Hans-Ulrich Kauczor
Mark Oliver Wielpütz   *Editors*

MRI of the Lung

Second Edition

Springer

Medical Radiology

Diagnostic Imaging

Series Editors

Hans-Ulrich Kauczor
Paul M. Parizel
Wilfred C. G. Peh

Hans-Ulrich Kauczor
Mark Oliver Wielpütz
Editors

MRI of the Lung

Second Edition

Springer

Editors
Hans-Ulrich Kauczor
Department of Diagnostic and
Interventional Radiology,
University Hospital Heidelberg,
Heidelberg
Germany

Mark Oliver Wielpütz
Department of Diagnostic and
Interventional Radiology,
University Hospital Heidelberg,
Heidelberg
Germany

Preface

For a long time the lung has been regarded as the black hole in MRI. In the 1980s courageous physicists and radiologists have tried to investigate different lung diseases using MRI, but they could neither produce convincing image quality within a reasonable examination time nor generate a substantial clinical impact. This has clearly changed in the last 15 years. Since then, however, the investigation of the potential application of MRI for the study of lung diseases is a challenging and exciting field of clinical research driven by the rapid development of new techniques and sequences for cardiac MRI as well as by the use of hyperpolarized noble gases as novel contrast agents.

The specific ability of MRI to visualize simultaneously morphological changes and modifications in perfusion, ventilation and gas exchange has opened up totally new perspectives to lung imaging and subsequently entered the clinical arena. Thus, the great success of the first edition of *MRI of the Lung* and the rapid development since then clearly encouraged us to prepare an updated second edition. This book again eminently illustrates the mutation of radiology from pure morphology to combined morphological–functional imaging. The original chapters were kept, updated and extended in order to cover the basics, such as

– the rationale and recommendation of a suggested standard protocol
– non-contrast and contrast-enhanced pulmonary MR angiography
– non-contrast and contrast-enhanced MR perfusion imaging
– ventilation imaging using hyperpolarized gases (^{3}He, ^{129}Xe) as alternative nuclei, or fluorinated gases as well as oxygen for dynamic proton MRI

Further, international world-renowned experts describe how MRI can be used in the clinical setting to diagnose, characterize and quantify different lung diseases such as pulmonary hypertension and thromboembolic disease, vascular anomalies and diseases, chronic obstructive airways disease (asthma, COPD, cystic fibrosis), lung cancer, mediastinal disease, pneumonia, diffuse parenchymal disease (fibrosis) and diseases of the pleura and the chest wall.

To further reflect the current developments in MRI of the lung, three new chapters were added to the second edition. They highlight the novel role of pulmonary MRI in animal models of respiratory diseases and in clinical trials as well as the specific challenges when using 3 T systems and the integration of lung imaging into whole body MRI protocols, such as staging in oncological disease.

We are very grateful to the contributing authors, all outstanding experts in their fields, for preparing this fine volume on a highly active topic for our series. The second edition again represents the leading handbook to provide a comprehensive overview of our current knowledge on the clinical role of MRI of the lung. In addition it outlines future perspectives for potential new applications of this imaging modality at the cutting edge of radiology.

This volume is highly recommended to certified radiologists, particularly those with a special interest in chest imaging and/or MRI, and to radiologists in training. However, pneumologists, cardiologists and chest surgeons will also find it a very useful source of information for better diagnostic and therapeutic management of their patients. We have no doubt that this volume will again meet the appropriate interest and well-deserved success with our readership.

Heidelberg, Germany   Hans-Ulrich Kauczor
Heidelberg, Germany   Mark O. Wielpütz

Contents

Contributors

Talissa A. Altes Department of Radiology, University of Missouri, Columbia, MO, USA

Grzegorz Bauman Division of Radiological Physics, Department of Radiology, University of Basel Hospital, Basel, Switzerland

Department of Biomedical Engineering, University of Basel, Basel, Switzerland

Nicolau Beckmann Department of Musculoskeletal Diseases, Novartis Institutes for BioMedical Research, Basel, Switzerland

Edwin J.R. van Beek Edinburgh Imaging, Queen's Medical Research Institute, University of Edinburgh, Edinburgh, UK

Donald Benson Department of Radiology, UW-Madison School of Medicine and Public Health, University of Wisconsin-Madison, Madison, WI, USA

Juergen Biederer Diagnostic and Interventional Radiology, University Hospital Heidelberg, Heidelberg, Germany

Radiologie Darmstadt, Gross-Gerau County Hospital, Gross-Gerau, Germany

German Center for Lung Research (DZL), Translational Lung Research Center Heidelberg (TLRC), Heidelberg, Germany

Dante P.I. Capaldi Robarts Research Institute and Department of Medical Biophysics, Western University, London, Canada

Ho-Fung Chan POLARIS, Unit of Academic Radiology, University of Sheffield, Sheffield, UK

Yannick Crémillieux Institut des Sciences Moléculaires, Université de Bordeaux, CNRS, Bordeaux, France

Olaf Dietrich Josef Lissner Laboratory for Biomedical Imaging, Institute for Clinical Radiology, Ludwig-Maximilians-University Hospital Munich, Munich, Germany

Julien Dinkel Institute for Clinical Radiology, Ludwig-Maximilians-University Hospital Munich, Munich, Germany

German Center for Lung Research (DZL), Comprehensive Pneumology Center (CPC), Munich, Germany

Department of Clinical Radiology, University of Munich Hospital (LMU), Munich, Germany

Rachel L. Eddy Robarts Research Institute and Department of Medical Biophysics, Western University, London, Canada

Roger Eibel Department of Radiology, Pediatric- and Neuroradiology, HELIOS Kliniken Schwerin, Teaching Hospital of the University of Rostock, Schwerin, Germany

Monika Eichinger Department of Diagnostic and Interventional Radiology, University Hospital Heidelberg, Heidelberg, Germany

German Center for Lung Research (DZL), Translational Lung Research Center Heidelberg (TLRC), Heidelberg, Germany

Department of Diagnostic and Interventional Radiology with Nuclear Medicine, Thoraxklinik at University Hospital Heidelberg, Heidelberg, Germany

Sean B. Fain Departments of Medical Physics, Radiology, and Biomedical Engineering, University of Wisconsin, Madison, WI, USA

2488 Wisconsin Institutes for Medical Research (WIMR), University of Wisconsin, Madison, WI, USA

Christopher J. Francois Department of Radiology, UW-Madison School of Medicine and Public Health, University of Wisconsin-Madison, Madison, WI, USA

Department of Medicine, UW-Madison School of Medicine and Public Health, University of Wisconsin-Madison, Madison, WI, USA

Marcel Gutberlet Hannover Medical School, Institute of Diagnostic and Interventional Radiology, Hannover, Germany

Biomedical Research in Endstage and Obstructive Lung Disease Hannover (BREATH), Hannover, Germany

Claus Peter Heussel Department of Interventional and Diagnostic Radiology with Nuclear Medicine, Clinic for Thoracic Diseases, University Heidelberg, Heidelberg, Germany

Department of Diagnostic and Interventional Radiology, University Hospital Heidelberg, Heidelberg, Germany

Translational Lung Research Center, Member of the German Center of Lung Research, University of Heidelberg, Heidelberg, Germany

Hans-Ulrich Kauczor Department of Diagnostic and Interventional Radiology, University Hospital Heidelberg, Heidelberg, Germany

Department of Interventional and Diagnostic Radiology with Nuclear Medicine, Clinic for Thoracic Diseases, University Heidelberg, Heidelberg, Germany

Translational Lung Research Center, Member of the German Center of Lung Research, University of Heidelberg, Heidelberg, Germany

Hisanobu Koyama Division of Radiology, Department of Radiology, Kobe University Graduate School of Medicine, Dallas, TX, USA

Department of Radiology, Kobe University Graduate School of Medicine, Kobe, Japan

Karl-Friedrich Kreitner Department Diagnostic and Interventional Radiology, Johannes Gutenberg-University Mainz, Mainz, Germany

Sebastian Ley Chirurgisches Klinikum München Süd, Diagnostic and Interventional Radiology, Munich, Germany

Institute of Clinical Radiology, Ludwig-Maximilians University Hospital Munich, Munich, Germany

Julia Ley-Zaporozhan Klinik und Poliklinik für Radiologie, Ludwig-Maximilians University Hospital Munich, Munich, Germany

Francesco Molinari Centre Hospitalier de Tourcoing, Lille, France

Jan Mueller Diagnostic and Interventional Radiology, University Hospital Heidelberg, Heidelberg, Germany

David G. Mummy Department of Biomedical Engineering, University of Wisconsin, Madison, WI, USA

Iga Muradyan Department of Radiology, Brigham and Women's Hospital, Harvard Medical School, Boston, MA, USA

Scott K. Nagle Department of Radiology, University of Wisconsin, Madison, WI, USA

K. Nakajima Department of Radiation Oncology, Asahikawa Medical College, Asahikawa, Japan

Yoshiharu Ohno Division of Functional and Diagnostic Imaging Research, Department of Radiology, Kobe University Graduate School of Medicine, Kobe, Japan

Advanced Biomedical Imaging Research Center, Kobe University Graduate School of Medicine, Kobe, Japan

Grace Parraga Robarts Research Institute and Department of Medical Biophysics, Western University, London, Canada

Samuel Patz Department of Radiology, Brigham and Women's Hospital, Harvard Medical School, Boston, MA, USA

Michael Puderbach Department of Radiology, Community Hospital Bad Langensalza, Bad Langensalza, Germany

Translational Lung Research Center Heidelberg (TLRC), German Center for Lung Research (DZL), Heidelberg, Germany

Department of Diagnostic and Interventional Radiology with Nuclear Medicine, Thoraxklinik at University Hospital Heidelberg, Heidelberg, Germany

Department of Diagnostic and Interventional Radiology, University Hospital Heidelberg, Heidelberg, Germany

Frank Risse Department of Translational Medicine and Clinical Pharmacology, Boehringer Ingelheim Pharma GmbH & Co KG, Biberach, Germany

T. Sasaki Department of Radiology, Asahikawa Medical College, Asahikawa, Japan

Mark L. Schiebler Department of Radiology, UW-Madison School of Medicine and Public Health, University of Wisconsin-Madison, Madison, WI, USA

Tilman Schubert Clinic of Radiology and Nuclear Medicine, University Hospital, Basel, Switzerland

Department of Radiology, UW-Madison School of Medicine and Public Health, University of Wisconsin-Madison, Madison, WI, USA

Ronald L. Sorkness School of Pharmacy and Morris Institute for Respiratory Research, University of Wisconsin, Madison, WI, USA

Neil J. Stewart POLARIS, Unit of Academic Radiology, University of Sheffield, Sheffield, UK

K. Takahashi Department of Radiology, Asahikawa Medical College, Asahikawa, Japan

Masaya Takahashi Advanced Imaging Research Center, Department of Radiology, University of Texas, Southwestern Medical Center at Dallas, Dallas, TX, USA

Jens Vogel-Claussen Hannover Medical School, Institute of Diagnostic and Interventional Radiology, Hannover, Germany

Biomedical Research in Endstage and Obstructive Lung Disease Hannover (BREATH), Hannover, Germany

Mark Oliver Wielpütz Department of Diagnostic and Interventional Radiology, University Hospital Heidelberg, Heidelberg, Germany

Department of Interventional and Diagnostic Radiology with Nuclear Medicine, Clinic for Thoracic Diseases, University Heidelberg, Heidelberg, Germany

Translational Lung Research Center, Member of the German Center of Lung Research, University of Heidelberg, Heidelberg, Germany

Jim M. Wild POLARIS, Unit of Academic Radiology, University of Sheffield, Sheffield, UK

Takeshi Yoshikawa Division of Functional and Diagnostic Imaging Research, Department of Radiology, Kobe University Graduate School of Medicine, Kobe, Japan

Advanced Biomedical Imaging Research Center, Kobe University Graduate School of Medicine, Kobe, Japan

Wei Zha Department of Medical Physics, University of Wisconsin, Madison, WI, USA

General Requirements of MRI of the Lung and Suggested Standard Protocol

Juergen Biederer

Contents

J. Biederer
Diagnostic and Interventional Radiology,
University Hospital Heidelberg,
Im Neuenheimer Feld 410,
D-69120 Heidelberg, Germany

Radiologie Darmstadt, Gross-Gerau County Hospital,
Wilhelm-Seipp-Str. 3, D-64521
Gross-Gerau, Germany

German Center for Lung Research (DZL),
Translational Lung Research Center Heidelberg
(TLRC), Heidelberg, Germany
e-mail: biederer@radiologie-darmstadt.de

Abstract

Among the modalities for lung imaging, proton magnetic resonance imaging (MRI) has been the latest to be introduced into clinical practice. MRI is taking its place as an alternative and supplementary, third method for the assessment of pulmonary diseases besides chest radiography (the most commonly employed first line test for chest disorders) and computed tomography (CT, so far the most comprehensive and detailed modality for cross-sectional and three-dimensional imaging of the lung). Once broadly available and sufficiently robust, it will likely become a modality of choice for cases in which exposure to ionizing radiation should be strictly avoided. Moreover, lung MRI offers particular advantages beyond the scope of CT such as dynamic studies of respiratory mechanics and first pass perfusion imaging. This chapter discusses the strategies to overcome major challenges for lung MRI such as motion artifacts and low signal. A set of protocols for different clinical applications to be used as a "starter kit" by any interested reader of this book will be suggested. This comprises a basic selection of non-contrast-enhanced sequences and can be extended by contrast-enhanced series: Breath-hold T1-weighted 3D gradient echo sequences (3D-GRE) are applied for the detection of solid lesions and airways. T2-weighted fast spin echo sequences (FSE) contribute to detection of

infiltrates and soft lesions, T2-weighted FSE with fat suppression or inversion recovery series visualize enlarged lymph nodes and skeletal lesions. Steady-state free precession sequences (SSFP) in free breathing contribute to the detection of pulmonary embolism, cardiac dysfunction, and impairment of respiratory mechanics. Tumors, suspicious pleural effusions, and inflammatory diseases warrant additional contrast-enhanced sequences. Fast gradient echo imaging with dynamic contrast enhancement (DCE) for the assessment of lung and tumor perfusion contributes to imaging of thromboembolic vascular and obstructive airway diseases and characterization of lung lesions. Additional diffusion weighted imaging (DWI) with fat signal suppression can be applied for the assessment of lymph nodes and lung lesion characterization.

1   Introduction

Evolving from a research tool, MRI of the lung is becoming increasingly important for specific clinical applications. The image quality has become reasonably robust and experience with multi-center, multi-vendor, and multi-platform implementation of MRI of the lung is increasing worldwide. The advantages over CT are not only limited to the lack of ionizing radiation, which is of particular interest for the assessment of lung disease in children (e.g., pneumonia, cystic fibrosis), pregnant patients, or in patients who require frequent follow-up examinations (e.g., immunocompromised patients with fever of unknown origin). Chest wall invasion by a tumor and mediastinal masses are traditional indications benefiting from the superior soft tissue contrast of MRI. Dynamic examinations to study respiratory mechanics and contrast-enhanced first pass perfusion imaging reach far beyond the scope of CT. High quality lung MRI can contribute significantly to clinical decision-making in numerous pulmonary diseases from lung cancer over malignant pleural mesothelioma, acute pulmonary embolism, pulmonary arterial hypertension, airways disease such as cystic fibrosis to interstitial

lung disease and pneumonia. In order to plan surgery or radiotherapy, lung MRI may serve as "the ace up the sleeve," e.g., for assessment of unclear pulmonary masses, for exclusion or confirmation of malignancy, or for separation of lung tumor and atelectasis. In whole body MRI for screening and staging thoracic MRI completes the study with full coverage of the lungs.

Given all potential benefits, MRI is still an under-utilized imaging modality for evaluating thoracic disorders—mainly because it is considered more complex than other modalities (Boiselle et al. 2013). Furthermore, professionals who are used to work with chest X-ray and CT may feel uncomfortable with the different image appearance and lower spatial resolution of lung MRI. It is therefore the major purpose of this book to familiarize the interested reader with the diagnostic scope of lung MRI and its potential benefits. In respect for the technology, the following chapter outlines the strategies to overcome the challenges for lung MRI such as motion artifacts and low signal. It introduces a standardized protocol concept which may be used as a "starter kit" by any interested reader of this book based on already available or easy to implement sequences packages (Biederer et al. 2012). Further strategies beyond this basic concept are introduced throughout the dedicated chapters of this book and can be added to this protocol tree according to the advanced users growing experience and expertise in the field.

2   Proton-MRI of the Lung: The Challenge

One major problem in imaging thoracic organs is the continuous motion of all components induced by heart pulsation and respiratory motion. Both are most prominent in the lower and anterior sections of the chest where classical T1- and T2-weighted spin-echo and fast spin-echo techniques therefore yield poor image quality. More specific problems are encountered, if MRI is applied to imaging of the lung parenchyma. MRI uses the subtle resonant signal that can be obtained from hydrogen nuclei (protons) of water

or organic substances when they are brought into a strong magnet and excited by precise radio frequency pulses. Since the lungs have an a priori low proton density with about 800 g of tissue and blood distributed over a volume of 4–6 L, signal intensity is extremely low compared to other parts of the body (Albertin 1996; Wild et al. 2012). Further, local field inhomogeneities due to susceptibility artifacts at tissue-air or liquid-air interfaces of the alveoli result in rapid dephasing of the low signal with extremely short T2* (Su et al. 1995). Therefore, the lungs usually appear without any visible signal on most clinical MR images. For diagnostic use, this is not necessarily a problem, since all pathologies with higher proton density and therefore higher signal appear with a strong inherent contrast against the black background of aerated lung tissue. With recent improvements in image quality, only very small lesions or fine reticulations of lung tissue might be missed, in particular if motion artifacts are not sufficiently suppressed (Wild et al. 2012).

3 Strategies for Motion Compensation

For most protocols with reasonably high spatial resolution, image acquisition times of MRI are still too long to cover the lungs and heart in free breathing without motion artifacts. Therefore, technical solutions for gating have a long tradition in chest imaging. Principally, the problems encountered in motion compensation for lung imaging are well known from MRI of the heart. By "gating," image data are split into multiple short sections that fit into a predefined phase of the respiratory or cardiac cycle. Retrospective gating uses continuously sampled image data that are correlated, grouped, or reordered by means of a simultaneously acquired respiratory or cardiac signal. Motion corrected images result from using only a part of heavily oversampled data that were acquired within a desired phase of the respiratory curve (Remmert et al. 2007). "Triggering" as a sub-entity of prospective gating describes the active start of MR data acquisition after detection of a physiologic event (an R-wave or signal from a respiratory monitoring device) (Lutterbey et al. 2005). However, independent of the method of physiologic signal acquisition, any triggering or gating multiplies acquisition times while the compensation of motion artifacts usually remains incomplete (Biederer et al. 2010). In general, higher respiration frequencies are appreciated to reduce the prolongation of examination times. This facilitates respiration-triggered imaging in pediatric patients, in particular in very small children, who are too young to comply with respiration commands or even have to be examined in sedation (Biederer et al. 2012; Wielpütz et al. 2013).

An appropriate respiratory signal can be obtained with a simple pneumatic belt or a compressible cushion placed at the upper abdomen or the chest of the patient. The pressure changes due to compression and decompression of the device are directly registered by the MR scanner. The ideal position of such a device depends on the individual respiratory pattern of the patient at rest. The trigger signal is usually set to expiration, usually the longest and most reproducible phase of the respiratory cycle (Biederer et al. 2002a; Both et al. 2005). End-expiration is principally most favorable for imaging lung parenchyma, since proton density and lung signal intensity increase with deflation. However, appropriate instructions of the patient how to comply with gating are still the key to high image quality without respiratory motion artifacts.

Navigator sequences replace the respiration belt by continuous real-time image acquisition from a small volume at the top of the diaphragm. The images are evaluated electronically for movements of the diaphragm and trigger settings can be applied interactively by the operator. As a disadvantage, respiratory motion is not tracked during the acquisition of the diagnostic images when the navigator has to be suppressed. For uninterrupted control of the breathing maneuvers, a respiratory belt or similar mechanic devices can be used on addition, if needed. The same navigator-technique can be used to adjust several slice blocks of a multi-breath-hold acquisition in case of variable respiratory levels.

As the straightforward further development of navigator triggering, advanced approaches use

the inherent periodic changes of the not spatially encoded k-space center (DC) signal of the MR image data themselves. This signal correlates to the respiratory cycle during continuous image acquisition. Just like an external signal, this "intrinsic" signal can be used for retrospective gating of continuously acquired image data. Based on this approach, Weick et al. suggested a motion-compensated 3D gradient echo sequence with intrinsic gating (Weick et al. 2013). The combination of intrinsic triggering with a radial acquisition scheme further increases robustness to motion artifacts. This approach was suggested for perfusion imaging of solid lung lesions and motion compensated MRI in integrated MRI-PET hybrid systems (Lin et al. 2008; Bauman and Bieri 2016; Rank et al. 2016).

Principally, additional control for cardiac pulsation artifacts can be achieved with either ECG monitoring or peripheral pulse oximetry—but only at the expense of even longer examination times. Therefore, simultaneous double-triggering or gating for respiration and cardiac pulsation is usually not favorable and not generally recommended (Leutner and Schild 2001). In conclusion, simply scaling up the sequence packages from cardiac MRI does not lead to a lean protocol for lung imaging (Wild et al. 2012).

For practical use, the easiest and fastest way to overcome respiratory motion is therefore to use breath-hold techniques with full anatomic coverage (ideally the whole thorax) within a single 20 s breath-hold—and to ignore cardiac action. This is facilitated by the broad introduction of parallel imaging techniques, which has significantly reduced examination times and facilitates full volume coverage of the chest (Heidemann et al. 2003). Parallel imaging uses arrangements of multiple coils to acquire additional information along the phase encoding direction. K-space data are partially reconstructed from spatial information, which originates from differences in the signal intensities depending on the distance of a location to the individual coils. The result is a substantial improvement in image acquisition speed, usually two- or threefold. Current 1.5 T or 3 T scanners with parallel imaging capabilities allow for the acquisition of a 3D-data sets of the whole chest with voxel sizes down to $1.6 \times 1.6 \times 4$ mm or isotropic voxels of $2 \times 2 \times 2$ mm within one breath-hold. For the lung, acceleration factors of 2–3 are reasonable, more than 3 can so far not be recommended.

If acquisition time still exceeds this limit or if a patient cannot hold his breath for 20 s, the examination can be split into blocks that are acquired within several breath-holds. However, splitting the acquisition introduces additional artifacts if the level of the breath-holds is not reproducible (Biederer et al. 2001). Furthermore, either rotating sets of phase encoding bars (PROPELLER or BLADE (Pipe 1999; Deng et al. 2006)) or radial K-space acquisition (Bauman and Bieri 2016) provides inherent motion compensation of images and contribute to the robustness of lung MRI image quality. Rotating phase encoding has already become broadly available while radial acquisition sequences and self-navigating approaches are currently being implemented for routine use. Therefore, respiratory motion artifacts are no more an issue in most patients and further improvement is expected.

Fast image acquisition schemes also contribute to the compensation of cardiac pulsation, i.e., very fast single shot techniques such as fast spin-echo imaging using partial Fourier acquisition (e.g., T2-HASTE), fast steady-state gradient echo imaging (SS-GRE, TrueFISP), or very short echo times (e.g., ultrafast turbo-spin-echo UTSE) (Leutner et al. 1999). This type of sequences can also be used to acquire sets of single shot images without any instructions to the patient—a helpful approach in noncompliant individuals. Fast spin-echo imaging using partial Fourier acquisition techniques (e.g., T2-HASTE) or axial steady-state gradient echo imaging (SS-GRE, TrueFISP) can be acquired with a slice overlap of, e.g., 50% during free breathing for pseudo-cine visualization of respiratory motion and cardiac action. The SS-GRE series is particularly attractive for this purpose, since its T1/T2-weighted contrast displays blood bright with good contrast against thrombotic material. It yields basic information on pulmonary motion during the respiratory cycle as well as on size, shape, and patency of the

central pulmonary vessels. Thus, it can be used as a fast technique to exclude massive acute pulmonary embolism even in noncompliant patients during free breathing (Kluge et al. 2005).

Fast low angle shot gradient echo and T1-weighted 3D gradient echo (e.g., Volume Interpolated Breath-hold Examination (VIBE)) also tend to be quite robust to cardiac motion, even without cardiac triggering or gating. Their image quality largely depends on the breath-hold capability and compliance of the patient more than the compensation for cardiac motion. Sometimes, readout-frequencies or their multiples appear to synchronize with heart action so that a "pseudo-gating" results in very sharp delineation of the heart. To our knowledge, this has not been further investigated so far, but it might be a useful approach to achieve more robustness of the gradient echo sequences against cardiac pulsation. The suggestions for a standard protocol in this chapter appreciate these benefits and use breath-hold sequences with acceptable robustness against cardiac pulsation but without cardiac triggering to keep within an acceptable time frame for clinical routine. To be compatible with state-of-the-art clinical scanners, all protocols are based on broadly available technology. Upcoming improvements such as radial acquisition schemes or intrinsic gating can be easily implemented by adding or replacing protocol components, once available.

4 Strategies for Imaging Lung Parenchyma Disease

In respect to MR imaging, diseases of the lung can be divided into two groups: diseases which increase proton density ("plus pathology") and diseases which reduce proton density of the lung ("minus pathology"). Any increase in lung proton density due to solid lesions or infiltration with liquids—fortunately the vast majority of cases—is easy to detect with MRI, in particular against the dark background of the healthy aerated lung parenchyma. This implies that the visualization of the lung parenchyma itself is clinically not too important for morphologic imaging of lung dis-

ease—except for the few entities which produce "minus pathology." These are mainly overinflation due to air trapping, emphysema, or pneumothorax. These conditions can be only visualized, if intact lung structure and pathologic lesions have a different signal. This can be achieved with contrast-enhanced perfusion imaging or ventilation studies with hyperpolarized gases—while the first can be addressed within a standard protocol suggestion, the latter remains to be reserved for specialized centers.

The key plus-pathologies in clinical lung imaging are solid lesions inside the lung (nodules or masses as found in metastatic lung disease or primary lung cancer) or increased density of the lung parenchyma itself (i.e., intra-alveolar or interstitial fluid accumulation as found in pneumonia). For any new imaging method it has to be proven that these situations are diagnosed correctly with reasonable sensitivity and specificity.

For lung nodules, MRI has been proven to yield a higher sensitivity than plain chest X-rays, but it does not yet match CT. Depending on the water content, nodules can be detected either on fast T1-weighted 3D-gradient echo images (VIBE), T2-weighted single shot partial Fourier acquisition spin echo images (HASTE) or inversion recovery series (TIRM). Schäfer et al. have shown a similar detection rate of small pulmonary nodule of T1- and T2-weighted sequences, but the number of false positives was lower with fast T1-weighted gradient echo sequences (Schäfer et al. 2005). The sensitivity for lung nodules larger than 4 mm ranges between 80 and 90% and reaches 100% for lesions larger than 8 mm. Overall, it appears realistic to assume a threshold size of 3–4 mm for lung nodule detection with MRI, given that conditions are optimal (i.e., patient can keep a breath-hold for 20 s or perfect gating/triggering) (Biederer et al. 2003; Both et al. 2005; Schroeder et al. 2005; Bruegel et al. 2007; Fink et al. 2007). Exceptions are calcified nodules which appear black. Thus, lung MRI cannot be recommended for staging chondrosarcoma or other entities with calcified metastases. Tools for lung nodule detection and computer-aided lung nodule volumetry for MRI are under investigation, but so far not commercially available.

Unfortunately, accumulation of fluid inside the lung such as in pneumonia appears with only low signal on T1-GRE images. Experimental results show that the signal intensity of fluid inside lung tissue on T1-GRE is much too low to be of diagnostic use (Biederer et al. 2002b). Lung infiltration, e.g., due to pneumonia, can instead be readily detected on T2-weighted images as well as on TrueFISP and T2-TIRM (Fink et al. 2007). It is therefore commonly accepted to add T2-weighted sequences for the evaluation of pulmonary infiltrates. Fast T2-weighted single shot imaging techniques can be performed with partial Fourier acquisition (e.g., HASTE) or ultra-short TE (UTSE). A dark blood preparation pulse may be favorable for particular purposes such as imaging of the mediastinum. As an alternative to breath-hold imaging, fast T2-weighted spin-echo sequences with respiratory triggering have produced reasonable results (Leutner and Schild 2001; Biederer et al. 2002a).

5 Suggestions for a Lean Standard Protocol

The following suggestions for a lung imaging protocol are derived from MR sequence components of current standard installations and based on parallel acquisition techniques as they are nowadays available at most sites. This facilitates to achieve full anatomic coverage of the chest within one breath-hold for most parts of the protocol and reduces respiratory motion artifacts. Some parts of the protocol are still acquired with multiple breath-hold acquisitions and if parallel imaging techniques are not available, the full protocol can be readily changed to multi-breath-hold acquisitions. In this case some overlap is recommended to avoid loss of information between different breath-holds and slice blocks. In practice, it has been shown to be helpful to use a common basic protocol trunk for the majority of expected clinical scenarios and to extend this for specific questions such as

the staging of malignancy, evaluation of pulmonary vessels and perfusion, etc. (Biederer et al. 2012). Besides this, short dedicated programs for emergency conditions, such as acute pulmonary embolism, are warranted. Examination time for the standard procedure should not exceed 15 min plus 5–10 min for protocol extensions. Solutions for typical scenarios such as patients not being able to hold their breath or young children should be available (fast real-time imaging, triggered sequences). Table 1 outlines the general protocol concepts for different groups of clinical indications (Biederer et al. 2012). Table 2 gives an overview over the available sequences and imaging parameters including the acronyms of compatible sequences from different vendors (Biederer et al. 2012).

Generally, the fields of view (FOVs) would be adjusted to the size of the patient (e.g., 450–500 mm in coronal and approximately 400 mm in transverse acquisitions) with matrices of 256–384 pixels (for triggered fast spin echo series up to 512) resulting in pixel sizes smaller than 1.8×1.8 mm. Slice thicknesses for the 2D acquisitions would range from 4 to 6 mm (Biederer et al. 2012). 3D GRE for lung morphology in transverse and coronal orientation would use slice thicknesses of 4 mm or less, pulmonary angiography in coronal orientation 2 mm or less (Biederer et al. 2004).

The preparation for the examination includes instruction of the patient for the breathing maneuvers and selection of a phased array body coil for thoracic imaging. The application of a respiratory belt is optional and ECG is not required on a routine basis unless cardiac imaging sequences are planned, e.g., in case of tumor infiltration into the pericardium or large vessels of the mediastinum.

The basic imaging protocol starts with a gradient echo localizer in inspiration to plan the study. The first sequences are acquired in breath-hold, usually starting with the coronal T2-HASTE (Fig. 1) followed by the transverse T1-3D-GRE (VIBE) (Fig. 2, Table 1). As defined above, these

Table 1 Protocol suggestion for lung MRI (adapted from Biederer et al. 2012)

Sequence	Sequence combinations dedicated to clinical problems				Patients compliant, able to hold breath for 20 s			i.v. contrast	Alternative approach if unable to hold breath for 20 s, e.g., children
	General questions (15')	Thoracic mass (20')	Pulmonary embolism, AVM (15')	Mass/vessel invasion (25')	Slice orientation	Slice thickness	Respiration maneuver		
3D gradient echo T1-w.	X	X		X	Transverse	4 mm (interpolated)	Breath-hold	No	Radial 3D GRE with intrinsic gating
Fast spin echo T2-w. half Fourier	X	X		X	Coronal	6–8 mm	Breath-hold	No	Triggered or non-triggered acquisition in free breathing (0–5 min acquisition time)
Steady-state GRE	X	X	X	X	Coronal	4–6 mm	Free breathing	No	Not needed
Fast spin echo T2-w., rotating phase encoding	X	X		X	Coronal (non-fat sat.)	4–6 mm	Breath-hold	No	Triggered acquisition in free breathing (5 min increase in acquisition time)
Fast spin echo T2-w. rotating phase encoding	X	(X)		(X)	Transverse (fat sat. or IR)	4–6 mm	Breath-hold	No	Triggered acquisition in free breathing (5 min increase in acquisition time)
Diffusion weighted imaging		X		(X)			Multi-breath-hold	No	Triggered acquisition in free breathing (5 min increase in acquisition time)
3D gradient echo T1-w. dynamic angio			X	X	Coronal	5 mm	Breath-hold	Yes	Acquisition in shallow free breathing possible (no increase in acquisition time)
3D gradient echo T1-w. max. spatial res. angio			X	X	Coronal	1.5–3 mm	Breath-hold	Yes	Not available/to be developed
3D gradient echo T1-w. fat saturated	X	X	X	X	Transverse	4 mm (interpolated)	Breath-hold	Yes	Radial 3D GRE with intrinsic gating
3D gradient echo T1-w. fat saturated	X	X			Coronal	4 mm (interpolated)	Breath-hold	Yes	Radial 3D GRE with intrinsic gating

Table 2 Sequences for lung MRI (adapted from Biederer et al. 2012)

Sequence type	Features or variations	Vendor specific acronyms					Respiration maneuver (Typical acquisition time)	Spatial resolution (Typical pixel size)	Temporal resolution (S per slice or volume)	Particular use for lung MRI (pathology)	Protocol suggestion B—basic T—tumor V—vessel
		Siemens	Philips	GE	Hitachi	Toshiba					
3D gradient echo T1-weighted	Volume interpolation (ce with fat saturation, Figs. 2 and 8)	VIBE	THRIVE	LAVA	TIGRE	Quick3D	Breath-hold (21 s)	High (1.5 × 1.5 mm)	Low	Pulmonary nodules, masses, airways	B, T, V
	Max. spatial resolution for angiography (Figs. 7 and 9)	Flash 3D	FFE	SPGR	RF spoiled SARGE	FE, FFE	Breath-hold (21 s)	High (1.2 × 1 mm)	Low	High resolution angiogram (embolism AVM)	V
	Echo sharing (Fig. 6)	TWIST	TRAK	TRICKS	TRAQ	DRKS	Breath-hold or shallow breathing	Low (3.5 × 2 mm)	High (<1.5 s/ vol)	First pass lung perfusion (embolism, hypoxic vasoconstriction)	V (T)
Fast spin echo T2-weighted	Half Fourier acquisition (Figs. 1 and 8)	HASTE	Halfscan FSE	½ NEX FSE	Half scan single shot FSE	AFI RO	Multiple breath-hold (2 × 20 s)	Low (1.8 × 1.8 mm)	High	Infiltrates	B, T
	Rotating phase encoding (Fig. 8)	BLADE	MultiVane	PROPELLER	RADAR	JET	Multiple breath-hold (4–5 × 20 s)	Moderate (1.8 × 1.5 mm)	Moderate	Nodules and masses	B, T
	Respir. triggered, high res. (Fig. 5)	TSE-rt	TSE	FSE	FSE	FSE	Respiration triggered (5–10 min)	Moderate-high (1.3 × 1 mm)	Low	Masses	(B), (T)
	Fat saturated	TSE fs BLADE fs	TSE fs or MultiVane	FSE fs or PROPELLER	FSE fs or RADAR	FSE fs or JET fs	Multiple breath-hold (4–5 × 20 s) or respiration triggered (4–8 min)	Moderate (1.8 × 1.5 mm)	Moderate	Lymph nodes Bone metastases	B, T
Short tau inversion recovery	Fast spin echo (Fig. 4)	STIR	STIR	STIR	STIR	STIR					

Diffusion weighted imaging (DWI)	Echo planar imaging or other fast technique	REVEAL (DWI)	DWIBS (DWI)	Whole body diffusion (DWI)	DWI	Body vision (DWI)	Multiple breath-hold (3–4 × 20 s) or respiration triggered (4–5 min)	Low (3 × 2 mm)	Low	Nodules and masses	T
Steady-state GRE	T1/T2 contrast (Fig. 3a, b)	TrueFISP	bFFE	FIESTA	BASG	TrueSSFP	Free breathing (60 s) or instructed br. maneuvers	Moderate (2.4 × 1.6 mm)	High (<0.5 s/sl.)	Pulmonary embolism	B, T, V
										Respiration mechanics	T

Fig. 1 T2-weighted single shot partial Fourier (T2 HASTE, coronal acquisition in breath-hold, healthy, 30-year-old male subject)

Fig. 2 T1-weighted volumetric interpolated 3D gradient echo sequence (VIBE, transverse acquisition in breath-hold, healthy, 30-year-old male subject)

sequences cover infiltrative disease and solid lung pathology, respectively. The fast T2-weighted single shot images provide high signal and good lesion-to-background contrast but due to partial Fourier acquisition and long echo trains the delineation of structures is slightly blurred. The overall signal of the T1-weighted 3D-GRE images is lower, but sharpness is improved due to a higher spatial resolution. If needed, the signal of the lung parenchyma with this type of sequence can be enhanced with i.v. application of Gd-based contrast material (see below for protocol variations). Both sequences usually do not show a visible signal of healthy lung tissue, unless infiltrates, atelectasis, or solid lesions are present.

A coronal T1/T2-weighted, free breathing SS-GRE sequence (TrueFISP) is acquired next (Fig. 3a). This allows the patient to recover from the first set of breath-hold maneuvers. Signal intensity of the SS-GRE images is intermediate, but basic information on pulmonary motion during the respiratory cycle and on cardiac action are generated within a very short time. This part of
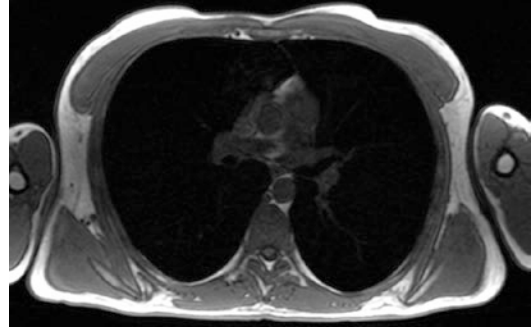
the protocol also allows for an exclusion of relevant pulmonary embolism due to a bright signal of the lung vessels with a good contrast against hypointense thrombotic material. The signal of healthy lung parenchyma on SS-GRE images is low, but still significantly higher than on the first sequences of the protocol.

Finally, two sets of multi-breath-hold images are acquired. First, a motion-compensated inversion recovery (IR) or fat signal suppressed T2-weighted image series in transverse orientation (Fig. 4). These images contribute significantly to the detection of mediastinal lymph nodes and edematous bone lesions while healthy lung parenchyma signal appears completely black. Then, the same type of sequence but without fat signal suppression is used for a coronal, multi-breath-hold acquisition. This T2-weighted fast spin echo series in high spatial resolution improves the depiction of masses with chest-wall invasion and mediastinal lesions. In case of pulmonary masses the higher spatial resolution and improved soft tissue contrast compared to the initial T2-weighted images contribute to lesion characterization.

This basic protocol can be concluded after a total room time of approximately 15 min. Specific variations of the protocol and additional series as extensions to this protocol are added depending on the indication, i.e., post i.v. contrast scans.
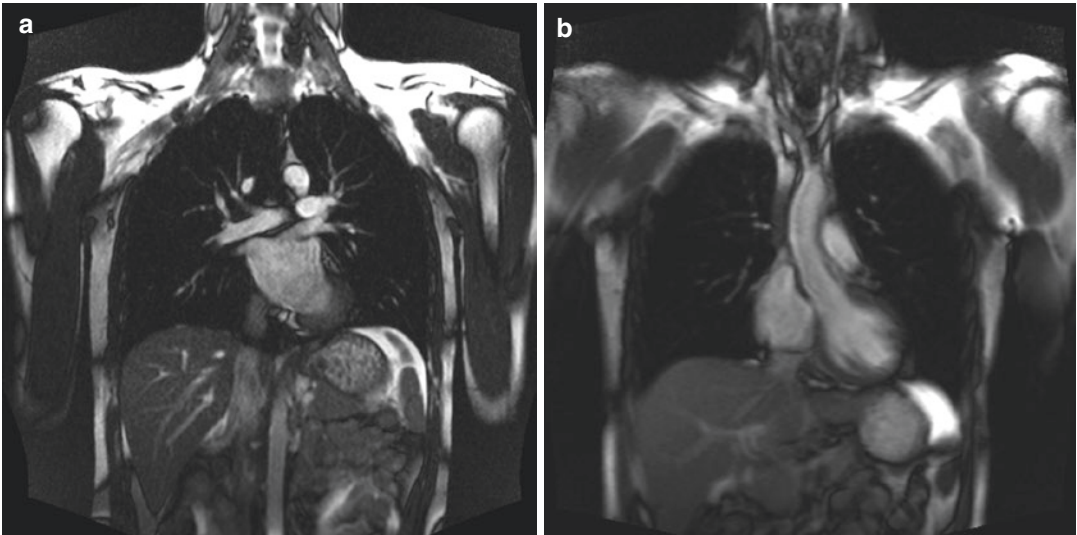
Fig. 3 T1/T2-weighted steady-state gradient echo sequence (TrueFISP), (**a**) coronal acquisition in free breathing to cover the whole chest in a semi-dynamic acquisition, (**b**) coronal acquisition in forced respiratory maneuver to study respiratory mechanics. The FEV1-maneuver includes maximum ins- and expiration and requires good interaction with the operator (healthy, 30-year-old male subject)
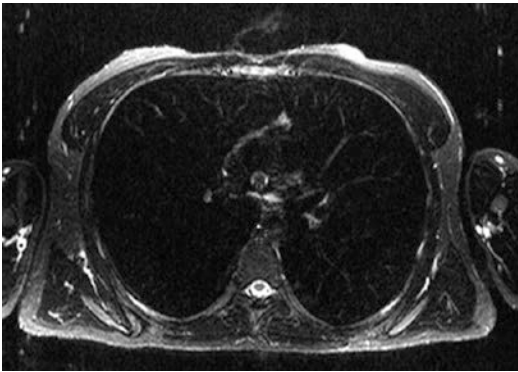

Fig. 4 Inversion recovery fast spin echo sequence (TIRM, STIR, transverse acquisition in breath-hold, healthy, 30-year-old male subject)

mode (Fig. 3b). The series is focused on the structure of interest, e.g., the highest elevation of the diaphragmatic dome or an intrapulmonary lesion to be acquired with a temporal resolution of three to ten images per second, depending on the performance of the MR scanner (Plathow et al. 2006). Otherwise the parameters are identical to the third acquisition. The patient is instructed to breathe deeply in and out just like during a lung function test, so-called forced expiratory volume in 1 s (FEV1)-maneuver. This short part of the protocol appreciates the potential of time-resolved MR image series to visualize functional aspects, i.e., on diaphragmatic function, as a significant advantage compared to CT.

6 Specific Variations of the Protocol

6.1 Respiratory Mechanics

For the further evaluation of respiratory mechanics and diaphragmatic motion, the dynamic SS-GRE series can be acquired in a single slice

6.2 Lung Tumors/Thoracic Masses

For the assessment of lung malignancy or other thoracic masses, the protocol should be extended by transverse and coronal T1-weighted 3D GRE acquisitions, each acquired in a single breath-hold. These post-contrast scans improve the

diagnostic yield of the study by clearer depiction of vessels, hilar structures, and pleural enhancement. Parenchymal disease and solid pathologies are also enhanced. Thus, a study to exclude pulmonary malignancies, e.g., for staging purposes, should usually comprise contrast-enhanced series, preferably with a fat-saturated 3D-GRE sequence. Contrast enhancement is also recommended in case of pleural processes (empyema, abscess, metastatic spread of carcinoma, mesothelioma) for the further evaluation of solid masses as well as functional imaging or angiography (Biederer et al. 2004). Since the so far listed sequences only include a 3D-GRE sequence without fat saturation, it might be favorable to acquire an additional fat-saturated scan before i.v. contrast administration to allow for a direct comparison of contrast uptake. The other sequence parameters are identical with the initial non-contrast-enhanced acquisition.

Significant differences of the available paramagnetic contrast agents in respect to image quality have not been shown so far. For simple post-contrast imaging, reasonable results are achieved with a manual i.v.-injection of a contrast agent containing 0.1–0.2 mmol Gadolinium per kg body weight. Lung perfusion imaging with time resolved contrast-enhanced magnetic resonance angiography is preferably done with a power injector.

Further options to extend the standard protocol are T1- and T2-weighted SE or FSE sequences with respiratory triggering (or gating; Fig. 5). Traditionally, T1-weighted images are recommended for the detection of lymph nodes and tumor infiltration into the chest wall, but since T2-weighted sequences additionally contribute to the evaluation of lung parenchyma pathology and provide equal information about the chest wall and mediastinum, they are the method of choice to conclude the study, if desired.

At the current state of development, we would not yet suggest diffusion-weighted imaging (DWI) as a mandatory component of a general protocol. Basically, DWI serves for whole-body staging of lung cancer, including mediastinal metastases (Kim et al. 2015). DWI's contribution to lung nodule detection is limited due to low spatial resolution. Regier et al. found a sensitivity

Fig. 5 Respiration-triggered T2-weighted fast spin echo sequence (T2-TSE, coronal acquisition in free breathing, healthy, 30-year-old male subject)

of 44% for lung nodules of 5 mm, which increased to 97% at 10 mm (threshold size around 6 mm) (Regier et al. 2011). Koyama et al. demonstrated a lower nodule detection rate with DWI compared to IR-T2-weighted images (Koyama et al. 2010). For the assessment of pulmonary malignancy with DWI, a meta-analysis of 10 studies including 545 patients revealed a pooled sensitivity of 84% and a pooled specificity of 84%. In patients with high pretest probabilities, DWI enabled the confirmation of malignant pulmonary lesions. In patients with low pretest probabilities, DWI enabled the exclusion of malignant pulmonary lesions (Wu et al. 2013). However, the applied protocols vary widely and DWI cannot yet be considered as robust, highly standardized, and simple technique for clinical use (Kim et al. 2015). In the author's own experience, DWI helps to delineate lesions adjacent to the pleura, assess mediastinal extension, and may serve as a "second reader" for detection of small nodules (Biederer et al. 2012). We therefore suggest including DWI as an optional sequence of the lung tumor protocol.

6.3 Lung Vessel Disorders

Irregularities of pulmonary perfusion and diseases of the lung vessels are among the most common clinical scenarios to be addressed with MRI. Our suggestion for MRI of lung vessel disease therefore comprises two variations of T1-weighted ultra-short TR and TE contrast-enhanced three-dimensional gradient echo sequences for breath-hold magnetic resonance angiography (MRA): a dynamic series with high temporal resolution for first pass perfusion studies of the lung parenchyma (this can be only achieved on the cost of a lower spatial resolution) and an angiogram with high spatial resolution (resulting in lower temporal resolution). Further technical aspects and recommendations for image post-processing of first pass contrast-enhanced lung parenchyma perfusion imaging and pulmonary MR angiography are addressed in the dedicated chapters in this book.

6.3.1 Temporally Resolved Perfusion Imaging

For multiphasic lung perfusion imaging, the scan time for each 3D data set should be reduced to less than 5 s (Fink et al. 2004). This can be achieved by most clinical MR scanners with parallel imaging capability. For lower performance systems, 2D perfusion MRI may still be favorable to provide optimum temporal resolution (Levin et al. 2001), but anatomic coverage and spatial resolution in the *z*-axis are usually not acceptable for clinical applications. The easiest approach to perfusion studies is to start contrast injection and the MR sequence simultaneously without bolus timing. Arterial-venous discrimination is improved by high temporal resolution and the study is robust to motion artifacts even in patients with severe respiratory disease and limited breath-hold capability. For documentation and viewing, contrast-enhanced 3D perfusion MRI is usually processed by subtraction of mask image data acquired before contrast bolus arrival (Fig. 6). Since the acquisition time and diagnostic yield completely cover the information provided by a test bolus, the dynamic perfusion series may be used to calculate bolus timing for
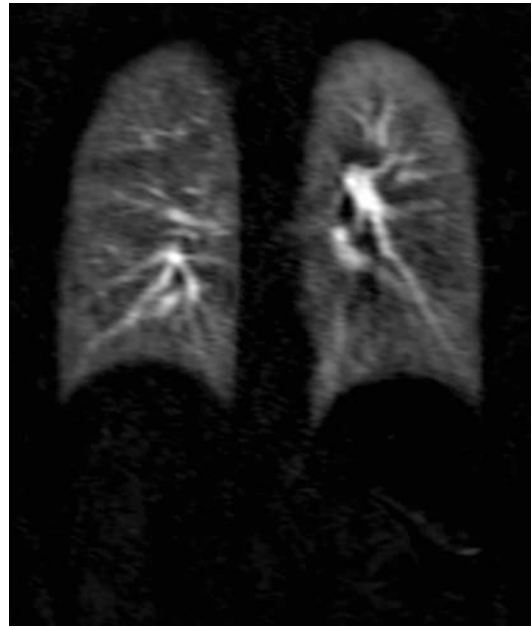

Fig. 6 T1-weighted 4D contrast-enhanced first pass perfusion study (T1-weighted 3D-GRE with echo sharing, TWIST, subtracted image, coronal acquisition in breath-hold, healthy, 30-year-old male subject)

the following high spatial resolution angiogram (Biederer et al. 2012). Disadvantages compared to the test bolus method are the additional time needed for image post-processing and the slightly higher amount of contrast medium. To synchronize bolus profiles with the angiogram, injection speed and the volume of the bolus plus sodium chloride chaser (at least 20 mL sodium chloride) should be equal. A highly performant image reconstruction system and a power injector are prerequisites for this approach.

6.3.2 High Resolution Pulmonary Angiography

The pulmonary arteriogram is acquired with a minimum relaxation time (TR) of less than 5 ms and an echo time (TE) of less than 2 ms and with a high spatial resolution (typically a voxel size of $1.2 \times 1.0 \times 1.6$ mm requiring a breath-hold of 20–30 s). The short TR allows for short breath-hold acquisitions and the short TE minimizes background signal and susceptibility artifacts. The ability of the patient to hold the breath is crucial for image quality. Full anatomic coverage is

achieved with image acquisition in coronal orientation and a single injection of contrast (0.1–0.2 mmol/kg flow rates between 2 and 5 mL/s, minimum 20 mL saline flush administered by an automatic power injector) is sufficient. Vascular signal intensity is determined by the gadolinium concentration at the time of central k-space acquisition; thus the scan delay should be individually adjusted using a care bolus procedure or a test bolus examination. Ideally this is achieved with a first pass perfusion study as described above. One of the most frequent clinical problems to be addressed with MRA and perfusion imaging is the exclusion of pulmonary embolism in young women with or without potential pregnancy. For this particular purpose, it appears favorable to adjust the center of the k-space to maximum parenchymal perfusion (approx. 2 s later than central pulmonary artery peak contrast). The reconstructed MIP provides a very illustrative image of the lung parenchyma (see the example in Fig. 7). Image subtractions, multiplanar reformations (MPR), and maximum intensity projections (MIP) are the standard tools for viewing and documentation of the results.

Fig. 7 T1-weighted 3D contrast-enhanced MRA (MIP reconstruction, healthy 24-year-old female subject, clinical study to exclude pulmonary embolism)

6.4 Mediastinum

The mediastinum contains the heart and the large vessels, the trachea, the esophagus, neural structures as well as lymphatic tissues and the thoracic duct. Anatomically the mediastinum is traditionally divided into three compartments even though there is no physical barrier between them. These are the anterior, middle, and posterior mediastinum, mainly defined by the organs of the middle part like the heart and large vessels (Strollo et al. 1997a, b). The typical indications for cross-sectional imaging of the mediastinum are masses originating from the present structures. While size and position of a tumor can be assessed with MRI as well as with CT, both modalities contribute to the characterization of tumors, e.g., with the detection of fat or calcifications inside a teratoma. For this purpose, it can be recommended to use a Dixon technique for fat saturation of 3D GRE to produce in phase- and out of phase-images (chemical shift imaging), just as it is applied to assess the fat content of lung lesions (hamartoma) (Hochhegger et al. 2012). In this case, CT has a higher sensitivity for small calcifications. Usually, CT is acquired with the administration of contrast media to obtain a sufficient contrast between vessels and soft tissues while most mediastinal masses can be readily identified on non-enhanced MRI due to its inherent and excellent soft tissue contrast (Landwehr et al. 1999). Observations on MRI such as a central hypointensity in enlarged mediastinal lymph nodes in sarcoidosis (dark lymph node sign) can be of specific clinical value (Chung et al. 2013). However, for the assessment of unclear masses, the administration of a paramagnetic contrast agent provides more insights into tumor composition and differentiation.

Basically, the mediastinum is fully covered with the above made suggestions for lung imaging within this chapter. Identification and classification of mediastinal processes is possible by using unsaturated and fat-saturated non-enhanced 3D gradient echo sequences and repeating the latter after contrast administration. With an in-plane resolution of 1.6 mm even very small lymph nodes can be detected. It is imperative however to apply fat saturation to contrast-

enhanced images, otherwise enhanced lymph nodes do not show within the surrounding fatty tissue. The T2-weighted inversion recovery images (TIRM) or fat saturated T2-weighted images of the protocol are well appreciated for the visualization of mediastinal lymph nodes (Ohno et al. 2004). STIR sequences are highly sensitive for the detection of lymph nodes with bright contrast against mediastinal fat and might be even more sensitive for the detection and classification of lung cancer and mediastinal metastases than DWI (Koyama et al. 2010). DWI, as recommended for whole body staging of lung cancer, also covers mediastinal metastases, but a clear advantage of DWI over other MRI protocols has not been confirmed so far (Hasegawa et al. 2008; Pauls et al. 2012). A recent meta-analysis by Wu et al. (2012), based on 19 studies with a total of 2845 pathologically proven cases, confirmed an equal pooled sensitivity of DWI (72%) compared to PET/CT (75%; P = 0.09). The optional DWI sequence in the protocol suggestions of this chapter would be therefore recommended for mediastinal imaging.

However, beyond the suggested standards, specific protocols are appreciated, if the clinical scenario is directly related to the mediastinum and its structures. A quick method for scanning mediastinal masses is a black blood prepared partial Fourier fast spin echo sequence (HASTE) (Hintze et al. 2006). Non-enhanced MRI benefits from black blood techniques, which reduce flow artifacts. It allows for the identification of vessel walls and better differentiation to lymph nodes, but is used on the cost of signal intensity. The disadvantages of all available breath-hold techniques are their limited spatial resolution and their only partially T1- or T2-weighted contrast. For the chest wall and the mediastinum, clear T1- and T2-contrast can be very helpful, in particular for the characterization of mediastinal masses. Conventional spin-echo and fast spin-echo imaging require acquisition times of a couple of minutes so that cardiac and respiratory motion have to be compensated for, i.e., with triggering or gating. Since respiratory motion usually plays a minor role, in particular while imaging the upper mediastinum, the benefits of respiration-triggered sequences are limited and do not pay off for the significantly higher acquisition times. Conventional ECG-triggered T1-weighted spin echo and T2-weighted fast spin echo sequences provide excellent detail of structures close to the heart. Depiction of lymph nodes on both sequences is equal. Appropriate sequences are available on any standard scanner. Thus, they were not specifically adapted for the purposes of our protocol suggestions. However, an excellent visualization of both, mediastinal lymph nodes and lung parenchyma, is achieved with the optional respiration-triggered T2-weighted fast spin echo sequence of the protocol (Fig. 5).

6.5 Chest Wall and Apex

A typical indication for imaging the lung apices, the upper thoracic outlet, and the posterior chest wall is malignant infiltration of this region, e.g., a Pancoast tumor. The structures of interest are the large vessels, the cervico-brachial plexus, and the spine with the spinal cord. They can be examined without specific motion compensation, since motion artifacts are sparse with the given distance from the heart and diaphragm. Therefore appropriate protocols based on conventional spin echo and fast (turbo-) spin echo sequences are already available on most scanners (Shiotani et al. 2000). However, all diagnostic questions in this area are fully covered with our standard protocol suggestions for lung tumor imaging.

Towards the lower thoracic aperture, imaging the posterior chest wall remains easy while imaging the anterior chest wall and the sternum becomes difficult due to respiratory motion. Using a conventional protocol approach, the solution is as easy as effective: The examination can be performed in prone position. This has been used on a routine basis for breast MRI for many years and it is extremely helpful to remember this simple trick when a study is planned for imaging any other component of this location, e.g., an unclear mass or destruction of the sternum. The fast breath-hold sequences of our suggested protocol, however, produce excellent images of the sternum even with the patient in supine position.

6.6 Pediatric Applications

The use of lung MRI is of particular interest for pediatric radiology. Besides ultrasound, which is particularly challenging in the lungs, lung MRI is the only imaging modality for the chest without radiation exposure. The limitations of the suggested standard protocol in this chapter are twofold: The first is that breath-hold imaging requires a reasonable compliance of the patient. The authors have made good experience with children of 10 years and older (Eichinger et al. 2006). Acceptable results were achieved even in younger children between 6 and 10 years—if the interaction with the patient was good; even with breath-hold techniques. Single shot steady-state imaging (TrueFISP) has been successfully implemented for children of less than 6 years (Rupprecht et al. 2002). In smaller children, the fast breathing frequency is in favor of respiration-triggered sequences. Appropriate protocol modifications are suggested in Table 2. The second limitation refers to the T1-weighted 3D-GRE (VIBE) acquisition, which suffers from low signal in small volumes and voxels, if the matrix is adapted to very small children.

7 Protocol Adaptions for 3 T and Below 1.5 T

The particular challenges of lung imaging with MR imply that imaging at 3 T might be unfavorable due to increasing susceptibility artifacts while a lower field strength, e.g., of 0.5 T, should achieve a relative increase in the signal intensity for the lung parenchyma compared to 1.5 T.

Practice shows that 3 T images obtained with the protocol suggestions for 1.5 T are of comparable quality (Lutterbey et al. 2005; 2007; Regier et al. 2007). In observer preference studies the imaging characteristics of different pulse sequences used for lung MRI did not substantially differ between 1.5 and 3 T (Fink et al. 2007; Fabel et al. 2009). At both field strengths T2-weighted partial Fourier single shot sequences (HASTE) showed the highest signal-to-background ratio for infiltrates and were rated best for the delineation of infiltrates. 3D gradient echo sequences (VIBE) achieved the highest signal-to-background ratio for nodules and the best rating for the depiction of nodules at both field strengths. At 3 T, contrast and signal of gradient echo sequences improved slightly while steady-state gradient echo sequences suffered from increasing off-resonance artifacts. To study respiratory dynamics at 3 T, gradient echo sequences should be preferred to steady-state sequences. Image quality of inversion recovery sequences decreased minimally at 3 T. The respiration-triggered fast spin echo sequence was the preferred sequence for the visualization of the mediastinum at both field strengths. Thus, at present no specific advantage can be seen in using high-field MR for scanning the lungs, but the above given protocol suggestions can be readily transferred to 3 T. However, the given advantages in 3D GRE imaging with higher lesion to background contrast and shortened scan times suggest to focus on this part of the protocol and on contrast-enhanced studies as well as angiographic studies when using 3 T scanners (Fig. 8, 9) (Dewes et al. 2016). Additional benefits of dedicated protocols specifically adapted to the requirements of lung MRI at 3 T have not been evaluated so far.

Principally, low-field scanners are economic and yield the advantages of open systems regarding patient compliance, in particular for children. Unfortunately, the protocol recommendations for 1.5 T systems cannot be transferred one by one. So far, T1-GRE and T2-FSE sequences have been successfully implemented on 0.5 T scanners (Schäfer et al. 2002; Abolmaali et al. 2004). Due to the lower gradient performance of the systems, 2D gradient echo sequences were preferred to 3D
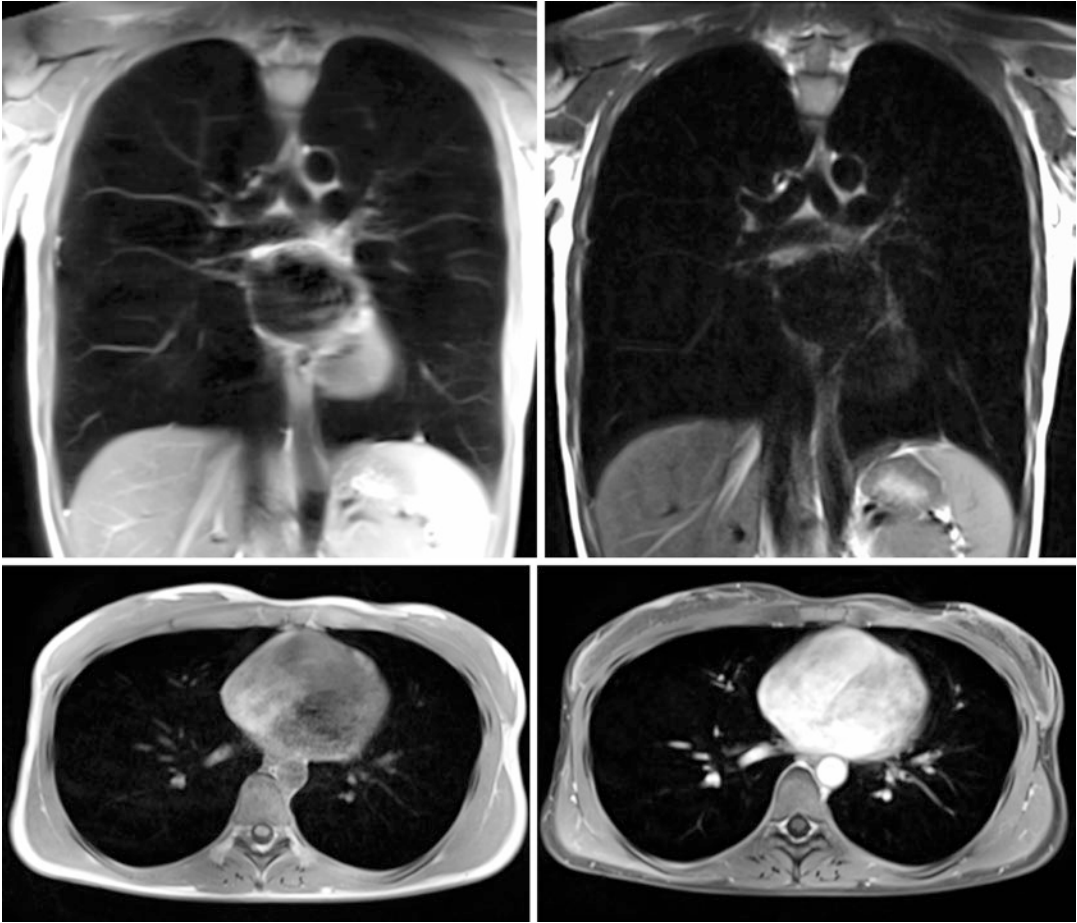
Fig. 8 Lung MRI at 3 T, 26-year-old female, clinical study for unclear chest pain: T2-weighted single shot partial Fourier (T2 HASTE, coronal acquisition in breath-hold, *upper left*), T2-weighted fast spin echo with rotating phase encoding (T2 BLADE, coronal acquisition in multiple breath-holds, *upper right*), T1-weighted volumetric interpolated 3D gradient echo sequence (VIBE, transverse acquisition in breath-hold) pre (*bottom left*) and post contrast (*bottom right*)

techniques. Steady-state gradient echo sequences with strong T1/T2-contrast producing high signal of solid and liquid pathology have been found to be particularly useful as well. The lower prevalence of susceptibility artifacts at lower field strength is in favor of steady-state imaging techniques. Also known as SS-FFE, TrueFISP or balanced steady-state acquisition with rewound gradi-

ent echo (BASG), they can be applied as 2D- or 3D-multislice-acquisitions or as single thick-slice technique (Heussel et al. 2002). Comprehensive protocol suggestions as defined for 1.5 T have not been published for low field MRI scanners so far, but the general sequences parameters are available from the cited publications.
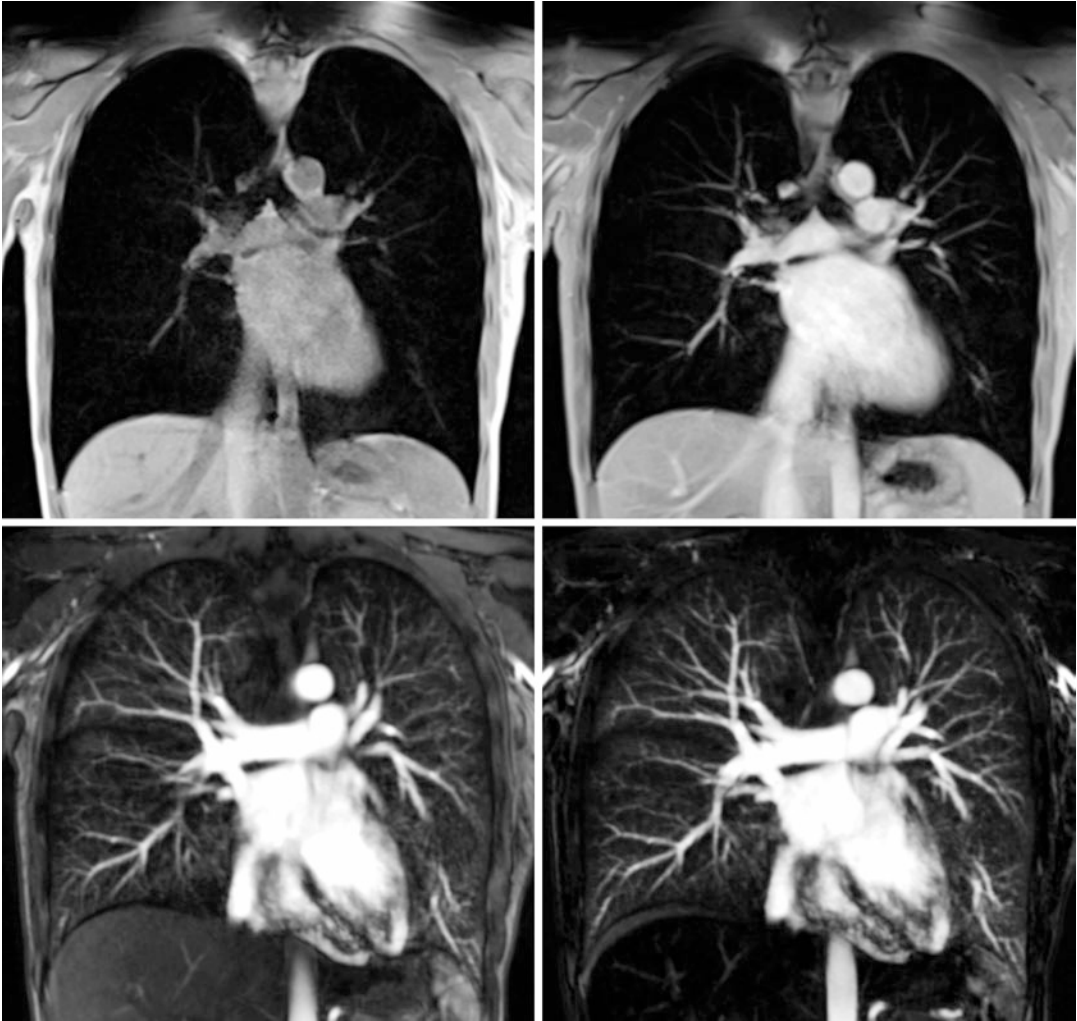
Fig. 9 Lung MRI at 3 T, same subject as in Fig. 8: T1-weighted volumetric interpolated 3D gradient echo sequence (VIBE, coronal acquisition in breath-hold) pre (*top left*) and post contrast (*top right*), T1-weighted 3D contrast-enhanced MRA as coronal acquisition in breath-hold, non-subtracted (*bottom left*) and subtracted (*bottom right*)

References

Abolmaali ND, Schmitt J, Krauss S, Bretz F, Deimling M, Jacobi V, Vogl TJ (2004) MR imaging of lung parenchyma at 0.2 T: evaluation of imaging techniques, comparative study with chest radiography and interobserver analysis. Eur Radiol 14:703–708

Albertin K (1996) Structural organization and quantitative morphology of the lung. In: Cutillo AG (ed) Application of magnetic resonance to the study of lung; hrsg. v. Futura Pub. Co., Armonk, NY, pp 73–114

Bauman G, Bieri O (2016) Reversed half-echo stack-of-stars TrueFISP (TrueSTAR). Magn Reson Med 76:583–590

Biederer J, Graessner J, Heller M (2001) Magnetic resonance imaging of the lung with a volumetric interpolated 3D-gradient echo sequence. RöFo Fortschritte Auf Dem Geb Röntgenstrahlen Nukl 173:883–887

Biederer J, Reuter M, Both M, Muhle C, Grimm J, Graessner J, Heller M (2002a) Analysis of artefacts and detail resolution of lung MRI with breath-hold T1-weighted gradient-echo and T2-weighted fast spin-echo sequences with respiratory triggering. Eur Radiol 12:378–384

Biederer J, Busse I, Grimm J, Reuter M, Muhle C, Freitag S, Heller M (2002b) Sensitivity of MRI in detecting alveolar infiltrates: experimental studies. RöFo Fortschritte Auf Dem Geb Röntgenstrahlen Nukl 174:1033–1039

Biederer J, Schoene A, Freitag S, Reuter M, Heller M (2003) Simulated pulmonary nodules implanted in a dedicated porcine chest phantom: sensitivity of MR imaging for detection. Radiology 227:475–483

Biederer J, Liess C, Charalambous N, Heller M (2004) Volumetric interpolated contrast-enhanced MRA for the diagnosis of pulmonary embolism in an ex vivo system. J Magn Reson Imaging 19:428–437

Biederer J, Hintze C, Fabel M, Dinkel J (2010) Magnetic resonance imaging and computed tomography of respiratory mechanics. J Magn Reson Imaging 32:1388–1397

Biederer J, Beer M, Hirsch W, Wild J, Fabel M, Puderbach M, Beek EJR (2012) MRI of the lung (2/3). Why … when … how? Insights Imaging 3:355–371

Boiselle PM, Biederer J, Gefter WB, Lee EY (2013) Expert opinion: why is MRI still an under-utilized modality for evaluating thoracic disorders? J Thorac Imaging 28:137

Both M, Schultze J, Reuter M, Bewig B, Hubner R, Bobis I, Noth R, Heller M, Biederer J (2005) Fast T1- and T2-weighted pulmonary MR-imaging in patients with bronchial carcinoma. Eur J Radiol 53:478–488

Bruegel M, Gaa J, Woertler K, Ganter C, Waldt S, Hillerer C, Rummeny EJ (2007) MRI of the lung: value of different turbo spin-echo, single-shot turbo spin-echo, and 3D gradient-echo pulse sequences for the detection of pulmonary metastases. J Magn Reson Imaging 25:73–81

Chung JH, Cox CW, Forssen AV, Biederer J, Puderbach M, Lynch DA (2013) The dark lymph node sign on magnetic resonance imaging: a novel finding in patients with sarcoidosis. J Thorac Imaging 29:125–129

Deng J, Miller FH, Salem R, Omary RA, Larson AC (2006) Multishot diffusion-weighted PROPELLER magnetic resonance imaging of the abdomen. Investig Radiol 41:769–775

Dewes P, Frellesen C, Al-Butmeh F, Albrecht MH, Scholtz J-E, Metzger SC, Lehnert T, Vogl TJ, Wichmann JL (2016) Comparative evaluation of non-contrast CAIPIRINHA-VIBE 3T-MRI and multidetector CT for detection of pulmonary nodules: in vivo evaluation of diagnostic accuracy and image quality. Eur J Radiol 85:193–198

Eichinger M, Puderbach M, Fink C, Gahr J, Ley S, Plathow C, Tuengerthal S, Zuna I, Müller F-M, Kauczor H-U (2006) Contrast-enhanced 3D MRI of lung perfusion in children with cystic fibrosis—initial results. Eur Radiol 16:2147–2152

Fabel M, Wintersperger BJ, Dietrich O, Eichinger M, Fink C, Puderbach M, Kauczor H-U, Schoenberg SO, Biederer J (2009) MRI of respiratory dynamics with 2D steady-state free-precession and 2D gradient echo sequences at 1.5 and 3 Tesla: an observer preference study. Eur Radiol 19:391–399

Fink C, Puderbach M, Bock M, Lodemann K-P, Zuna I, Schmähl A, Delorme S, Kauczor H-U (2004) Regional lung perfusion: assessment with partially parallel three-dimensional MR imaging. Radiology 231:175–184

Fink C, Puderbach M, Biederer J, Fabel M, Dietrich O, Kauczor H-U, Reiser MF, Schönberg SO (2007) Lung MRI at 1.5 and 3 Tesla: observer preference study and lesion contrast using five different pulse sequences. Investig Radiol 42:377–383

Hasegawa I, Boiselle PM, Kuwabara K, Sawafuji M, Sugiura H (2008) Mediastinal lymph nodes in patients with non-small cell lung cancer: preliminary experience with diffusion-weighted MR imaging. J Thorac Imaging 23:157–161

Heidemann RM, Griswold MA, Kiefer B, Nittka M, Wang J, Jellus V, Jakob PM (2003) Resolution enhancement in lung 1H imaging using parallel imaging methods. Magn Reson Med 49:391–394

Heussel CP, Sandner A, Voigtländer T, Heike M, Deimling M, Kuth R, Rupprecht T, Schreiber WG, Kauczor HU (2002) Prospective feasibility study of chest X-ray vs. thoracic MRI in breath-hold technique at an open low-field scanner. ROFO Fortschr Geb Rontgenstr Nuklearmed 174:854–861

Hintze C, Biederer J, Wenz HW, Eberhardt R, Kauczor HU (2006) MRI in staging of lung cancer. Radiology 46:251–4, 256–9

Hochhegger B, Marchiori E, dos Reis DQ, Souza AS, Souza LS, Brum T, Irion KL (2012) Chemical-shift MRI of pulmonary hamartomas: initial experience using a modified technique to assess nodule fat. AJR Am J Roentgenol 199:W331–W334

Kim HS, Lee KS, Ohno Y, van Beek EJR, Biederer J (2015) PET/CT versus MRI for diagnosis, staging, and follow-up of lung cancer. J Magn Reson Imaging 42:247–260

Kluge A, Gerriets T, Müller C, Ekinci O, Neumann T, Dill T, Bachmann G (2005) Thoracic real-time MRI: experience from 2200 examinations in acute and ill-defined thoracic diseases. RöFo Fortschritte Auf Dem Geb Röntgenstrahlen Nukl 177:1513–1521

Koyama H, Ohno Y, Aoyama N, Onishi Y, Matsumoto K, Nogami M, Takenaka D, Nishio W, Ohbayashi C, Sugimura K (2010) Comparison of STIR turbo SE imaging and diffusion-weighted imaging of the lung: capability for detection and subtype classification of pulmonary adenocarcinomas. Eur Radiol 20:790–800

Landwehr P, Schulte O, Lackner K (1999) MR imaging of the chest: mediastinum and chest wall. Eur Radiol 9:1737–1744

Leutner C, Schild H (2001) MRI of the lung parenchyma. RöFo Fortschritte Auf Dem Geb Röntgenstrahlen Nukl 173:168–175

Leutner C, Gieseke J, Lutterbey G, Kuhl CK, Flacke S, Glasmacher A, Theisen A, Wardelmann E, Grohe C, Schild HH (1999) MRT versus CT in the diagnosis of pneumonias: an evaluation of a T2-weighted ultrafast turbo-spin-echo sequence (UTSE). ROFO Fortschr Geb Rontgenstr Nuklearmed 170:449–456

Levin DL, Chen Q, Zhang M, Edelman RR, Hatabu H (2001) Evaluation of regional pulmonary perfusion using ultrafast magnetic resonance imaging. Magn Reson Med 46:166–171

Lin W, Guo J, Rosen MA, Song HK (2008) Respiratory motion-compensated radial dynamic contrast-enhanced (DCE)-MRI of chest and abdominal lesions. Magn Reson Med 60:1135–1146

Lutterbey G, Gieseke J, von Falkenhausen M, Morakkabati N, Schild H (2005) Lung MRI at 3.0 T: a comparison of helical CT and high-field MRI in the detection of diffuse lung disease. Eur Radiol 15:324–328

Lutterbey G, Grohé C, Gieseke J, von Falkenhausen M, Morakkabati N, Wattjes MP, Manka R, Trog D, Schild HH (2007) Initial experience with lung-MRI at 3.0T: comparison with CT and clinical data in the evaluation of interstitial lung disease activity. Eur J Radiol 61:256–261

Ohno Y, Hatabu H, Takenaka D, Higashino T, Watanabe H, Ohbayashi C, Yoshimura M, Satouchi M, Nishimura Y, Sugimura K (2004) Metastases in mediastinal and hilar lymph nodes in patients with non-small cell lung cancer: quantitative and qualitative assessment with STIR turbo spin-echo MR imaging. Radiology 231:872–879

Pauls S, Schmidt SA, Juchems MS, Klass O, Luster M, Reske SN, Brambs H-J, Feuerlein S (2012) Diffusion-weighted MR imaging in comparison to integrated [^{18}F]-FDG PET/CT for N-staging in patients with lung cancer. Eur J Radiol 81:178–182

Pipe JG (1999) Motion correction with PROPELLER MRI: application to head motion and free-breathing cardiac imaging. Magn Reson Med 42:963–969

Plathow C, Hof H, Kuhn S, Puderbach M, Ley S, Biederer J, Claussen CD, Huber PE, Schaefer J, Tuengerthal S, Kauczor H-U (2006) Therapy monitoring using dynamic MRI: analysis of lung motion and intrathoracic tumor mobility before and after radiotherapy. Eur Radiol 16:1942–1950

Rank CM, Heußer T, Buzan MTA, Wetscherek A, Freitag MT, Dinkel J, Kachelrieß M (2016) 4D respiratory motion-compensated image reconstruction of free-breathing radial MR data with very high undersampling. Magn Reson Med 77:1170–1183

Regier M, Kandel S, Kaul MG, Hoffmann B, Ittrich H, Bansmann PM, Kemper J, Nolte-Ernsting C, Heller M, Adam G, Biederer J (2007) Detection of small pulmonary nodules in high-field MR at 3 T: evaluation of different pulse sequences using porcine lung explants. Eur Radiol 17:1341–1351

Regier M, Schwarz D, Henes FO, Groth M, Kooijman H, Begemann PG, Adam G (2011) Diffusion-weighted MR-imaging for the detection of pulmonary nodules at 1.5 Tesla: intraindividual comparison with multidetector computed tomography. J Med Imaging Radiat Oncol 55:266–274

Remmert G, Biederer J, Lohberger F, Fabel M, Hartmann GH (2007) Four-dimensional magnetic resonance imaging for the determination of tumour movement and its evaluation using a dynamic porcine lung phantom. Phys Med Biol 52:N401–N415

Rupprecht T, Böwing B, Kuth R, Deimling M, Rascher W, Wagner M (2002) Steady-state free precession projec-tion MRI as a potential alternative to the conventional chest X-ray in pediatric patients with suspected pneumonia. Eur Radiol 12:2752–2756

Schäfer JF, Vollmar J, Schick F, Seemann MD, Mehnert F, Vonthein R, Aebert H, Claussen CD (2002) Imaging diagnosis of solitary pulmonary nodules on an open low-field MRI system—comparison of two MR sequences with spiral CT. ROFO Fortschr Geb Rontgenstr Nuklearmed 174:1107–1114

Schäfer JF, Vollmar J, Schick F, Seemann MD, Kamm P, Erdtmann B, Claussen CD (2005) Detection of pulmonary nodules with breath-hold magnetic resonance imaging in comparison with computed tomography. ROFO Fortschr Geb Rontgenstr Nuklearmed 177:41–49

Schroeder T, Ruehm SG, Debatin JF, Ladd ME, Barkhausen J, Goehde SC (2005) Detection of pulmonary nodules using a 2D HASTE MR sequence: comparison with MDCT. AJR Am J Roentgenol 185:979–984

Shiotani S, Sugimura K, Sugihara M, Kawamitsu H, Yamauchi M, Yoshida M, Kushima T, Kinoshita T, Endoh H, Nakayama H et al (2000) Diagnosis of chest wall invasion by lung cancer: useful criteria for exclusion of the possibility of chest wall invasion with MR imaging. Radiat Med 18:283–290

Strollo DC, Rosado de Christenson ML, Jett JR (1997a) Primary mediastinal tumors. Part 1: tumors of the anterior mediastinum. Chest 112:511–522

Strollo DC, Rosado-de-Christenson ML, Jett JR (1997b) Primary mediastinal tumors: part II. Tumors of the middle and posterior mediastinum. Chest 112: 1344–1357

Su S, Saunders JK, Smith IC (1995) Resolving anatomical details in lung parenchyma: theory and experiment for a structurally and magnetically inhomogeneous lung imaging model. Magn Reson Med 33:760–765

Weick S, Breuer FA, Ehses P, Völker M, Hintze C, Biederer J, Jakob PM (2013) DC-gated high resolution three-dimensional lung imaging during free-breathing. J Magn Reson Imaging 37:727–732

Wielpütz MO, Eichinger M, Puderbach M (2013) Magnetic resonance imaging of cystic fibrosis lung disease. J Thorac Imaging 28:151–159

Wild JM, Marshall H, Bock M, Schad LR, Jakob PM, Puderbach M, Molinari F, Van Beek EJR, Biederer J (2012) MRI of the lung (1/3): methods. Insights Imaging 3:345–353

Wu L-M, Xu J-R, Gu H-Y, Hua J, Chen J, Zhang W, Haacke EM, Hu J (2012) Preoperative mediastinal and hilar nodal staging with diffusion-weighted magnetic resonance imaging and fluorodeoxyglucose positron emission tomography/computed tomography in patients with non-small-cell lung cancer: which is better? J Surg Res 178:304–314

Wu L-M, Xu J-R, Hua J, Gu H-Y, Chen J, Haacke EM, Hu J (2013) Can diffusion-weighted imaging be used as a reliable sequence in the detection of malignant pulmonary nodules and masses? Magn Reson Imaging 31:235–246

Noncontrast and Contrast-Enhanced Pulmonary Magnetic Resonance Angiography

Mark L. Schiebler, Donald Benson,
Tilman Schubert, and Christopher J. Francois

Contents

M.L. Schiebler, M.D. (✉) • D. Benson, M.D., Ph.D.
Department of Radiology, UW-Madison School of
Medicine and Public Health, University of
Wisconsin-Madison, Madison, WI, USA
e-mail: Mschiebler@uwhealth.org

T. Schubert, M.D.
Clinic of Radiology and Nuclear Medicine, Basel,
University Hospital, Basel, Switzerland

Department of Radiology, UW-Madison School of
Medicine and Public Health, University of
Wisconsin-Madison, Madison, WI, USA

C.J. Francois, M.D.
Department of Radiology, UW-Madison School of
Medicine and Public Health, University of
Wisconsin-Madison, Madison, WI, USA

Department of Medicine, UW-Madison School of
Medicine and Public Health, University of
Wisconsin-Madison, Madison, WI, USA

Abstract

Single breath hold 3D contrast-enhanced pulmonary MRA should be considered an important part of the imaging toolbox for the assessment of diseases affecting the pulmonary arteries. Some clinical sites are already using this method for the primary assessment of pulmonary embolism in younger patients. The advantages of CE-MRA over Computed Tomographic Angiography (CTA), in the assessment of the pulmonary vasculature, are: (1) lack of ionizing radiation, (2) time-resolved imaging for perfusion, and (3) lack of iodinated contrast material. Although artifacts can be a source of interpretive error, CE-MRA is a good alternative to CTA for patients with borderline renal function or iodinated contrast allergies. Free breathing CE-MRA methods using ultrashort time to echo pulse sequences, which can also show the lung parenchyma, will improve MRA even further.

1   Introduction

For most radiology departments the primary focus of vascular imaging of the lungs is for the evaluation of pulmonary embolism (PE). There are a number of excellent review articles on this subject (Goldhaber and Bounameaux 2012; Stein et al. 2011b; Tapson 2008; West 1986). The essential problem with this disorder of clotting that affects approximately 1/1000 in the normal population annually (Spencer et al. 2008), is that it can be a cause of sudden death. Many decisions need to be made by the clinician when dealing with the possible risk for venous thromboembolic (VTE) disease. The range of clinical issues begins with prevention and ends with surgical thromboembolectomy. Finding the right balance for each patient on the scale of risks and benefits of treatment is critical for improving patient outcomes.

The wholesale introduction of CE-MRA has been limited for use in pulmonary angiography due to the accuracy, speed, and safety of multidetector computed tomographic angiography (CTA) (Remy-Jardin et al. 2007, 1996; Tillie-Leblond et al. 2002). With the publication of the PIOPED III (Stein et al. 2010, 2008) results showing that the sensitivity and specificity of MRA was 79% and 98%, respectively, when compared with CTA, it became clear that CE-MRA needed technical refinement before it would be ready for routine clinical use.

The reader should ask the following question: "Why bother with pulmonary CE-MRA for the diagnosis of PE when CTA is so good?" The answer for most of the world has been to "not bother" with MRA at all because it takes too long to do, it is of unproven benefit, and CTA is quick and accurate. In this chapter, we will show that MRA is worth the effort to master as one of the important imaging test choices for studying pulmonary pathophysiology (Nagle et al. 2016; Schiebler et al. 2013). There have also been early reports that CTA exams are associated with an increase in the number of double-stranded DNA breaks in circulating lymphocytes (Popp et al. 2016). There is no DNA damage after gadolinium-based contrast-enhanced cardiovascular MR exams (Brand et al. 2015). Iodinated contrast material is associated with anaphylaxis and acute renal failure. Thus, the use of pulmonary MRA can *improve patient safety* by allowing for the use of a non-ionizing modality without iodinated contrast material for the study of the pulmonary vasculature (Nagle et al. 2016).

2   Contrast-Enhanced Pulmonary MRA

As of today, MRA of the pulmonary vasculature is best performed after contrast enhancement using a breath hold 3D gradient echo with time to repetition (TR) less than 6 ms and time to echo (TE) as short as possible to minimize the magnetic susceptibility effects of the lung. While there is the belief that any pulmonary arterial exam must have an arterial phase acquisition to

minimize the effects of venous contamination, we have not found this to be an essential component for the detection of PE. The basis for a successful clinical pulmonary MRA exam is a robust, reliable, and reproducible MRA technique. As proposed in 1999, the principal idea behind creating high quality MRA images requires centering the contrast agent bolus peak signal enhancement with the center of the k-space acquisition (Meaney and Prince 1999a, b). The use of elliptical centric readout takes advantage of this requirement by filling the center of k-space first. This allows the MRI technologist to track the bolus and start the scan when the artery of interest is maximally enhanced. Another approach is to use a timing bolus to determine the delay time needed for the scan acquisition. The scan is timed to begin at the exact time when the vessel in question shows peak enhancement with the test bolus. The disadvantage with using a test bolus is that it is not real time. Many issues can occur to limit the quality of those examinations that solely rely on a test bolus to determine when to start their MRA acquisition: (1) breath in with new influx of nonopacified blood (transient interruption of the bolus), (2) patient respiratory or bulk motion during the acquisition, (3) kinking of the vein or arm during the bolus injection of contrast. There are artifacts that can mimic thrombus. These result from improper timing of the

scan. For instance, the effect of filling the center of k-space before the peak of the contrast agent bolus has been reached is the Maki artifact (Maki et al. 1996). In this situation, the contrast is not present during the acquisition of the center of k-space but is at the periphery. This causes a characteristic high signal intensity rim to the inner lumen of the vessels in the acquisition volume and may mimic thrombus.

The introduction of parallel imaging (Griswold et al. 2000) has allowed for the possibility of obtaining 3D high resolution pulmonary MRA. Compared with conventional MRI k-space trajectories, parallel imaging techniques acquire only a fraction of the phase encoding lines. The missing information is reconstructed to a full field-of-view using the inherent spatial encoding of the different receiver coils (Griswold et al. 2000). The amount of time savings (acceleration factor) is in the range of 2–4× shorter than when using conventional reconstruction methods (Blaimer et al. 2006; Breuer et al. 2005; Fink et al. 2003; Griswold et al. 2000). Because there is time that can be bought using the parallel imaging acceleration, we can use that to either simply reduce the total acquisition time or increase the spatial resolution to submillimeter isotropic resolution without prolonging the acquisition time.

We have used our current protocol for pulmonary MRA (Table 1) continuously since 2008 (Nagle et al. 2016; Schiebler et al. 2013). We use

Table 1 UW-Madison Basic MRA PE—5-min scan protocol description

MRI acquisition number	Description	Pulse sequence	Scan length in minutes
1	Localizer	Single shot Fast spin echo	<1
2	Pre-contrast MRA	T1 weighted Gradient echo	<1
3	Post-contrast MRA—Bolus phase	T1 weighted Gradient echo	<1
4	Post-contrast MRA—immediate post-contrast	T1 weighted Gradient echo	<1
5	Post-contrast Equilibrium phase Lower flip angle	T1 weighted Gradient echo	<1
(Extra)	*Free breathing salvage examination*	*4 average No parallel imaging 3D T1 Weighted MRA*	*3*
6	Post-contrast T1 fat saturated images of thorax	T1 weighted chemical fat saturation axial or 3D spoiled gradient recalled echo with fat saturation	<1

This has not changed in the last 8 years of use

Fig. 1 Normal contrast-enhanced MRA maximum intensity projection at the equilibrium phase showing both the pulmonary arteries and the aorta and great vessels

it for other MRA exams as well such as thoracoabdominal aorta, renal arterial, and pelvic MRA exams using the same basic protocol with modifications to the matrix, number of slices, and number of coil elements. The secret of high quality examinations with few nondiagnostic examinations is experience, with repetition of the examination by the MR technologist staff (Fig. 1). Practice makes for better MRA chest examinations! Another technical component to this specific protocol is the use of elliptical centric phase ordering to capture the peak contrast enhancement of the dextrophase at the very beginning of the k-space trajectory. Another feature is the use of a sagittal excitation slab to minimize the wrap encountered from the shoulders and arms. This allows a smaller field of view to be chosen. The timing of the contrast bolus administration is also important. We have a slow infusion of contrast material that lasts over the entire bolus phase of acquisition (Nagle et al. 2016). This limits the variation in enhancement

for that early phase and prevents significant Maki artifacts (Maki et al. 1996) from occurring. We have also found that each patient will vary with respect to which one of the angiographic phases is the most diagnostic. Sometimes it is the bolus phase, while other times one of the delayed phase acquisitions is better. These software parameters and hardware configurations are now all routinely available on current MRI scanners. We do not currently use a perfusion sequence or time-resolved MR angiography sequence for the routine evaluation of PE. This would potentially require a second injection and we have tried to keep the protocol short so that these emergency room patients can be squeezed into the very busy (already full) MRI clinical schedule.

2.1 Time-Resolved Imaging

Several studies used time-resolved strategies pulmonary perfusion and *t*ime-*r*esolved *i*nterpolated *c*ontrast *k*inetic*s* (TRICKS), which is the major method that has made it into routine clinical practice (Fink et al. 2003, 2004; Nikolaou et al. 2005; Ohno et al. 2003). TRICKS is based on view sharing. In view sharing the central regions of k-space are updated more often than others leading to an effective shortening of the total acquisition time. In 1996, 3-dimensional view sharing for MRA (TRICKS) was introduced to visualize the transit of a contrast agent bolus (Korosec et al. 1996). This was initially spurred by the issue of differential flows in the legs in the setting of peripheral vascular disease. In TRICKS, the low frequency k-space data, which contributes most significantly to the image contrast, is sampled more frequently than the high frequency k-space data, which contributes to resolution. The high frequency components of k-space are not sampled as frequently and need to be interpolated between consecutive time frames (Frayne et al. 1996; Korosec et al. 1996). Many other combinations that can be used to acquire time-resolved MRA are as follows: (A) non-Cartesian k-space sampling (e.g., spiral k-space sampling) and (B) spiral-TRICKS MRA with a spatial resolution of $0.6 \times 0.6 \times 2$ mm^3 and a temporal reso-

lution of approximately 2 s for pulmonary MRA (Du and Bydder 2007). Many other time-resolved MRA acquisition solutions have sprung from this k-space sampling strategy ever since (Carroll et al. 2000, 2001; Du et al. 2003, 2002). In the scenario of chest disease and pulmonary embolism, time-resolved imaging can be performed as a perfusion like acquisition; however the price to be paid for higher temporal resolution is lower spatial resolution (Velikina et al. 2010). There are reconstruction solutions for this problem as well that involve compressed sensing and more extensive view sharing methodologies that are applicable in the cranial circulation (Chang et al. 2015), but these cannot be used in the chest due to the confounding motion of the diaphragms and heart during the acquisition of the contrast bolus.

One of the interesting features of time-resolved MRA in the chest is the determination of circulation time (Francois et al. 2003). This is the time it takes for the bolus to travel from the pulmonary artery to the aorta. This is measured by an ROI placed in the pulmonary trunk (PA) and Aorta (Ao) to help find the time of peak signal intensity (SI) (time = 0) after the bolus injection of contrast. The contrast needs to be the same iodine concentration or GBCA for all subjects used in the study. The bolus must use a defined amount of contrast material at a defined rate from a catheter placed in the antecubital vein or another location that is standardized. The transit time is the time it takes for the bolus peak signal intensity to reach the ascending aorta (time 1) from the PA time 0 (Time1 − time0 = Transit time). There are many diseases that affect the circulation time, but the most common cause is left heart dysfunction (Francois et al. 2003) Transit time is an underutilized metric in cardiopulmonary imaging.

2.2 Importance of Breath Holding

For the preservation of pulmonary CE-MRA image quality, there is nothing more important than a proper breath hold. The problem of the dyspneic patient is of course the central issue of why pulmonary MRA has had such a difficult

time gaining traction in the clinic. If they can hold their breath, they are less likely to have a symptomatic pulmonary embolism. On the other hand, those patients that the radiologist needs to study are not able to hold their breath. Without suspension of respiration, the amount of noise generated can make these 10–20 second MRA exams unreadable. Other strategies like free breathing acquisitions must be used if the patient is unable to hold their breath. Modification of the slice thickness—upward to a maximum of 3 mm—will decrease the overall acquisition time. One can use a larger parallel imaging acceleration factor but the artifacts from the higher G-factor might impede image interpretation (Fig. 2). The patient is requested to hold his/her breath at maximum inspiration rather than at maximum expiration, and the administration of 2–4 L of nasal cannula oxygen can also be added. The technologist can request the patient to hyperventilate to decrease $PaCO_2$ levels slightly by using the following strategy: breathe in, hold for 5 s and then breathe out, breathe in and hold for

Fig. 2 G-factor image degradation. This bothersome feature of parallel imaging propagates image noise into the center of the image. To limit wrap artifacts and G-factor noise increase the AP dimension of the acquisition volume

5 s and breathe out, breathe in and hold your breath. Sometimes these additional strategies still do not work and a free breathing heavily averaged examination can be tried, in particular after using an intravascular contrast agent (ferumoxytol or gadofosveset trisodium).

The use of free breathing contrast-enhanced MRA methods for the examination of PE would be preferable to any current breath hold dependent method when the patient is unable to hold his/her breath. This strategy is useful when there is a need to salvage a pulmonary MRA examination that is uninterpretable due to breathing artifacts. By turning off parallel imaging, opening up the field of view, increasing the phase acquisition matrix, decreasing the slice thickness, increasing the total number of acquisitions the imaging physician can make a trip down "memory lane" and use the methods that were in vogue in the 1990s for MRI of the chest and abdomen. While there will be motion unsharpness, these are highly readable exams and can be a good option in those select cases where no other breath hold option works.

With the recent introduction of a new pulse sequence for the lung that relies on an ultrashort time to echo (UTE) (Johnson et al. 2013), there will be a new chance for free breathing pulmonary MRA. This limits the amount of dephasing that occurs from the differences in magnetic susceptibility between the protons of the lung parenchyma/vessels and air within the bronchi and alveoli. This pulse sequence can be a good choice for free breathing acquisitions. The utility of combining a free breathing acquisition with the UTE pulse sequence has recently been shown to successfully image subsegmental pulmonary emboli in an animal model (Bannas et al. 2016). They showed that efficacy of a free breathing UTE exam was significantly better than traditional MRA when an intravascular contrast agent was used (Bannas et al. 2016). Bauml et al. have reported on their preliminary results of using a UTE-free breathing strategy in patients being evaluated for PE (Bauml et al. 2016). They showed that the interobserver ICC was 0.60 for MRA (moderate agreement) and 0.78 for UTE (strong agreement). Total image quality scores were significantly better for the UTE exams (74.4) than for the routine MRA exams (62.9) (p-value −0.02) (Bauml et al. 2016). The reason for this is rather straightforward. The quality of an MRA exam relies on the patient's ability to hold their breath, while the quality of the UTE-free breathing exam relied on the regularity of the breathing, the summated diastolic cardiac chamber position, and the absence of bulk motion by the subject. Patients evaluated for possible PE have a variable ability to hold their breath, hence the utility of the UTE exam.

2.3   Navigator 3D Free Breathing bSSFP Pre- or Post-contrast MRA

The 3D navigator methods (Wang et al. 1996) are excellent to track respiratory variation of the diaphragm to limit binning of cardiac data to those portions of the respiratory cycle that are quiescent (e.g., near end expiration). However, this method is harder to implement for the lung and pulmonary arteries. This is because the navigator is a separate saturation band that is used to track motion of the hemi-diaphragm. This works well for the heart when the band is over the liver, but this position will not work if the area of interest is the lungs, as that portion of the lung is saturated by the repeated application of the saturation band.

3   Choice of MRA Contrast Agent

Pulmonary MRA is an off-label use of gadolinium-based contrast agents (GBCA) and ferumoxytol. The MRA signal quality of single dose gadobenate dimeglumine was shown to be superior to double dose gadopentetate dimeglumine (Woodard et al. 2012). While any GBCA can be used, those formulations with higher relaxivity are preferred for MRA exams. With the concern for nephrogenic systemic fibrosis (NSF) and gadolinium deposition within the basal ganglia, the choice of formulations with more thermal stabil-

ity is preferred (Grobner 2006; Suzuki et al. 2010; Thomson et al. 2015). The use of gadofosveset trisodium (Ablavar™) is now problematic as the vendor will no longer be making and distributing this intravascular MRI contrast agent for use. This agent has been successfully used to determine the presence of both PE and deep venous thrombosis (Hansch et al. 2011; Pfeil et al. 2012). The only remaining MRA contrast agent that is completely intravascular is ferumoxytol. Its use as an MRA contrast agent (1–4 mg/kg) is an off-label use of this product that is approved for intravenous administration in chronic kidney disease patients with refractory iron deficiency anemia. This is a nonstoichiometric superparamagnetic iron oxide coated with poly glucose sorbitol carboxymethylether with an overall size of 17–31 nm. The relaxivity of this agent is very high and can be exploited for both bright and dark blood imaging. The bright blood images rely on the T1 effects using a short TE. The black blood relies on the T2*/T2 shortening found at longer echo times with this agent. The FDA has recently issued a black box warning on the bolus infusion of this agent. It is most safely administered as a slow infusion diluted in saline outside of the scanner, and is used in the steady state of its pharmacokinetic distribution within the circulation. Ferumoxytol is contraindicated in those patients with prior allergies or anaphylaxis, and the risks and benefits of its use in patients with known hemosiderosis/hemochromatosis should be carefully considered (Hope et al. 2015).

4 Dosing of Contrast Agents for Pulmonary MRA Exams

There is now an easy to use and free mobile app (**GadCalc**—University of Wisconsin) for determining the IV contrast dose of MR imaging agents. This mobile phone application also allows for easy access to the product's FDA's package insert (pdf). This reference can aid the MRI technologists in determining the correct dose in milliliters for each one of the approved MRI contrast agents. It also covers the dosing for ferumoxytol.

For pulmonary MRA with gadobenate dimeglumine the standard dose we use is 0.15 mmol/kg diluted up to 30 ml with a 30 ml saline chase. For ferumoxytol, a dose of 1–3 mg/kg can be used diluted in 150 ml of saline and administered as a slow infusion over 15 min (10 ml/min).

5 Safety of Gadolinium-Based Contrast Agents (GBCAs)

Just when the "black cloud" of nephrogenic systemic fibrosis (NSF) had begun to dissipate (Bruce et al. 2016; Haemel et al. 2011; Sadowski et al. 2007; Soulez et al. 2015), we must now deal with a new issue: Gadolinium deposition in the deep brain nuclei and the bony skeleton (Gd^{3+} is a calcium analogue) in both children and adults from the prior use of gadolinium-based contrast agents (GBCAs) (Huckle et al. 2016; Suzuki et al. 2010). This deposition is more significant for the linear agents than the macrocyclics. At this point, we do not know what the long-term effects of this deposition will be. While it is entirely possible that this will not prove to be a significant finding or have any lasting effects on our patients, we must be cognizant of the fact that this could potentially continue to affect them for many years. The current best evidence on this topic suggests that this is an interesting side effect of GBCA use, but it is not important at all for patient survival, morbidity, or normal brain function at the concentrations used clinically. One side note to this issue is that we must begin to rethink the use of GBCAs in normal volunteers, particularly those that are getting repeated doses of these agents.

6 Noncontrast Pulmonary MRA

Noncontrast MRA methods have a long history of use in the heart (bSSFP), but not the lungs. The reasons for the poor image quality of the lungs and pulmonary vasculature using bSSFP pulse sequences are multifactorial. First, the vessels in the lung are smaller than the cardiac chambers and the great vessels. Second, the pulmonary ves-

sels move almost as much as the cardiac chambers (particularly in the left upper lobe lingular segment), and cardiac gating has not traditionally been used. Lastly, there is a larger amount of magnetic susceptibility artifact present between the smaller pulmonary arteries/veins and the surrounding lung/bronchi than is seen for the cardiac chambers which is very deleterious for bSSFP imaging. A recent study by Heredia et al. (2012) compared the use of bSSFP MRA in pregnant patients to contrast-enhanced 3D gradient echo (3D-GRE) in young women (Heredia et al. 2012) and found that in 21 subjects the central and lobar arteries were visible 100% of the time and the segmental arteries were seen in 90% of the cases. The lower image quality of the segmental vessels was related to poor blood signal intensity and motion for both the noncontrast bSSFP MRA exam and the post-gadolinium MRA examination. Kalb et al. showed lower performance for the bSSFP images when compared to perfusion imaging or post-contrast 3D MRA (Kalb et al. 2012). They found that the specificity for the detection of pulmonary emboli was 67% for triggered true FISP imaging and 73% for 3D GRE imaging. Certainly, bSSFP can evaluate the central pulmonary arteries, but for smaller vessels the addition of contrast material is still needed.

Arterial spin labeling can work well in the abdomen where the arterial inflows are predictable from a superior to inferior direction (Bley et al. 2016; Miyazaki and Akahane 2012). While this approach has the potential to become useful in the evaluation of pulmonary arterial flow, it has had limited application in patients (Mai and Berr 1999).

Time of flight methods for noncontrast MRA work very well in the head and neck. The arterial blood flow is usually from an inferior to superior direction and the organ stays still. The chest is nearly a polar opposite in its suitability for TOF angiography. There is nearly constant motion of either the heart or diaphragms. While breath holding can help with this, patients that are sick or have tachypnea from shortness of breath have a limited ability to quiet their breathing. In addition, the flow of blood in the chest is multidirec-

tional. The cardiopulmonary system is one of the more difficult locations for successful application of the noncontrast TOF MRA method. Edelman has introduced a noncontrast 2D time of flight MRA method for use that simply takes advantage of a number of recent advances (Edelman et al. 1990). Quiescent-interval single shot (QISS) is such a method that began by simply using a bSSFP technique with cardiac gated acquisition to the maximal systolic inflow with the addition of saturation slabs. The contrast mechanism for the signal intensity found using this method is principally provided by the inflowing spins of fresh blood. The application of a saturation slab is the primary way to separate venous from arterial flow. While this method works well for flow suppression in the head and lower extremities, it cannot be relied on for the chest. In the chest application of saturation of the pulmonary trunk can suppress the pulmonary arterial signal intensity, while saturation of the left ventricle can suppress the aorta. The addition of an ASL method using disc excitation can also help to further select a discrete volume of blood for rephasing of spins.

6.1 Black Blood Imaging

The trouble with routine spin echo imaging for analysis of blood flow is that slow flow will be rephased and show up as confounding high signal intensity within the vessel lumen. To combat this issue for use in the study of arterial vessel wall and ventricular myocardial wall imaging, sequences to null all nonstationary spins were developed (Edelman et al. 1990). Later a double inversion recovery method was introduced for use in the coronary arteries (Fayad et al. 2000; Worthley et al. 2001). This pulse sequence is particularly robust with regard to the nulling of those intraluminal slow moving spins that can contaminate the juxta intimal region of black blood images. The primary application of this method was to help in the analysis of lipid plaque in the wall of the coronary arteries and aorta. It is also a mainstay of helping to null signal intensity in the right ventricle chamber for the analysis of the

right ventricular wall in the setting of arrhythmogenic right ventricular cardiomyopathy (ARVC). In principle, this method can be applied to the pulmonary arteries using a free breathing 3D approach with binning of the cardiac and respiratory cycles to limit the motion artifacts. Some sites use the high signal intensity of the pulmonary arteries on routine fast spin echo images to act as an index of slow flow in the setting of chronic pulmonary arterial hypertension (Swift et al. 2014).

6.2   Phase Contrast MRA

The workhorse of velocity sensitized flow imaging is the single slice, breath hold, cardiac gated cine 2D-phase contrast pulse sequence (Firmin et al. 1990, 1987; Klipstein et al. 1987; Nayler et al. 1986; Parsons et al. 1990; Rees et al. 1987). This is often used for the analysis of pulmonary arterial flows (main pulmonary arteries) and aortic flows to calculate Qp/Qs. This analysis is critical in the setting of congenital heart disease for the evaluation of left to right shunts and pulmonary valve insufficiency. All MR cardiovascular imaging sites use this methodology on a daily basis for flow quantification. Since flow encoded gradients must be applied in the positive and negative directions for each slice, the examination times are much longer for 3D phase contrast MRA. This method can work in those parts of the body that do not move at all (head and neck) and those that move a just a little (mesenteric arteries) (Wasser et al. 1996). However, for those areas in the body that move a lot, such as the chest, 3D phase contrast MRA sequences are challenging. In a new radial pattern of k-space sampling all lines of k-space traverse the center, but the overall volume of k-space is only partially sampled, for a 3D phase contrast pulse sequence that is called PC-VIPR (*P*hase *C*ontrast—*V*astly undersampled *I*sotropic-voxel *R*adial *P*rojection imaging) (Barger et al. 2002). Using this time-saving methodology the velocity-dependent phase in all three dimensions can be acquired from user-defined velocity-encoding gradients in a reasonable time period. These data can also be binned to

the cardiac and respiratory cycles. These cardiac- and respiratory-gated 3D phase contrast studies are known by the moniker of 4D flow MRI. The reconstruction of PC-VIPR images is performed using non-Cartesian methods and requires a standalone workstation for post–processing (Markl et al. 2011). The vendors have now entered the market with smaller field of view 4D flow acquisitions that rely on Cartesian-based reconstruction methodology and these image reconstructions of 4D flow can be seen at the time of the exam. 4D flow MRI has been used in many parts of the body for the evaluation of flow rates, internal flow patterns within a vessel, wall sheer stress, vessel compliance, pulse wave velocity, pressure difference, and turbulent kinetic energy. While 4D flow methods are currently used for pulmonary arterial hypertension, its use for other diseases of the pulmonary arterial system has lagged (Barker et al. 2015; Chelu et al. 2016).

The signal-to-noise for 4D flow methodology can be increased through the administration of an intravascular MRA contrast agent (Dyverfeldt et al. 2015; Markl et al. 2011). In the scenario of possible pulmonary embolism, the use of 4D flow has been limited. There are very slow flows involved and the resolution of the magnitude images is best for the larger vessels of the pulmonary arteries and veins and is quite limited at this point for the segmental and subsegmental vasculature. The longer imaging times needed for 4D flow necessitates careful attention to the cardiac and respiratory cycles before reconstruction.

Computational fluid dynamics (CFD) is now being used commercially for the determination of coronary artery stenosis from coronary computed tomographic angiography images (Zarins et al. 2013). The principle behind this work lies in the fact that as vessel stenosis increases, flow decreases and this can be determined by evaluating the contrast density within the vessel lumen. This methodology has also been applied to the pulmonary arterial system and a mathematical model of pulmonary embolism has been generated by Clark et al. (Burrowes et al. 2011). They found that proximal obstruction by pulmonary embolism does not explain the degree of pulmo-

nary hypertension. They suggest that the combination of the lack of functional information, pulmonary vasoconstriction, and any peripheral clots are very important components leading to hypoxia (Burrowes et al. 2014; Clark et al. 2012, 2014).

7 MRA Artifacts: Causes and Solutions

Without a clear understanding of what artifacts to expect, there will be incorrect interpretations of these exams.

7.1 Gibbs' Truncation Artifact

The Gibbs' truncation artifact is caused by the abrupt truncation of data at the edges of the sampled region of k-space (Wood and Henkelman 1985). These are formed when high-contrast (sharp) edges are present in the reconstructed image; this results in "ringing" adjacent to those sharp edges. When a vessel is approximately 3–5 pixels in diameter, these "rings" can superimpose in the exact center of the vessel, causing an appearance of a central filling defect (Fig. 3) (Bannas et al. 2014). On pulmonary MRA exams, these artifacts are seen in both the pulmonary arteries and veins. In addition, one helpful clue for their presence, versus a true pulmonary embolism, is the presence of linear low signal intensity

Fig. 3 Central filling defect in the interlobar artery (*arrow*). Gibbs' truncation artifact in the left lower lobe pulmonary artery (*dashed arrow*)

lines in the proximal larger vessel (Fig. 4) that summate to form the truncation artifact in the more distal vessel. Distinguishing a free floating centrally located embolus from the Gibbs' truncation artifact can be performed using a simple method as recently shown by Bannas et al. (2014). Their method is to divide the ROI signal intensity (SI) of the "presumed PE" by the average SI of four ROI from the surrounding enhanced pulmonary artery lumen(ROI SI PE/average ROI of lumen enhancement). If this value is found to be greater than or equal to 50%, then a PE is present. Values lower than 50% suggest that this region is a truncation artifact (Fig. 4). There is a confounding issue that also needs to be considered and that is the centrally located PE that is dissolving from thrombolytic therapy. These emboli can imbibe gadolinium-based contrast material and be of intermediate signal intensity. Another imaging feature of central PE that can be helpful is the observation that those vessels with a PE floating in them can be dilated when compared to their accompanying bronchi. This is due to vasodilation of the vessel (autoregulation) in response to the decrease in flow. If the PE was occlusive before the imaging exam, there may also be an area of hemorrhage in the pulmonary parenchyma that is fed by the vessel in question.

Bronchi of a certain size can also show this artifact (a reverse Gibbs') as a central area of high signal intensity on the post-contrast-enhanced images only. These are only seen on the post-contrast MRA because after contrast the bronchial wall enhances. It is the bright signal intensity of the wall that in turn causes the formation of the rippling in image space from the Fourier transform to form this high signal intensity dot, which is the reverse of the low signal intensity seen in the spinal cord and normal pulmonary vessels (of a defined size). Interestingly enough there is a second reverse Gibbs' artifact found in PE of a certain size. This is cause by the abrupt transition between the bright contrast-enhanced lumen of the vessel and the black low signal intensity of the outer surface of the clot. We have termed this the "bright central dot." This is one of the direct findings of PE that helps to distinguish it from a Gibbs' artifact on MRA exams (Fig. 5).
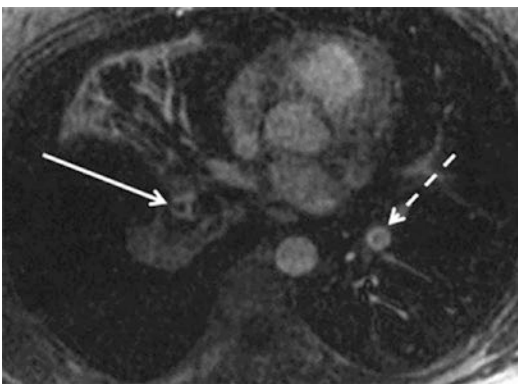
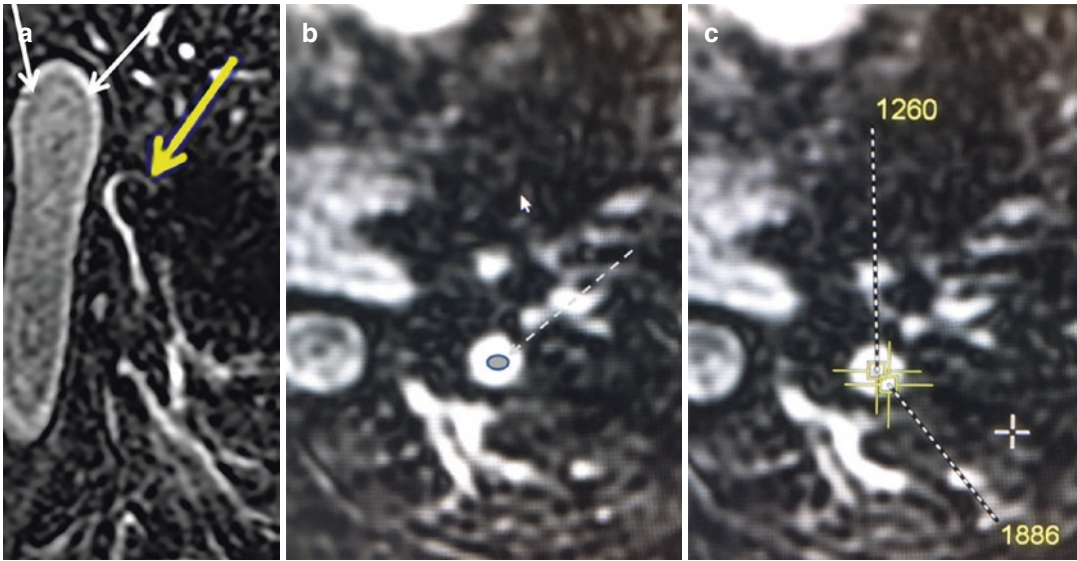**Fig. 4** (**a**) The low signal artifact is seen remote from the center of a vessel (*white arrows*) and summates to form the central truncation artifact that can mimic a pulmonary embolism. *Yellow arrow* is a pulmonary embolism in the left lower lobe pulmonary artery. (**b**) Gibbs' truncation artifact (enhanced by a *gray circle* and *outlined with a blue rim*). (**c**) Bannas' method for the determination of pulmonary embolus versus clot by measuring region of interest of the central vessel and comparing that measurement to the surrounding lumen. In this example the center measures 1260 signal intensity units and the lumen measures 1886 signal intensity units for a ratio of (1260/1886 = 67%). Since this is greater than 50%, this area is most consistent with a truncation artifact. Pulmonary emboli will typically have a ratio of less than 50%
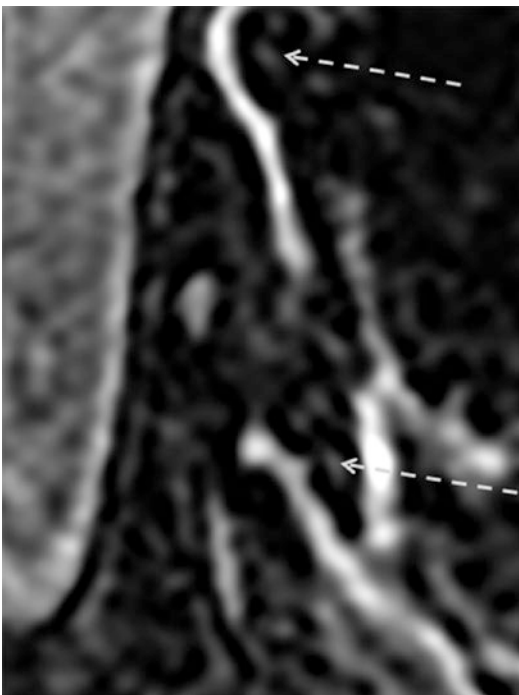
Fig. 5 Pulmonary embolism (PE) with reverse Gibbs' artifact is shown by the *dashed arrows*. This is a direct sign of pulmonary embolism and is a way to distinguish PE from Gibbs' truncation artifact

7.2 Transient Interruption of the Bolus

This is a very interesting artifact for both CTA and MRA exams. One must understand pulmonary physiology and the influence of intrathoracic pressure on the flow of blood into the right atrium to appreciate how this is created. This issue is related to the simple fact that if the patient breathes in during the injection of contrast material there will be the sudden influx of unopacified blood from the IVC that will prevent contrast enhancement of the pulmonary arteries (Wittram 2003; Wittram and Yoo 2007). The *sine qua non* imaging appearance of this artifact is as follows: (1) contrast material in the superior vena cava, (2) very little opacification of the pulmonary arteries, and (3) opacification of the pulmonary veins, left heart and aorta. There is in effect a hiatus of contrast material due to the breath in as prescribed by the technologist for the patient prior to the initiation of scanning. This may occur in the bolus phase images but is not relevant for the equilibrium phase exam. This issue can be prevented by simply having the patient breathe

quietly and then stop breathing (or to have the patient hold his/her breath at end expiration). These methods will prevent the sudden decrease in intrapulmonary pressure. Most patients with PE will have difficulty holding their breath at end expiration for the length of an MRA exam.

7.3 Over-Ranging and Noise Enhancement in Parallel Imaging

There is aliasing that is produced from the undersampling of k-space that is used for parallel imaging (Deshmane et al. 2012). Sense reconstruction relies on the aliased images for reconstruction and the GRAPPA type reconstruction relies on reconstructing the missing data in k-space. Residual aliasing can be identified as ghosts inside or outside the object being imaged. On the other hand noise enhancement makes the image appear grainy and is often nonuniform (Deshmane et al. 2012).

7.4 Field of View Wrap

One of the more problematic issues with pulmonary MRA is wrap from the arms down by the patient's sides folding over into the field of view. While a larger field of view (FOV) can be employed to prevent this problem, this strategy will prolong the acquisition time. In most pulmonary MRA exams, there is some wrap from the undersampling of k-space. The use of sagittal slice excitation or having the patient hold their arms over their heads can help to limit this problem.

7.5 Fontan and Glenn Shunts

The post-surgical venous connections of the Glenn and Fontan shunts can mimic pulmonary embolism on those acquisitions acquired during the pulmonary arterial bolus (dextrophase). This can be very confusing and is an issue for CTA, MRA, and nuclear medicine ventilation/perfusion exams (Chow et al. 2001). When one of the pulmonary arteries receives blood primarily from one of the vena cavas after Glenn or Fontan sur-

gery, there is the likelihood that injection of contrast material will only go into that caval connection's corresponding pulmonary artery. These cases look like a large PE in one of the main pulmonary arteries, but on the delayed images, these fill in normally. Some centers are working to model these flow patterns with computational fluid dynamics, 4D flow and 3D printing. The flow modeling of these patient's venous-pulmonary arterial connections can help to plan the surgical revision of these shunts. It is well known that when there is poor mixing of the IVC blood with the SVC blood small peripheral arteriovenous malformations develop in the lung (Ashrafian and Swan 2002).

8 Clinical Applications

8.1 MRA for the Primary Diagnosis of Acute Pulmonary Embolism: UW-Madison Experience

We started doing MRA for the primary diagnosis of pulmonary embolism from the Emergency Department (Fig. 6) after the success visualizing the artery of Adamkiewicz with MRA (Bley et al. 2010). This method was modified and relied on
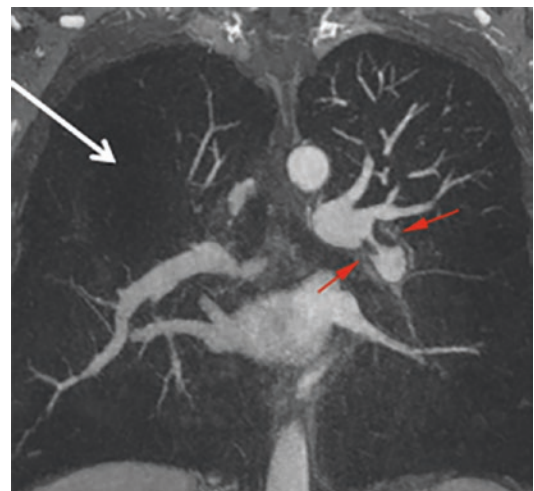

Fig. 6 MRA of a PE (*red arrows*), and a perfusion defect is also shown by the *white arrow* in the right upper lobe (Case courtesy of Dr. J. Paul Finn, UCLA Medical Center)

the availability of a 2D autocalibration method (ARC) for the center of k-space filling that was adapted to 3D MRA acquisitions (Brau et al. 2008; Lum et al. 2009). Table 1 shows the basic protocol description with special attention to the amount of time it takes to scan the patient. This protocol has less than 5 min of acquisition time needed which allows these studies to be added onto the busy MRI clinical schedule from the emergency department. Please note that in rare instances the patient may not be able to cooperate at all for breath hold acquisitions. In those cases, a free breathing strategy can be helpful to salvage the examination. In less than 1% of the cases, there is a complete failure and a follow-up CTA or nuclear medicine ventilation/perfusion examination needed. From our recent experience, MRA is best suited for stable patients with a low to intermediate risk of pulmonary embolism.

9 Patient Selection

9.1 Clinical Decision Rules

The routine use of clinical decision rules (CDRs) is important to limit the amount of overutilization of imaging testing for the diagnosis of PE (Rybicki et al. 2016). The use of the Wells' score, Geneva rule, or revised Geneva rule can be helpful to control the desire to image all chest pain and improve the rate of positive cases. Lucassen et al. have performed a meta-analysis on the efficacy of various pre-imaging CDRs for the prediction of pulmonary embolism (Lucassen et al. 2011). They found the following performance: (1) Wells' rule with a cutoff value <2, sensitivity 0.84; specificity 0.58, (2) Wells cutoff value ≤4, sensitivity 0.60; specificity 0.80, (3) the Geneva rule, sensitivity 0.84; specificity 0.50, and (4) the revised Geneva rule, sensitivity 0.91; specificity 0.37 (Lucassen et al. 2011). This group also repeated this study using a prospective cohort and found that the simplified Wells' rule with a cutoff value of 96% sensitive and 49% specific for the diagnosis of PE (Hendriksen et al. 2015). The problem with CDRs is that there is still at least a 2% incidence of PE found on CTA in patients that are considered to be of low risk (Dentali et al. 2006).

9.2 The Ideal Patient

The ideal patient for pulmonary MRA is younger than 50 years old, able to hold his/her breath for more than 13 s and to follow verbal commands (Table 2). The short-term follow-up of younger patients with known pulmonary embolism on

Table 2 Optimal patient selection for CE-MRA versus CTA for the primary diagnosis of pulmonary embolism depends on patient age, ability to cooperate, and the renal function

Patient presentation	CE-MRA	CTA
Young female (<30 years of age)	Yes	Ok
Pediatric Patients	Yes	Ok
Known PE follow-up	Yes	Ok
Renal failure not on dialysis (30 < eGFR < 60)	Yes (ferumoxytol or gadobenate dimeglumine)	No
Renal failure on dialysis	Yes—ferumoxytol	Yes
Pregnancy	Perhaps—ferumoxytol or non-CE-MRA	Yes
Very dyspneic	Ok—heavily averaged exam	Yes
Allergy to Iodinated contrast material	Yes	Ok—needs premedication
Anaphylaxis to Iodinated contrast material	Yes	Not recommended
Pacemaker and implantable defibrillators	Ok—needs to be turned off by cardiology	Yes
CTEPH	Yes	Yes

The utility of MRA and CTA is demonstrated in this table for various patient scenarios

prior CTA is also a good indication for the use of pulmonary MRA (Kluge et al. 2005; Stein et al. 2016). This helps to minimize the potential effects of medical radiation induced malignancy (Brenner 2014). For patients with renal failure or borderline renal function CE-MRA can also be considered as an alternative to CTA. The use of a GBCA in patients with compromised renal function has recently been shown to be safe, without evidence for the induction of nephrogenic fibrosis (Soulez et al. 2015). The use of ferumoxytol can also be helpful in these instances (Hope et al. 2015). For those patients that have an iodinated contrast allergy, CE-MRA and NM V/Q scanning should be considered to be suitable alternatives to premedication of the patient prior to a CTA (Ersoy et al. 2007).

10   MRA Efficacy for PE: the Good, the Bad, and the Ugly

Twenty-five years ago contrast-enhanced pulmonary magnetic resonance angiography (CE-MRA) was found to be a promising new research modality for the detection of PE (Grist et al. 1993; Meaney and Prince 1999a, b; Meaney et al. 1997; Schiebler et al. 1993). Since then a number of investigators have worked tirelessly to determine whether or not this modality could achieve a similar sensitivity and specificity as other recognized imaging studies for this clotting disorder (Table 3) (Blum et al. 2005; Ersoy et al. 2007; Gefter et al. 1993, 1995; Grist et al. 1993; Gupta et al. 1999; Kluge et al. 2006a, b, c; Meaney et al. 1997; Ohno et al. 2004; Oudkerk et al. 2002; Pleszewski et al. 2006; Revel et al. 2012; Schiebler et al. 1993; Stein et al. 2010; Goodman et al. 2000). After the fine work by Martine Remy-Jardin and colleagues CTA was established as the new gold standard imaging test for the presence of pulmonary embolism (Remy-Jardin et al. 1996) Mayo et al. 1997) and used to evaluate the efficacy of each incremental gain in MRA methodologies

for the primary diagnosis of PE. The largest, best, and probably the last funded efficacy study comparing MRA to CTA for PE was PIOPED III (Stein et al. 2010). This prospective study compared MRA exams performed after a CTA exam in patients with possible pulmonary embolism. This showed that MRA was difficult to perform well with an aggregate technical failure rate of 25% (range of 11–51%). The technical success rate at expert academic centers in the PIOPED network was 50%, and the sensitivity of MRA for PE was modest (80%). On the positive side, the PIOPED investigators did find a very high specificity (99%) (Table 4).

10.1   MRA and MRV Methods

Pulmonary MRA can easily be performed at either 1.5 T or 3 T. The image quality is better at 3 T; however the motion artifacts are also more significant. If the patient is dyspneic, there are a series of interventions that are available to ensure good image quality (see above). MRV can be used to reliably quantify the amount of deep venous thrombus (DVT) (Mani et al. 2015). Thus, MRV is able to quantify the response of DVT to thrombolytic agents and long-term anticoagulation.

11   Post-processing

Subtraction of pre- and post-pulmonary MRA images is not recommended, as there is too much misregistration between breath hold acquisitions and the pre-contrast mask to allow for any meaningful subtraction image. Maximum intensity projection images (MIP) and multiplanar reconstructions (MPR) are helpful supplements of the MRA images. Volume rendering (VR) can also be useful for demonstration purposes and scientific presentations. This is particularly true if a vascular malformation is being shown to an audience, as the VR images are most similar to standard angiography.

Table 3 Patient-based efficacy of MRA for acute pulmonary embolism: use of CTA as the gold standard for the determination of test accuracy, sensitivity, specificity, PPV, and NPV

Publication	Test	Total patients (% diagnostic)	Accuracy% (TP + TN/total) (95%; C.I.) [prevalence]	Sensitivity% (TP/TP + FN) [95%; C.I.]	Specificity% (TN/TN + FP) [95%; C.I.]	PPV% (TP/TP + FP) [95%; C.I.]	NPV% (TN/ TN + FN) [95%; C.I.]
Grist et al. (1993)	MRA	14	78% (11/14) [42%]	100% (6/6)	63% (5/8)	66% (6/9)	100% (5/5)
Schiebler et al. (1993)	MRA	18 (100%)	– – [77%]	85%	–	–	–
Kalb et al. (2012)	MRA	22		55%	95%		
	FISP	22		67%	100%		
	3D GRE	22		73%	100%		
	All 3	22		84%	100%		
Stein et al. (2010)	MRA	371 (75%)	93% (260/279) [28%]	78% (59/76) [67–86]	99% (201/203) [96–100]	97% (59/61) [91–98]	92% (201/218) [82–97]
Stein et al. (2010)	MRA and MRV	370 [48%]	94% (166/176) [28%]	92% (65/71) [83–97]	96% (101/105) [91–99]	94% (65/69) [74–98]	94% (101/107) [92–99]
Revel et al. (2012)	MRA	274 [72%]	92% (182/198) [37.5%]	84.5% (71/84) [75–91]	99.1% (111/112) [95–100]	98.6% (71/72) [93–100]	89.5% (111/124) [83–94]
Kluge et al. (2006c)	MRA	62 87%	94% (51/54) [30%]	81% (13/16)	100% (38/38)	100% (13/13)	93% (38/41)
Ersoy et al. (2007)	MRA	27 100%	96% (26/27) [15.4%]	100% (4/4)	95% (22/23)	80% (4/5)	100% 22/22
Pleszewski et al. (2006)	MRA	48 100%	95% (46/48) [23%]	82% (9/11)	100% (37/37)	100% (9/9)	95% (37/39)
Blum et al. (2005)	MRA	89 100%	77% (69/89) [71%]	71% (44/62) (60–82)	92% (25/27) (82–100)	96% (44/46) (90–100)	58% (25/43) (42–72)
Ohno et al. (2004)	MRA	48 100%	94% 45/48 [25%]	92% 11/12	94% 34/36	85% 11/13	97% 34/35
Meaney et al. (1997)	MRA	30	100% (30/30) [26%]	100% (8/8)	95% (21/22)	89% (8/9)	100% (21/21)
Oudkerk et al. (2002)	MRA	128 92%	91% [30%]	77% [61–90]	98 [92–100]	93% [78–99]	91% [83–96]
Gupta et al. (1999)	MRA	36	92% (33/36) [36.1%]	85% (11/13) [64–98]	96% (22/23) [85–100]	92% (11/12) [74–100]	92% (22/24) [83–100]
Zhang et al. (2013)	MRA	27 100%	100% (27/27) [89%]	100% (24/24)	100% (3/3)	100% (24/24)	100% (3/3)

Table 4 Direct comparison of PIOPED III and UW-Madison Methodologies, protocols, and results

Study parameter	PIOPED III	UW-Madison experience
Protocol implementation date	May 1, 2007	April 1, 2008
Efficacy trial	Yes	No
Effectiveness trial	No	Yes
Prospective multicenter	Yes	No
Randomized	No	No
Multiple readers of MRA after index study reached consensus	Yes	No
MRA was index study	No	Yes
MRA results determined patient treatment	No	Yes
MR venography	Sometimes (194/371)	No
Central readers (at least 2)	Yes	No
Range of reader MRA experience (years)	unknown	5–30 years
Reference tests used for the determination of test efficacy	CTA; Normal V/Q lung scan; Low probability V/Q lung scan; Low clinical probability Wells criteria, and negative venous ultrasound Negative pulmonary DSA	Not applicable
Outcome variable used	Not applicable	All-cause mortality, minor or major hemorrhage, venous thromboembolism
Follow-up period	3 months (Telephone call) 6 months (Telephone call if eGFR 60–90)	6 months Electronic medical record review
Number of cases analyzed	371	675
Number lost to follow-up or excluded	Not applicable	58
Number of cases included	371	617
CTA reference test (+)	102	Not applicable
CTA reference test (−)	166	Not applicable
No CTA performed	8	Not applicable
Percentage of (+) PE exams	28% (104/371)[a]	8.2% (46/617)
Death over 6 months F/U	No recorded adverse events[b]	16
Technically limited exams	24.8% (92/371)	7.5% (54/617)
Sensitivity	45–100	93.8%
Specificity	95–100	100%
Positive predictive value	96.6%	100%
Negative predictive value	92.2%	99.4%
MRA methods		
Field strength (T)	1.5 and 3.0	1.5
Hardware vendors	Multiple	Single
Field of view	40 (fixed)	18–45 (to fit the patient)
Slice acquisition plane	Coronal	Sagittal
Interpolated resolution (mm^3) (2 × zero filling of k-space)	SI 0.5 × RL 0.7 × AP 1.5	SI 0.7 × RL 0.7 × AP 1.0
Number of slices	44 (88)	140–160
Number of signal averages	One	One

Table 4 (continued)

Study parameter	PIOPED III	UW-Madison experience
Contrast agent and dose (mmol/kg)	Gadobenate dimeglumine (Multihance™) 0.1–0.2	Gadobenate dimeglumine (Multihance™) 0.1
Minimum eGFR (ml/min)	60	none
Test bolus	Yes (1–2 ml)	No
Real time bolus tracking	No	Yes
Bolus injection rate (ml/s)	2	1.5
Normal saline flush (ml)	15	30
Contrast dilution	No	Bring up to a total volume of 30 ml with normal saline
Type of Pulse sequence	3D gradient recalled echo	3D T1 weighted fat saturated spoiled gradient recalled echo
Time to repetition (TR)	≤6.6 ms	2.9 ms
Time to echo (TE)	≤2.3 ms	1.0 ms
Number of surface coils	6–12	8
Parallel imaging factor	Varied depending on size of patient	3.6
MRA acquisitions	Six	Three
Flip angle for primary and delay # 1 MRA	20–35°	28°
Flip angle for delay # 2 MRA	20–35°	15° (lower)
Bandwidth (kHz/pixel)	±38–150	±88
Breath hold length (s)	14–22	15–21
Respiratory phase	Full inspiration	variable

[a]This was an enriched population of subjects and not a sequential enrollment of all qualifying patients. In other words this was not a real world accrual of patients with symptoms suspicious for pulmonary embolism
[b]An important shortfall in the methodologyused for PIOPED III was the lack of attention to the all-cause mortality at six months for their subject population

12 Recent Improvements of Pulmonary MRA

In the PIOPED III trial, MRA still fell short of meeting any of the critical efficacy goals that would have ensured meaningful adoption of this new technology, despite many efforts. However, since the closure of PIOPED III the MRA acquisition methods have improved substantially. There have been changes in the use of multi-coil technology, parallel imaging, bolus strategies, injection rates and duration, use of autocalibration of k-space strategy (Brau et al. 2008), and the use of a combination of pulse sequences for the total exam. Table 4 highlights the similarities and differences between the current UW-Madison and PIOPED III methods. Thus, a modern strategy does not just rely on a single acquisition in the dextroarterial bolus phase (Brau et al. 2008; Ohno et al. 2004). In addition, physician experience level, familiarity with

MRA artifacts, technologist training, and making pulmonary MRA a frequently performed examination help to improve the technical success rate for this study (Nagle et al. 2016). While CE-MRA of the pulmonary arteries is not a perfect test, we have learned from our experience and the shortcomings of the PIOPED III trial to make this test work effectively.

In a prospective efficacy trial the combination of MRA, MR perfusion, and 3D gradient echo imaging pulse sequences was shown to improve the sensitivity and specificity of MRI for the detection of PE (Kalb et al. 2012). Using CTA as the gold standard for comparison of test efficacy, they found a sensitivity of 55% for MRA, 67% for triggered true FISP, and 73% for 3D GRE MRI. The combination of all three pulse sequences improved the sensitivity to 84% (Kalb et al. 2012). Ohno et al. (2010) also used perfusion MRA to help with the diagnosis of PE (Ohno et al. 2010). They also

generated estimates of pulmonary blood flow (PBF), pulmonary blood volume (PBV), and mean transit time (MMT) maps from the perfusion MRA data; they found that the pulmonary blood volume was the most accurate parameter for determining patient outcomes (Ohno et al. 2010). This is an interesting result in that the lung perfused blood volume is a proxy for how much gas exchange is still available after pulmonary embolism. It takes into account the amount of diseased lung as well as that portion of the pulmonary arterial circulation that is still patent. This measure was of more importance than any of obstruction indices and was more closely related to survival than the RV/LV index (Ohno et al. 2010).

13   MRA Characteristics of Pulmonary Emboli

13.1   Direct Findings

The direct findings of pulmonary embolism at MRA are very similar to what one would expect from a contrast-enhanced cross-sectional imaging exam (Table 5). Our experience mirrors that of the extensive CTA literature in this area and extends knowledge regarding these direct findings based on the multiparametric features of MRA exams (Kluge et al. 2006b, c, 2004;

Wittram et al. 2004). These direct findings are as follows: The most obvious of these findings is visualization of the **(A) occlusive PE—** these present as low signal intensity clot completely obstructing the pulmonary artery (the average clot to vessel signal intensity ratio is 0.26 ± 0.23 S.D.) (Fig. 7). In 60 of our positive MRA PE studies we found totally occlusive clots in 33% of the cases (20/60 occlusive clot); these occlusive clots are a cause of the well-known angiographic finding of **(B) vessel "cutoff"** seen on the MIP images of the MRA (11/60 vessel cutoff); the embolus may also be nonocclusive and be either centrally located or **(C) eccentrically located PE** with respect to the vessel centerline (40/60 nonocclusive clot) (Fig. 8). Only on MRI is the finding of two low signal intensity lumens side-by-side, named the **(D) double bronchus sign** (20/60 cases of the double bronchus sign) (Fig. 9). The double bronchus sign is caused by the low signal intensity clot completely obstructing a pulmonary artery that is always next to a bronchus, which is also of low signal intensity; **(E) chronic clots/webs** from CTEPH tend to be more eccentrically located as a rule, but some patients with a single PE can also have this configuration as the clot resolves (Fig. 8b); **(F)** the **bright central dot** is a reverse Gibbs' truncation artifact in the center of emboli of a certain size. Gibbs' artifact in a ves-

Table 5 Comparison of the direct findings of pulmonary embolism found at CTA and MRA and the underlying mechanism responsible for their imaging appearances

Mechanism for imaging appearance	CTA	MRA
Filling defect within the pulmonary artery after contrast enhancement	Nonocclusive filling defect	Nonocclusive filling defect
Vessel completely obstructed and amputated on angiographic projection images	Vessel cutoff	Vessel cutoff not visible if vessel too small
Methemoglobin in PE	Not applicable	High signal intensity T1 of PE
Obstructing PE with its adjacent bronchus	Not named	"Double bronchus" sign
Imbibition of Contrast by dissolving clot	Webs	Web and the "Chameleon" clot
Gibbs' truncation artifact	Not applicable	High signal intensity dot within clot
Chronic clot with eccentric effacement of pulmonary artery wall after contrast enhancement	Pulmonary artery wall irregularity	Pulmonary artery wall irregularity
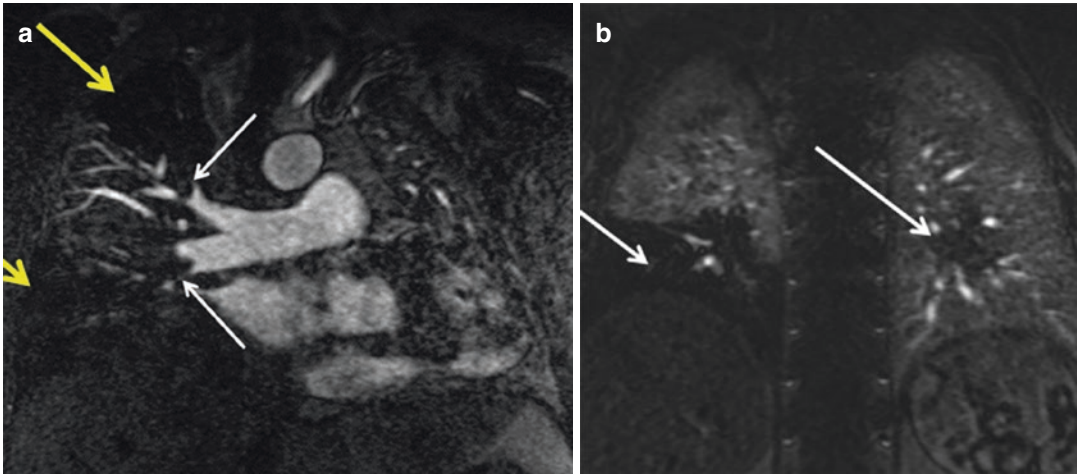
Fig. 7 (**a**) Occlusive PE are shown in the right upper and-interlobar arteries (*white arrows*) and their corresponding perfusion defects (*yellow arrows*). (**b**) Perfusion defects in the right lower and left lower lobes from pulmonary embolism (*arrows*)
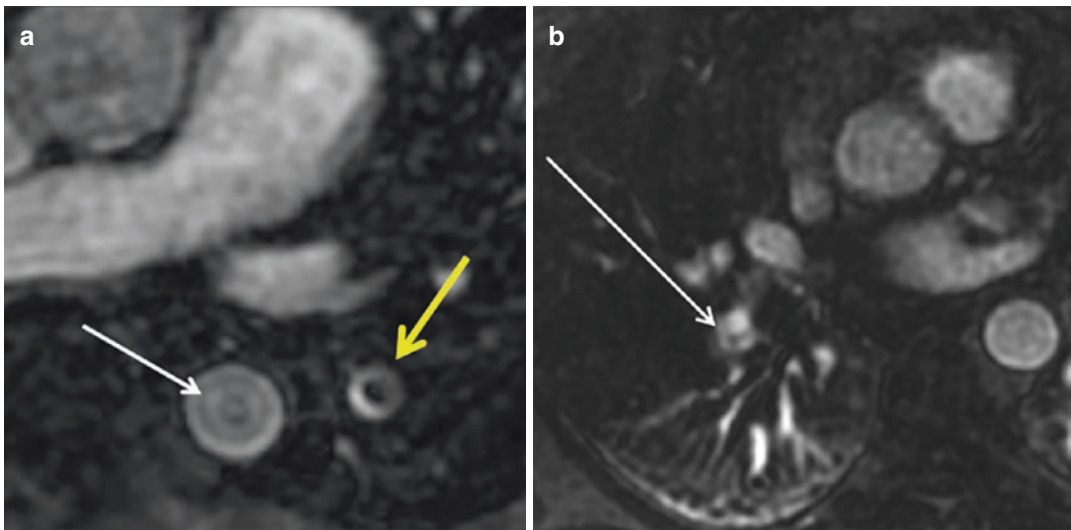

Fig. 8 (**a**) Nonocclusive PE shown in the left lower lobe (*yellow arrow*) and the Gibbs' truncation (ringing) artifact is shown in the aorta (*white arrow*). (**b**) Chronic pulmonary embolism web (*white arrow*) in the right lower lobe pulmonary artery

sel without PE will not have a bright dot centrally, so this is one of the key distinguishing features between an embolus and the Gibbs' artifact (Fig. 10). On occasion there are (**G**) higher signal intensity emboli seen; we have termed these **"Chameleon Clots."** These are defined by the fact that these PE become of higher signal intensity on the post-contrast MRA images than would normally be expected for an embolus. We suspect that the reason for this is that there are different ages of emboli within the pulmonary arterial tree. As pulmonary emboli age they tend to fragment, get smaller and eccentric, and as the webs of fibrin are surrounded by the contrast agent. These types of PE at MRA may not show the 50% loss of signal intensity that is found with PE using the Bannas method, because they have lost their
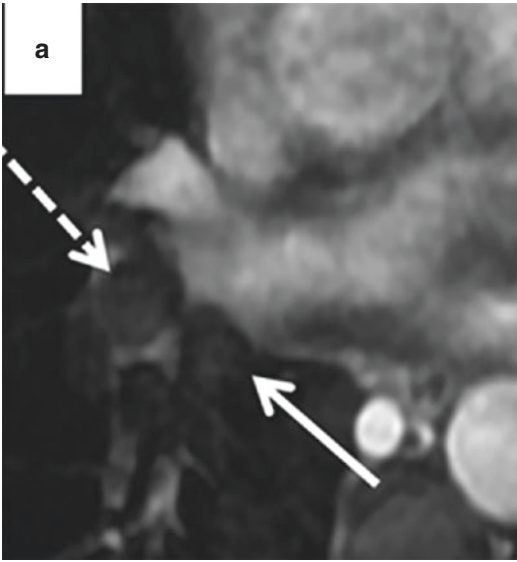
Fig. 9 Double bronchus sign is shown in this spoiled gradient echo image of an occlusive PE in the right lower lobe pulmonary artery (*dashed arrow*) and in the right interlobar bronchus (*solid arrow*). This is a direct sign of PE on MRA. (**a**) Right lung
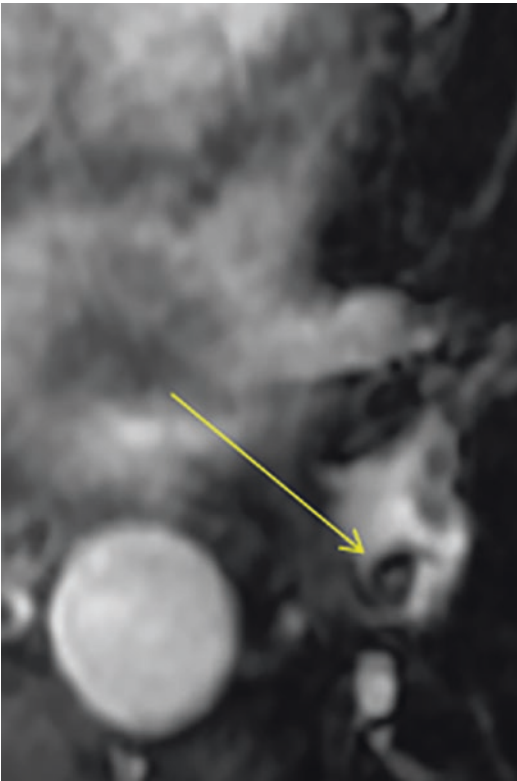
Fig. 10 Bright central dot seen in reverse Gibbs' truncation artifact of pulmonary embolism

normal low signal intensity due to the imbibition of GBCA. As the clot lyses, there are more spaces for contrast to enter it. This is only seen in the follow-up CE-MRAs of patients on anticoagulation for known VTE. The end stage of this process is a web. These chameleon clots may be indistinguishable from Gibbs' artifact at MRA. In these cases, a CTA is needed to solve the problem. Another feature of PE on MRA exams is that occasionally the PE has a **(H) high T1 weighted signal intensity embolus** (Fig. 11) on the pre-contrast MRA T1 weighted images. This is because there is enough methemoglobin to shorten the T1 (Gomori and Grossman 1988) of the embolus and observed on the pre-contrast examination. While the high T1 signal intensity from methemoglobin within the clot is better seen in the head, occasionally it can also be seen in the body as well, and may be occasionally seen on the pre-contrast MRA exams used for field of view calibration (5/60 high T1W signal intensity clot). Multiparametric MRI of ex vivo human clots and emboli (Vidmar et al. 2015) exhibits some unique apparent diffusion coefficient (ADC) T1, T2, and T2* features of thrombi as they age. Of interest for the radiologist is that the ADC and T2 are sufficiently different for the red cell and platelet rich portions of the thrombus compared to the fibrin rich portion of thrombi. These could potentially be used in vivo for characterization of clot age. Not all emboli are related to thrombi. As Bach et al. have shown man made materials can be filtered out by the lungs as well and sometimes be mistaken for pulmonary embolism (Bach et al. 2013).

13.1.1 Direct Binding of Fibrin by Molecular Imaging Agents

A novel agent (^{64}Cu-FBP8) that binds fibrin can also be chemically bound to gadolinium or a radioactive isotope (Blasi et al. 2014, 2015a, b; Oliveira et al. 2015; Overoye-Chan et al. 2008). It is now undergoing testing in animals and will soon have a human trial started. The interesting feature of this agent is being able to identify areas of active fibrin formation and chronic fibrin in clots. The resolution of this agent (how
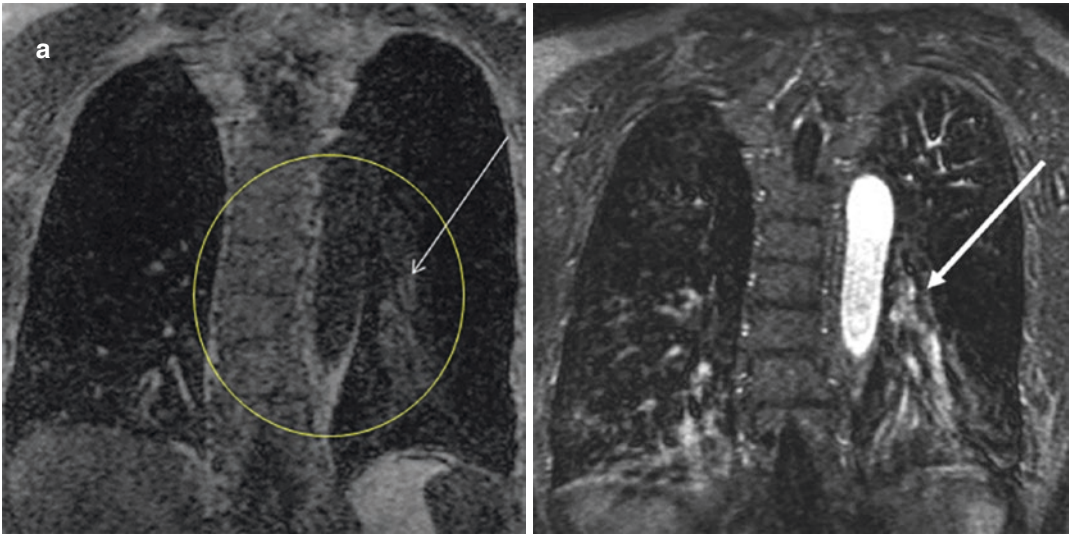
Fig. 11 (**a**) High T1W signal of pulmonary embolism in the left lower lobe (*white arrow*), (**b**) confirmed on the CE-MRA images

small of a clot can be found) depends on the tracer used, its activity/relaxivity, and the inherent detector sensitivity/resolution of the imaging device employed to image it. Recently, with the introduction of PET/MR instruments for humans use, the simultaneous MRI and PET imaging of pulmonary emboli and their reservoir in the systemic venous system has now become possible (Uppal et al. 2011). Non-invasive real-time imaging of the effectiveness of thrombolytic therapy may also be possible using this technology. It may be interesting to use such imaging biomarkers for the personalization of thrombolytic and anticoagulation therapy.

13.1.2 Pitfalls and Mimics in the MRA Diagnosis of PE

It is more difficult to find pulmonary emboli on MRA exams than on CTA examinations because the perceptual event has a lower intrinsic signal for the observer to find. In the case of an occlusive embolus, there is low signal intensity thrombus filling the pulmonary arterial lumen surrounded by lung that is of a similar degree of low signal intensity. We have termed this situation as a "black on black" event (Table 6). There is nothing to see but the absence of where a vessel should be. Therefore, the first pitfall is simply

that the vessel involved is too small to find/observe because it is occluded. Hence the problem of why MRA exams have lower sensitivity for PE, particularly in the subsegmental vessels (Stein et al. 2010).

There are also mimics of pulmonary embolism at MRA (Table 6). The most common MRA pitfall is the central vessel low signal intensity from the Gibbs' truncation artifact (Bannas et al. 2014). This is differentiated from a true embolus by its location and signal intensity. Another common pitfall is "transient interruption of the bolus." Breathing just before the exam suddenly lowers the intrathoracic pressure and causes a rapid inflow of unopacified blood from the inferior vena cava that destroys the opacification of the pulmonary arteries coming from the superior vena cava (upper extremity injection). Primary and secondary malignancy can also cause intraluminal defects seen at MRA (Attina et al. 2013). These may be suspected in the appropriate clinical scenario. Primary pulmonary artery sarcoma is rare, often centrally located, has a frond-like interface with the lumen, may invade the pulmonary artery wall, and will not improve after thrombolytic therapy or anticoagulation (Attina et al. 2013). Secondary malignancies can embolize to the lung and be a cause of intrapulmonary arterial metastatic disease. While this can

Table 6 The pitfalls in interpretation of pulmonary emboli are discussed along with their underlying etiology

	CTA	MRA
Poor bolus	Variable density	Variable signal intensity
Fontan shunt baffle	Complete lack of contrast within one of the pulmonary arteries	Complete lack of contrast within one of the pulmonary arteries
Incomplete mixing	Right ventricle will have a variegated appearance	Right ventricle may have a variegated appearance but this is uncommon given the 15+ s acquisitions
Transient interruption of the bolus during inspiration	Normal contrast in SVC and aorta but very little in the pulmonary arteries	Normal contrast in SVC and aorta but very little in the pulmonary arteries
Gibbs' truncation artifact	Not applicable	Very common area of central low signal intensity with the lower lobe arteries
Volume averaging	Can cause low density within a subsegmental vessel	Less of an issue given the three separate acquisitions
Motion artifact	Common problem in the left lower lobe adjacent to the heart	Smoothing of the pulmonary arteries adjacent to the heart without a significant limitation for interpretation
Primary pulmonary artery sarcoma	Large irregular intra-arterial mass with multiple fronds of tissue that does not resolve after thrombolytic therapy and is PET (+)	Large irregular intra-arterial mass with enhancement and ADC different from thrombus
Intrapulmonary hematogenous spread of metastatic disease	Can be indistinguishable from PE	Can be indistinguishable from PE

occur with any malignancy, renal cell cancer is the most common (Restrepo et al. 2012).

13.2 Indirect Findings

There are a number of secondary imaging findings that are associated with pulmonary embolism that are well known from the CTA literature and some additional findings that are only found on MRA exams (He et al. 2006), In our own experience of 60 MRA (+) of pulmonary embolism we found the following distribution of indirect findings: (a) perfusion defect in 71% (43/60). There is also the issue of (b) 20/60 pulmonary venous stasis. This finding is related to differential venous return in the lobes affected by PE wherein the transit time is increased when compared with the normal adjacent vein. The signal intensity of the vein in the affected lobe will be either higher or lower than its adjacent venous comparison. This difference is dependent on

when the peak of the bolus reaches each one of the veins. Frequently, for the first time point of the MRA exam (bolus phase), this finding is reflected as an increase in the signal intensity of those lobes with PE that have diminished flow in and out of them. We have also found (c) 15/60 high T2W signal intensity pulmonary infarctions and (d) (13/60) pleural effusions. (e) The wall of the vessel has also been observed to enhance after contrast (8/60) or (f) the parietal pleura (6/60). A few cases (g) (6/60) exhibit atelectasis, and rarely we have found (h) (3/60) enhancing pleural effusions.

13.2.1 Follow-Up of Known Pulmonary Embolism

One of the unsung uses of pulmonary MRA is in the follow-up of known pulmonary embolism (Kluge et al. 2005). Skeptics of using MRA as a first-line test should be willing to try this imaging exam lacking ionizing radiation for follow-up of known disease under treatment to determine if

the emboli are smaller or if new emboli have occurred. In a review of 600 patients with CTA evidence of PE, at least one follow-up exam was performed in 141 of 600 patients (23.5 %), with two follow-up exams in 1 year found in 40/600 (6.7%) (Stein et al. 2016). Since a number of these cases were in young women, they conclude that the use of *alternative imaging modalities* would be useful for young women with known pulmonary embolism (Todua et al. 2016).

13.3 Ancillary Findings

One of the concerns regarding the use of pulmonary MRA as a primary examination for non-STEMI chest pain is that this modality will not be able to find the cause of pain as well as CTA (Richman et al. 2004), particularly if the cause is related to a primary pulmonary parenchymal process (Stein et al. 2011a; Wittram et al. 2004). While it is true that the traditional MRA pulse sequences using gradient echo imaging do not show lung parenchymal detail well, the full protocol for an MRA chest also includes Fast Spin Echo pulse sequences as well as post-gadolinium fat-subtracted pulse sequences that can be employed to troubleshoot any contemporaneous lung pathology. In addition, the use of contrast enhancement means that inflammation and cancer will be nicely shown on the MRA pulse sequences as high signal intensity regions within the lung parenchyma. Our own experience with ancillary findings when using pulmonary MRA as a primary imaging modality for the diagnosis of pulmonary embolism confirms that almost all critical tissues in the chest are well evaluated with MRI; these include the following: mediastinal compartments, lymphadenopathy, bone pathology, thoracic spinal cord, lung masses, pneumonia, pulmonary infarcts, areas of decreased pulmonary perfusion, cardiac chamber enlargement, pericardial effusion, pericarditis, pleural effusions, atelectasis, pleural-based and chest wall masses, liver masses and cysts, renal masses and pyelonephritis, splenic masses, adrenal masses, gallstones, cholecystitis, sternal
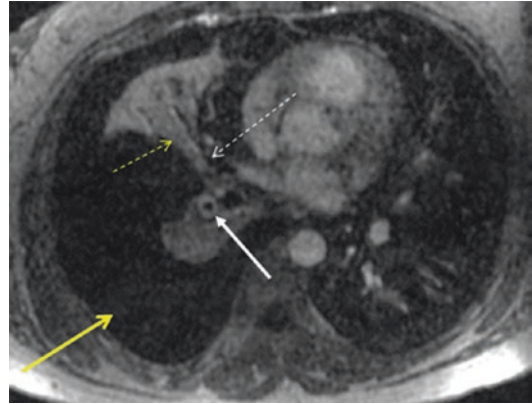
Fig. 12 Right pleural effusion (*yellow arrow*), nonocclusive embolus (*white arrow*), and the right middle lobe medial segment paired bronchus (*dashed white arrow*) adjacent to its pulmonary artery (*dashed yellow arrow*)
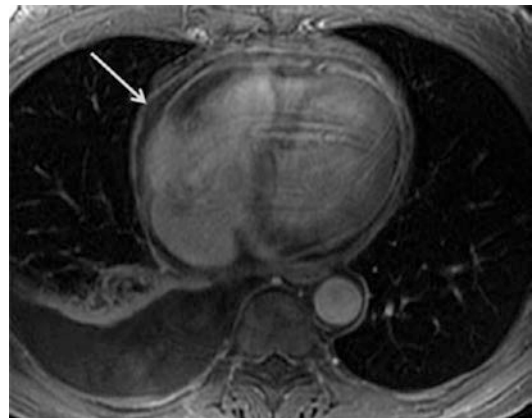
Fig. 13 Pericarditis (*white arrow*) is shown on this fat saturated spoiled gradient echo image. The visceral and parietal (*arrow*) pericardial surfaces are enhancing in this individual with malignancy

osteomyelitis, rib fractures, costochondritis (Figs. 12, 13, and 14) (Richman et al. 2004; Schiebler et al. 2016b). We have found that the percentage of actionable findings reported on final MRA examinations of the chest was similar to the percentage reported for CTA in the same clinical scenario (Richman et al. 2004; Schiebler et al. 2016b). One of the added benefits of MRA of the chest, with respect to ancillary findings, is the larger craniocaudal field of view than CTA. This allows for more coverage of the upper
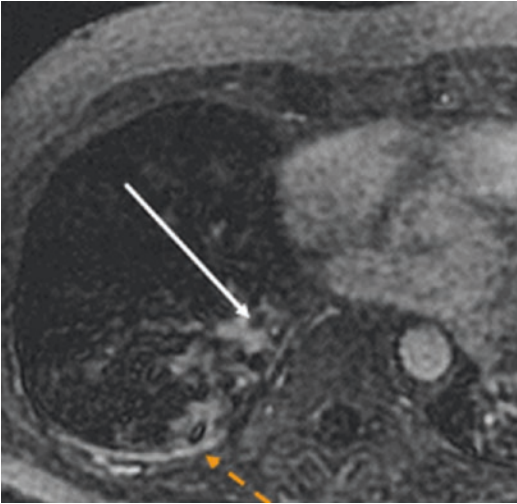
Fig. 14 Pulmonary infarct shown as high signal intensity debris in the lung parenchyma surrounding a pulmonary embolus (*arrow*). Note the enhancing parietal pleural surface (*yellow arrow*). The irritation of the parietal pleura by the hemorrhage of the pulmonary infarct is what initiates the symptom of chest pain for a patient presenting with pulmonary embolism
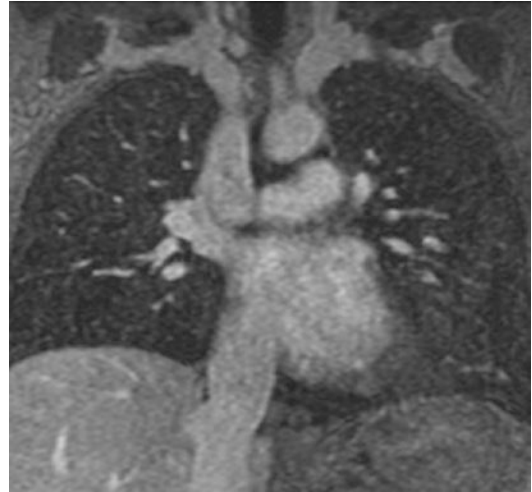

Fig. 15 Pneumomediastinum on coronal contrast-enhanced MRA is of low signal intensity and mimics fluid in the pericardial space

abdomen and the cervicothoracic junction with MRA; thus any pathologies involving those areas are also included as part of the exam. This is particularly helpful in the situation of venous catheter related fibrin sheaths and acquired upper extremity thrombosis which is not well identified on routine CTA.

The Achilles heel for MRA of the chest is collections of air. We have found that small pneumothoraces and/or a pneumomediastinum can be difficult to observe if the radiologist is not specifically looking for these pathologies (Fig. 15). The lung parenchyma is of low signal intensity as are the pneumothoraces and areas of pneumomediastinum. Often these are on the chest x-ray performed before the MRA, and thus are not an issue for patient care. Sometimes however these are found on follow-up CTA examinations. The presence of emphysematous blebs, paraseptal emphysema, and centrilobular emphysema is difficult to observe on standard MRA exams. There is likely a role for MRI using ultrashort time to echo (UTE) imaging for these disorders (Johnson et al. 2013; Ohno et al. 2014; Roach et al. 2016).

14 MRA Effectiveness for PE

In our studies of MRA test effectiveness for PE, the outcome metric used was interval venous thromboembolism (VTE). This follow-up metric has been used for years in the CTA and nuclear medicine literature for ventilation/perfusion scans to show test effectiveness in this specific clinical setting. These CTA effectiveness studies (Table 7) show that on average the likelihood for an interval VTE, after a negative CTA, is about 1% (Ferretti et al. 1997; Garg et al. 1999; Goodman 2000; Lomis et al. 1999; Mayo et al. 1997; Nilsson et al. 2002; Ost et al. 2001; Tillie-Leblond et al. 2002; van Belle et al. 2006). In addition to evaluating for venous thromboembolism as the outcome metric, some studies have also used the presence of all-cause mortality, hemorrhage requiring transfusion of at least 2 units of packed cells and/or significant bleeding requiring hospitalization. We have recently reported our experience in 563 patients (Schiebler et al. 2016a) and show that there are very good outcomes, as good as those for CTA, using pulmonary MRA as a primary test for the diagnosis of PE.

The confounding issue of the excellent patient outcomes (test effectiveness) found in patients after the primary use of MRA for the detection

Table 7 Meta-analysis of MRA for the diagnosis of acute pulmonary embolism—combining both efficacy and effectiveness studies (Zhou et al. 2015)

Sub-study classifier	Number of publications	Sensitivity 95% CI	Specificity 95% CI
High quality studies	3 studies	96% (85–100%)	96% (86–100%)
Low quality studies	10 studies	72% (67–77%)	79% (76–82%)
Publication date <2004	5 studies	90% (80–90%)	92% (85–97%)
Publication date 2004–2009	5 studies	82% (73–88%)	96% (91–98%)
Publication date ≥2010	3 studies	67% (60–73%)	72% (67–76%)
Gadopentetate dimeglumine	3 studies	95% (84–99%)	98% (91–100%)
Gadodiamide	2 studies	74% (62–83%)	94% (83–99%)
Gadodiamide hydrate	1 study	92% (N.A.)	94% (N.A.)

of PE is difficult to explain because the known efficacy for MRA is so much lower than CTA (Schiebler et al. 2016a, 2013; Stein et al. 2010; Li et al. 2016). This is essentially a "performance gap" wherein the outcomes are better than would have initially been expected based solely on the sensitivity and specificity of MRA for the primary detection of PE, and simply it might be too early to make any informed judgment about this issue. In addition, MRA might be preferentially used in younger persons that are healthier than the CTA population for this disorder. Also, the presence of subsegmental PE (SSPE) emboli, which are difficult to find at MRA, may have little to no importance. In other words, these SSPE are not clinically significant, particularly for those with good cardiopulmonary reserve and normal underlying lung function. Perhaps CTA is finding too much disease. This is the concept of "over-diagnosis" wherein a test, in this case CTA, is finding PE that does not merit treatment, as the treatment has not affected the death rate from the disease (Burge et al. 2008; Sheh et al. 2012). However, a retrospective multi-center study demonstrated that any PE, even a small SSPE, is as problematic as larger PE and was found to have the same incidence of adverse events during follow-up (den Exter et al. 2013).

Otherwise, CTA exams may be "overcalling the presence of PE" by up to 50% (Hutchinson et al. 2015). Consensus reads by thoracic radiologists found most cases of erroneous PE diagnosis in the smaller vessels and that these errors were related to beam hardening artifact, motion, and volume averaging. Obviously, the current MRA protocol with better gradients, longer injection times, shorter time to echo, 3D acquisition strategy with autocalibration of the center of k-space (Brau et al. 2008), and near isotropic voxels is much more powerful than the one used in PIOPED III (see Table 4). As such, the leap in image quality could help to explain this performance gap and possibly a better efficacy of 3D MRA than was found in PIOPED III (Zhang et al. 2013). Overall, a multicenter prospective randomized trial comparing MRA and CTA for an age, sex, and Wells' score matched case control study is warranted to show whether this test can be safely used for the primary diagnosis/exclusion of PE.

The old adage is that, "all politics are local." In the translation of any new imaging method from the bench to the clinic there need to be champions ("cheerleaders") in radiology and clinical medicine to help jump start the program. There is also the need to explore the local

reimbursement for pulmonary MRA. Currently in the USA a pulmonary MRA for PE is not covered, whereas MR of the chest with contrast for other chest-related pathologies is, e.g., pleural effusion, pericardial effusion, pneumonia, mediastinal mass, and lung cancer. The reader is also referred to a recently published road map for successfully starting a pulmonary MRA program (Nagle et al. 2016).

Conclusion

We have demonstrated that pulmonary MRA is indeed a safe alternative test for the primary diagnosis of clinically significant pulmonary embolism. Radiologists should be comfortable knowing that the current hardware/software configurations of all MRI vendors are more than sufficient to perform this exam in almost all of their patients. In the specific situation of pulmonary MRA for acute PE, we started by comparing MRA to concurrent CTA and then evolved to using pulmonary MRA as an alternative to CTA for young women and those patients with iodinated contrast allergies. While our experience is very strong on the performance of MRA at one site, how this translates to implementation at multiple new sites, with the expected variation in reader experience, remains to be determined. The reason this book chapter is so detailed is that we want you, the reader, to be successful in performing and interpreting these exams for your patients.

References

Ashrafian H, Swan L (2002) The mechanism of formation of pulmonary arteriovenous malformations associated with the classic Glenn shunt (superior cavopulmonary anastomosis). Heart 88(6):639

Attina D, Niro F, Tchouante P, Mineo G, Russo V, Palazzini M, Galie N, Fanti S, Lovato L, Zompatori M (2013) Pulmonary artery intimal sarcoma. Problems in the differential diagnosis. Radiol Med 118(8):1259–1268

Bach AG, Restrepo CS, Abbas J, Villanueva A, Lorenzo Dus MJ, Schöpf R, Imanaka H, Lehmkuhl L, Tsang FH, Saad FF, Lau E, Rubio Alvarez J, Battal B, Behrmann C, Spielmann RP, Surov A (2013) Imaging of nonthrombotic pulmonary embolism: biological materials, nonbiological materials, and foreign bodies. Eur J Radiol 82(3):e120–e141

Bannas P, Bell LC, Johnson KM, Schiebler ML, François CJ, Motosugi U, Consigny D, Reeder SB, Nagle SK (2016) Pulmonary embolism detection with three-dimensional ultrashort echo time MR imaging: experimental study in canines. Radiology 278(2):413–421

Bannas P, Schiebler ML, Motosugi U, Francois CJ, Reeder SB, Nagle SK (2014) Pulmonary MRA: differentiation of pulmonary embolism from truncation artefact. Eur Radiol 24(8):1942–1949

Barger AV, Block WF, Toropov Y, Grist TM, Mistretta CA (2002) Time-resolved contrast-enhanced imaging with isotropic resolution and broad coverage using an undersampled 3D projection trajectory. Magn Reson Med 48(2):297–305

Barker AJ, Roldan-Alzate A, Entezari P, Shah SJ, Chesler NC, Wieben O, Markl M, Francois CJ (2015) Four-dimensional flow assessment of pulmonary artery flow and wall shear stress in adult pulmonary arterial hypertension: results from two institutions. Magn Reson Med 73(5):1904–1913

Bauml J, Schiebler ML, Francois CJ, Johnson KM, Nagle SK (2016) Comparison of traditional MRA and free-breathing UTE in comprehensive evaluation of the vascular and non-vascular anatomy of the chest in patients with suspected pulmonary embolism. ISMRM abstracts 2016 annual meeting (Singapore), 12 May 2016

Blaimer M, Breuer FA, Mueller M, Seiberlich N, Ebel D, Heidemann RM, Griswold MA, Jakob PM (2006) 2D-GRAPPA-operator for faster 3D parallel MRI. Magn Reson Med 56(6):1359–1364

Blasi F, Oliveira BL, Rietz TA, Rotile NJ, Day H, Looby RJ, Ay I, Caravan P (2014) Effect of chelate type and radioisotope on the imaging efficacy of 4 fibrin-specific PET probes. J Nucl Med 55(7):1157–1163

Blasi F, Oliveira BL, Rietz TA, Rotile NJ, Day H, Naha PC, Cormode DP, Izquierdo-Garcia D, Catana C, Caravan P (2015a) Radiation dosimetry of the fibrin-binding probe ^{64}Cu-FBP8 and its feasibility for PET imaging of deep vein thrombosis and pulmonary embolism in rats. J Nucl Med 56(7):1088–1093

Blasi F, Oliveira BL, Rietz TA, Rotile NJ, Naha PC, Cormode DP, Izquierdo-Garcia D, Catana C, Caravan P (2015b) Multisite Thrombus Imaging and Fibrin Content Estimation With a Single Whole-Body PET Scan in Rats. Arterioscler Thromb Vasc Biol 35(10):2114–2121

Bley TA, Duffek CC, Francois CJ, Schiebler ML, Acher CW, Mell M, Grist TM, Reeder SB (2010) Presurgical localization of the artery of Adamkiewicz with time-resolved 3.0-T MR angiography. Radiology 255(3):873–881

Bley TA, Francois CJ, Schiebler ML, Wieben O, Takei N, Brittain JH, Del Rio AM, Grist TM, Reeder SB (2016) Non-contrast-enhanced MRA of renal artery stenosis: validation against DSA in a porcine model. Eur Radiol 26(2):547–555

Blum A, Bellou A, Guillemin F, Douek P, Laprevote-Heully MC, Wahl D, Group, G. S (2005) Performance of

magnetic resonance angiography in suspected acute pulmonary embolism. Thromb Haemost 93(3):503–511

Brand M, Ellmann S, Sommer M, May MS, Eller A, Wuest W, Engert C, Achenbach S, Kuefner MA, Baeuerle T, Lell M, Uder M (2015) Influence of cardiac MR imaging on DNA double-strand breaks in human blood lymphocytes. Radiology 277(2):406–412

Brau AC, Beatty PJ, Skare S, Bammer R (2008) Comparison of reconstruction accuracy and efficiency among autocalibrating data-driven parallel imaging methods. Magn Reson Med 59(2):382–395

Brenner DJ (2014) What we know and what we don't know about cancer risks associated with radiation doses from radiological imaging. Br J Radiol 87(1035):20130629

Breuer FA, Blaimer M, Heidemann RM, Mueller MF, Griswold MA, Jakob PM (2005) Controlled aliasing in parallel imaging results in higher acceleration (CAIPIRINHA) for multi-slice imaging. Magn Reson Med 53(3):684–691

Bruce R, Wentland AL, Haemel AK, Garrett RW, Sadowski DR, Djamali A, Sadowski EA (2016) Incidence of nephrogenic systemic fibrosis using gadobenate dimeglumine in 1423 patients with renal insufficiency compared with gadodiamide. Invest Radiol. 51(11):701–705

Burge AJ, Freeman KD, Klapper PJ, Haramati LB (2008) Increased diagnosis of pulmonary embolism without a corresponding decline in mortality during the CT era. Clin Radiol 63(4):381–386

Burrowes KS, Clark AR, Marcinkowski A, Wilsher ML, Milne DG, Tawhai MH (2011) Pulmonary embolism: predicting disease severity. Philos Trans A Math Phys Eng Sci 369(1954):4255–4277

Burrowes KS, Clark AR, Wilsher ML, Milne DG, Tawhai MH (2014) Hypoxic pulmonary vasoconstriction as a contributor to response in acute pulmonary embolism. Ann Biomed Eng 42(8):1631–1643

Carroll TJ, Korosec FR, Swan JS, Grist TM, Frayne R, Mistretta CA (2000) Method for rapidly determining and reconstructing the peak arterial frame from a time-resolved CE-MRA exam. Magn Reson Med 44(5):817–820

Carroll TJ, Korosec FR, Swan JS, Hany TF, Grist TM, Mistretta CA (2001) The effect of injection rate on time-resolved contrast-enhanced peripheral MRA. J Magn Reson Imaging 14(4):401–410

Chang W, Wu Y, Johnson K, Loecher M, Wieben O, Edjlali M, Oppenheim C, Roca P, Hald J, Aagaard-Kienitz B, Niemann D, Mistretta C, Turski P (2015) Fast contrast-enhanced 4D MRA and 4D flow MRI using constrained reconstruction (HYPRFlow): potential applications for brain arteriovenous malformations. AJNR Am J Neuroradiol 36(6):1049–1055

Chelu RG, Wanambiro KW, Hsiao A, Swart LE, Voogd T, van den Hoven AT, van Kranenburg M, Coenen A, Boccalini S, Wielopolski PA, Vogel MW, Krestin GP, Vasanawala SS, Budde RPJ, Roos-Hesselink JW, Nieman K (2016) Cloud-processed 4D CMR flow imaging for pulmonary flow quantification. Eur J Radiol 85(10):1849–1856

Chow B, Wittram C, Lee VW (2001) Unilateral absence of pulmonary perfusion mimicking pulmonary embolism. AJR Am J Roentgenol 176(3):712

Clark AR, Bajaj M, Wilsher ML, Milne DG, Tawhai MH (2012) Ventilatory and cardiac responses to pulmonary embolism: consequences for gas exchange and blood pressure. Conf Proc IEEE Eng Med Biol Soc 2012:6657–6660

Clark AR, Milne D, Wilsher M, Burrowes KS, Bajaj M, Tawhai MH (2014) Lack of functional information explains the poor performance of 'clot load scores' at predicting outcome in acute pulmonary embolism. Respir Physiol Neurobiol 190:1–13

den Exter PL, van Es J, Klok FA, Kroft LJ, Kruip MJ, Kamphuisen PW, Buller HR, Huisman MV (2013) Risk profile and clinical outcome of symptomatic subsegmental acute pulmonary embolism. Blood 122(7):1144–1149. quiz 1329

Dentali F, Crowther M, Ageno W (2006) Thrombophilic abnormalities, oral contraceptives, and risk of cerebral vein thrombosis: a meta-analysis. Blood 107(7):2766–2773

Deshmane A, Gulani V, Griswold MA, Seiberlich N (2012) Parallel MR imaging. J Magn Reson Imaging 36(1):55–72

Du J, Bydder M (2007) High-resolution time-resolved contrast-enhanced MR abdominal and pulmonary angiography using a spiral-TRICKS sequence. Magn Reson Med 58(3):631–635

Du J, Carroll TJ, Block WF, Fain SB, Korosec FR, Grist TM, Mistretta CA (2003) SNR improvement for multiinjection time-resolved high-resolution CE-MRA of the peripheral vasculature. Magn Reson Med 49(5):909–917

Du J, Carroll TJ, Wagner HJ, Vigen K, Fain SB, Block WF, Korosec FR, Grist TM, Mistretta CA (2002) Time-resolved, undersampled projection reconstruction imaging for high-resolution CE-MRA of the distal runoff vessels. Magn Reson Med 48(3):516–522

Dyverfeldt P, Bissell M, Barker AJ, Bolger AF, Carlhall CJ, Ebbers T, Francios CJ, Frydrychowicz A, Geiger J, Giese D, Hope MD, Kilner PJ, Kozerke S, Myerson S, Neubauer S, Wieben O, Markl M (2015) 4D flow cardiovascular magnetic resonance consensus statement. J Cardiovasc Magn Reson 17:72

Edelman RR, Mattle HP, Wallner B, Bajakian R, Kleefield J, Kent C, Skillman JJ, Mendel JB, Atkinson DJ (1990) Extracranial carotid arteries: evaluation with "black blood" MR angiography. Radiology 177(1):45–50

Ersoy H, Goldhaber SZ, Cai T, Luu T, Rosebrook J, Mulkern R, Rybicki F (2007) Time-resolved MR angiography: a primary screening examination of patients with suspected pulmonary embolism and contraindications to administration of iodinated contrast material. AJR Am J Roentgenol 188(5):1246–1254

Fayad ZA, Fuster V, Fallon JT, Jayasundera T, Worthley SG, Helft G, Aguinaldo JG, Badimon JJ, Sharma SK (2000) Noninvasive in vivo human coronary artery lumen and wall imaging using black-blood magnetic resonance imaging. Circulation 102(5):506–510

Ferretti GR, Bosson JL, Buffaz PD, Ayanian D, Pison C, Blanc F, Carpentier F, Carpentier P, Coulomb M

(1997) Acute pulmonary embolism: role of helical CT in 164 patients with intermediate probability at ventilation-perfusion scintigraphy and normal results at duplex US of the legs. Radiology 205(2):453–458

Fink C, Bock M, Puderbach M, Schmahl A, Delorme S (2003) Partially parallel three-dimensional magnetic resonance imaging for the assessment of lung perfusion—initial results. Invest Radiol 38(8):482–488

Fink C, Puderbach M, Bock M, Lodemann KP, Zuna I, Schmahl A, Delorme S, Kauczor HU (2004) Regional lung perfusion: assessment with partially parallel three-dimensional MR imaging. Radiology 231(1):175–184

Firmin DN, Nayler GL, Kilner PJ, Longmore DB (1990) The application of phase shifts in NMR for flow measurement. Magn Reson Med 14(2):230–241

Firmin DN, Nayler GL, Klipstein RH, Underwood SR, Rees RS, Longmore DB (1987) In vivo validation of MR velocity imaging. J Comput Assist Tomogr 11(5):751–756

Francois CJ, Shors SM, Bonow RO, Finn JP (2003) Analysis of cardiopulmonary transit times at contrast material-enhanced MR imaging in patients with heart disease. Radiology 227(2):447–452

Frayne R, Grist TM, Korosec FR, Willig DS, Swan JS, Turski PA, Mistretta CA (1996) MR angiography with three-dimensional MR digital subtraction angiography. Top Magn Reson Imaging 8(6):366–388

Garg K, Sieler H, Welsh CH, Johnston RJ, Russ PD (1999) Clinical validity of helical CT being interpreted as negative for pulmonary embolism: implications for patient treatment. AJR Am J Roentgenol 172(6):1627–1631

Gefter WB, Gupta KB, Holland GA (1993) MR, CT enhance diagnosis of pulmonary emboli. Diagn Imaging (San Franc) 15(8):80–85

Gefter WB, Hatabu H, Holland GA, Gupta KB, Henschke CI, Palevsky HI (1995) Pulmonary thromboembolism: recent developments in diagnosis with CT and MR imaging. Radiology 197(3):561–574

Goldhaber SZ, Bounameaux H (2012) Pulmonary embolism and deep vein thrombosis. Lancet 379(9828):1835–1846

Gomori JM, Grossman RI (1988) Mechanisms responsible for the MR appearance and evolution of intracranial hemorrhage. Radiographics 8(3):427–440

Goodman LR, Lipchik RJ, Kuzo RS, Liu Y, McAuliffe TL, O'Brien DJ (2000) Subsequent pulmonary embolism: risk after a negative helical CT pulmonary angiogram--prospective comparison with scintigraphy. Radiology 215(2):535–542

Goodman PC (2000) Spiral CT for pulmonary embolism. Semin Respir Crit Care Med 21(6):503–510

Grist TM, Sostman HD, MacFall JR, Foo TK, Spritzer CE, Witty L, Newman GE, Debatin JF, Tapson V, Saltzman HA (1993) Pulmonary angiography with MR imaging: preliminary clinical experience. Radiology 189(2):523–530

Griswold MA, Jakob PM, Nittka M, Goldfarb JW, Haase A (2000) Partially parallel imaging with localized sensitivities (PILS). Magn Reson Med 44(4):602–609

Grobner T (2006) Gadolinium—a specific trigger for the development of nephrogenic fibrosing dermopathy and nephrogenic systemic fibrosis? Nephrol Dial Transplant 21(4):1104–1108

Gupta A, Frazer CK, Ferguson JM, Kumar AB, Davis SJ, Fallon MJ, Morris IT, Drury PJ, Cala LA (1999) Acute pulmonary embolism: diagnosis with MR angiography. Radiology 210(2):353–359

Haemel AK, Sadowski EA, Shafer MM, Djamali A (2011) Update on nephrogenic systemic fibrosis: are we making progress? Int J Dermatol 50(6):659–666

Hansch A, Betge S, Poehlmann G, Neumann S, Baltzer P, Pfeil A, Waginger M, Boettcher J, Kaiser WA, Wolf G, Mentzel HJ (2011) Combined magnetic resonance imaging of deep venous thrombosis and pulmonary arteries after a single injection of a blood pool contrast agent. Eur Radiol 21(2):318–325

He H, Stein MW, Zalta B, Haramati LB (2006) Pulmonary infarction: spectrum of findings on multidetector helical CT. J Thorac Imaging 21(1):1–7

Hendriksen JM, Geersing GJ, Lucassen WA, Erkens PM, Stoffers HE, van Weert HC, Büller HR, Hoes AW, Moons KG (2015) Diagnostic prediction models for suspected pulmonary embolism: systematic review and independent external validation in primary care. BMJ 351:h4438

Heredia V, Altun E, Ramalho M, de Campos R, Azevedo R, Pamuklar E, Semelka RC (2012) MRI of pregnant patients for suspected pulmonary embolism: steady-state free precession vs postgadolinium 3D-GRE. Acta Med Port 25(6):359–367

Hope MD, Hope TA, Zhu C, Faraji F, Haraldsson H, Ordovas KG, Saloner D (2015) Vascular imaging with ferumoxytol as a contrast agent. AJR Am J Roentgenol 205(3):W366–W373

Huckle JE, Altun E, Jay M, Semelka RC (2016) Gadolinium deposition in humans: when did we learn that gadolinium was deposited in vivo? Invest Radiol 51(4):236–240

Hutchinson B, Navin P, Marom EM, Truong MT, Bruzzi JF (2015) Overdiagnosis of pulmonary embolism by CT angiography. AJR 205:271–277

Johnson KM, Fain SB, Schiebler ML, Nagle S (2013) Optimized 3D ultrashort echo time pulmonary MRI. Magn Reson Med 70(5):1241–1250

Kalb B, Sharma P, Tigges S, Ray GL, Kitajima HD, Costello JR, Chen Z, Martin DR (2012) MR imaging of pulmonary embolism: diagnostic accuracy of contrast-enhanced 3D MR pulmonary angiography, contrast-enhanced low-flip angle 3D GRE, and nonenhanced free-induction FISP sequences. Radiology 263(1):271–278

Klipstein RH, Firmin DN, Underwood SR, Nayler GL, Rees RS, Longmore DB (1987) Colour display of quantitative blood flow and cardiac anatomy in a single magnetic resonance cine loop. Br J Radiol 60(710):105–111

Kluge A, Gerriets T, Lange U, Bachman G (2005) MRI for short-term follow-up of acute pulmonary embolism. Assessment of thrombus appearance and pulmonary perfusion: a feasibility study. Eur Radiol 15(9):1969–1977

Kluge A, Gerriets T, Stolz E, Dill T, Mueller KD, Mueller C, Bachmann G (2006a) Pulmonary perfusion in acute

pulmonary embolism: agreement of MRI and SPECT for lobar, segmental and subsegmental perfusion defects. Acta Radiol 47(9):933–940

Kluge A, Luboldt W, Bachmann G (2006b) Acute pulmonary embolism to the subsegmental level: diagnostic accuracy of three MRI techniques compared with 16-MDCT. AJR Am J Roentgenol 187(1):W7–14

Kluge A, Mueller C, Strunk J, Lange U, Bachmann G (2006c) Experience in 207 combined MRI examinations for acute pulmonary embolism and deep vein thrombosis. AJR Am J Roentgenol 186(6):1686–1696

Kluge A, Muller C, Hansel J, Gerriets T, Bachmann G (2004) Real-time MR with TrueFISP for the detection of acute pulmonary embolism: initial clinical experience. Eur Radiol 14(4):709–718

Korosec FR, Frayne R, Grist TM, Mistretta CA (1996) Time-resolved contrast-enhanced 3D MR angiography. Magn Reson Med 36(3):345–351

Li SJ, Tu YM, Zhou CS, Zhang LH, Liu ZH (2016) Risk factors of venous thromboembolism in focal segmental glomerulosclerosis with nephrotic syndrome. Clin Exp Nephrol 20(2):212–217

Lomis NN, Yoon HC, Moran AG, Miller FJ (1999) Clinical outcomes of patients after a negative spiral CT pulmonary arteriogram in the evaluation of acute pulmonary embolism. J Vasc Interv Radiol 10(6):707–712

Lucassen W, Geersing GJ, Erkens PM, Reitsma JB, Moons KG, Büller H, van Weert HC (2011) Clinical decision rules for excluding pulmonary embolism: a meta-analysis. Ann Intern Med 155(7):448–460

Lum DP, Busse RF, Francois CJ, Brau AC, Beatty PJ, Huff J, Brittain JH, Reeder SB (2009) Increased volume of coverage for abdominal contrast-enhanced MR angiography with two-dimensional autocalibrating parallel imaging: initial experience at 3.0 Tesla. J Magn Reson Imaging 30(5):1093–1100

Mai VM, Berr SS (1999) MR perfusion imaging of pulmonary parenchyma using pulsed arterial spin labeling techniques: FAIRER and FAIR. J Magn Reson Imaging 9(3):483–487

Maki JH, Prince MR, Londy FJ, Chenevert TL (1996) The effects of time varying intravascular signal intensity and k-space acquisition order on three-dimensional MR angiography image quality. J Magn Reson Imaging 6(4):642–651

Mani V, Alie N, Ramachandran S, Robson PM, Besa C, Piazza G, Mercuri M, Grosso M, Taouli B, Goldhaber SZ, Fayad ZA (2015) A multicenter MRI protocol for the evaluation and quantification of deep vein thrombosis. J Vis Exp (100):e52761

Markl M, Geiger J, Kilner PJ, Foll D, Stiller B, Beyersdorf F, Arnold R, Frydrychowicz A (2011) Time-resolved three-dimensional magnetic resonance velocity mapping of cardiovascular flow paths in volunteers and patients with Fontan circulation. Eur J Cardiothorac Surg 39(2):206–212

Mayo JR, Remy-Jardin M, Muller NL, Remy J, Worsley DF, Hossein-Foucher C, Kwong JS, Brown MJ (1997) Pulmonary embolism: prospective comparison of spi-ral CT with ventilation-perfusion scintigraphy. Radiology 205(2):447–452

Meaney JF, Prince MR (1999a) Pulmonary MR angiography. Magn Reson Imaging Clin N Am 7(2):393–409

Meaney JF, Prince MR (1999b) Method and apparatus for magnetic resonance angiography using contrast agents. United States patent 5,924,987, 1–35

Meaney JF, Weg JG, Chenevert TL, Stafford-Johnson D, Hamilton BH, Prince MR (1997) Diagnosis of pulmonary embolism with magnetic resonance angiography. N Engl J Med 336(20):1422–1427

Miyazaki M, Akahane M (2012) Non-contrast enhanced MR angiography: established techniques. J Magn Reson Imaging 35(1):1–19

Nagle SK, Schiebler ML, Repplinger MD, Francois CJ, Vigen KK, Yarlagadda R, Grist TM, Reeder SB (2016) Contrast enhanced pulmonary magnetic resonance angiography for pulmonary embolism: Building a successful program. Eur J Radiol 85(3):553–563

Nayler GL, Firmin DN, Longmore DB (1986) Blood flow imaging by cine magnetic resonance. J Comput Assist Tomogr 10(5):715–722

Nikolaou K, Schoenberg SO, Attenberger U, Scheidler J, Dietrich O, Kuehn B, Rosa F, Huber A, Leuchte H, Baumgartner R, Behr J, Reiser MF (2005) Pulmonary arterial hypertension: diagnosis with fast perfusion MR imaging and high-spatial-resolution MR angiography—preliminary experience. Radiology 236(2):694–703

Nilsson T, Olausson A, Johnsson H, Nyman U, Aspelin P (2002) Negative spiral CT in acute pulmonary embolism. Acta Radiol 43(5):486–491

Ohno Y, Higashino T, Takenaka D, Sugimoto K, Yoshikawa T, Kawai H, Fujii M, Hatabu H, Sugimura K (2004) MR angiography with sensitivity encoding (SENSE) for suspected pulmonary embolism: comparison with MDCT and ventilation-perfusion scintigraphy. AJR Am J Roentgenol 183(1):91–98

Ohno Y, Kawamitsu H, Higashino T, Takenaka D, Watanabe H, van Cauteren M, Fujii M, Hatabu H, Sugimura K (2003) Time-resolved contrast-enhanced pulmonary MR angiography using sensitivity encoding (SENSE). J Magn Reson Imaging 17(3):330–336

Ohno Y, Koyama H, Matsumoto K, Onishi Y, Nogami M, Takenaka D, Yoshikawa T, Matsumoto S, Sugimura K (2010) Dynamic MR perfusion imaging: capability for quantitative assessment of disease extent and prediction of outcome for patients with acute pulmonary thromboembolism. J Magn Reson Imaging 31(5):1081–1090

Ohno Y, Nishio M, Koyama H, Yoshikawa T, Matsumoto S, Seki S, Obara M, van Cauteren M, Takahashi M, Sugimura K (2014) Pulmonary 3 T MRI with ultrashort TEs: influence of ultrashort echo time interval on pulmonary functional and clinical stage assessments of smokers. J Magn Reson Imaging 39(4):988–997

Oliveira BL, Blasi F, Rietz TA, Rotile NJ, Day H, Caravan P (2015) Multimodal molecular imaging reveals high target uptake and specificity of 111In- and 68Ga-labeled fibrin-binding probes for thrombus detection in rats. J Nucl Med 56(10):1587–1592

Ost D, Rozenshtein A, Saffran L, Snider A (2001) The negative predictive value of spiral computed tomography for the diagnosis of pulmonary embolism in patients with nondiagnostic ventilation-perfusion scans. Am J Med 110(1):16–21

Oudkerk M, van Beek EJ, Wielopolski P, van Ooijen PM, Brouwers-Kuyper EM, Bongaerts AH, Berghout A (2002) Comparison of contrast-enhanced magnetic resonance angiography and conventional pulmonary angiography for the diagnosis of pulmonary embolism: a prospective study. Lancet 359(9318):1643–1647

Overoye-Chan K, Koerner S, Looby RJ, Kolodziej AF, Zech SG, Deng Q, Chasse JM, McMurry TJ, Caravan P (2008) EP-2104R: a fibrin-specific gadolinium-Based MRI contrast agent for detection of thrombus. J Am Chem Soc 130(18):6025–6039

Parsons JM, Baker EJ, Hayes A, Ladusans EJ, Qureshi SA, Anderson RH, Maisey MN, Tynan M (1990) Magnetic resonance imaging of the great arteries in infants. Int J Cardiol 28(1):73–85

Pfeil A, Betge S, Poehlmann G, Boettcher J, Drescher R, Malich A, Wolf G, Mentzel HJ, Hansch A (2012) Magnetic resonance VIBE venography using the blood pool contrast agent gadofosveset trisodium—an inter-rater reliability study. Eur J Radiol 81(3):547–552

Pleszewski B, Chartrand-Lefebvre C, Qanadli SD, Déry R, Perreault P, Oliva VL, Prenovault J, Belblidia A, Soulez G (2006) Gadolinium-enhanced pulmonary magnetic resonance angiography in the diagnosis of acute pulmonary embolism: a prospective study on 48 patients. Clin Imaging 30(3):166–172

Popp HD, Meyer M, Brendel S, Prinzhorn W, Naumann N, Weiss C, Seifarth W, Schoenberg SO, Hofmann WK, Henzler T, Fabarius A (2016) Leukocyte DNA damage after reduced and conventional absorbed radiation doses using 3rd generation dual-source CT technology. Eur J Radiol Open 3:134–137

Rees RS, Somerville J, Underwood SR, Wright J, Firmin DN, Klipstein RH, Longmore DB (1987) Magnetic resonance imaging of the pulmonary arteries and their systemic connections in pulmonary atresia: comparison with angiographic and surgical findings. Br Heart J 58(6):621–626

Remy-Jardin M, Pistolesi M, Goodman LR, Gefter WB, Gottschalk A, Mayo JR, Sostman HD (2007) Management of suspected acute pulmonary embolism in the era of CT angiography: a statement from the Fleischner Society. Radiology 245(2):315–329

Remy-Jardin M, Remy J, Deschildre F, Artaud D, Beregi JP, Hossein-Foucher C, Marchandise X, Duhamel A (1996) Diagnosis of pulmonary embolism with spiral CT: comparison with pulmonary angiography and scintigraphy. Radiology 200(3):699–706

Restrepo CS, Betancourt SL, Martinez-Jimenez S, Gutierrez FR (2012) Tumors of the pulmonary artery and veins. Semin Ultrasound CT MR 33(6):580–590

Revel MP, Sanchez O, Couchon S, Planquette B, Hernigou A, Niarra R, Meyer G, Chatellier G (2012) Diagnostic accuracy of magnetic resonance imaging for acute pulmonary embolism: results of the "IRM-EP" study. J Thromb Haemost 10(5):743–750

Richman PB, Courtney DM, Friese J, Matthews J, Field A, Petri R, Kline JA (2004) Prevalence and significance of nonthromboembolic findings on chest computed tomography angiography performed to rule out pulmonary embolism: a multicenter study of 1,025 emergency department patients. Acad Emerg Med 11(6):642–647

Roach DJ, Cremillieux Y, Serai SD, Thomen RP, Wang H, Zou Y, Szczesniak RD, Benzaquen S, Woods JC (2016) Morphological and quantitative evaluation of emphysema in chronic obstructive pulmonary disease patients: a comparative study of MRI with CT. J Magn Reson Imaging 44(6):1656–1663

Rybicki FJ, Udelson JE, Peacock WF, Goldhaber SZ, Isselbacher EM, Kazerooni E, Kontos MC, Litt H, Woodard PK (2016) 2015 ACR/ACC/AHA/AATS/ACEP/ASNC/NASCI/SAEM/SCCT/SCMR/SCPC/SNMMI/STR/STS appropriate utilization of cardiovascular imaging in emergency department patients with chest pain: a joint document of the American College of Radiology Appropriateness Criteria Committee and the American College of Cardiology Appropriate Use Criteria Task Force. J Am Coll Radiol 13(2):1–29

Sadowski EA, Bennett LK, Chan MR, Wentland AL, Garrett AL, Garrett RW, Djamali A (2007) Nephrogenic systemic fibrosis: risk factors and incidence estimation. Radiology 243(1):148–157

Schiebler M, Francois C, Repplinger M, Hamedani A, Lindholm C, Vigen K, Munoz del Rio A, Grist T, Reeder S, Nagle S (2016a) Effectiveness of pulmonary contrast enhanced magnetic resonance angiography for the primary workup of pulmonary embolism. International Society for Magnetic Resonance in Medicine, book of meeting abstracts (Singapore annual meeting and exhibition, 7–13 May 2016), Oral abstract presentation number 1074, Friday 09:12 am

Schiebler M, Francois C, Repplinger M, Vigen K, Reeder S, Kramer H, Grist T, Munoz Del Rio A, Hamedani A, Nagle S (2013) Effectiveness of pulmonary MRA for the primary diagnosis of PE: outcomes analysis of 578 consecutive symptomatic patients. Poster LL-CHS-SU4A. Radiological Society of North America (RSNA) 99th scientific assembly and annual meeting Chicago, IL

Schiebler ML, Ahuja J, Repplinger MD, Francois CJ, Vigen KK, Grist TM, Hamedani AG, Reeder SB, Nagle SK (2016b) Incidence of actionable findings on contrast enhanced magnetic resonance angiography ordered for pulmonary embolism evaluation. Eur J Radiol 85(8):1383–1389

Schiebler ML, Holland GA, Hatabu H, Listerud J, Foo T, Palevsky H, Edmunds H, Gefter WB (1993) Suspected pulmonary embolism: prospective evaluation with pulmonary MR angiography. Radiology 189(1):125–131

Sheh SH, Bellin E, Freeman KD, Haramati LB (2012) Pulmonary embolism diagnosis and mortality with

pulmonary CT angiography versus ventilation-perfusion scintigraphy: evidence of overdiagnosis with CT? AJR Am J Roentgenol 198(6):1340–1345

Soulez G, Bloomgarden DC, Rofsky NM, Smith MP, Abujudeh HH, Morgan DE, Lichtenstein RJ, Schiebler ML, Wippold FJ, Russo C, Kuhn MJ, Mennitt KW, Maki JH, Stolpen A, Liou J, Semelka RC, Kirchin MA, Shen N, Pirovano G, Spinazzi A (2015) Prospective cohort study of nephrogenic systemic fibrosis in patients with stage 3-5 chronic kidney disease undergoing mri with injected gadobenate dimeglumine or gadoteridol. AJR Am J Roentgenol 205(3):469–478

Spencer FA, Gore JM, Lessard D, Douketis JD, Emery C, Goldberg RJ (2008) Patient outcomes after deep vein thrombosis and pulmonary embolism: the Worcester Venous Thromboembolism Study. Arch Intern Med 168(4):425–430

Stein PD, Chenevert TL, Fowler SE, Goodman LR, Gottschalk A, Hales CA, Hull RD, Jablonski KA, Leeper KV Jr, Naidich DP, Sak DJ, Sostman HD, Tapson VF, Weg JG, Woodard PK (2010) Gadolinium-enhanced magnetic resonance angiography for pulmonary embolism: a multicenter prospective study (PIOPED III). Ann Intern Med 152(7):434–443. W142-3

Stein PD, Gottschalk A, Sostman HD, Chenevert TL, Fowler SE, Goodman LR, Hales CA, Hull RD, Kanal E, Leeper KV Jr, Nadich DP, Sak DJ, Tapson VF, Wakefield TW, Weg JG, Woodard PK (2008) Methods of prospective investigation of pulmonary embolism diagnosis III (PIOPED III). Semin Nucl Med 38(6):462–470

Stein PD, Matta F, Hughes PG, Hourmouzis ZN, Hourmouzis NP, Schweiss RE, Bach JA, Kazan VM, Kakish EJ, Keyes DC, Hughes MJ (2016) Follow-up CT pulmonary angiograms in patients with acute pulmonary embolism. Emerg Radiol 23:463

Stein PD, Matta F, Sedrick JA, Saleh T, Badshah A, Denier JE (2011) Ancillary findings on CT pulmonary angiograms and abnormalities on chest radiographs in patients in whom pulmonary embolism was excluded. Clin Appl Thromb Hemost 18(2):201–205

Stein PD, Sostman HD, Dalen JE, Bailey DL, Bajc M, Goldhaber SZ, Goodman LR, Gottschalk A, Hull RD, Matta F, Pistolesi M, Tapson VF, Weg JG, Wells PS, Woodard PK, Consensus G (2011b) Controversies in diagnosis of pulmonary embolism. Clin Appl Thromb Hemost 17(2):140–149

Suzuki K, Masuya M, Matsumoto T, Ito N, Ohishi K, Maeda M, Katayama N (2010) High-intensity signals in the basal ganglia from gadolinium-enhanced T1-weighted MRI as an early change in toxoplasma encephalitis in an AIDS patient. J Infect Chemother 16(2):135–138

Swift AJ, Wild JM, Nagle SK, Roldan-Alzate A, Francois CJ, Fain S, Johnson K, Capener D, van Beek EJ, Kiely DG, Wang K, Schiebler ML (2014) Quantitative magnetic resonance imaging of pulmonary hypertension: a practical approach to the current state of the art. J Thorac Imaging 29(2):68–79

Tapson VF (2008) Acute pulmonary embolism. N Engl J Med 358(10):1037–1052

Thomson LK, Thomson PC, Kingsmore DB, Blessing K, Daly CD, Cowper SE, Roditi GH (2015) Diagnosing nephrogenic systemic fibrosis in the post-FDA restriction era. J Magn Reson Imaging 41(5):1268–1271

Tillie-Leblond I, Mastora I, Radenne F, Paillard S, Tonnel AB, Remy J, Remy-Jardin M (2002) Risk of pulmonary embolism after a negative spiral CT angiogram in patients with pulmonary disease: 1-year clinical follow-up study. Radiology 223(2):461–467

Todua F, Akhvlediani M, Vorobiova E, Baramidze A, Tsivtsivadze G, Gachechiladze D (2016) Prognostic value of some hemostasis-related, homocysteine, high sensitive CRP and multidetector computed tomography parameters in pulmonary embolism. Georgian Med News (254):37–42

Uppal R, Catana C, Ay I, Benner T, Sorensen AG, Caravan P (2011) Bimodal thrombus imaging: simultaneous PET/MR imaging with a fibrin-targeted dual PET/MR probe—feasibility study in rat model. *Radiology* 258(3):812–820

van Belle A, Büller HR, Huisman MV, Huisman PM, Kaasjager K, Kamphuisen PW, Kramer MH, Kruip MJ, Kwakkel-van Erp JM, Leebeek FW, Nijkeuter M, Prins MH, Sohne M, Tick LW, Investigators CS (2006) Effectiveness of managing suspected pulmonary embolism using an algorithm combining clinical probability, D-dimer testing, and computed tomography. JAMA 295(2):172–179

Velikina JV, Johnson KM, Wu Y, Samsonov AA, Turski P, Mistretta CA (2010) PC HYPR flow: a technique for rapid imaging of contrast dynamics. J Magn Reson Imaging 31(2):447–456

Vidmar J, Kralj E, Bajd F, Sersa I (2015) Multiparametric MRI in characterizing venous thrombi and pulmonary thromboemboli acquired from patients with pulmonary embolism. J Magn Reson Imaging 42(2):354–361

Wang Y, Grimm RC, Felmlee JP, Riederer SJ, Ehman RL (1996) Algorithms for extracting motion information from navigator echoes. Magn Reson Med 36(1):117–123

Wasser MN, Geelkerken RH, Kouwenhoven M, van Bockel JH, Hermans J, Schultze Kool LJ, de Roos A (1996) Systolically gated 3D phase contrast MRA of mesenteric arteries in suspected mesenteric ischemia. J Comput Assist Tomogr 20(2):262–268

West JW (1986) Pulmonary embolism. Med Clin North Am 70(4):877–894

Wittram C (2003) Pulmonary artery enhancement at CT pulmonary angiography. Radiology 229(3):932. author reply 932–933

Wittram C, Maher MM, Yoo AJ, Kalra MK, Shepard JA, McLoud TC (2004) CT angiography of pulmonary embolism: diagnostic criteria and causes of misdiagnosis. Radiographics 24(5):1219–1238

Wittram C, Yoo AJ (2007) Transient interruption of contrast on CT pulmonary angiography: proof of mechanism. J Thorac Imaging 22(2):125–129

Wood ML, Henkelman RM (1985) Truncation artifacts in magnetic resonance imaging. Magn Reson Med 2(6):517–526

Woodard PK, Chenevert TL, Sostman HD, Jablonski KA, Stein PD, Goodman LR, Londy FJ, Narra V, Hales CA, Hull RD, Tapson VF, Weg JG (2012) Signal quality of single dose gadobenate dimeglumine pulmonary MRA examinations exceeds quality of MRA performed with double dose gadopentetate dimeglumine. Int J Cardiovasc Imaging 28(2):295–301

Worthley SG, Helft G, Fayad ZA, Fuster V, Rodriguez OJ, Zaman AG, Badimon JJ (2001) Cardiac gated breath-hold black blood MRI of the coronary artery wall: an in vivo and ex vivo comparison. Int J Cardiovasc Imaging 17(3):195–201

Zarins CK, Taylor CA, Min JK (2013) Computed fractional flow reserve (FFTCT) derived from coronary CT angiography. J Cardiovasc Transl Res 6(5):708–714

Zhang LJ, Luo S, Yeh BM, Zhou CS, Tang CX, Zhao Y, Li L, Zheng L, Huang W, Lu GM (2013) Diagnostic accuracy of three-dimensional contrast-enhanced MR angiography at 3-T for acute pulmonary embolism detection: comparison with multidetector CT angiography. Int J Cardiol 168(5):4775–4783

Zhou M, Hu Y, Long X, Liu D, Liu L, Dong C, Wang J, Kong X (2015) Diagnostic performance of magnetic resonance imaging for acute pulmonary embolism: a systematic review and meta-analysis. J Thromb Haemost 13(9):1623–1634

MR Perfusion in the Lung

Frank Risse and Grzegorz Bauman

Contents

F. Risse, PhD (✉)
Department of Translational Medicine and Clinical
Pharmacology, Boehringer Ingelheim Pharma
GmbH & Co KG, Birkendorfer Strasse 65, 88397
Biberach, Germany
e-mail: frank.risse@boehringer-ingelheim.com

G. Bauman, PhD
Division of Radiological Physics, Department
of Radiology, University of Basel Hospital,
Petersgraben 4, 4031 Basel, Switzerland

Department of Biomedical Engineering, University
of Basel, Gewerbestrasse 14, 4123 Basel, Switzerland

Abstract

Perfusion is the blood flow of an organ at the capillary level. It is closely related to the blood supply of the lung and moreover to lung function. It is altered in various diseases of the lung such as pulmonary hypertension or cystic fibrosis, etc. Therefore, perfusion is an important functional parameter in the diagnosis of pulmonary diseases, and quantitative values are required to study physiology and pathophysiology of various lung diseases as well as to monitor treatment response. The most popular and clinically established approach to measure the pulmonary perfusion using MRI is based on three-dimensional time-resolved contrast-enhanced T1-weighted sequences. The rapid acquisition of perfusion images facilitates the tracking of the first pass of a contrast agent through the lung parenchyma. Based on this information, it is possible to quantify perfusion in the entire lung using the indicator dilution theory. Quantification is challenging due to potential extravasation of the contrast agent during the first pass as well as the nonlinear relationship between the concentration of the contrast agent and signal intensity. Some of these challenges can be addressed by a dual-bolus technique. Alternatively, pulmonary perfusion can be assessed using contrast agent-free approaches such as arterial spin labeling or Fourier decomposition MRI. Application of these techniques can especially benefit patients for whom the contrast agent administration is contraindicated.

1 Introduction

Perfusion is the blood flow of an organ at the capillary level, i.e., it is the amount of arterial blood delivered to a tissue in a certain time period. The unit of perfusion is mL min^{-1} 100 g^{-1} or, more commonly in lung perfusion imaging, mL min^{-1} 100 mL^{-1}.

Perfusion is closely related to the supply of organs and moreover to the function of the organ and can be altered in various diseases of the lung such as pulmonary hypertension, chronic obstructive pulmonary disease (COPD), or cystic fibrosis (CF). Not only can lung perfusion alterations occur directly due to diseases affecting pulmonary blood supply but also indirectly by hypoxic vasoconstriction, a reaction to alveolar hypoxia, which leads to a shifting of blood to better ventilated lung regions. Therefore, perfusion is an important functional parameter in diagnosis of pulmonary diseases. Currently, the standard clinical tool for the assessment of perfusion is still 99m-technetium-labeled macroaggregated albumin scintigraphy or single-photon emission computed tomography (SPECT). The nuclear medicine modalities, however, are limited by poor spatial resolution and by the use of radioactive substances. MRI has proven to be a promising alternative providing morphological and functional information. First experiments in rats using a spin echo sequence after the administration of contrast agent had already shown the potential of pulmonary perfusion MRI in an experimental setup (Berthezene et al. 1992). As a result of the advancing development of MR scanners, Hatabu et al. (1996) were able to visualize the signal enhancement during the first pass of a contrast agent through the lungs in humans by utilizing a two-dimensional T1-weighted gradient echo sequence with short echo time (TE). In the last decade, investigation of three-dimensional (3D) pulmonary perfusion by time-resolved or dynamic contrast-enhanced (DCE) MRI with acceptable temporal resolution and volume coverage has been proposed (Fink et al. 2004a, 2005a; Nikolaou et al. 2004; Ohno et al. 2004) and became available on most clinical MR scanners today.

The rapid acquisition of perfusion images facilitates the tracking of the first pass of a gadolinium-based contrast agent through the lung parenchyma. Based on this information, it is possible to quantify perfusion in 2D (Hatabu et al. 1999; Levin et al. 2001) or in 3D (Fink et al. 2004b; Nikolaou et al. 2004; Ohno et al. 2004). The latter allows for the investigation of perfusion changes in lung diseases affecting the entire lung. Quantitative values of perfusion may be particularly useful in studying physiology and pathophysiology as well as to monitor treatment response (Wielpütz et al. 2014).

Despite the fact that the gadolinium-based contrast agents are generally well tolerated by the majority of subjects, its intravenous administration causes patient discomfort as well as additional complications for the clinical setup. In a limited subset of patients, the use of contrast agents may cause a risk of acute allergic reactions and severe complications such as nephrogenic systemic fibrosis in patients with impaired renal function or lead to accumulation of gadolinium in various tissues (Rogosnitzky and Branch 2016). Administration of contrast agents should also be carefully considered in neonates, infants, pregnant women, or patients requiring frequent follow-up. For these reasons, noninvasive and contrast agent-free techniques such as arterial spin labeling (ASL) or Fourier decomposition (FD) MRI have gained much attention in the recent years (Hopkins et al. 2005; Bauman et al. 2009).

2 Technical Challenges

MRI of the lung is challenging in general, but to obtain functional information is even more complex than to perform mere morphological images. Reasons are on the one hand the large gas-filled space with only a small percentage of parenchyma, on the other hand respiratory and cardiac motion.

Conventional MRI is based on the measurement of the macroscopic magnetization of protons within the defined volume. Air is virtually invisible to MRI but represents the majority of

the lung volume. The percentage of parenchyma with a proton density sufficient to be detected by MRI is rather small (ca. 20–30 %). Additionally, the large area of air-tissue interfaces – the lung surface has an area of approximately 140 m^2 (Thews 1997) – leads to strong susceptibility gradients, which makes use of fast acquisition techniques like echo planar imaging virtually impossible. Furthermore, the T2* of the lung is very short, only in the range of 1.0–2.5 ms (Pracht et al. 2005). The signal-to-noise ratio (SNR) is therefore low compared to other organs as a result of the low proton density and the rapid decay of the measured signal. However, due to recent advances in MR technology, pulmonary MRI has significantly improved. Specifically, rapid short TE pulse sequences with optimized k-space sampling schemes combined with multichannel phased-array coils for parallel imaging have shown great promise to overcome the limitations of standard imaging methods.

Furthermore, when performing DCE-MRI perfusion scans, it is important to take into account the respiration-induced proton density variations, which cause a modulation of the MR signal. The most common solution for these problems is to acquire the perfusion images using optimized fast sampling schemes within one breath hold (Attenberger et al. 2009). The acquisition time of perfusion measurements using such a breath-hold technique is limited to a maximum of 20–25 s depending on the subject's constitution but is often much shorter in patients with impaired ventilation. In addition, the high pulmonary blood flow, which leads to short transit times through the lungs and potentially also to inflow artifacts in the feeding arteries, has to be taken into account. Thus, fast acquisition techniques are required in DCE-MRI to measure the contrast agent bolus properly when the blood flow is high. Furthermore, artifacts due to cardiac motion can alter perfusion information in the region of the heart since usually no ECG triggering is used for lung perfusion MRI to achieve the required high temporal resolution.

In contrast to DCE-MRI, contrast agent-free techniques benefit especially from using rapid balanced steady-state free precession or spin echo-based imaging techniques, which in general provide much higher native signal intensity from the blood pool in the lung than the gradient echo-based sequences.

3 Measurement Techniques

Several MRI techniques have been described to measure the pulmonary perfusion: The clinically most established and increasingly popular technique is DCE-MRI, which uses contrast media to measure the regional blood flow at the capillary level. It is relatively easy to use and provides a good contrast-to-noise ratio (CNR) but cannot be repeated arbitrarily, or used if the administration of contrast agent is contraindicated. Thus, alternative imaging methods which do not rely on the administration of an intravenous contrast agent have received much attention. One of them is ASL MRI, which utilizes the water protons of the blood as an endogenous, freely diffusible tracer by labeling the spins with dedicated radio-frequency pulses. The evolution of the spin labeling is then measured in the lung parenchyma to assess information about perfusion (Mai and Berr 1999). In the recent years, an alternative method to study lung function, the Fourier decomposition (FD) MRI, has been introduced (Bauman et al. 2009). This noninvasive technique allows for the simultaneous assessment of both the regional perfusion and ventilation-related information of the lung.

3.1 Dynamic Contrast-Enhanced Perfusion Imaging

DCE-MRI is based on the tracking of the signal change due to the first passage of a contrast media bolus through the lung capillaries (Fig. 1). It is therefore referred to as the "bolus-tracking" or "first pass" technique. Originally the bolus-tracking technique was introduced for perfusion imaging of the brain (Rosen et al. 1990) and later adapted for the lungs by Hatabu et al. (1996). In pulmonary perfusion MRI, the tracking is performed using dynamic T1-weighted pulse sequences during the intravenous injection of a
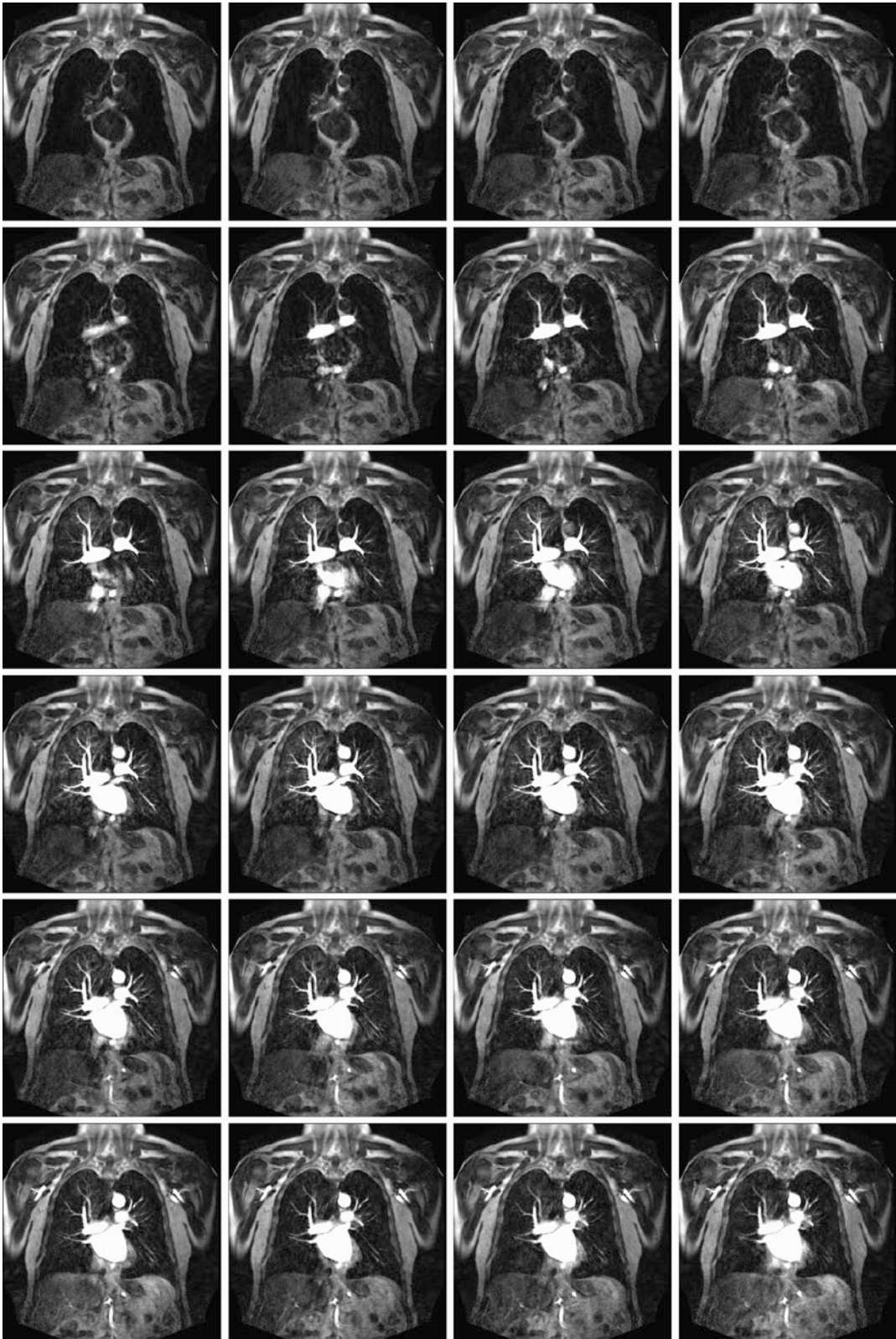
contrast agent with a high flow rate between 3 and 5 mL/s to achieve a compact and high bolus profile. A high temporal resolution of about 1.5 s is required for an adequate acquisition of the bolus due to the high injection rates and the short contrast agent transit times through the lungs of approximately of 3–4 s (Fishman 1963).

Typical pulse sequences used for DCE-MRI in the lungs are fast spoiled gradient echo techniques like fast low-angle shot (FLASH) or turbo FLASH. Both should be applied with short echo times below 1 ms due to the low T2* of 1.0–2.5 ms in lung parenchyma (Pracht et al. 2005) to achieve sufficient CNR. Nowadays, most lung DCE-MRI studies are performed using 3D techniques to acquire images of the entire chest since the whole lung is affected in the majority of pulmonary diseases. Very short repetition times are therefore used to achieve the temporal resolution required to track the short signal change induced by the contrast agent. Present parallel imaging techniques like SENSE (Pruessmann et al. 1999) or GRAPPA (Griswold et al. 2002) allow for a reduction of k-space lines and thus for shorter acquisition times per image. These techniques can also be used to improve the spatial resolution when further improvement of the acquisition time is not required. Furthermore, the amount of k-space data can be reduced by acquiring only the central part of the k-space, i.e., the part that determines the image contrast, with high temporal resolution and updating the outer parts at a lower rate. This "view-sharing" technique was originally developed for contrast-enhanced MR angiography by Korosec et al. (1996). Different variants of the view-sharing technique are currently used in clinical routine and known as time-resolved echo-shared angiographic technique (TREAT), time-resolved imaging of contrast

Table 1 Example for a time-resolved 3D perfusion pulse sequence

Name	T1-weighted 3D spoiled gradient echo technique with view sharing and parallel imaging
Field strength	1.5 T
Orientation	Coronal
No. of slices	40
No. of acquisitions	25–35
Flip angle/echo time/ repetition time	25°/0.81 ms/2.04 ms
Bandwidth	1116 Hz
Voxel size	$1.6 \times 1.6 \times 5.5$ mm^3
FOV	500×500 mm^2
Matrix	224×320
Acquisition time	0.8 s
Parallel imaging technique (acceleration factor)	2
Respiratory phase	Inspiration

kinetics (TRICKS) (Fink et al. 2005b, c), or time-resolved angiography with interleaved stochastic trajectories (TWIST) (Lim et al. 2008). When combined with parallel imaging, these imaging techniques offer a very good spatial resolution of about 1.5×1.5 mm^2 with 5 mm slice thickness at the acquisition rate of about 1 s. An example for a clinical 3D perfusion sequence is given in Table 1. Only recently, 3D radial ultrashort echo time (UTE) MRI was applied for simultaneous acquisition of a high-resolution isotropic structural dataset and a DCE dataset for the lung perfusion assessment (Bell et al. 2015). The main advantage of this technique is improved native SNR in the lung tissue due to extremely short echo times and its inherent robustness against motion and pulsation artifacts. However, significant radial undersampling is required to achieve sufficient

Fig. 1 First pass of a contrast agent through a central lung slice of a patient with chronic obstructive disease. The image acquisition was performed with a time-resolved 3D gradient echo pulse sequences with view sharing and parallel imaging (Images courtesy of Gregor Sommer, MD, Clinic of Radiology and Nuclear Medicine, University of Basel Hospital, Basel, Switzerland)

temporal resolution when using 3D UTE scans. Thus, it is beneficial to employ the high level of sparsity of DCE-MRI data in the spatial-temporal domain and apply an iterative reconstruction approach for improved quantification of perfusion parameters (Bauman et al. 2015).

In general, the use of 3D pulse sequences is done on the cost of a lower temporal resolution compared to 2D techniques with acquisition times in the range of milliseconds. The application of simple view-sharing methods in 3D acquisitions may lead to temporal interpolation artifacts in the presence of rapid signal changes caused by high blood flow. Hence, the temporal resolution is particularly important for perfusion quantification, where an exact tracking of the bolus is crucial. Nevertheless, a sufficient CNR has to be maintained and should be balanced against temporal resolution (Ingrisch et al. 2010).

3.2   Arterial Spin Labeling

Besides contrast-enhanced perfusion MRI, ASL has been proposed as a method for the assessment of lung perfusion with MRI. In contrast to DCE-MRI, no intravenous contrast agent administration is necessary, but the water protons of the blood are labeled with dedicated inversion pulses and used as an endogenous tracer. Usually, a control and a tag image are acquired and then subtracted to suppress the static background. The labeling can either be done in a continuous or pulsed mode, where the pulsed techniques allow for the quantification of perfusion mostly based on the general kinetic model of Buxton et al. (1998). Several acquisitions are often required in ASL to achieve a sufficiently high SNR which makes it particularly difficult in lung perfusion imaging. Initial experiments were successfully performed by Mai and Berr (1999), and more recently, ASL techniques were used to determine the heterogeneity of lung perfusion (Hopkins et al. 2005) and to quantify perfusion imaging (Bolar et al. 2006).

However, ASL is usually not used in routine lung diagnostics for several reasons. A major drawback apart from generally low signal is the subtraction of two images which makes the technique particularly sensitive to respiratory and cardiac motion (Mai and Berr 1999), especially when several acquisitions are necessary. ECG and cardiac triggering can reduce these artifacts but without omitting them totally. Single-shot ASL techniques do not require separate control images and might overcome these limitations also allowing for quantitative measurements within a single breath hold (Bolar et al. 2006; Pracht et al. 2006, Fischer et al. 2008). For the reasons mentioned above, the ASL-based techniques are currently limited to study lung physiology (Hopkins and Prisk 2010) and rarely applied in clinical studies, e.g., in a group of CF patients (Schraml et al. 2012).

3.3   Fourier Decomposition

An alternative, noninvasive method to study lung function called Fourier decomposition (FD) MRI has been introduced in recent years (Bauman et al. 2009). FD MRI allows for simultaneous assessment of regional pulmonary perfusion, blood arrival time, and ventilation-related information without the need for the administration of an intravenous or inhaled contrast agent. A current implementation of this approach utilizes ultrafast balanced steady-state free precession (uf-bSSFP) imaging (Bieri 2013) for time-resolved free-breathing acquisitions of 2D lung datasets. Neither ECG nor any respiratory triggering method is required during the scan. The technique takes advantage from variations of regional MR signal intensity in the lung parenchyma caused by respiratory and cardiac cycles. In inspiration the regional lung volume increases while the signal intensity decreases. The opposite takes place during expiration. Thus, the signal intensity in the lung is determined by the phase of the respiratory cycle and can be scaled linearly in the tidal volume breathing region. The signal intensity in the lung parenchyma is also modulated by the cardiac cycle. Fresh unsaturated blood entering the slice being imaged increases the regional signal intensity. Both physiological cycles correspond to different frequencies and
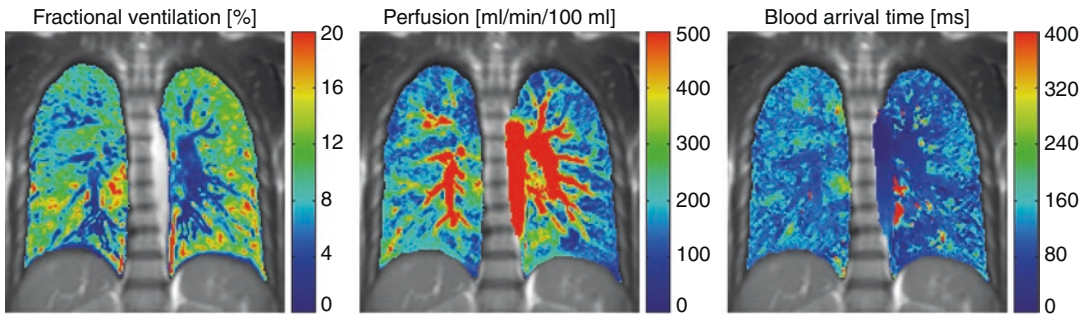
Fig. 2 Fractional ventilation, perfusion, and blood arrival time maps obtained using FD MRI in a healthy volunteer

can be spectrally retrieved in the time-resolved dataset. However, prior to further post-processing, the acquired datasets are subject to nonrigid image registration for the compensation of respiratory motion. Subsequently, pixel-wise spectral analysis is performed on the motion-corrected data using fast Fourier transform, or more robust and stable methods such as matrix pencil decomposition (Bauman and Bieri 2016) to identify frequency components of the physiological cycles. The amplitudes and phases of the respiratory and cardiac signal modulations are used to generate ventilation-weighted, perfusion-weighted, and blood inflow time maps (Bauman and Bieri 2016).

FD MRI has been primarily developed for 1.5 T clinical MR scanners. Very short repetition time of uf-bSSFP imaging mitigates the so-called banding artifacts and improves SNR in the lung. The image acquisition is usually performed at the in-plane spatial resolution of 2.8 × 2.8–3.5 × 3.5 mm^2 with 10–15 mm slice thickness and temporal resolution of about 3–4 images per second. The whole lung volume can be covered in less than 10 min using a sequential multi-slice acquisition. Since the banding artifacts caused by the off-resonance effects at 3 T can negatively affect the image quality of bSSFP sequences, an acquisition based on gradient echo sequence was proposed by Schönfeld et al. (2015).

Quantification approaches for of the perfusion- and ventilation-weighted FD MRI have been recently presented by Kjørstad et al. (2014). However, clinical studies validating the quantitative FD MRI still need to be conducted. Figure 2

shows example maps generated from the data acquired in a healthy volunteer.

The technique was validated in animal experiments against well-established modalities including SPECT, DCE-MRI, and hyperpolarized helium-3 MRI (Bauman et al. 2011, Bauman et al. 2013a). The first clinical data on FD MRI were obtained in patients with different pulmonary diseases (Bauman et al. 2013b, Capaldi et al. 2015; Schönfeld et al. 2015; Sommer et al. 2013). An example of functional maps obtained in CF patients is shown in Fig. 3.

4 Image Processing of DCE-MRI Data

The investigation of contrast-enhanced perfusion datasets requires usually post-processing of the acquired images to achieve either a better visualization of perfusion or to obtain quantitative perfusion parameters.

The idea of most visualization methods is to condense the information of the time-resolved 3D images. The reading of several hundred images is very time consuming and requires an experienced radiologist. Additionally, the visual presentation of the diagnostic findings to non-radiologists is difficult. Therefore, perfusion-weighted subtraction images are useful and can be generated on most MR scanners (Fig. 4). A pre-contrast image is subtracted from a dedicated contrast-enhanced image, typically with the one exhibiting maximum lung signal enhancement. The choice of the images is often done by choos-
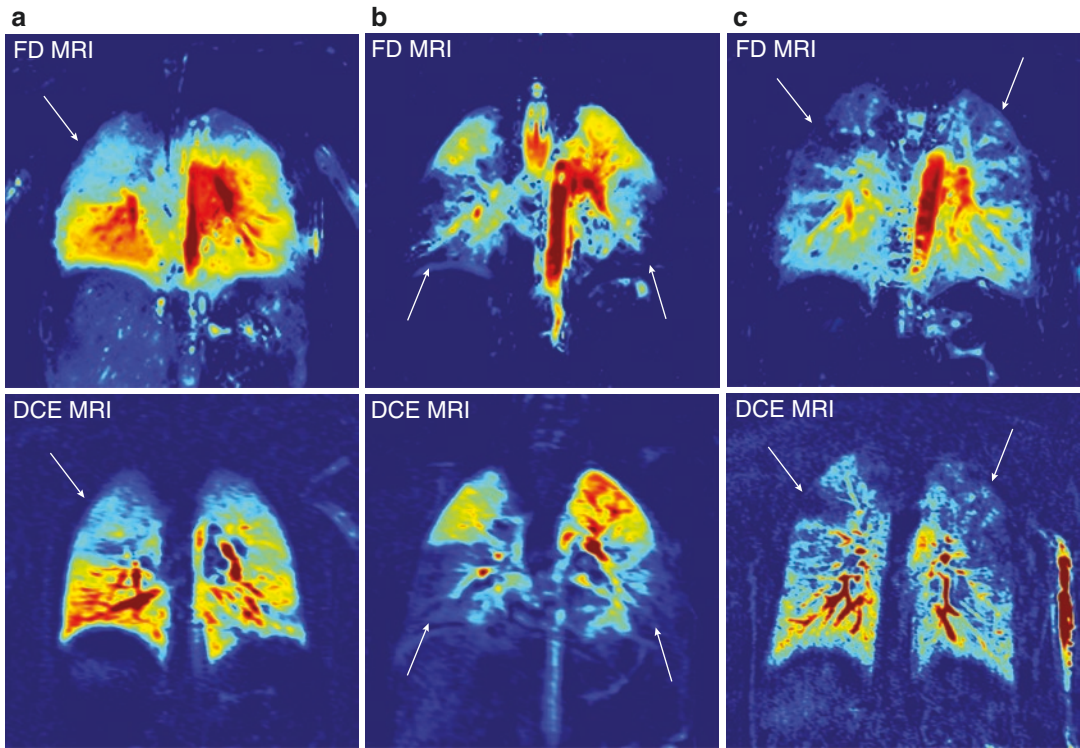
Fig. 3 Examples showing perfusion-weighted FD MRI and perfusion DCE-MRI at corresponding section locations obtained in three CF patients: (**a**) 4-year-old male, (**b**) 5-year-old male, and (**c**) 23-year-old female. Regions with perfusion defects were indicated with arrows (From Bauman et al. (2013b) with permission)
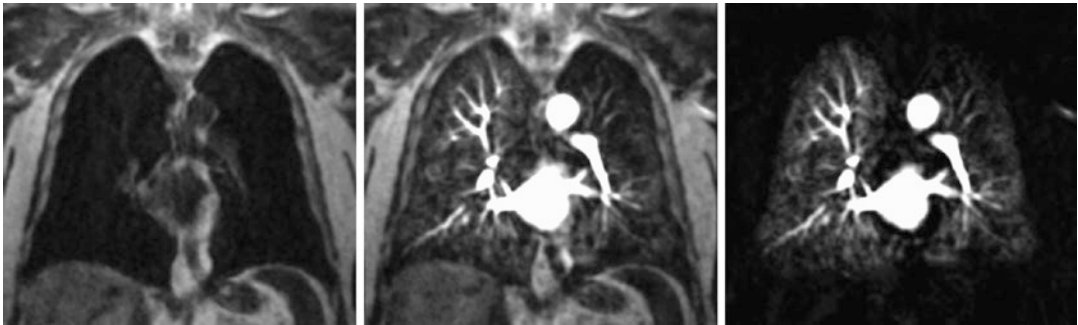
Fig. 4 Perfusion-weighted subtraction image (*right*) of a patient with chronic obstructive pulmonary disease. The image is generated by subtracting a pre-contrast image (*left*) from the image with the signal maximum (*middle*) and shows multiple patchy perfusion defects, particularly in the left lung. (Original images courtesy of Gregor Sommer, MD, Clinic of Radiology and Nuclear Medicine, University of Basel Hospital, Basel, Switzerland)

ing the eligible image frames from signal-time curves generated from a drawn region of interest (ROI) (Fink et al. 2004a). However, this approach has some drawbacks. Usually an additional investigation of a selection of original images has to be carried out. Furthermore, the choice of the images to be processed is observer-dependent and not always reproducible, particularly when a ROI analysis is performed. A suboptimal selection might mask regions of impaired perfu-

Fig. 5 Color-coded parameter maps of a patient. Maximum signal enhancement or peak map on the *left*. Time-to-peak map on the *right*
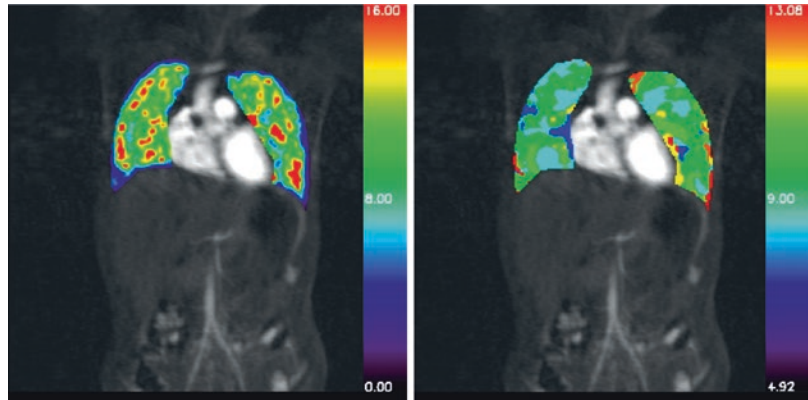
sion in the subtraction images. Moreover, the temporal information is lost, although this is of utmost importance in diseases with inhomogeneous and delayed perfusion.

A possible solution is to compute qualitative and/or quantitative parameters. Common practice is to generate parameter images in which the pixel-wise computed parameters are displayed as color-coded overlays (Fig. 5). These parameter images can be generated automatically on the MR scanners of most manufacturers. Usually the following parameters are calculated: the maximum signal enhancement or peak, the bolus arrival time, the time to peak, and the mean transit time. Some recent scanner software has also the option to compute quantitative parameters as described in Sect. 4.1. The advantage compared to subtraction images is the consideration of the temporal information. For instance, delayed perfusion cannot be masked by the choice of a suboptimal ROI (Risse et al. 2011). Recently, the implementation of an algorithm for a 3D visualization of functional perfusion parameters for better anatomic orientation and an improved representation of perfusion changes was presented to fully exploit the volumetric information (Kuder et al. 2008). The perfusion parameters calculated from 3D MR datasets were visualized in different cutting planes using a specially adapted interpolation algorithm as well as 3D volume rendering (Fig. 6). This might be helpful for the investigation of the exact localization and dimensions of abnormal perfusion by using the additional two cutting planes, e.g., for the plan-

ning of surgical therapy of lung emphysema or tumors. Furthermore, 3D parametric perfusion visualization might be used for radiation therapy planning to limit radiation dose to healthy perfused lung.

4.1 Perfusion Quantification in DCE-MRI

Beside the visual and qualitative analysis of the perfusion images, quantitative analysis can be desirable for the estimation of regional lung function for monitoring purposes or as an endpoint in interventional trials to assess treatment effects.

The pioneering work in the area of lung perfusion quantification was done by the group of Robert Edelman (Chen et al. 1999; Hatabu et al. 1999; Stock et al. 1999). Levin et al. (2001) presented an approach to lung perfusion quantification using the so-called "gamma variate" function on a pixel-by-pixel basis in healthy volunteers. In more recent studies, quantification of pulmonary perfusion is mostly done based on the indicator dilution theory (Meier and Zierler 1954) modified for the use with MRI (Fink et al. 2004b, 2005a, b; Ohno et al. 2004, 2007). Initially, an arterial input function (AIF) is defined in the feeding artery, i.e., the large pulmonary artery in case of the lung. The quantification is either done for the mean signal-time course of a defined region or for each pixel of the lung. Assuming a linear relationship between the measured MR signal and the contrast agent
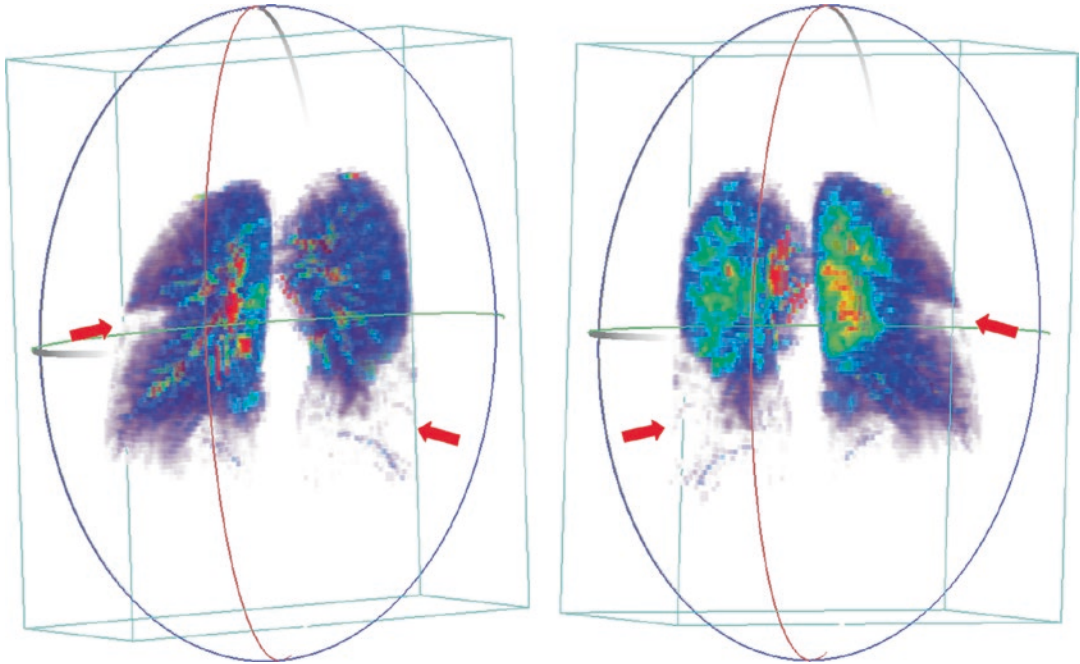
Fig. 6 3D volume rendering of the regional pulmonary blood flow in a patient with acute pulmonary embolism (*arrows*) (From Kuder et al. (2008) with permission)

concentration, the signal can be converted to a relative concentration by

$$C\left(t\right) = k\,\frac{S\left(t\right) - S_0}{S_0},\qquad(1)$$

where $S(t)$ is the signal-time course, S_0 the mean signal before the arrival of contrast agent (the baseline), and k an unknown constant depending on the specific tissue characteristics,

parameters of the pulse sequence, the contrast agent, and the inspiration level. The inspiration level affects the density of the lung parenchyma and must therefore be constant during the measurement (Fink et al. 2005a).

If the amount of contrast agent extravasating during the first pass through the lung is negligible, the measurement volume can be described by the convolution integral

$$C(t) = PBF\left[C_a\left(t\right) \otimes R(t)\right] = PBF\int_0^\infty C_a\left(t\right) \cdot R(t - \tau)\,d\tau,\qquad(2)$$

where $\otimes$ denotes the convolution. $C_a(t)$ is the concentration-time course of the AIF, *PBF* the regional blood flow, and $R(t)$ the amount of contrast agent remaining in the measurement volume at time point t (Fig. 7). The pulmonary blood flow is therefore the initial height of $R(t_0)$ or the maximum of $R(t)$ in case of a delay between $C_a(t)$

and $C(t)$ and can be assessed by the deconvolution of the measured $C_a(t)$ and $C(t)$.

The regional blood volume may generally be calculated by

$$PBV = \int_0^\infty C\left(t\right)dt\,/\int_0^\infty C_a\left(t\right)dt.\qquad(3)$$
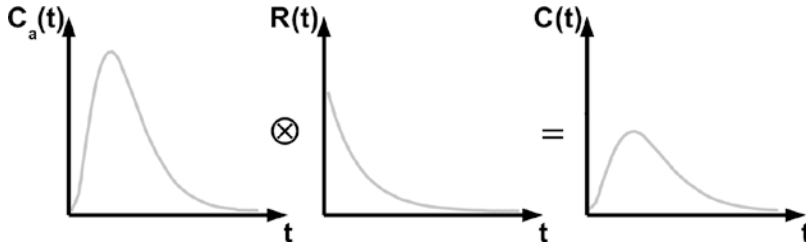
Fig. 7 Schematic representation of Eq. (2). The arterial input function $C_a(t)$ is measured in the large pulmonary artery, in the tissue response $C(t)$ in a region of interest in the lung parenchyma, or for each pixel in the lungs. The residual function $R(t)$ can be determined by the deconvolution of $C_a(t)$ and $C(t)$

However, the difference in the hematocrit of the large pulmonary artery and the lung parenchyma should be corrected by the additional factor $c_H = (1 - h_G)/(1 - h_C)$ (Brix et al. 1997), where h_G is the hematocrit of the artery and h_C of the capillaries.

According to the central volume theorem (Zierler 1962), the mean transit time (MTT), the mean time a tracer particle needs to pass through the measurement volume, is

$$MTT = PBV \: / \: PBF = \int_0^\infty R(t) \: / \: R(t_0). \quad (4)$$

A problem in quantification arises from Eq. (2) or actually from the discrete form of Eq. (2)

$$C(t) = PBF \cdot \Delta t \sum_{i=1}^{j} C_a(t_i) \cdot R(t_{j\text{-}}t_i) \quad (5)$$

as used in MRI. The solution starts to oscillate, i.e., generate meaningless results, when solved directly by, e.g., Fourier transformation in the presence of noise. Therefore, regularization tools are needed for the calculation of $R(t)$. A simple tool is the truncated singular value decomposition (tSVD), which provides stable solutions in the presence of noise as shown in brain perfusion MRI (Østergaard et al. 1996). tSVD was successfully used in several lung perfusion studies (Fink et al. 2004a, b, 2005a, b; Ohno et al. 2004). However, the application of a fixed threshold with very variable noise levels and tissue characteristics as in lung perfusion MRI will lead to a suboptimal regularization of Eq. (5). Alternatives like the Tikhonov regularization

with a modified L-curve criterion are proposed for perfusion MRI, which estimates the optimal level of regularization automatically (Sourbron et al. 2004). This method has performed best in the presence of highly heterogeneous CNR ratios in a study by Salehi Ravesh et al. (2013) in which four algebraic deconvolution/regularization methods were evaluated using simulations and human lung data.

The administration of contrast agents is mostly done at doses up to 0.1 mmol/kg body weight to achieve a sufficient CNR for diagnosis of perfusion defects. Similar to quantitative perfusion MRI in other body regions, e.g., cardiac perfusion MRI, linearity between local tissue contrast agent concentrations and the MR signal intensity, especially in the central pulmonary arteries, is a prerequisite. However, the most commonly used pulse sequence FLASH has only a limited range of linearity for low contrast agent concentrations, whereas signal saturation occurs for higher concentrations (Fig. 8).

Nikolaou et al. (2004) found a dose of 0.05 mmol/kg body weight as appropriate for their lung perfusion protocol. In another study, Ohno et al. (2007) investigated bolus injection protocols with constant bolus volumes of 5 mL but different contrast agent concentrations as a function of the subject's body weight and compared the perfusion parameters to perfusion SPECT measurements. Based on their results, a concentration of 0.3 mmol/mL Gd-DTPA was recommended for patients with a body weight <70 kg and a concentration of 0.5 mmol/mL for patients with ≥70 kg body weight. This is in accordance with a study in a porcine model using

Fig. 8 Simulated normalized signal of a 3D FLASH sequence for different contrast agent concentrations. The nonlinear behavior for higher concentrations can be clearly seen
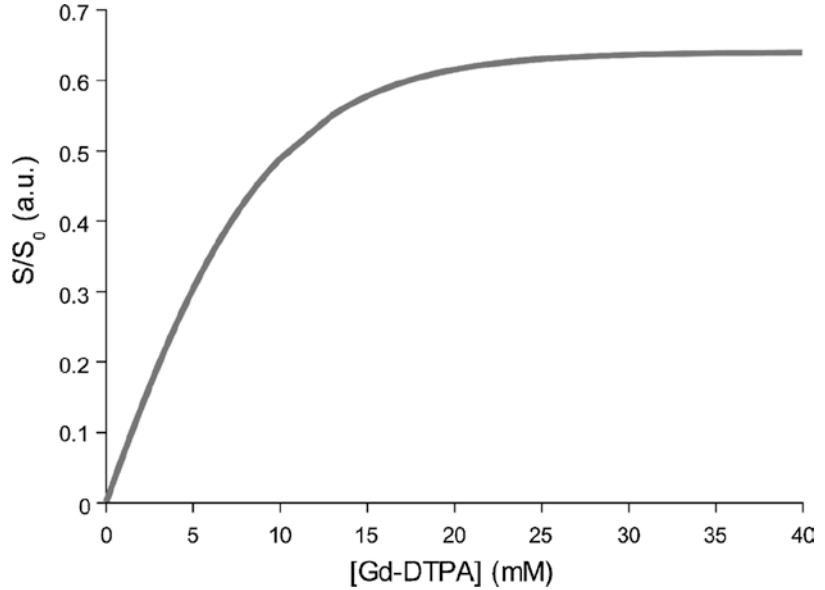
Gd-enhanced MRI and computed tomography to estimate the contrast agent concentration in vivo (Puderbach et al. 2008), which showed that the linear range was exceeded in the pulmonary artery already at a concentration of 0.5 mmol/mL in three out of five measurements.

The total dose of contrast agent may not be reduced arbitrarily because of the resulting low CNR of the lung parenchyma, particularly in low-perfused regions. As a consequence, the AIF signal is often saturated due to the high contrast agent concentration in the pulmonary artery leading to an overestimation of perfusion parameters. Signal saturation might even occur in well-perfused healthy tissue for high administered doses (Risse et al. 2006). Therefore, a dual-bolus approach to T1-weighted perfusion MRI was introduced, first to cardiac imaging (Christian et al. 2004; Köstler et al. 2004) and subsequently also to lung perfusion MRI (Risse et al. 2006, Oechsner et al. 2009). In addition to the "normal" contrast agent bolus, a prebolus with a low dose to achieve linearity is administered before the normal clinical dose. This prebolus is only used for the determination of the AIF in the large pulmonary artery, whereas the dataset acquired during the administration of the higher "clinical" dose yields the tissue signal. Admittedly, the prebolus cannot be used directly since the dose dif-

ferences between AIF and lung parenchyma would appear as an underestimation of the AIF signal, i.e., the calculation of perfusion parameters would yield too low values. Thus, assuming a linear and time-invariant system, the AIF bolus is calculated from the prebolus according to the dose of the second "high-dose" bolus. In brief, the new AIF $C_a(t)$ is constructed by adding up the prebolus volume V_p until the volume of the corresponding second bolus V is reached. To take into account not only the volumes but also the kinetics, the prebolus is shifted by its injection duration τ during the construction process (Köstler et al. 2004)

$$C_a(t) = \sum_{q=0}^{V/V_p} C_p(t + q\tau) \qquad (6)$$

The construction of the AIF is also described in Fig. 9. The new AIF can then be used to calculate the regional perfusion parameters without the influence of saturation effects in the arterial input leading to more reliable perfusion quantification even when high clinical doses are needed. However, the application of a dual-bolus technique is more complicated, and the complete washout of the contrast agent is required before the second bolus is administered. Furthermore, keeping to the linear relationship between con-
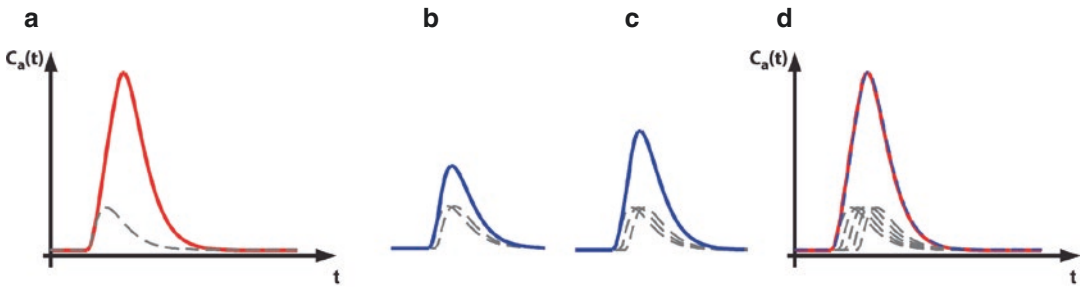
Fig. 9 (**a**–**d**) Calculation of the arterial input function for the dual-bolus approach. (**a**) The theoretical input according to the second "clinical" bolus (*red*) and the measured low-dose bolus. (**b**) In the first step, the prebolus volume is shifted according to its injection rate and added to the original prebolus. This results in the new input function (*blue*). (**c**) In the second step, the prebolus volume is again shifted and added to the intermediate result of step 1. (**d**) The procedure is repeated until the volume of the predicted volume of the second bolus (*red*) is reached (*blue*)

trast agent concentration and MR signal for both measurements is still crucial. Veldhoen et al. (2016) provided recommendations for feasible doses for three commonly used contrast agents when using a dual-bolus approach.

Despite these efforts to improve quantification methods, quantitative lung perfusion MRI in the clinic remains challenging due to the lack of standardization and widely accepted segmentation and analysis software. Hence, most clinical applications are restricted to visual assessments using scoring systems such as the morpho-functional MRI score by Eichinger et al. (2012) or to single center studies using bespoken in-house analysis software. Only recently, Hueper et al. (2013) reported a multicenter study investigating lung perfusion in COPD patients and controls with acceptable intra- and interobserver coefficients of variation below 10 %. In contrast, Ley-Zaporozhan et al. (2011) found good reproducibility of perfusion parameters but a strong interobserver dependence. This may result from differences in delineating and positioning of ROIs as automatic segmentation approaches were not used; for instance, the inclusion of large blood vessels can lead to a significant overestimation of quantitative perfusion parameters (Risse et al. 2009). Ingrisch et al. (2010) proposed a simple semiautomatic segmentation algorithm that uses information from the AIF and cross correlation analysis to identify lung tissue and to exclude large blood vessels at the same time. In general,

the repeatability and reproducibility of quantitative lung DCE-MRI would benefit from automated segmentation algorithms and an increased level of standardization.

References

Attenberger U, Ingrisch M, Dietrich O et al (2009) Time-resolved 3D pulmonary perfusion MRI: comparison of different k-space acquisition strategies at 1.5 and 3 T. Investig Radiol 44:525–531

Bauman G, Bieri O (2016) Matrix pencil decomposition of time-resolved proton MRI for robust and improved assessment of pulmonary ventilation and perfusion. Magn Reson Med. doi:10.1002/mrm.26096

Bauman G, Puderbach M, Deimling M et al (2009) Non-contrast-enhanced perfusion and ventilation assessment of the human lung by means of Fourier decomposition in proton MRI. Magn Reson Med 62:656–664

Bauman G, Lützen U, Ullrich M et al (2011) Pulmonary functional imaging: qualitative comparison of Fourier decomposition MR imaging with SPECT/CT in porcine lung. Radiology 260:551–559

Bauman G, Scholz A, Rivoire J et al (2013a) Lung ventilation- and perfusion-weighted Fourier decomposition magnetic resonance imaging: in vivo validation with hyperpolarized 3He and dynamic contrast-enhanced MRI. Magn Reson Med 69:229–237

Bauman G, Puderbach M, Heimann T et al (2013b) Validation of Fourier decomposition MRI with dynamic contrast-enhanced MRI using visual and automated scoring of pulmonary perfusion in young cystic fibrosis patients. Eur J Radiol 82:2371–2377

Bauman G, Johnson KM, Bell LC et al (2015) Three-dimensional pulmonary perfusion MRI with radial ultrashort echo time and spatial-temporal constrained reconstruction. Magn Reson Med 73:555–564

Bell LC, Johnson KM, Fain SB et al (2015) Simultaneous MRI of lung structure and perfusion in a single breath-hold. J Magn Reson Imaging 41(1):52–59

Berthezene Y, Vexler V, Clement O et al (1992) Contrast-enhanced MR imaging of the lung: assessments of ventilation and perfusion. Radiology 183:667–672

Bieri O (2013) Ultra-fast steady state free precession and its application to in vivo (1)H morphological and functional lung imaging at 1.5 tesla. Magn Reson Med 70:657–663

Bolar DS, Levin DL, Hopkins SR et al (2006) Quantification of regional pulmonary blood flow using ASL-FAIRER. Magn Reson Med 55:1308–1317

Brix G, Schreiber W, Hoffmann U et al (1997) Methodological approaches to quantitative evaluation of microcirculation in tissues with dynamic magnetic resonance tomography. Radiol 37:470–480

Buxton RB, Frank LR, Wong EC et al (1998) A general kinetic model for quantitative perfusion imaging with arterial spin labeling. Magn Reson Med 40:383–396

Capaldi DP, Sheikh K, Guo F et al (2015) Free-breathing pulmonary 1H and Hyperpolarized 3He MRI: comparison in COPD and bronchiectasis. Acad Radiol 22:320–329

Chen Q, Levin DL, Kim D et al (1999) Pulmonary disorders: ventilation-perfusion MR imaging with animal models. Radiology 213:871–879

Christian TF, Rettmann DW, Aletras AH et al (2004) Absolute myocardial perfusion in canines measured by using dual-bolus first-pass MR. Radiology 232:677–684

Eichinger M, Elzbieta Optazaitea DE, Kopp-Schneider A et al (2012) Morphologic and functional scoring of cystic fibrosis lung disease using MRI. Eur J Radiol 81:1321–1329

Fink C, Puderbach M, Bock M et al (2004a) Regional lung perfusion: assessment with partially parallel three-dimensional MR imaging. Radiology 231:175–184

Fink C, Risse F, Buhmann R et al (2004b) Quantitative analysis of pulmonary perfusion using time-resolved parallel 3D MRI – initial results. Rofo 176:170–174

Fink C, Ley S, Risse F et al (2005a) Effect of inspiratory and expiratory breathhold on pulmonary perfusion: assessment by pulmonary perfusion magnetic resonance imaging. Investig Radiol 40:72–79

Fink C, Ley S, Kroeker R et al (2005b) Time-resolved contrast-enhanced three-dimensional magnetic resonance angiography of the chest: combination of parallel imaging with view sharing (TREAT). Investig Radiol 40:40–48

Fink C, Puderbach M, Ley S et al (2005c) Time-resolved echo-shared parallel MRA of the lung: observer preference study of image quality in comparison with non-echoshared sequences. Eur Radiol 156:2070–2074

Fischer A, Pracht ED, Arnold JF (2008) Assessment of pulmonary perfusion in a single shot using SEEPAGE. J Magn Reson Imaging 27:63–70

Fishman AP (1963) Dynamic of the pulmonary circulation. In: Hamilton WF (ed) Handbook of physiology. American Physiological Society, Washington, DC, p. 1708

Griswold MA, Jakob PM, Heidemann RM et al (2002) Generalized auto-calibrating partially parallel acquisitions (GRAPPA). Magn Reson Med 47:1202–1210

Hatabu H, Gaa J, Kim D et al (1996) Pulmonary perfusion: qualitative assessment with dynamic contrast-enhanced MRI using ultra-short TE and inversion recovery turbo FLASH. Magn Reson Med 36:503–508

Hatabu H, Tadamura E, Levin DL et al (1999) Quantitative assessment of pulmonary perfusion with dynamic contrast-enhanced MRI. Magn Reson Med 42:1033–1038

Hopkins SR, Prisk GK (2010) Lung perfusion measured using magnetic resonance imaging: New tools for physiological insights into the pulmonary circulation. J Magn Reson Imaging 32(6):1287–1301

Hopkins SR, Garg J, Bolar DS et al (2005) Pulmonary blood flow heterogeneity during hypoxia and high-altitude pulmonary edema. Am J Respir Crit Care Med 171:83–87

Hueper K, Parikh MA, Prince MR et al (2013) Quantitative and semiquantitative measures of regional pulmonary microvascular perfusion by magnetic resonance imaging and their relationships to global lung perfusion and lung diffusing capacity: the multiethnic study of atherosclerosis chronic obstructive pulmonary disease study. Investig Radiol 48:223–230

Ingrisch M, Dietrich O, Attenberger UI et al (2010) Quantitative pulmonary perfusion magnetic resonance imaging: influence of temporal resolution and signal-to-noise ratio. Investig Radiol 45:7–14

Kjørstad Å, Corteville DM, Fischer A et al (2014) Quantitative lung perfusion evaluation using Fourier decomposition perfusion MRI. Magn Reson Med 72:558–562

Korosec FR, Frayne R, Grist TM, Mistretta CA (1996) Time-resolved contrast-enhanced 3D MR angiography. Magn Reson Med 36:345–351

Köstler H, Ritter C, Lipp M et al (2004) Prebolus quantitative MR heart perfusion imaging. Magn Reson Med 52:296–299

Kuder TA, Risse F, Eichinger M et al (2008) New method for 3D parametric visualization of contrast-enhanced pulmonary perfusion MRI data. Eur Radiol 18:291–297

Levin DL, Chen O, Zhang M et al (2001) Evaluation of regional pulmonary perfusion using ultrafast magnetic resonance imaging. Magn Reson Med 46:166–171

Ley-Zaporozhan J, Molinari F, Risse F et al (2011) Repeatability and reproducibility of quantitative whole-lung perfusion magnetic resonance imaging. J Thorac Imaging 26:230–239

Lim RP, Shapiro M, Wang EY et al (2008) 3D time-resolved MR angiography (MRA) of the carotid arteries with time-resolved imaging with stochastic trajectories: comparison with 3D contrast-enhanced Bolus-Chase MRA and 3D time-of-flight MRA. AJNR Am J Neuroradiol 29:1847–1854

Mai VM, Berr SS (1999) MR perfusion imaging of pulmonary parenchyma using pulsed arterial spin labeling techniques: FAIRER and FAIR. J Magn Reson Imaging 9:483–487

Meier P, Zierler KL (1954) On the theory of the indicator-dilution method for measurement of blood flow and volume. J Appl Physiol 6:731–744

Nikolaou K, Schoenberg SO, Brix G et al (2004) Quantification of pulmonary blood flow and volume in healthy volunteers by dynamic contrast-enhanced magnetic resonance imaging using a parallel imaging technique. Investig Radiol 39:537–545

Oechsner M, Mühlhäusler M, Ritter CO et al (2009) Quantitative contrast-enhanced perfusion measurements of the human lung using the prebolus approach. J Magn Reson Imaging 30:104–111

Ohno Y, Hatabu H, Murase K et al (2004) Quantitative assessment of regional pulmonary perfusion in the entire lung using three-dimensional ultrafast dynamic contrast-enhanced magnetic resonance imaging: preliminary experience in 40 subjects. J Magn Reson Imaging 20:353–365

Ohno Y, Murase K, Higashino T et al (2007) Assessment of bolus injection protocol with appropriate concentration for quantitative assessment of pulmonary perfusion by dynamic contrast-enhanced MR imaging. J Magn Reson Imaging 25:55–65

Ostergaard L, Weisskoff RM, Chesler DA et al (1996) High resolution measurement of cerebral blood flow using intravascular tracer bolus passages. Part I: Mathematical approach and statistical analysis. Magn Reson Med 36:715–725

Pracht ED, Arnold JF, Wang T, Jacob PM (2005) Oxygen-enhanced proton imaging of the human lung using T2*. Magn Reson Med 53:1193–1196

Pracht ED, Fischer A, Arnold JF et al (2006) Single-shot quantitative perfusion imaging of the human lung. Magn Reson Med 56:1347–1351

Pruessmann KP, Weiger M, Scheidegger MB, Boesiger P (1999) SENSE: sensitivity encoding for fast MRI. Magn Reson Med 30:952–962

Puderbach M, Risse F, Biederer J et al (2008) In vivo Gd-DTPA concentration for MR lung perfusion measurements: assessment with computed tomography in a porcine model. Eur Radiol 18:2102–2107

Risse F, Semmler W, Kauczor HU, Fink C (2006) Dual bolus approach to quantitative measurement of pulmonary perfusion by contrast-enhanced MRI. J Magn Reson Imaging 24:1284–1290

Risse F, Kuder TA, Kauczor HU et al (2009) Suppression of pulmonary vasculature in lung perfusion MRI using correlation analysis. Eur Radiol:2569–2575

Risse F, Eichinger M, Kauczor HU et al (2011) Improved visualization of delayed perfusion in lung MRI. Eur J Radiol 77:105–110

Rogosnitzky M, Branch S (2016) Gadolinium-based contrast agent toxicity: a review of known and proposed mechanisms. Biometals 29(3):365–376 [Epub ahead of print]. Review

Rosen BR, Belliveau JW, Vevea JM et al (1990) Perfusion imaging with NMR contrast agents. Magn Reson Med 14:249–265

Salehi Ravesh M, Brix G, Laun FB et al (2013) Quantification of pulmonary microcirculation by dynamic contrast-enhanced magnetic resonance imaging: comparison of four regularization methods. Magn Reson Med 69:188–199

Schönfeld C, Cebotari S, Voskrebenzev A et al (2015) Performance of perfusion-weighted Fourier decomposition MRI for detection of chronic pulmonary emboli. J Magn Reson Imaging 42(1):72–79

Schraml C, Schwenzer NF, Martirosian P et al (2012) Non-invasive pulmonary perfusion assessment in young patients with cystic fibrosis using an arterial spin labeling MR technique at 1.5 T. MAGMA 25:155–162

Sommer G, Bauman G, Koenigkam-Santos M et al (2013) Non-contrast-enhanced preoperative assessment of lung perfusion in patients with non-small-cell lung cancer using Fourier decomposition magnetic resonance imaging. Eur J Radiol 82: e879–e887

Sourbron S, Luypaert R, Van Schuerbeek P et al (2004) Deconvolution of dynamic contrast-enhanced MRI data by linear inversion: choice of the regularization parameter. Magn Reson Med 52:209–213

Stock KW, Chen Q, Levin DL et al (1999) Demonstration of gravity-dependent lung perfusion with contrast-enhanced magnetic resonance imaging. J Magn Reson Imaging 9:557–561

Thews G (1997) Atmung. In: Schmidt RF, Thews G (eds) Physiologie des Menschen, 27th edn. Springer, Berlin/Heidelberg/New York, pp. 565–591

Veldhoen S, Oechsner M, Fischer A et al (2016) Dynamic contrast-enhanced magnetic resonance imaging for quantitative lung perfusion imaging using the dual-bolus approach. Investig Radiol 51:186–193

Wielpütz MO, Puderbach M, Kopp-Schneider A et al (2014) Magnetic resonance imaging detects changes in structure and perfusion, and response to therapy in early cystic fibrosis lung disease. Am J Respir Crit Care Med 189:956–965

Zierler KL (1962) Theoretical basis of indicator-dilution methods for measuring flow and volume. Circ Res 10:393–407

Hyperpolarised Helium-3 (³He) MRI: Physical Methods for Imaging Human Lung Function

Jim M. Wild, Neil J Stewart, and Ho-Fung Chan

Contents

J.M. Wild, PhD (✉) • N.J. Stewart, PhD
H.-F. Chan, MEng
POLARIS, Unit of Academic Radiology,
University of Sheffield, Sheffield, UK
e-mail: j.m.wild@sheffield.ac.uk

Key Points

Hyperpolarised gas imaging has opened up the possibility of direct imaging of pulmonary ventilation by MRI. The use of hyperpolarised helium-3 (³He) gas for MRI of the lung has been pioneered by a number of groups worldwide. Due to the enormous progress in the fields of hyperpolarisation technology, administration of hyperpolarised ³He, MR hardware, and MR pulse sequences, translation into the clinical arena has been accomplished. This chapter gives an overview of the technical methods for hyperpolarised ³He MRI for human lung imaging, focusing on gas polarisation methods, MR physics, hardware and software considerations, safety considerations for inhaled ³He, and pulse sequence design for probing several aspects of lung physiology and anatomy. Where possible, the methods will be highlighted with reference to the literature and illustrated with clinical examples of images from the authors' home group. We conclude the chapter with an appraisal of how ³He methods can be translated to the more clinically scalable gas isotope ¹²⁹Xe and provide preliminary evidence of how the MRI techniques compare between the two gases, in order to lead into the following chapter on hyperpolarised ¹²⁹Xe techniques.

1   Introduction

It is now around 30 years since the first images of hyperpolarised (HP) helium-3 (^{3}He) gas in human lungs were acquired (Middleton et al. 1995; Ebert et al. 1996; MacFall et al. 1996). In that time, gas polarisation techniques and MRI methodology have developed such that HP gas MRI can now provide images of gas ventilation of unsurpassed quality, and simultaneous sensitivity to various aspects of lung physiology in a wide range of human lung diseases. Despite the obvious potential for these images to shed new light on lung function, the technique has still to find general acceptance in the clinical mainstream for a variety of reasons. These include advances in other techniques such as CT and pulmonary function testing that are already well established and accepted in the chest radiology and physiology communities, limited accessibility to the necessary technology for polarising and imaging ^{3}He and perhaps most importantly, the clear-cut identification of clinical applications that will positively benefit from the technology.

Several comprehensive reviews have been written to date on both the physics of gas polarisation and non-clinical applications of HP gas NMR (Goodson 2002; Oros and Shah 2004) and the growing number of applications in biomedical science and clinical radiology (Möller et al. 2002; van Beek et al. 2004; Fain et al. 2007; Walkup and Woods 2014). It is fair to say that ^{3}He has made more impact to date than ^{129}Xe in human lung imaging applications, with numerous clinical research exams having been performed at over ten sites worldwide using whole-body MRI scanners in a wide range of chest diseases, including asthma (Altes et al. 2001; Samee et al. 2003; Tzeng et al. 2009); cystic fibrosis (Donnelly et al. 1999; Koumellis et al. 2005; Bannier et al. 2010); emphysema/COPD (Kauczor et al. 1996; Saam et al. 2000; Salerno et al. 2002; Stavngaard et al. 2005; Swift et al. 2005; Parraga et al. 2007; van Beek et al. 2009); lung transplantation (Gast et al. 2002); lung cancer (Ireland et al. 2007); and pulmonary embolism (Altes et al. 2005). However, there are global concerns over the longevity of ^{3}He supplies, since ^{3}He has a negligible natural abundance and is predominantly derived as a by-product of the nuclear industry. In recent years, significant efforts

to improve ^{129}Xe polarisation levels (Hersman et al. 2008; Nikolaou et al. 2013; Norquay et al. 2013) have facilitated high quality human lung imaging with ^{129}Xe (Mugler and Altes 2013; He et al. 2014; Stewart et al. 2015), and preliminary comparisons of the sensitivity of the two gases to different lung pathologies (Kirby et al. 2012b; Svenningsen et al. 2013) suggest that similar functional information can be obtained with ^{129}Xe.

2   Physical, Chemical, and Medical Properties of ^{3}He and Gas Polarisation

^{3}He gas is a monatomic radio-stable isotope of the inert gas helium, with a very low natural abundance on earth (0.000137% of natural abundant helium), and is mostly derived from beta decay of the tritium nucleus in the nuclear industry. From an MRI perspective, the spin 1/2 of the ^{3}He atom coupled with its relatively high gyromagnetic ratio ($\gamma_{3He} = 32.3$ MHz/T) makes it very sensitive to NMR techniques. ^{3}He is a highly diffusive gas due to its low atomic weight, having a self-diffusion coefficient of 2 cm^2/s, which is reduced to around 0.9 cm^2/s in air. The ^{3}He diffusion coefficient can be measured with NMR, and, when introduced into a porous medium whose walls inhibit free diffusion, the ^{3}He apparent diffusion coefficient (ADC) exhibits a dependence upon the surrounding microstructure. This feature can be used to probe alveolar length scales in the lungs. As an inert gas, the NMR T_1 relaxation time of ^{3}He is potentially very long and can approach the dipole–dipole limit of days providing the gas is stored in a magnetically homogeneous environment. However, when in the presence of paramagnetic molecular oxygen, the T_1 of ^{3}He reduces in direct proportionality to the inverse of the oxygen concentration (Saam et al. 1995), leading to values of the order of tens of seconds in the lungs. ^{3}He can be detected by NMR in the gaseous state using conventional Boltzmann thermal polarisation arising from the Zeeman effect, however, the low spin density of the gaseous state makes the signal too weak for in vivo MRI. The ^{3}He nuclear spin polarisation can, however, be increased by using an alternative mechanism.

3 Polarising the ^{3}He Nuclear Spin by Optical Pumping

Laser optical pumping with circularly polarised light at selective wavelengths can be used to drive the electronic spins of certain atoms into non-Boltzmann energy level distributions. This phenomenon was first discovered over 50 years ago (Kastler 1950) and since then it has been used to transfer electronic spin polarisation to nuclear spin systems by the process of spin exchange (Walker and Happer 1997). In optical pumping, the laser photons are wavelength-matched to a chosen electronic orbital transition of the atomic system. For polarisation of noble gas nuclei, this system is generally the orbital energy levels of an alkali metal atom such as rubidium or the electron levels of meta-stable atoms of ^{3}He. The laser photons are circularly polarised with respect to the direction of an external B_0 field using a $\lambda/4$ optical polariser. The B_0 field produces a Zeeman splitting in the orbital energies, and subject to the angular momentum selection rules for transitions between available orbital levels and their Zeeman sub-levels, a net exchange of angular momentum between the spin polarised photons and the electronic system can be made, resulting in a non-Boltzmann occupancy of selected electronic Zeeman states. Having established a hyper-populated electron Zeeman sub-level, spin polarisation is then transferred to the nuclear Zeeman system of the spin 1/2 noble gas atom of interest, e.g. ^{3}He or ^{129}Xe; the overall process is thus called spin exchange optical pumping (SEOP). The mechanism of spin polarisation exchange is the Fermi contact hyperfine interaction that relies on an overlap of the $^2S_{1/2}$ electron wave function with the noble gas nucleus. This interaction predominantly takes place, in the case of ^{3}He SEOP, during binary collisions between ^{3}He and alkali metal atoms in the vapour state. In the case of ^{129}Xe SEOP the spin polarisation exchange process may involve the temporary formation of an intermediate van der Waal's molecule with N_2 gas in the optical pumping cell. The rate of spin polarisation transfer is influenced by a number of physical factors inside the optical pumping cell, which include gas pressure, vapour pressure of the alkali metal, incident photon flux, gas temperature, and propensity for formation of intermediate

molecules. A fundamental limiting factor is the electron-nuclear cross section, i.e. the probability of interaction, σ, which is larger for ^{129}Xe-Rb than for ^{3}He-Rb, leading to longer SEOP polarisation "spin-up times" for ^{3}He. The implementation of SEOP was pioneered and refined by the Happer group at Princeton (Walker and Happer 1997), and led to the design of a prototype commercial SEOP polariser with the formation of the Magnetic Imaging Technologies Inc. (MITI) company. The patents for this design were subsequently bought by Nycomed-Amersham and then GE Healthcare, and despite phase II clinical trials, the device was never properly commercialised. Recently, the company Polarean Inc. acquired these patents and established dedicated sales of polarisation systems. However, at the time of writing there exists some uncertainty over future routes to commercialisation of SEOP for ^{3}He MRI, a fact which is hampered by the rapid decline in ^{3}He availability. From a practical perspective, the prototype ^{3}He MITI polariser uses a 60-W FAP laser at 795 nm and is capable of polarising approximately 1 L of ^{3}He to a polarisation of 25–40% in a total spin-up time period of around 25 h (5× spin-up time constant of approximately 5 h). This system provides sufficient HP ^{3}He gas to perform 3–4 in vivo imaging exams only, and hence large throughput clinical research studies would require either multiple systems, or a single system with higher volume polarisation rate. High power lasers with narrowed optics (Babcock et al. 2005; Zhu et al. 2005) provide more effective transfer of the polarised photon beam energy to the alkali metal electron spin transition and are now routinely enabling high polarisation levels of ^{3}He with SEOP. Fig. 1a shows a prototype MITI polariser retrofitted with a 125-W solid-fibre laser diode array, currently in use at the University of Sheffield.

^{3}He can also be polarised by the alternative method of *meta-stability* exchange optical pumping (MEOP) (Colegrove et al. 1963) whereby the paired electrons in the ^{3}He ground state 1^1S_0 are excited to the meta-stable 2^3S_1 state by means of a weak RF discharge. Thereafter optical pumping of the $2^3S_1 \rightarrow 2^3P_0$ transition can take place with circularly polarised photons at $\lambda = 1{,}083$ nm and nuclear spin polarisation is built up through collisions of the meta-stable ^{3}He atoms in the low
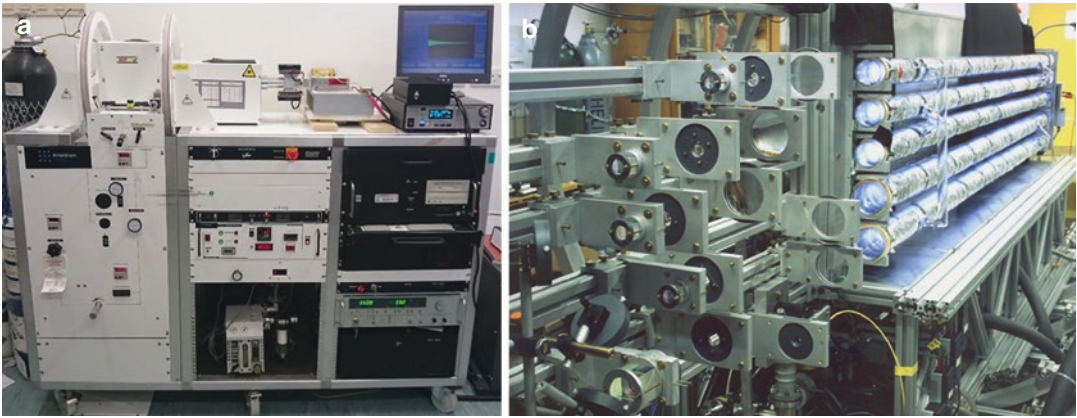
Fig. 1 (**a**) MITI prototype ^{3}He polariser in Sheffield retrofitted with a 125-W laser diode array at 795 nm. (**b**) The Mainz group meta-stable ^{3}He polariser and compressor (image courtesy of Professor Werner Heil and Professor Ernst Otten)

pressure optical pumping cell. The process of meta-stable spin exchange is faster than collisional spin exchange during SEOP, however, because of the low pressure regime required for optimal polarisation build-up efficiency, the volume of polarised ^{3}He gas must be compressed upon extraction from the optical pumping cell for in vivo use. It is fair to say that the MEOP process is more demanding than SEOP in terms of reliable extraction of large volumes of polarised gas for in vivo MRI, despite its higher polarisation efficiency. The Mainz meta-stable ^{3}He polariser and compressor (Fig. 1b) was originally built for production of HP ^{3}He for neutron spin filter work; however, it is now around 20 years since the group first obtained polarised gas for in vivo MRI with the prototype system (Ebert et al. 1996).

4 Storage, Transfer, and NMR of HP Species: The Importance of T_1

Having polarised the ^{3}He nucleus, it is vital that the polarisation is preserved in transit from the polariser to the NMR magnet. This journey may involve taking the polarised nuclear system from one B_0 to another through inhomogeneous field gradients. In noble gas optical pumping, the polarising fields are typically very weak ($B_0 \sim 2$ mT) whereas the NMR system may have a B_0 of several T. Therefore, precautions need to be taken to prevent a non-adiabatic field change. Typically, the Zeeman polarisation is preserved in a "holding" B_0 field (which can be weak; the Earth's field may suffice for short journeys) to ensure the sample is not taken through a zero field condition (i.e. field direction change). In the context of a hyperpolarised nuclear spin ensemble, the *adiabatic* condition has the meaning that when an external factor such as the B_0 is changed the population of the Zeeman levels remains unchanged (i.e. no transitions are induced).

The T_1 of the hyperpolarised nuclear spin sample depends strongly upon the physical environment. For example, pure ^{3}He gas has minimal spin–lattice interactions and has a T_1 governed by the dipole–dipole interaction, which is extremely long (>700 h at 1 atm pressure (Newbury et al. 1993)). This opens up the possibility of transporting the polarised gas large distances from polarisation source to NMR site. In the early 2000s, the Mainz group polarised and delivered gas to more than ten sites worldwide by road and air, and have been extremely supportive of the development of clinical applications of ^{3}He MRI (Wild et al. 2002b). By comparison, these T_1s are much greater than the half-life of fluorodeoxyglucose (FDG) used in PET (110 min), a technique that is performed routinely by external delivery in hospitals without access to on-site cyclotrons.

During optical pumping, a practical limit on ^{3}He T_1 is imposed by the microscopic field perturbations experienced by ^{3}He nuclei during collisional contact with magnetic impurities in the walls of the optical pumping and storage cells, although T_1s > 100 h can be obtained by coating

the cells with metallic films (Heil et al. 1995). In addition, Brownian diffusion of HP gas in the presence of macroscopic B_0 field gradients will reduce the T_1 (Schearer and Walters 1965). Furthermore, mixing with a paramagnetic gas such as oxygen will radically reduce the T_1 (Saam et al. 1995), such that the T_1 of ^{3}He in air is ~20 s. Nevertheless, as discussed later, this effect can be utilised as a means of probing lung oxygenation (Deninger et al. 1999).

5   In Vivo Administration of ^{3}He

Polarised ^{3}He is typically mixed with a larger volume of nitrogen prior to delivery to the subject for inhalation either by manual means from a sealed plastic bag or by an automated respirator device. The volume of ^{3}He used directly affects the signal to noise ratio (SNR) of the acquired images; in our experience, with gas polarised to ~25%, ~150 ml of ^{3}He typically provides sufficient SNR for a complete imaging sequence at 1.5 T. To put the raw material costs into perspective, this volume of ^{3}He currently would cost approximately 120 USD, as of our most recent quote in early 2015. One possibility to improve the cost efficacy and hence clinical viability of the technique is to scavenge the exhaled gas. Since helium is insoluble in the blood, around 90% of the inhaled gas is exhaled within about ten breaths making recycling, e.g. by cryogenic separation of ^{3}He from exhaled air (Salhi et al. 2012), a potentially cheap and viable option.

The most crucial factor to consider during breath-hold imaging exams is patient safety. In Sheffield, subjects have always been imaged with full vital signs monitoring throughout the MRI protocol. Blood oxygen saturation levels often decrease slightly towards the end of a long breath-hold (20 s), however, these levels rarely fall below 90% (Lutey et al. 2008), and this decrease can typically be pre-empted by pre-washing the lungs with a high concentration of oxygen in patients without signs of emphysema. This procedure can, however, degrade the SNR of the images by virtue of the T_1 shortening effect of oxygen as introduced above. In a study which compared patients' vital signs when ^{3}He gas was delivered as an anoxic 1-L dose from a bag or as a bolus chased by room air

via a respirator device, it was observed that the latter mode of delivery prevented the blood O_2 saturation from falling (Woodhouse et al. 2006).

Typically, the pulse rate also starts to rise towards the end of the breath-hold exam, as might be expected, nevertheless these effects are rapidly reversible. No lasting adverse effects have been found in our experience in Sheffield (with around 300 subjects). In similar experience published by the University of Virginia (with 528 subjects over a 7 year period), mild respiratory adverse events were reported in only 6% of the subjects, and one severe adverse event possibly related to the inhalation procedure was reported in a patient with atypical asthma who had an uncontrolled cough after inhalation (Altes et al. 2007). This data is also in agreement with observations in 100 subjects at the University of Washington (Lutey et al. 2008). From a regulatory perspective, ^{3}He is classed as an investigational medicinal product in Europe and the USA. However, in early 2015, the Sheffield group received a regulatory licence from the UK Medicines and Healthcare products Regulatory Agency (MHRA) to manufacture the gas as a routine diagnostic agent for lung MRI.

6   MRI Hardware Considerations for HP ^{3}He

6.1 B_0 Field Strength

The polarisation of ^{3}He is independent of the static magnetic field (B_0) of the MRI magnet and as such there is scope for high SNR imaging at low field strengths (Durand et al. 2002; Owers-Bradley et al. 2003; Salerno et al. 2005; Tsai et al. 2008); indeed both ^{3}He and ^{1}H MRI of lungs may benefit from lesser magnetic susceptibility artefacts than are found at clinical imaging field strengths of 1.5 T (Müller et al. 2001). Some theoretical discussion has taken place as to the optimum theoretical field strength for HP gas imaging (Parra-Robles et al. 2005); the answer is still very much dependent on the size of the object which dictates the electromagnetic field regime for RF coil coupling to the sample and the associated noise regime. Although interesting from a technical and theoretical point of view, this optimum B_0 has yet to be fully experimentally

proven (Dominguez-Viqueira et al. 2011) and from a practical point of view it is fair to say that high quality ^{3}He images are routinely acquired at 1.5 T at a number of groups (Diaz et al. 2008; Fain et al. 2008; de Lange et al. 2009; van Beek et al. 2009). Low field imaging of HP gas represents a cheap solution and allows the possibility of probing the physiological effects of posture with magnets oriented in an upright position (Tsai et al. 2008); however, the larger commercial MRI vendors are pushing their multi-nuclear imaging efforts on to higher field systems (1.5 T and above) and results at 3 T from Sheffield and the Robarts Institute, Canada (Parraga et al. 2008) in particular are encouraging, despite the increased B_0 inhomogeneity and associated susceptibility artefacts (Deppe et al. 2009) (see Fig. 2).

Fig. 2 (**a**, **b**) ^{3}He lung ventilation images acquired at 1.5 T and 3 T, respectively, with arrows highlighting susceptibility artefacts (Deppe et al. 2009). (**c**, **d**) T_2* maps and histograms obtained at 1.5 T and 3 T, respectively

6.2   Radio-Frequency Hardware

Although non-proton imaging is possible on commercial MRI spectrometers, none of the major vendors offer a complete integrated hardware solution for ^{3}He MRI. Thus, the interested party either has to build their own transmit-receive switches and transmit-receive coils or purchase them from a third party vendor. Transceiver coils for HP gas MRI need to be large enough to cover the FOV of the adult lungs and airways (approximately $40 \times 40 \times 25$ cm^3) without subject discomfort. Furthermore, the coils must be able to function safely and efficiently, often within the confines of a clinical whole-body scanner, which has limited bore access. Most whole-body MR systems are fitted with integrated proton body transmit coils and therefore resonant coupling between these volume resonators and the HP gas coil needs to be considered in the design process. Other design constraints include portability and minimisation of scanner dead time due to hardware changes between ^{1}H and HP nuclei imaging exams. From an application perspective, HP gas MRI is very sensitive to flip angle by virtue of the non-renewable polarisation (see Sect. 7.1); thus, the transmit coil must provide a uniform flip angle across the whole of the lungs for a range of transmit powers. A large volume resonator such as an insert birdcage provides a good solution to these requirements (De Zanche et al. 2008).

A close fitting transmit-receive coil (Fig. 3a) will invariably have a poorer B_1 spatial homogeneity but more power efficiency than a birdcage coil, which can cause problems with broadband RF amplifiers. A solution may be to use a volume birdcage coil with a dedicated ^{3}He receiver array, as shown in Fig. 3b (Deppe et al. 2011b). This not only offers increased sensitivity, but also opens up the opportunity for parallel receiver imaging with ^{3}He for acceleration of image acquisition (Lee et al. 2006).
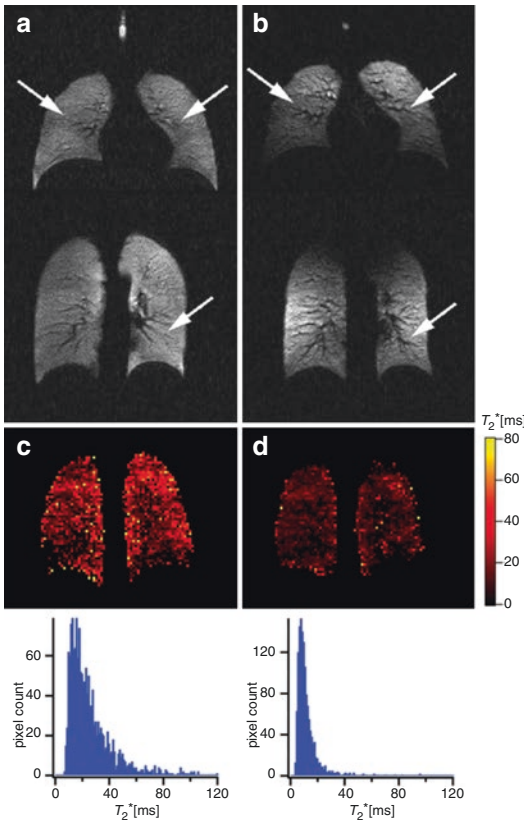
Fig. 3 (**a**) Transmit-receive vest RF coil for ^{3}He lung MRI (Clinical MR Solutions, Brookfield, WI), and (**c**) associated flip angle map. (**b**) Custom birdcage quadrature transmit-receive body coil (De Zanche et al. 2008) with 32-channel receiver array (Deppe et al. 2011b) for ^{3}He. (**d**) Flip angle map for the birdcage coil
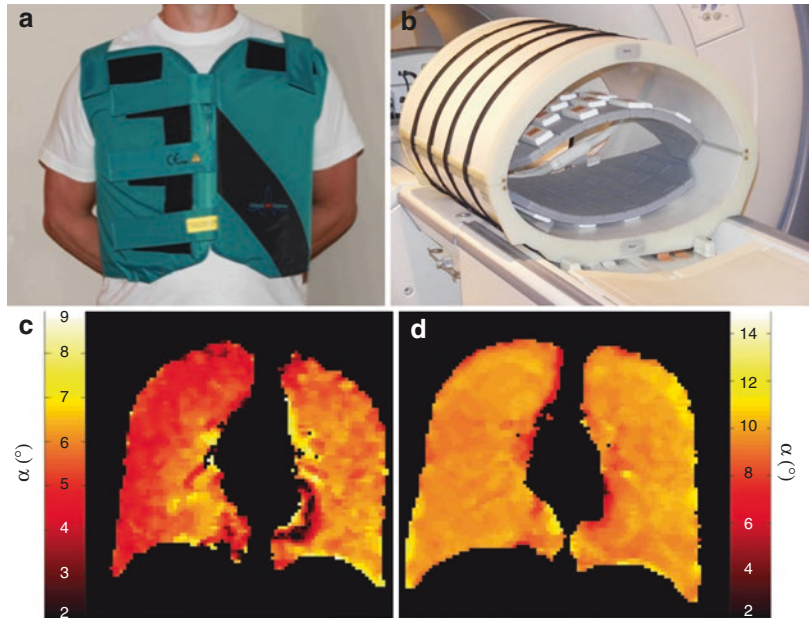
7 ^{3}He Imaging Pulse Sequence Considerations

Having delivered the HP ^{3}He to the MRI system and administered to the subject, the T_1 rapidly decreases due to exposure to residual oxygen in the lungs (Saam et al. 1995), leading to T_1 s of the order of tens of seconds. For hyperpolarised media, T_1 is the time constant of "recovery" to thermal (Boltzmann) equilibrium polarisation, and thus acts as a time constant of "decay" of the induced polarisation. Thus, the in vivo acquisition window for a HP ^{3}He pulse sequence is generally short and is constrained by the subject's breath-holding capability in addition to T_1 decay; for sick patients a breath-hold duration of less than 15 s is usually well tolerated (Woodhouse et al. 2006). The remaining challenge is effective use of the finite ^{3}He polarisation for high SNR MRI, since upon excitation the ^{3}He magnetisation returns to thermal equilibrium.

Pulse sequence optimisation should also take into account the fact that the lungs are a magnetically inhomogeneous medium with a 9 ppm difference in susceptibility between the parenchyma and airspaces, creating microscopic (sub-pixel) field gradients. As such, susceptibility artefacts may be misdiagnosed as impaired ventilation (Wild et al. 2003a; Deppe et al. 2009). Moreover, the high diffusivity of ^{3}He poses a potential problem in that the imaging gradients act to dephase the transverse magnetisation of moving ^{3}He spins.

7.1   Polarisation Usage

For a spoiled gradient echo (SPGR) sequence built up with a series of $n = 1$ to N RF pulses of constant flip angle (CFA) α, the transverse magnetisation of a HP gas during a breath-hold acquisition decays as:

$$M_{xy}(n) = M_0 \sin a \left(\cos a\right)^{n-1} \exp\left[-t / T_1\left(pO_2\right)\right]$$

(1)

where T_1 depends on the regional oxygen partial pressure, pO_2, which itself changes during the breath-hold (Deninger et al. 1999). This polarisation depletion from view to view using a SPGR sequence imposes a k-space filter on the data in the phase encoding dimension (Wild et al. 2002a) which can cause blurring or signal attenuation.

As such the choice of phase encoding trajectory is closely related to the flip angle used.

For a Cartesian (spin-warp) SPGR sequence with constant flip angle, a centric encoding order will provide higher SNR at the expense of blurring in the image, whilst a sequential ordering will result in lower SNR in the images whilst preserving the fine structure. A partial-Fourier acquisition which exploits the phase conjugate symmetry in the higher spatial frequencies represents a compromise that relies on less RF pulses for sequential ordering. As the number of RF views is reduced either by partial-Fourier methods (Wild et al. 2002a), parallel imaging with receive coil arrays (Lee et al. 2006), or radial under-sampling (Wild et al. 2003b; Holmes et al. 2008) or interleaved-spiral acquisitions (Salerno et al. 2001), the flip angle can be increased in order to utilise all the available polarisation. This provides the interesting possibility with HP gas MRI of image SNR that is independent of the number of RF encoding steps (N) (Mugler and Brookeman 2005), in contrast to the familiar $SNR \propto \sqrt{N}$ relation for conventional thermally polarised MRI.

A variable flip angle (VFA) approach can also be used in SPGR imaging with HP gases (Zhao et al. 1996); here the flip angle is increased from view to view to maintain a constant transverse magnetisation thus minimise the k-space filtering effect. The flip angle for the nth RF pulse is given by:

$$a(n) = \tan^{-1}\left[1 / \sqrt{(N-n)} \right] \qquad (2)$$

The VFA approach potentially presents the optimum strategy for SPGR imaging of ^{3}He; however,

the idealised constant magnetisation profile can diverge if there is slight mis-calibration in the RF transmit amplitude. Similarly, in 2D SPGR imaging the distribution of flip angles across the 2D slice profile (Wild et al. 2002a) can cause similar problems of divergence (Deppe et al. 2010). An alternative to spoiling the precious transverse magnetisation from view to view is to recycle it using steady state (Mugler et al. 2002; Wild et al. 2006), EPI (Saam et al. 1999) or CPMG (Durand et al. 2002) -based refocusing strategies. All of these approaches allow potentially increased SNR by using a higher excitation flip angle and subsequently refocusing residual transverse magnetisation with the finite longitudinal magnetisation. Of these approaches, steady state free precession (SSFP) acquisitions have been utilised most extensively for high SNR imaging with hyperpolarised ^{3}He (Fig. 4) (Wild et al. 2006; Qing et al. 2015). The flip angle across the slice profile is better preserved in SSFP compared with SPGR acquisitions (Deppe et al. 2010), and furthermore, variable flip angles can be employed with SSFP to enable further improvements in image quality (Deppe and Wild 2012).

However, any sequence that employs refocusing is constrained by the effect of diffusion attenuation of the transverse magnetisation which can be considerable for ^{3}He in the lungs. The diffusion related signal loss is quantified by the signal attenuation at the centre of the readout echo according to the expression $\exp(-b(\tau)D)$, where:

$$b(\tau) = \int_0^\tau |k(t)|^2 \, dt \qquad (3)$$
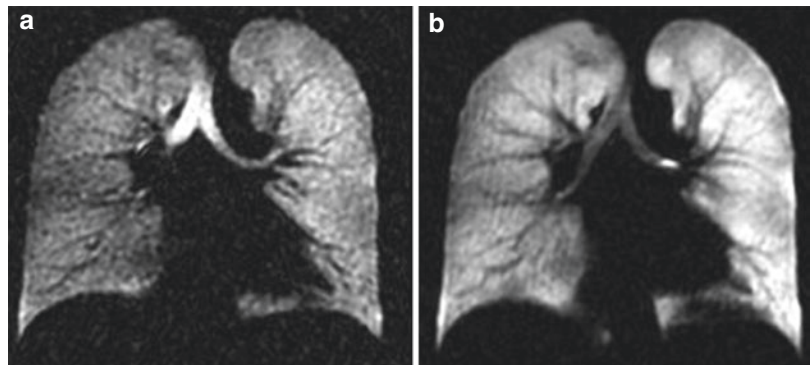
Fig. 4 2D coronal (**a**) SPGR and (**b**) SSFP images of HP ^{3}He in the lungs of a healthy volunteer, acquired at 1.5 T

is the time-dependent *b*-value derived from the time integral of the imaging gradient. $k(t) = \gamma \int_0^t G(t')dt'$ is the *k*-space encoding vector, and *G* is the time varying imaging gradient waveform.

In light of potential diffusion related signal losses, short echo time imaging, e.g. with radial and spiral sequences which start to sample the centre of *k*-space at TE ~ 0, can provide SNR advantages. This is most beneficial when imaging with small FOVs (Driehuys et al. 2007) or where gas diffusion is considerable such as in the upper airways (Wild et al. 2004). The same constraint of diffusion dephasing imposed by the imaging gradients applies to EPI sequences, and as such, limits the achievable echo train length and spatial resolution (Saam et al. 1999). Nevertheless, single shot EPI provides an attractive means of rapidly tracking gas flow dynamics and has been used more recently to estimate global lung ventilation volume with time during exhalation (Teh et al. 2007). Diffusion dephasing also limits the minimum achievable slice thickness in 2D imaging; when striving for high resolution images a 3D sequence is less prone to this source of attenuation in the slice direction and can yield higher image SNR for a given spatial resolution (Wild et al. 2004). A secondary effect in 2D imaging is the mixing of gas polarisation by diffusion of gas between the slice being excited and the adjacent slice. This effect is mitigated by keeping the sequence TR to a minimum and acquiring slices in an interleaved fashion. This slice mixing effect can be quantified by the expression below which describes the dissipation of the slice profile *f(z)* with time due to diffusion with a Gaussian distribution:

$$f(z,t) = \frac{1}{2\sqrt{\pi D t}} \int_{-\infty}^{\infty} f_0(z') \exp{-\frac{(z-z')^2}{4\pi D t}} dz'$$

(4)

This process of slice mixing can in fact be used to measure long-range diffusion coefficients (Fichele et al. 2005) and is discussed later.

8 Physiological and Anatomical Sensitivity with HP ^{3}He

The remainder of the chapter will focus on how ^{3}He MR images can be used to probe lung function. The emphasis of the following sections is on how to sensitise MR pulse sequences to different aspects of lung physiology and microstructure, and how to quantify the results with image processing techniques.

8.1 Ventilation Imaging

The obvious and most common use for HP ^{3}He images is to visualise lung ventilation distribution and homogeneity. For this purpose, high resolution images at breath-hold are needed and 2D multi-slice and 3D SPGR and SSFP sequences with Cartesian encoding routinely provide good lung coverage at voxel resolutions of around 4 mm^3. Ventilation homogeneity can be expressed qualitatively with radiological scoring procedures (Kauczor et al. 1997; Donnelly et al. 1999; Altes et al. 2001; Gast et al. 2002; Stavngaard et al. 2005; van Beek et al. 2007). The degree of ventilation heterogeneity can potentially be further quantified by texture analysis (Tustison et al. 2010), and lacunarity scoring methods that were initially used in CT. A more direct quantitative approach is evaluation of regional ventilation volumes (Woodhouse et al. 2005). ^{1}H lung images add additional information on the potentially viable ventilated volume and can be used in tandem with the ^{3}He MRI ventilation images to calculate an index of percentage ventilated volume (VV%). A 3D imaging sequence (Wild et al. 2004) with its contiguous data format allows direct calculation of regional lung volume, with the added ability to reformat images in any orientation, as shown in Fig. 5.

The ventilated volume can also be expressed by the reciprocal measure; the ventilation defect percentage (VDP), i.e. the percentage volume of unventilated lung (where VV% + VDP = 100%), as a quantitative metric of lung ventilation. Lung ventilation volume from ^{3}He MRI has been shown to correlate both with spirometry in normal and smokers (Woodhouse et al. 2005), and patients with chronic
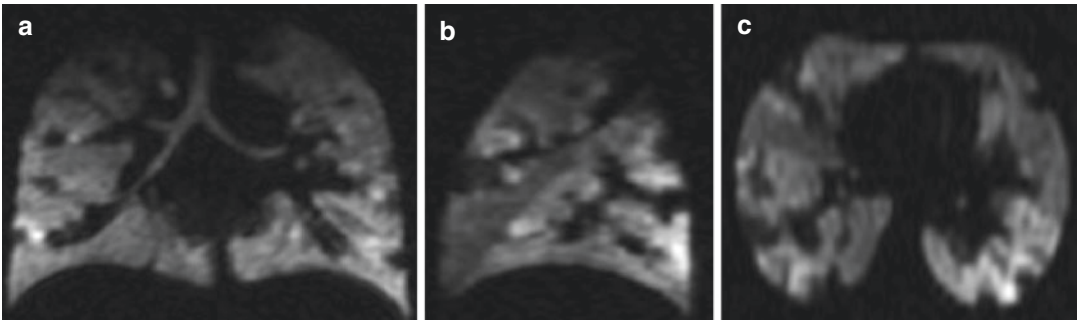
Fig. 5 Three-dimensional ³He ventilation images formatted into (**a**) coronal, (**b**) sagittal, and (**c**) axial slices, acquired from a 9-year-old child with cystic fibrosis

obstructive pulmonary disease (Mathew et al. 2011) and cystic fibrosis (Kirby et al. 2011b). Since the images supply spatially resolved data, it is a shame to sacrifice the regional ventilation sensitivity by summing up all ventilated pixels into a global index of ventilated volume. Techniques which evaluate changes in ventilation heterogeneity on a voxel-wise basis show promise in this respect (Tzeng et al. 2009), and there are a number of methods routinely used in CT that could possibly be adapted for this purpose in future (Evans et al. 2008).

The non-invasive nature of hyperpolarised ³He MRI makes it well suited to longitudinal examinations of disease progression (Kirby et al. 2010) and assessment of response to treatment (Samee et al. 2003; Woodhouse et al. 2009; Kirby et al. 2011a). For these applications, the baseline repeatability of the ventilation imaging is of great importance; this depends upon the respiratory manoeuvre and distribution of ventilation defects, which has been shown to change with time and posture in healthy subjects (Mata et al. 2008). ³He images obtained pre- and post-administration of a bronchodilator in a subject with asthma are shown in Fig. 6, along with a "treatment response" map of the improvement in ventilation.

8.2 Dynamic Imaging

HP gas MRI is not constrained by saturation recovery of the signal and as such it is possible to acquire images at very short TRs and high SNR. This opens up the possibility of imaging gas flow dynamics, wash-in and wash-out, and other time resolved processes such as air trapping, which occur over time
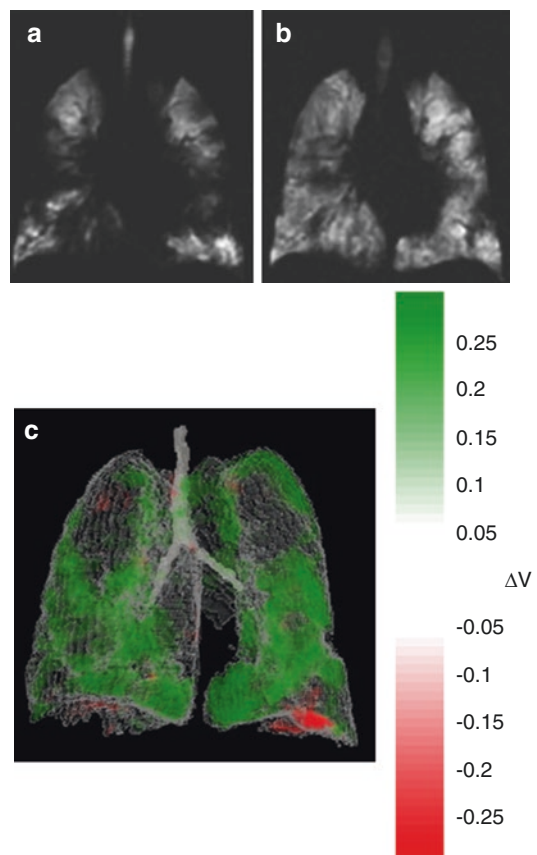
Fig. 6 2D SPGR ³He ventilation images acquired in a subject with asthma, (**a**) pre- and (**b**) post-administration of a bronchodilator. (**c**) Map of the response to bronchodilator treatment, presented as the fractional change in ventilation between the two images, overlaid by a 3D render of the thoracic cavity

scales of the order of milliseconds. Work to date in humans has largely focused on using very rapid time resolved 2D acquisitions with partial-Fourier Cartesian SPGR (Schreiber et al. 2000), spiral

(Salerno et al. 2001) and radial (Wild et al. 2003b; Holmes et al. 2008) sequences; an example of the latter is shown in Fig. 7. The non-Cartesian methods oversample the centre of *k*-space and can be readily adapted to sliding window reconstruction and thus seem to be particularly effective for 2D dynamic imaging. These sequences provide a 2D planar view of the lungs with very fast temporal resolution and have been used to elucidate rates of gas flow in the major airways and periphery on a voxel-wise basis (Gast et al. 2003; Koumellis et al. 2005). By modulating the flip angle used with respect to the rate of inhalation, the time series of images can be weighted according to gas flow rate in order to delineate the major airways where gas flux is highest (Tooker et al. 2003).

Dynamic imaging sequences can potentially be run directly after a volumetric breath-hold exam in order to investigate the gas clearance rate (Holmes et al. 2007). In addition, these acquisition techniques allow for the possibility of assessing pulmonary mechanics including shear motion and strain, during inhalation (Cai et al. 2009). With the advent of faster volumetric imaging sequences that use compressed sensing undersampling (Ajraoui et al. 2010) and parallel imaging (Deppe et al. 2011b) techniques (see Sect. 9), the possibility also exists for high temporal resolution 3D imaging of ventilation.

An alternative approach to imaging the rapid influx of HP gas during inspiration is to monitor the slower multiple-breath wash-in of signal in a fashion similar to that used in nuclear medicine ventilation studies. In this approach the regional fractional ventilation – i.e. the volume of gas turned over per breath – can be derived (Deninger et al. 2002b; Emami et al. 2010; Hamedani et al. 2016) as a quan-titative index of regional gas ventilation. More recently, these techniques have been adapted to monitor ^{3}He gas wash-out dynamics over several breathing cycles in order to quantify fractional ventilation (Deppe et al. 2011a; Horn et al. 2014) (Fig. 8).

A final dynamic imaging approach involves exploiting the phase contrast (PC) sensitivity to steady flow provided by MRI. Work in this field has adapted methods developed for phase contrast MR angiography to enable mapping of gas flow profiles and turbulence in the upper airways (de Rochefort et al. 2006; Collier and Wild 2015) (see Fig. 9). Recently, these techniques have been employed to probe the effect of the heartbeat on gas flow dynamics in the lungs (Collier et al. 2015).

8.3   Measurement of Regional Oxygen Uptake

As described in Sect. 7.1 (see Eq. (1)), the T_1 decay of HP ^{3}He is strongly affected by the effect of mixing with oxygen in the air. The dependence of the ^{3}He T_1 on oxygen concentration was quantified by Saam et al. (1995); the longitudinal relaxation rate $(1/T_1)$ is given by $\Gamma_{O_2}(t) = pO_2(t)/\xi$, where the coefficient ξ was determined empirically as 2.61 bars at 310 K. This pO_2 dependence of the ^{3}He T_1 was subsequently used by Deninger et al. (1999) for in vivo quantification of pO_2 in breath-hold experiments on pigs and humans. Under breath-hold conditions, the HP ^{3}He image signal intensity, A_n, in a time series of *n* images acquired with *N* RF pulses per image, can be derived from Eq. (1) as:

$$A_n = A_0 \left(\cos \alpha \right)^{nN} \exp\left(-\frac{1}{\xi} \int_0^{t_n} pO_2(t) dt \right) \quad (5)$$
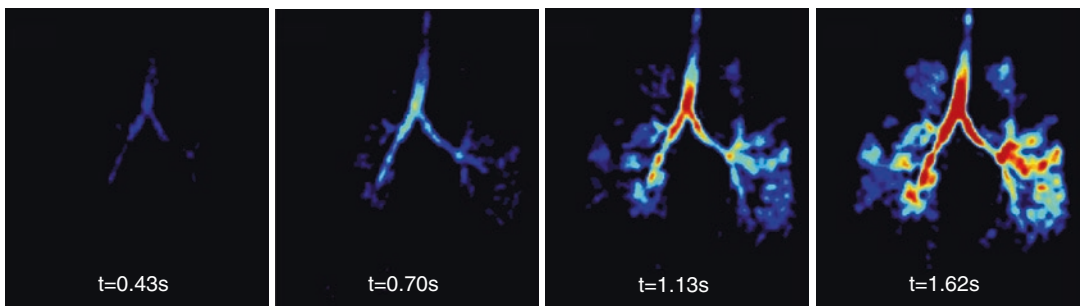
Fig. 7 Selected time frames from a dynamic time series of ^{3}He images acquired with a 2D radial sequence (Wild et al. 2003b) in a patient with severe COPD
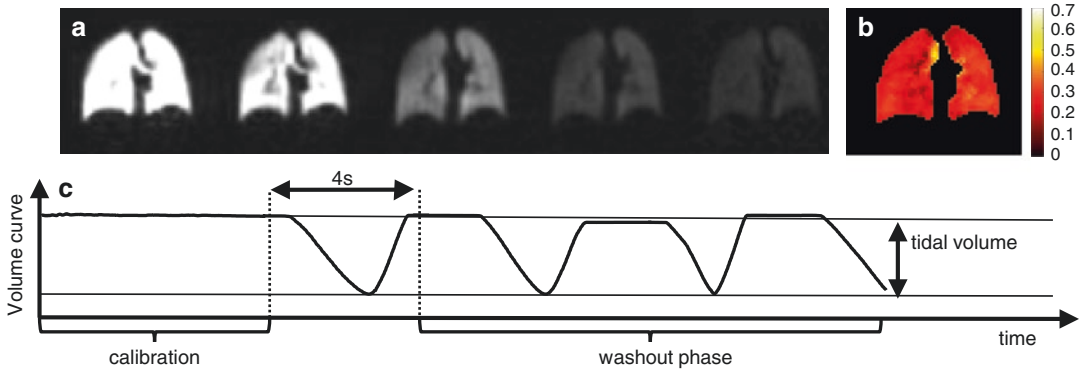
Fig. 8 (a) Time series of ³He ventilation images acquired from a healthy volunteer during a multiple-breath wash-out imaging experiment (Horn et al. 2016). (b) Fractional ventilation map derived from the time series of images in (a). (c) Lung volume derived from flow measurements at the mouth during the multiple-breath wash-out acquisition. The first two images in (a) are acquired in one breath-hold to calibrate for RF and T_1 decay between acquisitions, and hence normalise subsequent acquisitions such that decay in signal can be attributed to gas wash-out only
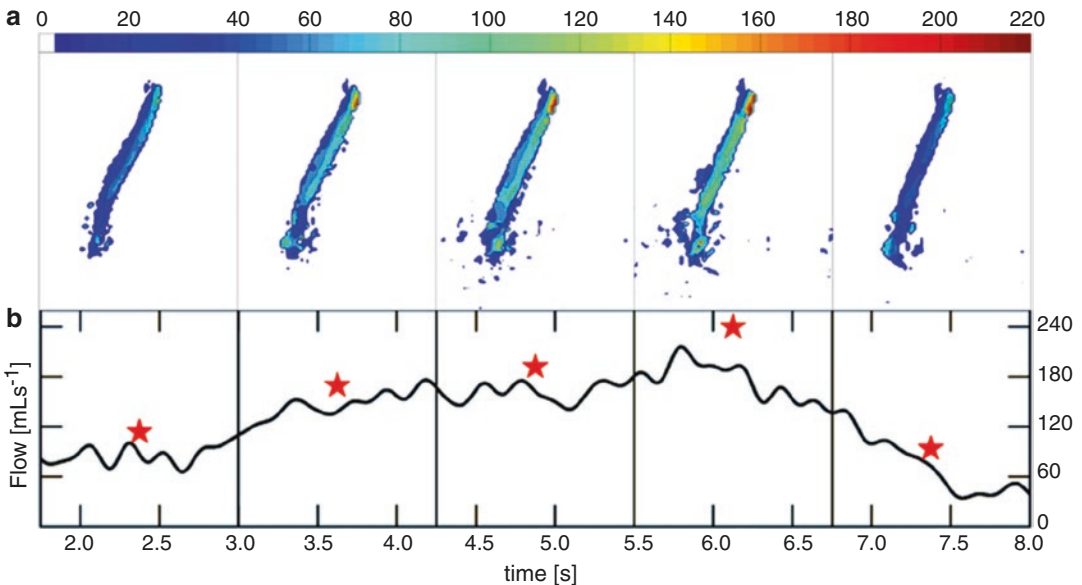
Fig. 9 (a) Time series of ³He gas velocity maps in the trachea during steady breathing through a flowmeter (Collier and Wild 2015). (b) Flowmeter recordings at the mouth (red stars represent flow estimates derived from the MR images)

Thus, by acquiring a time series of images with different inter-image delay times (t_n), the RF depletion and $T_1(pO_2)$ effects can be separated to give an estimate of the regional $pO_2(t)$. This method relies on the assumption that oxygen uptake in the human lung can be approximated by a linear rate constant (R), such that $pO_2(t) = p_0 - Rt$, (where $p_0 = pO_2(t = 0)$); this could represent a short time scale approximation to the exponential behaviour reported in rat lungs by ³He T_1 measurements (Cieślar et al. 2007). Practically, in vivo

experiments use thick slice 2D images (whole lung projections) acquired with two sets of weightings – either different flip angles or different inter-image delays. This dual scan approach is ³He intensive and prone to registration and breath-hold irreproducibility, as such single breath-hold versions of the method have been proposed (Deninger et al. 2002a; Fischer et al. 2004). For accurate fitting of the decay curve, high image SNR is important whilst the spatial resolution of the images is less paramount. Furthermore, the effect of inter-

slice diffusion of gas during the significant inter-image delay time (up to 7 s) can introduce erroneous decay rates which can be circumvented by using a 3D imaging sequence (Wild et al. 2005) (Fig. 10). However, the major limitation of this technique to date is diffusional mixing of HP ^{3}He gas and consequent collateral ventilation in emphysematous lungs (Marshall et al. 2012).

8.4 Diffusion Measurement

One of the most powerful and proven aspects of HP ^{3}He MRI is its sensitivity to gas diffusion (random Brownian motion of the atoms). In air (at standard temperature and pressure conditions) the diffusion coefficient (D) of ^{3}He is on the order of 0.88 cm^2/s (Liner and Weissman 1972), and it can travel root-mean-square distances of millimeters over the timescale of milliseconds, as calculated from the solution to the 1D diffusion equation $\bar{x} = \sqrt{2Dt}$. For example, in an MR experimental time frame of 5 ms, ^{3}He gas atoms can travel a root-mean-squared (RMS) distance of $\approx$1 mm. Considering the smallest confining structure in the lungs to be an alveolus, which is approximately 0.3 mm in diameter, gas atoms can encounter the tissue walls multiple times during a MR sequence repetition time (TR), which is typically ~5 ms. The confinement by the alveolar walls leads to a "restriction" in gas diffusion and hence the measured apparent diffusion coefficient (ADC) is much smaller in healthy lungs than that of diffusion in free-space. Diffusion-weighted MRI measurements reveal that the ^{3}He ADC is between 0.1 cm^2/s and 0.2 cm^2/s in healthy lungs (Saam et al. 2000; Salerno et al. 2002; Swift et al. 2005; Fain et al. 2006), in comparison to the free diffusion coefficient in room air of 0.88 cm^2/s. The restricted diffusion process in healthy lungs (and emphysematous lungs wherein the diffusion restriction is altered by tissue destruction) is depicted in the schematic in Fig. 11.
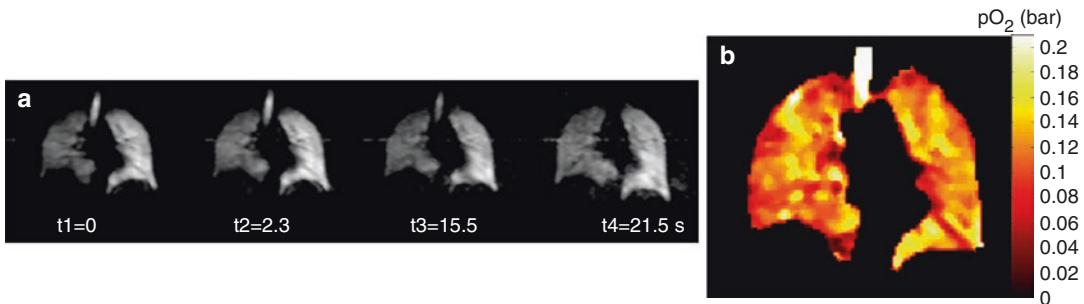
Fig. 10 (**a**) Time course of images from one slice of a 3D single scan pO_2 imaging acquisition (Wild et al. 2005), and (**b**) the calculated pO_2 map
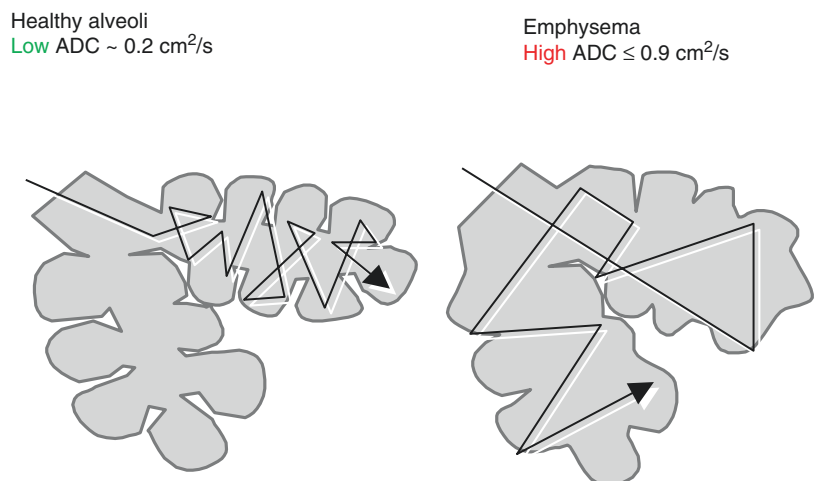
Fig. 11 Schematic of a healthy and an emphysematous alveolar sac and the effect on diffusion path length

8.4.1   Measuring Diffusion: Time-Length Scale Dependence

As discussed earlier, diffusion acts to attenuate irreversibly the MR signal whenever a magnetic field gradient is present. Hence, MRI sequences can be used to measure diffusion by using pulsed or static gradients after the application of the excitation RF pulse. These methods stem from the seminal work of Carr and Purcell (1954) and Stejskal and Tanner (1965). For HP ^{3}He, the most commonly employed method is the pulsed-gradient-spin-echo (PGSE) technique. It is easily implemented, robust, and most importantly, it can be incorporated into fast sequences that can be performed within a breath-hold. The standard PGSE method utilises two pulsed gradients separated by a time Δ, and a 180° refocusing pulse, all situated after the slice-selection gradient and usually before the phase encode step of the sequence. The same diffusion measurement can also be made without the 180° refocusing pulse; instead by modifying the polarity of the two gradient pulses, as shown in Fig. 12. However, this essentially limits experiments to short values of Δ, since T_2^* causes signal attenuation. Furthermore, the refocusing pulse can mitigate

some of the measurement errors introduced due to superposition of background gradients.

The simplified PGSE diffusion-weighted SPGR sequence block, as typically used for HP gases, is depicted in Fig. 12. The diffusion b-values are computed from Eq. (3), and for the PGSE sequence in Fig. 12, b-values can be expressed in terms of the gradient waveform parameters:

$$b = \gamma^2 G^2 \left[\begin{array}{l} \delta^2 \left(\Delta - \dfrac{\delta}{3} \right) + \\[2mm] \tau \left(\delta^2 - 2\Delta\delta + \Delta\tau - \dfrac{7}{6}\delta\tau + \dfrac{8}{15}\tau^2 \right) \end{array} \right]$$

(6)

where γ is the gyromagnetic ratio, G is the applied field gradient, Δ is the diffusion time, δ is the pulse duration, and τ is the ramp time. The ADC is subsequently evaluated by an exponential fit to the expression exp $(-b \cdot \text{ADC})$. This sequence is best run in an interleaved mode where the acquisition of each line of k-space is repeated at different diffusion weightings: the first interleave typically has no diffusion weighting ($b = 0$), while the subsequent interleaves incorporate bipolar gradient waveforms of differ-
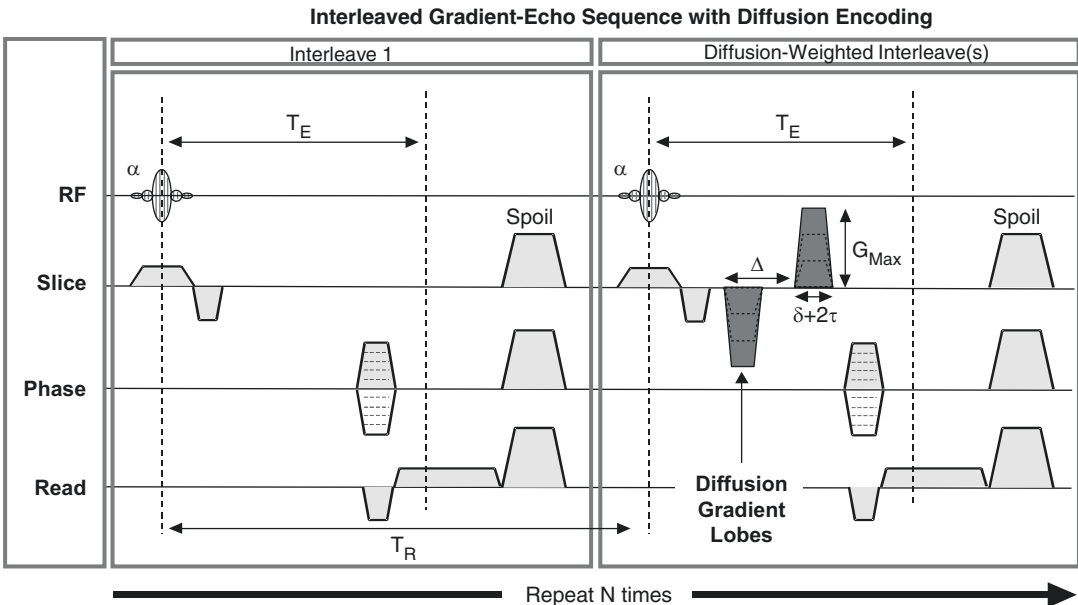
Fig. 12 Diffusion-weighted spoiled gradient echo (SPGR) sequence, based on the PGSE sequence, typically used for measuring ^{3}He ADC

ent non-zero *b*. Interleaving in this fashion ensures a reduced sensitivity to motion artefacts and greatly reduces any flip angle and T_1 relaxation bias in the resulting ADC measurement. However, it is crucial that each interleave has the same time-to-echo (TE) and repetition time (TR).

Various investigations into diffusion in the human lungs have been performed using variations of the PGSE sequence shown in Fig. 12. The first reported measurements of ^{3}He diffusion were by Mugler et al. (1998) at a field strength of 1.5 T, using a bipolar gradient waveform with four *b*-values of 0.4, 0.8, 1.2, and 1.6 s/cm^2. ADC values were calculated on a pixel-by-pixel basis using a linear, least-squares fit to yield a single average ADC value for all four *b*-values. The overall mean ADC value over all healthy volunteers was found to be 0.25 cm^2/s, almost a factor of four times smaller than the unrestricted diffusion coefficient of ^{3}He in air.

A more comprehensive study, using 11 healthy volunteers and 5 patients with severe emphysema, was performed by Saam et al. (2000). Here, diffusion was encoded using

only two *b*-values: for the healthy volunteers the values were $b = 0$ s/cm^2, and $b = 2.75$ s/cm^2, whilst for the emphysema patients a lower second *b*-value of 1.375 s/cm^2 was selected. Diffusion in both cases was encoded with a relatively long diffusion time of 7.5 ms. The results from the healthy volunteers yielded an average ADC value of 0.20 cm^2/s, whereas the ADC values from the emphysema patients were greatly elevated, with an average of 0.50 cm^2/s. The results clearly demonstrated that destruction of the lung tissue led to higher ADC values, closer to the unrestricted diffusion coefficient of ^{3}He (see Fig. 13). Following this study, Salerno et al. (2002) conducted a study in sixteen healthy volunteers, and eleven patients suffering from emphysema, using identical encoding methods to those of Mugler et al. (1998). The ADC average was found to be 0.23 cm^2/s for healthy volunteers, and 0.45 cm^2/s for the patients with emphysema. In addition, the ADC values were compared to spirometry measurements taken before each scan. The ADC values were found to correlate
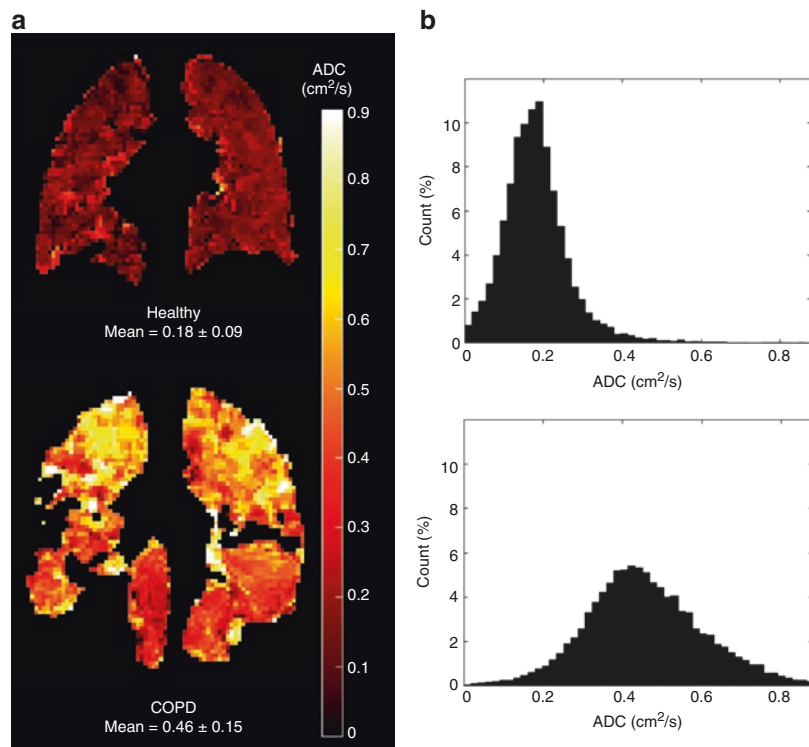
Fig. 13 (**a**) Single slice ^{3}He ADC map and (**b**) corresponding whole lung histogram from a healthy subject and a COPD patient

significantly with the forced expiratory volume in 1 s (FEV_1), which is of great importance given that spirometry is routinely used to assess disease severity. Several groups have since used PGSE sequences such as these to elucidate early emphysematous changes in smokers (Swift et al. 2005; Fain et al. 2006), bronchodilator effects in severe COPD (Kirby et al. 2012a), growth of alveoli with age (Fain et al. 2005), postural and anatomical gradients within the lung (Fichele et al. 2004c), and subtle changes in asthma (Wang et al. 2008). In addition, preliminary evidence of ADC change in patients with radiation induced lung injury (Mathew et al. 2010) and in transplanted lungs of patients with pulmonary fibrosis (Bink et al. 2007) is promising for wider applications of the technique. Importantly, ^{3}He ADC results have been shown to match well with the alveolar dimensions measured from histological sections in experiments made in animal (Peces-Barba et al. 2003) and human lungs (Woods et al. 2006).

The mean ADC value is clearly an indicator of alveolar size and hence disease severity in the case of emphysema; however, the diffusion regime of measurement of gases in the alveolar microstructure imposes a dependence of the ADC upon the diffusion weighting gradient strengths and timings (Fichele et al. 2004b). This sequence timing dependence of the ADC means that care should be taken when making a direct comparison of ADC results from different sites made with sequences with different diffusion weightings.

8.4.2   Theoretical Models of Gas Diffusion

Whilst the calculation of ADC assumes that gas diffusion is associated with a Gaussian distribution of phases (c.f. Eq. (4)), leading to a mono-exponential decay of MR signal, the diffusion regime of ^{3}He gas in the lungs results in a non-Gaussian phase dispersion and non-mono-exponential signal decay. This effect is experimentally seen in the dependence of the ADC upon the diffusion weighting gradient strengths and timings (Fichele et al. 2004b), and is caused by the numer-

ous airways with different sizes and orientations with respect to the diffusion sensitising gradient contained within one voxel. These different diffusion regimes result in differences of apparent diffusion rates, which are not fully compensated by motional averaging for the relatively short diffusion times used in typical ^{3}He diffusion-weighted MR measurements (Parra-Robles and Wild 2012). The heterogeneity of the apparent diffusivity is further increased by localised diffusion effects (Hurlimann et al. 1995) caused by strong gradients at structural edges (Parra-Robles et al. 2010a), as well as effects related to the airway connectivity (e.g. branching) (Parra-Robles and Wild 2012) and background susceptibility gradients (Parra-Robles et al. 2012).

The dependence of the observed ^{3}He signal on these factors of the local diffusion regime causes difficulties when extracting quantitative information about lung microstructure from in vivo diffusion-weighted MR imaging. Much work has been performed in modelling the effect of restricted diffusion of ^{3}He inside analytical/geometrical (Yablonskiy et al. 2002; Conradi et al. 2004; Grebenkov et al. 2007; Sukstanskii and Yablonskiy 2008) and numerical (Fichele et al. 2004a, b) models of lung microstructure. However, to date, only cylindrical geometrical models (Yablonskiy et al. 2002; Sukstanskii and Yablonskiy 2008), stretched exponential models (Parra-Robles et al. 2014), and q-space transforms (Shanbhag et al. 2006) have been used to provide estimates of alveolar length scales in vivo from ^{3}He gas diffusion measurements. A fundamental requirement for the application of each of these models is that multiple (>2) high b-value diffusion measurements are acquired to sufficiently sample the non-mono-exponential diffusion signal.

The first in vivo measurements of alveolar geometrical parameters were reported by Yablonskiy et al. (2002), using an analytical model of respiratory airways as infinitely long cylinders, based upon the Weibel model of acinar geometry (Fig. 14a). Multiple b-value diffusion-weighted MR measurements were used to estimate alveolar duct diameters from a model of anisotropic diffusion in healthy subjects and patients with emphysema. This cylindrical geometrical model was
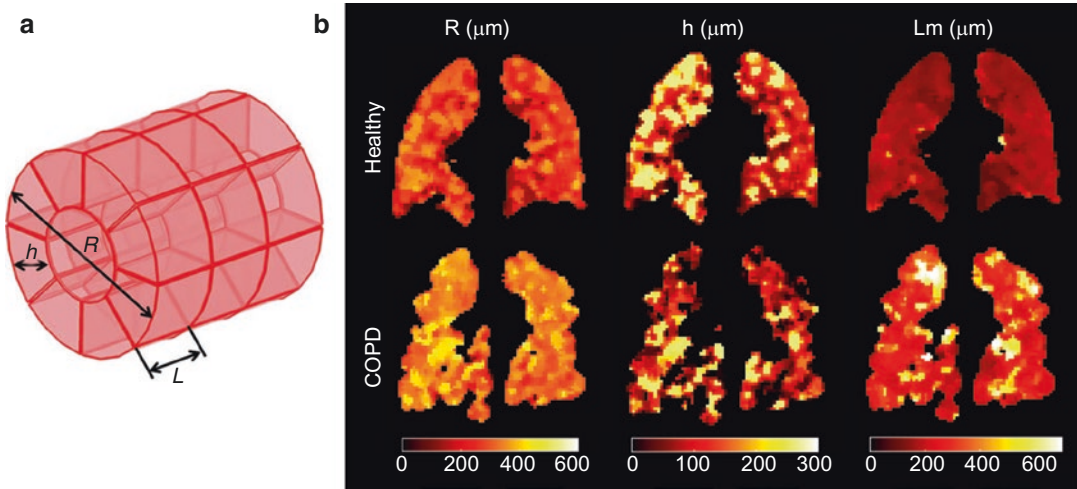
Fig. 14 (**a**) Geometric model of alveolar ducts used in the cylinder model. Each duct consists of infinitely repeating alveolar segments that are described by alveolar radii (*R*) and alveolar depth (*h*) and effective alveolar diameter (*L*) (Parra-Robles et al. 2012). (**b**) Example of healthy subject and COPD patient parametric maps of *R*, *h*, and mean linear intercept (*Lm*) derived from the cylindrical geometric model

subsequently updated (Sukstanskii and Yablonskiy 2008) to permit the evaluation of parameters of lung morphometry (including mean linear intercept (*Lm*), surface-area-to-volume ratio (*S/V*), and density of alveoli (N_a)) from the model parameters of alveolar radius (*R*) and alveolar depth (*h*).

Lm measurements derived from ^{3}He diffusion MRI analysed with this cylindrical geometrical model have been found to be strongly correlated with histological measurements of *Lm* in specimens of healthy and emphysematous lungs (Yablonskiy et al. 2009). Various groups have since used this model to study changes in lung microstructure associated with smoking-related early emphysema (Quirk et al. 2011; Paulin et al. 2015), age (Quirk et al. 2016), lung inflation (Hajari et al. 2012), and adult lung growth (Butler et al. 2012).

An alternative theoretical model of ^{3}He diffusion signal behaviour in the lungs is the stretched exponential model (Grebenkov and Guillot 2006; Parra-Robles et al. 2014). This model does not require any assumptions about the lung geometry to derive in vivo estimates of alveolar length scales. In the stretched exponential model, the measured macroscopic (voxel) signal can be represented as the superposition of signals with different apparent diffusivities *D*:

$$\frac{S_b}{S_0} = \int_0^{D_0} p(D) e^{-bD} dD \tag{7}$$

where S_0 is the signal when $b = 0$, S_b is the signal when b is non-zero, and D_0 is the free diffusion coefficient of ^{3}He in air. The continuous summation of exponential decay functions modulated by the probability density function $p(D)$ can be represented with a stretched exponential function such that:

$$\frac{S_b}{S_0} = e^{[-b \cdot DDC]^\alpha} \tag{8}$$

where DDC is the distributed diffusion coefficient and α is a heterogeneity index that describes the amount of deviation from mono-exponential signal decay behaviour (Berberan-Santos et al. 2005; Parra-Robles et al. 2010b). Recently, it was demonstrated that DDC and α values were significantly different in healthy subjects and patients with COPD, and that α values were independent of diffusion time and lung inflation size (Parra-Robles et al. 2013).

A probability distribution of diffusion length scales ($p(L_D)$) can be determined from $p(D)$ by using the diffusion equation, $L_D = (2D\Delta)^{½}$ (i.e. the root-mean-squared displacement, where Δ is the

diffusion time). The $p(L_D)$ distribution is a measure of the distribution of microscopic dimensions of the airways (i.e. the diffusion-restricting boundaries) contained within a given voxel, and the shape of the distribution is similar to that of intercept length measured in histological studies. The $p(L_D)$ distribution can thus be used to derive a mean diffusion length scale (Lm_D), analogous to the histological mean linear intercept. The first in vivo Lm_D values were reported in a population of asthmatic subjects, and Lm_D was shown to significantly correlate with %-predicted functional residual capacity (FRC) measurements from spirometry, in addition to CT density (Parra-Robles et al. 2014). With the implementation of compressed sensing acquisition for scan time reduction (see Sect. 9.2), 3D whole lung Lm_D maps have been recently acquired in a single breath-hold from healthy subjects and patients with COPD (Chan et al. 2016). Examples of stretched exponential model data is presented in Fig. 15.

Global spectroscopic measurements of HP gas diffusion can also provide an alternative means to obtain lung microstructural information. At the expense of spatial information, diffusion-weighted spectroscopy experiments offer shorter acquisition times and require less hyperpolarised ^{3}He gas than the imaging-based methods discussed above, and therefore may be ideally suited

for longitudinal monitoring of paediatric patients. Multiple b-value diffusion-weighted spectroscopy data can be analysed using q-space theory (Callaghan et al. 1988) to derive displacement probability profiles and root-mean-square displacements (X_{rms}) (Shanbhag et al. 2006). Shanbhag et al. (2006) used a bi-Gaussian model to derive narrow (X_{rms1}) and broad (X_{rms2}) root-mean-square displacements in healthy children and adults, and COPD patients. X_{rms1} and X_{rms2} correspond to two different diffusion length scales in the lung, and both values correlated well with age and conventional ADC measurements, suggesting that these MR spectroscopy-derived displacements may be similarly sensitive to changes in lung microstructure. Recently, O'Halloran et al. (2010) further developed the hyperpolarised ^{3}He MR q-space imaging technique to obtain 3D spatially resolved X_{rms} maps in a healthy volunteer using an under-sampled radial stack-of-stars acquisition.

8.4.3 Long Time Scale Diffusion

As discussed earlier, the dependence of the HP gas diffusion MR signal on the PGSE sequence timing indicates that with longer diffusion times it is possible to probe longer diffusion length scales in the lungs, associated with inter-acinar connectivity and disease processes that lead to
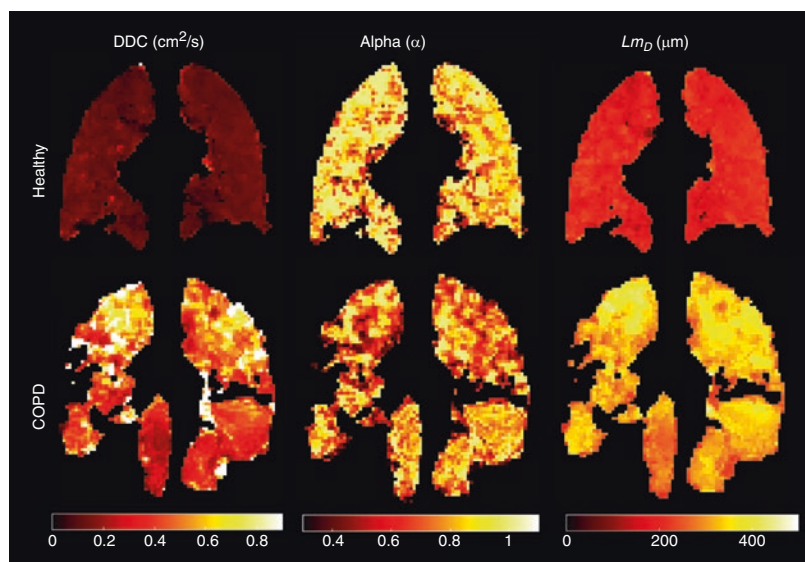
Fig. 15 Example of healthy subject and COPD patient parametric maps of effective distributed diffusion coefficient (DDC), heterogeneity index (α), and mean diffusion length scale (Lm_D) derived from the stretched exponential model

different gas mixing and wash-out times. The problem with extending the diffusion time Δ to the order of tens of milliseconds needed to probe longer length scales is that T_2^* decay ($T_2^* \approx 25$ ms for ³He in the lungs at 1.5 T (Salerno et al. 2005)) can significantly attenuate the MR signal before application of the second gradient pulse. To address this, the diffusion-encoded magnetisation can be stored in the longitudinal direction (with a flip back RF pulse of the opposite phase to the excitation pulse, i.e. as in stimulated echo sequence), such that the longer T_1 (~20 s) allows longer diffusion times, and the magnetisation can then be read out with a third pulse with the same phase as the original excitation pulse.

Various manifestations of pulse sequences for measurement of long time scale diffusion have been proposed (Owers-Bradley et al. 2003; Woods et al. 2004; Fichele et al. 2005; Wang et al. 2006); in each case, the reported ADC values were approximately an order of magnitude less than those measured with PGSE, which indicates that long time scale diffusion experiments measure gas mixing by diffusion through inter-acinar connectivity over a much longer length scale than in conventional short time scale experiments (Conradi et al. 2008). Whether this method is more or less sensitive than the short time scale measurements to different aspects of lung microstructure in healthy and diseased lungs remains to be fully investigated, although preliminary comparisons have shown differences in sensitivity (Wang et al. 2008).

9 Future Perspectives: Accelerated HP ³He Lung MRI

All the above applications of HP ³He lung MRI, despite their clinical potential, are fundamentally limited by both the non-renewable polarisation ($T_1 \sim 20$ s and RF-induced) and feasible patient breath-hold times (~15 s). As such, HP gas MRI is a prime candidate for k-space under-sampling schemes that permit the number of RF excitations, and thus the total scan time to be reduced. However, as in conventional ¹H MRI, violation of the Nyquist sampling criterion introduces aliasing artefacts in the reconstructed images that must be minimised by specialised techniques. In particular, compressed sensing (CS) and parallel imaging (PI) strategies have considerable potential for accelerated HP gas lung MRI, and form the focus of this section.

9.1 Parallel Imaging

The concept of PI relies on utilising the sensitivity profiles of multiple receiver coils as prior knowledge to reduce the number of RF pulses required to reconstruct an image and therefore reduce acquisition time. PI with HP gases is not constrained by the typical SNR trade-off in PI of thermally polarised nuclei when the number of RF pulses is reduced, because the HP gas signal per excitation can be increased by using larger flip angles (Lee et al. 2006). Thus, PI is an attractive option for HP gas lung imaging applications. To date, PI reconstruction with HP ³He has typically been done either in the image domain with SENSE (Pruessmann et al. 1999) or in the k-space domain with GRAPPA (Griswold et al. 2002).

Teh et al. (2006) demonstrated in vivo acquisition of HP ³He images with PI using a simultaneous slice excitation approach to reduce the number of RF pulses required to acquire a full image volume. This technique differs from conventional PI in that it does not require the use of multiple-channel receiver arrays to reduce acquisition time. The first in vivo ³He lung images acquired with a multiple-channel receiver array coil were presented by Lee et al. (2006). A 2-channel transmit and 24-channel receive ³He phased-array system and SENSE reconstruction was shown to maintain ³He lung image SNR at reduction factors of 2 and 4. Larger receiver arrays comprising 32-channels (Meise et al. 2010) and up to 128-channels (Lee et al. 2008) have also been developed for high SNR parallel imaging with ³He. Deppe et al. (2011b) further improved ³He lung image quality by combining an asymmetric birdcage transmit coil with a 32-channel receiver array to maintain a homogeneous B_1 transmit field across the thorax (Fig. 16).
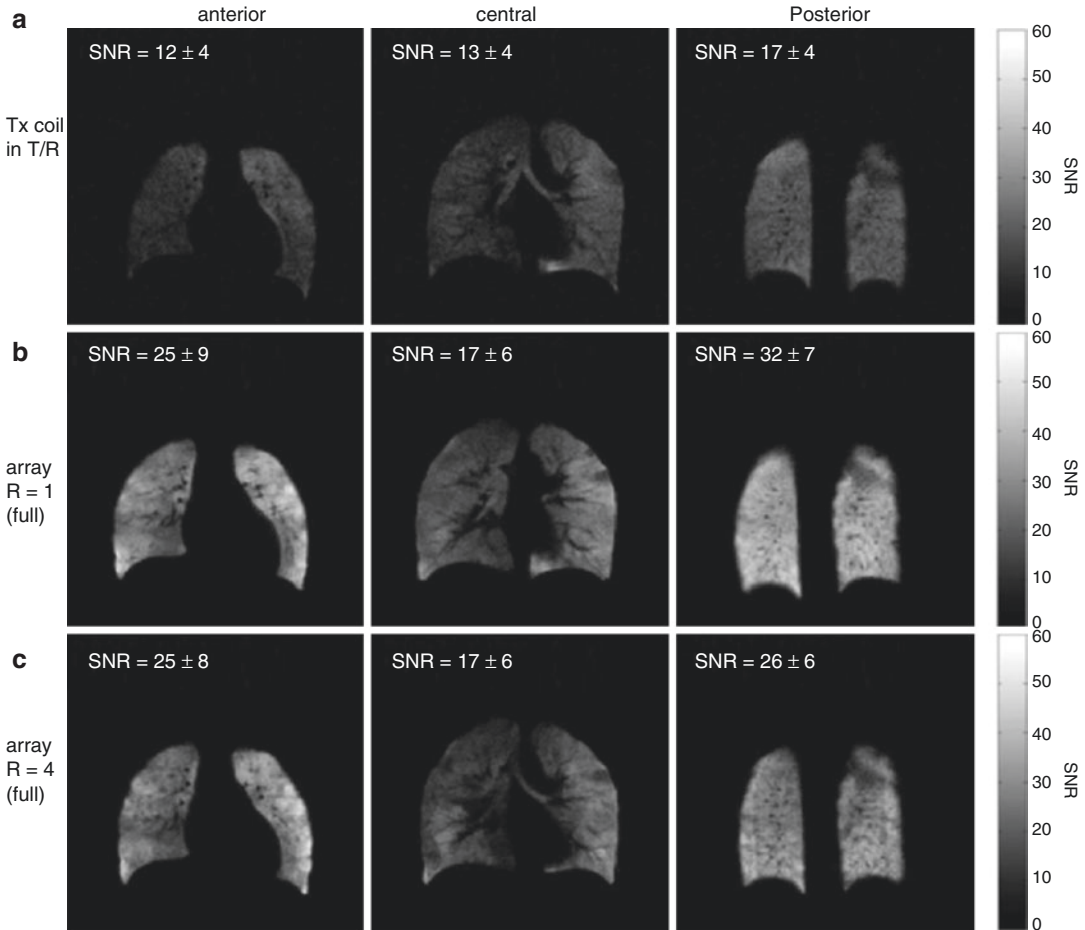
Fig. 16 SNR maps acquired from a healthy volunteer using a flexible 32-channel receive array and asymmetric birdcage transmit coil (Deppe et al. 2011b). (**a**) Images acquired with the birdcage coil in transmit and receive mode; (**b**) images acquired with the birdcage in transmit mode and the receive array, fully sampled (i.e. acceleration factor, $R = 1$); (**c**) images acquired as in (**b**) but with fourfold under-sampling ($R = 4$). Mean and standard deviation of SNR in the lungs are given for each SNR map

Very few applications of PI for HP gases outside of conventional ^{3}He ventilation imaging have been reported. Meise et al. (2010) demonstrated the first morphologic lung images using a 32-channel array coil with GRAPPA reconstruction. SNR enhancement allowed ADC maps to be calculated from images acquired at a higher spatial resolution (1.37×1.37 mm^2) than with a standard transmit-receive coil. In a recent study comparing fully sampled and under-sampled multiple b-value diffusion data acquired with an 8-channel receive coil (Chang et al. 2015), quantitative lung morphometry measurements were shown to be largely preserved with GRAPPA reconstruction, highlighting the potential of PI for acceleration of multiple b-value DW-MRI

acquisitions. Other PI studies with HP ^{3}He have demonstrated accelerated acquisition of maps of the B_1-field (Santoro et al. 2011), fractional ventilation (Emami et al. 2013), and partial oxygen pressure (Kadlecek et al. 2013).

9.2 Compressed Sensing

CS is an alternative acceleration technique that exploits the inherent sparsity of MR images to reconstruct images from under-sampled k-space data (Lustig et al. 2007). In contrast to PI, CS does not require the use of multiple-channel RF coils, facilitating translation of the technique across different sites and scanners.

Three requirements must be satisfied to ensure good CS image reconstruction: (1) image data must be sparse in either the image domain or a transform domain; (2) k-space must be under-sampled randomly with variable-density schemes to ensure that associated artefacts produced during reconstruction are incoherent/noise-like and can be smoothed by the CS algorithm; (3) a non-linear reconstruction method must be used to enforce sparsity and data fidelity.

The feasibility of acquisition and reconstruction of HP ³He lung MR ventilation images with CS was first investigated by Ajraoui et al. (2010). Retrospective under-sampling and reconstruction of fully sampled 2D and 3D ³He ventilation images, and subsequent prospective acquisition of under-sampled images, showed that approximately two-fold reductions in scan time could be achieved in ³He ventilation imaging without compromising image quality (Fig. 17a, b). In the same work, prospective under-sampled 2D ³He diffusion-weighted MRI
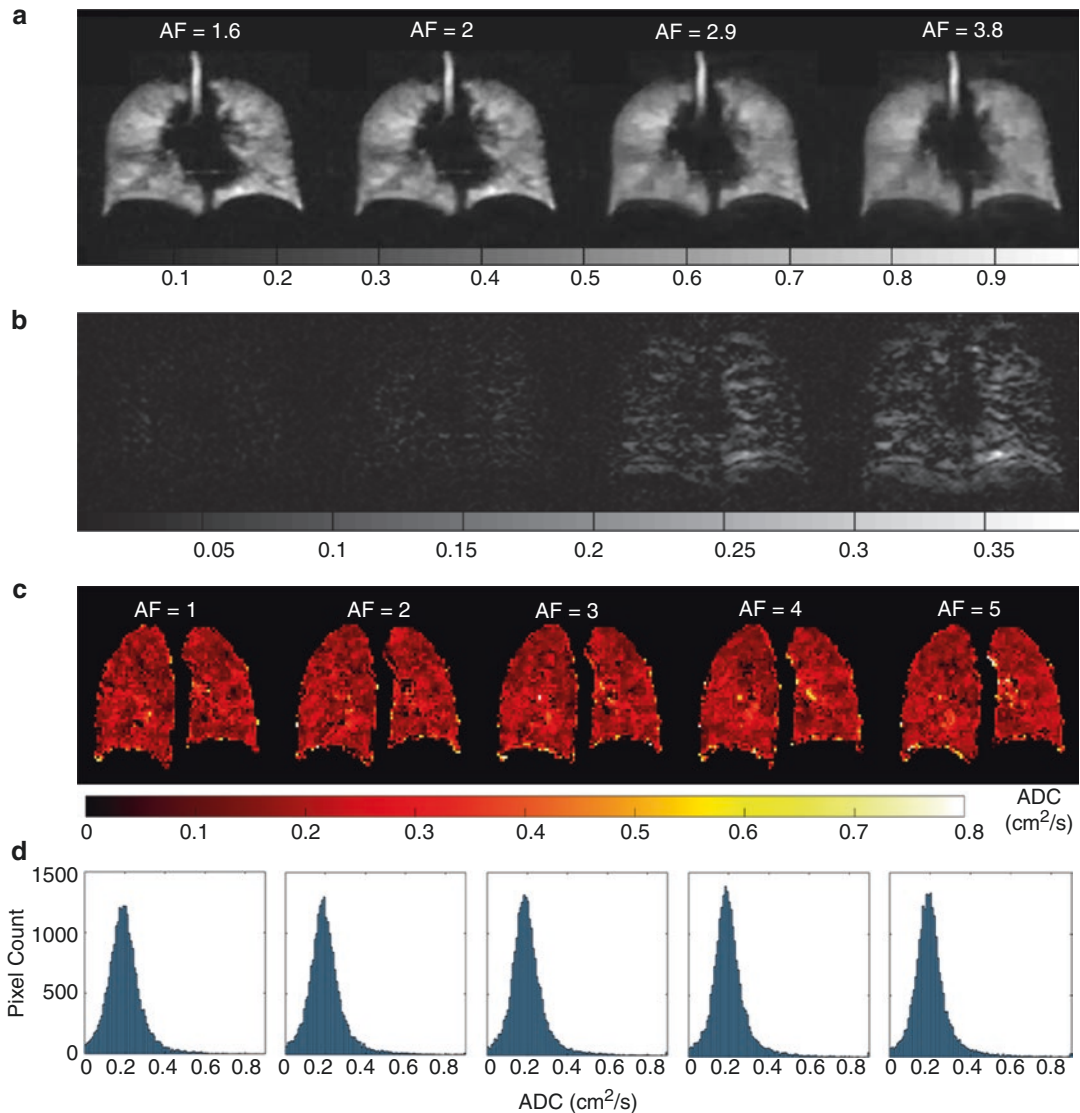
Fig. 17 (**a**) Effects of retrospective under-sampling on an example slice from a 2D ³He ventilation imaging acquisition (AF = acceleration factor) (Ajraoui et al. 2010); (**b**) corresponding difference images between fully sampled and under-sampled CS images. (**c**) Effects of retrospective under-sampling on an example slice from a 3D ³He diffusion-weighted MR acquisition (Chan et al. 2016); (**d**) corresponding whole lung ADC histograms for each AF

data reconstructed using CS demonstrated good preservation of quantitative ADC information.

The reduction in acquisition time offered by CS has allowed isotropic resolution ^{3}He and ^{1}H lung MR images to be acquired in the same breath-hold (Qing et al. 2015). Furthermore, the acquisition of ^{1}H structural images as prior knowledge for use in the CS reconstruction was shown to reduce error in the reconstruction of ^{3}He ventilation images (Ajraoui et al. 2013). CS techniques have also been implemented to enable high temporal resolution gas flow measurements in the upper airways with phase contrast velocimetry (Collier and Wild 2015). Further HP ^{3}He studies have incorporated CS to permit acquisition of additional functional or structural data within a single breath-hold, such as 2D multi-interleaved ^{3}He MRI data for mapping of ADC, T_2^*, and B_1 (Ajraoui et al. 2012), and 3D multiple b-value diffusion-weighted MRI data for whole lung morphometry mapping (Chan et al. 2016) (Fig. 17c, d).

Conclusion

The development of several key methods for lung MRI with hyperpolarised ^{3}He has facilitated clinical translation of the technique to evaluate multiple aspects of lung function in a number of pulmonary disorders. However, whilst HP ^{3}He is arguably a highly sensitive and powerful gas isotope for lung MR applications, its rapidly declining availability has somewhat limited its widespread clinical application. In recent years, there has been significant evidence of a steady transition in the field from using ^{3}He to ^{129}Xe for both physics and engineering development work, and clinical investigations. Despite the approximately three-fold inferior MR sensitivity of ^{129}Xe, preliminary comparisons of the two techniques suggest that equivalent functional and structural information can be obtained with the two nuclei (Kirby et al. 2012b; Svenningsen et al. 2013; Kirby et al. 2014) (Fig. 18). ^{129}Xe also possesses several advantageous properties to probe additional aspects of lung function that cannot be investigated with ^{3}He (Mugler and Altes 2013), as discussed in the following chapter of this
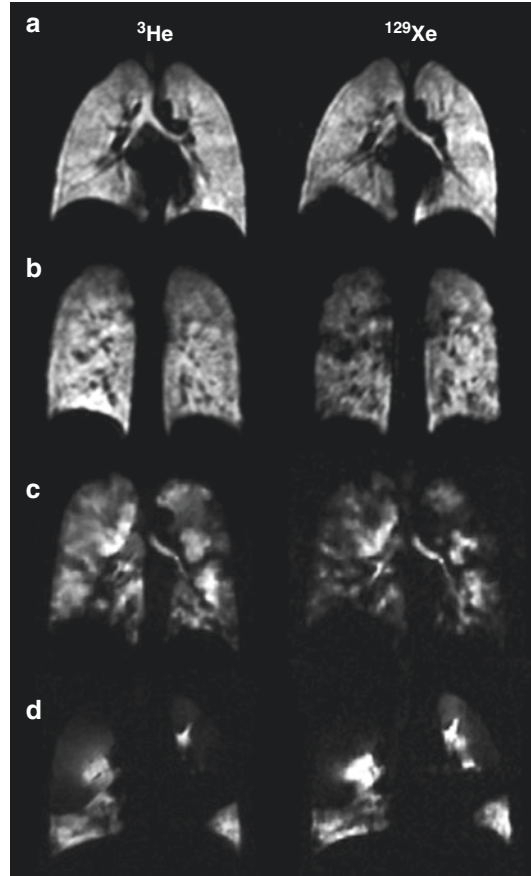
Fig. 18 Comparison of 3D SSFP ^{3}He and ^{129}Xe ventilation images of the lungs of (**a**) a healthy never-smoker, (**b**) a "healthy" smoker, (**c**) a patient with asthma, and (**d**) a patient with COPD. The slice thickness and spatial resolution for acquisitions (**a**, **b**) were identical, whilst ^{3}He images in (**c**, **d**) were acquired with half the slice thickness of the corresponding ^{129}Xe images and reconstructed to mimic the equivalent slice thickness

book. In Sheffield, we believe that there is still life in HP ^{3}He lung MRI for certain research questions alongside the more clinically viable ^{129}Xe, and in fact, complementary functional information can be obtained by using the two hyperpolarised gas nuclei in tandem (Wild et al. 2013; Rao and Wild 2016).

References

Ajraoui S, Lee KJ, Deppe MH, Parnell SR, Parra-Robles J, Wild JM (2010) Compressed sensing in hyperpolarized ^{3}He lung MRI. Magn Reson Med 63(4):1059–1069

Ajraoui S, Parra-Robles J, Marshall H, Deppe MH, Clemence M, Wild JM (2012) Acquisition of ^{3}He ventilation images, ADC, T_2*and B_1 maps in a single scan with compressed sensing. NMR Biomed 25(1):44–51

Ajraoui S, Parra-Robles J, Wild JM (2013) Incorporation of prior knowledge in compressed sensing for faster acquisition of hyperpolarized gas images. Magn Reson Med 69(2):360–369

Altes TA, Powers PL, Knight-Scott J, Rakes G, Platts-Mills TAE, De Lange EE, Alford BA, Mugler JP III, Brookeman JR (2001) Hyperpolarized ^{3}He MR lung ventilation imaging in asthmatics: preliminary findings. J Magn Reson Imaging 13(3):378–384

Altes TA, Mai VM, Munger TM, Brookeman JR, Hagspiel KD (2005) Pulmonary embolism: comprehensive evaluation with MR ventilation and perfusion scanning with hyperpolarized helium-3, arterial spin tagging, and contrast-enhanced MRA. J Vasc Interv Radiol 16(7):999–1005

Altes TA, Gersbach JC, Mata JF, Mugler JP III, Brookeman JR, de Lange EE (2007) Evaluation of the safety of hyperpolarized helium-3 gas as an inhaled contrast agent for MRI. In: Proceedings of the 15th meeting of the international society of magnetic resonance in medicine, Berlin, Germany, p 1305

Babcock E, Chann B, Nelson IA, Walker TG (2005) Frequency-narrowed diode array bar. Appl Opt 44(15):3098–3104

Bannier E, Cieslar K, Mosbah K, Aubert F, Duboeuf F, Salhi Z, Gaillard S, Berthezène Y, Crémillieux Y, Reix P (2010) Hyperpolarized ^{3}He MR for sensitive imaging of ventilation function and treatment efficiency in young cystic fibrosis patients with normal lung function. Radiology 255(1):225–232

Berberan-Santos MN, Bodunov EN, Valeur B (2005) Mathematical functions for the analysis of luminescence decays with underlying distributions 1. Kohlrausch decay function (stretched exponential). Chem Phys 315(1–2):171–182

Bink A, Hanisch G, Karg A, Vogel A, Katsaros K, Mayer E, Gast KK, Kauczor H-U (2007) Clinical aspects of the apparent diffusion coefficient in 3He MRI: results in healthy volunteers and patients after lung transplantation. J Magn Reson Imaging 25(6):1152–1158

Butler JP, Loring SH, Patz S, Tsuda A, Yablonskiy DA, Mentzer SJ (2012) Evidence for adult lung growth in humans. N Engl J Med 367(3):244–247

Cai J, Sheng K, Benedict SH, Read PW, Larner JM, Mugler JP, de Lange EE, Cates GD, Miller GW (2009) Dynamic MRI of grid-tagged hyperpolarized helium-3 for the assessment of lung motion during breathing. Int J Radiat Oncol Biol Phys 75(1):276–284

Callaghan PT, Eccles CD, Xia Y (1988) NMR microscopy of dynamic displacements: k-space and q-space imaging. Journal of Physics E: Scientific Instruments 21(8):820

Carr HY, Purcell EM (1954) Effects of diffusion on free precession in nuclear magnetic resonance experiments. Phys Rev 94(3):630–638

Chan H-F, Stewart NJ, Parra-Robles J, Collier GJ, Wild JM (2016) Whole lung morphometry with 3D multiple b-value hyperpolarized gas MRI and compressed sensing. Magn Reson Med. doi:10.1002/mrm.26279

Chang YV, Quirk JD, Yablonskiy DA (2015) In vivo lung morphometry with accelerated hyperpolarized ^{3}He diffusion MRI: a preliminary study. Magn Reson Med 73(4):1609–1614

Cieślar K, Stupar V, Canet-Soulas E, Gaillard S, Crémillieux Y (2007) Alveolar oxygen partial pressure and oxygen depletion rate mapping in rats using ^{3}He ventilation imaging. Magn Reson Med 57(2):423–430

Colegrove F, Schearer L, Walters G (1963) Polarization of He^3 gas by optical pumping. Phys Rev 132(6):2561

Collier GJ, Wild JM (2015) In vivo measurement of gas flow in human airways with hyperpolarized gas MRI and compressed sensing. Magn Reson Med 73(6):2255–2261

Collier GJ, Marshall H, Rao M, Stewart NJ, Capener D, Wild JM (2015) Observation of cardiogenic flow oscillations in healthy subjects with hyperpolarized ^{3}He MRI. J Appl Physiol. doi:10.1152/japplphysiol.01068.02014

Conradi MS, Bruns MA, Sukstanskii AL, Gross SS, Leawoods JC (2004) Feasibility of diffusion-NMR surface-to-volume measurements tested by calculations and computer simulations. J Magn Reson 169(2):196–202

Conradi MS, Yablonskiy DA, Woods JC, Gierada DS, Bartel S-ET, Haywood SE, Menard C (2008) The role of collateral paths in long-range diffusion of ^{3}He in lungs. Acad Radiol 15(6):675–682

de Lange EE, Altes TA, Patrie JT, Battiston JJ, Juersivich AP, Mugler JP, Platts-Mills TA (2009) Changes in regional airflow obstruction over time in the lungs of patients with asthma: evaluation with ^{3}He MR imaging. Radiology 250(2):567–575

de Rochefort L, Maître X, Fodil R, Vial L, Louis B, Isabey D, Croce C, Darrasse L, Apiou G, Caillibotte G, Bittoun J, Durand E (2006) Phase-contrast velocimetry with hyperpolarized ^{3}He for in vitro and in vivo characterization of airflow. Magn Reson Med 55(6):1318–1325

De Zanche N, Chhina N, Teh K, Randell C, Pruessmann KP, Wild JM (2008) Asymmetric quadrature split birdcage coil for hyperpolarized ^{3}He lung MRI at 1.5T. Magn Reson Med 60(2):431–438

Deninger AJ, Eberle B, Ebert M, Großmann T, Heil W, Kauczor HU, Lauer L, Markstaller K, Otten E, Schmiedeskamp J, Schreiber W, Surkau R, Thelen M, Weiler N (1999) Quantification of regional intrapulmonary oxygen partial pressure evolution during apnea by ^{3}He MRI. J Magn Reson 141(2):207–216

Deninger AJ, Eberle B, Bermuth J, Escat B, Markstaller K, Schmiedeskamp J, Schreiber WG, Surkau R, Otten

E, Kauczor HU (2002a) Assessment of a single-acquisition imaging sequence for oxygen-sensitive ³He-MRI. Magn Reson Med 47(1):105–114

Deninger AJ, Månsson S, Petersson JS, Pettersson G, Magnusson P, Svensson J, Fridlund B, Hansson G, Erjefeldt I, Wollmer P, Golman K (2002b) Quantitative measurement of regional lung ventilation using ³He MRI. Magn Reson Med 48(2):223–232

Deppe MH, Wild JM (2012) Variable flip angle schedules in bSSFP imaging of hyperpolarized noble gases. Magn Reson Med 67(6):1656–1664

Deppe MH, Parra-Robles J, Ajraoui S, Parnell SR, Clemence M, Schulte RF, Wild JM (2009) Susceptibility effects in hyperpolarized He-3 lung MRI at 1.5T and 3T. J Magn Reson Imaging 30(2):418–423

Deppe MH, Teh K, Parra-Robles J, Lee KJ, Wild JM (2010) Slice profile effects in 2D slice-selective MRI of hyperpolarized nuclei. J Magn Reson 202(2):180–189

Deppe MH, Parra-Robles J, Ajraoui S, Wild JM (2011a) Combined measurement of pulmonary inert gas washout and regional ventilation heterogeneity by MR of a single dose of hyperpolarized He-3. Magn Reson Med 65(4):1076–1084

Deppe MH, Parra-Robles J, Marshall H, Lanz T, Wild JM (2011b) A flexible 32-channel receive array combined with a homogeneous transmit coil for human lung imaging with hyperpolarized ³He at 1.5 T. Magn Reson Med 66(6):1788–1797

Diaz S, Casselbrant I, Piitulainen E, Pettersson G, Magnusson P, Peterson B, Wollmer P, Leander P, Ekberg O, Akeson P (2008) Hyperpolarized ³He apparent diffusion coefficient MRI of the lung: reproducibility and volume dependency in healthy volunteers and patients with emphysema. J Magn Reson Imaging 27(4):763–770

Dominguez-Viqueira W, Ouriadov A, O'Halloran R, Fain SB, Santyr GE (2011) Signal-to-noise ratio for hyperpolarized ³He MR imaging of human lungs: a 1.5 T and 3 T comparison. Magn Reson Med 66(5):1400–1404

Donnelly LF, MacFall JR, McAdams HP, Majure JM, Smith J, Frush DP, Bogonad P, Charles HC, Ravin CE (1999) Cystic fibrosis: combined hyperpolarized ³He-enhanced and conventional proton MR imaging in the lung—preliminary observations. Radiology 212(3):885–889

Driehuys B, Walker J, Pollaro J, Cofer GP, Mistry N, Schwartz D, Johnson GA (2007) ³He MRI in mouse models of asthma. Magn Reson Med 58(5):893–900

Durand E, Guillot G, Darrasse L, Tastevin G, Nacher PJ, Vignaud A, Vattolo D, Bittoun J (2002) CPMG measurements and ultrafast imaging in human lungs with hyperpolarized helium-3 at low field (0.1 T). Magn Reson Med 47(1):75–81

Ebert M, Grossmann T, Heil W, Otten EW, Surkau R, Thelen M, Leduc M, Bachert P, Knopp MV, Schad LR (1996) Nuclear magnetic resonance imaging with hyperpolarised helium-3. Lancet 347(9011):1297–1299

Emami K, Kadlecek SJ, Woodburn JM, Zhu J, Yu J, Vahdat V, Pickup S, Ishii M, Rizi RR (2010) Improved technique for measurement of regional fractional ventilation by hyperpolarized ³He MRI. Magn Reson Med 63(1):137–150

Emami K, Xu Y, Hamedani H, Profka H, Kadlecek S, Xin Y, Ishii M, Rizi RR (2013) Accelerated fractional ventilation imaging with hyperpolarized gas MRI. Magn Reson Med 70(5):1353–1359

Evans A, McCormack DG, Santyr G, Parraga G (2008) Mapping and quantifying hyperpolarized ³He magnetic resonance imaging apparent diffusion coefficient gradients. J Appl Physiol 105(2):693–699

Fain SB, Altes TA, Panth SR, Evans MD, Waters B, Mugler JP III, Korosec FR, Grist TM, Silverman M, Salerno M, Owers-Bradley J (2005) Detection of age-dependent changes in healthy adult lungs with diffusion-weighted ³He MRI. Acad Radiol 12(11):1385–1393

Fain SB, Panth SR, Evans MD, Wentland AL, Holmes JH, Korosec FR, O'Brien MJ, Fountaine H, Grist TM (2006) Early emphysematous changes in asymptomatic smokers: detection with ³He MR imaging. Radiology 239(3):875–883

Fain SB, Korosec FR, Holmes JH, O'Halloran R, Sorkness RL, Grist TM (2007) Functional lung imaging using hyperpolarized gas MRI. J Magn Reson Imaging 25(5):910–923

Fain SB, Gonzalez-Fernandez G, Peterson ET, Evans MD, Sorkness RL, Jarjour NN, Busse WW, Kuhlman JE (2008) Evaluation of structure-function relationships in asthma using multidetector CT and hyperpolarized He-3 MRI. Acad Radiol 15(6):753–762

Fichele S, Paley MNJ, Woodhouse N, Griffiths PD, van Beek EJR, Wild JM (2004a) Finite-difference simulations of ³He diffusion in 3D alveolar ducts: comparison with the cylinder model. Magn Reson Med 52(4):917–920

Fichele S, Paley MNJ, Woodhouse N, Griffiths PD, Van Beek EJR, Wild JM (2004b) Investigating ³He diffusion NMR in the lungs using finite difference simulations and in vivo PGSE experiments. J Magn Reson 167(1):1–11

Fichele S, Woodhouse N, Swift AJ, Said Z, Paley MNJ, Kasuboski L, Mills GH, van Beek EJR, Wild JM (2004c) MRI of helium-3 gas in healthy lungs: posture related variations of alveolar size. J Magn Reson Imaging 20(2):331–335

Fichele S, Paley MNJ, Woodhouse N, Griffiths PD, van Beek EJR, Wild JM (2005) Measurements and modeling of long range ³He diffusion in the lung using a slice-washout method. J Magn Reson 174(1):28–33

Fischer MC, Spector ZZ, Ishii M, Yu J, Emami K, Itkin M, Rizi R (2004) Single-acquisition sequence for the measurement of oxygen partial pressure by hyperpolarized gas MRI. Magn Reson Med 52(4):766–773

Gast KK, Viallon M, Eberle B, Lill J, Puderbach MU, Hanke AT, Schmiedeskamp J, Kauczor H-U (2002) MRI in lung transplant recipients using hyperpolarized ³He: comparison with CT. J Magn Reson Imaging 15(3):268–274

Gast KK, Puderbach MU, Rodriguez I, Eberle B, Markstaller K, Knitz F, Schmiedeskamp J, Weiler N,

Schreiber WG, Mayer E (2003) Distribution of ventilation in lung transplant recipients: evaluation by dynamic ^{3}He-MRI with lung motion correction. Investig Radiol 38(6):341–348

Goodson BM (2002) Nuclear magnetic resonance of laser-polarized noble gases in molecules, materials, and organisms. J Magn Reson 155(2):157–216

Grebenkov DS, Guillot G (2006) Localization regime of restricted diffusion in a model pulmonary acinus. In: Proceedings of the 14th Meeting of the International Society of Magnetic Resonance in Medicine, Seattle, WA, p 1624

Grebenkov DS, Guillot G, Sapoval B (2007) Restricted diffusion in a model acinar labyrinth by NMR: theoretical and numerical results. J Magn Reson 184(1):143–156

Griswold MA, Jakob PM, Heidemann RM, Nittka M, Jellus V, Wang J, Kiefer B, Haase A (2002) Generalized autocalibrating partially parallel acquisitions (GRAPPA). Magn Reson Med 47(6):1202–1210

Hajari AJ, Yablonskiy DA, Sukstanskii AL, Quirk JD, Conradi MS, Woods JC (2012) Morphometric changes in the human pulmonary acinus during inflation. J Appl Physiol 112(6):937–943

Hamedani H, Clapp JT, Kadlecek SJ, Emami K, Ishii M, Gefter WB, Xin Y, Cereda M, Shaghaghi H, Siddiqui S, Rossman MD, Rizi RR (2016) Regional fractional ventilation by using multibreath wash-in ^{3}He MR imaging. Radiology 279(3):917–924

He M, Kaushik SS, Robertson SH, Freeman MS, Virgincar RS, McAdams HP, Driehuys B (2014) Extending semi-automatic ventilation defect analysis for hyperpolarized 129Xe ventilation MRI. Acad Radiol 21(12):1530–1541

Heil W, Humblot H, Otten E, Schafer M, Sarkau R, Leduc M (1995) Very long nuclear relaxation times of spin polarized helium 3 in metal coated cells. Phys Lett A 201(4):337–343

Hersman FW, Ruset IC, Ketel S, Muradian I, Covrig SD, Distelbrink J, Porter W, Watt D, Ketel J, Brackett J, Hope A, Patz S (2008) Large production system for hyperpolarized 129Xe for human lung imaging studies. Acad Radiol 15(6):683–692

Holmes JH, Korosec FR, Du J, O'Halloran RL, Sorkness RL, Grist TM, Kuhlman JE, Fain SB (2007) Imaging of lung ventilation and respiratory dynamics in a single ventilation cycle using hyperpolarized He-3 MRI. J Magn Reson Imaging 26(3):630–636

Holmes JH, O'Halloran RL, Brodsky EK, Jung Y, Block WF, Fain SB (2008) 3D hyperpolarized He-3 MRI of ventilation using a multi-echo projection acquisition. Magn Reson Med 59(5):1062–1071

Horn FC, Deppe MH, Marshall H, Parra-Robles J, Wild JM (2014) Quantification of regional fractional ventilation in human subjects by measurement of hyperpolarized He-3 washout with 2D and 3D MRI. J Appl Physiol 116(2):129–139

Horn FC, Rao M, Stewart NJ, Wild JM (2016) Multiple breath washout of hyperpolarized 129Xe and ^{3}He in human lungs with three-dimensional balanced steady-state free-precession imaging. Magn Reson Med. doi:10.1002/mrm.26319

Hurlimann MD, Helmer KG, Deswiet TM, Sen PN (1995) Spin echoes in a constant gradient and in the presence of simple restriction. J Magn Reson Ser A 113(2):260–264

Ireland RH, Bragg CM, McJury M, Woodhouse N, Fichele S, van Beek EJR, Wild JM, Hatton MQ (2007) Feasibility of image registration and intensity-modulated radiotherapy planning with hyperpolarized helium-3 magnetic resonance imaging for non–small-cell lung cancer. Int J Radiat Oncol Biol Phys 68(1):273–281

Kadlecek S, Hamedani H, Xu Y, Emami K, Xin Y, Ishii M, Rizi R (2013) Regional alveolar partial pressure of oxygen measurement with parallel accelerated hyperpolarized gas MRI. Acad Radiol 20(10):1224–1233. doi:10.1016/j.acra.2013.1007.1002

Kastler A (1950) Quelques suggestions concernant la production optique et la détection optique d'une inégalité de population des niveaux de quantifigation spatiale des atomes. Application à l'expérience de stern et Gerlach et à la résonance magnétique. J phys radium 11(6):255–265

Kauczor HU, Hofmann D, Kreitner KF, Nilgens H, Surkau R, Heil W, Potthast A, Knopp MV, Otten EW, Thelen M (1996) Normal and abnormal pulmonary ventilation: visualization at hyperpolarized He-3 MR imaging. Radiology 201(2):564–568

Kauczor HU, Ebert M, Kreitner KF, Nilgens H, Surkau R, Heil W, Hofmann D, Otten EW, Thelen M (1997) Imaging of the lungs using ^{3}He MRI: preliminary clinical experience in 18 patients with and without lung disease. J Magn Reson Imaging 7(3):538–543

Kirby M, Mathew L, Wheatley A, Santyr GE, McCormack DG, Parraga G (2010) Chronic obstructive pulmonary disease: longitudinal hyperpolarized ^{3}He MR imaging. Radiology 256(1):280–289

Kirby M, Mathew L, Heydarian M, Etemad-Rezai R, McCormack DG, Parraga G (2011a) Chronic obstructive pulmonary disease: quantification of bronchodilator effects by using hyperpolarized He MR imaging. Radiology 261(1):283–292

Kirby M, Svenningsen S, Ahmed H, Wheatley A, Etemad-Rezai R, Paterson NAM, Parraga G (2011b) Quantitative evaluation of hyperpolarized helium-3 magnetic resonance imaging of lung function variability in cystic fibrosis. Acad Radiol 18(8):1006–1013

Kirby M, Heydarian M, Wheatley A, McCormack DG, Parraga G (2012a) Evaluating bronchodilator effects in chronic obstructive pulmonary disease using diffusion-weighted hyperpolarized helium-3 magnetic resonance imaging. J Appl Physiol 112(4):651–657

Kirby M, Svenningsen S, Owrangi A, Wheatley A, Farag A, Ouriadov A, Santyr GE, Etemad-Rezai R, Coxson HO, McCormack DG, Parraga G (2012b) Hyperpolarized ^{3}He and 129Xe MR imaging in healthy volunteers and patients with chronic obstructive pulmonary disease. Radiology 265(2):600–610

Kirby M, Ouriadov A, Svenningsen S, Owrangi A, Wheatley A, Etemad-Rezai R, Santyr GE, McCormack DG, Parraga G (2014) Hyperpolarized ^{3}He and 129Xe magnetic resonance imaging apparent diffusion coef-

ficients: physiological relevance in older never- and ex-smokers. Physiol Rep 2(7):pii: e12068

Koumellis P, van Beek EJR, Woodhouse N, Fichele S, Swift AJ, Paley MNJ, Hill C, Taylor CJ, Wild JM (2005) Quantitative analysis of regional airways obstruction using dynamic hyperpolarized ³He MRI—preliminary results in children with cystic fibrosis. J Magn Reson Imaging 22(3):420–426

Lee RF, Johnson G, Grossman RI, Stoeckel B, Trampel R, McGuinness G (2006) Advantages of parallel imaging in conjunction with hyperpolarized helium—a new approach to MRI of the lung. Magn Reson Med 55(5):1132–1141

Lee RF, Chang M, Stefanescu C, Stoeckel B, Santoro D, Strick D, Xue R, Oessingman N, Johnson G, Sodickson D (2008) A 128-channel helium-3 phased array at 3T for highly accelerated parallel imaging in hyperpolarized gas MRI. In: Proceedings of the 16th meeting of the international society of magnetic resonance in medicine, Toronto, Canada, p 440

Liner JC, Weissman S (1972) Determination of the temperature dependence of gaseous diffusion coefficients using gas chromatographic apparatus. J Chem Phys 56(5):2288–2290

Lustig M, Donoho D, Pauly JM (2007) Sparse MRI: the application of compressed sensing for rapid MR imaging. Magn Reson Med 58(6):1182–1195

Lutey BA, Lefrak SS, Woods JC, Tanoli T, Quirk JD, Bashir A, Yablonskiy DA, Conradi MS, Bartel ST, Pilgram TK, Cooper JD, Gierada DS (2008) Hyperpolarized ³He MR imaging: physiologic monitoring observations and safety considerations in 100 consecutive subjects. Radiology 248(2):655–661

MacFall JR, Charles HC, Black RD, Middleton H, Swartz JC, Saam B, Driehuys B, Erickson C, Happer W, Cates GD, Johnson GA, Ravin CE (1996) Human lung air spaces: potential for MR imaging with hyperpolarized He-3. Radiology 200(2):553–558

Marshall H, Deppe MH, Parra-Robles J, Hillis S, Billings CG, Rajaram S, Swift A, Miller SR, Watson JH, Wolber J, Lipson DA, Lawson R, Wild JM (2012) Direct visualisation of collateral ventilation in COPD with hyperpolarised gas MRI. Thorax 67(7):613–617

Mata J, Altes T, Knake J, Mugler J III, Brookeman J, de Lange E (2008) Hyperpolarized ³He MR imaging of the lung: effect of subject immobilization on the occurrence of ventilation defects. Acad Radiol 15(2):260–264

Mathew L, Gaede S, Wheatley A, Etemad-Rezai R, Rodrigues GB, Parraga G (2010) Detection of longitudinal lung structural and functional changes after diagnosis of radiation-induced lung injury using hyperpolarized He3 magnetic resonance imaging. Med Phys 37(1):22–31

Mathew L, Kirby M, Etemad-Rezai R, Wheatley A, McCormack DG, Parraga G (2011) Hyperpolarized ³He magnetic resonance imaging: preliminary evaluation of phenotyping potential in chronic obstructive pulmonary disease. Eur J Radiol 79(1):140–146

Meise FM, Rivoire J, Terekhov M, Wiggins GC, Keil B, Karpuk S, Salhi Z, Wald LL, Schreiber LM (2010) Design and evaluation of a 32-channel phased-array coil for lung imaging with hyperpolarized 3-helium. Magn Reson Med 63(2):456–464

Middleton H, Black RD, Saam B, Cates GD, Cofer GP, Guenther R, Happer W, Hedlund LW, Alan Johnson G, Juvan K, Swartz J (1995) MR imaging with hyperpolarized ³He gas. Magn Reson Med 33(2):271–275

Möller HE, Chen XJ, Saam B, Hagspiel KD, Johnson GA, Altes TA, de Lange EE, Kauczor H-U (2002) MRI of the lungs using hyperpolarized noble gases. Magn Reson Med 47(6):1029–1051

Mugler JP III, Altes TA (2013) Hyperpolarized 129Xe MRI of the human lung. J Magn Reson Imaging 37(2):313–331

Mugler JP III, Brookeman JR (2005). Signal-to-Noise considerations for parallel imaging with hyperpolarized gases. In: Proceedings of the 13th meeting of the international society of magnetic resonance in medicine, Miami Beach, FL

Mugler JP III, Brookeman JR, Knight-Scott J, Maier T, De Lange EE, Bogorad PL (1998) Regional measurement of the ³He diffusion coefficient in the human lung. In: Proceedings of the 6th meeting of the international society of magnetic resonance in medicine, Sydney, Australia, p 1906

Mugler JP III, Salerno M, de Lange EE, Brookeman JR (2002) Optimized TrueFISP hyperpolarized ³He MRI of the lung yields a 3-fold SNR increase compared to FLASH. In: Proceedings of the 10th meeting of the international society of magnetic resonance in medicine, Honolulu, HI, p 2019

Müller CJ, Löffler R, Deimling M, Peller M, Reiser M (2001) MR lung imaging at 0.2 T with T_1-weighted true FISP: native and oxygen-enhanced. J Magn Reson Imaging 14(2):164–168

Newbury NR, Barton AS, Cates GD, Happer W, Middleton H (1993) Gaseous ³He-³He magnetic dipolar spin relaxation. Phys Rev A 48(6):4411–4420

Nikolaou P, Coffey AM, Walkup LL, Gust BM, Whiting N, Newton H, Barcus S, Muradyan I, Dabaghyan M, Moroz GD, Rosen MS, Patz S, Barlow MJ, Chekmenev EY, Goodson BM (2013) Near-unity nuclear polarization with an open-source 129Xe hyperpolarizer for NMR and MRI. Proc Natl Acad Sci 110(35):14150–14155

Norquay G, Parnell SR, Xu X, Parra-Robles J, Wild JM (2013) Optimized production of hyperpolarized 129Xe at 2 bars for in vivo lung magnetic resonance imaging. J Appl Phys 113(4):044908–044909

O'Halloran RL, Holmes JH, Wu Y-C, Alexander A, Fain SB (2010) Helium-3 MR q-space imaging with radial acquisition and iterative highly constrained back-projection. Magn Reson Med 63(1):41–50

Oros AM, Shah NJ (2004) Hyperpolarized xenon in NMR and MRI. Phys Med Biol 49(20):R105–R153

Owers-Bradley JR, Fichele MS, Bennattayalah A, Smith McGloin CJ, Bowtell RW, Morgan PS, Moody AR (2003) MR tagging of human lungs using

hyperpolarized ^{3}He gas. J Magn Reson Imaging 17(1):142–146

Parraga G, Ouriadov A, Evans A, McKay S, Lam WW, Fenster A, Etemad-Rezai R, McCormack D, Santyr G (2007) Hyperpolarized ^{3}He ventilation defects and apparent diffusion coefficients in chronic obstructive pulmonary disease: preliminary results at 3.0 tesla. Investig Radiol 42(6):384–391

Parraga G, Mathew L, Etemad-Rezai R, McCormack DG, Santyr GE (2008) Hyperpolarized ^{3}He magnetic resonance imaging of ventilation defects in healthy elderly volunteers: initial findings at 3.0 tesla. Acad Radiol 15(6):776–785

Parra-Robles J, Wild JM (2012) The influence of lung airways branching structure and diffusion time on measurements and models of short-range ^{3}He gas MR diffusion. J Magn Reson 225(0):102–113

Parra-Robles J, Cross AR, Santyr GE (2005) Theoretical signal-to-noise ratio and spatial resolution dependence on the magnetic field strength for hyperpolarized noble gas magnetic resonance imaging of human lungs. Med Phys 32(1):221–229

Parra-Robles J, Ajraoui S, Deppe MH, Parnell SR, Wild JM (2010a) Experimental investigation and numerical simulation of ^{3}He gas diffusion in simple geometries: implications for analytical models of ^{3}He MR lung morphometry. J Magn Reson 204(2):228–238

Parra-Robles J, Ajraoui S, Wild JM (2010b) Modelling non-Gaussian ^{3}He diffusion signal behaviour using a fractional dynamics approach. In: Proceedings of the 18th Meeting of the international society of magnetic resonance in medicine, Stockholm, Sweden, p 2538

Parra-Robles J, Ajraoui S, Marshall H, Deppe MH, Xu X, Wild JM (2012) The influence of field strength on the apparent diffusion coefficient of ^{3}He gas in human lungs. Magn Reson Med 67(2):322–325

Parra-Robles J, Marshall H, Wild JM (2013) Characterization of ^{3}He diffusion in lungs using a stretched exponential model. In: Proceedings of the 21st annual meeting of the international society for magnetic resonance in medicine, Salt Lake City, UT, p 820

Parra-Robles J, Marshall H, Hartley RA, Brightling CE, Wild JM (2014) Quantification of lung microstructure in asthma using a ^{3}He fractional diffusion approach. In: Proceedings of the 22nd annual meeting of the international society for magnetic resonance in medicine, Milan, Italy, p 3529

Paulin GA, Ouriadov A, Lessard E, Sheikh K, McCormack DG, Parraga G (2015) Noninvasive quantification of alveolar morphometry in elderly never- and ex-smokers. Physiol Rep 3(10):e12583

Peces-Barba G, Ruiz-Cabello J, Cremillieux Y, Rodríguez I, Dupuich D, Callot V, Ortega M, Rubio Arbo ML, Cortijo M, Gonzalez-Mangado N (2003) Helium-3 MRI diffusion coefficient: correlation to morphometry in a model of mild emphysema. Eur Respir J 22(1):14–19

Pruessmann KP, Weiger M, Scheidegger MB, Boesiger P (1999) SENSE: sensitivity encoding for fast MRI. Magn Reson Med 42(5):952–962

Qing K, Altes TA, Tustison NJ, Feng X, Chen X, Mata JF, Miller GW, de Lange EE, Tobias WA, Cates GD, Brookeman JR, Mugler JP (2015) Rapid acquisition of helium-3 and proton three-dimensional image sets of the human lung in a single breath-hold using compressed sensing. Magn Reson Med 74(4):1110–1115

Quirk JD, Lutey BA, Gierada DS, Woods JC, Senior RM, Lefrak SS, Sukstanskii AL, Conradi MS, Yablonskiy DA (2011) In vivo detection of acinar microstructural changes in early emphysema with ^{3}He lung morphometry. Radiology 260(3):866–874

Quirk JD, Sukstanskii AL, Woods JC, Lutey BA, Conradi MS, Gierada DS, Yusen RD, Castro M, Yablonskiy DA (2016) Experimental evidence of age-related adaptive changes in human acinar airways. J Appl Physiol 120(2):159–165

Rao M, Wild JM (2016) RF instrumentation for same-breath triple nuclear lung MR imaging of 1H and hyperpolarized ^{3}He and 129Xe at 1.5T. Magn Reson Med 75(4):1841–1848

Saam B, Happer W, Middleton H (1995) Nuclear relaxation of ^{3}He in the presence of O^2. Phys Rev A 52(1):862–865

Saam B, Yablonskiy DA, Gierada DS, Conradi MS (1999) Rapid imaging of hyperpolarized gas using EPI. Magn Reson Med 42(3):507–514

Saam BT, Yablonskiy DA, Kodibagkar VD, Leawoods JC, Gierada DS, Cooper JD, Lefrak SS, Conradi MS (2000) MR imaging of diffusion of ^{3}He gas in healthy and diseased lungs. Magn Reson Med 44(2): 174–179

Salerno M, Altes TA, Brookeman JR, De Lange EE, Mugler JP III (2001) Dynamic spiral MRI of pulmonary gas flow using hyperpolarized ^{3}He: preliminary studies in healthy and diseased lungs. Magn Reson Med 46(4):667–677

Salerno M, Lange EE d, Altes TA, Truwit JD, Brookeman JR, Mugler IJP (2002) Emphysema: hyperpolarized helium 3 diffusion MR imaging of the lungs compared with spirometric indexes—initial experience. Radiology 222(1):252–260

Salerno M, Brookeman JR, de Lange EE, Mugler JP (2005) Hyperpolarized ^{3}He lung imaging at 0.5 and 1.5 tesla: a study of susceptibility-induced effects. Magn Reson Med 53(1):212–216

Salhi Z, Großmann T, Gueldner M, Heil W, Karpuk S, Otten EW, Rudersdorf D, Surkau R, Wolf U (2012) Recycling of ^{3}He from lung magnetic resonance imaging. Magn Reson Med 67(6):1758–1763

Samee S, Altes T, Powers P, de Lange EE, Knight-Scott J, Rakes G, Mugler JP III, Ciambotti JM, Alford BA, Brookeman JR, Platts-Mills TAE (2003) Imaging the lungs in asthmatic patients by using hyperpolarized helium-3 magnetic resonance: assessment of response to methacholine and exercise challenge. J Allergy Clin Immunol 111(6):1205–1211

Santoro D, Rivoire J, Meise F, Terekhov M, Salhi Z, Gast K, Schreiber LM (2011) Three-dimensional mapping of the B$_1$ field using an optimized phase-based method:

application to hyperpolarized ³He in lungs. Magn Reson Med 65(4):1166–1172

Schearer LD, Walters GK (1965) Nuclear spin-lattice relaxation in the presence of magnetic-field gradients. Phys Rev 139(5A):A1398–A1402

Schreiber WG, Weiler N, Kauczor HU, Markstaller K, Eberle B, Hast J, Surkau R, Grossmann T, Deninger A, Hanisch G, Otten EW, Thelen M (2000) Ultrafast MRI of lung ventilation using hyperpolarized helium-3. RoFo 172(2):129–133

Shanbhag DD, Altes TA, Miller GW, Mata JF, Knight-Scott J (2006) Q-space analysis of lung morphometry in vivo with hyperpolarized ³He spectroscopy. J Magn Reson Imaging 24(1):84–94

Stavngaard T, Søgaard LV, Mortensen J, Hanson LG, Schmiedeskamp J, Berthelsen AK, Dirksen A (2005) Hyperpolarised ³He MRI and 81mKr SPECT in chronic obstructive pulmonary disease. Eur J Nucl Med Mol Imaging 32(4):448–457

Stejskal EO, Tanner JE (1965) Spin diffusion measurements: spin echoes in the presence of a time-dependent field gradient. J Chem Phys 42(1):288–292

Stewart NJ, Norquay G, Griffiths PD, Wild JM (2015) Feasibility of human lung ventilation imaging using highly polarized naturally abundant xenon and optimized three-dimensional steady-state free precession. Magn Reson Med 74(2):346–352

Sukstanskii AL, Yablonskiy DA (2008) In vivo lung morphometry with hyperpolarized ³He diffusion MRI: theoretical background. J Magn Reson 190(2):200–210

Svenningsen S, Kirby M, Starr D, Leary D, Wheatley A, Maksym GN, McCormack DG, Parraga G (2013) Hyperpolarized ³He and 129Xe MRI: differences in asthma before bronchodilation. J Magn Reson Imaging 38(6):1521–1530

Swift AJ, Wild JM, Fichele S, Woodhouse N, Fleming S, Waterhouse J, Lawson RA, Paley MNJ, Van Beek EJR (2005) Emphysematous changes and normal variation in smokers and COPD patients using diffusion ³He MRI. Eur J Radiol 54(3):352–358

Teh K, Lee KJ, Paley MNJ, Wild JM (2006) Parallel imaging of hyperpolarized helium-3 with simultaneous slice excitation. Magn Reson Med 55(2):258–262

Teh K, Parnell SR, Woodhouse N, Wild JM (2007) Time resolved lung ventilation volume measurement with multislice EPI using hyperpolarized 3He. In: Proceedings of the 15th meeting of the international society of magnetic resonance in medicine, Berlin, p 944

Tooker AC, Hong KS, McKinstry EL, Costello P, Jolesz FA, Albert MS (2003) Distal airways in humans: dynamic hyperpolarized ³He MR imaging—feasibility. Radiology 227(2):575–579

Tsai LL, Mair RW, Rosen MS, Patz S, Walsworth RL (2008) An open-access, very-low-field MRI system for posture-dependent ³He human lung imaging. J Magn Reson 193(2):274–285

Tustison NJ, Altes TA, Song G, de Lange EE, Mugler JP, Gee JC (2010) Feature analysis of hyperpolarized helium-3 pulmonary MRI: a study of asthmatics

versus nonasthmatics. Magn Reson Med 63(6):1448–1455

Tzeng Y-S, Lutchen K, Albert M (2009) The difference in ventilation heterogeneity between asthmatic and healthy subjects quantified using hyperpolarized ³He MRI. J Appl Physiol 106(3):813–822

van Beek EJR, Wild JM, Kauczor H-U, Schreiber W, Mugler JP, de Lange EE (2004) Functional MRI of the lung using hyperpolarized 3-helium gas. J Magn Reson Imaging 20(4):540–554

van Beek EJR, Hill C, Woodhouse N, Fichele S, Fleming S, Howe B, Bott S, Wild JM, Taylor CJ (2007) Assessment of lung disease in children with cystic fibrosis using hyperpolarized 3-helium MRI: comparison with Shwachman score, Chrispin-Norman score and spirometry. Eur Radiol 17(4):1018–1024

van Beek EJR, Dahmen AM, Stavngaard T, Gast KK, Heussel CP, Krummenauere F, Schmiedeskamp J, Wild JM, Søgaard LV, Morbach AE, Schreiber LM, Kauczor HU (2009) Hyperpolarised ³He MRI versus HRCT in COPD and normal volunteers: PHIL trial. Eur Respir J 34(6):1311–1321

Walker TG, Happer W (1997) Spin-exchange optical pumping of noble-gas nuclei. Rev Mod Phys 69(2):629–642

Walkup LL, Woods JC (2014) Translational applications of hyperpolarized ³He and 129Xe. NMR Biomed 27(12):1429–1438

Wang C, Miller GW, Altes TA, de Lange EE, Cates Jr GD, Mugler JP (2006) Time dependence of ³He diffusion in the human lung: measurement in the long-time regime using stimulated echoes. Magn Reson Med 56(2):296–309

Wang C, Altes TA, Mugler JP III, Miller GW, Ruppert K, Mata JF, Cates GD, Borish L, de Lange EE (2008) Assessment of the lung microstructure in patients with asthma using hyperpolarized ³He diffusion MRI at two time scales: comparison with healthy subjects and patients with COPD. J Magn Reson Imaging 28(1):80–88

Wild JM, Paley MN, Viallon M, Schreiber WG, van Beek EJ, Griffiths PD (2002a) K-space filtering in 2D gradient-echo breath-hold hyperpolarized ³He MRI: spatial resolution and signal-to-noise ratio considerations. Magn Reson Med 47:687–695

Wild JM, Schmiedeskamp J, Paley MNJ, Filbir F, Fichele S, Kasuboski L, Knitz F, Woodhouse N, Swift A, Heil W, Mills GH, Wolf M, Griffiths PD, Otten E, van Beek EJR (2002b) MR imaging of the lungs with hyperpolarized helium-3 gas transported by air. Phys Med Biol 47(13):N185

Wild JM, Fichele S, Woodhouse N, Paley MNJ, Swift A, Kasuboski L, van Beek EJR (2003a) Assessment and compensation of susceptibility artifacts in gradient echo MRI of hyperpolarized ³He gas. Magn Reson Med 50(2):417–422

Wild JM, Paley MNJ, Kasuboski L, Swift A, Fichele S, Woodhouse N, Griffiths PD, Van Beek EJR (2003b) Dynamic radial projection MRI of inhaled hyperpolarized ³He gas. Magn Reson Med 49(6):991–997

Wild JM, Woodhouse N, Paley MNJ, Fichele S, Said Z, Kasuboski L, van Beek EJR (2004) Comparison

between 2D and 3D gradient-echo sequences for MRI of human lung ventilation with hyperpolarized ^{3}He. Magn Reson Med 52(3):673–678

Wild JM, Fichele S, Woodhouse N, Paley MNJ, Kasuboski L, van Beek EJR (2005) 3D volume-localized pO2 measurement in the human lung with ^{3}He MRI. Magn Reson Med 53(5):1055–1064

Wild JM, Teh K, Woodhouse N, Paley MNJ, Fichele S, de Zanche N, Kasuboski L (2006) Steady-state free precession with hyperpolarized ^{3}He: experiments and theory. J Magn Reson 183(1):13–24

Wild JM, Marshall H, Xu X, Norquay G, Parnell SR, Clemence M, Griffiths PD, Parra-Robles J (2013) Simultaneous imaging of lung structure and function with triple-nuclear hybrid MR imaging. Radiology 267(1):251–255

Woodhouse N, Wild JM, Paley MNJ, Fichele S, Said Z, Swift AJ, van Beek EJR (2005) Combined helium-3/proton magnetic resonance imaging measurement of ventilated lung volumes in smokers compared to never-smokers. J Magn Reson Imaging 21(4):365–369

Woodhouse N, Wild JM, Mills GH, Fleming S, Fichele S, van Beek EJ (2006) Comparison of hyperpolarized 3-He administration methods in healthy and diseased subjects. In: Proceedings of the 14th meeting of the international society of magnetic resonance in medicine, Seattle, WA, p 1288

Woodhouse N, Wild JM, van Beek EJR, Hoggard N, Barker N, Taylor CJ (2009) Assessment of hyperpolarized ^{3}He lung MRI for regional evaluation of interventional therapy: a pilot study in pediatric cystic fibrosis. J Magn Reson Imaging 30(5):981–988

Woods JC, Yablonskiy DA, Chino K, Tanoli TSK, Cooper JD, Conradi MS (2004) Magnetization tagging decay to measure long-range ^{3}He diffusion in healthy and emphysematous canine lungs. Magn Reson Med 51(5):1002–1008

Woods JC, Choong CK, Yablonskiy DA, Bentley J, Wong J, Pierce JA, Cooper JD, Macklem PT, Conradi MS, Hogg JC (2006) Hyperpolarized ^{3}He diffusion MRI and histology in pulmonary emphysema. Magn Reson Med 56(6):1293–1300

Yablonskiy DA, Sukstanskii AL, Leawoods JC, Gierada DS, Larry Bretthorst G, Lefrak SS, Cooper JD, Conradi MS (2002) Quantitative in vivo assessment of lung microstructure at the alveolar level with hyperpolarized ^{3}He diffusion MRI. Proc Natl Acad Sci U S A 99(5):3111–3116

Yablonskiy DA, Sukstanskii AL, Woods JC, Gierada DS, Quirk JD, Hogg JC, Cooper JD, Conradi MS (2009) Quantification of lung microstructure with hyperpolarized ^{3}He diffusion MRI. J Appl Physiol 107(4):1258–1265

Zhao L, Mulkern R, Tseng CH, Williamson D, Patz S, Kraft R, Walsworth RL, Jolesz FA, Albert MS (1996) Gradient-echo imaging considerations for hyperpolarized 129Xe MR. J Magn Reson B 113(2):179–183

Zhu H, Ruset IC, Hersman FW (2005) Spectrally narrowed external-cavity high-power stack of laser diode arrays. Opt Lett 30(11):1342–1344

Hyperpolarized ¹²⁹Xenon MRI of the Lung

Iga Muradyan and Samuel Patz

Contents

1   Introduction

Pulmonary imaging is the least evolved branch of proton MRI, primarily due to the low volume fraction of tissue in the lung; only ~20% of the volume contains tissue or blood while the remainder is filled with air. By comparison, most of the volume in other organs is hydrogen. Another source of the inherently weak MR signal in the lungs is the extremely large area of the tissue-gas interface. The 3 ppm difference in magnetic susceptibility between tissue and air causes an alteration of the local magnetic field resulting in very short signal coherence times. Despite having limited SNR, several promising techniques have been developed (Edelman et al. 1996; Mai et al. 2001; Hatabu et al. 2001; Jakob et al. 2004; Detre et al. 1994; Hopkins and Prisk 2010; Deimling et al. 2008; Bauman et al. 2009). These techniques work better at low magnetic fields (such as 1.5 T) because of the air/tissue susceptibility issue. This may be problematic for the future as the overall drive for clinical imaging is in the direction of higher field strengths. In preclinical small animal imaging, Kuethe et al. (2007) used 1.89 T field strength system to produce lung images approaching the quality of CT.

An ideal technique for pulmonary imaging would enable independent imaging of gaseous and tissue regions of the lung to allow for independent evaluation of overall ventilation and perfusion, their distributions, and be sensitive to early changes in the structure and/or function of the lungs, at the same time avoiding exposure to radiation, and having a short half-life for rapid repeat measurements, if necessary. Hyperpolarized Xenon (HPXe) MRI may satisfy most of these criteria: (i) NMR techniques inherently lack

I. Muradyan (✉) • S. Patz
Radiology Department, Brigham and Women's
Hospital, Harvard Medical School, 221 Longwood
Ave, Suite BRB-34K, Boston, MA 02115, USA
e-mail: muradian@bwh.harvard.edu;
patz@bwh.harvard.edu

exposure to an ionizing radiation; HPXe's relaxation time ranges from seconds to hours depending on the holding field strength and temperature (frozen HPXe has a much longer T_1 than gaseous or liquid Xe) making possible repeat measurements using a batch of previously polarized gas; (ii) because the Xe nucleus has a large electron cloud, it is sensitive to the composition of its surroundings, exhibiting a significant chemical shift (~200 ppm) between Xe in a gaseous state and dissolved in a soft tissue, fat, and blood. However, there are also significant shortcomings in this approach, such as the necessity for preparing the hyperpolarized gas separately using spin exchange optical pumping, which, in turn, requires a relatively expensive and complicated apparatus, a Xe polarizer; polarizing large quantities of Xe to a high degree for human imaging can be challenging; and relatively short coherence times, i.e., T_2, inherent to pulmonary proton MRI still hold for Xe imaging of the lungs. Nevertheless, the large 200 ppm chemical shift between gaseous and dissolved phases of Xe allows for the unique possibility of measuring both these phases separately and simultaneously. There is also a smaller but sufficient chemical shift between the two dissolved phases of Xe, tissue and blood, that allows quantitation of each of these dissolved phase components. These attributes of HPXe MRI make it possible to gather simultaneous information about early structural and functional changes in the lungs.

Despite the challenges and shortcomings of the technology over the last two decades, interest has been maintained, primarily because only with HPXe can one obtain in vivo parameters describing important aspects of pulmonary structure and function affecting gas exchange. Further, because it is a noninvasive approach, in preclinical imaging, it can remedy many issues associated with methods that rely on tissue fixation as different fixation approaches can never duplicate in vivo physiology. Moreover, in clinical imaging, there is a significant need for better noninvasive diagnostic tools as pulmonary disease is a major public health issue. For example, chronic obstructive pulmonary disease, COPD, is the fourth leading cause of death in the world and the only major

disease that is still on the rise (American Lung Association 2010). Current pulmonary function tests (PFTs) provide measurements such as forced expiratory volume in 1 s (FEV1), but lack disease specificity as they are not a measure of a specific pathology, but rather, of how the lung functions as a whole. Carbon monoxide diffusing capacity, D_{LCO}, while specifically measuring gas exchange, is a global rather than regional measurement and can be highly variable due to a dependence on blood volume. Computed tomography, CT, is the current imaging modality of choice for the lungs as it provides very high spatial resolution maps of lung density. The fact that CT uses ionizing radiation, however, is a significant issue. Since CT quantifies local tissue density but does not measure lung function, it can lack specificity. For example, consider a patient that has a combination of functional problems corresponding to emphysema as well as fibrosis. Emphysema, which involves loss of septal tissue, and fibrosis have opposite effects on tissue density and thus may be undetected with CT. HPXe, however, can separately evaluate alveolar surface area that is lost in emphysema as well as fibrosis through a functional measurement of time-dependent diffusion of Xe from alveolar gas spaces into the septal tissue.

HPXe MRI could significantly contribute to both preclinical and clinical pulmonary imaging capabilities. Pulmonary HPXe MRI allows observation of separate peaks for inhaled Xe in a gaseous state (referred to as 0 ppm), and at least two separate peaks for dissolved states: one for Xe dissolved into tissue and blood plasma (at 197 ppm relative to the gas peak) and another for Xe in erythrocytes (at 217 ppm relative to the gas peak). Time-dependent measurements of the septal uptake offers a unique opportunity to noninvasively monitor gas exchange. Several mathematical models of Xe septal uptake have been developed to quantify subcomponents of gas exchange. In vivo data provided quantitative estimates of fundamental pulmonary parameters, such as the alveolar surface area per unit volume (S/V), the total thickness of the septal tissue (h), the thickness of the gas to blood barrier (d), and blood transit time through gas exchange region

(t). Widespread effort is underway to extend this unique and very promising approach to regional measurements (Månsson et al. 2003; Driehuys et al. 2006; Ruppert et al. 2004; Chang 2013; Stewart et al. 2014).

Another important feature of HPXe is that the intrinsic decay of the magnetization depends on the local oxygen concentration, similar to conditions in ^{3}He-MRI. The decay of the longitudinal magnetization is exponential, with the time constant denoted as T_1. In the presence of O_2, T_1 drops from hours to seconds. This sensitivity has been exploited (initially in HPHe and then in HPXe) to map pulmonary partial pressure of oxygen in vivo using the inverse relationship of p_AO_2 as a function of T_1 (Deninger et al. 2000). This, in turn, can be interpreted as a measure of the regional mismatch between ventilation and perfusion. This is true as although the relationship between p_AO_2 and local V/Q is complex, it is known, and typically displayed as in the Rahn/Fenn O_2/CO_2 diagram (Rahn 1964). For example, regions with high V/Q have abnormally high p_AO_2 (such as a region with a pulmonary embolus (PE)); regions with low V/Q have abnormally low p_AO_2 (such as in poorly ventilated units in COPD or in ventilation defects in asthma).

2   Polarizer

As part of an NIH funded grant, Dr. Samuel Patz created a consortium of scientists from Southern Illinois University at Carbondale (SIUC), Vanderbilt University, Harvard University, and our group at Brigham and Women's Hospital. The main goal of the consortium is to develop a low-cost open-source alternative to the commercially available polarizers that is capable of producing sufficient amounts of Xe for human studies. Our lab houses the first prototype polarizer, Xenon polarizatioN Automated (XeNA), built by the collaboration (Nikolaou et al. 2013, 2014). XeNA is largely based on existing designs and technologies. The polarization is achieved via spin-exchange optical pumping (SEOP), whereby the spins of unpaired electrons of an alkali metal vapor (in this case Rb) is polarized

via optical pumping with circularly polarized light. This polarization is then transferred to the Xe nucleus by means of hyperfine interaction during Rb vapor Xe gas collisions. XeNA runs in a batch mode in a high-pressure mode (2000 Torr) with high Xe partial pressure (200–1800 Torr range) in a half liter glass cell. Having a Xe-rich mixture in the cell allows skipping the cryo-collection step used by most other polarizers. Since cryo-collection also aided in preventing Rb leakage into the tedlar bag where hyperpolarized Xe is collected, we use an alternative method, a Teflon filter in the transfer line, with XeNA, to filter out the Rb. XeNA is modular and portable (Fig. 1a); it uses an open-source design and special care was taken to use off-the-shelf components whenever possible to allow for easy reproduction of the apparatus. It is largely automated: an open-source microcontroller (Arduino Mega 2560) controls all time-dependent operations driven by sensor measurements, such as vacuuming and filling the cell with the desired xenon-nitrogen mixture and evacuating the gas transfer lines and the tedlar bag for transfer of hyperpolarized gas, etc. Various controller outputs activate external devices via TTL level logic, such as shutting down the laser power supply unit if the door of the black box containing the laser is opened or triggering the low-field NMR spectrometer (Kea2, Magritek, Wellington, New Zealand) to run a NMR pulse sequence to evaluate Xe polarization. Additionally, the microcontroller interacts with a computer GUI through commands sent over the built-in USB-serial interface; all programmed gas manifold load/transfer sequences are stored on the microcontroller board's memory. The GUI itself is designed and programmed in open-source software (processing.org). The GUI also allows one to manually operate the polarizer: the gas manifold with active valves is depicted on the GUI with a manual control option also available for each valve. The GUI's schematic of the plumbing makes manual operation of the polarizer more intuitive (Fig. 1b). Finally, XeNA is also equipped with a high-resolution near-IR spectrometer (Ocean Optics HR2000+) that detects transmitted laser photons. The low-field NMR
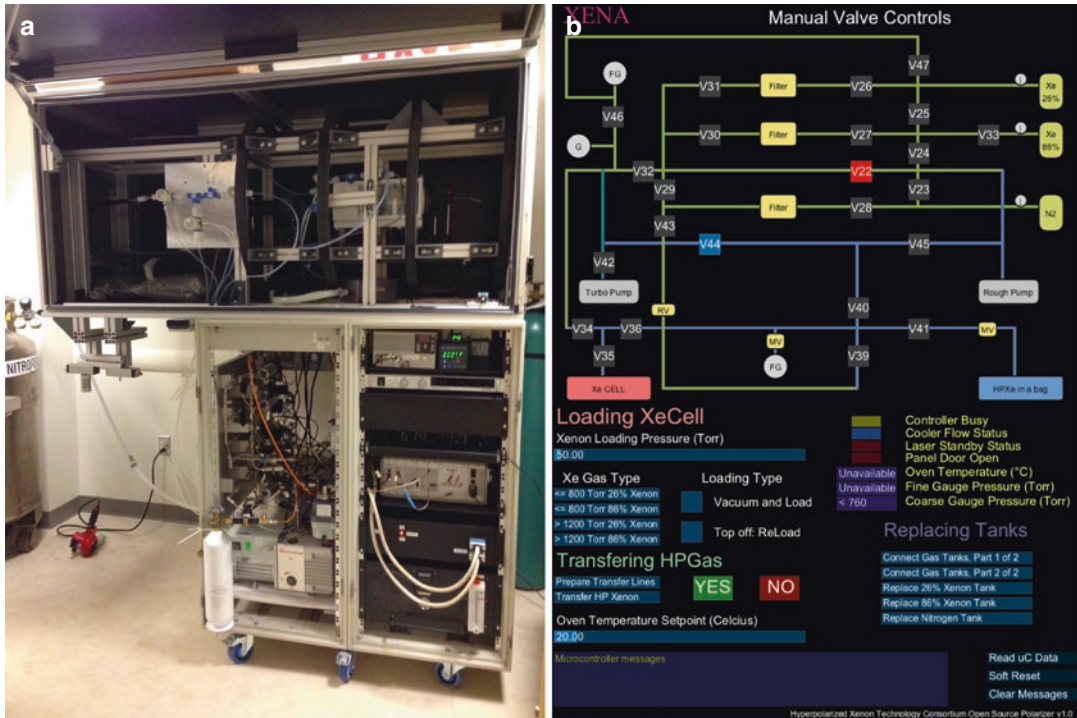
Fig. 1 Open-source polarizer, XeNA, located in our laboratory. (**a**) The chassis holding the black box on *top*, shown here with the side open, containing the polarizing hardware, while the gas panel, vacuuming systems and gas tanks are on the *lower left-hand side* of the chassis. On the *right*, we have temperature and pressure gauges, a laser power supply and its chiller, a NMR spectrometer and a microcontroller that orchestrates all automated protocols. (**b**) GUI controlling valves and protocols on the polarizer

spectrometer is used to detect nuclear spin-polarization of ^{129}Xe using a small surface coil (approximately 1.5 in. O.D., tuned to 62 kHz). Xe polarization is calibrated by comparison to the signal from a thermal proton phantom of identical geometry.

During an approximately 20-min run, slightly more than 600 mL of HPXe is polarized to approximately 25–30%. XeNA can achieve ^{129}Xe nuclear spin polarization values (PXe) of approximately 90%, 57%, 50%, and 30% for Xe loadings of approximately 300, 500, 760, and 1570 Torr, respectively (Nikolaou et al. 2013). Furthermore, little polarization loss is suffered during cell cool-down and gas transfer from the device to tedlar bags. There is a 30-min overhead for the subsequent run: the system needs to cool down; a new batch of the gas mixture needs to be loaded into the cell for a new polarization process

to commence. In parallel with the polarization process, a tedlar bag attached to the system is vacuumed and prepared to receive the polarized gas, taking about 20 min. We observed very long (about 6 h) spin-lattice relaxation times of gaseous HPXe in a tedlar bag in the center (uniform region) of a 3 T MRI scanner allowing for preparation of several samples of HPXe before the human imaging session.

To preserve the gas polarization during transport from the polarizer lab to the imaging suite, we built a transport box. It contains a set of three battery-powered solenoids, together producing a 16 Gauss magnetic field uniform over the region where the bag is placed. HPXe relaxation times are longer at higher fields. We measured the T_1 relaxation time of the hyperpolarized gas within our transport box as approximately 30 min, which is more than adequate to allow transport

to the scanner, a distance <100 m. It takes less than 5 min from the moment the gas is transferred into the bag to the moment the bag is placed inside the uniform region of an MRI scanner. The transport box is brought to the stray field region of the MRI scanner, the tedlar bag is taken out of the transport box and brought to the subject inside the scanner where it is then used for hyperpolarized Xe MRI. As noted above, long decay times of almost 6 h were observed for tedlar bags containing HP ^{129}Xe when placed in the central homogeneous field region of a clinical 3 T scanner.

3 HPXe Inhalation Protocol

With the development of the new polarizer, we also obtained a new FDA IND for this polarizer (FDA IND #116,662). Based on our previous experience and experience of other research groups working with HPXe MRI (Lutey et al. 2008; Shukla et al. 2012; Driehuys et al. 2012; Patz et al. 2008), we changed the breathing protocol: 800 mL of anoxic gas (Xe and nitrogen) is produced and available for inhalation. The Xe content can vary from 20 to 80% by volume. To standardize the inhalation process, participating subjects are directed to inhale to total lung capacity (TLC) and exhale to functional residual capacity. They then inhale the hyperpolarized gas mixture from a tedlar bag followed by a breath-hold of a maximum of 16 s. We perform baseline measurements of heart and respiratory rates, blood pressure, and blood oxygen saturation (SpO$_2$). We repeat these measurements 5 min post breath-hold. A physician is present in the MR room, continuously monitoring the subject during the breath-hold and observing the SpO$_2$.

4 In Vivo Spectroscopy

Xenon's wide chemical shift allows for separate measurements of gaseous and dissolved states, and the Xe uptake by the tissue and blood mimics the oxygen uptake in the lungs. During the last 20

years, there has been significant interest in developing a theoretical framework to describe the Xe uptake (Abdeen et al. 2006; Månsson et al. 2003; Driehuys et al. 2006; Ruppert et al. 2004; Chang 2013). In 2002, Butler et al. (2002) developed the first analytical model describing a simplified case of Xe diffusion in a porous medium. They assumed semi-infinite geometry in which diffusion times are kept sufficiently short that dissolved Xe does not reach the other phase change boundary. Small Xe-soluble porous polymer granulate phantoms with varying pore sizes ranging from 20 to 250 µm (Porex Corp., Atlanta, GA) were used to measure the surface area per unit gas volume (not the Euclidean volume of the sample) using NMR and the results were correlated with the mean linear intercept measured via confocal microscopy. We developed the chemical shift saturation recovery (CSSR) NMR technique by which a frequency-selective RF pulse is applied at Xe dissolved state frequencies to quench the signal rising from those frequencies, thereby essentially creating initial conditions such that at time $t = 0$, the dissolved-state magnetization $MD(t = 0)$ is zero, while the gas state initial magnetization $MG(t = 0)$ is essentially unaffected by this RF pulse. After some time t_{diff}, a fraction $F(t_{\text{diff}}) = MD(t_{\text{diff}})/MG(t = 0)$ of the initial gaseous Xe magnetization diffuses into the solid. The measured dissolved and gaseous signals (SD and SG) can be analytically described as:

$$F\left(t_{\text{diff}}\right) = \frac{M_D\left(t_{\text{diff}}\right)}{M_G\left(t=0\right)} = \frac{S_D\left(t_{\text{diff}}\right)}{S_G\left(t=0\right)}\frac{\sin\left(\alpha_G\right)}{\sin\left(\alpha_D\right)}$$
$$= \lambda \frac{S}{V}\sqrt{\frac{4Dt_{\text{diff}}}{\pi}} \tag{1}$$

where the ratio of the sines accounts for flip angle differences experienced by gaseous and dissolved states, λ is the partition coefficient, D is the dissolved Xe diffusivity, S is the alveolar surface area, and V is the gaseous Xe volume. Note that if there are unventilated regions of the lung, they will not contribute to both signals.

Although this simplified semi-infinite slab model does not describe the real alveolar septum

with finite thickness, nevertheless, it is applicable to in vivo measurements so long as Xe molecules entering the dissolved state from opposite ends of the realistic tissue-blood-tissue slab do not meet. As the alveolar septa containing tissue and blood can be extremely thin—less than a micron—the diffusion times at which this model is applicable are very short, less than a millisecond. Generally, we cannot make measurements for such short times because of hardware limitations, so a DC offset term was added to account for these very thin regions that are saturated with Xe early on and add a constant contribution independent of the diffusion time used for a particular measurement.

A more realistic approach has to account for the finite thickness of the tissue-blood-tissue slab (Fig. 2a). We applied the well-known solution to the 1D diffusion equation with periodic boundary conditions to our geometry and initial conditions in the absence of a blood flow. In order to incorporate the blood flow into the model, we made three simplifying assumptions about the Xe uptake by the blood and the blood flow (Patz et al. 2011):

1. Xenon dissolves directly into the blood, skipping the parenchymal layer separating blood from gas (Fig. 2b).
2. Diffusion is strictly orthogonal to the direction of the blood flow.
3. Plug flow describes the blood flow.

Within the time interval [0 t], allowed for diffusion, a segment of the blood that was just upstream of the gas exchange region (GER) prior to the start of diffusion (region R1, see Fig. 2c) will make its way into the GER. If the diffusion time t is greater than the time τ it takes blood to exit the gas exchange region ($t \geq \tau$), then at time t, R1 will occupy the whole GER. For shorter times, however, there will be another segment R2 that will spend the entire time from 0 to t inside the GER.

Finally, at time 0, the space between R2 and the right edge of the GER (Fig. 2c) will contain R3, a segment that will completely exit the GER at time t. If v is the velocity of the blood flow, then both R1 and R3 are length vt, and hence,
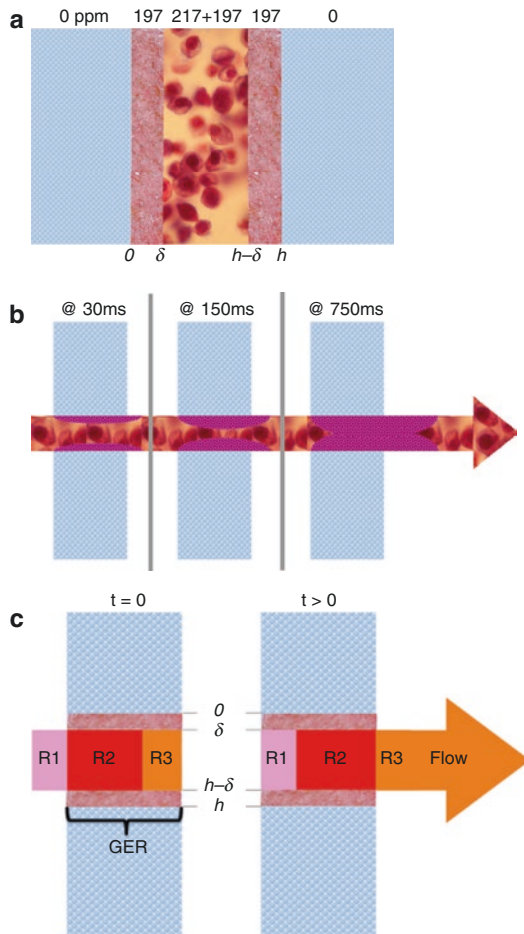
Fig. 2 A schematic of the simple geometry considered in the CSSR model. (**a**) The gas, tissue, and blood compartments used in modeling xenon septal uptake. (**b**) Cross-sectional depiction of the xenon uptake by the tissue/blood at different diffusion times. (**c**) Position of three spatially distinct regions of blood flow, labeled R1, R2, and R3 at time $t = 0$ and $t > 0$. The distance the blood travels in time t is $\Delta x = vt$. Blood in regions R1 and R3 experience gas exchange for only a fraction of the time t, whereas region R2 experiences gas exchange for the entire time t. Note that blood in region R1 on the *left* and in region R3 on the *right* correspond to blood in the pulmonary arterioles and venules and are therefore both located physically within the lung. Since we observe Xe within the lung, Xe diffusing into the blood within the gas exchange region and afterwards traveling downstream into the venules is observed as part of the xenon septal uptake data. Reproduced from Muradyan et al. (2012) with permission from The Royal Society of Chemistry

R1 + R2 is of the same length as R2 + R3, and both are equal to the total length of GER.

Since the entire R2 is involved in the diffusion between 0 and t, for this portion, the fraction of the septal thickness containing Xe (the distance of Xe's diffusion into the segment) will be uniform over its length. The fraction of the alveolar surface area associated with R2 is $(\tau - t)/\tau$, where τ is the capillary transit time. By contrast, some parts of R1 and R3, respectively, move in and out of the GER, causing the fractions of septal thickness containing Xe to change along their lengths. In this case, the average fractions must be calculated by integrating septal thickness over the diffusion time. The fraction of the surface associated with both R1 and R3 is t/τ. By combining the three contributions, the total fraction of Xe is calculated. The resulting expression, describing the Xe uptake from alveoli, is as follows:

$$F(t) = F_0 + \frac{\lambda h}{2} \cdot \frac{S}{V} \cdot \left(\frac{\tau - t}{\tau} \right) \cdot f\left(\frac{Dt}{h^2} \right)$$
$$+ \lambda h \frac{S}{V} \cdot \left[\frac{t}{\tau} + \frac{8h^2}{D\pi^4 \tau} \cdot g\left(\frac{Dt}{h^2} \right) \right] \quad (2)$$

where h is the septal thickness and f and g are

$$f\left(\frac{Dt}{h^2} \right) = 1 - \sum_{k, \, odd} \frac{8}{(\pi k)^2} \exp\left(-Dt\left(\frac{\pi k}{h} \right)^2 \right) \quad (3)$$

and

$$g\left(\frac{Dt}{h^2} \right) = \sum_{k, \, odd} \frac{1}{k^4} \left[\exp\left(-Dt\left(\frac{\pi k}{h} \right)^2 \right) - 1 \right] \quad (4)$$

As noted earlier, the term F_0 is due to very thin portions of the gas-blood barrier that are saturated before the shortest diffusion time. However, there is another mechanism that would result in such an offset: if the quenching of the dissolved state signal is not ideal, there will be a residual dissolved state signal to offset the measurements.

We used this model to fit the data previously collected on a 0.2 T scanner: 13 different diffusion times ranging from 17 ms to 1 s were used to obtain a Xe uptake curve. A sample curve from a healthy nonsmoking volunteer is presented in Fig. 3. Data were acquired at three different lung volumes for healthy nonsmokers, at a single volume for two subjects with COPD, and two subjects
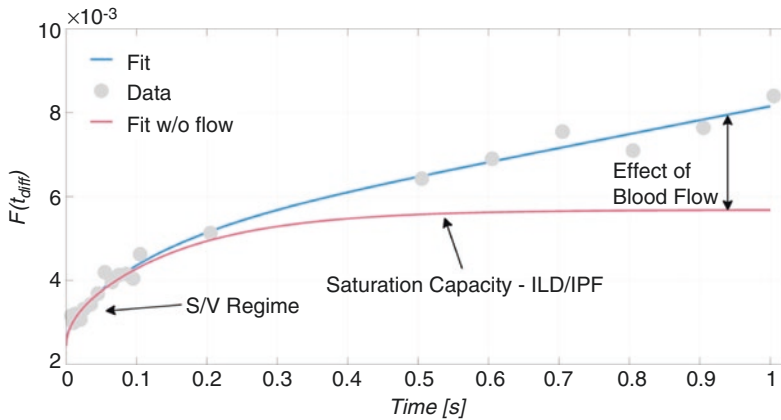
Fig. 3 Example of $F(t)$ data plotted versus t. The data here are for a subject with COPD Gold Stage 1. Also shown is the fit to the theoretical expression in Eq. (2) (*blue curve*). Using the fitted parameters S/V and h obtained for the *blue curve*, but setting $\tau \to \infty$, a separate curve was plotted (*red curve*) that shows the behavior for no blood flow. Note that the dissolved state data were corrected for T_1 decay during the diffusion time t. Reproduced from Muradyan et al. (2012) with permission from The Royal Society of Chemistry

Fig. 4 Results of data analysis for (**a**) *S/V*, (**b**) *h*, and (**c**) *τ* as a function of lung volume normalized to TLC. The results shown are for four healthy nonsmoker subjects (Healthy NS), two subjects with mild ILD, and two subjects with COPD, one with mild and one with mild/moderate disease. Reproduced from Muradyan et al. (2012) with permission from The Royal Society of Chemistry
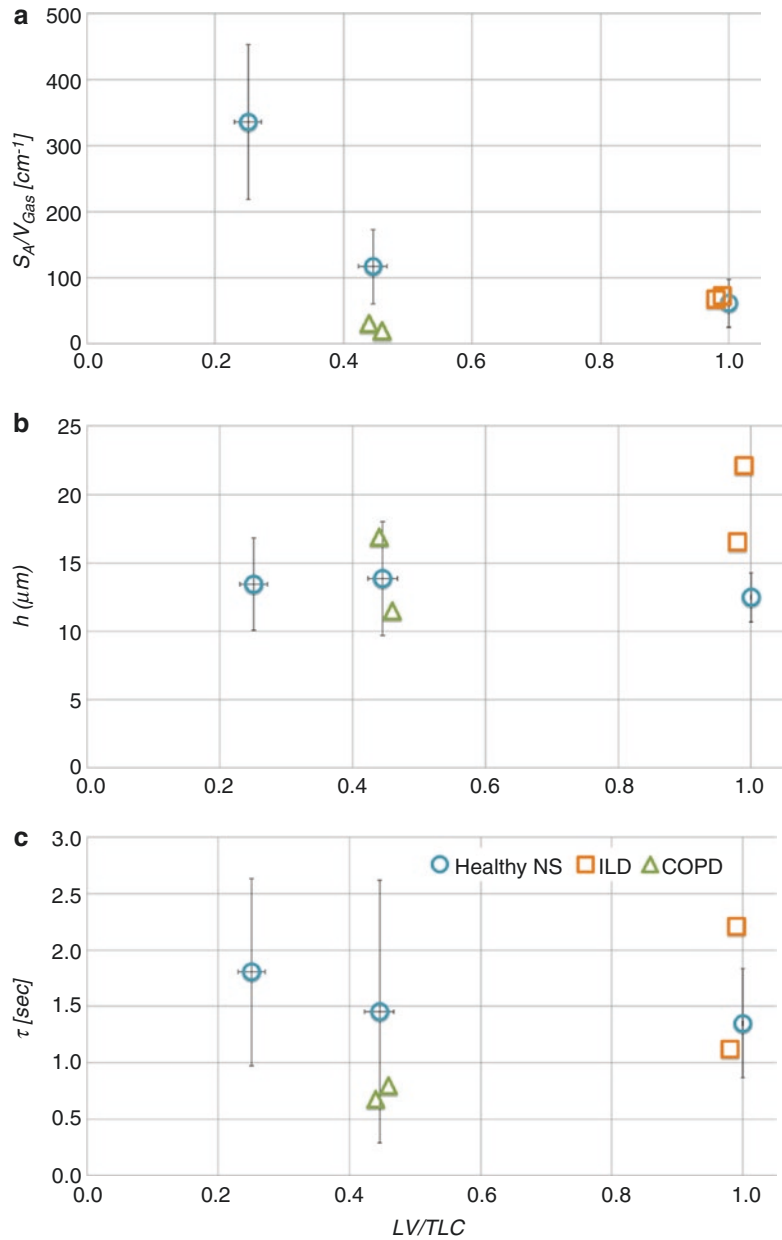
with interstitial lung disease. To enable inter-subject comparison, lung volumes (LV) were normalized to their respective total lung capacities (TLC). In the fitting routine, we used literature values for $\lambda = 0.1$ *and* $D = 3 \times 10^{-6} \frac{cm^2}{s}$. The *S/V*, *h*, and *τ* values are summarized in Fig. 4. Despite the use of such a simplified analytical model, the values for the parenchymal thickness are remarkably similar to those measured with histology on

fixed lungs (Coxson et al. 1999). Further, for blood transit time we measured $\tau \approx 1.5$ s, very close to the range of the values (mean 1.6 s, median 1.2 s, with a wide spread) reported in the literature (Hogg et al. 1994). Our surface area per unit volume measurements, on the other hand, are nearly 40% lower than the reported values (Coxson et al. 1999) obtained using histology on fixed lungs, possibly also explained by the lower

bound on our diffusion time window being too long so that the thinner sections of septal tissue between capillaries may have already been saturated. The S/V values of the subjects with ILD fall within the range of values for healthy subjects, consistent with a lack of parenchymally destructive disease; their h values are 36 and 97% larger than the mean value of the healthy volunteers at TLC, consistent with laying down of excess connective tissue and increased interstitial fluid in progressive fibrotic diseases. For COPD subjects, on the other hand, one would expect to observe loss of tissue due to the emphysema, which would result in a decreased S/V. For the two subjects we studied, we observed a striking loss compared to volunteers (more than by a factor of three!) of S/V measured near functional residual capacity, while there was no significant deviation from healthy volunteers for h. Values for the capillary transit time as a function of normalized lung volume are fairly constant but exhibited relatively high variability. We observed no significant difference in transit times for ILD patients and healthy subjects; for COPD subjects, the values of τ were somewhat reduced, but remained within the range observed in the healthy volunteers.

Although morphometric measurements on the fixed lungs demonstrated that S/V decreases as LV increases—most probably it is a power function between S and V—the details of the functional dependence remain obscure. Moreover, there are really no means for making such measurements in live humans, and one can argue that CSSR with hyperpolarized Xe is uniquely poised to address such a question. We used CSSR to perform simultaneous measurements of the Xe uptake at a single exchange time and the lung volume at which a particular spectrum was taken. To change the lung volume, we asked the subjects to inhale HPXe and air to total lung capacity, and wait for the NMR sequence to begin. Then the subject exhaled from TLC to residual volume in approximately 8 s as the NMR data were collected. A MR safe spirometer, triggered by the spectrometer, was used to measure the exhaled volume simultaneous with NMR data collection. We measured F versus LV for two diffusion times, 20 and 323 ms. The data and their fit to a power-law $F = F_0 + cV\alpha$ (Fig. 5). For both, t_{diff} of 20 and 323 ms, $\alpha = -1.86$, $R^2 = 0.99$ and 0.97, respectively. Unfortunately, we cannot translate the values of F to S/V values because due to the offset F_0, it requires several time points to evaluate the slope of F versus $\sqrt{t_{\mathrm{diff}}}$.
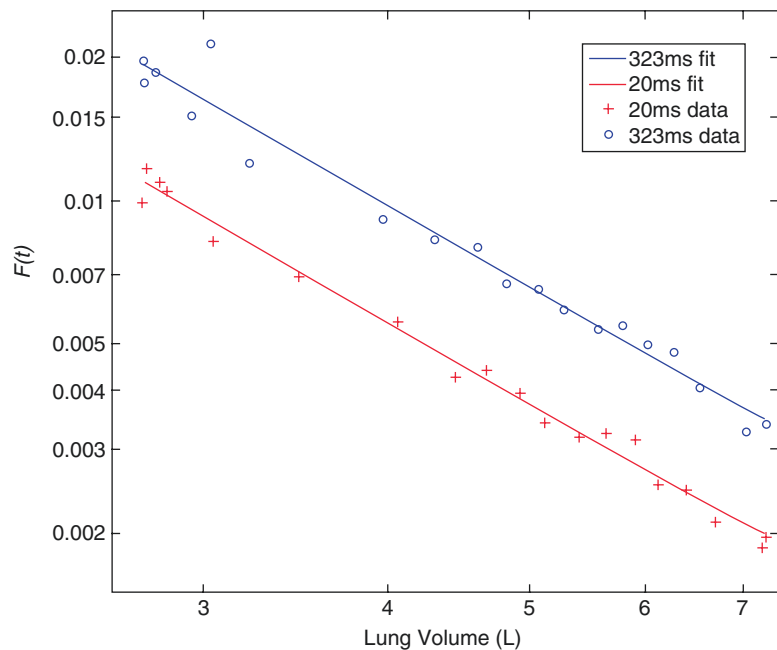
Fig. 5 Examples of $F(t)$ versus lung volume V acquired at a fixed diffusion time. Data are from a healthy, male subject, 32 years old, who exhaled from TLC to close to RV. Two different diffusion times (20 and 323 ms) were measured. Reproduced from Patz et al. (2008) with permission

5 In Vivo Imaging

5.1 Ventilation Maps

When, upon an inhalation and a breath-hold of HPXe, an MRI is acquired, the resulting image is essentially a map of the ventilation distribution in vivo. Only the regions where Xe has reached will be visible on the image; the signal intensity in a pixel is proportional to the number of Xe molecules in the corresponding voxel. We used such maps to address the basic physiology question of whether closing volume in healthy young adults is due to frank airway closure or to flow limitation of patent airways.

Closing volume (CV) is traditionally measured using a single-breath nitrogen washout test during which a volunteer expires to residual volume (RV), then inspires from RV with 100% oxygen to total lung capacity (TLC). Then, while the subject slowly exhales, the concentration of expired nitrogen is plotted against the volume over the expiration. An examination of the plateau and the presence of a sharp change in slope of $[N_2]$ versus lung volume on this plot allow CV to be determined. CV is defined as the lung volume (relative to RV) at which this change in slope occurs. This change in slope is interpreted as reflecting the abrupt onset of asynchronous emptying of lung units with different specific ventilations (and hence different N_2 concentrations) due to either frank airway closure or flow limitation on the prior exhalation. It is traditionally thought that if the mechanism responsible for this change is frank airway closure, and if these airways do not reopen on a subsequent inspiration, absorption atelectasis, shunt, and hypoxemia will result. In such a case, substantial ventilatory inhomogeneities and patchiness would be revealed in the HPXe MRI, associated with the sequential reopening of units and the continued presence of closed units. On the other hand, if "closure" on the prior exhalation is associated with patent but flow-limited airways, then the fact that they remain open would preclude, on the subsequent inspiration, any marked degree of inhomogeneity.

In most fit, healthy young individuals, this is not physiologically significant for two reasons: lung volume generally stays above closing volume and even if it dips below CV, the resulting ventilation-perfusion (V/Q) mismatch is managed with regional vasoconstriction, and any residual gas exchange effect is minor. However, in those older than approximately 30 years, CV increases almost linearly with age (Bode et al. 1976) and after approximately 45 years of age approaches FRC. In young healthy adults, CV is close to RV, which makes it difficult to measure. We studied two young elite divers who were capable of achieving lung volumes below RV through glossopharyngeal exsufflation (Muradyan et al. 2010). This maneuver is performed by sequentially using laryngeal and glossopharyngeal muscles to lower mouth pressure below gas pressure in the lungs, followed by a transient opening of the glottis, thus extracting air out of the lungs into the pharynx. Performed repeatedly, this exsufflation maneuver can lower lung volumes by a few hundred milliliters below RV (RV is defined as the lowest lung volume that can be attained using the expiratory muscles, with mouth and glottis open). Each of the subjects performed two breath-holds for HPXe MRI at different lung volumes. Figure 6 shows the ventilation maps observed at nearly RV and close to FRC for these subjects. As shown on the maps, there are several regions in the lower lung volume maps that have no Xe signal, i.e., that stayed unventilated upon inhalation of a small volume of gas, while the same regions were ventilated when more gas was inhaled. This suggests that the mechanism behind the CV is frank airway closure and not flow limitation in otherwise open airways. To further appreciate the degree of heterogeneity in ventilation at such low volumes, we also studied two age matching healthy volunteers and two older healthy volunteers. They inhaled approximately 1 L of Xe gas from RV, reaching lung volumes close to their FRCs; even in older
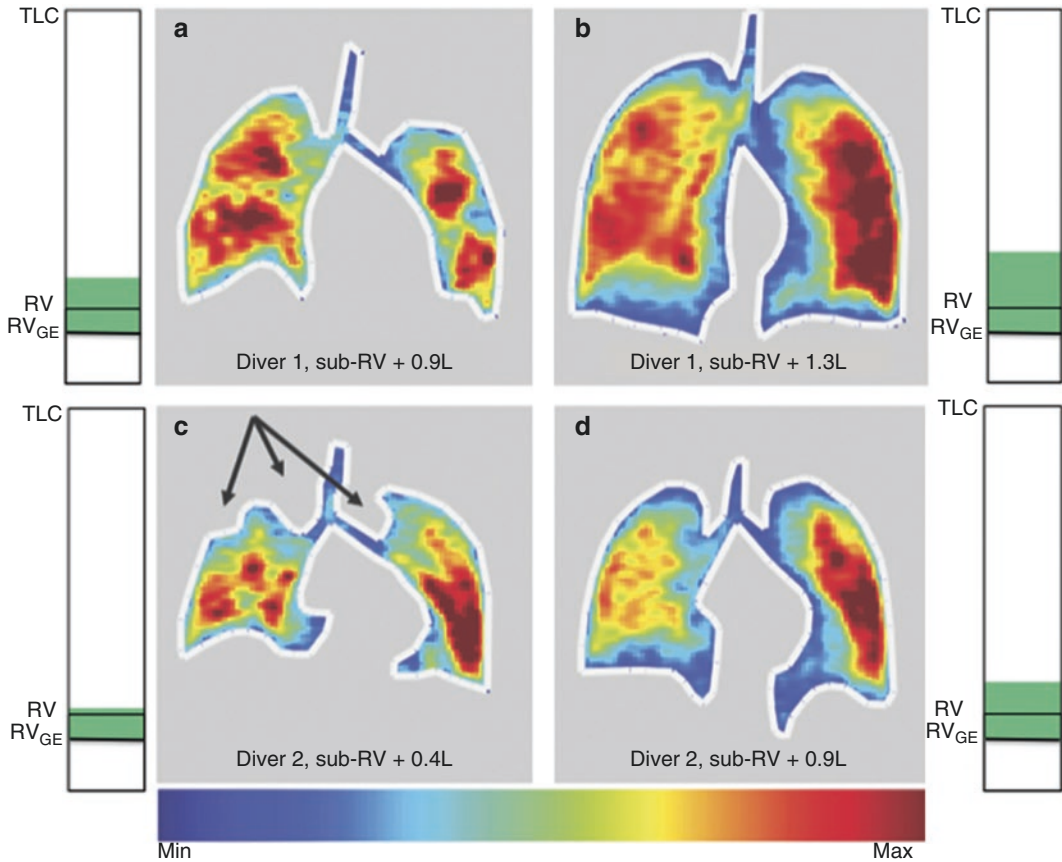
Fig. 6 Ventilation maps from two divers. Subjects performed glossopharyngeal exsufflation (GE) to reach sub-RV (RV$_{GE}$), after which they inhaled a Xe gas mixture. Here the *vertical bars* on the sides of the ventilation maps provide information about the lung and inhaled gas volumes. The *black horizontal lines* show RV and RV$_{GE}$ with respect to total lung capacity (TLC), while the bottom of the *green* region represents the lung volume at which the divers started inhalation of the Xe gas mixture. The top of the *green* region shows the lung volume (again, with respect to TLC) at which the breath-hold was done and data acquired. (**a**) Diver 1 (28 yo) following inhalation of 0.9 L from sub-RV. (**b**) Diver 1, 1.3 L from sub-RV. (**c**) Diver 2 (28 yo), 0.4 L from sub-RV. (**d**) Diver 2, 0.9 L from sub-RV. Note especially the regions remaining closed in (**c**) (*arrows*), and significant patchiness at both lung volumes in (**a**) and (**c**). The background color (*gray*) of the images shows the regions where no xenon signal was detected. *Dark blue* corresponds to minimum signal, while *dark red* represents the maximum signal measured. Reproduced from Muradyan et al. (2010) with permission

volunteers, for whom it was expected that CV would be greater than RV, following inhalation of approximately 1 L of gas, the ventilation maps were less patchy than the divers' maps (Fig. 7). Eight years later, we imaged one of the older volunteers who had participated in the study with the divers (Control 3). Figure 8 shows the ventilation distribution in this sub-ject following inhalation of 0.8 L of gas after exhaling to RV (twice) and FRC. As can be seen from comparison of the maps in Figs. 7c and 8, there was a significant increase in heterogeneity after 8 years if Xe was inhaled from RV, which largely disappeared when inhalation was from FRC, consistent with CV approaching FRC in older adults.
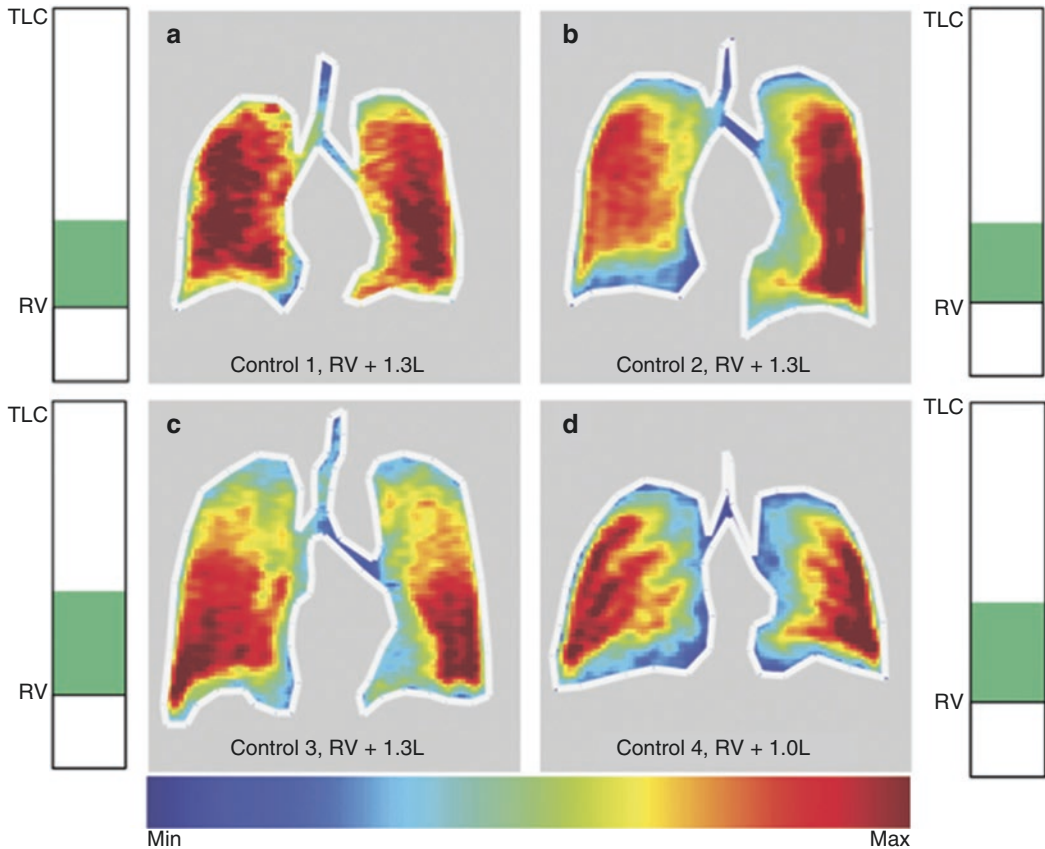
Fig. 7 Ventilation maps from controls. Subjects exhaled to RV, then inhaled a Xe gas mixture to reach lung volumes near FRC. The bars on the sides of the ventilation maps provide information about the lung volumes and inhaled gas amounts. The *black horizontal line* shows RV with respect to TLC, while the bottom of the *green* region represents the lung volume at which the controls started inhalation of Xe gas mixture (in these cases it coincided with RV). The top of the *green* region shows the lung volume (with respect to TLC) at which the breath-hold was done and data acquired. (**a**) Control 1 (31 yo), following inhalation of 1.3 L from RV. (**b**) Control 2 (31 yo), 1.3 L from RV. (**c**) Control 3 (55 yo), 1.3 L from RV. (**d**) Control 4 (56 yo), 1 L from RV. Color scheme is same as in Fig. 6. Reproduced from Muradyan et al. (2010) with permission

5.2 Direct Measurement of Xenon Uptake: Three-Point Dixon Approach

Regional maps of the parameters obtainable by the CSSR technique would be a welcome addition to pulmonary diagnostic tests. However, due to the low tissue density (only approximately 20% of the lung volume is tissue) and low solubility of Xe into the blood (the partition coefficient is approximately 0.1) only 2% of the Xe ends up in the dissolved state, thus limiting direct imaging of the dissolved state. Nevertheless, there is a strong effort by many groups involved in HPXe MRI research to obtain such maps (Cleveland et al. 2010; Mugler et al. 2010; Kaushik et al. 2013; Qing et al. 2014b). As described earlier, in CSSR, we quenched the dissolved Xe signal by applying a 90° pulse at a dissolved state frequency, then allowed for the gas to diffuse into the tissue for some time t_{diff}, which was then followed by an application of another 90° pulse and data acquisition. Here we combined the CSSR method with the Dixon method to map gas and dissolved state signals simultaneously during a short breath-hold in two healthy volunteers at approximately 40 and 70% of TLC. The three-point Dixon technique was

Inhalation from RV Inhalation from FRC Inhalation from RV
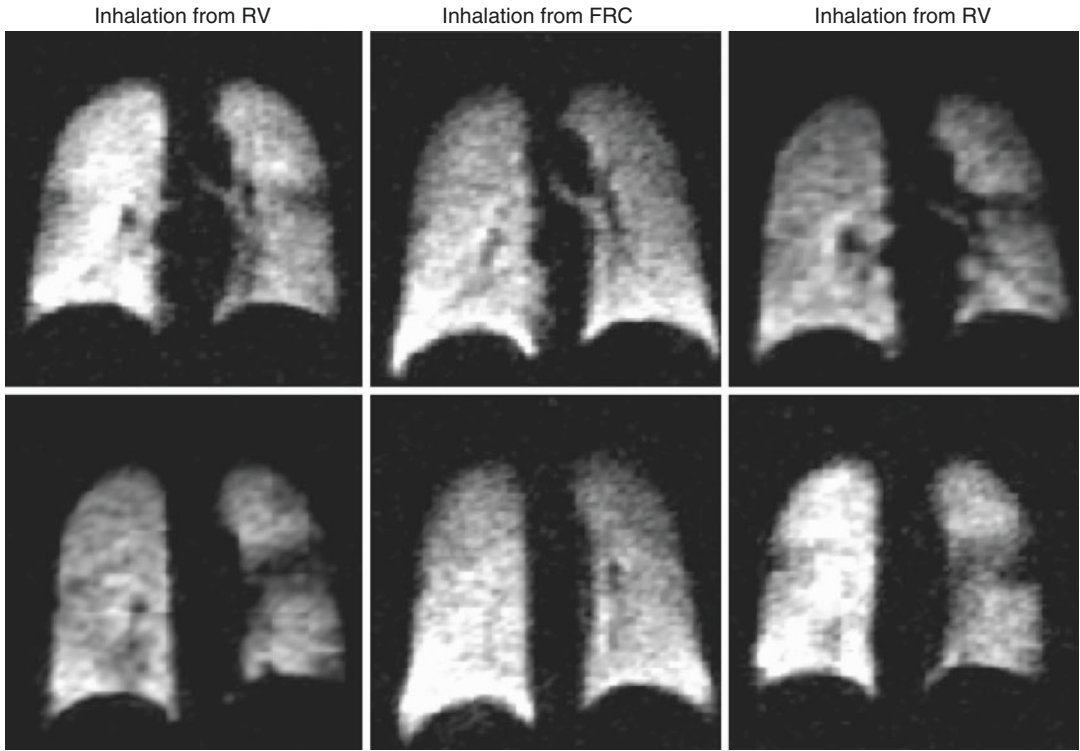
Fig. 8 Ventilation maps from control 3 (Fig. 7c), inhaling 800 mL of xenon gas mixture from RV (*right and left columns*) and FRC (*center column*). These data were taken 8 years after the data in Fig. 7c. As can be appreciated from the maps, if inhalation started from RV (below CV), there are reproducible patches of unventilated regions, which disappear if inhalation is started from FRC

chosen as it allows for correction of possible field nonuniformity in the measurement region. The measurements were performed at 0.2 T magnetic field strength; the difference between gaseous and dissolved state Xe resonance frequencies was $\Delta\nu = 485$ Hz. We collected three coronal projection images with three echo times such that the dissolved and gaseous states were in "parallel," "anti-parallel," and "parallel again" phases, i.e., values for TE were:

$$T_{E,n} = T_{E,0} + (n-1)\cdot\Delta T_E \qquad (5)$$

where *n* is the number of the image to be collected with *TE, n* echo time, $\Delta T_E = \dfrac{1}{2\Delta\nu}$, and *TE,* $_0$ is the minimum echo time we could reach. We used a 90° flip angle centered at the dissolved state signal, which tipped the gas state signal with only 2° RF pulse. By collecting interleaved images, we avoided relaxation effects. In one of the volunteers, we repeated the experiments twice to check the reproducibility of the measurements.

Because the dissolved phase Xe signal was very low, we used phased reconstruction to avoid noise rectification during image reconstruction. The first and third images (both had gas and dissolved state signals in phase) were used to obtain time-dependent phase accumulated during the time ΔTE, which is then used to phase-correct the second image. The sum of the first and second images provided dissolved state images, while their difference provided the gas state image. In order to calculate the fractional gas transport, *F*, we calculated a ratio of these two images. However, the dissolved and gas state images had shifted positions with respect to each other due to the chemical shift experienced by the off-resonance phase (in this case, the gas phase was off-resonance). We corrected for this shift by transferring the images into the time domain, per-

forming a time-dependent phase-correction for data points during the acquisition time and then transferred back to the image domain. This corrected the shift in the off-resonance image, which was then used to calculate $F(t_{\text{diff}})$ maps. A set of sample images and F-maps for each lung volume is presented in Fig. 9a, b. Unfortunately, we collected images for only a single diffusion time point during a breath-hold, and could not translate measured F values to S/V maps because of the unknown offset F_0. Despite the relatively low SNR of the images (average SNR for gas and dis-
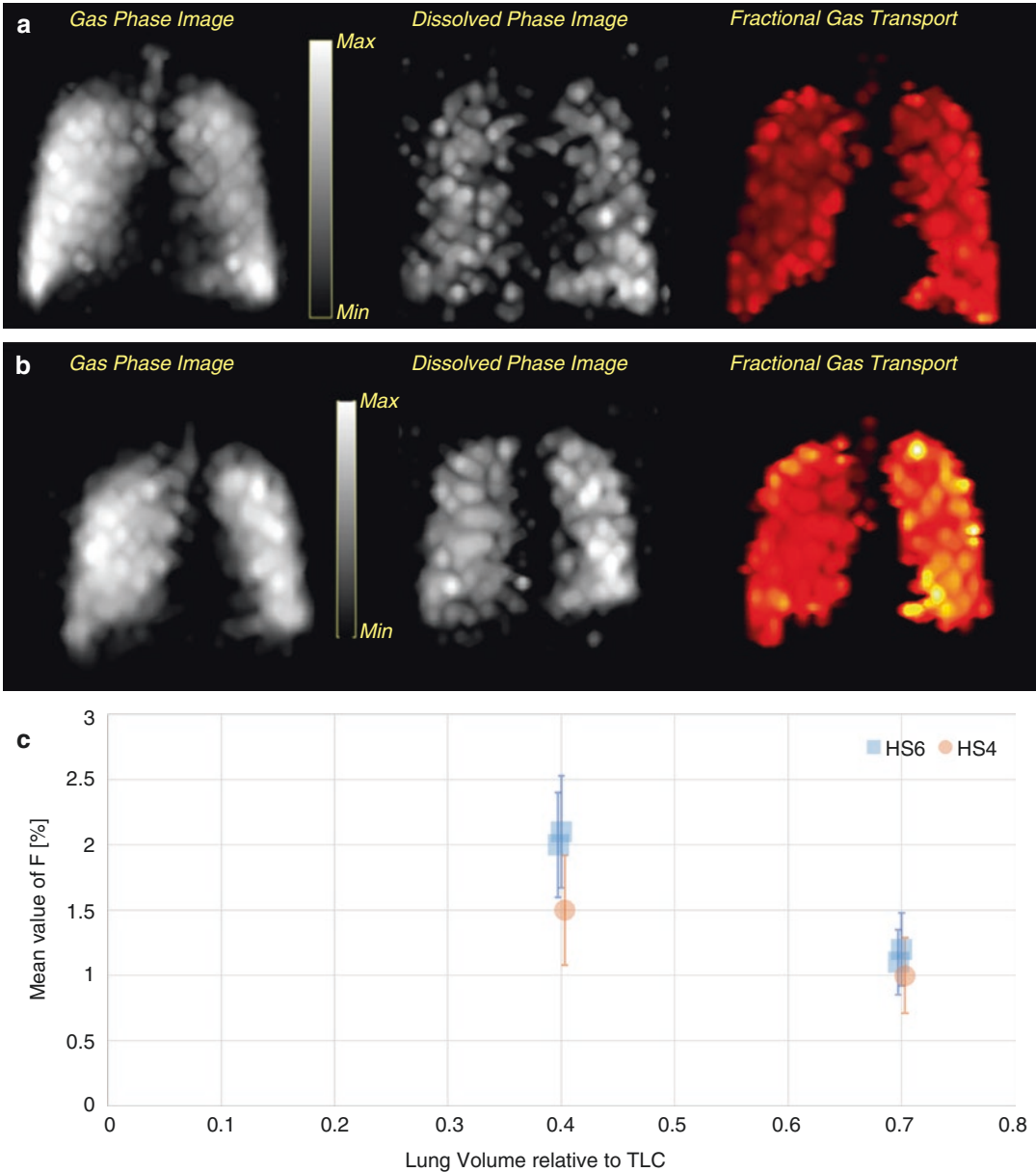
Fig. 9 Sample data from a subject at two different lung volumes. (**a**) Data at higher lung volume (~70% TLC); Reproduced from Muradyan et al. (2012) with permission from The Royal Society of Chemistry. (**b**) Data at ~FRC; (**c**) Mean and standard deviations for three data sets we collected in two healthy volunteers. As expected, the higher lung volume shows more homogeneous distribution of the gas exchange. Also, $F(t)$ values at higher LV are lower than those at lower LV

solved state images were 20.5, 10.9, and 17.4, 6.5 for 40% and 70% TLC, respectively), we were able to obtain F-maps for both subjects at two lung volumes. Features to note are: for both subjects, the distribution of F at a higher LV is more uniform than that of lower LV; the mean values of F at lower LV are greater than those at a higher LV for both subjects; the mean values of F from two measurements are in good agreement for both lung volumes (see Fig. 9c for details).

5.3 Indirect Measurement of Xenon Uptake—SB-XTC

We are using a modified version of Xe transfer contrast technique (Ruppert et al. 2000), in which all necessary calibration information is collected during a single breath-hold, the so-called single breath Xe transfer contrast (SB-XTC) technique, to map fractional gas transport in vivo (Patz et al. 2007). Briefly, XTC allows for measurement of Xe septal uptake by measuring the loss of gas phase magnetization following repeated saturations of the dissolved phase. Each saturation allows Xe transport from gas to dissolved phase during a time t_{diff}. SB-XTC is designed as follows. The Xe gas signal is measured prior to (image I_1) and following (image I_2), the XTC sequence with RF pulses applied at the dissolved phase frequency (+205 ppm relative to the gas phase). In addition to the measured loss of signal between images I_1 and I_2 due to Xe septal uptake, there are other loss mechanisms including: (1) T_1 relaxation in the lungs; (2) application of small flip angle RF pulses to collect the gas phase images; and (3) the effect of the XTC saturation pulses on the gas phase (although they are applied at +205 ppm, one needs to account for their tail at the Larmor frequency, possibly exciting the gas phase). To account for these contributions, a third image (I_3) is collected following application of an identical XTC sequence, except that the RF pulses are at −205 ppm. This procedure corrects for all relaxation contributions other than septal uptake of Xe, yielding an unbiased estimate of $F(t_{\text{diff}})$. To account for the RF flip angle spatial distribution, a fourth image (I_4) is

acquired immediately following image I_3. The ratio I_2/I_1 is used to map the fractional Xe uptake $F(t_{\text{diff}})$; I_3/I_2 is used to correct for the above confounding contributions, and I_4/I_3 is used to map the distribution of the B_1 field. Details of the SB-XTC technique and our implementation in human subjects can be found in reference (Muradyan et al. 2012).

We studied the fractional depolarization F as a function of lung volume in eight healthy subjects for a wide range of lung volumes, from 18 to 82% of TLC. We observed an increase in the value of $<F>$ with the decrease of the lung volume (Fig. 10a). We separated the physiological heterogeneity of the lung from the overall measured heterogeneity and observed a reduction of physiological heterogeneity with the lung volume decrease (Fig. 10b).

With SB-XTC, we also studied two nonsmokers, nine smokers (with a smoking history ranging between 1.5 and 33 pack years (PY)) and three nonsmokers, who have experienced heavy second hand exposure to smoke (approximately 13–22 years of more than 10 h of daily exposure). We measured their average fractional gas transport $<F>$ as a function of smoking history or exposure. As can be appreciated from Fig. 11, in almost all smokers (except the smoker with the longest smoking history, 33 PY), we observed elevated $<F>$ at both low and high lung volumes. Similarly, high values of $<F>$ were observed in second hand smokers, suggestive of ongoing inflammation in the lungs. The lower value of $<F>$ in the subject with 33 PY smoking history may be due to the interplay between inflammation that results in an increase of the measured septal thickness and lung tissue/capillary bed destruction, which lowers $<F>$. Interestingly, the subjects with second hand exposure exhibited an increase in $<F>$ almost identical to that seen in active smokers.

We further extended the technique to 3D in vivo measurements for three diffusion times (20, 44, 66 ms) short enough to maintain the validity of the semi-infinite slab model. We used the Xe uptake model valid for short diffusion times to fit the data and obtain regional S/V in healthy subjects (Fig. 12). It should be noted that in order to utilize the analytical CSSR
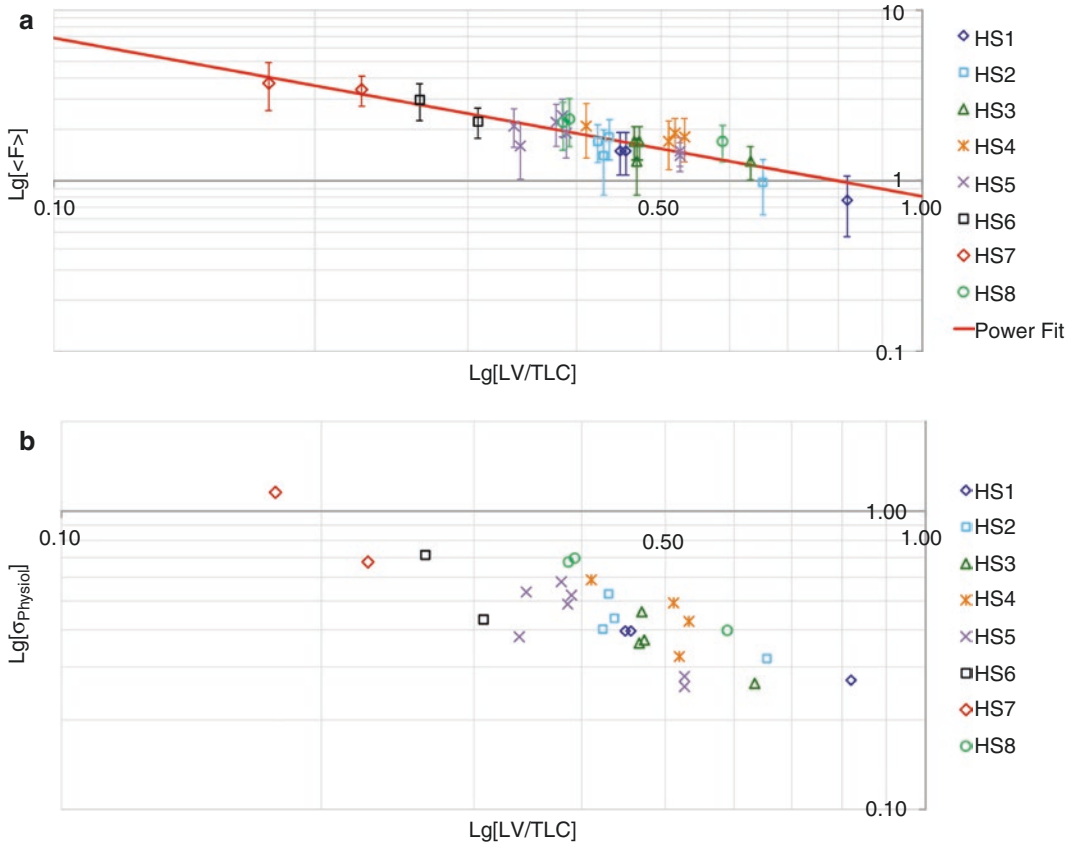
Fig. 10 Volume dependence of the mean fractional gas transport *<F(t)>* (**a**) and physiological heterogeneity $\sigma_{Physiol}$ (**b**), both plotted on a Log-Log scale. To enable inter-subject comparison, the lung volumes are normalized to TLC of each subject. *<F(t)>* from all subjects is in good agreement within the error, which is represented here by the contribution of the noise to the width of the fractional gas transport distribution. In most cases the largest contribution to the width of *<F(t)>* distribution comes from the physiological heterogeneity. Each human subject is indicated as "HS" followed by a number. Reproduced from Muradyan et al. (2012) with permission

Fig. 11 Mean Fractional transport *<F>* versus smoking history at two lung volumes. Purple and red data points (*triangles*) are from two second hand smokers. Interestingly, the effect of second hand smoke is similar to that of active smoking. Reproduced from Muradyan et al. (2012) with permission from The Royal Society of Chemistry
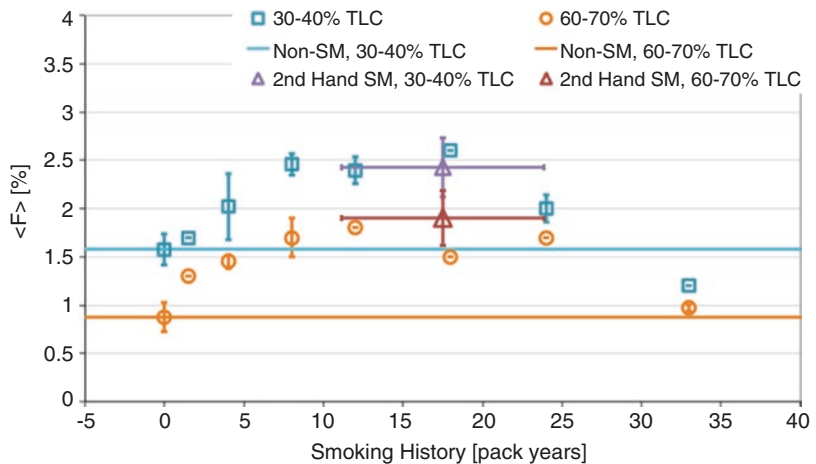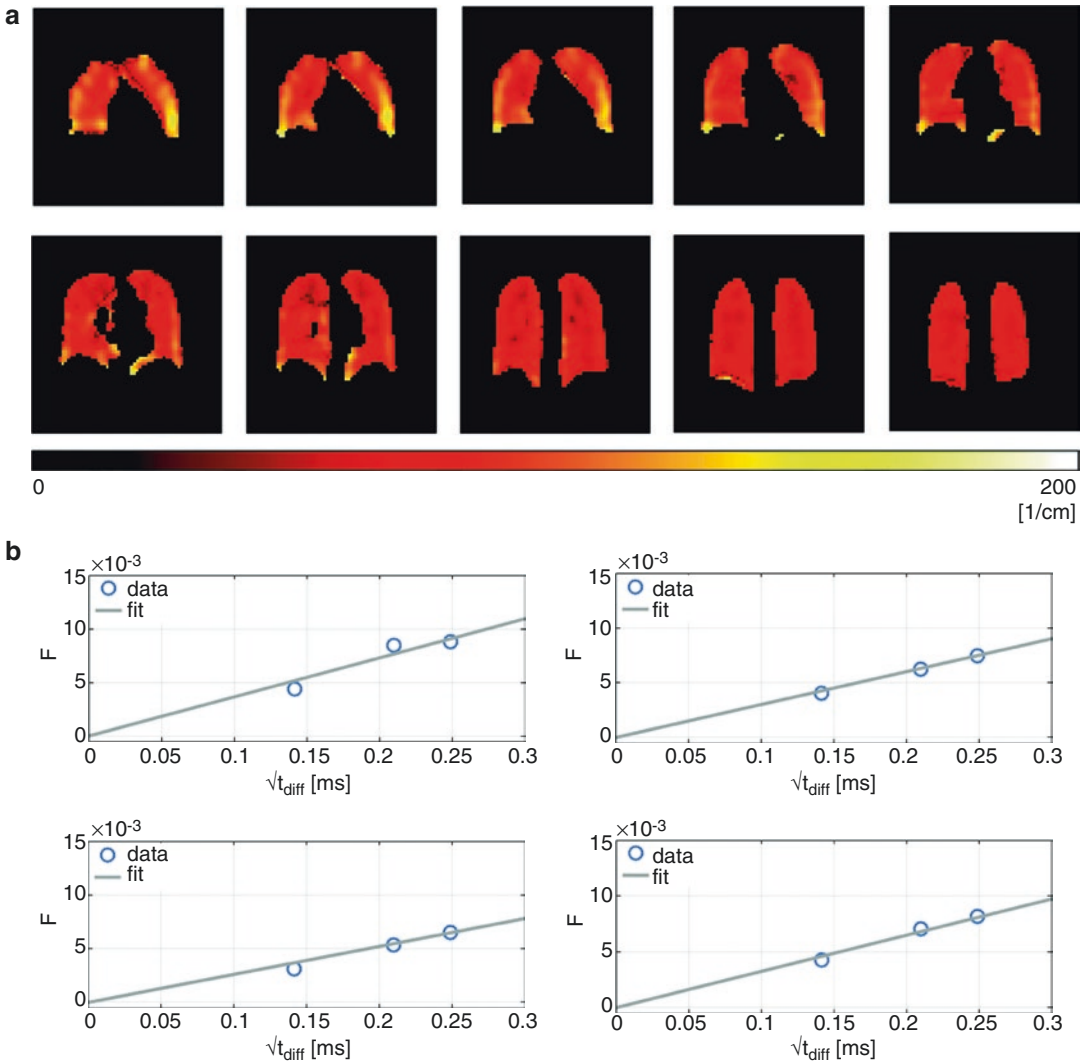
Fig. 12 (**a**) Map of *S/V* in units of inverse cm calculated from a pixel-wise fit to the semi-infinite slab model. The global mean value for *S/V* is 89 ± 30 cm^{-1} (mean $\pm$ standard deviation). The data are collected at RV + 260 mL gas, resulting in near 40% of TLC for this subject. (**b**) Representative voxel-wise fits of *F* to the short-time model from four different voxels measured at three diffusion times demonstrating the quality of the fit. Reproduced from Muradyan et al. (2012) with permission from The Royal Society of Chemistry

framework to calculate morphological parameters of the lung such as *S/V*, *h*, and τ, it is necessary to use saturation pulses in XTC-type experiments and not inversion pulses, as was originally proposed (Ruppert et al. 2000). Additionally, we demonstrated the importance of the proper estimation of the fractional depolarization at higher fields, as it is necessary to account for B_1 distribution.

5.4 Mapping the Partial Pressure of Alveolar Oxygen with SB-XTC

Mismatches in the ventilation/perfusion ratio (V/Q) in the lung are the hallmark of a wide spectrum of pulmonary diseases including COPD, asthma, interstitial diseases, and pulmonary embolism (PE). The consequences of V/Q mis-

matches are important both in diagnosis and in patient management. V/Q heterogeneity is a major factor in impaired gas exchange: regionally low V/Q ratios (e.g., COPD) lead to locally low alveolar oxygen tension ($p_A O_2$) and systemic hypoxia; high V/Q ratios (e.g., in PE) lead to wasted ventilation, locally high $p_A O_2$, and contribute to pulmonary hypertension.

The basic technique for measuring $p_A O_2$ utilizing the oxygen-dependent T_1 relaxation rate of ^{3}He was introduced more than 15 years ago. Deninger et al. (2002) showed that the only significant source of relaxation other than oxygen was due to the RF pulses used to interrogate the HPG signal. This can be quantified through a series of images, collected such that there is no extra delay between the first two images, minimizing the magnetization decay due to O_2, thereby quantifying the reduction in magnetization due to the RF pulses and permitting a calculation of the direct effect of O_2. Development has continued in both 3D technique or through sophisticated interleaved multi-slice approaches, correcting for confounding effects such as the high diffusivity of He (Deninger et al. 1999; Wild et al. 2005; Yu et al. 2008, 2009; Miller et al. 2010; Marshall et al. 2013). In contrast to ^{3}He, ^{129}Xe is naturally available and inexpensive, has a significant solubility in tissue, and therefore, is subject not only to local $p_A O_2$, but also to local perfusion. Ignoring septal uptake of Xe leads to a systematic bias such that the estimates of local $p_A O_2$ are artifactually high. We implemented a correction to this bias by explicitly taking into account Xe uptake in tissue and blood.

At the theoretical level, the measureable quantity is the longitudinal magnetization decay time constant T_1. This time constant is proportional to the harmonic mean of three characteristic times: the decay associated with the interrogatory RF pulses, the decay associated with wall interactions, and the decay associated with O_2. The latter is driven by the intermolecular dipolar coupling between the electron spin of oxygen and nuclear spin of a noble gas (Jameson et al. 1988; Saam et al. 1995). The first of these is directly measureable; the second is known from experimentation to be sufficiently long that it can

be ignored; the third has a known field/frequency dependence (Saam et al. 1995). The relation between the measured T_1 and $p_A O_2$ is thus given by:

$$\frac{1}{T_1} = \frac{1}{T_{1,RF}} + \frac{1}{T_{1,p_{AO_2}}} = \frac{1}{T_{1,RF}} + \frac{p_{AO_2}}{\xi(T)} \cdot \left(1 - f(T)\sqrt{\omega}\right) \tag{6}$$

where T is the temperature and ω is the Larmor frequency; ξ and f are, in general, temperature dependent.

Earlier, we reported on local measurements of a quantity we called the "$p_A O_2$-equivalent" as part of measurements with the single breath Xe transfer contrast (SB-XTC) technique without accounting for Xe uptake (Patz et al. 2007). We assumed the saturation RF pulses at −205 ppm had a negligible effect on the gas phase signal and, because Xe septal uptake is estimated as *approximately 2%* of the gas phase signal during the time interval between images 2 and 3, we neglected it as well. As a result, the T_1 values were underestimated and $p_A O_2$ values were overestimated: the mean $p_A O_2$-equivalent in 17 healthy volunteers was estimated to be 165 Torr. In this study, we highlighted the complications with $p_A O_2$ data interpretations when measured with Xe, and, in particular, that ignoring Xe uptake and nonoptimal pulse sequences leads to a systematic overestimation in $p_A O_2$. After accounting for the extra RF depletion effect, we calculated a mean $p_A O_2$-equivalent of 127 ± 17 Torr (mean ± standard deviation) of the same data, a significant change from 165 Torr. These mean values agreed with other $p_A O_2$ measurements with HPXe, but are still higher than expected in healthy volunteers: in all of our experiments, the subjects inhaled 21% oxygen and we expected an initial $p_A O_2$ of ~*approximately 100 Torr* (Weibel 1984).

To account for Xe uptake during the measurement, we used SB-XTC and CSSR data from the same subject to calculate $p_A O_2$ after correcting for Xe uptake. With CSSR, we demonstrated that for diffusion times more than *approximately 100 ms*, the tissue is saturated with Xe and the assumption of linear bulk blood flow is supported

Fig. 13 (**a**) Simulated Xe uptake curve based on the mean values of surface area per unit volume, thickness of the gas-blood barrier, and blood transit time. This curve is used to estimate the linearity region where p_AO_2 measurements can be performed. (**b**) Sample p_AO_2 map from a volunteer, calculated from SB-XTC data. The volunteer inhaled HPXe gas mixture containing 21% O_2. Mean p_AO_2 of 127 Torr is calculated before accounting for Xe uptake. Subject's CSSR data at the same lung volume provided amount of xenon uptake to obtain unbiased mean p_AO_2 of 97 Torr
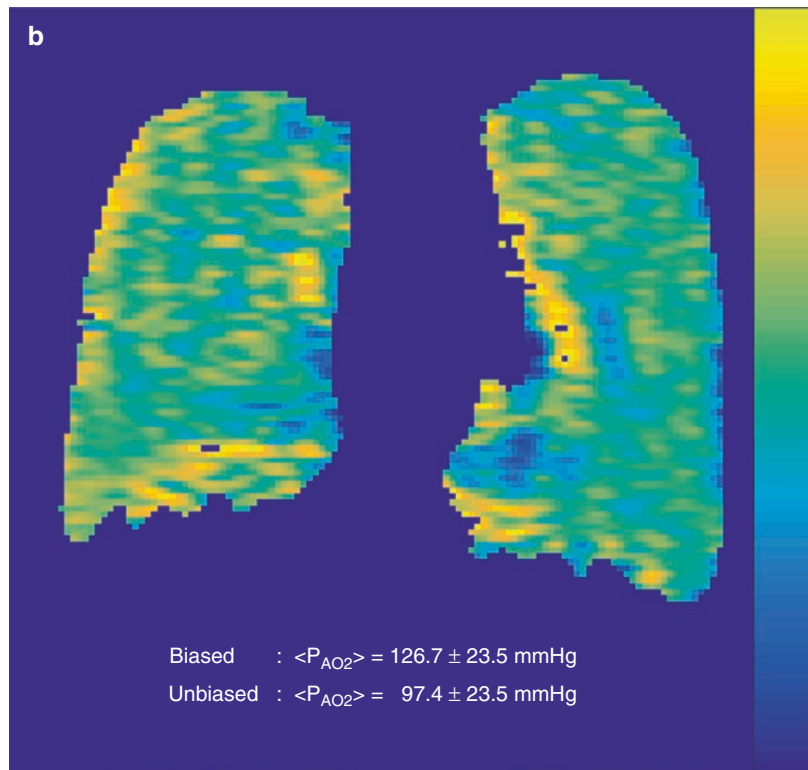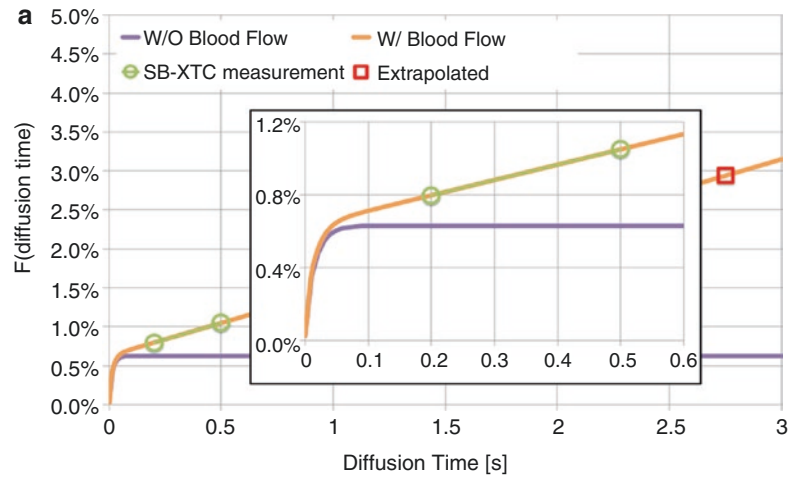
by the in vivo data (Patz et al. 2011; Chang et al. 2014; Stewart et al. 2014). Figure 13a shows a simulated Xe uptake curve using the mean values of the surface area per unit volume available for gas exchange, tissue thickness, and pulmonary blood transit time measured on healthy volunteers (based on data from Patz et al. (2011)). For times greater than 100 ms, the Xe uptake curve is linear with time and it can be used to extrapolate and estimate the amount of Xe lost during the measurement of p_AO_2.

We used the Xe uptake curve to estimate that in a healthy subject, approximately 2.5–3% of Xe was taken away from the pulmonary region by the blood (for some of the volunteers, we measured the uptake curves; for the remainder, we

used an averaged curve to predict the amount of the Xe loss, Fig. 13a). When the uptake loss was accounted for, the unbiased mean p_AO_2 in all subjects was *102 ± 14 Torr*, which was in agreement with the expected value (Fig. 13b).

The ability to measure local alveolar p_AO_2 has long been one of the holy grails of pulmonary physiology. Any pulmonary disease necessarily affects local ventilation, perfusion, or both, and as the local p_AO_2 is the product of a complicated interplay of the local ventilation and perfusion, it will reflect the mismatch between the two. Therefore, local p_AO_2 is definitely a clinically important parameter and can inform the evaluation of regional V/Q mismatch in pulmonary disease.

6 Recent Studies with HPXe MRI in Adult and Pediatric Patients

There have been several studies in patients with various pulmonary diseases published over the last couple of years. Most of them included only a small number of patients, but provided enough information to warrant a larger scale study.

Ebner et al. (2017) studied 20 patients with asthma and 10 healthy volunteers (10 young patients with 5 age-matched controls, and 10 older patients with 5 age-matched controls). They obtained 3D ventilation maps and calculated ventilation defect percentage (VDP) in all subjects. They observed significant difference in VDP ($p = 0.031$) between young patient ($8.4 ± 3.2\%$) and matching control ($5.6 ± 1.7\%$) groups, while in the older subjects the observed difference was not significant ($16.8 ± 10.3\%$ in patients versus $11.6 ± 6.6\%$ in controls, $p = 0.13$). They also reported a moderate correlation between VDP and some PFT results (FEV1%, FEF25–75%, RV/TLC). However, more notably, they demonstrated that the spread between repeat measurements of VDP was significantly narrower compared to that in FEV1 measurements: with Bland-Altman analysis they obtained a bias ± standard deviation of −0.88 ± 1.52 for VDP and −0.33 ± 7.18 for FEV1.

Qing et al. (2014a) have obtained Xe uptake in 45 subjects: 23 healthy, 13 with COPD, and 9 with asthma, using both spectroscopic CSSR and 3D dissolved phase imaging approaches. In CSSR they separated signal from Xe dissolved into the tissue and plasma (TP) from the signal from Xe dissolved into red blood cells (RBC), and reported the ratio of RBC/TP; they also obtained alveolar septal thickness (ST). While for the COPD cohort they observed RBC/TP ratios below the average values for the controls, the same ratio in subjects with asthma was either significantly higher or significantly lower (each two standard deviations removed), with the mean value not significantly different from the controls' mean value. ST in COPD subjects was significantly higher than that in controls.

For 3D dissolved phase imaging they used radial interleaved acquisition to obtain maps of Xe signal distributions in gas (G) phase, dissolved into TP, and dissolved into RBC. For the COPD cohort, all measured ratios (TP/G, RBC/G, and RBC/TP) were lowered compared to those in healthy volunteers, while between asthmatic subjects these ratios varied drastically. In ten of the subjects they also obtained the diffusing capacity of the lung for carbon monoxide (DLCO); in this subset of the subjects they observed a high correlation between RBC/G and DLCO ($R = 0.91$).

Stewart et al. (2016) used CSSR to assess the reproducibility of the spectroscopic functional measurements of pulmonary parameters, alveolar septal thickness (ST) and surface area per unit volume available for gas exchange (*S/V*). They studied five controls on 3 separate days; three of the controls were also studied at three different lung volumes. They reported that *S/V* decreased with increase in lung volume, which agrees with our previous observations, however they also reported lower ST values at higher lung volume; our previous measurements did not show a significant difference in ST at different lung volumes (Patz et al. 2011). They also studied five COPD patients and nine age-matched controls on three occasions to evaluate the reproducibility of the measurement: the mean coefficient of variation (CV) of ST was 3.9 ± 1.9% in controls and 6.0 ± 4.5% in COPD patients, similar to CV

values for DLCO measurements. For *S/V* measurements, the mean CV was $14.1 \pm 8.0\%$ in volunteers and $18.0 \pm 19.3\%$ in patients.

Ouriadov et al. (2014) used diffusion weighted HPXe imaging to obtain unrestricted Xe diffusion coefficient, which they then used to estimate alveolar oxygen partial pressure (p_AO_2) in four controls and four COPD patients. They reported significantly higher ($p < 0.04$) free diffusion constant values in COPD subjects (0.14 ± 0.03 cm^2/s) compared to the never-smoker controls (0.12 ± 0.02 cm^2/s); COPD subjects also had higher p_AO_2 values compared to the controls ($18 \pm 3\%$ vs. $15 \pm 3\%$, $p < 0.01$).

Stewart et al. (2014) used CSSR to quantify changes in Xe signal dissolved into TP and RBC in four patients with idiopathic pulmonary fibrosis (IPF), four patients with systemic sclerosis (SS), and ten healthy volunteers. They observed a reduced Xe uptake into the pulmonary capillaries in both patient groups; IPF patients also had significant thickening of the septal wall. Additionally, they reported a good correlation between ST measured with CSSR and DLCO percent predicted values ($R = -0.91$, $p < 0.001$).

Kaushik et al. (2014) obtained HPXe spectra in 11 controls and 6 IPF patients to evaluate the differences in the Xe uptake. They reported a more than threefold lower RBC/TP ratio in IPF subjects compared to healthy volunteers; this was due to 52% reduction in RBC signal and 58% increase in TP signal. They also reported that the RBC/TP ratio showed a strong correlation with the subjects' DLCO ($r = 0.89$, $p < 0.0001$).

Thomen et al. (2016) published the first HPXe MRI study report in pediatric subjects. They imaged 11 healthy controls (age 6–16 years) and 11 patients with cystic fibrosis (CF) (age 8–16 years) and evaluated the ventilation defect percentage in each group. They observed a significantly higher VDP for CF subjects ($18.3 \pm 8.6\%$) compared to controls ($6.4 \pm 2.8\%$). Even for a subset of CF patients with normal FEV1 (>85%, with mean FEV1 = $103.1 \pm 12.3\%$ comparable to controls' FEV1 = $100.3 \pm 8.5\%$), the difference in VDP values ($15.4 \pm 6.3\%$) was statistically significant ($p < 0.002$).

Above is just a small subset of the studies done in different patient groups, meant to demonstrate the utility of HPXe MRI for aiding clinical diagnosis and evaluating treatment efficiency. Still, even based on the studies listed here one can argue that HPXe offers unique capabilities for noninvasive radiation-free pulmonary structural and functional assessment.

7 Safety of HPXe Human Studies in Children and Adults

An extensive body of work over the past couple of decades shows that 15–40 s periods of breath-hold after the inhalation of 1 L of hyperpolarized inert gases are tolerated well by most healthy as well as diseased subjects; over 1000 subjects have inhaled polarized ^{3}He or ^{129}Xe with no adverse effects other than "dry mouth"- and "dizziness"-related symptoms that are resolved spontaneously upon breathing room air again. "Dry mouth"-related symptoms result from the fact the gas is produced without water vapor that is always present in room air, while "dizziness" is due to xenon's anesthetic effect.

In our laboratory, we have performed nearly 500 breath-holds for practice breath-holds and HPXe MRI tests. According to our old protocol (Patz et al. 2007), we have instructed the subjects to fully inhale and exhale three times, and then administered up to 2 L of Xe with addition of O_2 and air, so that the gas mixture prepared for inhalation contained 21% of O_2 and no more than 70% Xe, while the resulting concentration of Xe in the lungs did not exceed 35%. We administered up to eight breath-holds per subject per study, separated by 10 min. We measured their baseline SpO_2, blood pressure (BP), heart rate (HR), and respiratory rate (RR) and recorded their electrocardiographs (ECG). During the breath-hold (up to 40 s long for healthy and 20 s for diseased patient) we continuously monitored their SpO_2 and HR and recorded nadir SpO_2. Over these breath-holds we have observed no adverse events in any of the subjects. None of the subjects withdrew from the study. No significant

changes were observed in the vital signs in either healthy volunteers or patients. Most of the subjects reported experiencing some degree of dizziness that subsided within a minute of breathing room air.

Lutey et al. (2008) conducted a study that involved 100 subjects from five distinct groups: 20 healthy subjects, 35 heavy smokers (more than 30 pack/years) who are otherwise healthy, 7 asthma, 1 lung cancer, and 37 lung volume reduction surgery (27 participated before and 10 after the surgery, 12 of these 37 patients were on supplemental oxygen) patients. Their criteria excluded subjects who had or were suspected to have cardiac or cerebrovascular disease and anemia and those who were or might had been pregnant. Their protocol required subjects to exhale to FRC, and then inhale from a bag containing 300–500 mL of ^{3}He mixed with 0–2700 mL of N_2 gas. The first 23 subjects were administered up to 3 L of asphyxiant gas, while for the following 77 subjects a standard inhaled dose of 1 L (300–500 mL of which was hyperpolarized ^{3}He) was adapted. All breath-holds were limited to 15 s. At the baseline they measured the subject's HR, BP, RR, and SpO_2 and reviewed his/her ECG. These parameters were reassessed immediately after the imaging session was completed, and any symptoms were addressed. The HR and SpO_2 were continuously monitored during the breath-hold, and SpO_2 nadir and times of its occurrence and return to baseline with respect to breath-hold commencement were recorded. All subjects were contacted the following day for a 24-h follow-up. For the 216 runs that they reported no clinically important effects of ^{3}He breath-holds on vital signs, nadir SpO_2 of 4%, nadir SpO_2 during a breath-hold over 95% in 28% of the runs, in the range 90–94% in 56% of the runs, below 85–89% in 14% of the cases and 81–84% in 2% of the cases. All returned to the baseline within 2 min. Based on the results they concluded that SpO_2 should be continuously monitored during the breath-hold, and careful screening should be implemented to exclude subjects with conditions in which even a transient drop of SpO_2 to ~80% would be inadvisable.

Shukla et al. (2012) presented data on 136 anoxic inhalations of 500 mL of hyperpolarized Xe mixed in 500 mL of helium buffer gas from 33 healthy and diseased subjects (12 healthy subjects, 7 with asthma, 10 with COPD, 3 with cystic fibrosis, and 1 with radiation-induced lung injury). The subjects requiring day- or night-time supplementary oxygen were included in the study. The only exclusion criterion was baseline supine $SpO_2 < 90\%$ while on supplemental oxygen. At the baseline they recorded BP, HR, RR, and SpO_2. HR and SpO_2 were continually monitored during the breath-holds. They defined Adverse Event (AE) as any unfavorable and unintended symptom temporarily associated with the use of Xe, whether or not it was considered related to the gas or expected based on its known properties. Subjects were continually monitored for AEs, and asked to report any AEs experienced within 24 h of the last breath-hold. AEs were evaluated by a qualified pulmonologist as mild (awareness of the sigh or symptom, but easily tolerated), moderate (discomfort enough to cause interference with usual activity), or severe (incapacitating with inability to perform usual activity); AEs were also judged by a qualified pulmonologist as not related, possibly related, and related to Xe gas inhalation. Hypoxic AEs were defined as a reduction from baseline SpO_2 of more than 5% that had not quickly resolved after Xe inhalation.

There were no serious or severe AEs reported, none of the subjects withdrew from the study. They reported a total of two mild AEs in 136 breath-holds (less than 1.5%) by one COPD subject and one with asthma. One (head ache 7 h after the last inhalation) was considered not related to the inhalation, while the other (light-headedness) was judged possibly related to Xe breath-hold. This symptom subsided within 2 min.

While there were no hypoxic AEs reported, there was small change in SpO_2 during the breath-hold compared to the baseline (baseline $SpO_2 = 97.9 \pm 1.3\%$, breath-hold $SpO_2 = 96 \pm 2.9\%$), which was judged clinically insignificant. No significant differences in handling Xe inhalations were observed between healthy and diseased subjects.

In another report Driehuys et al. (Virgincar et al. 2012) studied the safety and tolerability

of xenon breath-holds in healthy volunteers and patients. Their subject pool consisted of 24 healthy volunteers, 10 patients with COPD (GOLD stage I–III), and 10 age-matched controls. According to their protocol, the subjects were instructed to fully inhale and exhale twice and then administered 1 L of 100% Xe without adding of O_2. They administered up to four 1 L xenon inhalations per study. At the baseline they measured HR, RR, BP, and ECG and performed neurologic and neurobehavioral examinations. During a breath-hold they continuously monitored subjects' SpO_2 and three-lead ECG. Within 10 min following the breath-hold they measured HR, RR, BP, and SpO_2 six times and conducted another brief neurological examination. These were followed by similar measurements at 1-h post breath-hold and 24-h follow-up visit, during which all vitals, ECG, neurologic and neurobehavioral examination and a limited physical examination were performed. Moreover, at the screening and 24-h follow-up clinical laboratory tests (Serum Biochemistry and Hematology) were obtained to assess the biochemical effect of dissolved Xe on the blood chemistry.

They defined an adverse event as any unintended symptom temporally associated with Xe, which was classified by the medical personnel as mild (tolerable), moderate (interferes with normal activity), or severe (incapacitating). Further, hypoxic adverse event was defined as a drop in SpO_2 of over 5% that did not resolve in 1 min after the breath-hold.

All subjects tolerated the xenon inhalations well; none of them withdrew from the study; no serious adverse events were recorded; no significant changes in vital signs were observed following the breath-holds and up to 24 h after the inhalation, none of the subjects exhibited any change in serum biochemistry or hematology values. Most subjects (40 of 44) experienced mild, transient symptoms, related to the known anesthetic properties of xenon (most commonly dizziness), which resolved without clinical intervention in less than 2 min. Two subjects (one healthy, one age-matched control) experienced four moderate adverse events.

They concluded that inhalation of hyperpolarized ^{129}Xe is well tolerated in healthy subjects and in those with mild or moderate COPD. The exclusion of O_2 from the gas mixture has a significant effect on the resulting image quality, while having very little effect on the safety and tolerability of the inhalation by the subjects. This study showed that SpO_2 after inhalation and breath-hold changed by less than 1%, and that inhalation of Xe has no biochemical effect on blood chemistry.

And, lastly, Walkup et al. (2016) evaluated feasibility, tolerability, and safety of pediatric HPXe MRI in healthy volunteers and children with cystic fibrosis. They enrolled 17 healthy volunteers (age 6–16 years) and 11 children with clinically diagnosed CF (age 8–16 years). Their inclusion criterion was the ability to hold their breaths for 16 s for all children; the exclusion criteria were a history of poorly controlled asthma, history of heart defect, use of an asthma rescue inhaler more than twice within the last month, symptoms of respiratory or sinus infection a week prior to Xe study, baseline $SpO_2 < 95\%$, positive pregnancy test, and standard MRI exclusions. A registered nurse or a physician oversaw all Xe inhalations. They obtained subjects' baseline HR and SpO_2, and monitored them for 2 min following the inhalation. They recorded nadir SpO_2, its duration, as well as the HR at that instance. Immediately after the inhalation, with the child still in the scanner, the gas administrator asked the child to describe any dizziness, lightheadedness, numbness, or euphoria that he/she might have experienced during the inhalation. A maximum of three inhalations were performed per child, with at least 2-min delays between the runs for the children to rest and breath room air. They assessed adverse events during and up to 30th day post imaging (via day 1 and day 30 follow-up phone call). First five of the volunteers were given HPXe volume equal to 1/12th of their predicted TLC. No adverse events were reported; thus, the rest of the healthy volunteers and all CF subjects inhaled volume of HPXe equal to 1/6th of their TLC, with a maximum dose of 1 L.

Baseline SpO_2 was measured at 98.5 ± 1.2% and 97.3 ± 1.6% for control and CF subjects,

respectively; their nadir values were significantly reduced to $93.9 \pm 4.0\%$ ($p \leq 0.001$) and $89.9 \pm 9.8\%$ ($p < 0.02$), correspondingly; 2 min post inhalation the SpO_2 values for the control group were lower compared to the baseline ($97.5 \pm 1.7\%$, $p = 0.02$), while for the CF group the values returned to the baseline ($97.3 \pm 1.8\%$, $p = 1.0$).

No central nervous system effects were reported by those children who inhaled lower dose of HPXe (1/12 of TLC). While all children receiving larger dose of HPXe (1/6 of TLC) reported some degree of tingling, dizziness, and euphoria, all deemed mild and consistent with the expected effects of Xe inhalations; all side effects resolved spontaneously within 30 s after breathing room air for 2 min.

Four adverse events were reported, none determined to be related to the study: on day 1 after the study, one control subject ate his/her food too quickly and vomited, but the child had reported history of such behavior; on day 30 there were reported a cough from one of the CF subjects, influenza B from another CF subject, and an upper respiratory tract infection from yet another CF subject.

All these studies indicate that Xe is a well-tolerated and safe contrast agent for pulmonary structural and functional imaging. This is even more important for pediatric patients, as there are very limited options for noninvasive, radiation-free imaging for children.

References

Abdeen N, Cross A, Cron G, White S, Rand T, Miller D, Santyr G (2006) Measurement of xenon diffusing capacity in the rat lung by hyperpolarized 129Xe MRI and dynamic spectroscopy in a single breath-hold. Magn Reson Med 56(2):255–264. doi:10.1002/mrm.20943

American Lung Association (2010) Chronic obstructive pulmonary disease COPD. ALA, Washington, DC, pp 1–6. http://action.lung.org/site/DocServer/state-of-lung-disease-in-diverse-communities-2010.pdf?docID=8744

Bauman G, Puderbach M, Deimling M, Chefdhotel C, Schad L, Kauczor H-U, Geiger B, Jellus V, Dinkel J, Hintze C (2009) Functional MRI of the lung by means of Fourier decomposition. Abstract:1-1

Bode FR, Dosman J, Martin RR, Ghezzo H, Macklem PT (1976) Age and sex differences in lung elasticity, and in closing capacity in nonsmokers. J Appl Physiol 41(2):129–135

Butler JP, Mair RW, Hoffmann D, Hrovat MI, Rogers RA, Topulos GP, Walsworth RL, Patz S (2002) Measuring surface-area-to-volume ratios in soft porous materials using laser-polarized xenon interphase exchange nuclear magnetic resonance. J Phys Condens Matter 14(13):L297–L304

Chang YV (2013) MOXE: a model of gas exchange for hyperpolarized 129Xe magnetic resonance of the lung. Magn Reson Med 69(3):884–890. doi:10.1002/mrm.24304

Chang YV, Quirk JD, Ruset IC, Atkinson JJ, Hersman FW, Woods JC (2014) Quantification of human lung structure and physiology using hyperpolarized 129Xe. Magn Reson Med 71(1):339–344. doi:10.1002/mrm.24992

Cleveland ZI, Cofer GP, Metz G, Beaver D, Nouls J, Kaushik SS, Kraft M, Wolber J, Kelly KT, McAdams HP, Driehuys B (2010) Hyperpolarized 129 Xe MR imaging of alveolar gas uptake in humans. PLoS One 5(8):e12192. doi:10.1371/journal.pone.0012192

Coxson H, Rogers R, Whittall K, D'yachkova Y, Pare P, Sciurba F, Hogg J (1999) A quantification of the lung surface area in emphysema using computed tomography. Am J Respir Crit Care Med 159(3):851–856

Deimling M, Jellus V, Geiger B, Chefdhotel C (2008) Time resolved lung ventilation imaging by Fourier decomposition. Intl Soc Mag Reson Med 16:2639

Deninger A, Eberle B, Ebert M, Grossmann T, Heil W, Kauczor H, Lauer L, Markstaller K, Otten E, Schmiedeskamp J, Schreiber W, Surkau R, Thelen M, Weiler N (1999) Quantification of regional intrapulmonary oxygen partial pressure evolution during apnea by (3)He MRI. J Mag Reson 141(2):207–216. doi:10.1006/jmre.1999.1902S109078079991902X. [pii]

Deninger A, Eberle B, Ebert M, Grossmann T, Hanisch G, Heil W, Kauczor H, Markstaller K, Otten E, Schreiber W, Surkau R, Weiler N (2000) (3)he-MRI-based measurements of intrapulmonary p(O2) and its time course during apnea in healthy volunteers: first results, reproducibility, and technical limitations. NMR Biomed 13(4):194–201. doi:10.1002/1099-1492(200006)13:4<194::AID-NBM643>3.0.CO;2-D. [pii]

Deninger AJ, Månsson S, Petersson JS, Pettersson G, Magnusson P, Svensson J, Fridlund B, Hansson G, Erjefeldt I, Wollmer P, Golman K (2002) Quantitative measurement of regional lung ventilation using 3He MRI. Magn Reson Med 48(2):223–232. doi:10.1002/mrm.10206

Detre JA, Zhang W, Roberts DA, Silva AC, Williams DS, Grandis DJ, Koretsky AP, Leigh JS (1994) Tissue specific perfusion imaging using arterial spin labeling. NMR Biomed 7(1–2):75–82

Driehuys B, Cofer G, Pollaro J, Mackel J, Hedlund L, Johnson G (2006) Imaging alveolar-capillary gas transfer using hyperpolarized 129Xe MRI. Proc Natl Acad Sci U S A 103(48):18278–18283. doi:10.1073/pnas.0608458103. [pii] 0608458103

Driehuys B, Driehuys B, Martinez-Jimenez S, Martinez-Jimenez S, Cleveland ZI, Cleveland ZI, Metz GM, Metz

GM, Beaver DM, Beaver DM, Nouls JC, Nouls JC, Kaushik SS, Kaushik SS, Firszt R, Firszt R, Willis C, Willis C, Kelly KT, Kelly KT, Wolber J, Kraft M, McAdams HP (2012) Chronic obstructive pulmonary disease: safety and tolerability of hyperpolarized 129Xe MR imaging in healthy volunteers and patients. Radiology 262(1):279–289. doi:10.1148/radiol.11102172

Ebner L, He M, Virgincar RS, Heacock T, Kaushik SS, Freemann MS, McAdams HP, Kraft M, Driehuys B (2017) Hyperpolarized 129Xenon magnetic resonance imaging to quantify regional ventilation differences in mild to moderate asthma. Investig Radiol 52(2):120–127. doi:10.1097/RLI.0000000000000322

Edelman R, Hatabu H, Tadamura E, Li W, Prasad P (1996) Noninvasive assessment of regional ventilation in the human lung using oxygen-enhanced magnetic resonance imaging. Nat Med 2(11):1236–1239

Hatabu H, Tadamura E, Chen Q, Stock KW, Li W, Prasad PV, Edelman RR (2001) Pulmonary ventilation: dynamic MRI with inhalation of molecular oxygen. Eur J Radiol 37(3):172–178

Hogg J, Coxson H, Brumwell M, Beyers N, Doerschuk C, MacNee W, Wiggs B (1994) Erythrocyte and poly-morphonuclear cell transit time and concentration in human pulmonary capillaries. J Appl Physiol 77(4):1795–1800

Hopkins SR, Prisk GK (2010) Lung perfusion measured using magnetic resonance imaging: new tools for physiological insights into the pulmonary circulation. J Magn Reson Imaging 32(6):1287–1301. doi:10.1002/jmri.22378

Jakob P, Wang T, Schultz G, Hebestreit H, Hebestreit A, Hahn D (2004) Assessment of human pulmonary function using oxygen-enhanced T1 imaging in patients with cystic fibrosis. Magn Reson Med 51(5):1009–1016

Jameson CJ, Jameson AK, Hwang JK (1988) Nuclear spin relaxation by intermolecular magnetic dipole coupling in the gas phase. 129 Xe in oxygen. J Chem Phys 89(7):4074

Kaushik SS, Freeman MS, Cleveland ZI, Davies J, Stiles J, Virgincar RS, Robertson SH, He M, Kelly KT, Foster WM (2013) Probing the regional distribution of pulmonary gas exchange through single-breath gas- and dissolved-phase 129Xe MR imaging. J Appl Physiol 115(6):850–860

Kaushik SS, Freeman MS, Yoon SW, Liljeroth MG, Stiles JV, Roos JE, Michael Foster WS, Rackley CR, McAdams HP, Driehuys B (2014) Measuring diffusion limitation with a perfusion-limited gas—hyperpolarized 129Xe gas-transfer spectroscopy in patients with idiopathic pulmonary fibrosis. J Appl Physiol 117(6):577–585. doi:10.1152/japplphysiol.00326.2014

Kuethe DO, Adolphi NL, Fukushima E (2007) Short data-acquisition times improve projection images of lung tissue. Magn Reson Med 57(6):1058–1064. doi:10.1002/mrm.21230

Lutey BA, Lefrak SS, Woods JC, Tanoli T, Quirk JD, Bashir A, Yablonskiy DA, Conradi MS, Bartel ST, Pilgram TK, Cooper JD, Gierada DS (2008) Hyperpolarized 3He MR imaging: physiologic monitoring observations and safety considerations in 100 consecutive subjects. Radiology 248(2):655–661. doi:10.1148/radiol.2482071838

Mai VM, Bankier AA, Prasad PV, Li W, Storey P, Edelman RR, Chen Q (2001) MR ventilation-perfusion imaging of human lung using oxygen-enhanced and arterial spin labeling techniques. J Magn Reson Imaging 14(5):574–579

Månsson S, Wolber J, Driehuys B, Wollmer P, Golman K (2003) Characterization of diffusing capacity and perfusion of the rat lung in a lipopolysaccaride disease model using hyperpolarized 129Xe. Magn Reson Med 50(6):1170–1179. doi:10.1002/mrm.10649

Marshall H, Parra-Robles J, Deppe MH, Lipson DA, Lawson R, Wild JM (2013) 3He pO₂ mapping is limited by delayed-ventilation and diffusion in chronic obstructive pulmonary disease. Magn Reson Med 71(3):1172–1178. doi:10.1002/mrm.24779

Miller GW, Mugler JP, Altes TA, Cai J, Mata JF, De Lange EE, Tobias WA, Cates GD, Brookeman JR (2010) A short-breath-hold technique for lung pO₂ mapping with 3He MRI. Magn Reson Med 63(1):127–136. doi:10.1002/mrm.22181

Mugler JP, Altes TA, Ruset IC, Dregely IM, Mata JF, Miller GW, Ketel S, Ketel J, Hersman FW, Ruppert K (2010) Simultaneous magnetic resonance imaging of ventilation distribution and gas uptake in the human lung using hyperpolarized xenon-129. Proc Natl Acad Sci 107(50):21707–21712. doi:10.1073/pnas.1011912107

Muradyan I, Loring S, Ferrigno M, Lindholm P, Topulos G, Patz S, Butler J (2010) Inhalation heterogeneity from subresidual volumes in elite divers. J Appl Physiol (1985) 109(6):1969

Muradyan I, Butler JP, Dabaghyan M, Hrovat M, Dregely I, Ruset I, Topulos GP, Frederick E, Hatabu H, Hersman WF, Patz S (2012) Single-breath xenon polarization transfer contrast (SB-XTC): implementation and initial results in healthy humans. J Magn Reson Imaging 37(2):457–470. doi:10.1002/jmri.23823

Nikolaou P, Coffey AM, Walkup LL, Gust BM, Whiting N, Newton H, Barcus S, Muradyan I, Dabaghyan M, Moroz GD, Rosen MS, Patz S, Barlow MJ, Chekmenev EY, Goodson BM (2013) Near-unity nuclear polarization with an open-source 129Xe hyperpolarizer for NMR and MRI. Proc Natl Acad Sci 110(35):14150–14155. doi:10.1073/pnas.1306586110

Nikolaou P, Coffey AM, Walkup LL, Gust BM, Whiting N, Newton H, Muradyan I, Dabaghyan M, Ranta K, Moroz GD, Rosen MS, Patz S, Barlow MJ, Chekmenev EY, Goodson BM (2014) XeNA: an automated 'open-source'; (129)Xe hyperpolarizer for clinical use. Magn Reson Imaging 32(5):541–550. doi:10.1016/j.mri.2014.02.002

Ouriadov A, Farag A, Kirby M, McCormack DG, Parraga G, Santyr GE (2014) Pulmonary hyperpolarized 129Xe morphometry for mapping xenon gas concentrations and alveolar oxygen partial pressure:

proof-of-concept demonstration in healthy and COPD subjects. Mag Reson Med. doi:10.1002/mrm.25550

Patz S, Hersman FW, Muradyan I, Hrovat MI, Ruset IC, Ketel S, Jacobson F, Topulos GP, Hatabu H, Butler JP (2007) Hyperpolarized (129)Xe MRI: a viable functional lung imaging modality? Eur J Radiol 64(3):335–344. doi:10.1016/j.ejrad.2007.08.008

Patz S, Muradyan I, Hrovat MI, Ruset IC, Topulos G, Covrig SD, Frederick E, Hatabu H, Hersman FW, Butler JP (2008) Human pulmonary imaging and spectroscopy with hyperpolarized 129Xe at 0.2T. Acad Radiol 15(6):713–727. doi:10.1016/j.acra.2008.01.008

Patz S, Muradyan I, Hrovat M, Dabaghyan M, Washko G, Hatabu H, Butler J (2011) Diffusion of hyperpolarized 129Xe in the lung: a simplified model of 129Xe septal uptake and experimental results. New J Phys 13:015009

Qing K, Mugler JP III, Altes TA, Jiang Y, Mata JF, Miller GW, Ruset IC, Hersman FW, Ruppert K (2014a) Assessment of lung function in asthma and COPD using hyperpolarized 129Xe chemical shift saturation recovery spectroscopy and dissolved-phase MRI. NMR Biomed 27(12):1490–1501. doi:10.1002/nbm.3179

Qing K, Ruppert K, Jiang Y, Mata JF, Miller GW, Shim YM, Wang C, Ruset IC, Hersman FW, Altes TA, Mugler JP (2014b) Regional mapping of gas uptake by blood and tissue in the human lung using hyperpolarized xenon-129 MRI. J Magn Reson Imaging 39(2):346–359. doi:10.1002/jmri.24181

Rahn F (1964) Handbook of physiology: respiration, vol 1. Williams and Wilkins, Baltimore

Ruppert K, Brookeman JR, Hagspiel KD, Mugler JP (2000) Probing lung physiology with xenon polarization transfer contrast (XTC). Magn Reson Med 44(3):349–357

Ruppert K, Mata JF, Brookeman JR, Hagspiel KD, Mugler JP (2004) Exploring lung function with hyperpolarized (129)Xe nuclear magnetic resonance. Magn Reson Med 51(4):676–687. doi:10.1002/mrm.10736

Saam B, Happer W, Middleton H (1995) Nuclear relaxation of 3He in the presence of O2. Phys Rev A 52(1):862–865

Shukla Y, Wheatley A, Kirby M, Svenningsen S, Farag A, Santyr GE, Paterson NAM, McCormack DG, Parraga G (2012) Hyperpolarized [129]Xe magnetic resonance imaging: tolerability in healthy volunteers and subjects with pulmonary disease. Acad Radiol 19:941–951. doi:10.1016/j.acra.2012.03.018

Stewart NJ, Leung G, Norquay G, Marshall H, Parra-Robles J, Murphy PS, Schulte RF, Elliot C, Condliffe R, Griffiths PD, Kiely DG, Whyte MK, Wolber J, Wild JM (2014) Experimental validation of the hyperpolarized 129Xe chemical shift saturation recovery technique in healthy volunteers and subjects with interstitial lung disease. Magn Reson Med 74(1):196–207. doi:10.1002/mrm.25400

Stewart NJ, Horn FC, Norquay G, Collier GJ, Yates DP, Lawson R, Marshall H, Wild JM (2016) Reproducibility of quantitative indices of lung function and microstructure from [129]Xe chemical shift saturation recovery (CSSR) MR spectroscopy. Magn Reson Med:1–7. doi:10.1002/mrm.26310

Thomen RP, Walkup LL, Roach DJ, Cleveland ZI, Clancy JP, Woods JC (2016) Hyperpolarized [129]Xe for investigation of mild cystic fibrosis lung disease in pediatric patients. J Cyst Fibros:1–8. doi:10.1016/j.jcf.2016.07.008

Virgincar RS, Cleveland ZI, Sivaram Kaushik S, Freeman MS, Nouls J, Cofer GP, Martinez-Jimenez S, He M, Kraft M, Wolber J, Page McAdams H, Driehuys B (2012) Quantitative analysis of hyperpolarized [129]Xe ventilation imaging in healthy volunteers and subjects with chronic obstructive pulmonary disease. NMR Biomed 26(4):424–435. doi:10.1002/nbm.2880

Walkup LL, Thomen RP, Akinyi TG, Watters E, Ruppert K, Clancy JP, Woods JC, Cleveland ZI (2016) Feasibility, tolerability and safety of pediatric hyperpolarized [129]Xe magnetic resonance imaging in healthy volunteers and children with cystic fibrosis. Pediatr Radiol:1–12. doi:10.1007/s00247-016-3672-1

Weibel ER (1984) The pathway for oxygen. Harvard University Press, Cambridge, MA

Wild J, Fichele S, Woodhouse N, Paley M, Kasuboski L, van Beek E (2005) 3D volume-localized pO2 measurement in the human lung with 3He MRI. Magn Reson Med 53(5):1055–1064. doi:10.1002/mrm.20423

Yu J, Rajaei S, Ishii M, Law M, Emami K, Woodburn J, Kadlecek S, Vahdat V, Rizi R (2008) Measurement of pulmonary partial pressure of oxygen and oxygen depletion rate with hyperpolarized helium-3 MRI: a preliminary reproducibility study on pig model. Acad Radiol 15(6):702–712. doi:10.1016/j.acra.2008.01.024. [pii] S1076-6332(08)00088-3

Yu J, Law M, Kadlecek S, Emami K, Ishii M, Stephen M, Woodburn JM, Vahdat V, Rizi RR (2009) Simultaneous measurement of pulmonary partial pressure of oxygen and apparent diffusion coefficient by hyperpolarized 3He MRI. Magn Reson Med 61(5):1015–1021. doi:10.1002/mrm.21854

Fluorinated-Gas MRI

Marcel Gutberlet and Jens Vogel-Claussen

Contents

Key Points

Fluorinated-gas MRI for ventilation imaging is an alternative approach to hyperpolarized-gas MRI using ³He or ¹²⁹Xe, which may have the potential to be translated into clinical routine in the future. Although in general the contrast-to-noise ratio is less in fluorinated-gas MRI than that achieved with hyperpolarized gases, fluorinated-gas MRI has the advantage of comparatively simple technical requirements: An MRI system with multinuclear imaging capabilities and a dedicated fluorine-19 (¹⁹F) MRI coil is required. Manufactured fluorinated gases do not need a complex preparatory treatment on site before their use in patients and their signal-enhancing capabilities do not show a rapid decay. This makes their application less demanding for the local infrastructure and also reduces costs. These gases have not been approved as contrast agents for routine clinical ventilation MR imaging in most countries yet, which is the only major drawback to date.

M. Gutberlet • J. Vogel-Claussen (✉)
Hannover Medical School, Institute of Diagnostic and Interventional Radiology, Carl-Neuberg Str. 1, Hannover 30625, Germany

Biomedical Research in Endstage and Obstructive Lung Disease Hannover (BREATH), Hannover, Germany
e-mail: Vogel-claussen.jens@mh-hannover.de

1   Introduction

Already in the early stages of clinical MRI, the potential application of fluorinated-gas tracers for visualization of lung ventilation was recognized, when Rinck et al. performed ¹⁹F gas MRI in dogs in 1984 (Rinck et al. 1984a, b). However, it took until the late 1990s when fluorinated-gas

tracers regained interest in the MR community. First, the feasibility and several methods of ^{19}F MRI were shown in animal and ex vivo studies. Signal-to-noise ratio (SNR) improvements were achieved by hardware and pulse sequence optimization using different fluorinated gases. After first human use in 2008 by Wolf et al. (Wolf et al. 2008), ^{19}F MRI has been performed in COPD, asthma, CF, and lung transplant patients (Couch et al. 2013; Halaweish et al. 2013; Soher et al. 2015; Gutberlet et al. 2016).

2   Principle of ^{19}F MRI of Fluorinated Gases

2.1   Fluorinated Gases

^{19}F is the only isotope of fluorine naturally occurring in abundance. Due to the high gyromagnetic ratio and short relaxation times of fluorinated gases, it is well suited for MRI applications. Negligible endogenous fluorine in the human body facilitates reliable application of ^{19}F contrast media without any notable interfering back-ground signal. Lung MRI can be performed with different fluorinated gases like sulfur hexafluoride (SF_6), hexafluoroethane (C_2F_6), tetrafluoromethane (CF_4), octafluoropropane or perfluoropropane (C_3F_8), and octafluorobutane (C_4F_8) (Table 1). All these gases are nontoxic and chemically inert and have a low solubility in water and blood. Therefore, they have no systemic side effects and only visualize the respiratory tract. However, these gases have significantly higher molecular weight than air, which, however, has insufficient magnetic properties for MR imaging. Molecular weight and viscosity influence the spatiotemporal distribution of different fluorinated gases in the lung and have to be considered for regional lung ventilation imaging with fluorinated gases.

Fluorinated gases are extremely potent greenhouse gases (Nations 1998); thus recycling of the gases has to be discussed if it is upscaled for clinical routine use. SF_6 (Sonovue®) and C_3F_8 (Optison®) are already in medical use as ultrasound agents (Lindner 2004). SF_6 is also routinely used in multiple inert gas washout tests (Wagner 2012; Stahl et al. 2016).

Table 1 Properties of gases relevant for pulmonary MRI
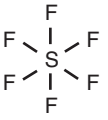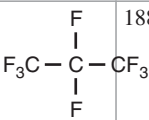
Gas	Chemical structure	Molecular weight	Density (kg/m³) @ 288 K, 1.013 bar	Viscosity (µPa s) @ 273 K	Solubility in water (mg/L) @ 288 K, 1.013 bar	Larmor frequency (MHz) @ 1.5 T	T_1 (ms) @ 1.5 T, 293 K	Self-diffusion coefficient (cm²/s) @ 288 K, 1.013 bar
SF_6	F, F, F, S, F, F, F	146.1	6.27	14.2	41	59.8103	1.8	0.033 (Ruiz-Cabello et al. 2005)
CF_4	F—C—F, F, F	88.0	3.72	16.1	20	59.8031	1.9	N.a.
C_2F_6	F_3C—CF_3	138.0	5.83	13.6	N.a.	59.8017	7.8	0.033 (Chang and Conradi 2006)
C_3F_8	F_3C—C—CF_3, F, F	188.0	8.17	12.5	5.7	59.8906 (Couch et al. 2014) 59.8877	18.0 (Chang and Conradi 2006)	0.023 (Chang and Conradi 2006)

Table 1 (continued)

Gas	Chemical structure	Molecular weight	Density (kg/m³) @ 288 K, 1.013 bar	Viscosity (µPa s) @ 273 K	Solubility in water (mg/L) @ 288 K, 1.013 bar	Larmor frequency (MHz) @ 1.5 T	T_1 (ms) @ 1.5 T, 293 K	Self-diffusion coefficient (cm²/s) @ 288 K, 1.013 bar
C_4F_8	F_2C-CF_2 | | F_2C-CF_2	200.0	8.82	10.9	140	59.8988	47.0	N.a.
^{3}He		3.0	0.13	20.0	1.2	48.6509		1.8 (Salerno et al. 2001)
^{129}Xe		129.0	5.90	23.2	755	17.6655		0.06 (Salerno et al. 2001)
N_2		28.0	1.19	16.6	20			
O_2		32.0	1.35	19.1	39			
CO_2		44.0	1.87	13.7	2000			

2.2 SNR Considerations

Because of the lower spin density and increased diffusivity, intrapulmonary gas tracers provide three orders of magnitude lower MR signal when compared to that of solid tissue or fluids. At 1.5 T, the fluorinated gases used in lung MRI have a short longitudinal relaxation time T_1 ranging from a few milliseconds for SF_6 (1.7 ms) up to 42 ms for C_4F_8 at atmospheric pressure and room temperature (Table 1) (Chang and Conradi 2006; Conradi et al. 2006).

The SNR of gas MRI can be optimized by significantly enhancing the level of nuclear polarization (i.e., hyperpolarized ^{3}He or ^{129}Xe), or alternatively by using extensive spatial and temporal signal averaging. For example, increasing typical voxel dimensions of proton MRI ($1 \times 1 \times 5$ mm³) to acceptable voxel dimensions for intrapulmonary gas MRI ($5 \times 5 \times 20$ mm³) results in an SNR improvement of $5 \times 5 \times 4 = 100$ times if all other imaging parameters are kept fixed.

Additionally, due to the short T_1 time of fluorinated gases the signal recovers very fast after radio frequency (RF) excitation and therefore facilitates signal acquisition at very short repetition times T_R compared to typical proton MRI. Comparing the T_1 of ^{19}F atoms in SF_6 (1.6 ms) with T_1 of protons in blood (1400 ms) shows that T_R could in theory be reduced by a factor of 1400 ms/1.6 ms = 875 without losing signal intensity from saturation of the magnetization due to excessive radio frequency pulsing. Accordingly, the faster data acquisition can be used for signal averaging (SNR improvement by a factor of $\sqrt{875} \approx 30$).

The combination of increasing voxel dimensions and signal averaging due to shorter T_R is sufficient to obtain reasonable SNR from intrapulmonary fluorinated gases: the total SNR improvement at scan times similar to that required for ^{1}H MRI of blood can be more than a factor of $100 \times 30 = 3000$. This is sufficient to compensate for the three orders of magnitude lower spin density of gases when compared with that of solid tissue or fluids.

The T_1 relaxation time determines not only the optimum T_R but also the required echo time and, hence, imaging bandwidth. Shorter T_R allows more efficient signal averaging and reduces the possible T_E but also increases the minimal imaging bandwidth and correspondingly decreases the readout time per echo. Adequate sequence parameters for optimal SNR depend on the T_1 and T_2 relaxation times of the fluorinated gas. For gases with T_1/T_2 of about 1 ms like CF_4 or SF_6, it is more SNR efficient to shorten T_E in order to

reduce signal loss by T_2 relaxation than decreasing imaging bandwidth to increase the readout period. Contrarily, because of the slower signal decay for gases with T_1/T_2 of several milliseconds such as C_2F_6, C_3F_8, and C_4F_8, better SNR is obtained at lower bandwidth and higher T_E.

Additionally, the different fluorinated gases contain multiple ^{19}F atoms per gas molecule and thus per mol/L as opposed to purely ^{19}F gas, which therefore increases the SNR. Exclusively, C_3F_8 resonates at two different frequencies separated by about 48 ppm (Couch et al. 2014) (Table 1). However, no systematic study comparing the SNR of the different fluorinated-gas tracers has been published so far. For fluorinated gases with short T_1, the short T_E required for optimal SNR may be demanding for MR systems. Therefore, gases with longer T_1 might be favored for application in pulmonary MRI on a broader scale.

Different pulse sequence types have been tested for optimal SNR of ^{19}F gas MRI. Since T_2 / T_2^* of ^{19}F intrapulmonary gas tracers is relatively short, different methods to shorten T_E were tested such as asymmetric echoes, ultrashort echo time (UTE) imaging, and non-slice selective excitation with 2D projection of a 3D volume (Schreiber et al. 2000, 2001; Couch et al. 2013; Ouriadov et al. 2015; Tibiletti et al. 2016). In ex vivo imaging, Conradi et al. found that spin-echo imaging is superior to gradient echo imaging due to dephasing effects across large voxels (Conradi et al. 2006). However,

the use of spin-echo imaging in human subjects may exceed the maximum specific absorption rate (SAR) limit. Further SNR improvements may be achieved at higher field strengths, which has not been studied systematically yet.

^{19}F MRI requires dedicated transmit and receive coils, which have to be optimized for the low SNR and for a large FOV due to the size of the lung. While in transmission mode a large coil delivers a more homogeneous B_1 field, in receive mode a close-fitting coil provides a better SNR. Corresponding to the fact that the main challenge of ^{19}F gas MRI is the low SNR, using close-fitting flexible vestlike transmit/receive coils in ^{19}F gas MRI significantly improved image quality compared to typically used birdcage coils (Couch et al. 2013). Combination of a birdcage transmit coil and a separate surface receive coil could additionally improve image quality of ^{19}F gas MRI (Fig. 1) (Charles et al. 2015b). Diagnostic lung MRI requires both ^{19}F gas MRI for visualization of regional lung ventilation and ^1H MRI for morphologic and additional functional lung imaging. The close resonance frequencies of ^{19}F and ^1H give the opportunity to use ^{19}F coils in off-resonance mode or for human scanners to use the integrated ^1H body coil but of course at slightly lower image quality. Due to the close resonance frequencies of ^{19}F and ^1H, design of dual-tuned coils is complex but technically feasible (Maunder et al. 2016).

Fig. 1 Custom-built transmit birdcage coil and 16-channel phased-array receive coil for ^{19}F MRI at 1.5 T at Hannover Medical School

Table 2 Parameters of pulmonary MRI using different gas tracers (modified from Ebner et al. (2017))

	^{3}He	^{129}Xe	^{19}F
Costs	Very high	High	Average
Supply	Low	Good	Good
Polarization	30–40%	10–40%	5 ppm (@1.5 T)
Volume required (L)	0.25–1.0	0.25–1.0	1.0–25
Scan length (s)	5–10	5–10	5–20
Breath hold	+	+	+/Free breathing
Nominal resolution (mm^3)	$3 \times 3 \times 10$	$3 \times 3 \times 10$	$6 \times 6 \times 15$
Ventilation	+	+	+
Lung parenchyma	−	+	−
Blood	−	+	−
Gas exchange	−	+	−
Microstructure	+	+	+
Perfusion	−	+	−

Because of high costs for ^{3}He, low throughput of approximately 1–2 L/h of hyperpolarized gas with current hyperpolarizers, and considering the anesthetic effect of xenon at higher dosages, pulmonary hyperpolarized-gas MRI is typically applied with about a maximum of 1 L of gas in a single breath hold depending on body size (Table 2). Another advantage is that paramagnetic oxygen results in substantial decay of polarization and subsequent signal loss in pulmonary hyperpolarized-gas MRI (Saam et al. 1995), and fluorinated gases can be mixed with oxygen without any remarkable signal loss. Therefore, ^{19}F gas MRI can be performed over several minutes while continuously breathing a normoxic gas mixture of fluorinated gas, allowing for dynamic studies of ventilation.

A comprehensive review of pulmonary gas MRI describing the properties, applications but also drawbacks of hyperpolarized-gas tracers and thermally polarized fluorinated gases can be found in several articles (Halaweish et al. 2013; Wolters et al. 2013; Couch et al. 2014; Kruger et al. 2016; Ebner et al. 2017).

3 Applications of Fluorinated-Gas Imaging

First studies of ^{19}F gas MRI were performed in animals and in ex vivo settings. In addition to static gas imaging, different methods of ^{19}F gas MRI were developed providing quantitative parameters, which may serve as new biomarkers of regional lung ventilation. ^{19}F gas MRI has been shown to be feasible and safe in humans and its first applications in different lung pathologies show promise to add new diagnostic value in mapping of regional lung ventilation.

3.1 Static Imaging

In 1998, static ^{19}F gas imaging of rat lungs at 1.9 T while breathing continuously normoxic C_2F_6 gas tracer resulted in a mean SNR of 8 with an acquisition time of more than 4 h (Kuethe et al. 1998). After pulse sequence and hardware optimization the required acquisition time for sufficient SNR could be significantly reduced which is essential for human use. Schreiber et al. obtained 3D images of the whole lung in a breath hold of 49 s in a pig by using RF pulses with short duration (e.g., non-slice selective hard pulses with 3D readout of the whole lung) and using asymmetric readouts to shorten the T_E (Schreiber et al. 2000, 2001).

The SNR could be improved by a factor of two when imaging in breath hold after continuous breathing of 5 L of normoxic C_3F_8 compared to a single breath of 1 L of the gas mixture (Couch et al. 2013). This indicates that the gas does not instantaneously diffuse into the peripheral lung parenchyma and equilibrium gas

concentration forms only after several breaths of the gas mixture. Charles et al. reduced the required scan time for static 3D MRI of the ^{19}F gas-filled lung to a 6-s breath hold at sufficient SNR by using dedicated hardware and parallel imaging, i.e., a Helmholtz transmit coil and a separate surface multichannel receive coil instead of a combined transmit and receive volume coil (Charles et al. 2015b).

3.2 Dynamic Imaging

Quantitative evaluation of regional lung ventilation by using static intrapulmonary gas MRI may be challenging. Typically, using image segmentation, quantitative parameters like ventilated volume (VV), ventilation defect volume (VDV), and ventilation defect percentage (VDP) can be derived (Kirby et al. 2012). However, the gas signal may be affected by B_1-field inhomogeneity and by the receiver sensitivity if additional surface receive coils are used.

When changing from breathing room air or pure oxygen to breathing continuously a normoxic fluorinated gas mixture, an equilibrium gas concentration forms after several breaths. The time constant for this wash-in phase allows for quantification of regional lung ventilation. Correspondingly, the washout time can be measured when switching from breathing fluorinated gas to room air or pure oxygen. Thus extending results from static imaging (basically dichotomous readout, ventilated vs. non-ventilated lung), regional lung ventilation can be quantified by the wash-in/washout time in units of seconds or by the number of breathing cycles or by fractional ventilation (Gutberlet et al. 2016).

First, Schreiber et al. measured wash-in and washout times of SF_6 in a machine-ventilated pig with sufficient temporal resolution of 9.1 s using non-slice selective excitation without spatial encoding in slice direction resulting in a 2D projection of the 3D lung volume (Schreiber et al. 2000, 2001). Wolf et al. could achieve a temporal resolution of less than 1 s by using C_2F_6 instead and by optimizing the acquisition bandwidth (Wolf et al. 2006). Using this technique, high-frequency oscillatory ventilation, which potentially improves conventional ventilation, was visualized (Wolf et al. 2010). Using dynamic ^{19}F gas MRI in rats, Ouriadov et al. found washout constants comparable to ^{3}He and ^{129}Xe MRI (Ouriadov et al. 2015). In a rat model of fibrosis and inflammation, fractional ventilation derived by dynamic fluorinated-gas MRI was reduced compared to the control group (Couch et al. 2016). Using parallel imaging and a free breathing washout MRI protocol, Gutberlet et al. reported a strong linear correlation of ^{19}F washout parameters and FEV1 in a cohort of COPD patients (Gutberlet et al. 2016).

3.3 Ventilation/Perfusion (V/Q) Imaging

Kuethe et al. could show that intrapulmonary ^{19}F gas can be used to determine regional V/Q ratio in the lung (Kuethe et al. 2000). The fluorinated gas concentration in the lung depends not only on gas transport, i.e., regional ventilation, but also on the removal of oxygen due to diffusion and perfusion. When a gas mixture of oxygen and fluorinated gas with a high fraction of oxygen is inhaled, the concentration of the fluorinated gas is substantially increased in obstructed alveoli compared to normally ventilated alveoli and therefore ^{19}F gas MRI is sensitive to reduced V/Q ratios in comparison to normal V/Q ratios. Two different techniques using ^{19}F gas to determine V/Q ratios were proposed: (1) ^{19}F gas imaging is performed at high oxygen concentration (e.g., 75% O_2 and 25% fluorinated gas) where the ^{19}F MR signal is very sensitive to changes of V/Q ratios. Additionally, at a low oxygen concentration and correspondingly high fluorinated gas concentration (e.g., 21% O_2 and 79% fluorinated gas), where the ^{19}F MR signal shows nearly no dependency on changes of V/Q ratios, ^{19}F gas MRI is used to normalize for other sources of MR signal variations like B_1 field inhomogeneities (Kuethe et al. 2000). (2) Alternatively, because the T_1 and T_2 relaxation times of fluorinated gases are proportional to its concentration, V/Q ratio was measured with a single ^{19}F gas scan, by measuring T_1 at high oxygen concentration (70%) (Adolphi and Kuethe 2008).

The dependency of the fluorinated gas concentration on V/Q ratios is strong for low values of V/Q (approximately in the range of $0.01 \leq V/Q \leq 1$) and becomes weak for increased ratios of $V/Q > 1$. Therefore, this method is suitable to detect V/Q mismatch due to obstructed ventilation but not due to perfusion defects like pulmonary embolism. The usefulness of this technique to detect lung obstruction was verified in a rat model: Adolphi et al. used inversion recovery imaging to determine T_1 (Adolphi and Kuethe 2008). However, the narrow range of T_1 depending on the ^{19}F gas concentration (SF$_6$: 0.7–1.3 ms; C$_2$F$_6$: 4–8 ms) (Chang and Conradi 2006) is challenging due to sequence timing, limited SAR, and long scan times of about 1 h and requires very accurate determination of the T_1 values.

Terekhov et al. showed the feasibility of T_1 mapping of intrapulmonary ^{19}F gas using the variable flip angle method (Terekhov et al. 2007). Since this method is less SAR intensive and can be performed within 1 min, this seems to be an interesting alternative to inversion recovery imaging to determine regional ^{19}F intrapulmonary gas concentrations.

3.4   Diffusion Imaging

Similar to hyperpolarized-gas imaging, restricted diffusion of fluorinated gas can be measured to probe the lung's microstructure. Two factors complicate the measurement of the apparent diffusion coefficient (ADC) of a fluorinated gas in the lung: (1) Because of the higher molecular weight of fluorinated gases compared with ^{3}He, diffusion is much slower; that is, diffusion gradients need to be stronger and/or longer. (2) The short T_1 and T_2 relaxation times limit the maximum T_E to achieve a reasonable SNR and therefore limit the duration of the diffusion gradients and, thus, the achievable diffusion weighting. Despite these complications, the feasibility to measure the ADC of ^{19}F gases in the lung was shown in several in vivo rat studies and in a study of excised human lungs, respectively (Jacob et al. 2005; Pérez-Sánchez et al. 2005; Ruiz-Cabello

et al. 2005; Conradi et al. 2006; Carrero-González et al. 2013). In the latter study, a reduction of the free diffusivity of C$_2$F$_6$ gas (ADC$_0$ = 0.033 cm^2/s) to 0.018 cm^2/s was found in normal lung tissue, while in emphysematous lungs the diffusivity was almost equal to that of freely diffusing C$_2$F$_6$ gas (0.031 cm^2/s) (Table 1). In elastase-treated rats, serving as a model for lung emphysema, Carrero-Gonzalez et al. found an increased ADC compared to the control group (Carrero-González et al. 2013).

Using a diffusion model, lung microstructure parameters can be derived from intrapulmonary gas diffusion MRI. With the maximum diffusion weighting achievable with the available animal and human MR scanners, surface-to-volume ratio of the lung can be derived with this model. However, this method additionally requires correction of the local free diffusivity, which is proportional to the regional ^{19}F gas concentration (Chang and Conradi 2006). Since the latter is proportional to the T_1 and T_2 time of the fluorinated gas, additional mapping of the relaxation constants, e.g., with the variable flip angle method described above (Terekhov et al. 2007), can be used to determine the gas concentration.

3.5   Clinical Translation

Under conditions of a controlled clinical investigation and with approval of the local ethics committee, Wolf et al. provided the first images in a healthy human volunteer after inspiration of four breaths of a mixture of 78% SF$_6$ gas and 22% oxygen (Wolf et al. 2008). Since the fluorinated gases have significantly higher molecular weight than the respiratory gases, it was unclear how it distributes in the lung and whether inhalation of gas mixtures of fluorinated gases and oxygen may induce hypoxia. Therefore, monitoring of respiration and other physiological parameters like ECG, oxygen saturation, inspiratory/expiratory O$_2$ and CO$_2$ levels (in the mouthpiece/breathing mask), and respiratory frequency is essential to guarantee its safe use in humans (Halaweish and Charles 2014). In our institution, during the whole scan time, a physician supervises the MR

scan, who can switch immediately to pure oxygen in case of hypoxia or patient discomfort. In accordance to the experience by Charles et al. no significant impact of multiple breaths of normoxic C_3F_8 gas mixture on patient condition was found in healthy volunteers and patients with chronic lung disease in our experiments (Charles et al. 2015a).

An MRI conditional apparatus is required for continuous breathing of oxygen/fluorinated gas mixture consisting of gas reservoirs, tubing, valves, filters for multiuse of the apparatus, and monitoring system. Dead space and resistance of the apparatus to airflow while breathing have to be minimized to ensure its safety. Because of the higher molecular weight of the fluorinated gas than room air, the exhaled gas has to be collected in a bag. If ^{19}F gas MRI will be translated to clinical use, recycling of these extremely potent greenhouse gases has to be considered.

First studies of intrapulmonary fluorinated-gas MRI using C_3F_8 have shown its feasibility in human use and provided promising results for its diagnostic value in patients with chronic obstructive lung disease (COPD) (Couch et al. 2013; Halaweish et al. 2013; Gutberlet et al. 2016). Using optimized pulse sequences and hardware, sufficient SNR in the range of 10–30 was obtained both in healthy subjects and in patients with lung diseases such as asthma and COPD and in lung transplant patients

with typical acquisition times of 15 s in breath hold (Halaweish et al. 2013) (Fig. 2). Using a birdcage transmit coil and a separate receive coil, comparable SNR was achieved with a breath hold of about 6 s (Charles et al. 2015b). In a pilot study of 11 healthy nonsmokers, 2 asthmatics, 3 patients after lung transplantation, and 12 COPD patients, visually, the gas distribution over the lung was found to be very homogeneous in healthy subjects. In contrast, in asthmatics and COPD patients the gas seemed to be distributed more heterogeneously and ventilation defects were detected (Halaweish et al. 2013). Comparing ^{19}F gas MRI with hyperpolarized ^{3}He imaging in five healthy volunteers, despite its worse image quality with respect to SNR and spatial resolution, no statistically significant difference in the detection of ventilation defects was found (Couch et al. 2015). Dynamic multi-breath ^{19}F gas MRI of the whole lung in 3D has been shown to be feasible in humans. Charles et al. acquired wash-in and washout of ^{19}F gas in 15-s breath holds alternating to several breaths (Halaweish et al. 2013; Soher et al. 2015) (Fig. 2). Alternatively, using parallel imaging, ^{19}F dynamics were measured in free breathing with a scan time of 2 s per 3D block in healthy volunteers and COPD patients (Gutberlet et al. 2016) (Fig. 3). A significantly delayed wash-in and washout was found in COPD, asthma, and lung transplant patients (Soher et al. 2015; Gutberlet et al. 2016) (Fig. 4).
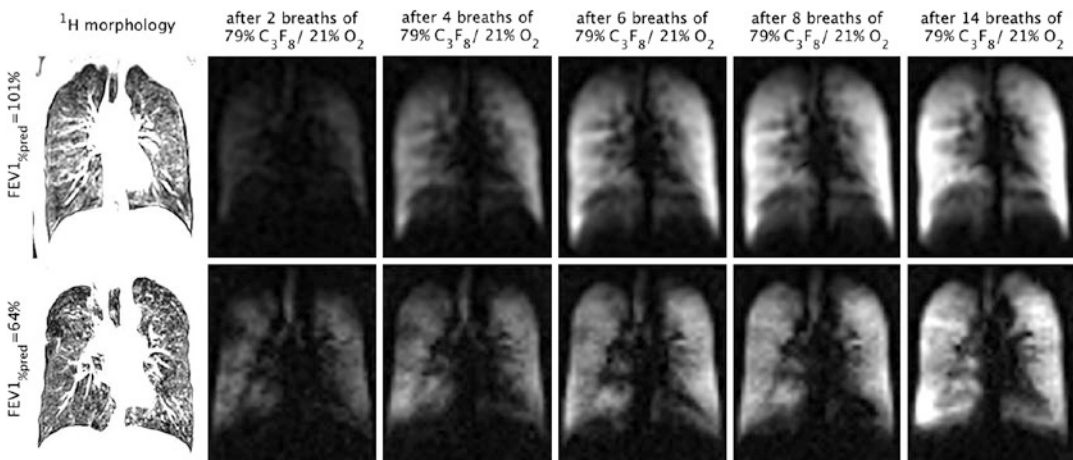
Fig. 2 A healthy volunteer (forced expiratory volume in 1 s in % predicted (FEV1$_{\%pred}$) = 101%) (*first row*) and a COPD patient (FEV1$_{\%pred}$ = 64%) (*second row*) at 1.5 T with morphologic ^{1}H MRI (*first column*) and ^{19}F gas MRI (*second–sixth column*) in 16-s breath holds with a spatial resolution of 7.8 × 7.8 × 20 mm^3 after several breaths of a gas mixture of 79% C_3F_8 and 21% O_2

a

b
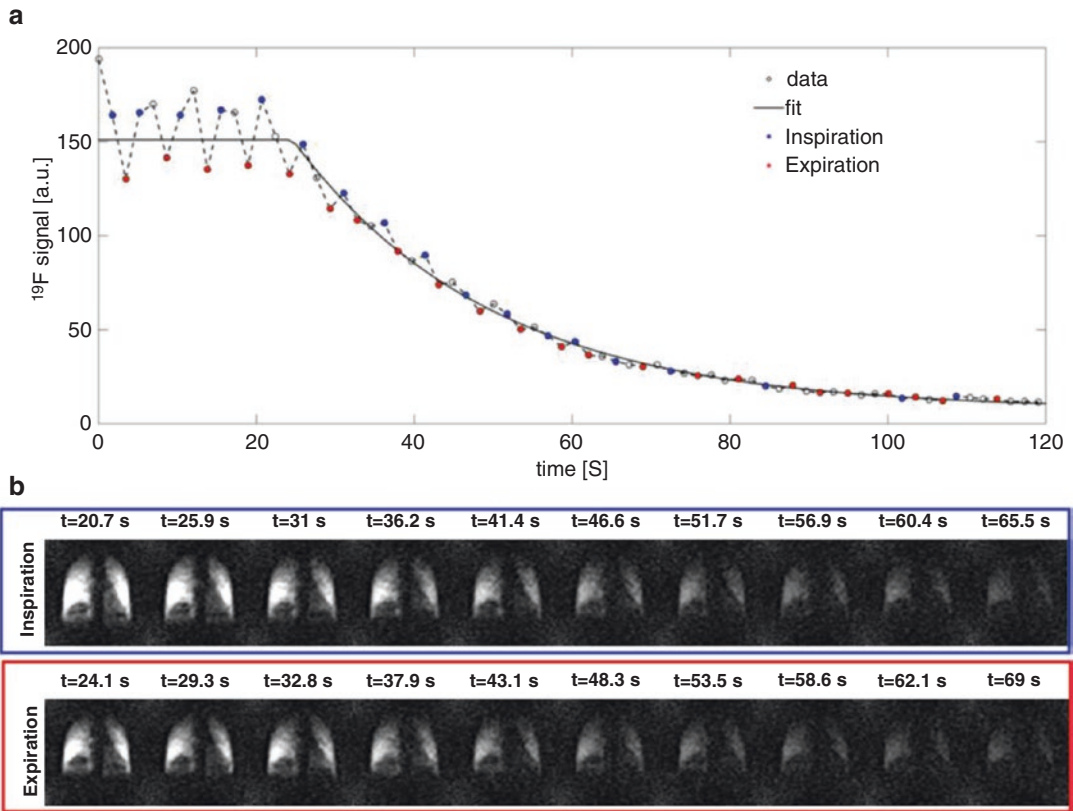
Fig. 3 ^{19}F gas washout MRI in free breathing. The ^{19}F gas signal averaged over a region of interest in the lung (*black dots* in (**a**)) is sorted according to the respiratory phase (*blue* and *red dots* in (**a**)). The corresponding washout dynamics of a healthy volunteer is shown in inspiration and expiration for one exemplary slice of 3D MRI (**b**)
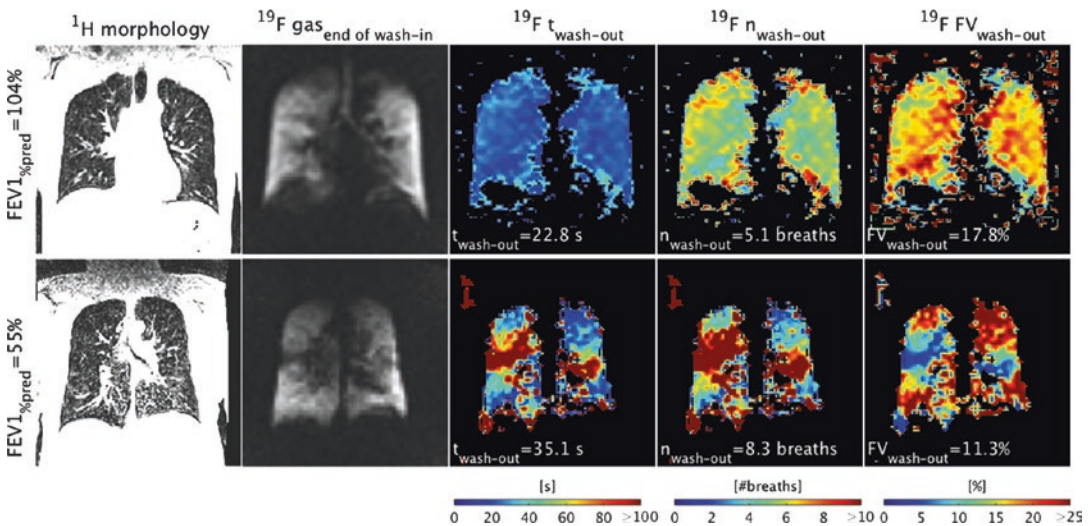
Fig. 4 A healthy volunteer (*first row*) and a COPD patient (*second row*) examined with ^{19}F gas washout MRI in free breathing. Shown is ^{1}H MRI (*first column*), ^{19}F gas MRI directly before starting the ^{19}F gas washout (*second column*), washout time maps in units of seconds ($t_{wash-out}$, *third column*), in number of breaths ($n_{wash-out}$, *fourth column*) and as fractional ventilation (FV$_{wash-out}$, *fifth column*). Median of $t_{wash-out}$, $n_{wash-out}$, and FV$_{wash-out}$ of the whole lung and FEV$_{1pred}$ from spirometry are given

Conclusion

Through recent advances in MRI scanner technology and coil design most of the measurement techniques available with hyperpolarized gases may also become available with fluorinated gases without the need for polarization at comparatively lower cost and with sufficient signal to obtain clinically relevant functional information on regional ventilation dynamics throughout the lung parenchyma. This makes this technique a promising new diagnostic tool in the future for patients with lung disease.

References

Adolphi NL, Kuethe DO (2008) Quantitative mapping of ventilation-perfusion ratios in lungs by 19F MR imaging of T1 of inert fluorinated gases. Magn Reson Med 59:739–746. doi:10.1002/mrm.21579

Carrero-González L, Kaulisch T, Stiller D (2013) In vivo diffusion-weighted MRI using perfluorinated gases: ADC comparison between healthy and elastase-treated rat lungs. Magn Reson Med 70:1761–1764. doi:10.1002/mrm.24627

Chang YV, Conradi MS (2006) Relaxation and diffusion of perfluorocarbon gas mixtures with oxygen for lung MRI. J Magn Reson 181:191–198. doi:10.1016/j.jmr.2006.04.003

Charles C, Moon RE, Macintyre NR, et al (2015a) Cardio-respiratory tolerability of perfluoropropane-enhanced MRI of pulmonary ventilation. In: American Thoracic Society International conference abstracts, pp A3509–A3509

Charles HC, Jones RW, Halaweish AF, Ainslie MD (2015b) Parallel imaging for short breath hold times in perfluorinated gas imaging of the lung. In: Proceedings of International Society for Magnetic Resonance in Medicine, p 3984

Conradi MS, Saam BT, Yablonskiy DA, Woods JC (2006) Hyperpolarized 3He and perfluorocarbon gas diffusion MRI of lungs. Prog Nucl Magn Reson Spectrosc 48:63–83. doi:10.1016/j.pnmrs.2005.12.001

Couch MJ, Ball IK, Li T, et al (2015) Comparing pulmonary MRI using inert fluorinated gases and hyperpolarized 3He: is 19F MRI good enough? In: Proceedings of International Society for Magnetic Resonance in Medicine, p 1501

Couch MJ, Ball IK, Li T et al (2014) Inert fluorinated gas MRI: a new pulmonary imaging modality. NMR Biomed 27:1525–1534. doi:10.1002/nbm.3165

Couch MJ, Ball IK, Li T et al (2013) Pulmonary ultrashort echo time 19F MR imaging with inhaled fluorinated gas mixtures in healthy volunteers: feasibility. Radiology 269:903–909. doi:10.1148/radiol.13130609

Couch MJ, Fox MS, Viel C et al (2016) Fractional ventilation mapping using inert fluorinated gas MRI in rat models of inflammation and fibrosis. NMR Biomed 29:545–552. doi:10.1002/nbm.3493

Ebner L, Kammerman J, Driehuys B et al (2017) The role of hyperpolarized 129xenon in MR imaging of pulmonary function. Eur J Radiol 86:343–352. doi:10.1016/j.ejrad.2016.09.015

Gutberlet M, Kaireit T, Voskrebenzev A, et al (2016) Real-time dynamic fluorinated gas MRI in free breathing for mapping of regional lung ventilation in patients with COPD and healthy volunteers using a 16 channel receive coil at 1.5T. In: Proceedings of International Society for Magnetic Resonance in Medicine, p 1140

Halaweish AF, Charles HC (2014) Physiorack: an integrated MRI safe/conditional, gas delivery, respiratory gating, and subject monitoring solution for structural and functional assessments of pulmonary function. J Magn Reson Imaging 39:735–741. doi:10.1002/jmri.24219

Halaweish AF, Moon RE, Foster WM et al (2013) Perfluoropropane gas as a magnetic resonance lung imaging contrast agent in humans. Chest 144:1300–1310. doi:10.1378/chest.12-2597

Jacob RE, Chang YV, Choong CK et al (2005) 19F MR imaging of ventilation and diffusion in excised lungs. Magn Reson Med 54:577–585. doi:10.1002/mrm.20632

Kirby M, Heydarian M, Svenningsen S et al (2012) Hyperpolarized 3He magnetic resonance functional imaging semiautomated segmentation. Acad Radiol 19:141–152. doi:10.1016/j.acra.2011.10.007

Kruger SJ, Nagle SK, Couch MJ et al (2016) Functional imaging of the lungs with gas agents. J Magn Reson Imaging 43:295–315. doi:10.1002/jmri.25002

Kuethe DO, Caprihan A, Fukushima E, Waggoner RA (1998) Imaging lungs using inert fluorinated gases. Magn Reson Med 39:85–88. doi:10.1002/mrm.1910390114

Kuethe DO, Caprihan A, Gach HM et al (2000) Imaging obstructed ventilation with NMR using inert fluorinated gases. J Appl Physiol 88:2279–2286

Lindner JR (2004) Microbubbles in medical imaging: current applications and future directions. Nat Rev Drug Discov 3:527–532. doi:10.1038/nrd1417

Maunder A, Rao M, Robb F, Wild J (2016) RF coil design for multi-nuclear lung MRI of 19F fluorinated gases and 1H using MEMS. In: Proceedings of International Society for Magnetic Resonance in Medicine, p 3504

Nations U (1998) Kyoto Protocol to the United Nations Framework Convention on Climte Change. http://unfccc.int/resource/docs/convkp/kpeng.pdf. Accessed 21 Mar 2017

Ouriadov AV, Fox MS, Couch MJ et al (2015) In vivo regional ventilation mapping using fluorinated gas MRI with an x-centric FGRE method. Magn Reson Med 74:550–557. doi:10.1002/mrm.25406

Pérez-Sánchez JM, Pérez De Alejo R, Rodríguez I et al (2005) In vivo diffusion weighted 19F MRI using SF6. Magn Reson Med 54:460–463. doi:10.1002/mrm.20569

Rinck PA, Petersen SB, Heidelberger E, et al (1984a) NMR ventilation imaging of the lungs using perfluorinated gases. In: Proceedings of International Society for Magnetic Resonance in Medicine, p 237

Rinck PA, Petersen SB, Lauterbur PC (1984b) NMR-Imaging von fluorhaltigen Substanzen: 19Fluor-Ventilations- und Perfusionsdarstellungen. Fortschr Röntgenstr 140:239–243

Ruiz-Cabello J, Pérez-Sánchez JM, Pérez De Alejo R et al (2005) Diffusion-weighted 19F-MRI of lung periphery: influence of pressure and air-SF6 composition on apparent diffusion coefficients. Respir Physiol Neurobiol 148:43–56. doi:10.1016/j.resp.2005.04.007

Saam B, Happer W, Middleton H (1995) Nuclear relaxation of He3 in the presence of O2. Phys Rev A 52:862–865. doi:10.1103/PhysRevA.52.862

Salerno M, Altes TA, Mugler JP et al (2001) Hyperpolarized noble gas MR imaging of the lung: potential clinical applications. Eur J Radiol 40:33–44

Schreiber WG, Eberle B, Laukemper-Ostendorf S et al (2001) Dynamic 19F-MRI of pulmonary ventilation using sulfur hexafluoride (SF6) gas. Magn Reson Med 45:605–613. doi:10.1002/mrm.1082

Schreiber WG, Markstaller K, Weiler N et al (2000) F-MRT der Lungenventilation in – Atemanhaltetechnik mittels SF -Gas. Fortschr Röntgenstr 172:500–503

Soher BJ, Halaweish AF, Charles HC (2015) Modeling of the spatio-temporal distribution of pulmonary ventilation via perfluoropropane gas enhanced MRI. In: Proceedings of International Society for Magnetic Resonance in Medicine, p 4006

Stahl M, Wielpütz MO, Graeber SY, et al (2016) Comparison of lung clearance index and magnetic resonance imaging for assessment of lung disease in children with cystic fibrosis. Am J Respir Crit Care Med rccm.201604-0893OC. doi: 10.1164/rccm.201604-0893OC

Terekhov M, Wolf U, Scholz A, Schreiber WG (2007) Rapid in-vivo MRI measurement of fluorinated gas concentration in lungs using T1 – mapping. In: Proceedings of International Society for Magnetic Resonance in Medicine, p 1336

Tibiletti M, Tschechne M, Bianchi A, et al (2016) Ventilation imaging with sulfur hexafluoride in free-breathing mice: initial experience. In: Proceedings of International Society for Magnetic Resonance in Medicine, p 2912

Wagner PD (2012) The multiple inert gas elimination technique (MIGET). In: Applied physiology in intensive care medicine 1: physiological notes – technical notes – seminal studies in intensive care, 3rd ed, pp 35–42

Wolf U, Scholz A, Heussel CP et al (2006) Subsecond fluorine-19 MRI of the lung. Magn Reson Med 55:948–951. doi:10.1002/mrm.20859

Wolf U, Scholz A, Terekhov M, et al (2008) Fluorine-19 MRI of the lung: first human experiment. In: Proceedings of International Society for Magnetic Resonance in Medicine, p 3207

Wolf U, Scholz A, Terekhov M et al (2010) Visualization of inert gas wash-out during high-frequency oscillatory ventilation using fluorine-19 MRI. Magn Reson Med 64:1479–1483. doi:10.1002/mrm.22528

Wolters M, Mohades ÞSG, Hackeng TM et al (2013) Clinical perspectives of hybrid proton-fluorine magnetic resonance imaging and spectroscopy. Invest Radiol 48:341–350

Proton MRI Based Ventilation Imaging: Oxygen-Enhanced Lung MRI and Alternative Approaches

Olaf Dietrich

Contents

O. Dietrich, PhD
Josef Lissner Laboratory for Biomedical Imaging,
Institute for Clinical Radiology, Ludwig-Maximilians-
University Hospital Munich, Marchioninistr. 15,
81377 Munich, Germany
e-mail: od@dtrx.net

Abstract

The direct visual assessment of the lung parenchyma and of lung ventilation using proton MRI is considerably more difficult than MRI of most other organs due to the very low signal intensity of the lung parenchyma. The low signal intensity is caused by the low average proton density and the short T_2^* relaxation time of lung tissue.

Several methods for proton MRI based ventilation measurements have been proposed to overcome these difficulties. Currently, the most established technique is oxygen-enhanced MRI of the lung, employing inhaled molecular oxygen as a T_1-reducing contrast agent, which enhances the signal of the protons in the lung. Clinical applications of oxygen-enhanced lung MRI have been assessed in a relatively large number of studies. Main advantages of oxygen-enhanced MRI are the general availability of oxygen and the relative safety of oxygen administration. Potential limitations of oxygen-enhanced lung MRI are the relatively low signal enhancement corresponding to a T_1 reduction of about 10 %, and the complex contrast mechanism with contributions from ventilation, perfusion, and oxygen-diffusion properties of the lung tissue.

Newer emerging techniques such as Fourier decomposition pulmonary MRI based on non-enhanced dynamic MR acquisitions appear to be a promising tool for ventilation assessment that may be clinically available in the

near future. Other proposed techniques such as imaging after administration of aerosolized gadolinium contrast agents or after infusion of water-in-perfluorocarbon emulsions into the lung require still considerably more research before they might become applicable in clinical MR imaging.

1   Introduction

Magnetic resonance proton imaging of the human lung is considerably more difficult than proton MRI of most other organs or tissues due to respiratory and cardiac motion as well as the very low signal intensity of the lung parenchyma in acquisitions with most available pulse sequences.[1] The low signal intensity is caused by the low average proton density and the short T_2^* relaxation time of lung tissue. Both properties are a consequence of the heterogeneous microstructure of the lung parenchyma, which consists mainly of microscopic air-filled alveoli with a large interface between air spaces and tissue or blood. Hence, the physical density (and consequently the proton density) of the lung tissue is very low and, in addition, large local variations of susceptibility occur within small spatial scales. These susceptibility variations influence the homogeneity of the static magnetic field and, thus, the Larmor frequencies of the protons within a single image voxel, which leads to substantially reduced T_2^* relaxation times of, for example, 1–2 ms at a field strength of 1.5 T and of values below 1 ms at 3 T (Zapp et al. 2016). A direct visual assessment of the lung parenchyma is therefore generally difficult with conventional proton MRI (Kauczor and Kreitner 1999; Kruger et al. 2016).

Several techniques have been proposed to overcome these limitations of proton MRI of the lung and to improve the visualization either of the lung parenchyma or of inhaled gas in order to directly depict pulmonary ventilation. Direct visualization of the inhaled gas is possible with hyperpolarized noble gases such as helium-3 or xenon-129 and is described in detail in Chaps. 4 and 5 of this book, respectively. An alternative approach is based on fluorine-19 MRI of inert fluorinated gases and is discussed in Chap. 6 of this book. All these techniques require a certain amount of additional hardware – at least specifically adapted radio frequency (RF) equipment (such as RF transmit and receive coils tuned to the Larmor frequency of the used helium, xenon, or fluorine nuclei) and, for MRI of hyperpolarized noble gases, also complex and expensive hardware devices to prepare the hyperpolarized state of the gases.

Alternative approaches are based on the visualization of the optimized or enhanced proton signal of the lung tissue, that is, ventilation is measured indirectly in contrast to the direct visualization of the inhaled gases mentioned above. Several different methods have been proposed that will be described in detail below:

- Oxygen-enhanced lung MRI (Edelman et al. 1996; Chen et al. 1998; Löffler et al. 2000) exploiting the T_1-shortening effect of inhaled molecular oxygen (O_2)
- Nonenhanced ventilation measurements based on signal changes (Zapke et al. 2006; Topf et al. 2006; Marcus et al. 2007) in dynamic MR acquisitions during respiration
- Tissue-displacement tracking (Voorhees et al. 2005) in dynamic MR acquisitions during respiration
- Nonenhanced ventilation measurements based on Fourier decomposition pulmonary MRI (Bauman et al. 2009),
- Contrast-enhanced lung MRI using inhaled aerosols of gadolinium-based contrast agents (Berthezene et al. 1992; Suga et al. 2002a; Haage et al. 2005),
- Contrast-enhanced lung MRI using the administration of water-in-perfluorocarbon emulsions (Huang et al. 2002, 2004).

An obvious advantage of these techniques is that standard RF equipment available for conventional proton MRI can be used. However, the contrast is generally lower than that in direct

---

[1]This introduction and the subsequent subsection on oxygen-enhanced lung MRI are modified and extensively updated from Chap. 38 "Oxygen-enhanced Imaging of the Lung" of the book "Parallel Imaging in Clinical MR Applications" (Dietrich 2007b).

visualization of ventilation, and the interpretation of the measured signal is more difficult due to the indirect nature of these imaging approaches.

Of these proton MRI approaches, oxygen-enhanced imaging of the lung is by far the most established technique with a large number of published technical and clinical studies. Consequently, the main focus of the following sections lies on oxygen-enhanced lung MRI including the introduction of its physiological and technical basis, details of implementation such as multislice acquisition techniques as well as triggering schemes, and discussion of the specific advantages and applications of parallel imaging techniques. The alternative proton MRI approaches for pulmonary ventilation MRI (and, in particular, Fourier decomposition pulmonary MRI) are subsequently presented in Sect. 3.

2 Oxygen-Enhanced Lung MRI

2.1 Contrast Mechanism and Physiology

Molecular oxygen (O_2) is a paramagnetic gas, that is, O_2 molecules act similar as miniature magnets and can be oriented by an external magnetic field such that a field-amplifying magnetization is induced. The volume magnetic susceptibility[2] of gaseous O_2 is 1.79 ppm corresponding to a molar magnetic susceptibility of 43.0×10^{-9} m³/mol; in contrast, many other gases including, for example, hydrogen, nitrogen, carbon dioxide, methane, and the noble gases are diamagnetic with considerably lower molar susceptibilities between -0.02×10^{-9} and -0.6×10^{-9} m³/mol (Lide 2005). Inhaled molecular oxygen was first suggested in 1996 by Edelman et al. as a paramagnetic contrast agent for in vivo proton MRI of the lung; effects of O_2 in excised lung tissue of rats were already demonstrated in 1992 by Goodrich et al. (1992)

The underlying contrast mechanism of molecular oxygen is similar to the one of gadolinium-based contrast agents (although of a substantially smaller magnitude): the longitudinal relaxation time constant (T_1) of the protons in the tissue is shortened depending on the O_2 concentration due to the paramagnetism of the O_2 molecule. The measured absolute T_1 values of lung tissue vary to a certain degree in different publications, and oxygen-induced relative T_1 reductions between 7 and 14 % were observed in healthy subjects after inhalation of pure oxygen (Table 1). This effective reduction results from differently changed T_1 values of all protons that contribute to the voxel signal, that is, it is averaged over all kinds of tissue such as blood, blood vessels, alveolar cells, and connective tissue within each single voxel. The weighting of these different compartments can be influenced, for example, by choosing different echo times as demonstrated by Triphan et al. (2015b); generally, shorter T_1 values of the lung (presumably associated with extravascular pulmonary tissue components) are observed at ultrashort echo times (70 µs) than at longer echo times. The most important contribution to oxygen-induced T_1 changes, however, is caused by the increased concentration of dissolved molecular oxygen in the capillary blood of the lung. Hence, oxygen-based lung imaging has been described to provide combined information about three physiological parameters (Edelman et al. 1996; Löffler et al. 2000):

- The inhaled oxygen must reach the lung area under consideration; thus, sufficient *ventilation* of the area is a necessary precondition for oxygen-induced reduction of T_1 relaxation.
- In addition, fresh capillary blood must be supplied, in which the oxygen can be dissolved; lung *perfusion* therefore is a second requirement for the observation of reduced T_1 values.
- Finally, the transition of the oxygen from the alveoli into the capillaries of the lung, that is, molecular oxygen *diffusion*, is required for signal enhancement.

Thus, oxygen-enhanced lung MRI can be regarded as imaging of "lung function" understood as the combination of these three parame-

---

[2]All magnetic susceptibilities are given at normal temperature (20 °C) and pressure (1 atm, 1013.25 hPa), and in SI units, i.e., multiplied by 4π when converted from cgs units.

Table 1 T_1 relaxation time constants of lung tissue

	B_0 (T)	T_1 (ms) breathing room air	T_1 (ms) breathing pure oxygen	T_1 reduction (%)
Edelman et al. (1996)	1.5	913	837	9.3
Chen et al. (1998)	1.5	1352	1183	12.5
Stock et al. (1999)	1.5	904	790	12.6
	0.2	632	586	7.3
Löffler et al. (2000)	1.5	1219	1074	11.9
Nakagawa et al. (2001)	1.5	1147	1070	6.7
Jakob et al. (2001)	1.5	1249	1141	8.6
Mai et al. (2002)	1.5	1399	1207	13.7
Jakob et al. (2004)[a]	1.5	1298	1160	10.6
Dietrich et al. (2006b)	3.0	1281	1102	14.0
Molinari et al. (2008)	1.5	1110	1016	8.5
Beer et al. (2009)	0.2	686	631	8.0
Renne et al. (2015b)[b]	1.5	1173	1038	11.5
Renne et al. (2015c)	1.5	1250	1093	12.6
Triphan et al. (2015a), expiration	1.5	1027	922	10.2
Triphan et al. (2015a), inspiration	1.5	1017	923	9.3

[a]T_1 relaxation times calculated from $T_1(0)$ and OTF
[b]In patients after lung transplantation with bronchiolitis obliterans syndrome level 0

ters. With respect to the contribution of perfusion in oxygen-enhanced lung MRI, a result by Ley et al. (2007) is noteworthy. The authors demonstrated that lung perfusion is influenced by the inhaled oxygen concentration: significantly increased perfusion was found during inhalation of oxygen compared to inhalation of room air. Similarly, Nogami et al. (2007) showed that oxygen inhalation modulated cardiac blood flow parameters. In contrast, Arai et al. (2009) found no significant differences of blood flow between hypoxia, normoxia, and mild hyperoxia. Looking at the opposite causality, Lee et al. (2013) demonstrated in rabbits that changing the pulmonary blood flow had only little effect on the oxygen-induced signal enhancement. The consequences of these observations effect on oxygen-enhanced lung MRI have not yet been fully evaluated.

As an alternative to T_1-based oxygen-enhanced proton MRI, the measurement of the oxygen-induced reduction of the transverse T_2^* relaxation time constant was proposed by Pracht et al. (2005). This technique is based on the T_2^* reduction of the lung parenchyma signal by about 10 % due to inhalation of pure oxygen compared to inhalation of room air. Typical T_2^* relaxation times of the lung parenchyma are short and range from 1.4 to about 2.0 ms in different studies at a field strength of 1.5 T; at lower field strengths, T_2^* is considerably longer with values of, for example, about 10 ms at 0.2 T, but again the oxygen-induced shortening of T_2^* is about 10 % (cf. Table 2). The measurement of this effect is more difficult than that for T_1-based experiments and prone to systematic errors because of the very short T_2^* relaxation times. This approach, however, might be useful to determine ventilation properties with reduced contributions of perfusion and diffusion effects (Pracht et al. 2005). A new (but related) approach for oxygen-enhanced lung MRI was recently proposed by Carinci et al. (2016): Based on an asymmetric spin-echo preparation, the spectral line broadening within the lung tissue is measured and demonstrated to significantly increase from a mean value of 1.48 ppm (under room air conditions) to 1.69 ppm (i.e., by about 14 %) under inhalation of pure oxygen.

Different approaches and technical solutions for the administration of oxygen during MRI are available and have been compared. Molinari

Table 2 T_2^* relaxation time constants of lung tissue

	B_0 (T)	T_2^* (ms) breathing room air	T_2^* (ms) breathing pure oxygen	T_2^* reduction (%)
Pracht et al. (2005), right lung	1.5	1.84	1.64	10.9
Pracht et al. (2005), upper left lung	1.5	1.88	1.50	20.2
Beer et al. (2009)	0.2	10.7	9.6	10.3
Oechsner et al. (2009)	0.2	10.6	9.5	10.4
Triphan et al. (2015a), expiration	1.5	1.47	1.36	7.5
Triphan et al. (2015a), inspiration	1.5	1.45	1.33	8.3
Hemberger et al. (2015), expiration[a]	1.5	2.10	1.89	10.0
Hemberger et al. (2015), inspiration[a]	1.5	1.98	1.76	8.9

[a]In a coronal posterior slice

et al. (2008) compared a closed (tightly fitting) oxygen delivery system and a clinically available nontight standard face mask; they did not find relevant differences between the results with both systems. In contrast, Renne et al. (2015c) found higher oxygen-induced T_1 shortening and lower variability with a full, closed face mask than with a nontight standard face mask. An integrated solution for gas delivery, respiratory gating, and subject monitoring was described and evaluated recently by Halaweish and Charles (2014).

2.2 MRI Pulse Sequences

Several pulse sequences can be employed for oxygen-enhanced T_1-weighted lung MRI, provided the following prerequisites are fulfilled:

- The pulse sequences must provide sufficient T_1 weighting to be sensitive to the oxygen-induced T_1 shortening. This is usually achieved by a magnetization preparation with an inversion pulse (180° pulse, inversion recovery technique). Typical inversion times between the 180° pulse and the readout are either about 700–900 ms (Edelman et al. 1996; Stock et al. 1999; Ohno et al. 2001, 2008b, 2011, 2012a, b, 2014a, b; Vaninbroukx et al. 2003; Naish et al. 2005) or about 1100–1300 ms (Löffler et al. 2000; Müller et al. 2002; Mai et al. 2003; Dietrich et al. 2005, 2010; Thieme et al. 2011; Maxien et al. 2012; Morgan et al. 2014).
- Fast data acquisition is recommendable to reduce motion artifacts caused by cardiac motion, blood flow, and respiration. Single-shot

sequences (with complete data acquisition after a single excitation) and very fast gradient-echo sequences have successfully been employed in order to avoid motion-related effects.

- The pulse sequences should be insensitive to variations of susceptibility and to short T_2^* relaxation times; this requirement excludes echoplanar imaging techniques or gradient-echo sequences with intermediate or longer echo times.

A pulse sequence with the listed properties that has frequently been employed for oxygen-enhanced lung MRI is, for example, the single-shot turbo spin-echo sequence with centrically reordered k-space sampling, which is also known as RARE (rapid acquisition with relaxation enhancement) sequence (Chen et al. 1998; Stock et al. 1999; Löffler et al. 2000; Müller et al. 2002; Vaninbroukx et al. 2003; Morgan et al. 2014; Zhang et al. 2015). A similar sequence with even shorter acquisition time is the half Fourier-acquired single-shot turbo spin-echo (HASTE) sequence (Edelman et al. 1996; Ohno et al. 2001, 2011, 2012a, b, 2014a, b; Nakagawa et al. 2001; Mai et al. 2003; Dietrich et al. 2005; Thieme et al. 2011; Maxien et al. 2012). Ohno et al. (2004) confirmed that the signal-to-noise ratio of HASTE sequences improves if the shortest possible interecho spacing, that is, the shortest readout time, is used.

An alternative to single-shot turbo spin-echo sequences are fast spoiled gradient-echo (or field-echo) sequences with short (below about 2 ms) or ultrashort (below about 0.5 ms) echo times. Snapshot-FLASH sequences with very short echo times below 2 ms have been used for oxygen-

enhanced lung MRI; these sequences are particularly suited for the measurement of quantitative T_1 maps of the lung (Jakob et al. 2001; Arnold et al. 2007; Molinari et al. 2008; Kershaw et al. 2010; Renne et al. 2015a, b, c; Jobst et al. 2015). Ultrashort echo time (UTE) acquisitions for oxygen-enhanced lung MRI were performed first in small animals (Togao et al. 2011; Zurek et al. 2014, 2016) and recently also in humans (Kruger et al. 2014; Hemberger et al. 2015; Triphan et al. 2015a) with echo times between 70 and 80 μs. These UTE techniques are particularly useful for T_2*-based oxygen-enhanced lung MRI and for mapping of the very short T_2* relaxation times. Finally, oxygen MRI of the lung at low fields below 0.5 T has also been performed with fast steady-state free precession (SSFP) techniques such as the True FISP sequence (Müller et al. 2001).

The listed pulse sequences are typically combined with an inversion recovery preparation to achieve sufficient T_1 weighting. Puderbach et al. (2007) demonstrated that the chosen inversion pulse type may influence the assessment of oxygen enhancement. T_1-weighted *saturation recovery* measurements instead of inversion recovery measurements can be utilized for oxygen-enhanced lung MRI as well. The dynamic signal range of saturation recovery experiments is only half as large as that of inversion recovery experiments; consequently, the contrast-to-noise ratio of oxygen-induced signal changes is smaller as well. On the other hand, the saturation preparation is generally more robust than inversion preparation, particularly in the presence of B_1 inhomogeneities. Thus, especially at higher field strengths such as 3 T, saturation recovery measurements may be advantageous compared to inversion recovery measurements (Dietrich et al. 2006b). In addition, imaging time can be reduced with saturation recovery techniques, since no longitudinal relaxation is required between readout and the following preparation (Naish et al. 2005).

2.3 Acquisition Paradigms and Data Evaluation

Several approaches for the acquisition and qualitative or quantitative data evaluation of oxygen-enhanced lung MRI have been proposed. They can be divided into techniques based on the T_1-weighted signal time course and those based on quantitative T_1 mapping results.

2.3.1 Signal-Intensity Based Techniques

A straightforward technique for the visualization of the ventilated lung tissue is based on difference images: Difference maps of T_1-weighted images acquired during the inhalation of oxygen on the one hand and of room air on the other hand show the lung parenchyma hyperintense relative to the surrounding tissue due to the change of longitudinal relaxation after O_2 inhalation. Typically, a block paradigm is used for data acquisition consisting of alternating blocks with inhalation of room air and oxygen as illustrated in Fig. 1. The acquisition of several repetitions is required, since both the expected signal difference and the signal-to-noise ratio of the lung tissue are relatively small. Thus, averaging of, for example, 20–40 times repeated acquisitions breathing oxygen and of a similar number of acquisitions breathing room air is used to increase the signal-to-noise ratio of the resulting difference maps.

The signal difference, ΔS, between the pixelwise averaged oxygen-enhanced signal S_{O_2} and the averaged room air signal $S_{\text{room air}}$ can be either visualized directly (Chen et al. 1998; Stock et al. 1999; Mai et al. 2000; Nakagawa et al. 2001):

$$\Delta S = S_{O_2} - S_{\text{room air}}$$

or as relative difference, $\Delta S_{\text{relative}}$ (or relative enhancement ratio, RER) after pixelwise normalization to the room air signal (Edelman et al. 1996; Müller et al. 2002; Ohno et al. 2002; Dietrich et al. 2005; Arnold et al. 2007; Hemberger et al. 2015):

$$\Delta S_{\text{relative}} = RER = \frac{S_{O_2} - S_{\text{room air}}}{S_{\text{room air}}}.$$

Calculating absolute or relative difference maps is a straightforward way to visualize lung function and can be performed on most MRI systems without additional postprocessing software. To calculate these difference maps, however, it must be taken into consideration that a certain
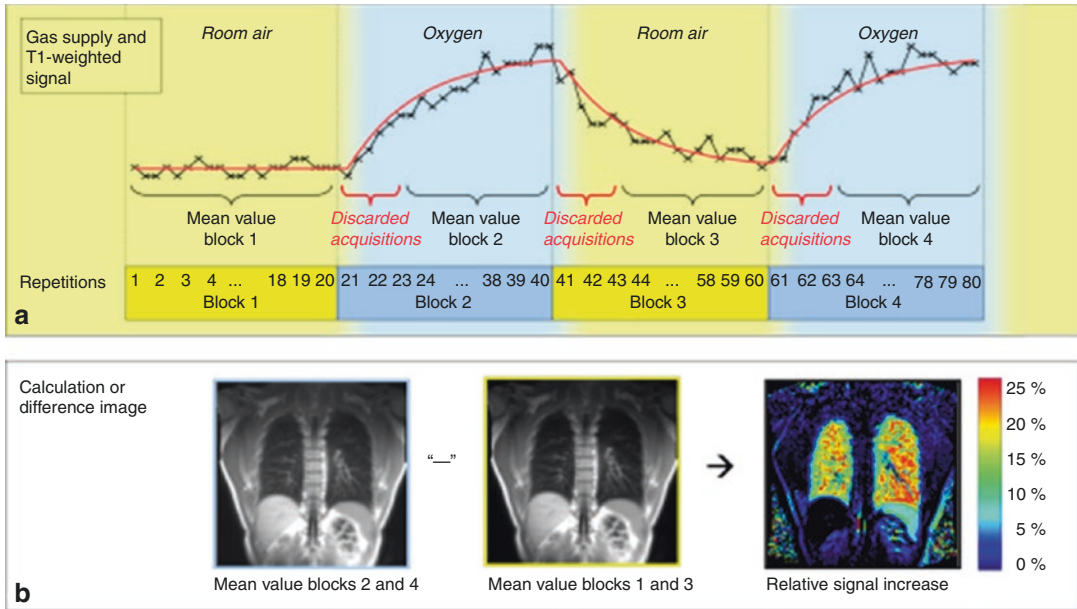
Fig. 1 (**a**, **b**) Block paradigm for oxygen-enhanced lung MRI. (**a**) Data acquisition: T_1-weighted images are continuously acquired in four blocks with 4×20 repetitions; in blocks 1 and 3, room air is supplied; in blocks 2 and 4, pure oxygen. The T_1-weighted signal varies relatively slowly after switching the gas supply and reaches exponentially its new steady state. Thus, several repetitions should be discarded before calculating the pixel-by-pixel mean value of each block. (**b**) The relative signal increase (or relative enhancement ratio) is calculated as the difference of the averaged images in blocks 2 and 4 on the one hand and 1 and 3 on the other hand, normalized to the averaged room air image. The lung parenchyma and the spleen appear hyperintense in the difference map (Figure reprinted with permission of Springer from: Dietrich (2007b))

time interval is required after switching the gas supply from air to oxygen (and vice versa) until T_1 (and, hence, the T_1-weighted signal intensity) reaches a steady-state value as demonstrated in Fig. 1. This process is described by an exponential change with time constants between 23 and 83 s in healthy volunteers (Arnold et al. 2004; Naish et al. 2005; Dietrich et al. 2010).

The interval of intermediate signals between the steady states could be avoided by waiting a few minutes after switching the gas supply before the data acquisition is being continued (Mai et al. 2003). However, Müller et al. (2002) demonstrated that the slope of the signal increase correlates well with other clinical parameters. Hence, it appears useful to acquire data continuously to measure the intermediate signal dynamics as well and, thus, to be able to determine both the difference image and the time constants or slopes of the signal change. When calculating relative or absolute difference maps from such continuously acquired data, a certain number of acquisitions within each block of the paradigm

should be discarded after switching the gas supply to avoid systematically decreased differences. For example, in a paradigm of 4×20 respiratory-triggered acquisitions, an optimized ratio of signal difference and statistical error was found if about five to eight acquisitions were discarded (Dietrich et al. 2006a).

To assess pixelwise the dynamics of oxygen wash-in and wash-out, it was shown that a piecewise exponential model function provides a better signal fit (quantified by the Akaike information criterion) than rectangular or piecewise linear model functions (Dietrich et al. 2010). Thus, from an oxygen-enhanced acquisition with repeated blocks of room air inhalation and oxygen inhalation, the (exponential) time constants τ_{in} for oxygen wash-in and τ_{out} for oxygen wash-out can be quantified as additional ventilation-associated parameters.

As an alternative to the evaluation of the absolute or relative difference of T_1-weighted images, it was proposed by Mai et al. (2003) to compute the cross-correlation between the time-response

function of each pixel in a series of T_1-weighted acquisitions and the input function representing the paradigm of alternating room air and oxygen administration. Based on this approach, Molinari et al. (2007) have introduced the fraction of oxygen-activated pixels (OAP%), that is, the number of pixels with a correlation coefficient greater than 0.5 divided by the total number of pixels in the considered region of interest, to compare acquisitions of, for example, healthy volunteers and patients. Improved cross-correlation results, that is, higher median cross-correlation coefficients, can be obtained if a piecewise exponential function is used as input function instead of a simpler (rectangular) box function (Dietrich et al. 2010). Combining the correlation-based analysis with a dynamic oxygen wash-in and wash-out model, Sá et al. (2010, 2014) estimated the specific ventilation from the oxygen-modulated signal time course.

2.3.2 T_1 Relaxation Time-Based Methods

In addition to the above-mentioned intensity-based evaluation strategies, which use the T_1-weighted signal modulation due to oxygen inhalation, postprocessing of oxygen-enhanced MRI can also be performed based on relaxometry techniques, that is, on T_1 (or T_2^*) mapping. These T_1 (or T_2^*) maps of the lungs can be computed from appropriate acquisitions during the inhalation of room air and of pure oxygen, respectively. The influence of oxygen can now be displayed in difference maps showing the reduction of relaxation time (or the increase of the relaxation rates $R_1 = 1/T_1$ and $R_2^* = 1/T_2^*$) due to oxygen inhalation. These differences can be displayed as absolute differences (Oechsner et al. 2009; Hemberger et al. 2015) or relative differences (Beer et al. 2009; Triphan et al. 2015a).

The change of the relaxation rates in the lung parenchyma between room air and oxygen inhalation can also be used to estimate the partial pressure ΔP_{O2} of oxygen dissolved in blood plasma (and tissue water):

$$\Delta P_{O_2} = \frac{1}{r_1}\left(R_1\left(O_2\right) - R_1\left(\text{air}\right)\right)$$

where $r_1 = 2.49 \times 10^{-4} \text{s}^{-1}\text{mmHg}^{-1}$ is the longitudinal relaxivity of O_2 in water (Zaharchuk et al. 2006; Kershaw et al. 2010; Morgan et al. 2014; Zhang et al. 2015). With this value for the relaxivity, typical changes of the relaxation rate of about 0.1 s^{-1} in healthy subjects correspond to oxygen partial pressures of about 400 mmHg. Similarly, as for the T_1-weighted signal, wash-in and wash-out time constants can also be determined from the time course of R_1 or of the partial pressure ΔP_{O_2} (Kershaw et al. 2010; Morgan et al. 2014; Zhang et al. 2015).

Instead of the alternating administration of room air and pure oxygen, such quantitative measurements can also be performed at more than two different concentrations of oxygen, for example, at 21 % (room air), 40 %, 60 %, 80 %, and 100 %. Based on quantitative T_1 measurements at these different O_2 levels, the oxygen transfer function (OTF) can be determined as illustrated in Fig. 2 (Jakob et al. 2004). The OTF describes the change of relaxation rate $R_1 = 1/T_1$ in lung tissue depending on the concentration of oxygen, C_{O2}, in the administered gas, that is, it is similarly defined as the relaxivity of oxygen but does not require the measurement of the actual tissue concentration (in units of mmol/L) of oxygen. The OTF is expressed in units of s^{-1} (%O$_2$)$^{-1}$, and the change of T_1 is described by

$$\frac{1}{T_1\left(C_{O_2}\right)} = \frac{1}{T_1\left(0\right)} + \text{OTF} \times C_{O_2}.$$

Typical OTF values of healthy lung tissue range from 0.9×10^{-3} s^{-1}(%O$_2$)$^{-1}$ to 1.5×10^{-3} s^{-1}(%O$_2$)$^{-1}$ (Jakob et al. 2004; Renne et al. 2015a, b, c), which is consistent with a change of $1/T_1$ by about 0.1 s^{-1} when increasing the O$_2$ concentration by 79 % (from 21 % at room air to 100 %). Similarly, T_2^* at different concentrations of oxygen can be measured and exhibits an approximately linear behavior with a slope in the order of 500×10^{-3} s^{-1}(%O$_2$)$^{-1}$ at 1.5 T (Triphan et al. 2015a).

To accelerate the acquisition of the required T_1 maps for OTF measurements, a technique proposed by Arnold et al. (2007) can be used. T_1 can be estimated for different concentrations of oxygen based on a single T_1 map measured dur-
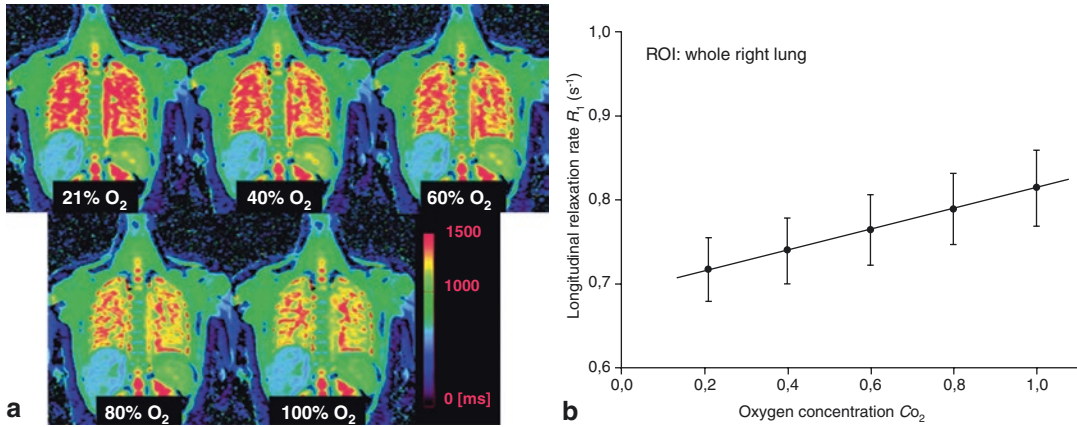
Fig. 2 (**a**, **b**) Measurement of the oxygen transfer function (OTF). (**a**) T_1 maps of a 30-year-old healthy female volunteer breathing different oxygen concentrations, C_{O_2}. (**b**) A linear relationship between the oxygen concentration, C_{O_2}, and the longitudinal relaxation rate, R_1, in the whole right lung. The fitted OTF and extrapolated relaxation time without oxygen, $T_1(0)$, were $(0.12\pm0.00)\times10^{-2}$ s^{-1}(%O$_2$)$^{-1}$ and 1449 ± 2 ms, respectively, with an excellent correlation coefficient (R) of 1 (Reprinted with permission of John Wiley and Sons from: Jakob et al. (2004))

ing inhalation of room air, and on T_1-weighted images acquired for all other oxygen concentrations. In contrast to almost all other studies evaluating oxygen-enhanced lung MRI, Arnold et al. (2007) used carbogen (i.e., 95 % oxygen, 5 % carbon dioxide) instead of pure oxygen as T_1-reducing contrast agent, because carbogen is thought to be advantageous as a breathing gas during radiation therapy of patients with non-small-cell lung cancer.

2.4   Advanced Acquisition Techniques

Almost all studies using oxygen-enhanced MRI have been performed at a field strength of 1.5 T or at low-field systems with, for example, 0.2 T. Only a single study by Thieme et al. (2011) demonstrated the feasibility of oxygen-enhanced MRI (using an inversion recovery HASTE sequence) at a field strength of 3 T, but the obtained oxygen-induced signal enhancement was more heterogeneous and slightly lower than that in the same subjects at 1.5 T. Consequently, the technical development of oxygen-enhanced MRI is still focusing on acquisition improvements at 1.5 T, as illustrated in the subsequent sections.

2.4.1   Multislice Imaging

Oxygen-enhanced MRI of the lung is based on T_1-weighting sequences such as single-shot turbo spin-echo techniques or ultrafast gradient-echo techniques. Both sequence types require an additional T_1-sensitizing magnetization preparation that is usually realized as an inversion pulse. This 180° RF pulse (as well as the refocusing RF pulses of the turbo spin-echo sequence) can be implemented either as *slice-selective* pulses that influence only the spins in a two-dimensional section or as *non-selective* pulses that invert all spins within the RF coil (Takenaka et al. 2011). Interleaved multislice acquisitions with the same inversion time for all slices can only be performed with slice-selective inversion and refocusing pulses.

Most oxygen-enhanced imaging studies have been performed with nonselective inversion or refocusing pulses (Jakob et al. 2001; Nakagawa et al. 2001; Mai et al. 2003; Molinari et al. 2007; Zhang et al. 2015), such that an interleaved inversion and acquisition of multiple slices is not possible. Hence, either single-slice imaging was used or the total duration of acquisition had to be prolonged to acquire several slices in successive imaging experiments.

a Single-slice inversion recovery HASTE sequence

b Multi-slice inversion recovery HASTE sequence
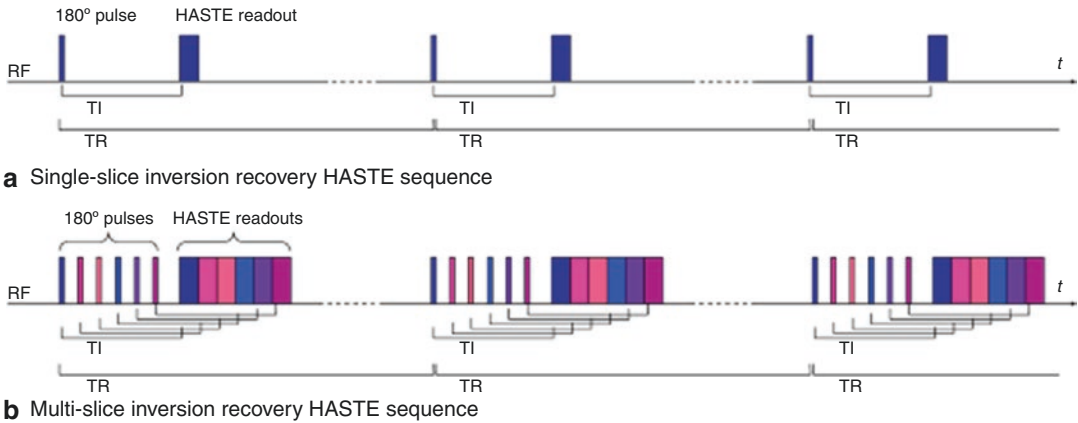
Fig. 3 (**a**) Three repetitions of a single-slice inversion recovery HASTE sequence. Only a single slice is acquired; the inversion (180°) pulse as well as the refocusing pulses may be nonselective. (**b**) Three repetitions of a multislice inversion recovery HASTE sequence. Six slices

(shown in different colors) are acquired; inversion (180°) pulses and readouts are interleaved. All 180° RF pulses must be slice-selective (Figure reprinted with permission of Springer from: Dietrich (2007b))

The acquisition time of multiple slices can be decreased by employing slice-selective RF pulses and interleaving inversion preparation and image data readout, that is, the inversion time, TI, between inversion and readout of a single slice is used to invert one or several more slices as demonstrated in Fig. 3. A potential disadvantage of using slice-selective inversion can be an increased sensitivity to perfusion effects: the signal within the slice will be influenced by inflowing noninverted spins from outside the slice. To minimize this effect, the thickness of the inverted slice can be increased, for example, by a factor of 2, relative to the thickness of the image slice.

It has been demonstrated in a comparison of nonselective inversion and slice-selective inversion with doubled inversion slice thickness that similar results can be obtained with both techniques (Dietrich et al. 2005). The T_1-weighted images and calculated maps of relative signal increase showed some differences with respect to the signal within the pulmonary vessels. However, the signal increase in the large pulmonary vessels is less important for evaluation of the lung function than the signal distribution in the lung parenchyma which was similar for both techniques.

2.4.2 ECG and Respiratory Triggering, Motion Correction

Reliable triggering is particularly important for MRI of the lung because of the high level of motion in the thorax due to pulsatile blood flow, cardiac motion, and respiration. Vaninbroukx et al. (2003) as well as Molinari et al. (2006) demonstrated that oxygen-enhanced MRI of the lung benefits from both ECG triggering and respiratory triggering in comparison to MRI without triggering. ECG triggering helps to acquire all repetitions in identical cardiac phases and to avoid motion artifacts due to acquisition during the systolic phase. Even more important is respiratory triggering to acquire all repetitions with identical positions of the diaphragm, since the signal intensity of the lung parenchyma depends substantially on the respiratory phase (Mai et al. 2000; Bankier et al. 2004). The signal intensity typically varies by at least 50 % due to the change of proton density during respiration, and this signal variation is superimposed on the oxygen-induced signal increase. Different techniques for respiratory triggering have been applied including the frequently used pneumatic respiratory belts, pneumotachographic triggering (Molinari et al. 2006), or navigator techniques (Molinari et al. 2007). It appears advantageous to choose end-expiration for image
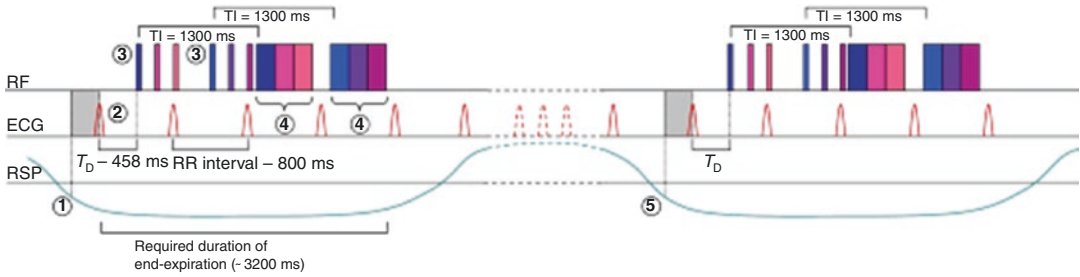
Fig. 4 Inversion recovery HASTE sequence with respiratory (RSP) and ECG triggering. (*1*) Sequence starts in end-expiration. (*2*) After the next R wave, the delay T_D is inserted, and (*3*) the slice-selective inversion pulses for 2×3 slices are applied. (*4*) The delay T_D has been calculated from the current heart rate such that all six HASTE readouts lie in the diastole. (*5*) The sequence is repeated in the next respiratory cycle (Figure reprinted with permission of Springer from: Dietrich (2007b))

acquisition to obtain the maximal lung signal and a more uniform diaphragm position than that after repeated inspirations (Losert et al. 2002).

The preceding considerations motivate the combined application of ECG and respiratory triggering in fast T_1-weighting pulse sequences to facilitate robust oxygen-enhanced MRI of the lung in clinical routine. However, ECG and respiratory triggering in combination with a multislice inversion recovery single-shot turbo spin-echo sequence requires a complex trigger scheme to move the data readout into the diastolic phase. A possible trigger and sequence scheme, which has been evaluated by Dietrich et al. (2005), is shown in Fig. 4; the acquisition is respiratory-triggered to start in end-expiration, and an additional short delay, T_D, is calculated from the ECG signal such that the actual data readout takes place in the diastolic cardiac phase. Since the acquisition of all six slices cannot be fitted into a single RR interval, the readout is divided into two parts with three HASTE readouts.

In addition to respiratory triggering, Molinari et al. (2012) demonstrated that the image quality of oxygen-enhanced MRI can be further improved by fully automatic nonrigid image registration; the mean coefficients of variation of the oxygen enhancement maps decreased by about 11 % after image registration.

2.4.3 Parallel Imaging

Parallel imaging, which has been developed since the mid-1990s with the aim to accelerate image acquisition (Sodickson and Manning 1997;

Pruessmann et al. 1999; Griswold et al. 2002; Larkman and Nunes 2007; Schoenberg et al. 2007), has been an important innovation in MRI. The basic idea of parallel imaging is to employ several independent receiver coil elements in parallel to reduce the number of required phase-encoding steps for a given image matrix size by decreasing the sampling density in k-space, that is, by k-space undersampling. Parallel imaging has been demonstrated to provide several advantages for single-shot MRI in general (Griswold et al. 1999; Dietrich 2007a) and, in particular, for single-shot MRI of the lung (Heidemann et al. 2003; Eibel 2007) due to shorter echo trains, shorter echo times, and reduced blurring.

For oxygen-enhanced MRI of the lung with the ECG-triggered and respiratory-triggered multislice sequence shown in Fig. 4, parallel imaging exhibits specific advantages as a consequence of the shorter turbo spin-echo readout. Using parallel imaging with an acceleration factor of 2, Dietrich et al. (2005) showed that the number of echoes required for the acquisition of a 128×128 matrix with a HASTE sequence could be reduced from 72 to 36; thus, the total readout time decreased from 214 ms/slice to 115 ms/slice (for an echo spacing of 2.7 ms) including the time for signal excitation and spoiler gradients. As a consequence of the shorter total readout time, the number of interleaved slices with inversion recovery preparation acquired during end-expiration could be increased to six or more in contrast to

a complete difference map

b difference map inserted in T_1-weighted image
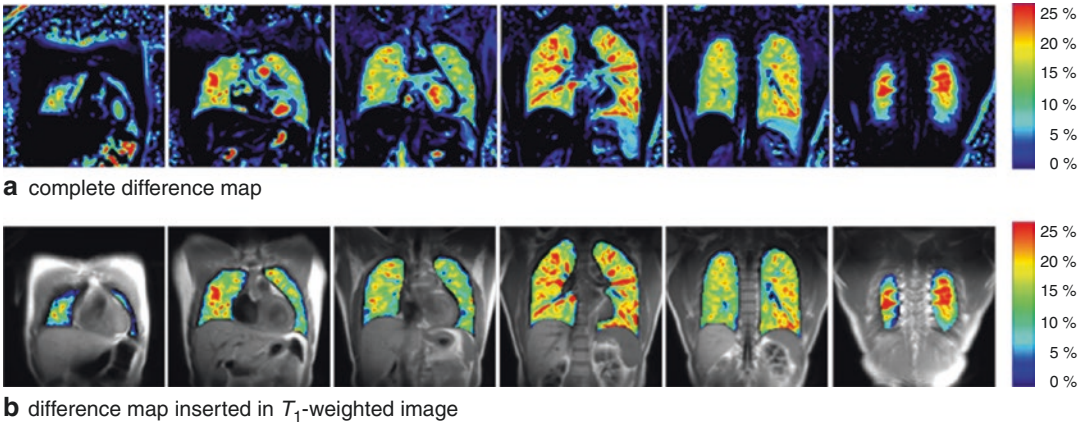
Fig. 5 (**a**, **b**) Parameter maps displaying the oxygen-induced relative signal increase in a healthy volunteer acquired with parallel imaging. The complete parameter maps (**a**) demonstrate that oxygen-induced signal enhancement is observed predominantly in the lung, in the large cardiopulmonary vessels, in the spleen, and in the cardiac ventricles. The same data is shown inserted in the T_1-weighted acquisition (**b**) after manual segmentation of the lungs (Figure (modified) reprinted with permission of Springer from: Dietrich (2007b))

only four slices without parallel imaging. The average required end-expiration time per repetition (cf. Fig. 4) to acquire six slices without motion artifacts could be significantly reduced from 4112 ms without parallel imaging to 2727 ms with parallel imaging (Dietrich et al. 2005), resulting in considerably increased robustness of the sequence against respiratory motion artifacts. The synergistic effects of parallel imaging and oxygen-enhanced multislice MRI of the lung are discussed in much more detail in publications by Dietrich et al. (2005) and Dietrich (2007b).

Examples of oxygen-enhanced lung MRI in six coronal slices of a healthy volunteer are shown in Fig. 5. These data were acquired with the T_1-weighted respiratory-triggered and ECG-triggered inversion recovery multislice HASTE sequence described above. The echo time was 11 ms with GRAPPA parallel imaging (Griswold et al. 2002).

2.5 Clinical Applications

Oxygen-enhanced lung imaging has been evaluated in several studies demonstrating a good correlation between MRI parameters and conventional methods of lung diagnostics such as evaluation of the diffusion capacity of carbon monoxide (DLCO), the forced expiratory volume in 1 s (FEV$_1$), or results of ventilation scintigraphy. Ohno et al. (2001, 2002) examined patients with lung cancer and with lung emphysema and demonstrated a good correlation of the maximum signal enhancement in oxygen-enhanced MRI on the one hand and FEV$_1$ and DLCO on the other hand. The same group described that oxygen-enhanced MRI could be used to successfully predict the postoperative FEV$_1$ in patients with bronchogenic carcinoma (Ohno et al. 2005). Nakagawa et al. (2001) demonstrated in patients with pulmonary embolism that oxygen-enhanced MRI did not show any ventilation defects in agreement with ventilation scintigraphy; in these patients, ventilation contrast appears to dominate over the perfusion-based and diffusion-based contributions. A study by Müller et al. (2002) in patients with various pulmonary diseases showed a good correlation between the signal slope after switching the gas supply to pure oxygen and the DLCO. Jakob et al. (2004) found in patients with cystic fibrosis that the oxygen transfer function correlates well with affected lung areas characterized by perfusion defects. A study in 33 patients with pulmonary hypertension demonstrated good sensitivity of oxygen-enhanced MRI for detecting ventilation defects when compared to ventilation scintigraphy (Maxien et al. 2012).

Oxygen-enhanced MRI and thin-section computed tomography (CT) were correlated or compared in several studies by Ohno et al. (2008a, b, 2011, 2012a, b, 2014a, b). In patients with smoking-related chronic obstructive pulmonary disease (COPD), signal enhancement and wash-in time in dynamic oxygen-enhanced MRI were demonstrated to have potential for pulmonary functional loss assessment (Ohno et al. 2008a, b, 2012a). In asthmatics, the same group found oxygen-enhanced MRI to be as effective as CT for the assessment of pulmonary functional loss and classification of the clinical stage (Ohno et al. 2011); effects of treatment could be assessed by signal enhancement and, particularly, by wash-in time analysis of oxygen-enhanced MRI in good correlation with FEV_1 results (Ohno et al. 2014a). In patients who were examined before lung-volume reduction surgery, oxygen-enhanced MRI could be demonstrated to be comparably reliable as thin-section CT with respect to clinical outcome measurements (Ohno et al. 2012b). In a study in patients with connective tissue disease, oxygen-enhanced MRI was also shown to be as useful as thin-section CT for disease severity assessment (Ohno et al. 2014b).

In a study by Molinari et al. (2007), a significantly smaller fraction of oxygen-activated pixels (OAP%) was found in patients with interstitial lung diseases than in healthy volunteers. Two recent studies evaluated oxygen-enhanced MRI for the assessment of COPD: Jobst et al. (2015) determined the oxygen-induced T_1 shortening in 20 COPD patients and concluded that this parameter correlates with lung perfusion deficits and with the severity of COPD (cf. Fig. 6); Morgan et al. (2014) found that oxygen-enhanced MRI parameters (based on T_1 measurements and on wash-out dynamics) showed the response to treatment (in 40 COPD patients) with a β_2-antagonist and with inhaled corticosteroids. A study in 10 asthmatic patients also assessed T_1 values and dynamic parameters (oxygen wash-in/wash-out time constants) and demonstrated sensitivity to the severity of disease as well as good reproducibility and intraobserver agreement (Zhang et al. 2015); cf. Fig. 7. In another study in asthmatic patients, oxygen-enhanced MRI was shown to visualize and quantify the regional allergic reactions after segmental endobronchial allergen challenge (Renne et al. 2015a). Finally, Renne et al. (2015b) demonstrated that the oxygen transfer function may be used as an early marker for detecting chronic lung allograft dysfunction in a study that included 76 recipients of double lung allografts.

3 Alternative Approaches

3.1 Non-contrast-Enhanced Dynamic Lung Imaging

Although the signal of lung tissue in non-contrast-enhanced proton MRI is very low as described in Sec. 1, it is still possible to employ this signal directly to assess ventilation properties of the lung. One approach to deduce ventilation information from non-contrast-enhanced lung MRI is based on the evaluation of a series of dynamic lung images acquired during the respiratory cycle (Rupprecht et al. 2003; Topf et al. 2004, 2005, 2006; Zapke et al. 2006; Voorhees et al. 2005; Marcus et al. 2007). These images are acquired with temporal resolutions between 119 ms (Marcus et al. 2007) and 2 s (Topf et al. 2005, 2006). Typically, only a single slice is acquired to optimize the temporal resolution.

Different MR imaging techniques have been proposed to obtain a sufficiently strong signal of the native lung tissue. For instance, it has been suggested to use MRI systems with low field strengths of, for example, 0.2 T (Wagner et al. 2001; Rupprecht et al. 2002; Abolmaali et al. 2004). In spite of the generally lower signal-to-noise ratio (SNR) at low field strengths, the relative signal of the lung tissue is increased because of the substantially reduced susceptibility effects, which are proportional to the field strength. Balanced SSFP sequences such as the True FISP sequence are particularly suited for lung MRI at 0.2 T because of their high SNR efficiency. At higher field strengths, single-shot fast spin-echo techniques such as the HASTE sequence with relatively short echo times are generally preferred for visualization of the lung tissue.
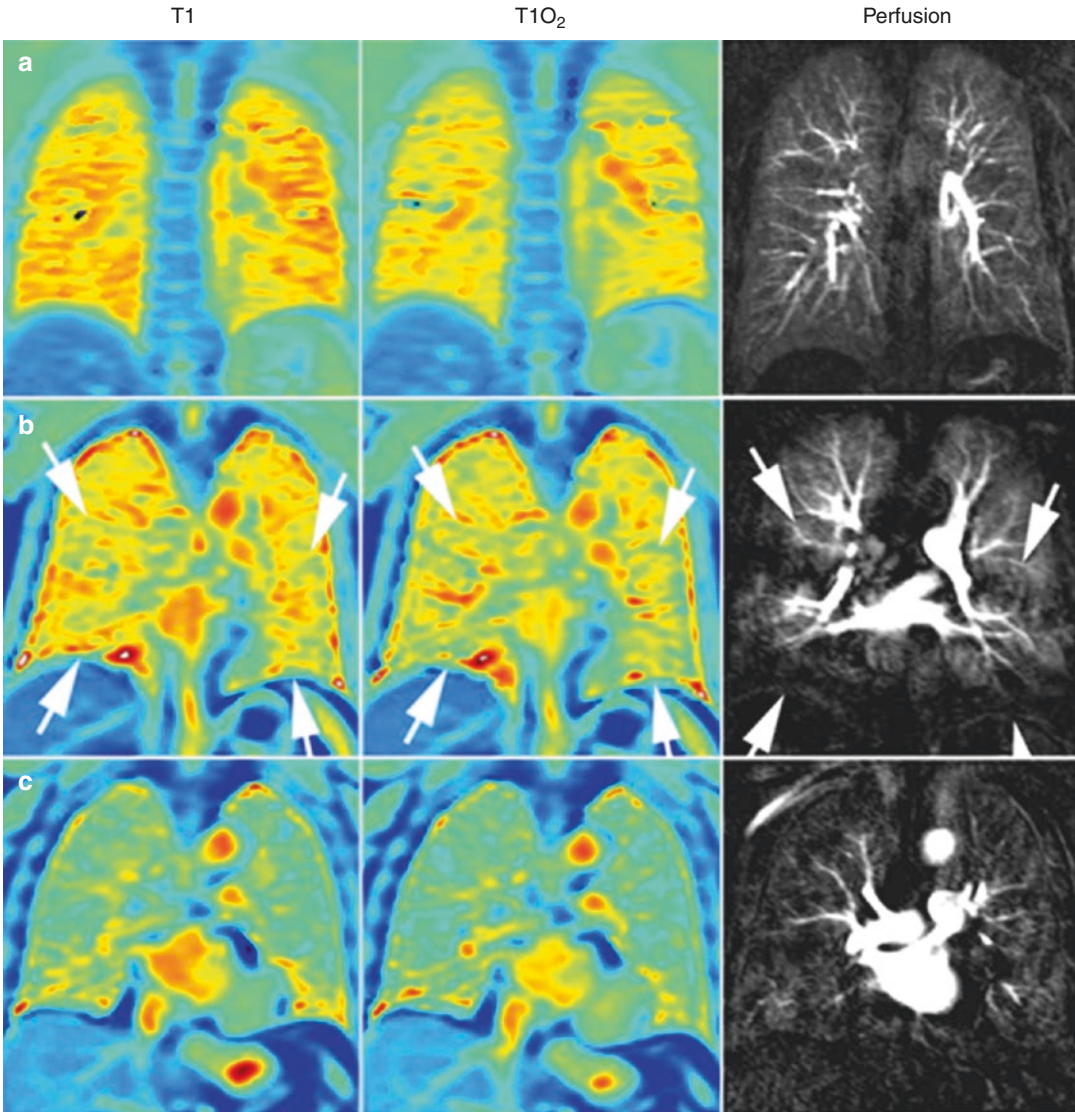
Fig. 6 Comparison of T_1 and perfusion characteristics. Normal T_1 mapping at room air (*left*), T_1 mapping after 100 % O_2 (*middle*), and DCE lung perfusion (*right*) (zonal scores = 0 each) of a 29-year-old healthy proband (**a**). Fifty-nine-year-old patient with GOLD stage II showing minor T_1 abnormalities at room air (score = 1), normal ΔT_1 after 100 % O_2 (score = 0), and minor perfusion abnormalities (score = 1) of the middle and lower lung zones (area between *white arrows*), reflecting lung areas with intact ventilation and simultaneous perfusion impairment (**b**). Severe T_1 abnormalities at room air, abnormal ΔT_1 after 100 % O_2 and perfusion abnormalities (score = 2 each) affecting the entire lung of a 75-year-old patient with GOLD stage II (**c**) (Figure reprinted (CC BY license) from: Jobst et al. (2015))

Rupprecht et al. (2003) proposed that information about the pulmonary ventilation can be deduced directly from regional variations of the MR signal intensity during the respiratory cycle. In their study, the ratio of the volume of inhaled air (V_{air}) and the volume of lung parenchyma (V_{tissue}) in expiration was calculated from the signal during inspiration, S_{insp}, expiration, S_{exp}, as well as the noise signal, S_{noise}, as

$$\frac{V_{air}}{V_{tissue}} = \frac{S_{exp} - S_{insp}}{S_{exp} - S_{noise}}.$$
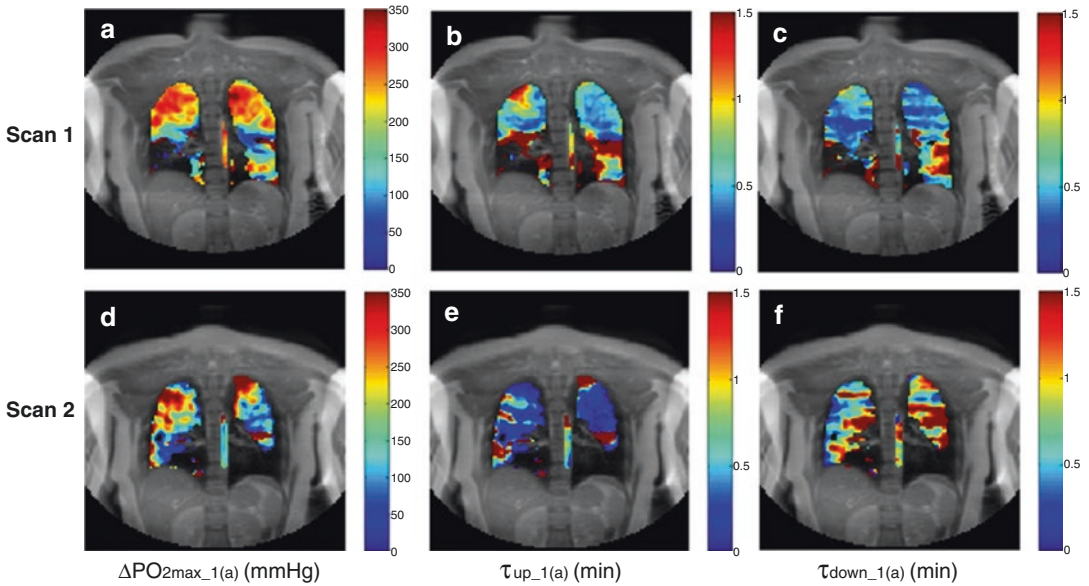
Fig. 7 Dynamic oxygen-enhanced MRI parameter maps from a severe asthmatic participant (female, 19 years old, FEV$_1$% predicted = 64 %) from the scan (V1) and rescan (V2). (**a–c**) Maps of ΔPO_{2max}, τ_{up_1} and τ_{down_1} from the first scan, respectively. (**d–f**) Maps of ΔPO_{2max}, τ_{up_1} and τ_{down_1} from the second scan, respectively. The enhancing fraction is 82 % in the first scan and 67 % in the second scan (Figure reprinted (CC BY license) from: Zhang et al. (2015))

More generalized, this ratio can also be determined for every time, t, of the respiratory cycle, based on the lung signal, $S(t)$, at time t:

$$\frac{V_{air}(t)}{V_{tissue}} = \frac{S_{exp} - S(t)}{S_{exp} - S_{noise}}$$

This quantitative approach has been evaluated in volunteers and patients using a True FISP sequence at 0.2 T (Rupprecht et al. 2003; Topf et al. 2004; Zapke et al. 2006) and with a HASTE sequence at 1.5 T (Topf et al. 2005, 2006). A good correlation was found between lung ventilation determined by MRI and the vital capacity derived from conventional pulmonary function test as shown in Fig. 8 (Zapke et al. 2006). This method, however, is complicated by the fact that lung tissue is moving significantly during the respiratory cycle. Hence, a substantial amount of postprocessing is required to (nonrigidly) register all images acquired during the respiratory cycle to a reference image (Zapke et al. 2006) before evaluating the variation of MR signal intensity. A related approach which correlates the signal intensity and the lung area during the respiratory cycle (Bankier et al. 2004) was suggested by Marcus et al. (2007).

Instead of evaluating the time dependence of the MR signal intensity during the respiratory cycle, ventilation information can also be deduced from direct monitoring of the spatial displacement of lung tissue. Two different approaches for tissue displacement mapping have been suggested: motion tracking after a grid preparation using SPAMM tagging of the lung (Chen et al. 2001; Napadow et al. 2001; Voorhees et al. 2005) and direct tracking of the lung tissue analyzing the motion of vessels and other hyperintense structures (Gee et al. 2003; Sundaram and Gee 2005). Only a few results based on these techniques have been published; however, Voorhees et al. (2005) demonstrated a good agreement of the regional lung volume change derived from the directly segmented volume and from the volume that was calculated using the regional tissue displacement measurements.

More MRI studies have been performed that evaluate only global spirometric properties of the lung such as static or dynamic lung volumes (Eichinger et al. 2007). These techniques for non-contrast-enhanced lung imaging and MR spirometry-based ventilation measurements are discussed in Chap. 8 of this book.
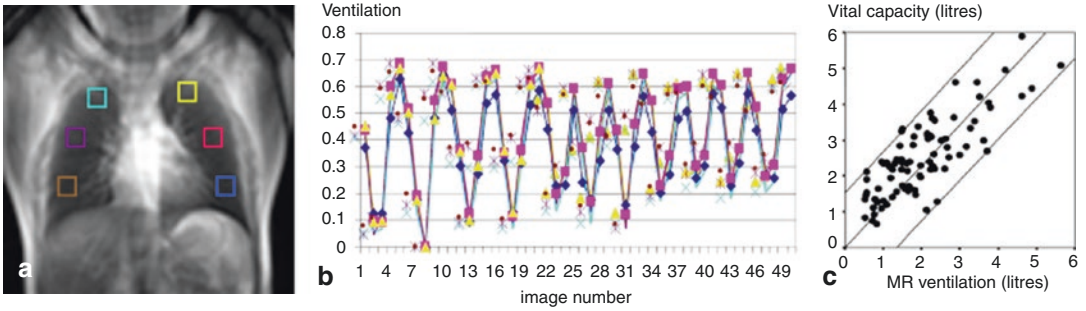
Fig. 8 (**a–c**) Non-contrast-enhanced dynamic lung MRI. (**a**) MR ventilation image of a patient with normal pulmonary function test. (**b**) Ventilation graphs that show the ventilation (i.e., the ratio of the volume of inhaled air, V_{air}, and the volume of lung parenchyma, V_{tissue}) in 50 images for each rectangular region shown in **a** during the respiratory cycles. The 50 measurements span a total of 1 min. Ventilation measurements: *Right*: *upper* field (*turquoise*) 0.64 mL/cm³; *middle* field (*violet*) 0.68 mL/cm³; *lower* field (*brown*) 0.65 mL/cm³. *Left*: *upper* field (*yellow*) 0.67 mL/cm³; *middle* field (*pink*) 0.68 mL/cm³; *lower* field (*blue*) 0.62 mL/cm³. (**c**) Correlation of MR ventilation and vital capacity measured by conventional pulmonary function test ($r = 0.8$; $p \leq 0.001$, *black lines*: regression line and 95 % confidence interval) (Figure reprinted (CC BY license) from Zapke et al. (2006)))

3.2 Fourier Decomposition Pulmonary MRI

The underlying idea of exploiting pulmonary signal variations during respiration is also the basis for an emerging technique known as "Fourier decomposition" pulmonary MRI, which was first proposed in 2009 by Bauman et al. For Fourier decomposition pulmonary MRI, dynamically acquired images of the lung (e.g., using a fast 2D True FISP pulse sequence) are first nonrigidly registered (as described above), preserving the respiration-induced signal variations of each voxel. Then, this signal time course is analyzed pixelwise by a one-dimensional temporal Fourier transform, which enables to separate fast (i.e., high-frequency) signal variations due to pulsatile blood flow and slower (low-frequency) signal variations due to respiratory lung motion within each pixel. After choosing the appropriate frequency ranges, the area under the respiratory (and the cardiac) peaks of the Fourier power spectrum is calculated and used as signal intensity of a ventilation (and perfusion) map, respectively. The calculation of ventilation and perfusion data with the Fourier decomposition approach is illustrated in Fig. 9. The initial part of a simulated signal time course of a typical lung tissue pixel is shown in Fig. 9a. The total signal (blue) contains contributions from respiration

(green) with respiratory cycle durations between 6.4 and 6.7 s, and from pulsatile blood flow (red) with heart rates 66.8 and 68.2 bpm; a low level of image noise is added as well. The Fourier transform of this signal is shown in Fig. 9b, in which the peaks due to respiration are highlighted in green (with a principal frequency of about $1/(6.5$ s) ≈ 0.16 s⁻¹, and higher harmonics at multiples of this frequency) and a separate (red) peak corresponding to the pulsatile blood flow at about $68/60$ s ≈ 1.13 s⁻¹.

Examples of resulting ventilation and perfusion maps from three healthy volunteers are shown in Fig. 10 (Bauman et al. 2009); the separation of ventilation and perfusion components is particularly obvious in the aorta, which shows bright signal only on the perfusion maps (b, d, f). Typical acquisition strategies for Fourier decomposition MRI (at a field strength of 1.5 T) are based on fast balanced SSFP pulse sequences (such as the True FISP sequence), with TRs of 1.5–1.9 ms to acquire a single coronal slice of the lung with a thickness of 12–15 mm at a matrix size between 128×128 and 256×256 pixels; the data acquisition is usually accelerated by parallel imaging with reduction factors of 2–3. With these sequences, temporal resolutions of 250–300ms/image (i.e., about 3–4 images/s) can be achieved. The total measurement durations for one slice range from about 30 s (Kjørstadt et al. 2014) over 60 s (Bauman et al.
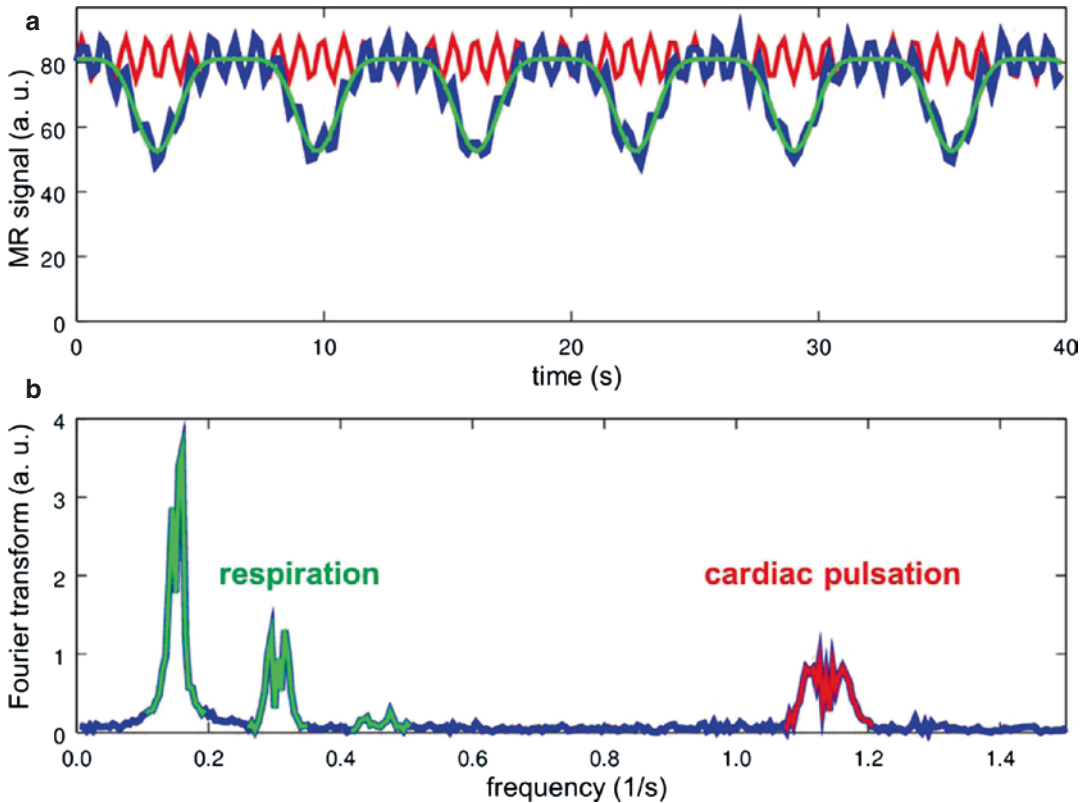
Fig. 9 (**a**, **b**) Basic principle of Fourier decomposition pulmonary MRI. (**a**) A simulated MR signal time course of lung tissue (*blue*) with signal variations due to respiration (*green*) with a cycle duration of 6.4–6.7 s and due to pulsatile blood flow (*red*) with a heart frequency of 66.8– 68.2 bpm. (**b**) Frequency spectrum (obtained by Fourier analysis from the signal time course in (a)) containing the low-frequency contributions of respiration (*green*) and pulsatile blood flow (*red*)

2009) to 2 min (Capaldi et al. 2015), resulting in series of about 100–500 images, respectively. Multiple slices can be acquired sequentially increasing the total acquisition duration (Bauman et al. 2013). As an alternative to fast SSFP sequences, fast spoiled gradient-echo sequences were applied in a few studies (Fischer et al. 2014; Voskrebenzev et al. 2015).

In a subsequent study, Bauman and colleagues demonstrated the qualitative agreement of Fourier decomposition results on the one hand and of ventilation and perfusion SPECT acquisitions on the other hand in the porcine lung (Bauman et al. 2011). In a second study in pigs, they validated Fourier decomposition MRI for different pulmonary pathologies with hyperpolarized helium-3 and dynamic contrast-enhanced MRI (Bauman et al. 2013). They also found a

high reproducibility of the Fourier decomposition results in healthy volunteers (Lederlin et al. 2013). Recently, Bauman et al. (2016) demonstrated that the performance of Fourier decomposition pulmonary MRI can be improved with an ultrafast SSFP sequence (TE/TR = 0.67/1.46 ms) compared to a conventional SSFP sequence (TE/ TR = 0.87/1.9 ms) and by postprocessing with a technique known as matrix pencil decomposition (Bauman and Bieri 2016). To improve the separation of ventilation and perfusion information in Fourier decomposition MRI, Wujcicki et al. (2015) proposed a new subject-adaptive algorithm for filter design, which was shown to reduce the amount of mutual information in perfusion and ventilation maps.

A first study comparing ventilation results of Fourier decomposition MRI and hyperpolarized
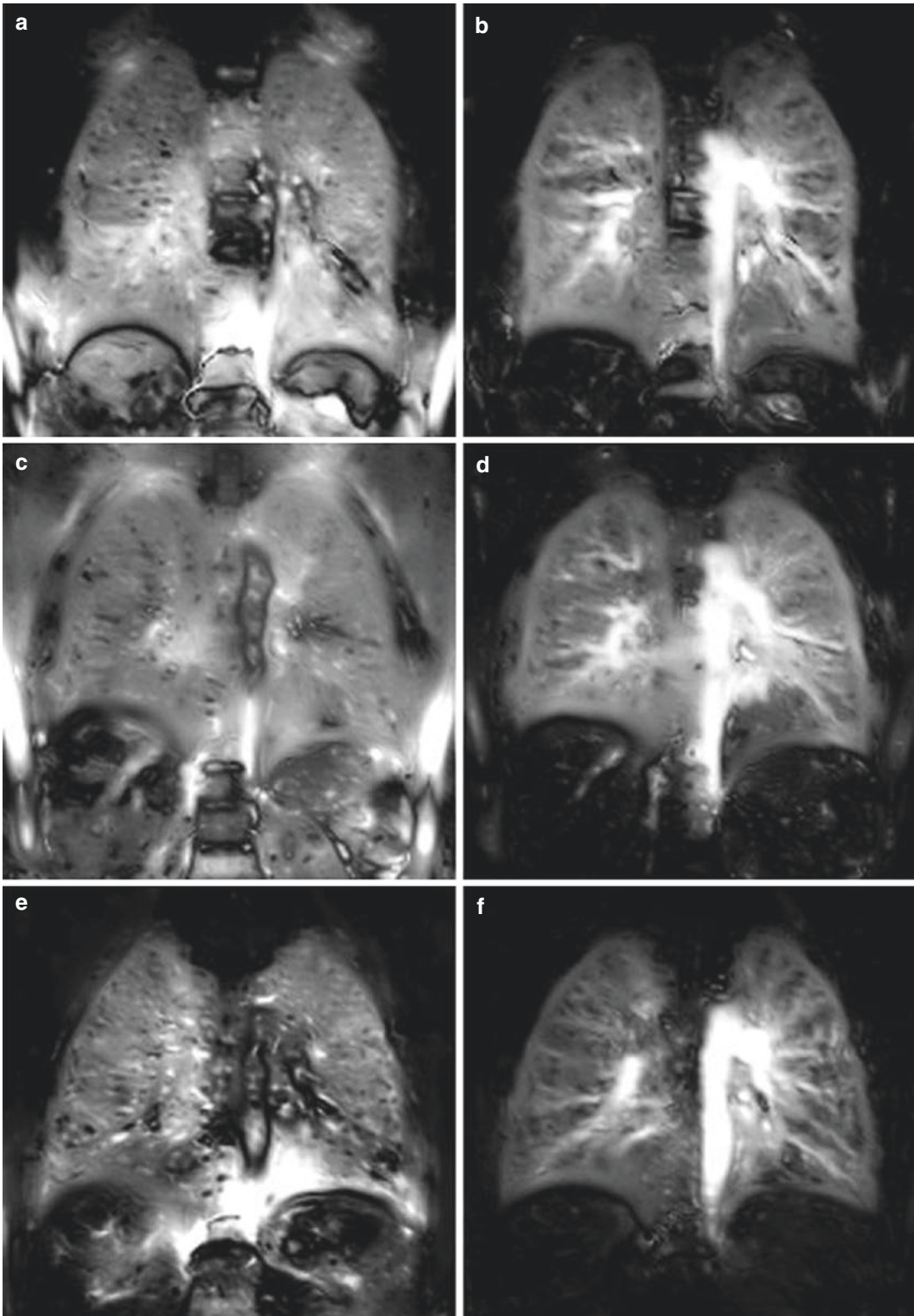
Fig. 10 (**a**–**f**) Qualitative ventilation-weighted (**a**, **c**, **e**) and perfusion-weighted (**b**, **d**, **f**) images in coronal view from three healthy subjects obtained using the Fourier decomposition approach (Figure reprinted with permission of John Wiley and Sons from: Bauman et al. (2009))

helium-3 MRI in 26 patients with COPD or bronchiectasis was published by Capaldi et al. (2015); they found a significant correlation ($r = 0.88$; $p < 0.01$) of ventilation defect percent values in COPD patients between both techniques, but no significant correlations in subjects with bronchiectasis. Another patient study in 15 patients with lung cancer demonstrated the feasibility to calculate ventilation–perfusion (V/Q) values from Fourier decomposition MRI (Kjørstad et al. 2015); however, the approach showed only limited robustness, which required the exclusion of 5 out of 15 patients.

While the original Fourier decomposition approach results in purely qualitative ventilation maps, Kjørstad et al. (2014) have proposed and validated an approach to *quantify* lung ventilation based on Fourier decomposition. With this technique, they obtained mean minute ventilation values of about 700 mL/min for the evaluated 2D slice in a study in 10 healthy volunteers. In a second study of the same group, an improved signal-to-noise ratio of Fourier decomposition MRI was demonstrated with a variable flip-angle SSFP sequence in comparison to a conventional SSFP sequence with constant flip angle (Corteville et al. 2015). Another technical modification of the original SSFP-based Fourier decomposition method was proposed by Fischer et al. (2014) as "SElf-gated Non-Contrast-Enhanced FUnctional Lung imgaing" (SENCEFUL), which is based on a FLASH acquisition with quasirandom phase encoding and self-gating using an additionally acquired nonphase-encoded signal; images in different respiratory and cardiac states can be retrospectively reconstructed with this technique and postprocessed with Fourier decomposition techniques. To improve the reproducibility of fractional ventilation results obtained by Fourier decomposition MRI, Voskrebenzev et al. (2015) proposed to include the tidal volume in the postprocessing of ventilation data.

3.3 Aerosolized Gadolinium-Based Contrast Agents

Already in 1987, Montgomery et al. (1987) proposed to administer an aerosolized gadolinium-based contrast agent to decrease the T_1 relaxation time and to enhance the signal of extravascular water in the lungs; first MR experiments were performed in excised lung tissue of rats, demonstrating a significant decrease of T_1. Berthezène et al. (1992) used a T_1-weighting spin-echo sequence (TR≈250 ms, TE=6 ms) and measured an MRI signal increase by more than 70 % in rats in vivo after inhalation of an aerosolized gadolinium contrast agent for 5 min. More animal studies were performed in the following years, investigating safety aspects (Berthezène et al. 1993), modified gadolinium formulations (Misselwitz et al. 1997), MRI in larger animals such as domestic pigs (Haage et al. 2000) and dogs (Suga et al. 2002a), the signal enhancement behavior of various gadolinium-containing contrast agents (Haage et al. 2001b, 2002), and improved delivery devices for the administration of the gadolinium-DTPA aerosol (Haage et al. 2001a; Suga et al. 2002b). The used aerosols had mean particle sizes between 0.2 and 5.0 μm, and the original contrast agent concentration before aerosolization ranged between 100 and 500 mmol/L. In these studies, Haage and coworkers applied a respiratory-gated T_1-weighting two-dimensional multislice fast spin-echo sequence with repetition times between 141 and 199 ms and an echo time of 8.5 ms for dynamic lung imaging. Suga and coworkers acquired T_1-weighted data with a fast three-dimensional spoiled gradient-echo sequence with repetition time of 3.5 ms and an echo time of 0.9 ms. An alternative measurement approach is described by Price et al. (2004, 2005), who propose a single-point imaging sequence for signal detection; this technique has the advantage to be very insensitive to susceptibility effects and short T_2^* relaxation times in lung tissue.

The application of aerosolized gadolinium contrast agents in animals with functional impairments of the lung was demonstrated by Suga et al. (2002a, b, 2003) and by Ogasawara et al. (2004); MRI was performed in dogs with acute airway obstruction with a balloon catheter and after pulmonary arterial embolization with enbucrilate. Areas of acute airway obstruction showed matched perfusion and aerosol deposit defects, while small areas affected by embolization

showed only perfusion defects but normal aerosol images. The clearance of a gadolinium-based aerosol in bleomycin-injured dog lungs was investigated by Suga et al. (2003). They found a heterogeneously reduced aerosol deposition in the affected lungs as well as a significantly decreased clearance half-time. Sood et al. (2008, 2010, 2012) used aerosolized gadolinium contrast agents to assess general aerosol delivery with different ventilation systems (e.g., of prostaglandins in neonates) in pig models as well as in a lung phantom. Two recent studies in mice (Bianchi et al. 2013) and spontaneously breathing rats (Wang et al. 2016) demonstrated the feasibility of ultrashort echo-time (UTE) sequences with echo times of 276 and 400 µs for the visualization of Gd-DOTA based aerosol deposition in the lungs.

The first applications of lung ventilation MRI with aerosolized gadolinium chelates in human volunteers were described by Haage et al. (2003, 2005). An average signal enhancement of about 35 % was observed after 10 min inhalation of the gadolinium-DTPA aerosol; data was acquired with a T_1-weighting fast spin-echo sequence as described above. Examinations in 15 healthy volunteers were performed without any procedure-related complications or acute or delayed allergic reactions to the aerosolized contrast medium. The examination was followed by an 18-month observation period to exclude any delayed side effects such as pulmonary inflammations. No further studies are published until now about the application of gadolinium aerosols in human volunteers or in patients.

3.4 Water-In-Perfluorocarbon Emulsions

A further approach for proton MRI ventilation measurements is based on the infusion of a water-in-perfluorocarbon emulsion into the lung (Huang et al. 2002, 2004). Perfluorocarbon compounds have been used for liquid ventilation since the 1960s (Lowe 1987), exploiting the excellent solubility of O_2 and CO_2 in these substances. Fluorine-19 perfluorocarbon has been utilized in fluorine-19 MRI for lung visualization (cf. Chap. 6 of this book); however, no signal is emitted by these substances in proton MRI because of the lack of protons in perfluorocarbons. To employ perfluorocarbon-based liquid ventilation in proton MRI, Huang et al. (2002) proposed to use water-in-perfluorocarbon emulsions that can provide both a fluorine-19 and a proton MRI signal. After infusion of the water-in-perfluorocarbon emulsion into rat lungs, a substantial signal enhancement can be observed in proton MRI using, for example, a spin-echo sequence with a repetition time of 900 ms and an echo time of 6 ms. Huang et al. (2002) also performed diffusion-weighted proton MRI and found apparent diffusion coefficients (ADCs) of about 1×10^{-3} mm²/s in healthy lungs in contrast to substantially increased ADCs of about 3×10^{-3} mm²/s in injured lungs with induced pulmonary edema. The latter results are in parallel to diffusion measurements based on helium-3 lung MRI (cf. Chap. 4 of this book).

In a second study performed in mice, Huang et al. (2004) measured the T_2^* relaxation time in lung tissue after infusion of a water-in-perfluorocarbon emulsion. Using a multi-echo spin-echo sequence with echo times between 5 and 120 ms, they found T_2^* values between 25 and 35 ms for a sufficiently high administered infusion dose. Thus, T_2^* is substantially increased compared to the relaxation times of typically less than 5 ms without infusion of the water-in-perfluorocarbon emulsion. This observation is explained by the considerably reduced susceptibility variation in lung tissue after filling of the air spaces with the liquid emulsion.

No further studies about applications of water-in-perfluorocarbon emulsions in animals or humans have been published yet.

Conclusions

Several methods for proton MRI based ventilation measurements are available. Currently, the most established technique is oxygen-enhanced MRI of the lung, employing inhaled molecular oxygen as a T_1-reducing contrast agent, which enhances the signal of the protons in the lung. The main advantages of

oxygen-enhanced MRI are the general availability of oxygen in every clinical environment and the relative safety of oxygen administration in volunteers or patients. A large number of publications describe the application of oxygen-enhanced lung MRI in patients with several different lung pathologies. Technically, a certain amount of hardware is required to administer alternately room air and oxygen (pure or in several different concentrations) via a mask or a mouthpiece to the examined subject in the scanner. Disadvantages of oxygen-enhanced lung MRI are the relatively low signal enhancement corresponding to the T_1 reduction of about 10 %, and the complex contrast mechanism with contributions from ventilation, perfusion, and oxygen-diffusion properties of the lung tissue.

A second, newer approach for proton MRI of lung ventilation is based on the evaluation of a sequence of dynamic MR images acquired during the respiratory cycle without any additional exogenous contrast enhancement. The obvious advantage of this technique is that no additional hardware is required which reduces costs and increases patient comfort during the examination. However, the proposed techniques are based on complex postprocessing including sophisticated nonrigid image registration, which is not generally available as standard postprocessing tools on MRI scanners or PACS workstations. The number of publications that evaluate this new promising approach is now increasing, particularly, since Fourier decomposition pulmonary MRI was proposed in 2009 by Bauman et al. More clinical studies are still required to establish this technique for use in routine imaging.

Other available techniques for ventilation MRI are imaging after administration of aerosolized gadolinium contrast agents or water-in-perfluorocarbon emulsions into the lung. The former technique, however, involves complex and expensive hardware devices to prepare and administer the contrast agent aerosol; a further disadvantage is that the inhalation of gadolinium-based contrast agents is still controversial and not yet thoroughly evaluated in humans. Until now,

no studies with aerosolized gadolinium contrast agents have been conducted in patients. Even less data are available on proton MRI during (partial) liquid ventilation employing water-in-perfluorocarbon emulsions, which has yet been tested only in small rodents.

In conclusion, proton-based ventilation MR imaging of the lungs is clinically feasible and well established with oxygen-enhanced MRI. Newer techniques based on nonenhanced dynamic MR acquisitions appear to be a promising and emerging tool for ventilation assessment that may be available in the near future. Other proposed techniques require still considerably more research before they might be applicable in clinical MR imaging.

References

Abolmaali ND, Schmitt J, Krauss S, Bretz F, Deimling M, Jacobi V, Vogl TJ (2004) MR imaging of lung parenchyma at 0.2T: evaluation of imaging techniques, comparative study with chest radiography and interobserver analysis. Eur Radiol 14:703–708

Arai TJ, Henderson AC, Dubowitz DJ, Levin DL, Friedman PJ, Buxton RB, Prisk GK, Hopkins SR (2009) Hypoxic pulmonary vasoconstriction does not contribute to pulmonary blood flow heterogeneity in normoxia in normal supine humans. J Appl Physiol 106:1057–1064

Arnold JF, Fidler F, Wang T, Pracht ED, Schmidt M, Jakob PM (2004) Imaging lung function using rapid dynamic acquisition of T1-maps during oxygen enhancement. MAGMA 16:246–253

Arnold JF, Kotas M, Fidler F, Pracht ED, Flentje M, Jakob PM (2007) Quantitative regional oxygen transfer imaging of the human lung. J Magn Reson Imaging 26:637–645

Bankier AA, O'Donnell CR, Mai VM, Storey P, De Maertelaer V, Edelman RR, Chen Q (2004) Impact of lung volume on MR signal intensity changes of the lung parenchyma. J Magn Reson Imaging 20:961–966

Bianchi A, Lux F, Tillement O, Crémillieux Y (2013) Contrast enhanced lung MRI in mice using ultra-short echo time radial imaging and intratracheally administrated Gd-DOTA-based nanoparticles. Magn Reson Med 70:1419–1426

Bauman G, Bieri O (2016) Matrix pencil decomposition of time-resolved proton MRI for robust and improved assessment of pulmonary ventilation and perfusion. Magn Reson Med. doi:10.1002/mrm.26096 [Epub ahead of print]

Bauman G, Puderbach M, Deimling M, Jellus V, Chefd'hotel C, Dinkel J, Hintze C, Kauczor HU, Schad LR (2009) Non-contrast-enhanced perfusion and ventilation assessment of the human lung by means of fourier decomposition in proton MRI. Magn Reson Med 62:656–664

Bauman G, Lützen U, Ullrich M, Gaass T, Dinkel J, Elke G, Meybohm P, Frerichs I, Hoffmann B, Borggrefe J, Knuth HC, Schupp J, Prüm H, Eichinger M, Puderbach M, Biederer J, Hintze C (2011) Pulmonary functional imaging: qualitative comparison of Fourier decomposition MR imaging with SPECT/CT in porcine lung. Radiology 260:551–559

Bauman G, Scholz A, Rivoire J, Terekhov M, Friedrich J, de Oliveira A, Semmler W, Schreiber LM, Puderbach M (2013) Lung ventilation- and perfusion-weighted Fourier decomposition magnetic resonance imaging: in vivo validation with hyperpolarized 3He and dynamic contrast-enhanced MRI. Magn Reson Med 69:229–237

Bauman G, Pusterla O, Bieri O (2016) Ultra-fast steady-state free precession pulse sequence for fourier decomposition pulmonary MRI. Magn Reson Med 75:1647–1653

Beer M, Stäb D, Oechsner M, Hahn D, Köstler H, Hebestreit H, Jakob P (2009) Sauerstoffverstärkte funktionelle MR-Lungenbildgebung. Radiologe 49:732–738

Berthezene Y, Vexler V, Clement O, Muhler A, Moseley ME, Brasch RC (1992) Contrast-enhanced MR imaging of the lung: assessments of ventilation and perfusion. Radiology 183:667–672

Berthezène Y, Mühler A, Lang P, Shames DM, Clément O, Rosenau W, Kuwatsuru R, Brasch RC (1993) Safety aspects and pharmacokinetics of inhaled aerosolized gadolinium. J Magn Reson Imaging 3:125–130

Capaldi DP, Sheikh K, Guo F, Svenningsen S, Etemad-Rezai R, Coxson HO, Leipsic JA, McCormack DG, Parraga G (2015) Free-breathing pulmonary 1H and Hyperpolarized 3He MRI: comparison in COPD and bronchiectasis. Acad Radiol 22:320–329

Carinci F, Meyer C, Breuer FA, Jakob PM (2016) In vivo imaging of the spectral line broadening of the human lung in a single breathhold. J Magn Reson Imaging 44(3):745–757

Chen Q, Jakob PM, Griswold MA, Levin DL, Hatabu H, Edelman RR (1998) Oxygen enhanced MR ventilation imaging of the lung. MAGMA 7:153–161

Chen Q, Mai VM, Bankier AA, Napadow VJ, Gilbert RJ, Edelman RR (2001) Ultrafast MR grid-tagging sequence for assessment of local mechanical properties of the lungs. Magn Reson Med 45:24–28

Corteville DM, Kjørstad Å, Henzler T, Zöllner FG, Schad LR (2015) Fourier decomposition pulmonary MRI using a variable flip angle balanced steady-state free precession technique. Magn Reson Med 73: 1999–2004

Dietrich O (2007a) Single-shot pulse sequences. In: Schoenberg SO, Dietrich O, Reiser MF (eds) Parallel imaging in clinical MR applications. Springer, Berlin/Heidelberg/New York, pp. 119–126

Dietrich O (2007b) Oxygen-enhanced imaging of the lung. In: Schoenberg SO, Dietrich O, Reiser MF (eds) Parallel imaging in clinical MR applications. Springer, Berlin/Heidelberg/New York, pp. 429–440

Dietrich O, Losert C, Attenberger U, Fasol U, Peller M, Nikolaou K, Reiser MF, Schoenberg SO (2005) Fast oxygen-enhanced multislice imaging of the lung using parallel acquisition techniques. Magn Reson Med 53:1317–1325

Dietrich O, Losert C, Attenberger U, Reuter C, Fasol U, Peller M, Nikolaou K, Reiser MF, Schoenberg SO (2006a) Sauerstoff-MRT der Lunge: Optimierte Berechnung von Differenzbildern. Radiologe 46:300–308

Dietrich O, Raya JG, Fasol U, Peller M, Reiser MF, Schoenberg SO (2006b) Oxygen-enhanced MRI of the lung at 3Tesla: feasibility and T1 relaxation times. Proc Int Soc Magn Reson Med 14:1307

Dietrich O, Attenberger UI, Ingrisch M, Maxien D, Peller M, Nikolaou K, Reiser MF (2010) Analysis of signal dynamics in oxygen-enhanced magnetic resonance imaging. Invest Radiol 45:165–173

Edelman RR, Hatabu H, Tadamura E, Li W, Prasad PV (1996) Noninvasive assessment of regional ventilation in the human lung using oxygen-enhanced magnetic resonance imaging. Nat Med 2:1236–1239

Eibel R (2007) Lung imaging. In: Schoenberg SO, Dietrich O, Reiser MF (eds) Parallel imaging in clinical MR applications. Springer, Berlin/Heidelberg/New York, pp. 209–217

Eichinger M, Tetzlaff R, Puderbach M, Woodhouse N, Kauczor HU (2007) Proton magnetic resonance imaging for assessment of lung function and respiratory dynamics. Eur J Radiol 64:329–334

Fischer A, Weick S, Ritter CO, Beer M, Wirth C, Hebestreit H, Jakob PM, Hahn D, Bley T, Köstler H (2014) SElf-gated Non-Contrast-Enhanced FUnctional Lung imaging (SENCEFUL) using a quasi-random fast low-angle shot (FLASH) sequence and proton MRI. NMR Biomed 27:907–917

Gee J, Sundaram T, Hasegawa I, Uematsu H, Hatabu H (2003) Characterization of regional pulmonary mechanics from serial magnetic resonance imaging data. Acad Radiol 10:1147–1152

Goodrich KC, Hackmann A, Ganesan K, Ailion DC, Cutillo AG (1992) Spin-lattice relaxation in excised rat lung. Proc Int Soc Magn Reson Med 11:1307

Griswold MA, Jakob PM, Chen Q, Goldfarb JW, Manning WJ, Edelman RR, Sodickson DK (1999) Resolution enhancement in single-shot imaging using simultaneous acquisition of spatial harmonics (SMASH). Magn Reson Med 41:1236–1245

Griswold MA, Jakob PM, Heidemann RM, Nittka M, Jellus V, Wang J, Kiefer B, Haase A (2002) Generalized autocalibrating partially parallel acquisitions (GRAPPA). Magn Reson Med 47:1202–1210

Haage P, Adam G, Misselwitz B, Karaagac S, Pfeffer JG, Glowinski A, Döhmen S, Tacke J, Günther RW (2000) Aerosoliertes Gadolinium-DTPA zur Darstellung der Lungenventilation in der Magnetresonanztomographie. Rofo Fortschr Röntgenstr 172:323–328

Haage P, Adam G, Karaagac S, Pfeffer J, Glowinski A, Döhmen S, Günther RW (2001a) Mechanical delivery of aerosolized gadolinium-DTPA for pulmonary ventilation assessment in MR imaging. Invest Radiol 36:240–243

Haage P, Karaagac S, Adam G, Glowinski A, Günther RW (2001b) Comparison of aerosolized gadoteridol and gadopentetate dimeglumine for magnetic resonance ventilation imaging of the lung. Magn Reson Med 46:803–806

Haage P, Karaagac S, Adam G, Spüntrup E, Pfeffer J, Günther RW (2002) Gadolinium containing contrast agents for pulmonary ventilation magnetic resonance imaging: preliminary results. Invest Radiol 37:120–125

Haage P, Karaagac S, Spüntrup E, Adam G, Günther RW (2003) MR-Bildgebung der Lungenventilation mittels aerosolierter Gadolinium-Chelate. Rofo Fortschr Röntgenstr 175:187–193

Haage P, Karaagac S, Spuntrup E, Truong HT, Schmidt T, Gunther RW (2005) Feasibility of pulmonary ventilation visualization with aerosolized magnetic resonance contrast media. Invest Radiol 40:85–88

Halaweish AF, Charles HC (2014) Physiorack: an integrated MRI safe/conditional, gas delivery, respiratory gating, and subject monitoring solution for structural and functional assessments of pulmonary function. J Magn Reson Imaging 39:735–741

Heidemann RM, Griswold MA, Kiefer B, Nittka M, Wang J, Jellus V, Jakob PM (2003) Resolution enhancement in lung 1H imaging using parallel imaging methods. Magn Reson Med 49:391–394

Hemberger KR, Jakob PM, Breuer FA (2015) Multiparametric oxygen-enhanced functional lung imaging in 3D. MAGMA 28:217–226

Huang MQ, Ye Q, Williams DS, Ho C (2002) MRI of lungs using partial liquid ventilation with water-in-perfluorocarbon emulsions. Magn Reson Med 48:487–492

Huang MQ, Basse PH, Yang Q, Horner JA, Hichens TK, Ho C (2004) MRI detection of tumor in mouse lung using partial liquid ventilation with a perfluorocarbon-in-water emulsion. Magn Reson Imaging 22:645–652

Jakob PM, Hillenbrand CM, Wang T, Schultz G, Hahn D, Haase A (2001) Rapid quantitative lung 1H T1 mapping. J Magn Reson Imaging 14:795–799

Jakob PM, Wang T, Schultz G, Hebestreit H, Hebestreit A, Hahn D (2004) Assessment of human pulmonary function using oxygen-enhanced T(1) imaging in patients with cystic fibrosis. Magn Reson Med 51:1009–1016

Jobst BJ, Triphan SM, Sedlaczek O, Anjorin A, Kauczor HU, Biederer J, Ley-Zaporozhan J, Ley S, Wielpütz MO (2015) Functional lung MRI in chronic obstructive pulmonary disease: comparison of T1 mapping, oxygen-enhanced T1 mapping and dynamic contrast enhanced perfusion. PLoS One 10:e0121520

Kauczor HU, Kreitner KF (1999) MRI of the pulmonary parenchyma. Eur Radiol 9:1755–1764

Kershaw LE, Naish JH, McGrath DM, Waterton JC, Parker GJ (2010) Measurement of arterial plasma oxygenation in dynamic oxygen-enhanced MRI. Magn Reson Med 64:1838–1842

Kjørstad Å, Corteville DM, Henzler T, Schmid-Bindert G, Hodneland E, Zöllner FG, Schad LR (2014) Quantitative lung ventilation using Fourier decomposition MRI; comparison and initial study. MAGMA 27:467–476

Kjørstad Å, Corteville DM, Henzler T, Schmid-Bindert G, Zöllner FG, Schad LR (2015) Non-invasive quantitative pulmonary V/Q imaging using Fourier decomposition MRI at 1.5T. Z Med Phys 25:326–332

Kruger SJ, Fain SB, Johnson KM, Cadman RV, Nagle SK (2014) Oxygen-enhanced 3D radial ultrashort echo time magnetic resonance imaging in the healthy human lung. NMR Biomed 27:1535–1541

Kruger SJ, Nagle SK, Couch MJ, Ohno Y, Albert M, Fain SB (2016) Functional imaging of the lungs with gas agents. J Magn Reson Imaging 43:295–315

Larkman DJ, Nunes RG (2007) Parallel magnetic resonance imaging. Phys Med Biol 52:R15–R55

Lederlin M, Bauman G, Eichinger M, Dinkel J, Brault M, Biederer J, Puderbach M (2013) Functional MRI using Fourier decomposition of lung signal: reproducibility of ventilation- and perfusion-weighted imaging in healthy volunteers. Eur J Radiol 82:1015–1022

Lee HJ, Park J, Hur J, Kim YJ, Nam JE, Choi BW, Choe KO (2013) The effect of pulmonary blood flow changes on oxygen-enhanced lung magnetic resonance imaging. Magn Reson Med 69:1645–1649

Ley S, Puderbach M, Risse F, Ley-Zaporozhan J, Eichinger M, Takenaka D, Kauczor HU, Bock M (2007) Impact of oxygen inhalation on the pulmonary circulation: assessment by magnetic resonance (MR)-perfusion and MR-flow measurements. Invest Radiol 42:283–290

Lide DR (ed) (2005) CRC handbook of chemistry and physics, 85th edn. CRC Press, Boca Raton

Löffler R, Müller CJ, Peller M, Penzkofer H, Deimling M, Schwaiblmair M, Scheidler J, Reiser M (2000) Optimization and evaluation of the signal intensity change in multisection oxygen-enhanced MR lung imaging. Magn Reson Med 43:860–866

Losert C, Nikolaou K, Scheidler J, Mueller CJ, Schwaiblmair M, Reiser MF (2002) Optimized respiratory and ECG gating in oxygen-enhanced MR ventilation imaging of the lung. Proc Int Soc Magn Reson Med 10:1971

Lowe KC (1987) Perfluorocarbons as oxygen-transport fluids. Comp Biochem Physiol A Comp Physiol 87:825–838

Mai VM, Chen Q, Li W, Hatabu H, Edelman RR (2000) Effect of respiratory phases on MR lung signal intensity and lung conspicuity using segmented multiple inversion recovery turbo spin echo (MIR-TSE). Magn Reson Med 43:760–763

Mai VM, Liu B, Li W, Polzin J, Kurucay S, Chen Q, Edelman RR (2002) Influence of oxygen flow rate on signal and T(1) changes in oxygen-enhanced ventilation imaging. J Magn Reson Imaging 16:37–41

Mai VM, Tutton S, Prasad PV, Chen Q, Li W, Chen C, Liu B, Polzin J, Kurucay S, Edelman RR (2003) Computing oxygen-enhanced ventilation maps using correlation analysis. Magn Reson Med 49:591–594

Marcus JT, Korporaal JG, Rietema H, Boonstra A, Vonk Noordegraaf A (2007) MRI estimation of dynamic regional lung ventilation, derived from pulmonary density changes during respiration. Proc Int Soc Magn Reson Med 15:2777

Maxien D, Dietrich O, Thieme SF, Förster S, Behr J, Reiser MF, Nikolaou K (2012) Value of oxygen-enhanced MRI of the lungs in patients with pulmonary hypertension: a qualitative and quantitative approach. J Magn Reson Imaging 35:86–94

Misselwitz B, Mühler A, Heinzelmann I, Böck JC, Weinmann HJ (1997) Magnetic resonance imaging of pulmonary ventilation. Initial experiences with a gadolinium-DTPA-based aerosol. Invest Radiol 32:797–801

Molinari F, Gaudino S, Fink C, Corbo GM, Valente S, Pirronti T, Bonomo L (2006) Simultaneous cardiac and respiratory synchronization in oxygen-enhanced magnetic resonance imaging of the lung using a pneumotachograph for respiratory monitoring. Invest Radiol 41:476–485

Molinari F, Eichinger M, Risse F, Plathow C, Puderbach M, Ley S, Herth F, Bonomo L, Kauczor HU, Fink C (2007) Navigator-triggered oxygen-enhanced MRI with simultaneous cardiac and respiratory synchronization for the assessment of interstitial lung disease. J Magn Reson Imaging 26:1523–1529

Molinari F, Puderbach M, Eichinger M, Ley S, Fink C, Bonomo L, Kauczor HU, Bock M (2008) Oxygen-enhanced magnetic resonance imaging: influence of different gas delivery methods on the T1-changes of the lungs. Invest Radiol 43:427–432

Molinari F, Bauman G, Paolantonio G, Geisler T, Geiger B, Bonomo L, Kauczor HU, Puderbach M (2012) Improvement of multislice oxygen-enhanced MRI of the lung by fully automatic non-rigid image registration. Eur J Radiol 81:2900–2906

Montgomery AB, Paajanen H, Brasch RC, Murray JF (1987) Aerosolized gadolinium-DTPA enhances the magnetic resonance signal of extravascular lung water. Invest Radiol 22:377–381

Morgan AR, Parker GJ, Roberts C, Buonaccorsi GA, Maguire NC, Hubbard Cristinacce PL, Singh D, Vestbo J, Bjermer L, Jögi J, Taib Z, Sarv J, Bruijnzeel PL, Olsson LE, Bondesson E, Nihlén U, McGrath DM, Young SS, Waterton JC, Nordenmark LH (2014) Feasibility assessment of using oxygen-enhanced magnetic resonance imaging for evaluating the effect of pharmacological treatment in COPD. Eur J Radiol 83:2093–2101

Müller CJ, Löffler R, Deimling M, Peller M, Reiser M (2001) MR lung imaging at 0.2T with T1-weighted true FISP: native and oxygen-enhanced. J Magn Reson Imaging 14:164–168

Müller CJ, Schwaiblmair M, Scheidler J, Deimling M, Weber J, Löffler RB, Reiser MF (2002) Pulmonary diffusing capacity: assessment with oxygen-enhanced lung MR imaging preliminary findings. Radiology 222:499–506

Naish JH, Parker GJ, Beatty PC, Jackson A, Young SS, Waterton JC, Taylor CJ (2005) Improved quantitative dynamic regional oxygen-enhanced pulmonary imaging using image registration. Magn Reson Med 54:464–469

Nakagawa T, Sakuma H, Murashima S, Ishida N, Matsumura K, Takeda K (2001) Pulmonary ventilation-perfusion MR imaging in clinical patients. J Magn Reson Imaging 14:419–424

Napadow VJ, Mai V, Bankier A, Gilbert RJ, Edelman R, Chen Q (2001) Determination of regional pulmonary parenchymal strain during normal respiration using spin inversion tagged magnetization MRI. J Magn Reson Imaging 13:467–474

Nogami M, Ohno Y, Higashino T, Takenaka D, Yoshikawa T, Koyama H, Kawamitsu H, Fujii M, Sugimura K (2007) Influences of prolonged apnea and oxygen inhalation on pulmonary hemodynamics during breath holding: quantitative assessment by velocity-encoded MR imaging with SENSE technique. Eur J Radiol 64:375–380

Oechsner M, Pracht ED, Staeb D, Arnold JF, Köstler H, Hahn D, Beer M, Jakob PM (2009) Lung imaging under free-breathing conditions. Magn Reson Med 61:723–727

Ogasawara N, Suga K, Kawakami Y, Yamashita T, Zaki M, Matsunaga N (2004) Assessment of regional lung function impairment in airway obstruction and pulmonary embolic dogs with combined noncontrast electro-cardiogram-gated perfusion and gadolinium diethylenetriaminepentaacetic acid aerosol magnetic resonance images. J Magn Reson Imaging 20:46–55

Ohno Y, Hatabu H, Takenaka D, Adachi S, Van Cauteren M, Sugimura K (2001) Oxygen-enhanced MR ventilation imaging of the lung: preliminary clinical experience in 25 subjects. AJR Am J Roentgenol 177:185–194

Ohno Y, Hatabu H, Takenaka D, Van Cauteren M, Fujii M, Sugimura K (2002) Dynamic oxygen-enhanced MRI reflects diffusing capacity of the lung. Magn Reson Med 47:1139–1144

Ohno Y, Oshio K, Uematsu H, Nakatsu M, Gefter WB, Hatabu H (2004) Single-shot half-Fourier RARE sequence with ultra-short inter-echo spacing for lung imaging. J Magn Reson Imaging 20:336–339

Ohno Y, Hatabu H, Higashino T, Nogami M, Takenaka D, Watanabe H, Van Cauteren M, Yoshimura M, Satouchi M, Nishimura Y, Sugimura K (2005) Oxygen-enhanced MR imaging: correlation with postsurgical lung function in patients with lung cancer. Radiology 236:704–711

Ohno Y, Iwasawa T, Seo JB, Koyama H, Takahashi H, Oh YM, Nishimura Y, Sugimura K (2008a) Oxygen-enhanced magnetic resonance imaging versus computed tomography: multicenter study for clinical stage classification of smoking-related chronic obstructive pulmonary disease. Am J Respir Crit Care Med 177:1095–1102

Ohno Y, Koyama H, Nogami M, Takenaka D, Matsumoto S, Obara M, Sugimura K (2008b) Dynamic oxygen-enhanced MRI versus quantitative CT: pulmonary functional loss assessment and clinical stage classification of smoking-related COPD. AJR Am J Roentgenol 190:W93–W99

Ohno Y, Koyama H, Matsumoto K, Onishi Y, Nogami M, Takenaka D, Matsumoto S, Sugimura K (2011) Oxygen-enhanced MRI vs. quantitatively assessed thin-section CT: pulmonary functional loss assessment and clinical stage classification of asthmatics. Eur J Radiol 77:85–91

Ohno Y, Koyama H, Yoshikawa T, Matsumoto K, Aoyama N, Onishi Y, Takenaka D, Matsumoto S, Nishimura Y, Sugimura K (2012a) Comparison of capability of dynamic O_2-enhanced MRI and quantitative thin-section MDCT to assess COPD in smokers. Eur J Radiol 81:1068–1075

Ohno Y, Nishio M, Koyama H, Yoshikawa T, Matsumoto S, Takenaka D, Sugimura K (2012b) Oxygen-enhanced MRI, thin-section MDCT, and perfusion SPECT/CT: comparison of clinical implications to patient care for lung volume reduction surgery. AJR Am J Roentgenol 199:794–802

Ohno Y, Nishio M, Koyama H, Seki S, Yoshikawa T, Matsumoto S, Obara M, van Cauteren M, Sugimura K (2014a) Asthma: comparison of dynamic oxygen-enhanced MR imaging and quantitative thin-section CT for evaluation of clinical treatment. Radiology 273:907–916

Ohno Y, Nishio M, Koyama H, Yoshikawa T, Matsumoto S, Seki S, Tsubakimoto M, Sugimura K (2014b) Oxygen-enhanced MRI for patients with connective tissue diseases: comparison with thin-section CT of capability for pulmonary functional and disease severity assessment. Eur J Radiol 83:391–397

Pracht ED, Arnold JF, Wang T, Jakob PM (2005) Oxygen-enhanced proton imaging of the human lung using T2*. Magn Reson Med 53:1193–1196

Price A, Prior M, Busza A, Morris P (2004) Single point imaging (SPI) of lung tissue. Proc Int Soc Magn Reson Med 12:858

Price A, White A, Busza A, Morris P (2005) Gadolinium enhanced SPI to assess lung ventilation. Proc Int Soc Magn Reson Med 13:45

Pruessmann KP, Weiger M, Scheidegger MB, Boesiger P (1999) SENSE: sensitivity encoding for fast MRI. Magn Reson Med 42:952–962

Puderbach M, Ohno Y, Kawamitsu H, Koyama H, Takenaka D, Nogami M, Obara M, Van Cauteren M, Kauczor HU, Sugimura K (2007) Influence of inversion pulse type in assessing lung-oxygen-enhancement by centrically-reordered non-slice-selective inversion-recovery half-Fourier single-shot turbo spin-echo (HASTE) sequence. J Magn Reson Imaging 26:1133–1138

Renne J, Hinrichs J, Schönfeld C, Gutberlet M, Winkler C, Faulenbach C, Jakob P, Schaumann F, Krug N, Wacker F, Hohlfeld JM, Vogel-Claussen J (2015a) Noninvasive quantification of airway inflammation

following segmental allergen challenge with functional MR imaging: a proof of concept study. Radiology 274:267–275

Renne J, Lauermann P, Hinrichs JB, Schönfeld C, Sorrentino S, Gutberlet M, Jakob P, Haverich A, Warnecke G, Welte T, Wacker FK, Gottlieb J, Vogel-Claussen J (2015b) Chronic lung allograft dysfunction: Oxygen-enhanced T1-mapping MR imaging of the lung. Radiology 276:266–273

Renne J, Lauermann P, Hinrichs J, Schönfeld C, Sorrentino S, Gutberlet M, Jakob P, Wacker F, Vogel-Claussen J (2015c) Clinical use of oxygen-enhanced T1 mapping MRI of the lung: reproducibility and impact of closed versus loose fit oxygen delivery system. J Magn Reson Imaging 41:60–66

Rupprecht T, Böwing B, Kuth R, Deimling M, Rascher W, Wagner M (2002) Steady-state free precession projection MRI as a potential alternative to the conventional chest X-ray in pediatric patients with suspected pneumonia. Eur Radiol 12:2752–2756

Rupprecht T, Kuth R, Deimling M, Wagner M (2003) Functional lung imaging by MRI – is there a simple solution for a complex problem? Proc Int Soc Magn Reson Med 11:1371

Sá RC, Cronin MV, Henderson AC, Holverda S, Theilmann RJ, Arai TJ, Dubowitz DJ, Hopkins SR, Buxton RB, Prisk GK (2010) Vertical distribution of specific ventilation in normal supine humans measured by oxygen-enhanced proton MRI. J Appl Physiol 109:1950–1959

Sá RC, Asadi AK, Theilmann RJ, Hopkins SR, Prisk GK, Darquenne C (2014) Validating the distribution of specific ventilation in healthy humans measured using proton MR imaging. J Appl Physiol 116:1048–1056

Schoenberg SO, Dietrich O, Reiser MF (eds) (2007) Parallel imaging in clinical MR applications. Springer, Berlin/Heidelberg/New York

Sodickson DK, Manning WJ (1997) Simultaneous acquisition of spatial harmonics (SMASH): fast imaging with radiofrequency coil arrays. Magn Reson Med 38:591–603

Sood BG, Shen Y, Latif Z, Chen X, Sharp J, Neelavalli J, Joshi A, Slovis TL, Haacke EM (2008) Aerosol delivery in ventilated newborn pigs: an MRI evaluation. Pediatr Res 64:159–164

Sood BG, Shen Y, Latif Z, Galli B, Dawe EJ, Haacke EM (2010) Effective aerosol delivery during high-frequency ventilation in neonatal pigs. Respirology 15:551–555

Sood BG, Latif Z, Shen Y, Galli RJ, Dunlap CW, Gelmini MJ, Haacke EM (2012) Aerosol delivery during high frequency jet ventilation: an MRI evaluation. Respir Care 57:1901–1907

Stock KW, Chen Q, Morrin M, Hatabu H, Edelman RR (1999) Oxygen-enhanced magnetic resonance ventilation imaging of the human lung at 0.2 and 1.5 T. J Magn Reson Imaging 9:838–841

Suga K, Ogasawara N, Okada M, Matsunaga N, Arai M (2002a) Regional lung functional impairment in acute airway obstruction and pulmonary embolic dog mod-

els assessed with gadolinium-based aerosol ventilation and perfusion magnetic resonance imaging. Invest Radiol 37:281–291

Suga K, Ogasawara N, Tsukuda T, Matsunaga N (2002b) Assessment of regional lung ventilation in dog lungs with Gd-DTPA aerosol ventilation MR imaging. Acta Radiol 43:282–291

Suga K, Yuan Y, Ogasawara N, Tsukuda T, Matsunaga N (2003) Altered clearance of gadolinium diethylenetri-aminepentaacetic acid aerosol from bleomycin-injured dog lungs: initial observations. Am J Respir Crit Care Med 167:1704–1710

Sundaram TA, Gee JC (2005) Towards a model of lung biomechanics: pulmonary kinematics via registration of serial lung images. Med Image Anal 9:524–537

Takenaka D, Puderbach M, Ohno Y, Risse F, Ley S, Sugimura K, Kauczor HU (2011) Oxygen-enhanced lung magnetic resonance imaging: influence of inversion pulse slice selectivity on inversion recovery half-Fourier single-shot turbo spin-echo signal. Jpn J Radiol 29:244–250

Thieme SF, Dietrich O, Maxien D, Nikolaou K, Schoenberg SO, Reiser M, Fink C (2011) Oxygen-enhanced MRI of the lungs: intraindividual comparison between 1.5 and 3 Tesla. Rofo Fortschr Röntgenstr 183:358–364

Togao O, Ohno Y, Dimitrov I, Hsia CC, Takahashi M (2011) Ventilation/perfusion imaging of the lung using ultra-short echo time (UTE) MRI in an animal model of pulmonary embolism. J Magn Reson Imaging 34:539–546

Topf HG, Wagner M, Kuth R, Kreisler P, Deimling M, Geiger B, Chefd'hotel C, Rupprecht T (2004) Measuring quantitative regional lung ventilation by alveolar ventilation imaging (AVI) – phantom data and results of a feasibility study in 50 patients. Proc Int Soc Magn Reson Med 12:671

Topf HG, Zapke M, Kuth R, Kreisler P, Deimling M, Geiger B, Chefd'hotel C, Rupprecht T (2005) 1.5 Tesla can do too – measuring quantitative regional lung ventilation by AVI (alveolar ventilation imaging) – phantom data and results of a feasibility study in 10 patients. Proc Int Soc Magn Reson Med 13:–46

Topf HG, Biondetti P, Zapke M, Kuth R, Deimling M, Chefd'hotel C, Geiger B, Rupprecht T (2006) Quantitative regional lung ventilation – results in 15 single lung transplanted patients. Proc Int Soc Magn Reson Med 14:1660

Triphan SM, Breuer FA, Gensler D, Kauczor HU, Jakob PM (2015a) Oxygen enhanced lung MRI by simulta-neous measurement of T1 and T2* during free breath-ing using ultrashort TE. J Magn Reson Imaging 41:1708–1714

Triphan SM, Jobst BJ, Breuer FA, Wielpütz MO, Kauczor HU, Biederer J, Jakob PM (2015b) Echo time depen-dence of observed T1 in the human lung. J Magn Reson Imaging 42:610–616

Vaninbroukx J, Bosmans H, Sunaert S, Demedts M, Delcroix M, Marchal G, Verschakelen J (2003) The use of ECG and respiratory triggering to improve the sensitivity of oxygen-enhanced proton MRI of lung ventilation. Eur Radiol 13:1260–1265

Voorhees A, An J, Berger KI, Goldring RM, Chen Q (2005) Magnetic resonance imaging-based spirometry for regional assessment of pulmonary function. Magn Reson Med 54:1146–1154

Voskrebenzev A, Gutberlet M, Becker L, Wacker F, Vogel-Claussen J (2016) Reproducibility of fractional ventilation derived by Fourier decomposition after adjusting for tidal volume with and without an MRI compatible spirometer. Magn Reson Med. 76:1542–1550

Wagner M, Böwing B, Kuth R, Deimling M, Rascher W, Rupprecht T (2001) Low field thoracic MRI – a fast and radiation free routine imaging modality in chil-dren. Magn Reson Imaging 19:975–983

Wang H, Sebrié C, Ruaud JP, Guillot G, Bouazizi-Verdier K, Willoquet G, Maître X, Darrasse L, de Rochefort L (2016) Aerosol deposition in the lungs of spontane-ously breathing rats using Gd-DOTA-based contrast agents and ultra-short echo time MRI at 1.5 Tesla. Magn Reson Med 75:594–605

Wujcicki A, Corteville D, Materka A, Schad LR (2015) Perfusion and ventilation filters for Fourier-decomposition MR lung imaging. Z Med Phys 25:66–76

Zaharchuk G, Busse RF, Rosenthal G, Manley GT, Glenn OA, Dillon WP (2006) Noninvasive oxygen partial pressure measurement of human body fluids in vivo using magnetic resonance imaging. Acad Radiol 13:1016–1024

Zapke M, Topf HG, Zenker M, Kuth R, Deimling M, Kreisler P, Rauh M, Chefd'hotel C, Geiger B, Rupprecht T (2006) Magnetic resonance lung func-tion – a breakthrough for lung imaging and functional assessment? A phantom study and clinical trial. Respir Res 7:106

Zapp J, Domsch S, Weingärtner S, Schad LR (2016) Gaussian signal relaxation around spin echoes: impli-cations for precise reversible transverse relaxation quantification of pulmonary tissue at 1.5 and 3 Tesla. Magn Reson Med. doi:10.1002/mrm.26280 [Epub ahead of print]

Zhang WJ, Niven RM, Young SS, Liu YZ, Parker GJ, Naish JH (2015) Dynamic oxygen-enhanced magnetic resonance imaging of the lung in asthma – initial expe-rience. Eur J Radiol 84:318–326

Zurek M, Johansson E, Risse F, Alamidi D, Olsson LE, Hockings PD (2014) Accurate T(1) mapping for oxy-gen-enhanced MRI in the mouse lung using a seg-mented inversion-recovery ultrashort echo-time sequence. Magn Reson Med 71:2180–2185

Zurek M, Sladen L, Johansson E, Olsson M, Jackson S, Zhang H, Mayer G, Hockings PD (2016) Assessing the relationship between lung density and function with oxygen-enhanced magnetic resonance imaging in a mouse model of emphysema. PLoS One 11:e0151211

Dynamic MRI of Respiratory Mechanics and Pulmonary Motion

Jürgen Biederer, Monika Eichinger,
and Julien Dinkel

Contents

Abstract

Insights into the global and local pathophysiology of respiratory motion, e.g., in patients with chronic obstructive lung disease (COPD), are increasingly appreciated in clinical imaging and research. Dynamic MRI accelerated by parallel imaging and echo sharing reaches temporal resolutions of up to ten images per second in single plane acquisitions or one volume per second in time-resolved 3D imaging. Recently developed, externally, navigator- or self-navigated sequences allow for oversampling of image data during free breathing and retrospective reconstruction of high resolution data sets for different phases of the respiratory cycle. Dynamic MRI allows for repeated and prolonged measurements without radiation exposure to analyze respiratory motion of the lung, the diaphragm, and the chest wall in

J. Biederer, M.D. (✉)
Diagnostic and Interventional Radiology,
University Hospital Heidelberg, Heidelberg, Germany

Radiologie Darmstadt, Gross-Gerau County Hospital,
Gross-Gerau, Germany

German Center for Lung Research (DZL),
Translational Lung Research Center Heidelberg
(TLRC), Heidelberg, Germany
e-mail: biederer@radiologie-darmstadt.de

M. Eichinger, M.D.
Diagnostic and Interventional Radiology, University
Hospital Heidelberg, Heidelberg, Germany

German Center for Lung Research (DZL),
Translational Lung Research Center Heidelberg
(TLRC), Heidelberg, Germany

Department of Diagnostic and Interventional
Radiology with Nuclear Medicine, Thoraxklinik at
University Hospital Heidelberg, Heidelberg, Germany

J. Dinkel, M.D.
Institute for Clinical Radiology, Ludwig-Maximilians-
University Hospital Munich, Munich, Germany

German Center for Lung Research (DZL),
Comprehensive Pneumology Center (CPC),
Munich, Germany

healthy subjects as well as patients. The analysis of respiratory motion has direct clinical impact for adaptive radiotherapy of moving organs like the lung or the liver. This has motivated the development of dynamic volume lung imaging with computed tomography (4D-CT) or MRI (4D-MRI). Both, 4D-CT and 4D-MRI, are principally capable of capturing respiratory motion. Additional morpho-functional imaging capacities of MRI and the radiation exposure involved with 4D-CT give good reasons to prefer dynamic MRI for this purpose. Near-isotropic imaging can be used to assess general and local respiratory mechanics of the lung as well as tumor displacement for adaptive radiotherapy. Dedicated systems with integrated MRI into the radiotherapy equipment are under development or already being installed. Beyond applications for radiation therapy, recent work has shown that 4D-MRI can be used to analyze regional lung ventilation without hyperpolarized gases or oxygen enhancement. This could be a valuable adjunct to classical spirometry giving deeper insights into local lung ventilation in healthy subjects and in patients opening the perspective for a broad spectrum of clinical applications.

1   Introduction

The continuous development of fast acquisition techniques has substantially increased the capacities of MRI for time-resolved large volume imaging. Most prominent fields are cardiac and abdominal imaging, for which MRI has become well recognized. Less known are the capacities of fast MRI to study respiratory mechanics and pulmonary motion. Respiratory mechanics include passive and active components. The passive components are the bones, ligaments, and articulations of the thoracic cage. The active components are the several muscle groups carrying out volume changes. This system is also called the respiratory pump. Of all respiratory muscles, the diaphragm effects most of the volume change.

Other muscles with minor contributions to lung volume are the external and internal intercostal muscles with in- and expiratory action, and the so-called auxiliary muscles (mainly the scalene and sternocleidomastoid muscles), which can contribute to respiratory action if needed, but have other primary functions. The forces generated by the respiratory pump are transmitted to the lungs through the pleural space, which reduces friction and allows the lung to deform freely. Pulmonary motion follows these forces and further depends on the elastic and resistant properties of the lung tissue. Diseases can affect any one of these components, by example in scoliosis the rib cage can be deformed in a way that limits its response to muscular contraction, phrenic paresis immobilizes the affected hemidiaphragm, inflammation of the pleural space can lead to increased friction or immobilization through scarring, and various diseases of the lung can increase or reduce its compliance through alteration of the tissues elasticity or increasing flow resistance in the airways (D'Angelo 1998).

To date, routine clinical assessment of the respiratory system has to rely mainly on indirect lung function tests like spirometry and plethysmography. These do not directly measure the motion of the lung, but the resulting gas flow at the level of the mouth (spirometry) or overall thoracic and abdominal volume changes (plethysmography). Consequently, these measurements do not provide any regional function indices. Since regional deficits are compensated for by healthy parts in other regions of the lung, these global lung function tests are insensitive to localized disease or early manifestations of a diffuse disease (Plathow et al. 2004).

With fluoroscopy and ultrasound it has been possible to directly observe and measure the motion of the hemithorax or single lung for a period of time. However, quantification of regional volume changes with these methods is difficult. Cross-sectional imaging with CT and MRI instead is principally capable of monitoring and quantifying regional volume changes (Biederer et al. 2010). Radiation exposure involved with 4D-CT and additional morphofunctional imaging capacities of MRI give good

reasons to prefer dynamic MRI for this purpose. Moreover, depending on the acquisition technique, dynamic 4D-CT images are usually retrospectively composed from several respiratory cycles and are thus not a "real-time" technique. This averages out any inter-cycle variability and represents only measurement of an average motion. Dynamic MRI is far more sensitive to capture individual inter-cycle variability. This was one of the major motivations to develop radiotherapy systems with integrated MRI equipment (Lagendijk et al. 2014). This chapter is thus intended to give an overview of the application of MRI for the analysis of respiratory mechanics, i.e., the movement of the wall of the thoracic cavity and the motion of pulmonary tissue.

1.1 Technical Concepts

There are essentially two different approaches to imaging of respiratory motion. The static approach uses standard imaging sequences at breath hold to obtain images at two or more different respiratory positions/lung volumes. This approach relies on the same imaging techniques as described for morphological imaging in the other chapters. It has the advantage of providing anatomical detail usable for further analysis like the application of registration algorithms. As a drawback, the lung is allowed to come to a state

of uniform stress and pressure distribution during breath hold (usually patients perform a Valsalva's maneuver when breath-holding, which cannot be controlled for easily). Local differences in movement speed, caused, e.g., by airway stenosis, or hysteresis cannot be detected.

The second approach uses fast imaging to capture images during free breathing in real time. Unfortunately, in MRI, gains in speed are always paid with a reduction in detail. During quiet breathing, respiratory rates are around 12 cycles per minute (5 s per respiratory cycle) and normal respiratory excursion of the diaphragmatic dome is about 1.5 cm. Thus, the maximum speed of the diaphragm is about 0.94 cm/s. Therefore, to avoid motion smear, imaging times should be well below 1 s for imaging of quiet breathing (Biederer et al. 2010).

Dynamic MRI in single plane (2D + t) uses fast 2D-GRE (Gradient-echo-) and SSFP (steady state free precession-) sequences with a temporal resolution of approximately three to ten images per second (Fig. 1). This is achieved with parallel imaging (GRAPPA, SENSE) and is superior to 4D-CT, where temporal resolution depends on the rotation speed of the system. Typical parameters for a dynamic 2D-GRE sequence (acronyms: FLASH, Siemens; SPGR, General Electric; T1-FFE, Philips) and a dynamic SSFP sequence (acronyms: trueFISP, Siemens; FIESTA, General Electric; balanced FFE,

Residual volume ⟶ Vital capacity
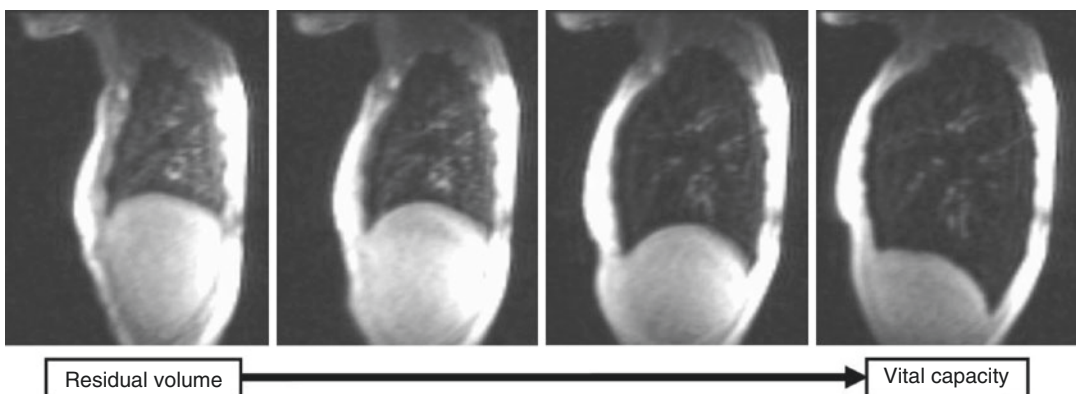
Fig. 1 Selected images from a sagittal 2D FLASH series of the right lung. The original series had a temporal resolution of 8.5 images per second and contained 13 images for inspiration from residual volume to vital capacity. The limited regional information inside the lung stems from the pulmonary blood vessels

Table 1 Imaging parameters for dynamic MRI

Sequ. type	FOV (mm)	Matrix	ST (mm)	TR (ms)	TE (ms)	FA	BW (Hz/px)	Pat	Temp. res. (im/s)
2D-SS-GRE (TrueFISP)	400	159 × 256	10	37.7	1.7	65°	977	2	3
2D-GRE (FLASH)	500	98 × 128	15	2.49	1.03	5°	980	2	10
3D-GRE (FLASH)	450	128 × 128	8	1.38	0.5	10°	1500	4	2

Image parameters for sequences typically used for dynamic MRI. The acronyms stated are for Siemens scanners, acronyms for other manufacturers can be found in the text

Philips) with parallel imaging using an acceleration factor of 2 are listed in Table 1 (Fabel et al. 2009). While fast 2D-GRE sequences have the advantage of higher temporal resolution (Fig. 1), SSFP sequences offer a higher signal from the blood vessels that provide the main spatial information in dynamic lung MRI and may be used for segmentation landmarks (Plathow et al. 2005b). 2D + t imaging with MRI has the capacity to observe the motion of lung and chest wall over more than one respiratory cycle. Instructed and forced breathing maneuvers can be performed in real time with free choice of imaging planes (Swift et al. 2007).

For 1.5 and 3 T systems, acceleration factors of 2–3 are recommended. At 1.5 T, the modified SSFP sequence with parallel imaging achieved a superior spatial resolution to the GRE sequence (with equal temporal resolution). In experimental work at 3 T, contrast-to-noise ratios for the GRE sequence improved while the SSFP sequence was impaired by increasing flow artifacts and field inhomogeneities. It is therefore suggested to use SSFP sequences on 1.5 T and GRE sequences on 3 T systems (Fabel et al. 2009).

Dynamic MRI of the total lung volume (3D + t = 4D) is usually realized with very fast 3D-GRE or SSFP sequences. Echo sharing and parallel imaging allow to use a primary matrix of 128 × 128 pixel and a voxel size of approximately 4 mm in all dimensions at up to two volumes per second (Fig. 2) (Biederer et al. 2009). Typical parameters are listed in Table 1. As discussed above, imaging times of less than 1 s per volume are necessary to capture lung motion at normal respiration frequencies. However, the trade-off

between imaging speed and spatial resolution results in inferior image quality of very fast 4D series. As a workaround, very slow controlled breathing helped to obtain reasonably good results for dynamic 3D studies (Plathow et al. 2005a). Still, image quality and detail resolution of 3D + t-MRI are inferior to 2D + t. Signal to noise in the normal lung is low when these sequences (originally designed for contrast-enhanced angiography) are used without contrast. The delineation of fast moving structures necessarily remains blurry during the rapid phases of the respiratory cycle.

A simple approach to combine the advantages of 2D + t and 3D + t imaging are retrospectively gated 4D-MRI with 2D-GRE sequences using redundant acquisitions of 2D-GRE sequences that are retrospectively sorted by respiratory phase by an external trigger signal, e.g., a respiration belt. Compared to "real-time" 4D acquisitions, image quality and detail resolution are improved. Remmert et al. achieved a pixel size of 2.7 × 2.7 mm at 10 mm slice thickness (typical parameters are TR = 3.4 ms, TE = 1.5 ms, acquisition time per image = 160 ms, flip angle = 10°, band width 980 Hz/pixel, FOV 400 mm, matrix 128 × 128, pixel-size 3.1 × 3.1 mm, slice thickness 10 mm) (Remmert et al. 2007). Due to the short acquisition time of each single slice, motion artifacts were markedly reduced in comparison to dynamic volume acquisitions.

A very recent development is self-navigated MRI. Typically, this technology is based on 3D-GRE sequences with radial K-space acquisition and highly redundant acquisition of data. The signal obtained in the central K-space varies throughout the respiratory cycle and is used to
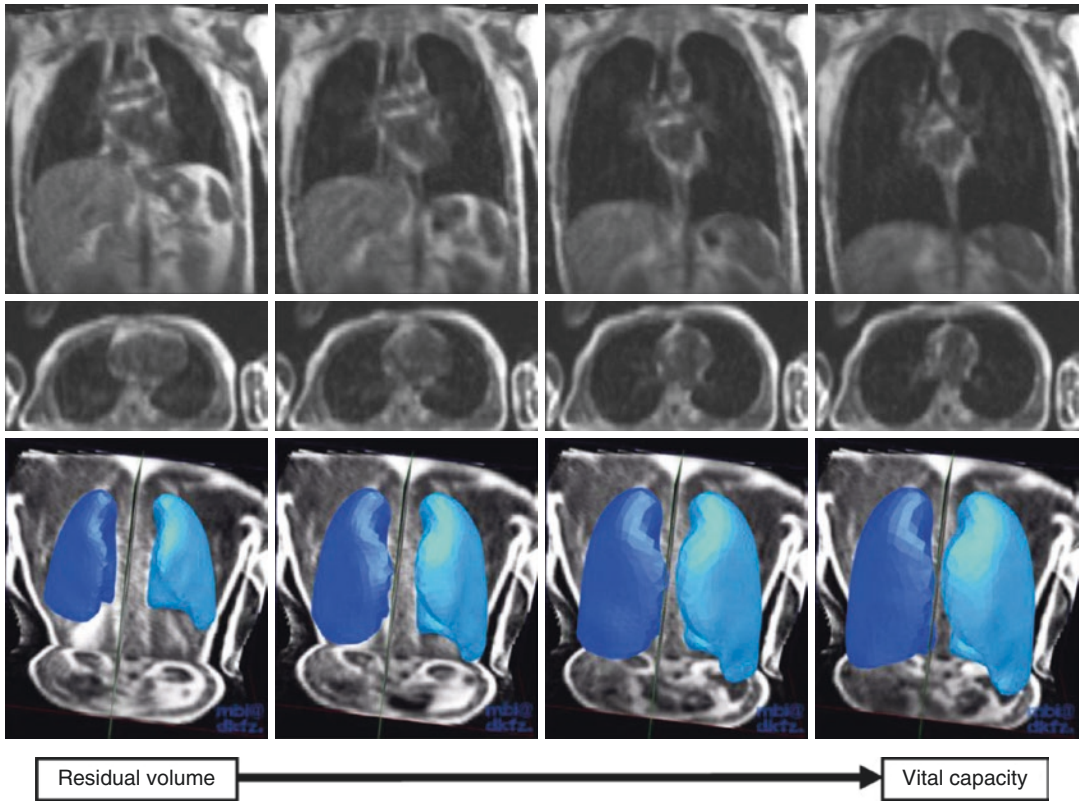
Fig. 2 Selected images from a sagittal 3D FLASH series with a temporal resolution of one image per second with 3D reconstruction of the lung by automatic segmentation. At this temporal resolution mostly noise is visible inside the lung. Nevertheless, the images are well suited for analysis of the thoracic configuration and lung volumetry, e.g., through automatic segmentation

group or bin data for respiratory phases. 3D images can then be reconstructed for each bin/respiratory phase. Additional features such as auto-focusing, 3D image correlation, K-space weighted image contrast, and principal component analysis contribute to improvement of image quality (Lin et al. 2008; Weick et al. 2013). Since images are obtained during free breathing, image quality can be optimized with very long acquisitions (Fig. 3a, b). If 4D-MRI is recorded over a longer period of time, it covers the individual range of changes in respiration depth and frequency (Blackall et al. 2006). Dinkel et al. showed with 4D-MRI, how the individual motion pattern of lung tumors may vary in patients with diaphragmatic palsy (Dinkel et al. 2009). This included lateral components of tumor motion up to displacement of the mass in the opposite of the

expected direction due to unilateral palsy. It was concluded that 4D-MRI over several respiratory cycles may provide valuable additional information for radiotherapy planning.

A major obstacle for the implementation of 4D-MRI in clinical practice is the lack of appropriate tools for 4D-viewing and interpretation in most current medical image viewing software packages. Some workstations are capable of 4D image display incorporating basic MPR as well as volume rendering functionality. The overlay of a metric crosshair grid may be useful to follow the displacement of structures throughout the respiratory cycle. Unless comfortable software solutions become more broadly available, successful implementation of 4D imaging technology outside academic centers will remain exceptional (Biederer et al. 2010).
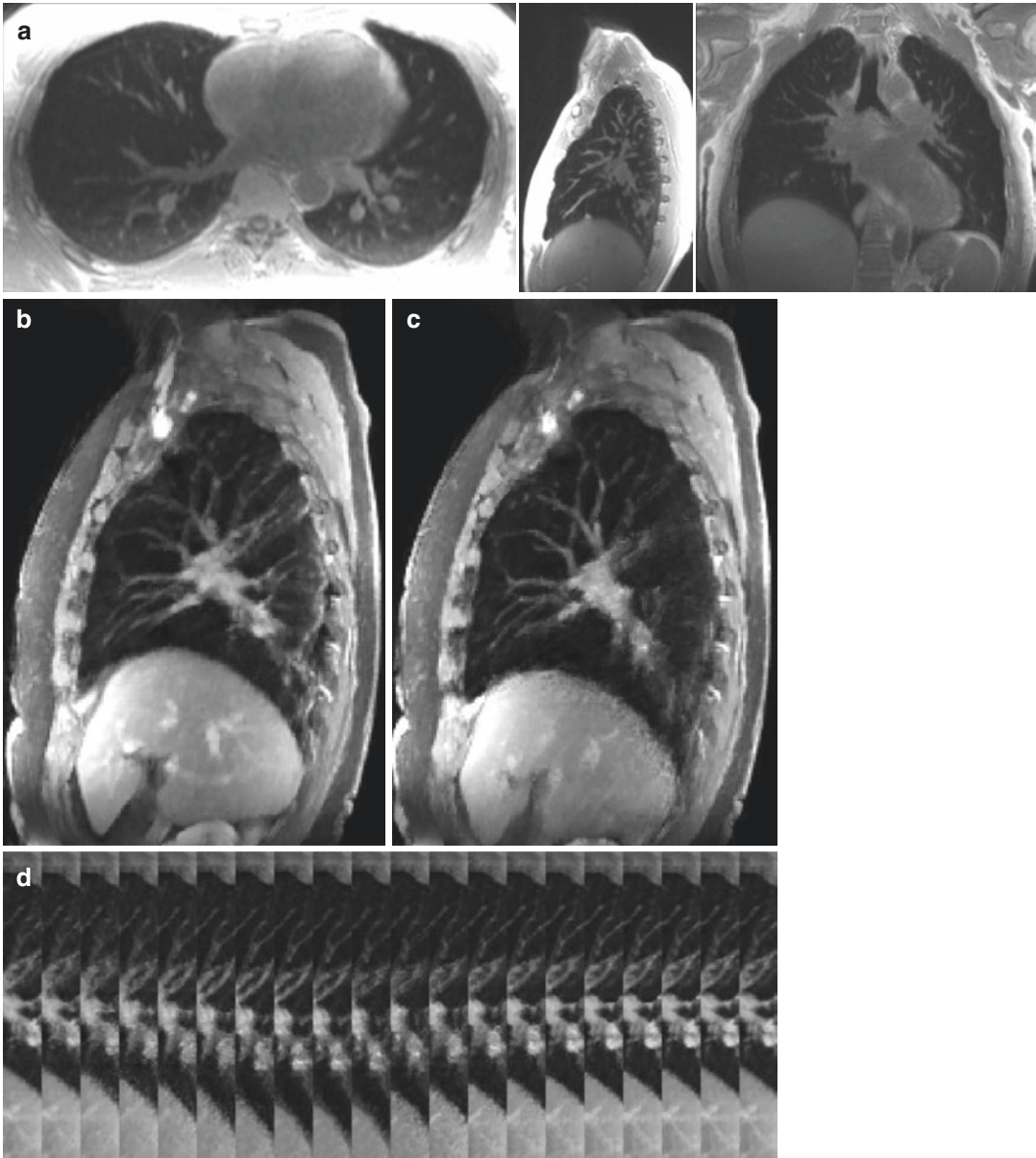
Fig. 3 (**a**) MPR of self-navigated GRE images. The 3D data were acquired in free breathing during 5 min. Pictures are reconstructed in expiratory phase with a 1.5 mm³ isotropic resolution. (**b**) The images show a sagittal slice of the right lung in a 4D-MRI dataset. (**b**) and (**c**) show a slice in end-expiration and end-inspiration phases, respectively. (**c**) shows a central part of each slice for each of the 20 retrospectively reconstructed phases

1.2 Magnetic Resonance Compatible Spirometry

Spirometry and plethysmography are the gold standard techniques for lung function testing. Diagnostic parameters derived from MRI measurements will have to be compared to these techniques. But both spirometry and plethysmography are characterized by high intrapersonal variability (Miller et al. 2005). Therefore, imaging and lung function tests should be acquired simultaneously. Unfortunately, most spirometers are made with at least some metal parts or contain electronic components and are therefore unsuitable for use inside

the MRI suite. To overcome these obstacles, commercially available spirometers can be adapted successfully for MR compatibility with some modifications. Two approaches have been reported so far (Kondo et al. 2000; Eichinger et al. 2007). Both worked with spirometers using pneumotachographs. These make subjects breath through a small air flow resistance. The resistance causes a pressure drop which changes linearly with the air flow and is measured by an electronic component. To ensure MR compatibility, metal parts are replaced by plastic substitutes and the pressure sensitive electronics are mounted outside the scanner cabin and connected by pressure transducing plastic tubes. Such modifications can be made without affecting the measurement precision of the spirometer (Eichinger et al. 2007). Naturally, the spirometric measurements obtained during MRI differ from measurements obtained under standard conditions. The supine position as well as the use of surface coils reduces air flow during maximal respiratory maneuvers (Meysman and Vincken 1998; Eichinger et al. 2007). One problem for comparative analysis of spirometry with MRI measurements is the missing temporal synchronization of the measurements that are acquired with two different computer systems. Kondo et al. (2005) solved this by recording the scanner noise on the spirometry system and using the increase in noise during image for temporal matching. Another solution would be to synchronize the system timers of the spirometer and the MRI scanner to the same network time server, so that the time information in the image header and spirometry record can be used directly.

2 Respiratory Mechanics

MRI is an ideal tool for analysis of the motion of diaphragm and thoracic wall. The low signal of lung tissue leads to an excellent contrast to the surrounding high signal soft tissue structures. Thus, the combined action of the different components of the respiratory pump can be visualized and the functional principle analyzed.

Generally speaking, published research can be divided in two categories. The first analyzes the movement of individual components (lung, diaphragm, and rib cage) for better understanding of their individual action. The second approach attempts to calculate the lung volume changes by segmentation of measurement of surrogate markers on the acquired images.

Imaging techniques are basically the same for both approaches, as always the whole thorax (in the case of 2D dynamic MRI one slice through the thorax) is imaged. The differences between the studies lie in the measurements and analysis on the images. The images can then be subjected to a qualitative analysis, and in many cases, meaningful information can be derived, e.g., a phrenic paresis is immediately evident from two images in inspiration and expiration. But for differentiation of severity of a disease or for detection of small abnormalities, quantitative measures are necessary. As the field of research is still rather new and only a limited number of publications exist, no standards for imaging procedures, the location of measurements, and the analysis of measurements have emerged. This limits the comparability of results from different studies, but it appears to be only a matter of time for clinical meaningful measures and applicable measurement methods to emerge.

2.1 Movement of the Diaphragm

The diaphragm is the biggest respiratory muscle and by itself responsible for most of the volume changes during quiet and to a somewhat lesser degree during forced respiration. It is a flat muscle sheet with a central tendinous component. By its muscular insertions it can be divided in two components. The muscular fibers of the crural part arise from the first three lumbar vertebral bodies and the medial and lateral arcuate ligaments. The costal part inserts on the inner surfaces of the lower six ribs. During quiet breathing, a considerable fraction of the diaphragm is opposed to the inner rib cage and thus forms the cylindrical "area of apposition" which is capped by the diaphragmatic dome (Mead et al. 1986). As it is normally hidden inside the body, the exact area distribution between the apposition zone and the diaphragmatic dome and the three-dimensional configuration are difficult to measure. Tomographic imaging has been a breakthrough in this respect.

2.1.1 Static Imaging

Several groups used static MRI at different respiratory volumes to gain further insight into the function of the diaphragm. Images were acquired during breath hold with relaxed diaphragm in sagittal and coronal orientation. On each of the resulting images, the diaphragmatic contour was traced. The combined tracings form a wireframe representation of the diaphragmatic contour (Fig. 4). From this, changes in diaphragmatic length (Table 2), area (Table 3), and curvature can be derived and correlated to the respective changes in lung volumes. According to these results, the Laplace law is applicable to at least the posterior part of the diaphragmatic dome. As the Laplace law links the pressure across a surface with the surface's curvature and the pressure gradient across the surface, this allows the calculation of the diaphragmatic tension from its curvature and the transdiaphragmatic pressure (Paiva et al. 1992). Further results confirm the remarkable ability of diaphragmatic fibers to shorten up to 55% during contraction (Gauthier et al. 1994; Cluzel et al. 2000). This ability allows the diaphragm to effect the respiratory volume changes descending like a piston in a cylinder. While the diaphragmatic dome does change in form with anteroposterior widening, flattening, and dorsal rotation, the effect of these changes on transdiaphragmatic pressure are small. Consequently, the
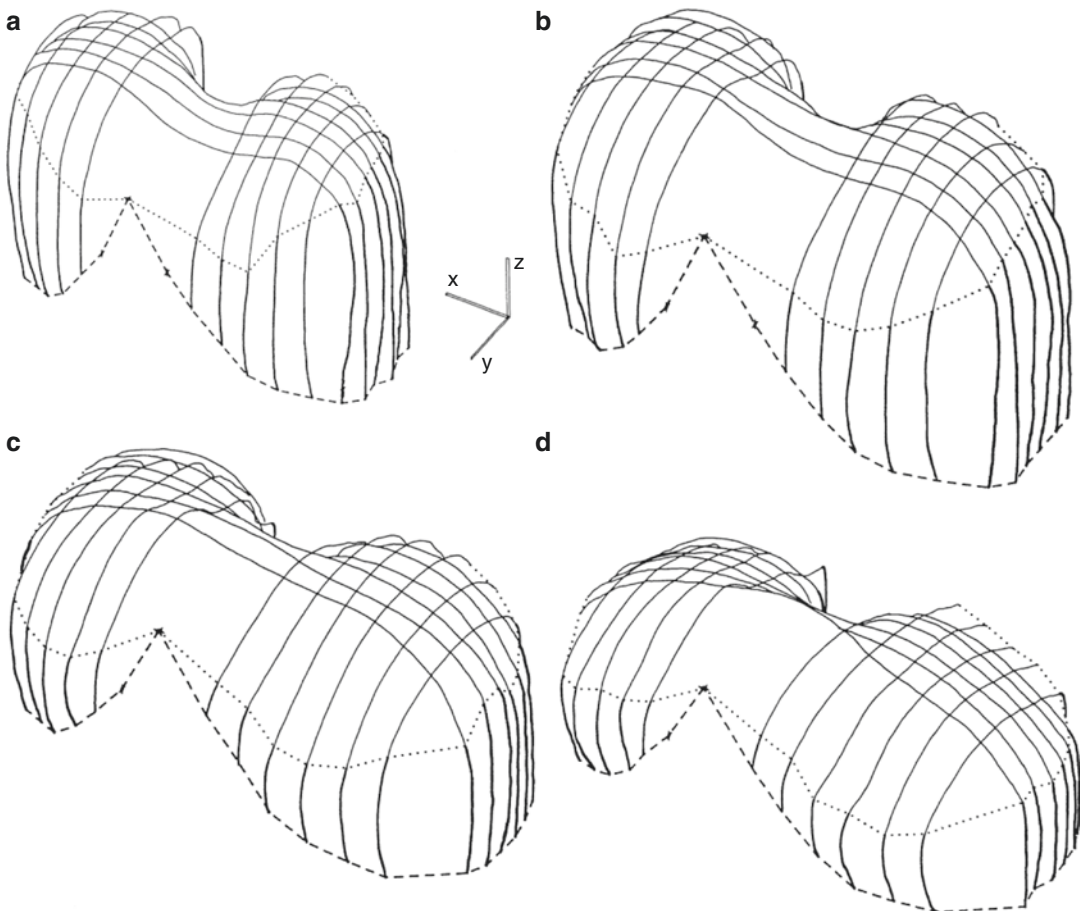
Fig. 4 Wireframe reconstructions of the diaphragm at residual volume (**a**), functional residual capacity (**b**), FRC plus one-half inspiratory capacity (**c**), and vital capacity (**d**). *Dashed lines* show the lower costal margin, *dotted lines* the upper limit of the zone of apposition. The *3D axis* indicates spatial orientation and scaling with line length of 50 mm. Reprinted with permission of the American Physiological Society (Gauthier et al. 1994)

Table 2 Diaphragmatic lengths as a whole and separately for its appositional part (part that is directly apposed to the thoracic wall) and the diaphragmatic zone (apposed to the lung) at different lung volumes as measured by Cluzel et al. (2000)

	RV	FRC	TLC
Diaphragm			
Coronal	507 ± 72	485 ± 77	365 ± 79
Sagittal left	330 ± 15	301 ± 17	208 ± 12
Sagittal right	368 ± 20	354 ± 22	228 ± 23
Appositional zone			
Coronal	254 ± 17	221 ± 35	0 or close to 0
Sagittal left	163 ± 16	127 ± 21	0 or close to 0
Sagittal right	196 ± 11	161 ± 25	0 or close to 0
Diaphragmatic zone			
Coronal	253 ± 69	264 ± 64	365 ± 79
Sagittal left	167 ± 13	174 ± 15	208 ± 12
Sagittal right	173 ± 17	194 ± 8	228 ± 23

RV residual volume, *FRC* functional residual capacity, *TLC* total lung capacity

Table 3 Areas of the whole diaphragm, the appositional part, the diaphragmatic dome and the diaphragmatic muscle surface (diaphragmatic area minus central tendon area) as measured by Cluzel et al. (2000)

	RV	FRC	TLC
Total diaphragmatic area	1128 ± 129	997 ± 93	584 ± 89
Apposition area	757 ± 121	597 ± 91	0 or close to 0
Diaphragmatic dome area	371 ± 28	399 ± 27	584 ± 89
Diaphragmatic muscle surface area	985 ± 129	854 ± 93	441 ± 98
Percentage decrease	Reference	13 ± 8	55 ± 11

RV residual volume, *FRC* functional residual capacity, *TLC* total lung capacity

diaphragmatic action is described with the term of a widening piston in a widening cylinder, which means that volume changes through diaphragmatic action are nearly linearly related to diaphragmatic muscle fiber length (Gauthier et al. 1994). These conclusions depend on the assumption that the apposition zone does not entirely disappear even at total lung capacity. This is controversial as the location of the diaphragmatic costal attachment can only be derived indirectly and Cluzel et al. found the apposition zone to disappear at TLC (Cluzel et al. 2000). Thus, at least at volumes near TLC, the above results might not be entirely valid. As a further limitation, the results are based on imaging of the relaxed diaphragm. Thus, its form should be considerably influenced by the adjacent structures. The configuration during contraction, i.e., inspiration, might differ considerably. Also, the configuration will be different when not in the supine position, as described further on.

2.1.2 Dynamic Imaging

During most of the respiratory cycle, the diaphragm is in motion, either actively contracting during inspiration or passively expanding during expiration. To truly understand its mode of function in contributing to lung volume changes, static analysis as described above is not ideal. While dynamic 3D + *t* MRI is not yet fast enough to allow comparable experimental designs, dynamic 2D + *t* MRI offers the necessary speed. The sacrifice of spatial coverage can be compensated for by acquiring several sagittal image series at different lateral positions. Under the assumption that diaphragmatic motion is more or less constant during quiet respiration, these measurements show that the craniocaudal displacement of the diaphragm in supine position is not evenly distributed. The diaphragmatic excursion increases from anterior to posterior and at each anteroposterior position from medially to

Fig. 5 Excursion of the diaphragm relative to its maximal excursion. The *three lines* represent the motion at three different anteroposterior positions, the middle line (*D*) was measured at the diaphragmatic dome, the top line (*P*) in the middle between *D* and the posterior costophrenic angle, the lower line (*A*) in the middle between *D* and the anterior costophrenic angle. Numbers on the horizontal axis indicate different lateral positions: Midline (*4*), 2 cm to the right (*3*) and left (*5*) of midline, middle of right (*2*) and left (*6*) hemithorax, positions *1* and *7* are in the middle between *3* and *5* and the lateral chest wall, respectively. Reprinted with permission of RSNA (Gierada et al. 1995)
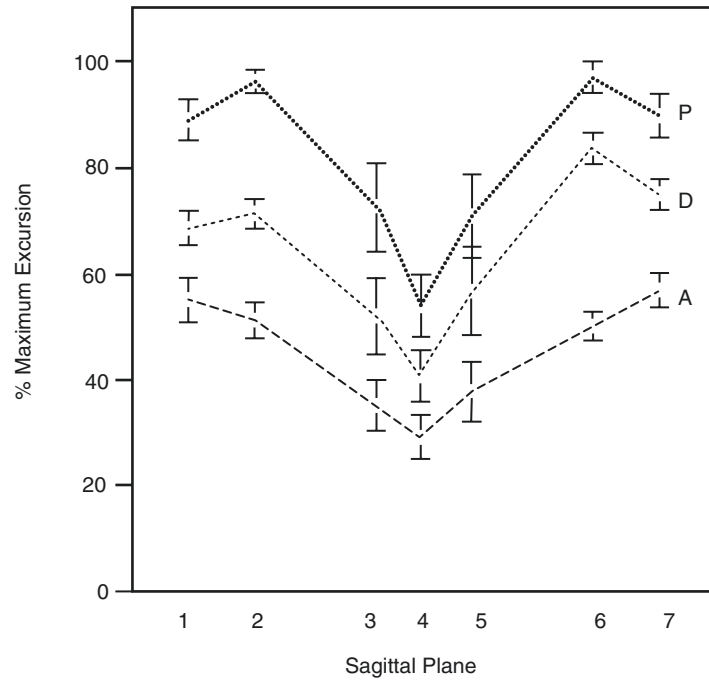
Table 4 Excursion of left and right hemidiaphragm at different body positions

	n	Body position	Right (cm)	Left (cm)
Gierada et al. (1995)	10	Supine	4.4 ± 1.3	4.2 ± 0.9
Ünal et al. (2000)	15	Supine	6.0	5.0
Takazakura et al. (2004)	10	Sitting	8 ± 2.3	8 ± 2.4
		Supine	9.2 ± 2.1	10.3 ± 2
Kiryu et al. (2006)	8	Supine	8.9 ± 1	7.5 ± 1.1
		Prone	9.3 ± 0.3	8.1 ± 0.6
		Right lateral	9.1 ± 0.9	7.7 ± 1.1
		Left lateral	8.4 ± 1.2	8.2 ± 1.2

laterally (Fig. 5). Using dynamic 2D-MRI in coronal orientation it is possible to directly compare the movement of the left and right hemidiaphragm. Apparently the two sides can move synchronously or one side can move slightly ahead of the other. The respective pattern can also change from inspiration to expiration. There is some discussion whether one hemidiaphragm moves more than the other one (see Table 4 for excursion data). Kiryu et al. (2006) found a larger excursion on the right and attributes the different findings of earlier studies to the averaging effect of the respective lower temporal resolution (Gierada et al. 1995; Unal et al. 2000; Takazakura et al. 2004; Craighero et al. 2005; Kiryu et al. 2006).

The results discussed so far are all based on imaging in the supine position. As postural changes have an effect on intraabdominal pressure, diaphragmatic motion should differ in the upright position. In a study conducted in a vertical MRI, diaphragmatic excursion was 1–2 cm less than in the supine position. Differences were more pronounced in the posterior diaphragm. This reduces the difference of excursion between anterior and posterior diaphragm from maximally 51–38 mm. This effect could be explained by the steeper anteroposterior abdominal pressure gradient in the supine position. The posterior diaphragm is consequently pushed more cranially. This has the side effect that the force-tension characteristic of the diaphragm is improved

through increased muscle fiber length (Takazakura et al. 2004). The same effect can be observed when changing from supine to prone and either lateral decubitus position. The respective dependent diaphragm lies more cranially and starts to move later in inspiration and earlier in expiration (Kiryu et al. 2006).

2.2 Chest Wall Movement

Under physiologic conditions, the chest wall contributes less to lung volume changes than the diaphragm. Nevertheless, imaging of respiratory mechanics has to account for this significant component of the respiratory pump. MRI with its high contrast between air filled lung and adjacent thoracic wall is an ideal instrument to quantitatively analyze chest wall movement. As in diaphragmatic imaging, dynamic analysis requires high temporal resolutions and consequently, time-resolved 2D imaging is the method of choice in most of the studies.

Under normal conditions, both sides of the thorax move synchronously and have the equal maximal excursions (Suga et al. 1999). Differences are found between the upper and lower chest wall, which do not seem to move as a single functional unit. While the anteroposterior movement of the upper thorax is linearly related to lung volume changes, the lower thorax is poorly synchronized to lung volumes (Kondo et al. 2000). It is possible to deduct the respective contributions to lung volume changes. In comparison to diaphragmatic displacements, the anteroposterior thoracic expansion contributes only two-fifth to lung volume changes. The contribution of transverse expansion of the thorax again is only half of the latter (Kondo et al. 2000). These patterns have primarily been found in healthy young subjects but a later study with elderly healthy subjects found no significant differences between age groups (Kondo et al. 2005).

2.3 Volumetry

Comparison of dynamic MRI measurements to standard lung function tests has received a lot of interest in scientific work. As dynamic MRI makes it possible to image single lungs and to some degree even distinguish lung lobes, a good agreement of MRI measures to spirometry could pave the way to regional lung function testing on a split lung or even lobar basis.

Many studies used 3D imaging of the thorax to determine the volume of the low signal lung tissue. With this approach the temporal resolution is limited by the measurement time of the MRI. The fastest measurements of 3D images of the lung reported take about 1 s per volume (Plathow et al. 2005a). This is not sufficient to measure lung volumes during tidal breathing at normal respiratory frequencies. In intentionally slow breathing, continuous volume measurements with 3D-MRI correlate well to spirometric measurements (Gierada et al. 1998; Plathow et al. 2005a). Alternatively, i.e., to achieve higher temporal resolution, 2D imaging can be used. The area of the lung in sagittal and transversal sections is well correlated to spirometric lung volume ($r > 0.8$) (Kondo et al. 2000). From 2D imaging in different orientations, diameter measurements can be used to calculate lung volumes using a geometrical model of the lung. This has been reported to provide volume measurements with a high correlation to spirometric measurements (Plathow et al. 2004). The forced expiratory volume in the first second (FEV1) is a standard test for assessment of obstructive lung disease. In this maneuver, the subject is asked to expire as fast as possible from maximal inspiration. The volume expired during the first second of this maneuver is measured. To derive this measure from dynamic MRI, only very fast imaging techniques are applicable. Swift et al. (2007) used 2D spoiled gradient echo sequence to image the thorax in coronal and sagittal orientation with a temporal resolution of five to ten images per second (Swift et al. 2007). From these images, volumes were calculated with an elliptical model, the long and short axis measured on the sagittal and coronal image. They found a very high correlation to spirometric for FEV1 and FVC (correlation coefficients of 0.95 and 0.83, respectively).

These results indicate that static and dynamic volume measurements with MRI are feasible with adequate precision. Therefore, volume measurements of single lungs should give meaningful

Table 5 Volume distribution between left and right lung

Publication	Collective	Phase	Sample size	Left	Right
Chapman et al. (1990)	Infants (2–10 months)	Mid-tidal	9	47.2%	52.8%
Qanadli et al. (1999)	Young adults (24–32 years)	Insp	15	48%	52%
		Exp	15	45%	55%
		VC	15	49.7%	50.3%
Plathow et al. (2005a)	Young adults (19–35 years)	VC	20	45%	55%

results. Table 5 shows the MRI-derived volumes of single lungs found in different studies. All found a significant difference between both lungs with the right lung having slightly higher volume. This agrees well with anatomical data and can easily be explained by the volume taken up by the heart on the left (Mead et al. 1986).

Measurements of thoracic diameters on dynamic MRI of single lungs also show good correlation (correlation coefficients above 0.85 for anteroposterior, craniocaudal, and lateral thoracic diameters) to spirometrically measured VC and FEV1%. Even though the spirometric data available for comparison are global, the high correlation indicates the validity of measurements on single lungs. Further results, gained by inserting diameter measurements in a more complicated geometric model as the one used by Swift et al. (2007), show that craniocaudal movement contributes most and lateral expansion less to lung volume changes which is in good agreement with other physiological studies (Plathow et al. 2004; Swift et al. 2007).

The results described so far are based on the diameter differences between only two images of the multitude of images acquired (e.g., the images with highest and lowest position of the diaphragm for VC or the image acquired 1 s after the highest diaphragm position for FEV1). With a simultaneous spirometric measurement using an MRI-compatible spirometer, the volume changes occurring between the acquisitions of two images (approx. 120 ms) can be compared to the corresponding dynamic MRI measurements. This is illustrated in Fig. 6a, where the volume changes calculated from 2D-MRI of the right lung are plotted together with simultaneously measured

spirometric volume changes. From such 2D-MRI measurements realistic flow volume curves of single lungs can be derived as shown in Fig. 6b.

The normalized craniocaudal diameter changes for each hemithorax are highly correlated to normalized spirometric volumes (correlation coefficient of 0.93). The surrogate for FEV1% calculated from MRI measurements was also highly correlated to spirometric FEV1% for each hemithorax (correlation coefficient of 0.71) (Tetzlaff et al. 2008).

When comparing lung volume measured with MRI to spirometrically measured volumes it is important to keep in mind that the former usually contains also volume occupied by the lung tissue and blood content. From MRI volumetry at maximal inspiration combined with plethysmographic measurement of TLC this volume can be calculated to be around 840 mL (Qanadli et al. 1999) which is in good agreement with indicator dilution studies that found the blood volume in healthy subjects to be about 250 mL (Dock et al. 1961) and the tissue volume about 600 mL (Cander and Forster 1959).

In all MRI measurements, post-processing is needed to extract the volumes or volume surrogates from the images. The post-processing techniques range from manual (O'Callaghan et al. 1987; Chapman et al. 1990; Plathow et al. 2004) to semiautomatic (Tetzlaff et al. 2008). Even though the post-processing method very likely influences the precision of measurements, this error is rarely evaluated. That time savings from semiautomatic measurement comes at a cost was recently shown for the measurement of thoracic diameters. This could be accelerated by a factor of four compared to manual measurements and

Fig. 6 (**a**) Normalized
volume-time curves
from spirometric
measurement and
calculated from 2D-MRI
(product of
anteroposterior and
craniocaudal diameter)
(**b**) Flow-volume curve
calculated from the same
data as used in (**a**). The
curve derived from
2D-MRI closely follows
the course of the
spirometric curve and
only fails to exactly
reproduce the sharp
downturn at the
beginning of the
measurement
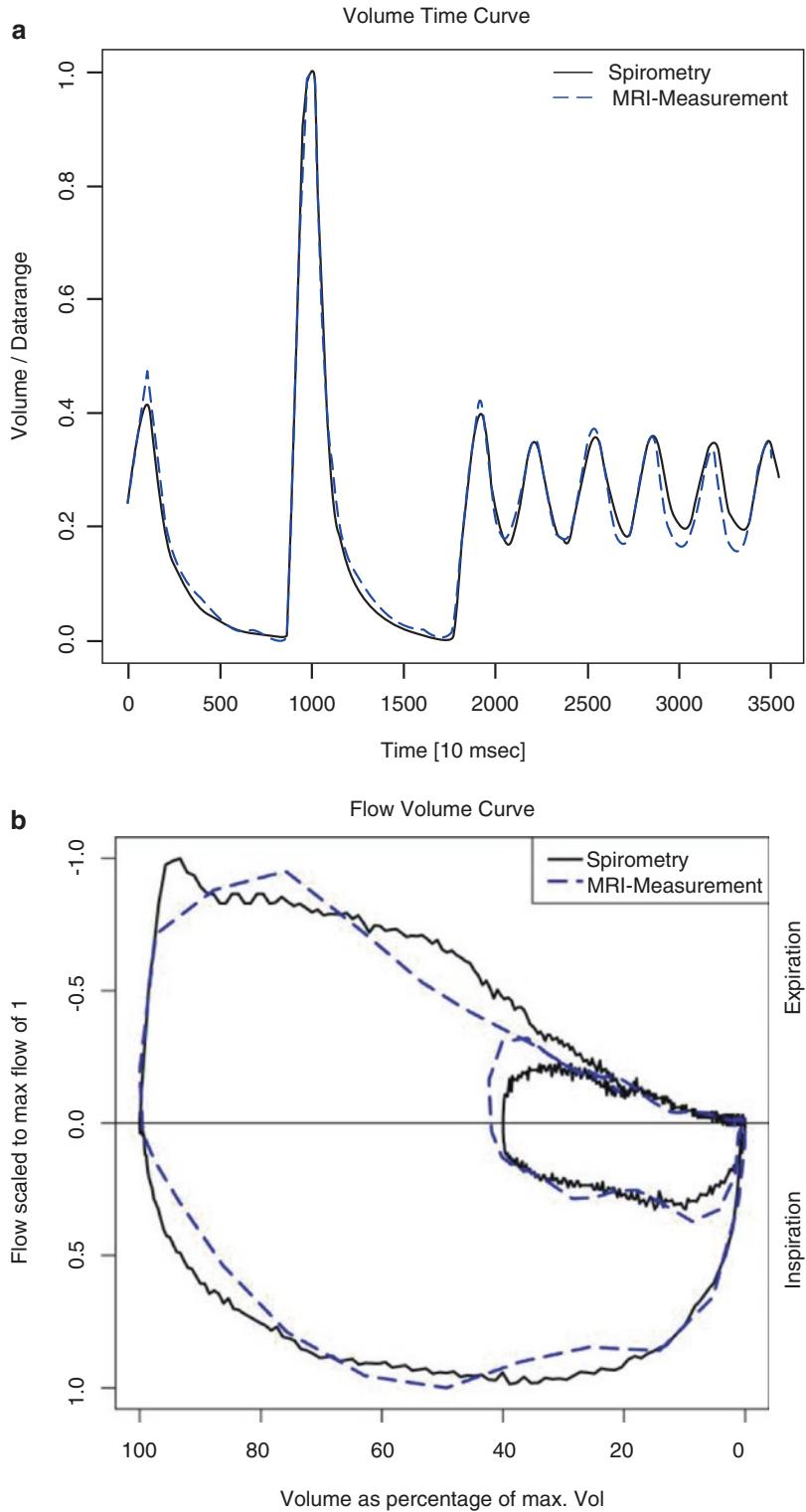
the agreement with manual measurement was reduced by about 3 mm, the side length of a single voxel in the study (Tetzlaff et al. 2008).

Semiautomatic measurement of lung area from 2D-time-resolved MRI shows an even better agreement to simultaneously acquired spirometry with mean correlation coefficients >0.97. This post-processing method proved fast enough for application in a clinical context and possibly provides increased sensitivity for lung functional measurement of inhomogeneously distributed lung disease (Tetzlaff et al. 2010).

3 Pulmonary Motion

3.1 Displacement of Lung Parenchyma

The quantification of parenchymal lung motion is the most challenging, but at the same time the most promising field of investigation in dynamic MRI of the lung. While the low signal of aerated lung tissue facilitates the measurement of chest wall or diaphragm motion, registration of tissue motion itself requires the detection of recognizable landmarks throughout the lung parenchyma. In currently available sequences for dynamic MRI, the central vessels mainly provide suffi-

cient signal as landmarks. Towards the periphery, the vessel contrast to lung tissue rapidly decreases and the number of useful landmarks is low.

A promising approach to the imaging of pulmonary motion lies in creating landmarks by MRI grid-tagging. Grid-tagging has been previously used to assess the motion and deformation of myocardial tissue. Using an ultra-short-TE fast low-angle shot pulse sequence it has been applied for assessment of pulmonary mechanics with limited success. The critical point is the rapid signal decay with short T2* times in lung tissue. Nevertheless, it has been shown that a rectangular grid of saturation stripes can still be identified approximately 1000 ms after its application. Using 2D-MRI with a temporal resolution of up to eight images per second allows imaging of pulmonary tissue motion over the short time span of at least 1 s (Chen et al. 2001). From these images, the 2D tissue strain tensor (represented by a 2×2 matrix) can be calculated (Fig. 7). From its elements, measures to quantitatively describe lung deformation can be derived. The trace of the vector (sum of the diagonal elements) can be considered to be a generalized direction-independent strain magnitude. In coronal images of healthy volunteers, this was maximal at the base and apex of the lung, with lower values at the hilum where the large bronchi and vessels
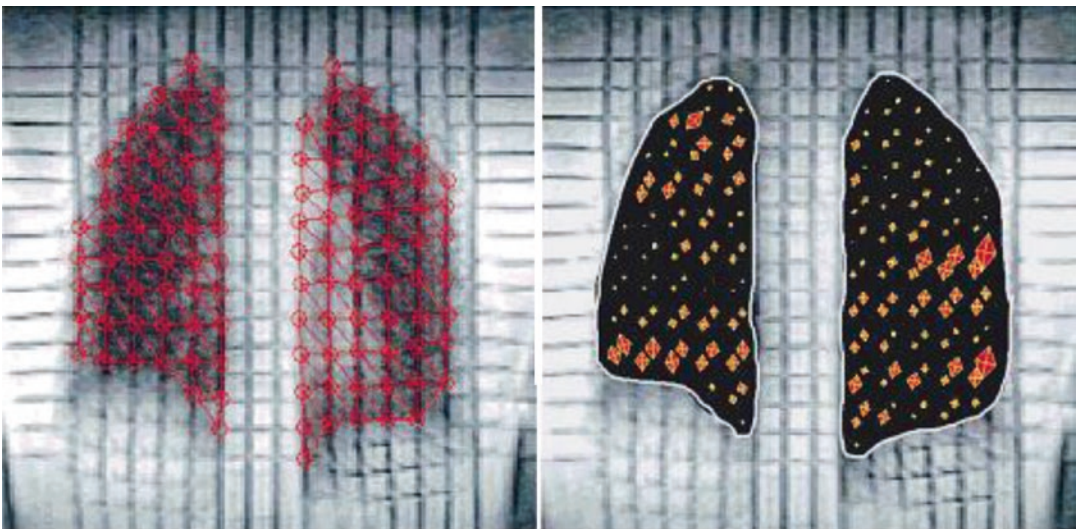
Fig. 7 Quantitative evaluation of the lung deformation in coronal plane during forced inspiration by grid-tagging MRI. The *left* image shows mesh triangular elements fitted to the tagging grid for calculation of the strain tensor that is visualized in the image on the *right* (reprinted with permission of John Wiley & Sons, Inc. (Chen et al. 2001))

reduced the lung elasticity. The directional dominance of shear could also be calculated and showed that the craniocaudally oriented strain was predominant at the apex and base of the lung. In the middle lung field, strain was more laterally oriented. On sagittal images, the maximum tissue expansion occurred at the apex and was greater posteriorly than anteriorly (Napadow et al. 2001). The imaging sequence was further improved to allow for continuous measurement through repeated grid application. In extension to the work described above the authors were able to calculate the regional air flow rate and volumetric strain, and to derive volume time and flow-volume curves for the upper, middle, and lower lung zones (Voorhees et al. 2005). These results indicate the potential to considerably improve lung function diagnostics in the future with dynamic MRI. However, clinical applications have not been reported so far.

Alternatively to relying on native 1H-MRI signal of lung tissue, dynamic multinuclear MRI with hyperpolarized (HP) inert noble gas isotopes, i.e., He-3 and Xe-129, can make gridding of lung parenchyma more efficient. HP gases act as positive contrast agents that distribute rapidly in the airspaces of the lungs. 2D + t and 3D + t MRI are applied to study lung ventilation dynamics with frame rates in the order of 5–10 ms (Wild et al. 2003; Cai et al. 2009). Grid-tagging of the bright lung signal with the HP gases allows following local respiratory mechanics, giving new insights into the biomechanics of the healthy and diseased lung. However, the potential role for clinical imaging is questionable due to logistic concerns, cost, and availability of the He-3 gas and the need for additional equipment.

Alternative methods of assessing regional lung tissue motion are deformable registration algorithms. These match series of images by deforming them in order to achieve congruence of structural image information. Unfortunately, the limited signal of pulmonary tissue only implies the relative absence of such structural information. On the other hand, the registration approach is not dependent on a specific imaging sequence and could make a more general application of motion detection possible. Registration techniques have been applied to 2D-MRI with

only a small error of the registration process in comparison to landmarks defined by experts. Naturally, the landmarks were set according to the present structural information, namely, the central vessel structures. The performance in the peripheral lung tissue was not accessible to evaluation. In general, the available algorithms can quantify lung motion where it would be also visible for a human observer. At contrast levels below visibility, the algorithms also fail (Gee et al. 2003). In a following study, the same group investigated healthy volunteers and mice (Sundaram and Gee 2005). Motion detection worked well over the diaphragm and hilar vessels, but performance was worse in the periphery. Further improvements of the technology can be anticipated with improvement of sequence techniques with higher signal even in the periphery of the lung.

3.2 Regional Volume Change

Based on the experience with the analysis of lung parenchyma displacement with registration algorithms, recent investigations have been focused on the quantification of regional lung ventilation as a function of local lung volume change calculated from dynamic MRI. Most of these studies on regional lung volume changes are based on the assumption that an analysis of the regional patterns of movement of the lung tissue is related to lung ventilation and might contribute to the assessment of the type and severity of pulmonary diseases with impairment of the elasticity of the lung tissue (i.e., lung fibrosis, Fig. 8).

The basic requirement for the analysis of the movement patterns and the recognition of pathological changes is a time-resolved image acquisition or reconstruction that represents lung parenchyma and its respiratory-dependent movements with reasonably high signal. A 2D or 3D balanced SSFP sequence with very short TE is presently the best choice for this purpose. Retrospective 4D resorting techniques could be used as an alternative.

Only recently, Kolb et al. created an atlas-derived reference system in which the regional lung tissue motion can be quantified using a

shape model-based segmentation and registration workflow (Kolb et al. 2016). The model-based temporal registration of the lung surfaces in 4D-MRI was compared with that of 4D-CT images. A ventilation analysis was performed on 4D MR images of patients with lung fibrosis. The ventilation maps were superimposed on static CT images and visually correlated well with the CT patho-morphology (Fig. 9). Similar to spirometry, flow-volume diagrams for individual lung lobes can be calculated for the regional analysis

of the respiration. In addition, a visualization of the regional ventilation can be extracted from the data, which shows the local expansion of the tissue during breathing.

In first feasibility studies, the methodology was used in healthy subjects, then in patients with a known impairment of lung structure, e.g., restrictive ventilation disorder in the case of lung fibrosis. This technique has the potential to provide new diagnostic information on the regional parenchymal movement of healthy and diseased lungs during the respiratory cycle. Further studies will be necessary to elaborate the diagnostic value of this method.
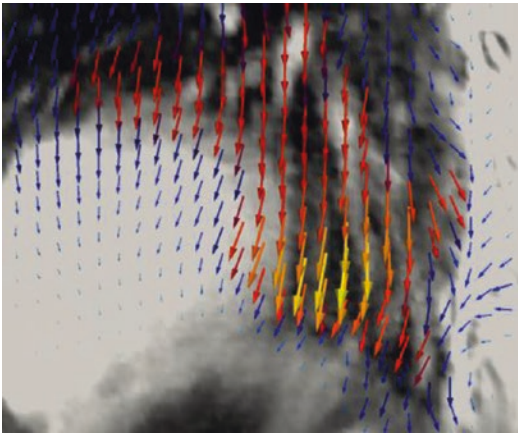
Fig. 8 The image visualizes the result of a deformable image registration during breathing cycle as *3D arrows*, pointing from locations in an end-expiration image to their corresponding locations in the depicted end-inspiration image. The image registration was initialized with a prediction of the surface motion

4   Applications in Lung Disease

Since lung emphysema is a very common chronic pulmonary disease with typically severe impairment of respiratory mechanics and on the other hand available treatment options, this was one of the first conditions to be investigated with dynamic MRI of the lungs. In severe emphysema, dynamic MRI shows the diaphragm flattened and with reduced and irregular movement. Occasionally an asynchronous movement was seen between the hemidiaphragms. The minimum craniocaudal dimensions of the lung in expiration are significantly increased compared to normal subjects and correlate well with residual lung vol-
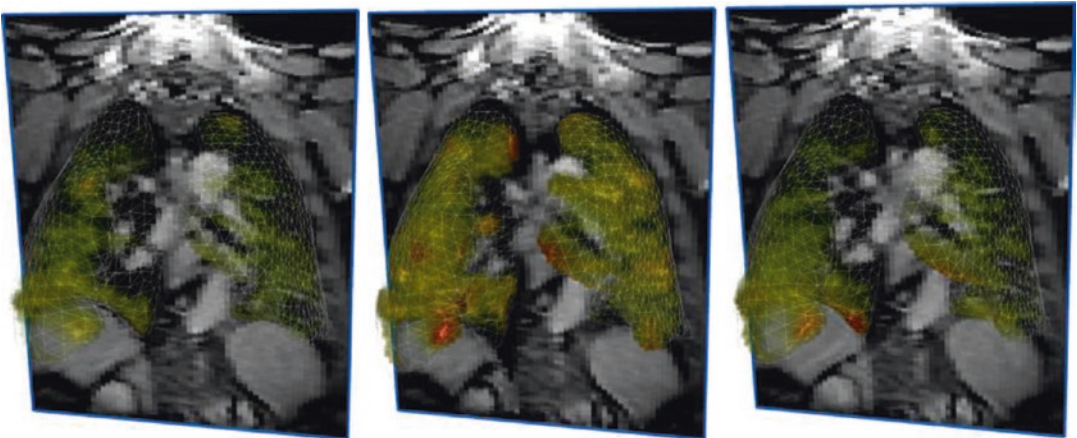
Fig. 9 Ray-casting visualization of regional volume increases in three respiration phases. The lung surfaces in which the volumes have been calculated are delineated as a wire frame
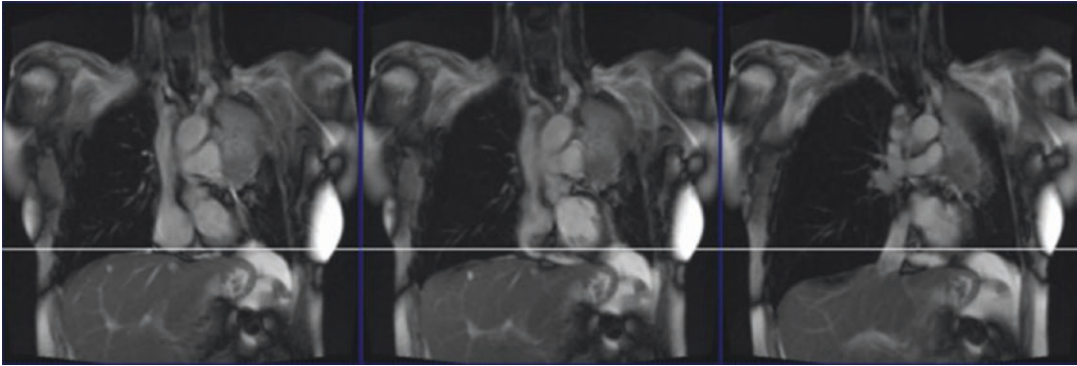
Fig. 10 Three images from a dynamic SSFP (TrueFISP) image series acquisition in a patient with *left* central tumor. A *line* is placed in the vicinity of the diaphragm in order to facilitate the visualization of the *left* hemidiaphragmatic paralysis

ume (%RV). The maximum craniocaudal dimension of the lung was found to correlate well with total lung capacity (TLC%) and is not significantly changed in emphysema patients (Iwasawa et al. 2011). Effects of therapy (e.g., lung volume reduction surgery) can be documented by an increase in craniocaudal motion of the diaphragm in the operated hemithorax. The effect can even be observed in the contralateral hemithorax. The results from dynamic MRI correlated well with improved scores on the Fletcher dyspnea scale (Suga et al. 1999). For the lateral and anteroposterior thoracic dimension, similar findings were reported (Gierada et al. 1998; Iwasawa et al. 2002). Therefore, emphysema is a good example of how dynamic MRI can contribute to monitoring the effects of therapy for disorders of respiratory mechanics. Consequently, the suggestions for a standard protocol include a simplified approach with SSFP images to be acquired during free breathing to implement the capacity of lung MRI with 2D + *t* imaging in routine imaging (Chapter "General Requirements of MRI of the Lung and Suggested Standard Protocol"). Impairments of diaphragmatic function due to tumor invasion into the mediastinum with phrenic nerve palsy could be easily detected (Fig. 10).

Adolescent idiopathic scoliosis is another condition, in which patients suffer from insufficient respiratory function due to a dysfunctional respiratory pump. Compared to normal subjects, 2D dynamic MRI shows how the anteroposterior thoracic movement in these patients is limited (Kotani et al. 2004). The diaphragm is elevated in inspiration just as in expiration but the amplitude of its motion is unchanged when compared to healthy subjects. After surgery, dynamic MRI shows an improvement in the amplitude of thoracic expansion and an increase in diaphragmatic movement (Chu et al. 2006, 2007).

Pompe's disease is a progressive metabolic myopathy with involvement of respiratory muscles leading to progressive pulmonary dysfunction, particularly in supine position. Diaphragmatic weakness is considered to be the most important component. Using static spirometer-controlled MRI scans during maximum inspiration and expiration, striking dysfunction of the diaphragm up to a lacking displacement was diagnosed in Pompe patients. Patients had a significant smaller cranial-caudal length ratio than volunteers ($p < 0.001$), indicating diaphragmatic weakness. These cranial-caudal length ratios correlated strongly with forced vital capacity in supine position ($r = 0.88$) and postural drop ($r = 0.89$) (Wens et al. 2015; Mogalle et al. 2016).

4.1 Applications in Radiotherapy

A large field for dynamic MRI are applications in radiotherapy. Dynamic MRI can be used either to monitor side effects of therapy or as a sophisticated tool for planning adaptive therapy.

One example of monitoring side effects was a study that compared lung motion before and after radiotherapy for lung cancer with 2D dynamic MRI. It could be shown that craniocaudal lung motion in the irradiated hemithorax was reduced after radiotherapy. In contrast to this, global lung function tests showed no significant difference to measurements obtained before radiotherapy. This result is a good example how dynamic MRI can be used to detect functional pulmonary changes with higher sensitivity than spirometric measurements (Plathow et al. 2006).

The main scientific focus in dynamic MRI for radiotherapy lies in planning therapy of moving objects such as the lungs or the liver. Conservative radiotherapy plans account for the displacement of a target structure by extending the planning target volume. This includes all volumes of healthy surrounding tissues that pass the planned target volume during the breathing cycle (Keall et al. 2006). The safety margins are estimated from a population of lung tumor patients but cannot be defined individually: A large inter-individual variability of motion patterns and the overall displacement of lung tumors—even paradox displacement against the expected directions during in- and expiration—have been documented (Dinkel et al. 2009). An ideal task for 4D-MRI within the radiooncology workflow would be to analyze individual motion patterns and to select patients for motion adapted radiotherapy in the first line.

One step further in the application of 4D imaging in the workflow for motion adapted radiotherapy would be to monitor changes in displacement, motion pattern, and lesion size in real time during therapy (inter-fractional changes) at the linear accelerator prior to each radiation fraction (Cai et al. 2008). This would account for the multiple factors that may change lung ventilation and motion between treatment sessions: pleural effusion, lung collapse, pericardial effusion, changes in heart function and size, changes in tumor size, phrenic nerve paralysis, radiation fibrosis in the lung, interval pneumonia, and obstructive disease. Each of these can change the tumor position within the chest quite rapidly, in particular for peripheral lung lesions rather than for mediastinal masses. Nowadays, dedicated systems use either an integrated X-ray unit or the therapeutic beam itself (Dietrich et al. 2006). This approach could be improved with on-board real-time-MRI using the recently developed, integrated Linac-MRI scanners (Lagendijk et al. 2014).

A more sophisticated application would be directly planning MRI-guided adaptive radiotherapy. To minimize the volume of irradiated healthy tissue and to maximize the tumor dose, tailored treatment plans would incorporate detailed information of the individual breathing cycle of each patient. Full 4D imaging-based radiotherapy planning (4D-RT) is not yet clinically practiced. Validated, standardized planning tools, including deformable image registration, multiple target contouring, adaptive dose calculation, and motion control delivery mechanism are missing. Ideally, dynamic real-time planning and iterative modification of any treatment port in the chest would be implemented at the linear accelerator itself. Tumor motion could be accounted for with either gating the beam to the respiratory phases in which the tumor is inside the target volume or tracking of the moving target with the beam (Keall et al. 2006).

Nevertheless, uncertainties in spatial encoding are a major point of critique in the discussion of MRI for radiotherapy planning. The quality of spatial encoding depends on the quality of the system and can be severely impaired by local inhomogeneities of the magnetic field. Stents within the bronchi or other metallic objects can add to local field distortions (Chen et al. 2006). Careful compensation of spatial distortion using the 3D-distortion correction of images with individual correction factors for the particular MR scanner and optimized shimming are warranted (Biederer et al. 2010; Torfeh et al. 2016). Limited temporal resolution of dynamic volume acquisitions with 4D-MRI (in their current implementation) may lead to an overestimation of tumor size as the mass is volume averaged into many voxels during motion (Biederer et al. 2009). Furthermore, while CT produces radiation transmission data for therapy planning, estimating transmission data from MRI can be difficult (Dowling et al. 2015). Proton- or particle therapy based on spot scanning, in which precision will be considerably

Table 6 Comparison of 4D-MRI and 4D-CT (adapted from Biederer et al. 2010)

4D-MRI	4D-CT
Temporal resolution 　Dynamic 2D approx. 100 ms 　Dynamic 3D >1000 ms	Temporal resolution 200–500 ms
Typical spatial resolutions (voxel size) 　Dynamic 2D 2 × 3 × 8 mm 　Dynamic 3D 3 × 3 × 4 mm	Typical spatial resolution (voxel size) 0.5 × 0.5 × 1 mm
Covers individual changes in respiration frequency and depth	Representative for the recumbent, slow breathing patient at rest
Instructed breathing maneuvers possible	Fixed acquisition scheme
Free choice of imaging plane (i.e., dynamic 2D)	Limited gantry tilt
Transmission data need to be estimated	Provides radiation transmission data
Suitable for uncooperative patients	Suitable for uncooperative patients
Linear accelerator integration under development	Verification can be integrated in linear accelerator (cone beam CT)
No radiation exposure	Effective dose 30–40 mSv
To be repeated virtually ad libidum	Radiation exposure limits repetition

affected by respiratory motion, is yet another upcoming challenge and warrants a further development of 4D imaging technology (Saito et al. 2009). For quick reference, Table 6 gives an overview of the advantages and disadvantages of 4D-CT and 4D-MRI for planning motion adapted radiotherapy (Biederer et al. 2010).

In summary, the great potential of dynamic MRI for clinical use whether for radiotherapy or other clinical fields is not yet fully recognized. In the near future, both will profit substantially from the rapid technical development and intense research on the upcoming new indications.

References

Biederer J, Dinkel J, Remmert G, Jetter S, Nill S, Moser T, Bendl R, Thierfelder C, Fabel M, Oelfke U et al (2009) 4D-Imaging of the lung: reproducibility of lesion size and displacement on helical CT, MRI, and cone beam CT in a ventilated ex vivo system. Int J Radiat Oncol Biol Phys 73:919–926

Biederer J, Hintze C, Fabel M, Dinkel J (2010) Magnetic resonance imaging and computed tomography of respiratory mechanics. J Magn Reson Imaging 32:1388–1397

Blackall JM, Ahmad S, Miquel ME, McClelland JR, Landau DB, Hawkes DJ (2006) MRI-based measurements of respiratory motion variability and assessment of imaging strategies for radiotherapy planning. Phys Med Biol 51:4147–4169

Cai J, Read PW, Larner JM, Jones DR, Benedict SH, Sheng K (2008) Reproducibility of interfraction lung motion probability distribution function using dynamic MRI: statistical analysis. Int J Radiat Oncol Biol Phys 72:1228–1235

Cai J, Sheng K, Benedict SH, Read PW, Larner JM, Mugler JP, de Lange EE, Cates GD, Miller GW (2009) Dynamic MRI of grid-tagged hyperpolarized helium-3 for the assessment of lung motion during breathing. Int J Radiat Oncol Biol Phys 75:276–284

Cander L, Forster RE (1959) Determination of pulmonary parenchymal tissue volume and pulmonary capillary blood flow in man. J Appl Physiol 14:541–551

Chapman B, O'Callaghan C, Coxon R, Glover P, Jaroszkiewicz G, Howseman A, Mansfield P, Small P, Milner AD, Coupland RE (1990) Estimation of lung volume in infants by echo planar imaging and total body plethysmography. Arch Dis Child 65:168–170

Chen Q, Mai VM, Bankier AA, Napadow VJ, Gilbert RJ, Edelman RR (2001) Ultrafast MR grid-tagging sequence for assessment of local mechanical properties of the lungs. Magn Reson Med 45:24–28

Chen Z, Ma C-M, Paskalev K, Li J, Yang J, Richardson T, Palacio L, Xu X, Chen L (2006) Investigation of MR image distortion for radiotherapy treatment planning of prostate cancer. Phys Med Biol 51:1393–1403

Chu WC, Ng BK, Li AM, Lam T-P, Lam WW, Cheng JC (2007) Dynamic magnetic resonance imaging in assessing lung function in adolescent idiopathic scoliosis: a pilot study of comparison before and after posterior spinal fusion. J Orthop Surg 2:20

Chu WCW, Li AM, Ng BKW, Chan DFY, Lam T, Lam WWM, Cheng JCY (2006) Dynamic magnetic resonance imaging in assessing lung volumes, chest wall, and diaphragm motions in adolescent idiopathic scoliosis versus normal controls. Spine 31:2243–2249

Cluzel P, Similowski T, Chartrand-Lefebvre C, Zelter M, Derenne JP, Grenier PA (2000) Diaphragm and chest wall: assessment of the inspiratory pump with MR imaging-preliminary observations. Radiology 215:574–583

Craighero S, Promayon E, Baconnier P, Lebas JF, Coulomb M (2005) Dynamic echo-planar MR imaging of the diaphragm for a 3D dynamic analysis. Eur Radiol 15:742–748

D'Angelo E (1998) Static and dynamic behaviour of the respiratory system. In: Milic-Emili PJ (ed) Applied physiology in respiratory mechanics; hrsg. v. Springer, Milan, pp 39–49

Dietrich L, Jetter S, Tücking T, Nill S, Oelfke U (2006) Linac-integrated 4D cone beam CT: first experimental results. Phys Med Biol 51:2939–2952

Dinkel J, Hintze C, Tetzlaff R, Huber PE, Herfarth K, Debus J, Kauczor HU, Thieke C (2009) 4D-MRI analysis of lung tumor motion in patients with hemidiaphragmatic paralysis. Radiother Oncol 91:449–454

Dock DS, Kraus WL, McGUIRE LB, Hyland JW, Haynes FW, Dexter L (1961) The pulmonary blood volume in man. J Clin Invest 40:317–328

Dowling JA, Sun J, Pichler P, Rivest-Hénault D, Ghose S, Richardson H, Wratten C, Martin J, Arm J, Best L et al (2015) Automatic substitute computed tomography generation and contouring for magnetic resonance imaging (MRI)-alone external beam radiation therapy from standard MRI sequences. Int J Radiat Oncol Biol Phys 93:1144–1153

Eichinger M, Puderbach M, Smith H-J, Tetzlaff R, Kopp-Schneider A, Bock M, Biederer J, Kauczor H-U (2007) Magnetic resonance-compatible-spirometry: principle, technical evaluation and application. Eur Respir J 30:972–979

Fabel M, Wintersperger BJ, Dietrich O, Eichinger M, Fink C, Puderbach M, Kauczor H-U, Schoenberg SO, Biederer J (2009) MRI of respiratory dynamics with 2D steady-state free-precession and 2D gradient echo sequences at 1.5 and 3 Tesla: an observer preference study. Eur Radiol 19:391–399

Gauthier AP, Verbanck S, Estenne M, Segebarth C, Macklem PT, Paiva M (1994) Three-dimensional reconstruction of the in vivo human diaphragm shape at different lung volumes. J Appl Physiol (1985) 76:495–506

Gee J, Sundaram T, Hasegawa I, Uematsu H, Hatabu H (2003) Characterization of regional pulmonary mechanics from serial magnetic resonance imaging data. Acad Radiol 10:1147–1152

Gierada DS, Curtin JJ, Erickson SJ, Prost RW, Strandt JA, Goodman LR (1995) Diaphragmatic motion: fast gradient-recalled-echo MR imaging in healthy subjects. Radiology 194:879–884

Gierada DS, Hakimian S, Slone RM, Yusen RD (1998) MR analysis of lung volume and thoracic dimensions in patients with emphysema before and after lung volume reduction surgery. AJR Am J Roentgenol 170:707–714

Iwasawa T, Kagei S, Gotoh T, Yoshiike Y, Matsushita K, Kurihara H, Saito K, Matsubara S (2002) Magnetic resonance analysis of abnormal diaphragmatic motion in patients with emphysema. Eur Respir J 19:225–231

Iwasawa T, Takahashi H, Ogura T, Asakura A, Gotoh T, Shibata H, Inoue T (2011) Influence of the distribution of emphysema on diaphragmatic motion in patients with chronic obstructive pulmonary disease. Jpn J Radiol 29:256–264

Keall PJ, Mageras GS, Balter JM, Emery RS, Forster KM, Jiang SB, Kapatoes JM, Low DA, Murphy MJ, Murray BR et al (2006) The management of respiratory motion in radiation oncology report of AAPM Task Group 76. Med Phys 33:3874–3900

Kiryu S, Loring SH, Mori Y, Rofsky NM, Hatabu H, Takahashi M (2006) Quantitative analysis of the velocity and synchronicity of diaphragmatic motion: dynamic MRI in different postures. Magn Reson Imaging 24:1325–1332

Kolb C, Wetscherek A, Buzan MT, Werner R, Rank CM, Kachelrie M, Kreuter M, Dinkel J, Heuel CP, Maier-Hein K (2016) Regional lung ventilation analysis using temporally resolved magnetic resonance imaging. J Comput Assist Tomogr, vol 40, pp 899–906

Kondo T, Kobayashi I, Taguchi Y, Ohta Y, Yanagimachi N (2000) A dynamic analysis of chest wall motions with MRI in healthy young subjects. Respirology 5:19–25

Kondo T, Kobayashi I, Taguchi Y, Hayama N, Tajiri S, Yanagimachi N (2005) An analysis of the chest wall motions using the dynamic MRI in healthy elder subjects. Tokai J Exp Clin Med 30:15–20

Kotani T, Minami S, Takahashi K, Isobe K, Nakata Y, Takaso M, Inoue M, Maruta T, Akazawa T, Ueda T, Moriya H (2004) An analysis of chest wall and diaphragm motions in patients with idiopathic scoliosis using dynamic breathing MRI. Spine 29:298–302

Lagendijk JJW, Raaymakers BW, van Vulpen M (2014) The magnetic resonance imaging-linac system. Semin Radiat Oncol 24:207–209

Lin W, Guo J, Rosen MA, Song HK (2008) Respiratory motion-compensated radial dynamic contrast-enhanced (DCE)-MRI of chest and abdominal lesions. Magn Reson Med 60:1135–1146

Mead J, Fishman AP, Geiger SR, Macklem PT (1986) Mechanics of breathing. American Physiological Society, Bethesda, MD. Distributed by Williams & Wilkins

Meysman M, Vincken W (1998) Effect of body posture on spirometric values and upper airway obstruction indices derived from the flow-volume loop in young non-obese subjects. Chest 114:1042–1047

Miller MR, Hankinson J, Brusasco V, Burgos F, Casaburi R, Coates A, Crapo R, Enright P, van der Grinten CPM, Gustafsson P et al (2005) Standardisation of spirometry. Eur Respir J 26:319–338

Mogalle K, Perez-Rovira A, Ciet P, Wens SCA, van Doorn PA, Tiddens HAWM, van der Ploeg AT, de Bruijne M (2016) Quantification of diaphragm

mechanics in Pompe disease using dynamic 3D MRI. PLoS One 11:e0158912

Napadow VJ, Mai V, Bankier A, Gilbert RJ, Edelman R, Chen Q (2001) Determination of regional pulmonary parenchymal strain during normal respiration using spin inversion tagged magnetization MRI. J Magn Reson Imaging 13:467–474

O'Callaghan C, Small P, Chapman B, Coxon R, Glover P, Turner R, Jaroszkiewicz G, Howseman A, Mansfield P, Coupland R (1987) Determination of individual and total lung volumes using nuclear magnetic resonance echo-planar imaging. Ann Radiol (Paris) 30:470–472

Paiva M, Verbanck S, Estenne M, Poncelet B, Segebarth C, Macklem PT (1992) Mechanical implications of in vivo human diaphragm shape. J Appl Physiol (1985) 72:1407–1412

Plathow C, Ley S, Fink C, Puderbach M, Heilmann M, Zuna I, Kauczor H-U (2004) Evaluation of chest motion and volumetry during the breathing cycle by dynamic MRI in healthy subjects: comparison with pulmonary function tests. Investig Radiol 39:202–209

Plathow C, Schoebinger M, Fink C, Ley S, Puderbach M, Eichinger M, Bock M, Meinzer H-P, Kauczor H-U (2005a) Evaluation of lung volumetry using dynamic three-dimensional magnetic resonance imaging. Investig Radiol 40:173–179

Plathow C, Klopp M, Fink C, Sandner A, Hof H, Puderbach M, Herth F, Schmähl A, Kauczor H-U (2005b) Quantitative analysis of lung and tumour mobility: comparison of two time-resolved MRI sequences. Br J Radiol 78:836–840

Plathow C, Hof H, Kuhn S, Puderbach M, Ley S, Biederer J, Claussen CD, Huber PE, Schaefer J, Tuengerthal S, Kauczor H-U (2006) Therapy monitoring using dynamic MRI: analysis of lung motion and intrathoracic tumor mobility before and after radiotherapy. Eur Radiol 16:1942–1950

Qanadli SD, Orvoen-Frija E, Lacombe P, Di Paola R, Bittoun J, Frija G (1999) Estimation of gas and tissue lung volumes by MRI: functional approach of lung imaging. J Comput Assist Tomogr 23:743–748

Remmert G, Biederer J, Lohberger F, Fabel M, Hartmann GH (2007) Four-dimensional magnetic resonance imaging for the determination of tumour movement and its evaluation using a dynamic porcine lung phantom. Phys Med Biol 52:N401–N415

Saito N, Bert C, Chaudhri N, Gemmel A, Schardt D, Durante M, Rietzel E (2009) Speed and accuracy of a beam tracking system for treatment of moving targets with scanned ion beams. Phys Med Biol 54:4849–4862

Suga K, Tsukuda T, Awaya H, Takano K, Koike S, Matsunaga N, Sugi K, Esato K (1999) Impaired respiratory mechanics in pulmonary emphysema: evaluation with dynamic breathing MRI. J Magn Reson Imaging 10:510–520

Sundaram TA, Gee JC (2005) Towards a model of lung biomechanics: pulmonary kinematics via registration of serial lung images. Med Image Anal 9:524–537

Swift AJ, Woodhouse N, Fichele S, Siedel J, Mills GH, van Beek EJR, Wild JM (2007) Rapid lung volumetry using ultrafast dynamic magnetic resonance imaging during forced vital capacity maneuver: correlation with spirometry. Investig Radiol 42:37–41

Takazakura R, Takahashi M, Nitta N, Murata K (2004) Diaphragmatic motion in the sitting and supine positions: healthy subject study using a vertically open magnetic resonance system. J Magn Reson Imaging 19:605–609

Tetzlaff R, Eichinger M, Schöbinger M, Puderbach M, Meinzer H-P, Kauczor H-U (2008) Semiautomatic assessment of respiratory motion in dynamic MRI— comparison with simultaneously acquired spirometry. RöFo 180:961–967

Tetzlaff R, Schwarz T, Kauczor H-U, Meinzer H-P, Puderbach M, Eichinger M (2010) Lung function measurement of single lungs by lung area segmentation on 2D dynamic MRI. Acad Radiol 17:496–503

Torfeh T, Hammoud R, Perkins G, McGarry M, Aouadi S, Celik A, Hwang K-P, Stancanello J, Petric P, Al-Hammadi N (2016) Characterization of 3D geometric distortion of magnetic resonance imaging scanners commissioned for radiation therapy planning. Magn Reson Imaging 34:645–653

Unal O, Arslan H, Uzun K, Ozbay B, Sakarya ME (2000) Evaluation of diaphragmatic movement with MR fluoroscopy in chronic obstructive pulmonary disease. Clin Imaging 24:347–350

Voorhees A, An J, Berger KI, Goldring RM, Chen Q (2005) Magnetic resonance imaging-based spirometry for regional assessment of pulmonary function. Magn Reson Med 54:1146–1154

Weick S, Breuer FA, Ehses P, Völker M, Hintze C, Biederer J, Jakob PM (2013) DC-gated high resolution three-dimensional lung imaging during free-breathing. J Magn Reson Imaging 37:727–732

Wens SCA, Ciet P, Perez-Rovira A, Logie K, Salamon E, Wielopolski P, de Bruijne M, Kruijshaar ME, Tiddens HAWM, van Doorn PA, van der Ploeg AT (2015) Lung MRI and impairment of diaphragmatic function in Pompe disease. BMC Pulm Med 15:54

Wild JM, Paley MNJ, Kasuboski L, Swift A, Fichele S, Woodhouse N, Griffiths PD, van Beek EJR (2003) Dynamic radial projection MRI of inhaled hyperpolarized 3He gas. Magn Reson Med 49:991–997

Pulmonary Hypertension and Thromboembolic Disease

Sebastian Ley and Karl-Friedrich Kreitner

Contents

S. Ley, M.D. (✉)
Chirurgisches Klinikum München Süd, Diagnostic
and Interventional Radiology, Munich, Germany

Institute of Clinical Radiology, Ludwig-Maximilians
University Hospital Munich, Munich, Germany
e-mail: ley@gmx.de

K.-F. Kreitner, M.D.
Department Diagnostic and Interventional Radiology,
Johannes Gutenberg-University Mainz,
Langenbeckstrasse 1, 55131 Mainz, Germany
e-mail: kreitner@radiologie.klinik.uni-mainz.de

Key Points
Pulmonary hypertension (PH) is a disease group
that includes a wide variety of entities leading to
an increased pulmonary arterial pressure. This
chapter describes the basic mechanisms that lead
to PH and the possibilities of MRI in diagnosing
different aspects. A MR imaging protocol is pro-
vided making MRI a comprehensive modality for
the classification of the underlying disease and
assessment of hemodynamics.

1   Introduction

Pulmonary hypertension (PH) is characterized by
an elevation of the arterial pressure and vascular
resistance within the pulmonary circulation.
Precapillary PH has to be differentiated from
postcapillary PH (Rosenkranz 2007). In patients
with postcapillary PH, diseases of the left heart
(atrial, ventricular, valvular) cause pulmonary
venous congestion, which in turn leads to an ele-
vation of pulmonary capillary pressure (PCP)
and pulmonary arterial pressure (PAP). In con-
trast, precapillary PH is characterized by an iso-
lated elevation of PAP with normal PCP and
accounts for the majority of patients referred to
tertiary pulmonary hypertension centers. Since in
this setting the pulmonary hypertensive state is
limited to the arterial component of the pulmo-
nary vasculature, pulmonary arterial hyperten-
sion (PAH) is distinguished from other forms of
PH. The most important consequence of PAH is

chronic overload of the right heart (cor pulmonale) which ultimately leads to right heart failure and is thus responsible for the poor prognosis of patients with severe PAH. Based on invasive measurements by right heart catheterization, PAH is defined as an elevation of the mean pulmonary arterial pressure (PAPm) above 25 mmHg at rest and/or above 30 mmHg during exercise in the setting of normal or reduced cardiac output and normal PCP. Pulmonary vascular resistance (PVR) is elevated above 3 mmHg/L/min (Wood units).

In 1998, the WHO (Evian) classification system of PH was proposed, which sought to categorize different forms of pulmonary hypertension (PH) according to similarities in pathophysiological mechanisms, clinical presentation, and therapeutic options. Since then several world symposia have been held, the most recent 2013 in Nice, France (Simonneau et al. 2013). The most recent classification is summarized in Table 1.

Patients suffering from PH often present with nonspecific symptoms, namely shortness of breath on minimal physical exertion, fatigue, chest pain, and fainting. Therefore, correct diagnosis is often made late in the course of the disease when prognosis is poor and treatment options are limited (Tuder et al. 2007).

The incidence of IPAH is approximately 2–3 persons per one million per year (f:m = 1.7–3:1) (Taichman and Mandel 2007). It is a genetic disorder with a familial accumulation. For acquired ("secondary") forms of PH which are a common complication of many different disease entities only some examples are given: 50% of patients with chronic hypoxemia, such as in chronic obstructive pulmonary disease (COPD), develop PH. COPD is the third most frequent cause of death worldwide, mostly related to late complications, such as PH. Of patients with scleroderma, 40% develop PH. There are more than 500,000 cases of acute pulmonary embolism per year in the United States with subsequent obstruction of the pulmonary arterial vascular bed. Approximately 3–10% of these patients will develop a chronic and fatal late form called chronic thromboembolic pulmonary hypertension

Table 1 Classification of pulmonary hypertension according to the 5th world conference on pulmonary hypertension (Simonneau et al. 2013)

1. Pulmonary arterial hypertension (PAH)
1.1 Idiopathic PAH—cause unknown
1.2 Heritable PAH with subgroups—genetic background
1.3 Drug and toxin induced
1.4 Associated with connective tissue disease, HIV infection, portal hypertension, congenital heart disease, schistosomiasis
1′ Pulmonary veno-occlusive disease and/or pulmonary capillary hemangiomatosis
1″ Persistent pulmonary hypertension of the newborn (PPHN)
2. Pulmonary hypertension with left heart disease Left-sided ventricular or atrial heart disease, left-sided valvular heart disease, congenital/acquired left heart inflow/outflow tract obstruction and congenital cardiomyopathies
3. Pulmonary hypertension associated with lung disease and/or hypoxemia COPD, interstitial lung disease, sleep-disordered breathing, alveolar hypo-ventilation disorders, chronic exposure to high altitude, developmental abnormalities
4. Pulmonary hypertension due to chronic thrombotic and/or embolic disease (CTEPH) Thromboembolic obstruction of the proximal/distal pulmonary arteries; non-thrombotic pulmonary embolism (tumor, parasites, foreign material)
5. Pulmonary hypertension with unclear multifactorial mechanisms Hemotologic disorders, systemic disorders, metabolic disorders, others

(CTEPH) (Fernandes et al. 2016). So, overall, recent registries suggest an incidence of PH of at least five per million inhabitants per year (Delcroix et al. 2016).

Naturally, different types of PH require different treatment regimens, making a precise categorization mandatory. The diagnostic workup of these patients needs to differentiate between the different causes of PH (McLaughlin et al. 2015). This includes, besides patient history and laboratory findings, the assessment of cardiac function, lung function, pulmonary blood pressures, and pulmonary vasculature. Thus, the actual diagnostic pathway includes a broad spectrum of examinations, mainly echocardiography, invasive right heart catheterization, and ventilation/perfusion scintigraphy.

Table 2 Proposed MR imaging protocol for imaging patients with suspected pulmonary hypertension

Rationale	Sequences
Morphology I	Half-Fourier acquisition single-shot turbo spin echo tra & cor, 3D volume isotropic turbo spin echo acquisition tra
Function (perfusion)	FLASH 3D (time resolved), 0.1 mmol/kg BW
Morphology II	3D volume isotropic turbo spin echo acquisition tra & cor
Function (cardiac)	Cine of the right ventricle, flow
Vasculature	FLASH 3D (high spatial resolution), 0.1 mmol Gd/kg BW

Magnetic resonance imaging (MRI) has emerged as a versatile diagnostic tool allowing for combined morphological evaluation of the lung parenchyma and pulmonary arteries, and cardiac function (Ley and Kauczor 2008; Nagendran and Michelakis 2007; Kreitner 2014; Swift et al. 2014a). The diagnostic capabilities in the context of PH are described in detail in the following paragraphs. A basic MR imaging protocol is given in Table 2.

2 Lung Parenchyma

Pulmonary hypertension (PH) associated with respiratory systemic disorders is a distinct group in the categorization of PH. It is evolving as an important factor that can adversely affect prognosis and outcome in chronic lung disease (Presberg and Dincer 2003). Especially chronic obstructive pulmonary disease (COPD) and idiopathic pulmonary fibrosis (IPF) are associated with intimal thickening or medial smooth muscle cell hypertrophy leading to mild to moderate PH (Tuder et al. 2007; Wright et al. 2005; Ryu et al. 2007). The most common cause is COPD; PH occurs in approximately 5% of patients with severe emphysema. In a series with 215 patients with severe COPD, moderate (9.8%) or severe (3.7%) PH was found more frequently than observed before (Thabut et al. 2005). In advanced COPD, therapy directed at controlling the pulmonary artery pressure has been recommended. Many patients with COPD and severe PH have an additional cause of pulmonary pressure elevation, such as left ventricular disease, pulmonary embolism, or sleep apnea syndrome; these conditions should be ruled out routinely, as they may be treatable (Chaouat et al. 2008).

Evaluation of the lung parenchyma using MRI is not yet common but possible even in severe COPD patients with reduced parenchymal structure (Ley-Zaporozhan et al. 2007, 2008, 2010; Jobst et al. 2015).

Iwasawa et al. 2007 reported that lung signal change measured by MRI correlates with airflow obstruction in COPD patients.

Idiopathic pulmonary fibrosis (IPF) is a disease of unknown etiology associated with progressive parenchymal fibrosis. Little is known about PH in IPF but several retrospective analyses indicate that PH in IPF may be frequent (Cuttica 2016). In a large trial in patients awaiting lung transplantation due to IPF, it was found that PH affects approximately 45% of these patients; however, severe PH was relatively infrequent. Typical lung parenchymal changes due to fibrosis can be nicely visualized by MRI (Primack et al. 1994; Jung et al. 2000; Altes et al. 2007). The detailed description of the possibilities of MRI in the detection and characterization of lung parenchymal changes can be found in the respective chapters.

3 Macro- and Microvasculature

3.1 Pulmonary Hypertension

The exact processes that initiate the pathological changes seen in PAH are still unknown even if we now understand more and more of the mechanisms involved. It is recognized that PAH has a multifactorial pathobiology that involves various biochemical pathways and cell types (Tuder et al. 2007). The imaging hallmark in PH is vasoconstriction predominantly on a subsegmental level. The increased vascular resistance leads to dilation of the central pulmonary arteries (Perloff et al. 2003). Thus, a vascular pruning towards the lung periphery can be seen and the subpleural space is often spared (Chatterjee et al. 2002). An additional

finding of hypoxic pulmonary hypertension is an increase in vasomotor tone (Shimoda et al. 2000). The peripheral vascular bed is the location where current pharmaceutical approaches are aiming at. First, the vasomotor tone should be decreased and second, vascular remodeling should be stopped or even reversed. Therefore, visualization and quantification of blood flow in the most peripheral zone is crucial for treatment monitoring or even human drug trials in patients suffering from PH. The overall possibilities for assessment of the pulmonary blood flow in different diseases leading to PH, including a detailed technical description, are summarized elsewhere (Kreitner 2014; Ley 2015; Freed et al. 2016).

In an early study analyzing the MRA features of PH the most obvious finding was an abnormal proximal-to-distal tapering of all vessels being present (Bergin et al. 1997). Collateral blood supply, via bronchial arteries to the lung parenchyma was only observed in 1 out of 10 patients. Compared to healthy volunteers, the central pulmonary arteries were significantly enlarged. In a more recent study using parallel MR imaging techniques, the predominant MR angiographic findings were proximal-to-distal tapering and a tortuous course of the pulmonary arteries towards the periphery (Fig. 1) (Ley et al. 2005). In this series, no dilated bronchial arteries were found in PAH patients. Further technical developments will allow for more detailed evaluation of the pulmonary vasculature as demonstrated in a recent study where a spatial resolution of 1 mm isotropic datasets was achieved in a 20-s breath-hold (3-T MRI, dedicated 32 channel chest coil) (Nael et al. 2007).

As PH predominantly affects the small vessels, detailed analysis of pulmonary perfusion is the most promising technique. 3D MRI pulmonary perfusion in patients suffering from PH (except CTPEH) showed a predominantly peripheral, diffuse reduction of pulmonary perfusion (=patchy pattern) (80% of pulmonary lobes) and 20% of the lobes showed a normal perfusion (Ley et al. 2005). One advantage of MR perfusion measurements is the ability of absolute quantification, as demonstrated in an initial study with 40 PH patients (Ohno et al. 2004). In larger populations, quantitative perfusion analysis showed a marked reduction in pulmonary blood flow and an increase in mean transit time (Ohno et al. 2007; Ley et al. 2007a).

Seventy-nine patients with PAH were examined with contrast enhanced perfusion MRI and followed up for clinical outcome. MR perfusion transit times predicted mortality in patients with PAH and were closely associated with clinical gold standards CI and PVRI (Swift et al. 2014b).
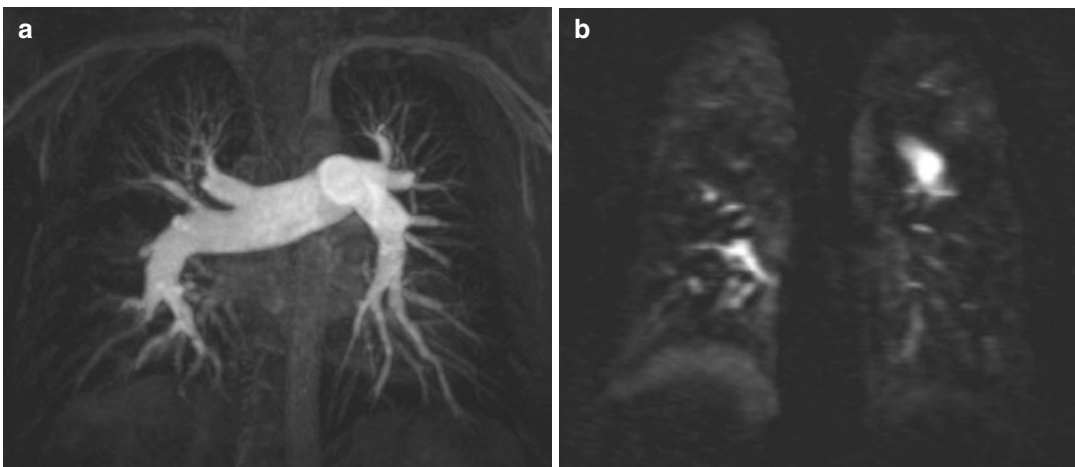
Fig. 1 Patient suffering from PAH. Two years before this MRI examination an invasive pressure measurement revealed a mean pulmonary arterial pressure of 56 mmHg. (**a**) MR angiography (50 mm MIP) shows the dilated main and central pulmonary arteries and the tortuous course towards the periphery. However, all segmental arteries are visible. (**b**) MR perfusion (10 mm MIP) shows a massive reduction of pulmonary perfusion with a patchy pattern. No lobar perfusion defects can be found

3.2 Chronic Thromboembolic Pulmonary Hypertension

The main contributor of CTEPH is the obstruction of the large pulmonary arteries by acute and recurrent pulmonary emboli, and organization of these blood clots (Lang 2015). Up to now, the exact pathological pathways of the development of CTEPH are not yet fully understood: in more than 50% of cases, patients with CTEPH lack a documented history of prior deep venous thrombosis (DVT) or PE. Thus, other conditions may be relevant for the onset of the disease. It has been suggested that a primary arteriopathy and an endothelial dysfunction may lead to in-situ (local) thrombosis in the lung, and that this could contribute to a subsequent failure of thrombus resolution—the thrombotic hypothesis. Furthermore, in some cases, a pulmonary arteriopathy could be the initial pathology, and thromboembolic events may occur as clinical sequelae rather than as the initiating factor (McNeil and Dunning 2007). Additionally, small-vessel hypertensive arteriopathy, similar to that seen in other forms of pulmonary hypertension (PH), develops in small unobstructed vessels.

In the THESEE study, in which scintigraphy perfusion lung scans were performed in 157 patients 8 days and 3 months after acute PE, a residual obstruction after 3 months was found in 66% of patients, and 10% of patients showed no resolution at all (Wartski and Collignon 2000). In a CTA series including 62 patients, at follow-up 13% of patients presented with only partial or no thrombus resolution despite adequate anticoagulation therapy (Remy-Jardin et al. 2007). Based on these data, it can be understood that Pengo et al. found a cumulative incidence of symptomatic CTEPH of 3.8% after 2 years in patients with an acute episode of pulmonary embolism (Pengo et al. 2004).

The combination of a high diagnostic sensitivity together with a radiation-free technique makes perfusion MRI the optimal tool for monitoring of thrombus resolution during anticoagulation therapy (Kluge et al. 2005). In a follow-up study, 33 patients with acute PE were examined with pulmonary perfusion MRI initially and 1 week later.

A subgroup of eight patients also underwent a second follow-up examination. Between both examinations, pulmonary perfusion changed noticeably, i.e., the time-to-peak enhancement decreased, and the peak enhancement of affected areas increased (Kluge et al. 2005).

In CTEPH, the thromboembolic material follows an aberrant path of organization and recanalization—instead of thrombolysis—leading to characteristic abnormalities such as intraluminal webs and bands, pouch-like endings of arteries, irregularities of the arterial wall, and stenotic lesions (Fig. 2) (Kreitner 2014; Wirth et al. 2014; Gopalan et al. 2016). This aberrant path of obstruction and reopening occurs in repeated cycles over many years. Patients become symptomatic if approximately 60% of the total diameter of the pulmonary arterial bed is obstructed. This obstruction leads to an increase in pulmonary arterial pressure and vascular resistance with subsequent cor pulmonale ending in right heart failure with a corresponding 5-year-survival of only 30%.

The primary treatment of CTEPH is surgical pulmonary endarterectomy (PEA), which leads to a permanent improvement of the pulmonary hemodynamics (Jenkins et al. 2016). The technical feasibility and success of surgery mainly depend on the localization of the thromboembolic material: surgical accessibility is given if the organized thrombi are not located distal to the lobar arteries or to the origin of the segmental vessels in order to develop a safe dissection plane for endarterectomy (de Perrot 2016). Between 10 and 50% of referred patients may not be considered eligible for this procedure either because of inaccessible distal thromboembolism or due to other serious comorbidities (Peacock et al. 2006). In these subjects, PAH-specific drug treatment can reduce the symptoms (Charalampopoulos et al. 2016). More recently, the possibility of percutaneous transluminal pulmonary angioplasty has been developed to either be used combined with PEA or alone (Stricker 2016). Lung (or heart-lung) transplantation can also be considered in selected cases where PEA is not indicated, or when significant pulmonary hypertension persists following PEA.
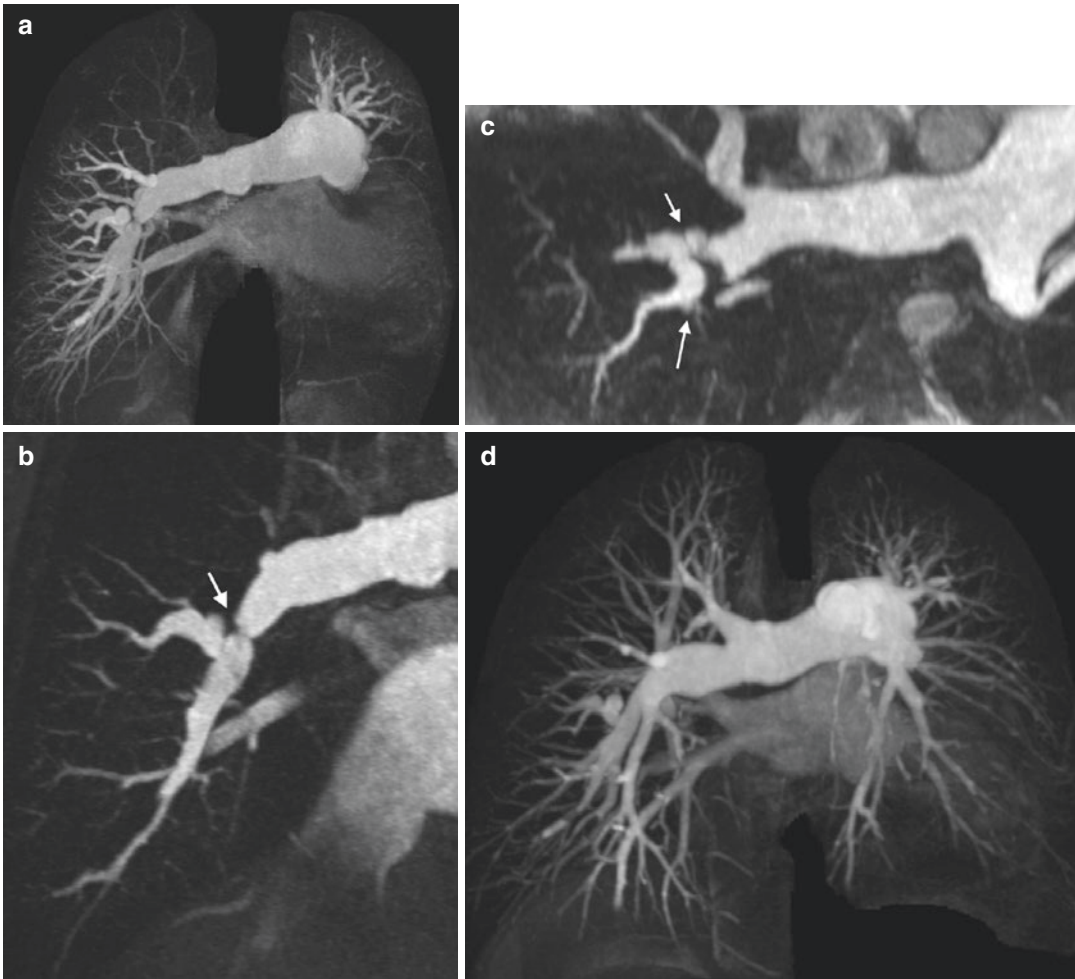
Fig. 2 Thirty-two-year-old female CTEPH patient with the characteristic angiographic findings: intraluminal webs and bands, abrupt vessels cutoffs, and abnormal proximal-to-distal tapering. (**a**) Maximum intensity projection (MIP) reconstruction of preoperative ce-MRA (TR/TE = 3.34/1.23 ms; flip angle = 25°, iPAT-factor = 2, GRAPPA algorithm). (**b**, **c**) Multiplanar reconstructions demonstrate intraluminal webs and bands in the pulmonary arteries (*arrows*). (**d**) Postoperatively, there is a nearly complete normalization of pulmonary arterial vasculature in the right lung and a reopening of many segmental pulmonary arteries in the left

Especially for diagnosis and follow-up of CTEPH patients MRI is well suited (Ley 2015; Gopalan et al. 2016). However, there are only few studies available exploring the usefulness of contrast-enhanced-(CE-) MRA in the diagnostic workup of CTEPH. In a study with 34 patients, depiction of typical findings for CTEPH could be done using CE-MRA (Kreitner et al. 2004). This comprised the detection of wall-adherent thromboembolic material in the central parts of the pulmonary arteries down to the segmental level, intraluminal webs and bands, abnormal proximal-

to-distal tapering, and abrupt vessel cutoffs (Fig. 2). A thorough analysis of source images and the creation of multiplanar reformations were most important for the exact assessment of the morphological findings. Maximum intensity projections on the other hand provided an overview and an impression of the arterial vascular tree that was comparable to those provided by the DSA images. Compared with selective DSA, pulmonary CE-MRA depicted all patent vessel segments down to the level of segmental arteries (533/533 vessel segments). For subsegmental arteries, DSA

significantly detected more patent vessel segments than MRA (733 vs. 681). MRA was superior to DSA in delineating the exact central beginning of the thromboembolic material. In all cases, the most proximal site as assessed by MRA corresponded to the beginning of the dissection procedure during PEA. However, as all patients suffered from CTEPH and were candidates for surgery, there was no statement regarding the ability of CE-MRA in the differentiation of other causes of pulmonary hypertension. Postoperatively, CE-MRA enabled the delineation of reopened segmental arteries and a decrease in the diameter of the central pulmonary arteries. A complete normalization of pulmonary arterial vasculature was not documented in any of the cases. This was confirmed in a recent study in 20 patients applying MR perfusion before and after PEA (Schoenfeld et al. 2016). After adjustment for cardiac output only a significant increase of perfusion was measured in the lower lobes.

CE-MRA of the PA in coronal orientation can be acquired in approximately 15–20 s which is tolerated by most of the CTEPH patients. In a series of 15 patients with CTEPH the diagnostic accuracy of coronal MRA was compared to a sagittal approach with two separate datasets. Sagittal CE-MRA provided a higher resolution and shorter acquisition time (Fig. 3). It proved to be superior in all assessed criteria like image quality, vessel coverage, depiction of patent peripheral arteries, and pathological findings compared to coronal MRA, especially on a segmental level (Oberholzer et al. 2004).

In a study on 29 patients with either CTEPH or primary pulmonary hypertension (PPH), CE-MRA $(1.0 \times 0.7 \times 1.6 \text{ mm}^3)$ was compared with DSA and/or CT angiography (Nikolaou et al. 2005). CE-MRA had sensitivities between 83% and 86% for the detection of complete vessel obstructions and free-floating thrombi, and sensitivities between 50% and
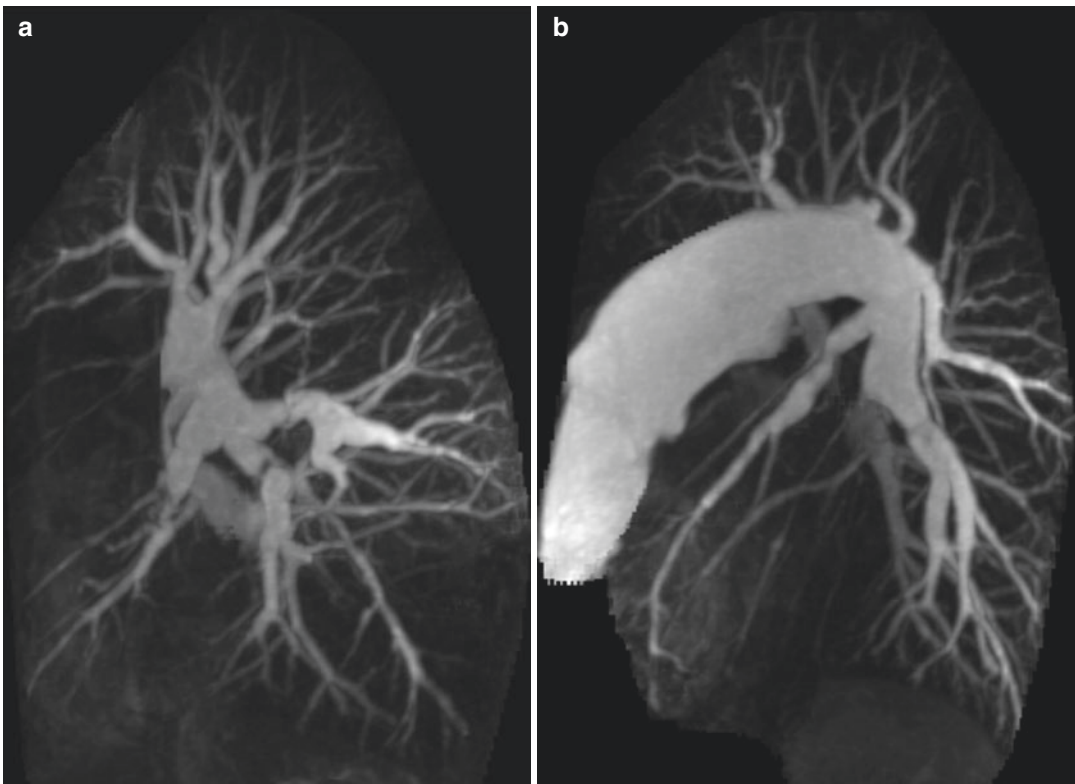
Fig. 3 Sagittal data sets of right (**a**) and left (**b**) pulmonary arteries. MIP reconstructions of preoperative ce-MRA ((TR/TE = 3.34/1.24 ms; flip angle = 25°, iPAT-factor = 2, GRAPPA algorithm), acquisition time = 13 s, 10 mL of gadobutrol). Complete coverage of the pulmonary arterial vasculature

71% for the depiction of older and/or organized thrombi, webs and bands. The specificities ranged between 73% and 95% for non-obstructing findings, and from 91% to 96% for occluding findings, respectively. CE-MRA enabled correct differentiation of PPH and CTEPH in 24 of 29 patients (83%). As in acute PE, pulmonary perfusion MRI should be performed for identification of the typical wedge-shaped perfusion defects (Nikolaou et al. 2005). Perfusion defects were classified either as patchy and/or diffuse (indicative of PPH) or segmental and/or circumscribed (indicative of CTEPH). Compared with perfusion scintigraphy as the standard of reference, MRI had an overall sensitivity of 77% in detecting perfusion defects on a per-patient basis. Compared with the final diagnosis, MR perfusion enabled a correct diagnosis of PPH or CTEPH in 20 (69%) of 29 patients. The combined interpretation of MR perfusion and CE-MRA led to a correct diagnosis of PPH or CTEPH in 26 (90%) of 29 patients when compared with the final reference diagnosis (combination of perfusion scintigraphy with DSA or CT angiography). In another study, MR perfusion was used to differentiate patients with idiopathic pulmonary arterial hypertension (IPAH), CTEPH, and healthy volunteers (Ley et al. 2005). Based on a per-segment analysis, patients with PPH showed a patchy and/or diffuse reduction of perfusion in 71 (79%) of 90 segments, a normal finding in 18 (20%) of 90 segments, and one focal defect (1%). Patients with CTEPH showed focal perfusion defects in 47 (52%), an absent segmental perfusion in 23 (26%), and a normal perfusion in 20 (22%) of 90 segments. On a per-patient basis, there was no difficulty in differentiating the two pathologic entities and in depicting the healthy volunteers. Semiquantitative analysis showed that healthy volunteers demonstrated a significantly shorter transit time than patients with IPAH and CTEPH (14 ± 1 s vs. 22 ± 4 s and 25 ± 11 s, respectively). No difference was found between both patient populations.

A study comparing the capability of MR perfusion compared to scintigraphy was performed in 132 patients (Rajaram et al. 2013). Seventy-eight patients were diagnosed as having CTEPH. Lung perfusion MR correctly identified 76 patients as having CTEPH with an overall sensitivity of 97%, specificity 92%, positive predictive value 95%, and negative predictive value 96% compared with perfusion scintigraphy (sensitivity 96%, specificity 90%).

3.3 Systemic Blood Supply to the Lungs (Bronchosystemic Shunt)

Beside the pulmonary arteries, the lung parenchyma is maintained by bronchial arteries—the direct systemic arterial blood supply of the airways and lung parenchyma (Carvalho et al. 2007; Sopko and Smith 2011). The bronchial arteries arise from the aorta, with a high level of variability, and drain into the pulmonary veins (Baile et al. 1985; Hartmann et al. 2007). In pathological conditions even arteries from the celiac trunk and intercostal arteries can supply to the lung parenchyma (Remy-Jardin et al. 2004). Normally they only contribute to nutrition supply and do not take part in gas exchange. During baseline condition, they have a maximum diameter of 1.5 mm and are rarely seen on helical CT (Kauczor et al. 1994a). In special pathologic conditions (e.g., occlusion of one main pulmonary artery), they also participate in blood oxygenation—up to 25% of bronchial circulation can do so (Robertson et al. 1984). In CTEPH, the flow through the bronchial arteries increases and they become visible on helical CT angiography due to dilatation of the vessels (Fig. 4). Another important finding is that dilated bronchial arteries are positively correlated with a lower mortality rate after pulmonary thromboendarterectomy (Kauczor et al. 1994b). Perloff et al. (2003) evaluated patients with Eisenmenger syndrome and patients with PPH. There was no bronchosystemic shunt seen in patients with Eisenmenger syndrome, but in PPH. Dilated bronchial arteries are also found in patients with inflammatory bronchial arterial disease (like asthma and cystic fibrosis), being a major cause of hemoptysis (Flume et al. 2010; Green et al. 2006).

Up to now, direct visualization of the bronchial arteries was a domain of CT. Due to improved spatial resolution of MRA it is possible to visualize them also with MRI. Functional assessment of the shunt volume was performed by MRI in patients suffering from CTEPH (Ley et al. 2002). The shunt volume, calculated by phase-contrast flow measurements in the pulmonary arteries and ascending aorta, correlated well ($r = 0.86$) with the cross-sectional area of the bronchial arteries, measured on CTA.

Fig. 4 Sixty-seven-year-old male patient with CTEPH. Coronary MPR shows a good delineation of dilated bronchial arteries (*arrows*) supplying the parenchyma of both lungs. Note wall-adherent thromboembolic material in the left pulmonary artery (*asterisk*)

4 Functional Assessment

4.1 Morphology

The enlargement of the central pulmonary arteries can be used as an indirect sign to estimate the increase of the pressure, although this is just a rough estimation as the individual pressure is heavily dependent on the cardiac condition. In a study of 32 patients with PH a diameter of the main pulmonary artery above 28.6 mm readily predicted the presence of pulmonary hypertension (Kuriyama et al. 1984). A diameter of 29 mm or greater has a sensitivity of 87% and specificity of 89% for the diagnosis of PH. If this finding is associated with a segmental artery-to-bronchus ratio greater than one in three or more pulmonary lobes, the specificity for the diagnosis of PH rises to 100% (Bugnone et al. 2002).

4.2 Flow and Pulsatility of Pulmonary Arteries

Phase-contrast measurements of flow and velocity can be regarded as a link between macro- and microcirculation. They enable the determination of cardiac output of the right and left ventricles with low inter- and intraobserver variability and can be performed selectively in the right and left pulmonary arteries (Gatehouse et al. 2010). Furthermore, they allow for a flow-profile analysis that could be the basis for an estimation of mean pulmonary arterial pressure (PAPm) and pulmonary vascular resistance (PVR). In an animal model of pulmonary hypertension (pigs with infusion of thromboxane A2) the acceleration time showed the highest linear correlation with invasively measured PAPm ($r^2 = 0.75$) (Abolmaali et al. 2007). By multiple linear regression analysis, the estimate of PAPm was further increased by taking the maximum of mean velocities into account ($r = 0.897$). In another animal study, systolic pressure measurements in the main pulmonary artery showed good linear correlation with average flow per minute ($r = 0.66$), peak velocity ($r = 0.66$), and average velocity ($r = 0.62$) (Ley et al. 2008).

The pressure wave velocity, determined by phase-contrast flow measurements, correlated well with invasively determined mean pressure in the main pulmonary artery ($r = 0.82$) in 15 PH patients (Laffon et al. 2001). However, calculation of the pressure wave velocity is not yet an established parameter for pressure estimation. Flow measurements allow for discrimination of volunteers and patients with PH (Ley et al. 2007b). The patients showed a significantly reduced peak velocity (cm/s) and pulmonary blood flow (L/min). In this group of PH patients, no relevant bronchosystemic shunting was found. In a large study on 59 patients of whom 42 patients had PAH, the average velocity showed the best correlation with PAPm ($r = -0.73$) and

sPAP ($r = −0.76$). Average velocity (cutoff value = 11.7 cm/s) revealed PAH with a sensitivity of 92.9% (39 of 42) and a specificity of 82.4% (14 of 17) (Sanz et al. 2007).

Pulmonary artery stiffness is increased in the presence of PH and correlates with invasive PA pressures (capacitance to PAPm: $r = −0.75$). Reduced PA pulsatility (<40%) detected the presence of PH at rest with a sensitivity of 93% and a specificity of 63% (Sanz et al. 2009).

Before treatment of PH can be initiated, the individuals' response to the application of vasodilators has to be tested. This is usually performed during invasive right heart catheterization with direct pressure measurements (Rosenkranz 2007). The mean pulmonary artery distensibility was used as a noninvasive marker of acute vasodilator responsiveness in IPAH patients (Jardim et al. 2007). The pulmonary artery distensibility was significantly higher in responders to treatment. A receiver operating characteristic curve analysis has shown that 10% distensibility was able to differentiate responders from nonresponders with 100% sensitivity and 56% specificity.

In CTEPH patients, a good correlation between maximum peak velocity in the pulmonary arteries and PAPm was found; however, the maximum peak velocity did not enable a reliable estimation of PAPm (Kreitner et al. 2004). This was mainly due to the limited temporal resolution of 110 ms. In the meantime, phase-contrast sequences with a temporal resolution between 10 and 12 ms were implemented for better assessment of pulmonary arterial flow (Abolmaali et al. 2004).

A recent study investigated 19 patients with CTEPH using a 1.5 T MR system with simultaneous invasive pressure measurements (Kreitner et al. 2013). A temporal resolution for phase-contrast flow measurements of 10 ms was achieved with an acquisition time of approx. 9 min. A linear combination equation was used to calculate PAPm (mPAP_cal): mPAP_cal = 69.446 − (0.521 × absolute acceleration time) − (0.570 × maximum of mean velocities) + (1.507 × volume of acceleration) + (0.002 × maximum flow acceleration). There was a statistically significant equivalence of

mPAP_cal and simultaneously measured mPAP with a fit of 0.892. Therefore, high temporal resolution phase-contrast flow measurements may be used for noninvasive estimation of mPAP.

A new imaging technique is called 4D phase-contrast flow (4D PC) allowing for visualization and analysis of complex flow pattern (Reiter et al. 2016). Acquisition of a volume of 4D flow data requires approx. 10 min with time resolution below 50 ms and spatial resolution in the order of $2.5 × 2.5 × 2.5$ mm^3. These data can be further postprocessed with vectorial flow presentation.

Employing 4D PC imaging the presence of a vortex of blood flow along the main PA in PH was found, which was not detected in patients with normal PAPm (Reiter et al. 2015). The typical rotation direction of the vortex is forward flow at the anterior side of the main PA and backward flow at its posterior side (Reiter et al. 2016).

The duration of vortical blood flow along the mPA relative to the cardiac interval (t vortex) turned out to be clearly linked to PAPm (Reiter et al. 2016). A proposed segmented linear model increasing from t vortex = 0% (below PAPm = 16 mmHg) linearly with a slope of 1.59% per mmHg. This model allowed for an accurate estimation of PAPm with a standard deviation of 3.9 mmHg, regardless of the PH group. Moreover, the model-based cutoff value for 25 mmHg (t vortex = 14.3%) revealed a high diagnostic accuracy for identifying PH (sensitivity/specificity, 97%/96%).

Another parameter suitable for estimating the pressure is the wall shear stress (Schafer et al. 2016). Wall shear stress is defined as the tangential force per unit area that is exerted by blood flow to the surface of the vessel. In-plane main PA wall shear stress showed strong inverse correlations with multiple hemodynamic indices, including pulmonary resistance ($\rho = −0.74$, $P < 0.001$), mean pulmonary pressure (rho = $−0.64$, $P = 0.006$), and elastance ($\rho = −0.70$, $P < 0.001$) (Schafer et al. 2016).

In CTEPH patients the net forward volume in the pulmonary artery was significantly lower than that in the aorta (Kreitner et al. 2004). This flow difference can be explained by the

bronchosystemic shunt volume that is caused by dilatation of bronchial arteries that originate from the aorta and supply the lung parenchyma. In a former study performed on a subset of CTEPH patients, there was a significant correlation between the cross-sectional area of bronchial arteries as determined by helical CT and the shunt volume between the systemic arterial and pulmonary venous circulation as determined by MR phase-contrast flow measurements (Ley et al. 2002). After surgery, there was a complete resolution of this bronchosystemic shunt volume.

4.3 Evaluation of the Right Ventricle and the Interventricular Septum

With increasing severity of PH, there is progressive right ventricular myocardial hypertrophy, dilatation of the right ventricle and atrium, and a reduction in right ventricular contractility. Moreover, changes in right ventricular relaxation time are observed (Caso et al. 2001). As the right ventricular systolic pressure approaches that of the left ventricle, a paradoxical systolic motion of the interventricular septum is observed (Fig. 5). However, the progress of right
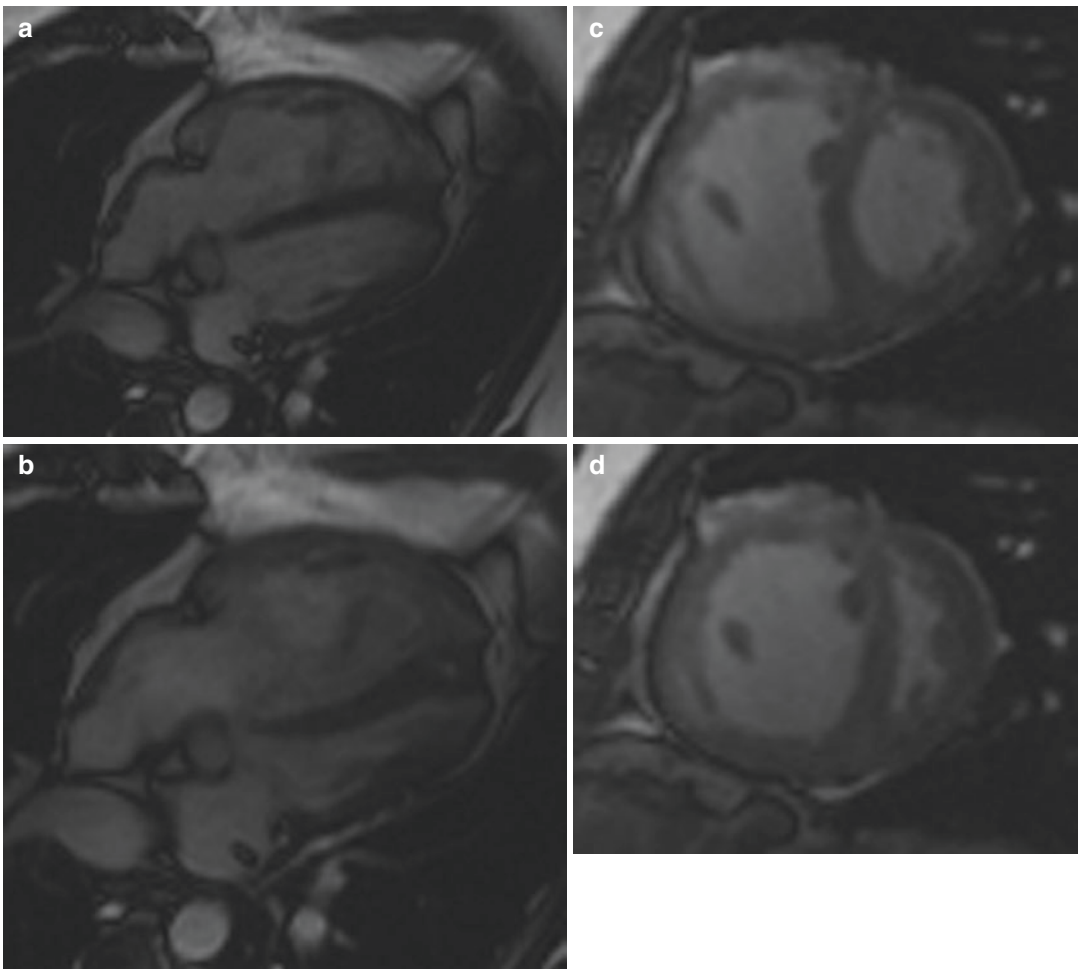
Fig. 5 Patient suffering from PAH. Four chamber view of the patient shows a dilated right ventricle with myocardial hypertrophy in the diastolic phase (**a**) and bowing of the interventricular septum towards the left ventricle (paradoxical septal movement) in the systole (**b**). Short axis view during diastole (**c**) and systole (**d**) even better illustrates the paradoxical septal movement

ventricular dysfunction may vary considerably in time, probably dependent on the duration of the underlying disease and the ability of the right ventricle to adapt to the increased afterload.

Cine MR imaging is an accepted reference standard for the assessment of global and regional left and right ventricular function (Alfakih et al. 2003; Kunz et al. 2005). Furthermore, MRI has shown to be more independent of the experience of the examining physician or technician (Pattynama et al. 1995).

MRI datasets allow for a detailed geometric analysis of the interventricular septal curvature (Moses and Axel 2004). In 37 patients with pulmonary hypertension, systolic PAP higher than 67 mmHg may be expected when leftward curvature of the interventricular septum is observed (Roeleveld et al. 2005). The left ventricular cavity deformation (expressed as the septal-to-free wall curvature ratio) was assessed in 46 PH patients (systolic PAP > 46 mmHg). A direct linear correlation between the pressure rise in the right ventricle during systole and the curvature ratio was observed ($r = 0.85$, $P < 0.001$) (Dellegrottaglie et al. 2007).

Sixty-four successive, unselected, treatment naive patients with suspected pulmonary hypertension were studied using cardiac MR and RHC (Swift et al. 2013). A strong correlation between PAPm and MR-estimated PAPm was demonstrated ($R^2 = 0.67$) based on the equation: cardiac MR-predicted PAPm = −4.6 + (interventricular septal angle × 0.23) + (ventricular mass index × 16.3).

Cine imaging in CTEPH patients typically reveals a hypertrophy and dilatation of the right ventricle, a reduced right ventricular ejection fraction without substantial impairment of left ventricular interventricular septum (Kreitner et al. 2007). After successful PEA, there is a significant improvement or normalization of the right ventricular ejection fraction with the interventricular septum returning to a normal movement in most cases (Kreitner et al. 2004). The increased vascular resistance in CTEPH patients goes along with a decreased ejection fraction: the right ventricular ejection fraction showed a good negative correlation with the PAPm. However,

analogous to the maximum peak velocity in the same study, a precise estimation of PAPm was not possible. Interestingly, the differences between the pre- and postoperative results of the right ventricular ejection fraction and PAPm showed the best correlation ($r = 0.8$, slope = 0.98).

Another study examined 17 patients with CTEPH, before and at 4 months after PEA using Cine-MRI and invasive pressure measurements. After PEA pulmonary hemodynamics improved, and right and left ventricular volumes and leftward ventricular septal bowing normalized; right ventricular mass decreased significantly ($P < 0.0005$), but did not completely normalize. The change in total pulmonary resistance correlated with the change in right ventricular ejection fraction, right ventricular mass, and leftward ventricular septal bowing (Reesink et al. 2007).

In a study on 20 patients before and after PEA the PAPm determined by RHC decreased from 46 to 24 mmHg (Schoenfeld et al. 2016). The RV ejection fraction increased significantly from 30% to 52% and the RV mass/BSA decreased from 41.7 g/m^2 to 34 g/m^2 within 2 weeks.

At present, cine and phase-contrast MR imaging enable a reliable assessment of the functional improvement of the CTEPH patient after technically successful (Kreitner et al. 2004).

References

Abolmaali ND, Esmaeili A, Feist P, Ackermann H, Requardt M, Schmidt H, Vogl TJ (2004) Reference values of MRI flow measurements of the pulmonary outflow tract in healthy children. Fortschr Röntgenstr 176(6):837–845

Abolmaali N, Seitz U, Esmaeili A, Kock M, Radeloff D, Ackermann H, Vogl TJ (2007) Evaluation of a resistance-based model for the quantification of pulmonary arterial hypertension using MR flow measurements. J Magn Reson Imaging 26(3):646–653

Alfakih K, Plein S, Thiele H, Jones T, Ridgway JP, Sivananthan MU (2003) Normal human left and right ventricular dimensions for MRI as assessed by turbo gradient echo and steady-state free precession imaging sequences. J Magn Reson Imaging 17(3):323–329

Altes TA, Eichinger M, Puderbach M (2007) Magnetic resonance imaging of the lung in cystic fibrosis. Proc Am Thorac Soc 4(4):321–327

Baile EM, Ling H, Heyworth JR, Hogg JC, Pare PD (1985) Bronchopulmonary anastomotic and noncoronary

collateral blood flow in humans during cardiopulmonary bypass. Chest 87(6):749–754

Bergin CJ, Hauschildt J, Rios G, Belezzuoli EV, Huynh T, Channick RN (1997) Accuracy of MR angiography compared with radionuclide scanning in identifying the cause of pulmonary arterial hypertension. AJR Am J Roentgenol 168(6):1549–1555

Bugnone AN, Viamonte M, Jr., Garcia H (2002) Imaging findings in human immunodeficiency virus-related pulmonary hypertension: report of five cases and review of the literature. Radiology 223(3): 820–827

Carvalho P, Anderson DK, Charan NB (2007) Bronchial arterial imaging using helical computed tomography. Pulm Pharmacol Ther 20(2):104–108

Caso P, Galderisi M, Cicala S, Cioppa C, D'Andrea A, Lagioia G, Liccardo B, Martiniello AR, Mininni N (2001) Association between myocardial right ventricular relaxation time and pulmonary arterial pressure in chronic obstructive lung disease: analysis by pulsed Doppler tissue imaging. J Am Soc Echocardiogr 14(10):970–977

Chaouat A, Naeije R, Weitzenblum E (2008) Pulmonary hypertension in COPD. Eur Respir J 32(5):1371–1385

Charalampopoulos A, Gibbs JS, Davies RJ, Gin-Sing W, Murphy K, Sheares KK, Pepke-Zaba J, Jenkins DP, Howard LS (2016) Exercise physiological responses to drug treatments in chronic thromboembolic pulmonary hypertension. J Appl Physiol (1985) 121(3):623–628. doi:10.1152/japplphysiol.00087.2016

Chatterjee K, De Marco T, Alpert JS (2002) Pulmonary hypertension: hemodynamic diagnosis and management. Arch Intern Med 162(17):1925–1933

Cuttica MJ (2016) Pulmonary hypertension associated with lung diseases and hypoxemia. Heart Fail Rev 21(3):299–308. doi:10.1007/s10741-016-9551-x

Delcroix M, Kerr K, Fedullo P (2016) Chronic thromboembolic pulmonary hypertension. Epidemiology and risk factors. Ann Am Thorac Soc 13(Suppl 3):S201–S206. doi:10.1513/AnnalsATS.201509-621AS

Dellegrottaglie S, Sanz J, Poon M, Viles-Gonzalez JF, Sulica R, Goyenechea M, Macaluso F, Fuster V, Rajagopalan S (2007) Pulmonary hypertension: accuracy of detection with left ventricular septal-to-free wall curvature ratio measured at cardiac MR. Radiology 243(1):63–69

Fernandes T, Planquette B, Sanchez O, Morris T (2016) From acute to chronic thromboembolic disease. Ann Am Thorac Soc 13(Suppl 3):S207–S214. doi:10.1513/AnnalsATS.201509-619AS

Flume PA, Mogayzel PJ Jr, Robinson KA, Rosenblatt RL, Quittell L, Marshall BC (2010) Cystic fibrosis pulmonary guidelines: pulmonary complications: hemoptysis and pneumothorax. Am J Respir Crit Care Med 182(3):298–306. doi:10.1164/rccm.201002-0157CI182/3/298

Freed BH, Collins JD, Francois CJ, Barker AJ, Cuttica MJ, Chesler NC, Markl M, Shah SJ (2016) MR and CT imaging for the evaluation of pulmonary hypertension. JACC Cardiovasc Imaging 9(6):715–732. doi:10.1016/j.jcmg.2015.12.015

Gatehouse PD, Rolf MP, Graves MJ, Hofman MB, Totman J, Werner B, Quest RA, Liu Y, von Spiczak J, Dieringer M, Firmin DN, van Rossum A, Lombardi M, Schwitter J, Schulz-Menger J, Kilner PJ (2010) Flow measurement by cardiovascular magnetic resonance: a multi-centre multi-vendor study of background phase offset errors that can compromise the accuracy of derived regurgitant or shunt flow measurements. J Cardiovasc Magn Reson 12:5

Gopalan D, Blanchard D, Auger WR (2016) Diagnostic evaluation of chronic thromboembolic pulmonary hypertension. Ann Am Thorac Soc 13(Suppl 3):S222–S239. doi:10.1513/AnnalsATS.201509-623AS

Green FH, Butt JC, James AL, Carroll NG (2006) Abnormalities of the bronchial arteries in asthma. Chest 130(4):1025–1033

Hartmann IJ, Remy-Jardin M, Menchini L, Teisseire A, Khalil C, Remy J (2007) Ectopic origin of bronchial arteries: assessment with multidetector helical CT angiography. Eur Radiol 17(8):1943–1953

Jardim C, Rochitte CE, Humbert M, Rubenfeld G, Jasinowodolinski D, Carvalho CR, Souza R (2007) Pulmonary artery distensibility in pulmonary arterial hypertension: an MRI pilot study. Eur Respir J 29(3):476–481

Jenkins DP, Biederman A, D'Armini AM, Dartevelle PG, Gan HL, Klepetko W, Lindner J, Mayer E, Madani MM (2016) Operability assessment in CTEPH: lessons from the CHEST-1 study. J Thorac Cardiovasc Surg. doi:10.1016/j.jtcvs.2016.02.062

Jobst BJ, Wielputz MO, Triphan SM, Anjorin A, Ley-Zaporozhan J, Kauczor HU, Biederer J, Ley S, Sedlaczek O (2015) Morpho-functional 1H-MRI of the lung in COPD: short-term test-retest reliability. PLoS One 10(9):e0137282. doi:10.1371/journal.pone.0137282

Jung JI, Park SH, Lee JM, Hahn ST, Kim KA (2000) MR characteristics of progressive massive fibrosis. J Thorac Imaging 15(2):144–150

Kauczor H-U, Cagil H, Fischer B, Schickert HC, Mildenberger P (1994a) CT-Angiographie der Bronchialarterien. Fortschr Röntgenstr 160(5):477–479

Kauczor H-U, Schwickert HC, Mayer E, Schweden F, Schild HH, Thelen M (1994b) Spiral CT of bronchial arteries in chronic thromboembolism. J Comput Assist Tomogr 18(6):855–861

Kluge A, Gerriets T, Lange U, Bachmann G (2005) MRI for short-term follow-up of acute pulmonary embolism. Assessment of thrombus appearance and pulmonary perfusion: a feasibility study. Eur Radiol 15(9):1969–1977

Kreitner KF (2014) Noninvasive imaging of pulmonary hypertension. Semin Respir Crit Care Med 35(1):99–111. doi:10.1055/s-0033-1363456

Kreitner KF, Ley S, Kauczor HU, Mayer E, Kramm T, Pitton MB, Krummenauer F, Thelen M (2004) Chronic thromboembolic pulmonary hypertension: pre- and postoperative assessment with breath-hold MR imaging techniques. Radiology 232(2):535–543

nance imaging: preliminary experience in 40 subjects. J Magn Reson Imaging 20(3):353–365

Ohno Y, Hatabu H, Murase K, Higashino T, Nogami M, Yoshikawa T, Sugimura K (2007) Primary pulmonary hypertension: 3D dynamic perfusion MRI for quantitative analysis of regional pulmonary perfusion. AJR Am J Roentgenol 188(1):48–56

Pattynama PMT, Lamb HJ, van der Velde EA, van der Geest RJ, van der Wall EE, de Roos A (1995) Reproducibilty of MRI-derived measurements of right ventricular volumes and myocardial mass. J Magn Reson Imaging 13(1):53–63

Peacock A, Simonneau G, Rubin L (2006) Controversies, uncertainties and future research on the treatment of chronic thromboembolic pulmonary hypertension. Proc Am Thorac Soc 3(7):608–614

Pengo V, Lensing AW, Prins MH, Marchiori A, Davidson BL, Tiozzo F, Albanese P, Biasiolo A, Pegoraro C, Iliceto S, Prandoni P (2004) Incidence of chronic thromboembolic pulmonary hypertension after pulmonary embolism. N Engl J Med 350(22):2257–2264

Perloff JK, Hart EM, Greaves SM, Miner PD, Child JS (2003) Proximal pulmonary arterial and intrapulmonary radiologic features of Eisenmenger syndrome and primary pulmonary hypertension. Am J Cardiol 92(2):182–187

de Perrot M (2016) Operability assessment in chronic thromboembolic pulmonary hypertension (CTEPH): don't miss the chance of a second opinion! J Thorac Cardiovasc Surg. doi:10.1016/j.jtcvs.2016.05.049

Presberg KW, Dincer HE (2003) Pathophysiology of pulmonary hypertension due to lung disease. Curr Opin Pulm Med 9(2):131–138

Primack SL, Mayo JR, Hartman TE, Miller RR, Muller NL (1994) MRI of infiltrative lung disease: comparison with pathologic findings. J Comput Assist Tomogr 18(2):233–238

Rajaram S, Swift AJ, Telfer A, Hurdman J, Marshall H, Lorenz E, Capener D, Davies C, Hill C, Elliot C, Condliffe R, Wild JM, Kiely DG (2013) 3D contrast-enhanced lung perfusion MRI is an effective screening tool for chronic thromboembolic pulmonary hypertension: results from the ASPIRE registry. Thorax 68(7):677–678. doi:10.1136/thoraxjnl-2012-203020

Reesink HJ, Marcus JT, Tulevski II, Jamieson S, Kloek JJ, Vonk Noordegraaf A, Bresser P (2007) Reverse right ventricular remodeling after pulmonary endarterectomy in patients with chronic thromboembolic pulmonary hypertension: utility of magnetic resonance imaging to demonstrate restoration of the right ventricle. J Thorac Cardiovasc Surg 133(1):58–64

Reiter G, Reiter U, Kovacs G, Olschewski H, Fuchsjager M (2015) Blood flow vortices along the main pulmonary artery measured with MR imaging for diagnosis of pulmonary hypertension. Radiology 275(1):71–79. doi:10.1148/radiol.14140849

Reiter U, Reiter G, Fuchsjager M (2016) MR phase-contrast imaging in pulmonary hypertension. Br J Radiol 89(1063):20150995. doi:10.1259/bjr.20150995

Remy-Jardin M, Bouaziz N, Dumont P, Brillet PY, Bruzzi J, Remy J (2004) Bronchial and nonbronchial systemic arteries at multi-detector row CT angiography: comparison with conventional angiography. Radiology 233(3):741–749

Remy-Jardin M, Pistolesi M, Goodman LR, Gefter WB, Gottschalk A, Mayo JR, Sostman HD (2007) Management of suspected acute pulmonary embolism in the era of CT angiography: a statement from the Fleischner society. Radiology 245(2):315–329

Robertson HT, Jindal SK, Lakshminarayan S, Albert R, Kirk W, Hlastala MP, Butler J (1984) Gas exchange properties of the bronchial circulation in a dog lobe maintained in zone 1 conditions. Am Rev Respir Dis 129(4):A229

Roeleveld RJ, Marcus JT, Faes TJ, Gan TJ, Boonstra A, Postmus PE, Vonk-Noordegraaf A (2005) Interventricular septal configuration at mr imaging and pulmonary arterial pressure in pulmonary hypertension. Radiology 234(3):710–717

Rosenkranz S (2007) Pulmonary hypertension: current diagnosis and treatment. Clin Res Cardiol 96(8):527–541

Ryu JH, Krowka MJ, Pellikka PA, Swanson KL, McGoon MD (2007) Pulmonary hypertension in patients with interstitial lung diseases. Mayo Clin Proc 82(3):342–350

Sanz J, Kuschnir P, Rius T, Salguero R, Sulica R, Einstein AJ, Dellegrottaglie S, Fuster V, Rajagopalan S, Poon M (2007) Pulmonary arterial hypertension: noninvasive detection with phase-contrast MR imaging. Radiology 243(1):70–79

Sanz J, Kariisa M, Dellegrottaglie S, Prat-Gonzalez S, Garcia MJ, Fuster V, Rajagopalan S (2009) Evaluation of pulmonary artery stiffness in pulmonary hypertension with cardiac magnetic resonance. JACC Cardiovasc Imaging 2(3):286–295

Schafer M, Kheyfets VO, Schroeder JD, Dunning J, Shandas R, Buckner JK, Browning J, Hertzberg J, Hunter KS, Fenster BE (2016) Main pulmonary arterial wall shear stress correlates with invasive hemodynamics and stiffness in pulmonary hypertension. Pulm Circ 6(1):37–45. doi:10.1086/685024PC2013254

Schoenfeld C, Cebotari S, Hinrichs J, Renne J, Kaireit T, Olsson KM, Voskrebenzev A, Gutberlet M, Hoeper MM, Welte T, Haverich A, Wacker F, Vogel-Claussen J (2016) MR imaging-derived regional pulmonary parenchymal perfusion and cardiac function for monitoring patients with chronic thromboembolic pulmonary hypertension before and after pulmonary Endarterectomy. Radiology 279(3):925–934. doi:10.1148/radiol.2015150765

Shimoda LA, Sham JS, Sylvester JT (2000) Altered pulmonary vasoreactivity in the chronically hypoxic lung. Physiol Res 49(5):549–560

Simonneau G, Gatzoulis MA, Adatia I, Celermajer D, Denton C, Ghofrani A, Gomez Sanchez MA, Krishna Kumar R, Landzberg M, Machado RF, Olschewski H, Robbins IM, Souza R (2013) Updated clini-

cal classification of pulmonary hypertension. J Am Coll Cardiol 62(25 Suppl):D34–D41. doi:10.1016/j.jacc.2013.10.029

Sopko DR, Smith TP (2011) Bronchial artery embolization for hemoptysis. Semin Interv Radiol 28(1):48–62. doi:10.1055/s-0031-1273940

Stricker H (2016) Chronic thromboembolic pulmonary hypertension--a diagnostic and therapeutic update. VASA Zeitschrift fur Gefasskrankheiten 45(3):195–199. doi:10.1024/0301-1526/a000525

Swift AJ, Rajaram S, Hurdman J, Hill C, Davies C, Sproson TW, Morton AC, Capener D, Elliot C, Condliffe R, Wild JM, Kiely DG (2013) Noninvasive estimation of PA pressure, flow, and resistance with CMR imaging: derivation and prospective validation study from the ASPIRE registry. JACC Cardiovasc Imaging 6(10):1036–1047. doi:10.1016/j.jcmg.2013.01.013

Swift AJ, Wild JM, Nagle SK, Roldan-Alzate A, Francois CJ, Fain S, Johnson K, Capener D, van Beek EJ, Kiely DG, Wang K, Schiebler ML (2014a) Quantitative magnetic resonance imaging of pulmonary hypertension: a practical approach to the current state of the art. J Thorac Imaging 29(2):68–79. doi:10.1097/RTI.0000000000000079

Swift AJ, Telfer A, Rajaram S, Condliffe R, Marshall H, Capener D, Hurdman J, Elliot C, Kiely DG, Wild JM (2014b) Dynamic contrast-enhanced magnetic resonance imaging in patients with pulmonary arterial hypertension. Pulm Circ 4(1):61–70. doi:10.1086/674882

Taichman DB, Mandel J (2007) Epidemiology of pulmonary arterial hypertension. Clin Chest Med 28(1):1–22. vii

Thabut G, Dauriat G, Stern JB, Logeart D, Levy A, Marrash-Chahla R, Mal H (2005) Pulmonary hemodynamics in advanced COPD candidates for lung volume reduction surgery or lung transplantation. Chest 127(5):1531–1536. doi:10.1378/chest.127.5.1531

Tuder RM, Marecki JC, Richter A, Fijalkowska I, Flores S (2007) Pathology of pulmonary hypertension. Clin Chest Med 28(1):23–42, vii

Wartski M, Collignon MA (2000) Incomplete recovery of lung perfusion after 3 months in patients with acute pulmonary embolism treated with antithrombotic agents. THESEE study group. Tinzaparin ou heparin standard: evaluation dans l'Embolie Pulmonaire study. J Nucl Med 41(6):1043–1048

Wirth G, Bruggemann K, Bostel T, Mayer E, Duber C, Kreitner KF (2014) Chronic thromboembolic pulmonary hypertension (CTEPH) – potential role of multidetector-row CT (MD-CT) and MR imaging in the diagnosis and differential diagnosis of the disease. Rofo 186(8):751–761. doi:10.1055/s-0034-1366425

Wright JL, Levy RD, Churg A (2005) Pulmonary hypertension in chronic obstructive pulmonary disease: current theories of pathogenesis and their implications for treatment. Thorax 60(7):605–609

Vascular Anomalies and Diseases

Sebastian Ley and Julia Ley-Zaporozhan

Contents

S. Ley, M.D. (✉)
Chirurgisches Klinikum München Süd, Diagnostic and Interventional Radiology, Munich, Germany

Institute of Clinical Radiology, Ludwig-Maximilians University Hospital Munich, Munich, Germany
e-mail: ley@gmx.net

J. Ley-Zaporozhan, M.D.
Klinik und Poliklinik für Radiologie, Ludwig-Maximilians University Hospital Munich, Munich, Germany
e-mail: julia.leyzaporozhan@gmail.com

Key Points

The spectrum of the congenital vascular malformations includes abnormalities of the pulmonary arterial system, partial or total abnormal pulmonary venous return, and anomalies of the aorta. Acquired diseases of the pulmonary vessels, other than thromboembolic diseases, are either primary tumors of the vessels or external compression. The following sections are organized accordingly—covering congenital vascular malformations, arteriovenous malformations, and other diseases of the pulmonary vasculature.

With increasing experience and development of new surgical techniques more and more complex forms of congenital cardiovascular diseases can be corrected. All surgical approaches significantly benefit from detailed three-dimensional (3D) presentation of the complex anatomy, which can be acquired using MRI.

1 Imaging of Congenital Heart Disease

The heterogeneity of anatomy, age, surgical procedure, and institutional management protocols contradicts development of clear imaging guidelines (Bhat and Sahn 2004).

Echocardiography is the primary examination in neonates, infants, and young children, and therefore the most frequently used noninvasive technique to examine cardiac morphology

and function. In older patients, particularly those with complex or surgically corrected (congenital) malformations, information acquired with transthoracic echocardiography may not be satisfactory. Scar and bone or lung tissue and chest deformations interfere with small acoustic windows. Transesophageal echocardiography obviously provides a better field of view in adults, especially since biplanar probes have become available. Still, echocardiography is often not sufficient in imaging of the pulmonary arteries and remains to be user dependent.

Conventional digital catheter angiography (DA) has long been the gold standard for the evaluation of cardiac anatomy and function. Additionally, it is the only method to determine pulmonary vascular pressure and oxygen saturation. However, DA is invasive and has a considerable complication rate, and requires the use of ionizing radiation and intra-arterial administration of iodinated contrast media (Hoeper et al. 2006).

Due to fast acquisition of high-spatial-resolution images, allowing for 3D post-processing, MDCT is actually a very common imaging modality. However, the lack of hemodynamic measurements, application of radiation, and iodinated contrast media makes it an unfavorable imaging technique for pediatric patients as it is known that children are more sensitive to the effects of ionizing radiation than adults are.

With the technical development of magnetic resonance imaging (MRI) this technique has increasingly been used for noninvasive assessment of the pulmonary vasculature (Eichhorn et al. 2004; Simonetti and Cook 2006). As the pulmonary arteries are rarely affected alone, it is important to examine the heart, pulmonary, and systemic vasculature in the first workup with a focus on the vascular diameters for surgical connectivity. If only the pulmonary arteries are affected, then contrast-enhanced techniques are well suited for sufficient imaging. If the placement of a conduit is considered, the most important task for imaging is to

preoperatively provide accurate luminal diameters in order to determine the prospective size of the conduits. Postoperatively conduit stenosis or insufficiency has to be ruled out frequently. In case of slow and/or turbulent flow, contrast-enhanced imaging may be quite difficult as the contrast material might not fill the vascular lumen homogenously. The visualization of all the vascular pathologies in complex congenital heart disease (CHD) is still a challenge for CT and MRI. In these cases, the contrast bolus is often diluted due to intracardial or extracardial shunts with mixing of non-contrast-enhanced blood. Severe imaging artifacts can occur in CT and MRI after surgical and interventional procedures due to metal artifacts originating from conduits with valves, coil material, or stents from former interventions (Maintz et al. 2003).

Today, cardiovascular MRI is most often performed using 1.5 T scanners due to the optimized coil and sequence technology (Naganawa et al. 2004). The increased specific absorption rate at high-field MRI (3 T) is still a challenge for imaging using the standard steady-state free precession techniques (Gilmore et al. 2004).

MRI in children younger than 5 years usually requires some form of sedation to tolerate the examination. Subsequently, free breathing techniques are necessary with increasing examination times. To acquire sharp images of the pulmonary vasculature single-shot techniques like half-Fourier single-shot turbo-spin-echo (HASTE) or steady-state free-precession (SSFP) sequences are utilized (Fig. 1) (Weiss et al. 2005). Combining those with a saturation pulse, the vessels are dark and can be well delineated. However, they can still be hazy and the saturation is not perfect in case of turbulent flow. Turbo-spin-echo (TSE) sequences are also fast imaging techniques with sharp delineation of the vessels (Weiss et al. 2005). For reduction of blurriness, averaging of the sequences (e.g., three averages) may be preferable. Usual acquisition times for a three times averaged TSE sequence of the thorax are
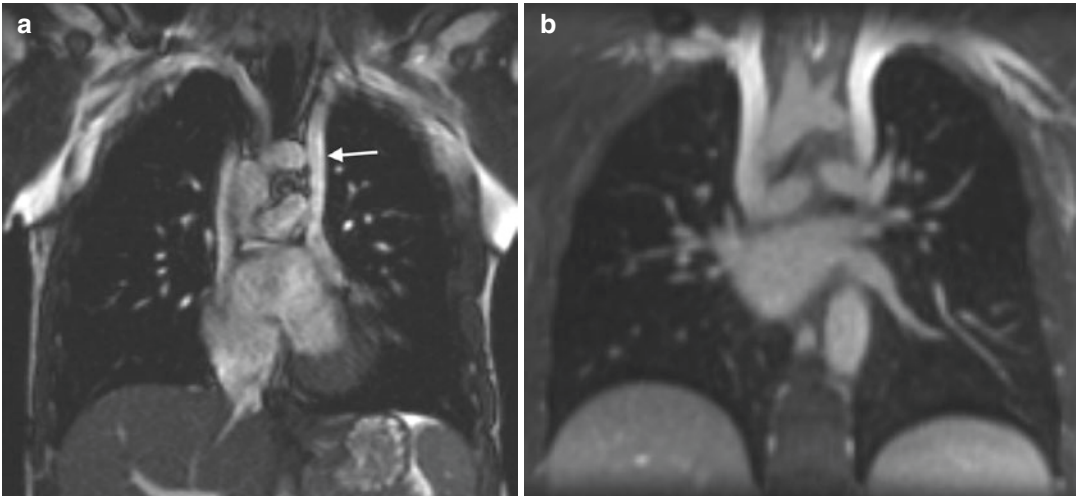
Fig. 1 Steady-state free-precession (SSFP) sequence (**a**) compared with a T1 GRE (VIBE) (**b**) acquired in coronal orientation. Images show a persistent left vena cava supe- rior (*arrow*). Note the good inherent vascular signal of the SSFP technique. These fast acquisition techniques allow for a rapid evaluation of vascular pathologies

3 min. Using spin-echo sequences the internal vascular diameter is underestimated compared to DA. In a phantom study an underestimation of 10–20% of linear dimensions was found (Holmqvist et al. 2001).

Another possible solution for visualization of the vasculature is the use of time-resolved MR angiography techniques. The spatial resolution is reduced ($1.4 \times 1.4 \times 2.0$ mm^3) to increase tempo- ral resolution (6 s per 3D dataset) (Fink et al. 2003). Thus, motion artifacts are minimized and a separation of arteries and veins can be achieved. Also, due to the time-resolved approach contrast media timing is not necessary.

The low body weight (b.w.) of children makes it necessary to apply 0.2 mmol/kg b.w. of a 0.5 M contrast media (Macgowan et al. 2005). However, for evaluation of subtle stenoses time-resolved MR angiography may not be sufficient. In a study including children from 2 days to 5 years the delineation of the vascular lumen was therefore further increased by injection of 0.2 mmol/kg b.w. of a 1 M contrast media (Fries et al. 2005). However, the use of this contrast agent (e.g., gadobenate dimeglumine (Gd-BOPTA)) in chil- dren is off-label and requires special permission (Grist and Thornton 2005).

Especially in children with unknown CHD time-resolved MR angiography also allows for characterization of the pulmonary perfusion due to the time course of contrast enhancement in the lung parenchyma (i.e., pulmonary arterial or sys- temic) (Boll et al. 2005).

In patients compliant in performing a breath- hold, acquisition of high spatial resolution angi- ography datasets ($1.2 \times 1.0 \times 1.6$ mm^3) can be performed (Ley et al. 2005). Using this tech- nique, even subtle variations in luminal diameters can be assessed.

A volume interpolated breath-hold tech- nique (VIBE) (breath-hold preferred, averag- ing possible) allows for high-spatial-resolution T1-weighted imaging. After contrast media injection it can be used to demonstrate the rela- tionship between airways and the pulmonary vasculature (Biederer et al. 2003). This tech- nique was already successfully combined with cardiac and respiratory gating and used in non- contrast-enhanced coronary arterial imaging in adults (Jhooti et al. 2000). Due to double gat- ing this technique may be promising for pedi- atric imaging.

Another technique, also adapted from coro- nary imaging, is a free-breathing 3D double-slab

fast imaging with steady-precession MR angiography (3D FISP MRA) (Sorensen et al. 2004; Sorensen et al. 2005). The resolution with a voxel size of $1.25 \times 1.25 \times 1.25$ mm^3 enables excellent diagnosis even in infants with vascular rings and slings (Greil et al. 2005).

Major aortopulmonary collateral arteries (MAPCA) can also be visualized by MRA but only if these arteries are markedly dilated (Boechat et al. 2005).

The creation of multiplanar reformats is necessary to accurately assess the vascular diameter after surgery (Sorensen et al. 2005). After arterial switch operation (ASO) for complete transposition of the great arteries in some cases narrowing of pulmonary arteries is associated with oval vessel diameters. In these patients special attention should be focused on the central part of the pulmonary arteries and MPRs have to be performed. Conventional angiography should only be performed when intervention is planned (Weiss et al. 2005).

Besides good visualization of the vasculature, MRI is capable of assessing the blood flow through arteries and veins by phase-contrast flow measurements (Roman et al. 2005; Gatehouse et al. 2005). This enables quantification of shunt volumes and can also be used to identify stenosis by an increased peak velocity. The pressure gradient across a stenosis can be calculated with the modified Bernoulli equation (Varaprasathan et al. 2002). However, quantitative pressure estimates of the pulmonary arterial system are still not possible using MRI. Therefore invasive pressure measurements are still mandatory (Nakanishi 2005).

A basic MRI examination protocol should include a contrast-enhanced angiography and techniques for non-contrast-enhanced visualization of the pulmonary vasculature. The FOV should cover the entire thorax of the patient to include secondary anomalies not suspected before. Overall, MRI enables good visualization of the pulmonary vasculature with and without contrast media. It is capable of acquiring functional cardiac information or blood flow distribution to the pulmonary and systemic circulation. As the main drawback, rather long examination times and the use of sedatives are to be mentioned.

A typical MR examination protocol is the following suggested MRI protocol for pediatric patients with proven or suggested congenital vascular disease (taken from (Ley et al. 2007 #2690)) (note that these techniques are aimed for optimal visualization of the pulmonary arteries and include no functional cardiac information; functional sequences may be added at the expense of additional examination time):

- Localizer
- HASTE coronal dark blood (ECG and respiratory gated)
- HASTE transversal dark blood (ECG and respiratory gated)
- T1 TSE transversal dark blood (ECG gated, breath-hold, or three averages)
- T1 TSE coronal dark blood (ECG gated, breath-hold, or three averages)
- Time-resolved angiography (4 s per 3D dataset)
- Postcontrast T1 VIBE (breath-hold or three averages)
- 3D true fast imaging with steady-state precession (TrueFISP) coronal or transversal with ECG and respiratory gating ($1.0 \times 1.0 \times 1.0$ mm^3)
- Phase-contrast flow measurements (pulmonary trunk, right and left pulmonary artery, and ascending aorta)

Recent advances in rapid MR imaging have enabled fully MR-guided intravascular interventions in closed-bore clinical whole-body MR scanners (Sequeiros et al. 2005). Dedicated active catheters and fast imaging sequences with automatic slice positioning in combination with a dedicated user interface for intravascular procedures are a mandatory prerequisite for safe application of the technique (Bock et al. 2006). First reports in animal models demonstrate the possibility of placing, i.e., Amplatzer septal occluders® under MRI guidance (Rickers et al. 2003). MRI guidance of percutaneous transluminal balloon angioplasty (PTCA) of aortic coarctation was shown as a suitable alternative to conventional fluoroscopy for catheter-based treatment in a pilot study with patients (Krueger et al. 2006).

Coils, stents, occluders, and clips lead to enormous artifacts making it sometimes impossible to perform MRI. After catheter interventional

therapy for patent ductus arteriosus left pulmonary arterial stenosis may occur. Therefore, MDCT using a low-dose protocol should be performed to rule out pulmonary stenosis. Because of artifacts echocardiography often does not provide enough information in this particular condition. DA should only be considered if a pressure measurement is necessary.

2 Congenital Pulmonary Vascular Diseases

Congenital heart disease (CHD) is the collective term for congenital malformations affecting the heart, pulmonary arteries, and aorta. Most cases of CHD are thought to be multifactorial and a result from a combination of genetic predisposition and environmental stimulus. Due to the complex nature of CHD single numbers for uniform types of malformations affecting the pulmonary arteries are not known. In general, CHD occurs in 0.5–0.8% of live births, indicating that about 1.5 million children are born with a cardiac malformation worldwide each year (Hoffman 1995). The spectrum of anatomic malformations is reaching from relatively simple to very complex

entities. About 2–3 out of 1000 newborn infants will become symptomatic with heart disease in the first year of life. Nowadays the diagnosis is most often established within the first month (Bernstein 2004).

2.1 Congenital Pulmonary Arterial Disorders

2.1.1 Stenosis of the Pulmonary Valve, the Pulmonary Artery, and Its Branches

The most common right ventricular outflow obstruction is isolated pulmonary stenosis, which accounts for 7–10% of all CHD. Stenosis may occur anywhere along the major branches of the pulmonary arteries and ranges from mild to severe and from circumscript to extensive forms (Fig. 2). Frequently, these anomalies are associated with other types of CHD, including tetralogy of Fallot (TOF), ventricular septal defect (VSD), and atrial septal defect (ASD). Moderate stenosis of the pulmonary arteries can be treated with repeated balloon angioplasty. In case of severe stenosis or hypoplasia of the pulmonary artery (Fig. 3), surgical interposition of
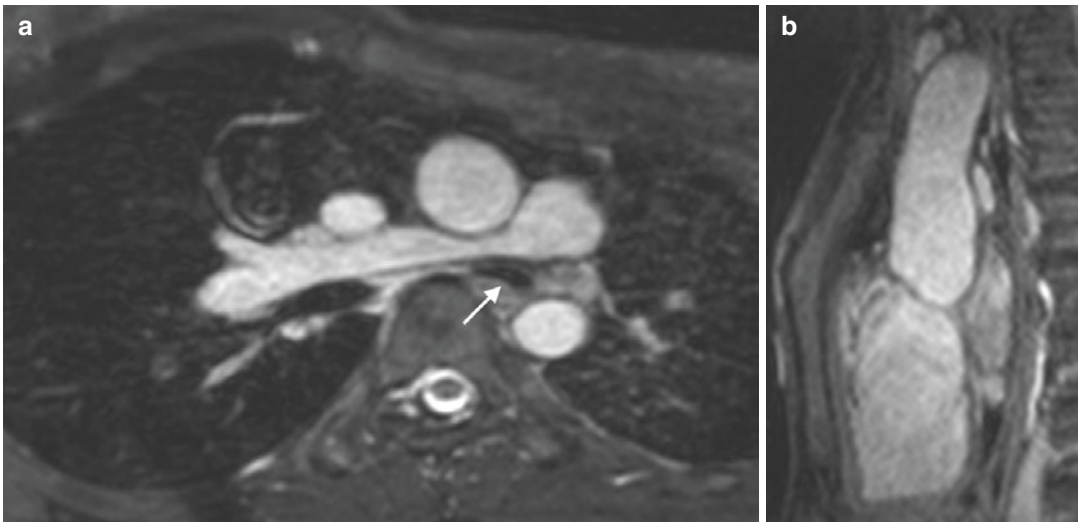
Fig. 2 Stenosis of the right pulmonary artery in a 12-year-old girl. Images were acquired using an ECG-gated and respiratory-triggered 3D steady-state free-precession technique (SSFP) with isotropic 1 mm spatial resolution.

Primary image acquisition was axial (**a**); however the datasets allow for any reformation, like sagittal (**b**). The *arrow* points at the subsequent stenosis of the left main bronchi
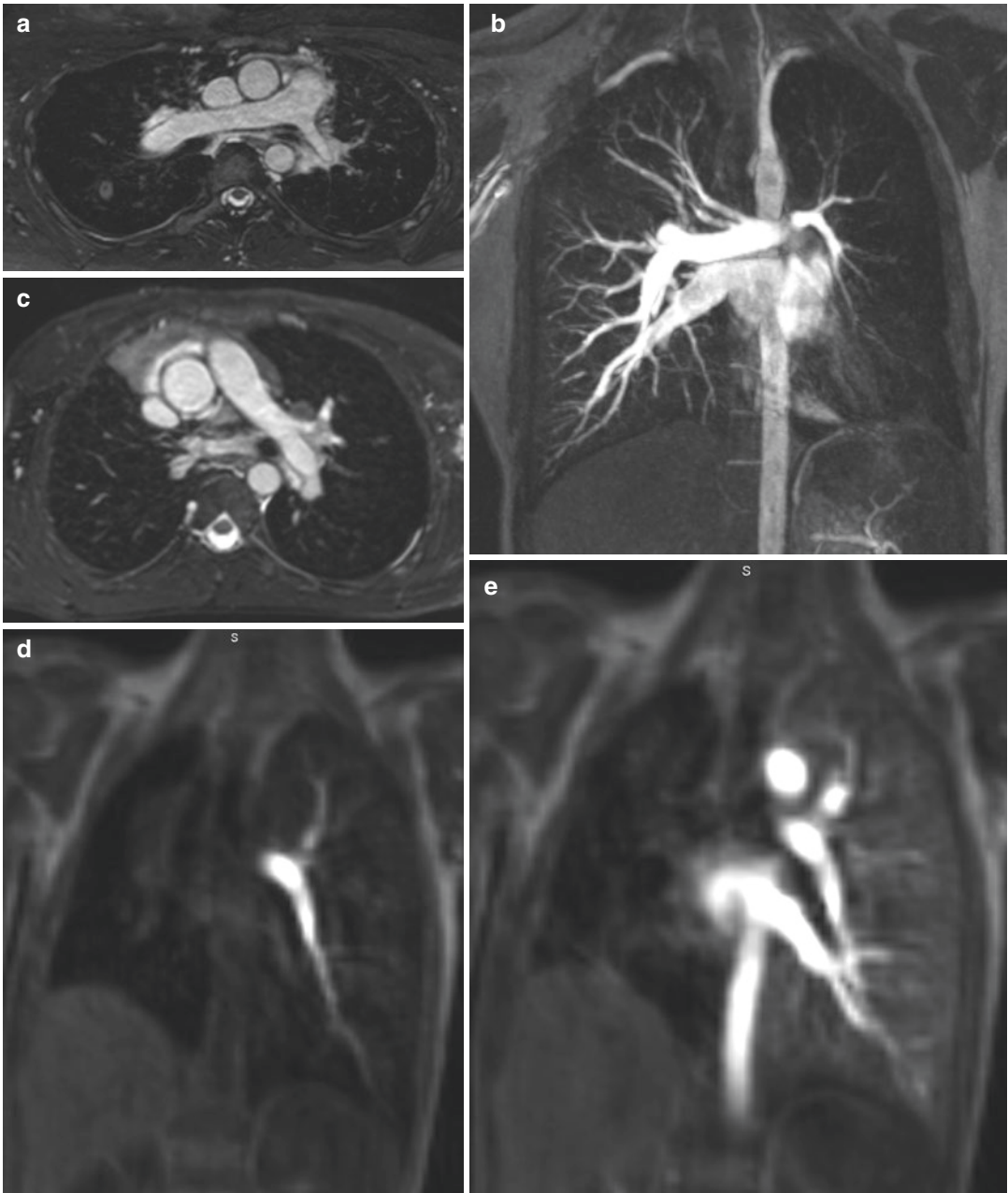
Fig. 3 Example presents a patient with a hypoplastic left pulmonary artery. (**a**) Is an image acquired by using an ECG-gated and respiratory-triggered 3D steady-state free-precession technique (SSFP) with isotropic 1 mm spatial resolution. Note the difference in size between the right (normal) and hypoplastic left pulmonary artery. (**b**) Is a high-spatial-resolution contrast-enhanced MR angi-ography showing furthermore the difference in blood dis-tribution between both lungs. (**c**) Another patient with an aplasia of the right pulmonary artery as shown by the 3D SSFP technique. The contrast-enhanced time-resolved (**d**, **e**) angiographic images nicely depict the lack of perfusion of the right lung as well as a smaller pulmonary volume of the right side

patch material or a conduit becomes necessary. After this procedure stenosis may occur at any structure within or in the neighborhood of the central pulmonary artery or the conduit. Therefore, visualization of the internal lumen of the conduit, its wall structure, and the anastomosis to the left and right pulmonary artery is important in the follow-up.

Circumscript malformations of the pulmonary artery and its post-interventional course can be visualized well using high-resolution MRA. Additional information about valve regurgitation can be obtained by MR phase-contrast imaging (Gatehouse et al. 2005). In a large study on 28 infants aged younger than 3 months with CHD mainly affecting the PA or RVOT, MRA proved to be in consensus with DA. However, in this study, a high dose of contrast media of 0.4–0.5 mmol/kg/b.w. was applied and scanning was performed in suspended mechanical ventilation. However, no adverse contrast media effects were found, and the pulmonary vessels were sharply delineated (Prakash et al. 2007).

2.1.2 Pulmonary Sling (Origin of the Left Pulmonary Artery from the Right Pulmonary Artery)

The left pulmonary artery arises aberrantly from the right pulmonary artery and runs behind the trachea and esophagus to the left side (Fig. 4) (Berdon 2000). This situation leads to either an acute and severe airway compression (infants) or signs of chronic obstructive lung disease or asthma (childhood and young adults). In a large series the prevalence of a pulmonary sling was 1 in 17,000 (186,213 school-aged children were examined) (Yu et al. 2008). Surgical correction is performed with attachment of the left pulmonary artery to the pulmonary trunk ventrally to the aorta. Imaging needs to display the pulmonary arterial anatomy as well as the relationship to the airways. MR imaging in ten patients (aged 6 months to 11 years) with clinically suspected ring or sling malformation (three of them with pulmonary sling) was able to demonstrate the topographic relation to the adjacent soft-tissue structures (esophagus, trachea, or bronchi). MR findings were confirmed surgically (Eichhorn et al. 2004).

2.1.3 Anomalous Origin of One Pulmonary Artery

In this rare malformation one pulmonary artery originates abnormally from the aorta leading to an unbalanced blood flow and unilateral pulmonary hypertension (Kutsche and Van Mierop 1988). Mainly the right pulmonary artery shows an anomalous origin (82%). Surgical intervention includes resection of the abnormal pulmonary artery and anastomosis with the pulmonary trunk using a small conduit. In order to achieve sufficient growth of the pulmonary vessels, conduits need to be replaced once or twice during childhood and adolescence. MRI is well suited for pre- and postoperative evaluation (Kim et al. 1995).

2.1.4 Tetralogy of Fallot or Pulmonary Atresia with VSD or Hypoplastic Pulmonary Artery

In these situations blood flow through the pulmonary valve or artery is highly diminished or even absent, leading to severe cyanosis. Tetralogy of Fallot (TOF) is the most common type of cyanotic CHD with an incidence of 356 per million live births (Dorfman and Geva 2006). The degree of right ventricular outflow tract (RVOT) obstruction varies from mild to complete obstruction. Pulmonary blood flow is dependent on a patent ductus arteriosus (PDA) or collateral vessels (MAPCA) (Fig. 5). In order to obtain sufficient pulmonary blood flow and vessel growth of the pulmonary arteries, a stable aortopulmonary connection needs to be established. Later, further operations are usually necessary to palliate the malformation. The so-called Blalock–Taussig procedure was first
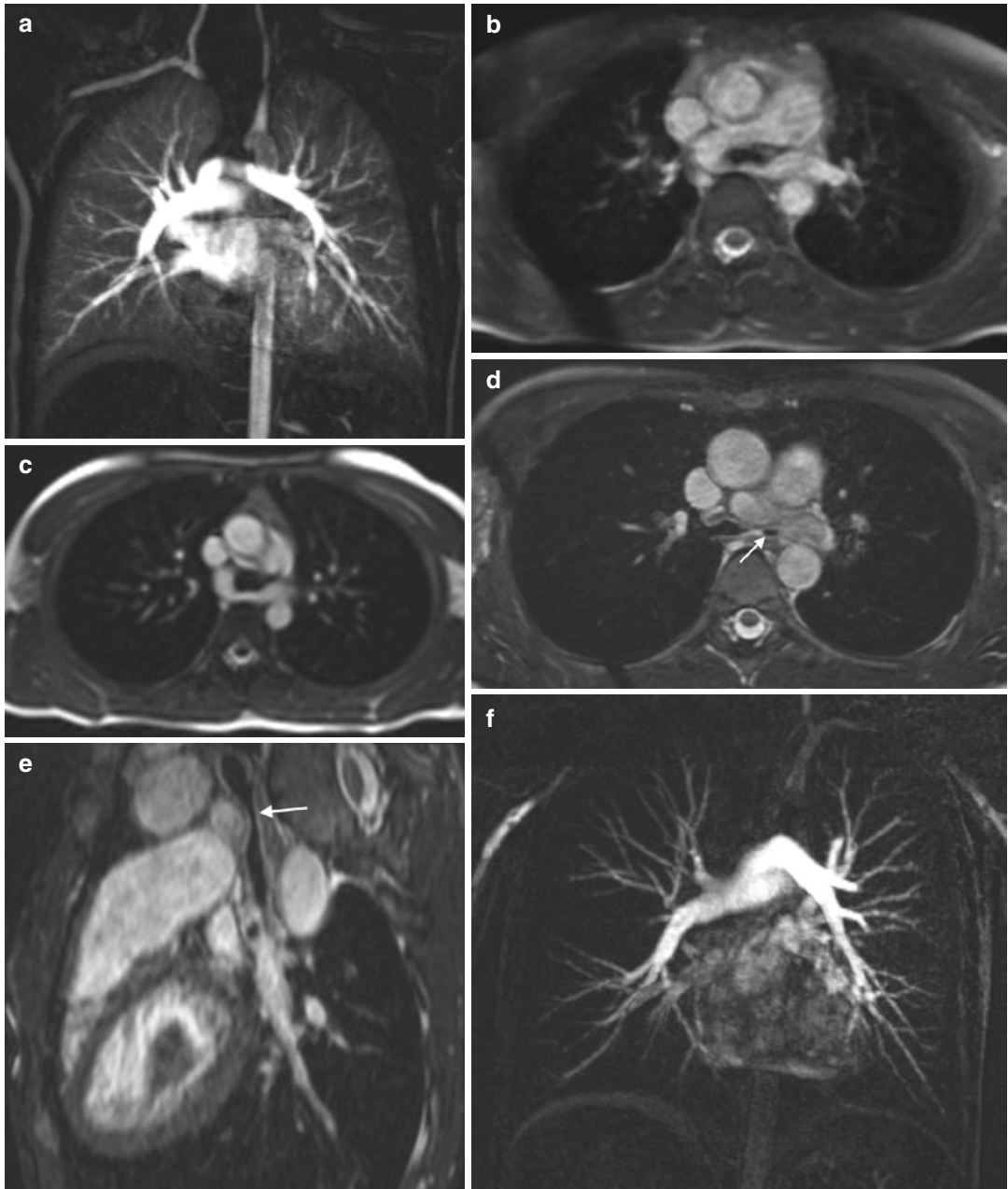
Fig. 4 Pulmonary sling. (**a**) Presents the coronal angiographic dataset with the left pulmonary artery (PA) originating from the right PA. The left PA encircles the trachea during its course through the mediastinum. This can also be demonstrated without contrast media (**b**) using an ECG-gated and respiratory-triggered 3D steady-state free-precession technique. MRI allows for functional assessment of the effect on the trachea. (**c**) Shows one frame from a steady-state free-precession cine sequence without tracheal compression. (**d**) Shows a patient after surgical correction of a pulmonary sling. However, the reinsertion of the left pulmonary artery was too far distally with subsequent compression of the left main bronchus (*arrow*). The same is shown in the sagittal reformated image (**e**). (**f**) Shows the contrast-enhanced MRA with nearly the same anatomy as in (**a**)
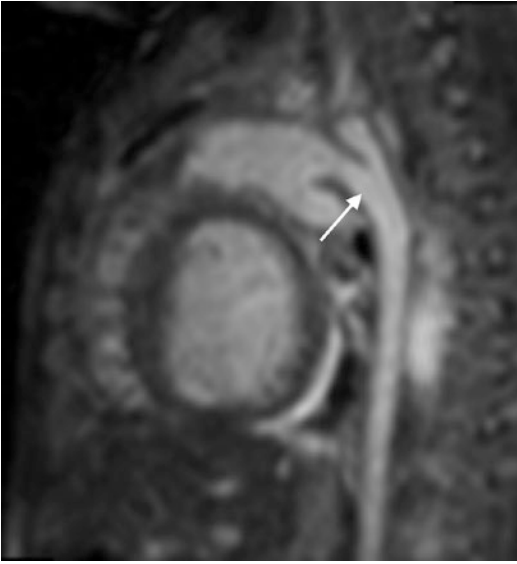
Fig. 5 Presentation of a large open ductus arteriosus botalli in a newborn with a time-of-flight acquisition. Time-resolved contrast-enhanced MR angiography presents the vascular anatomy. The arrow points at the patent ductus arteriosus botalli

successfully performed in 1944. The right or left subclavian artery and the ipsilateral pulmonary artery were connected in cyanotic patients with TOF (Blalock and Taussig 1945). Nowadays, this operation is not performed often as only one pulmonary artery will be sufficiently perfused. Central aortopulmonary shunts or a direct connection of the hypoplastic pulmonary trunk to the aorta is preferred as it leads to a balanced growth of both pulmonary arteries (Duncan et al. 2003).

Preoperative assessment of the vascular structures (pulmonary arteries, aorta, and collaterals) is possible with MRI but requires relatively long scan times for complete anatomical coverage, and small vessels (<2 mm) may not be detected. Still DA is preferred in most centers because of the potential risk of a cyanotic spell and the necessity of high-quality coronary imaging in very small infants. However, one study showed the excellent capabilities of MRI in ten patients in whom the central pulmonary arteries had not been visualized at DA, and showed that angiography

had failed to demonstrate the main pulmonary artery in seven cases, the proximal left pulmonary artery in two cases, and the entire pulmonary arterial tree in one case (Choe et al. 1998). At follow-up growth of the pulmonary arteries can be evaluated excellently using MRI, and MRI should be preferred over MDCT. The time of re-intervention may be determined without serial DA or CTA.

Collateral vessels arising from the aortic arch (MAPCA) are mostly found in TOF or pulmonary atresia with VSD and with hypoplastic pulmonary artery. Lung perfusion is partly established by these systemic vessels. Surgeons are especially interested if these vessels are suitable for connection to the pulmonary arteries or if they provide an unbalanced, high-pressure blood flow situation, leading to pulmonary hypertension (Eisemenger's reaction). Compared with DA, MRA has been shown to be highly accurate in depicting all sources of pulmonary blood supply in patients with complex pulmonary stenosis or atresia, including infants with multiple small aortopulmonary collaterals (Geva et al. 2002).

2.1.5 Pulmonary Sequestration

Pulmonary sequestration is a multifocal malformation, which is defined as a segment of lung parenchyma that is separated from the tracheobronchial tree and is supplied with blood from a systemic rather than a pulmonary artery. The blood supply usually comes from the descending thoracic aorta, but in about 20% of cases, it comes from the upper abdominal aorta, celiac artery, or splenic artery (Konen et al. 2003). Surgical procedures include ligation of the afferent vessels and/or resection of the pulmonary malformation.

In these malformations, MDCT is superior to most other techniques, providing excellent information of both the vessels supporting the malformation (arterial and venous) and especially the structure of the lung parenchyma inside the malformation. Visualization of the lung parenchyma is challenging using MRI, however being an essential part of the diagnosis.

2.1.6 Single-Ventricle Morphology

In single-ventricle morphology of the heart (tricuspid atresia, double-inlet left ventricle) cavity volume increases as a consequence of the excessive volume load associated with parallel pulmonary and systemic circulations (Gewillig 2005). The Glenn procedure (hemi-Fontan) was conceived as a means of accomplishing early reduction of the volume load of the single ventricle, in anticipation of eventual completion with a Fontan-like operation. The Glenn procedure includes association of the superior vena(e) cava(e) (SVC) with the branch pulmonary arteries, augmentation of the central pulmonary arteries, occlusion of the inflow of the SVC into the right atrium, and elimination of other sources of pulmonary blood flow (like patent ductus arteriosus). Other cardiac malformations have to be corrected at the same time, or at least before a Fontan-like operation. This may include atrial septectomy, relief of aortic arch obstruction, repair or revision of anomalous pulmonary venous connection, and other procedures (Jacobs and Pourmoghadam 2003).

During total cavopulmonary connection (TCPC), the inferior vena cava (IVC) is connected to one pulmonary artery using an extra- or intracardiac conduit (Fig. 6) (Ohye and Bove 2001). Throughout the different surgical stages visualization and quantification of the caval connections to the pulmonary arteries are essential. Due to the complex and slow flow pattern contrast-enhanced imaging can be difficult in ruling out stenosis. Time-resolved MRA techniques describe the main blood flow direction and visualize pulmonary blood distribution. In addition, information of function of the single ventricle can be obtained. Still DA is performed, mainly because exact estimation of pulmonary pressure is mandatory before Glenn procedure or TCPC.

2.1.7 Transposition of the Great Arteries (TGA)

Transposition of the great arteries (TGA) accounts for approximately 5% of all CHD. In this anomaly, the aorta arises from the right ventricle and the pulmonary artery from the left ventricle, while the systemic and pulmonary veins return normally. In contrast to the normal situation, where
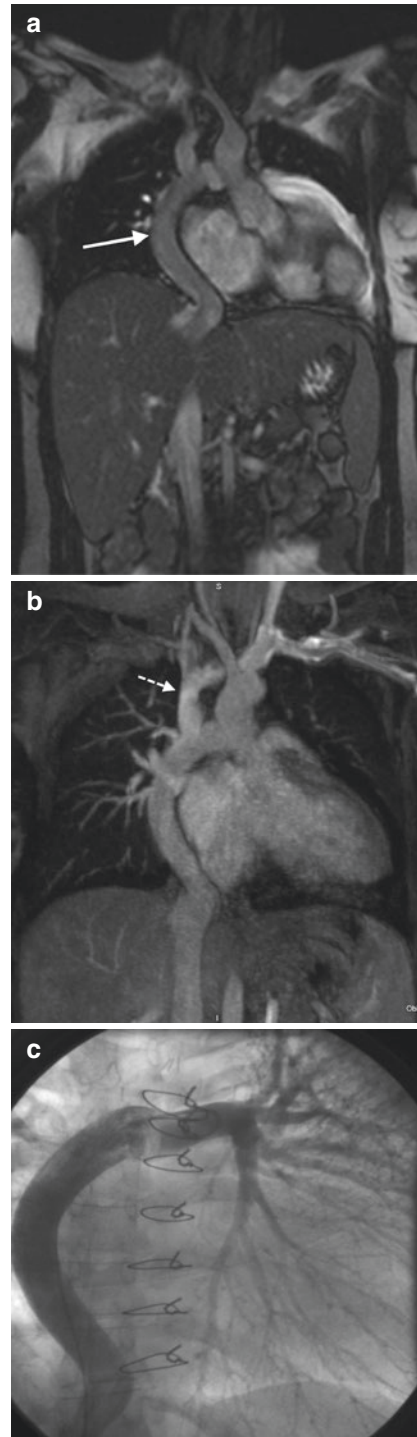
Fig. 6 Female patient with a functional single ventricle after a TCPC. A large patch was built running at the right lateral side of the heart (**a**, *arrow*). The superior vena cava was connected directly to the pulmonary arteries (**b**, *dotted arrow*). (**c**) Shows the conventional angiographic image of the inferior "vein" being connected to the pulmonary arteries

the aorta is posterior to the pulmonary artery, the aorta is anterior and to the right of the pulmonary artery in de-transposition of the great arteries. Since the original report from Jatene and colleagues in 1976 the arterial switch operation (ASO) has become the procedure of choice for neonates with complete transposition of the great arteries. The operation involves dividing the aorta and pulmonary artery just above the sinuses and re-anastomosing them in their correct anatomic positions. The coronary arteries need to be removed from the former aortic root along with a button of aortic wall and reimplanted into the so-called neoaorta (former pulmonary root). Although anatomic correction is achieved, there is still concern about the mid- and long-term outcome of these patients. Postoperatively there are three major problems requiring cardiac imaging (Losay et al. 2001). The first is the detection of coronary pathology, leading to myocardial dysfunction of both ventricles. The second is the aortic root dilation, leading to aortic regurgitation. The third and most frequent problem is the postoperative supravalvular pulmonary stenosis. In most cases there is a stenosis of one or both pulmonary branches as they take their way around the ascending aorta. This region cannot be visualized sufficiently by echocardiography, and therefore supplementary imaging is necessary. Assessment of the systemic right ventricular function is a key point in the follow-up of patients with TGA. Ejection fraction determined by cine-MRI of the right ventricle correlates well with echocardiography in these patients (Salehian et al. 2004). Furthermore, MRI allows for excellent 3D visualization of the central and peripheral pulmonary vasculature after correction of TGA and is therefore the modality of choice for follow-up (Fig. 7) (Weiss et al. 2005). In the case of severe pulmonary stenosis, additional DA is needed to measure pressure gradients across the stenosis (Gutberlet et al. 2000).

2.2 Congenital Pulmonary Venous Disorders

Generally there are a total of four pulmonary veins (PVs), with one pair of veins opening into

Fig. 7 Example of the anatomy following surgical correction of TGA. This volume-rendered image shows the anatomy with the ventral position of the main pulmonary artery and the dorsal ascending aorta. The right and left pulmonary arteries run anterior of the aorta to the periphery

the left atrium on each side. Anomalous pulmonary venous drainage may be partial or complete resulting in different levels of magnitude of left-to-right shunts. Young patients are usually asymptomatic; dyspnea on exertion becomes increasingly common in the third and fourth decades of live.

The complete form, known as total anomalous pulmonary venous connection (TAPVC), is compatible with life only in patients with a coexisting ASD or patent foramen ovale (Stein 2007). Three main types are distinguished, in descending order of frequency:

- Supracardiac type: The anomalous PVs unite posterior to the atria and drain into a left ascending vessel that opens into a persistent superior vena cava. The blood then enters the right atrium by way of the left innominate vein and right superior vena cava (Fig. 8).
- Intracardiac type: The anomalous PVs unite to form a short vessel that opens into the coronary sinus.
- Infracardiac type: The anomalous PVs drain into the portal vein, hepatic vein, left gastric vein, directly into the inferior vena cava, directly into the right atrium, or into the right atrium by way of a collecting vessel.

In partial anomalous pulmonary venous connection (PAPVC) some of the PVs are not connected to

the right atrium (RA), and in few cases only a single vein communicates with that chamber. Evidence of right ventricular overload with no apparent intracardiac shunt should prompt a search for PAPVC. In

Fig. 8 Fourteen-year-old boy with palpations during exercise. At echocardiography a turbulent flow profile in the SVC was detected. Contrast-enhanced 3D MRA (oblique coronal subvolume maximal intensity projection) demonstrates the partially anomalous pulmonary venous connection of the left upper pulmonary vein (*arrow*) to the left innominate vein

the most common configuration, the right superior pulmonary vein opens into the superior vena cava or RA. A special form is the scimitar syndrome, with a hypoplastic right lung and partial or total anomalous drainage of the right pulmonary vein into the inferior vena cava (Fig. 9) (Holt et al. 2004).

The relative frequency of PAPVC is approximately 0.6% of all congenital anomalies, while TAPVC accounts for 0.4% (Moos 2001). Anomalous pulmonary venous drainage imposes a volume overload on the pulmonary circulation with subsequent volume loading and dilatation of the left ventricle. PAPVC is usually asymptomatic and is often detected incidentally.

If a clinical concern for PAPVC cannot be resolved by echocardiography with confidence, then MRI is the most appropriate additional test. PVs are generally adequately visualized in axial T1-weighted SE sequences. Adding thin-slice acquisitions or a dynamic GE sequence with bright-blood vascular imaging may also be beneficial in patients with more complex vascular anatomy.

Several studies assessing the accuracy and utility of contrast-enhanced 3D MRA have shown a high level of agreement between findings on MRA compared with surgical inspection and DA. For preoperative planning 3D MIP reconstructions are valuable as they clearly define the

Fig. 9 MRA of a female patient with a scimitar vein. The venous blood of the right lung drains into this collecting vein, which is connected to the inferior vena cava. This results in a shunt volume of 55% (as proven by MR flow measurements and during invasive measurements). (**a**) Gives the coronal 10 mm MIP and (**b**) is a sagittal reformat (20 mm MIP)
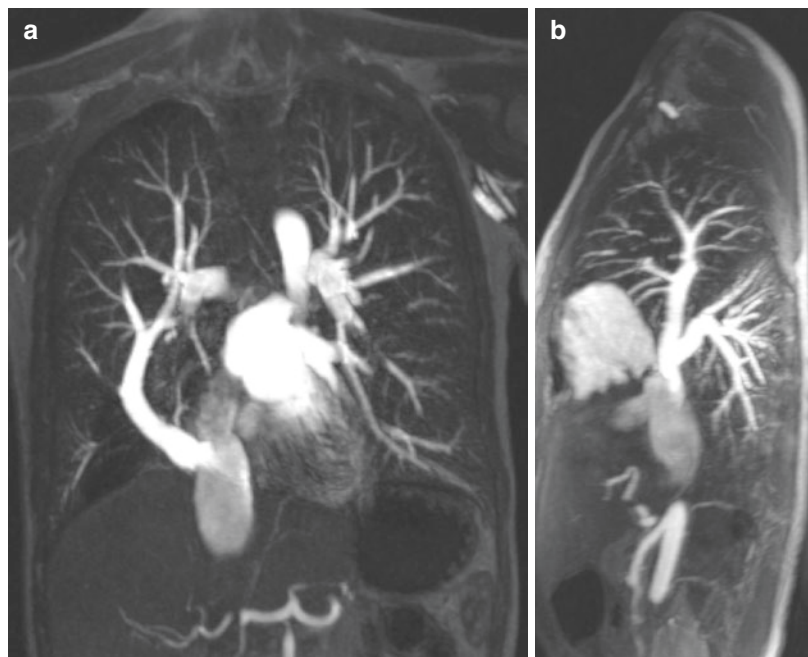
course of the PVs. MRA was uniformly more accurate than transthoracic and transesophageal echocardiography. MR studies often diagnosed previously unknown PAPVC or added new clinically important information regarding PAPVC anatomy (Kivelitz et al. 1999; Greil et al. 2002; Prasad et al. 2004; Wald and Powell 2006). The shunt volume can be quantified by performing flow measurements in the ascending aorta and pulmonary trunk. It is worth noting that in patients with PAPVC, systemic blood flow/pulmonary blood flow (Qp/Qs) ratio measurements by oximetry in the catheterization laboratory are inherently inaccurate because of the difficulty in obtaining a reliable, representative mixed systemic venous saturation.

2.3 Pulmonary Arteriovenous Malformations

Pulmonary arteriovenous malformations (PAVMs) result from fistula formation between the pulmonary arteries and veins. Blood flow bypasses the pulmonary capillary bed, giving rise to a functional right-to-left shunt. The prevalence of PAVM is approximately 2–3 per 100,000 population. The great majority of PAVMs (80%) are congenital. Within this group, PAVMs are present in 47–80% of patients with autosomal dominant Osler-Weber-Rendu syndrome (hereditary hemorrhagic telangiectasia) (Khurshid and Downie 2002). Other cases are not referable to a specific syndrome, although a genetic link to the 9q3 chromosome has been suggested.

Acquired AV shunts may have various causes like trauma, infection, metastatic carcinoma, mitral stenosis, and hepatic cirrhosis. AV shunts may develop due to metastatic involvement of the lung parenchyma. This possibility should be considered in patients who develop sudden hemoptysis after successful chemotherapy (Choi et al. 2003).

A large, long-term follow-up study documented the superiority of cross-sectional imaging modalities over DA. CTA (incremental and single-slice spiral CT) achieved a detection rate of 98% of all PAVMs, while angiography detected only 60% (Remy et al. 1992). In a study

comparing DA and MRA, MRA could correctly define the location of the PAVMs in 16 of 16 cases. The parent vessel and the size of the feeding vessel could be accurately determined in 14 of 16 cases. In two cases the feeding vessels were not contained in the slice package (Mohrs et al. 2002). This limitation no longer exists in the current generation of scanners, and both cross-sectional modalities may be considered equivalent in the evaluation of PAVMs.

3 Acquired Pulmonary Venous Disorders

In the absence of congenital anomalies, there is rarely an indication for diagnostic imaging of the pulmonary veins. The most frequent indication at present is pre- and postinterventional imaging of the pulmonary veins before and after radiofrequency ablation. Atrial fibrillation is the most common cardiac arrhythmia, with a prevalence of approximately 5% in persons over 65 years of age (Falk 2001). Percutaneous catheter ablation using radiofrequency or cryoablation is a minimally invasive procedure for destroying arrhythmogenic foci. Because the origin of the pulmonary vein slightly varies due to the rotation of the left atrium during embryonic development, preinterventional imaging is recommended (also to exclude previously undetected normal variants or anomalous origin). 3D imaging is useful for planning the optimum size of the catheter balloon. The most frequent complication of catheter ablation (prevalence of 1.5–42%) is stenosis of the pulmonary veins. Other possible complications are thrombosis or dissection. Pulmonary vein stenosis develops during the first few days after the procedure, as initial tissue swelling is followed by the development of fibrotic changes. Clinical manifestations are progressive dyspnea, orthopnea, nonproductive cough, infection, and hemoptysis (Ghaye et al. 2003). Time-resolved angiographic techniques with adequate in-plane resolution should be used to achieve optimum timing of the contrast bolus for pulmonary vein imaging (Rahmani and White 2008). Optimum bolus timing varies in different patients (and in

different PV segments), especially in the presence of pulmonary vein stenosis. After contrast media application MRI can be used for therapy control by using late-enhancement imaging techniques. This allows for the precise localization of the scar tissue and the relationship to the orifice of the PV (Peters et al. 2007).

4 Tumors of the Pulmonary Vessels

4.1 Central Pulmonary Arteries: Leiomyosarcoma

Leiomyosarcoma is the most frequent tumor of the pulmonary arteries and veins (pulmonary artery sarcomas (PAS) and pulmonary vein sarcomas (PVS)). It arises from the smooth muscle cells of the media (Mayer et al. 2007). Completely intravascular leiomyosarcomas are usually nodular, polypoid tumors that are fixed to the inner vessel wall. Intraluminal tumor growth expands the vessel diameter, and intracardiac tumor extension may occur. Besides leiomyosarcoma, the differential diagnosis of intrathoracic sarcomas should include angiosarcoma, rhabdomyosarcoma, and sarcomatoid variant of mesothelioma.

Primary PAS affect both sexes equally and occur at a slightly earlier average age (50 years) than the venous forms. The incidence ratio of PAS to PVS is approximately 20:1. Only 17 cases (mean age at radiologic diagnosis was 48 years) of PVS have been described in the literature.

PAS most commonly involve the main pulmonary artery trunk and may spread from there toward the peripheral arterial branches or may extend back into the right ventricle. Tumor growth may be completely extravascular (62%), completely intravascular (5%), or both extra- and intravascular (33%) (Kreft et al. 2004). Other studies indicate that approximately 50% of PAS are intravascular when diagnosed. The remaining half undergoes transmural spread into the lung parenchyma (Fasse et al. 1999). The clinical

manifestations of PAS are nonspecific and may include dyspnea, chest pain, cough, hemoptysis, and signs of right heart failure. Because these tumors are often intraluminal, they may embolize and cause peripheral infarctions, producing clinical symptoms similar to those of acute or chronic recurrent pulmonary embolism. PVS are generally larger than PAS are. They remain asymptomatic until their growth interferes with pulmonary venous return. The most frequent clinical manifestations are dyspnea, hemoptysis, cough, chest pain, and weight loss. PVS have a tendency to spread into the left atrium (Yi 2004). PAS appears on CT and MR images as a convex intraluminal mass that usually begins in the pulmonary trunk and spreads in a peripheral or occasionally central fashion. Both primary and metastatic tumors of the pulmonary arteries may cause intraluminal filling defects that are similar in appearance to chronic recurrent pulmonary emboli.

The tumors may be inhomogeneous as a result of hemorrhage, necrosis, or different tissue components. Thrombi may adhere to intraluminal tumor components and may in turn be infiltrated by tumor (Kauczor et al. 1994). Thus, delayed T1-weighted images after contrast administration are an essential part of the MRI protocol. Tumor enlargement over time may lead to vascular expansion with complete obliteration of the lumen. A convex shape of the filling defect does not support a diagnosis of chronic pulmonary embolism. Contrast enhancement on MRI is another indicator of intravascular tumor growth. Delayed imaging after contrast administration shows a highly variable degree of tumor enhancement, which is an important differentiating feature from chronic thromboembolic pulmonary hypertension (CTEPH) (Kaminaga et al. 2003).

The treatment of choice is complete tumor resection based on an early preoperative diagnosis. Modern surgical techniques can be used to reconstruct the vascular defect with prosthetic material. Even if curative treatment is not an option, it appears that palliative surgery can significantly prolong patient survival.

4.2 Peripheral Pulmonary Arteries: Pulmonary Capillary Hemangioma

Most cases of pulmonary capillary hemangioma (PCH) involve bilateral disease with an unknown cause. Capillaries proliferate into the alveolar septa and other structures such as bronchial walls, pleura, and regional lymph nodes. Extrathoracic growth or metastases have not been described. The disease is most prevalent in the third and fourth decades, with a range from 6 to 71 years, and affects males and females equally. Life expectancy after symptom onset is 2–12 years in untreated cases.

Typical clinical manifestations are progressive shortness of breath, pleuritic chest pain, and frequent hemoptysis, often prompting a misdiagnosis of chronic thromboembolic pulmonary hypertension. With the progression of disease, patients develop clinical signs of cor pulmonale with elevated pulmonary artery pressures but normal pulmonary capillary wedge pressures on right-heart catheterization.

To date, CT is the only cross-sectional imaging modality that has been investigated in the literature. The principal CT findings are enlarged pulmonary arteries and numerous small, bilateral, ill-defined densities (Eltorky et al. 1994). Compared with idiopathic pulmonary artery hypertension, perfusion scanning shows increased perfusion in the hemangiomatous tissue and decreased perfusion in occluded vessels, resulting in an inhomogeneous perfusion pattern.

The only curative treatment is bilateral lung transplantation, for which patients must be selected at a very early stage.

5 Anomalies of the Thoracic Aorta

5.1 Aortic Coarctation

The most frequent systemic arterial anomaly (up to 1 in 3000–4000 live births) affects the thoracic aorta in the early descending part with narrowing of the aorta, so-called aortic coarctation. Coarctation of the aorta can range from mild to severe, and might not be detected until adulthood, depending on the degree of stenosis. The narrowing of the aorta is traditionally classified based on the anatomic relationship to the arterial duct or ligament: proximal to (preductal or infantile) or at the level or distal (postductal or adult form) of the arterial duct (Eichhorn 2007 #3180). However, as the clinical symptoms depend on the degree of stenosis even many preductal lesions are only detected during adulthood; thus this concept is now regarded as too simplistic (Kau 2007 #4667). Most often a short stenotic segment is seen being only some mm long. The less frequently seen type is the hypoplastic stenosis which is a long-segment stenosis, usually associated with a hypoplasia of the aortic arch (Ulmer 2012 #4518) (Singh 2015 #4664). Patients with aortic coarctation have frequently associated cardiac malformations, in up to 80% a bicuspid aortic valve and approx. 20% a ventricular septal defect (Tanous 2009 #4091). Coarctation is associated with Turner syndrome. Most patients become clinically evident during childhood with hypertension in the upper extremities, low or unobtainable arterial blood pressure in the lower extremities, and cardiac murmurs. The mean age of diagnosis is 9 years. If it remains unnoticed the adult form of coarctation develops. Treatment of coarctation can be done surgically or by interventional balloon angioplasty (Torok 2015 #4666) (Schneider 2016 #4665). As a complication of a surgical repair in infancy a re-coarctation or aneurysm formation can occur (Tanous 2009 #4091).

For diagnostic purposes in childhood echocardiography is the primary imaging modality. For exact measurement of the degree of the stenosis and treatment planning MRI or CT imaging is used. As the patients are rather young with a normal life expectancy the radiation burden should be kept to a minimum, thus favoring the use of MRI. Current MR techniques allow for an excellent visualization by contrast-enhanced MRA and acquisition of flow-relevant parameters (Darabian 2013 #4521) (Fig. 10). By combination of the morphological and flow variables, MRI showed

Fig. 10 Five-month-old female patient with aortic coarctation, approx. 50% stenosis. (**a**) Shows a 3D non-contrast-enhanced respiratory- and cardiac-gated MR angiography displaying the aortic configuration accurately. The *arrow* points out the aortic coarctation. (**b**) Shows the contrast-enhanced MR angiography. Given the small venous access only a slow injection speed could be used. Furthermore, the patient was examined in sedation, without intubation. Therefore, image quality is slightly degraded due to breathing artifacts

excellent sensitivity (95%) and good specificity (82%) for assessment of the severity of aortic coarctation (Nielsen 2005 #2089). More recently MR techniques have been developed allowing for a non-contrast-enhanced visualization of the vasculature. These techniques are applied with ECG and respiratory gating and show excellent agreement with other techniques (Ley-Zaporozhan 2007 #3130) (Amano 2008 #3443). In a pediatric study with patients suffering from aortic coarctation an excellent agreement (r = 0.96) was found for this 3D-FISP MR angiography and invasive catheterization.

5.2 Patent Ductus Arteriosus

During the fetal period the arterial duct ensures a continuous blood flow between the proximal descending aorta and the pulmonary arteries. Usually this connection closes soon after birth (in a full-term infant within 48 h after birth). If

the ductus arteriosus remains patent (patent ductus arteriosus—PDA) a left-to-right shunt is present (Fig. 5). This leads to a volume overload of the pulmonary arterial system and of the left ventricle. Depending on the shunt volume an early left heart insufficiency can occur. Small shunt volumes remain asymptomatic and may be detected incidentally in adults (Eichhorn 2007 #3180). If a relevant defect remains undetected an Eisenmenger's syndrome can develop. Usually, a clinically relevant shunt is detected in early childhood by a cardiac murmur and subsequent echocardiography. A further evaluation using CT or MR is not required.

5.3 Aortic Vascular Rings and Slings

During the embryologic development the aorta and aortic arch is doubled. During gestation the vascular system fuses and partly becomes

atretic. Especially the right fourth primitive aortic arch disappears producing the normal left-sided aortic arch. In some cases the right part of the aorta persists while the left part disappears forming a right-sided aortic arch (Kau 2007 #4667) (Cina 2004 #4668) (Fig. 11). This condition is seen in approx. 0.05–0.1% of

radiological series. Normally, a right-sided aortic arch will be asymptomatic.

If both primitive aortic arches persist (to a varying degree) a double-aortic arch is formed passing to either side of the esophagus and trachea and reunites to form the descending aorta (Kau 2007 #4667) (Fig. 12). Most commonly, one arch is dominant, whereas the other may be of small caliber or just represented by a fibrous band.

In both settings, more frequently if a double-aortic arch is present, symptoms are related to compression of mediastinal structures such as the trachea or the esophagus. In adulthood, symptoms are more often the result of early atherosclerotic changes of the anomalous vessels, dissection, or aneurysmal dilatation with compression of surrounding structures causing dysphagia, dyspnea, stridor, wheezing, cough, choking spells, recurrent pneumonia, obstructive emphysema, or chest pain (Cina 2004 #4668).

Fig. 11 Two-year-old girl with a right-sided aortic arch (*long arrow*). The *short arrow* shows the left-sided brachiocephalic trunk
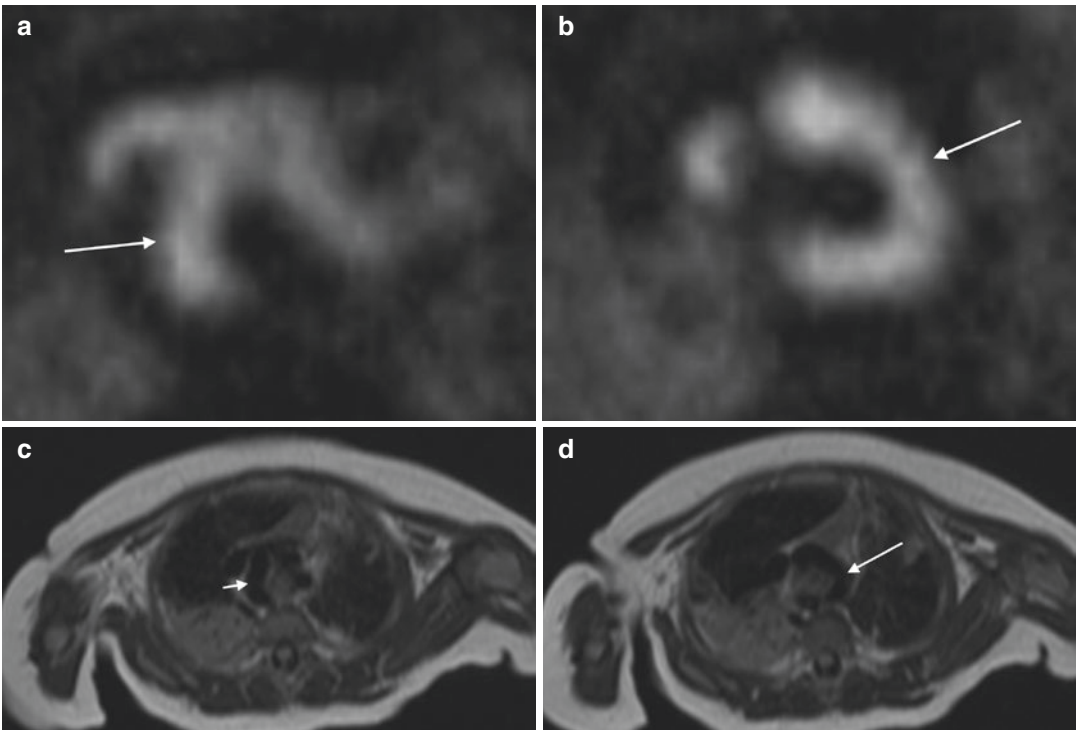
Fig. 12 Young patient with a double-aortic arch. (**a**, **b**) Show the right and left sides of the aortic arch (*arrows*), respectively. (**c**, **d**) Shows a dark-blood T2w-TSE image of the aortic configuration (*arrows point to the right and left aortic arch*). Note that this morphological image provides a better insight into the mediastinal structures that are encircled than the contrast-enhanced MR angiography

Especially of note is the development of a tracheomalacia, which persists even if the vascular or fibrotic ring is surgically relieved. MDCT and MR are well-established imaging techniques for visualization of the vasculature and relationship between vessels and other mediastinal structures, especially the trachea (Simoneaux 1995 #4524) (Berdon 2000 #2439) (Sebening 2000 #2904). Depending on the institutional setting these examinations are performed in intubated patients, which subsequently make an evaluation of a potential tracheomalacia impossible. CT allows for an easier 3D reconstruction of the dataset, which is a crucial issue for the cardiothoracic surgeon. However (to limit radiation exposure) CT is limited to static images while MR images can be acquired dynamically (i.e., by axial CINE acquisitions) to demonstrate the pulsatile and respiratory effects on the mediastinal structures.

6   Extravascular Disorders

The most frequent extravascular disorder affecting the PA is mediastinal tumor spread with compression or infiltration of the PA and/or PV. Studies have documented the value of MRI in the detection and evaluation of mediastinal and arterial invasion by bronchial carcinoma. This information is critical in planning the resection of the carcinoma. When vascular invasion is present, a heart-lung machine has to be used during the operation and a suitable vascular interposition graft available. The long-term survival rate is significantly reduced in patients with pulmonary vascular invasion (Chunwei et al. 2003; Ohno et al. 2001). The lung parenchyma should also be evaluated during preoperative staging; thus, a CT is most often performed despite the high diagnostic quality of MRI.

The presence of aneurysms in the setting of Behçet disease or Hughes-Stovin syndrome (Kindermann et al. 2003; Oliver et al. 1997) and involvement by vasculitis are relatively rare indications for imaging of the pulmonary vessels. The primary cross-sectional imaging study in these cases is still CT, whose capabilities have been greatly augmented by the advent of multide-

tector technology. MRA should be considered in cases where CT is contraindicated due to renal failure or thyroid dysfunction, and should be avoided in young patients.

References

Amano Y, Takahama K, Kumita S (2008) Non-contrast-enhanced MR angiography of the thoracic aorta using cardiac and navigator-gated magnetization-prepared three-dimensional steady-state free precession. J Magn Reson Imaging 27(3):504–509

Berdon WE (2000) Rings, slings, and other things: vascular compression of the infant trachea updated from the midcentury to the millennium – the legacy of Robert E. Gross, MD, and Edward B. D. Neuhauser, MD. Radiology 216(3):624–632

Bernstein D (2004) Congenital heart disease. In: Behrman RE, Kliegman R, Jenson HB (eds) Nelson textbook of pediatrics, 17th edn. Saunders, Philadelphia, pp 1499–1554

Bhat AH, Sahn DJ (2004) Congenital heart disease never goes away, even when it has been 'treated': the adult with congenital heart disease. Curr Opin Pediatr 16:500–507

Biederer J, Both M, Graessner J, Liess C, Jakob P, Reuter M, Heller M (2003) Lung morphology: fast MR imaging assessment with a volumetric interpolated breath-hold technique: initial experience with patients. Radiology 226:242–249

Blalock A, Taussig HB (1945) The surgical treatment of malformations of the heart in which there is pulmonary stenosis or pulmonary atresia. JAMA 128:189–202

Bock M, Umathum R, Zuehlsdorff S, Volz S, Fink C, Hallscheidt P, Zimmermann H, Nitz W, Semmler W (2006) Interventional magnetic resonance imaging: an alternative to image guidance with ionising radiation. Radiat Prot Dosim 117:74–78

Boechat MI, Ratib O, Williams PL, Gomes AS, Child JS, Allada V (2005) Cardiac MR imaging and MR angiography for assessment of complex tetralogy of Fallot and pulmonary atresia. Radiographics 25:1535–1546

Boll DT, Lewin JS, Young P, Siwik ES, Gilkeson RC (2005) Perfusion abnormalities in congenital and neoplastic pulmonary disease: comparison of MR perfusion and multislice CT imaging. Eur Radiol 15:1978–1986

Choe YH, Ko JK, Lee HJ, Kang IS, Park PW, Lee YT (1998) MR imaging of non-visualized pulmonary arteries at angiography in patients with congenital heart disease. J Korean Med Sci 13:597–602

Choi SH, Goo JM, Kim HC, Im JG (2003) Pulmonary arteriovenous fistulas developed after chemotherapy of metastatic choriocarcinoma. AJR Am J Roentgenol 181:1544–1546

Chunwei F, Weiji W, Xinguan Z, Qingzen N, Xiangmin J, Qingzhen Z (2003) Evaluations of bronchoplasty and

pulmonary artery reconstruction for bronchogenic carcinoma. Eur J Cardiothorac Surg 23:209–213

Cina CS, Althani H, Pasenau J, Abouzahr L (2004) Kommerell's diverticulum and right-sided aortic arch: a cohort study and review of the literature. J Vasc Surg 39(1):131–139

Darabian S, Zeb I, Rezaeian P, Razipour A, Budoff M (2013) Use of noninvasive imaging in the evaluation of coarctation of aorta. J Comput Assist Tomogr 37(1):75–78

Dorfman AL, Geva T (2006) Magnetic resonance imaging evaluation of congenital heart disease: conotruncal anomalies. J Cardiovasc Magn Reson 8:645–659

Duncan BW, Mee RB, Prieto LR, Rosenthal GL, Mesia CI, Qureshi A, Tucker OP, Rhodes JF, Latson LA (2003) Staged repair of tetralogy of Fallot with pulmonary atresia and major aortopulmonary collateral arteries. J Thorac Cardiovasc Surg 126:694–702

Eichhorn JG, Ley S (2007) Angeborene Fehlbildungen der Aorta im Kindes- und Jugendalter. Radiologe 47(11):974–981

Eichhorn J, Fink C, Delorme S, Ulmer H (2004) Rings, slings and other vascular abnormalities. Ultrafast computed tomography and magnetic resonance angiography in pediatric cardiology. Z Kardiol 93:201–208

Eltorky MA, Headley AS, Winer-Muram H, Garrett HE Jr, Griffin JP (1994) Pulmonary capillary hemangiomatosis: a clinicopathologic review. Ann Thorac Surg 57:772–776

Falk RH (2001) Atrial fibrillation. N Engl J Med 344:1067–1078

Fasse A, Kauczor HU, Mayer E, Kreitner KF, Heussel CP, Thelen M (1999) Sarcoma of the pulmonary artery—pre- and postoperative radiologic findings in initial tumor manifestation and recurrence. Rofo Fortschr Geb Rontgenstr Neuen Bildgeb Verfahr 170:112–118

Fink C, Eichhorn J, Kiessling F, Bock M, Delorme S (2003) Time-resolved multiphasic 3D MR angiography in the diagnosis of the pulmonary vascular system in children. Rofo Fortschr Geb Rontgenstr Neuen Bildgeb Verfahr 175:929–935

Fries P, Altmeyer K, Seidel R, Massmann A, Kirchin MA, Schneider G (2005) Dynamic contrast enhanced MRA in pediatric patients after application of Gd-BOPTA. Eur Radiol 15:E8

Gatehouse PD, Keegan J, Crowe LA, Masood S, Mohiaddin RH, Kreitner KF, Firmin DN (2005) Applications of phase-contrast flow and velocity imaging in cardiovascular MRI. Eur Radiol 15:2172–2184

Geva T, Greil GF, Marshall AC, Landzberg M, Powell AJ (2002) Gadolinium-enhanced 3-dimensional magnetic resonance angiography of pulmonary blood supply in patients with complex pulmonary stenosis or atresia: comparison with x-ray angiography. Circulation 106:473–478

Gewillig M (2005) The Fontan circulation. Heart 91:839–846

Ghaye B, Szapiro D, Dacher JN, Rodriguez LM, Timmermans C, Devillers D, Dondelinger RF (2003) Percutaneous ablation for atrial fibrillation: the role of cross-sectional imaging. Radiographics 23:S19–S33; discussion S48–S50

Gilmore JH, Zhai G, Wilber K, Smith JK, Lin W, Gerig G (2004) 3 Tesla magnetic resonance imaging of the brain in newborns. Psychiatry Res 132:81–85

Greil GF, Powell AJ, Gildein HP, Geva T (2002) Gadolinium-enhanced three-dimensional magnetic resonance angiography of pulmonary and systemic venous anomalies. J Am Coll Cardiol 39:335–341

Greil GF, Kramer U, Dammann F, Schick F, Miller S, Claussen CD, Sieverding L (2005) Diagnosis of vascular rings and slings using an interleaved 3D double-slab FISP MR angiography technique. Pediatr Radiol 35:396–401

Grist TM, Thornton FJ (2005) Magnetic resonance angiography in children: technique, indications, and imaging findings. Pediatr Radiol 35:26–39

Gutberlet M, Boeckel T, Hosten N, Vogel M, Kuhne T, Oellinger H, Ehrenstein T, Venz S, Hetzer R, Bein G, Felix R (2000) Arterial switch procedure for D-transposition of the great arteries: quantitative midterm evaluation of hemodynamic changes with cine MR imaging and phase-shift velocity mapping-initial experience. Radiology 214:467–475

Hoeper MM, Lee SH, Voswinckel R, Palazzini M, Jais X, Marinelli A, Barst RJ, Ghofrani HA, Jing ZC, Opitz C, Seyfarth HJ, Halank M, McLaughlin V, Oudiz RJ, Ewert R, Wilkens H, Kluge S, Bremer HC, Baroke E, Rubin LJ (2006) Complications of right heart catheterization procedures in patients with pulmonary hypertension in experienced centers. J Am Coll Cardiol 48:2546–2552

Hoffman JI (1995) Incidence of congenital heart disease: II. Prenatal incidence. Pediatr Cardiol 16:155–165

Holmqvist C, Hochbergs P, Bjorkhem G, Brockstedt S, Laurin S (2001) Pre-operative evaluation with MR in tetralogy of fallot and pulmonary atresia with ventricular septal defect. Acta Radiol 42:63–69

Holt PD, Berdon WE, Marans Z, Griffiths S, Hsu D (2004) Scimitar vein draining to the left atrium and a historical review of the scimitar syndrome. Pediatr Radiol 34:409–413

Jacobs ML, Pourmoghadam KK (2003) The hemi-Fontan operation. Semin Thorac Cardiovasc Surg Pediatr Card Surg Annu 6:90–97

Jatene AD, Fontes VF, Paulista PP, Souza LC, Neger F, Galantier M, Sousa JE (1976) Anatomic correction of transposition of the great vessels. J Thorac Cardiovasc Surg 72:364–370

Jhooti P, Gatehouse PD, Keegan J, Bunce NH, Taylor AM, Firmin DN (2000) Phase ordering with automatic window selection (PAWS): a novel motion-resistant technique for 3D coronary imaging. Magn Reson Med 43:470–480

Kaminaga T, Takeshita T, Kimura I (2003) Role of magnetic resonance imaging for evaluation of tumors in the cardiac region. Eur Radiol 13(Suppl 4):L1–10

Kau T, Sinzig M, Gasser J, Lesnik G, Rabitsch E, Celedin S et al (2007) Aortic development and anomalies. Semin Intervent Radiol 24(2):141–152

Kauczor HU, Schwickert HC, Mayer E, Kersjes W, Moll R, Schweden F (1994) Pulmonary artery sarcoma

mimicking chronic thromboembolic disease: computed tomography and magnetic resonance imaging findings. Cardiovasc Intervent Radiol 17:185–189

Khurshid I, Downie GH (2002) Pulmonary arteriovenous malformation. Postgrad Med J 78:191–197

Kim TK, Choe YH, Kim HS, Ko JK, Lee YT, Lee HJ, Park JH (1995) Anomalous origin of the right pulmonary artery from the ascending aorta: diagnosis by magnetic resonance imaging. Cardiovasc Intervent Radiol 18:118–121

Kindermann M, Wilkens H, Hartmann W, Schafers HJ, Bohm M (2003) Images in cardiovascular medicine. Hughes-Stovin Syndr Circ 108:e156

Kivelitz DE, Scheer I, Taupitz M (1999) Scimitar syndrome: diagnosis with MR angiography. AJR 172:1700

Konen E, Raviv-Zilka L, Cohen RA, Epelman M, Boger-Megiddo I, Bar-Ziv J, Hegesh J, Ofer A, Konen O, Katz M, Gayer G, Rozenman J (2003) Congenital pulmonary venolobar syndrome: spectrum of helical CT findings with emphasis on computerized reformatting. Radiographics 23:1175–1184

Kreft B, Flacke S, Zhou H, Textor J, Remig J, Schild HH (2004) Diagnostic imaging of vascular leiomyosarcomas. Rofo Fortschr Geb Rontgenstr Neuen Bildgeb Verfahr 176:183–190

Krueger JJ, Ewert P, Yilmaz S, Gelernter D, Peters B, Pietzner K, Bornstedt A, Schnackenburg B, Abdul-Khaliq H, Fleck E, Nagel E, Berger F, Kuehne T (2006) Magnetic resonance imaging-guided balloon angioplasty of coarctation of the aorta: a pilot study. Circulation 113:1093–1100

Kutsche LM, Van Mierop LH (1988) Anomalous origin of a pulmonary artery from the ascending aorta: associated anomalies and pathogenesis. Am J Cardiol 61:850–856

Ley S, Fink C, Zaporozhan J, Borst MM, Meyer FJ, Puderbach M, Eichinger M, Plathow C, Grunig E, Kreitner KF, Kauczor HU (2005) Value of high spatial and high temporal resolution magnetic resonance angiography for differentiation between idiopathic and thromboembolic pulmonary hypertension: initial results. Eur Radiol 15:2256–2263

Ley-Zaporozhan J, Ley S, Eberhardt R, Weinheimer O, Fink C, Puderbach M et al (2007) Assessment of the relationship between lung parenchymal destruction and impaired pulmonary perfusion on a lobar level in patients with emphysema. Eur J Radiol 63(1):76–83

Ley S, Zaporozhan J, Arnold R, Eichhorn J, Schenk JP, Ulmer H, Kreitner KF, Kauczor HU (2007) Preoperative assessment and follow-up of congenital abnormalities of the pulmonary arteries using CT and MRI. Eur Radiol 17:151–162

Losay J, Touchot A, Serraf A, Litvinova A, Lambert V, Piot JD, Lacour-Gayet F, Capderou A, Planche C (2001) Late outcome after arterial switch operation for transposition of the great arteries. Circulation 104:I121–I126

Macgowan CK, Al-Kwifi O, Varodayan F, Yoo SJ, Wright GA, Kellenberger CJ (2005) Optimization of 3D contrast-enhanced pulmonary magnetic resonance angiography in pediatric patients with congenital heart disease. Magn Reson Med 54:207–212

Maintz D, Juergens KU, Wichter T, Grude M, Heindel W, Fischbach R (2003) Imaging of coronary artery stents using multislice computed tomography: in vitro evaluation. Eur Radiol 13:830–835

Mayer F, Aebert H, Rudert M, Konigsrainer A, Horger M, Kanz L, Bamberg M, Ziemer G, Hartmann JT (2007) Primary malignant sarcomas of the heart and great vessels in adult patients--a single-center experience. Oncologist 12:1134–1142

Mohrs OK, Voigtlander T, Heussel CP, Bardeleben S, Duber C, Kreitner KF (2002) Morphologic and functional assessment of vascular abnormalities of the pulmonary vasculature by breath-hold MR techniques. Rofo Fortschr Geb Rontgenstr Neuen Bildgeb Verfahr 174:467–473

Moos A (2001) Heart disease in infants, children and adolescents. Including the fetus and yound adult. Lippincott Williams & Wilkins, Philadelphia

Naganawa S, Kawai H, Fukatsu H, Ishigaki T, Komada T, Maruyama K, Takizawa O (2004) High-speed imaging at 3 Tesla: a technical and clinical review with an emphasis on whole-brain 3D imaging. Magn Reson Med Sci 3:177–187

Nakanishi T (2005) Cardiac catheterization is necessary before bidirectional Glenn and Fontan procedures in single ventricle physiology. Pediatr Cardiol 26:159–161

Nielsen JC, Powell AJ, Gauvreau K, Marcus EN, Prakash A, Geva T (2005) Magnetic resonance imaging predictors of coarctation severity. Circulation 111(5):622–628

Ohno Y, Adachi S, Motoyama A, Kusumoto M, Hatabu H, Sugimura K, Kono M (2001) Multiphase ECG-triggered 3D contrast-enhanced MR angiography: utility for evaluation of hilar and mediastinal invasion of bronchogenic carcinoma. J Magn Reson Imaging 13:215–224

Ohye RG, Bove EL (2001) Advances in congenital heart surgery. Curr Opin Pediatr 13:473–481

Oliver TB, Stevenson AJ, Gillespie IN (1997) Pulmonary artery pseudoaneurysm due to bronchial carcinoma. Br J Radiol 70:950–951

Peters DC, Wylie JV, Hauser TH, Kissinger KV, Botnar RM, Essebag V, Josephson ME, Manning WJ (2007) Detection of pulmonary vein and left atrial scar after catheter ablation with three-dimensional navigator-gated delayed enhancement MR imaging: initial experience. Radiology 243:690–695

Prakash A, Torres AJ, Printz BF, Prince MR, Nielsen JC (2007) Usefulness of magnetic resonance angiography in the evaluation of complex congenital heart disease in newborns and infants. Am J Cardiol 100:715–721

Prasad SK, Soukias N, Hornung T, Khan M, Pennell DJ, Gatzoulis MA, Mohiaddin RH (2004) Role of magnetic resonance angiography in the diagnosis of major aortopulmonary collateral arteries and partial anomalous pulmonary venous drainage. Circulation 109:207–214

Rahmani N, White CS (2008) MR imaging of thoracic veins. Magn Reson Imaging Clin N Am 16:249–262

Remy J, Remy-Jardin M, Wattinne L, Deffontaines C (1992) Pulmonary arteriovenous malformations: eval-

uation with CT of the chest before and after treatment. Radiology 182:809–816

Rickers C, Seethamraju RT, Jerosch-Herold M, Wilke NM (2003) Magnetic resonance imaging guided cardiovascular interventions in congenital heart diseases. J Interv Cardiol 16:143–147

Roman KS, Kellenberger CJ, Farooq S, MacGowan CK, Gilday DL, Yoo SJ (2005) Comparative imaging of differential pulmonary blood flow in patients with congenital heart disease: magnetic resonance imaging versus lung perfusion scintigraphy. Pediatr Radiol 35:295–301

Salehian O, Schwerzmann M, Merchant N, Webb GD, Siu SC, Therrien J (2004) Assessment of systemic right ventricular function in patients with transposition of the great arteries using the myocardial performance index: comparison with cardiac magnetic resonance imaging. Circulation 110:3229–3233

Schneider H, Uebing A, Shore DF (2016) Modern management of adult coarctation: transcatheter and surgical options. J Cardiovasc Surg (Torino) 57(4):557–568

Sebening C, Jakob H, Tochtermann U, Lange R, Vahl CF, Bodegom P et al (2000) Vascular tracheobronchial compression syndromes – experience in surgical treatment and literature review. Thorac Cardiovasc Surg 48(3):164–174

Sequeiros RB, Ojala R, Kariniemi J, Perala J, Niinimaki J, Reinikainen H, Tervonen O (2005) MR-guided interventional procedures: a review. Acta Radiol 46:576–586

Simonetti OP, Cook S (2006) Technical aspects of pediatric CMR. J Cardiovasc Magn Reson 8:581–593

Simoneaux SF, Bank ER, Webber JB, Parks WJ (1995) MR imaging of the pediatric airway. Radiographics 15(2):287–298, discussion 98-9

Singh S, Hakim FA, Sharma A, Roy RR, Panse PM, Chandrasekaran K et al (2015) Hypoplasia, pseudocoarctation and coarctation of the aorta – a systematic review. Heart Lung Circ 24(2):110–118

Sorensen TS, Beerbaum P, Korperich H, Pedersen EM (2005) Three-dimensional, isotropic MRI: a unified approach to quantification and visualization in congenital heart disease. Int J Card Imaging 21:283–292

Sorensen TS, Korperich H, Greil GF, Eichhorn J, Barth P, Meyer H, Pedersen EM, Beerbaum P (2004) Operator-independent isotropic three-dimensional magnetic resonance imaging for morphology in congenital heart disease: a validation study. Circulation 110:163–169

Stein P (2007) Total anomalous pulmonary venous connection. AORN J 85:509–520; quiz 521-504

Tanous D, Benson LN, Horlick EM (2009) Coarctation of the aorta: evaluation and management. Curr Opin Cardiol 24(6):509–515

Torok RD, Campbell MJ, Fleming GA, Hill KD (2015) Coarctation of the aorta: management from infancy to adulthood. World J Cardiol 7(11):765–775

Ulmer H (2012) Aortenisthmusstenose: Viel mehr als eine angeborene Engstelle der Hauptschlagader. Herzblatt 2012:1.

Varaprasathan GA, Araoz PA, Higgins CB, Reddy GP (2002) Quantification of flow dynamics in congenital heart disease: applications of velocity-encoded cine MR imaging. Radiographics 22:895–905; discussion 905-896

Wald RM, Powell AJ (2006) Simple congenital heart lesions. J Cardiovasc Magn Reson 8:619–631

Weiss F, Habermann CR, Lilje C, Nimz M, Rasek V, Dallmeyer J, Stork A, Graessner J, Weil J, Adam G (2005) MRI of pulmonary arteries in follow-up after arterial-switch-operation (ASO) for transposition of great arteries (d-TGA). Rofo Fortschr Geb Rontgenstr Neuen Bildgeb Verfahr 177:849–855

Yi ES (2004) Tumors of the pulmonary vasculature. Cardiol Clin 22:431–440, vi–vii

Yu JM, Liao CP, Ge S, Weng ZC, Hsiung MC, Chang JK, Chen FL (2008) The prevalence and clinical impact of pulmonary artery sling on school-aged children: a large-scale screening study. Pediatr Pulmonol 43(7):656–661

Asthma

David G. Mummy, Wei Zha, Ronald L. Sorkness,
and Sean B. Fain

Contents

D.G. Mummy, MS, MBA
Department of Biomedical Engineering,
University of Wisconsin, Madison, WI, USA

W. Zha, PhD
Department of Medical Physics,
University of Wisconsin, Madison, WI, USA

R.L. Sorkness, PhD
School of Pharmacy and Morris Institute for
Respiratory Research, University of Wisconsin,
Madison, WI, USA

Abstract

Asthma is a disease with significant clinical impact and growing incidence, particularly in children. It is characterized by a complex interplay of environmental and genetic factors that affect airway structure and function, leading to recurrent and spatially heterogeneous airway obstruction. Conventional methods for evaluating lung function using spirometry and plethysmography are neither capable of assessing regional obstruction nor the regional dynamics of airway obstruction. MRI methods that exploit gas contrast agents have emerged as an attractive approach for evaluating heterogeneity and mechanisms of airway obstruction in the asthmatic lung without requiring ionizing radiation. Specific gas agents that show promise include hyperpolarized gases, oxygen enhancement, and fluorinated gases. Hyperpolarized (HP) helium-3 (³He) and xenon-129 (¹²⁹Xe) MRI techniques in particular have enabled visualization of the

S.B. Fain, PhD (✉)
Departments of Medical Physics, Radiology, and
Biomedical Engineering, University of Wisconsin,
Madison, WI, USA

2488 Wisconsin Institutes for Medical Research
(WIMR), University of Wisconsin,
1111 Highland Ave, Madison, WI 53795, USA
e-mail: sfain@wisc.edu

airspaces of the lungs, including the large airways and lung parenchyma, during breath-held and dynamic respiratory maneuvers. This method has been applied to study disease progression, response to therapy, and asthma phenotypes. Diffusion-weighted MRI may be used to measure the dimensions of small airways and alveolar microstructure, allowing for the determination of structural changes associated with disease progression. Ultrashort echo time (UTE) MRI, an emerging technique, allows for rapid 3D acquisition of lung images at a resolution approaching that of CT. Patterns of poor ventilation observed on HP MRI identify regions of obstruction that may reflect underlying structural changes in the airway such as remodeling or chronic inflammation. HP MRI has also been used in conjunction with CT to perform image-guided sampling of airways leading to areas of poor ventilation in the lung, enabling the development of biomarkers of disease. These multi-modality comparisons between CT and HP MRI may help evaluate regional structure-function relationships to assess causal mechanisms of disease and response to therapy and potentially to develop new disease phenotypes associated with clinical outcomes and healthcare utilization.

Glossary of Acronyms

%DL$_{CO}$	Percent predicted diffusing capacity of the lung for carbon monoxide
ACOS	Asthma-COPD overlap syndrome
ADC	Apparent diffusion coefficient
BAL	Bronchoalveolar lavage
BT	Bronchial thermoplasty
CF	Cystic fibrosis
COPD	Chronic obstructive pulmonary disease
DWI	Diffusion-weighted imaging
FEV$_1$	Forced expiratory volume in 1 s
FID	Free induction decay
FLASH	Fast low-angle shot
FRC	Functional residual capacity
FSE	Fast spin echo
FVC	Forced vital capacity

GRE	Gradient-recalled echo
HP	Hyperpolarized
IOS	Impulse oscillometry
IPF	Idiopathic pulmonary fibrosis
MDCT	Multi-detector computed tomography
OE	Oxygen enhanced
OTF	Oxygen transfer function
PET	Positron emission tomography
PFT	Pulmonary function test
PSE	Percent signal enhancement
qCT	Quantitative CT
RF	Radio frequency
RV	Residual volume
SEOP	Spin-exchange optical pumping
SNR	Signal-to-noise ratio
SPECT	Single-photon emission computed tomography
SSFSE	Single shot fast spin echo
SV	Specific Ventilation
TLC	Total lung capacity
UTE	Ultrashort echo time
V/Q	Ventilation/perfusion
VDP	Ventilation defect percent
Xrms	Chi root-mean-square acinar dimension

Key Points

Asthma is characterized by recurrent airway obstruction and has a significant and increasing clinical impact worldwide. Since conventional methods of evaluating lung function cannot assess spatial patterns and regional dynamics of airway obstruction, MRI methods that exploit gas contrast agents, including hyperpolarized (HP) helium-3 and xenon-129, oxygen enhancement, and fluorinated gases, are an attractive approach for evaluating airway obstruction without the use of ionizing radiation. HP gas MRI techniques enable visualization of the airspaces of the lungs and have been most extensively applied to study asthma, including severity, therapy response, and disease phenotypes. Diffusion-weighted imaging with HP gas MRI is capable of measuring the dimen-

sions of the small airways that are a locus of ventilation heterogeneity in asthma. Both oxygen-enhanced and fluorinated gas MRI are less well developed in asthma, but may hold promise for broader dissemination. Ultra-short echo time (UTE) MRI, is also an emerging technique, capable of volumetric lung images at a resolution approaching that of CT. Ultimately, HP gas MRI in conjunction with CT or UTE MRI may be used to perform image-guided sampling or therapy of airways associated with areas of poor ventilation in the lung. A regional evaluation of the relationships between structure and function remains a promising approach for understanding and phenotyping asthma for new therapies.

1 Introduction

This chapter describes the application of MR imaging of lung function to the study of asthma. Asthma affects millions of people worldwide, and trends indicate increasing incidence, particularly among children. The first section of the chapter focuses on a general overview of asthma as a disease, characterizes the obstructive physiology involved in asthma, and describes its clinical presentation. This section includes the rationale for imaging in asthma specifically as a useful tool to advance our understanding of the basic phenotypes of this disease and for characterizing regional heterogeneity in the lungs. Subsequent sections are dedicated to the role of different gas agents used for both breath-held and dynamic MRI of ventilation, including hyperpolarized (^{3}He and ^{129}Xe), oxygen-enhanced, and fluorinated gases. These techniques also serve to advance our current understanding of the physiologic meaning of observed "ventilation defects." While the emphasis is on the role of hyperpolarized (HP) gases, resurgent methods using oxygen-enhanced and fluorinated gas are included given their potential. Approaches to the measurement and quantification of ventilation defects observed in asthma are

reviewed, with a focus on the use of ventilation images to explore mechanisms of airway closure and disease progression and to target and evaluate regional disease and response to therapy. Diffusion-weighted MRI with HP gas is given treatment, with emphasis on its potential to investigate lung microstructure and small airways disease in asthma. The next sections present preliminary clinical results derived from the use of these techniques, including studies of asthma phenotypes and clinical correlates of ventilation heterogeneity. The final sections are dedicated to emerging techniques likely to impact the study of asthma using MRI, especially the growing role of ultrashort echo time (UTE) MRI, 3D radial imaging, and the ongoing transition from HP ^{3}He to HP ^{129}Xe MRI.

2 Background

Asthma is a significant cause of disease, disability, and healthcare utilization. It is estimated that over 600 million people worldwide are affected by some form of the disease (To et al. 2012). There are over seven million asthmatic children in the United States alone, and prevalence is increasing (Akinbami et al. 2012). In addition to the substantial strain this imposes on the healthcare system, asthma disease burden results in millions of school- and work-days lost each year (Akinbami et al. 2012).

Asthma is an obstructive airways disease characterized by chronic inflammation of the airways, resulting in obstruction of airflow and symptoms of wheezing, chest tightness, cough, and overall difficulty breathing. These symptoms are often reversible, but persistent airway limitation may also occur. Acute episodes of airway obstruction may be triggered by stimuli such as respiratory viral infections, exposure to allergens, or exercise, which are superimposed on an underlying chronic inflammatory process that renders the airways hyperresponsive to perturbations that in normal airways would evoke a negligible response. The etiology of the disease is recognized as a complex combination of genetic and environmental risk factors. Differing patterns

of asthma (e.g., inception, lability, responsiveness to treatment, severity) likely represent differences in underlying airway pathophysiology, but definitions of distinct asthma phenotypes suitable for guiding treatment remain elusive (Lotvall et al. 2011). Structural remodeling likely has a role in driving the obstructive physiology. This remodeling includes wall thickening stemming from a combination of subepithelial and smooth muscle thickening and an increase in the mucus-producing structures (goblet cells and submucosal glands), as illustrated in Fig. 1. Moreover, there is a wide spectrum of severity in patients with asthma and considerable debate as to the relative roles of the environmental and remodeling factors in determining disease severity.

This uncertainty is in part due to the indirect nature of the information used to study asthma thus far. Much of what is known about asthma, and obstructive lung diseases in general, was gleaned from careful studies using whole-lung measurements of airflow (i.e., spirometry), lung volume (i.e., plethysmography) (Levitzky 2013; Evans and Scanlon 2003), and direct bronchoscopic assessment (Jarjour et al. 2012). Spirometry shows that obstructive lung diseases including asthma and chronic obstructive pulmonary disease (COPD) are characterized by a reduction in forced expiratory volume at 1 s (FEV_1), forced vital capacity (FVC; an indicator of the air trapping component of obstruction), and the FEV_1/FVC ratio (an indicator of the airflow limitation component of obstruction) (Evans and Scanlon 2003). However, spirometry is relatively nonspecific for distinguishing asthma from COPD, and substantial overlap is common. Generally, COPD refers to a spectrum of obstructive lung diseases including chronic bronchitis, emphysema, and asthmatic bronchitis (Petty 2003), as opposed to typical asthma, which is largely characterized
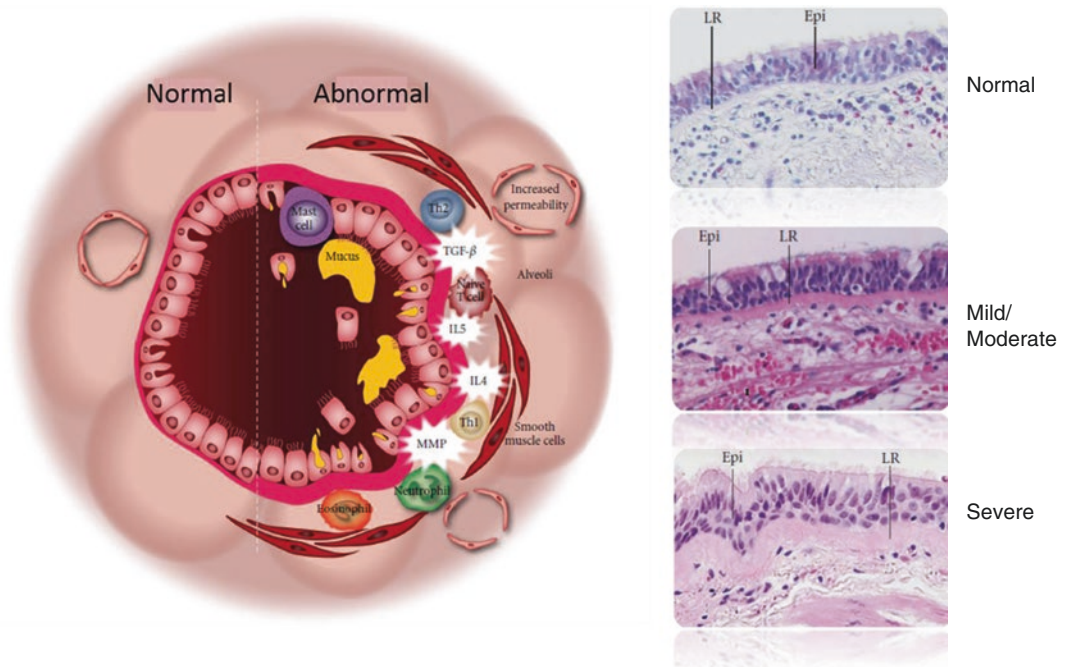
Fig. 1 Pathophysiological processes governing airway injury and remodeling in asthma. Basal membrane thickening and smooth muscle hypertrophy and hyperreactivity are believed to occur due to chronic injury and airway remodeling. In particular, wall thickening in the epithelium (*Epi*) and lamina reticulata (*LR*) has been shown to be associated with severe asthma on histology (*panels in right column*) and using CT imaging (Adapted from Shifren et al. (2012) with permission)

by more reversible obstruction. However, airway remodeling may lead to a nonreversible component in asthma as well as chronic reduction in FEV_1/FVC ratio and persistent airflow limitation (Sorkness et al. 2008). Bronchoscopic assessment and postmortem histology support the existence of airway remodeling as a significant component of more severe asthma (James et al. 2009; Jarjour et al. 2012). In several studies, more severe asthma is associated with decreased FVC and increased residual lung volume (RV) that also suggest increased air trapping at low lung volumes (Sorkness et al. 2008; Brown et al. 2006).

Conventionally, lung obstruction is assessed using spirometry and plethysmography (Levitzky 2013; Evans and Scanlon 2003), global measurements commonly referred to collectively as "pulmonary function tests" or PFTs (Fig. 2). PFTs are derived from respiratory maneuvers designed to measure fixed lung volumes and dynamic airflow curves (Winn et al. 2003). Both FEV_1 and FEV_1/FVC (Levitzky 2013) are reduced in asthma because the large and small airways in the lungs have increased resistance to airflow due to narrowing and collapse, limiting both the total volume of air exhaled and the rate of exhaled airflow. Plethysmography, using Boyle's law and a "body box" (Levitzky 2013), is less commonly used than spirometry but is capable of measuring absolute lung volumes, including the total lung capacity (TLC), functional residual capacity (FRC), and RV. Both FRC and RV are typically increased in asthma due to hyperinflation and air trapping, respectively (Sorkness et al. 2008).

Impulse oscillometry (IOS) is another important global method for characterizing heterogeneity in the biomechanical properties of the airways. IOS has also been a useful correlate in imaging studies and has shown potential for characterizing early disease changes and heterogeneity of disease as it relates to mechanical properties of the airways, especially in pediatric asthma (Rabinovitch et al. 2014; Guilbert et al. 2014b).

Conventional PFTs are inexpensive and widely accessible and are standardized to reference values for different populations, gender, and body size (Hankinson et al. 1999; Quanjer et al. 2012). Standardization makes it possible to make general comparisons of disease severity across different populations in order to screen and monitor disease progression. Spirometry and plethysmography cannot explore the regional mechanics of airway obstruction, however, and direct bronchoscopic assessment is invasive and can only sample very limited regional structure (Benayoun et al. 2003). Therefore, imaging methods are well positioned for in vivo studies of regional heterogeneity and dynamics of airway obstruction in asthma. This has led to the
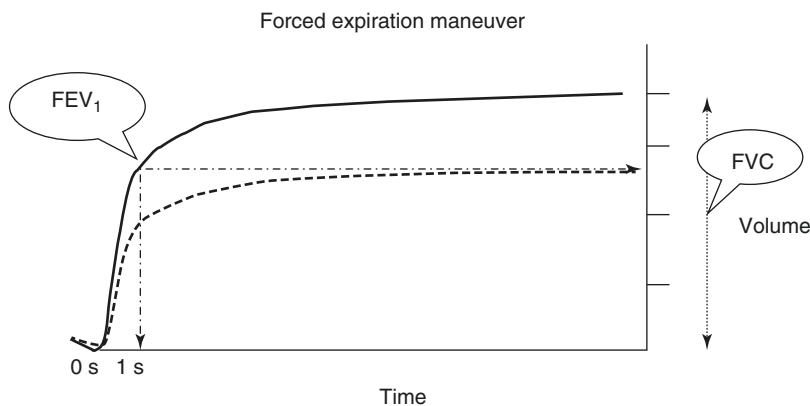
Fig. 2 Global lung function can be assessed using pulmonary function tests such as spirometry and plethysmography. The time-volume curves shown here illustrate the decrease in forced expiratory volume in 1 s (*FEV$_1$*) and forced vital capacity (*FVC*) in asthma subjects vs. healthy subjects, suggesting airway obstruction to flow. However, these whole-lung methods do not provide the regional specificity that may be obtained via imaging

increasing role of multiple detector computed tomography (MDCT) and functional lung imaging using MRI. In asthma, most of this work has focused on imaging of gas ventilation of the lungs, principally with HP ³He (though increasingly with HP ¹²⁹Xe), but oxygen-enhanced and fluorinated gas MRI are likely to find increased applications as well.

2.1 Role of Imaging in Asthma

The clinical standard of care for diagnosis of lung disease in general is MDCT. While MDCT provides high contrast and resolution in the airways and lung parenchyma, it cannot readily assess lung function. Typically, a high CT radiation dose is associated with regional ventilation and perfusion studies of lung function. This raises challenges for the study of asthma in particular, which often involves pediatric subjects (Miglioretti et al. 2013) and the need for longitudinal and interventional studies requiring repeated imaging exams (Hurwitz et al. 2007). However, MDCT remains important as a tool for understanding airway and parenchymal structure in asthma. For example, the application of MDCT provides direct measurement of structures in the central airways (Fig. 3) such as wall thickening, airway lumen narrowing and closure, and mucus plugging associated with increased asthma severity (Aysola et al. 2008), often measured in con-

junction with various respiratory maneuvers such as deep inspiration (Brown et al. 2000). Quantitative CT (qCT) measures (Lynch and Al-Qaisi 2013) of airway morphology and lung parenchymal density in multi-center trials suggest that structural remodeling of the central airways drives some aspects of the obstructive physiology, especially for severe asthma, where wall thickness and air trapping measures correlate to more severe outcomes (Aysola et al. 2008; Busacker et al. 2009; Gupta et al. 2015). Despite such advances in the noninvasive imaging of lung structure using qCT, the functional consequences of airway remodeling and the spatial and temporal dynamics of airway obstruction in asthma remain only partially characterized. Moreover, safety concerns raise significant question as to the viability of both X-ray CT (given the risk of ionizing radiation dose (Mayo 2008)) and invasive bronchoscopy in pediatric populations and in the longitudinal studies necessary for a comprehensive study of asthma phenotypes and disease progression.

The primary clinical approaches for evaluating ventilatory patterns in the lungs are single-photon emission computed tomography (SPECT) and nuclear scintigraphy with inhaled technegas, i.e., technetium (Tc)-99m-labeled aerosol or ¹³³Xe (Howarth et al. 1999; Newman et al. 2003). However, these conventional nuclear imaging methods remain limited in resolution, coverage, and signal-to-noise ratio (SNR). Nuclear imaging
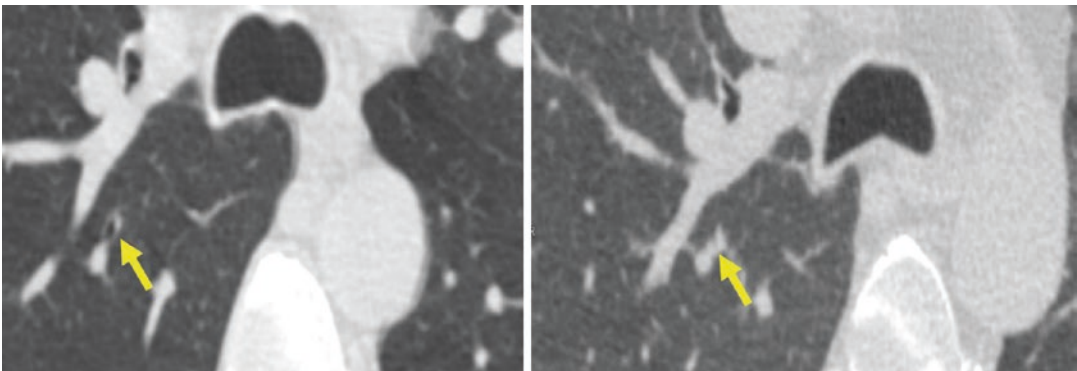
Fig. 3 Inspiratory (*left*) and expiratory (*right*) CT of the central airways in a subject with asthma. A case of airway collapse is indicated by changes in the airway lumen indicated (*yellow arrow*). Airway collapse is one mechanism driving obstruction and air trapping at lower lung volumes, functional reserve capacity (*FRC*) in this case

methods are challenged to depict the heterogeneity and dynamics of airway obstruction in asthma due to reduced spatial and temporal resolution. Nonetheless, $^{13}N_2$ gas positron emission tomography (PET) has been successfully applied to the study of asthma in the research setting (Vidal Melo et al. 2003) but with limited spatial coverage and a requirement for extended breath-hold times.

MRI is well positioned for longitudinal investigations of in vivo heterogeneity and dynamics of airway obstruction in asthma. The low sensitivity of PFTs has driven pulmonary clinicians and radiologists to seek more sensitive regional measures of asthma. A niche exists for MRI applications of functional lung imaging that can exploit the modality's three-dimensional (3D) and time-resolved imaging capabilities while providing sufficient contrast resolution in the airways and lung parenchyma. In general, visualization of the airspaces of the large airways and parenchyma using functional lung MRI in asthma is similar in concept to nuclear imaging with inhaled ^{133}Xe gas, but with superior SNR and 3D coverage, and without the use of ionizing radiation. Consequently, there has been significant interest and activity in MRI techniques, especially in HP ^3He (and also ^{129}Xe) MRI, among the pulmonary research community, including its use in several large-scale longitudinal clinical research studies (Jarjour et al. 2012; Bel et al. 2011).

3 Characterization of the Asthmatic Lung with MRI

3.1 Functional Lung Imaging with MRI

Various gas agents are used to produce contrast in the ventilated lungs using MRI (Fig. 4 and Table 1). These include oxygen, fluorinated gases (typically sulfur hexafluoride (SF_6) and hexafluoroethane (C_2F_6)), and hyperpolarized gases (^3He and ^{129}Xe). Protocols, methodology, and analysis approaches used for each gas are

described with some detail in other chapters in this book and below. Both HP ^3He and ^{129}Xe are dependent on polarizer and multinuclear technology that is not widely available (Fain et al. 2010), and gas shortages, limited accessibility, and high cost of these gases have hampered the dissemination of these techniques until recently. In response to these disadvantages, other gas agents used in functional lung imaging have become resurgent. These include oxygen-enhanced (Edelman et al. 1996) and fluorinated gas MRI (Kuethe et al. 1998) methods that have emerged as possible alternatives, with lower-cost profiles and potential for wider accessibility than HP gases (Table 1). Both of these alternative gases are described in terms of their basic implementation and their potential application to the study of asthma.

3.2 Hyperpolarized Gas Imaging

Clinical research applications of HP ^3He MRI have been demonstrated in childhood asthma (Cadman et al. 2013; Altes et al. 2016), severe asthma (Jarjour et al. 2012; Bel et al. 2011), and exercise-induced asthma (Kruger et al. 2014b). However, the gases involved are expensive, require hardware modifications to the typical clinical MRI to enable multinuclear imaging (similar to those needed for fluorinated gases), and require a polarizer system. The basics of hyperpolarized gas preparation have already been described elsewhere, and either metastability (Gentile et al. 2000) or SEOP (Walker and Happer 1997) methods can be used. The patient or research subject is generally imaged in the supine position; consequently, gradients in ventilation and alveolar size are expected from anterior to posterior due to gravity dependence. Minimizing the duration of the study mitigates the development of posterior atelectasis, which is not a problem for typical exam times of 30 min or less. Both 2D multi-slice and 3D spoiled gradient-recalled echo (GRE) pulse sequences are routinely used for breath-held and dynamic MRI in clinical research (Table 2). Spin density images of ventilation during a breath-hold have been
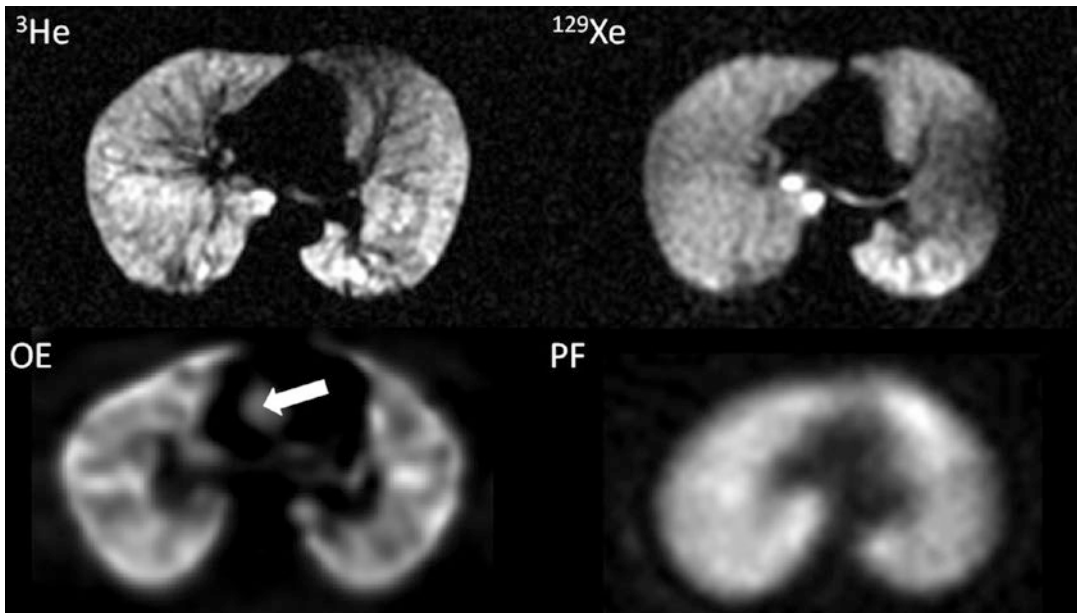
Fig. 4 Representative images of the four main gas agents used in ventilation-weighted MRI: helium-3, xenon-129, oxygen-enhanced (*OE*) and perfluorinated gas (*PF*). The PF image is adapted from (Kruger et al. 2016). In the OE contrast image, enhancement extends beyond the lung parenchyma and includes the blood pool as indicated by the enhancement in the aorta (*arrow*)

most commonly used to date for the study of asthma because of ease of implementation and repeatability across different visits and collaborating institutions (Niles et al. 2013; Mathew et al. 2008). HP gases have a unique ability to measure the regional dimensions of lung microstructures during a single breath-hold. For example, diffusion-weighted imaging (DWI) can quantitatively measure change in small airway and alveolar microstructures due to aging and disease (Salerno et al. 2002; Yablonskiy et al. 2002; Fain et al. 2005), especially in emphysema due to tissue loss caused by smoking (Fain et al. 2006) or α-1-antitrypsin deficiency (Salerno et al. 2002).

3.2.1 Image Analysis Methods

The development of more objective quantitative measures of the severity and extent of ventilation defects is critical to the advance of HP MRI technology. The most common metric currently in use is the ventilation defect percent (VDP), which is calculated by summing the defect volume over a given region of the lung and then normalizing to the total regional lung volume (Woodhouse et al.

2005; Pike et al. 2015). Proton MRI is generally used in conjunction with this method to segment the lung volume. VDP is commonly reported as a whole-lung metric but is also used over subregions of the lung to provide a quantitative measure of both defect extent and spatial heterogeneity. Multiple investigators have independently converged on the use of VDP as a biomarker of the severity of obstruction, which has prompted recent, more coordinated efforts to develop automated methods of defect segmentation (Tustison et al. 2011; He et al. 2014). These pipelines include steps to exclude the pulmonary vascular structure using the vesselness filter (Frangi et al. 1999) and intensity correction of the gas images (Tustison et al. 2010). Recent methods have integrated these approaches with an adaptive k-means clustering algorithm for segmenting ventilation defects, allowing for rapid, reproducible calculation of VDP (Zha et al. 2016). These semiautomated approaches typically require supervised segmentation of the lung volume, but otherwise use automated classifiers to define four clusters of signal intensity (Fig. 5). The lowest signal intensity

Table 1 Strengths and challenges of different gas contrast agents for pulmonary functional imaging

	HP ³He MRI	HP ¹²⁹Xe MRI	OE MRI	¹⁹F MRI
SNR	High	Med-high	Low	Low
Breath-hold imaging	Yes	Yes	No	Both
Cost	~$800–1200/L	$170/L (enriched) $15/L (natural abundance)	<$1/L	$15–20/L
Hardware requirements	MNS T/R polarizer	MNS T/R polarizer	Conventional clinical MRI	MNS T/R
IND required	Yes	Yes	No	Yes
Scan length	5–10 s	5–10 s	5–30 min	12–15 s
Typical spatial resolution	3 mm × 3 mm × 10 mm	3 mm × 3 mm × 10 mm	2 mm × 2 mm × 10 mm	6 mm × 6 mm × 15 mm
Most common quantitative measures	ADC, VDP, pO_2	ADC, VDP, pO2	MRSER, PSE, OTF	VDP
Signal weightings	Ventilation, diffusion, oxygen mapping	Ventilation, diffusion, oxygen mapping, gas exchange	Ventilation and perfusion	Ventilation and oxygen mapping
Clinical research strengths	High spatial-temporal resolution regional measures of emphysema and gas trapping and airflow obstruction	Regional measures of emphysema and gas trapping and airflow obstruction. Dissolved phases in tissue and blood are a measure of gas exchange	Inexpensive, widely accessible method for ventilation-weighted imaging. Potential for quantitative ventilation	Less expensive method for ventilation-weighted imaging. Potential for quantitative ventilation

Abbreviations: HP hyperpolarized, *OE* oxygen enhanced, *SNR* signal-to-noise ratio, *IND* Investigational New Drug (FDA) application, *ADC* apparent diffusion coefficient, *VDP* ventilation defect percentage, *pO2* oxygen partial pressure, *MNS* multinuclear spectroscopy, *MRSER* mean relative signal enhancement ratio, *PSE* percent signal enhancement, *OTF* oxygen transfer function, *T/R* transmit/receive, *V/Q* ventilation-to-perfusion ratio

Table 2 Typical imaging parameters based on applications of ^{3}He MRI described in the literature. All imaging was performed at 1.5 Tesla. SPGR spoiled gradient, SSFP steady state free precession.

Method	Pulse sequence type	TR/TE (ms)	Flip (deg)	Matrix	FOV (cm)	Slice (mm)	Polarized gas dose	Temporal resolution	Technique-specific parameters
Ventilation	Cartesian (Samee et al. 2003)	9/3.7	10	256 × 100	50 × 38	10	300 ml ^{3}He in 1 L	10–13 s breath-hold from FRC	14–16 coronal slices or 20–25 axial slices
	3D SPGR (Wild et al. 2004)	9/4.47	2.1	108 × 100	43	0.9–1.3	300 ml ^{3}He in 1 L	19 s	32–48 slices
	SSFP (Wild et al. 2006)	10/5	5–20	128 × 256	48 × 48	13	300 ml ^{3}He in 1 L	Regular breath-hold	37 slices
	3D b-SSFP (Qing et al. 2015)	1.86/0.79	9	128 × 88	49.9 × 34.3	3.9	^{3}He diluted with N2 to 1/3 of TLC	16.4 s (fully sampled) 10.9 s (2× acceleration factor) 6.9 s (3× acceleration factor)	52 slices
Dynamic	2D Radial (Koumellis et al. 2005; Marshall et al. 2012)	5.4/2	7	128 × 100 (proj. angles)	41 × 41	10	5 ml ^{3}He/kg body wgt. in 0.5 L	0.54 s	128 projection angles/frame
	3D Radial (Hahn et al. 2016a, b)	4.4/0.22 (first TE)	~ 1	128 × 128	42 × 42	3.3	4.5 mM polarized ^{3}He in volume equal to 14% of subject's TLC	0.5 s	25 projection angles/frame
Diffusion	Cartesian (Fain et al. 2006; Mugler and Altes 2013)	8.4/4.5	7	128 × 80	38 × 30	15	4.5 mM polarized ^{3}He in 1 L	14 s breath-hold from FRC	10 coronal slices or 14–16 axial slices; b-value = 1.6 s/cm^2 (10 s/cm^2 for Xenon)
	Stack-of-stars (Cadman et al. 2013)	7.2/5.4	2	128 × 128 reconstructed	42 × 42	30	4.5 mM polarized ^{3}He in volume equal to 14% of subject's TLC	15 s breath-hold from FRC	256 radial lines, 8 phase-encoded axial slices, undersampled by acquiring each nonzero b-value on only 16 radial lines, b = 0.15, 0.61, 1.4, 2.4, 3.8, 5.5, 7.5, 9.8 s/cm^2

pixels (or a fraction thereof) are classified as ventilation defects. More sophisticated analyses have recently incorporated measurements of higher intensity pixels that may reflect more highly inflated lung regions stemming from ventilation heterogeneity. Although early in development, it is reasonable to assume that a more complete picture of both low and high ventilated regions will better capture the regional picture of ventilation heterogeneity in asthma.

3.2.2 Applications to Asthma

HP gas MRI has a distinct advantage in its ability to perform repeated breath-held images of ventilation, and it has uniquely shown the natural dynamics of ventilation defects over intervals of weeks (Niles et al. 2013), months, and years (de Lange et al. 2009; Svenningsen et al. 2014a). The visualization of elements of airway dynamics and heterogeneity over short time intervals can also be achieved using interventions such as breath-hold maneuvers, or before and after airway interventions. For example, HP ^{3}He MRI can be performed during breath-hold before and after

bronchodilation (Fig. 6), exercise (Fig. 7), methacholine challenge (Samee et al. 2003; Kruger et al. 2014b; Niles et al. 2013), or deep breathing maneuvers (Sani et al. 2008; Black et al. 2004) to assess airway response. The VDP and similar measures of ventilation on HP ^{3}He MRI have been variously correlated with spirometric measures of both FEV_1 and FEV_1/FVC percent predicted (PP), with degree and significance of the correlation differing among study populations (Kruger et al. 2014b; Svenningsen et al. 2014b; Zha et al. 2016). HP gas MRI is also useful in validating more accessible surrogate biomarkers of obstructive physiology, such as serum markers (Johansson et al. 2013a) including von Willebrand factor and P-selectin. Regional assessment of defect volume allows cross-modality comparisons with abnormalities and airway morphology on MDCT and with localized measurements performed via bronchoscopy, as will be discussed later in this chapter.

Breath-held images acquired at a fixed lung volume (approximately 1 L above FRC) are only measuring a short snapshot of the temporally
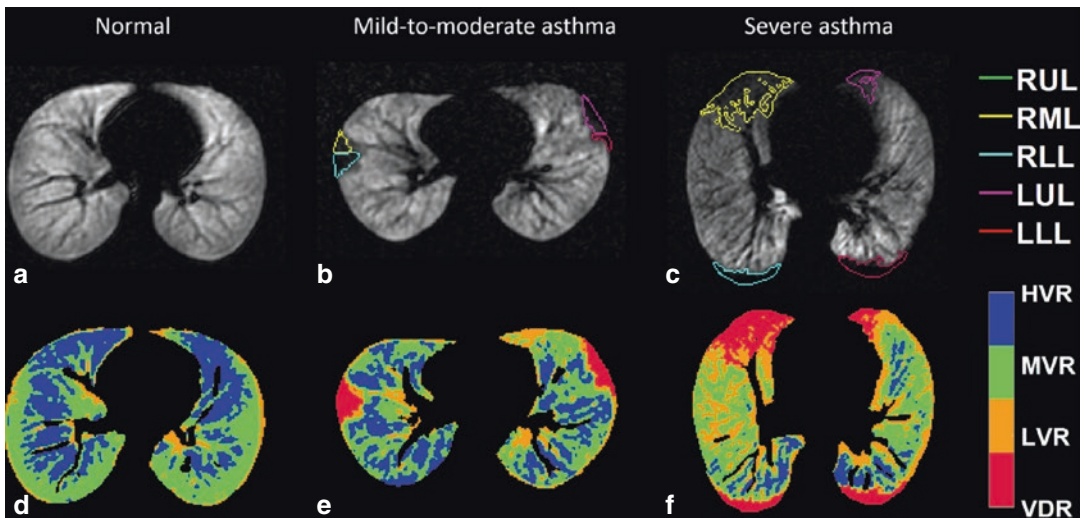
Fig. 5 Typical examples of segmented defects and the corresponding ventilation maps at middle slices of three subjects on HP ^{3}He MRI. The segmented defects for a normal subject (**a**), mild-to-moderate asthma (**b**), and severe asthma (**c**) are outlined with color-coding by lung lobe: right upper lobe (*RUL*) in *green*, right middle lobe (*RML*) in *yellow*, right lower lobe (*RLL*) in *cyan*, left

upper lobe (*LUL*) in *magenta*, and left lower lobe (*LLL*) in *red*. In the second row, the corresponding semiquantitative ventilation maps (**d, e, f**) contain four ventilation levels: the ventilation defect region (*VDR*) in *red*, low-ventilated region (*LVR*) in *orange*, moderately ventilated region (*MVR*) in *green*, and highly ventilated region (*HVR*) in *blue*
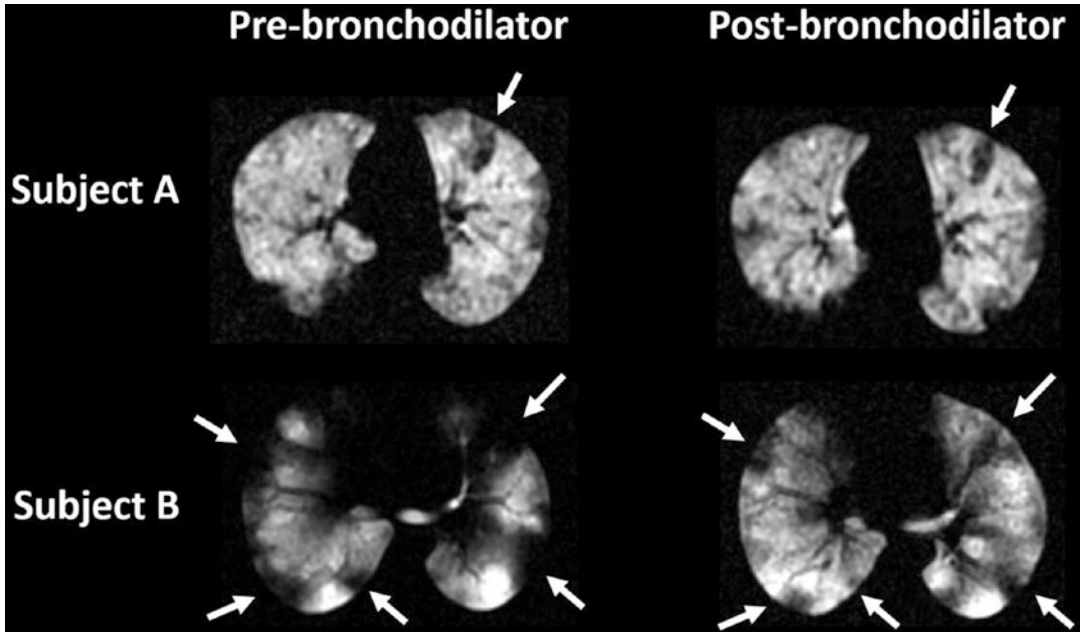
Fig. 6 Ventilation defects observed on HP ³He MRI before and after administration of albuterol, an inhaled bronchodilator. In subject A (*top row*), a ventilation defect observed pre-bronchodilator (*left column*) appears refractory to the bronchodilator, as it is still present in the post-bronchodilator image (*right column*). In subject B, however, multiple ventilation defects (*white arrows*) exhibit substantial reduction in extent following treatment

complex evolution of airway obstruction in asthma during the respiratory cycle. A more complete study of this obstruction would ideally capture the dynamic components of the disease that have been shown to depend on airway size, lung volume, and respiratory effort (Mead et al. 1967, 1970; Sa et al. 2014). Temporally resolved imaging of gas flow and kinetics is possible with HP gas MRI, and several acquisition methods have shown early promise. MRI in combination with inspiratory or forced expiratory maneuvers can capture regional obstruction within a single respiratory cycle. Spiral (Salerno et al. 2001) and projection acquisition (Wild et al. 2003) trajectories have been used to accelerate temporal and spatial resolution for assessing inspiratory obstruction in cystic fibrosis (CF) patients (Koumellis et al. 2005) and COPD patients (Salerno et al. 2001). Specific to asthma, forced exhalation with dynamic HP ³He MRI has shown a retained signal intensity that correlates well with air trapping on MDCT and residual volume measurements that correlate with plethys-

mography (Holmes et al. 2008, 2009). Most recently, this technique has been used to explore temporal dynamics of HP ³He gas during a single breath-hold (Hahn et al. 2016a).

However, the full realization of regional quantitative ventilation maps faces significant technical challenges, principally due to inconsistent lung volume over the duration of the gas wash-in and washout. Several mechanical ventilation techniques (Hamedani et al. 2016) or coached breath-hold methods (Horn et al. 2014) have shown promise, but more technical advances in the area of constrained reconstruction (Holmes et al. 2009; Collier and Wild 2015) and simultaneous anatomic and gas imaging (Wild et al. 2013) are necessary to perform dynamic respiratory maneuvers and fractional ventilation studies robustly within a clinical setting.

Diffusion-weighted HP gas MRI is a potential noninvasive probe for investigating small airway disease in asthma. The capability to measure small airway and alveolar structures at the scale
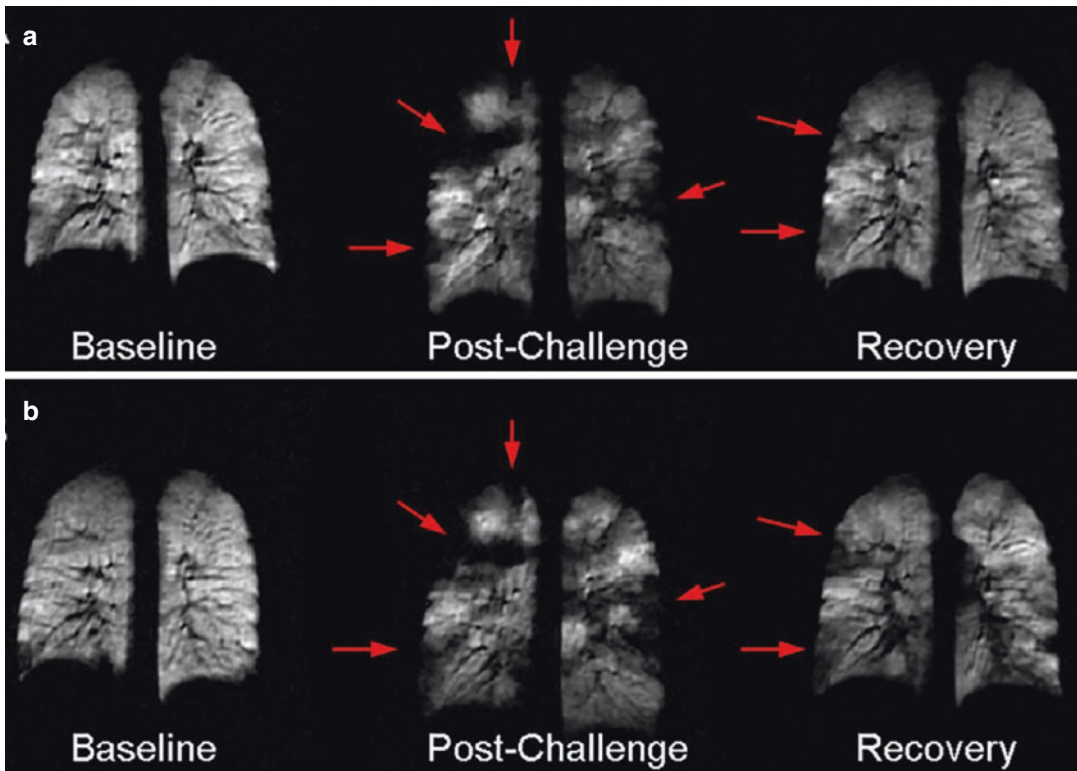
Fig. 7 Repeated HP ³He MRI in exercise-induced asthma showing two separate visits 1 week apart in the same patient in rows *A* and *B*. Columns correspond to pre-challenge (baseline), 10 min. after exercise challenge (post-challenge) on a treadmill, and 45 min after challenge (recovery), respectively. *Red arrows* indicate defects that recur in the same regional pattern (From reference Niles 2013; used with permission)

of 10–100 microns is a currently underappreciated advantage for the study of asthma, a disease in which small airways disease is known to be a major, but difficult to study, component. However, using just two b-values to determine the apparent diffusion coefficient (ADC), the method commonly used to investigate emphysema, has been less useful in asthma, likely due to the complexity of small airways disease. In asthma, air trapping, hyperinflation, and small airway narrowing may be occurring simultaneously. Interestingly, children with asthma were found to have restricted gas diffusion compared to healthy subjects, consistent with smaller bronchioles and alveolar spaces (Cadman et al. 2013). Further refinement of these measures – especially to address the simultaneous conditions of small airway narrowing and gas trapping – requires more

realistic models of the acinar (gas exchange) units of the lungs similar to that by Sukstanskii and Yablonskiy (2012) and demonstrated recently in healthy aging (Quirk et al. 2016). Such approaches show promise for illuminating the microstructural airway and alveolar changes associated with asthma disease progression.

3.3 Oxygen-Enhanced Imaging

Oxygen-enhanced (OE) T1 mapping techniques (Chen et al. 1998; Hatabu et al. 2001) enable assessment of ventilation patterns in chronic obstructive pulmonary disease (Ohno et al. 2008a), and specific ventilation patterns have been assessed using dynamic wash-in and wash-out methods (Sa et al. 2010b). Oxygen is widely

available in the clinic, including in most MRI suites, and does not require specialized hardware or modifications to clinical scanners (Table 1). While this technique has shown strong correlations with other functional lung imaging methods and PFTs in numerous studies of obstructive lung disease, studies in asthma are presently limited. Although promising, further investigation of the reproducibility of quantitative measures of ventilation derived from OE MRI is needed (Kruger et al. 2016). Typically, OE is performed using a dual acquisition: one during inhalation of 21% O_2 (normoxic) and the other during inhalation of 100% O_2. Most researchers allow 1–2 min between changes in fractions of inhaled O_2 to avoid transient effects. The change in T1 between these two scans is widely considered to be predominantly ventilated weighted. Both respiratory (Vaninbroukx et al. 2003) and cardiac triggering have been implemented successfully for 2D OE MRI (Dietrich et al. 2005; Molinari et al. 2007). Typically, non-rebreather face masks are used with a constant flow of oxygen at 15 L/min (Renne et al. 2015; Molinari et al. 2008).

OE MRI shows promise for providing a more quantitative evaluation of ventilation than is currently possible with direct imaging of gas contrast agents such as HP and fluorinated gases. The most promising aspect of OE MRI in asthma is its ability to capture wash-in and washout kinetics of oxygen. Dynamic 2D OE MRI images were obtained by averaging single-shot fast spin echo (SSFSE) images over a moving temporal averaging window and calculating percent signal enhancement (PSE) relative to baseline. Recent works by Ohno et al. (2008b, 2002) with dynamic OE MRI found a correlation of PSE with the percent predicted diffusing capacity of the lung for carbon monoxide (%DL_{CO}). Oxygen wash-in time was also shown to correlate inversely with %DL_{CO} and FEV_1. In one implementation, dynamic OE MRI has also been used to measure regional specific ventilation (SV) (Sa et al. 2014). In this method, oxygen is cycled between wash-in and washout by switching from normoxic to 100% oxygen and back again several times. Fitting the time course of wash-in as a means of estimating SV has the advantage of being inde-

pendent of the absolute level of enhancement, avoiding the ambiguity inherent in the use of oxygen-enhanced contrast due to mixing of gas ventilation and blood perfusion. A similar 3D approach has been developed to measure time constants of oxygen wash-in and washout as regional measures of obstruction in asthma (Naish et al. 2005). A basic limitation of OE MRI is that it does not provide diffusion-weighted contrast within the physical lung airspaces.

3.3.1 Applications to Asthma

The ready availability of oxygen and the freedom from dedicated multinuclear imaging hardware make OE MRI a promising research tool with high potential for clinical research applications in asthma. The technique has shown strong correlations with other reference standards for pulmonary function such as PFT, CT, %DL_{CO}, scintigraphy, and HP ^{3}He MRI. Using dynamic OE MRI, the oxygen wash-in slope was found to inversely correlate with %DL_{CO} in smoking-related COPD (Ohno et al. 2008b) and in idiopathic pulmonary fibrosis (IPF) (Müller et al. 2002). Before OE MRI can move into routine clinical use, however, further work in improving SNR and time efficiency, quantitative analysis, and reproducibility of the various OE MRI metrics is needed.

3.4 Fluorinated Gas Imaging

Fluorinated gases are an attractive choice as a contrast agent because the ^{19}F isotope is 100% naturally abundant, with a high gyromagnetic ratio approximately equal to that of ^{1}H (Ruiz-Cabello et al. 2011). Though fluorinated gases themselves are relatively inexpensive, dedicated multinuclear transmit and receive radio frequency (RF) coils are required. Thus, fluorinated gases fall somewhere between oxygen and HP gases on the scale of cost and technical complexity (Table 1). While modeling of fluorinated gas kinetics has not been fully realized, technical advances in image acquisition and engineering have made dynamic imaging of gas wash-in and washout feasible. Respiratory-controlled breath-

ing (Halaweish and Charles 2014) is used to enable both dynamic imaging and multiple breath wash-in to improve SNR for normoxic steady-state breath-hold imaging. The short T1 recovery time of fluorinated gases combined with the use of equilibrium phase polarization allows for repeated acquisitions over short temporal windows. Therefore, fluorinated gases are well suited for dynamic imaging of ventilation. For dynamic imaging applications, fast low-flip angle GRE sequences with non-Cartesian readout trajectories and frequent sampling of the central region of k-space are used. The first feasibility study of dynamic fluorinated gas MRI was done in a pig model by Schreiber et al. (2001), who measured SF_6 washout time constants and demonstrated an inverse correlation between washout time and tidal volume. In a rat study comparing SF_6 and C_3F_8 for the purpose of mapping regional fractional ventilation, Ouriadov et al. (2014) showed that while SF_6 baseline images had superior SNR, both gases yielded similar values for fractional ventilation. Moreover, a gravitational dependence of fractional ventilation was observed, in good agreement with previous results using nuclear imaging, HP MRI, and OE MRI (Kruger 2013; Kruger et al. 2013; Sa et al. 2010a; Petersson et al. 2007).

Diffusion-weighted imaging of fluorinated gases within the lung airspaces is feasible. To mitigate rapid T2 and T2* decay, radial free induction decay (FID) sequences with short TE are most commonly employed for DWI with ${}^{19}F$. The first example was a 2005 study in which Perez-Sanchez et al. (2005) measured an average ADC of SF_6 in five rats as $2.22 \cdot 10^{-6}$ m/s^2. The expected anisotropy of diffusion was in agreement with previous studies (Chen et al. 1999; Yablonskiy et al. 2002). Interestingly, ADC measured at FRC was not significantly different from the ADC measured at TLC. This result differed from previous ${}^3He$ results that showed that ADC increased with lung inflation volume (Chen et al. 2000).

3.4.1 Applications to Asthma

Fluorinated gas MRI techniques have only recently experienced a resurgence and have not been extensively applied to the study of asthma, although feasibility has been shown (Halaweish et al. 2013). Fluorinated gas MRI has the potential for providing information similar to that provided by HP gases but without the complexity and cost required to site and operate a polarizer system.

3.5 Multimodality Airway Assessment

Combining functional images of ventilation with other measures of lung disease is a potentially powerful approach to characterizing mechanisms of airway obstruction in asthma. For example, it is possible to establish spatial relationships between regional measures of ventilation and overlapping biomarkers of airway inflammation and morphology using either a structural imaging modality such as MDCT or direct bronchoscopic assessment. Such approaches provide a means of characterizing localized disease mechanisms of observed regional obstruction.

Thus far, cross-modality studies in asthma use functional images of ventilation from MRI to guide localized quantitative measures of airway inflammation and remodeling. MDCT can be registered with hyperpolarized gas MR images to associate quantitative measures of the central airways and lung parenchyma with regional ventilation patterns. Refinement of lobar anatomy further enables measurements of VDP at the sublobar level (Thomen et al. 2015). Preliminary work has indicated that regional measures of airway wall thickness and area measured on CT are associated with local VDP, indicating that airway remodeling is a possible mechanism underlying ventilation defects observed on HP MRI (Svenningsen et al. 2014b; Mummy et al. 2016). In addition, lobar mucus plugging scores determined from CT have been positively associated with lobar VDP (Dunican et al. 2016), indicating that submucosal gland hypersecretion or goblet cell hyperplasia may be another such obstructive mechanism. This approach is not limited to imaging-based biomarkers. Analysis of bronchoalveolar lavage (BAL) fluid from bronchoscopic sampling of sites

CT / MRI Analysis Results					
Lobe	Segment	Emergent Defect %, Rank		Overall Defect %, Rank	
LUL	LB1	10.4%	18	14.5%	2
	LB2	18.5%	10	34.3%	10
	LB3	13.4%	16	34.8%	11
	LB4	13.7%	14	23.6%	5
	LB5	26.8%	3	41.5%	14
LLL	LB6	19.7%	8	42.3%	15
	LB8	14.4%	11	32.2%	7
	LB9	25.2%	4	50.6%	18
	LB10	13.8%	13	29.0%	6
RUL	RB1	3.0%	19	3.6%	1
	RB2	13.5%	15	20.9%	3
	RB3	28.1%	2	50.2%	17
RML	RB4	21.1%	5	33.1%	9
	RB5	29.5%	1	68.9%	19
RLL	RB6	20.3%	7	36.1%	12
	RB7	11.5%	17	23.0%	4
	RB8	18.9%	9	39.1%	13
	RB9	13.9%	12	32.8%	8
	RB10	20.8%	6	44.8%	16

Neutrophils

Fig. 8 Distribution of the longitudinal ventilation defect percent (*VDP*) at the sublobar (segmental) level can guide bronchoscopic sampling. Each lung segment is located spatially using CT and VDP is determined via HP ^{3}He MRI. Defects are used as targets for bronchoscopy (top three candidates shown in *red text* in table). The most well-ventilated segments (*blue text*) are used as control sites. Image-guided bronchoscopy may be used to obtain lavage, brushings, and tissue biopsies. In a small population of asthma subjects ($N = 10$), defected sites were found to have elevated levels of neutrophils vs. control sites (boxplot shown at right; $p = 0.05$)
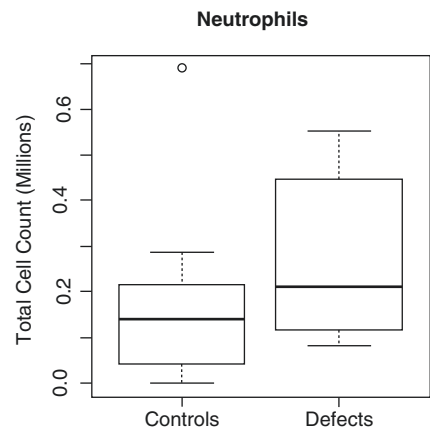
of ventilation defect has shown increased levels of granulocytes relative to well-ventilated control sites when performed both retrospectively (Fain et al. 2008) and prospectively (Mummy et al. 2015), as illustrated in Fig. 8.

4 Initial Clinical Results

The vast majority of clinical research studies have been performed using HP gas MRI in asthma (Fain et al. 2008; Tzeng et al. 2009; Niles et al. 2013; de Lange et al. 2006; Kruger et al. 2014b; Altes et al. 2001; Samee et al. 2003) but also in COPD (Virgincar et al. 2013; Salerno et al. 2002; Kirby et al. 2010), with a growing number of recent studies also focusing on CF in children and adults (Kirby et al. 2011; Mentore et al. 2005; Paulin et al. 2015). Multiple small studies with HP ^{3}He MRI in subjects with asthma have revealed regional ventilation heterogeneity that has changed the way in which clinicians and researchers view this disease. Relatively larger cross-sectional and longitudinal studies (de Lange et al. 2006, 2007, 2009) have revealed that up to half of ventilation defects persist in the same locations over time intervals of several days to a year (de Lange et al. 2007). The persistence of ventilation defects in these studies was independent of asthma severity and medication use,

suggesting that persistent defects were refractory to therapy. Because defects are observed even in asymptomatic patients and involve both the central and peripheral airways, conventional assumptions that asthma is predominantly a small airways disease have been challenged (Castro et al. 2011; Teague et al. 2014; Castro and Woods 2013). Multiple longitudinal studies of defects in asthma have confirmed pioneering work by a group at the University of Virginia (de Lange et al. 2009) that demonstrated persistence of up to 50% of ventilation defects over months to years. This pattern of ventilation defects recurring in the same locations (Fig. 6) has been confirmed in multiple studies (Niles et al. 2013; Svenningsen et al. 2014a). Emerging analysis tools for quantifying temporal patterns can identify fixed vs. reversible defects, with possible clinical consequences for identifying different processes of airway injury for local therapies and better phenotyping based on predominant mechanisms.

4.1 Imaging-Based Asthma Phenotypes

Asthma is likely the result of multiple distinct disease processes (Wenzel 2006) and multiple mechanistic phenotypes are currently undergoing investigation and refinement (Moore et al. 2007; Jarjour et al. 2012; Guilbert et al. 2014a). Several possible roles for HP MRI in the clinic include improved characterization of asthma phenotypes, visualization and testing of mechanisms underlying regional heterogeneity, and the evaluation of response to asthma therapies. These applications all exploit the ability of HP MRI to safely obtain repeated image sets for longitudinal studies without accumulating ionizing radiation dose. Interventions with methacholine (de Lange et al. 2007; Sani et al. 2008) and exercise challenge (Niles et al. 2013) have been safely performed and can provide a unique window into the dynamics of airway obstruction in asthma compared to normal subjects.

As described in the previous section, HP MRI also provides a means of multimodal assessment of regional structure-function relationships in asthmatic lungs, which may facilitate potentially valuable insights into the obstructive mechanisms underlying ventilation defects, and the creation and refinement of disease phenotypes. The image-guided assessment of biomarkers of inflammatory response (Fig. 8) and obstruction (including BAL/tissue biopsy, mucus plugging, and airway wall thickness on CT) is providing insights into active disease processes at sites of ventilation defect. Simultaneous analysis of a suite of standardized image biomarkers could allow for ventilation defects to be scored on a rubric based on their etiology and extent. Predictive cluster-based approaches (Moore et al. 2010) could then be used to refine asthma phenotypes based on an observed distribution of defect scores. If these phenotypes are found to be associated with clinical outcomes such as disease progression, propensity for exacerbation, or response to specific therapies, this approach could provide a strong motivation for the translation of HP gas as a clinical tool for guiding biologic therapies (Hilvering and Pavord 2015).

4.2 Correlates of Ventilation Heterogeneity

Imaging, including both CT and HP gas MRI, has played an important role in identifying possible biomarkers of lung injury in asthma. Serum vascular markers of inflammation (von Willebrand factor) and structural remodeling (P-selectin) correlated to VDP and lung density in adult asthma (Johansson et al. 2013a). Similar findings in airway biopsy and bronchoalveolar lavage derived from bronchoscopic assessment of airways proximal to ventilation defects found multiple inflammatory markers (Fain et al. 2008) as well as epithelial wall injury and thickening (Marozkina et al. 2015) suggesting airway injury and remodeling at these locations. Such use of image-guided bronchoscopy can investigate correlations between local regions of disease and more accessible biomarkers, such as sputum inflammatory markers. Both VDP and ADC-related

measures are also associated with differences in lung microstructure in asthma compared with controls (Wang et al. 2008) and with asthma risk factors in adults (Johansson et al. 2013b; Marozkina et al. 2014) and children (Cadman et al. 2013; Castro and Woods 2013).

Both pediatric and adult asthma remain challenging to phenotype in clinically meaningful ways, especially in efforts to screen for inflammatory phenotypes that can help to guide treatment approach for exacerbation-prone patients. Several studies have associated image-based biomarkers with severe clinical outcomes to better identify these patients. Air trapping measured on CT has been investigated in severe asthma and found to be associated with hospitalizations (Busacker et al. 2009), and more recently VDP has been associated with severe exacerbations requiring hospitalization in COPD (Kirby et al. 2014). Similar studies to determine the relationship between VDP and clinical outcomes in asthma remain an important area of research with the goal of proving the clinical relevance of the longitudinal imaging capabilities of MRI.

The role of DWI in investigating the restricted diffusion of hyperpolarized helium within the lung airspaces has been more complicated in asthma than in COPD. Partly, small airways disease in asthma is complex and may not be universal in all forms of disease, a revelation due in part to advanced imaging techniques. Moreover, involvement of the alveoli – the main unit affected by emphysema – is probably minimal in pure asthma, although recent interest has focused on the asthma-COPD overlap syndrome (ACOS) suggesting another potential role for HP gas MRI (Gelb et al. 2016). Nonetheless, a handful of studies have found interesting associations between asthma and increased restriction – measured as smaller ADC (Wang et al. 2008) and Xrms (Cadman et al. 2013) – at the scale of the alveoli and small airways. In Cadman et al. (2013), lung microstructure was found to be smaller in children aged 9 and 10 with asthma compared to age-matched children without asthma (Fig. 9). This study also found

that ventilation defect score was greater in asthma (Fig. 10) and in girls vs. boys, with the latter finding possibly presaging the known predominance of asthma in girls postpuberty (Thomas et al. 2015).

In many ways, however, these DWI results raise more questions than answers about the role of the lung development in obstructive physiology. Multiple studies of pediatric lung development have used DWI measures in an attempt to answer physiologic questions about the processes of lung growth and development (Narayanan et al. 2012; Altes et al. 2006), including alveolarization (Narayanan et al. 2013) vs. alveolar recruitment (Hajari et al. 2012) as lung volume increases with age. Lung models of restricted diffusion that allow calculation of measureable histological features such as mean length and surface area to volume are in development (O'Halloran et al. 2010; Narayanan et al. 2012; Woods et al. 2006; Parra-Robles et al. 2010, 2012) and have been reviewed previously (Yablonskiy et al. 2014b). More refined models that account for terminal airway branching (Parra-Robles et al. 2012; Parra-Robles and Wild 2012) have stimulated healthy debate (Yablonskiy et al. 2014a; Parra-Robles and Wild 2014b) and have challenged the field to develop more rigorous quantitative methods (Narayanan et al. 2014; Parra-Robles and Wild 2014a). Follow-up studies that are investigating age-related changes in alveolar and small airway dimension in the same subjects postpuberty and in adult healthy normal and asthma subjects will help to clarify the clinical meaning of these observations (Fain et al. 2005; Quirk et al. 2016).

4.3 Obstructive Mechanisms in Asthma

Improving our understanding of ventilation defects in asthma has been an important focus of the field. Several multimodality and dynamic imaging studies have enabled a more specific understanding of the underlying causes of
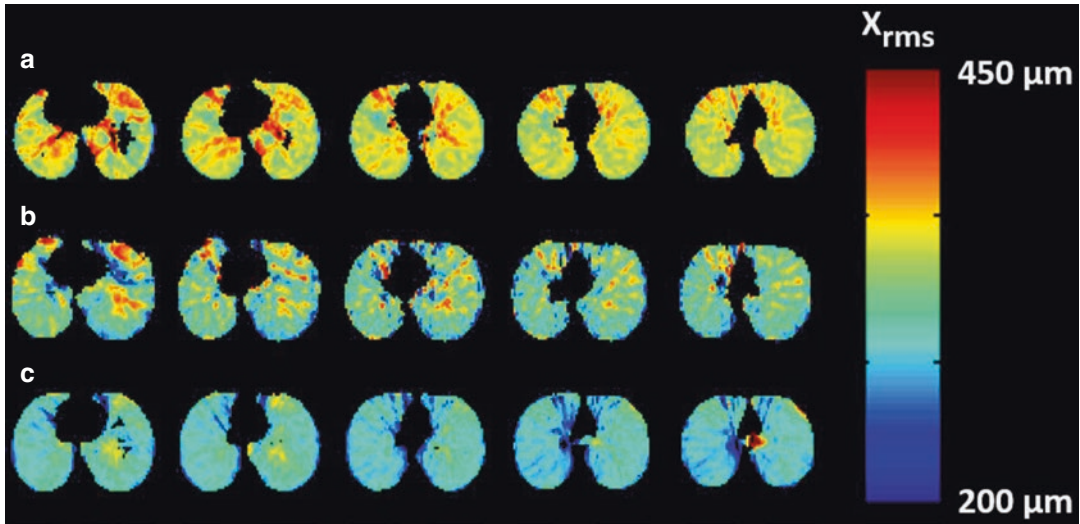
Fig. 9 Example of the evaluation of small airway dimensions using HP ³He MRI diffusion imaging. Xrms lung maps are shown for three subjects: (**a**) a healthy 10-year-old child, (**b**) a 9-year-old child with asthma, and (**c**) a 10-year-old child who was not diagnosed with asthma at the time of imaging, but did experience a wheezing illness with rhinovirus infection during the first 3 years of life
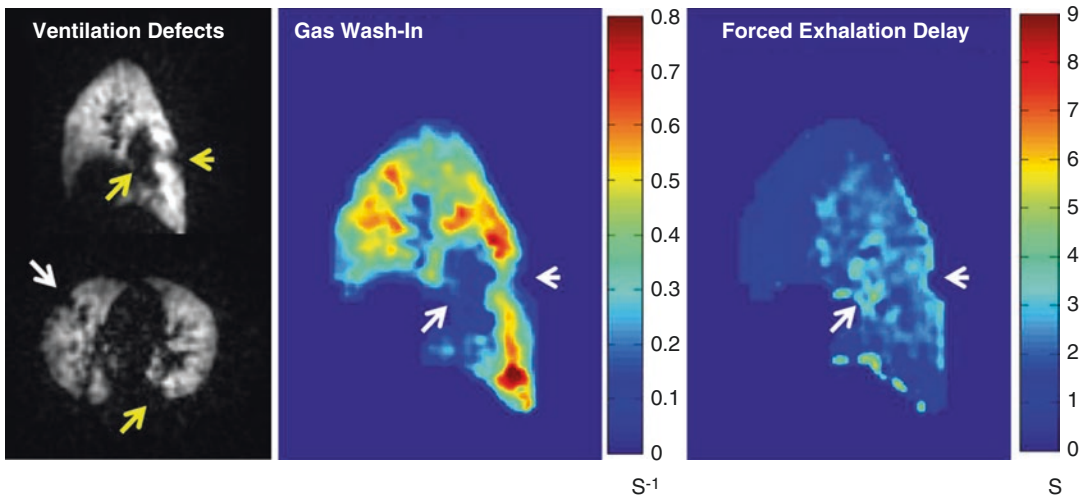
Fig. 10 HP ³He MRI in a 9-year-old asthmatic indicating defect regions (*left, arrows*) similar to those seen in adult asthma. Dynamic imaging of ³He gas wash-in and washout shows delayed rates of wash-in (*middle, arrows*) and washout (*right, arrows*) near regions of ventilation defect (Far left image reformatted from Reference (Cadman et al. 2013) with permission)

obstruction observed on ventilation-weighted MRI using gas agents. Cross-validation of ventilation defects on HP ³He MRI with CT has continued to be an important area of research. Early work suggested substantial overlap between ventilation defects and air trapping (Fain et al. 2008). More recent comparisons of dynamic ventilation on CT confirm that ventilation defects are associated with reduced volumetric change between inspiratory and expiratory CT (Tahir et al. 2015). In dynamic HP ³He MRI studies, gas distribution during forced exhalation maneuvers

and over the duration of a fixed breath-hold has demonstrated gas trapping, delayed filling, and washout of both defect and hyperintense regions in asthma (Fig. 11). Importantly, even for a fixed breath-held lung volume, these rates of filling and washout differ in severe vs. mild-to-moderate asthma, suggesting that regional compliance differences driving redistribution of gas flow (the "pendelluft" effect) are associated with asthma severity.

Ventilation heterogeneity observed in asthma has been corroborated with other gas agents. In one recent study, the oxygen transfer function (OTF) was shown to decrease in asthmatics after allergen challenge and correlated with the percentage of eosinophils in bronchoalveolar lavage at the site of challenge (Renne et al. 2014). As discussed previously, the OE signal reflects a longer time interval or "steady state" of ventilation rather than the snapshot of ventilation presented in most breath-held HP gas MRI images. Discrete ventilation defects similar to those on HP gas MRI are visualized in OE MR images, especially in instances of mucus plugging of central airways as is commonly the case in CF; however, obstruction in asthma is often partial, causing delayed rather than complete absence of ventilation in effected regions. On OE MRI such regions result in a diminished signal enhancement rather than a discrete ventilation defect (Fig. 12). This speaks to the need to evaluate ventilation dynamically, especially in asthma, and several approaches for dynamic imaging with OE MRI have been explored as described previously. To this end, in a small study of mild/moderate and severe asthma, reduced oxygen wash-in time constants and mean peak enhancement were associated with greater severity (Zhang et al. 2015). In addition, using dynamic OE MRI, the oxygen wash-in slope was found to inversely correlate with %DL_{CO} in smoking-related COPD (Ohno et al. 2008b) and IPF (Müller et al. 2002).

Preliminary studies of ventilation with fluorinated gases in human subjects by Halaweish et al. (2013) also found that asthmatic subjects did not present with ventilation defects, but rather a more heterogeneous distribution of ^{19}F signal than in healthy normal subjects. In this feasibility study, 28 subjects were imaged (eleven normal, two asthma, seven COPD, three transplant, one COPD/transplant, four emphysema) using 2D fast low-angle shot (FLASH) MRI with C_3F_8 to evaluate the suitability of ^{19}F breath-hold MRI for characterization of disease. Normal subjects demonstrated the expected homogeneous distribution of ^{19}F gas, while diseased subjects showed heterogeneity patterns that varied based on disease.

4.4 Improved Regional Specificity of Therapy

The characterization of ventilation defects on a local scale may ultimately have its greatest impact as a means to guide treatment. For example, bronchial thermoplasty (BT) has emerged as an effective treatment for severe persistent asthma that is unresponsive to conventional therapies (Wechsler et al. 2013; Cox et al. 2007) and quantification of regional ventilation using HP ^3He MRI has been shown to be a feasible method of assessing changes in ventilation patterns after the procedure (Thomen et al. 2015). In a small population of asthmatic subjects, ventilation defects decreased as a function of time following BT. The advancement of methods for characterizing and identifying local sites of airway injury for treatment planning would potentially minimize treatment time, cost, and possibly side effects by focusing therapy only at the airways where treatment will have the most impact.

Improved characterization of individual defects also enables locally guided bronchoscopic assessment of disease mechanisms. This type of approach has been shown to be feasible as a prospective method to identify inflammatory phenotypes of asthma (Mummy et al. 2015; Marozkina et al. 2014) and may ultimately help guide local therapy approaches. The ability to image pre- and post-intervention has similarly benefited studies of non-severe asthma phenotypes such as exercise-induced bronchoconstriction. Assessment of ventilation defects before
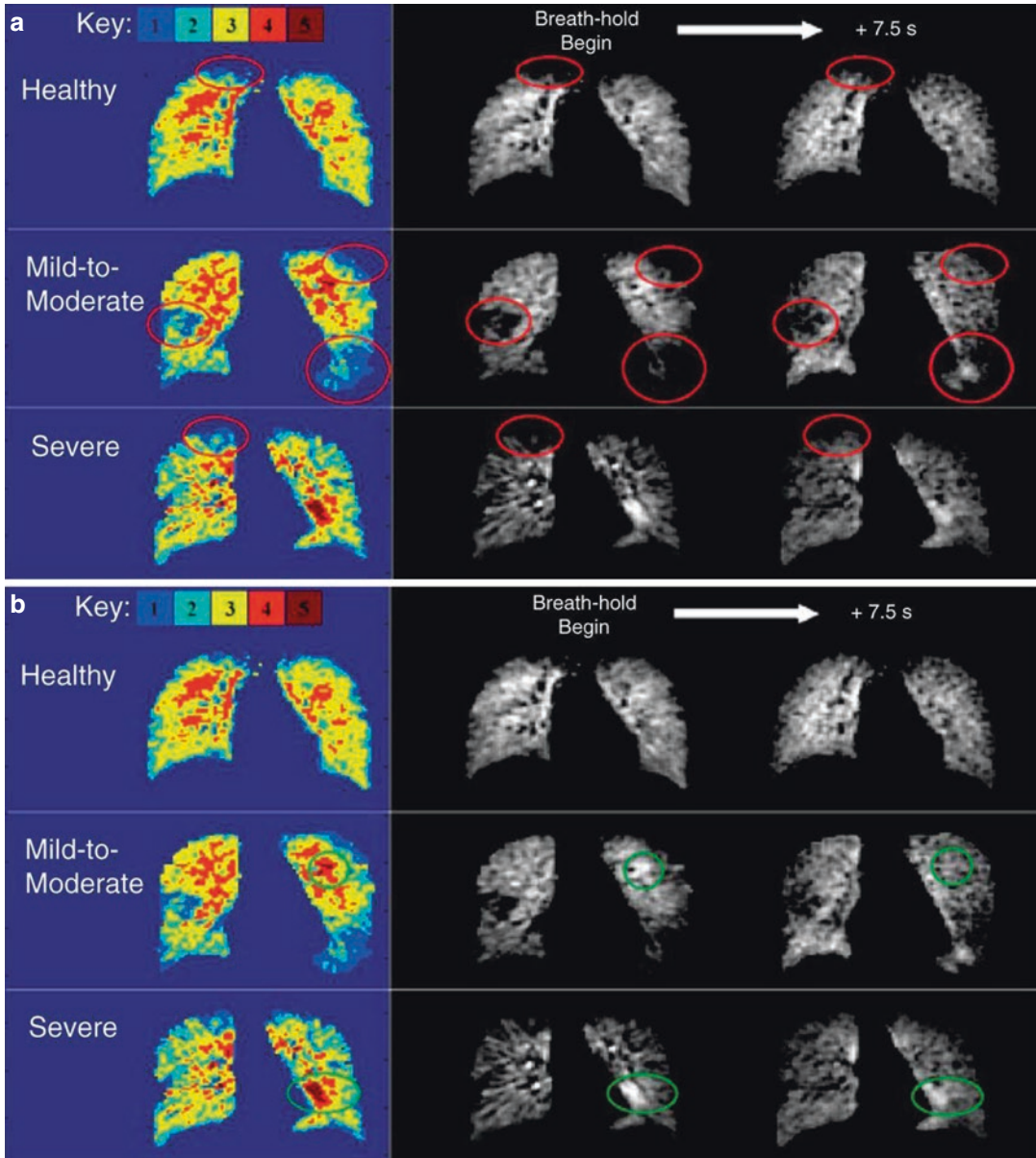
Fig. 11 Delayed wash-in and wash-out phenomena of HP 3He gas during fixed breath-hold MRI in healthy (female, 21-year-old), mild-to-moderate asthmatic (male, 36-year-old), and severe asthmatic (male, 45-year-old) subjects. *Color-coded maps* indicate initial ventilation classification in the displayed coronal slices. (**a**) Regions of interest are *circled*, *highlighting* areas of initially poor ventilation (level 1 or 2), which fill to varying degrees following 7.5 s of breath-hold. (**b**) Same slices from the same subjects, instead highlighting regions of initial hyperintensity (level 5) that alternatively wash out to varying degrees following breath-hold

and after exercise challenge has allowed investigation of ephemeral obstruction that only manifests upon stress (Samee et al. 2003). In a blinded, placebo-controlled prospective study (Kruger et al. 2014b), prophylactic treatment with leukotriene receptor blockade was shown to mitigate regional airway hyperresponsiveness during exercise using the VDP as an outcome measure, which significantly decreased with treatment.
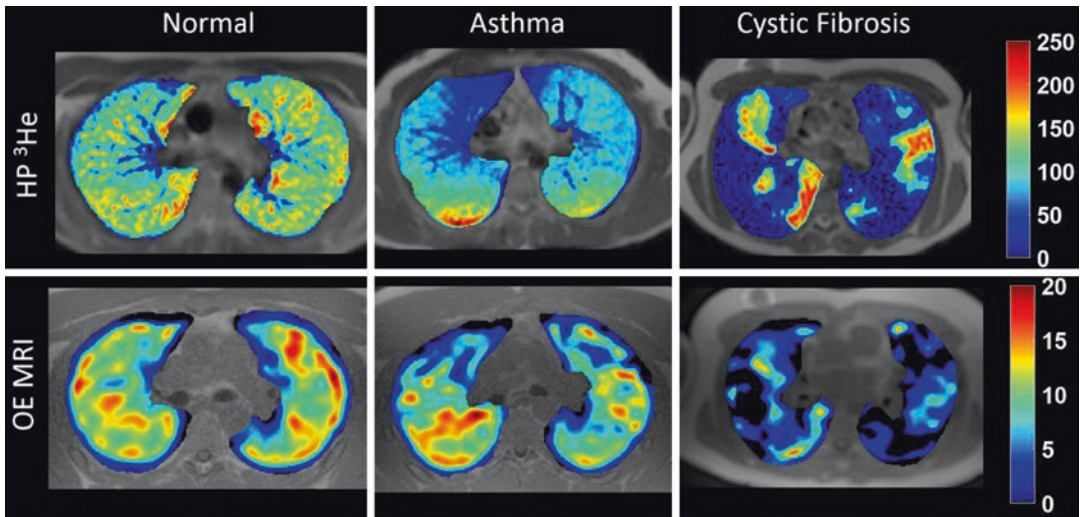
Fig. 12 Comparison of hyperpolarized (HP) ³He MR images (*top*) with OE MRI (*bottom*) acquired in the same healthy normal (*left*) asthma (*middle*) and cystic fibrosis (*right*) subjects. In-plane spatial resolution for HP ³He MRI is about 3 mm vs. 6 mm for OE MRI. *Color bars* are in arbitrary units for HP ³He and percent signal enhancement (*PSE*) for OE MRI

5   Emerging Techniques

5.1   Ultrashort Echo Time Imaging

Imaging without gas agents in the lungs is challenging due to the short T2* (<2 ms) properties (Hatabu et al. 1999; Stock et al. 1999) associated with the parenchymal microstructure, specifically air-tissue interfaces of the alveoli. Moreover, the low proton density of the lung tissue requires high SNR efficiency and signal averaging to provide whole-lung coverage within a breath-hold. However, conventional proton MRI has several advantages for imaging of lung disease in asthma given concerns about X-ray CT dose and the aforementioned advantages of relating structure and function.

UTE MRI techniques with 3D radial and cone trajectories have shown promise in addressing the challenges of pulmonary imaging in adults (Gibiino et al. 2015; Weick et al. 2013; Johnson et al. 2013; Dournes et al. 2015) and children (Hahn et al. 2016b; Higano et al. 2016). The advantages of the 3D radial UTE approach include full coverage of the chest and lungs at isotropic spatial resolution, approaching that typically obtained with CT, without requiring ioniz-

ing radiation. 3D radial UTE MRI to study asthma has been limited thus far, but several studies in other obstructive lung diseases show promise for the detection of central airway bronchiectasis and air trapping in CF (Roach et al. 2016). Recently Ma et al. (2015) have investigated local deformation changes between different lung inflation volumes with breath-held UTE as a measure of air trapping in COPD. UTE MRI has also shown promise for investigating neonatal lung diseases in free-breathing non-sedated infants (Hahn et al. 2016b) supporting the potential benefits of this modality in pediatric lung disease generally.

UTE with 3D radial acquisition has also shown important applications to improve pulmonary MRI using gas agents. Several studies have demonstrated the feasibility of 3D isotropic OE MRI in healthy human subjects (Kruger et al. 2014a; Triphan et al. 2015), and this has been extended recently to the study of both CF and asthma (Fig. 12). Similarly, by implementing a 3D radial UTE FID sequence, Couch et al. (2013) were able to perform volumetric ventilation imaging in a 15-s breath-hold of C_3F_8. Image quality was quite good, and a relatively homogeneous distribution of ventilation was observed (Fig. 4). Importantly, SNR

increased by nearly a factor of two when ^{19}F gas was allowed to wash into the lungs by controlled breathing of a mixture of O_2 and C_3F_8 over several respiratory cycles prior to imaging. This observation supports the feasibility of dynamic imaging with the 3D UTE technique to assess fractional ventilation (defined as the ratio of fresh gas entering a volume "region" of the lung to the total end-inspiratory volume of the region [Wagner 1979; Horn et al. 2014]).

5.2 Transition to ^{129}Xe MRI

Global quantities of ^3He are limited, leading to high cost (Cho 2009) (Table 1). This has motivated migration to the more widely available HP ^{129}Xe gas (Woods 2013). The technical challenges of this migration have been made easier by advances in ^{129}Xe SEOP polarization (Ruset et al. 2006; Hersman et al. 2008). All the major types of contrast-weighting demonstrated for ^3He MRI have now been replicated robustly with enriched HP ^{129}Xe (Kirby and Parraga 2013; Mugler and Altes 2013) but are only now being applied systematically in studies of asthma. As of this writing, only a handful of studies in asthma using HP ^{129}Xe MRI have been published (Svenningsen et al. 2013; Qing et al. 2014a). It should be noted that larger values for VDP are observed with ^{129}Xe MRI than with ^3He MRI in the same individual (Svenningsen et al. 2013). This bias is likely attributable to the difference in gas densities, although this remains a matter for further research.

There are also potentially important advantages to the ability to investigate gas exchange by exploiting the solubility of xenon in tissues and red blood cells. The soluble "dissolved phase" fraction of ^{129}Xe in blood and tissues is approximately 2% of the total signal after accounting for the lower density of lung tissue and blood. The dissolved phase of ^{129}Xe has a different chemical shift frequency than the gas phase. Compartmental modeling of these components has advanced relatively rapidly (Chang 2013). The recent introduction of spectroscopic imaging methods with 3D radial UTE has made it possible to study xenon exchange ratios in asthma and COPD

(Qing et al. 2014a, b); thus, HP ^{129}Xe MRI may provide a new functional marker of gas exchange in asthma in the near future.

6 Summary

Asthma is widespread and will continue to be a leading cause of respiratory disease worldwide. The gas agents described in this chapter underscore the unique ability of pulmonary MRI to measure the functional consequences of asthma. While widespread adoption has been slow, functional lung MRI is now poised for more widespread use in the clinic as new and more costly biologic treatments become available for treating severe asthma that is refractory to conventional therapies. In fact, a "virtuous cycle" is now emerging for the use of functional lung MRI in severe and pediatric asthma, which still has significant unmet needs in terms of pharmaceutical development, minimally invasive interventions, longitudinal follow-up, and prognosis as patients age. The expansion of functional lung MRI using a wider array of gas agents will further benefit translation. Complementary approaches that use the technique best suited to the available hardware capabilities of a given site will better support widespread adoption of pulmonary MRI within the clinical research community. Moreover, continued dissemination and advances in UTE MRI will support an emerging clinical role for combined structure-function MRI.

References

Akinbami LJ, Moorman JE, Bailey C, Zahran HS, King M, Johnson CA, Liu X (2012) Trends in asthma prevalence, health care use, and mortality in the United States, 2001-2010. NCHS (National Center for Health Statistics) Data Brief 94:1–8

Altes TA, Mata J, de Lange EE, Brookeman JR, Mugler JP (2006) Assessment of lung development using hyperpolarized helium-3 diffusion MR imaging. J Magn Reson Imaging 24(6):1277–1283

Altes TA, Mugler JP 3rd, Ruppert K, Tustison NJ, Gersbach J, Szentpetery S, Meyer CH, de Lange EE, Teague WG (2016) Clinical correlates of lung ventilation defects in asthmatic children. J Allergy Clin Immunol 137(3):789–796 . doi:10.1016/j.jaci.2015.08.045e787

Altes TA, Powers PL, Knight-Scott J, Rakes G, Platts-Mills TA, de Lange EE, Alford BA, Mugler JP 3rd, Brookeman JR (2001) Hyperpolarized 3He MR lung ventilation imaging in asthmatics: preliminary findings. J Magn Reson Imaging 13(3):378–384

Aysola RS, Hoffman EA, Gierada D, Wenzel S, Cook-Granroth J, Tarsi J, Zheng J, Schechtman KB, Ramkumar TP, Cochran R, Xueping E, Christie C, Newell J, Fain S, Altes TA, Castro M (2008) Airway remodeling measured by multidetector CT is increased in severe asthma and correlates with pathology. Chest 134(6):1183–1191. doi:10.1378/chest.07-2779

Bel EH, Sousa A, Fleming L, Bush A, Chung KF, Versnel J, Wagener AH, Wagers SS, Sterk PJ, Compton CH, Unbiased Biomarkers for the Prediction of Respiratory Disease Outcome Consortium CG (2011) Diagnosis and definition of severe refractory asthma: an international consensus statement from the Innovative Medicine Initiative (IMI). Thorax 66(10):910–917. doi:10.1136/thx.2010.153643

Benayoun L, Druilhe A, Dombret MC, Aubier M, Pretolani M (2003) Airway structural alterations selectively associated with severe asthma. Am J Respir Crit Care Med 167(10):1360–1368. doi:10.1164/rccm.200209-1030OC

Black LD, Henderson AC, Atileh H, Israel E, Ingenito EP, Lutchen KR (2004) Relating maximum airway dilation and subsequent reconstriction to reactivity in human lungs. J Appl Physiol (1985) 96(5):1808–1814. doi:10.1152/japplphysiol.01170.2003

Brown RH, Croisille P, Mudge B, Diemer FB, Permutt S, Togias A (2000) Airway narrowing in healthy humans inhaling methacholine without deep inspirations demonstrated by HRCT. Am J Respir Crit Care Med 161(4 Pt 1):1256–1263. doi:10.1164/ajrccm.161.4.9806051

Brown RH, Pearse DB, Pyrgos G, Liu MC, Togias A, Permutt S (2006) The structural basis of airways hyperresponsiveness in asthma. J Appl Physiol (1985) 101(1):30–39. doi:10.1152/japplphysiol.01190.2005

Busacker A, Newell JD, Keefe T, Hoffman EA, Granroth JC, Castro M, Fain S, Wenzel S (2009) A multivariate analysis of risk factors for the air-trapping asthmatic phenotype as measured by quantitative CT analysis. Chest 135(1):48–56. doi:10.1378/chest.08-0049

Cadman RV, Lemanske RF Jr, Evans MD, Jackson DJ, Gern JE, Sorkness RL, Fain SB (2013) Pulmonary 3He magnetic resonance imaging of childhood asthma. J Allergy Clin Immunol 131(2):369–376 . doi:10.1016/j.jaci.2012.10.032e361-365

Castro M, Fain SB, Hoffman EA, Gierada DS, Erzurum SC, Wenzel S, Sever NHLBI (2011) Lung imaging in asthmatic patients: the picture is clearer. J Allergy Clin Immunol 128(3):467–478. doi:10.1016/j.jaci.2011.04.051

Castro M, Woods J (2013) Insights into pediatric asthma with hyperpolarized magnetic resonance imaging of the lung. J Allergy Clin Immunol 131(2):377–378. doi:10.1016/j.jaci.2012.12.669

Chang YV (2013) MOXE: a model of gas exchange for hyperpolarized 129Xe magnetic resonance of the lung. Magn Reson Med 69(3):884–890

Chen Q, Jakob PM, Griswold MA, Levin DL, Hatabu H, Edelman RR (1998) Oxygen enhanced MR ventilation imaging of the lung. Magn Reson Mater Phy 7(3):153–161

Chen XJ, Hedlund LW, Möller HE, Chawla MS, Maronpot RR, Johnson GA (2000) Detection of emphysema in rat lungs by using magnetic resonance measurements of 3He diffusion. Proc Natl Acad Sci 97(21):11478–11481

Chen XJ, Möller HE, Chawla MS, Cofer GP, Driehuys B, Hedlund LW, Johnson GA (1999) Spatially resolved measurements of hyperpolarized gas properties in the lung in vivo. Part I: diffusion coefficient. Magn Reson Med 42(4):721–728

Cho A (2009) Physics. Helium-3 shortage could put freeze on low-temperature research. Science 326(5954):778–779. doi:10.1126/science.326_778

Collier GJ, Wild JM (2015) In vivo measurement of gas flow in human airways with hyperpolarized gas MRI and compressed sensing. Magn Reson Med 73(6):2255–2261. doi:10.1002/mrm.25348

Couch MJ, Ball IK, Li T, Fox MS, Littlefield SL, Biman B, Albert MS (2013) Pulmonary ultrashort echo time 19F MR imaging with inhaled fluorinated gas mixtures in healthy volunteers: feasibility. Radiology 269(3):903–909. doi:10.1148/radiol.13130609

Cox G, Thomson NC, Rubin AS, Niven RM, Corris PA, Siersted HC, Olivenstein R, Pavord ID, McCormack D, Chaudhuri R, Miller JD, Laviolette M, Group AIRTS (2007) Asthma control during the year after bronchial thermoplasty. N Engl J Med 356(13):1327–1337. doi:10.1056/NEJMoa064707

de Lange EE, Altes TA, Patrie JT, Battiston JJ, Juersivich AP, Mugler JP 3rd, Platts-Mills TA (2009) Changes in regional airflow obstruction over time in the lungs of patients with asthma: evaluation with 3He MR imaging. Radiology 250(2):567–575. doi:10.1148/radiol.2502080188

de Lange EE, Altes TA, Patrie JT, Gaare JD, Knake JJ, Mugler JP, Platts-Mills TA (2006) Evaluation of asthma with hyperpolarized helium-3 MRI – correlation with clinical severity and spirometry. Chest 130(4):1055–1062. doi:10.1378/chest.130.4.1055

de Lange EE, Altes TA, Patrie JT, Parmar J, Brookeman JR, Mugler JP 3rd, Platts-Mills TA (2007) The variability of regional airflow obstruction within the lungs of patients with asthma: assessment with hyperpolarized helium-3 magnetic resonance imaging. J Allergy Clin Immunol 119(5):1072–1078. doi:10.1016/j.jaci.2006.12.659

Dietrich O, Losert C, Attenberger U, Fasol U, Peller M, Nikolaou K, Reiser MF, Schoenberg SO (2005) Fast oxygen-enhanced multislice imaging of the lung using parallel acquisition techniques. Magn Reson Med Off J Soc Magn Reson Med Soc Magn Reson Med 53(6):1317–1325. doi:10.1002/mrm.20495

Dournes G, Grodzki D, Macey J, Girodet P-O, Fayon M, Chateil J-F, Montaudon M, Berger P, Laurent F (2015) Quiet submillimeter MR imaging of the lung is feasible with a PETRA sequence at 1.5 T. Radiology 276(1):258–265

Dunican E, Fahy JV, Mummy DG, Fain S, Hoffman EA, Elicker BM, Gierada DS, Newell J, Castro NNJM, Nagle S (2016) Regional ventilation defects measured on hyperpolarized 3He MRI are associated with mucus plugging measured on CT in asthma. Am J Respir Crit Care Med 193:A1052

Edelman RR, Hatabu H, Tadamura E, Li W, Prasad PV (1996) Noninvasive assessment of regional ventilation in the human lung using oxygen-enhanced magnetic resonance imaging. Nat Med 2(11):1236–1239

Evans SE, Scanlon PD (2003) Current practice in pulmonary function testing. Mayo Clin Proc 78(6):758–763

Fain S, Schiebler ML, McCormack DG, Parraga G (2010) Imaging of lung function using hyperpolarized helium-3 magnetic resonance imaging: review of current and emerging translational methods and applications. J Magn Reson Imaging JMRI 32(6):1398–1408. doi:10.1002/jmri.22375

Fain SB, Altes TA, Panth SR, Evans MD, Waters B, Mugler JP 3rd, Korosec FR, Grist TM, Silverman M, Salerno M, Owers-Bradley J (2005) Detection of age-dependent changes in healthy adult lungs with diffusion-weighted 3He MRI. Acad Radiol 12(11):1385–1393. doi:10.1016/j.acra.2005.08.005

Fain SB, Gonzalez-Fernandez G, Peterson ET, Evans MD, Sorkness RL, Jarjour NN, Busse WW, Kuhlman JE (2008) Evaluation of structure-function relationships in asthma using multidetector CT and hyperpolarized He-3 MRI. Acad Radiol 15(6):753–762. doi:10.1016/j.acra.2007.10.019

Fain SB, Panth SR, Evans MD, Wentland AL, Holmes JH, Korosec FR, O'Brien MJ, Fountaine H, Grist TM (2006) Early emphysematous changes in asymptomatic smokers: detection with 3He MR imaging. Radiology 239(3):875–883. doi:10.1148/radiol.2393050111

Frangi AF, Niessen WJ, Hoogeveen RM, van Walsum T, Viergever MA (1999) Model-based quantitation of 3-D magnetic resonance angiographic images. IEEE Trans Med Imaging 18(10):946–956. doi:10.1109/42.811279

Gelb AF, Christenson SA, Nadel JA (2016) Understanding the pathophysiology of the asthma–chronic obstructive pulmonary disease overlap syndrome. Curr Opin Pulm Med 22(2):100–105

Gentile TR, Jones GL, Thompson AK, Rizi RR, Roberts DA, Dimitrov IE, Reddy R, Lipson DA, Gefter W, Schnall MD, Leigh JS (2000) Demonstration of a compact compressor for application of metastability-exchange optical pumping of 3He to human lung imaging. Magn Reson Med 43(2):290–294

Gibiino F, Sacolick L, Menini A, Landini L, Wiesinger F (2015) Free-breathing, zero-TE MR lung imaging. MAGMA 28(3):207–215

Guilbert TW, Bacharier LB, Fitzpatrick AM (2014a) Severe asthma in children. J Allergy Clin Immunol Pract 2(5):489–500. doi:10.1016/j.jaip.2014.06.022

Guilbert TW, Mauger DT, Lemanske RF (2014b) Childhood asthma-predictive phenotype. J Allergy Clin Immunol Pract 2(6):664–670

Gupta S, Hartley R, Singapuri A, Hargadon B, Monteiro W, Pavord ID, Sousa AR, Marshall RP, Subramanian D, Parr D, Entwisle JJ, Siddiqui S, Raj V, Brightling CE (2015) Temporal assessment of airway remodeling in severe asthma using quantitative computed tomography. Am J Respir Crit Care Med 191(1):107–110. doi:10.1164/rccm.201406-1128LE

Hahn AD, Cadman RV, Sorkness RL, Jarjour NN, Nagle SK, Fain SB (2016a) Redistribution of inhaled hyperpolarized 3He gas during breath-hold differs by asthma severity. J Appl Physiol (1985) 120(5):526–536. doi:10.1152/japplphysiol.00197.2015

Hahn AD, Higano NS, Walkup LL, Thomen RP, Cao X, Merhar SL, Tkach JA, Woods JC, Fain SB (2016b) Pulmonary MRI of neonates in the intensive care unit using 3D ultrashort echo time and a small footprint MRI system. J Magn Reson Imaging DOI: 10.1002/jmri.25394

Hajari AJ, Yablonskiy DA, Sukstanskii AL, Quirk JD, Conradi MS, Woods JC (2012) Morphometric changes in the human pulmonary acinus during inflation. J Appl Physiol 112(6):937–943

Halaweish AF, Charles HC (2014) Physiorack: an integrated MRI safe/conditional, gas delivery, respiratory gating, and subject monitoring solution for structural and functional assessments of pulmonary function. J Magn Reson Imaging 39(3):735–741. doi:10.1002/jmri.24219

Halaweish AF, Moon RE, Foster WM, Soher BJ, McAdams HP, MacFall JR, Ainslie MD, MacIntyre NR, Charles HC (2013) Perfluoropropane gas as a magnetic resonance lung imaging contrast agent in humans. CHEST J 144(4):1300–1310

Hamedani H, Clapp JT, Kadlecek SJ, Emami K, Ishii M, Gefter WB, Xin Y, Cereda M, Shaghaghi H, Siddiqui S, Rossman MD, Rizi RR (2016) Regional fractional ventilation by using multibreath wash-in (3)He MR imaging. Radiology 279(3):917–924. doi:10.1148/radiol.2015150495

Hankinson JL, Odencrantz JR, Fedan KB (1999) Spirometric reference values from a sample of the general U.S. population. Am J Respir Crit Care Med 159(1):179–187. doi:10.1164/ajrccm.159.1.9712108

Hatabu H, Alsop DC, Listerud J, Bonnet M, Gefter WB (1999) T2* and proton density measurement of normal human lung parenchyma using submillisecond echo time gradient echo magnetic resonance imaging. Eur J Radiol 29(3):245–252

Hatabu H, Tadamura E, Chen Q, Stock KW, Li W, Prasad PV, Edelman RR (2001) Pulmonary ventilation: dynamic MRI with inhalation of molecular oxygen. Eur J Radiol 37(3):172–178. doi:10.1016/S0720-048x(00)00298-9

He M, Kaushik SS, Robertson SH, Freeman MS, Virgincar RS, McAdams HP, Driehuys B (2014) Extending semiautomatic ventilation defect analysis for hyperpolarized (129)Xe ventilation MRI. Acad Radiol 21(12):1530–1541. doi:10.1016/j.acra.2014.07.017

Hersman FW, Ruset IC, Ketel S, Muradian I, Covrig SD, Distelbrink J, Porter W, Watt D, Ketel J, Brackett J, Hope A, Patz S (2008) Large production system for hyperpolarized 129Xe for human lung imaging studies. Acad Radiol 15(6):683–692. doi:10.1016/j.acra.2007.09.020

Higano NS, Hahn AD, Tkach JA, Cao X, Walkup LL, Thomen RP, Merhar SL, Kingma PS, Fain SB, Woods JC (2016) Retrospective respiratory self-gating and removal of bulk motion in pulmonary UTE MRI of neonates and adults. Magn Reson Med DOI: 10.1002/mrm.26212

Hilvering B, Pavord ID (2015) What goes up must come down: biomarkers and novel biologicals in severe asthma. Clin Exp Allergy 45(7):1162–1169

Holmes JH, O'Halloran RL, Brodsky EK, Bley TA, Francois CJ, Velikina JV, Sorkness RL, Busse WW, Fain SB (2009) Three-dimensional imaging of ventilation dynamics in asthmatics using multiecho projection acquisition with constrained reconstruction. Magn Reson Med 62(6):1543–1556. doi:10.1002/mrm.22150

Holmes JH, O'Halloran RL, Brodsky EK, Jung Y, Block WF, Fain SB (2008) 3D hyperpolarized He-3 MRI of ventilation using a multi-echo projection acquisition. Magn Reson Med 59(5):1062–1071. doi:10.1002/mrm.21437

Horn FC, Deppe MH, Marshall H, Parra-Robles J, Wild JM (2014) Quantification of regional fractional ventilation in human subjects by measurement of hyperpolarized 3He washout with 2D and 3D MRI. J Appl Physiol (1985) 116(2):129–139. doi:10.1152/japplphysiol.00378.2013

Howarth DM, Lan L, Thomas PA, Allen LW (1999) 99mTc technegas ventilation and perfusion lung scintigraphy for the diagnosis of pulmonary embolus. J Nucl Med 40(4):579–584

Hurwitz LM, Reiman RE, Yoshizumi TT, Goodman PC, Toncheva G, Nguyen G, Lowry C (2007) Radiation dose from contemporary cardiothoracic multidetector CT protocols with an anthropomorphic female phantom: implications for cancer induction. Radiology 245(3):742–750. doi:10.1148/radiol.2453062046

James AL, Bai TR, Mauad T, Abramson MJ, Dolhnikoff M, McKay KO, Maxwell PS, Elliot JG, Green FH (2009) Airway smooth muscle thickness in asthma is related to severity but not duration of asthma. Eur Respir J 34(5):1040–1045. doi:10.1183/09031936.00181608

Jarjour NN, Erzurum SC, Bleecker ER, Calhoun WJ, Castro M, Comhair SA, Chung KF, Curran-Everett D, Dweik RA, Fain SB, Fitzpatrick AM, Gaston BM, Israel E, Hastie A, Hoffman EA, Holguin F, Levy BD, Meyers DA, Moore WC, Peters SP, Sorkness RL, Teague WG, Wenzel SE, Busse WW, Program NSAR (2012) Severe asthma: lessons learned from the National Heart, Lung, and Blood Institute Severe Asthma Research Program. Am J Respir Crit Care Med 185(4):356–362. doi:10.1164/rccm.201107-1317PP

Johansson MW, Kruger SJ, Schiebler ML, Evans MD, Sorkness RL, Denlinger LC, Busse WW, Jarjour NN, Montgomery RR, Mosher DF, Fain SB (2013a) Markers of vascular perturbation correlate with airway structural change in asthma. Am J Resp Crit Care 188(2):167–178. doi:10.1164/rccm.201301-0185OC

Johansson MW, Kruger SJ, Schiebler ML, Evans MD, Sorkness RL, Denlinger LC, Busse WW, Jarjour NN, Montgomery RR, Mosher DF, Fain SB (2013b) Markers of vascular perturbation correlate with airway structural change in asthma. Am J Respir Crit Care Med 188(2):167–178. doi:10.1164/rccm.201301-0185OC

Johnson KM, Fain SB, Schiebler ML, Nagle S (2013) Optimized 3D ultrashort echo time pulmonary MRI. Magn Reson Med 70(5):1241–1250

Kirby M, Mathew L, Wheatley A, Santyr GE, McCormack DG, Parraga G (2010) Chronic obstructive pulmonary disease: longitudinal hyperpolarized (3)He MR imaging. Radiology 256(1):280–289. doi:10.1148/radiol.10091937

Kirby M, Parraga G (2013) Pulmonary functional imaging using hyperpolarized noble gas MRI: six years of start-up experience at a single site. Acad Radiol 20(11):1344–1356. doi:10.1016/j.acra.2013.02.020

Kirby M, Pike D, Coxson HO, McCormack DG, Parraga G (2014) Hyperpolarized (3)He ventilation defects used to predict pulmonary exacerbations in mild to moderate chronic obstructive pulmonary disease. Radiology 273(3):887–896. doi:10.1148/radiol.14140161

Kirby M, Svenningsen S, Ahmed H, Wheatley A, Etemad-Rezai R, Paterson NA, Parraga G (2011) Quantitative evaluation of hyperpolarized helium-3 magnetic resonance imaging of lung function variability in cystic fibrosis. Acad Radiol 18(8):1006–1013. doi:10.1016/j.acra.2011.03.005

Koumellis P, van Beek EJ, Woodhouse N, Fichele S, Swift AJ, Paley MN, Hill C, Taylor CJ, Wild JM (2005) Quantitative analysis of regional airways obstruction using dynamic hyperpolarized 3He MRI-preliminary results in children with cystic fibrosis. J Magn Reson Imaging Sep; 22(3):420–426. doi:10.1002/jmri.20402

Kruger SJ (2013) 3D radial oxygen enhanced imaging in normal and asthmatic human subjects. In: International Society for Magnetic Resonance in Medicine, Salt Lake City

Kruger SJ, Fain SB, Johnson KM, Cadman RV, Nagle SK (2014a) Oxygen-enhanced 3D radial ultrashort echo time magnetic resonance imaging in the healthy human lung. NMR Biomed 27(12):1535–1541. doi:10.1002/nbm.3158

Kruger SJ, Nagle SK, Couch MJ, Ohno Y, Albert M, Fain SB (2016) Functional imaging of the lungs with gas agents. J Magn Reson Imaging 43(2):295–315. doi:10.1002/jmri.25002

Kruger SJ, Niles DJ, Dardzinski B, Harman A, Jarjour NN, Ruddy M, Nagle SK, Francois CJ, Sorkness RL, Burton RM, Munoz del Rio A, Fain SB (2014b) Hyperpolarized Helium-3 MRI of exercise-induced bronchoconstriction during challenge and therapy. J Magn Reson Imaging 39(5):1230–1237. doi:10.1002/jmri.24272

Kruger SJ, Niles DJ, Dardzinski BJ (2013) Exercise-induced bronchoconstriction: hyperpolarized helium-3

MRI during challenge and therapy. J Magn Reson Med 39(5):1230–1237. doi:10.1002/jmri.24272

Kuethe DO, Caprihan A, Fukushima E, Waggoner RA (1998) Imaging lungs using inert fluorinated gases. Magn Reson Med 39(1):85–88

Levitzky MG (2013) Pulmonary physiology, 8th edn. McGraw-Hill, New York

Lotvall J, Akdis CA, Bacharier LB, Bjermer L, Casale TB, Custovic A, Lemanske RF, Wardlaw AJ, Wenzel SE, Greenberger PA (2011) Asthma endotypes: a new approach to classification of disease entities within the asthma syndrome. J Allergy Clin Immunol 127(2):355–360. doi:10.1016/j.jaci.2010.11.037

Lynch DA, Al-Qaisi MA (2013) Quantitative computed tomography in chronic obstructive pulmonary disease. J Thoracic Imaging 28(5):284–290. doi:10.1097/RTI.0b013e318298733c

Ma WJ, Sheikh K, Svenningsen S, Pike D, Guo FM, Etemad-Rezai R, Leipsic J, Coxson HO, McCormack DG, Parraga G (2015) Ultra-short echo-time pulmonary MRI: evaluation and reproducibility in COPD subjects with and without bronchiectasis. J Magn Reson Imaging 41(5):1465–1474. doi:10.1002/jmri.24680

Marshall H, Ajraoui S, Deppe MH, Parra-Robles J, Wild JM. NMR Biomed. (2012) K-space filter deconvolution and flip angle self-calibration in 2D radial hyperpolarised 3He lung MRI. Feb; 25(2):389–399. doi:10.1002/nbm.1766

Marozkina NV, Wang XQ, Stsiapura V, Fitzpatrick A, Carraro S, Hawkins GA, Bleecker E, Meyers D, Jarjour N, Fain SB, Wenzel S, Busse W, Castro M, Panettieri RA Jr, Moore W, Lewis SJ, Palmer LA, Altes T, de Lange EE, Erzurum S, Teague WG, Gaston B (2014) Phenotype of asthmatics with increased airway S-nitrosoglutathione reductase activity. Eur Respir J 45(1):87–97. doi:10.1183/09031936.00042414

Marozkina NV, Wang XQ, Stsiapura V, Fitzpatrick A, Carraro S, Hawkins GA, Bleecker E, Meyers D, Jarjour N, Fain SB, Wenzel S, Busse W, Castro M, Panettieri RA, Moore W, Lewis SJ, Palmer LA, Altes T, de Lange EE, Erzurum S, Teague WG, Gaston B (2015) Phenotype of asthmatics with increased airway S-nitrosoglutathione reductase activity. Eur Respir J 45(6):87–97. doi:10.1183/09031936.50042414

Mathew L, Evans A, Ouriadov A, Etemad-Rezai R, Fogel R, Santyr G, McCormack DG, Parraga G (2008) Hyperpolarized He-3 magnetic resonance imaging of chronic obstructive pulmonary disease: reproducibility at 3.0 tesla. Acad Radiol 15(10):1298–1311. doi:10.1016/j.acra.2008.04.019

Mayo JR (2008) Radiation dose issues in longitudinal studies involving computed tomography. Proc Am Thorac Soc 5(9):934–939. doi:10.1513/pats.200808-079QC

Mead J, Takishima T, Leith D (1970) Stress distribution in lungs: a model of pulmonary elasticity. J Appl Physiol 28(5):596–608

Mead J, Turner JM, Macklem PT, Little JB (1967) Significance of the relationship between lung recoil and maximum expiratory flow. J Appl Physiol 22(1):95–108

Mentore K, Froh DK, de Lange EE, Brookeman JR, Paget-Brown AO, Altes TA (2005) Hyperpolarized HHe 3 MRI of the lung in cystic fibrosis: assessment at baseline and after bronchodilator and airway clearance treatment. Acad Radiol 12(11):1423–1429. doi:10.1016/j.acra.2005.07.008

Miglioretti DL, Johnson E, Williams A, Greenlee RT, Weinmann S, Solberg LI, Feigelson HS, Roblin D, Flynn MJ, Vanneman N, Smith-Bindman R (2013) The use of computed tomography in pediatrics and the associated radiation exposure and estimated cancer risk. JAMA Pediatr 167(8):700–707. doi:10.1001/jamapediatrics.2013.311

Molinari F, Eichinger M, Risse F, Plathow C, Puderbach M, Ley S, Herth F, Bonomo L, Kauczor HU, Fink C (2007) Navigator-triggered oxygen-enhanced MRI with simultaneous cardiac and respiratory synchronization for the assessment of interstitial lung disease. J Magn Reson Imaging JMRI 26(6):1523–1529. doi:10.1002/jmri.21043

Molinari F, Puderbach M, Eichinger M, Ley S, Fink C, Bonomo L, Kauczor HU, Bock M (2008) Oxygen-enhanced magnetic resonance imaging: influence of different gas delivery methods on the T1-changes of the lungs. Investig Radiol 43(6):427–432. doi:10.1097/RLI.0b013e318169012d

Moore WC, Bleecker ER, Curran-Everett D, Erzurum SC, Ameredes BT, Bacharier L, Calhoun WJ, Castro M, Chung KF, Clark MP, Dweik RA, Fitzpatrick AM, Gaston B, Hew M, Hussain I, Jarjour NN, Israel E, Levy BD, Murphy JR, Peters SP, Teague WG, Meyers DA, Busse WW, Wenzel SE, National Heart LBIsSARP (2007) Characterization of the severe asthma phenotype by the National Heart, Lung, and Blood Institute's Severe Asthma Research Program. J Allergy Clin Immunol 119 (2):405-413. doi:10.1016/j.jaci.2006.11.639

Moore WC, Meyers DA, Wenzel SE, Teague WG, Li H, Li X, D'Agostino R Jr, Castro M, Curran-Everett D, Fitzpatrick AM (2010) Identification of asthma phenotypes using cluster analysis in the Severe Asthma Research Program. Am J Resp Crit Care 181(4):315–323

Mugler JP 3rd, Altes TA (2013) Hyperpolarized 129Xe MRI of the human lung. J Magn Reson Imaging JMRI 37(2):313–331. doi:10.1002/jmri.23844

Müller CJ, Schwaiblmair M, Scheidler J, Deimling M, Weber J, Löffler RB, Reiser MF (2002) Pulmonary diffusing capacity: assessment with oxygen-enhanced lung MR imaging – preliminary findings. Radiology 222:499–506. doi:10.1148/radiol.2222000869

Mummy DG, Sorkness RL, Denlinger LC, Jarjour NN, Fain SB (2015) Magnetic resonance image-guided bronchoscopic sampling in asthma indicates increased levels of granulocytes in areas of hyperpolarized 3He

ventilation defect compared with control sites. Am J Respir Crit Care Med 191:A6143

Mummy DG, Zha W, Sorkness RL, Denlinger LC, Quirk JD, Gierada DS, Woods JC, Castro M, Jarjour NN, Fain SB (2016) Segmental ventilation defect percentage in hyperpolarized 3He MRI in asthma is associated with airway wall thickness measured on CT. Am J Respir Crit Care Med 193(2016):A1053

Naish JH, Parker GJM, Beatty PC, Jackson A, Young SS, Waterton JC, Taylor CJ (2005) Improved quantitative dynamic regional oxygen-enhanced pulmonary imaging using image registration. Magn Reson Med 54(2):464–469. doi:10.1002/mrm.20570

Narayanan M, Beardsmore CS, Owers-Bradley J, Dogaru CM, Mada M, Ball I, Garipov RR, Kuehni CE, Spycher BD, Silverman M (2013) Catch-up alveolarization in ex-preterm children. Evidence from 3He magnetic resonance. Am J Resp Crit Care 187(10):1104–1109

Narayanan M, Kuehni CE, Silverman M (2014) On the use of ^{3}He diffusion magnetic resonance as evidence of neo-alveolarization during childhood and adolescence/reply. Am J Resp Crit Care 189(4):501

Narayanan M, Owers-Bradley J, Beardsmore CS, Mada M, Ball I, Garipov R, Panesar KS, Kuehni CE, Spycher BD, Williams SE, Silverman M (2012) Alveolarization continues during childhood and adolescence: new evidence from helium-3 magnetic resonance. Am J Respir Crit Care Med 185(2):186–191. doi:10.1164/rccm.201107-1348OC

Newman SP, Pitcairn GR, Hirst PH, Rankin L (2003) Radionuclide imaging technologies and their use in evaluating asthma drug deposition in the lungs. Adv Drug Deliv Rev 55(7):851–867

Niles DJ, Kruger SJ, Dardzinski BJ, Harman A, Jarjour NN, Ruddy M, Nagle SK, Francois CJ, Fain SB (2013) Exercise-induced bronchoconstriction: reproducibility of hyperpolarized He-3 MR imaging. Radiology 266(2):618–625. doi:10.1148/radiol.12111973

O'Halloran RL, Holmes JH, Wu Y-C, Alexander A, Fain SB (2010) Helium-3 MR q-space imaging with radial acquisition and iterative highly constrained backprojection. Magn Reson Med 63(1):41–50. doi:10.1002/mrm.22158

Ohno Y, Hatabu H, Takenaka D, Van Cauteren M, Fujii M, Sugimura K (2002) Dynamic oxygen-enhanced MRI reflects diffusing capacity of the lung. Magn Reson Med 47(6):1139–1144

Ohno Y, Iwasawa T, Seo JB, Koyama H, Takahashi H, Oh YM, Nishimura Y, Sugimura K (2008a) Oxygen-enhanced magnetic resonance imaging versus computed tomography – multicenter study for clinical stage classification of smoking-related chronic obstructive pulmonary disease. Am J Resp Crit Care 177(10):1095–1102. doi:10.1164/rccm.200709-1322OC

Ohno Y, Koyama H, Nogami M, Takenaka D, Matsumoto S, Obara M, Sugimura K (2008b) Dynamic oxygen-enhanced MRI versus quantitative CT: pulmonary functional loss assessment and clinical stage classification of smoking-related COPD. Am J Roentgenol 190(2):W93–W99

Ouriadov AV, Fox MS, Couch MJ, Li T, Ball IK, Albert MS (2014) In vivo regional ventilation mapping using fluorinated gas MRI with an x-centric FGRE method. Magn Reson Med Off J Soc Magn Reson Med Soc Magn Reson Med 74(2):550–557. doi:10.1002/mrm.25406

Parra-Robles J, Ajraoui S, Deppe M, Parnell S, Wild J (2010) Experimental investigation and numerical simulation of 3 He gas diffusion in simple geometries: implications for analytical models of 3 He MR lung morphometry. J Magn Reson 204(2):228–238

Parra-Robles J, Wild JM (2012) The influence of lung airways branching structure and diffusion time on measurements and models of short-range 3 He gas MR diffusion. J Magn Reson 225:102–113

Parra-Robles J, Wild JM (2014a) On the use of 3He diffusion magnetic resonance as evidence of neo-alveolarization during childhood and adolescence. Am J Resp Crit Care 189(4):501–502

Parra-Robles J, Wild JM (2014b) Response to Commentary on "The influence of lung airways branching structure and diffusion time on measurements and models of short-range 3 He gas MR diffusion". J Magn Reson 239:143–146

Parra-Robles J, Ajraoui S, Marshall H, Deppe M, Xu X, Wild J (2012) The influence of field strength on the apparent diffusion coefficient of 3He gas in human lungs. Magn Reson Med 67(2):322–325

Paulin GA, Svenningsen S, Jobse BN, Mohan S, Kirby M, Lewis JF, Parraga G (2015) Differences in hyperpolarized (3) He ventilation imaging after 4 years in adults with cystic fibrosis. J Magn Reson Imaging 41(6):1701–1707. doi:10.1002/jmri.24744

Pérez-Sánchez JM, de Alejo RP, Rodríguez I, Cortijo M, Peces-Barba G, Ruiz-Cabello J (2005) In vivo diffusion weighted 19F MRI using SF6. Magn Reson Med 54(2):460–463

Petersson J, Rohdin M, Sanchez-Crespo A, Nyren S, Jacobsson H, Larsson SA, Lindahl SG, Linnarsson D, Neradilek B, Polissar NL, Glenny RW, Mure M (2007) Posture primarily affects lung tissue distribution with minor effect on blood flow and ventilation. Respir Physiol Neurobiol 156(3):293–303. doi:10.1016/j.resp.2006.11.001

Petty TL (2003) Definition, epidemiology, course, and prognosis of COPD. Clin Cornerstone 5(1):1–10

Pike D, Kirby M, Guo F, McCormack DG, Parraga G (2015) Ventilation heterogeneity in ex-smokers without airflow limitation. Acad Radiol 22(8):1068–1078. doi:10.1016/j.acra.2015.04.006

Qing K, Mugler JP, Altes TA, Jiang Y, Mata JF, Miller GW, Ruset IC, Hersman FW, Ruppert K (2014a) Assessment of lung function in asthma and COPD using hyperpolarized 129Xe chemical shift saturation recovery spectroscopy and dissolved-phase MRI. NMR Biomed 27(12):1490–1501

Qing K, Ruppert K, Jiang Y, Mata JF, Miller GW, Shim YM, Wang C, Ruset IC, Hersman FW, Altes TA (2014b) Regional mapping of gas uptake by blood and tissue in the human lung using hyperpolarized xenon-129 MRI. J Magn Reson Imaging 39(2):346–359

Qing K, Altes TA, Tustison NJ, Feng X, Chen X, Mata JF, Miller GW, de Lange EE, Tobias WA, Cates GD, Brookeman JR, Mugler JP (2015) Rapid Acquisition of Helium-3 and Proton Three-Dimensional Image Sets of the Human Lung in a Single Breath-Hold Using Compressed Sensing. Magnetic Resonance in Medicine 74(4):1110–1115. doi:10.1002/mrm.25499

Quanjer PH, Stanojevic S, Cole TJ, Baur X, Hall GL, Culver BH, Enright PL, Hankinson JL, Ip MS, Zheng J (2012) Multi-ethnic reference values for spirometry for the 3–95-yr age range: the global lung function 2012 equations. Eur Respir J 40(6):1324–1343

Quirk JD, Sukstanskii AL, Woods JC, Lutey BA, Conradi MS, Gierada DS, Yusen RD, Castro M, Yablonskiy DA (2016) Experimental evidence of age-related adaptive changes in human acinar airways. J Appl Physiol 120(2):159–165. doi:10.1152/japplphysiol.00541.2015

Rabinovitch N, Mauger DT, Reisdorph N, Covar R, Malka J, Lemanske RF, Morgan WJ, Guilbert TW, Zeiger RS, Bacharier LB (2014) Predictors of asthma control and lung function responsiveness to step 3 therapy in children with uncontrolled asthma. J Allergy Clin Immunol 133(2):350–356

Renne J, Hinrichs J, Schönfeld C, Gutberlet M, Winkler C, Faulenbach C, Jakob P, Schaumann F, Krug N, Wacker F (2014) Noninvasive quantification of airway inflammation following segmental allergen challenge with functional MR imaging: a proof of concept study. Radiology 274(1):267–275

Renne J, Lauermann P, Hinrichs J, Schonfeld C, Sorrentino S, Gutberlet M, Jakob P, Wacker F, Vogel-Claussen J (2015) Clinical use of oxygen-enhanced T1 mapping MRI of the lung: reproducibility and impact of closed versus loose fit oxygen delivery system. J Magn Reson Imaging JMRI 41(1):60–66. doi:10.1002/jmri.24535

Roach DJ, Cremillieux Y, Fleck RJ, Brody AS, Serai SD, Szczesniak RD, Kerlakian S, Clancy JP, Woods JC (2016) Ultrashort echo-time magnetic resonance imaging is a sensitive method for the evaluation of early cystic fibrosis lung disease. Ann Am Thorac Soc. 13(11):1923–1931. doi:10.1513/AnnalsATS.201603-203OC

Ruiz-Cabello J, Barnett BP, Bottomley PA, Bulte JW (2011) Fluorine (19F) MRS and MRI in biomedicine. NMR Biomed 24(2):114–129

Ruset IC, Ketel S, Hersman FW (2006) Optical pumping system design for large production of hyperpolarized. Phys Rev Lett 96(5):053002

Sa RC, Asadi AK, Theilmann RJ, Hopkins SR, Prisk GK, Darquenne C (2014) Validating the distribution of specific ventilation in healthy humans measured using proton MR imaging. J Appl Physiol (1985) 116(8):1048–1056. doi:10.1152/japplphysiol.00982.2013

Sa RC, Cronin MV, Henderson AC, Holverda S, Theilmann RJ, Arai TJ, Dubowitz DJ, Hopkins SR, Buxton RB, Prisk GK (2010a) Vertical distribution of specific ventilation in normal supine humans measured by oxygen-enhanced proton MRI. J Appl Physiol 109(6):1950–1959. doi:10.1152/japplphysiol.00220.2010

Sa RC, Cronin MV, Henderson AC, Holverda S, Theilmann RJ, Arai TJ, Dubowitz DJ, Hopkins SR, Buxton RB, Prisk GK (2010b) Vertical distribution of specific ventilation in normal supine humans measured by oxygen-enhanced proton MRI. J Appl Physiol (1985) 109(6):1950–1959. doi:10.1152/japplphysiol.00220.2010

Salerno M, Altes TA, Brookeman JR, de Lange EE, Mugler JP 3rd (2001) Dynamic spiral MRI of pulmonary gas flow using hyperpolarized (3)He: preliminary studies in healthy and diseased lungs. Magn Reson Med 46(4):667–677

Salerno M, de Lange EE, Altes TA, Truwit JD, Brookeman JR, Mugler JP 3rd (2002) Emphysema: hyperpolarized helium 3 diffusion MR imaging of the lungs compared with spirometric indexes – initial experience. Radiology 222(1):252–260. doi:10.1148/radiol.2221001834

Samee S, Altes T, Powers P, de Lange EE, Knight-Scott J, Rakes G, Mugler JP, Ciambotti JM, Alford BA, Brookeman JR, Platts-Mills TAE (2003) Imaging the lungs in asthmatic patients by using hyperpolarized helium-3 magnetic resonance: assessment of response to methacholine and exercise challenge. J Allergy Clin Immunol 111(6):1205–1211. doi:10.1067/mai.2003.1544

Sani SZ, Tzeng YS Cho MH, Y Sun, Israel E, Albert MS, Lutchen KR (2008) Linking mechanical and ventilation heterogeneity in asthma via deep inspirations. In: Proceedings of the international conference of the ATS, Toronto, p A563

Schreiber WG, Eberle B, Laukemper-Ostendorf S, Markstaller K, Weiler N, Scholz A, Burger K, Heussel CP, Thelen M, Kauczor HU (2001) Dynamic (19) F-MRI of pulmonary ventilation using sulfur hexafluoride (SF(6)) gas. Magn Reson Med Off J Soc Magn Reson Med Soc Magn Reson Med 45(4):605–613

Shifren A, Witt C, Christie C, Castro M. (2012) Mechanisms of remodeling in asthmatic airways. J Allergy (Cairo) 2012:316049

Sorkness RL, Bleecker ER, Busse WW, Calhoun WJ, Castro M, Chung KF, Curran-Everett D, Erzurum SC, Gaston BM, Israel E, Jarjour NN, Moore WC, Peters SP, Teague WG, Wenzel SE, Severe NHLBI (2008) Lung function in adults with stable but severe asthma: air trapping and incomplete reversal of obstruction with bronchodilation. J Appl Physiol 104(2):394–403. doi:10.1152/japplphysiol.00329.2007

Stock KW, Chen Q, Hatabu H, Edelman RR (1999) Magnetic resonance T 2∗ measurements of the normal human lung in vivo with ultra-short echo times. Magn Reson Imaging 17(7):997–1000

Sukstanskii AL, Yablonskiy DA (2012) Lung morphometry with hyperpolarized 129Xe: theoretical background. Magn Reson Med 67(3):856–866. doi:10.1002/mrm.23056

Svenningsen S, Guo F, Kirby M, Choy S, Wheatley A, McCormack DG, Parraga G (2014a) Pulmonary functional magnetic resonance imaging: asthma temporal–spatial maps. Acad Radiol 21(11):1402–1410. doi:10.1016/j.acra.2014.08.002

Svenningsen S, Kirby M, Starr D, Coxson HO, Paterson NAM, McCormack DG, Parraga G (2014b) What are ventilation defects in asthma? Thorax 69(1):63–71. doi:10.1136/thoraxjnl-2013-203711

Svenningsen S, Kirby M, Starr D, Leary D, Wheatley A, Maksym GN, McCormack DG, Parraga G (2013) Hyperpolarized 3He and 129Xe MRI: differences in asthma before bronchodilation. J Magn Reson Imaging 38(6):1521–1530

Tahir BA, Van Holsbeke C, Ireland RH, Swift AJ, Horn FC, Marshall H, Kenworthy JC, Parra-Robles J, Hartley R, Kay R (2015) Comparison of CT-based lobar ventilation with 3He MR imaging ventilation measurements. Radiology 278(2):585–592

Teague WG, Tustison NJ, Altes TA (2014) Ventilation heterogeneity in asthma. J Asthma 51(7):677–684. doi:10.3109/02770903.2014.914535

Thomas AO, Jackson DJ, Evans MD, Rajamanickam V, Gangnon RE, Fain SB, Sorkness RL, Okupa AY, Thomas A, Gern JE (2015) Sex-related differences in pulmonary physiologic outcome measures in a high-risk birth cohort. J Allergy Clin Immunol 136(2):282–287

Thomen RP, Sheshadri A, Quirk JD, Kozlowski J, Ellison HD, Szczesniak RD, Castro M, Woods JC (2015) Regional ventilation changes in severe asthma after bronchial thermoplasty with (3)He MR imaging and CT. Radiology 274(1):250–259. doi:10.1148/radiol.14140080

To T, Stanojevic S, Moores G, Gershon AS, Bateman ED, Cruz AA, Boulet L-P (2012) Global asthma prevalence in adults: findings from the cross-sectional world health survey. BMC Public Health 12(1):1

Triphan SM, Breuer FA, Gensler D, Kauczor HU, Jakob PM (2015) Oxygen enhanced lung MRI by simultaneous measurement of T1 and T2* during free breathing using ultrashort TE. J Magn Reson Imaging 41(6):1708–1714

Tustison NJ, Avants BB, Cook PA, Zheng Y, Egan A, Yushkevich PA, Gee JC (2010) N4ITK: improved N3 bias correction. IEEE Trans Med Imaging 29(6):1310–1320. doi:10.1109/TMI.2010.2046908

Tustison NJ, Avants BB, Flors L, Altes TA, de Lange EE, Mugler JP 3rd, Gee JC (2011) Ventilation-based segmentation of the lungs using hyperpolarized (3)He MRI. J Magn Reson Imaging 34(4):831–841. doi:10.1002/jmri.22738

Tzeng YS, Lutchen K, Albert M (2009) The difference in ventilation heterogeneity between asthmatic and healthy subjects quantified using hyperpolarized 3He MRI. J Appl Physiol (1985) 106(3):813–822. doi:10.1152/japplphysiol.01133.2007

Vaninbroukx J, Bosmans H, Sunaert S, Demedts M, Delcroix M, Marchal G, Verschakelen J (2003) The use of ECG and respiratory triggering to improve the sensitivity of oxygen-enhanced proton MRI of lung ventilation. Eur Radiol 13(6):1260–1265. doi:10.1007/s00330-002-1694-6

Vidal Melo MF, Layfield D, Harris RS, O'Neill K, Musch G, Richter T, Winkler T, Fischman AJ, Venegas JG (2003) Quantification of regional ventilation-perfusion ratios with PET. J Nucl Med 44(12):1982–1991

Virgincar RS, Cleveland ZI, Kaushik SS, Freeman MS, Nouls J, Cofer GP, Martinez-Jimenez S, He M, Kraft M, Wolber J, McAdams HP, Driehuys B (2013) Quantitative analysis of hyperpolarized 129Xe ventilation imaging in healthy volunteers and subjects with chronic obstructive pulmonary disease. NMR Biomed 26(4):424–435. doi:10.1002/nbm.2880

Wagner PD (1979) Information content of the multibreath nitrogen washout. J Appl Physiol 46(3):579–587

Walker TG, Happer W (1997) Spin-exchange optical pumping of noble-gas nuclei. Rev Mod Phys 69(2):629–642. doi:10.1103/RevModPhys.69.629

Wang C, Altes TA, Mugler JP 3rd, Miller GW, Ruppert K, Mata JF, Cates GD Jr, Borish L, de Lange EE (2008) Assessment of the lung microstructure in patients with asthma using hyperpolarized 3He diffusion MRI at two time scales: comparison with healthy subjects and patients with COPD. J Magn Reson Imaging 28(1):80–88. doi:10.1002/jmri.21408

Wild JM, Teh K, Woodhouse N, Paley MN, Fichele S, de Zanche N, Kasuboski L (2006) Steady-state free precession with hyperpolarized 3He: experiments and theory. Journal of Magnetic Resonance 183(1):13–24.

Wild JM, Woodhouse N, Paley MN, Fichele S, Said Z, Kasuboski L, van Beek EJ (2004) Comparison between 2D and 3D gradient-echo sequences for MRI of human lung ventilation with hyperpolarized 3He. Magnetic resonance in medicine 52(3):673–678.

Wechsler ME, Laviolette M, Rubin AS, Fiterman J, Lapa e Silva JR, Shah PL, Fiss E, Olivenstein R, Thomson NC, Niven RM, Pavord ID, Simoff M, Hales JB, McEvoy C, Slebos DJ, Holmes M, Phillips MJ, Erzurum SC, Hanania NA, Sumino K, Kraft M, Cox G, Sterman DH, Hogarth K, Kline JN, Mansur AH, Louie BE, Leeds WM, Barbers RG, Austin JH, Shargill NS, Quiring J, Armstrong B, Castro M, Asthma Intervention Research 2 Trial Study G (2013) Bronchial thermoplasty: long-term safety and effectiveness in patients with severe persistent asthma. J Allergy Clin Immunol 132(6):1295–1302. doi:10.1016/j.jaci.2013.08.009

Weick S, Breuer FA, Ehses P, Völker M, Hintze C, Biederer J, Jakob PM (2013) DC-gated high resolution three-dimensional lung imaging during free-breathing. J Magn Reson Imaging 37(3):727–732

Wenzel SE (2006) Asthma: defining of the persistent adult phenotypes. Lancet 368(9537):804–813. doi:10.1016/S0140-6736(06)69290-8

Wild JM, Marshall H, Xu X, Norquay G, Parnell SR, Clemence M, Griffiths PD, Parra-Robles J (2013) Simultaneous imaging of lung structure and function with triple-nuclear hybrid MR imaging. Radiology 267(1):251–255. doi:10.1148/radiol.12121153

Wild JM, Paley MN, Kasuboski L, Swift A, Fichele S, Woodhouse N, Griffiths PD, van Beek EJ (2003) Dynamic radial projection MRI of inhaled hyperpolarized 3He gas. Magn Reson Med 49(6):991–997. doi:10.1002/mrm.10477

Winn R, Chan E, McKinley S, Geraci M (2003) Laboratory evaluation: pulmonary function testing. In: Current diagnosis and treatment in pulmonary medicine. McGraw-Hill, San Francisco, pp 39–56

Woodhouse N, Wild JM, Paley MN, Fichele S, Said Z, Swift AJ, van Beek EJ (2005) Combined helium-3/proton magnetic resonance imaging measurement of ventilated lung volumes in smokers compared to never-smokers. J Magn Reson Imaging 21(4):365–369. doi:10.1002/jmri.20290

Woods JC (2013) Mine the moon for 3He MRI? Not yet. J Appl Physiol 114(6):705–706. doi:10.1152/japplphysiol.00035.2013

Woods JC, Choong CK, Yablonskiy DA, Bentley J, Wong J, Pierce JA, Cooper JD, Macklem PT, Conradi MS, Hogg JC (2006) Hyperpolarized 3He diffusion MRI and histology in pulmonary emphysema. Magn Reson Med 56(6):1293–1300

Yablonskiy DA, Sukstanskii AL, Conradi MS (2014a) Commentary on "The influence of lung airways branching structure and diffusion time on measurements and models of short-range 3 He gas MR diffusion". J Magn Reson 239:139–142

Yablonskiy DA, Sukstanskii AL, Leawoods JC, Gierada DS, Bretthorst GL, Lefrak SS, Cooper JD, Conradi MS (2002) Quantitative in vivo assessment of lung microstructure at the alveolar level with hyperpolarized 3He diffusion MRI. Proc Natl Acad Sci U S A 99(5):3111–3116. doi:10.1073/pnas.052594699

Yablonskiy DA, Sukstanskii AL, Quirk JD, Woods JC, Conradi MS (2014b) Probing lung microstructure with hyperpolarized noble gas diffusion MRI: theoretical models and experimental results. Magn Reson Med 71(2):486–505

Zha W, Niles DJ, Kruger SJ, Dardzinski BJ, Cadman RV, Mummy DG, Nagle SK, Fain SB (2016) Semiautomated ventilation defect quantification in exercise-induced bronchoconstriction using hyperpolarized helium-3 magnetic resonance imaging: a repeatability study. Acad Radiol. doi:10.1016/j.acra.2016.04.005

Zhang W-J, Niven RM, Young SS, Liu Y-Z, Parker GJ, Naish JH (2015) Dynamic oxygen-enhanced magnetic resonance imaging of the lung in asthma – initial experience. Eur J Radiol 84(2):318–326

MRI of Chronic Obstructive Pulmonary Disease

Julia Ley-Zaporozhan and Edwin JR van Beek

Contents

Key Points

MRI is becoming increasingly useful for imaging of lung structure and function, in terms of airway imaging, assessment of ventilation, and evaluation of lung perfusion and right heart function. This modality is highly versatile and capable of generating a range of inherent and exogenously introduced contrast mechanisms while maintaining high resolution as well as incredible speed of data acquisition.

It is quite likely that MRI techniques will allow further evaluation of physiological and pathophysiological aspects of COPD, and this should ultimately lead to improved understanding and treatment of this complex heterogeneous disease.

1   Introduction

Chronic obstructive pulmonary disease (COPD) is the fourth most common cause of death among adults (Rabe et al. 2007). COPD is characterized by incompletely reversible (usually progressive) airflow limitation, which is associated with an abnormal inflammatory response of the lung to noxious particles or gases. It is caused by a mixture of airway obstruction (obstructive bronchiolitis) and parenchymal destruction (emphysema), the relative contributions of which are variable (Rabe et al. 2007). Chronic bronchitis, or the presence of cough and sputum production for at

J. Ley-Zaporozhan, M.D. (✉)
Institute for Clinical Radiology,
Ludwig-Maximilians University of Munich,
Lindwurmstrasse 4, 80337 Munich, Germany
e-mail: julia.leyzaporozhan@gmail.com

E.J. van Beek, M.D., Ph.D.
Edinburgh Imaging, Queen's Medical Research
Institute, University of Edinburgh,
47 Little France Crescent, Edinburgh EH16 4TJ, UK
e-mail: edwin-vanbeek@ed.ac.uk

least 3 months in each of the 2 consecutive years, remains a clinically and epidemiologically useful diagnostic classifying term. Pulmonary emphysema is a pathological term and is defined by the American Thoracic Society as an abnormal permanent enlargement of the air spaces distal to the terminal bronchioles, accompanied by the destruction of their walls. In a simplified way, obstructive airflow limitation leads to air trapping with subsequent hyperinflation of the airspaces, which combined with inflammatory lung injury leads to destruction of the lung parenchyma. For severity assessment of COPD lung function tests, such as forced expiration volume in 1 s (FEV_1), FEV_1/FVC (forced vital capacity) and diffusing capacity for carbon monoxide (DLco) are used. However, pulmonary function tests only provide a global measure without any regional information and are not suitable for determination of structural abnormalities or for distinguishing the causes of air outflow obstruction. Although extremely useful in clinical practice and for global management of patients, pulmonary function tests are known to be relatively insensitive to both early stages and small changes of manifest disease. Furthermore, pulmonary function tests are dependent upon the effort and compliance of the patient, and are difficult to be reliably performed in young children. Chronic hyperinflation impacts on diaphragmatic geometry with subsequent dysfunction due to dissociation of the breathing mechanics. The disease also affects the pulmonary arteries: intimal thickening, smooth muscle hypertrophy, and inflammation are described, which ultimately give rise to vascular remodeling (Szilasi et al. 2006). The direct vascular changes and hyperinflation lead to the precapillary type of pulmonary hypertension and pulmonary vascular flow disturbance (Rosenkranz 2007).

In contrast to pulmonary function tests, radiological imaging techniques may be able to differentiate the components of obstructive lung disease on a regional basis, with the possibility of detecting early disease stages prior to the onset of symptoms. Computed tomography (CT) is the mainstay diagnostic modality in this field with emphasis on structural imaging of lung parenchyma and airways. Magnetic resonance imaging (MRI) has the potential to provide regional information about the lung without the use of ionizing radiation, but is hampered by several challenges: the low amount of tissue relates to a small number of protons leading to low signal, countless air–tissue interfaces cause substantial susceptibility artifacts, and last but not least, respiratory and cardiac motion. In several lung diseases, such as tumors, the amount of protons or the blood volume is actually increased and motion is reduced, which provides better pre-conditions for MRI. In obstructive pulmonary disease, however, there are no facilitating disease-related effects as there is loss of tissue and reduced blood volume due to hypoxic vasoconstriction and the degree of hyperinflation has a negative correlation with the MR signal. The depiction of the airways by MRI is certainly limited to the central bronchi. Fortunately, MRI has shown significant potential beyond the mere visualization of structure by providing comprehensive information about "function," such as perfusion, hemodynamics, ventilation, and respiratory mechanics.

2   Parenchyma

The most frequently utilized sequences in MRI of COPD are acquired in a single breath-hold. The T2-weighted single-shot techniques with partial Fourier acquisition (HASTE) sequence in coronal and/or axial orientation allow for the depiction of pulmonary infiltrates, inflammatory bronchial wall thickening, and mucus collections (Figs. 1 and 2). T1-weighted 3D gradient echo sequences, such as volume-interpolated breath-hold examination (VIBE), are suitable for the assessment of the mediastinum and common nodular lesions. The intravenous application of contrast material markedly improves the diagnostic yield of T1-weighted sequences by a clearer depiction of vessels, hilar structures, and solid pathologies. A major goal in inflammatory obstructive airway disease is to differentiate inflammation within the wall from muscular hypertrophy, edema, and mucus collection which cannot be achieved by CT, but can be addressed
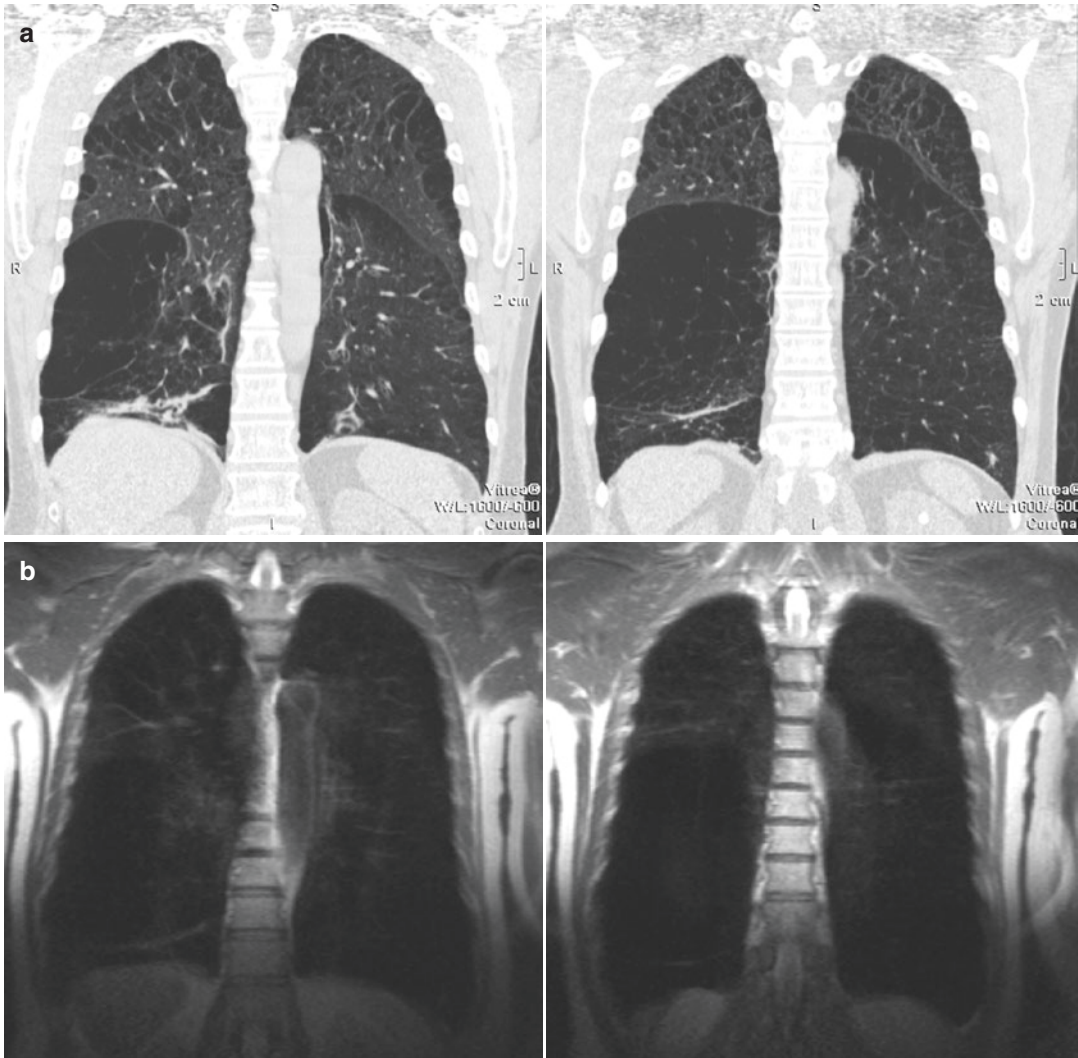
Fig. 1 Coronal CT reformats (**a**) and corresponding coronal T2-weighted (HASTE) images (**b**): severe emphysema with predominance of the right lower lobe on CT corresponds to a loss of MR signal (*arrows*) reflecting destruction of the parenchyma and rarefication of the pulmonary vasculature

by the use of T1- and T2-weighted images as well as contrast enhancement (Ley-Zaporozhan et al. 2008). Different MRI sequences were compared to CT for detection of the severity of emphysema and leading emphysema type on a lobar level. MRI matched the CT in only half of the cases: the sensitivity for emphysema severity was 44%, 48%, and 41%, and the leading type of emphysema was 68%, 55%, and 60% for T2w-HASTE, T1w-VIBE, and T1w-ce-VIBE, respectively (Ley-Zaporozhan et al. 2010). All sequences showed a similar diagnostic performance; however a combination of T2w-HASTE and ce-VIBE was recommended. The method proved very reproducible in a group of 19 patients, who were imaged on 2 consecutive days, resulting in a weighted kappa of 0.86, 95%CI = 0.81–0.91 (Jobst et al. 2015a).

The extent of hyperinflation and hypoxic vasoconstriction is directly associated with the loss of signal (Bankier et al. 2004). While emphysematous destruction can hardly be diagnosed by a loss of signal, it is much easier to detect hyperinflation just by the size or volume of the thorax.

Fig. 2 Coronal T2-weighted (HASTE) image shows the typical flattening of the diaphragm in emphysema

In one of the first studies, it was shown that the change of parenchymal signal intensity measured by multiple inversion-recovery sequence with a HASTE acquisition at inspiration and expiration correlates with FEV_1 ($r = 0.508$) and might warrant further studies as a predictor of airflow obstruction (Iwasawa et al. 2007).

Recently T1w VIBE was used in a few patients at different lung volumes (Pennati et al. 2014). After semiautomatic segmentation of lung parenchyma from the surrounding soft tissue, a deformable image registration algorithm was applied to follow the signal change between different inflation volumes, resulting in a map of ^{1}H signal change. These maps can be used for regional investigation of lung function.

In the last couple of years measurement of the lung density using ultrashort TE sequences showed promising results. These sequences significantly improve the pulmonary MR signal so that areas with less parenchyma can be visualized and quantified (Hoffman et al. 2016). In 15 patients with COPD the mean signal intensity of one coronal central slice showed good correlation with the amount of density-based emphysema from CT ($r = -0.71$) (Ma et al. 2015). Another

study on ten patients applied a 3D approach and defined emphysema at a threshold of <10% of mean thoracic soft-tissue signal to segment the lower signal regions from healthy lung. Emphysema amount measured on MRI and CT showed a high correlation ($r^2 = 0.79$) (Roach et al. 2016). In a larger study population of 40 smokers without COPD, UTE correlated with different clinical stages of COPD (Ohno et al. 2011). UTE-MRI with a short interval measured in 60 smokers without and with different clinical stages of COPD showed moderate correlation with CT ($r = 0.65$) and FEV1/FVC% ($r = 0.62$), and good correlation with FEV1% (0.75) and DLCO% ($r = 0.79$) (Ohno et al. 2014).

More recently T1 mapping using snapshot fast low angle shot (FLASH) was investigated as a potential biomarker in COPD. T1 was significantly shorter in 24 patients with COPD compared to 12 age-matched healthy volunteers (Alamidi et al. 2016). In a group of 20 patients with COPD, a strong correlation ($r = 0.81$) was found between T1 abnormalities and MR perfusion abnormalities using a zone-based approach (Fig. 3) (Jobst et al. 2015b).

3   Airways

Several pathological studies have shown that a major site of airway obstruction in patients with COPD is in airways smaller than 2 mm internal diameter (Hogg et al. 2004). The 2 mm airways are located between the 4th and the 14th generation of the tracheobronchial tree. Airflow limitation is closely associated with the severity of luminal occlusion by inflammatory exudates and thickening of the airway walls due to remodeling. Severe peripheral airflow obstruction can also affect the proximal airways from subsegmental bronchi to the trachea.

For assessment of tracheal instability MR cine acquisitions during continuous respiration or forced expiration are recommended (Heussel et al. 2004). The depiction of airway dimensions and thickness of the airway walls by MRI under physiological conditions is limited to the central bronchi. For depiction of the bronchiectasis high

T1   T1O$_2$ Perfusion
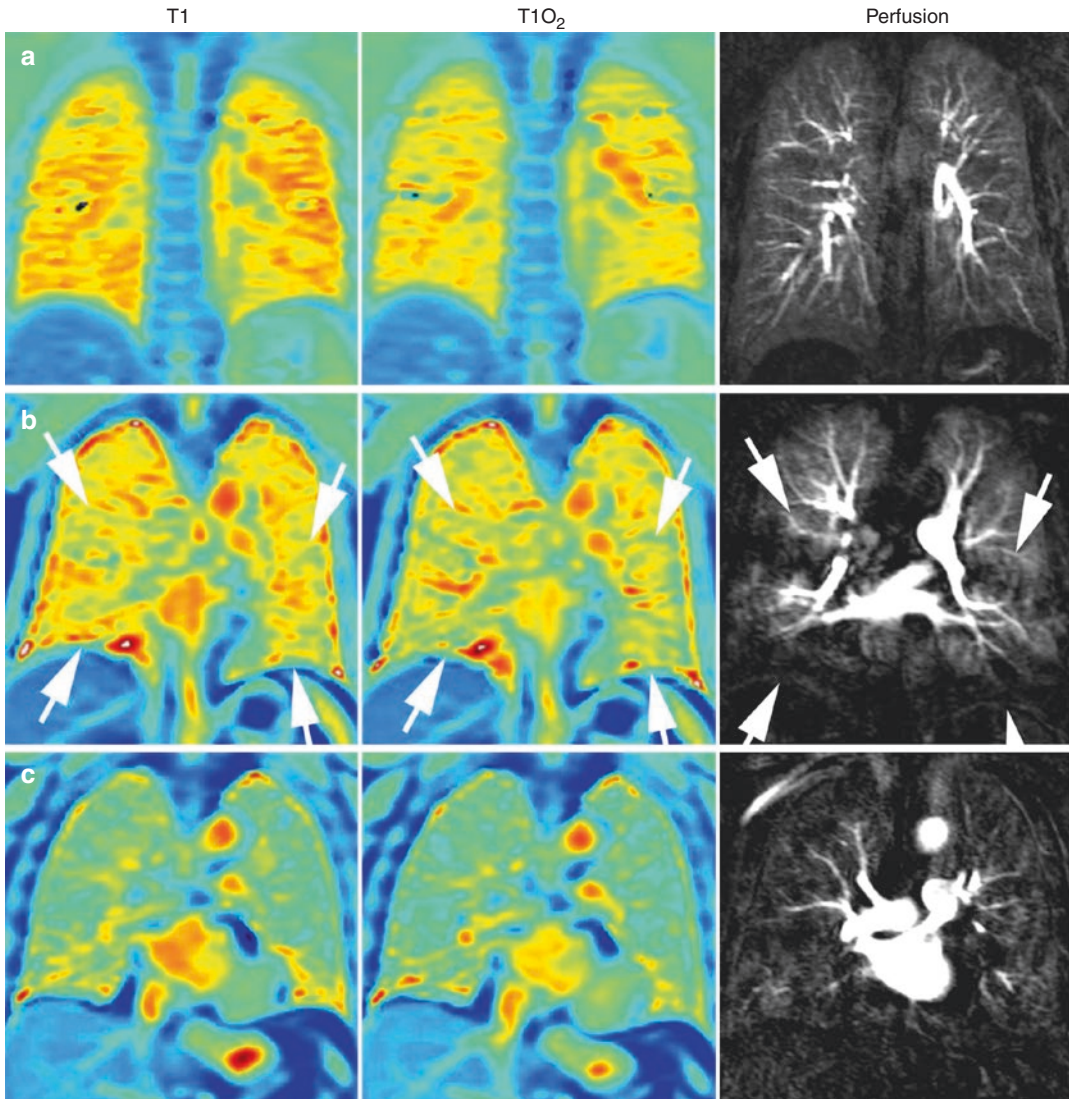
Fig. 3 Comparison of T1 and perfusion characteristics: Normal T1 mapping at room air (*left*), T1 mapping after 100% O2 (*middle*), and DCE lung perfusion (*right*) (zonal scores = 0 each) of a 29-year-old healthy volunteer (**a**). Fifty-nine-year-old patient with GOLD stage II showing minor T1 abnormalities at room air (score = 1), normal ΔT1 after 100% O2 (score = 0), and minor perfusion abnormalities (score = 1) of the middle and lower lung zones (area between *white arrows*), reflecting lung areas with intact ventilation and simultaneous perfusion impairment (**b**). Severe T1 abnormalities at room air, abnormal ΔT1 after 100% O2, and perfusion abnormalities (score = 2 each) affecting the entire lung of a 75-year-old patient with GOLD stage II (**c**). Reprinted with permission from Jobst et al. (2015a, b)

spatial resolution is essential. By using a 3D VIBE with a voxel size of approximately $0.9 \times 0.88 \times 2.5$ mm^3 a sensitivity of 79% and a specificity of 98% regarding the visual depiction of bronchiectasis were shown compared to CT (Biederer et al. 2003).

4   Respiratory Dynamics

Respiration is the result of the complex interaction between chest wall and diaphragm motion, and it can be visualized by 2D or 3D dynamic MR techniques (Cluzel et al. 2000; Plathow

et al. 2004, 2005). For data acquisition time-resolved techniques are used, which can be based on FLASH or trueFISP sequences. This allows for a high temporal resolution down to 100 ms per frame.

Hyperinflation of the lung severely affects diaphragmatic geometry with subsequent reduction of the mechanical properties, while the effects on the mechanical advantage of the neck and rib cage muscles are less pronounced (Decramer 1997). The common clinical measurements of COPD do not provide insights into how structural alterations in the lung lead to dysfunction in the breathing mechanics, although treatments such as lung volume reduction surgery (LVRS) are thought to improve lung function by facilitating breathing mechanics and increasing elastic recoil (Henderson et al. 2007).

In contrast to normal subjects with regular, synchronous diaphragm and chest wall motion, dynamic MRI in patients with emphysema frequently showed reduced, irregular, or asynchronous motion, with a significant decrease in the maximum amplitude and the length of apposition of the diaphragm (Suga et al. 1999). In some patients the ventral portion of the hemidiaphragm moved downward at MRI while the dorsal part moved upward like a seesaw (Iwasawa et al. 2000). The paradoxical diaphragmatic motion correlated with hyperinflation, although severe hyperinflation tended to restrict both normal and paradoxical diaphragmatic motion (Iwasawa et al. 2002). Another study showed that the distribution of emphysema might have an influence on the diaphragmatic motion. The lower zone emphysema on CT correlated significantly with diaphragmatic flattening and abnormal chest wall motion evaluated with dynamic MRI whereas emphysema of the upper lung zone did not correlate with these parameters (Iwasawa et al. 2011). After LVRS, patients showed improvements in diaphragm and chest wall configuration and mobility at MRI (Suga et al. 1999). Ultrafast dynamic proton MRI was shown to be able to demonstrate the rapid volume changes observed during forced vital capacity maneuver (Fig. 4) and correlated closely with pulmonary function tests, but with the added advantage of providing regional information on changes in lung volumes during this procedure (Swift et al. 2007; Eichinger et al. 2007).

5   Ventilation

As sufficient gas exchange depends on matched perfusion and ventilation, assessment of regional ventilation is important for the diagnosis and evaluation of pulmonary emphysema. The most established method for imaging regional lung ventilation is nuclear medicine studies using krypton-81m (Kr-81m), xenon-133 (Xe-133), radiolabeled aerosol (Technegas), and technetium-99m (Tc-99m)-labeled diethylentriamine-pentaacetic acid (DTPA). The utility of nuclear medicine in pulmonary diseases has been well documented. However, these techniques are hampered by low spatial and temporal resolution, and the necessity of inhalation of radioactive tracers. While 3D (SPECT) imaging requires approximately 20 min of imaging time, the diagnostic power of the technique is limited.

Although PFTs and nuclear medicine imaging have been established as the most common and reliable pulmonary function techniques, other techniques such as contrast-enhanced proton and hyperpolarized noble gas MRI are strong contenders in the functional imaging race. They provide a rapid, high-resolution regional quantification of disease progress and onset without the need for ionizing radiation tracers.

MRI signal changes inherent to lung tissue expansion and contraction that occur during normal breathing could be exploited to generate ventilation and perfusion maps. Fourier decomposition of the 1H signal intensity caused by compression and expansion of the lung parenchyma and pulmonary blood flow can be used to evaluate pulmonary ventilation and perfusion (Bauman et al. 2013). This method does not depend on inhaled gas or injected contrast agents. Despite these important advantages, there have been no large clinical COPD studies that have taken advantage of these novel pulmonary 1H MRI measurements (Coxson et al. 2014).
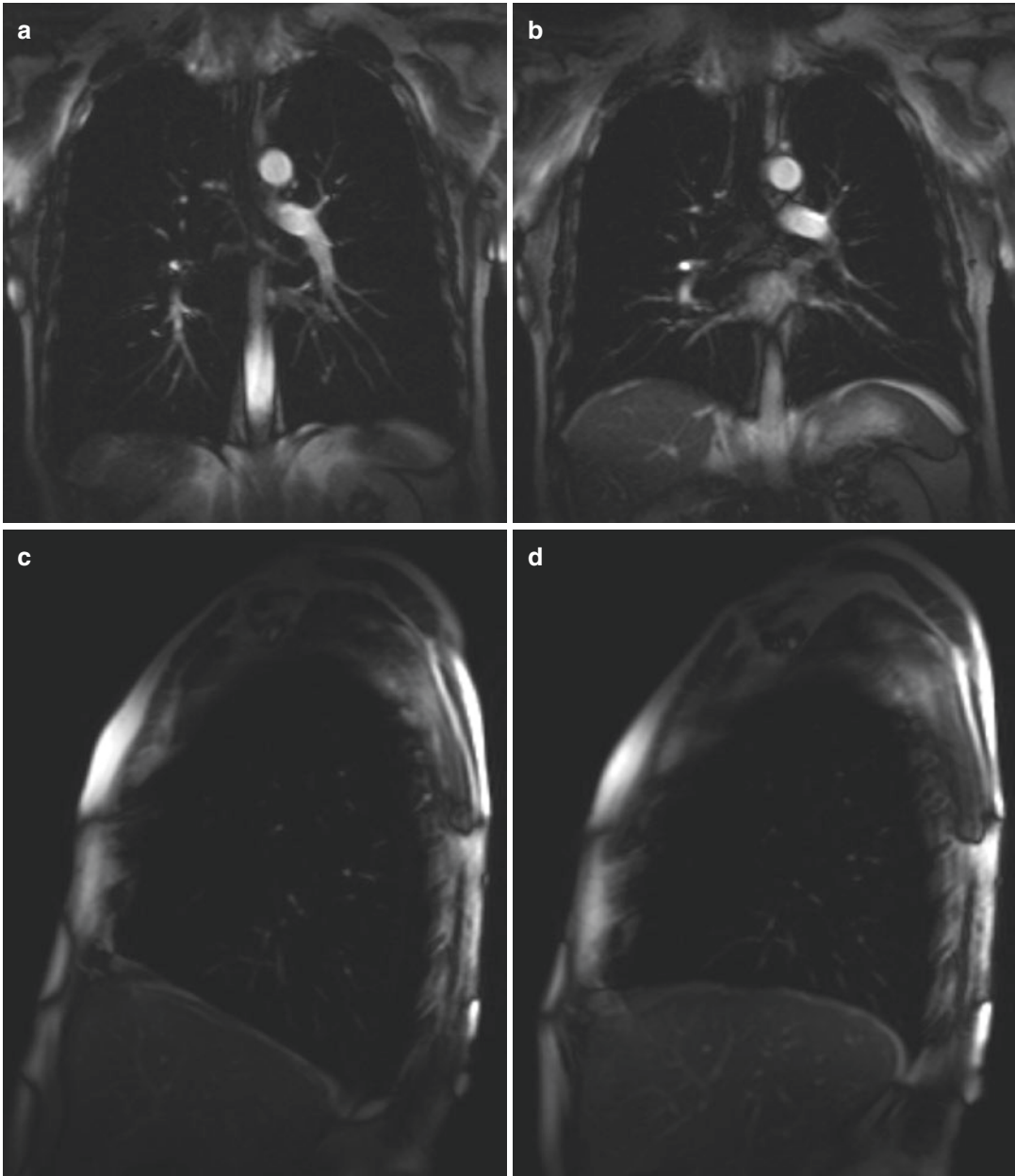
Fig. 4 Coronal and sagittal MR images taken from a dynamic series acquired in a COPD patient during forced expiration reflecting maximum inspiration (**a**, **c**) and maximum expiration (**b**, **d**) shows motion of the diaphragm and thoracic wall (*arrows*)

5.1 Oxygen-Enhanced Imaging

Oxygen-enhanced MRI does not require special scanner hardware and is easy to use and the overall material costs are low in comparison with noble gas imaging. The main idea behind this technique is to utilize the paramagnetic properties of inhaled oxygen (O_2) to obtain information regarding the pulmonary blood flow

volume and integrity of the lung parenchyma. Several investigators reported that oxygen-enhanced MRI could demonstrate regional ventilation (Edelman et al. 1996; Loffler et al. 2000; Ohno et al. 2001). Only few studies have successfully applied oxygen-enhanced MRI to patients with pulmonary diseases in a clinical setting. One of the reasons might be that the use of high oxygen concentrations (15 L/min) may not be without risk in patients with severe COPD and therefore vital parameters should be monitored during the procedure.

In some basic measurements it was shown that the T1 of the lung parenchyma is significantly shorter in patients with emphysema than in volunteers (Stadler et al. 2008). In a preliminary study an inhomogeneous and weak signal intensity increase after application of oxygen was observed, compared to healthy volunteers (Muller et al. 2002). Ohno et al. demonstrated that regional changes in ventilation as observed in oxygen-enhanced MR reflected regional lung function. The maximum mean relative enhancement ratio correlated with the diffusion capacity for carbon monoxide ($r^2 = 0.83$), while the mean slope of relative enhancement was strongly correlated with the FEV_1 ($r^2 = 0.74$) and the maximum mean relative enhancement with the high-resolution CT emphysema score ($r^2 = 0.38$) (Ohno et al. 2003). The simple administration of pure oxygen might induce the pulmonary arteries to dilate resulting in an increase of pulmonary blood volume and a consecutive increase in signal intensity (Ley et al. 2007).

This technique might be further refined by exploiting time-resolved acquisitions during oxygen wash-in and washout. Mean wash-in time showed good correlation with FEV1/FVC% and FEV1% ($r = -0.74$) and moderate correlation with DLCO% ($r = -0.57$) in a cohort of 10 non-smokers and 61 smokers without or with mild to severe COPD (Ohno et al. 2008a). Mean wash-in time was significantly different between non-smokers (smallest) and COPD patients at risk of or with mild COPD, while moderate and severe stages of the disease were significantly different to all other subgroups. In a larger study population of 160 smokers without and with mild to very

severe COPD, similar good correlation was found between mean relative enhancement ratio and FEV1/FVC% ($r = 0.68$), FEV1% ($r = 0.65$), and moderate correlation with DLCO% ($r = 0.61$), all slightly better than correlation coefficients between quantitative CT and pulmonary function tests (Ohno et al. 2008b). These results were confirmed in another study in 187 smokers (Ohno et al. 2012). Pulmonary functional parameters and mean relative enhancement ratio for each clinical subgroup showed significant differences among each other, thus suggesting that oxygen-enhanced MRI is effective for pulmonary functional loss assessment and clinical stage classification of smoking-related COPD.

The feasibility of oxygen-enhanced MRI to detect a response to a single-dose bronchodilator therapy as well as 8-week treatment with a combination of an inhaled corticosteroid and bronchodilator was tested in a recent study and demonstrated improvement of FEV1 and MRI ventilation parameters (Morgan et al. 2014).

5.2 Hyperpolarized Noble Gas Imaging

Over the past decade hyperpolarized noble gas MRI using [3]Helium and [129]Xenon was developed to improve imaging of pulmonary structure, ventilation, dynamics, and oxygen uptake (Ley-Zaporozhan and van Beek 2010). [3]Helium became the most widely used gas for these studies as it provides higher signal-to-noise ratios than [129]Xenon, due to its lower intrinsic gyromagnetic ratio, and its confinement to the airways and airspaces without dissolving into the surrounding tissue and bloodstream (van Beek et al. 2004). Areas with ventilation defects caused by airway obstruction and emphysema represent the only limitation because they cannot be assessed due to lack of the tracer gas entering these areas. Thus, there is almost no information about these affected lung regions. Overall, the intrinsic high cost of these noble gases, need for laser-induced hyperpolarization hardware, and need for non-proton imaging hardware and software remain the major drawbacks of this technology on its

way to broader clinical applications. The field of hyperpolarized noble gas imaging is currently undergoing some changes due to supply issues of [3]Helium, while development of [129]Xenon is increasingly encouraging due to novel polarizer systems that offer higher levels of polarization with resultant better signal (Ley-Zaporozhan and van Beek 2010).

5.2.1 Static Ventilation

Airflow obstruction leads to a reduced level of [3]Helium in the distal lung regions allowing for sensitive detection of ventilation abnormalities (Figs. 5 and 6) (Kauczor et al. 1996). In healthy smokers with normal lung function even subtle ventilation defects were visualized demonstrating the high sensitivity of the technique (Guenther et al. 2000). Ventilation defects correlated well with the parenchymal destruction assessed by

HRCT in patients with severe emphysema following single-lung transplantation (Gast et al. 2002). To date, the largest multicenter trial was performed in three European centers analyzing 94 subjects with COPD, α1-antitrypsin-deficiency patients, and healthy age-matched never-smokers (van Beek et al. 2009). The visually estimated non-ventilated lung volumes on [3]He-MRI were compared to percentage of diseased lung on HRCT. Using PFT as a reference, regional analysis of [3]He-MRI and HRCT correctly categorized normal volunteers in 100% and 97%, COPD in 42% and 69%, and α1-antitrypsin-deficiency patients in 69% and 85% of cases, respectively. Overall only a moderate agreement (kappa = 0.43) was found between [3]He-MRI and HRCT. Direct comparison revealed that 23% of subjects with moderate/severe structural abnormalities had only mild ventilation defects.
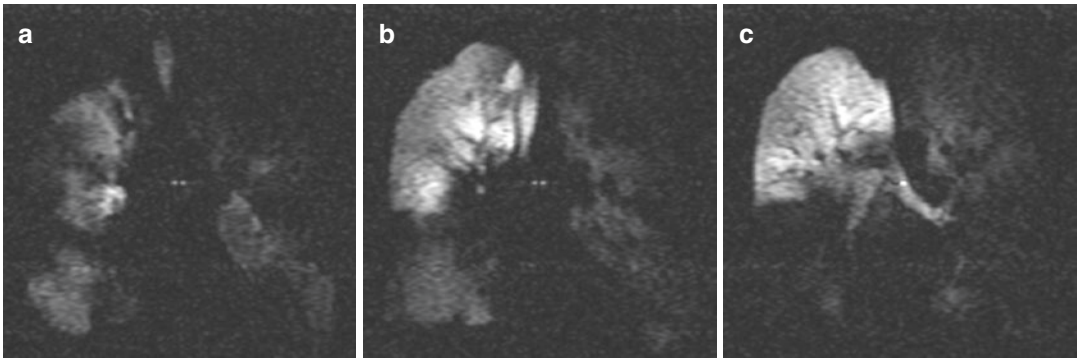
Fig. 5 MR ventilation images using hyperpolarized [3]Helium gas of a patient suffering from alpha1-antitrypsin deficiency: good ventilation of the right upper lobe and large wedge-shaped ventilation defects in all remaining lung areas
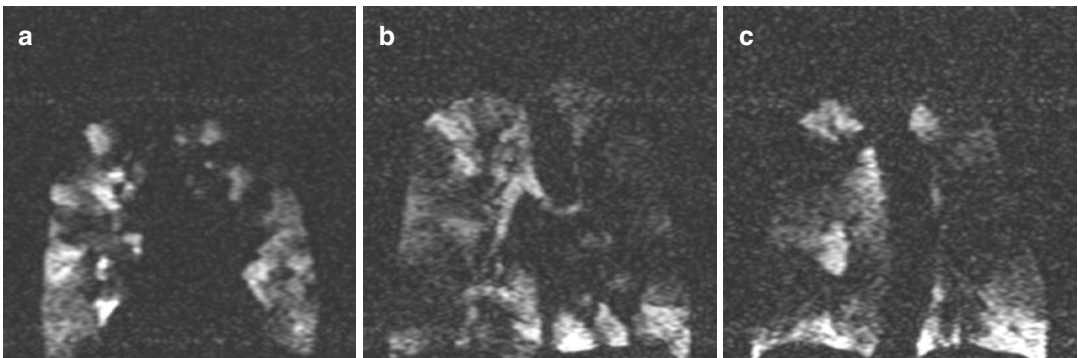
Fig. 6 MR ventilation images using hyperpolarized [3]Helium gas of a patient suffering from COPD: focal and wedge-shaped ventilation defects in all parts of the lung

The most common metric used in the early literature was the mean number of ventilation defects per slice without information about the size and regional distribution of the defect (Fain et al. 2010). By use of estimated lung boundaries the volume of ventilated lung areas on ^{3}He-MRI correlated well with vital capacity ($r = 0.9$) and the amount of non-emphysematous volume on CT ($r = 0.7$) in patients with severe emphysema following single-lung transplantation (Zaporozhan et al. 2004). Today an established approach is to calculate the ventilated lung volume and normalize it to total lung volume, resulting in percentage of lung volume ventilated or its derivate percentage volume of defect. These values are quantified by semiautomated segmentation of ^{3}He ventilation images and further registration to proton MR images for delineation of the lungs and defect boundaries. Repeatability and validity of this measure were shown in several studies in several disease entities (Kruger et al. 2016). Using this approach in small-scale studies, a good correlation between ventilation defect percentage and FEV_1% and FEV_1/FVC was found by Kirby et al. ($r = -0.84$) (Kirby et al. 2012a) but only fair correlation by Mathew et al. ($r = -0.58$ and -0.54, respectively) (Mathew et al. 2011). Even more reproducible quantification of percentage ventilation volume could be achieved by acquiring ^{3}He ventilation images and anatomical proton images during the same single breath-hold (Horn et al. 2014).

The voxel intensity of the ventilation images can be further classified into clusters representing graduations of signal intensity from no signal, hypointense signal to hyperintense signal, and generating ventilation cluster maps (Kirby et al. 2011). This in-depth distribution analysis might be of value for therapy monitoring. Advantages of this evaluation were shown in a small-scale study of patients with moderate to severe COPD, where ^{3}He-MRI depicted significant improvements in the regional gas distribution throughout the lung after bronchodilator therapy with and without clinically important changes in FEV_1 (Kirby et al. 2011). In a 2-year longitudinal study in patients with mild to moderate COPD, ventilation defect percentage worsened significantly in

the absence of significant decline in FEV1, suggesting sensitivity of ^{3}He-MRI for depicting disease progression (Kirby et al. 2010).

Given its greater availability and lower cost, ^{129}Xenon offers an alternative to ^{3}He-MRI. The associated lower signal-to-nose ratio of ^{129}Xenon images requires careful segmentation of the lung from background noise (Kaushik et al. 2011). The gas distribution at ^{129}Xe-MRI was qualitatively more regionally heterogeneous and the ventilation defect percentage was significantly greater than that with ^{3}He-MRI in patients with COPD but not in healthy volunteers, suggesting incomplete or delayed filling of lung regions (Kirby et al. 2012a). Lower diffusion coefficient and higher viscosity of xenon relative to helium may result in slower gas movement and filling into distal diseased lung regions. The ventilation defect percentage from ^{129}Xe-MRI showed a good correlation with FEV_1% and FEV_1/FVC in a small group of COPD patients and age-matched controls ($r = -0.79$ and $r = -0.71$, respectively) and also in a small group of COPD patients and healthy volunteers ($r = -0.89$ and $r = -0.95$, respectively) (Kirby et al. 2012a; Virgincar et al. 2013).

5.2.2 Dynamic

^{3}He-MR imaging with high temporal resolution via ultrafast echo-planar (EPI), gradient-echo, and interleaved spiral sequences allows for the visualization and assessment of the various inspiratory and expiratory phases of respiration. The instantaneous visualization of the bolus movement leads to a direct evaluation of the regional distribution of ventilation throughout the lungs, which may be quantified using a regional assessment (Lehmann et al. 2004). Evaluation of the overall usefulness of the technique has shown considerable airflow abnormalities in diseased lung states and normal respiration stages in normal lungs (Salerno et al. 2001; Wild et al. 2003). Normal respiration can be described by a rapid and homogenous distribution of the gas throughout the lung, whereas in diseased lungs, the airflow is inhomogeneous due to factors such as airway blockages and reduced lung compliance, leading to interspersed ventilation defects (Fig. 7). The observed ventilation defects vary
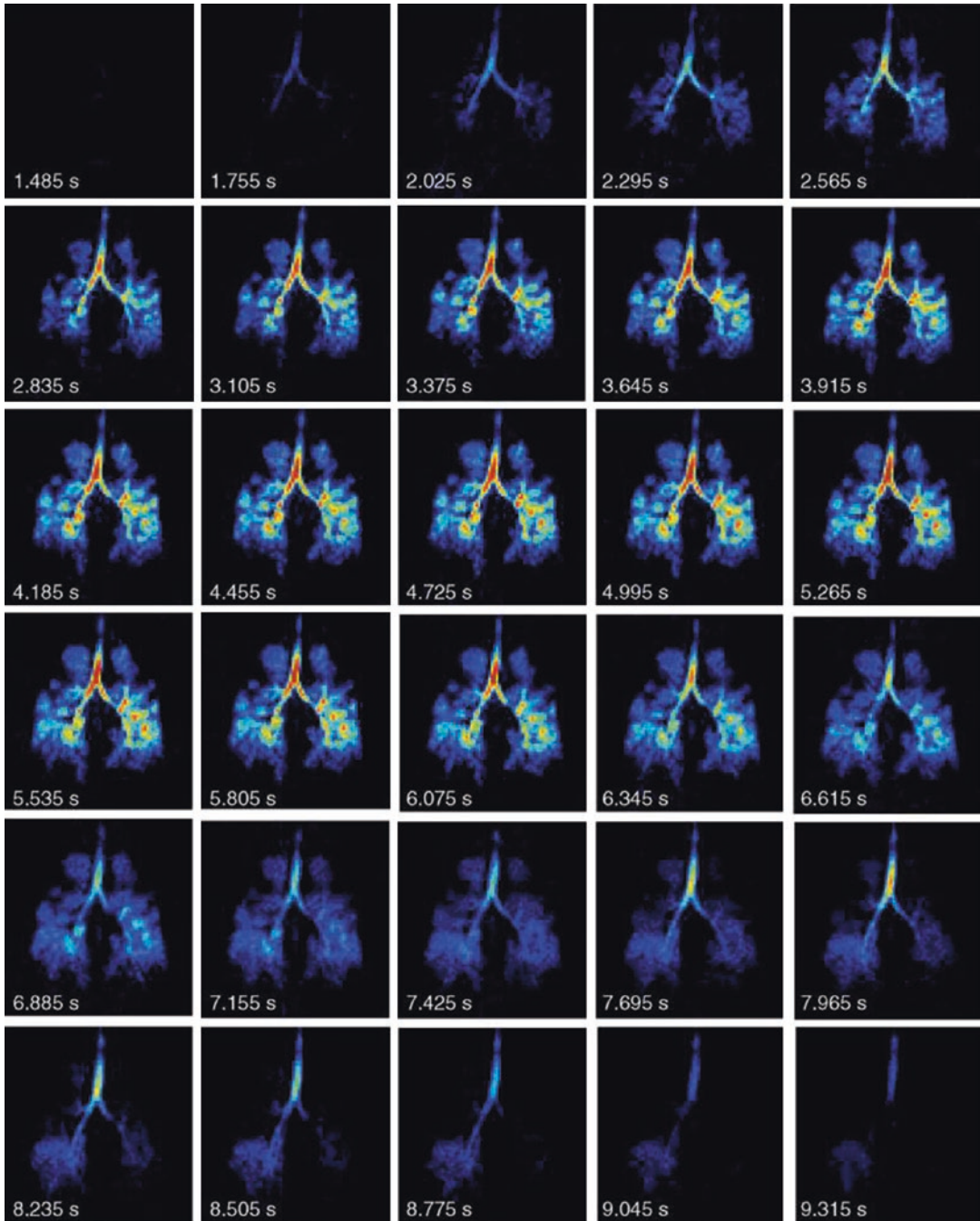
Fig. 7 Dynamic MR ventilation images using hyperpolarized ³Helium gas from a COPD patient showing regions of ventilation obstruction in both lungs, particularly in the upper lobes, and a delayed emptying/depolarization of gas in the lower left lobe, which could be indicative of air trapping. Reprinted with permission from van Beek et al. (2004)

from reduced inflow to air trapping as observed in the later phases of the respiratory cycle, which are more markedly visualized in subjects with CT-proven centrilobular emphysema (Wild et al. 2003; Gierada et al. 2000; Gast et al. 2003).

Another recently used approach was to evaluate delayed ventilation during the time course of breath-hold imaging by using time-resolved gradient-echo sequence with 3D whole-lung coverage (Marshall et al. 2012). The influx of polarized gas into initially non-ventilated defects might represent collateral ventilation and slow filling of peripheral airspaces due to increased flow resistance. Delayed filling was observed in eight of ten COPD patients.

5.2.3 ^{3}Helium Apparent Diffusion Coefficient (ADC)

The high diffusion coefficient of ^{3}Helium gas makes it very suitable for the evaluation of the lung microstructure, connecting pores and pathways, leading to an overall assessment of the integrity and size of such structures. The ADC is a reflection of the restricted diffusion of ^{3}Helium gas in a normal airway system due to the relatively small size of airways in relation to the diffusivity of the gas.

Similar to all other ^{3}Helium techniques, the ADC is accomplished throughout one single breath-hold, where a series of images are acquired and evaluated on a pixel-by-pixel basis. The introduction of the additional gradients into the sequences allows the monitoring of diffusion through signal decay incurred by motion of the helium molecules, thus creating a map of diffusion values representing the regional and global integrity of the lungs.

ADC maps of normal healthy volunteers have shown to be homogenous and uniform. On the other hand, in emphysematous subjects ADC maps were nonuniform and contained larger diffusion values. This nonuniformity of the ADC values correlates well with the nature of the disease, where the degree and location of destruction vary throughout the lung (Salerno et al. 2002; Ley et al. 2004a; Conradi et al. 2005). The ability to distinguish between normal and emphysematous lungs reflects the overall power

of determining and quantifying airway enlargement along with tissue destruction. The mean ADC for emphysema patients (0.452 cm^2/s) was found to be significantly larger ($p < 0.002$) than for normal volunteers (0.225 cm^2/s) (Salerno et al. 2002). In other studies, mean ADC values of emphysema patients were as low as 0.24 cm^2/s and as high as 0.55 cm^2/s (Conradi et al. 2005; Swift et al. 2005; Diaz et al. 2009). This wide distribution of ADC values for the emphysema population can be attributed to the variability in airspace size and morphological alterations of the distal airspaces caused by the disease. Values for ^{129}Xe-ADC are lower than ^{3}He-ADC by an order of magnitude due to higher density of xenon gas (Kruger et al. 2016). ^{129}Xe-ADC for emphysema patients (0.056 cm^2/s) was significantly different than for age-matched controls (0.043 cm^2/s) and for healthy volunteers (0.036 cm^2/s) (Kaushik et al. 2011).

Very high reproducibility of these ADC measures has been demonstrated—within 6% variation for consecutive scans at the same day (Morbach et al. 2005) and in another study with a correlation of $r^2 > 0.9$ for re-scanning on the same day as well as in a week interval (Mathew et al. 2008). In a small study combining ^{3}He and ^{129}Xe imaging in ten patients, mean ^{3}He-ADC within the regions only assessed by helium gas was significantly greater than for lung regions assessed by both gases (0.503 cm^2/s versus 0.470 cm^2/s) (Kirby et al. 2013). ^{3}He-ADC values showed a moderate correlation with FEV$_1$% ($r = -0.6$) (Swift et al. 2005) and good correlation with DLCO% ($r = -0.82$) (Diaz et al. 2009). ^{129}Xe-ADC showed good to moderate correlation with FEV$_1$%, FEV1/FVC%, and DLCO% in COPD patients and age-matched controls ($r = -0.77$) (Kaushik et al. 2011) as well as in COPD and healthy volunteers ($r = -0.67$, $r = -0.77$ and $r = -0.79$, respectively) (Kirby et al. 2012a).

Mean ADC probably underestimates the amount of destroyed lung tissue, as ventilation defects prevent ADC measurements, and some of the most destroyed emphysematous lung areas therefore are excluded from the analysis.

In a small study investigating ^{3}He-ADC before and after bronchodilator administration a signifi-

cant decrease in ADC value was detected within the lung regions containing the ³He signal at both time points (Kirby et al. 2012b). No difference was found between ventilated areas before bronchodilator administration and newly ventilated lung regions after the bronchodilator administration, suggesting that these regions have a similar degree of the disease.

6   Pulmonary Perfusion

Perfusion and ventilation are normally in balance, with hypoxic vasoconstrictive response providing a method to optimize lung function. In patients with COPD, ventilation is impaired due to airway obstruction and parenchymal destruction, leading to perfusion being moved to better ventilated lung regions or shunting of blood (moving through the lungs without reaching a capillary bed for gas exchange) (Moonen et al. 2005). The reduction of the pulmonary vascular bed is related to the severity of parenchymal destruction (Thabut et al. 2005); however the distribution of perfusion does not necessarily match parenchymal destruction (Sandek et al. 2002; Ley-Zaporozhan et al. 2007). Conventional radionuclide perfusion scintigraphy has been used to assess these abnormalities, but it has substantial limitations with respect to spatial and temporal resolution. A superior technique is SPECT, which is rarely used as it is rather time consuming and not routinely applied. Inflammation appears to play a critical role in the maintenance of the hypoxic vasoconstrictive response, and PET studies with endotoxin challenge have shown that this response is shut off when inflammation and lung injury occur (Schuster and Marklin 1986; Gust et al. 1998).

The basic principle of contrast-enhanced perfusion MRI is a dynamic acquisition during and after an intravenous bolus injection of a paramagnetic contrast agent. With the introduction of parallel imaging techniques, 3D perfusion imaging with a high spatial and temporal resolution as well as an improved anatomical coverage and *z*-axis resolution can be acquired (Ley et al. 2004b; Fink et al. 2004, 2005). These data sets are also well suited for high-quality multiplanar reformats. Due to high spatial resolution, detailed analysis of pulmonary perfusion and precise anatomical localization of the perfusion defects on a lobar and even segmental level can be performed (Fig. 8). Quantitative values for pulmonary perfusion can be obtained by applying the principles of indicator dilution techniques. The quantitative indices, such as mean transit time (MTT), pulmonary blood volume (PBV), and blood flow (PBF), are derived from the time intensity curve, defined by the dynamic series of perfusion MR images.

MR perfusion allows for a high diagnostic accuracy in detecting perfusion abnormalities (Fink et al. 2004; Sergiacomi et al. 2003). Furthermore, MR perfusion ratios correlate well with radionuclide perfusion scintigraphy ratios (Ohno et al. 2004a; Molinari et al. 2006). Lobar and segmental analysis of the perfusion defects can be achieved. In patients with severe emphy-
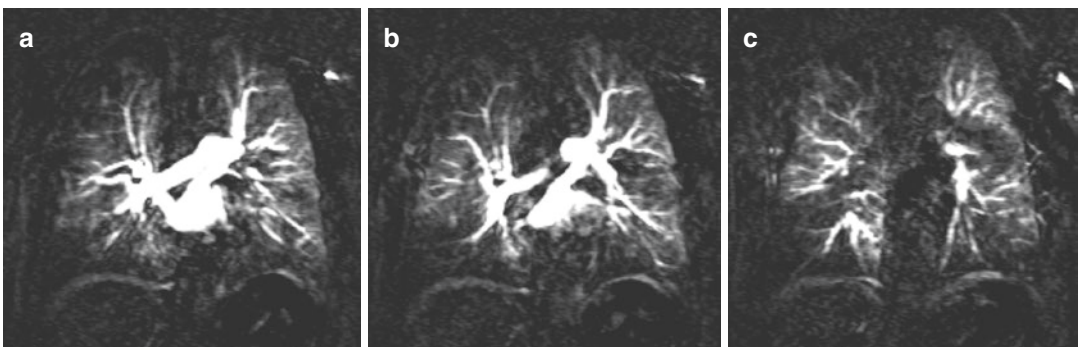
Fig. 8 Coronal contrast-enhanced MR perfusion images of a COPD patient acquired during an inspiratory breath-hold showing subpleural distribution of perfusion defects

sema there was a strong match between parenchymal destruction and reduction of perfusion; however the distribution patterns of emphysema and perfusion impairment were not necessarily in concordance (Ley-Zaporozhan et al. 2007). Here the severity score was higher on CT in 16% of the lobes and on MRI in 5%. In otherwise healthy smokers there were more MR perfusion defects than parenchymal abnormalities seen on CT, suggesting MR perfusion being a good approach to identify early evidence of COPD (Fan et al. 2013).

The perfusion abnormalities in COPD clearly differ from those caused by vascular obstruction. While wedge-shaped perfusion defects occur in embolic vascular obstruction, a low degree of contrast enhancement is generally found in patients with COPD/emphysema (Amundsen et al. 2002; Morino et al. 2006). Furthermore, the peak signal intensity is usually reduced. These features allow for easy visual differentiation. In patients with COPD, the quantitative evaluation of 3D perfusion showed that the mean PBF, PBV, and MTT were significantly decreased, and these changes showed a very heterogeneous distribution (Ohno et al. 2004b). It was discussed that patients with emphysema have hypoxia as well as destruction of lung parenchyma and fewer alveolar capillaries. This causes increased pulmonary arterial resistance and, secondarily to adaptive processes, pulmonary hypertension and right ventricular dysfunction. Ultimately, this results in decreased pulmonary blood flow in addition to heterogeneous perfusion and decreased PBV. MTT is determined by the ratio between PBV and PBF. The results suggested that MTT is significantly decreased, reflecting a larger degree of decrease in PBV compared with PBF, with concomitant increased heterogeneity of regional PBV. Obviously, accurate quantitative measurements of such regional changes are important for improved understanding of lung pathophysiology in COPD.

For visual assessment of the regional heterogeneity the area of perfusion impairment on color-coded maps covering 10–15 cm of the thorax was compared with the same area of emphysema on quantitative CT maps. Very good or good agreement was found in 9–10 of 14 patients (two readers) for PBF and in 11/14 patients (similar for both readers) for PBV (Jang et al. 2008). The quantitative evaluation was performed in small peripheral ROIs on each slice for upper, middle, and lower areas of the lung. Here only moderate correlation was found between PBV and emphysema fraction on volumetric CT ($r = -0.61$) and FEV1/FVC ($r = 0.69$).

An association between the emphysema type on CT and MR perfusion pattern was analyzed at a segmental level in patients with severe emphysema (Bryant et al. 2015). The centrilobular type of emphysema showed corresponding heterogeneous perfusion with focal defects in 70% (Fig. 9a), whereas panlobular emphysema presented with either homogeneous or heterogeneous absence of perfusion in 42% and 43%, respectively (Fig. 9b, c).

The repeatability and reproducibility of quantitative whole-lung perfusion in inspiration and expiration were analyzed in healthy volunteers by two observers (Ley-Zaporozhan et al. 2011). The intraobserver differences between the initial examination and follow-up after 24 h were not significantly different for PBV, MTT, and TTP for both observers. However, PBF showed a sig-

Fig. 9 (**a**) For the segments of the middle and lower lobes centrilobular emphysema was found to be the predominant type on CT, corresponding color-coded map of max. Peak enhancement of MR perfusion showed heterogeneous perfusion with defects as the predominant pattern. (**b**) The apical segment of both lungs showed centrilobular emphysema as the predominant type on CT (*arrows*), corresponding color-coded map of max. Peak enhancement of MR perfusion showed heterogeneous loss of perfusion as the predominant pattern. (**c**) For the segments of both lower lobes panlobular emphysema was found to be the predominant type on CT (*arrows*), corresponding color-coded map of max. Peak enhancement of MR perfusion showed homogeneous loss of perfusion as the predominant pattern (*arrows*). Reprinted with permission from Bryant et al. (2015)
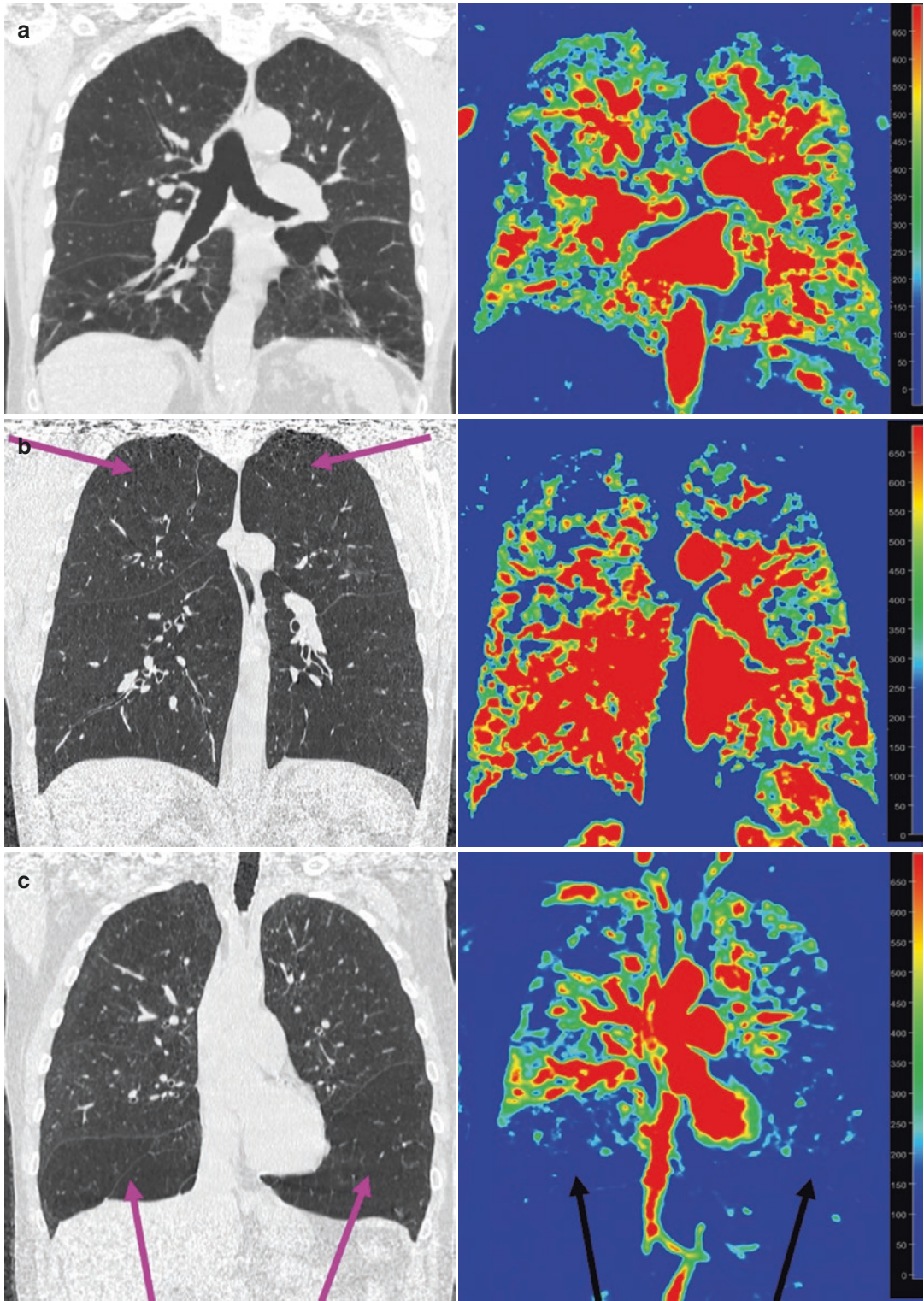
nificant difference for both observers but only on inspiration. For interobserver evaluation, all parameters except inspiratory PBF were significantly different ($P < 0.0001$). Thus, the quantitative perfusion MRI showed reproducible results, but the evaluation is highly dependent on the observer and the quantitative analysis of the serial examinations should be performed by the same person.

In the largest study to date, the quantitative perfusion parameters were markedly reduced in mild COPD as well as in more severe stages compared to healthy smokers; however evaluation was limited to one coronal slice (Hueper et al. 2015). Thus, there is a need for fast, dedicated post-processing software for whole-lung assessment, which is especially necessary in longitudinal studies or screening trials for further investigation of perfusion as a possible imaging biomarker. A fully automatic method was recently introduced by Kohlmann et al. (2015). Similar to ventilation imaging, the lungs were segmented on the morphological MR images with higher spatial resolution and the segmentation was then transferred to the perfusion images via nonlinear registration. The automatic segmentation took approximately 1 min and no user interaction was required, whereas the time for the manual segmentation ranged between 12 and 25 min. The reproducibility of the quantitative

analysis may also be improved by using automatic instead of manual lung segmentation.

In a recent study evaluating perfusion during acute exacerbation of COPD, two patient groups were identified—one presented with an improvement of quantitative perfusion parameters after clinical stabilization and another showed no response (Sergiacomi et al. 2014). This could assist in predicting early response to treatment, allowing more aggressive approaches in nonresponders.

7   Hemodynamics

Assessment of right ventricular function is important, as this is where the strain of perfusion obstruction and pulmonary hypertension eventually leads to the demise of the patient. MRI is able to assess right ventricular function through either phase-contrast flow measurements in the pulmonary trunk (Fig. 10) or short-axis cine acquisition of the right ventricle (Vonk-Noordegraaf et al. 2005; Gatehouse et al. 2005). Thus, early changes of the complex geometry of the right ventricular wall and chamber volume can be accurately measured.

Although pulmonary hypertension and cor pulmonale are rather common sequelae of COPD, the direct mechanism remains unclear (Szilasi
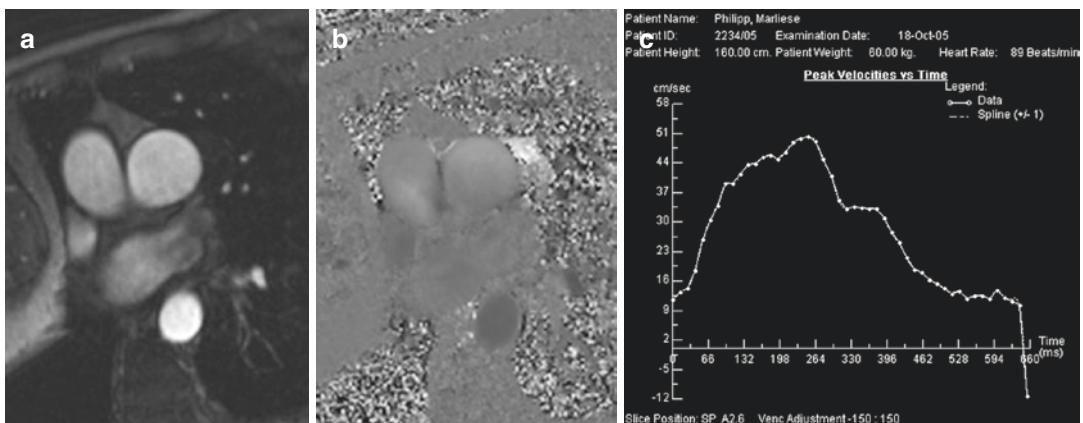
Fig. 10 Quantitative flow measurement of pulmonary blood flow. Magnitude (**a**) and velocity-encoded (**b**) image of the pulmonary trunk (*arrow*). Results of peak velocity over time (**c**) show the prolonged increase of velocity at the beginning of the systolic phase followed by an abnormal plateau during diastole

et al. 2006). In COPD patients the pulmonary vessels show a reduced capacity for vessel dilatation due to a defect in synthesis and/or release of nitric oxide. Prior to the onset of clinical symptoms patients exhibit signs of vascular bed obstruction and elevated pulmonary artery pressure including main pulmonary artery dilatation. Pulmonary hypertension is most often mild to moderate (mean pulmonary artery pressure in the range of 20–35 mm Hg), but it may worsen markedly during acute exacerbations, sleep, and exercise. Assessment of the pulmonary arterial pressure is necessary in COPD patients for at least two reasons: such patients have a poor prognosis; and they need adequate treatment that might include pulmonary vasodilators.

It has been demonstrated by several studies that the level of pulmonary hypertension has a prognostic impact on COPD patients. In one of these studies, the 5-year survival rates were 50% in patients with mild (20–30 mm Hg), 30% in those with moderate to severe (30–50 mm Hg), and 0% in the small group (n = 15) of patients with very severe pulmonary hypertension (>50 mm Hg). Thus, severe pulmonary hypertension carries a poor prognosis, and this has also been observed in COPD patients receiving long-term oxygen therapy (Weitzenblum and Chaouat 2005).

Initially, a rise in pulmonary blood pressure leads to pulmonary artery dilatation while right ventricular performance is usually maintained. Evaluation of the right ventricle and pulmonary blood flow by echocardiography is difficult in patients with emphysema as the acoustic window is limited. Therefore, MRI has been used for imaging the right ventricle, and a loose correlation between increased right ventricular mass and severity of emphysema was demonstrated (Boxt 1996).

In COPD patients with hypoxemia, increased right ventricular volumes, decreased right ventricular function, and impaired left ventricular diastolic function were shown (Budev et al. 2003). In a study by Vonk-Nordegraaf et al. the right ventricular mass and ejection fraction in 25 clinically stable, normoxic COPD patients

with emphysema were analyzed. The position of the heart appeared rotated and shifted to a more vertical position in the thoracic cavity due to hyperinflation of the lungs with an increase of the retrosternal space. The right ventricular wall mass was significantly higher (68 g) in the patient group compared to healthy volunteers (59 g). The right ventricular ejection fraction was unchanged (53%) (Vonk Noordegraaf et al. 1997). In another study from the same group structural and functional cardiac changes in COPD patients with normal P_aO_2 and without signs of right ventricular failure were evaluated. Compared to healthy volunteers there were no indications of pulmonary hypertension. However, the end-systolic and end-diastolic volumes of the right ventricle were significantly reduced (with normal ejection fraction), the right ventricular mass was significantly elevated while the left ventricular mass was within normal limits. The authors conclude that concentric right ventricular hypertrophy is the earliest sign of right ventricular pressure increase in patients with COPD. This structural adaptation of the heart initially does not alter right and left ventricular systolic function (Vonk-Noordegraaf et al. 2005). As this is the only study so far in patients with mild emphysema no strong conclusions can be drawn from this first description of the early adaptation mechanisms of the right ventricle in patients with normoxemia or mild hypoxemia and the consequences of any structural changes on right and left ventricular function.

References

Alamidi DF, Morgan AR, Hubbard Cristinacce PL, Nordenmark LH, Hockings PD, Lagerstrand KM et al (2016) COPD patients have short lung magnetic resonance T1 relaxation time. COPD 13(2):153–159. doi: 10.3109/15412555.2015.1048851

Amundsen T, Torheim G, Kvistad KA, Waage A, Bjermer L, Nordlid KK et al (2002) Perfusion abnormalities in pulmonary embolism studied with perfusion MRI and ventilation-perfusion scintigraphy: an intra-modality and inter-modality agreement study. J Magn Reson Imaging 15(4):386–394

Bankier AA, O'Donnell CR, Mai VM, Storey P, De Maertelaer V, Edelman RR et al (2004) Impact of lung volume on MR signal intensity changes of the lung parenchyma. J Magn Reson Imaging 20(6):961–966

Bauman G, Scholz A, Rivoire J, Terekhov M, Friedrich J, de Oliveira A et al (2013) Lung ventilation- and perfusion-weighted Fourier decomposition magnetic resonance imaging: in vivo validation with hyperpolarized 3He and dynamic contrast-enhanced MRI. Magn Reson Med 69(1):229–237. doi:10.1002/mrm.24236

van Beek EJ, Wild JM, Kauczor HU, Schreiber W, Mugler JP III, de Lange EE (2004) Functional MRI of the lung using hyperpolarized 3-helium gas. J Magn Reson Imaging 20(4):540–554

van Beek EJ, Dahmen AM, Stavngaard T, Gast KK, Heussel CP, Krummenauer F et al (2009) Hyperpolarised 3He MRI versus HRCT in COPD and normal volunteers: PHIL trial. Eur Respir J 34(6):1311–1321. doi:10.1183/09031936.00138508

Biederer J, Both M, Graessner J, Liess C, Jakob P, Reuter M et al (2003) Lung morphology: fast MR imaging assessment with a volumetric interpolated breath-hold technique: initial experience with patients. Radiology 226(1):242–249

Boxt LM (1996) MR imaging of pulmonary hypertension and right ventricular dysfunction. Magn Reson Imaging Clin N Am 4(2):307–325

Bryant M, Ley S, Eberhardt R, Menezes R, Herth F, Sedlaczek O et al (2015) Assessment of the relationship between morphological emphysema phenotype and corresponding pulmonary perfusion pattern on a segmental level. Eur Radiol 25(1):72–80. doi:10.1007/s00330-014-3385-5

Budev MM, Arroliga AC, Wiedemann HP, Matthay RA (2003) Cor pulmonale: an overview. Semin Respir Crit Care Med 24(3):233–244

Cluzel P, Similowski T, Chartrand-Lefebvre C, Zelter M, Derenne JP, Grenier PA (2000) Diaphragm and chest wall: assessment of the inspiratory pump with MR imaging-preliminary observations. Radiology 215(2):574–583

Conradi MS, Yablonskiy DA, Woods JC, Gierada DS, Jacob RE, Chang YV et al (2005) 3He diffusion MRI of the lung. Acad Radiol 12(11):1406–1413

Coxson HO, Leipsic J, Parraga G, Sin DD (2014) Using pulmonary imaging to move chronic obstructive pulmonary disease beyond FEV1. Am J Respir Crit Care med 190(2):135–144. doi:10.1164/rccm.201402-0256PP

Decramer M (1997) Hyperinflation and respiratory muscle interaction. Eur Respir J 10(4):934–941

Diaz S, Casselbrant I, Piitulainen E, Magnusson P, Peterson B, Wollmer P et al (2009) Validity of apparent diffusion coefficient hyperpolarized 3He-MRI using MSCT and pulmonary function tests as references. Eur J Radiol 71(2):257–263. doi:10.1016/j.ejrad.2008.04.013

Edelman RR, Hatabu H, Tadamura E, Li W, Prasad PV (1996) Noninvasive assessment of regional ventilation in the human lung using oxygen-enhanced magnetic resonance imaging. Nat Med 2(11):1236–1239

Eichinger M, Tetzlaff R, Puderbach M, Woodhouse N, Kauczor HU (2007) Proton magnetic resonance imaging for assessment of lung function and respiratory dynamics. Eur J Radiol 64(3):329–334

Fain S, Schiebler ML, McCormack DG, Parraga G (2010) Imaging of lung function using hyperpolarized helium-3 magnetic resonance imaging: review of current and emerging translational methods and applications. J Magn Reson Imaging 32(6):1398–1408. doi:10.1002/jmri.22375

Fan L, Xia Y, Guan Y, Yu H, Zhang TF, Liu SY et al (2013) Capability of differentiating smokers with normal pulmonary function from COPD patients: a comparison of CT pulmonary volume analysis and MR perfusion imaging. Eur Radiol 23(5):1234–1241. doi:10.1007/s00330-012-2729-2

Fink C, Puderbach M, Bock M, Lodemann KP, Zuna I, Schmahl A et al (2004) Regional lung perfusion: assessment with partially parallel three-dimensional MR imaging. Radiology 231(1):175–184

Fink C, Ley S, Kroeker R, Requardt M, Kauczor HU, Bock M (2005) Time-resolved contrast-enhanced three-dimensional magnetic resonance angiography of the chest: combination of parallel imaging with view sharing (TREAT). Investig Radiol 40(1):40–48

Gast KK, Viallon M, Eberle B, Lill J, Puderbach MU, Hanke AT et al (2002) MRI in lung transplant recipients using hyperpolarized (3)He: comparison with CT. J Magn Reson Imaging 15(3):268–274

Gast KK, Puderbach MU, Rodriguez I, Eberle B, Markstaller K, Knitz F et al (2003) Distribution of ventilation in lung transplant recipients: evaluation by dynamic 3He-MRI with lung motion correction. Investig Radiol 38(6):341–348

Gatehouse PD, Keegan J, Crowe LA, Masood S, Mohiaddin RH, Kreitner KF et al (2005) Applications of phase-contrast flow and velocity imaging in cardiovascular MRI. Eur Radiol 15(10):2172–2184

Gierada DS, Saam B, Yablonskiy D, Cooper JD, Lefrak SS, Conradi MS (2000) Dynamic echo planar MR imaging of lung ventilation with hyperpolarized (3)He in normal subjects and patients with severe emphysema. NMR Biomed 13(4):176–181

Guenther D, Eberle B, Hast J, Lill J, Markstaller K, Puderbach M et al (2000) (3)He MRI in healthy volunteers: preliminary correlation with smoking history and lung volumes. NMR Biomed 13(4):182–189

Gust R, Kozlowski J, Stephenson AH, Schuster DP (1998) Synergistic hemodynamic effects of low-dose endotoxin and acute lung injury. Am J Respir Crit Care Med 157(6 Pt 1):1919–1926

Henderson AC, Ingenito EP, Salcedo ES, Moy ML, Reilly JJ, Lutchen KR (2007) Dynamic lung mechanics in late-stage emphysema before and after lung volume reduction surgery. Respir Physiol Neurobiol 155(3):234–242

Heussel CP, Ley S, Biedermann A, Rist A, Gast KK, Schreiber WG et al (2004) Respiratory lumenal change of the pharynx and trachea in normal subjects and COPD patients: assessment by cine-MRI. Eur Radiol 14(12):2188–2197

Hoffman EA, Lynch DA, Barr RG, van Beek EJ, Parraga G (2016) Pulmonary CT and MRI phenotypes that help explain chronic pulmonary obstruction disease pathophysiology and outcomes. J Magn Reson Imaging 43(3):544–557. doi:10.1002/jmri.25010

Hogg JC, Chu F, Utokaparch S, Woods R, Elliott WM, Buzatu L et al (2004) The nature of small-airway obstruction in chronic obstructive pulmonary disease. N Engl J Med 350(26):2645–2653

Horn FC, Tahir BA, Stewart NJ, Collier GJ, Norquay G, Leung G et al (2014) Lung ventilation volumetry with same-breath acquisition of hyperpolarized gas and proton MRI. NMR Biomed 27(12):1461–1467. doi:10.1002/nbm.3187

Hueper K, Vogel-Claussen J, Parikh MA, Austin JH, Bluemke DA, Carr J et al (2015) Pulmonary microvascular blood flow in mild chronic obstructive pulmonary disease and emphysema. The MESA COPD study. Am J Respir Crit Care Med 192(5):570–580. doi:10.1164/rccm.201411-2120OC

Iwasawa T, Yoshiike Y, Saito K, Kagei S, Gotoh T, Matsubara S (2000) Paradoxical motion of the hemi-diaphragm in patients with emphysema. J Thorac Imaging 15(3):191–195

Iwasawa T, Kagei S, Gotoh T, Yoshiike Y, Matsushita K, Kurihara H et al (2002) Magnetic resonance analysis of abnormal diaphragmatic motion in patients with emphysema. Eur Respir J 19(2):225–231

Iwasawa T, Takahashi H, Ogura T, Asakura A, Gotoh T, Kagei S et al (2007) Correlation of lung parenchymal MR signal intensity with pulmonary function tests and quantitative computed tomography (CT) evaluation: a pilot study. J Magn Reson Imaging 26(6):1530–1536

Iwasawa T, Takahashi H, Ogura T, Asakura A, Gotoh T, Shibata H et al (2011) Influence of the distribution of emphysema on diaphragmatic motion in patients with chronic obstructive pulmonary disease. Jpn J Radiol 29(4):256–264. doi:10.1007/s11604-010-0552-8

Jang YM, Oh YM, Seo JB, Kim N, Chae EJ, Lee YK et al (2008) Quantitatively assessed dynamic contrast-enhanced magnetic resonance imaging in patients with chronic obstructive pulmonary disease: correlation of perfusion parameters with pulmonary function test and quantitative computed tomography. Investig Radiol 43(6):403–410. doi:10.1097/RLI.0b013e31816901ab

Jobst BJ, Wielputz MO, Triphan SM, Anjorin A, Ley-Zaporozhan J, Kauczor HU et al (2015a) Morpho-functional 1H-MRI of the lung in COPD: short-term test-retest reliability. PLoS One 10(9):e0137282. doi:10.1371/journal.pone.0137282

Jobst BJ, Triphan SM, Sedlaczek O, Anjorin A, Kauczor HU, Biederer J et al (2015b) Functional lung MRI in chronic obstructive pulmonary disease: comparison of T1 mapping, oxygen-enhanced T1 mapping and dynamic contrast enhanced perfusion. PLoS One 10(3):e0121520. doi:10.1371/journal.pone.0121520

Kauczor HU, Hofmann D, Kreitner KF, Nilgens H, Surkau R, Heil W et al (1996) Normal and abnormal pulmonary ventilation: visualization at hyperpolarized He-3 MR imaging. Radiology 201(2):564–568

Kaushik SS, Cleveland ZI, Cofer GP, Metz G, Beaver D, Nouls J et al (2011) Diffusion-weighted hyperpolarized 129Xe MRI in healthy volunteers and subjects with chronic obstructive pulmonary disease. Magn Reson Med 65(4):1154–1165. doi:10.1002/mrm.22697

Kirby M, Mathew L, Wheatley A, Santyr GE, McCormack DG, Parraga G (2010) Chronic obstructive pulmonary disease: longitudinal hyperpolarized (3)He MR imaging. Radiology 256(1):280–289. doi:10.1148/radiol.10091937

Kirby M, Mathew L, Heydarian M, Etemad-Rezai R, McCormack DG, Parraga G (2011) Chronic obstructive pulmonary disease: quantification of bronchodilator effects by using hyperpolarized (3)He MR imaging. Radiology 261(1):283–292. doi:10.1148/radiol.11110403

Kirby M, Svenningsen S, Owrangi A, Wheatley A, Farag A, Ouriadov A et al (2012a) Hyperpolarized 3He and 129Xe MR imaging in healthy volunteers and patients with chronic obstructive pulmonary disease. Radiology 265(2):600–610. doi:10.1148/radiol.12120485

Kirby M, Heydarian M, Wheatley A, McCormack DG, Parraga G (2012b) Evaluating bronchodilator effects in chronic obstructive pulmonary disease using diffusion-weighted hyperpolarized helium-3 magnetic resonance imaging. J Appl Physiol (1985) 112(4):651–657. doi:10.1152/japplphysiol.01295.2011

Kirby M, Svenningsen S, Kanhere N, Owrangi A, Wheatley A, Coxson HO et al (2013) Pulmonary ventilation visualized using hyperpolarized helium-3 and xenon-129 magnetic resonance imaging: differences in COPD and relationship to emphysema. J Appl Physiol (1985) 114(6):707–715. doi:10.1152/japplphysiol.01206.2012

Kohlmann P, Strehlow J, Jobst B, Krass S, Kuhnigk JM, Anjorin A et al (2015) Automatic lung segmentation method for MRI-based lung perfusion studies of patients with chronic obstructive pulmonary disease. Int J Comput Assist Radiol Surg 10(4):403–417. doi:10.1007/s11548-014-1090-0

Kruger SJ, Nagle SK, Couch MJ, Ohno Y, Albert M, Fain SB (2016) Functional imaging of the lungs with gas agents. J Magn Reson Imaging 43(2):295–315. doi:10.1002/jmri.25002

Lehmann F, Knitz F, Weiler N, Gast KK, Ley S, Schmiedeskamp J et al (2004) A software tool for analysis and quantification of regional pulmonary ventilation using dynamic hyperpolarised-(3) He-MRI. Fortschr Röntgenstr 176(10):1399–1408

Ley S, Zaporozhan J, Morbach A, Eberle B, Gast KK, Heussel CP et al (2004a) Functional evaluation of emphysema using diffusion-weighted 3Helium-

magnetic resonance imaging, high-resolution computed tomography, and lung function tests. Investig Radiol 39(7):427–434

Ley S, Fink C, Puderbach M, Plathow C, Risse F, Kreitner KF et al (2004b) Contrast-enhanced 3D MR perfusion of the lung: application of parallel imaging technique in healthy subjects. Fortschr Röntgenstr 176(3):330–334

Ley S, Puderbach M, Risse F, Ley-Zaporozhan J, Eichinger M, Takenaka D et al (2007) Impact of oxygen inhalation on the pulmonary circulation: assessment by magnetic resonance (MR)-perfusion and MR-flow measurements. Investig Radiol 42(5):283–290

Ley-Zaporozhan J, van Beek EJ (2010) Imaging phenotypes of chronic obstructive pulmonary disease. J Magn Reson Imaging 32(6):1340–1352. doi:10.1002/jmri.22376

Ley-Zaporozhan J, Ley S, Eberhardt R, Weinheimer O, Fink C, Puderbach M et al (2007) Assessment of the relationship between lung parenchymal destruction and impaired pulmonary perfusion on a lobar level in patients with emphysema. Eur J Radiol 63(1):76–83

Ley-Zaporozhan J, Puderbach M, Kauczor HU (2008) MR for the evaluation of obstructive pulmonary disease. Magn Reson Imaging Clin N Am 16(2):291–308

Ley-Zaporozhan J, Ley S, Eberhardt R, Kauczor HU, Heussel CP (2010) Visualization of morphological parenchymal changes in emphysema: comparison of different MRI sequences to 3D-HRCT. Eur J Radiol 73(1):43–49. doi:10.1016/j.Ejrad.2008.09.029

Ley-Zaporozhan J, Molinari F, Risse F, Puderbach M, Schenk JP, Kopp-Schneider A et al (2011) Repeatability and reproducibility of quantitative whole-lung perfusion magnetic resonance imaging. J Thorac Imaging 26(3):230–239. doi:10.1097/RTI.0b013e3181e48cc36

Loffler R, Muller CJ, Peller M, Penzkofer H, Deimling M, Schwaiblmair M et al (2000) Optimization and evaluation of the signal intensity change in multisection oxygen-enhanced MR lung imaging. Magn Reson Med 43(6):860–866

Ma W, Sheikh K, Svenningsen S, Pike D, Guo F, Etemad-Rezai R et al (2015) Ultra-short echo-time pulmonary MRI: evaluation and reproducibility in COPD subjects with and without bronchiectasis. J Magn Reson Imaging 41(5):1465–1474. doi:10.1002/jmri.24680

Marshall H, Deppe MH, Parra-Robles J, Hillis S, Billings CG, Rajaram S et al (2012) Direct visualisation of collateral ventilation in COPD with hyperpolarised gas MRI. Thorax 67(7):613–617. doi:10.1136/thoraxjnl-2011-200864

Mathew L, Evans A, Ouriadov A, Etemad-Rezai R, Fogel R, Santyr G et al (2008) Hyperpolarized 3He magnetic resonance imaging of chronic obstructive pulmonary disease: reproducibility at 3.0 tesla. Acad Radiol 15(10):1298–1311. doi:10.1016/j.acra.2008.04.019

Mathew L, Kirby M, Etemad-Rezai R, Wheatley A, McCormack DG, Parraga G (2011) Hyperpolarized (3)He magnetic resonance imaging: preliminary evaluation of phenotyping potential in chronic obstructive pulmonary disease. Eur J Radiol 79(1):140–146. doi:10.1016/j.ejrad.2009.10.028

Molinari F, Fink C, Risse F, Tuengerthal S, Bonomo L, Kauczor HU (2006) Assessment of differential pulmonary blood flow using perfusion magnetic resonance imaging: comparison with radionuclide perfusion Scintigraphy. Investig Radiol 41(8):624–630

Moonen M, Xu J, Johansson A, Thylen A, Bake B (2005) Effects of lung volume reduction surgery on distribution of ventilation and perfusion. Clin Physiol Funct Imaging 25(3):152–157

Morbach AE, Gast KK, Schmiedeskamp J, Dahmen A, Herweling A, Heussel CP et al (2005) Diffusion-weighted MRI of the lung with hyperpolarized helium-3: a study of reproducibility. J Magn Reson Imaging 21(6):765–774

Morgan AR, Parker GJ, Roberts C, Buonaccorsi GA, Maguire NC, Hubbard Cristinacce PL et al (2014) Feasibility assessment of using oxygen-enhanced magnetic resonance imaging for evaluating the effect of pharmacological treatment in COPD. Eur J Radiol 83(11):2093–2101. doi:10.1016/j.Ejrad.2014.08.004

Morino S, Toba T, Araki M, Azuma T, Tsutsumi S, Tao H et al (2006) Noninvasive assessment of pulmonary emphysema using dynamic contrast-enhanced magnetic resonance imaging. Exp Lung Res 32(1–2):55–67

Muller CJ, Schwaiblmair M, Scheidler J, Deimling M, Weber J, Loffler RB et al (2002) Pulmonary diffusing capacity: assessment with oxygen-enhanced lung MR imaging preliminary findings. Radiology 222(2):499–506

Ohno Y, Chen Q, Hatabu H (2001) Oxygen-enhanced magnetic resonance ventilation imaging of lung. Eur J Radiol 37(3):164–171

Ohno Y, Sugimura K, Hatabu H (2003) Clinical oxygen-enhanced magnetic resonance imaging of the lung. Top Magn Reson Imaging 14(3):237–243

Ohno Y, Hatabu H, Higashino T, Takenaka D, Watanabe H, Nishimura Y et al (2004a) Dynamic perfusion MRI versus perfusion scintigraphy: prediction of postoperative lung function in patients with lung cancer. AJR Am J Roentgenol 182(1):73–78

Ohno Y, Hatabu H, Murase K, Higashino T, Kawamitsu H, Watanabe H et al (2004b) Quantitative assessment of regional pulmonary perfusion in the entire lung using three-dimensional ultrafast dynamic contrast-enhanced magnetic resonance imaging: preliminary

experience in 40 subjects. J Magn Reson Imaging 20(3):353–365

Ohno Y, Koyama H, Nogami M, Takenaka D, Matsumoto S, Obara M et al (2008a) Dynamic oxygen-enhanced MRI versus quantitative CT: pulmonary functional loss assessment and clinical stage classification of smoking-related COPD. AJR Am J Roentgenol 190(2):W93–W99. doi:10.2214/AJR.07.2511

Ohno Y, Iwasawa T, Seo JB, Koyama H, Takahashi H, Oh YM et al (2008b) Oxygen-enhanced magnetic resonance imaging versus computed tomography: multicenter study for clinical stage classification of smoking-related chronic obstructive pulmonary disease. Am J Respir Crit Care Med 177(10):1095–1102. doi:10.1164/rccm.200709-1322OC

Ohno Y, Koyama H, Yoshikawa T, Matsumoto K, Takahashi M, Van Cauteren M et al (2011) T2* measurements of 3-T MRI with ultrashort TEs: capabilities of pulmonary function assessment and clinical stage classification in smokers. AJR Am J Roentgenol 197(2):W279–W285. doi:10.2214/AJR.10.5350

Ohno Y, Koyama H, Yoshikawa T, Matsumoto K, Aoyama N, Onishi Y et al (2012) Comparison of capability of dynamic O(2)-enhanced MRI and quantitative thin-section MDCT to assess COPD in smokers. Eur J Radiol 81(5):1068–1075. doi:10.1016/j.ejrad.2011.02.004

Ohno Y, Nishio M, Koyama H, Yoshikawa T, Matsumoto S, Seki S et al (2014) Pulmonary 3 T MRI with ultrashort TEs: influence of ultrashort echo time interval on pulmonary functional and clinical stage assessments of smokers. J Magn Reson Imaging 39(4):988–997. doi:10.1002/jmri.24232

Pennati F, Quirk JD, Yablonskiy DA, Castro M, Aliverti A, Woods JC (2014) Assessment of regional lung function with multivolume (1)H MR imaging in health and obstructive lung disease: comparison with (3)He MR imaging. Radiology 273(2):580–590. doi:10.1148/radiol.14132470

Plathow C, Fink C, Ley S, Puderbach M, Eichinger M, Schmahl A et al (2004) Measurement of diaphragmatic length during the breathing cycle by dynamic MRI: comparison between healthy adults and patients with an intrathoracic tumor. Eur Radiol 14(8):1392–1399

Plathow C, Schoebinger M, Fink C, Ley S, Puderbach M, Eichinger M et al (2005) Evaluation of lung volumetry using dynamic three-dimensional magnetic resonance imaging. Investig Radiol 40(3):173–179

Rabe KF, Hurd S, Anzueto A, Barnes PJ, Buist SA, Calverley P et al (2007) Global strategy for the diagnosis, management, and prevention of chronic obstructive pulmonary disease: GOLD executive summary. Am J Respir Crit Care Med 176(6):532–555

Roach DJ, Cremillieux Y, Serai SD, Thomen RP, Wang H, Zou Y et al (2016) Morphological and quantitative evaluation of emphysema in chronic obstructive pulmonary disease patients: a comparative study of MRI with CT. J Magn Reson Imaging 44(6):1656–1663. doi:10.1002/jmri.25309

Rosenkranz S (2007) Pulmonary hypertension: current diagnosis and treatment. Clin Res Cardiol 96:527–541

Salerno M, Altes TA, Brookeman JR, de Lange EE, Mugler JP III (2001) Dynamic spiral MRI of pulmonary gas flow using hyperpolarized (3)He: preliminary studies in healthy and diseased lungs. Magn Reson Med 46(4):667–677

Salerno M, de Lange EE, Altes TA, Truwit JD, Brookeman JR, Mugler JP III (2002) Emphysema: hyperpolarized helium 3 diffusion MR imaging of the lungs compared with spirometric indexes – initial experience. Radiology 222(1):252–260

Sandek K, Bratel T, Lagerstrand L, Rosell H (2002) Relationship between lung function, ventilation-perfusion inequality and extent of emphysema as assessed by high-resolution computed tomography. Respir Med 96(11):934–943

Schuster DP, Marklin GF (1986) Effect of changes in inflation and blood volume on regional lung density – a PET study: 2. J Comput Assist Tomogr 10(5):730–735

Sergiacomi G, Sodani G, Fabiano S, Manenti G, Spinelli A, Konda D et al (2003) MRI lung perfusion 2D dynamic breath-hold technique in patients with severe emphysema. In vivo 17(4):319–324

Sergiacomi G, Taglieri A, Chiaravalloti A, Calabria E, Arduini S, Tosti D et al (2014) Acute COPD exacerbation: 3 T MRI evaluation of pulmonary regional perfusion – preliminary experience. Respir Med 108(6):875–882. doi:10.1016/j.rmed.2014.04.002

Stadler A, Jakob PM, Griswold M, Stiebellehner L, Barth M, Bankier AA (2008) T(1) mapping of the entire lung parenchyma: influence of respiratory phase and correlation to lung function test results in patients with diffuse lung disease. Magn Reson med 59(1):96–101

Suga K, Tsukuda T, Awaya H, Takano K, Koike S, Matsunaga N et al (1999) Impaired respiratory mechanics in pulmonary emphysema: evaluation with dynamic breathing MRI. J Magn Reson Imaging 10(4):510–520

Swift AJ, Wild JM, Fichele S, Woodhouse N, Fleming S, Waterhouse J et al (2005) Emphysematous changes and normal variation in smokers and COPD patients using diffusion 3He MRI. Eur J Radiol 54(3):352–358

Swift AJ, Woodhouse N, Fichele S, Siedel J, Mills GH, van Beek EJ et al (2007) Rapid lung volumetry using ultrafast dynamic magnetic resonance imaging during forced vital capacity maneuver: correlation with spirometry. Investig Radiol 42(1):37–41

Szilasi M, Dolinay T, Nemes Z, Strausz J (2006) Pathology of chronic obstructive pulmonary disease. Pathol Oncol Res 12(1):52–60

Thabut G, Dauriat G, Stern JB, Logeart D, Levy A, Marrash-Chahla R et al (2005) Pulmonary hemody-

namics in advanced COPD candidates for lung volume reduction surgery or lung transplantation. Chest 127(5):1531–1536

Virgincar RS, Cleveland ZI, Kaushik SS, Freeman MS, Nouls J, Cofer GP et al (2013) Quantitative analysis of hyperpolarized 129Xe ventilation imaging in healthy volunteers and subjects with chronic obstructive pulmonary disease. NMR Biomed 26(4):424–435. doi:10.1002/nbm.2880

Vonk Noordegraaf A, Marcus JT, Roseboom B, Postmus PE, Faes TJ, de Vries PM (1997) The effect of right ventricular hypertrophy on left ventricular ejection fraction in pulmonary emphysema. Chest 112(3):640–645

Vonk-Noordegraaf A, Marcus JT, Holverda S, Roseboom B, Postmus PE (2005) Early changes of cardiac struc-

ture and function in COPD patients with mild hypoxemia. Chest 127(6):1898–1903

Weitzenblum E, Chaouat A (2005) Severe pulmonary hypertension in COPD: is it a distinct disease? Chest 127(5):1480–1482

Wild JM, Paley MN, Kasuboski L, Swift A, Fichele S, Woodhouse N et al (2003) Dynamic radial projection MRI of inhaled hyperpolarized 3He gas. Magn Reson Med 49(6):991–997

Zaporozhan J, Ley S, Gast KK, Schmiedeskamp J, Biedermann A, Eberle B et al (2004) Functional analysis in single-lung transplant recipients: a comparative study of high-resolution CT, (3)He-MRI, and pulmonary function tests. Chest 125(1):173–181

Magnetic Resonance Imaging of the Lung: Cystic Fibrosis

Scott K. Nagle, Michael Puderbach,
Monika Eichinger, and Talissa A. Altes

Contents

S.K. Nagle (✉)
Department of Radiology, University of Wisconsin,
Madison, WI, USA
e-mail: SNagle@uwhealth.org

M. Puderbach
Department of Radiology, Community Hospital Bad
Langensalza, Bad Langensalza, Germany

Translational Lung Research Center Heidelberg
(TLRC), German Center for Lung Research (DZL),
Heidelberg, Germany

Department of Diagnostic and Interventional
Radiology with Nuclear Medicine, Thoraxklinik at
University Hospital Heidelberg, Heidelberg, Germany

Department of Diagnostic and Interventional
Radiology, University Hospital Heidelberg,
Heidelberg, Germany

M. Eichinger
Translational Lung Research Center Heidelberg
(TLRC), German Center for Lung Research (DZL),
Heidelberg, Germany

Department of Diagnostic and Interventional
Radiology with Nuclear Medicine, Thoraxklinik at
University Hospital Heidelberg, Heidelberg, Germany

Department of Diagnostic and Interventional
Radiology, University Hospital Heidelberg,
Heidelberg, Germany

T.A. Altes
Department of Radiology, University of Missouri,
Columbia, MO, USA

Key Points

Proton MRI is able to depict the major changes
in CF lung disease in a similar way to CT,
albeit there will be shortcomings in the detec-
tion of more subtle or smaller abnormalities.
Further studies are warranted to determine
whether the additional structural detail pro-
vided by CT is necessary for the evaluation of
the severity and progression of CF lung dis-
ease. At the same time, proton and hyperpo-
larized gas MRI provide a broad spectrum of
additional functional information in CF lung
diseases that is otherwise not available to
patients and clinicians. The MRI techniques to
be applied in CF lung disease are novel and
further development and studies are required
to fully implement and assess their potential

impact in CF. It is currently unknown whether the combination of functional and structural information from MRI will be more useful than the mere structural information provided by CT in the clinical assessment of CF. It is conceivable that MRI and CT will be complementary as they have different advantages and disadvantages in elucidating the complex interrelation of lung structure and function.

1   Introduction

Cystic fibrosis (CF) is an autosomal recessive disorder caused by gene mutations of the long arm of chromosome 7. This gene codes for the cystic fibrosis transmembrane regulator-protein (CFTR), which functions as an anion channel in the cell membrane. The impaired CFTR function causes aberrations of volume and ion composition of airway surface fluid, leading to viscous secretions with the consequence of bacterial colonization, chronic lung infection, airway obstruction, and consecutive destruction of the lung parenchyma (Gibson et al. 2003). Despite improved understanding of the underlying pathophysiology and the introduction of new therapies, CF remains one of the most life-shortening inherited diseases in the Caucasian population. The median survival of CF patients approaches 40 years (Stern et al. 2008; Beall 2005). Although CF affects most body systems, the majority of morbidity and mortality in CF patients is due to chronic progressive lung disease.

The standard clinical tool for monitoring CF lung disease is pulmonary function testing. Pulmonary function tests provide a global measure of airflow obstruction and/or restriction, but provide no regional information about the lung function or information about lung structure. Although extremely useful, pulmonary function tests are known to be relatively insensitive to early lung disease and to small changes in the course of the disease. Furthermore, pulmonary function tests are dependent upon the effort and compliance of the patient and are difficult for young children

to perform. Yet pulmonary function tests remain one of the primary outcome measures in CF lung disease. A decrease of Forced Expiratory Volume in 1 s (FEV_1) was shown to be the most important prognostic factor for the course of the disease and the most significant predictor of mortality in a study of 673 patients with CF (Kerem et al. 1992). Over the last decade and particularly within the last 5 years, multiple breath washout techniques such as lung clearance index (LCI) have shown promise in overcoming the limitations of conventional spirometry in mild disease and in very young patients. Several authors have published data showing that LCI is more sensitive than FEV_1 to detect and grade lung disease in CF children (Lum et al. 2007; Aurora et al. 2005; Amin et al. 2010; Belessis et al. 2012; Hoo et al. 2012; Davies et al. 2013; Subbarao et al. 2013; Stahl et al. 2014).

The standard radiological tools for monitoring of lung disease in CF patients are chest x-ray and thin-section computed tomography (CT), evaluated using different scoring systems, e.g., the Chrispin-Norman Score (Chrispin and Norman 1974) or Wisconsin Score (Weatherly et al. 1993) for chest x-ray and the Bhalla (Bhalla et al. 1991), Helbich (Helbich et al. 1999), or Brody (Brody et al. 2006) Scores for thin-section CT. Chest CT provides submillimeter resolution images of lung structure and has been proposed as a possible outcome measure for CF lung disease (Brody et al. 2005). CT has been shown to be more sensitive to early CF lung disease than pulmonary function testing, likely due to the regional nature of the information obtained (Brody et al. 2005). Despite the promising early studies related to the use of CT scanning in CF, a major drawback remains the radiation exposure associated with CT (Brenner 2002; Frush et al. 2003; Huda and Vance 2007; Donadieu et al. 2007; O'Connell et al. 2012; Kuo et al. 2014). Even with more recent ultra-low-dose CT protocols involving model-based iterative reconstruction (de Jong et al. 2006; Loeve et al. 2009), there will continue to be resistance to the use of even small amounts of radiation in pediatric patient populations. Furthermore, in very young children and in those

with very mild disease, the sensitivity of existing CT scoring systems may be insufficient to detect subtle changes in disease (Thia et al. 2014). More sensitive manual scoring methods (Rosenow et al. 2015) or automated methods (DeBoer et al. 2014) are being developed to address this shortcoming, but radiation safety concerns may ultimately limit the utility of CT in CF lung disease for applications in which multiple CT scans in very young patients are required.

MRI of the chest was proposed as a potential imaging alternative in CF patients in the late 1980s (Fiel et al. 1987). At that time, MRI technology was not capable of producing comparable results to CT (Carr et al. 1995). Early studies compared low field MRI and chest x-ray or CT (Abolmaali et al. 2002). Other studies compared CT, chest x-ray, and proton MRI at 1.5 T (Puderbach et al. 2007a, b; Sileo et al. 2014; Renz et al. 2015; Tepper et al. 2016). However, the primary strength of MRI over CT, beyond its lack of ionizing radiation, is MRI's ability to depict lung *function* (e.g., ventilation and perfusion). Because cystic fibrosis affects the lungs very heterogeneously, the ability to depict the spatial distribution of functional abnormalities is a unique strength of MRI. Functional MRI techniques like oxygen-enhanced MRI (Jakob et al. 2004), hyperpolarized helium (^{3}He)-MRI (Donnelly et al. 1999; Koumellis et al. 2005; Mentore et al. 2005), or contrast-enhanced MR perfusion (Eichinger et al. 2006) have been used to assess the functional impairment of the lung in cystic fibrosis. As recent techniques have improved the ability of MRI to show lung structure, the possibility of simultaneous assessment of lung structure and function using a single cross-sectional imaging modality is becoming a reality.

Currently, research with MRI in CF lung disease lags behind that with CT, at least partially due to the tremendous range of possible MRI approaches. In the following, we review the common functional and structural findings of CF lung disease and discuss some of the emerging MRI techniques that promise to further expand the utility of MRI for assessment of cystic fibrosis lung disease.

2 Functional Lung MR Imaging

MRI can provide functional assessment of pulmonary hemodynamics and ventilation. Pulmonary perfusion imaging typically requires the administration of gadolinium-based intravenous contrast. An inhaled contrast agent, either oxygen or a hyperpolarized noble gas, is required for MR lung ventilation imaging.

2.1 Pulmonary Perfusion

In CF, regional ventilatory defects cause changes in regional lung perfusion due to the reflex of hypoxic vasoconstriction or tissue destruction. A variety of MRI methods have been employed to assess lung perfusion, including methods that rely on the endogenous signal from blood (Mai and Berr 1999) and others that require the administration of intravenous contrast (Hatabu et al. 1996; Levin and Hatabu 2004). Using a contrast-enhanced 3D MRI acquisition in 11 children with CF, it was found that MRI-perfusion defects correlated with the degree of tissue destruction (Fig. 1) (Eichinger et al. 2006). More recent, larger studies support the utility of perfusion MRI in detecting treatment effect in young children (Wielpütz et al. 2014; Stahl et al. 2017). Since the perfusion abnormalities in cystic fibrosis are likely to be matched to corresponding ventilation defects, it is possible that perfusion MRI and ventilation MRI may serve as equivalent biomarkers in this particular disease. In a study of 30 CF patients, ten of whom returned for a repeat scan within 1–2 weeks, perfusion MRI and ventilation MRI obtained using hyperpolarized ^{3}He gas performed similarly in differentiating a wide spectrum of CF disease severity, using FEV_1 as a reference standard (Fig. 2) (Poranski et al. 2016). Since perfusion MRI is much more widely available than hyperpolarized gas ventilation MRI, this could enable more widespread incorporation of functional measures into MRI protocols for assessing CF lung disease and treatment response. By combining time-resolved perfusion MRI with a 3D radial ultrashort echo time acquisition, it is possible to simultaneously obtain both perfusion
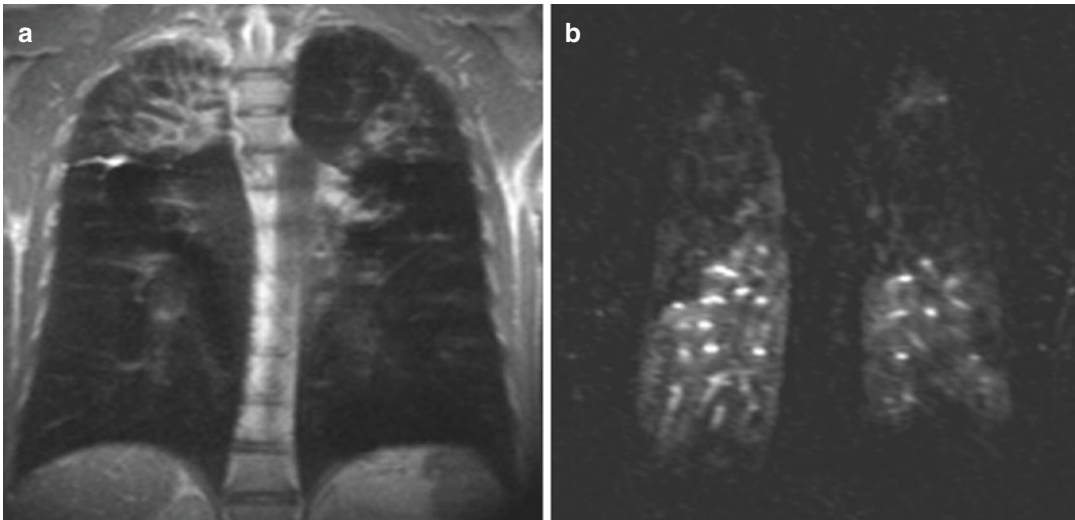
Fig. 1 (**a**) T2 weighted MR image of the patient shown in Fig. 2 showing lobar destruction of the right upper lobe and severe bronchiectasis and wall thickening of the left lobe. (**b**) MR-Perfusion map of the corresponding lung region showing large perfusion defects in both upper lobes and an inho-mogeneous perfusion in the peripheral lower lobe zones. Reprinted with permission of the American Thoracic Society. Copyright (c) 2017 American Thoracic Society. (Altes et al. 2007a). Proceedings of the American Thoracic Society is an official journal of the American Thoracic Society
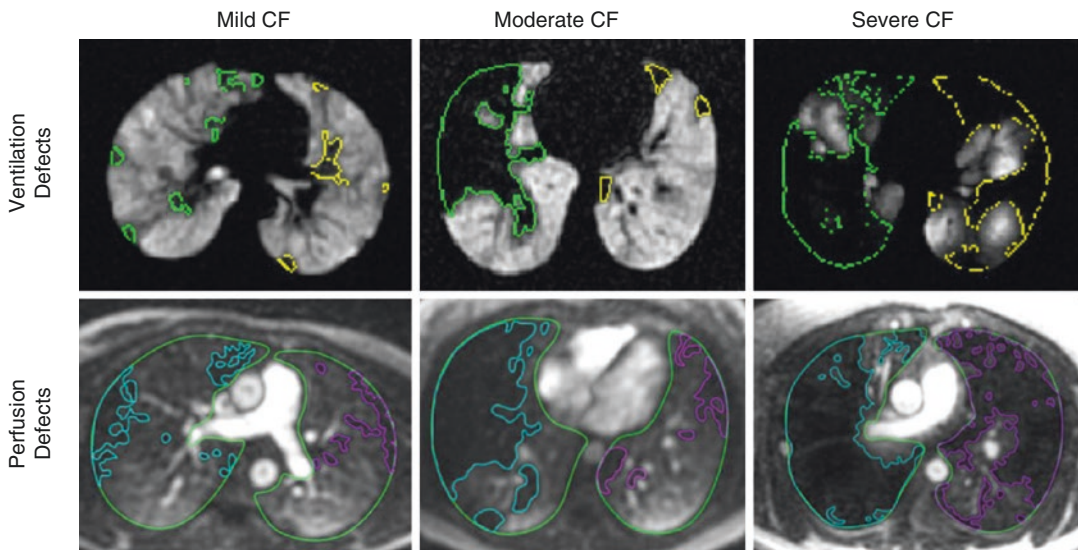
Fig. 2 Ventilation defects observed with hyperpolarized gas MRI (*top row*) are well matched to perfusion defects observed with dynamic contrast-enhanced perfusion MRI

and high resolution structural information during a single breath-hold (Bell et al. 2015a).

While it is numerically possible to calculate pulmonary blood flow (PBF), pulmonary blood volume (PBV), and mean transit time (MTT) maps from dynamic pulmonary perfusion datasets, the fact that the signal intensity in the image is not linearly proportional to the concentration of gadolinium in the blood makes absolute quantification very challenging (Puderbach et al. 2008; Bell et al. 2015b). However, if only qualitative detection and comparison of perfusion defects, then *relative* PBF and PBV can be very useful. Indeed, in the CF literature, the

majority of analyses using perfusion MRI use a maximum intensity projection through the time dimension or subtracted images (peak enhancement phase—pre-contrast phase) as the means for qualitatively identifying regions of relatively decreased perfusion.

2.2 Pulmonary Flow Measurements

Parenchymal destruction can lead to dilatation and flow augmentation of bronchial arteries. As bronchial arteries are part of the systemic circulation, they do not contribute to blood oxygenation. Thus, a higher flow in the bronchial arteries leads to a shunt volume, which can be assessed by MRI-based flow measurements. Decreased peak blood flow velocities in the right and left pulmonary arteries were found in ten CF patients as compared with 15 healthy volunteers, and this may represent early development of pulmonary hypertension in this patient group (Ley et al. 2005). A more recent study of 16 CF patients and 17 age- and sex-matched non-CF controls showed that aortopulmonary blood flow as measured using phase-contrast MRI was inversely correlated with FEV_1 (Fleck et al. 2013), and the authors suggest that this could serve as a sensitive marker for mild lung disease. In addition, pulmonary hemorrhage is a known risk of cystic fibrosis and may be related to bleeding from bronchial arteries; therefore, increased bronchial relative to pulmonary artery flow may provide useful prognostic information regarding the risk of subsequent pulmonary hemorrhage. However, the full clinical significance of the systemic arterial shunt volume is not yet known and direct comparison with the leading global biomarker for mild impairment of lung function, lung clearance index, has not yet been performed.

2.3 Oxygen-Enhanced MRI

Gaseous molecular oxygen is weakly paramagnetic and serves, if inhaled in high concentrations, as a contrast medium inducing a dose-dependent T1-signal increase which can be used to assess lung ventilation (Edelman et al. 1996). In a preliminary study of five CF patients and five healthy volunteers, the lungs of the CF patients had an inhomogeneous appearance following the inhalation of high oxygen concentrations suggesting inhomogeneous lung ventilation (Jakob et al. 2004). Since oxygen is quickly soluble in blood, the oxygen-enhanced MR images depict a combination of ventilation, diffusion, and perfusion (Keilholz et al. 2002). As with time-resolved perfusion imaging, it is possible to use 3D radial ultrashort echo time techniques to simultaneously acquire both structural and functional images using a single acquisition protocol (Kruger et al. 2014). One of the difficulties with oxygen-enhanced MRI in general is that there is a relatively low difference in signal from the lung parenchyma with 21% versus 100% inspired oxygen concentration. Furthermore, there is variability in oxygen delivery through different face mask systems, with peak inspired oxygen concentration rarely reaching the nominal 100% target. This results in a relatively low signal-to-noise level in the resulting MR oxygen-enhanced images.

2.4 Hyperpolarized Gas MRI

Hyperpolarized ^{3}He or ^{129}Xe are gaseous MRI contrast agents that, when inhaled, provide a very high MR signal from the airspaces of the lung when using dedicated coil systems. Hyperpolarized gas MRI can be used to obtain information about lung function using static spin density imaging (de Lange et al. 1999; Kauczor et al. 1996; Woodhouse et al. 2005), dynamic spin density imaging (Gast et al. 2002; Salerno et al. 2001), or oxygen-sensitive imaging (Eberle et al. 1999). In addition, lung structure at the alveolar and distal airway level can be assessed using diffusion-weighted imaging (Morbach et al. 2005; Salerno et al. 2002).

The majority of studies investigating the use of hyperpolarized gas MRI in CF have used static spin density imaging. Static spin density imaging, often referred to as ventilation imaging, is performed during a breath-hold following the inhalation of the

hyperpolarized gas (Altes et al. 2004). Well-ventilated areas of the lung receive more gas and thus appear brighter than poorly ventilated areas of the lung on the MR images. Typically, the entire lung volume can be imaged in a 4–20 s breath-hold, but the in plane spatial resolution is typically in the order of 3 mm and thus lower than with CT. Since children have smaller lungs than adults, the breath-hold duration is shorter for children, and hyperpolarized gas MRI has been successfully performed in children as young as 4 years who were able to breath-hold (Altes et al. 2008).

The first report of hyperpolarized ^{3}He MRI in CF found extensive abnormalities of ventilation on static spin density images in four subjects with moderate to severe pulmonary CF and abnormal FEV1% predicted (Donnelly et al. 1999). Also using static spin density imaging, a study of 31 subjects (16 healthy volunteers and 15 patients with CF) found the CF patients had a significantly higher number of ventilation defects on ^{3}He MRI than the normal subjects (Mentore et al. 2005). Even the four CF subjects with a normal FEV1% predicted had significantly higher ventilation defect score than the normal subjects, suggesting hyperpolarized gas MRI may be more sensitive to ventilation abnormalities than spirometry. Moderate correlations between the ventilation defect score and spirometry were found (Fig. 3). In this study, eight of the CF patients underwent a therapeutic intervention first with nebulized albuterol followed by DNase and chest physical therapy. Repeated ^{3}He MRI after ther-apy showed changes in the ventilation defect score. Thus, this study demonstrated the feasibility of using hyperpolarized ^{3}He MRI as an outcome measure in the evaluation of airway clearance techniques. Another study of 18 children with CF (age 5–17 years) confirmed that hyperpolarized ^{3}He MRI can be performed by children with CF and found moderate to weak correlations between static spin density hyperpolarized ^{3}He MRI and spirometry or chest x-ray (van Beek et al. 2007). It was the opinion of the authors that the weak correlations were the result of a greater sensitivity of hyperpolarized ^{3}He MRI to ventilatory abnormalities than spirometry or chest x-ray. Another study compared static spin density ^{3}He MRI with CT in eight adults with CF and found a strong correlation between the MRI percent ventilation and the Bhalla score (Bhalla et al. 1991) from CT (McMahon et al. 2006). Further, the correlations between hyperpolarized ^{3}He MRI and spirometry were stronger than those between CT and spirometry. Thus, this study suggests that hyperpolarized ^{3}He MRI may represent a safe alternative to CT for the evaluation of CF lung disease. Most recently, a pilot study of eight CF patients treated with ivacaftor demonstrated clear treatment effects on ^{3}He MRI on an individual basis (Fig. 4) (Altes et al. 2007b).

Due to the limited availability of ^{3}He, many research teams have been switching to the use of naturally occurring ^{129}Xe. In a recent study of 11 CF pediatric patients with mild disease and 11 healthy controls, ^{129}Xe MRI more effectively dis-

Normal	CF	CF	CF
FEV1 130%	109%	63%	35%
(%pred)			
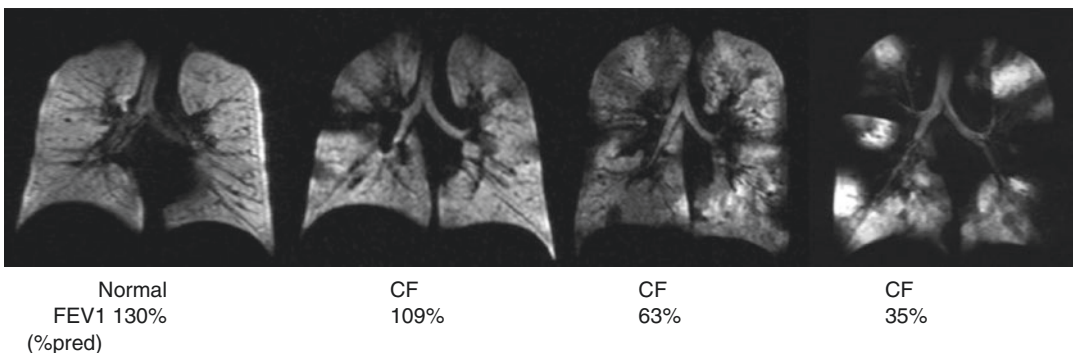
Fig. 3 Coronal hyperpolarized helium MR ventilation images from a normal subject and three different patients with CF. The CF patients have more ventilation defects than the normal subject, and the number of defects increases with worsening FEV1 (%predicted).

Reprinted with permission of the American Thoracic Society. Copyright (c) 2017 American Thoracic Society. (Altes et al. 2007a). Proceedings of the American Thoracic Society is an official journal of the American Thoracic Society
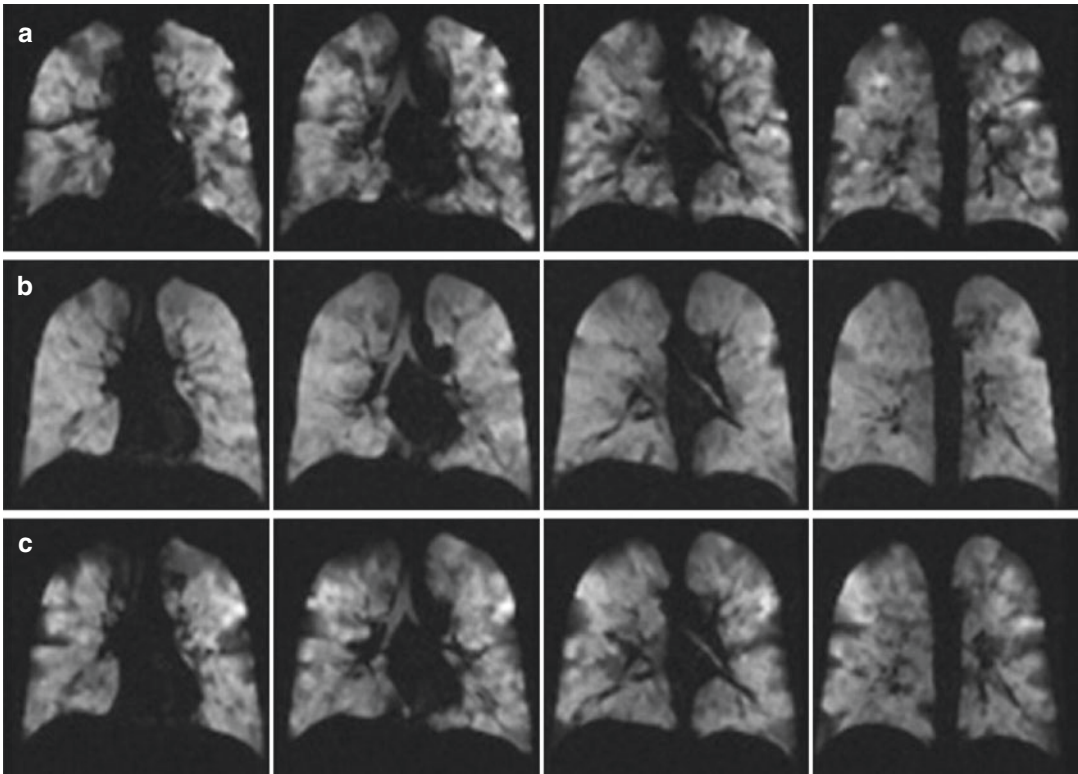
Fig. 4 Following inhalation of the hyperpolarized gas, well-ventilated lung regions appear bright white, and poorly ventilated regions (termed "ventilation defects") appear *dark gray/black*. (**a**) Baseline: ppFEV1: 62.2; TVDH: 51.7%; TVDC: 48.4%. (**b**) End of 4 weeks of ivacaftor treatment: ppFEV1: 83.0; TVDH: 27.1%; TVDC: 17.4%. (**c**) End of 2 weeks of placebo washout: ppFEV1: 71.6; TVDH: 57.4%; TVDC: 40.9%. (ppFEV1 = percent predicted forced expiratory volume in 1 s; TVDH = Total Ventilation Defect by Human; TVDC = Total Ventilation Defect by Computer). Reprinted with permission of Elsevier. (Altes 2007b)

criminated CF from normal subjects than did FEV_1 and demonstrated ventilation defects even in subjects with normal FEV_1 (Thomen et al. 2017). Unlike ^{3}He, ^{129}Xe is soluble in blood. In fact, its resonance frequency is slightly different in gaseous and blood phases, which offers the intriguing potential of using it to separately image ventilation and perfusion following a single inhalation (Mugler and Altes 2013). While initially there was some concern about potential anesthetic effects of ^{129}Xe in the pediatric population, recent literature supports the feasibility, safety, and tolerability of ^{129}Xe in patients as young as 6 years (Walkup et al. 2016).

To date, little work has been done in CF evaluating the other mechanisms of contrast possible with hyperpolarized gas MRI including dynamic ventilation (Koumellis et al. 2005), diffusion weighted, or oxygen sensitive imaging. Further, the special equipment required to perform hyperpolarized gas MRI is both expensive and not yet widely available, and hyperpolarized gas as a MRI contrast agent has not yet been approved by the Food and Drug Administration, so use of this technique is currently limited to a relatively small number of academic medical centers. More details on ^{3}He- and ^{129}Xe-MRI are discussed in the respective chapters in this book. Novel techniques for combined ventilation and perfusion imaging without application of exogenous contrast agents (e.g., Fourier Decomposition MRI) in the context of CF are also further explained in separate chapters.

3 Structural Changes of CF Lung Disease on Proton-MRI

In addition to visualization of lung function, it is possible using common proton-MRI sequences to visualize the structural changes of CF lung disease, including bronchial wall thickening, mucus
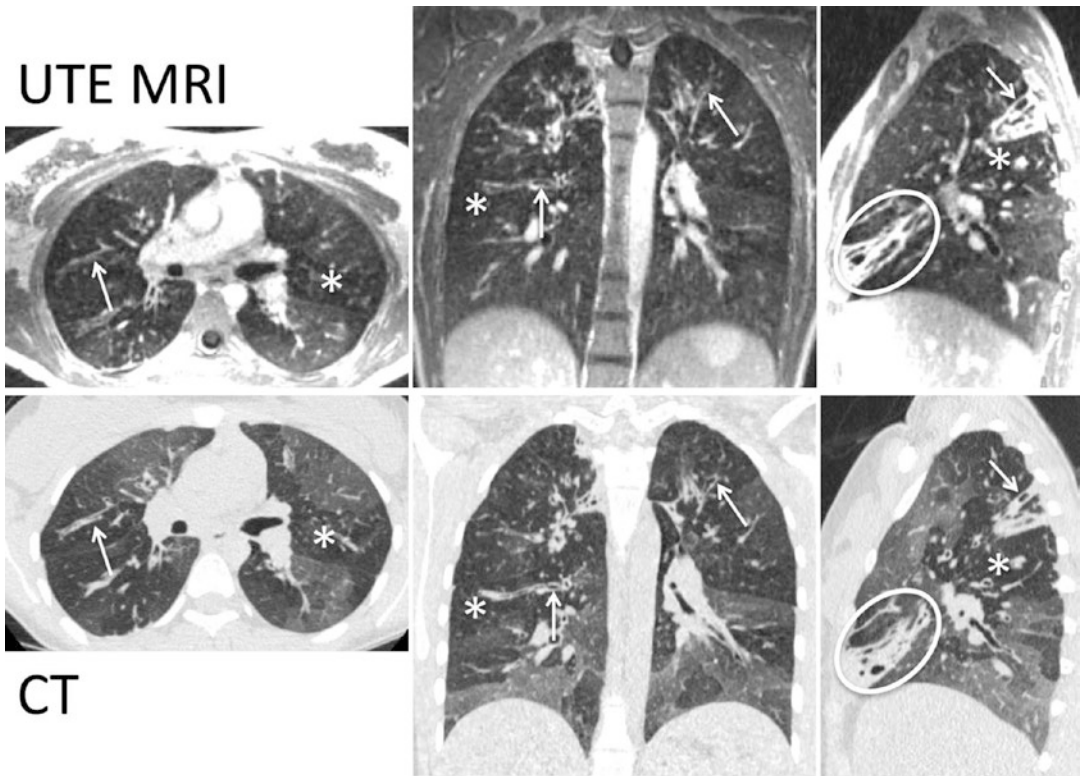
Fig. 5 Ultrashort echo time (TE < 0.1 ms) MRI of the lungs in cystic fibrosis clearly shows a mosaic pattern (*), likely to be air trapping based upon comparison with expiratory CT images, much better than conventional echo time methods. Although the UTE MRI images have slightly lower in-plane spatial resolution than CT, the depiction of bronchiectasis and bronchial wall thickening (arrows) is comparable to CT. As with conventional echo time MRI methods, consolidation (ovals) is shown well against the dark lung background. These UTE images were acquired during 5 min of quiet breathing, using retrospective respiratory gating based on respiratory bellows. Details of the pulse sequence can be found in Johnson KM, et al., Magn Res Med 70(5):1241–1250 (2013)

plugging, bronchiectasis, air fluid levels, consolidation, and segmental/lobar destruction, albeit with lower spatial and temporal resolution than with CT (Puderbach et al. 2007a). It seems likely that the lower spatial and temporal resolution of MRI will mean that MRI is less sensitive than CT to specific imaging features such as distal bronchiectasis. However, this does not necessarily mean that MRI will provide less useful information about CF since sensitivity to these imaging features may not be critical for the assessment of the overall burden of disease (Puderbach et al. 2007b). Indeed, some recent studies have shown that MRI methods approach the performance of CT (Teufel et al. 2012; Sileo et al. 2014; Renz et al. 2015; Tepper et al. 2016). Furthermore, recent improvements in ultrashort echo time MRI methods (Johnson et al. 2013; Dournes et al. 2016; Roach et al. 2016) have enabled much improved direct visualization of lung parenchyma and mosaic pattern in particular, further narrowing the gap between MRI and CT with respect to assessment of lung structure (Fig. 5) (Nagle et al. 2016).

3.1 Bronchial Wall Thickening

The visualization of bronchial wall thickening is dependent on bronchial size, bronchial wall thickness, and bronchial wall signal. In MRI studies of normal lung, only the central airways to the level of lobar bronchi are routinely visualized, and some segmental bronchi can be identified using conventional echo time methods. Emerging ultrashort echo time methods (TE < 0.1 ms) show promise in showing smaller airways. This is in contrast to CT in which the 6th to 8th generation bronchi can be iden-

tified. However in CF patients, bronchial wall thickening of small airways enhances their detectability by MRI so that small airways with thick walls can be visualized in the lung periphery (Fig. 6) (Puderbach et al. 2007a). Interestingly, the T2 weighted signal of the thickened bronchial walls in CF varies from high intensity to low intensity. Since water and edema produce a high T2 weighted signal, it would not be surprising if the high bronchial wall signal is due to edema possibly caused

by active inflammation. This is a phenomena not observed in CT. A T1 weighted sequence allows for evaluation of the contrast enhancement of the bronchial wall. In CF, different patterns of bronchial wall contrast enhancement have been observed. In some lung regions, bronchi demonstrate striking enhancement while in other regions weak contrast enhancement is observed. This phenomenon may also be related to inflammatory activity within the bronchial wall, but further stud-
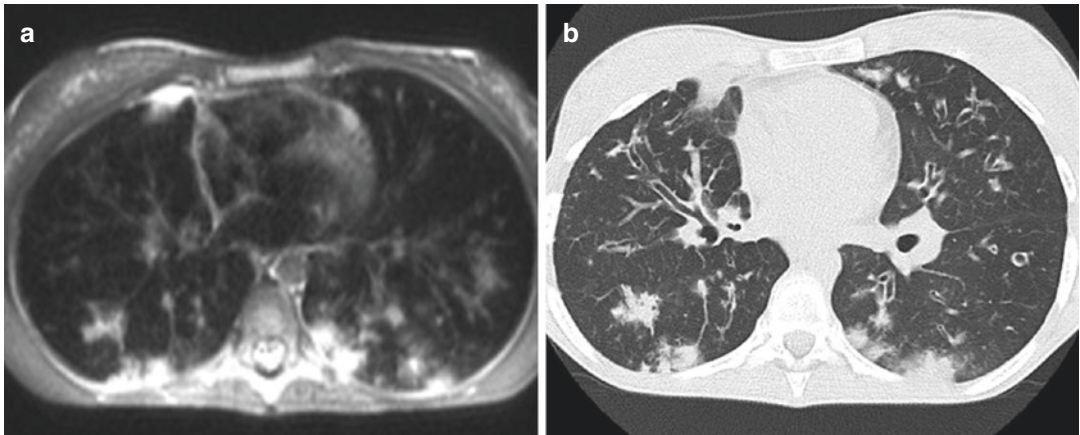
Fig. 6 Transverse MR T2 weighted (HASTE) image (**a**) and corresponding CT image (**b**) of a 14-year-old female with CF. In both images bronchial wall thickening, bronchiectasis, peripheral mucus plugging, and dorsal consolidations are demonstrated. Reprinted with permission of the American Thoracic Society. Copyright (c) 2017 American Thoracic Society. (Altes et al. 2007a). Proceedings of the American Thoracic Society is an official journal of the American Thoracic Society
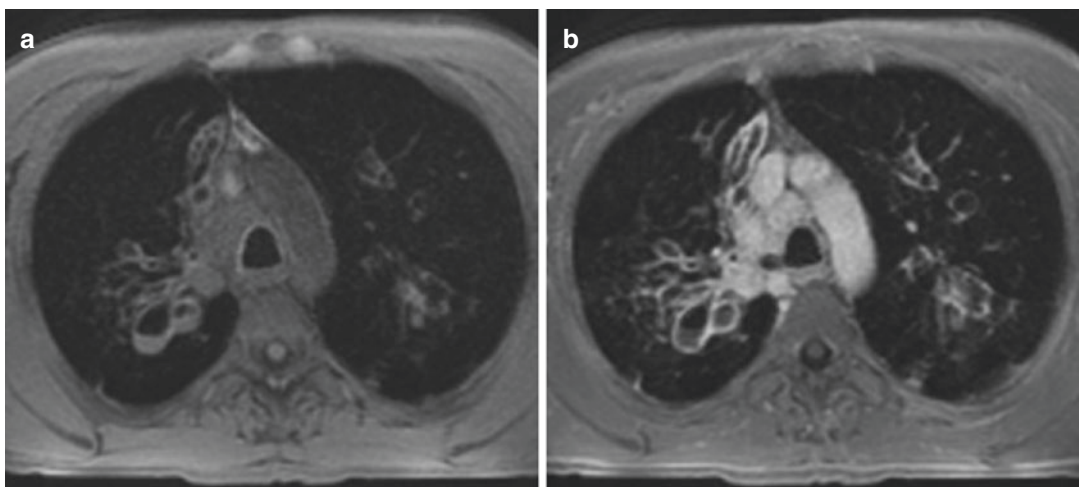
Fig. 7 T1 weighted MR images of a 43-year-old CF patient (**a**) pre- and (**b**) post-contrast media: contrast enhancement. The post-contrast images demonstrate extensive bronchial wall enhancement and permit differentiation of a thickened wall from intrabronchial secretions, with intrabronchial fluid having an air fluid level. Reprinted with permission of the American Thoracic Society. Copyright (c) 2017 American Thoracic Society. (Altes et al. 2007a). Proceedings of the American Thoracic Society is an official journal of the American Thoracic Society

ies are required to improve our understanding of these phenomena (Fig. 7).

3.2 Mucus Plugging

Mucus plugging is well visualized by MRI due to the high T2 weighted signal of its fluid content (Fig. 6). Mucus plugging in central large bronchi and peripheral small bronchi can be visualized on MRI. In central mucus plugging, there is high T2 weighted signal filling the bronchus within its course. Peripheral mucus plugging shows a grape like appearance of small T2 weighted high intensity areas, similar to the "tree in bud" phenomena in small airway inflammation on CT. Mucus plugging does not show contrast enhancement; thus mucus and bronchial wall thickening can be differentiated by the combination of T2 weighted and contrast-enhanced sequences. In CT, these two pathologic entities cannot be reliably distinguished because the CT attenuation of mucus and soft tissue are similar.

Depending on the stage of disease, CF patients have an increased risk of hemoptysis. The localization of the origin of bleeding can be crucial for the outcome of the patient. With CT, mucus and blood are similar in attenuation and cannot be distinguished. On MRI, using the combination of T1 and T2 weighted and contrast-enhanced sequences, mucus and fresh blood may be distinguishable. Mucus usually has high T2 weighted and low T1 weighted signal, while fresh blood usually has low T2 weighted and T1 weighted signal. Whether or not this difference is consistent enough to be used as a reliable differentiator remains to be seen.

3.3 Bronchiectasis

The MRI appearance of bronchiectasis is dependent on bronchial level, bronchial diameter, wall thickness, wall signal, and the signal within the bronchial lumen. Central bronchiectasis is well visualized on MRI independent of wall thickening or wall signal because of the anatomically thicker wall of the central bronchi. Peripheral

bronchi starting at the third to fourth generation are poorly visualized by MRI except when they are pathological with bronchial wall thickening and/or mucus plugging.

3.4 Air Fluid Levels

Air fluid levels are indicative of active infection and occur in saccular or varicose bronchiectasis. Bronchial air fluid levels can be visualized by MRI because of the high T2 weighted signal from the fluid. However, discriminating between a bronchus with an air fluid level and one with a partial mucus plug or a severely thickened wall can be difficult. By evaluating the signal characteristics on T1 and T2 weighted, and contrast-enhanced sequences, air fluid levels can frequently be differentiated (Fig. 7).

3.5 Consolidation

Consolidation in CF is mainly caused by alveolar filling with inflammatory fluid. The visualization of consolidation in MRI is based on both the high T2 weighted signal from inflammatory fluid and the increased proton density of a consolidation compared with healthy lung tissue. Comparable to CT, MRI is able to visualize air bronchograms as low signal areas following the course of the bronchi within the consolidation (Eibel et al. 2006; Rupprecht et al. 2002). With disease progression, complete destruction of lung segments or of a complete lung lobe can occur and these destructed lung areas have a similar appearance on MRI as CT.

3.6 Mosaic Pattern

On CT, a mosaic pattern of lung attenuation is a common finding in CF patients. This pattern can be observed on inspiratory scans as areas of relative hyperlucency, which can be due to air trapping or regional hypoperfusion (mosaic perfusion). These two entities can be distin-

guished on expiratory CT images since regions of air trapping will not change significantly in volume and thus change little in measured CT attenuation. Conversely, in areas of hypoperfusion without air trapping, the lung attenuation will increase with expiration.

On MRI, the phenomena of air trapping is not typically apparent because even normal lung parenchyma has a very low signal, and an increase of the air content does not cause a detectable decrease in lung parenchymal signal. However, two approaches offer potential to overcome this limitation: direct measurement of T1 relaxation times (Stadler et al. 2005) and ultrashort echo time methods (Fig. 5). Ultrashort echo time methods in particular offer potential by increasing the signal of normal lung so that areas of decreased proton density due to air trapping can be seen as dark areas surrounded by more dense normal lung. The previously described technique of time-resolved pulmonary perfusion MRI has the potential to directly show areas of mosaic perfusion (Fig. 1) (Eichinger et al. 2006).

4 Validation of MRI Biomarkers

Two major recent studies have taken important steps in validating MRI-based biomarkers of CF lung disease. Wielpütz et al. published in 2014 the results of a pivotal study showing the ability of MRI to depict structural and functional lung disease in CF as a way to both differentiate lung disease severity and also to show treatment effect following pulmonary exacerbation in very young patients 0–6 years of age (Wielpütz et al. 2014). Their study included 50 pediatric subjects with CF and 26 controls. Using a hybrid scoring system simplified from the Brody CT score, eliminating air trapping and adding a functional category for lung perfusion, they showed that abnormalities were seen even in very mild disease in young patients. Most importantly, they demonstrated a clear treatment effect in those subjects recruited during a pulmonary exacerbation ($n = 10$) (Fig. 8). This study provided the first evidence in a moderate sized subject population of the potential utility of MRI as a biomarker in very young CF

patients with mild lung diseaThe alternative leading contenders for lung disease biomarkers in very mild disease in young patients are LCI and CT. The second major study demonstrating the potential utility of MRI was published by Stahl et al. in 2017 (Stahl et al. 2017). In this study, the same MRI approach used in the Wielputz 2014 study was compared with LCI in 122 CF patients age 0.2–21.1 years. Of these, 97 were evaluated at their stable baseline state of health while 25 were evaluated before and after treatment for pulmonary exacerbation. While some of these subjects were also included in the earlier Wielputz 2014 study, no MRI exam was used in both studies. The results showed that both LCI and MRI were sensitive to mild lung disease and showed response to treatment. MRI has the additional benefit of showing the spatial locations of the lung disease, which could enable more precise measurements on a regional basis.

5 Future Directions for MRI in CF

MRI of the lung is a promising but relatively new field. Thus, the majority of studies exploring lung MRI in CF have involved small numbers of subjects and have been observational, simply describing the imaging findings of CF. One of the issues related to using imaging as an endpoint is that the images themselves are not an endpoint. Typically information about the disease in question has to be extracted from the images. With chest CT, a variety of scoring systems for CF have been proposed to do just this, reducing a large set of images to a single number or small set of numbers that characterize the disease severity/activity. The development of imaging-based endpoints or scores for lung MRI in CF is in its infancy. First the salient imaging features must be determined and a method, based on either human scoring or computer-based image analysis, must be devised for quantifying these features. For proton MRI, methods based on the CT scoring schemes could be developed. For the functional lung MRI techniques, new analysis methods will need to be developed and specifically validated in CF. It has been proposed that to validate an endpoint or out-
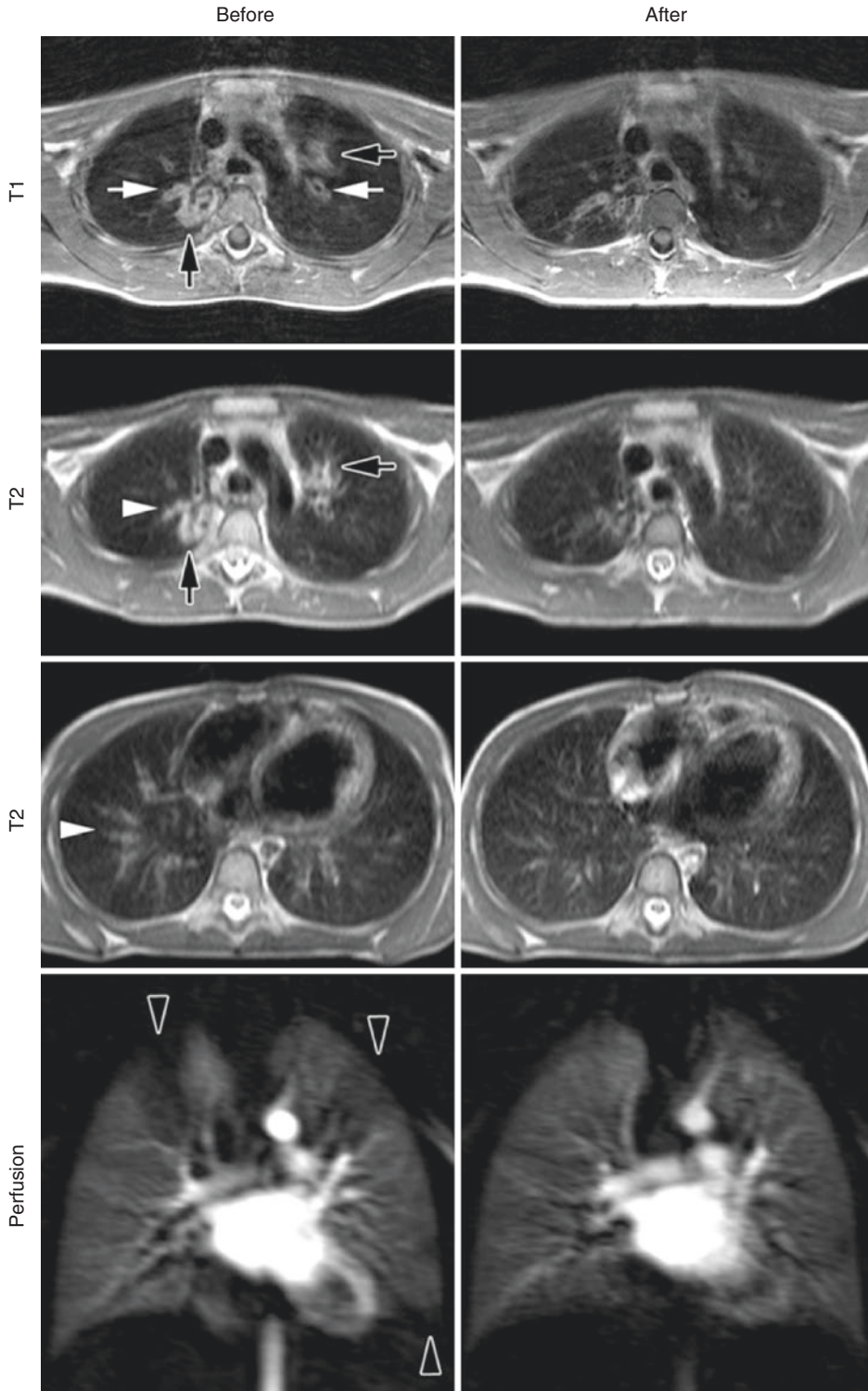
Fig. 8 The effect of treatment for pulmonary exacerbation is seen in a variety of structural and functional MRI techniques, including T1-weighted, T2-weighted, and perfusion-weighted methods. Reprinted with permission of the American Thoracic Society. Copyright (c) 2017 American Thoracic Society. (Wielputz et al. 2014). The American Journal of Respiratory and Critical Care Medicine is an official journal of the American Thoracic Society

come surrogate, it must be shown to be accurate, reproducible, feasible over time, biologically plausible, reflect the severity of disease, improve rapidly with effective treatment, and correlated with true clinical outcomes (Brody 2004; Smith et al. 2003). Of these characteristics, lung MRI is biologically plausible and likely feasible over time. Clinical trials are required to determine whether endpoints derived from any of the lung MRI methods discussed above possess the remainder of these characteristics.

References

Abolmaali N et al (2002) Chrispin-Norman-score and Ghalla-score of patients with cystic fibrosis: comparative study of chest radiographs and MR-Imaging. In: Presented at European congress of radiology 2002

Altes T et al (2008) Abnormalities of lung structure in children with bronchopulmonary dysplasia as assessed by diffusion hyperpolarized helium-3 MRI. In: International society of magnetic resonance in medicine

Altes TA et al (2004) Ventilation imaging of the lung: comparison of hyperpolarized helium-3 MR imaging with Xe-133 scintigraphy. Acad Radiol 11(7):729–734

Altes TA, Eichinger M, Puderbach M et al (2007a) Magnetic Resonance Imaging of the Lung in Cystic Fibrosis: Proceedings of the American Thoracic Society 4(4):322–325

Altes TA, Johnson M, Fidler M et al (2007b) Use of hyperpolarized helium-3 MRI to assess response to ivacaftor treatment in patients with cystic fibrosis. J Cyst Fibros 16(2):267–274

Amin R et al (2010) Hypertonic saline improves the LCI in paediatric patients with CF with normal lung function. Thorax 65(5):379–383

Aurora P et al (2005) Multiple-breath washout as a marker of lung disease in preschool children with cystic fibrosis. Am J Respir Crit Care Med 171(3):249–256

Beall RJ (2005) Executive vice president for medical affairs of the cystic fibrosis foundation. Statement at NACFC 2005

Belessis Y et al (2012) Early cystic fibrosis lung disease detected by bronchoalveolar lavage and lung clearance index. Am J Respir Crit Care Med 185(8):862–873

Bell LC, Johnson KM et al (2015a) Simultaneous MRI of lung structure and perfusion in a single breathhold. J Magn Reson Imaging 41(1):52–59

Bell LC, Wang K et al (2015b) Comparison of models and contrast agents for improved signal and signal linearity in dynamic contrast-enhanced pulmonary magnetic resonance imaging. Investig Radiol 50(3):174–178

Bhalla M et al (1991) Cystic fibrosis: scoring system with thin-section CT. Radiology 179(3):783–788

Brenner DJ (2002) Estimating cancer risks from pediatric CT: going from the qualitative to the quantitative. Pediatr Radiol 32(4):228-1. discussion 242-4

Brody AS (2004) Scoring systems for CT in cystic fibrosis: who cares? Radiology 231(2):296–298

Brody AS et al (2005) Computed tomography in the evaluation of cystic fibrosis lung disease. Am J Respir Crit Care Med 172(10):1246–1252

Brody AS et al (2006) Reproducibility of a scoring system for computed tomography scanning in cystic fibrosis. J Thorac Imaging 21(1):14–21

Carr DH et al (1995) Magnetic resonance scanning in cystic fibrosis: comparison with computed tomography. Clin Radiol 50(2):84–89

Chrispin AR, Norman AP (1974) The systematic evaluation of the chest radiograph in cystic fibrosis. Pediatr Radiol 2(2):101–105

Davies J et al (2013) Assessment of clinical response to ivacaftor with lung clearance index in cystic fibrosis patients with a G551D-CFTR mutation and preserved spirometry: a randomised controlled trial. Lancet Respir Med 1(8):630–638

de Jong PA, Long FR, Nakano Y (2006) Computed tomography dose and variability of airway dimension measurements: how low can we go? Pediatr Radiol 36(10):1043–1047

de Lange EE et al (1999) Lung air spaces: MR imaging evaluation with hyperpolarized 3He gas. Radiology 210(3):851–857

DeBoer EM et al (2014) Automated CT scan scores of bronchiectasis and air trapping in cystic fibrosis. Chest 145(3):593–603

Donadieu J et al (2007) Estimation of the radiation dose from thoracic CT scans in a cystic fibrosis population. Chest 132(4):1233–1238

Donnelly LF et al (1999) Cystic fibrosis: combined hyperpolarized 3He-enhanced and conventional proton MR imaging in the lung--preliminary observations. Radiology 212(3):885–889

Dournes G et al (2016) Lung morphology assessment of cystic fibrosis using MRI with ultra-short echo time at submillimeter spatial resolution. Eur Radiol 26(11):3811–3820

Eberle B et al (1999) Analysis of intrapulmonary O(2) concentration by MR imaging of inhaled hyperpolarized helium-3. J Appl Physiol (Bethesda, Md: 1985) 87(6):2043–2052

Edelman RR et al (1996) Noninvasive assessment of regional ventilation in the human lung using oxygen-enhanced magnetic resonance imaging. Nat Med 2(11):1236–1239

Eibel R et al (2006) Pulmonary abnormalities in immunocompromised patients: comparative detection with parallel acquisition MR imaging and thin-section helical CT. Radiology 241(3):880–891

Eichinger M et al (2006) Contrast-enhanced 3D MRI of lung perfusion in children with cystic fibrosis--initial results. Eur Radiol 16(10):2147–2152

Fiel SB et al (1987) Magnetic resonance imaging in young adults with cystic fibrosis. Chest 91(2):181–184

Fleck R et al (2013) Aortopulmonary collateral flow in cystic fibrosis assessed with phase-contrast MRI. Pediatr Radiol 43(10):1279–1286

Frush DP, Donnelly LF, Rosen NS (2003) Computed tomography and radiation risks: what pediatric health care providers should know. Pediatrics 112(4):951–957

Gast KK et al (2002) Dynamic ventilation (3)He-magnetic resonance imaging with lung motion correction: gas flow distribution analysis. Investig Radiol 37(3):126–134

Gibson RL, Burns JL, Ramsey BW (2003) Pathophysiology and management of pulmonary infections in cystic fibrosis. Am J Respir Crit Care Med 168(8):918–951

Hatabu H et al (1996) Pulmonary perfusion: qualitative assessment with dynamic contrast-enhanced MRI using ultra-short TE and inversion recovery turbo FLASH. Magn Reson Med 36(4):503–508

Helbich TH et al (1999) Cystic fibrosis: CT assessment of lung involvement in children and adults. Radiology 213(2):537–544

Hoo A-F et al (2012) Lung function is abnormal in 3-month-old infants with cystic fibrosis diagnosed by newborn screening. Thorax 67(10):874–881

Huda W, Vance A (2007) Patient radiation doses from adult and pediatric CT. Am J Roentgenol 188(2):540–546

Jakob PM et al (2004) Assessment of human pulmonary function using oxygen-enhanced T(1) imaging in patients with cystic fibrosis. Magn Reson Med 51(5):1009–1016

Johnson KM et al (2013) Optimized 3D ultrashort echo time pulmonary MRI. Magn Reson Med 70(5):1241–1250

Kauczor HU et al (1996) Normal and abnormal pulmonary ventilation: visualization at hyperpolarized He-3 MR imaging. Radiology 201(2):564–568

Keilholz SD et al (2002) The contributions of ventilation and perfusion in oxygen-enhanced pulmonary MR imaging. Proc Int Soc Mag Reson Med 10:409

Kerem E et al (1992) Prediction of mortality in patients with cystic fibrosis. N Engl J Med 326(18):1187–1191

Koumellis P et al (2005) Quantitative analysis of regional airways obstruction using dynamic hyperpolarized 3He MRI-preliminary results in children with cystic fibrosis. J Magn Reson Imaging 22(3):420–426

Kruger SJ et al (2014) Oxygen-enhanced 3D radial ultrashort echo time magnetic resonance imaging in the healthy human lung. NMR Biomed 27(12):1535–1541

Kuo W et al (2014) Monitoring cystic fibrosis lung disease by computed tomography. Radiation risk in perspective. Am J Respir Crit Care Med 189(11):1328–1336

Levin DL, Hatabu H (2004) MR evaluation of pulmonary blood flow. J Thorac Imaging 19(4):241–249

Ley S et al (2005) Assessment of hemodynamic changes in the systemic and pulmonary arterial circulation in patients with cystic fibrosis using phase-contrast MRI. Eur Radiol 15(8):1575–1580

Loeve M et al (2009) Cystic fibrosis: are volumetric ultra-low-dose expiratory CT scans sufficient for monitoring related lung disease? Radiology 253(1):223–229

Lum S et al (2007) Early detection of cystic fibrosis lung disease: multiple-breath washout versus raised volume tests. Thorax 62(4):341–347

Mai VM, Berr SS (1999) MR perfusion imaging of pulmonary parenchyma using pulsed arterial spin labeling techniques: FAIRER and FAIR. J Magn Reson Imaging 9(3):483–487

McMahon CJ et al (2006) Hyperpolarized 3helium magnetic resonance ventilation imaging of the lung in cystic fibrosis: comparison with high resolution CT and spirometry. Eur Radiol 16(11):2483–2490

Mentore K et al (2005) Hyperpolarized HHe 3 MRI of the lung in cystic fibrosis: assessment at baseline and after bronchodilator and airway clearance treatment. Acad Radiol 12(11):1423–1429

Morbach AE et al (2005) Diffusion-weighted MRI of the lung with hyperpolarized helium-3: a study of reproducibility. J Magn Reson Imaging 21(6):765–774

Mugler JP, Altes TA (2013) Hyperpolarized 129Xe MRI of the human lung. J Magn Reson Imaging 37(2):313–331

Nagle SK et al (2016) Conventional versus ultrashort echo time MRI of cystic fibrosis. In: Presented at the North American cystic fibrosis conference, Orlando, FL

O'Connell OJ et al (2012) Radiological imaging in cystic fibrosis: cumulative effective dose & changing trends over 2 decades. Chest 141(6):1575–1583

Poranski ME et al (2016) Ventilation and perfusion MRI of cystic fibrosis. In: Presented at North American cystic fibrosis conference, Orlando, FL

Puderbach M et al (2008) In vivo Gd-DTPA concentration for MR lung perfusion measurements: assessment with computed tomography in a porcine model. Eur Radiol 18(10):2102–2107

Puderbach M, Eichinger M, Gahr J et al (2007a) Proton MRI appearance of cystic fibrosis: comparison to CT. Eur Radiol 17(3):716–724

Puderbach M, Eichinger M, Haeselbarth J et al (2007b) Assessment of morphological MRI for pulmonary changes in cystic fibrosis (CF) patients: comparison to thin-section CT and chest x-ray. Investig Radiol 42(10):715–725

Renz DM et al (2015) Comparison between magnetic resonance imaging and computed tomography of the lung in patients with cystic fibrosis with regard to clinical, laboratory, and pulmonary functional parameters. Invest Radiol 50(10):733–742

Roach DJ et al (2016) Ultrashort echo-time magnetic resonance imaging is a sensitive method for the evaluation of early cystic fibrosis lung disease. Ann Am Thorac Soc 13(11):1923–1931

Rosenow T et al (2015) PRAGMA-CF. A quantitative structural lung disease computed tomography outcome in young children with cystic fibrosis. Am J Respir Crit Care Med 191(10):1158–1165

Rupprecht T et al (2002) Steady-state free precession projection MRI as a potential alternative to the conven-

tional chest X-ray in pediatric patients with suspected pneumonia. Eur Radiol 12(11):2752–2756

Salerno M et al (2001) Dynamic spiral MRI of pulmonary gas flow using hyperpolarized (3)He: preliminary studies in healthy and diseased lungs. Magn Reson Med 46(4):667–677

Salerno M et al (2002) Emphysema: hyperpolarized helium 3 diffusion MR imaging of the lungs compared with spirometric indexes – initial experience. Radiology 222(1):252–260

Sileo C et al (2014) HRCT and MRI of the lung in children with cystic. J Cyst Fibros 13(2):198–204

Smith JJ, Sorensen AG, Thrall JH (2003) Biomarkers in imaging: realizing radiology's future. Radiology 227(3):633–638

Stadler A et al (2005) T1 mapping of the entire lung parenchyma: influence of the respiratory phase in healthy individuals. J Magn Reson Imaging 21(6):759–764

Stahl M et al (2014) Multiple breath washout is feasible in the clinical setting and detects abnormal lung function in infants and young children with cystic fibrosis. Respiration 87(5):357–363

Stahl M et al (2017) Comparison of lung clearance index and magnetic resonance imaging for assessment of lung disease in children with cystic fibrosis. Am J Respir Crit Care Med 195(3):349–359

Stern M et al (2008) From registry to quality management: the German cystic fibrosis quality assessment project 1995–2006. Eur Respir J 31(1):29–35

Subbarao P et al (2013) Lung clearance index as an outcome measure for clinical trials in young children with cystic fibrosis. A pilot study using inhaled hypertonic saline. Am J Respir Crit Care Med 188(4):456–460

Tepper LA et al (2016) Validating chest MRI to detect and monitor cystic fibrosis lung disease in a pediatric cohort. Pediatr Pulmonol 51(1):34–41

Teufel M et al (2012) Comparison between high-resolution CT and MRI using a very short Echo time in patients with cystic fibrosis with extra focus on mosaic attenuation. Respiration 86(4):302–311

Thia LP et al (2014) Is chest CT useful in newborn screened infants with cystic fibrosis at 1 year of age? Thorax 69(4):320–327

Thomen RP et al (2017) Hyperpolarized 129Xe for investigation of mild cystic fibrosis lung disease in pediatric patients. J Cyst Fibros 16(2):275–282

van Beek EJR et al (2007) Assessment of lung disease in children with cystic fibrosis using hyperpolarized 3-Helium MRI: comparison with Shwachman score, Chrispin-Norman score and spirometry. Eur Radiol 17(4):1018–1024

Walkup LL et al (2016) Feasibility, tolerability and safety of pediatric hyperpolarized (129)Xe magnetic resonance imaging in healthy volunteers and children with cystic fibrosis. Pediatr Radiol 46(12):1651–1662

Weatherly MR et al (1993) Wisconsin cystic fibrosis chest radiograph scoring system. Pediatrics 91(2):488–495

Wielpütz MO et al (2014) Magnetic resonance imaging detects changes in structure and perfusion, and response to therapy in early cystic fibrosis lung disease. Am J Respir Crit Care Med 189(8):956–965

Woodhouse N et al (2005) Combined helium-3/proton magnetic resonance imaging measurement of ventilated lung volumes in smokers compared to never-smokers. J Magn Reson Imaging 21(4):365–369

Lung Cancer

Yoshiharu Ohno, Hisanobu Koyama,
and Julien Dinkel

Contents

Y. Ohno, MD, PhD (✉) • H. Koyama, MD
Department of Radiology, Kobe University Graduate
School of Medicine, 7-5-2 Kusunoki-cho, Chuo-ku,
Kobe 650-0017, Japan
e-mail: yosirad@kobe-u.ac.jp; yosirad@med.kobe-u.ac.jp

J. Dinkel, MD, MSc
Department of Clinical Radiology, University of
Munich Hospital (LMU), Marchioninistraße 15,
81377 Munich, Germany

Abstract

Since the publication of the Radiologic Diagnostic Oncology Group Report (RDOG) in 1991, the clinical application of pulmonary magnetic resonance (MR) imaging to patients with lung cancer has been limited. MDCT has been much more widely available for staging of lung cancer in clinical situations. Traditionally, FDG-PET or PET/CT is the only modality that reveals biological glucose metabolism of lung cancer, and ventilation and/or perfusion scintigraphy is the only modality that demonstrates pulmonary function. However, recent advances of MR systems and utilization of contrast media make it possible to overcome the limitation of chest MR imaging. Therefore, in the last years, several investigators have demonstrated the significant comprehensive potential of MR imaging to substitute for MDCT and nuclear medicine examinations in lung cancer staging. Currently, MR imaging in lung cancer patients can be applied for (1) detection of pulmonary nodules, (2) characterization of solitary pulmonary nodules, and (3) assessment of TNM classification in routine clinical practice. We believe that further basic studies, as well as clinical applications of newer MR techniques, will play an important role in the future management of patients with lung cancer including MRI.

Key Points

Since the publication of the Radiologic Diagnostic Oncology Group Report (RDOG) in 1991, the clinical application of pulmonary magnetic resonance (MR) imaging to patients with lung cancer has been limited. MDCT has been much more widely available for staging of lung cancer in clinical situations. Traditionally, FDG-PET or PET/CT is the only modality that reveals biological glucose metabolism of lung cancer, and ventilation and/or perfusion scintigraphy is the only modality that demonstrates pulmonary function. However, recent advances of MR systems and utilization of contrast media make it possible to overcome the limitation of chest MR imaging. Therefore, in the last years, several investigators have demonstrated the significant comprehensive potential of MR imaging to substitute for MDCT and nuclear medicine examinations in lung cancer staging. Currently, MR imaging in lung cancer patients can be applied for (1) detection of pulmonary nodules, (2) characterization of solitary pulmonary nodules, and (3) assessment of TNM classification in routine clinical practice. We believe that further basic studies, as well as clinical applications of newer MR techniques, will play an important role in the future management of patients with lung cancer including MRI.

1   Introduction

Lung cancer is the most common cause of cancer-related death in the Western world, Japan, and South Korea. Non-small cell lung carcinoma (NSCLC) accounts for approximately 80% of all lung cancers, with small cell lung carcinoma (SCLC) accounting for the remainder. Despite major efforts aimed at improving survival during recent years, survival remains dismal at 14% for all stages. Imaging techniques currently are essential for the diagnosis, staging, and follow-up of patients with lung cancer. The diagnosis of lung cancer has relied on findings on chest radiographs (CXRs) and detection of cells in sputum or biopsy specimens. Perhaps even more important, however, are specific findings on chest computed tomography (CT) and metabolic information on positron emission tomography with 2-[fluorine-18]-fluoro-2-deoxy-d-glucose (FDG-PET) or FDG-PET co-registered or integrated with CT (co-registered or integrated FDG-PET/CT). Moreover, the staging and follow-up of lung cancer have relied more on CT, FDG-PET, and/or FDG-PET/CT than on chest radiography. The goal of diagnosis and management of pulmonary nodules is to bring promptly to surgery all patients with operable malignant nodules while avoiding unnecessary thoracotomy for patients with benign lesions. It is therefore of utmost importance to differentiate malignant from benign nodules in the least invasive manner and to make as specific and accurate a diagnosis as possible. In addition, the preliminary goal of pre-therapeutic assessment of lung cancers is to avoid unnecessary surgery for patients with locally unresectable tumors and/or nodal or metastatic disease because the strongest prognostic indicator for survival in lung cancer is whether or not the tumor is resectable.

Currently, CT is considered to be the most widely applicable modality for evaluation of lung cancer, and a major breakthrough in CT technology has been the introduction of multidetector-row CT (MDCT), in which detector rows are exposed simultaneously. The performance of MDCT compared with single-detector CT is enhanced by a factor approximately equal to the number of rows. In addition, FDG-PET or PET/CT qualifies as another important innovation in lung cancer imaging. Standard imaging techniques are based on differences in the structure of tissues, whereas FDG-PET or PET/CT can show the enhanced glucose metabolism of lung cancer cells. For these reasons, MR imaging has been utilized for only a few cases, such as superior sulcus (Pancoast's) tumor, mediastinal invasion and chest wall invasion since 1991, when the Radiologic Diagnostic Oncology Group (RDOG) reported no significant difference in the diagnostic capability of CT and conventional T1-weighted imaging for the staging of lung cancer except for mediastinal invasion

(Webb et al. 1991). However, recent advances in MR imaging techniques and utilization of contrast media have resulted in further improvement of the image quality and diagnostic capability of MR imaging for lung cancer patients.

In this chapter we describe the utility and capability of MR imaging for (1) detection of pulmonary nodules, (2) characterization and management of pulmonary nodules, and (3) assessment of tumor-node-metastasis (TNM) stages in lung cancer patients.

2   Detection of Pulmonary Nodules

A pulmonary nodule is radiologically defined as an intraparenchymal lung lesion that is less than 30 mm in diameter and is not associated with atelectasis or adenopathy (Tuddenham 1984). While one in 500 CXRs shows a lung nodule, 90% of these nodules are incidental radiological findings, detected accidentally on CXRs obtained for unrelated diagnostic workups. More than 150,000 patients per year in the United States present their physicians with the diagnostic dilemma of a pulmonary nodule. This number has increased even further due to incidental findings of lung nodules on chest CT (Tuddenham 1984). The devastating effect of lung cancer is directly associated with its delayed presentation. Patients with the best prognosis are those with stage IA disease, although approximately one half of all lung cancers unfortunately show extrathoracic spread at the time of diagnosis. Timely and accurate detection and diagnosis of the etiology of pulmonary nodules are therefore essential for making it possible for patients with malignancy to be cured.

Spiral CT or MDCT can be considered the current gold standard for the detection of lung nodules (Davis 1991; Costello 1994; Henschke et al. 2001; Schaefer-Prokop and Prokop 2002; Swensen et al. 2005; Bach et al. 2007). However, repeated follow-up CT examinations for detection of pulmonary metastases may be undesirable, especially for young patients, because of radiation exposure. Although radiation exposure is usually no major issue for cancer patients and low-dose CT techniques have been proved feasi-

ble to reduce the radiation dose, MR imaging does not require any ionizing radiation at all. It would therefore be helpful if MR imaging could be used for the detection of pulmonary nodules without administration of contrast media.

Several investigators have addressed this issue by using various sequences with 1.5 and 3.0 T scanners since 1997. However, patient-related motion artifacts, susceptibility artifacts from the lungs, and inferior spatial and temporal resolution as compared with those of CT reduce the quality of MR images of the lungs (Kersjes et al. 1997; Vogt et al. 2004; Schroeder et al. 2005; Luboldt et al. 2006; Bruegel et al. 2007; Regier et al. 2007; Yi et al. 2007). All these studies assessed the detection rate (sensitivity) for pulmonary nodules, mainly pulmonary metastases, which was verified by single helical CT or MDCT. The sensitivities for nodules equal to or less than 5 mm in diameter were reportedly less than 45%, although various sequences such as electrocardiograph (ECG)-triggered proton density weighted (PDW) or T2-weighted turbo spin echo (SE), ECG-triggered PDW black-blood-prepared half-Fourier single-shot turbo SE (HASTE), respiratory-triggered T2-weighted short-inversion-time inversion recovery (STIR) turbo SE, pre- and post-contrast-enhanced Volumetric interpolated breath-hold examination (VIBE), T2-weighted triple inversion black blood turbo spin echo, etc. were tested with nodules equal to or more than 5 mm section thickness on 1.5 or 3.0 T scanners.

The detection rates or sensitivities of MR imaging using various sequences on 1.5 and 3.0 T systems have ranged from 36.0 to 96.0% (Kersjes et al. 1997; Vogt et al. 2004; Schroeder et al. 2005; Luboldt et al. 2006; Bruegel et al. 2007; Regier et al. 2007; Yi et al. 2007; Frericks et al. 2008; Koyama et al. 2008; Sommer et al. 2014). The study with 150 subjects considering as the large population to date compared CT and MR imaging on a 1.5 T system demonstrated that the overall detection rate of thin-section CT (97%) was superior to that of respiratory-triggered STIR turbo SE imaging (82.5%), although there were no significant differences between the methods in the detection rate for all types of malignant nodules (Koyama et al. 2008). Therefore, the currently available MR technique should be considered as
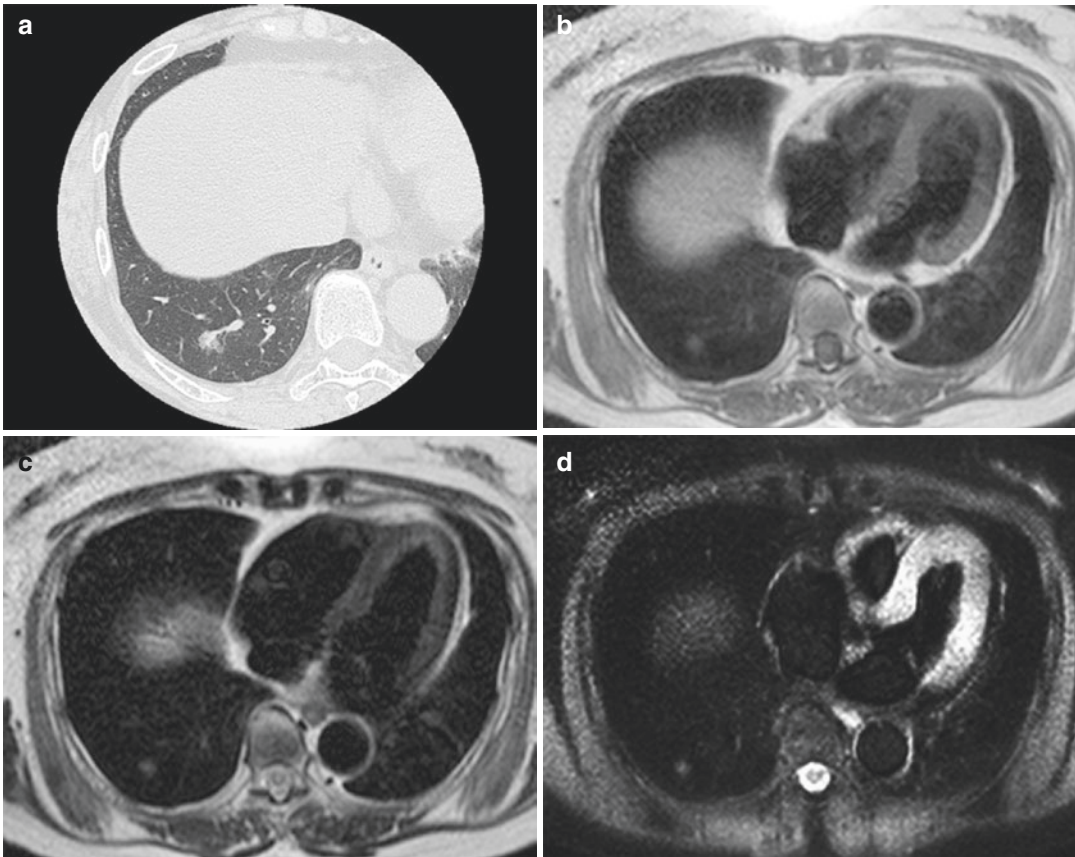
Fig. 1 A 71-year-old female with adenomatous hyper-plasia in the right lower lobe. Thin-section CT indicates ground-glass attenuation in the right lower lobe (**a**). Black-blood T1-weighted turbo SE (**b**), T2-weighted turbo SE (**c**), and STIR turbo SE (**d**) images show a nodule as, respectively, low, intermediate, and high signal intensity in the right lower lobe

capable of performing a complimentary function for intrathoracic metastasis detection, and radiologists need to carefully check the nodules on thoracic MR images of their oncology patients.

In addition, more recent study demonstrated that pulmonary thin-section MR imaging with ultrashort echo time (UTE) had almost similar capability for nodule detection as compared with standard- and low-dose thin-section CT in routine clinical practice (Ohno et al. 2016). Therefore, further improvements of MR systems and sequences can be expected to enable pulmonary metastasis surveillance and/or lung cancer screening as well as morphological lung nodule characterization similar to CT on not only dedicated chest but also whole-body MR imaging in the near future (Fig. 1).

3 Characterization and Management of Pulmonary Nodules or Masses on MR Imaging

Since the pulmonary nodule is one of the most common findings on chest radiographs and CT, it is important to differentiate malignant from benign nodules in the least invasive way and to make as specific and accurate a diagnosis as possible. Investigators have used CT, MR imaging, and FDG-PET or PET/CT to evaluate the radiological features, relaxation time, blood supply, and metabolism of pulmonary nodules to differentiate malignant from benign nodules with promising results (Table 1).

Table 1 Recommended MR protocol for nodule detection and characterization

No.	Recommended sequence	TR (ms)	TE (ms)	FA (°)	Black-blood TI (ms)	TI (ms)	Matrix	Respiration	Suggestion
1	Pre-contrast-enhanced ECG-gated T1-W-SE or TSE	1 <R-R>	15–25	N/A	N/A	N/A	256 × 256	RT or RG	N/A
	Pre-contrast-enhanced ECG-gated black-blood T1-W-TSE	1<R-R>	8	N/A	800–1000	N/A	256 × 256	BH	Parallel imaging should be applied. ETL should be less than 20
	Pre-contrast-enhanced 3D T1-GRE (VIBE, TTHRIVE, Quick 3D, etc.)	4	≤2	15	N/A	N/A	256 × 256	BH	Fat suppression technique should be applied
2	ECG- and respiratory-gated T2-W-TSE	2 or 3 <R-R>	90–100	N/A	N/A	N/A	256 × 256	RT or RG	ETL should be less than 15
	Pre-contrast-enhanced ECG-gated black-blood T2-W-TSE	2 or 3 <R-R>	102	N/A	2000–3000	N/A	256 × 256	BH	Parallel imaging should be applied. ETL should be less than 45
3	Respiratory-gated STIR TSE	Up to respiratory cycle	15	N/A	N/A	150–240	256 × 256	RG	ETL should be less than 5, if sequentially reordered phase encoding scheme is used
	ECG-gated black-blood STIR TSE	2<R-R>	5	N/A	1000–2000	150–240	256 × 256	BH	Parallel imaging should be applied. ETL should be less than 8
4	Diffusion-weighted imaging by EPI	∞	65	N/A	N/A	150–240	256 × 256	Free-breath	Number of excitation should be equal to or more than 6

(continued)

Table 1 (continued)

No.	Recommended sequence	TR (ms)	TE (ms)	FA (°)	Black-blood TI (ms)	TI (ms)	Matrix	Respiration	Suggestion
5	Dynamic MRI by using 3D ultrafast T1-GRE	2.4–2.7	0.6–0.7	20–40	N/A	N/A	128 × 128–256 × 256	BH	Dynamic MR images should be obtained every 1.1 s after contrast media injection. Increasing temporal resolution by parallel imaging technique
	Dynamic MRI by using ECG-gated T1-W-SE	150-1 <R-R>	10–15	N/A	N/A	N/A	128 × 128–256 × 256	BH	Dynamic MR images should be obtained at 0, 1, 2, 3, 4, 5, 6, and 8 min after contrast media injection
6	Post-contrast-enhanced ECG-gated T1-W-SE or TSE	1 <R-R>	15–25	N/A	N/A	N/A	256 × 256	RT or RG	N/A
	Post-contrast-enhanced ECG-gated black-blood T1-W-TSE	1<R-R>	8	N/A	800–1000	N/A	256 × 256	BH	Parallel imaging should be applied. ETL should be less than 20
	Post-contrast-enhanced 3D T1-GRE (VIBE, TTHRIVE, Quick 3D, etc.)	4	≤2	15	N/A	N/A	256 × 256	BH	Fat suppression technique should be applied

SE spin echo, *TSE* turbo spin echo, *GRE* gradient-echo, *TR* repetition time, *TE* echo time, *FA* flip angle, *RT* respiratory trigger, *RG* respiratory-gated, *ETL* echo train length, *VIBE* volumetric interpolated breath-hold examination, *THRIVE* T1 high resolution isotropic volume examination, *Quick 3D* segmented 3D T1-weighted spoiled gradient-echo

3.1 Conventional T1-Weighted and T2-Weighted MRI Without and with Contrast Media

Characterization of the primary tumor on CT and MR imaging is based on the imaging features of the nodule or mass itself and its relationship to the pleura, chest wall, airways, and mediastinum, as well as its relative enhancement by contrast media. Historically, non-contrast-enhanced MR imaging has shown limited potential for characterizing peripheral lung nodules and masses and identifying benign nature of nodules due to the low intrinsic signal intensity of the lung parenchyma, the relatively poor spatial resolution, and patient-related motion artifacts (Caskey et al. 1990; Feuerstein et al. 1992; Kono et al. 1993; Kersjes et al. 1997; McLoud and Swenson 1999). In general, many pulmonary nodules, including lung cancers, pulmonary metastases and low-grade malignancies such as carcinoids and lymphomas are demonstrated as low or intermediate signal intensities on T1-weighted images and as slightly high intensity on T2-weighted images when SE or turbo SE sequences are used (Caskey et al. 1990; Feuerstein et al. 1992; Kono et al. 1993; Kersjes et al. 1997; McLoud and Swensen 1999) (Fig. 2). Malignant pulmonary nodules less than 30 mm in diameter usually do not show macroscopic necrosis (Caskey et al. 1990; Feuerstein et al. 1992; Kono et al. 1993; Kersjes et al. 1997; McLoud and Swensen 1999). Although enhancement levels vary due to underlying microscopically determined pathologic conditions such as tumor angiogenesis, tumor interstitial spaces, the presence or absence of fibrosis, and scarring and necrosis within the tumor, malignant pulmonary nodules show homogeneous enhancement but at a variety of levels on T1-weighted images after administration of contrast media (Caskey et al. 1990; Feuerstein et al. 1992; Kono et al. 1993; Kersjes et al. 1997; McLoud and Swensen 1999). Consequently, when using pre- and post-contrast-enhanced conventional T1-weighted images and T2-weighted images, clinicians in routine clinical practice often face a diagnostic dilemma in distinguishing malignant from benign pulmonary nodules such as organizing pneumonia, benign tumors, and inflammatory nodules (Caskey et al. 1990; Feuerstein et al. 1992; Kono et al. 1993; Kersjes et al. 1997; McLoud and Swensen 1999) (Figs. 2 and 3). It has therefore been suggested that enhancement patterns or blood supply evaluated with dynamic contrast-enhanced MR imaging may be helpful for diagnosis and management of pulmonary nodules (Kono et al. 1993, 2007; Kusumoto et al. 1994; Hittmair et al. 1995; Gückel et al. 1996; Fujimoto et al. 2003; Ohno et al. 2002, 2004a; Schaefer et al. 2004, 2006; Donmez et al. 2007). However, it may be possible to diagnose several histological types of pulmonary nodules, such as bronchocele, tuberculoma, mucinous bronchoalveolar carcinoma (BAC), hamartoma, and aspergilloma, on pre- or post-contrast-enhanced T1-weighted images and T2-weighted image according to their specific MR findings.

3.1.1 Bronchocele

Bronchial atresia is a common focal pulmonary lesion, which can be diagnosed by using non-contrast-enhanced T1- and T2-weighted images. Bronchial atresia is an uncommon anomaly characterized by focal obliteration of the bronchial lumen and the absence of communication between lobar, segmental, or subsegmental bronchi and the central airway (Meng et al. 1978; Jederlinic et al. 1987; Finck and Milne 1988; Naidich et al. 1988; Bailey et al. 1990; Ko et al. 1998; Matsushima et al. 2002). Mucus secreted within the patent airways distal to the point of atresia accumulates in the form of a plug or bronchocele which appears as a pulmonary nodule or mass (Finck and Milne 1988; Naidich et al. 1988; Bailey et al. 1990; Ko et al. 1998; Matsushima et al. 2002). The MR image of bronchoceles reportedly appears as a branching lesion with high signal intensity on T1- and T2-weighted images due to the dilated mucus-filled bronchi and mucocele formation distal to the atelectatic segment (Finck and Milne 1988; Naidich et al. 1988; Bailey et al. 1990; Ko et al. 1998; Matsushima et al. 2002) (Fig. 4).
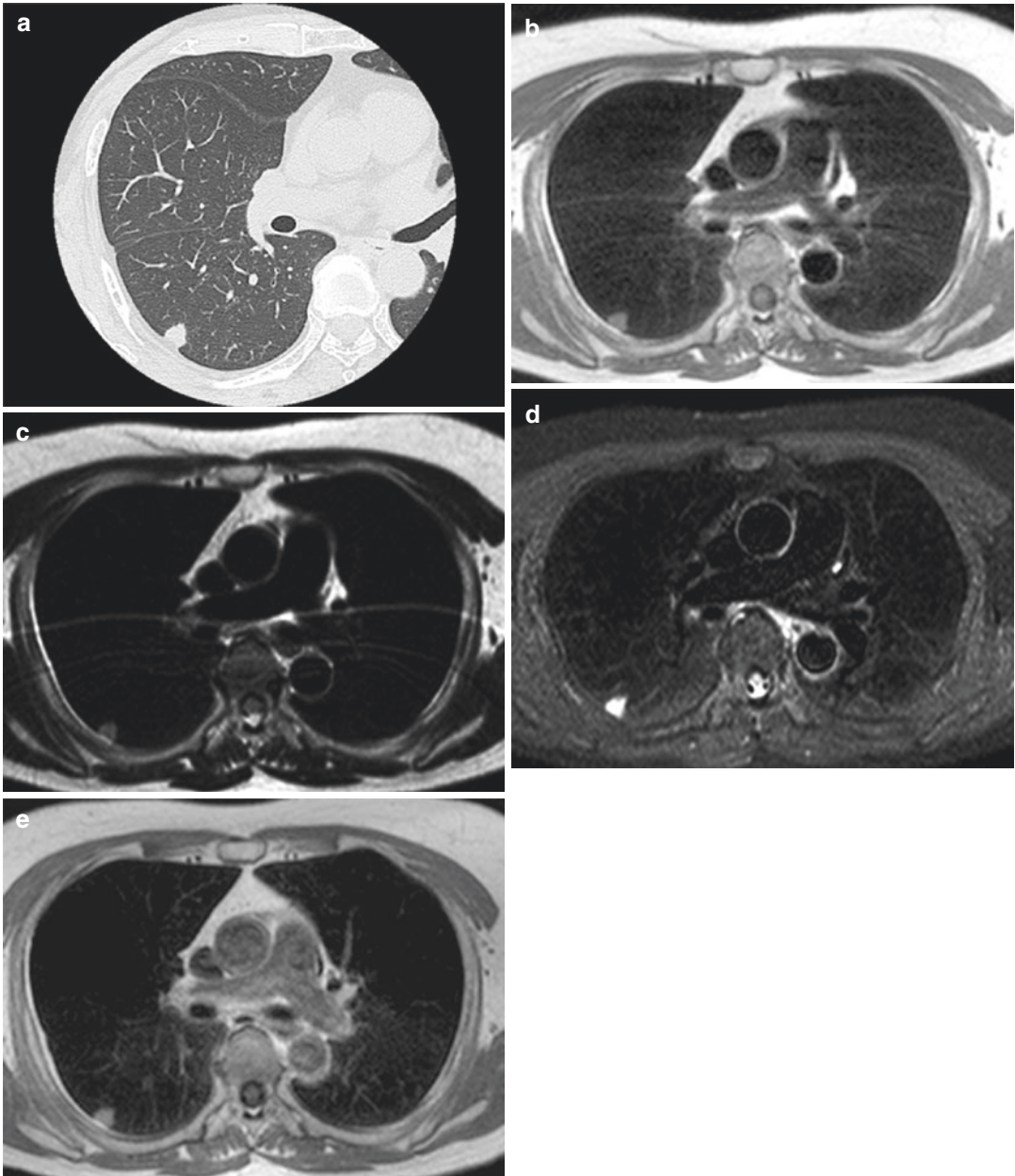
Fig. 2 A 56-year-old female with adenocarcinoma in the right lower lobe. Thin-section CT shows a solid nodule in the right lower lobe (**a**). Black-blood T1-weighted turbo SE (**b**), T2-weighted turbo SE (**c**), and STIR turbo SE (**d**) images show nodule as, respectively, low, intermediate, and high signal intensity in the right lower lobe. Post-contrast black-blood T1-weighted turbo SE image (**e**) showed homogeneous enhancement of the nodule

3.1.2 Tuberculoma

Tuberculomas, observed as well-defined nodules located mainly in the upper lobes, may appear after primary or reactivated tuberculosis. Calcification occurs in about 20–30% of cases (Sochocky 1958). CT yields superior visualization of the calcifications and characteristics of the nodules. In rare cases, areas of diminished attenuation are seen, which represent caseous necrosis. The latter may be identified as tuberculoma, a
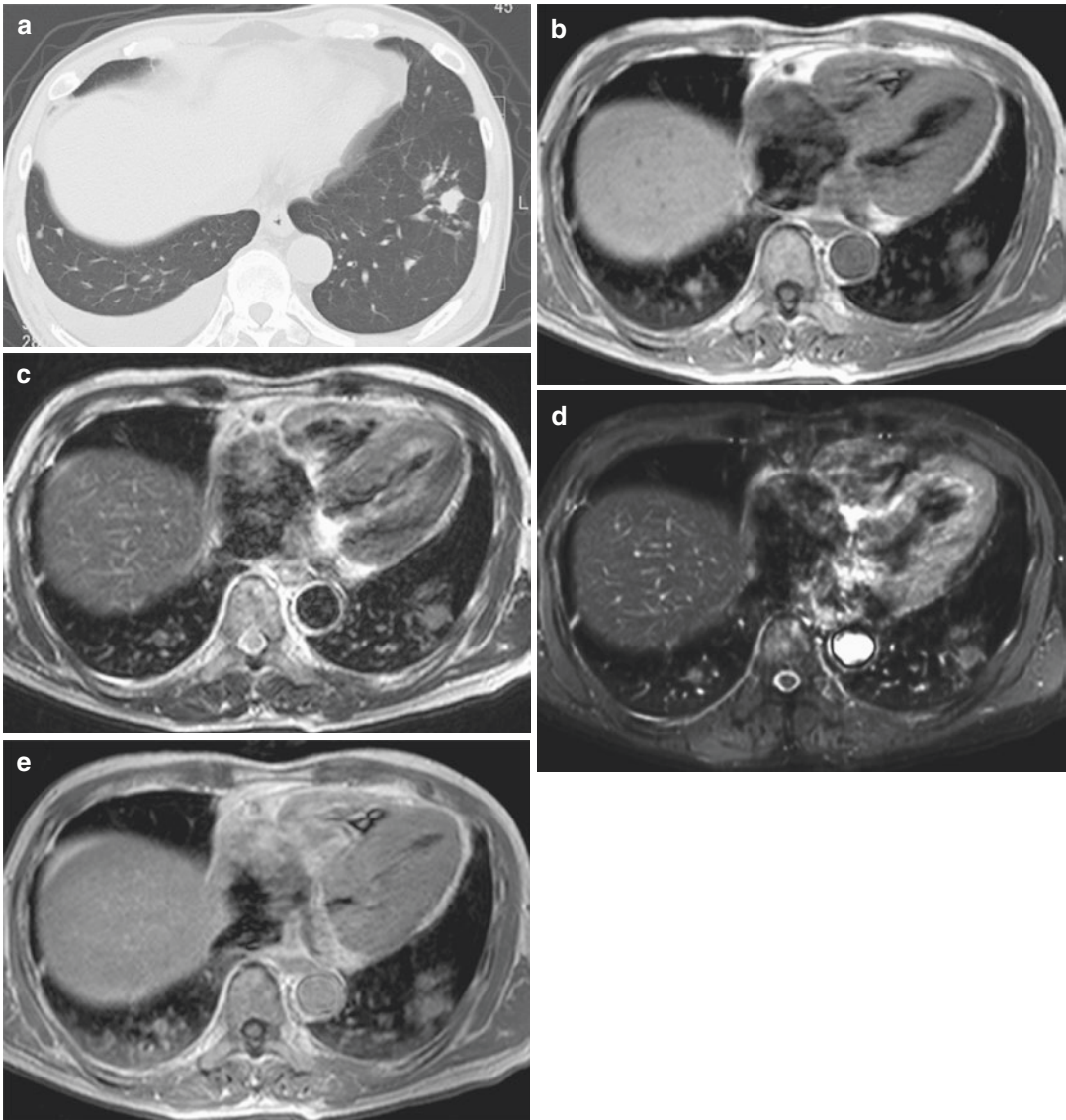
Fig. 3 A 55-year-old male with cryptococcosis in the left lower lobe. Thin-section CT shows a solid nodule in the left lower lobe (**a**). Black-blood T1-weighted turbo SE (**b**), T2-weighted turbo SE (**c**), and STIR turbo SE (**d**) images show nodule as, respectively, low, intermediate, and high signal intensity in the left lower lobe. Post-contrast black-blood T1-weighted turbo SE image (**e**) showed homogeneous enhancement of nodule

nodule with a relatively low signal intensity in comparison with that of other pulmonary nodules on T2-weighted SE or turbo SE images (Sakai et al. 1992; Kono et al. 1993; Kusumoto et al. 1994; Parmar et al. 2000; Chung et al. 2000; Schaefer et al. 2006). In addition, several investigators have reported on typical MR findings of tuberculoma on post-contrast-enhanced T1-weighted images known as "thin-rim enhancement" sign (Sakai et al. 1992) (Fig. 5). Signal intensity at the center of tuberculomas is low or slightly enhanced, but the signal intensity of the fibrotic rim is markedly enhanced. These MR findings correspond well to those of pathological specimens (Sakai et al. 1992; Kono et al. 1993; Kusumoto et al. 1994; Parmar et al. 2000; Chung et al. 2000; Schaefer et al. 2006). Therefore, when tuberculoma is suspected or attempts are
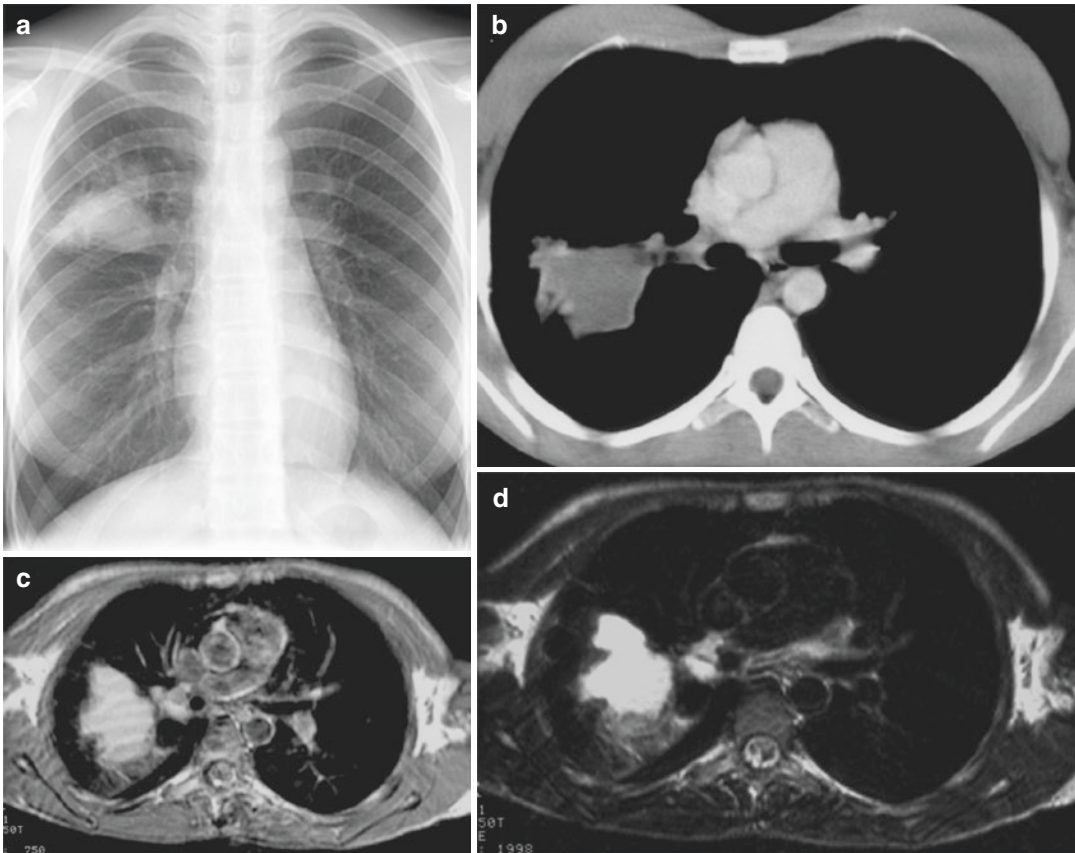
Fig. 4 A 15-year-old female with bronchocele in the right upper lobe. Chest radiograph shows a mass in the right upper lung field (**a**). Contrast-enhanced CT shows a mass with water density in the right upper lobe (**b**). Conventional T1-weighted SE (**c**) and T2-weighted turbo SE (**d**) images show the mass as high intensity due to mucus-filled bronchi and formation of a mucocele distal to the atelectatic segment, which was diagnosed as a bronchocele

made to distinguish it noninvasively from malignant nodules, pre- and post-contrast-enhanced conventional MR imaging may be the most suitable procedure because tuberculoma is one of the most well-known diseases that show intense FDG uptake and is difficult to distinguish from malignant nodules when FDG-PET or PET/CT is used (Chang et al. 2006).

3.1.3 Mucinous Bronchoalveolar Carcinoma

Adenocarcinoma of the lung constitutes a histologically and biologically heterogeneous group of tumors. Except for mucinous BAC, mucin production is seldom a truly prominent characteristic of this adenocarcinoma, so that there are no significant differences in the MR findings for adenocarcinoma of the lung and other subtypes of lung cancer. Mucinous BAC occasionally presents as a solitary pulmonary nodule with low or no uptake of contrast media on conventional post-contrast-enhanced T1-weighted image and thus may be difficult to differentiate from other benign nodules such as tuberculoma. However, many mucinous BACs demonstrate one of two radiological patterns, consolidation or diffuse disease. The consolidation may be segmental or may involve an entire lobe and, with the exception of pulmonary vasculature, shows as high signal intensity on T2-weighted turbo SE images, which is known as "white lung sign" (Fig. 6). In addition, intratumoral vessels may be detected on contrast-enhanced T1-weighted images (Gaeta et al. 2000, 2001, 2002).
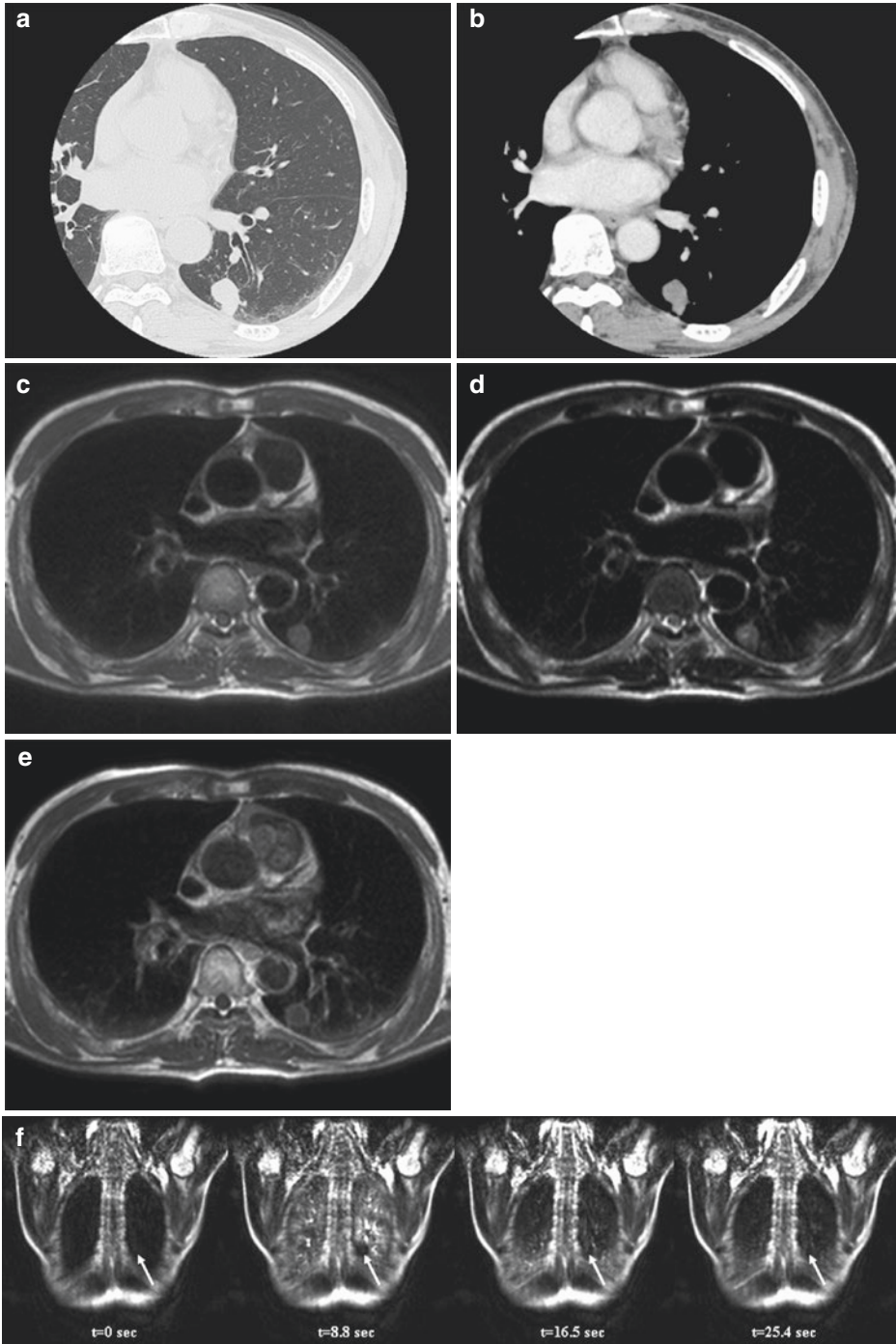
Fig. 5 A 67-year-old male with tuberculoma in the left lower lobe. Thin-section CT shows a solid nodule in the left lower lobe (**a**). Contrast-enhanced CT indicates homogeneity but little enhancement within the nodule (**b**). Black-blood T1-weighted turbo SE (**c**) and T2-weighted turbo SE (**d**) images show the nodule as, respectively, low and intermediate signal intensities in the left lower lobe. Post-contrast black-blood T1-weighted turbo SE image (**e**) showed thin-rim enhancement, which was diagnosed as tuberculoma. Dynamic MR imaging (**f**) with ultrafast GRE technique (L to R: $t = 0.0$ s, $t = 8.8$ s, $t = 16.5$ s, and $t = 25.4$ s) showed a slightly enhancing nodule in the left lower lung field. The nodule is not enhanced in the lung parenchymal phase ($t = 8.8$ s) and slightly enhanced in the systemic circulation phase ($t = 16.5$ and 25.4 s) due to low blood supply from bronchial circulation
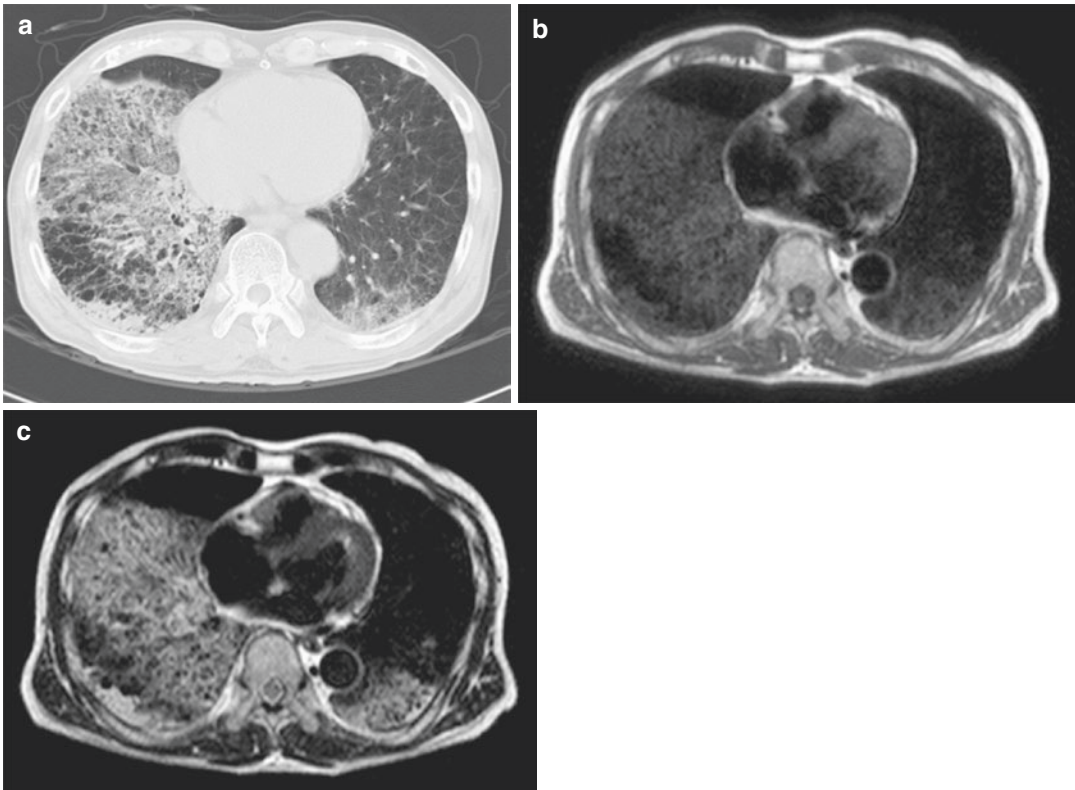
Fig. 6 A 73-year-old male with mucinous bronchoalveolar carcinoma (BAC) in the right middle and both lower lobes. Conventional CT shows ground-glass attenuation in the right middle and both lower lobes (**a**). Black-blood T1-weighted turbo SE (**b**) image shows mucinous BAC as low signal intensities. Black-blood T2-weighted turbo SE (**c**) image shows mucinous BAC with high signal intensities. These findings are known as "white lung sign"

3.1.4 Hamartoma

Pulmonary hamartomas, the third most common cause of solitary pulmonary nodules, are considered benign neoplasms that originate in fibrous connective tissue beneath the mucus membrane of the bronchial wall (Bateson 1973; Siegelman et al. 1986). A few investigators have reported on MR imaging of hamartomas. Sakai et al. (1994) found that all hamartomas appeared as a signal of intermediate intensity on T1-weighted SE images and as one of high intensity on T2-weighted SE images and four out of six hamartomas had a lobulated appearance separated by septa on T1- or T2-weighted SE images. In addition, pulmonary hamartomas pathologically diagnosed as lipomatous hamartoma sometimes show with high signal intensity on T1-weighted SE and T2-weighted turbo SE images (Yilmaz et al. 2004). Therefore, when these radiological findings are associated

with a pulmonary nodule, the nodule can be suspected of being a hamartoma, and the enhancement pattern within the nodule should be evaluated on post-contrast-enhanced T1-weighted SE images, where the regions with less enhancement correspond to core cartilaginous tissue and septa and areas of marked contrast enhancement correspond to branching cleft-like mesenchymal connective tissue that dip into the cartilaginous core (Sakai et al. 1994) (Fig. 7).

3.1.5 Aspergilloma

Saprophytic aspergillosis (aspergilloma) is characterized by Aspergillus infection without tissue invasion. It typically leads to conglomeration of intertwined fungal hyphae admixed with mucus and cellular debris within a pre-existing pulmonary cavity or ectatic bronchus (Gefter 1992; Aquino et al. 1994). A typical radiological finding of
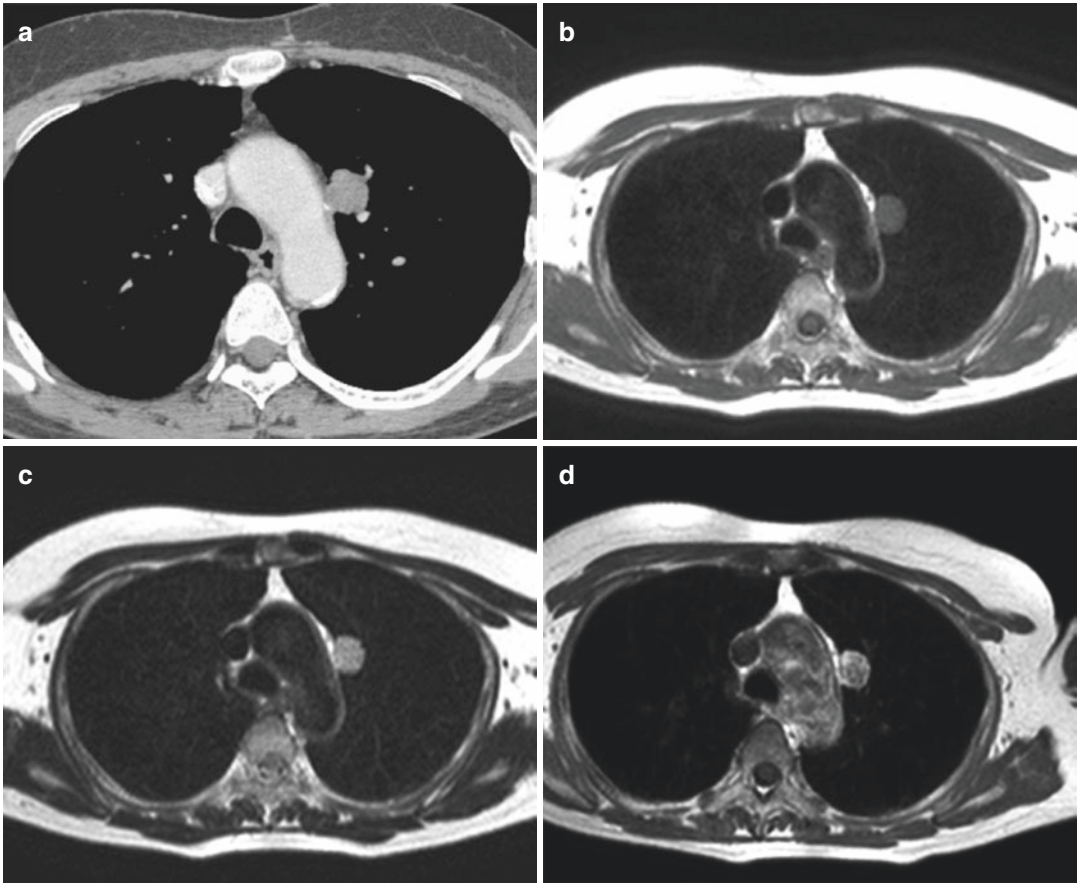
Fig. 7 A 54-year-old male with hamartoma in the left upper lobe. Conventional contrast-enhanced CT shows lobulated nodule in the left upper lobe (**a**). Black-blood T1-weighted turbo SE (**b**) and T2-weighted (**c**) images show a lobulated nodule as, respectively, low and high signal intensities in the left upper lobe. Post-contrast black-blood T1-weighted turbo SE (**d**) image shows less enhancement corresponding to core cartilaginous tissue, while areas of marked contrast enhancement correspond to cleft-like branching mesenchymal connective tissue

aspergilloma is a solid, round, or oval mass with soft-tissue opacity within a lung cavity. The mass is typically separated from the cavity wall by an airspace manifesting the so-called "air crescent" sign and is often associated with thickening of the wall and adjacent pleura (Gefter 1992; Park et al. 2007). The most common underlying causes are healed tuberculosis, bronchiectasis, bronchial cyst, and sarcoidosis. Other conditions that occasionally may be associated with aspergilloma include bronchogenic cyst, pulmonary sequestration, and pneumatoceles secondary to *Pneumocystis carinii* pneumonia in patients with acquired immunodeficiency syndrome.

The presence of a cavity within lung cancer is common and has been reported in 2–16% of cases (Felson and Wiot 1977). In general, lung cancer with a cavity typically shows a cavity wall with a thickness of more than 4 mm, spiculate or irregular inner and outer margins, enlarged lymph nodes, and a soft-tissue nodule or mass due to intracavitary tumorous mural regions associated with infiltration of the adjacent thoracic wall. In some cases, however, a lung cancer with a cavity may show a thin wall or "air crescent" sign on CXR or CT. It is therefore important to distinguish fungus ball from intracavitary tumorous mural regions by the "air crescent" sign in lung cancers with cavities, and pre- and post-contrast-enhanced conventional T1- and T2-weighted SE or turbo SE images are helpful for this purpose.

Although a cavity may be present within lung cancer, a viable lung cancer evidenced as a cavity and/or intracavitary mass shows a typical signal intensity pattern on pre- and post-contrast-enhanced conventional T1- and T2-weighted SE or turbo SE images with as its characteristics a signal of low or intermediate intensity on pre-contrast-enhanced T1-weighted images, one of intermediate or high intensity on T2-weighted images, and one of high intensity due to intensive and homogeneous enhancement on post-contrast-enhanced T1-weighted images (Ma et al. 1985; van der Heide et al. 1985; Zinreich et al. 1988; Herold et al. 1989; Fujimoto et al. 1994; Blum et al. 1994) (Fig. 8). In aspergilloma cases, on the other hand, the signal intensity of the intracavitary lesion is especially reduced on the T2-weighted SE or turbo SE image because of the presence of calcium, air, or ferromagnetic elements resulting from Aspergillus infection (Herold et al. 1989; Fujimoto et al. 1994; Blum et al. 1994) (Fig. 9). Because the presence of the ferromagnetic elements of iron, magnesium, and manganese is essential to the metabolism of amino acids by fungi, Fujimoto et al. (1994) have suggested that the reduction in signal intensity on T1-weighted images and the marked reduction on T2-weighted images are characteristics of aspergilloma as well as mycetomas and may be useful for differentiation of aspergilloma from intracavitary tumorous mural nodules.

3.2 New Non-Contrast-Enhanced MR Imaging of Pulmonary Nodules

To overcome limitations in differentiating benign from malignant nodules, STIR turbo SE imaging and diffusion-weighted imaging (DWI) were introduced in 2008 as more promising sequences than T2WI and pre- or post-CE T1WI for non-CE MR imaging for nodule assessment (Koyama et al. 2008; Mori et al. 2008). Koyama et al. demonstrated that the quantitative capability of STIR turbo SE imaging was significantly better than non-CE T1WI or T2WI for differentiating malignant from benign nodules, with sensitivity, speci-

ficity, and accuracy of 83.3%, 60.6%, and 74.5%, respectively (Koyama et al. 2008). DWI is usually assessed by the apparent diffusion coefficient (ADC), which evaluates the diffusivity of water molecules within tissue between 0 s/mm^2 and a maximum b value ranging from 500 to 1000 s/mm^2 in routine clinical practice. According to this ADC evaluation, the quantitative and/or qualitative sensitivities and specificities of DWI in this setting have been reported as 70.0–88.9% for sensitivity and 61.1–97.0% for specificity (Mori et al. 2008; Satoh et al. 2008; Uto et al. 2009). On the other hand, one study has suggested the signal intensity ratio between lesion and spinal cord is more useful than ADC and used this ratio to determine that sensitivity, specificity, and accuracy of DWI were 83.3%, 90.0%, and 85.7%, respectively, and that the accuracy of this new parameter was significantly higher than that of ADC (50.0%) (Uto et al. 2009). It would therefore be better to use the abovementioned two non-CE MR techniques as routine clinical protocols non-CE-T1WI, T2WI, and CE-T1WI to improve differentiation capability between malignant and in addition to benign nodules on non-CE-MR examinations.

3.3 Dynamic Contrast-Enhanced MR Imaging of Pulmonary Nodules

Although in some cases benign or malignant focal lesions can be differentiated from others by using pre- and post-contrast-enhanced conventional T1- or T2-weighted SE or turbo SE imaging, significant overlaps have been observed between benign and malignant lesions in routine clinical practice (Kono et al. 1993; Kusumoto et al. 1994). To overcome this problem, dynamic contrast-enhanced MR imaging has been proposed as an alternative technique for diagnosis and/or management of pulmonary nodules (Table 1). As a result of advances in MR systems and pulse sequences, there are now three major methods for dynamic MR imaging of the lung. Many investigators have proposed dynamic MR imaging be used for two-dimensional (2D) SE or turbo SE sequences or for various types
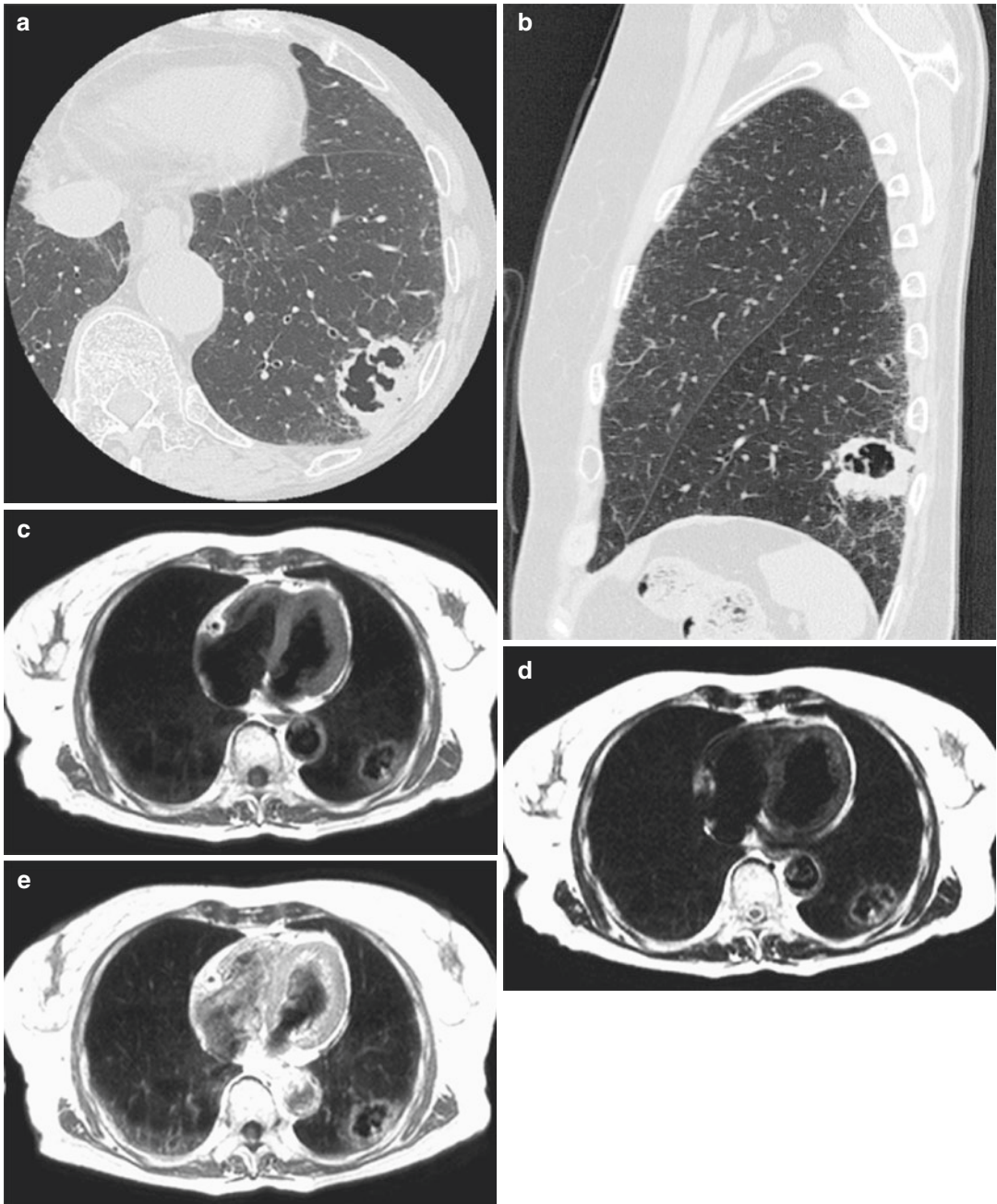
Fig. 8 A 74-year-old male with squamous cell carcinoma in the left lower lobe. Thin-section CT (**a**) and sagittal reformat (**b**) show mass with irregularly thickened cavity wall in the left lower lobe. Black-blood T1-weighted turbo SE (**c**) and T2-weighted (**d**) images show mass with irregularly thickened cavity wall as, respectively, low and high signal intensities in the left lower lobe. Post-contrast black-blood T1-weighted turbo SE (**e**) image shows well-enhanced cavity wall corresponding to lung cancer

of 2D or three-dimensional (3D) gradient-echo (GRE) sequences and that enhancement patterns within nodules and/or parameters determined from signal intensity-time course curves be assessed visually. These curves represent first transit and/or recirculation and washout of contrast media in
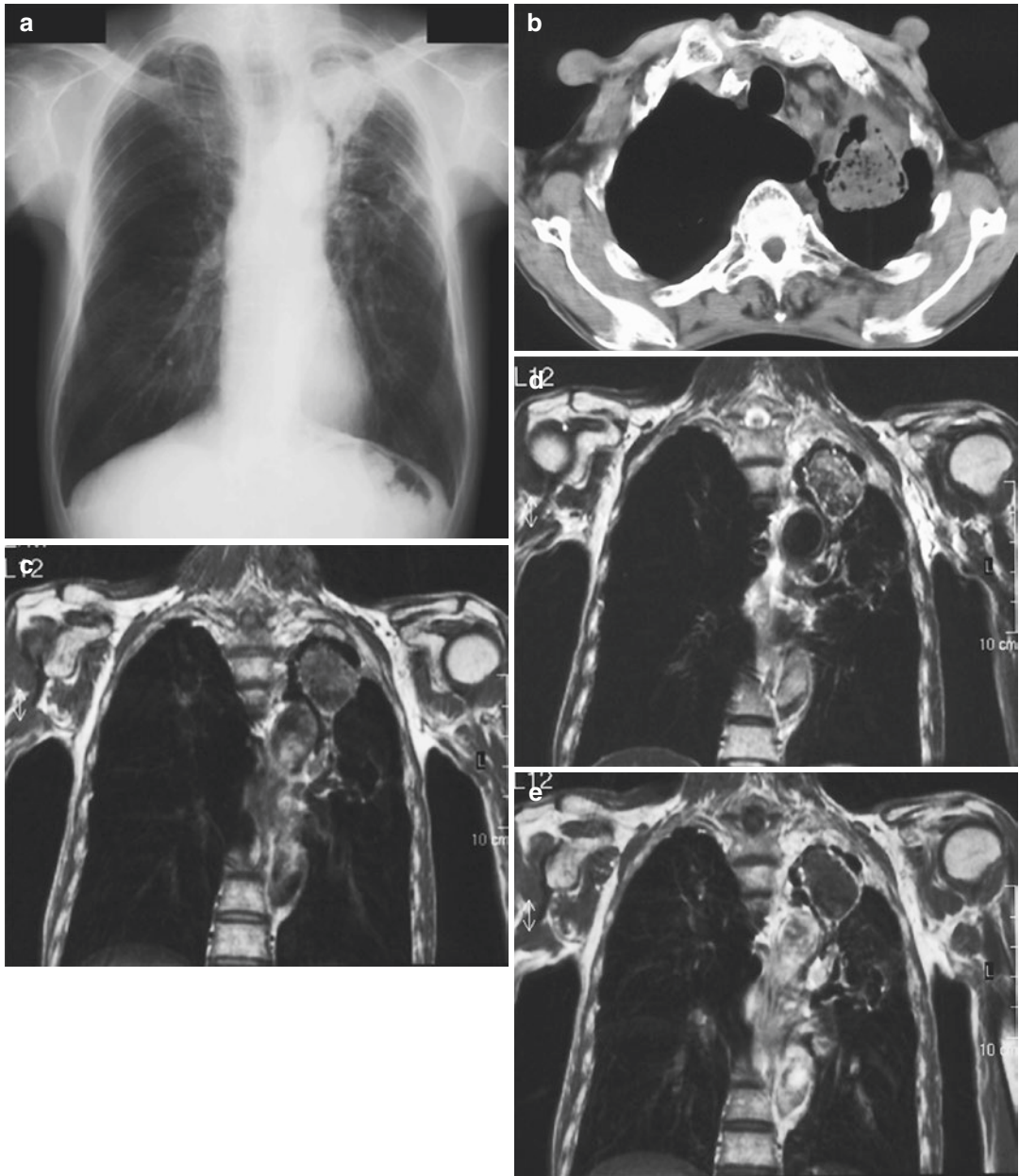
Fig. 9 A 60-year-old male with aspergilloma in the left upper lobe. Chest radiograph (**a**) shows "air crescent" sign in the left upper lung field. Conventional CT (**b**) shows fungus ball within cavity. Conventional T1-weighted SE (**c**) and T2-weighted turbo SE (**d**) images on coronal plane show intracavitary lesion as, respectively, low and very low signal intensities in the left upper lobe. Post-contrast T1-weighted SE image (**e**) shows well-enhanced cavity wall and no enhancement of intracavitary lesion

5 min or more with repeated breath holding (Kono et al. 1993, 2007; Kusumoto et al. 1994; Hittmair et al. 1995; Gückel et al. 1996; Ohno et al. 2002, 2004a; Fujimoto et al. 2003; Schaefer et al. 2004, 2006; Donmez et al. 2007). Taking into account the inherent inhomogeneous composition of many intraindividual lung cancers and even within benign lesions such as central necrosis, only a dynamic

contrast-enhanced 3D approach has the chance of depicting underlying histologies. This is important for the primary diagnosis as well as during follow up examinations to assure evaluation of the same region of interest again. Recently, dynamic contrast-enhanced MR perfusion imaging has been proposed for quantitative and qualitative assessment of regional pulmonary perfusion abnormalities by using 2D or 3D ultrafast GRE sequences with sharp bolus profiles (Hatabu et al. 1996, 1999; Amundsen et al. 1997, 2000; Levin et al. 2001; Matsuoka et al. 2001; Ohno et al. 2002, 2004c, 2005, 2007a, b; Fink et al. 2004). This technique allows for directly assessing the first passage of contrast media within nodules in less than 35 s within a single breath hold and to evaluate blood supply to nodules from pulmonary and/or bronchial circulation (Ohno et al. 2002, 2004c). It should be noted though that the ideal acquisition of contrast-enhanced dynamic studies of tumor perfusion should not be limited to the first pulmonary passage of the contrast agent. Tumors will be supplied by systemic, bronchial arteries instead of pulmonary arteries (Milne and Zerhouni 1987; Ohno et al. 2002, 2004c). In this case or due to inherent slow blood flow within a tumor an examination in a single breath hold might not be sufficient in detecting the full perfusion cycle of wash-in and wash-out (Ohno et al. 2002, 2004c). Examination of prolonged wash-out always reveals an underlying reperfusion of pulmonary tissue by both pulmonary and bronchial arteries. This circumstance has not been accounted for in the usual models for quantification of tissue perfusion so far.

Although there are various dynamic MR techniques, reported sensitivities range from 94 to 100%, specificities from 70 to 96%, and accuracies of more than 94% (Kono et al. 1993, 2007; Patz et al. 1993; Kusumoto et al. 1994; Hittmair et al. 1995; Gückel et al. 1996; Ohno et al. 2002, 2004a; Fujimoto et al. 2003; Schaefer et al. 2004, 2006; Donmez et al. 2007). These specificities and accuracies for dynamic MR imaging are superior to those reported for dynamic CT and almost equal to or superior to those for FDG-PET or PET/CT (Swensen et al. 1992, 1996, 2000; Dewan et al. 1993; Kono et al. 1993; Kusumoto et al. 1994; Hittmair et al. 1995; Yamashita et al.

1995; Bury et al. 1996; Gückel et al. 1996; Zhang and Kono 1997; Ohno et al. 2002, 2004a; Fujimoto et al. 2003; Herder et al. 2004; Schaefer et al. 2004, 2006; Yi et al. 2004, 2006; Jeong et al. 2005; Joshi et al. 2005; Mori et al. 2005; Bryant and Cerfolio 2006; Christensen et al. 2006; Donmez et al. 2007; Kim et al. 2007; Kono et al. 2007; Lee et al. 2007). Therefore, dynamic contrast-enhanced MR imaging may play a complementary role in the diagnosis of pulmonary nodules assessed with FDG-PET or PET/CT. Although these results are highly promising, further research in this field may be necessary in the light of recently published data regarding the MR signal dependency in perfusion studies on the contrast agent concentration. As quantification of perfusion parameters is dependent on an almost linear relationship of signal to concentration great care has to be taken regarding the dosage and application of contrast agents (Puderbach et al. 2008).

Although differentiation of malignant from benign pulmonary nodules by means of dynamic MDCT, dynamic MRI, and PET or PET/CT with FDG has been tried in several studies, accurate separation of active infectious nodules from malignant neoplasms on the basis of dynamic CT and MR parameters and uptakes of FDG can be extremely difficult in view of the underlying pharmacokinetical, pathological, and biological properties of malignant neoplasms and active infectious nodules. In addition, when considering the management of pulmonary nodules in clinical practice, it may be helpful to differentiate pulmonary nodules requiring further intervention and treatment (low- or high-grade malignant tumors and active infectious nodules) from pulmonary nodules requiring no further evaluation (benign tumors and chronic infectious nodules) rather than to differentiate between malignant nodules and other nodules. For this latter differentiation, ultrafast dynamic MR imaging can divide all nodules into the two categories (Figs. 5 and 10) (Ohno et al. 2002).

In addition, the results of several comparative studies of findings obtained with dynamic MR parameters and with immuno-histopathological examination of small peripheral lung cancers, the
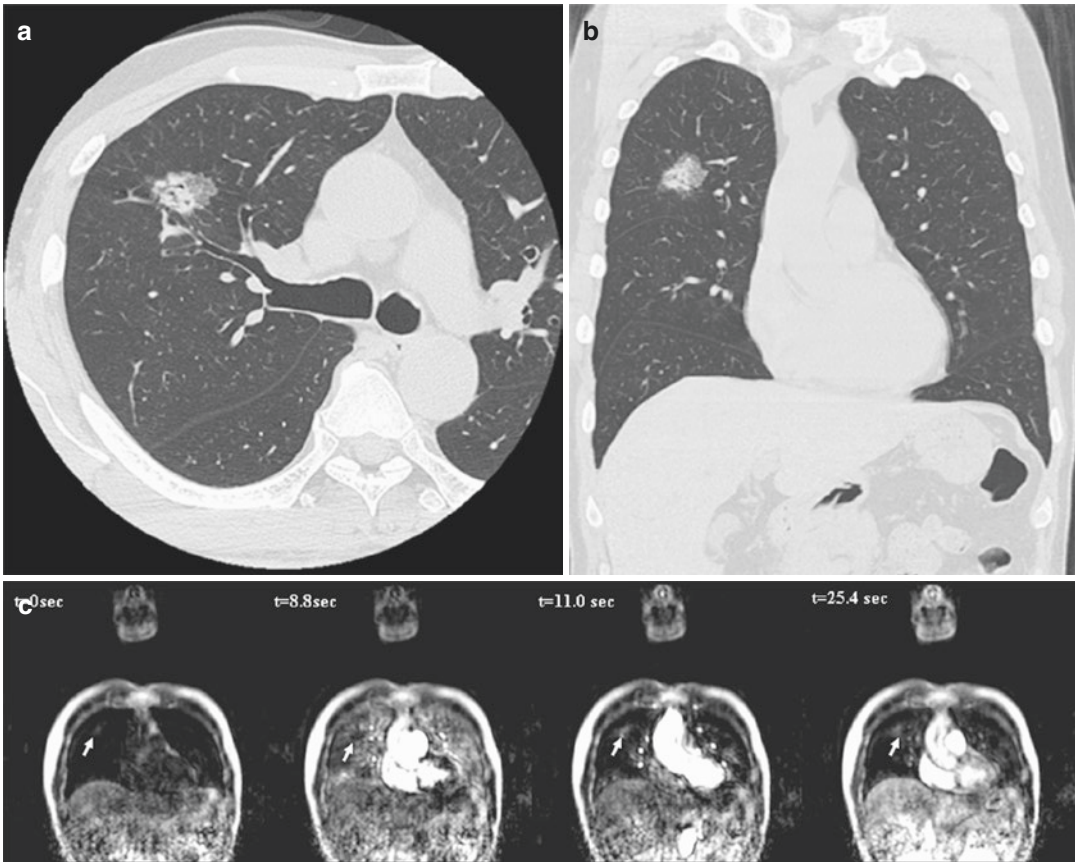
Fig. 10 A 57-year-old female with invasive adenocarcinoma. Thin-section CT (**a**) and coronal reformat (**b**) show partly solid nodule in the right upper lobe. Dynamic MR imaging (**c**) with ultrafast GRE technique (L to R: $t = 0.0$ s, $t = 8.8$ s, $t = 11.0$ s, and $t = 25.4$ s) shows well-enhanced nodule (*arrow*) in the right upper lung field. The nodule was not enhanced in the lung parenchymal phase ($t = 8.8$ s) and well enhanced in the systemic circulation phase ($t = 11.0$ and 25.4 s) due to enhanced blood supply from bronchial circulation

former showed good correlation with tumor angiogenesis (Fujimoto et al. 2003; Schaefer et al. 2006), and the potential for more accurate differentiation of subtypes of small peripheral adenocarcinomas than is possible with thin-section CT, or for prognosis both before and after treatment (Fujimoto et al. 2003; Ohno et al. 2005; Schaefer et al. 2006).

In the last a few decades, the diagnostic performance of these dynamic MR techniques for distinguishing malignant from benign nodules has been reported as comprising sensitivity ranging from 94 to 100%, specificity from 70 to 96%, and accuracy of more than 94% (Gückel et al. 1996; Ohno et al. 2002, 2004a, 2008a, 2014; Fujimoto et al. 2003; Schaefer et al. 2004; Kono et al. 2007; Cronin et al. 2008). In addition, a meta-analysis found that there were no significant differences in

diagnostic performance among dynamic CE-CT, dynamic CE-MR imaging, FDG-PET, and single photon emission tomography (SPECT) (Cronin et al. 2008), although dynamic MR imaging with the 3D GRE sequence and ultrashort TE proved its superior diagnostic performance in a direct and prospective comparison study of dynamic CE-CT and co-registered FDG-PET/CT (Ohno et al. 2008a). The use of dynamic MR imaging with the 3D GRE sequence and ultrashort TE is therefore likely to be more effective than that of other methods and may lead to improved diagnostic performance of dynamic CE-MR imaging. In addition, this method has the potential to play a complementary or substitutional role in the characterization of pulmonary nodules assessed with dynamic CE-CT, FDG-PET, and/or PET/CT.

Moreover, ultrafast 3D dynamic MR data can also be used for the prediction of postoperative lung function for NSCLC patients (Ohno et al. 2004b, 2007b, 2011a, b). The semiquantitative regional perfusion obtained from ultrafast dynamic MR imaging shows good correlation with that assessed by perfusion scintigraphy, with a reported limit of agreement of ± 6%, which is insignificant enough to make ultrafast dynamic MR imaging suitable for clinical purposes (Ohno et al. 2004b). Moreover, the prediction of postoperative lung function derived from dynamic MR imaging was more accurate than that derived from perfusion scintigraphy, single photon emission tomography (SPECT), SPECT fused with CT (SPECT/CT), or quantitatively and/or qualitatively assessed MDCT, which is predicted postoperative lung function from preoperative lung function and the number of lung segments in the total and resected lung evaluated by pulmonary surgeons, and the predictive accuracy is almost equal to that obtained with quantitatively assessed MDCT based on density-masked CT technique (Ohno et al. 2004b, 2007b, 2011a). Dynamic MR imaging may therefore be useful not only for the characterization of pulmonary nodules, but prediction of postoperative lung function may also assist the management of pulmonary nodules, including determination of whether further intervention and treatment and/or operability are indicated for lung cancer patients.

4 Assessment of TNM Stages

The international TNM classification proposed by the International Union against Cancer (UICC) has been widely used in the investigation and treatment of lung cancer (Tables 2, 3, 4, and 5), and shows that survival rates have improved with more accurate staging and more accurate differentiation between those patients who are candidates for surgical resection and those who are judged to be inoperable but would benefit from chemotherapy, radiotherapy, or both (Sobin and Wittekind 2002). Therefore, accurate radiological staging may affect the management as well as the prognosis of patients. However, only approximately one-half of the TNM stages determined with CT

Table 2 Stage according to Goldstraw et al. (2007)

TNM stage	T factor	N factor	M factor
0	Tis	N0	M0
IA	T1a or T1b	N0	M0
IB	T2a	N0	M0
IIA	T1a, T1b and T2a	N1	M0
	T2b	N0	
IIB	T2b	N1	M0
	T3	N0	
IIIA	T1a, T1b, T2a and T2b	N2	M0
	T3	N1	
	T3	N2	
	T4	N0	
	T4	N1	
IIIB	T4	N2	M0
	Any T	N3	
IV	Any T	Any N	M1a or M1b

systems in the past have agreed with operative staging, with patients being both under- and overstaged (Lewis et al. 1990; Gdeedo et al. 1997).

Currently, newly developed MDCT systems, FDG-PET or PET/CT, are considered useful for precise assessment of tumor extent because of their multiplanar capability and for accurate diagnosis of metastatic lymph nodes by analyzing the glucose metabolism of cancer cells in lung cancer patients. However, since 1991 it has been suggested that MR imaging, with its multiplanar capability and better contrast resolution of tumor and mediastinum or of tumor and chest wall or both than that of CT, may also be useful, but only for the assessment of mediastinal and chest wall invasions and determination of the short axis diameter of certain mediastinal lymph nodes (Webb et al. 1991). However, recent advancements in MR systems, improved or newly developed pulse sequences and/or utilization of contrast media has resulted in improved diagnosis of TNM staging for lung cancer patients (Table 6).

4.1 MR Assessment of T Classification

T classification is the descriptor given to the primary tumor and its local extent (Sobin and Wittekind 2002). The definitions are given in

Table 3 T classification – primary tumor according to Goldstraw et al. (2007)

TX	Primary tumor cannot be assessed or tumor proven by the presence of malignant cells in sputum or bronchial washings but not visualized by imaging or bronchoscopy
T0	No evidence of primary tumor
Tis	Carcinoma in situ
T1	Tumor 3 cm or less in greatest dimension, surrounded by lung or visceral pleura, without bronchoscopic evidence of invasion more proximal than the lobar bronchus (i.e., not in the main bronchus)[a] T1a: Tumor 2 cm or less in greatest dimension T1b: Tumor more than 2 cm but 3 cm or less in greatest dimension
T2	Tumor more than 3 cm but 7 cm or less or tumor with any of the following features (T2 tumors with these features are classified T2a if 5 cm or less): involves main bronchus, 2 cm or more distal to the carina; invades visceral pleura (PL1 or PL2); associated with atelectasis or obstructive pneumonitis that extends to the hilar region but does not involve the entire lung T2a: Tumor more than 3 cm but 5 cm or less in greatest dimension T2b: Tumor more than 5 cm but 7 cm or less in greatest dimension
T3	Tumor more than 7 cm or one that directly invades any of the following: parietal pleural (PL3), chest wall (including superior sulcus tumors), diaphragm, phrenic nerve, mediastinal pleura, parietal pericardium; or tumor in the main bronchus less than 2 cm distal to the carina1 but without involvement of the carina; or associated atelectasis or obstructive pneumonitis of the entire lung or separate tumor nodule(s) in the same lobe
T4	Tumor of any size that invades any of the following: mediastinum, heart, great vessels, trachea, recurrent laryngeal nerve, esophagus, vertebral body, carina, separate tumor nodule(s) in a different ipsilateral lobe

[a]The uncommon superficial spreading tumor of any size with its invasive component limited to the bronchial wall, which may extend proximally to the main bronchus, is also classified as T1a

Table 4 N classification – regional lymph nodes according Goldstraw et al. (2007)

NX	Regional lymph nodes cannot be assessed
N0	No regional lymph node metastasis
N1	Metastasis in ipsilateral peribronchial and/or ipsilateral hilar lymph nodes and intrapulmonary lymph nodes, including involvement by direct extension
N2	Metastasis in ipsilateral mediastinal and/or subcarinal lymph node(s)
N3	Metastasis in contralateral mediastinal, contralateral hilar, ipsilateral or contralateral scalene, or supraclavicular lymph node(s)

Table 5 M classification – distant metastasis according Goldstraw et al. (2007)

MX	Distant metastasis cannot be assessed
M0	No distant metastasis
M1	Distant metastasis M1a: Separate tumor nodule(s) in a contralateral lobe, tumor with pleural nodules or malignant pleural (or pericardial) effusion[a] M1b: Distant metastasis (in extrathoracic organs)

[a]Most pleural (and pericardial) effusions with lung cancer are due to tumor. In a few patients, however, multiple cytopathologic examinations of pleural (pericardial) fluid are negative for tumor, and the fluid is nonbloody and is not an exudate. Where these elements and clinical judgment dictate that the effusion is not related to the tumor, the effusion should be excluded as a staging element, and the patient should be classified as M0

Table 3. While the T factor is subdivided into four groups, the distinction between T3 and T4 tumors is critical because it represents the dividing line between conventional surgical and non-surgical management for NSCLC patients (Armstrong 2000). It is therefore more important to distinguish T3 from T4 tumors than to differ- entiate T1 and T2 tumors and determine nodal staging. For this reason, MR imaging may be helpful for assessment of mediastinal invasion, chest wall invasion, and distinguishing primary tumors from secondary changes such as atelecta- sis or obstructive pneumonia, although it may be difficult to distinguish simple extension of the tumor into the mediastinal pleura or pericardium (T3) from actual invasion (T4).

4.1.1 Mediastinal Invasion

Many surgeons consider minimal invasion of mediastinal fat as resectable (Quint and Francis 1999), so that clinicians want to know whether minimal mediastinal invasion (T3 disease) or actual invasion (T4 disease) has occurred before considering surgical resection. The accuracy of CT for evaluating hilar and mediastinal inva-

Table 6 Recommended MR protocol for lung cancer staging

No.	Recommended sequence	TR (ms)	TE (ms)	FA (°)	Black-blood TI (ms)	TI (ms)	Matrix	Respiration	Suggestion
1	Pre-contrast-enhanced ECG-gated T1-W-SE or TSE	1 <R-R>	15–25	N/A	N/A	N/A	256 × 256	RT or RG	N/A
	Pre-contrast-enhanced ECG-gated black-blood T1-W-TSE	1<R-R>	8	N/A	800–1000	N/A	256 × 256	BH	Parallel imaging should be applied. ETL should be less than 20
	Pre-contrast-enhanced 3D T1-GRE (VIBE, TTHRIVE, Quick 3D, etc.)	4	≤2	15	N/A	N/A	256 × 256	BH	Fat suppression technique should be applied
2	ECG- and respiratory-gated T2-W-TSE	2 or 3 <R-R>	90–100	N/A	N/A	N/A	256 × 256	RT or RG	ETL should be less than 15
	Pre-contrast-enhanced ECG-gated black-blood T2-W-TSE	2 or 3 <R-R>	102	N/A	2000–3000	N/A	256 × 256	BH	Parallel imaging should be applied. ETL should be less than 45
3	Respiratory-gated STIR TSE	Up to respiratory cycle	15	N/A	N/A	150–240	256 × 256	RG	ETL should be less than 5, if sequentially reordered phase encoding scheme is used
	ECG-gated black-blood STIR TSE	2<R-R>	5	N/A	1000–2000	150–240	256 × 256	BH	Parallel imaging should be applied. ETL should be less than 8
4	Diffusion-weighted imaging by EPI	∞	65	N/A	N/A	150–240	256 × 256	Free-breath	Number of excitation should be equal to or more than 6

Table 6 (continued)

No.	Recommended sequence	TR (ms)	TE (ms)	FA (°)	Black-blood TI (ms)	TI (ms)	Matrix	Respiration	Suggestion
5	ECG-gated contrast-enhanced MR angiography	5.7	1.9	20	N/A	256 × 128–256	BH	k-Space segmentation should be adapted	Dynamic MR images should be obtained every 1.1 s after contrast media injection. Increasing temporal resolution by parallel imaging technique
	Time-resolved contrast-enhanced MR angiography	4	1.2	20–30	N/A	512 × 333	BH	Temporal resolution should be less than 4 s	Dynamic MR images should be obtained at 0, 1, 2, 3, 4, 5, 6, and 8 min after contrast media injection
6	Post-contrast-enhanced ECG-gated T1-W-SE or TSE	1 <R-R>	15–25	N/A	N/A	N/A	256 × 256	RT or RG	N/A
	Post-contrast-enhanced ECG-gated black-blood T1-W-TSE	1<R-R>	8	N/A	800–1000	N/A	256 × 256	BH	Parallel imaging should be applied. ETL should be less than 20
	Post-contrast-enhanced 3D T1-GRE (VIBE, TTHRIVE, Quick 3D, etc.)	4	≤ 2	15	N/A	N/A	256 × 256	BH	Fat suppression technique should be applied

SE spin echo, *TSE* turbo spin echo, *GRE* gradient-echo, *EPI* echo planar imaging, *TR* repetition time, *TE* echo time, *FA* flip angle, *RT* respiratory trigger, *RG* respiratory-gated, *ETL* echo train length, *VIBE* volumetric interpolated breath-hold examination, *THRIVE* T1 high resolution isotropic volume examination, *Quick 3D* segmented 3D T1-weighted spoiled gradient-echo

sion of lung cancer has been investigated extensively over the last decades. Sensitivity for assessment of mediastinal invasion by single detector computed tomography with or without the use of helical scanning ranged from 40 to 84% and specificity from 57 to 94% (Baron et al. 1982; Martini et al. 1985; Quint et al. 1987, 1995; Rendina et al. 1987; Glazer et al. 1989; Herman et al. 1994; White et al. 1994; Takahashi et al. 1997).

The RDOG study compared CT with MR imaging for 170 patients with NSCLC, although only T1-weighted images obtained without the use of cardiac or respiratory gating techniques were assessed in this study (Webb et al. 1991). Although there was no significant difference between the sensitivity (63% and 56% for CT and MR imaging, respectively) and the specificity (84% and 80%) for distinguishing between T3-T4 tumors and T1-T2 tumors in this study, the RDOG reported that 11 patients showed mediastinal invasion and that the superior contrast resolution of MR imaging conferred a slight but statistically significant advantage over CT for accurate diagnosis of mediastinal invasion. In addition, delineation of tumor invasion of pericardium (T3) or heart (T4) was superior on MR imaging compared with CT scan when the cardiac-gated T1-weighted sequence was used for improved avoidance of cardiac motion artifacts (White 1996). The normal pericardium has low signal intensity. Direct invasion of the cardiac chambers is readily demonstrated on T1-weighted images, because blood flowing through the cardiac chambers is signal void, so that the tumor is conspicuous because of its higher signal intensity. However, the accuracy of minimal mediastinal invasion assessment by both CT scanning and MR imaging is limited because it depends on visualization of the tumor within the mediastinal fat (Wong et al. 1999). In contrast to the assessment of mediastinal invasion, Mayr et al. (1987) found CT scanning to be more accurate than MR imaging in visualizing and assessing both normal and abnormal airways. They evaluated 319 normal and 79 abnormal bronchoscopically visualized bronchi. Their study found that CT scanning was accurate in all

cases, whereas MR imaging correctly identified only 45% of normal bronchi and 72% of abnormal bronchi (Magdeleinat et al. 2001). This discrepancy can be attributed both to the higher spatial resolution of CT scanning and to the low intrinsic MR imaging signal of air. Therefore, the relationship of lung cancer to central endobronchial extension is more accurately demonstrated on CT scans.

Recent advancement in MR systems, improved pulse sequences, and utilization of contrast media have resulted in the introduction of new MR imaging techniques for assessment of mediastinal invasion of lung cancer. Contrast-enhanced MR angiography has been used for assessment of cardiovascular or mediastinal invasions (Takahashi et al. 2000; Ohno et al. 2001). Ohno et al. (2001) described a series of 50 NSCLC patients with suspected mediastinal and hilar invasion of lung cancer visualized with contrast-enhanced CT scans, cardiac-gated MR imaging, and non-cardiac- and cardiac-gated contrast-enhanced MR angiographies (Fig. 11). In this study, sensitivity, specificity, and accuracy of contrast-enhanced MR angiography ranged from 78% to 90%, 73% to 87%, and 75% to 88%, respectively. These values were higher than those of contrast-enhanced single helical CT and conventional T1-weighted imaging (Ohno et al. 2001). Thus, contrast-enhanced MR angiography is thought to improve the diagnostic capability of MR imaging for mediastinal and hilar invasion.

In 2005, another new technique, cine MR imaging obtained with a steady-state free precession (SSFP) sequence was introduced as useful for evaluation of cardiovascular invasion in patients with thoracic mass (Seo et al. 2005). In this study, as well as previous electron beam CT or traditional cine MR studies (Murata et al. 1994; Sakai et al. 1997), the assessment of sliding motions between thoracic masses and adjacent mediastinal structure demonstrated a very high diagnostic capability (sensitivity: 100%, specificity: 92.9%, accuracy: 94.4%) (Seo et al. 2005). However, only 9 of 26 lung cancer patients were included in this study since the others had mediastinal tumors. Further investigation thus
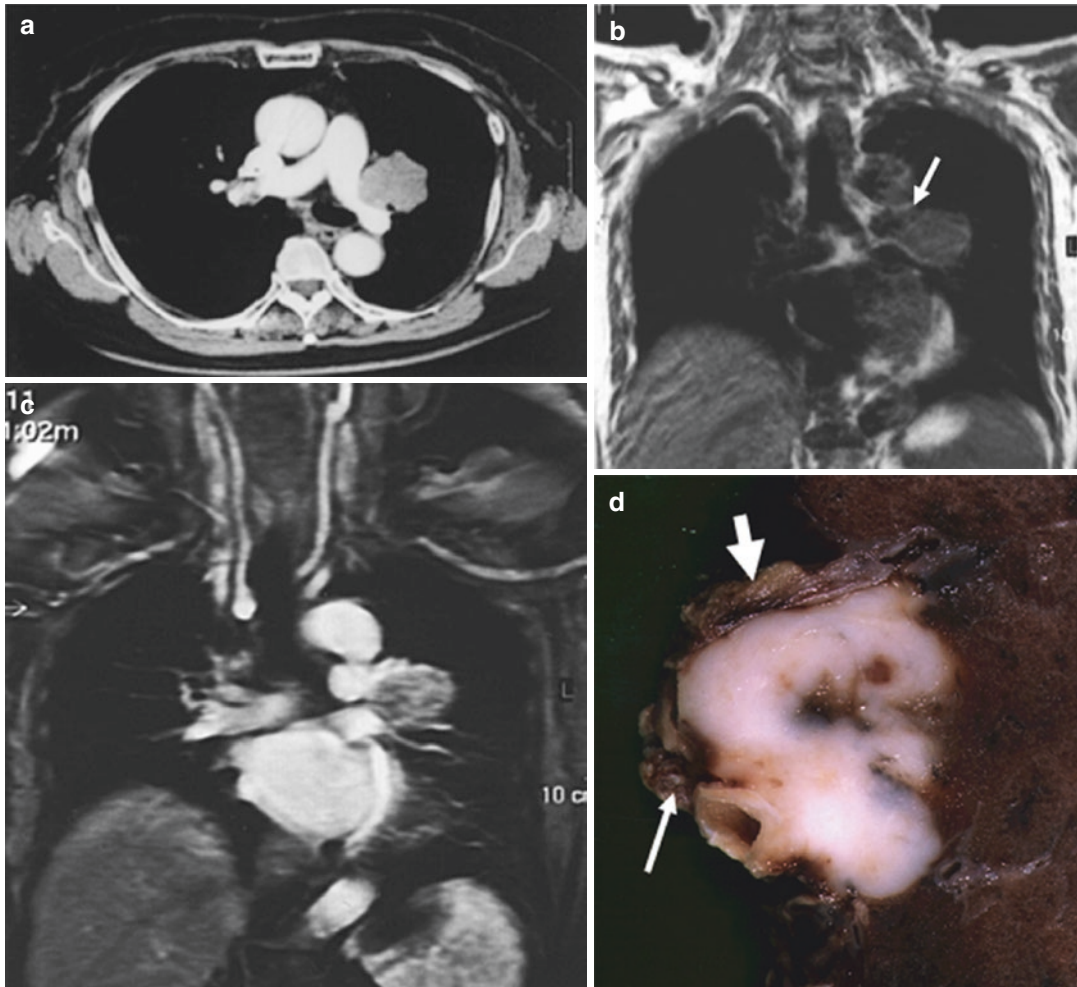
Fig. 11 A 68-year-old female with squamous cell carcinoma in the left upper lobe. Contrast-enhanced thin-section CT (**a**) suggests invasion to pulmonary vein and mediastinum, while conventional T1-weighted image (**b**) on coronal plane suggests invasion to pulmonary artery and mediastinum. Contrast-enhanced MR angiography (**c**) clearly shows invasion to pulmonary artery and vein, but not mediastinal invasion due to visualization of mediastinal fat between pulmonary artery and pulmonary vein as a *black area*. Macroscopical finding of the resected left upper lobe (**d**) shows invasion to left pulmonary artery (*arrow*) and left superior pulmonary vein (*large arrow*), but not mediastinal invasion

seems to be warranted to determine the actual diagnostic capability of cine MR imaging for mediastinal invasion in NSCLC patients.

MDCT is widely utilized for routine clinical practice, and it was found that thin-section multiplanar reformatted (MPR) imaging from thin-section volumetric MDCT data was useful for the evaluation of T classification due to its multiplanar capability (Higashino et al. 2005). Higashino et al. (2005) suggested that mediasti-nal invasion that can be assessed from thin-section coronal MPR images with 1 mm section thickness with greater sensitivity, specificity, and accuracy than can be achieved with routine MDCT with 5 mm section thickness and with slightly better specificity and accuracy than with thin-section axial MDCT with 1 mm section thickness. Although MR imaging is considered to show superior tissue contrast to that of MDCT, the similar multiplanar capability, faster scan
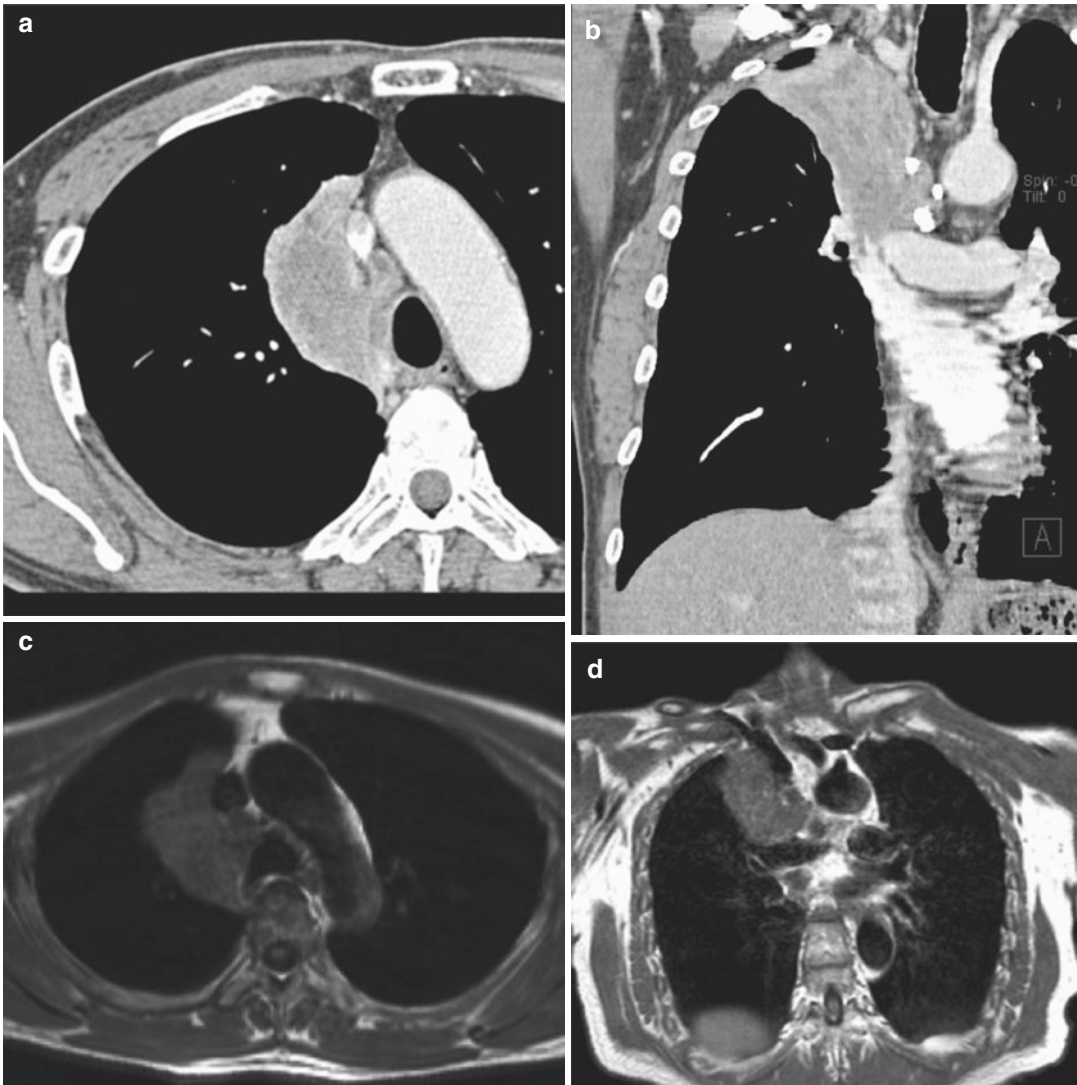
Fig. 12 A 61-year-old male with squamous cell carcinoma in the right upper lobe. Contrast-enhanced CT (**a**) suggests mediastinal invasion, while contrast-enhanced coronal reformat (**b**) clearly demonstrates mediastinal invasion. Black-blood T1-weighted images on axial (**c**) and coronal (**d**) planes also clearly demonstrate invasion to superior venous cava and mediastinum

time and better spatial resolution of thin-section MDCT may result in better assessment of mediastinal invasion in NSCLC patients than by previously described MR techniques (Fig. 12). Further investigations as well as comparative studies of thin-section MDCT and previously described or newly developed MR imaging techniques thus seem to be warranted to determine the actual significance of MR imaging for assessment of mediastinal invasion in routine clinical practice.

4.1.2 Distinguishing Lung Cancer from Secondary Change

Distinguishing primary lung cancer from secondary change is important for assessment of tumor extent and the therapeutic effect of chemotherapy and/or radiotherapy. While the therapeutic effect of conservative therapy has been assessed by using World Health Organization (WHO) criteria or response evaluation criteria in solid tumors (RECIST) (World Health Organization 1979;

Therasse et al. 2000), it would be difficult to use CXR or plain or contrast-enhanced CT to evaluate tumor extent or therapeutic effect for cases with atelectasis or obstructive pneumonia.

MR imaging, on the other hand, has potential for distinguishing lung cancer from secondary change due to atelectasis or pneumonitis (Kono et al. 1993). In some cases, it can be difficult to distinguish lung cancer from post-obstructive atelectasis or pneumonitis because these secondary changes tend to be enhanced to a similar degree as the central tumor on contrast-enhanced CT scan. On T2-weighted MR imaging, however, post-obstructive atelectasis and pneumonitis often show higher signal intensity than does the central tumor. Bourgounin et al. (1991) evaluated the histological findings of obstructive pneumonitis or atelectasis in patients who had undergone surgical resection of lung cancer and had been evaluated preoperatively with MR imaging. They found that cholesterol pneumonitis and mucus plugs displayed higher signal intensity than the tumor on T2-weighted images, while atelectasis and organizing pneumonitis were isointense to the tumor. Kono et al. (1993) described a series of 27 patients with central lung cancer associated with atelectasis or obstructive pneumonitis (Fig. 13). These patients were examined with post-contrast-enhanced T1-weighted MR imaging, and the central tumor could be differentiated from adjacent lung parenchymal disease in 23 out of 27 patients (85%). The tumor was of lower signal intensity than the adjacent lung disease in 18 cases (67%) and of higher signal intensity in 5 (18%). These differences in signal intensity between primary tumor and secondary change were considered to be due to the presence of invasion of pulmonary vasculatures. Therefore, the use of T2-weighted or post-contrast-enhanced T1-weighted images for assessment of tumor size and secondary change may be helpful for precise evaluation of tumor extent at the initial staging and for accurate prognosis for patients and assessment of therapeutic effect after conservative therapy and/or for comparative studies of standard and new chemo- and/or radiotherapy regimens (Ohno et al. 2000).

4.1.3 Chest Wall Invasion

Chest wall invasion used to be considered a contraindication for surgical excision of lung cancer, but recent surgical advances have made chest wall excision feasible for the treatment of locally aggressive lung cancer and giving patients a better chance of survival (Magdeleinat et al. 2001). Preoperative visualization of chest wall invasion may therefore be helpful for surgical planning. On conventional CT scan, rib destruction is the only reliable sign of chest wall invasion since soft-tissue masses in the chest wall correlate statistically with chest wall invasion. However, they are not reliable indicators for an individual patient, so that focal chest pain may still be the most reliable indicator of chest wall invasion. In fact, the reliability of conventional CT assessment of chest wall invasion in lung cancer patients varies widely with reported sensitivities ranging from 38 to 87% and specificities from 40 to 90% (Quint and Francis 1999). In addition to the technique of inducing artificial pneumothorax described elsewhere (Watanabe et al. 1991; Yokoi et al. 1991), Murata et al. (1994) reported that dynamic expiratory multi-section CT reviewed as a cine loop was 100% accurate for identification of both chest wall and mediastinal invasion.

Another study has suggested that ultrasound (US) is an effective technique for diagnosis of chest wall invasion (Suzuki et al. 1993). In this study, 120 lung cancer patients were examined, in 19 of whom invasion was pathologically proved. Sensitivity, specificity, and accuracy of US were 100%, 98%, and 98%, respectively, while the corresponding values for conventional CT used in the same study were only 68%, 66%, and 67% (Suzuki et al. 1993).

Because of its multiplanar capability and better tissue contrast resolution compared to CT, MR imaging has also been advocated as effective for assessment of chest wall invasion (Rapoport et al. 1988; Heelan et al. 1989; Webb et al. 1991; Padovani et al. 1993; Bonomo et al. 1996). Sagittal and coronal plane images are better than axial CT images for displaying the anatomical relationship between tumor and chest wall structures (Bonomo et al. 1996; Freundlich et al. 1996).
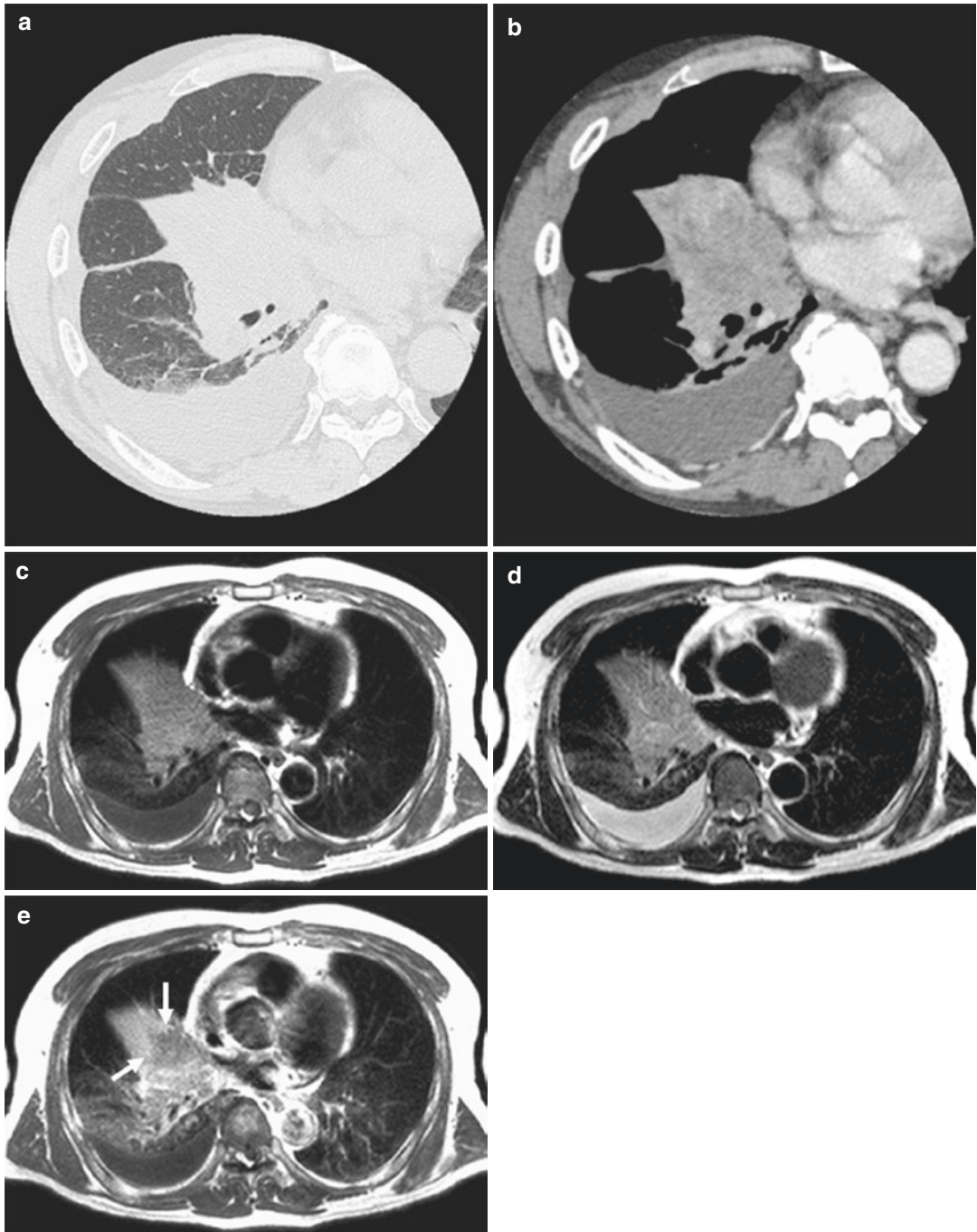
Fig. 13 A 59-year-old male with adenocarcinoma. Thin-section CT (**a**) shows atelectasis in the right middle and lower lobe. Contrast-enhanced thin-section CT (**b**) shows homogeneously enhanced atelectasis and pleural effusion, but the extent of the tumor cannot be determined. Black-blood T1-weighted (**c**) and T2-weighted (**d**) images show atelectasis and the tumor as, respectively, low and inter-mediate signal intensity. Mediastinal invasion is sus-pected, while pleural effusion is clearly seen. Post-contrast black-blood T1-weighted image (**e**) clearly shows lung cancer and secondary change (*arrow*)
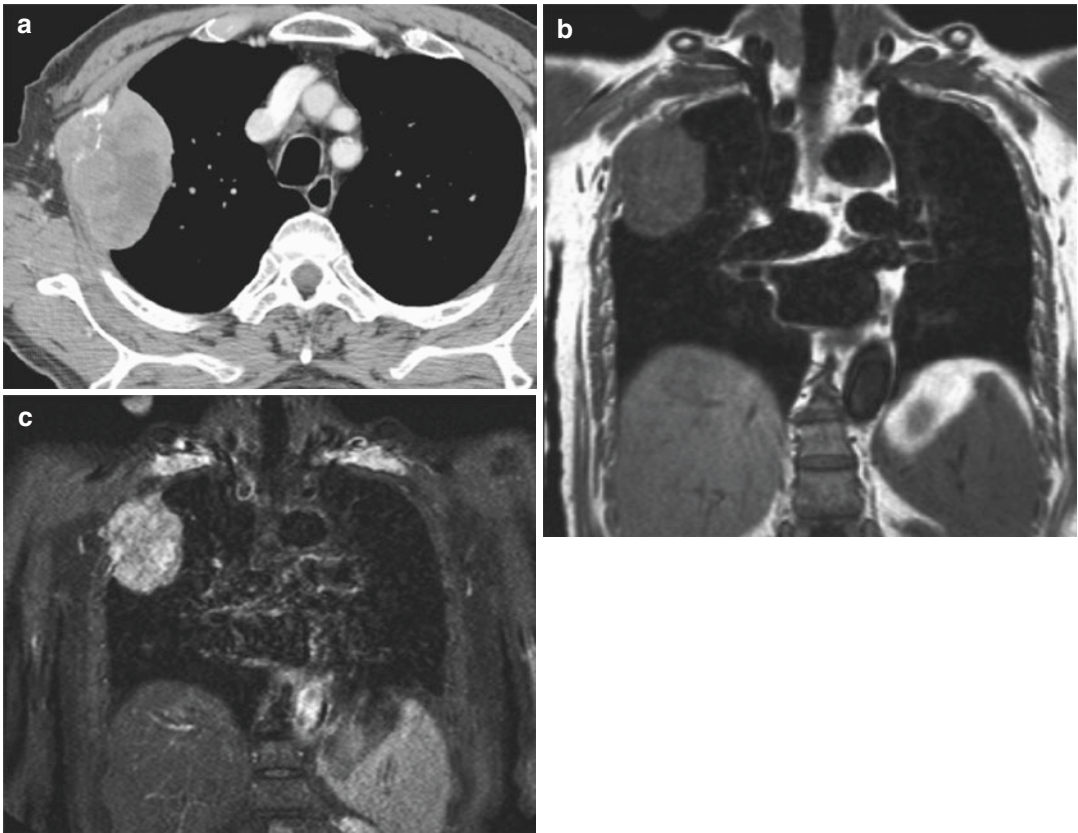
Fig. 14 A 71-year-old male with adenocarcinoma in the right upper lobe. Contrast-enhanced thin-section CT (**a**) and conventional T1-weighted SE (**b**) images suggest chest wall invasion, but tumor extent cannot be clearly determined on either image. However, STIR turbo SE (**c**) image clearly shows chest wall invasion and tumor extent

MR imaging shows infiltration or disruption of the normal extrapleural fat plane on T1-weighted images or parietal pleural signal hyperintensity on T2-weighted images (Fig. 14). In addition, when STIR turbo SE imaging is used for this purpose, it can demonstrate lung cancer as high signal intensity within the suppressed signal intensities of chest wall structures, enabling clinicians to easily determine the tumor extent within chest wall (Fig. 14c). Moreover, Padovani et al. (1993) have suggested that the diagnostic yield can be further improved by intravenous administration of contrast media. In addition, superior sulcus or Pancoast tumors are good candidates for the demonstration of chest wall invasion on MR imaging. Since superior sulcus tumors occur in close proximity to the lung apex, their imaging has to include an evaluation of the relationship between the tumor and the brachial plexus, subclavian artery and vein, and adjacent chest wall. The axial scan plane of a CT scan is suboptimal for examining the lung apex where superior sulcus tumors are located, while direct sagittal and coronal MR images are superior to CT for evaluating the local extent of disease in patients with superior sulcus tumors (Rapoport et al. 1988; Heelan et al. 1989; Webb et al. 1991; Padovani et al. 1993; Bonomo et al. 1996; Freundlich et al. 1996). Heelan et al. (1989) examined a series of 31 patients with superior sulcus tumors imaged with both CT and MR and found that MR imaging showed 94% correlation with surgical and clinical findings, whereas the CT scans had an accuracy of only 63% for evaluating tumor invasion through the superior sulcus.

Sakai et al. (1997) used dynamic cine MR imaging during breathing rather than static MR

imaging for evaluating chest wall invasion in lung cancer patients. This study evaluated the movement of the tumor along the parietal pleura during the respiratory cycle displayed with a cine loop in a manner similar to dynamic expiratory multi-section CT (Murata et al. 1994). Where the tumor had invaded the chest wall, it was fixed to the chest wall, while without invasion, the tumor was seen to move freely along the parietal pleura. In this study, the sensitivity, specificity, and accuracy of dynamic cine MR imaging for the detection of chest wall invasion were 100%, 70%, and 76%, respectively, and those of conventional CT and MR imaging were 80%, 65%, and 68% (Sakai et al. 1997). Of special significance is that the negative predictive value of dynamic cine MR imaging in this study was 100% without any need for ionizing radiation exposure. Dynamic cine MR imaging, when used in conjunction with static MR imaging, is therefore considered useful for further improvements of the assessment of chest wall invasion in lung cancer patients.

Currently, multiplanar capability, faster scan time and better spatial resolution of thin-section MDCT images may improve the diagnostic capability of CT for evaluation of chest wall invasion in NSCLC patients similar to that of mediastinal invasion. MR imaging is still considered to have superior tissue contrast compared with MDCT. Higashino et al. (2005) also reported that thin-section sagittal MPR imaging with 1 mm section thickness could significantly improve diagnostic accuracy for chest wall invasion in comparison with routine MDCT with 5 mm section thickness and showed slightly better diagnostic capability than thin-section MDCT with 1 mm section thickness. Therefore, further investigations as well as comparative studies of thin-section MDCT imaging and MR imaging used as described here, or of newly developed techniques will be needed to determine the actual significance of MR imaging for assessment of chest wall invasion in routine clinical practice.

4.1.4 MR Assessment of Respiratory Tumor Motion

The general objective of radiotherapy is to achieve tumor control by depositing a lethal dose in the target volume including potential microscopic spread of cancer cells, while sparing surrounding organs and tissue as best as possible. Therefore, precise localization of the target volume is needed. Actually, the recent advances in radiotherapy, including intensity-modulated radiotherapy, adaptive radiotherapy, as well as image-guided radiotherapy, allow for strong improvement of the accuracy of irradiation treatment. However, patient motion and especially respiratory motion has become a major obstacle for achieving high precision radiotherapy. Currently, in classic radiotherapy for lung tumors, such motion is accounted for with a generic target volume expansion, not considering the individual patient breathing characteristics and the mobility of the individual tumor. However, it has been widely recognized that the motion pattern of lung tumors and the breathing cycles vary greatly among patients. This empiric approach includes all surrounding healthy tissues that pass the planned target volume at any time of the breathing cycle to create a safety margin. Within this margin even the additional normal tissues will be irradiated unnecessarily, causing tissue damage or limiting the dose delivered to the target. Therefore it is attractive to define an individual treatment plan by limiting the irradiated volume to certain positions of the tumor on its path during respiration (gated technique) or to follow its respiratory movement (tracking techniques) (Li et al. 2008). Hence, the ultimate objective for radiotherapy of moving targets is to localize precisely the target in space and time in order to achieve a higher dose to be applied to the target while the maximum dose to the normal tissue is reduced, particularly for critical adjacent organs at risk. The better the delineation between target and normal tissue the lower the probability of complications and the higher the chance for tumor control eventually enhanced by the possibility to even increase tumor control by delivering an additional radiation dose solely to the target. For dedicated treatment planning, respiratory-gated four-dimensional (4D) MRI could be used to exactly define tumor size and its three-dimensional displacement during respiration in a single examination. The fourth dimension beyond the 3D space is time, in which patient motion and the

change of the position of the tumor will be recorded. Ideally, 4D MRI would not only encode tumor and organ motion information but also provide time-resolved 3D data sets with reduced motion artifacts.

Numerous MR-based investigations of lung and tumor motion in the literature have been limited to examining the motion in a single plane or in a small number of orthogonal planes through the tumor. Two non-coplanar image views provided critical motion characterization, while the most significant displacement was in the cranial-caudal direction (Shimizu et al. 2000). For this purpose, the MR sequences derived from cardiac imaging have been adapted for respiratory motion analysis. These sequences were compared, demonstrating that fast imaging with a free precession steady-state gradient-echo provided significantly higher SNR than any fast low-angle shot technique, while the latter had an advantage in higher temporal resolution.

The correlation between external fiducial markers (coils) and the internal organ motion was also studied using single-slice 4D MRI (Plathow et al. 2005). The correlation coefficients in the three orthogonal directions for different breathing types (thoracic or abdominal) were about 0.8, similar in magnitude to 4D CT. This quantitative information indicates that external fiducial markers might be satisfactory for predicting organ motion.

Volumetric 4D MR imaging was not possible before the recent introduction of multichannel parallel detection systems. Parallel acquisition improves the performance of MR imaging by over an order of magnitude compared to single-channel MR systems. The signal-to-noise ratio (SNR) is usually degraded when using multielement coils for multichannel imaging. Consequently, some of the gain in acceleration is sacrificed in order to maintain image quality. Compared with single-slice imaging, which requires multiple slice directions to view the critical motions of the moving organ, the volumetric 4D technique catches the entire volume in a single acquisition. However, single-slice 4D MR imaging has a higher speed and can be used to study fast heart beating and forced breathing maneuvers. Further improvement of 4D MR imaging may employ the view-sharing technique using a variable sampling rate

in k-space and shares elements between image sets, reducing the acquisition time by an appropriate approximation. This technique, combined with parallel imaging, allows for volumetric 4D MR imaging in respiratory motion studies. Then the acquisition time could be below 0.7 s for a 3D torso image using a 1.5-T MRI scanner.

A study directly compared 4D CT, 4D MR imaging, and cone beam CT (CBCT) and demonstrated that lesion sizes were exactly reproduced with 4D CT but overestimated on 4D MRI and CBCT with a larger variability due to limited temporal and spatial resolution (Biederer et al. 2009). In addition, all 4D modalities underestimate lesion displacement (Biederer et al. 2009). In addition, another study demonstrated that this technique was considered as a promising tool to analyze complex breathing patterns in patients with lung tumors and to use in planning of radiotherapy to account for individual tumor motion (Dinkel et al. 2009). Therefore, in the last decades, many investigators have assessed the influence of respiratory motion to radiation therapy as well as PET/MRI by 4D MR imaging as well as different motion correction methods (Dikaios et al. 2012, Tryggestad et al. 2013, Sawant et al. 2014, Dutta et al. 2015, Fayad et al. 2015, Stanescu and Jaffray 2016). Therefore, this part would be better to be more and more important for future lung MR imaging, especially oncologic fields.

4.2   MR Assessment of N Classification

The descriptor *N classification* refers to the presence or absence of regional lymph node metastases (Sobin and Wittekind 2002). The definitions are given in Table 4. In the absence of distant metastasis, locoregional lymph node spread will determine therapy and prognosis. For patients without positive lymph nodes (N0 disease) or with only intrapulmonary or hilar lymph nodes (N1 disease), direct resection remains standard therapy. In case of positive ipsilateral mediastinal lymph nodes (N2 disease), chemotherapy combined preoperatively with surgery or with concurrent or sequential radical radiotherapy is a legitimate choice (Martini et al. 1997;

Vansteenkiste et al. 1998). If patients have contralateral mediastinal lymph node metastases (N3 disease), however, they are generally rejected for surgery but will receive nonsurgical combination treatment.

CT has been the standard noninvasive modality for staging of lung cancer. Enlarged lymph nodes (i.e., with a short axis of more than 10 mm or a long axis of more than 15 mm) are considered to be metastatic. Although an increase in the size of mediastinal lymph nodes correlates with malignant involvement in patients with lung cancer, the sensitivity and specificity of this finding are not very high because lymph nodes can be enlarged due to infection or inflammation. In addition, small nodes can sometimes contain metastatic deposits. The RDOG reported that the sensitivity and specificity of CT for *N* classification were only 52% and 69%, respectively (Webb et al. 1991), while the corresponding values from the Leuven Lung Cancer Group (LLCG) were 69% and 71% (Dillemans et al. 1994). Due to the substantial limitation of CT for depicting mediastinal lymph node metastases, additional mediastinoscopy with biopsy is necessary for adequate assessment of hilar and mediastinal nodes (Glazer et al. 1984, 1985; Musset et al. 1986; Poon et al. 1987; Laurent et al. 1988; Webb et al. 1991, 1993; McLoud et al. 1992).

Since the 1990s, FDG-PET has been used for differentiation between metastatic and nonmetastatic lymph nodes based on the biochemical mechanism of increased glucose metabolism or tumor cell duplication (Wahl et al. 1994; Patz et al. 1995; Boiselle et al. 1998; Higashi et al. 1998; Gupta et al. 2000). However, elevated glucose metabolism may occur secondary to tumor, infection or inflammation (Dewan et al. 1993; Patz et al. 1993), and spatial resolution in PET is inferior to that of CT and MR, so that the diagnostic capability of the FDG-PET imaging is limited (Gupta et al. 2000). A large number of prospective studies have compared the diagnostic capability of N stage assessment using CT and FDG-PET. A meta-analysis demonstrated that FDG-PET was significantly more accurate than CT for identifying lymph node involvement (Gould et al. 2003). In addition, the respective median sensitivity and specificity of CT were 61% (interquartile range,

50–71%) and 79% (interquartile range, 66–89%), but those of FDG-PET were 85% (interquartile range, 67–91%) and 90% (interquartile range, 82–96%) (Gould et al. 2003). Moreover, it has been suggested that FDG-PET is more sensitive but less specific when CT showed enlarged lymph nodes [median sensitivity, 100% (interquartile range, 90–100%); median specificity, 78% (interquartile range, 68–100%)] than when CT showed no lymph node enlargement [median sensitivity, 82% (interquartile range, 65–100%); median specificity, 93% (interquartile range, 92–100%); ($P = 0.002$)] (Gould et al. 2003).

Since the introduction of MR imaging for assessment of lung cancer, the criteria for tumor involvement within lymph nodes depend solely on lymph node size and were very similar to CT criteria. In some cases, however, histological examination has shown that a normal-sized regional lymph node may have metastases and that nodal enlargement can be due to reactive hyperplasia or other nonmalignant conditions. The detectability of calcifications, which are indicative for a benign lesion, is also limited for MRI when compared with CT. The direct multiplanar capability of MR imaging, however, is an advantage for the detection of lymph nodes in areas that are suboptimally imaged in the axial plane, such as in the aortopulmonary (AP) window and subcarinal regions (Webb et al. 1991; Boiselle et al. 1998).

Recently, cardiac- and/or respiratory-triggered conventional or black-blood STIR turbo SE imaging has been recommended for detection of metastatic tumors and metastatic lymph nodes (Fujimoto et al. 1995; Eustace et al. 1998; Takenaka et al. 2002; Ohno et al. 2004d, 2007c; Kawai et al. 2006). These novel sequences may make to quantitatively assess the signal intensity of lymph nodes by means of comparison with a 0.9% normal saline phantom (Takenaka et al. 2002; Ohno et al. 2004d, 2007c). The STIR turbo spin echo (SE) is a simple sequence, which can be easily included in clinical protocols to yield net of T1- and T2-relaxation times. On STIR turbo SE images, metastatic lymph nodes exhibit high signal intensity and nonmetastatic lymph nodes low signal intensity (Figs. 15 and 16). According to previously published results (Fujimoto et al. 1995;
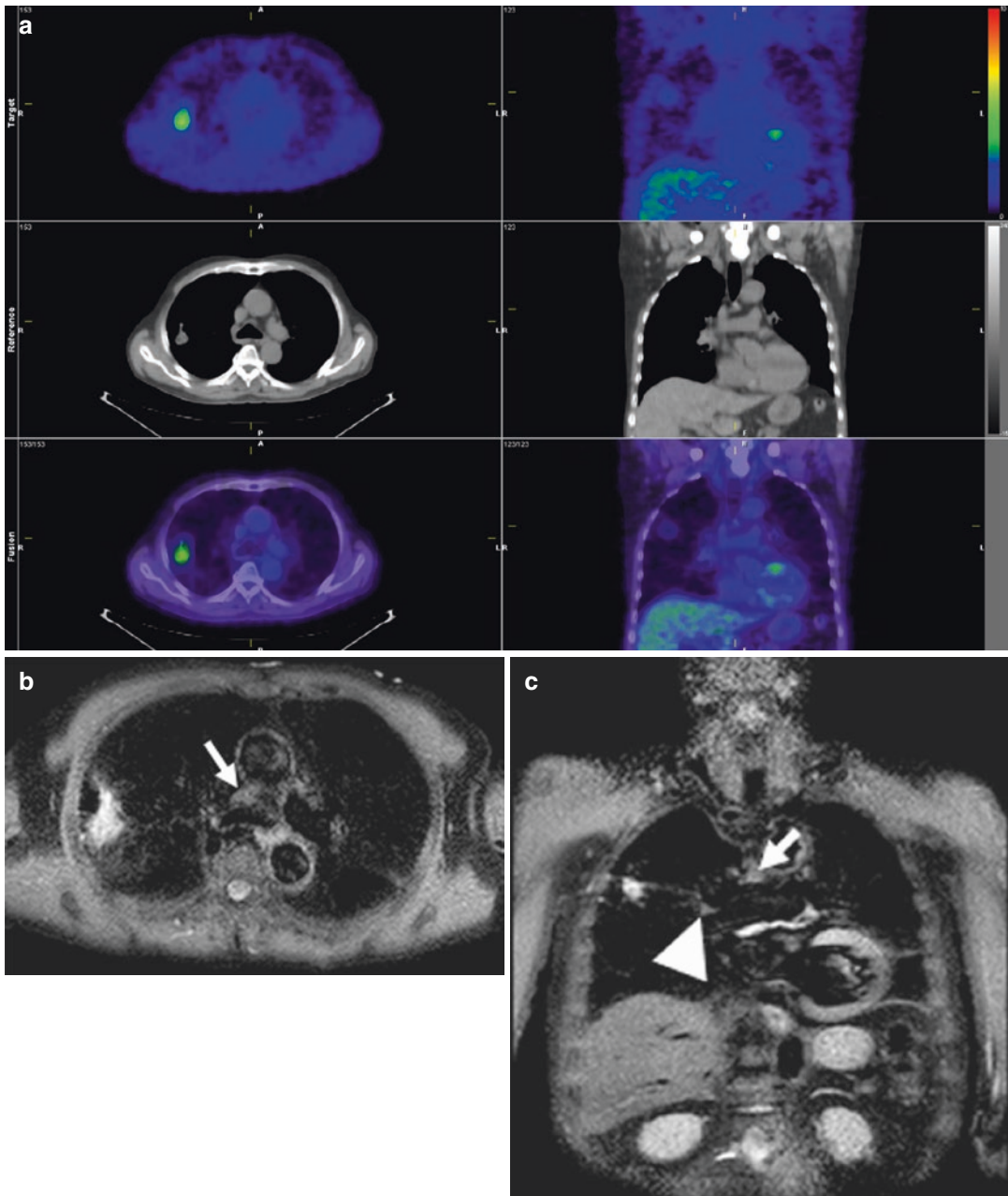
Fig. 15 A 77-year-old male with adenocarcinoma (N0). Integrated FDG-PET/CT (**a**) demonstrates high uptake of FDG in primary tumor, but no uptake in mediastinal and hilar lymph nodes, suggesting N0. Black-blood STIR turbo SE imaging on axial (**b**) and coronal (**c**) planes show the primary tumor as high intensity, but mediastinal (*arrow*) and hilar (*arrow head*) lymph nodes as low signal intensity, suggesting N0

Takenaka et al. 2002; Ohno et al. 2004d, 2007c, 2011b; Yi 2008; Morikawa et al. 2009), sensitivity of quantitatively and qualitatively assessed STIR turbo SE imaging ranged, on a per-patient basis, from 83.7 to 100.0%, specificity from 75.0 to 93.1%, and accuracy from 86.0 to 92.2%, and these values are equal to or higher than those for CE-CT, FDG-PET, or PET/CT. Yet another study showed that the quantitative and qualitative sensitivity, specificity, and accuracy of STIR turbo SE imaging were not significantly different from those of FDG-PET/CT. However, the combina-
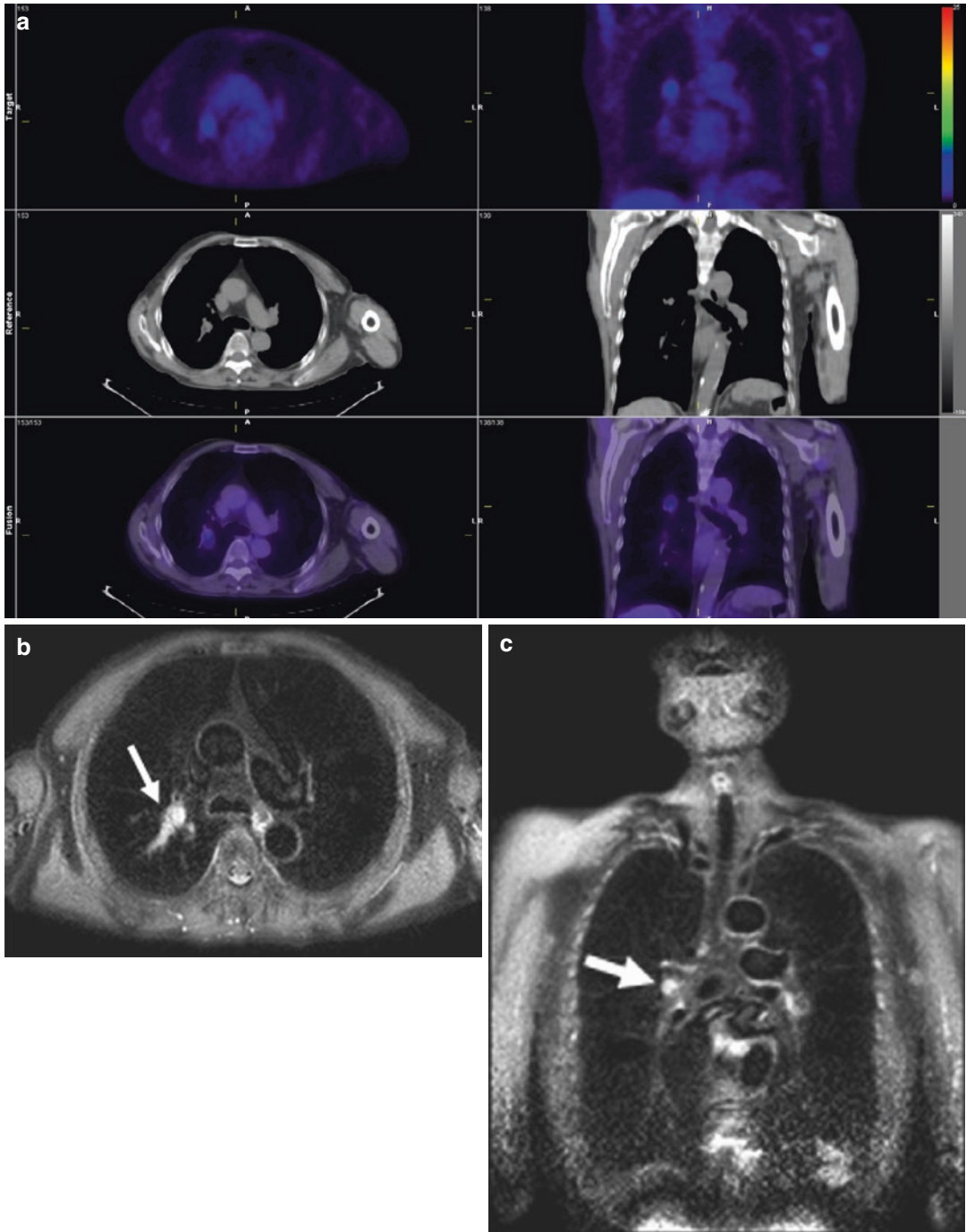
Fig. 16 A 74-year-old male with adenocarcinoma (N1). Integrated FDG-PET/CT (**a**) demonstrates no uptake of FDG in the mediastinal and faint uptake in the hilar lymph nodes, suggesting N0, which was false-negative. Black-blood STIR turbo SE imaging on axial (**b**) and coronal (**c**) planes shows the hilar lymph node (*arrow*) as high signal intensity, suggesting N1 which was true-positive

tion of FDG-PET/CT with STIR turbo SE imaging was found to be significantly more effective for detecting nodal involvement on a per-patient basis (96.9% specificity, 90.3% accuracy) than FDG PET/CT alone (65.6% specificity, 81.7% accuracy) (Morikawa et al. 2009).

Since 2008, DWI was introduced as another promising MR technique for this purpose (Hasegawa et al. 2008; Nomori et al. 2008; Ohno et al. 2011b; Pauls et al. 2012). Sensitivity, specificity, and accuracy of DWI reportedly range, on a per-patient basis, from 77.4% to 80.0%, 84.4% to 97.0%, and 89.0% to 95.0%, respectively, and these results appear to be equal to or better than those for FDG-PET or PET/CT (Hasegawa et al. 2008; Nomori et al. 2008; Ohno et al. 2011b; Pauls et al. 2012). Ohno et al. prospectively and directly compared these modalities to determine the clinical relevance of MR-based N-factor assessment as compared with that of FDG-PET/CT. In this study, sensitivity and/or accuracy of STIR turbo SE imaging (quantitative sensitivity: 82.8%, qualitative sensitivity: 77.4%, quantitative accuracy: 86.8%) proved to be significantly higher than those of DWI (74.2%, 71.0% and 84.4%, respectively) and FDG-PET/CT (quantitative sensitivity: 74.2%) (Ohno et al. 2011b). This means that quantitative and qualitative assessments of the N stage of NSCLC patients obtained with STIR turbo SE MR imaging are more sensitive and/or more accurate than those obtained with DWI and FDG PET/CT (Ohno et al. 2011b). According to these results and considering the limitations of DWI as well as FDG-PET/CT for detection of small metastatic foci or lymph nodes, STIR turbo SE imaging may be the better MR technique to use for this purpose before surgical treatment or lymph node sampling, during thoracotomy or mediastinoscopy for accurate pathologic TNM staging after surgical treatment, or before chemotherapy, radiation therapy, or both (Ohno et al. 2011b). However, further technical improvements in DWI are needed to overcome its current limitations and enable it to function in a complementary role or as a substitution for STIR turbo SE imaging in routine clinical practice. Thus, STIR turbo SE imaging should be considered as capable of enhancing the diagnostic capability of N classification not only due to its multiplanar capability but also its sensitive and accurate assessment of relaxation time differences between metastatic and nonmetastatic lymph nodes and play as complementary and/or substitution of PET or PET/CT as well as DWI in routine clinical practice.

Recently, PET/MRI at 3 T system was introduced for TNM staging in NSCLC patients. Although T staging had no significance with PET/CT, the diagnostic accuracy for N stage of MR imaging including STIR fast advanced spin echo (FASE) imaging, PET/MRI, and PET/CT was 98.6% for MR imaging; 98.6% and 92.1% for PET/MRI with and without signal intensity (SI) assessment based on STIR FASE imaging, respectively; and 92.1% for PET/CT (Ohno et al. 2015). In addition, the accuracy of STIR FASE imaging and PET/MRI with SI assessment was significantly higher than that of PET/MRI without SI assessment and of PET/CT (Ohno et al. 2015). Moreover, sensitivity of STIR FASE imaging (100%) and PET/MRI with SI assessment (100%) were significantly higher than that of whole-body PET/MRI without SI assessment (93.8%) and of PET/CT (93.8%) (Ohno et al. 2015) (Fig. 17). Therefore, PET/MRI may be more useful than PET/CT, when each investigator evaluates SI changes with FDG uptake in not only NSCLC, but also other oncologic patients in routine clinical practice.

Fig. 17 A-66-year-old male with right hilar lymph node metastasis due to adenocarcinoma. CE-thin-section MPR image (**a**) shows right hilar lymph node (*arrow*), whose short axis diameter was 6 mm, and diagnosed as N0 case. This patient was false-positive case on CT. PET/CT (**b**) and PET/MRI fused between PET and contrast-enhanced (CE) Quick 3D data (**c**) demonstrate small lymph node without high FDG uptake in right hilum (*arrow*) and also assessed as N0 case. This patient was false-negative case on PET/CT and PET/MRI. Whole-body STIR FASE image (**d**) shows high signal intensity at right hilar lymph node metastasis (*arrow*), although whole-body Quick 3D imaging (**e**) demonstrates small right hilar lymph node (*arrow*) in the right hilum. Moreover, whole-body MR image fused between diffusion-weighted image (DWI) and CE Quick 3D data (**f**) demonstrates small right hilar lymph node with low signal intensity color coded as heat (*arrow*). Therefore, whole-body MR imaging can correctly diagnose this case as N1 case, when applied STIR FASE image.
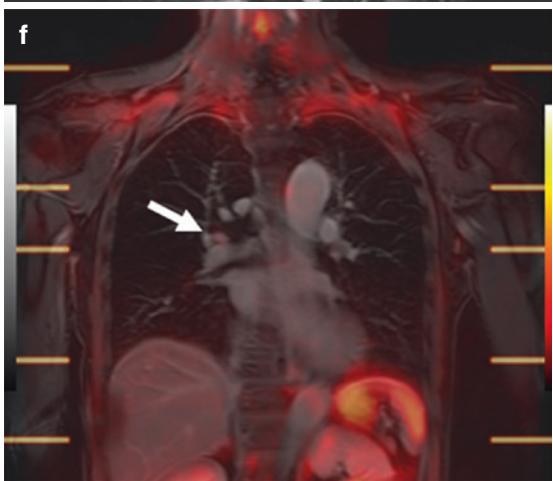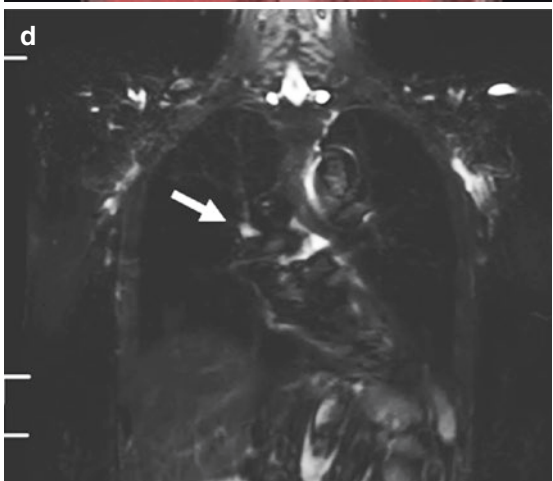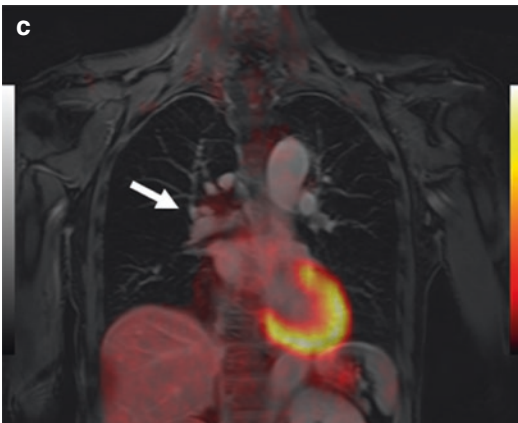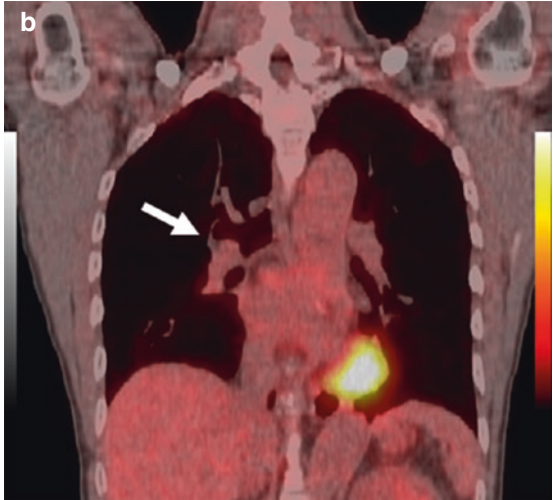
4.3   MR Assessment of M Classification

The descriptor *M* relates to the presence of distant metastasis (M1) or its absence (M0) (Sobin and Wittekind 2002). The definitions are given in Table 5. Lung cancer can metastasize widely and involve many organs, including the brain, bone, liver, and adrenal glands. The presence of metastasis beyond the intrathoracic lymph nodes is considered an indication of metastatic disease (M1) and implies surgical non-resectability. Patients with distant metastases carry a very poor prognosis and are generally treated with chemotherapy, radiotherapy, or both or with optimal supportive care. In most cases, extrathoracic imaging is indicated for patients with lung cancer and symptoms localized to a specific organ. At present, however, there is no consensus regarding the efficacy of extrathoracic imaging for presumably resectable lung cancer without signs or symptoms localized to a specific organ (Wong et al. 1999).

The observation of metastases in patients with NSCLC has major implications for management and prognosis. Extrathoracic metastases are present in approximately 40% of patients with newly diagnosed lung cancer at presentation, most commonly in the adrenal glands, bones, liver, or brain (Pantel et al. 1996; Quint et al. 1996). After radical treatment for apparently localized disease, 20% of the patients developed an early distant relapse, probably due to systemic micrometastases that were present but not detected or visualized at the point of initial staging (Pantel et al. 1996). Silvestri et al. (1995) updated a meta-analysis for the systemic evaluation of extrathoracic metastases in potentially resectable NSCLC patients. This study calculated that the negative predictive value was equal to or more than 90% for the clinical evaluation of patients asymptomatic for brain, abdominal, or bone metastases (Silvestri et al. 1995). These findings are consistent with the findings of a retrospective analysis of 755 patients with clinical stage T1-2 N0 disease, which found only five sites with silent metastasis after extensive imaging for extrathoracic disease (Tanaka et al. 1999). The current

recommendation from the American College of Chest Physicians (ACCP) therefore suggests that further diagnostic testing is necessary to confirm the presence of disease only in patients with abnormal findings on clinical evaluation, although the positive predictive values among the studies included in their meta-analysis were highly variable (Toloza et al. 2003; Silvestri et al. 2007). For purposes of TNM classification, however, it would be necessary to perform in-depth surveillance of potential sites of extrathoracic metastases for all lung cancer patients. In addition, accurate diagnosis of extrathoracic metastases may be helpful for clinicians to provide the most appropriate treatment and/or management for lung cancer patients.

4.3.1   Adrenal Gland Metastasis

Enlarged adrenal glands can be visualized on CT at initial presentation in nearly 10% of NSCLC patients, and approximately two-third of these adrenal lesions are benign or asymptomatic (Oliver et al. 1984; Ettinghausen and Burt 1991). Therefore, without pathologic proof of metastatic disease, the presence of an isolated adrenal mass in a patient with otherwise operable NSCLC should not preclude radical treatment. If the CT scan is performed without intravenous contrast media and an adrenal lesion is identified, measurement of the CT scan attenuation value can be helpful for distinguishing metastasis from adenoma (Boland et al. 1998; Szolar and Kammerhuber 1998). PET can also be a useful adjunct in this setting because the sensitivity and specificity of PET have been reported as ranging from 80 to 100% in the past literatures. This high sensitivity and specificity may result in a reduction of the number of unnecessary biopsies, which are not without risk and not always diagnostic (Erasmus et al. 1997; Marom et al. 1999). However, careful interpretation of PET is required for small lesions less than 10 mm in diameter, since experience with these is still limited (Schrevens et al. 2004). In addition, false-positive findings on PET have also been reported, and the incidence of false-positive findings is increasing. Currently, MR imaging is also considered helpful for distinguishing metastasis from adenoma when

an adrenal lesion is detected by CT. Visual assessment of adrenal lesions using chemical shift MR imaging may characterize a lesion as an adenoma on the basis of reduced signal intensity of the lesion on opposed-phase images as compared with that on in-phase images (Korobkin et al. 1995; Schwartz et al. 1998; Hussain and Korobkin 2004). Korobkin et al. (1995) applied this technique to 51 adrenal lesions and reported a sensitivity of 100% and specificity of 81% for the characterization of adenomas.

4.3.2 Bone Metastasis

Bone involvement is usually assessed by 99mTechnetium methylene diphosphate (^{99m}Tc-MDP) or hydroxymethylene diphosphate (^{99m}Tc-HMDP) bone scintigraphy. Although sensitivity of bone scintigraphy has been reported as high as 90%, its specificity was only about 60% due to false-positive findings caused by the nonselective uptake of the radionuclide tracer in any area of increased bone turnover (Schrevens et al. 2004). Consequently, additional imaging by X-ray, bone CT, and/or MR imaging is often required. PET is reported to have similar sensitivity, but higher specificity and accuracy (equal to or more than 90%, equal to or more than 98% and equal to or more than 96%, respectively) (Bury et al. 1998; Marom et al. 1999). PET is therefore considered superior to bone scintigraphy for the detection of bone metastases. Currently, MR imaging with the use of various sequences such as T1-weighted SE or turbo SE imaging, T2-weighted turbo SE imaging, STIR turbo SE imaging, contrast-enhanced T1-weighted SE or turbo SE imaging, or diffusion-weighted MR imaging is deemed useful for assessment of muscle-skeletal tumors and metastasis from various malignancies (Weinberger et al. 1995; Vanel et al. 1998; Mentzel et al. 2004; Park et al. 2004; Tokuda et al. 2004; Goo et al. 2005). However, only one study has directly compared the diagnostic capability of MR imaging and bone scintigraphy and found that sensitivity, specificity and accuracy of MR imaging were 80%, 96% and 93%, respectively, being superior to bone scintigraphy (40%, 92%, and 83%), although the difference was not significant (Earnest et al. 1999).

4.3.3 Brain Metastasis

Some investigators have reported that brain MR imaging is useful for evaluation of asymptomatic brain metastases in patients with operable lung cancer (Hillers et al. 1994; Earnest et al. 1999; Yokoi et al. 1999). FDG-PET is not suitable for the detection of brain metastases since the sensitivity of PET is low due to the high glucose uptake of normal surrounding brain tissue. CT and/or MR imaging remain the method of choice for screening brain metastases. Yokoi et al. (1999) compared the efficacy of MR imaging and CT scans of brain in 332 patients with potentially operable asymptomatic non-small cell lung cancer. Within 12 months of diagnosis, brain metastases were detected in 7% of the patients in this series. Preoperatively, brain metastases were detected in 3.4% of the patients by MR imaging and in 0.6% of the patients by CT scans. Other investigators have reported on the utility of contrast-enhanced brain MR imaging and found a high prevalence of asymptomatic brain metastasis in 28% of patients identified with contrast-enhanced brain MR imaging (Earnest et al. 1999). These findings suggest that preoperative brain MR imaging may be effective for patients with lung cancer.

4.3.4 Whole-Body MR Imaging for Assessment of M Classification in Lung Cancer Patients

Findings of a recent randomized trial suggest that the addition of whole-body FDG-PET scanning to a conventional workup can identify more patients with extrathoracic metastases among those with suspected NSCLC (van Tinteren et al. 2002). However, recent advances in MR techniques such as fast imaging and moving table techniques make it possible to perform whole-body MR imaging. Its usefulness has been investigated in the staging of breast cancer and the search for primary lesions in patients with metastatic carcinoma from an unknown primary lesion (Eustace et al. 1998; Walker et al. 2000; Antoch et al. 2003; Lauenstein et al. 2004; Takahara et al. 2004; Goehde et al. 2005; Schmidt et al. 2006). It was concluded that whole-body MR imaging

may constitute a single, cost-effective imaging test for patients with metastatic carcinoma from an unknown primary (Eustace et al. 1998; Walker et al. 2000; Antoch et al. 2003; Lauenstein et al. 2004; Takahara et al. 2004; Goehde et al. 2005; Schmidt et al. 2006). However, the potential of whole-body MR imaging for lung cancer staging has not yet been satisfactorily delineated. Ohno et al. (2007d) performed a direct comparison of the diagnostic capability of whole-body MR imaging and FDG-PET for the M classification. They reported that the interobserver agreement for whole-body MR imaging was substantially, but not significantly better than for whole-body FDG-PET on a per-site basis and a per-patient basis (Ohno et al. 2007d). For assessment of head and neck metastases, sensitivity (84.6%) and accuracy (95.0%) of whole-body MR imaging were significantly higher than those of FDG-PET (15.4% and 89.1%, respectively) on a per-site basis (Ohno et al. 2007d). In addition, the specificity (96.1%) and accuracy (94.8%) of whole-body MR imaging for bone metastasis were significantly higher than those of FDG-PET (88.3% and 88.2%, respectively) on a per-site basis (Ohno et al. 2007d). However, when brain metastases were excluded from head and neck metastases, sensitivity, specificity, and accuracy of whole-body MR imaging were not significantly different from those of FDG-PET, nor were they for diagnosis of thoracic, abdominal, and pelvic metastases (Ohno et al. 2007d). In addition, when evaluation on a per-patient basis of M classification included brain metastases as head and neck metastases, accuracy (80.0%) of whole-body MR imaging was significantly better than that of FDG-PET (73.3%), while exclusion of brain metastases from head and neck metastases resulted in no significant differences in sensitivity, specificity, and accuracy between whole-body MR imaging and FDG-PET (Ohno et al. 2007d). Whole-body MR imaging is therefore an accurate diagnostic technique and should be considered at least as effective as FDG-PET for M classification of lung cancer patients (Figs. 18 and 19).

Furthermore, whole-body DWI has been recommended as a promising new tool for whole-body MR examination of oncologic patients (64–66). Comparisons of the diagnostic performance of whole-body MR imaging for M-factor assessment with that of FDG-PET or PET/CT have shown that the diagnostic capability of whole-body MR imaging with or without DWI (sensitivity, 52.0–80.0%; specificity, 74.3–94.0%; accuracy, 80.0–87.7%) was equal to or significantly higher than that of FDG-PET or PET/CT (sensitivity, 48.0–80.0%; specificity, 74.3–96%; accuracy, 73.3–88.2%) (Ohno et al. 2007d, 2008b; Yi et al. 2008; Takenaka et al. 2009; Sommer et al. 2012). However, one drawback associated with the use of whole-body DWI in this setting needs to be carefully considered. The specificity (87.7%) and accuracy (84.3%) of whole-body DWI alone on a per-patient basis were significantly lower than those of FDG-PET/CT (specificity, 94.5%; accuracy, 90.4%) (Ohno et al. 2008b). On the other hand, the diagnostic accuracy of whole-body MR imaging combined with DWI (87.8%) was not significantly different from that of FDG-PET/CT, although that of whole-body MR imaging without DWI (85.8%) was lower than that of FDG-PET/CT (Ohno et al. 2008b). Therefore, it would be advisable to use whole-body DWI as part of whole-body MR examination in order to improve the diagnostic accuracy of M-factor assessment of NSCLC patients (Ohno et al. 2008b).

More recently, whole-body PET/MR imaging obtained with a hybrid PET/MR system or presented as PET fused with MR imaging has become clinically feasible, and a few investigators have conducted preliminary tests of their utility for lung cancer patients and reportedly found no significant differences in diagnostic capability between PET/MR imaging and PET/CT for M-factor assessment as well as for T- and N-factor assessments (Kohan et al. 2013; Heusch et al. 2014; Schaarschmidt et al. 2015). However, all these studies assessed only FDG uptake and anatomical information from PET/MR data as well as PET/CT, but not signal intensities on all sites detected on a variety of MR images. Correct evaluation of signal intensity changes at all suspected sites on PET/MR imaging may thus result in better diagnostic performance than PET/CT in the near future, especially when taking
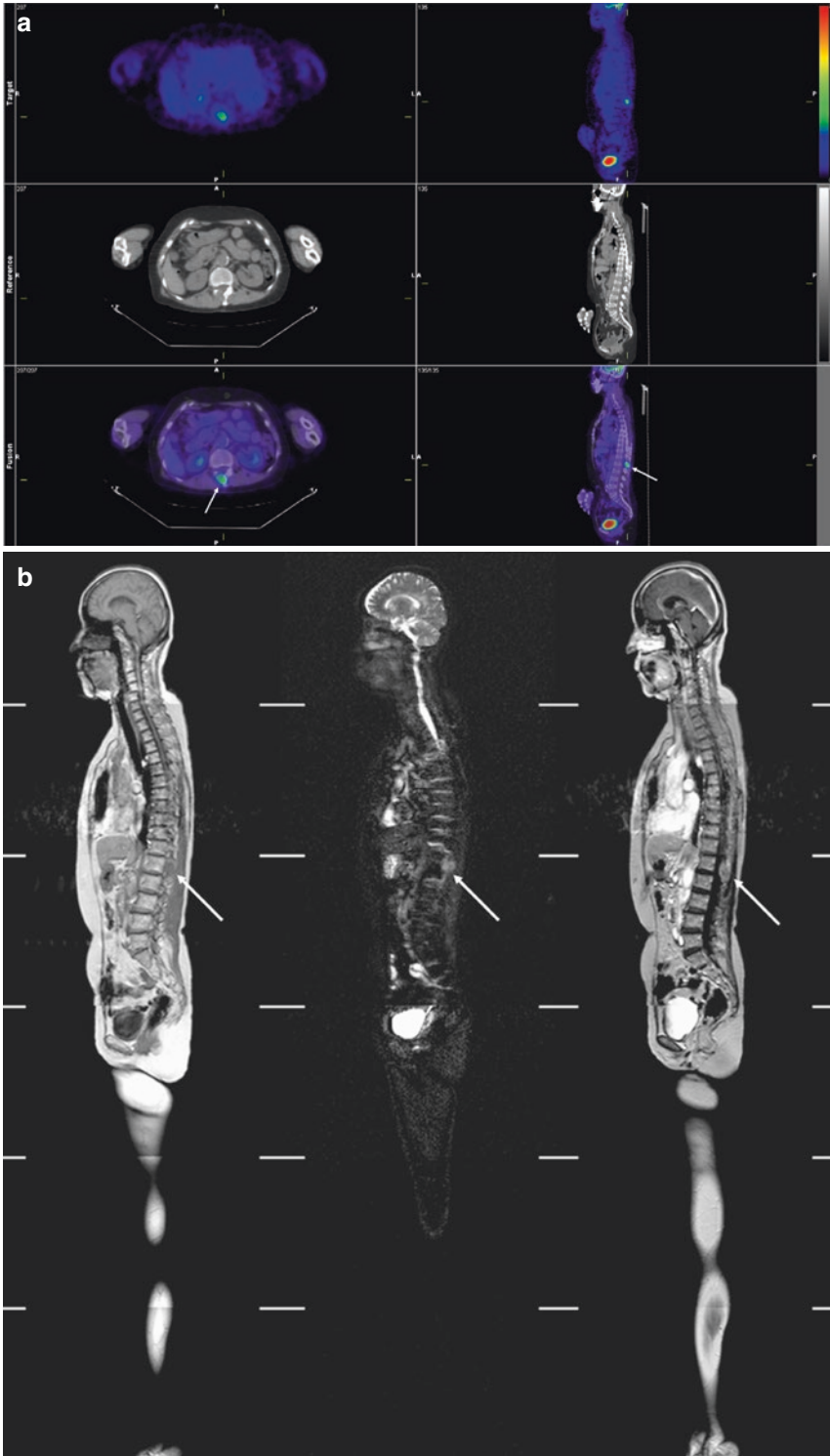
Fig. 18 A 68-year-old female with adenocarcinoma and lumbar vertebra (L1) metastasis. Integrated FDG-PET/CT (**a**) shows high uptake of FDG at the vertebral arch (*arrow*), suggesting bone metastasis, which was true-positive. On sagittal whole-body MR images (**b**) (L to R: non-contrast-enhanced T1-weighted GRE image, STIR turbo SE image, and contrast-enhanced T1-weighted GRE image), bone metastasis (*arrow*) is obvious, which was true-positive
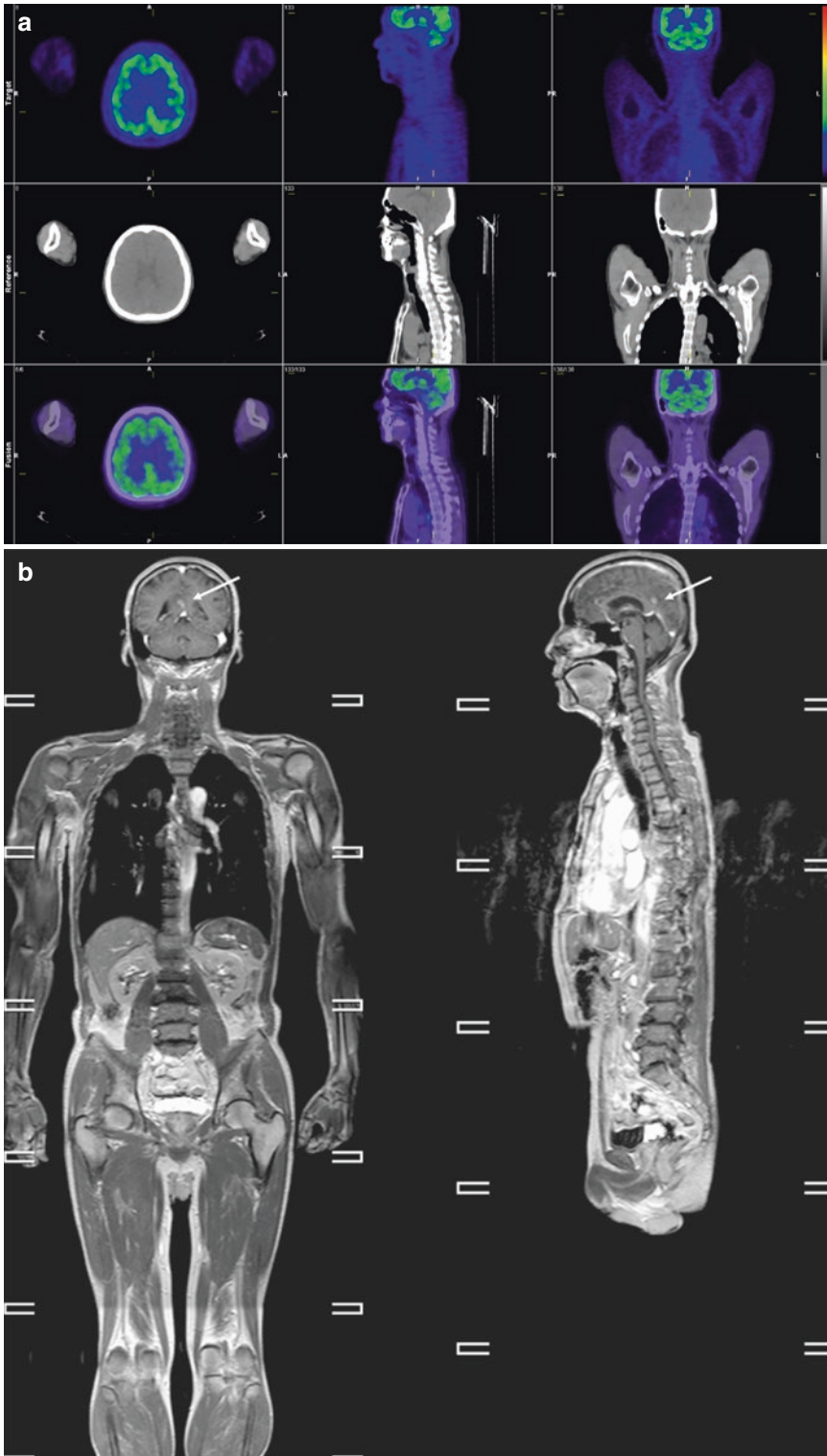
Fig. 19 A 67-year-old male with adenocarcinoma and brain metastasis. Integrated FDG-PET/CT (**a**) does not show any abnormal uptake, suggesting M0, which was false-negative. Contrast-enhanced whole-body T1-weighted GRE (**b**): L to R, coronal and sagittal planes clearly shows brain metastasis, suggesting M1, which was true-positive

into consideration MR results reported during the last few decades, which demonstrated the utility of MR imaging for differentiation of metastatic from nonmetastatic sites in lung cancer patients. A study showed the direct comparison of TNM staging capability among whole-body MRI, PET/MR, and PET/CT (Ohno et al. 2015). This study demonstrated that agreements of assessment of every factor (κ = 0.63–0.97) and clinical stage (κ = 0.65–0.90) were substantial or almost perfect. Regarding capability to assess operability, accuracy of whole-body MRI and PET/MR imaging with signal intensity assessment (97.1%) was significantly higher than that of MR/PET without signal intensity assessment and integrated FDG PET/CT (85.0%, $p < 0.001$). Therefore, when applying PET/MR in this setting, not only anatomical but also various information from MR part of PET/MR have to be evaluated for improving the potential PET/MR for TNM staging in lung cancer patients.

References

Amundsen T, Kvaerness J, Jones RA, Waage A, Bjermer L, Nilsen G, Haraldseth O (1997) Pulmonary embolism: detection with MR perfusion imaging of lung – a feasibility study. Radiology 203:181–185

Amundsen T, Torheim G, Waage A, Bjermer L, Steen PA, Haraldseth O (2000) Perfusion magnetic resonance imaging of the lung: characterization of pneumonia and chronic obstructive pulmonary disease. A feasibility study. J Magn Reson Imaging 12:224–231

Antoch G, Vogt FM, Freudenberg LS, Nazaradeh F, Goehde SC, Barkhausen J, Dahmen G, Bockisch A, Debatin JF, Ruehm SG (2003) Whole-body dual-modality PET/CT and whole-body MRI for tumor staging in oncology. JAMA 290:3199–3206

Aquino SL, Kee ST, Warnock ML, Gamsu G (1994) Pulmonary aspergillosis: imaging findings with pathologic correlation. AJR Am J Roentgenol 163:811–815

Armstrong P (2000) Neoplasms of the lung, airways and pleura. In: Armstrong P, Wilson AG, Dee P, Hansell DM (eds) Imaging of diseases of the chest, 3rd edn. Mosby, London, pp 305–401

Bach PB, Silvestri GA, Hanger M, Jett JR (2007) Screening for lung cancer: ACCP evidence-based clinical practice guidelines (2nd edition). American College of Chest Physicians. Chest 132:69S–77S

Bailey PV, Tracy T Jr, Connors RH, deMello D, Lewis JE, Weber TR (1990) Congenital bronchopulmonary malformations. Diagnostic and therapeutic considerations. J Thorac Cardiovasc Surg 99:597–602

Baron RL, Levitt RG, Sagel SS, White MJ, Roper CL, Marbarger JP (1982) Computed tomography in the preoperative evaluation of bronchogenic carcinoma. Radiology 145:727–732

Bateson EM (1973) So-called hamartoma of the lung – a true neoplasm of fibrous connective tissue of the bronchi. Cancer 31:1458–1467

Biederer J, Dinkel J, Remmert G, Jetter S, Nill S, Moser T, Bendl R, Thierfelder C, Fabel M, Oelfke U, Bock M, Plathow C, Bolte H, Welzel T, Hoffmann B, Hartmann G, Schlegel W, Debus J, Heller M, Kauczor HU (2009) 4D-Imaging of the lung: reproducibility of lesion size and displacement on helical CT, MRI, and cone beam CT in a ventilated ex vivo system. Int J Radiat Oncol Biol Phys 73:919–926

Blum U, Windfuhr M, Buitrago-Tellez C, Sigmund G, Herbst EW, Langer M (1994) Invasive pulmonary aspergillosis. MRI, CT, and plain radiographic findings and their contribution for early diagnosis. Chest 106:1156–1161

Boiselle PM, Patz EF Jr, Vining DJ, Weissleder R, Shepard JA, McLoud TC (1998) Imaging of mediastinal lymph nodes: CT, MR, and FDG PET. Radiographics 18:1061–1069

Boland GW, Lee MJ, Gazelle GS, Halpern EF, McNicholas MM, Mueller PR (1998) Characterization of adrenal masses using unenhanced CT: an analysis of the CT literature. AJR Am J Roentgenol 171:201–204

Bonomo L, Ciccotosto C, Guidotti A, Storto ML (1996) Lung cancer staging: the role of computed tomography and magnetic resonance imaging. Eur J Radiol 23:35–45

Bourgouin PM, McLoud TC, Fitzgibbon JF, Mark EJ, Shepard JA, Moore EM, Rummeny E, Brady TJ (1991) Differentiation of bronchogenic carcinoma from postobstructive pneumonitis by magnetic resonance imaging: histopathologic correlation. J Thorac Imaging 6:22–27

Bruegel M, Gaa J, Woertler K, Ganter C, Waldt S, Hillerer C, Rummeny EJ (2007) MRI of the lung: value of different turbo spin echo, single-shot turbo spin echo, and 3D gradient-echo pulse sequences for the detection of pulmonary metastases. J Magn Reson Imaging 25:73–81

Bryant AS, Cerfolio RJ (2006) The maximum standardized uptake values on integrated FDG-PET/CT is useful in differentiating benign from malignant pulmonary nodules. Ann Thorac Surg 82:1016–1020

Bury T, Dowlati A, Paulus P, Corhay JL, Benoit T, Kayembe JM, Limet R, Rigo P, Radermecker M (1996) Evaluation of the solitary pulmonary nodule by positron emission tomography imaging. Eur Respir J 9:410–414

Bury T, Barreto A, Daenen F, Barthelemy N, Ghaye B, Rigo P (1998) Fluorine-18 deoxyglucose positron emission tomography for the detection of bone metastases in patients with non-small cell lung cancer. Eur J Nucl Med 25:1244–1247

Caskey CI, Templeton PA, Zerhouni EA (1990) Current evaluation of the solitary pulmonary nodule. Radiol Clin N Am 28:511–520

Chang JM, Lee HJ, Goo JM, Lee HY, Lee JJ, Chung JK, Im JG (2006) False positive and false negative FDG-PET scans in various thoracic diseases. Korean J Radiol 7:57–69

Christensen JA, Nathan MA, Mullan BP, Hartman TE, Swensen SJ, Lowe VJ (2006) Characterization of the solitary pulmonary nodule: 18F-FDG PET versus nodule-enhancement CT. AJR Am J Roentgenol 187:1361–1367

Chung MH, Lee HG, Kwon SS, Park SH (2000) MR imaging of solitary pulmonary lesion: emphasis on tuberculomas and comparison with tumors. J Magn Reson Imaging 11:629–637

Costello P (1994) Spiral CT of the thorax. Semin Ultrasound CT MR 15:90–106

Cronin P, Dwamena BA, Kelly AM, Carlos RC (2008) Solitary pulmonary nodules: meta-analytic comparison of cross-sectional imaging modalities for diagnosis of malignancy. Radiology 246:772–782

Davis SD (1991) CT evaluation for pulmonary metastases in patients with extrathoracic malignancy. Radiology 180:1–12

Dewan NA, Gupta NC, Redepenning LS, Phalen JJ, Frick MP (1993) Diagnostic efficiency of PET-FDG imaging in solitary pulmonary nodules. Chest 104:997–1002

Dikaios N, Izquierdo-Garcia D, Graves MJ, Mani V, Fayad ZA, Fryer TD (2012) MRI-based motion correction of thoracic PET: initial comparison of acquisition protocols and correction strategies suitable for simultaneous PET/MRI systems. Eur Radiol 22:439–446

Dillemans B, Deneffe G, Verschakelen J, Decramer M (1994) Value of computed tomography and mediastinoscopy in preoperative evaluation of mediastinal nodes in non-small cell lung cancer. A study of 569 patients. Eur J Cardiothorac Surg 8:37–42

Dinkel J, Hintze C, Tetzlaff R, Huber PE, Herfarth K, Debus J, Kauczor HU, Thieke C (2009) 4D-MRI analysis of lung tumor motion in patients with hemidiaphragmatic paralysis. Radiother Oncol 91:449–454

Donmez FY, Yekeler E, Saeidi V, Tunaci A, Tunaci M, Acunas G (2007) Dynamic contrast enhancement patterns of solitary pulmonary nodules on 3D gradient-recalled echo MRI. AJR Am J Roentgenol 189:1380–1386

Dutta J, Huang C, Li Q, El Fakhri G (2015) Pulmonary imaging using respiratory motion compensated simultaneous PET/MR. Med Phys 42:4227–4240

Earnest F IV, Ryu JH, Miller GM, Luetmer PH, Forstrom LA, Burnett OL, Rowland CM, Swensen SJ, Midthun DE (1999) Suspected non-small cell lung cancer: incidence of occult brain and skeletal metastases and effectiveness of imaging for detection – pilot study. Radiology 211:137–145

Erasmus JJ, Patz EF Jr, McAdams HP, Murray JG, Herndon J, Coleman RE, Goodman PC (1997) Evaluation of adrenal masses in patients with bronchogenic carcinoma using 18F-fluorodeoxyglucose positron emission tomography. AJR Am J Roentgenol 168:1357–1360

Ettinghausen SE, Burt ME (1991) Prospective evaluation of unilateral adrenal masses in patients with operable non-small-cell lung cancer. J Clin Oncol 9:1462–1466

Eustace S, Tello R, DeCarvalho V, Carey J, Melhem E, Yucel EK (1998) Whole body turbo STIR MRI in unknown primary tumor detection. J Magn Reson Imaging 8:751–753

Fayad H, Schmidt H, Wuerslin C, Visvikis D (2015) Reconstruction-incorporated respiratory motion correction in clinical simultaneous PET/MR imaging for oncology applications. J Nucl Med 56:884–889

Felson B, Wiot JF (1977) Some less familiar roentgen manifestations of carcinoma of the lung. Semin Roentgenol 2:187–206

Feuerstein IM, Jicha DL, Pass HI, Chow CK, Chang R, Ling A, Hill SC, Dwyer AJ, Travis WD, Horowitz ME, Steinberg SM, Frank JA, Doppman JL (1992) Pulmonary metastases: MR imaging with surgical correlation – a prospective study. Radiology 182:123–129

Finck S, Milne EN (1988) A case report of segmental bronchial atresia: radiologic evaluation including computed tomography and magnetic resonance imaging. J Thorac Imaging 3:53–57

Fink C, Puderbach M, Bock M, Lodemann KP, Zuna I, Schmähl A, Delorme S, Kauczor HU (2004) Regional lung perfusion: assessment with partially parallel three-dimensional MR imaging. Radiology 231:175–184

Freundlich IM, Chasen MH, Varma DG (1996) Magnetic resonance imaging of pulmonary apical tumors. J Thorac Imaging 11:210–222

Frericks BB, Meyer BC, Martus P, Wendt M, Wolf KJ, Wacker F (2008) MRI of the thorax during whole-body MRI: evaluation of different MR sequences and comparison to thoracic multidetector computed tomography (MDCT). J Magn Reson Imaging 27:538–545

Fujimoto K, Meno S, Nishimura H, Hayabuchi N, Hayashi A (1994) Aspergilloma within cavitary lung cancer: MR imaging findings. AJR Am J Roentgenol 163:565–567

Fujimoto K, Edamitsu O, Meno S, Abe T, Honda N, Ogoh Y, Ohzono H, Nakaoda K, Kojima K, Nishimura H (1995) MR diagnosis for metastasis or non-metastasis of mediastinal and hilar lymph nodes in cases of primary lung cancer: detectability, signal intensity, and MR-pathologic correlation. Nippon Acta Radiol 55:162–171

Fujimoto K, Abe T, Müller NL, Terasaki H, Kato S, Sadohara J, Kono R, Edamitsu O, Ishitake T, Hayashi A, Rikimaru T, Hayabuchi N (2003) Small peripheral pulmonary carcinomas evaluated with dynamic MR imaging: correlation with tumor vascularity and prognosis. Radiology 227:786–793

Gaeta M, Blandino A, Scribano E, Vinci S, Minutoli F, Pergolizzi S, Pandolfo I (2000) Magnetic resonance imaging of bronchioloalveolar carcinoma. J Thorac Imaging 15:41–47

Gaeta M, Minutoli F, Ascenti G, Vinci S, Mazziotti S, Pandolfo I, Blandino A (2001) MR white lung sign: incidence and significance in pulmonary consolidations. J Comput Assist Tomogr 25:890–896

Gaeta M, Vinci S, Minutoli F, Mazziotti S, Ascenti G, Salamone I, Lamberto S, Blandino A (2002) CT and MRI findings of mucin-containing tumors and pseudotumors of the thorax: pictorial review. Eur Radiol 12:181–189

Gdeedo A, Van Schil P, Corthouts B, Van Mieghem F, Van Meerbeeck J, Van Marck E (1997) Comparison of imaging TNM [(i)TNM] and pathological TNM [pTNM] in staging of bronchogenic carcinoma. Eur J Cardiothorac Surg 12:224–227

Gefter WB (1992) The spectrum of pulmonary aspergillosis. J Thorac Imaging 7:56–74

Glazer GM, Orringer MB, Gross BH, Quint LE (1984) The mediastinum in non-small cell lung cancer: CT-surgical correlation. AJR Am J Roentgenol 142:1101–1105

Glazer GM, Gross BH, Aisen AM, Quint LE, Francis IR, Orringer MB (1985) Imaging of the pulmonary hilum: a prospective comparative study in patients with lung cancer. AJR Am J Roentgenol 145:245–248

Glazer HS, Kaiser LR, Anderson DJ, Molina PL, Emami B, Roper CL, Sagel SS (1989) Indeterminate mediastinal invasion in bronchogenic carcinoma: CT evaluation. Radiology 173:37–42

Goehde SC, Hunold P, Vogt FM, Ajaj W, Goyen M, Herborn CU, Forsting M, Debatin JF, Ruehm SG (2005) Full-body cardiovascular and tumor MRI for early detection of disease: feasibility and initial experience in 298 subjects. AJR Am J Roentgenol 184:598–611

Goldstraw P, Crowley J, Chansky K, Giroux DJ, Groome PA, Rami-Porta R, Postmus PE, Rusch V, Sobin L, International Association for the Study of Lung Cancer International Staging Committee; Participating Institutions (2007) The IASLC Lung Cancer Staging Project: proposals for the revision of the TNM stage groupings in the forthcoming (seventh) edition of the TNM Classification of malignant tumours. J Thorac Oncol 2:706–714

Goo HW, Choi SH, Ghim T, Moon HN, Seo JJ (2005) Whole-body MRI of paediatric malignant tumours: comparison with conventional oncological imaging methods. Pediatr Radiol 35:766–773

Gould MK, Kuschner WG, Rydzak CE, Maclean CC, Demas AN, Shigemitsu H, Chan JK, Owens DK (2003) Test performance of positron emission tomography and computed tomography for mediastinal staging in patients with non-small-cell lung cancer: a meta-analysis. Ann Intern Med 139:879–892

Gückel C, Schnabel K, Deimling M, Steinbrich W (1996) Solitary pulmonary nodules: MR evaluation of enhancement patterns with contrast – enhanced dynamic snapshot gradient – echo imaging. Radiology 200:681–686

Gupta NC, Graeber GM, Bishop HA (2000) Comparative efficacy of positron emission tomography with fluorodeoxyglucose in evaluation of small (<1 cm), intermediate (1 to 3 cm), and large (>3 cm) lymph node lesions. Chest 117:773–778

Hasegawa I, Boiselle PM, Kuwabara K, Sawafuji M, Sugiura H (2008) Mediastinal lymph nodes in patients with non-small cell lung cancer: preliminary experience with diffusion-weighted MR imaging. J Thorac Imaging 23:157–161

Hatabu H, Gaa J, Kim D, Li W, Prasad PV, Edelman RR (1996) Pulmonary perfusion: qualitative assessment with dynamic contrast-enhanced MRI using ultrashort TE and inversion recovery turbo FLASH. Magn Reson Med 36:503–508

Hatabu H, Tadamura E, Levin DL, Chen Q, Li W, Kim D, Prasad PV, Edelman RR (1999) Quantitative assessment of pulmonary perfusion with dynamic contrast-enhanced MRI. Magn Reson Med 42:1033–1038

Heelan RT, Demas BE, Caravelli JF, Martini N, Bains MS, McCormack PM, Burt M, Panicek DM, Mitzner A (1989) Superior sulcus tumors: CT and MR imaging. Radiology 170:637–641

Henschke CI, McCauley DI, Yankelevitz DF, Naidich DP, McGuinness G, Miettinen OS, Libby D, Pasmantier M, Koizumi J, Altorki N, Smith JP (2001) Early lung cancer action project: a summary of the findings on baseline screening. Oncologist 6:147–152

Herder GJ, Golding RP, Hoekstra OS, Comans EF, Teule GJ, Postmus PE, Smit EF (2004) The performance of (18)F-fluorodeoxyglucose positron emission tomography in small solitary pulmonary nodules. Eur J Nucl Med Mol Imaging 31:1231–1236

Herman SJ, Winton TL, Weisbrod GL, Towers MJ, Mentzer SJ (1994) Mediastinal invasion by bronchogenic carcinoma: CT signs. Radiology 190:841–846

Herold CJ, Kramer J, Sertl K, Kalhs P, Mallek R, Imhof H, Tscholakoff D (1989) Invasive pulmonary aspergillosis: evaluation with MR imaging. Radiology 173:717–721

Heusch P, Buchbender C, Köhler J, Nensa F, Gauler T, Gomez B, Reis H, Stamatis G, Kühl H, Hartung V, Heusner TA (2014) Thoracic staging in lung cancer: prospective comparison of 18F-FDG PET/MR imaging and 18F-FDG PET/CT. J Nucl Med 55:373–378

Higashi K, Nishikawa T, Seki H, Oguchi M, Nambu Y, Ueda Y, Yuasa K, Tonami H, Okimura T, Yamamoto I (1998) Comparison of fluorine-18-FDG PET and thallium-201 SPECT in evaluation of lung cancer. J Nucl Med 39:9–15

Higashino T, Ohno Y, Takenaka D, Watanabe H, Nogami M, Ohbayashi C, Yoshimura M, Satouchi M, Nishimura Y, Fujii M, Sugimura K (2005) Thin-section multiplanar reformats from multidetector-row CT data: utility for assessment of regional tumor extent in non-small cell lung cancer. Eur J Radiol 56:48–55

Hillers TK, Sauve MD, Guyatt GH (1994) Analysis of published studies on the detection of extrathoracic metastases in patients presumed to have operable non-small cell lung cancer. Thorax 49:14–19

Hittmair K, Eckersberger F, Klepetko W, Helbich T, Herold CJ (1995) Evaluation of solitary pulmonary

nodules with dynamic contrast-enhanced MR imaging – a promising technique. Magn Reson Imaging 13:923–933

Hussain HK, Korobkin M (2004) MR imaging of the adrenal glands. Magn Reson Imaging Clin N Am 12:515–544

Jederlinic PJ, Sicilian LS, Baigelman W, Gaensler EA (1987) Congenital bronchial atresia. A report of 4 cases and a review of the literature. Medicine 66:73–83

Jeong YJ, Lee KS, Jeong SY, Chung MJ, Shim SS, Kim H, Kwon OJ, Kim S (2005) Solitary pulmonary nodule: characterization with combined wash-in and washout features at dynamic multi-detector row CT. Radiology 237:675–683

Joshi U, Raijmakers PG, van Lingen A, Comans EF, Pijpers R, Teule GJ, Hoekstra OS (2005) Evaluation of pulmonary nodules: comparison of a prototype dual crystal (LSO/NAI) dual head coincidence camera and full ring positron emission tomography (PET). Eur J Radiol 55:250–254

Kawai Y, Sumi M, Nakamura T (2006) Turbo short tau inversion recovery imaging for metastatic node screening in patients with head and neck cancer. AJNR Am J Neuroradiol 27:1283–1287

Kersjes W, Mayer E, Buchenroth M, Schunk K, Fouda N, Cagil H (1997) Diagnosis of pulmonary metastases with turbo-SE MR imaging. Eur Radiol 7:1190–1194

Kim SK, Allen-Auerbach M, Goldin J, Fueger BJ, Dahlbom M, Brown M, Czernin J, Schiepers C (2007) Accuracy of PET/CT in characterization of solitary pulmonary lesions. J Nucl Med 48:214–220

Ko SF, Lee TY, Kao CL, Ng SH, Wan YL, Lin JW, Chen WJ (1998) Bronchial atresia associated with epibronchial right pulmonary artery and aberrant right middle lobe artery. Br J Radiol 71:217–220

Kohan AA, Kolthammer JA, Vercher-Conejero JL, Rubbert C, Partovi S, Jones R, Herrmann KA, Faulhaber P (2013) N staging of lung cancer patients with PET/MRI using a three-segment model attenuation correction algorithm: initial experience. Eur Radiol 23:3161–3169

Kono M, Adachi S, Kusumoto M, Sakai E (1993) Clinical utility of Gd – DTPA – enhanced magnetic resonance imaging in lung cancer. J Thorac Imaging 8:18–26

Kono R, Fujimoto K, Terasaki H, Müller NL, Kato S, Sadohara J, Hayabuchi N, Takamori S (2007) Dynamic MRI of solitary pulmonary nodules: comparison of enhancement patterns of malignant and benign small peripheral lung lesions. AJR Am J Roentgenol 188:26–36

Korobkin M, Lombardi TJ, Aisen AM, Francis IR, Quint LE, Dunnick NR, Londy F, Shapiro B, Gross MD, Thompson NW (1995) Characterization of adrenal masses with chemical shift and gadolinium-enhanced MR imaging. Radiology 197:411–418

Koyama H, Ohno Y, Kono A, Takenaka D, Maniwa Y, Nishimura Y, Ohbayashi C, Sugimura K (2008) Quantitative and qualitative assessment of non-contrast-enhanced pulmonary MR imaging for management of pulmonary nodules in 161 subjects. Eur Radiol 18:2120–2131

Kusumoto M, Kono M, Adachi S, Yamasaki K, Itouji E, Sakai E, Endo M, Nakamura T, Kimura K (1994) Gadopentetate dimeglumine – enhanced magnetic resonance imaging for lung nodules: differentiation of lung cancer and tuberculoma. Investig Radiol 29:S255–S256

Lauenstein TC, Goehde SC, Herborn CU, Goyen M, Oberhoff C, Debatin JF, Ruehm SG, Barkhausen J (2004) Whole-body MR imaging: evaluation of patients for metastases. Radiology 233:139–148

Laurent F, Drouillard J, Dorcier F, Velly JF, Barat JL, Grelet P, Martigne C, Tavernier J, Couraud L (1988) Bronchogenic carcinoma staging: CT versus MR imaging. Assessment with surgery. Eur J Cardiothorac Surg 2:31–36

Lee KS, Yi CA, Jeong SY, Jeong YJ, Kim S, Chung MJ, Kim HY, Kim YK, Lee KH (2007) Solid or partly solid solitary pulmonary nodules: their characterization using contrast wash-in and morphologic features at helical CT. Chest 131:1516–1525

Levin DL, Chen Q, Zhang M, Edelman RR, Hatabu H (2001) Evaluation of regional pulmonary perfusion using ultrafast magnetic resonance imaging. Magn Reson Med 46:166–171

Lewis JW Jr, Pearlberg JL, Beute GH, Alpern M, Kvale PA, Gross BH, Magilligan DJ Jr (1990) Can computed tomography of the chest stage lung cancer? Yes and no. Ann Thorac Surg 49:591–595

Li G, Citrin D, Camphausen K et al (2008) Advances in 4D medical imaging and 4D radiation therapy. Technol Cancer Res Treat 7:67–81

Luboldt W, Wetter A, Eichler K, Vogl TJ, Wagner TO, Seemann MD (2006) Determination of the optimal MRI sequence for the detection of malignant lung nodules. Eur J Med Res 11:336–342

Ma H, Kubicek CP, Röhr M (1985) Metabolic effects of manganese deficiency in Aspergillus niger: evidence for increased protein degradation. Arch Microbiol 141:266–268

Magdeleinat P, Alifano M, Benbrahem C, Spaggiari L, Porrello C, Puyo P, Levasseur P, Regnard JF (2001) Surgical treatment of lung cancer invading the chest wall: results and prognostic factors. Ann Thorac Surg 71:1094–1099

Marom EM, McAdams HP, Erasmus JJ, Goodman PC, Culhane DK, Coleman RE, Herndon JE, Patz EF Jr (1999) Staging non-small cell lung cancer with whole-body PET. Radiology 212:803–809

Martini N, Heelan R, Westcott J, Bains MS, McCormack P, Caravelli J, Watson R, Zaman M (1985) Comparative merits of conventional, computed tomographic, and magnetic resonance imaging in assessing mediastinal involvement in surgically confirmed lung carcinoma. J Thorac Cardiovasc Surg 90:639–648

Martini N, Kris MG, Ginsberg RJ (1997) The role of multimodality therapy in locoregional non-small cell lung cancer. Surg Oncol Clin N Am 6:769–791

Matsuoka S, Uchiyama K, Shima H, Terakoshi H, Nojiri Y, Oishi S, Ogata H (2001) Detectability of pulmonary

perfusion defect and influence of breath holding on contrast-enhanced thick-slice 2D and on 3D MR pulmonary perfusion images. J Magn Reson Imaging 14:580–585

Matsushima H, Takayanagi N, Satoh M, Kurashima K, Kanauchi T, Hoshi T, Kanazawa M (2002) Congenital bronchial atresia: radiologic findings in nine patients. J Comput Assist Tomogr 26:860–864

Mayr B, Heywang SH, Ingrisch H, Huber RM, Haussinger K, Lissner J (1987) Comparison of CT with MR imaging of endobronchial tumors. J Comput Assist Tomogr 11:43–48

McLoud TC, Swenson SJ (1999) Lung carcinoma. Clin Chest Med 20:97–713 , vii

McLoud TC, Bourgouin PM, Greenberg RW, Kosiuk JP, Templeton PA, Shepard JA, Moore EH, Wain JC, Mathisen DJ, Grillo HC (1992) Bronchogenic carcinoma: analysis of staging in the mediastinum with CT by correlative lymph node mapping and sampling. Radiology 182:319–323

Meng RL, Jensik RJ, Faber LP, Matthew GR, Kittle CF (1978) Bronchial atresia. Ann Thorac Surg 25:184–192

Mentzel HJ, Kentouche K, Sauner D, Fleischmann C, Vogt S, Gottschild D, Zintl F, Kaiser WA (2004) Comparison of whole-body STIR-MRI and 99mTc-methylene-diphosphonate scintigraphy in children with suspected multifocal bone lesions. Eur Radiol 14:2297–2302

Milne EN, Zerhouni EA (1987) Blood supply of pulmonary metastases. J Thorac Imaging 2:15–23

Mori K, Niki N, Kondo T, Kamiyama Y, Kodama T, Kawada Y, Moriyama N (2005) Development of a novel computer-aided diagnosis system for automatic discrimination of malignant from benign solitary pulmonary nodules on thin-section dynamic computed tomography. J Comput Assist Tomogr 29:215–222

Mori T, Nomori H, Ikeda K, Kawanaka K, Shiraishi S, Katahira K, Yamashita Y (2008) Diffusion-weighted magnetic resonance imaging for diagnosing malignant pulmonary nodules/masses: comparison with positron emission tomography. J Thorac Oncol 3:358–364

Morikawa M, Demura Y, Ishizaki T, Ameshima S, Miyamori I, Sasaki M, Tsuchida T, Kimura H, Fujibayashi Y, Okazawa H (2009) The effectiveness of 18F-FDG PET/CT combined with STIR MRI for diagnosing nodal involvement in the thorax. J Nucl Med 50:81–87

Murata K, Takahashi M, Mori M, Shimoyama K, Mishina A, Fujino S, Itoh H, Morita R (1994) Chest wall and mediastinal invasion by lung cancer: evaluation with multisection expiratory dynamic CT. Radiology 191:251–255

Musset D, Grenier P, Carette MF, Frija G, Hauuy MP, Desbleds MT, Girard P, Bigot JM, Lallemand D (1986) Primary lung cancer staging: prospective comparative study of MR imaging with CT. Radiology 160:607–611

Naidich DP, Rumancik WM, Ettenger NA, Feiner HD, Harnanz-Schulman M, Spatz EM, Toder ST, Genieser NB (1988) Congenital anomalies of the lungs in adults: MR diagnosis. AJR Am J Roentgenol 151:13–19

Nomori H, Mori T, Ikeda K, Kawanaka K, Shiraishi S, Katahira K, Yamashita Y (2008) Diffusion-weighted magnetic resonance imaging can be used in place of positron emission tomography for N staging of non-small cell lung cancer with fewer false-positive results. J Thorac Cardiovasc Surg 135:816–822

Ohno Y, Adachi S, Kono M, Kusumoto M, Motoyama A, Sugimura K (2000) Predicting the prognosis of non-small cell lung cancer patient treated with conservative therapy using contrast-enhanced MR imaging. Eur Radiol 10:1770–1781

Ohno Y, Adachi S, Motoyama A, Kusumoto M, Hatabu H, Sugimura K, Kono M (2001) Multiphase ECG-triggered 3D contrast-enhanced MR angiography: utility for evaluation of hilar and mediastinal invasion of bronchogenic carcinoma. J Magn Reson Imaging 13:215–224

Ohno Y, Hatabu H, Takenaka D, Adachi S, Kono M, Sugimura K (2002) Solitary pulmonary nodules: potential role of dynamic MR imaging in management initial experience. Radiology 224:503–511

Ohno Y, Hatabu H, Takenaka D, Uematsu H, Ohbayashi C, Higashino T, Nogami M, Yoshimura M, Fujii M, Sugimura K (2004a) Dynamic MR imaging: value of differentiating subtypes of peripheral small adenocarcinoma of the lung. Eur J Radiol 52:144–150

Ohno Y, Hatabu H, Higashino T, Takenaka D, Watanabe H, Nishimura Y, Yoshimura M, Sugimura K (2004b) Dynamic perfusion MRI versus perfusion scintigraphy: prediction of postoperative lung function in patients with lung cancer. AJR Am J Roentgenol 182:73–78

Ohno Y, Hatabu H, Murase K, Higashino T, Kawamitsu H, Watanabe H, Takenaka D, Fujii M, Sugimura K (2004c) Quantitative assessment of regional pulmonary perfusion in the entire lung using three-dimensional ultrafast dynamic contrast-enhanced magnetic resonance imaging: preliminary experience in 40 subjects. J Magn Reson Imaging 20:353–365

Ohno Y, Hatabu H, Takenaka D, Higashino T, Watanabe H, Ohbayashi C, Yoshimura M, Satouchi M, Nishimura Y, Sugimura K (2004d) Metastases in mediastinal and hilar lymph nodes in patients with non-small cell lung cancer: quantitative and qualitative assessment with STIR turbo spin echo MR imaging. Radiology 231:872–879

Ohno Y, Nogami M, Higashino T, Takenaka D, Matsumoto S, Hatabu H, Sugimura K (2005) Prognostic value of dynamic MR imaging for non-small-cell lung cancer patients after chemoradiotherapy. J Magn Reson Imaging 21:775–783

Ohno Y, Hatabu H, Murase K, Higashino T, Nogami M, Yoshikawa T, Sugimura K (2007a) Primary pulmonary hypertension: 3D dynamic perfusion MRI for quantitative analysis of regional pulmonary perfusion. AJR Am J Roentgenol 188:48–56

Ohno Y, Koyama H, Nogami M, Takenaka D, Matsumoto S, Yoshimura M, Kotani Y, Sugimura K (2007b)

Postoperative lung function in lung cancer patients: comparative analysis of predictive capability of MRI, CT, and SPECT. AJR Am J Roentgenol 189: 400–408

Ohno Y, Koyama H, Nogami M, Takenaka D, Yoshikawa T, Yoshimura M, Ohbayashi C, Sugimura K (2007c) STIR turbo SE MR imaging vs. coregistered FDG-PET/CT: quantitative and qualitative assessment of N-stage in non-small-cell lung cancer patients. J Magn Reson Imaging 26:1071–1080

Ohno Y, Koyama H, Nogami M, Takenaka D, Yoshikawa T, Yoshimura M, Kotani Y, Nishimura Y, Higashino T, Sugimura K (2007d) Whole-body MR imaging vs FDG-PET: comparison of accuracy of M-stage diagnosis for lung cancer patients. J Magn Reson Imaging 26:498–509

Ohno Y, Koyama H, Takenaka D, Nogami M, Maniwa Y, Nishimura Y, Ohbayashi C, Sugimura K (2008a) Dynamic MRI, dynamic multidetector-row computed tomography (MDCT), and coregistered 2-[fluorine-18]-fluoro-2-deoxy-D-glucose-positron emission tomography (FDG-PET)/CT: comparative study of capability for management of pulmonary nodules. J Magn Reson Imaging 27:1284–1295

Ohno Y, Koyama H, Onishi Y, Takenaka D, Nogami M, Yoshikawa T, Matsumoto S, Kotani Y, Sugimura K (2008b) Non-small cell lung cancer: whole-body MR examination for M-stage assessment – utility for whole-body diffusion-weighted imaging compared with integrated FDG PET/CT. Radiology 248:643–654

Ohno Y, Koyama H, Nogami M, Takenaka D, Onishi Y, Matsumoto K, Matsumoto S, Maniwa Y, Yoshimura M, Nishimura Y, Sugimura K (2011a) State-of-the-art radiological techniques improve the assessment of postoperative lung function in patients with non-small cell lung cancer. Eur J Radiol 77:97–104

Ohno Y, Koyama H, Matsumoto K, Onishi Y, Takenaka D, Fujisawa Y, Yoshikawa T, Konishi M, Maniwa Y, Nishimura Y, Ito T, Sugimura K (2011b) N stage disease in patients with non-small cell lung cancer: efficacy of quantitative and qualitative assessment with STIR turbo spin echo imaging, diffusion-weighted MR imaging, and fluorodeoxyglucose PET/CT. Radiology 261:605–615

Ohno Y, Nishio M, Koyama H, Miura S, Yoshikawa T, Matsumoto S, Sugimura K (2014) Dynamic contrast-enhanced CT and MRI for pulmonary nodule assessment. AJR Am J Roentgenol 202:515–529

Ohno Y, Koyama H, Yoshikawa T, Takenaka D, Seki S, Yui M, Yamagata H, Aoyagi K, Matsumoto S, Sugimura K (2015) Three-way comparison of whole-body MR, coregistered whole-body FDG PET/MR, and integrated whole-body FDG PET/CT imaging: TNM and stage assessment capability for non-small cell lung cancer patients. Radiology 275:849–861

Ohno Y, Koyama H, Yoshikawa T, Seki S, Takenaka D, Yui M, Lu A, Miyazaki M, Sugimura K (2016) Pulmonary high-resolution ultrashort TE MR imaging: Comparison with thin-section standard- and low-dose computed tomography for the assessment of pulmonary parenchyma diseases. J Magn Reson Imaging 43:512–532

Oliver TW Jr, Bernardino ME, Miller JI, Mansour K, Greene D, Davis WA (1984) Isolated adrenal masses in nonsmall-cell bronchogenic carcinoma. Radiology 153:217–218

Padovani B, Mouroux J, Seksik L, Chanalet S, Sedat J, Rotomondo C, Richelme H, Serres JJ (1993) Chest wall invasion by bronchogenic carcinoma: evaluation with MR imaging. Radiology 187:33–38

Pantel K, Izbicki J, Passlick B, Angstwurm M, Häussinger K, Thetter O, Riethmüller G (1996) Frequency and prognostic significance of isolated tumour cells in bone marrow of patients with non-small-cell lung cancer without overt metastases. Lancet 347:649–653

Park SW, Lee JH, Ehara S, Park YB, Sung SO, Choi JA, Joo YE (2004) Single shot fast spin echo diffusion-weighted MR imaging of the spine; Is it useful in differentiating malignant metastatic tumor infiltration from benign fracture edema? Clin Imaging 28:102–108

Park Y, Kim TS, Yi CA, Cho EY, Kim H, Choi YS (2007) Pulmonary cavitary mass containing a mural nodule: differential diagnosis between intracavitary aspergilloma and cavitating lung cancer on contrast-enhanced computed tomography. Clin Radiol 62:227–232

Parmar H, Shah J, Patkar D, Varma R (2000) Intramedullary tuberculomas. MR findings in seven patients. Acta Radiol 41:572–577

Patz EF Jr, Lowe VJ, Hoffman JM, Paine SS, Burrowes P, Coleman RE, Goodman PC (1993) Focal pulmonary abnormalities: evaluation with F-18 fluorodeoxyglucose PET scanning. Radiology 188:487–490

Patz EF Jr, Lowe VJ, Goodman PC, Herndon J (1995) Thoracic nodal staging with PET imaging with 18FDG in patients with bronchogenic carcinoma. Chest 108:1617–1621

Pauls S, Schmidt SA, Juchems MS, Klass O, Luster M, Reske SN, Brambs HJ, Feuerlein S (2012) Diffusion-weighted MR imaging in comparison to integrated [18F]-FDG PET/CT for N-staging in patients with lung cancer. Eur J Radiol 81:178–182

Plathow C, Zimmermann H, Fink C et al (2005) Influence of different breathing maneuvers on internal and external organ motion: use of fiducial markers in dynamic MRI. Int J Radiat Oncol Biol Phys 62:238–245

Poon PY, Bronskill MJ, Henkelman RM, Rideout DF, Shulman HS, Weisbrod GL, Steinhardt MI, Dunlap HJ, Ginsberg RJ, Feld R (1987) Mediastinal lymph node metastases from bronchogenic carcinoma: detection with MR imaging and CT. Radiology 162:651–656

Puderbach M, Risse F, Biederer J et al (2008) In vivo Gd-DTPA concentration for MR lung perfusion measurements: assessment with computed tomography in a porcine model. Eur Radiol 18:2102–2107

Quint LE, Francis IR (1999) Radiologic staging of lung cancer. J Thorac Imaging 14:235–246

Quint LE, Glazer GM, Orringer MB (1987) Central lung masses: prediction with CT of need for pneumonectomy versus lobectomy. Radiology 165:735–738

Quint LE, Francis IR, Wahl RL, Gross BH, Glazer GM (1995) Preoperative staging of non-small-cell carcinoma of the lung: imaging methods. AJR Am J Roentgenol 164:1349–1359

Quint LE, Tummala S, Brisson LJ, Francis IR, Krupnick AS, Kazerooni EA, Iannettoni MD, Whyte RI, Orringer MB (1996) Distribution of distant metastases from newly diagnosed non-small cell lung cancer. Ann Thorac Surg 62:246–250

Rapoport S, Blair DN, McCarthy SM, Desser TS, Hammers LW, Sostman HD (1988) Brachial plexus: correlation of MR imaging with CT and pathologic findings. Radiology 167:161–165

Regier M, Kandel S, Kaul MG, Hoffmann B, Ittrich H, Bansmann PM, Kemper J, Nolte-Ernsting C, Heller M, Adam G, Biederer J (2007) Detection of small pulmonary nodules in high-field MR at 3 T: evaluation of different pulse sequences using porcine lung explants. Eur Radiol 17:1341–1351

Rendina EA, Bognolo DA, Mineo TC, Gualdi GF, Caterino M, Di Biasi C, Facciolo F, Ricci C (1987) Computed tomography for the evaluation of intrathoracic invasion by lung cancer. J Thorac Cardiovasc Surg 94:57–63

Sakai F, Sone S, Maruyama A, Kawai T, Imai S, Aoki J, Morimoto M, Haniuda M, Ueda H, Honda T (1992) Thin-rim enhancement in Gd-DTPA-enhanced magnetic resonance images of tuberculoma: a new finding of potential differential diagnostic importance. J Thorac Imaging 7:64–69

Sakai F, Sone S, Kiyono K, Maruyama A, Kawai T, Aoki J, Ueda H, Ishii K, Honda T, Morimoto M (1994) MR of pulmonary hamartoma: pathologic correlation. J Thorac Imaging 9:51–55

Sakai S, Murayama S, Murakami J, Hashiguchi N, Masuda K (1997) Bronchogenic carcinoma invasion of the chest wall: evaluation with dynamic cine MRI during breathing. J Comput Assist Tomogr 21:595–600

Satoh S, Kitazume Y, Ohdama S, Kimula Y, Taura S, Endo Y (2008) Can malignant and benign pulmonary nodules be differentiated with diffusion-weighted MRI? AJR Am J Roentgenol 191:464–470

Sawant A, Keall P, Pauly KB, Alley M, Vasanawala S, Loo BW Jr, Hinkle J, Joshi S (2014) Investigating the feasibility of rapid MRI for image-guided motion management in lung cancer radiotherapy. Biomed Res Int 2014:485067

Schaarschmidt B, Buchbender C, Gomez B, Rubbert C, Hild F, Köhler J, Grueneisen J, Reis H, Ruhlmann V, Wetter A, Quick HH, Antoch G, Heusch P (2015) Thoracic staging of non-small-cell lung cancer using integrated (18)F-FDG PET/MR imaging: diagnostic value of different MR sequences. Eur J Nucl Med Mol Imaging 42:1257–1267

Schaefer JF, Vollmar J, Schick F, Vonthein R, Seemann MD, Aebert H, Dierkesmann R, Friedel G, Claussen CD (2004) Solitary pulmonary nodules: dynamic contrast-enhanced MR imaging – perfusion differences in malignant and benign lesions. Radiology 232:544–553

Schaefer JF, Schneider V, Vollmar J, Wehrmann M, Aebert H, Friedel G, Vonthein R, Schick F, Claussen CD (2006) Solitary pulmonary nodules: association between signal characteristics in dynamic contrast enhanced MRI and tumor angiogenesis. Lung Cancer 53:39–49

Schaefer-Prokop C, Prokop M (2002) New imaging techniques in the treatment guidelines for lung cancer. Eur Respir J Suppl 35:71s–83s

Schmidt GP, Haug AR, Schoenberg SO, Reiser MF (2006) Whole-body MRI and PET-CT in the management of cancer patients. Eur Radiol 16:1216–1225

Schrevens L, Lorent N, Dooms C, Vansteenkiste J (2004) The role of PET scan in diagnosis, staging, and management of non-small cell lung cancer. Oncologist 9:633–643

Schroeder T, Ruehm SG, Debatin JF, Ladd ME, Barkhausen J, Goehde SC (2005) Detection of pulmonary nodules using a 2D HASTE MR sequence: comparison with MDCT. AJR Am J Roentgenol 185:979–984

Schwartz LH, Ginsberg MS, Burt ME, Brown KT, Getrajdman GI, Panicek DM (1998) MRI as an alternative to CT-guided biopsy of adrenal masses in patients with lung cancer. Ann Thorac Surg 65:193–197

Seo JS, Kim YJ, Choi BW, Choe KO (2005) Usefulness of magnetic resonance imaging for evaluation of cardiovascular invasion: evaluation of sliding motion between thoracic mass and adjacent structures on cine MR images. J Magn Reson Imaging 22:234–241

Shimizu S, Shirato H, Aoyama H et al (2000) High-speed magnetic resonance imaging for four-dimensional treatment planning of conformal radiation therapy of moving body tumors. Int J Radiat Oncol Biol Phys 48:471–474

Siegelman SS, Khouri NF, Scott WW Jr, Leo FP, Hamper UM, Fishman EK, Zerhouni EA (1986) Pulmonary hamartoma: CT findings. Radiology 160:313–317

Silvestri GA, Littenberg B, Colice GL (1995) The clinical evaluation for detecting metastatic lung cancer. A meta-analysis. Am J Respir Crit Care Med 152:225–230

Silvestri GA, Gould MK, Margolis ML, Tanoue LT, McCrory D, Toloza E, Detterbeck F (2007) Noninvasive staging of non-small cell lung cancer: ACCP evidenced-based clinical practice guidelines, 2nd edn. American College of Chest Physicians. Chest 132:178S–201S

Sobin L, Wittekind C (2002) Lung cancer. In: Sobin L, Wittekind C (eds) TNM classification of malignant tumors, 6th edn. Wiley-Liss, New York, pp 99–103

Sochocky S (1958) Tuberculoma of the lung. Am Rev Tuber 78:403–410

Suzuki N, Saitoh T, Kitamura S (1993) Tumor invasion of the chest wall in lung cancer: diagnosis with US. Radiology 187:39–42

Sommer G, Wiese M, Winter L, Lenz C, Klarhöfer M, Forrer F, Lardinois D, Bremerich J (2012) Preoperative staging of non-small-cell lung cancer: comparison of

whole-body diffusion-weighted magnetic resonance imaging and 18F-fluorodeoxyglucose-positron emission tomography/computed tomography. Eur Radiol 22:2859–2867

Sommer G, Tremper J, Koenigkam-Santos M, Delorme S, Becker N, Biederer J, Kauczor HU, Heussel CP, Schlemmer HP, Puderbach M (2014) Lung nodule detection in a high-risk population: comparison of magnetic resonance imaging and low-dose computed tomography. Eur J Radiol 83:600–605

Stanescu T, Jaffray D (2016) Investigation of the 4D composite MR image distortion field associated with tumor motion for MR-guided radiotherapy. Med Phys 43:1550–1562

Swensen SJ, Morin RL, Schueler BA, Brown LR, Cortese DA, Pairolero PC, Brutinel WM (1992) Solitary pulmonary nodule: CT evaluation of enhancement with iodinated contrast media – a preliminary report. Radiology 182:343–347

Swensen SJ, Brown LR, Colby TV, Weaver AL, Midthum DE (1996) Lung nodule enhancement at CT: prospective findings. Radiology 201:447–455

Swensen SJ, Viggiano RW, Midthun DE, Müller NL, Sherrick A, Yamashita K, Naidich DP, Patz EF, Hartman TE, Muhm JR, Weaver AL (2000) Lung nodule enhancement at CT: multicenter study. Radiology 214:73–80

Swensen SJ, Jett JR, Hartman TE, Midthun DE, Mandrekar SJ, Hillman SL, Sykes AM, Aughenbaugh GL, Bungum AO, Allen KL (2005) CT screening for lung cancer: five-year prospective experience. Radiology 235:259–265

Szolar DH, Kammerhuber FH (1998) Adrenal adenomas and nonadenomas: assessment of washout at delayed contrast-enhanced CT. Radiology 207:369–375

Takahara T, Imai Y, Yamashita T, Yasuda S, Nasu S, Van Cauteren M (2004) Diffusion weighted whole body imaging with background body signal suppression (DWIBS): technical improvement using free breathing, STIR and high resolution 3D display. Radiat Med 22:275–282

Takahashi K, Furuse M, Hanaoka H, Yamada T, Mineta M, Ono H, Nagasawa K, Aburano T (2000) Pulmonary vein and left atrial invasion by lung cancer: assessment by breath-hold gadolinium-enhanced three-dimensional MR angiography. J Comput Assist Tomogr 24:557–561

Takahashi M, Shimoyama K, Murata K, Mori M, Nitta N, Mishina A, Matsuo H, Morita R, Fujino S, Inoue S, Kato H (1997) Hilar and mediastinal invasion of bronchogenic carcinoma: evaluation by thin-section electron-beam computed tomography. J Thorac Imaging 12:195–199

Takenaka D, Ohno Y, Hatabu H, Ohbayashi C, Yoshimura M, Ohkita Y, Sugimura K (2002) Differentiation of metastatic versus non-metastatic mediastinal lymph nodes in patients with non-small cell lung cancer using respiratory-triggered short inversion time inversion

recovery (STIR) turbo spin echo MR imaging. Eur J Radiol 44:216–224

Takenaka D, Ohno Y, Matsumoto K, Aoyama N, Onishi Y, Koyama H, Nogami M, Yoshikawa T, Matsumoto S, Sugimura K (2009) Detection of bone metastases in non-small cell lung cancer patients: comparison of whole-body diffusion-weighted imaging (DWI), whole-body MR imaging without and with DWI, whole-body FDG-PET/CT, and bone scintigraphy. J Magn Reson Imaging 30:298–308

Tanaka K, Kubota K, Kodama T, Nagai K, Nishiwaki Y (1999) Extrathoracic staging is not necessary for non-small-cell lung cancer with clinical stage T1-2 N0. Ann Thorac Surg 68:1039–1042

Therasse P, Arbuck SG, Eisenhauer EA, Wanders J, Kaplan RS, Rubinstein L, Verweij J, Van Glabbeke M, van Oosterom AT, Christian MC, Gwyther SG (2000) New guidelines to evaluate the response to treatment in solid tumors. J Natl Cancer Inst 92:205–216

Tokuda O, Hayashi N, Matsunaga N (2004) MRI of bone tumors: Fast STIR imaging as a substitute for T1-weighted contrast-enhanced fat-suppressed spin echo imaging. J Magn Reson Imaging 19:475–481

Toloza EM, Harpole L, McCrory DC (2003) Noninvasive staging of non-small cell lung cancer: a review of the current evidence. Chest 123:137S–146S

Tryggestad E, Flammang A, Han-Oh S, Hales R, Herman J, McNutt T, Roland T, Shea SM, Wong J (2013) Respiration-based sorting of dynamic MRI to derive representative 4D-MRI for radiotherapy planning. Med Phys 40:051909

Tuddenham WJ (1984) Glossary of terms for thoracic radiology: recommendations of the Nomenclature Committee of the Fleischner Society. AJR Am J Roentgenol 143:509–517

Uto T, Takehara Y, Nakamura Y, Naito T, Hashimoto D, Inui N, Suda T, Nakamura H, Chida K (2009) Higher sensitivity and specificity for diffusion-weighted imaging of malignant lung lesions without apparent diffusion coefficient quantification. Radiology 252:247–254

van der Heide S, Kauffman HF, de Vries K (1985) Cultivation of fungi in synthetic and semi-synthetic liquid medium. II Immunochemical properties of the antigenic and allergenic extracts. Allergy 40:592–598

van Tinteren H, Hoekstra OS, Smit EF, van den Bergh JH, Schreurs AJ, Stallaert RA, van Velthoven PC, Comans EF, Diepenhorst FW, Verboom P, van Mourik JC, Postmus PE, Boers M, Teule GJ (2002) Effectiveness of positron emission tomography in the preoperative assessment of patients with suspected non-small-cell lung cancer: the PLUS multicentre randomised trial. Lancet 359:1388–1393

Vanel D, Bittoun J, Tardivon A (1998) MRI of bone metastases. Eur Radiol 8:1345–1351

Vansteenkiste J, De Leyn P, Deneffe G, Menten J, Lerut T, Demedts M (1998) Present status of induction treatment in stage IIIA-N2 non-small cell lung cancer: a

review. The Leuven Lung Cancer Group. Eur J Cardiothorac Surg 13:1–12

Vogt FM, Herborn CU, Hunold P, Lauenstein TC, Schröder T, Debatin JF, Barkhausen J (2004) HASTE MRI versus chest radiography in the detection of pulmonary nodules: comparison with MDCT. AJR Am J Roentgenol 183:71–78

Wahl RL, Quint LE, Greenough RL, Meyer CR, White RI, Orringer MB (1994) Staging of mediastinal non-small cell lung cancer with FDG PET, CT, and fusion images: preliminary prospective evaluation. Radiology 191:371–377

Walker R, Kessar P, Blanchard R, Dimasi M, Harper K, DeCarvalho V, Yucel EK, Patriquin L, Eustace S (2000) Turbo STIR magnetic resonance imaging as a whole-body screening tool for metastases in patients with breast carcinoma: preliminary clinical experience. J Magn Reson Imaging 11:343–350

Watanabe A, Shimokata K, Saka H, Nomura F, Sakai S (1991) Chest CT combined with artificial pneumothorax: value in determining origin and extent of tumor. AJR Am J Roentgenol 156:707–710

Webb WR, Gatsonis C, Zerhouni EA, Heelan RT, Glazer GM, Francis IR, McNeil BJ (1991) CT and MR imaging in staging non-small cell bronchogenic carcinoma: report of the Radiologic Diagnostic Oncology Group. Radiology 178:705–713

Webb WR, Sarin M, Zerhouni EA, Heelan RT, Glazer GM, Gatsonis C (1993) Interobserver variability in CT and MR staging of lung cancer. J Comput Assist Tomogr 17:841–846

Weinberger E, Shaw DW, White KS, Winters WD, Stark JE, Nazar-Stewart V, Hinks RS (1995) Nontraumatic pediatric musculoskeletal MR imaging: comparison of conventional and fast-spin echo short inversion time inversion-recovery technique. Radiology 194:721–726

White CS (1996) MR evaluation of the pericardium and cardiac malignancies. Magn Reson Imaging Clin N Am 4:237–251

White PG, Adams H, Crane MD, Butchart EG (1994) Preoperative staging of carcinoma of the bronchus: can computed tomographic scanning reliably identify stage III tumours? Thorax 49:951–957

Wong J, Haramati LB, Rozenshtein A, Yanez M, Austin JH (1999) Non-small-cell lung cancer: practice patterns of extrathoracic imaging. Acad Radiol 6:211–215

World Health Organization (1979) WHO handbook for reporting the results of cancer treatment. World Health Organization, Geneva

Yamashita K, Matsunobe S, Tsuda T, Nemoto T, Matsumoto K, Miki H, Konishi J (1995) Solitary pulmonary nodules: preliminary study of evaluation with incremental dynamic CT. Radiology 194:399–405

Yi CA, Lee KS, Kim EA, Han J, Kim H, Kwon OJ, Jeong YJ, Kim S (2004) Solitary pulmonary nodules: dynamic enhanced multi-detector row CT study and comparison with vascular endothelial growth factor and microvessel density. Radiology 233:191–199

Yi CA, Lee KS, Kim BT, Choi JY, Kwon OJ, Kim H, Shim YM, Chung MJ (2006) Tissue characterization of solitary pulmonary nodule: comparative study between helical dynamic CT and integrated PET/CT. J Nucl Med 47:443–450

Yi CA, Jeon TY, Lee KS, Lee JH, Seo JB, Kim YK, Chung MJ (2007) 3-T MRI: usefulness for evaluating primary lung cancer and small nodules in lobes not containing primary tumors. AJR Am J Roentgenol 189:386–392

Yi CA, Shin KM, Lee KS, Kim BT, Kim H, Kwon OJ, Choi JY, Chung MJ (2008) Non-small cell lung cancer staging: efficacy comparison of integrated PET/CT versus 3.0-T whole-body MR imaging. Radiology 48:632–642

Yilmaz S, Ekici A, Erdogan S, Ekici M (2004) Endobronchial lipomatous hamartoma: CT and MR imaging features. Eur Radiol 14:1521–1524

Yokoi K, Mori K, Miyazawa N, Saito Y, Okuyama A, Sasagawa M (1991) Tumor invasion of the chest wall and mediastinum in lung cancer: evaluation with pneumothorax CT. Radiology 181:147–152

Yokoi K, Kamiya N, Matsuguma H, Machida S, Hirose T, Mori K, Tominaga K (1999) Detection of brain metastasis in potentially operable non-small cell lung cancer: a comparison of CT and MRI. Chest 115:714–719

Zhang M, Kono M (1997) Solitary pulmonary nodules: evaluation of blood flow patterns with dynamic CT. Radiology 205:471–4788

Zinreich SJ, Kennedy DW, Malat J, Curtin HD, Epstein JI, Huff LC, Kumar AJ, Johns ME, Rosenbaum AE (1988) Fungal sinusitis: diagnosis with CT and MR imaging. Radiology 169:439–444

Mediastinal Disease

K. Takahashi, T. Sasaki, and K. Nakajima

Contents

K. Takahashi, MD, PhD (✉) • T. Sasaki, MD, PhD
Department of Radiology, Asahikawa Medical
College, 2-1-1-1 Midorigaoka-higashi,
Asahikawa, Japan
e-mail: taka1019@asahikawa-med.ac.jp

K. Nakajima, MD
Department of Radiation Oncology, Asahikawa
Medical College, 2-1-1-1 Midorigaoka-higashi,
Asahikawa, Japan

Abstract

Cystic masses are generally congenital and arise anywhere in the mediastinum, and MR imaging is useful to confirm their cystic nature, especially in those cysts with soft tissue attenuation at CT. In the thymus, chemical shift MR imaging can characterize the normal thymus and thymic hyperplasia by detecting tiny amounts of fat tissue within the thymus and differentiate such benign processes from thymic tumors. Malignant lymphoma is a disease relatively common in the mediastinum, and MR provides important information, especially in the assessment of viability of residual masses in treated lymphoma. In the diagnosis of neurogenic tumors, MR imaging can precisely evaluate shape, location, intraspinal extension, and internal components of these tumors.

1 Introduction

In the assessment of mediastinal disease, CT is generally the first choice imaging modality. But not uncommonly, MR imaging provides important findings, which are diagnostic of a disease and facilitates precise assessment of location, pattern of extension, and anatomical relationship with adjacent structures of the disease. In addition to conventional T1- and T2-weighted spin-echo sequences, chemical shift imaging, dynamic studies with gradient-echo 2- or 3-dimensional sequences, and diffusion-weighted imaging are available to obtain specific findings of the mediastinal diseases.

We describe the role of MR imaging in the assessment of various mediastinal diseases, including congenital and acquired cystic masses, thymus and thymic tumors, germ cell tumors, Hodgkin and non-Hodgkin's lymphoma, and neurogenic tumors with emphasis of their characteristic and specific findings on MR imaging.

2 Mediastinal Cystic Masses

Cystic masses of the mediastinum are encapsulated lesions that contain fluid and are lined with epithelium. Most cystic lesions are congenital in origin and include foregut duplication cysts (i.e., bronchogenic cysts, esophageal duplication cysts, and neurenteric cysts) pericardial cysts, pleural cysts, and parathyroid cysts. Thymic cysts and thoracic duct cysts are either congenital or acquired in origin. Meningoceles, pancreatic pseudocysts, hydatid disease, abscess, hematoma, and various solid lesions associated with cystic degeneration (i.e., schwannoma, germ cell tumor, thymoma, and parathyroid adenoma) also appear as cystic mediastinal masses.

In a study of 105 cases with mediastinal cysts, cystic disease comprises 13.0 % of mediastinal masses and is more prevalent in adults (14.1 %) than in children (7.7 %) ($p < 0.05$). Overall, 36.2 % of the patients were symptomatic, and common symptoms were retrosternal chest pain (14.3 %), followed by dyspnea (7.6 %), cough (6.7 %), fever (5.7 %), and hoarseness (4.8 %). The incidence of cystic masses is 45 % in bronchogenic, 28 % in thymic, 11 % in pericardial, 7 % in pleural cysts, and 4 % in esophageal duplication cysts (Takeda et al. 2003).

On the radiographs, mediastinal cystic masses usually appear as focal deformity or obscuration of mediastinal contours and lines and may be associated with displacement of normal mediastinal structures. Generally, CT is the diagnostic modality of first choice for mediastinal cystic masses and the following typical features are diagnostic: (1) an encapsulated smooth round or oval mass, (2) homogeneous attenuation in the range of water attenuation (0–20 HU), (3) no enhancement of cyst contents, and (4) no infiltration of adjacent mediastinal structures (Kuhlman et al. 1988; Feung et al. 2002).

On MR images, mediastinal cysts that usually contain serous fluid typically show homogeneous low signal intensity on T1-weighted images and high signal intensity on T2-weighted images due to their long T1 and T2 relaxation time. In some mediastinal cysts, CT may reveal high attenuation similar to solid lesions due to a high level of protein and calcium oxalate in the cystic contents (Yemault et al. 1986). In such situations, MR imaging can be useful in the differentiation of cystic masses from solid lesions. High signal intensity corresponding to cerebrospinal fluid on T2-weighted images, a fluid-fluid level, and lack of contrast enhancement are highly suggestive of the cystic nature of the lesions. It should be noted that signal intensity on MR images of mediastinal masses also varies depending on its content including calcium, protein, and blood degradation products, especially on T1-weighted images (Murayama et al. 1995). The lesions with a proteinaceous or hemorrhagic content show high signal on T1-weighted images. One disadvantage of MR imaging is its inability to visualize calcifications, which may occur occasionally in the wall or within the lesion.

2.1 Bronchogenic Cyst

Bronchogenic cysts are the most common foregut cysts and result from defective development (abnormal budding of the ventral foregut) during

the fetal period (Ribet et al.1995). The cyst wall is lined by respiratory epithelium (pseudostriated ciliated columnar epithelium) and contains cartilage, smooth muscle, and mucous gland. Cyst fluid is usually serous but can contain various amounts of protein and calcium and can be hemorrhagic or highly viscous.

Bronchogenic cysts most commonly present in the first few decades of life, and the majority are incidentally detected on chest radiograph or on chest CT. However, they may occasionally be symptomatic due to compression of adjacent structures. In series of surgically diagnosed cases, 70–80 % of patients have symptoms including chest pain, cough, dyspnea, fever, and purulent sputum (St-Georges et al. 1991; Ribet et al. 1996). In infants and young children, they are usually symptomatic and sometimes life-threatening.

The bronchogenic cysts most commonly are located near to the carina (52 %) and in the paratracheal region (19 %), less often adjacent to the esophagus or retrocardiac region, and rarely in the anterior mediastinum, within the lung, in the pleura, and in the diaphragm (Reed and Sobonya 1974; MaAdams et al. 2000). As a rare case, a solitary pedunculated bronchogenic cyst that appeared as a pleural nodule located apart from the mediastinum has been reported (Yoshioka et al. 2000).

Bronchogenic cysts typically appear as a well-defined round or elliptical mass with a uniformly thin wall. On CT, 50 % of bronchogenic cysts reveal typical water attenuation, whereas in the other half, the cysts have variously higher attenuation and may be indistinguishable from soft tissue lesions (Yernault et al. 1986). At T2-weighted MR imaging, bronchogenic cysts constantly have high signal intensity, but variable patterns of signal intensity are seen at T1-weighted MR imaging depending on cystic contents including protein, hemorrhage, mucoid material, and calcium (Feung et al. 2002) (Figs. 1 and 2). McAdams et al. (2000) have reported that on T1-weighted MR images ($n = 23$), 18 cysts were hyperintense and 5 were isointense to cerebrospinal fluid and on T2-weighted MR images ($n = 18$), 17 cysts were isointense or hyperintense and 1 was hypointense to cerebrospinal fluid. Invariable high signal intensity on T2-weighted

MR images is diagnostic of the cystic nature of the lesion. Bronchogenic cysts may reveal a fluid-fluid level on MR images (Murayama et al. 1995). Rarely, bronchogenic cysts contain air that suggests secondary infection or communication with the tracheobronchial tree. Bronchogenic cysts are typically stable in size or may enlarge over years. Abrupt increase in size indicates hemorrhage or infection (Feung et al. 2002) and may result in rupture of the cyst (Fig. 3).

2.2 Esophageal Duplication Cyst

Esophageal duplication cysts may result from either abnormal budding of the foregut or a failure of complete vacuolation of the originally solid esophagus (Salo and Ala-Kulju 1987). The cysts are lined by gastrointestinal tract mucosa and have a double layer of smooth muscle. The cysts are commonly located in the lower mediastinum, adjacent to the esophagus. Imaging features of esophageal duplication cysts are similar to those of other mediastinal congenital cysts. However, the cyst walls may be thicker, and the lesions may be more tubular in shape and in more intimate contact with the esophagus.

2.3 Neurenteric Cyst

Neurenteric cysts result from incomplete separation of endoderm from notochord and usually have either a fibrous connection to the spine or an intraspinal component. The cysts occasionally are associated with various vertebral anomalies, such as hemivertebra, butterfly vertebra, or spina bifida. Findings of neurenteric cysts at CT and MR imaging are similar to those of other foregut cysts. MR imaging is indicated to exclude intraspinal extension of the cysts (Strollo et al. 1997).

2.4 Pericardial Cyst

Pericardial cysts are outpouchings of the parietal pericardium, which have no communication with the pericardial space and result from a defect in
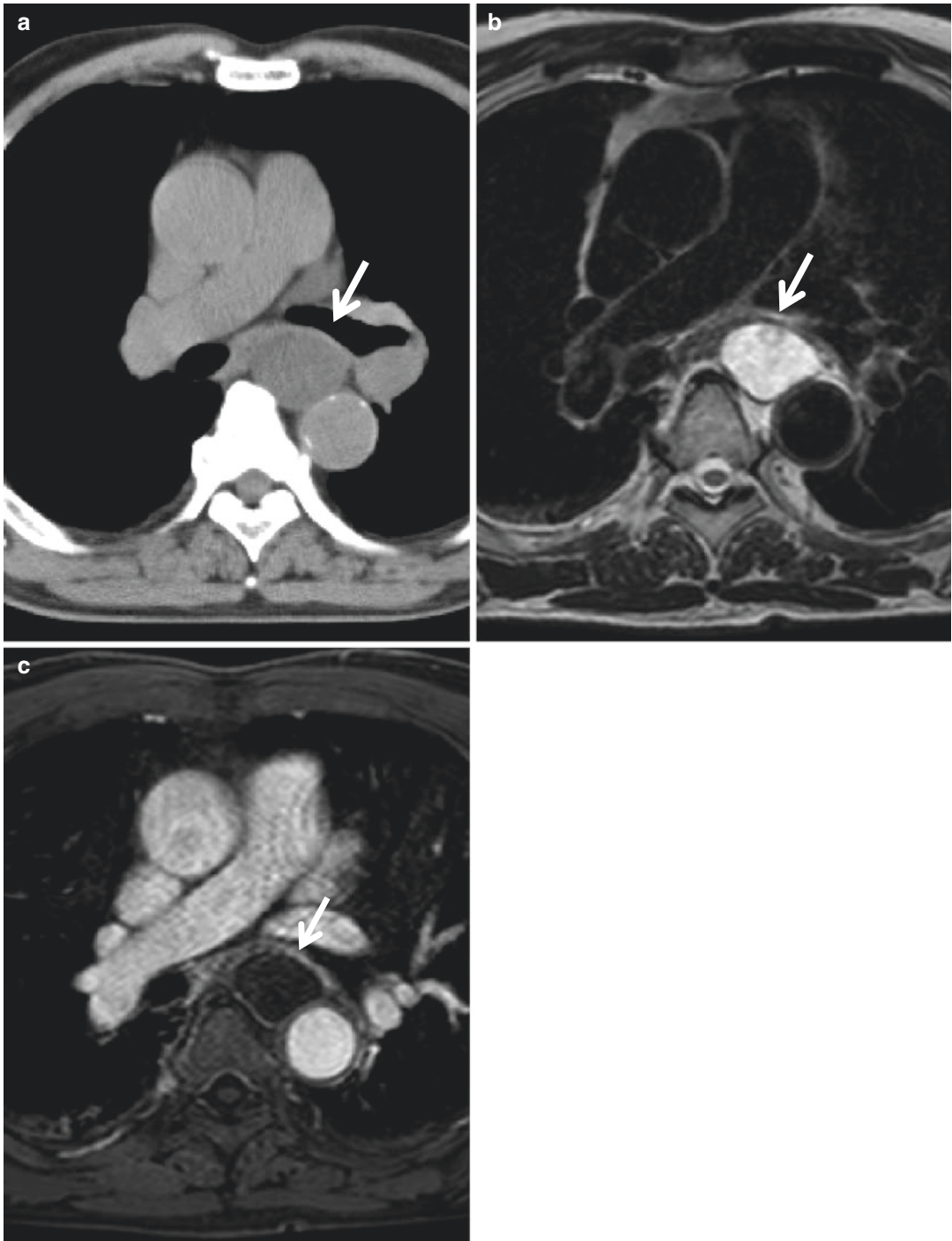
Fig. 1 Bronchogenic cyst. (**a**) Non-contrast-enhanced CT, (**b**) T2-weighted, and (**c**) contrast-enhanced MR images. There is a well-demarcated mass lesion in the subcarinal region (*arrows*). The mass shows soft tissue attenuation on CT but very high signal intensity on T2-weighted images (**b**) and no significant enhancement (**c**) suggesting the cystic nature of the lesion
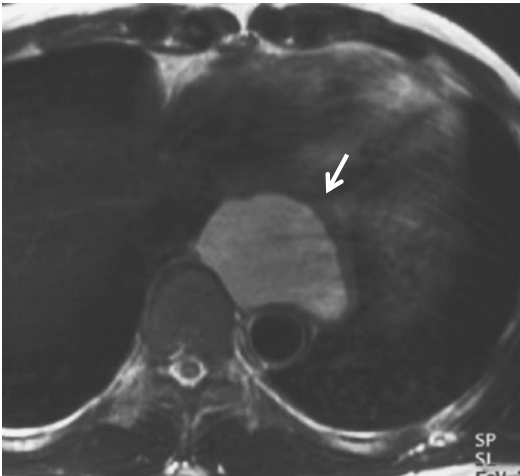
Fig. 2 Bronchogenic cyst. T2-weighted axial MR image (*arrow*) shows a mass at the paravertebral region of intermediate signal intensities suggesting proteinaceous fluid

Fig. 3 Ruptured bronchogenic cyst. The bronchogenic cyst ruptured after abrupt increase in size. T2-weighted MR image reveals a bronchogenic cyst at the carina (*arrow*) and right side pleural effusion

the embryogenesis of the coelomic cavity. These cysts are commonly round or spherical in shape, thin walled, unilocular, and contain clear or straw-colored fluid. Cyst walls consist of connective tissue and a single layer of mesothelial cells.

The majority of pericardial cysts are located in the cardiophrenic angles, and they are more frequent on the right side (Fig. 4). In one large series of 72 cases with pericardial cysts, 54 were located in the cardiophrenic angle, of which two thirds were on the right side, and the remaining 18 were found in the higher mediastinum up to the level of pericardial reflection (Wychulis et al. 1971). Patients are almost invariably asymptomatic, and cysts are incidentally detected on a screening chest radiograph.

On CT, the cysts characteristically show water attenuation, but occasionally its content is of soft tissue attenuation. At MR imaging, they typically have low or intermediate signal intensity on T1-weighted images and homogeneous high intensity on T2-weighted images. The cysts with proteinaceous fluid show high signal intensity on T1-weighted images. The cysts do not enhance with the administration of contrast material (Wang et al. 2003). Pericardial cysts in unusual locations, including upper and anterior mediastinum, may be indistinguishable from bronchogenic or thymic cysts.

2.5   Thymic Cyst

Congenital thymic cysts are derived from a remnant of the thymopharyngeal duct, and they are usually unilocular and generally small. Most patients with congenital thymic cyst are asymptomatic; however, patients can present with cough or dyspnea or with pain if intracystic bleeding occurs. Acquired thymic cysts, occasionally referred to multilocular thymic cysts, are probably pathologically unrelated to congenital cysts and may be associated with various inflammatory process or certain thymic neoplasms, including Hodgkin disease, seminoma, thymoma, and thymic carcinoma (Suster and Rosai 1991). Although some cysts develop after irradiation of the mediastinum or following chemotherapy (Baron et al. 1981), thymic cyst can coexist with Hodgkin disease, unrelated to therapy.

Thymic cysts show low signal intensity on T1-weighted MR images and high signal intensity on T2-weighted MR images (Fig. 5). Hemorrhage into the cysts results in increased signal on T1-weighted images. If the cyst is
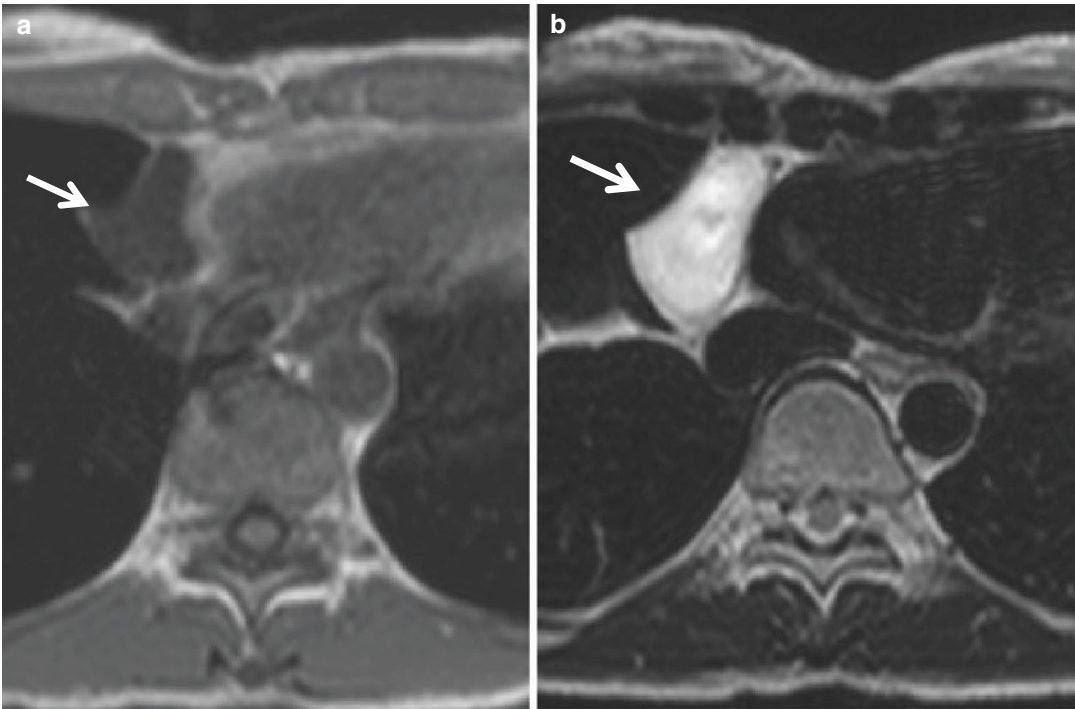
Fig. 4 Pericardial cyst. The right cardiophrenic angle is the most common site of pericardial cyst. The cyst typically shows low signal intensity on T1-weighted image (**a**) and high signal intensity on T2-weighted MR image (**b**) (*arrows*)

multilocular, thick walled, or associated with a soft tissue, biopsy or surgical resection may be indicated to exclude malignancy (Fig. 6).

2.6 Other Cystic and Cyst-Like Lesions

Thoracic duct cyst is an extremely rare cystic lesion in the mediastinum. The cysts occur anywhere along the course of the thoracic duct and occasionally communicate with the duct (Fig. 7). In a review of 29 patients with a thoracic duct cyst, the cyst was found in the mediastinum in 19, in the cervical region in 9, and in the abdomen in one (Mattila et al. 1999). The cysts may be associated with various conditions, including portal hypertension, liver cirrhosis, thoracic duct obstruction, and lymphangiomyomatosis.

Mediastinal pancreatic pseudocysts are rare complication of acute or chronic pancreatitis and result from the extension of pancreatic fluid through the diaphragm. Most mediastinal pseudocysts are retrocardiac as the inflammatory process extends

through the esophageal or the aortic hiatus (Tan et al. 2002). The multiplanar capability of MR imaging is beneficial in the pretreatment assessment of the precise location and range of extension of the pseudocysts (Tanaka et al. 2000).

Lateral thoracic meningocele is a rare disorder which occurs frequently in association with neurofibromatosis type I. MR imaging permits a diagnostic, noninvasive assessment of its cystic nature, communication with the spinal meninges, and associated spinal abnormalities (Nakasu et al. 1991).

3 Thymus and Thymic Tumors

3.1 Normal Thymus

The thymus is a bilobed, triangular-shaped organ that occupies retrosternal space and extends over the great vessel and the heart. The normal thymus varies widely in size and shape depending on the age (Francis et al. 1985). In infants and younger children, the thymus appears quadrilateral in shape rather than triangular in the axial plane. Its

Fig. 5 Thymic cyst. (**a**) Non-contrast-enhanced CT, (**b**) T1-weighted, and (**c**) T2-weighted MR images show a well-defined lesion at the anterior mediastinum (*arrows*). The thymic cyst reveals low and high signal intensity on T1-weighted (**b**) and T2-weighted (**c**) MR images, respectively
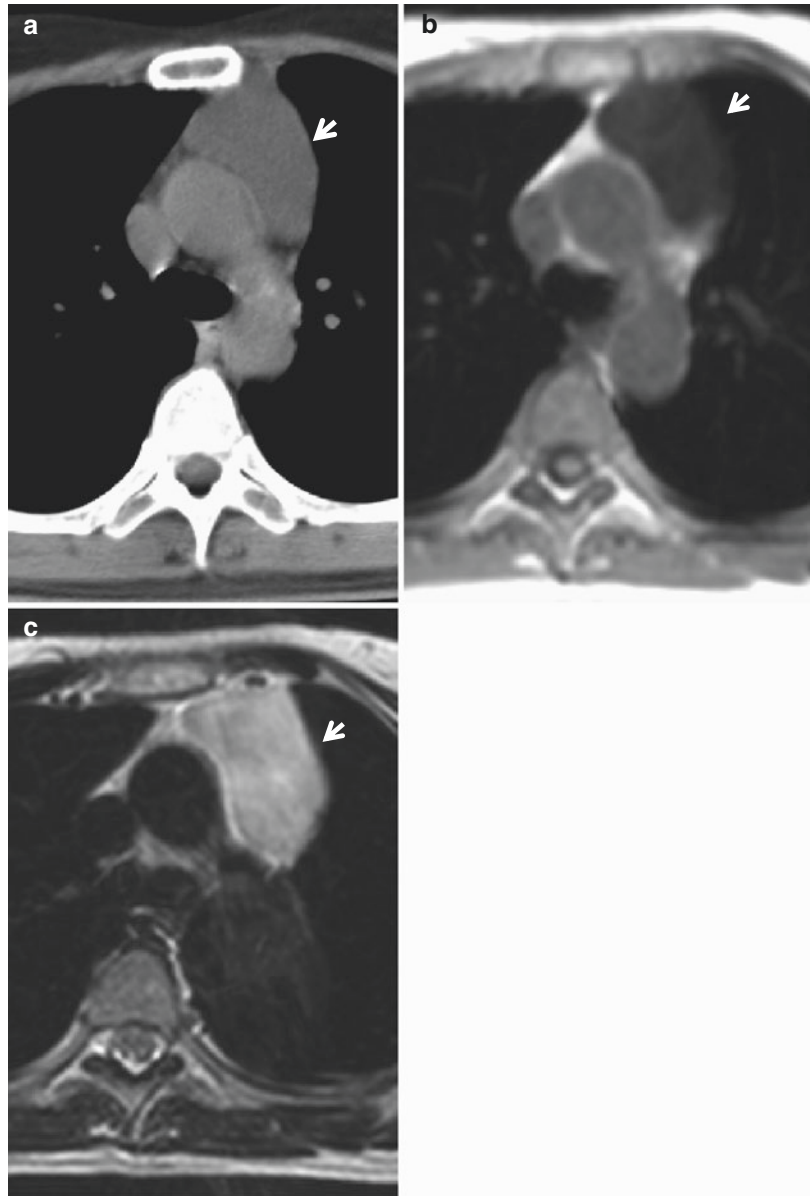
margins are convex in infants and usually become straight in older children (Baron et al. 1982). The thymus reaches a maximum weight during adolescence and then its weight and size decrease with age as the gland undergoes involution with fatty infiltration. From adolescence to young adulthood around 25 years, the thymus appears bilobed triangular structure, and its margins are flat or concave laterally.

The widely accepted CT measurement of the thymus is the thickness of the lobes measured perpendicular to their long axis. On CT, the normal maximal thickness of the thymus is 18 mm before the age of 20 years and 13 mm in older patients (Baron et al. 1982). On MR imaging, the thymus may appear to have a slightly greater thickness than measured on CT, when MR images are obtained under breathing. On CT, the thymus shows soft tissue attenuation similar to muscle in infants and young children. Its attenuation decreases with age after adolescence due to fatty infiltration. On MR imaging, the normal thymus characteristically
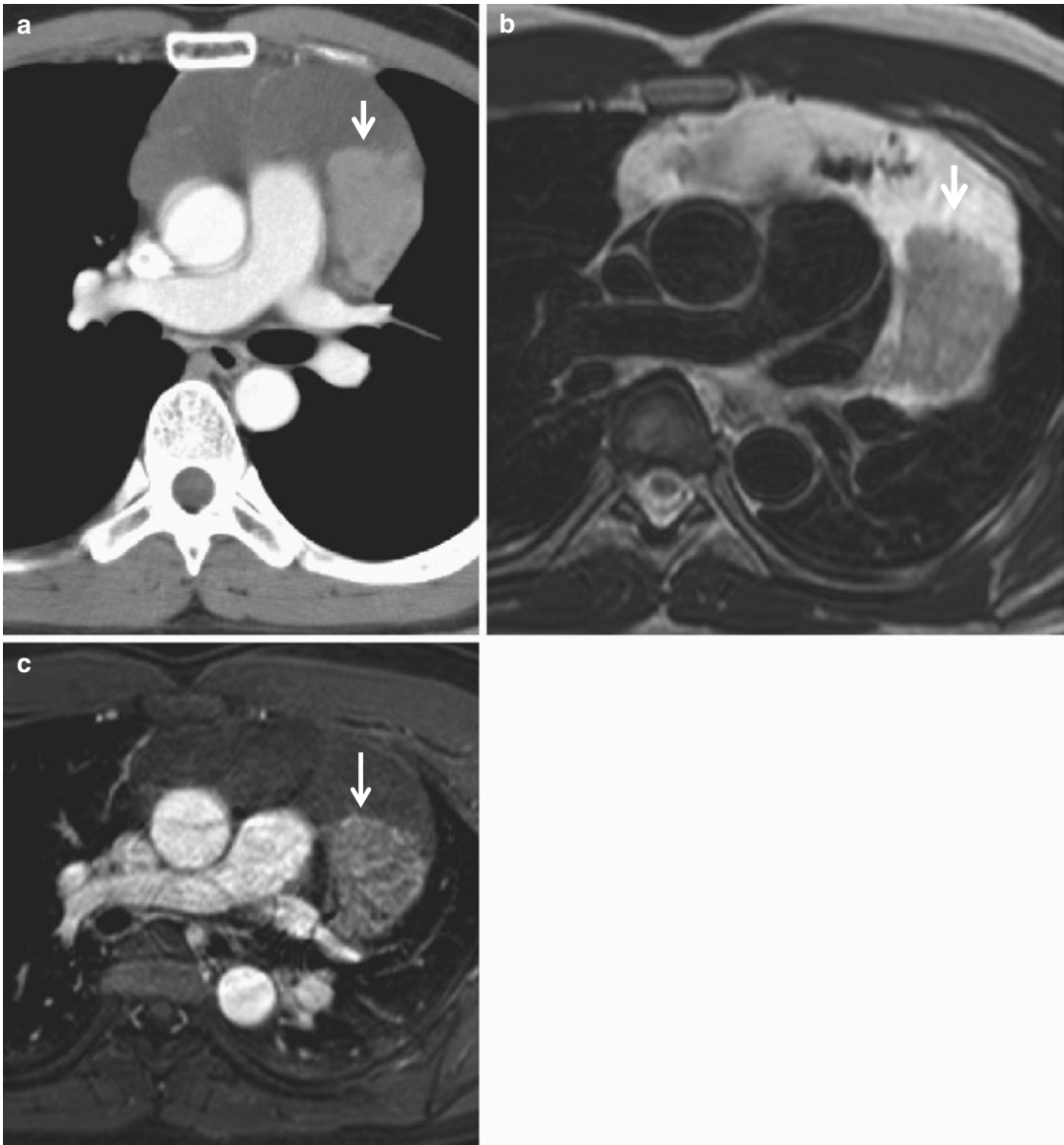
Fig. 6 Thymoma within a multiloculated thymic cyst. (**a**) Non-contrast-enhanced CT, (**b**) T2-weighted (**c**) contrast-enhanced MR images show a multiloculated cyst in the anterior mediastinum. A thymoma (*arrows*) within the cyst appears as a mass lesion of soft tissue attenuation (**a**) of intermediate signal (**b**) and with enhancement (**c**)

shows homogeneous and intermediate signal intensity on T1-weighted images that is less intense than mediastinal fat but greater than muscle. In older patients after adolescence, the T1-weighted signal intensity of the thymus increases with age since the thymus begins to involute and is replaced by fat. On T2-weighted images, the thymus shows high signal intensity similar to fat at all ages (de Geer et al. 1986; Boothroyd et al. 1992). Besides the measurement of the size, CT attenuation, and MR signal intensity, the shape of the thymus is also an important indicator for its abnormality. Focal contour abnormality of the thymus, especially when associated with displacement of the adjacent structures, is suggestive of underlying mass (de Geer et al. 1986).

Fig. 7 Thoracic duct cyst. T2-weighted coronal image shows a lobulated cyst adjacent to the aortic arch (*large arrow*) and a dilated thoracic duct (*small arrows*)

Chemical shift MR imaging can depict intravoxel fat and water within the tissue and has been used clinically to diagnose adrenal adenoma and assess fatty liver. It has been recently reported that chemical shift MR imaging is useful for characterizing the normal thymus by detecting the intravoxel fat tissue within the thymus. Chemical shift MR imaging can depict physiological fatty replacement of the normal thymus in nearly 50 % of subjects aged 11–15 years and in nearly 100 % of those over 15 years (Inaoka et al. 2005) (Fig. 8).

Ectopic thymus results from defective pathways of the embryologic descent of thymus and can occur anywhere along the path of the thymopharyngeal duct. Ectopic cervical thymus usually presents as an asymptomatic neck mass in infant, childhood, and early adulthood and is often located at submandibular region, adjacent to the thyroid gland, and near the carotid bifurcation

(He et al. 2008; Liu et al. 2006; Khariwala et al. 2004). CT reveals a homogeneous soft tissue mass with little or no contrast enhancement (Liu et al. 2006; Khariwala et al. 2004). MRI demonstrates an intensity equal to that of muscle on T1-weighted images and greater than that of muscle on T2-weighted images, identical to the mediastinal thymus. In the diagnosis of ectopic thymus, it should be noted that the normal thymus occasionally extends to the upper mediastinum or lower neck (Fig. 9).

Although a previous report has suggested that an apparent diffusion coefficient (ADC) lower than 1.22×10^{-3} mm^2/s for pediatric neck lesions indicates malignancy, there is a case report of ectopic cervical thymus which has a low ADC value of $0.35 \sim 0.40 \times 10^{-3}$ mm^2/s (Liu et al. 2006). The authors stated that the histological characteristics of normal thymic tissue, which consists of many lymphocytes with tight diffusion space of water protons in the extracellular dimension, might result in a low ADC (Liu et al. 2006).

3.2 Thymic Hyperplasia and Thymic Rebound

Lymphoid follicular hyperplasia is pathologically diagnosed by the presence of hyperplastic lymphoid germinal centers in the medulla of the thymus in association with a lymphocytic and plasma cell infiltrate (Goldstein and Mackey 1969). Lymphoid follicular thymic hyperplasia is seen in more than 50 % of patients with myasthenia gravis and is also associated with various conditions: thyrotoxicosis, systemic lupus erythematosus, Hashimoto thyroiditis, and polyarteritis nodosa (Levine and Rosai 1978).

In CT findings of the thymus in a series of 22 patients with myasthenia gravis and lymphoid follicular hyperplasia, ten had a normal appearance, seven had an enlarged thymus, and five had a focal thymic mass (Nicolaou et al. 1996). The usefulness of CT to establish the diagnosis of lymphoid follicular hyperplasia is limited. Also on MR imaging, thymic hyperplasia appears as diffuse enlargement of the thymus with MR signals similar to those of normal thymus (Molin et al. 1990).
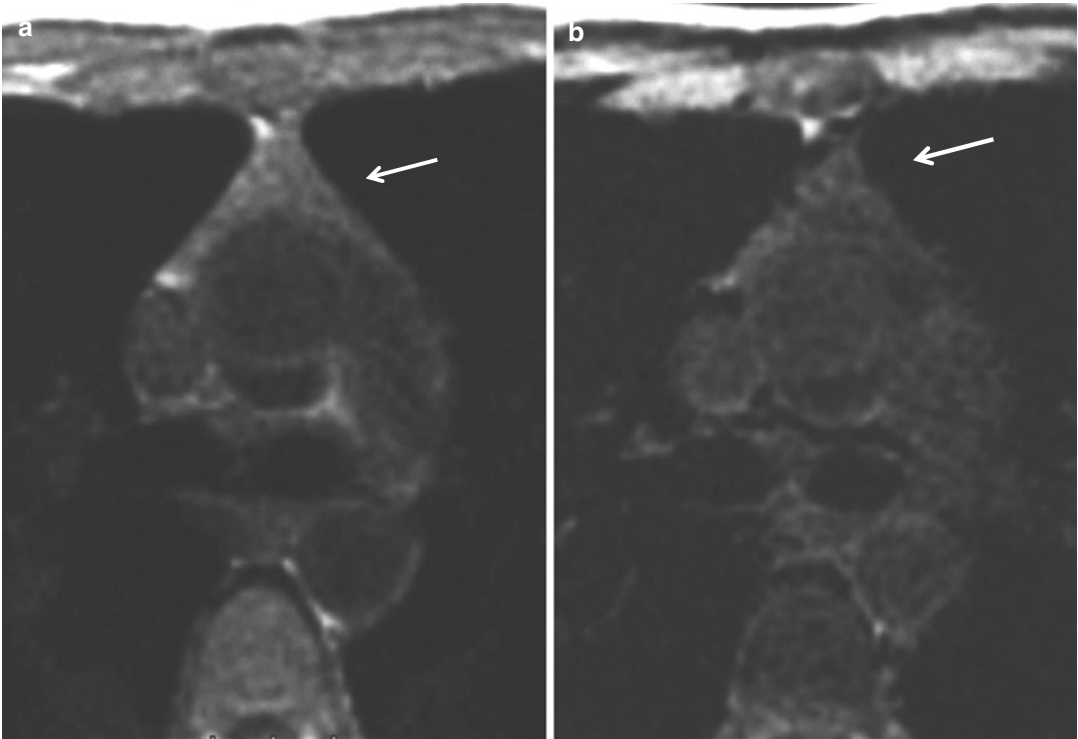
Fig. 8 Normal thymus in an 18-year-old girl. Chemical shift T1-weighted MR images. The thymus shows a homogeneous decrease in signal intensity at opposed-phase image (**b**) contrast to in-phase image (**a**) (*arrows*)

True thymic hyperplasia is defined as an increase in size of the thymus with normal gross and histologic appearance and commonly occurs as a rebound phenomenon secondary to atrophy caused by chemotherapy for malignancy, corticosteroid therapy, and radiotherapy (Linegar et al. 1993). In patients younger than 35 years and especially in children, the thymus may exhibit rebound to a size significantly larger than its original size (Chokye et al. 1987). When rebound thymic hyperplasia occurs in patients who previously underwent chemotherapy for malignancy, distinction of thymic rebound from recurrent neoplasm may be difficult. Clinically, thymic rebound is most problematic when it is seen in patients with malignant lymphoma who have undergone chemotherapy.

On CT and MR imaging, rebound thymic hyperplasia appears as an enlargement of the thymus, and its attenuation at CT and signal at MR imaging are similar to those of normal thymus (Siegel et al. 1989). In patients with enlarged thymus older than 15 years of age, chemical shift MR imaging can diagnose thymic hyperplasia by detecting fatty infiltration within the thymus and is

useful in its differentiation from neoplastic process (Takahashi et al. 2003; Inaoka et al. 2007). In a series of 41 patients consisting of 23 thymic hyperplasias and 18 thymic neoplasms, chemical shift MR imaging could differentiate thymic hyperplasia from thymic neoplasms in all patients. All patients with hyperplastic thymus showed an apparent decrease in the signal intensity of the thymus at opposed-phase images in contrast to in-phase images, while none of the patients with thymic tumors showed a decrease in signal intensity at opposed-phase images (chemical shift ratio (CSR) in Inaoka et al. 2007) (Figs. 9 and 10) Priola AM et al. also reported a high accuracy of chemical shift ratio of MR in the differentiation of thymic hyperplasia from thymic tumors, but it might overlap in both groups in early adulthood (Priola et al. 2015). Since the diagnosis of thymic hyperplasia by chemical shift MR imaging is based on the depiction of fatty degeneration within the thymus, we think its utility might be age dependent (Fig. 11). Actually, the CSR of pediatric patients with a thymic hyperplasia (particularly younger than 15 years) might overlap with CSR of tumors.
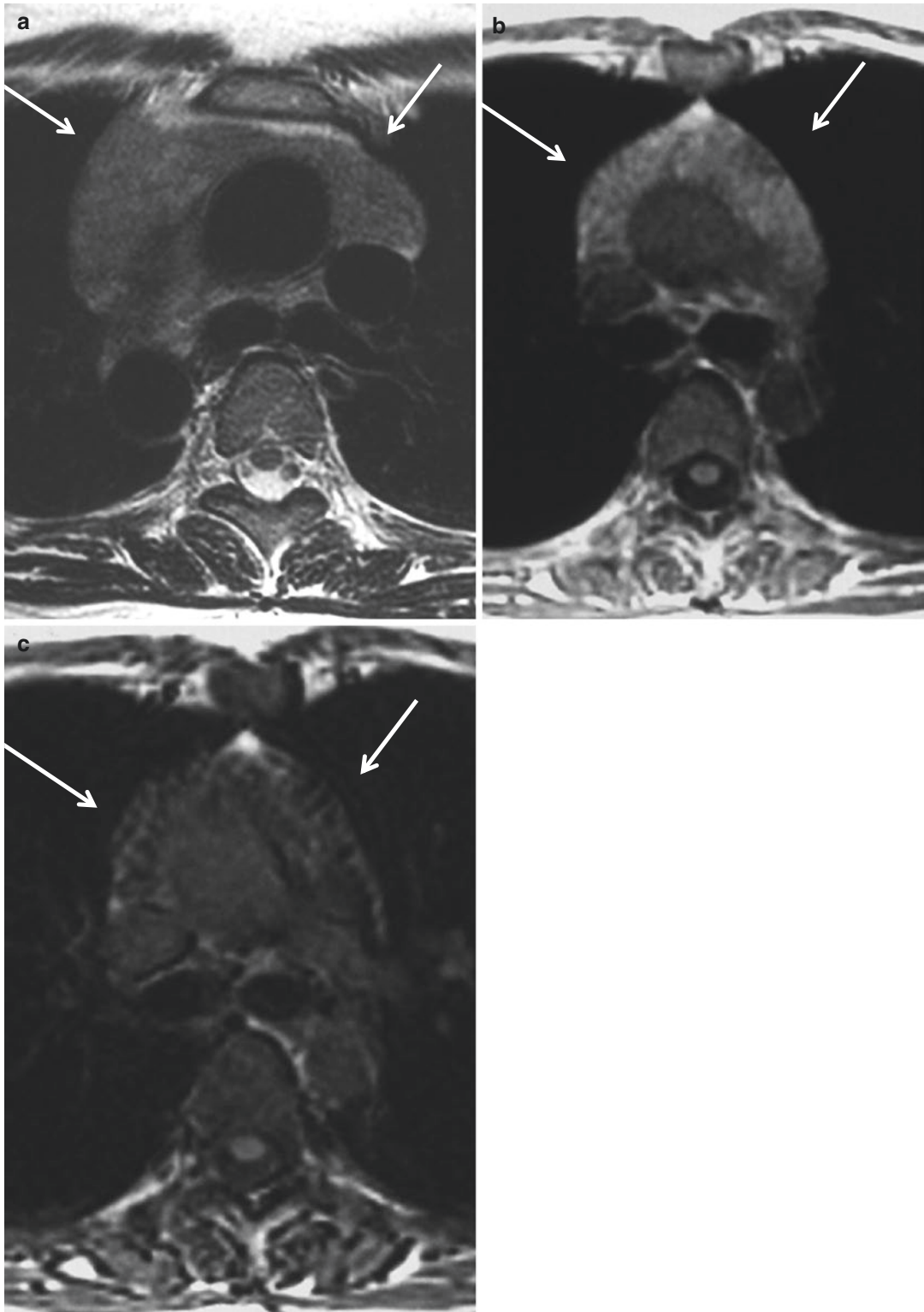
Fig. 9 Thymic hyperplasia in hyperthyroidism in a 25-year-old woman. T2-weighted (**a**) and in-phase (**b**) and opposed-phase (**c**) gradient-echo T1-weighted MR images. The thymus is diffusely enlarged but shows a decrease in signal at opposed-phase image (**c**) in contrast to in-phase image (**b**) due to physiologic fatty infiltration within the thymus (*arrows*)
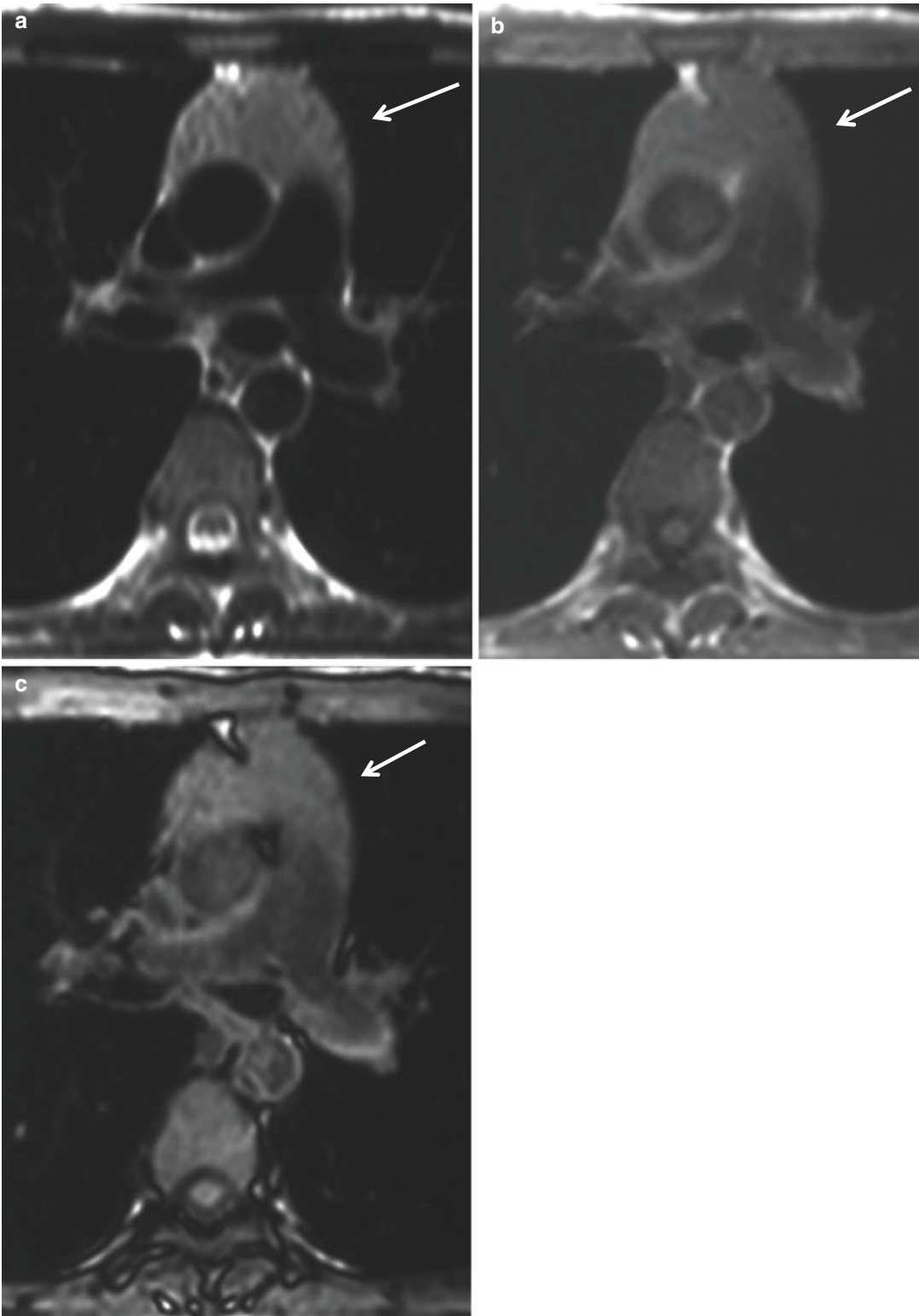
Fig. 10 Noninvasive thymoma. T2-weighted (**a**) and in-phase (**b**) and opposed-phase (**c**) gradient-echo T1-weighted MR images. A lobulated mass lesion is depicted in the anterior mediastinum. The contrast to the in-phase image (**b**) does not show a significant signal decrease in the opposed-phase image (**c**) (*arrows*)
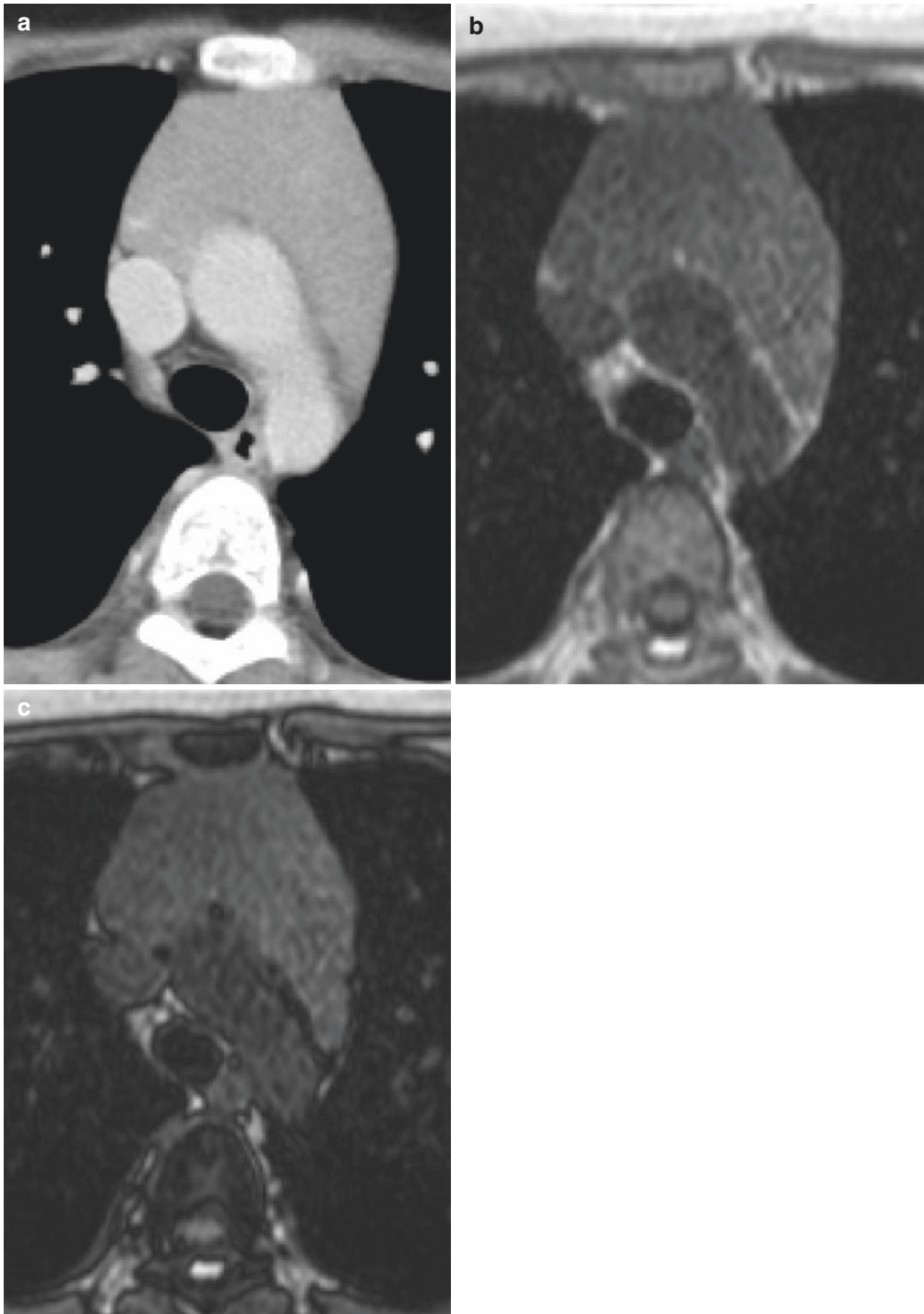
Fig. 11 Rebound thymic hyperplasia in a 12-year-old patient with nodular sclerosis classical Hodgkin's lymphoma after chemotherapy. Contrast-enhanced CT image (**a**) obtained 4 months after chemotherapy. Following shrinkage after chemotherapy, the thymus showed prominent enlargement. The findings are suggestive of rebound thymic hyperplasia, but recurrence of lymphoma should be excluded. (**b**, **c**) Chemical shift MR images of (**b**) in-phase (124/4.6) and (**c**) opposed-phase (124/2.3) images taken 4 months after systemic chemotherapy demonstrate no apparent change in the signal intensity of the thymus. The CSR is 0.93

3.3   Thymoma

Thymoma is the most common primary tumor in the entire mediastinum, and it comprises approximately 20 % of all mediastinal tumors (Hoffman et al. 1993). Thymoma is a benign or low-grade malignant tumor of the thymic epithelium, frequently associated with a variable population of immature but nonneoplastic T-cell lymphocytes. It is divided into an encapsulated noninvasive type and an invasive type that has spread beyond the capsule. 15–40 % of thymomas show invasion beyond the capsule and turn out to be of the invasive type. Invasive thymoma initially invades the adjacent mediastinal fat and eventually spreads to the pleura, pericardium, lung, or mediastinal vessels.

Thymomas most commonly arise in the upper part of the anterior mediastinum: anterior to the ascending aorta, the right ventricular outflow tract, and the main pulmonary artery. Uncommon locations of thymoma include inferior mediastinum as low as the cardiophrenic angle, middle or posterior mediastinum, the lower and upper neck as high as the submandibular region, or the lung parenchyma (Nagasawa et al. 2004; Yamazaki et al. 2006; Huang et al. 2007).

Thymomas usually occur in middle-aged adults, and the average age at diagnosis is approximately 50 years (Lewis et al. 1987). Thymomas are unusual below the age of 20 and extremely rare under the age of 15 years. Patients with an encapsulated thymoma are usually asymptomatic but may have symptoms such as chest pain, cough, dyspnea, dysphagia, or hoarseness due to compression to the adjacent structures. Most patients with invasive thymoma have clinical symptoms due to its invasion. Thymomas are occasionally associated with a paraneoplastic syndrome, and myasthenia gravis is the most common disease. Approximately 10–23 % of patients with myasthenia gravis have a thymoma, and 35–40 % of patients with a thymoma have myasthenia. Other paraneoplastic syndromes associated with a thymoma include pure red cell aplasia, acquired hypogammaglobulinemia, and nonthymic cancers.

Most thymomas show a lobulated external contour and are either completely or partially encapsulated by a fibrous capsule. The capsule connects with fibrous band within the tumor that divides it into multiple lobules (Fig. 12). Cystic change, hemorrhage, and necrosis are relatively common, and sometimes the tumor may be cystic.

The World Health Organization (WHO) proposed a consensus classification of thymic epithelial tumors, which is based on the morphology of epithelial cells and the lymphocyte-to-epithelial cell ratio in 1999 (Rosai and Sobin 1999). In 2004, the WHO updated the classification (Travis et al. 2004). In the latest classification (Table 1), the thymic epithelial tumors are classified into two major categories and five types of thymomas (types A, AB, B1, B2, and B3) and thymic carcinomas (various histologic types of carcinomas including neuroendocrine carcinoma). Thymomas were divided into two groups depending on whether the neoplastic epithelial cells and their nuclei have a spindle and/or oval shape (type A) or whether these cells have a dendritic or plump (epithelioid) appearance (type B). Tumors that combine these two morphologies are designated type AB. Type B tumors were subdivided further into three subtypes designated B1, B2, and B3, respectively, on the basis of the proportional increase of the epithelial component and the emergence of atypia of the neoplastic cells.

It has been suggested that the WHO classification reflects both the clinical and the functional features of thymic epithelial tumors and significantly correlates with the invasiveness and the prognosis of thymic epithelial tumors (Chen et al. 2002; Okumura et al. 2002; Kondo et al. 2004). A review of 273 patients with thymoma on the prognostic significance of the WHO classification system reported that in patients with type A, AB, B1, B2, and B3 tumors, the respective proportions of invasive tumor were 11.1, 41.6, 47.3, 69.1, and 84.6 %; the respective proportions of tumors with involvement of the great vessels were 0, 3.9, 7.3, 17.5, and 19.2 %; and the respective 20-year survival rates were 100, 87, 91, 59, and 36 % (Okumura et al. 2002). In a review of 200 patients with thymic epithelial tumors, 5-year survival rates of each subtype were 100 % in type A thymoma, 100 % in type
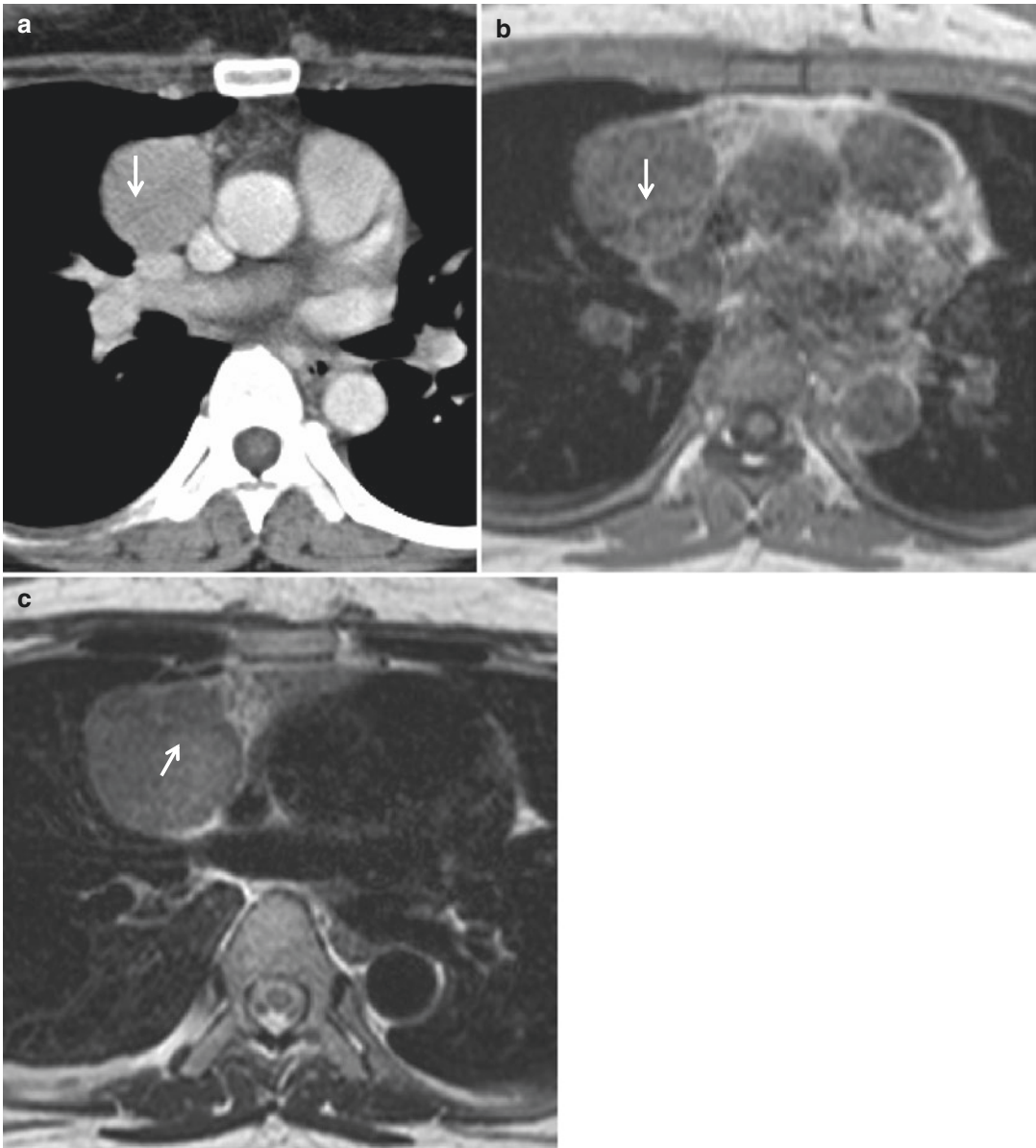
Fig. 12 Noninvasive thymoma. (**a**) Contrast-enhanced CT, (**b**) T1-weighted, and (**c**) T2-weighted MR images show a well-defined mass in the anterior mediastinum with a fibrous capsule and septae (*arrows*), characteristic of thymoma

AB, 94.1 % in type B1, 75.0 % in type B2, and 70.0 % in type B3 and 48.0 % in thymic carcinoma (Chen et al. 2002). Due to the significant correlation of the WHO histological classification and prognosis, the thymic epithelial tumors can be divided into three main groups: low-risk thymomas (types A, AB, B1), high-risk thymomas (types B2 and B3), and thymic carcinomas

(Jeong et al. 2004). But, on the basis of a clinico-pathological correlation of 250 cases, Moran CA et al. have recently stated that subtyping of thymomas should not be done on biopsy material, since according to subtyping more than 50 % of tumors fell into the mixed categories. He also said that all thymomas had the potential to become invasive tumors (Moran et al. 2012).

Table 1 The definitions of the World Health Organization classification of thymic epithelial tumors

Type A thymoma: an organotypical thymic epithelial neoplasm composed of bland spindle/oval epithelial tumor cells with few or no lymphocytes
Type AB thymoma: an organotypical thymic epithelial neoplasm composed of a mixture of a lymphocyte-poor type A thymoma component and a more lymphocyte-rich type B-like component. Both components are present in most sections
Type B1 thymoma: a tumor of thymic epithelial cells with a histological appearance practically indistinguishable from the normal thymus composed predominantly of areas resembling cortex with epithelial cells scattered in a prominent population of immature lymphocytes, and areas of medullary differentiation, with or without Hassall's corpuscles, similar to normal thymic medulla
Type B2 thymoma: an organotypical thymic epithelial neoplasm composed of large, polygonal tumor cells that are arranged in a loose network and exhibit large vascular nuclei with prominent large nucleoli, closely resembling the predominant epithelial cells of the normal thymic cortex. A background population of immature T cells is always present and usually outnumbers the neoplastic epithelial cells
Type B3 thymoma: an organotypical thymic epithelial neoplasm predominantly composed of medium-sized round or polygonal cells with slight atypia. The epithelial cells are mixed with a minor component of intraepithelial lymphocytes, resulting in a sheet-like growth of epithelial cell
Thymic carcinoma: all non-organotypical malignant epithelial neoplasms other than germ cell tumors are designated thymic carcinomas. Thymic carcinomas are termed according to their differentiation (squamous cell, mucoepidermoid, etc.). The term type C thymoma in the previous classification was eliminated. Thymic carcinomas lack immature T lymphocytes

Travis et al. (2004)

Table 2 Masaoka's clinical stage

Stage I: Macroscopically completely encapsulated and microscopically no capsular invasion
Stage II: 1. Macroscopic invasion into surrounding fatty tissue or mediastinal pleura 　　　　2. Microscopic invasion into capsule
Stage III: Macroscopic invasion into neighboring organs, i.e., the pericardium, great vessels, or lung
Stage IVa: Pleural or pericardial dissemination
Stage IVb: Lymphogenous or hematogenous metastasis

Masaoka et al. (1981)

For the clinical staging of thymic epithelial tumors, Masaoka's criteria (Masaoka et al. 1981) (Table 2), which were based on the presence of invasion of the surrounding organs, have been widely accepted, and modifications were suggested by Shimosato and Mukai (1997a, b, c). The staging significantly correlates with the prognosis, and the 20-year survival rates were 89, 91, 49, 0, and 0 % in patients with stage I, II, III, IVa, and IVb disease, respectively (Okumura et al. 2002). On multivariate analysis, WHO histologic classification and Masaoka clinical staging were independent prognostic factors (Chen et al. 2002; Okumura et al. 2002; Kondo et al. 2004).

On CT, thymomas usually present as sharply demarcated round or oval soft tissue masses in the region of the thymus. Tumors commonly reveal soft tissue attenuation and mild to moderate contrast enhancement. Occasionally, focal low attenuation areas are identified within tumors, reflecting hemorrhage, necrosis, or cyst formation. Rarely, a tumor appears entirely cystic. Linear or ringlike calcifications are occasionally seen in both encapsulated and invasive thymoma.

On MR images, thymomas typically appear as round, oval, or lobulated masses with a low signal intensity on T1-weighted images similar to that of muscle and relatively high signal intensity on T2-weighted images. T2-weighted images occasionally show scattered high-intensity regions and/or lobulated internal architecture within the tumors, which corresponded to cystic regions and fibrous septa, respectively, on pathologic specimen (Fig. 12). On T1-weighted images, the signal intensity of cystic regions was

variable, depending on the protein content of the cyst fluid or the presence of hemorrhage (Sakai et al. 1991).

Invasive thymomas invade the mediastinum beyond the capsule and occasionally spread to the pleura and pericardium. Although CT and MR imaging cannot detect minimal mediastinal invasion, it sometimes allows for distinction between invasive and noninvasive thymoma. Complete obliteration of the adjacent fat planes highly suggests mediastinal invasion, while partial obliteration is indeterminate (Figs. 13 and 14). Complete preservation of the adjacent fat planes usually excludes extensive invasive disease but not minimal capsular invasion (Chen et al. 1988). Transpleural spread either as a sheet of tumor or drop metastasis is a diagnostic finding of invasive thymoma (Figs. 13 and 14). Previous studies suggested MRI to be superior to CT in patients with invasive thymoma for defining invasion of contiguous structures, such as the pleura, lung, and pericardium (Fujimoto et al. 1992; Gualdi et al. 1994; Pirronti et al. 2002). MR imaging may be more efficient than CT in detecting tumor recurrence during postoperative follow-up in patients with invasive thymoma (Pirronti et al. 2002). In the recent review of CT findings of 99 thymomas by Marom et al., they stated radiologic tumor size >7 cm, a lobulated tumor contour, and infiltration of surrounding fat are more likely to have stage III or IV disease (Marom et al. 2011).

For the assessment of anterior mediastinal tumors, dynamic MR imaging has been suggested as useful in the differentiation between thymomas and non-thymomas including thymic carcinoma, malignant lymphoma, and malignant germ cell tumor. At dynamic MR imaging, thymoma tended to reach a peak in the time intensity curve relatively early and other mediastinal tumors relatively late. A cutoff point in the time intensity curve of 2–2.5 min could be used to differentiate thymomas and non-thymomas (Sakai et al. 2002).

Myasthenia gravis (MG) is commonly associated with thymic pathologies, including lymphoid follicular hyperplasia in 65–77 % and thymoma in 15–30 % (Pirronti et al. 2002). It is generally agreed that thymectomy is indicated in patients affected by generalized MG between adolescence and 50–60 years. Thymectomy is most likely to be effective in young female patients with MG of short duration, but its effectiveness is still under discussion in seronegative MG, ocular MG, and elderly patients with MG. Furthermore, thymectomy is indicated in all patients with thymoma. Therefore, the role of the radiologic assessment in MG patients is detection of thymomas and their differentiation from thymic hyperplasia.

In a study of 104 patients with MG who underwent thymectomy, CT showed thymoma in 46 of 52 patients (sensitivity 88.5 % and specificity 95 %) and thymic hyperplasia in 16 of 44 (sensitivity 36 % and specificity 95 %) (Pirronti et al. 2002). In a study of 16 patients with MG, MR imaging provided little additional information as compared with CT. A recent report suggested chemical shift MR imaging to be beneficial in the differentiation of thymomas from thymic hyperplasia in non-MG patients (Inaoka et al. 2007). Although no report has been published, MR imaging may provide similar information also in MG patients.

3.4 Thymic Carcinoma

Thymic carcinoma is a thymic epithelial tumor with a high degree of histologic anaplasia, obvious cell atypia, and increased proliferative activity and is unassociated with immature T cells (Shimosato and Mukai 1997a, b, c). The most common histologic variety is epidermoid or squamous cell carcinoma, followed by lymphoepithelioma-like carcinoma and anaplastic or undifferentiated carcinomas.

Thymic carcinomas predominantly occur in adults and are associated with poor prognosis even when treated with surgery and radiotherapy. At the time of diagnosis, most patients suffer from chest pain, dyspnea, cough, fever, weight loss, and superior vena cava syndrome (Hartmann et al. 1990). A paraneoplastic syndrome is uncommon in thymic carcinomas. Thymic carcinomas occasionally infiltrate the adjacent tissue
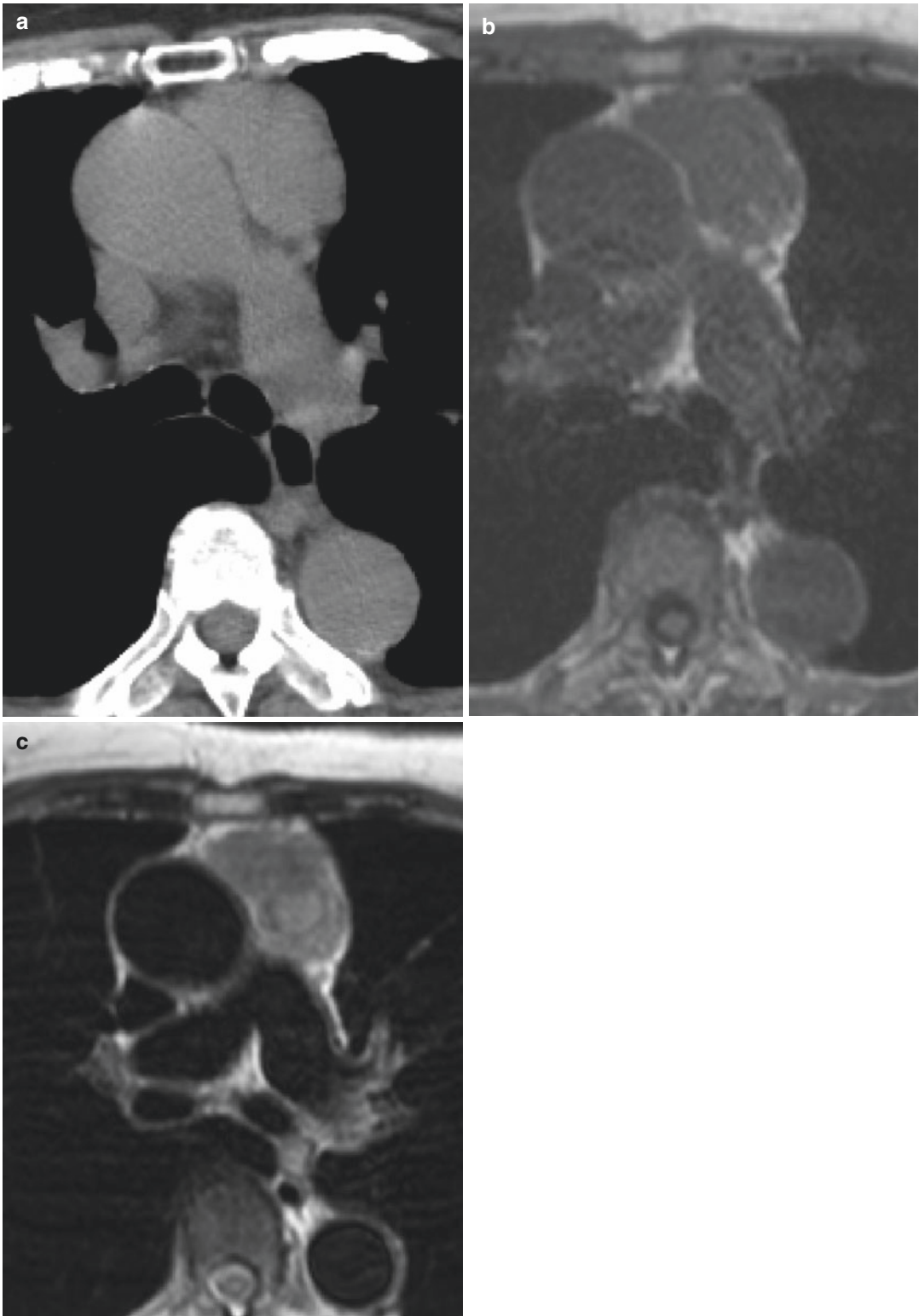
Fig. 13 Invasive thymoma. (**a**) Non-contrast-enhanced CT, (**b**) T1-weighted, and (**c**) T2-weighted MR images show an irregular mass with inhomogeneous intensity on T2-weighted image
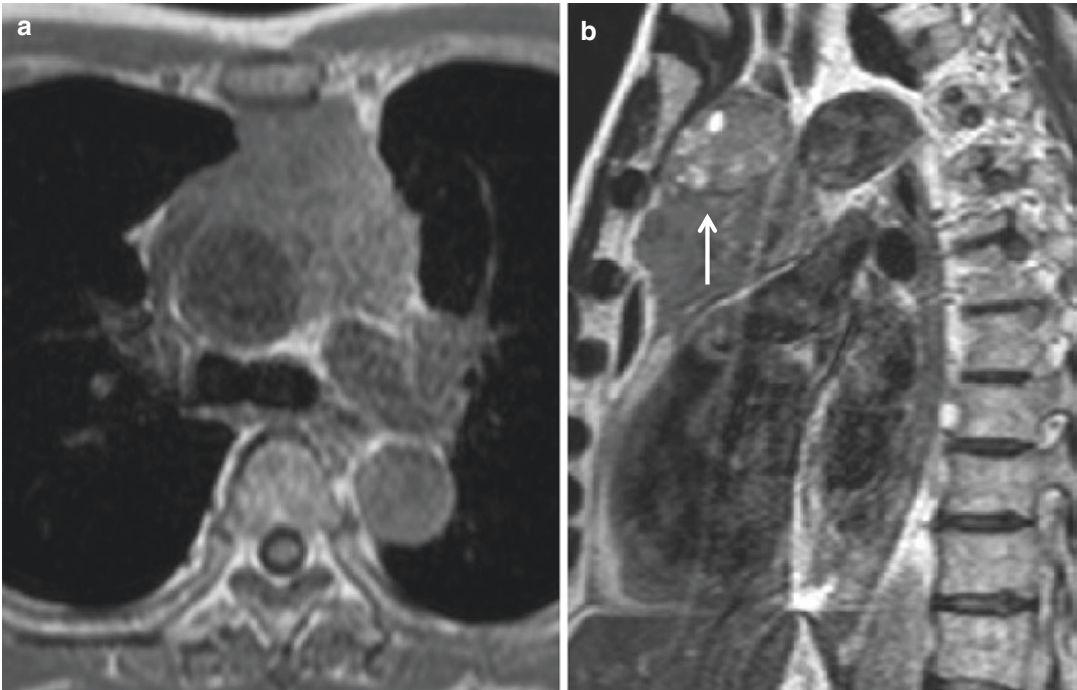
Fig. 14 Invasive thymoma. (**a**) T1-weighted axial and (**b**) T2-weighted coronal MR images show an irregular mass in the anterior mediastinum, surrounding the great vessel. The mass includes several foci of high intensity, representing degeneration (*arrows*)

and mediastinal vascular structures or extend into the pleura, the lungs, and the pericardium.

Although thymic carcinoma shows similar imaging findings to thymoma, they were more commonly associated with mediastinal lymph node and extrathoracic metastases but less commonly associated with pleural implants than invasive thymoma (Do et al. 1995). Jeong et al. correlated CT findings of thymic epithelial tumors with the WHO histopathologic subtypes. A lobulated contour was more often seen in high-risk thymomas (type B2 and B3) and thymic carcinomas than in low-risk thymomas (type A, AB, and B1). Mediastinal fat invasion was more often seen in thymic carcinomas than in low-risk thymomas (Jeong et al. 2004).

In the review of MR imaging of 64 patients with thymic epithelial tumors, foci of low signal intensity on T2-weighted images and mediastinal lymphadenopathy were highly suggestive of thymic carcinomas (Fig. 15). Most foci of low signal intensity within the tumor on T2-weighted

images were collagenous tissue on pathological examinations (Inoue et al. 2006).

Sadohara et al. assessed the correlation of MR findings with three main groups of the WHO histologic classification: low-risk thymomas (types A, AB, B1), high-risk thymomas (types B2 and B3), and thymic carcinomas. Thymic carcinomas were more likely to have irregular contours (75 %) than low-risk thymomas (3 %) and high-risk thymomas (22 %). Complete or almost complete capsule was seen in low-risk thymomas (27 %) and high-risk thymomas (17 %) but not in thymic carcinomas (0 %). A septum was more frequently seen in low-risk (57 %) and high-risk thymomas (44 %) than thymic carcinomas (8 %). A necrotic or cystic component was more frequently seen in thymic carcinomas (67 %) than low-risk thymomas (20 %) and high-risk thymomas (28 %). Thymic carcinomas had a higher prevalence of heterogeneous signal intensity (100 %) than low-risk thymomas (33 %) and high-risk thymomas (56 %) (Sadohara et al. 2006).
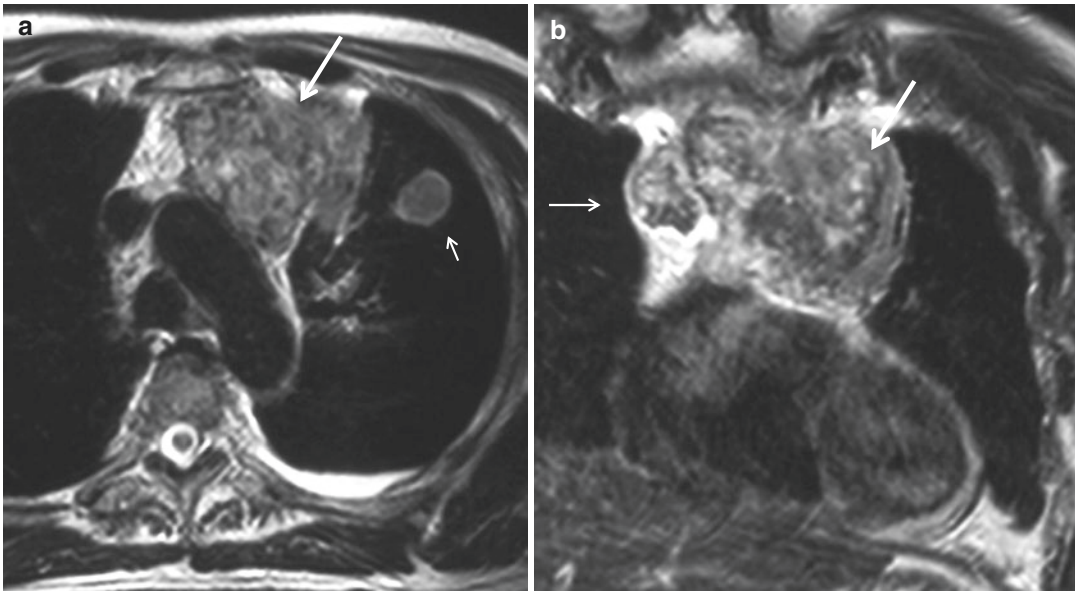
Fig. 15 Thymic carcinoma. T2-weighted axial (**a**) and coronal (**b**) MR images show an irregular mass in the anterior mediastinum. The tumor (*large arrows*) shows heterogeneous signal intensity with foci of low signal intensity on the T2-weighted image, representing collagenous tissue. Left side pleural effusion with drop metastasis (*small arrow* in **a**) and mediastinal lymphadenopathy (*small arrow* in **b**) are also demonstrated

3.5 Thymolipoma

Thymolipoma is a rare benign tumor composed of mature fat tissue and normal or involuted thymic tissue. The tumors commonly occur low in the anterior mediastinum and often in the cardiophrenic angle. The average age of the patients is 22–26 years, and most patients are asymptomatic (Rosado-de-Christenson et al. 1994).

On CT, thymolipomas appear as well-circumscribed masses that contain fat tissue intermingled with linear bands of soft tissue. The soft tissue histopathologically represents thymic tissue or fibrous septa. The amount of fat relative to the thymic tissue is variable.

On MR imaging, fat tissue within the tumors appears as an area of high signal intensity, and soft tissue component appears lower signal intensity bands that course through the mass (Rosado-de-Christenson et al. 1994; Shirkhoda et al. 1987).

3.6 Thymic Neuroendocrine Neoplasm

Primary neuroendocrine tumors of the thymus, previously known as carcinoid tumors of the thymus, are rare and account for less than 5 % of all anterior mediastinal tumors. Unlike carcinoids arising from the lungs, these tumors in the thymus are highly aggressive, and nearly 80 % of cases have been found to be malignant (Chaer et al. 2002). Based on histopathological findings, such as mitotic count, amount of necrosis, preservation of neuroendocrine architecture, and degree of cytologic atypia, Klemm and Moran have proposed classifications: well-differentiated, moderately-differentiated, and poorly-differentiated neuroendocrine neoplasms (Tiffet et al. 2003; Klemm and Moran 1999).

The mean age of the previously reported cases is 54 years. Nearly one third of patients are asymptomatic, and the remaining patients have symptoms resulting from the rapidly expanding mediastinal
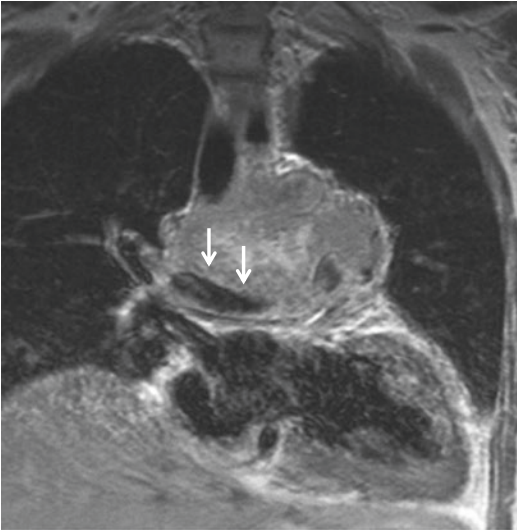
Fig. 16 Neuroendocrine tumor. Contrast-enhanced coronal MR image shows a lobulated mass displacing the pulmonary artery (*arrows*)

tumor. At least 20 % of patients have distant metastasis at presentation most commonly to the liver, lung, bone, pleura, and pancreas (Chaer et al. 2002). Approximately 40 % of patients have Cushing syndrome as a result of tumor secretion of adrenocorticotrophic hormone (Doppman et al. 1989), and up to 20 % have multiple endocrine neoplasia (MEN) syndromes I and II (Ferolla et al. 2005). In the literature, the overall survival rate at 5 years ranged from 31 to 82 % (Tiffet et al. 2003). As prognostic factors, unresectability and advanced clinical stage have been reported to be associated with poor survival (Gal et al. 2001).

Thymic neuroendocrine tumors do not differ significantly from thymoma in radiologic findings on CT and MR imaging. Neuroendocrine tumors are more aggressive than thymoma and often presenting in advanced stage, and superior vena cava obstruction is much more common with this tumor than with thymoma. On CT or MR imaging, the tumors appear as a lobulated thymic mass with heterogeneous enhancement and central areas of low attenuation secondary to necrosis or hemorrhage and may show local invasion (Chaer et al. 2002) (Fig. 16). Bone metastases are typically osteoblastic.

4 Mediastinal Germ Cell Tumors

Germ cell tumors are believed to develop from a germ cell during the process of maturation of a primordial germ cell into a gamete. The tumors mainly arise in the gonads but also in the midline of the body, including pineal region, anterior mediastinum, retroperitoneum, and sacrococcygeal region (Shimosato and Mukai 1997a, b, c). The mediastinum is the most common site of extragonadal germ cell tumors. The vast majority of mediastinal germ cell tumors arise within the anterior mediastinum within or in the proximity of the thymus, and only 3 % of them arise within the posterior mediastinum (Dehner 1983). Germ cell tumors include teratoma (mature, immature, and with malignant transformation), seminoma, embryonal carcinoma, endodermal sinus tumor, choriocarcinoma, and mixed germ cell tumor. Mature teratoma is the most common histologic type of mediastinal germ cell tumors and accounts for 75 % of them. Seminoma is the most common malignant subtype. In this text we divide mediastinal germ cell tumors into three subgroups: teratoma, seminoma, and non-seminomatous malignant germ cell tumor.

Germ cell tumors usually occur in young adults (mean age 27 years) (Erasmus et al. 2000). Malignant germ cell tumors are more common in men. To make a diagnosis of primary mediastinal germ cell tumors, the possibility of gonadal germ cell tumors should be clinically excluded. The important differential point is that gonadal germ cell tumors involving the mediastinum almost always have concomitant retroperitoneal lymph node metastases.

4.1 Teratoma

Teratomas contain elements of all three germ cell layers, ectoderm, endoderm, and mesoderm, and are frequently referred to "dermoid cyst" due to the frequent expression of the ectodermal component of the teratoma. Ectodermal

elements may be represented by the skin, teeth, and hair; mesodermal elements by the bone, cartilage, and muscle; and endodermal elements by bronchial, gastrointestinal, or pancreatic tissue. Histologically, teratoma can be divided into mature teratoma, immature teratoma, and teratoma with malignant transformation.

Mature teratomas are usually unilocular or multilocular cystic lesions and consist predominantly of ectoderm elements including skin and its appendages followed in order of frequency by bronchial tissue, gastrointestinal mucosa, smooth muscle, fat, bone, cartilage, and pancreatic tissue (Shimosato and Mukai 1997a, b, c). The presence of pancreatic tissue is unique in teratomas in the mediastinum, while it is not seen in those of the gonads. Although mature teratoma is usually silent, symptoms are due to local compression, rupture, or infection and include chest pain, cough, dyspnea, and fever.

A mature teratoma is a well-demarcated, occasionally lobulated anterior mediastinal mass on radiographs. On CT, mature teratomas most commonly appear as well-defined cystic lesions containing fluid, soft tissue, and fat attenuation. Calcifications of various morphological configurations also may be present within the lesion, and a tooth or a part of bone is rarely seen. Common combinations of internal components of mature teratomas include soft tissue, fluid, fat, and calcium in 39 %; soft tissue, fluid, and fat in 24 %; and soft tissue and fluid in 15 % (Moeller et al. 1997). In 15 % of cases, mature teratomas appear as nonspecific cystic lesions without fat or calcium. A capsule of teratoma is characteristically thickened, whereas that of other cystic lesions at the mediastinum is usually thin (Takahashi et al. 1998).

MR imaging typically demonstrates heterogeneous signal intensity, representing various internal elements, and this finding can be useful in differentiating teratomas from thymomas and lymphomas (Erasmus et al. 2000; Drevelegas et al. 2001). The soft tissue elements reveal isointensity with muscle, cystic components show low intensity on T1-weighted images and high intensity on T2-weighted images, and fat elements appear as a high-intensity area on T1-weighted images. The amount of fat tissue varies depending on the tumor (Figs. 17 and 18). The finding of fat-fluid level within the lesion on MR imaging is diagnostic of a teratoma.

Mediastinal mature teratomas may be associated with complications such as atelectasis or obstructive pneumonitis due to airway compression, pneumonitis due to rupture into the lung, and effusion due to rupture into the pleural space or pericardium. In nearly 30 % of mature teratomas, ruptures into the adjacent structures, the lung, pleural space, and pericardium and fat, have been reported as a complication (Sasaka et al. 1998). Proteolytic or digestive enzymes derived from the tumor have been considered to be the cause of tumoral rupture (Drevelegas et al. 2001).

Immature teratomas show various adult tissues derived from three germinal layers but in addition contain immature tissue most commonly primitive neuroepithelial tissue. Teratomas with malignant transformation contain foci of frankly malignant neoplasms such as angiosarcoma, rhabdomyosarcoma, adenocarcinoma, and squamous cell carcinoma. Most patients with immature teratoma and other malignant germ cell tumors are symptomatic, presenting with fatigue, weight loss, chest pain, cough, or dyspnea. Compared with benign teratomas, malignant teratomas are more likely to appear solid and poorly defined and compress adjacent structures and less often contain fat (Hoffman et al. 1993; Strollo et al. 2002).

Mediastinal growing teratoma syndrome is an unusual phenomenon associated with the treatment of malignant teratoma or seminoma. When the lesions consist of teratoma and other germ cell tumors and are mixed with malignant and benign components, benign part of the tumors can enlarge after chemotherapy despite sterilization of malignant components with normalization of tumor markers (Afifi et al. 1997; Iyoda et al. 2000).

4.2 Seminoma

Seminoma (mediastinal germinoma) occurs almost exclusively in males during the second to fourth decade. Macroscopically, the tumor is
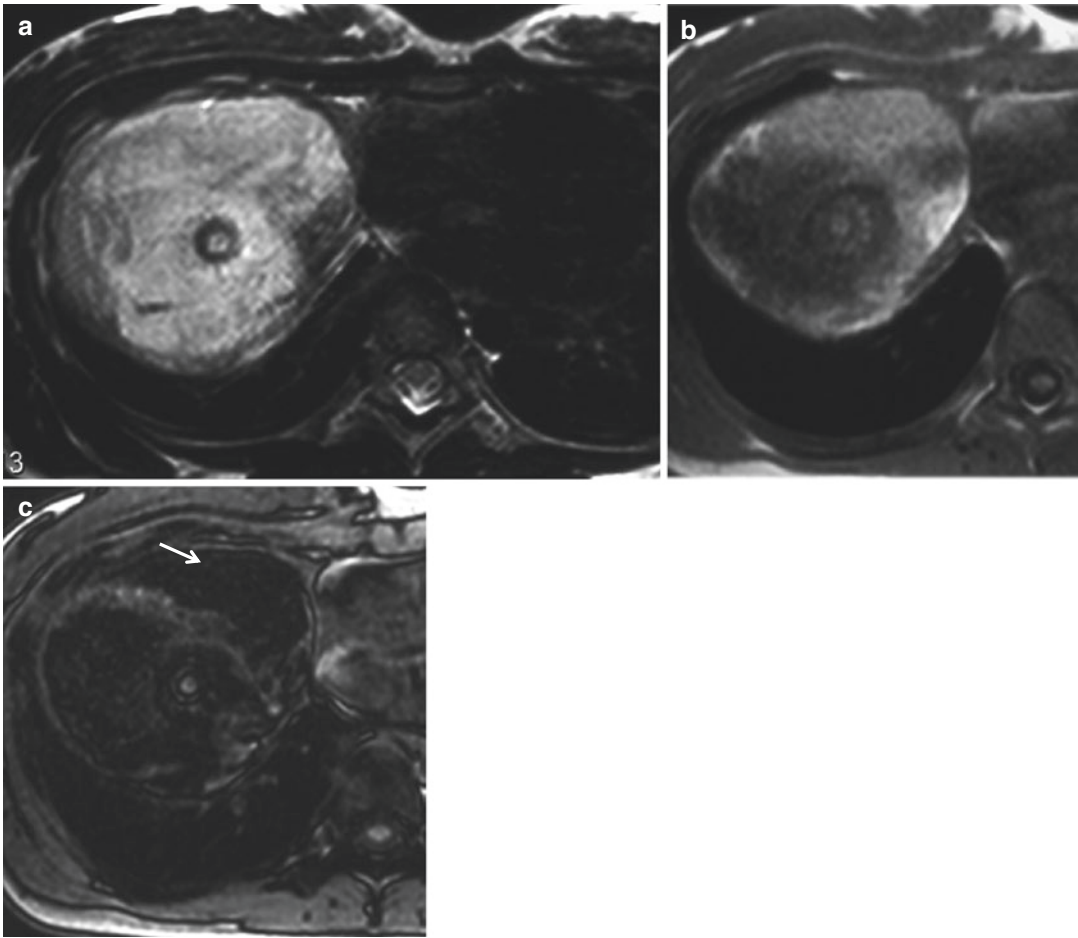
Fig. 17 Mature teratoma. A mass with a thick wall, which can be characteristic for mature teratoma, is demonstrated in the right paracardiac region. The mass entirely shows high signal intensity on T2-weighted image (**a**). Chemical shift MR images of (**b**) in-phase and (**c**) opposed-phase images: the area of mixture of water and fat within the tumor reveals a decrease in signal in the opposed phase (*arrow*)

well demarcated, large, and soft. The cut surface of the tumor is usually homogeneous but may show small foci of hemorrhage and necrosis (Shimosato and Mukai 1997a, b, c). Symptoms are usually related to the presence of invasion into the adjacent mediastinal structures (airways and vessels) and include chest pain, shortness of breath, and superior vena cava syndrome.

The tumor appears as a large anterior mediastinal mass, which protrudes in one or both sides of the mediastinum. On CT and MR imaging, the tumor most typically appears as a well-demarcated anterior mediastinal mass with homogeneous internal attenuation and signal intensity which shows only slight enhancement after administration of contrast material (Fig. 19). Areas of degeneration due to hemorrhage and coagulation necrosis may be present but is usually limited (Drevelegas et al. 2001; Lee et al. 1989). Seminoma most commonly metastasizes to the bone, lung, liver, and thoracic lymph nodes. Calcification and invasion of adjacent structures are uncommon (Drevelegas et al. 2001). Extension into the middle and posterior mediastinum and obliteration of the adjacent fat planes can be better evaluated by MRI (Drevelegas et al. 2001).
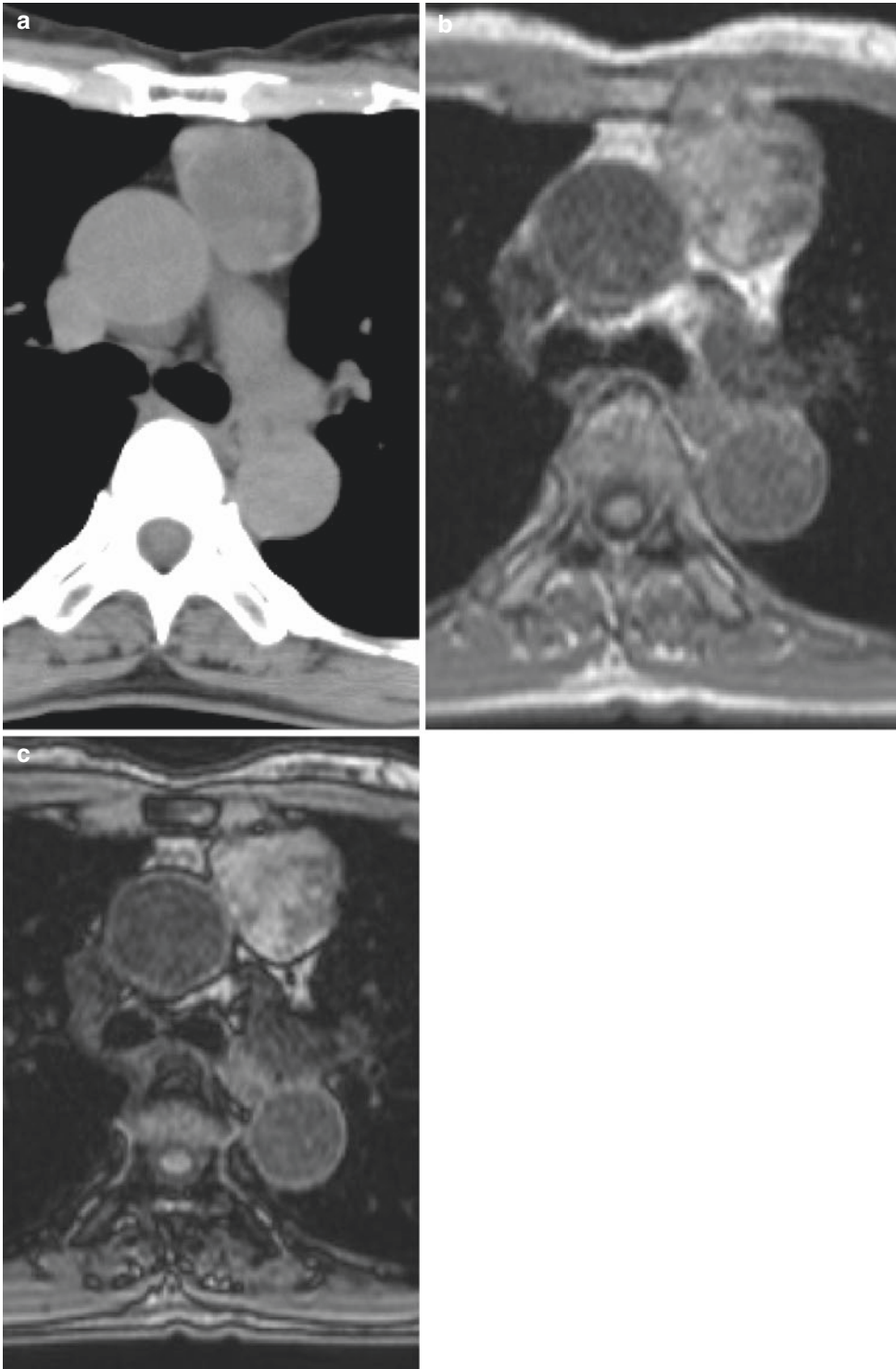
Fig. 18 Mature teratoma. (**a**) Non-contrast-enhanced CT, chemical shift MR images of (**b**) in-phase and (**c**) opposed-phase images. On CT, no fat component is seen within the tumor. No significant decrease in signal is iden-tified in the opposed-phase compared with the in-phase image, representing no apparent fat within the tumor. In nearly 10 % of mediastinal mature teratomas, imaging cannot identify the fat component
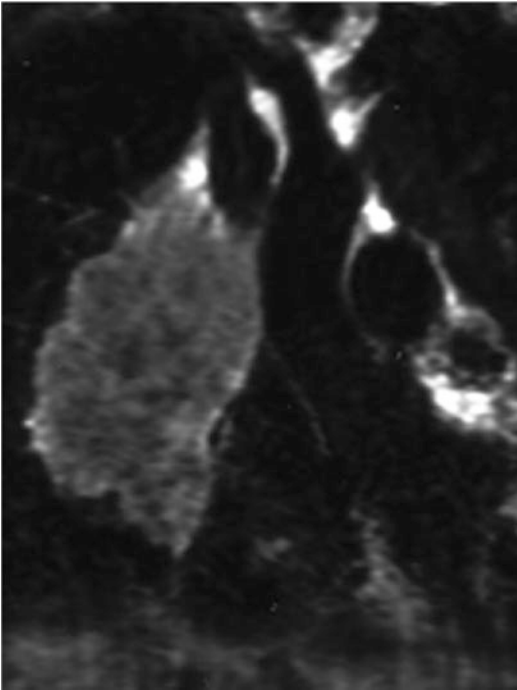
Fig. 19 Seminoma. T2-weighted coronal MR image shows a lobulated mass lesion in the anterior mediastinum with homogeneous intermediate signal intensity

4.3 Non-seminomatous Malignant Germ Cell Tumor

Non-seminomatous malignant germ cell tumors, including embryonal carcinoma, endodermal sinus (yolk sac) tumor, choriocarcinoma, and mixed types, are rare, highly malignant tumors which usually occur in young adults and are much more common in men than women. Tumors are usually associated with symptoms including chest pain, cough, fever, and dyspnea and occasional elevation of tumor markers: alpha-fetoprotein (AFP) from endodermal sinus tumor and embryonal carcinoma components and human chorionic gonadotropin (HCG) from choriocarcinoma component.

Tumors usually appear as a large anterior mediastinal mass on radiographs. On CT, the tumors consist of irregular soft tissue and multiple areas of low attenuation due to cystic necrosis and hemorrhage (Drevelegas et al. 2001; Lee et al. 1989). Obliteration of the adjacent fat

planes and invasion of the adjacent structures may occasionally be seen. Metastases to the regional lymph nodes and distant sites are also common (Shimosato and Mukai 1997a, b, c). On MR imaging, the tumors typically show internal heterogeneous intensities with areas of high signal intensity interspersed with areas of low signal intensity (Shimosato and Mukai 1997a, b, c) (Fig. 20). Patients with Klinefelter's syndrome are predisposed to develop germ cell tumors of extragonadal origin.

5 Mediastinal Malignant Lymphoma

Malignant lymphoma accounts for nearly 20 % of all mediastinum neoplasms in adults and 50 % in children. Most often lymphoma involves the mediastinum secondary to generalized disease, while a mediastinal disease can also be a primary lesion. Hodgkin's lymphoma is the most common primary mediastinal lymphoma. In non-Hodgkin's lymphoma, the two most common forms of primary mediastinal lymphoma are lymphoblastic lymphoma and diffuse large B-cell lymphoma, while virtually any histologic type of lymphoma may be identified. In addition to intrathoracic nodal disease, thymic involvement is also common in these primary mediastinal lymphomas. Clinically, most malignant lymphomas of the mediastinum affect individuals younger than those with thymoma. Hodgkin's lymphoma is staged using the Ann Arbor classification, which assesses the extent of nodal disease, the presence of extranodal disease, and clinical symptoms (Carbone et al. 1971). In non-Hodgkin's lymphoma, the clinical course depends more on histologic grade and parameters, including bulk and specific organ involvement than on the stage of disease.

5.1 Hodgkin's Lymphoma

Hodgkin's lymphoma is the most common lymphoma presenting with mediastinal adenopathy. Commonly involved lymph nodes are the
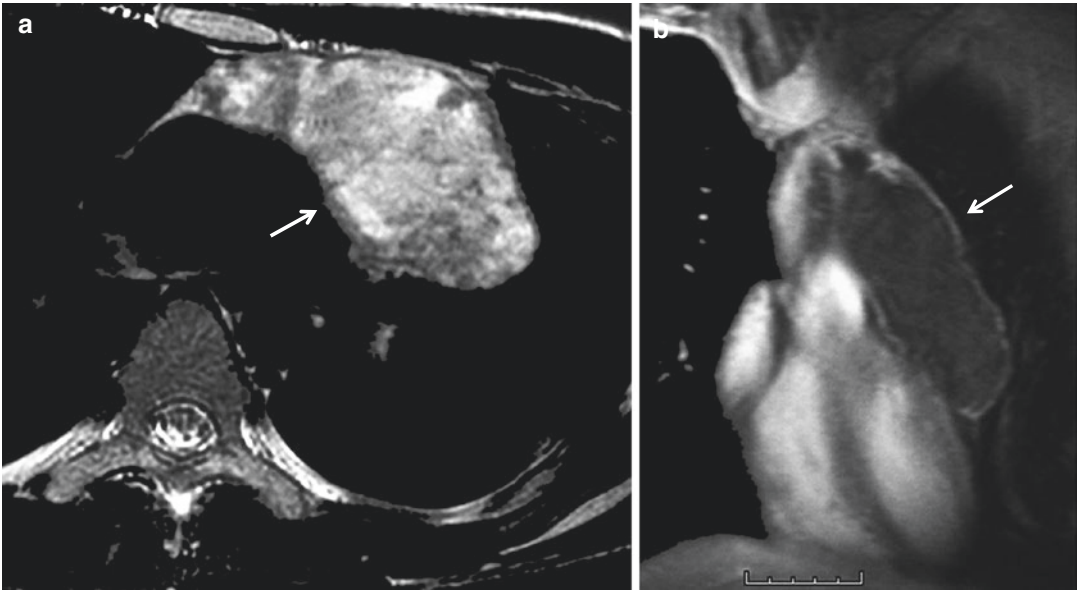
Fig. 20 Non-seminomatous malignant germ cell tumor. (**a**) T2-weighted axial image typically shows heterogeneous signal intensity with areas of low, intermediate, and high signal intensity (*arrow*). (**b**) Contrast-enhanced coronal image shows little enhancement (*arrow*) within the lesion probably due to prominent degeneration by hemorrhage and cystic necrosis

prevascular and paratracheal lymph nodes, followed by hilar, subcarinal, paracardiac, internal mammary, and posterior mediastinum nodes. In association with mediastinal lymphadenopathy, Hodgkin's lymphoma also has a predilection for thymic involvement. Most patients are young female adults.

Regarding the histologic subtypes, nodular sclerosis is by far the most common subtype and is characterized by orderly bands of interconnecting collagenous connective tissue that partially or entirely subdivides abnormal lymphoid tissue into isolated cellular nodules. The cellular proliferation within the nodules is polymorphic, with small and large lymphocytes, plasma cells, eosinophils, and histiocytes. The distinctive feature is the presence of Reed-Sternberg cells (Shimosato and Mukai 1997a, b, c).

On CT, involved nodes are commonly well defined and of homogeneous soft tissue attenuation, while cystic and necrotic changes are identified within the nodes in 10–21 % of cases (Pombo et al. 1994). Thymic involvement is another common manifestation of Hodgkin

disease, and thymic enlargement is seen in 40 % of adult patients. Typically, thymic lesions manifest as an anterior mediastinal mass of homogeneous soft tissue attenuation, which shows gradually increasing mild to moderate contrast enhancement on CT. Direct extension of the mediastinal lesion to the adjacent lung or chest wall is not uncommon in extensive mediastinal disease. Spread of lymph node disease is commonly contiguous to the adjacent lymph node groups, while skipping to adjacent lymph node groups is unusual.

On T2-weighted MR images, involved nodes usually demonstrate homogeneous high signal intensity greater than that of muscle and similar to that of fat (Rahmouni et al. 2001). The lesions of Hodgkin's lymphoma may reveal heterogeneous patterns with mixed areas of high and low signal intensity on T2-weighted images, which is typical of the nodular sclerosing subtype with its histological feature comprising fibrotic areas interspersed with more cellular areas. A thymic cyst may also be present in association with Hodgkin's lymphoma (Fig. 21).
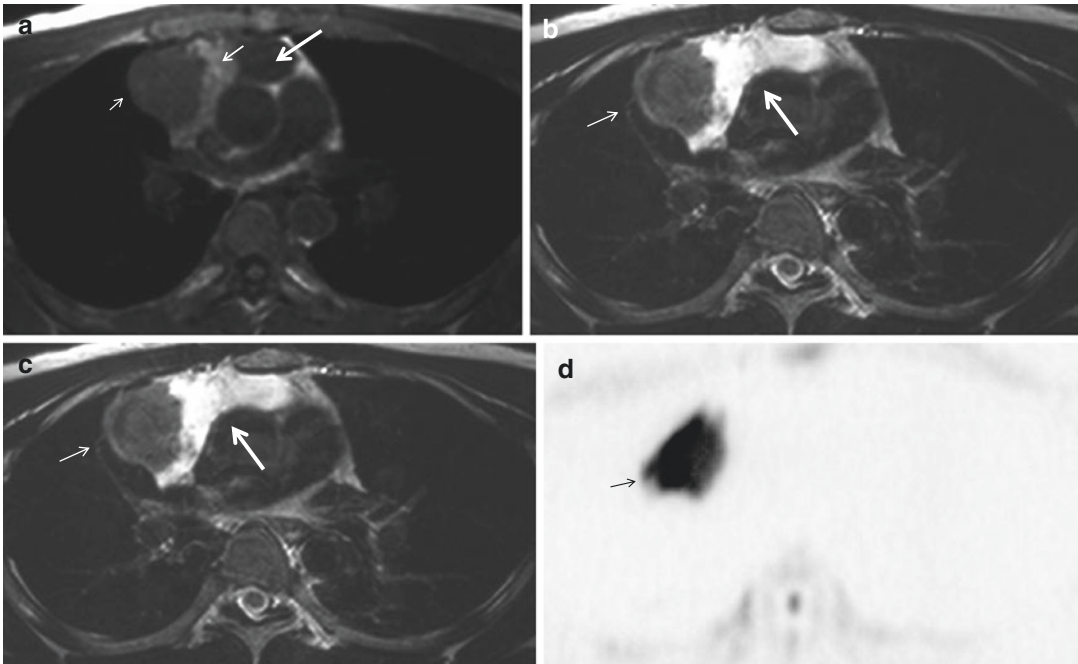
Fig. 21 Hodgkin's lymphoma associated with a thymic cyst. On T1-weighted image (**a**), the lymphoma (*small arrow*) shows intermediate signal similar to muscle, and the thymic cyst consists of high (*medium arrow*) and low signal (*large arrow*). On T2-weighted image (**b**), the lymphoma shows intermediate signal (*small arrow*), whereas the thymic cyst shows high signal intensity (*large arrow*). (**c**) On the contrast-enhanced image, the lymphoma (*small arrow*) shows enhancement, whereas the thymic cyst does not. (**d**) On the diffusion-weighted image (*b* = 1000), a prominent increase in signal is seen in the lymphoma (*small arrow*) due to high cellularity

5.2 Lymphoblastic Lymphoma

Lymphoblastic lymphoma mainly occurs in children and adolescents. Most tumors have features of thymic T cells on immunologic studies. Although lymphoblastic lymphoma and acute lymphoblastic leukemia show overlapping clinical, pathologic, cytogenetic, and molecular features, lymphoblastic lymphoma has no or minimal peripheral blood or bone marrow involvement, and lymphoblastic leukemia has predominant features of bone marrow and hematologic involvement (Shimosato and Mukai 1997a, b, c). Typically, patients present with respiratory distress and superior vena cava syndrome due to a large mediastinal mass (Picozzi and Coleman 1990).

The most common CT appearance is a large mediastinal mass representing thymic and lymph node enlargement, which compresses the airway and cardiovascular structures. Low attenuation areas reflecting necrosis are commonly seen after contrast enhancement. Pleural and pericardial effusions are also frequent. Lymphoblastic non-Hodgkin's lymphoma has a predilection for rapid dissemination, and the tumor spreads to extrathoracic lymph nodes, bone marrow, central nervous system, and gonads in extensive disease (Hamrick-Turner et al. 1994). Since recurrence 2–4 years after therapy is not unusual in lymphoblastic lymphoma, meticulous follow-up is necessary (Hamrick-Turner et al. 1994).

5.3 Primary Mediastinal Diffuse Large B-Cell Lymphoma

Primary mediastinal diffuse large B-cell lymphoma has been described as a distinct subtype of non-Hodgkin's lymphoma (Tateishi et al. 2004). Immunopathologic examination shows most tumors to be of B-cell origin. The majority of tumors tend
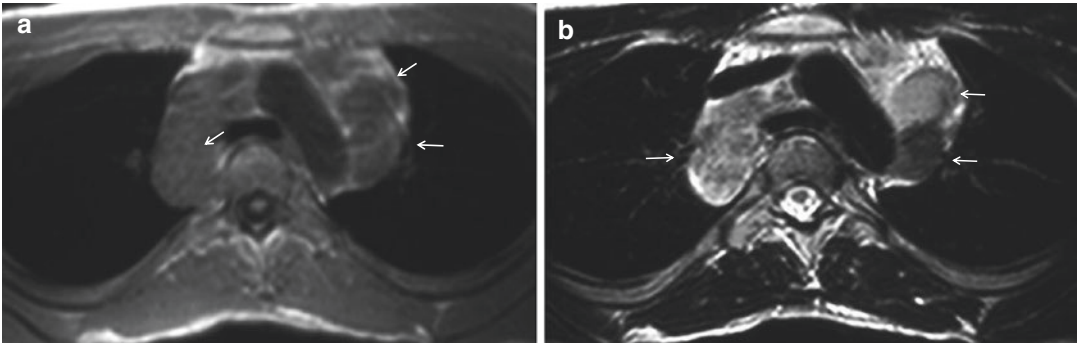
Fig. 22 Anaplastic diffuse large B-cell lymphoma. T1-weighted (**a**) and T2-weighted (**b**) images show multiple enlarged lymph nodes (*arrows*) in the anterior mediastinal, paratracheal, and posterior mediastinal regions

to occur in young to middle-aged adults with a mean age of 30 years (Shaffer et al. 1996). Common symptoms include dyspnea, cough, chest pain, malaise, and fever. Superior vena cava syndrome also occurs in nearly 40 % of patients.

The tumor appears as a large, smooth, or lobulated, anterior mediastinal mass in nearly all patients. Average diameters were 10 cm or greater (Shaffer et al. 1996). On CT, the tumors showed low attenuation areas, representing hemorrhage, necrosis, or cystic degeneration in 50 % of cases and heterogeneous enhancement in about 40 % of cases (Tateishi et al. 2004; Shaffer et al. 1996). The tumors are large and commonly invade the adjacent mediastinal structures, chest wall, and lung. Pleural and pericardial effusions are seen in about one third of patients.

In one study of 21 patients, mediastinal lymph node enlargement was seen in 67 %, but extrathoracic lymph node enlargement was unusual (Tateishi et al. 2004). The most commonly involved lymph nodes in the mediastinum are anterior mediastinal and paratracheal nodes followed by the subcarinal, hilar, internal mammary, pericardial, and posterior mediastinal nodes in decreasing order of frequency (Castellino et al. 1996) (Fig. 22).

5.4 Magnetic Resonance Imaging of Lymphoma

In general, lymphomas are relatively homogeneous on MR imaging and hypointense to fat and slightly hyperintense to muscle on T1-weighted images but isointense to fat and hyperintense to muscle on T2-weighted images (Negendank et al. 1990). Negendank et al. reported a unique finding: a greater brightness on T2-weighted images was seen in lymphomas with dense fibrosis, which contributes to the greater brightness of Hodgkin's lymphoma than that of non-Hodgkin's lymphomas (Negendank et al. 1990). The greater brightness of lymphomas may not to be caused by the fibrosis itself but by some other tissue element that has a very long T2 value, including edema, a greater proportion of vascular space, and inflammation (Negendank et al. 1990). If the initial mass shows high signal on T2-weighted images, the likelihood of recurrence might be higher (Nyman et al. 1989).

In mediastinal lymphomas, a residual mass is common after treatment, especially in cases with an initial bulk. MR imaging provides important information in distinguishing viable tumors from residual benign masses. Residual tumors can reveal various signal patterns on T1- and T2-weighted MR images. Heterogeneous signal intensity on T2-weighted images is seen in both residual and nonviable tumors. High signal intensity on T2-weighted images and low signal intensity on T1-weighted images may represent residual active lymphoma, areas of necrosis, and inflammation. In the mass lesions of nonviable tumors, heterogeneous signal patterns on T2- and T1-weighted images represent mixed fat and fibrous tissue. Inactive residual fibrotic masses characteristically show homogeneous hypointensity (Rahmouni et al. 1993; Rahmouni and
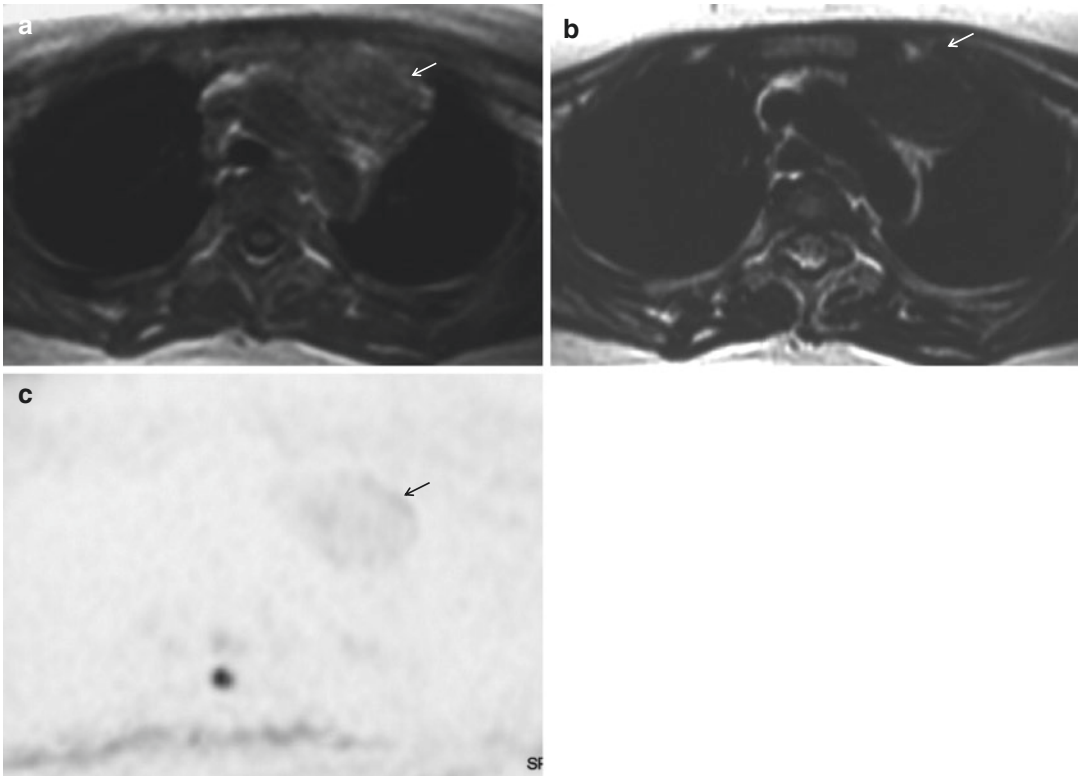
Fig. 23 A residual mass of non-Hodgkin's lymphoma after chemotherapy. T1-weighted (**a**) and T2-weighted (**b**) images show a well-demarcated mass of low signal intensity in the anterior mediastinum (*arrow*). (**c**) The mass does not show a significant signal increase on diffusion-weighted image (*b* = 1000) (*arrow*). Low signal intensity on T2-weighted and diffusion-weighted images and little enhancement on dynamic study suggest a nonviable residual mass

Zerhouni 1990). The use of contrast-enhanced MR imaging is also useful. In a study of 31 patients with bulky mediastinal lymphoma (17 with Hodgkin's lymphoma and 24 with non-Hodgkin's lymphoma), contrast enhancement of mediastinal masses in lymphoma decreases markedly after treatment in patients in complete remission but not in patients with relapse (Rahmouni et al. 2001) (Fig. 23).

6 Neurogenic Tumor

Neurogenic tumors account for approximately 9–20 % of primary mediastinal neoplasms in adults and 29–35 % in children (Strollo et al. 1997; Ribet and Cardot 1994). Nearly 90 % of neurogenic tumors occur in the posterior mediastinum. Tumors arise from peripheral nerve and nerve sheath (schwannoma, neurofibroma, malignant peripheral nerve sheath tumor), sympathetic ganglia (neuroblastoma, ganglioneuroblastoma, ganglioneuroma) and rarely parasympathetic ganglia (paraganglioma). Nerve sheath tumors are more common in adults, whereas sympathetic ganglia tumors are more common in children. The mean age at diagnosis is 5.8 years for neuroblastoma, 8.4 years for ganglioneuroblastoma, 19.6 years for ganglioneuroma, 29.7 years for neurofibroma, and 38 years for schwannoma.

6.1 Peripheral Nerve Sheath Tumor

Peripheral nerve sheath tumors of the mediastinum usually arise from intercostal nerves and rarely from the vagus, phrenic, or recurrent nerve.
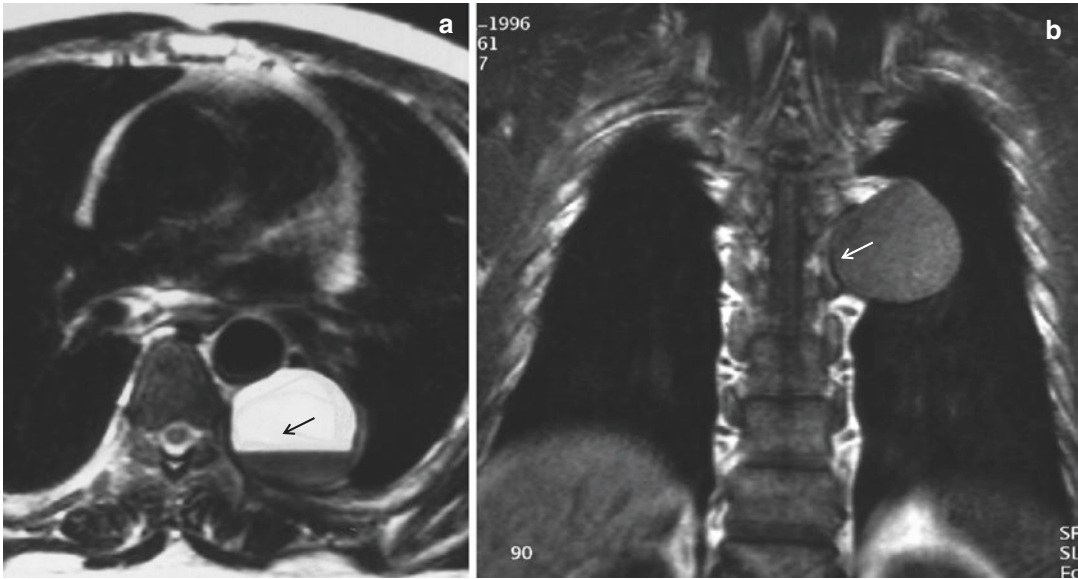
Fig. 24 Schwannoma with cystic degeneration. (**a**) T2-weighted axial image shows a well-defined mass in the paravertebral region. A fluid-fluid level is seen within the mass (*arrow*), suggesting a cystic nature of the lesion. T1-weighted coronal image (**b**) shows a flat deformity of the adjacent rib (*arrow*), representing pressure erosion by the mass

Schwannomas are encapsulated and arise from the nerve sheath. Neurofibromas are nonencapsulated and result from a disorganized proliferation of all nerve elements. Malignant peripheral nerve sheath tumors represent the malignant counterparts of schwannomas and neurofibromas, and nearly 50 % of them occur in patients with neurofibromatosis.

Schwannoma and neurofibroma typically appear as smooth, well-defined, rounded, or elliptical masses in the paravertebral region or along the course of other nerves (Fig. 24). Paravertebral tumors may extend into the spinal canal. On MR imaging, peripheral nerve sheath tumors typically show slightly higher signal intensity than muscle on T1-weighted images and markedly increased intensity on T2-weighted images (Burk et al. 1987; Sakai et al. 1991). On T2-weighted images, schwannomas occasionally reveal central high intensity due to cystic degeneration, whereas neurofibromas show central low intensity and peripheral high intensity (target sign), representing central tumor tissue and peripheral myxoid degeneration (Sakai et al. 1991). Neurofibromas may be associated with von Recklinghausen disease. Plexiform neurofibroma is pathognomonic of von Recklinghausen disease and appears as an extensive fusiform or infiltrating mass (Fig. 25).

Malignant peripheral nerve sheath tumors appear as a rounded well-defined mass in the posterior mediastinum but may locally invade mediastinal structures and adjacent chest wall (Strollo et al. 1997). Hematogenous metastases occur most commonly to the lung. Cystic degeneration due to hemorrhage and necrosis may be seen within the lesions.

6.2   Sympathetic Ganglia Tumor

Neuroblastoma, ganglioneuroblastoma, and ganglioneuroma are tumors of the sympathetic nervous system, and they originate from the primordial neural crest cells that form the sympathetic nervous system. Ganglioneuroma and ganglioneuroblastoma arise most commonly from the sympathetic ganglia in the posterior mediastinum. Fifty percent of neuroblastomas arise from the adrenal gland, and nearly 30 % arise in the mediastinum (Strollo et al. 1997). Ganglioneuroma is the most benign tumor, which is composed of gangliocytes and mature stroma;

Fig. 25 Plexiform neurofibroma in neurofibromatosis type 1 (von Recklinghausen disease). T2-weighted coronal image shows an extensive fusiform mass around the trachea (*arrows*)

ganglioneuroblastoma is of intermediate malignant potential and has both mature gangliocytes and immature neuroblasts; and neuroblastoma is the most malignant tumor of the three and composed primarily of neuroblasts. Ganglion cell tumors typically appear as a paravertebral mass.

On MR imaging, ganglioneuroma commonly shows low signal intensity on T1-weighted images and heterogeneous high signal intensity on T2-weighted images. The heterogeneous high signal intensity on T2-weighted images of ganglioneuroma has been considered to result from a combination of myxoid material and relatively low amounts of ganglion cells (Ichikawa et al. 1996; Serra et al. 1992; Sakai et al. 1991) (Fig. 26). Ganglioneuroma does not typically show early enhancement at dynamic MR but does accumulate contrast material over time (Lonergan et al. 2002; Ichikawa et al. 1996; Sakai et al. 1991) (Fig. 27). A ganglioneuroma containing fat has rarely been reported and is considered to result from spontaneous regression of the tumor with subsequent infiltration of fat tissue from the mediastinum (Hara et al. 1999) (Fig. 26).

Neuroblastoma and ganglioneuroblastoma are of relatively low signal intensity on T1-weighted
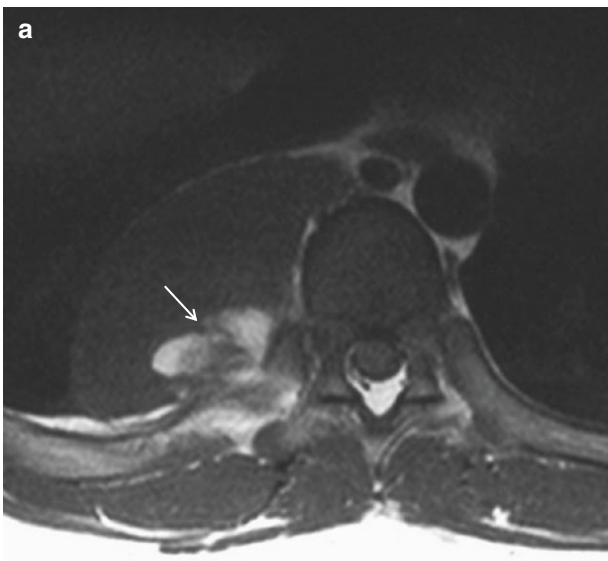
Fig. 26 Ganglioneuroma. T1-weighted image (**a**) shows a paravertebral mass of low signal intensity similar to muscle, which contains areas of high signal (*arrow*), representing mediastinal fat protruding into the mass. On the

T2-weighted coronal image (**b**), the mass shows heterogeneous high signal intensity, which may result from prominent myxoid material and a small amount of ganglion cells
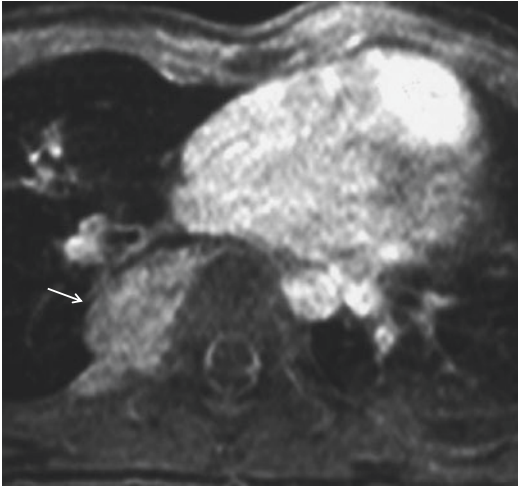
Fig. 27 Ganglioneuroma. Early phase (not shown) and equilibrium phase of a contrast-enhanced dynamic study. The mass shows no apparent enhancement in the early phase but homogeneous enhancement in the equilibrium phase (*arrow*)

images and high signal intensity on T2-weighted images (Figs. 28 and 29). They typically show a heterogeneous signal pattern due to hemorrhage and cystic change within the lesions, which manifest as areas of high signal intensity on T1- and T2-weighted images, respectively (Lonergan et al. 2002).

MR imaging has a few advantages over CT: the evaluation of intraspinal extension of primary tumor, detection of marrow disease, and detection of diffuse hepatic metastases (Abramson 1997; Couanet et al. 1988; King et al. 1975; Siegel et al. 1986). MR well demonstrates the range of extension of epidural tumor and its anatomical relation to the spinal cord and nerve roots. MR can depict marrow disease, which shows low signal on T1-weighted images and high signal on T2-weighted images.

6.3 Paraganglioma

Paraganglioma is a rare tumor originating from paraganglionic cells and accounts for 4 % of thoracic neurogenic tumors (Reed et al. 1978). The mediastinal paragangliomas predominantly arise in two locations: around the aortic arch (aortic

body tumors) and in the paravertebral region. Aortic body tumors may occur in the following four locations: lateral to the brachiocephalic artery, anterolateral to the aortic arch, at the angle of the ductus arteriosus, or above and to the right of the right pulmonary artery (Olson and Salyer 1978).

The appearance of thoracic paragangliomas is similar to that of paragangliomas seen in other locations, and the tumors have intermediate signal intensity on T1-weighted images and high signal intensity on T2-weighted images (Balcombe et al. 2007; Olsen et al. 1987). Smaller masses tend to have uniform intensity, whereas larger tumors are more likely to reveal heterogeneous appearance due to necrosis. Since paragangliomas are typically hypervascular, tumors generally reveal intense enhancement on CT or MR imaging after administration of intravenous contrast (Balcombe et al. 2007; Spizarny et al. 1987). Numerous serpiginous vascular channels may be seen within the large tumors.

7 Other Mediastinal Diseases

7.1 Mediastinal Goiter

Intrathoracic goiters almost always result from direct contiguous extension into the mediastinum from thyroid lesions, which are most commonly benign multinodular goiter. Thyroid carcinoma and thyroid enlargement due to thyroiditis may also extend into the mediastinum. Intrathoracic extension of thyroid masses is commonly into the anterior mediastinum (80 %) and anterior to the recurrent laryngeal nerve and the brachiocephalic vessels. Posterior mediastinal extension of goiters occurs in 10–25 % (Katlic et al. 1985; Shahian and Rossi 1988).

On T1-weighted MR images, the masses usually show intermediate signal intensity similar to muscle and occasionally can show high signal regions representing hemorrhage or colloid cyst formation (Higgins et al. 1986; Gefter et al. 1987). On T2-weighted images, the masses usually show heterogeneous intensity. Continuity of the mediastinal mass with the thyroid gland in the neck is an important diagnostic clue, and MR imaging is generally useful in its evaluation (Fig. 30).
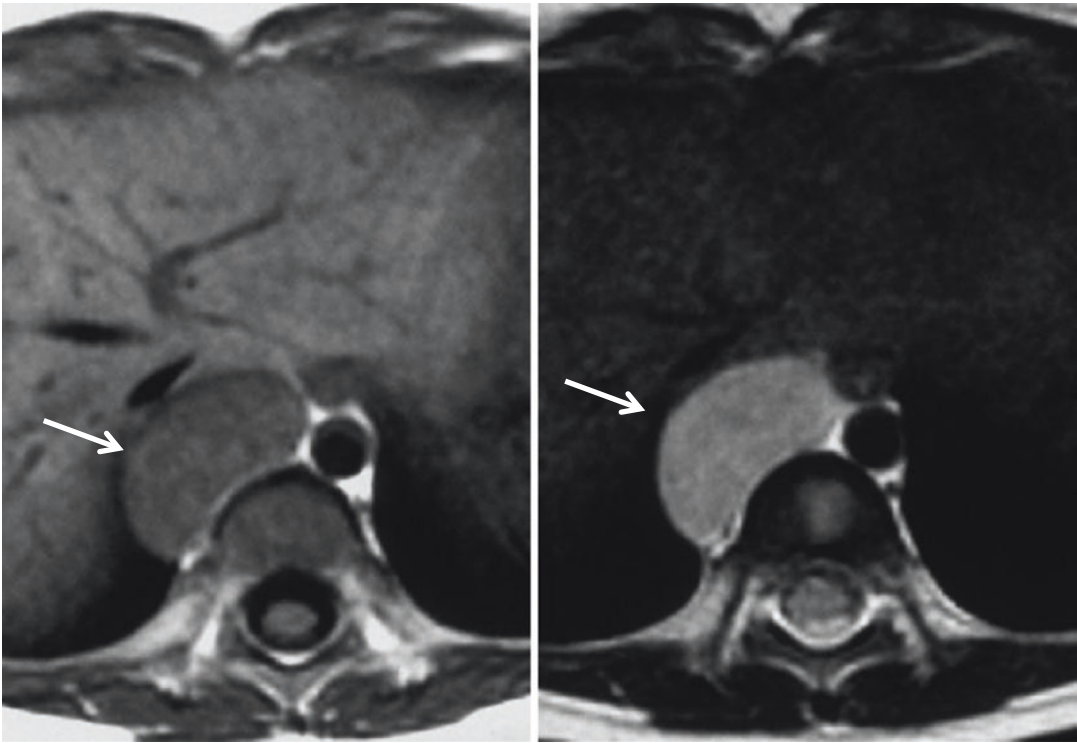
Fig. 28 Ganglioneuroblastoma. A right paravertebral mass shows low signal intensity on T1-weighted image (**a**) and high signal intensity on T2-weighted image (**b**) (*arrows*). Ganglion cell tumor typically arises in the anterior paravertebral region
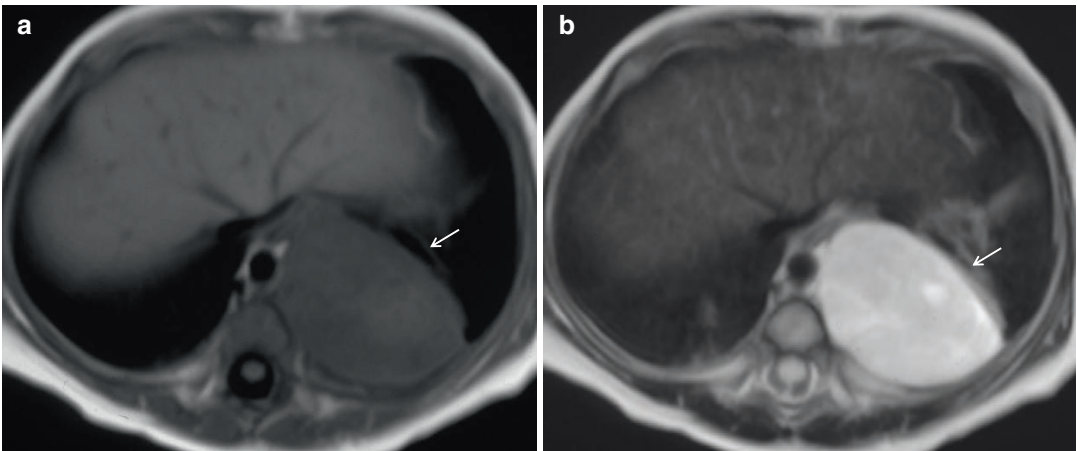
Fig. 29 Neuroblastoma. T1-weighted (**a**) and T2-weighted (**b**) axial images show a left paravertebral mass (*arrows*). The mass shows low signal intensity on T1-weighted image and high on T2-weighted image
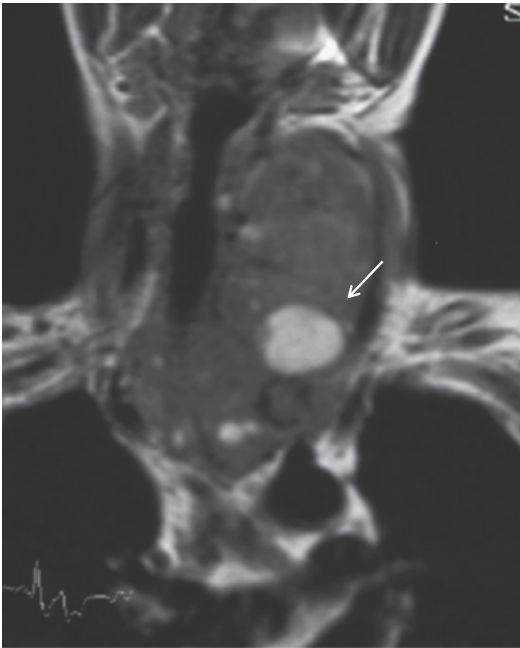
Fig. 30 Mediastinal goiter. A thyroid mass extends into the anterior mediastinum. The mass shows intermediate signal intensity with foci of high intensity (*arrow*), representing hemorrhage or cystic necrosis

7.2 Ectopic Parathyroid Gland

Parathyroid glands are located near the thyroid gland in 90 % and are ectopic in nearly 10 %. In a review of ectopic parathyroid glands, 81 % are located in the anterior mediastinum, and 19 % are in the posterior mediastinum (Clark 1988).

Generally, parathyroid adenomas are intermediate in signal intensity on T1-weighted images and show prominent high signal intensity on T2-weighted images (Spritzer et al. 1987). Due to fibrosis and hemorrhage, nearly 10 % of abnormal glands do not show high signal intensity on T2-weighted images (Spritzer et al. 1987).

7.3 Fibrosing Mediastinitis

Fibrosing mediastinitis is a rare disease manifested by chronic inflammation and fibrosis, which focally or diffusely involves the mediastinum. The most common causes of fibrosing mediastinitis are histoplasmosis and tuberculosis,

but it can also be related to autoimmune disease, radiation therapy, retroperitoneal fibrosis, methysergide therapy, or may be idiopathic (Mole et al. 1995). Histoplasmosis infection typically results in focal disease, whereas idiopathic fibrosing mediastinitis is usually diffuse. Complications result from obstruction of various mediastinal structures, most commonly the superior vena cava (39 %), followed by, in decreasing order, the bronchi (33 %), pulmonary artery (18 %), and esophagus (9 %) (Sherrck et al. 1994). The most common clinical symptoms are related to the superior vena cava syndrome: headache, cyanosis, and puffiness of the face, neck, and arms (Schowengerdt et al. 1969).

CT shows the enlarged calcified nodes most commonly in the right paratracheal region, whereas other regions, the left paratracheal, subcarinal, or posterior mediastinal regions, may also be involved (Sherrck et al. 1994). Calcification is rare in the diffuse form, which typically shows diffuse increase in attenuation of the mediastinal fat tissue. CT is useful for assessing involvement of mediastinal structures: narrowing and compression of superior vena cava, airway, pulmonary arteries, and veins. Although MR imaging and CT are equivalent in assessing the extent of adenopathy or fibrosis, MR allows for assessment of vascular involvement without contrast material. On MR imaging, fibrosing mediastinitis commonly show heterogeneous signal intensity on T1- and T2-weighted images (Rossi et al. 2001). Markedly decreased signal intensity on T2-weighted images is occasionally seen due to fibrosis and calcification within the lesions (Rholl et al. 1985). The major disadvantage of MR is that it cannot confidently identify calcifications.

7.4 Extramedullary Hematopoiesis

Extramedullary hematopoiesis is typically seen in patients with severe hemolytic anemia. Intrathoracic manifestations appear as multiple lobulated paravertebral masses. On CT, they appear as well-defined multiple masses of homo-

geneous soft tissue attenuation and may show areas of fat attenuation (Glazer et al. 1992). On T1-weighted MR images, the masses show heterogeneous signal intensity with increased signal intensity due to contained fat tissue.

8 Imaging Protocol

8.1 MRI Sequences for the Mediastinum

Recent advanced technology has improved MR images in the mediastinum. Generally, conventional T1- and T2- weighted spin-echo images provide basic information about mediastinal tumors, and the protocol of MR imaging in the mediastinum is similar to that in other organs. However, the main challenge is respiratory and cardiac motion, which frequently deteriorates image quality. To reduce these artifacts, selection of rapid sequences with or without breath-holding, respiratory gating, or ECG-gating techniques are needed (Takahashi and Al-Janabi 2010). Chemical shift imaging has an advantage for detecting minimal intravoxel fat deposition within a mass and consists of in- and opposed-phase gradient-echo T1-weighted images, which can be obtained during a single breath-hold's time. Its unique utility in the mediastinum is that it can characterize the normal thymus and differentiate thymic hyperplasia from thymic epithelial tumors (Inaoka etal. 2007; Priola et al. 2015).

MR imaging is particularly useful in distinguishing cystic and solid lesions. Since most cystic diseases in the mediastinum show nonspecific attenuation depending on their content on CT, MR imaging is often more beneficial. A bright signal on T2-weighted imaging, fluid-fluid level, and lack of contrast enhancement is a key to diagnose cystic masses. In addition, heavily T2-weighted imaging is optional. They are usually obtained by longer echo times enhancing the cystic components with remarkably high signal intensity. T2-weighted images could also have a potential to characterize other tissue components. Low signal intensity components in the mass may represent hemorrhage, flow voids, calcification,

Table 3 Suggested MR imaging protocol in the mediastinum

1. Initial coronal scout image
2. T1WI: gradient-refocused echo image with flow compensation, in-phase and opposed-phase image: axial (coronal, sagittal)
3. T2WI: first spin-echo: axial (coronal, sagittal) with/without cardiac gating
4. Gadolinium-enhanced T1WI: Gradient-refocused echo image with fat suppression and flow compensation: axial (coronal, sagittal) Dynamic study is indicated to evaluate vascularity of the lesion
5. For evaluation of vessels: breath-hold 3D contrast-enhanced study
6. Diffusion-weighted image ($b = 0,1000$) axial

or fibrosis. Low signal intensity areas within thymic carcinoma commonly represent collagenous fibrotic tissue, which is uncommon in thymoma (Takahashi and Al-Janabi 2010).

The recent fast gradient-echo sequences for dynamic studies can obtain multiple images with higher spatial resolution in a single breath-hold. A dynamic study using a spoiled gradient-echo sequence with contrast material is performed to evaluate the time-related enhancement of the lesion. For instance, we can assess tumor vascularity in the arterial phase and enhancement in the interstitial (extracellular) space in the equilibrium phase. Furthermore, we can use dynamic studies to distinguish between cystic and solid lesions and posttreatment fibrous scar and viable residual tumor and for tumor characterization. The earlier time peak on a dynamic study suggests thymoma instead of non-thymoma (Sakai et al. 2002).

Diffusion-weighted imaging (DWI) reflects differences of water diffusivity in the tissues. The b values used in the several reports ranged from 800 to 1000 s/mm^2 (Abdel et al. 2014; Gmustas et al. 2011). A b value higher than 1000 s/mm^2 might be inappropriate for mediastinal tumors, because a longer acquisition time might be needed and susceptibility artifacts from the lungs could not be ignored. Reduced water diffusivity usually correlates with higher cellular density, suggesting malignancy; DWI shows high

intensity in the area of higher cellular density in the tissue. It has been reported that the apparent diffusion coefficient (ADC) reflects tumor grades of thymic epithelial tumors. The ADC tends to be lower in high-risk thymomas or thymic carcinomas compared with low-risk thymomas (Abdel et al. 2014).

As generally accepted, the first step of imaging examination of the mediastinum tumors is CT, whereas MRI provides various unique information and occasionally contributes to the characterization of mediastinal tumors. Thus, the radiologist should know about the respective advantages and appropriate indications of the different sequences in MR imaging. Table 3 shows a suggested MR imaging protocol for the mediastinum.

References

Abdel Razek AA, Khairy M, Nada N (2014) Diffusion-weighted MR imaging in thymic epithelial tumors: correlation with World Health Organization classification and clinical staging. Radiology 273(1):268–275

Abramson SJ (1997) Adrenal neoplasms in children. Radiol Clin N Am 35:1415–1453

Afifi HY, Bosl GI, Burt ME (1997) Mediastinal growing teratoma syndrome. Ann Thorac Surg 64:359–362

Balcombe J, Torigian DA, Kim W, Miller WT Jr (2007) Cross-sectional imaging of paragangliomas of the aortic body and other thoracic branchiomeric paraganglia. Am J Roentgenol 188:1054–1058

Baron RL, Sagel SS, Baglan RJ (1981) Thymic cysts following radiation therapy for Hodgkin disease. Radiology 141:593–597

Baron RL, Lee JK, Sagel SS, Peterson RR (1982) Computed tomography of the normal thymus. Radiology 142:121–125

Boothroyd AE, Hall-Graggs MA, Dicks-Mireaux C, Shaw DG (1992) The magnetic resonance appearances of the normal thymus in children. Clin Radiol 45:378–381

Burk DL Jr, Brunberg JA, Kanal E, Brunberg JA, Latchaw RE, Wolf GL (1987) Spinal and paraspinal neurofibromatosis: surface coil MR imaging at 1.5 T. Radiology 162:797–801

Carbone PP, Kaplan HS, Musshoff K, Smithers DW, Tubiana M (1971) Report of the committee on Hodgkin's disease staging classification. Cancer Res 31:1860–1861

Castellino RA, Hilton S, O'Brien JP, Portlock CS (1996) Non-Hodgkin lymphoma: contribution of chest CT in the initial staging evaluation. Radiology 199:129–132

Chaer R, Massad MG, Evans A, Snow NJ, Geha AS (2002) Primary neuroendocrine tumors of the thymus. Ann Thorac Surg 74:1733–1740

Chen J, Weisbrod GL, Herman SJ (1988) Computed tomography and pathologic correlations of thymic lesions. J Thorac Imaging 3:61–65

Chen G, Marx A, Wen-Hu J (2002) New WHO histologic classification predicts prognosis of thymic epithelial tumors. A clinicopathologic study of 200 thymoma cases from china. Cancer 95:420–429

Choyke PL, Zeman RK, Gootenberg JE, Greenberg JN, Hoffer F, Frank JA (1987) Thymic atrophy and regrowth in response to chemotherapy: CT evaluation. Am J Roentgenol 149:269–272

Clark OH (1988) Mediastinal parathyroid tumors. Arch Surg 123:1096–1100

Couanet D, Geoffray A, Hartmann O, Leclere JG, Lumbroso JD (1988) Bone marrow metastases in children's neuroblastoma studied by magnetic resonance imaging. Prog Clin Biol Res 271:547–555

De Geer G, Webb WR, Gamsu G (1986) Normal thymus: associated with MR and CT. Radiology 158:313–317

Dehner LP (1983) Gonadal and extragonadal germ cell neoplasia of childhood. Hum Pathol 14:493–511

Do YS, Im J-G, Lee BH, Kim KH, Oh YW, Chin SY, Zo JI, Jang JJ (1995) CT findings in malignant tumors of thymic epithelium. J Comput Assist Tomogr 19:192–197

Doppman JL, Nieman L, Miller DL, Pass HI, Chang R, Cutler GB, Schaaf M, Chrousos G, Norton JA, Ziessman HA, Oldfield EH, Loriaux DL (1989) Ectopic adrenocorticotropic hormone syndrome: localization studies in 28 patients. Radiology 172:115–124

Drevelegas A, Palladas P, Scordalaki A (2001) Mediastinal germ cell tumors: a radiologic-pathologic review. Eur Radiol 11:1925–1932

Erasmus JJ, McAdams HP, Donnelly LF, Spritzer CE (2000) MR imaging of mediastinal masses. MRI Clin North Am 8:59–89

Ferolla P, Falchetti A, Filosso P, Tomassetti P, Tamburrano G, Avenia N, Daddi G, Puma F, Ribacchi R, Santeusanio F, Angeletti G, Brandi ML (2005) Thymic neuroendocrine carcinoma (carcinoid) in MEN 1 syndrome: the Italian series. J Clin Endocrinol Metab 90:2603–2609

Feung MY, Gasser B, Gangi A, Bogorin A, Charneau D, Wihlm FM, Dietemann FL, Catherine R (2002) Imaging of cystic masses of the mediastinum. RadioGraphics 22:s79–s93

Francis IR, Glazer GM, Bookstein FL, Gross BH (1985) The thymus: reexamination of age-related changes in size and shape. Am J Roentgenol 145:249–254

Fujimoto K, Nishihara H, Abe T, Edamitsu O, Uchida M, Kumabe T, Ueda H, Sakoda J, Kojima K, Uozumi J, Oshibuchi M, Hayabuchi N (1992) MR imaging of thymoma –comparison with CT, operative, and pathological findings. Nippon Igaku Hoshasen Gakkai Zasshi 25:1128–1138

Gal AA, Kornstein MJ, Cohen C, Duarte IG, Miller JI, Mansour KA (2001) Neuroendocrine tumors of the thymus: a clinicopathological and prognostic study. Ann Thorac Surg 72:1179–1182

Gefter WB, Spritzer CE, Eisenberg B, LiVolsi VA, Axel L, Velchik M, Alavi A, Schenck J, Kressel HY (1987) Thyroid imaging with high-field strength surface-coil MR. Radiology 164:483–490

Glazer HS, Wick MR, Anderson DJ, Semenkovich JW, Molina PL, Siegel MJ, Sagel SS (1992) CT of fatty thoracic masses. Am J Roentgenol 159:1181–1187

Goldstein G, Mackey IR (1969) The human thymus. Warren H. Green, St Louis

Gualdi GF, Volpe A, Polettini E, D'Agostino A, Ceroni AM, Pirolli FM (1994) Role of magnetic resonance in the evaluation of space-occupying mediastinal pathology. Clin Ter 145:141–147

Gumustas S, Inan N, Sarisoy HT (2011) Malignant versus benign mediastinal lesions: quantitative assessment with diffusion weigh ted MR imaging. Eur Radiol 21(11):2255–2260

Hamrick-Turner JE, Saif MF, Powers CI, Blumenthal BI, Royal SA, Iyer RV (1994) Imaging of childhood non-Hodgkin lymphoma: assessment by histologic subtype. RadioGraphics 14:11–28

Hara M, Ohba S, Andoh K, Kitase M, Sasaki S, Nakayama J, Fukai I, Goodman PC (1999) A case of ganglioneuroma with fatty replacement: CT and MRI findings. Radiat Med 17:172–178

Hartmann CA, Roth C, Minck C, Niedobitek G (1990) Thymic carcinoma. J Cancer Res Clin Oncol 116:69–82

He Y, Zhang Z-Y, Zhu H-G, Guo W, Wang L-Z (2008) Infant ectopic cervical thymus in submandibular region. Int J Oral Maxillofac Surg 37:186–189

Hoffman OA, Gillespie DJ, Aughenbaugh GL, Brown LR (1993) Primary mediastinal neoplasms (other than thymoma). Mayo Clin Proc 68:880–891

Huang TW, Cheng YL, Tzao C, Chang H, Tsai WC, Lee SC (2007) Middle mediastinal thymoma. Respirology 12:934–936

Higgins CB, McNamara MT, Fisher MR, Clark OH (1986) MR imaging of the thyroid. Am J Roentgenol 147:1255–1261

Ichikawa T, Ohtomo K, Araki T, Fujimoto H, Nemoto K, Nanbu A, Onoue M, Aoki K (1996) Ganglioneuroma: computed tomography and magnetic resonance features. Br J Radiol 69:114–121

Inaoka T, Takahashi K, Iwata K, Fajardo L, van Beek E, Sato Y, Yamada T, Nagasawa K, Shuke N, Aburano T (2005) Evaluation of normal fatty replacement of the thymus with chemical-shift MR imaging for identification of the normal thymus. J Magn Reson Imaging 22:341–346

Inaoka T, Takahashi K, Mineta M, Yamada T, Shuke N, Okizaki A, Nagasawa K, Sugimori H, Aburano T (2007) Thymic hyperplasia and thymus gland tumors: differentiation with chemical shift MR imaging. Radiology 243:869–876

Inoue A, Tomiyama N, Fujimoto K, Sadohara J, Nakamichi I, Tomita Y, Aozasa K, Tsubamoto M, Murai S, Natsag J, Sumikawa H, Mihara N, Honda O, Hamada S, Johkoh T, Nakamura H (2006) MR imaging of thymic epithelial tumors: correlation with world health organization classification. Radiat Med 24:171–181

Iyoda A, Hiroshima K, Yusa T, Toyozaki T, Fujisawa T, Ohwada H (2000) The primary mediastinal growing teratoma syndrome. Anticancer Res 20:3723–3728

Jeong YJ, Lee KS, Kim J, Shim YM, Han J, Kwon OJ (2004) Does CT of thymic epithelial tumors enable us to differentiate histologic subtypes and predict prognosis. Am J Roentgenol 183:283–289

Katlic MR, Wang C, Grillo HC (1985) Substernal goiter. Ann Thorac Surg 39:391–399

Khariwala SS, Nicollas R, Triglia JM, Garabedian EN, Marianowski R, Van Den Abbeele T, April M, Ward R, Koltai PJ (2004) Cervical presentations of thymic anomalies in children. Int J Pediatr Otorhinolaryngol 68:909–914

King D, Goodman J, Hawk T, Boles ET, Sayers MP (1975) Dumbbell neuroblastomas in children. Arch Surg 110:888–891

Klemm KM, Moran CA (1999) Primary neuroendocrine carcinomas of the thymus. Semin Diagn Pathol 16:32–41

Kondo K, Yoshizawa K, Tsuyuguchi M, Kimura S, Sumitomo M, Morita J et al (2004) WHO classification is a prognostic indicator in thymoma. Ann Thorac Surg 77:1183–1188

Kuhlman JE, Fishman EK, Wang KP, Zerhouni EA, Siegelman SS (1988) Mediastinal cysts; diagnosis by CT and needle aspiration. Am J Roentgenol 150:75–78

Lee KS, Gilm J, Han CH et al (1989) Malignant primary germ cell tumors of the mediastinum: CT features. Am J Roentgenol 153:947–951

Levine GD, Rosai J (1978) Thymic hyperplasia and neoplasia: a review of current concepts. Hum Pathol 9:495–515

Lewis JE, Wick MR, Scheithauer BW, Bernatz PE, Taylor WF (1987) Thymoma: a clinicopathological review. Cancer 60:2727–2743

Linegar AG, Odell JA, Fennell WM, Close PM, De Groot MK, Casserly DR, Perold JI (1993) Massive thymic hyperplasia. Ann Thorac Surg 55:1197–1201

Liu D, Kitajima M, Awai K, Nakayama Y, Tamura Y, Suda H, Asonuma K, Inomata Y, Yamashita Y (2006) Ectopic cervical thymus in an infant. Radiat Med 24:452–455

Lonergan GJ, Schwab CM, Suarez ES, Carlson CL (2002) Neuroblastoma, ganglioneuroblastoma, and ganglioneuroma: radiologic-pathologic correlation. Radiographics 22(4):911–934

Marom EA, Milito MA, Moran CA, Liu P, Correa AM, Kim ES, Komaki R, Erasmus JJ, Hofstetter WL, Rice DC, Swisher SG (2011) Computed tomography findings predicting invasiveness of thymoma. J Thorac Oncol 6:1274–1281

Masaoka A, Monden Y, Nakahara K, Tanioka T (1981) Follow-up study of thymomas with special reference to their clinical stages. Cancer 48:2485–2492

Mattila PS, Tarkkanen J, Mattila S (1999) Thoracic duct cyst: a case report and review of 29 cases. Ann Otol Rhinol Laryngol 108:505–508

McAdams HP, Kirejczyk WM, Posado-de-Christenson ML, Matsumoto S (2000) Bronchogenic cyst: imaging features with clinical and histopathologic correlation. Radiology 217:441–446

Moeller KH, Rosado-de-Christenson ML, Templeton PA (1997) Mediastinal mature teratoma: imaging features. Am J Roentgenol 169:985–990

Mole TM, Glover J, Sheppard MN (1995) Sclerosing mediastinitis: a report on 18 cases. Thorax 50: 280–283

Molica PL, Siegel MJ, Glazer HS (1990) Thymic masses on MR imaging. Am J Roentgenol 155:495–500

Molin PL, Siegel MJ, Glazer HS (1990) Thymic masses on MR imaging. Am J Roentgenol 155:495–500

Moran CA, Weissferdt A, Kalhor N, Solis LM, Behrens C, Wistuba II, Suster S (2012) A clinicopathological correlation of 250 cases with emphasis on the world health organization schema. Am J Clin Pathol 137:444–450

Murayama S, Murakami J, Watanabe H, Sakai S, Hinaga S, Soeda H, Nakata H, Masuda K (1995) Signal intensity characteristics of mediastinal cystic masses on T1-wieghted MRI. J Comput Assist Tomogr 19: 188–191

Nagasawa K, Takahashi K, Hayashi T, Aburano T (2004) Ectopic cervical thymus. Am J Roentgenol 182: 262–263

Nakasu Y, Minouchi K, Hatsuda N, Nakasu S, Handa J (1991) Thoracic meningocele in neurofibromatosis: CT and MR findings. J Comput Assist Tomogr 15:1062–1064

Negendank WG, Al-Katib AM, Karanes C, Smith MR (1990) Lymphomas: MR imaging contrast characteristics with clinical-pathologic correlations. Radiology 177:209–216

Nicolaou S, Muller NL, Li DKB, Oger JJF (1996) Thymus in myasthenia gravis: comparison of CT and pathologic findings and clinical outcome after thymectomy. Radiology 200:471–474

Nyman RS, Rehn SM, Glimelius BLG, Hagberg HE, Hemmingsson AL, Sundstrom CJ (1989) Residual mediastinal masses in Hodgkin disease: prediction of size with MR imaging. Radiology 170:435–440

Okumura M, Ohta M, Tateyama H, Nakagawa K, Matsumura A, Maeda H et al (2002) The world health organization histologic classification system reflects the oncologic behavior of thymoma. A clinical study of 273 patients. Cancer 94:624–632

Olson JL, Salyer WR (1978) Mediastinal paragangliomas (aortic body tumor): a report of four cases and a review of the literature. Cancer 41:2405–2412

Olsen WL, Dillon WP, Kelly WM, Norman D, Brant-Zawadzki M, Newton TH (1987) MR imaging of paragangliomas. Am J Roentgenol 148:201–204

Priola AM, Priola SM, Ciccone G, Evangelsta A, Cataldi A, Gned D, Ducco L, Moretti F, Brundu M, Veltri A (2015) Differentiation of rebound and lymphoid thynic hyperplasia from anterior mrdiastinal tumors with dual-echo chemical-shift imaging in adulthood. Radiology 274:238–248

Picozzi VJ, Coleman CN (1990) Lymphoblastic lymphoma. Semin Oncol 17:96–103

Pirronti T, Rinaldi P, Batocchi AP, Evoli A, Di Schino C, Marano P (2002) Thymic lesions and myasthenia gravis. Diagnosis based on mediastinal imaging and pathological findings. Acta Radiol 43:380–384

Pombo F, Rodriquez E, Caruncho MV (1994) CT attenuation values and enhancing characteristics of thoracoabdominal lymphomatous adenopathy. J Comput Assist Tomogr 18:59–64

Rahmouni A, Divine M, Lepage E, Jazaerli N, Belhadj K, Gaulard P, Golli M, Reyes F, Vasile N (2001) Mediastinal lymphoma: quantitative changes in gadolinium enhancement at MR imaging after treatment. Radiology 219:621–628

Rahmouni A, Tempany C, Jones R, Mann R, Yang A, Zerhouni E (1993) Lymphoma: monitoring tumor size and signal intensity with MR imaging. Radiology 188:445–451

Rahmouni AD, Zerhouni EA (eds) (1990) Role of MRI in the management of thoracic lymphoma. Churchill-Livingstone, New York

Rholl KS, Levitt RG, Glazer HS (1985) Magnetic resonance imaging of fibrosing mediastinitis. Am J Roentgenol 145:255–259

Rosado-de-Christenson ML, Pugatch RD, Moran CA, Galobardes J (1994) Thymolipoma: analysis of 27 cases. Radiology 193:121–126

Rosai J, Sobin LH (1999) Histological typing of tumors of the thymus. In: International histological classification of tumors, 2nd edn. Springer, NewYork, pp. 5–14

Rossi SE, McAdams HP, Rosado-de-Christenson ML, Franks TF, Galvin FR (2001) Fibrosing mediastinitis. RadioGraphics 21:737–757

Reed JC, Hallet KK, Feigin DS (1978) Neural tumors of the thorax: subject review from the AFIP. Radiology 126:9–17

Reed JC, Sobonya RE (1974) Morphologic analysis of foregut cysts in the thorax. Am J Roentgenol 120:851–860

Ribet ME, Cardot GR (1994) Neurogenic tumors of the thorax. Ann Thorac Surg 58:1091–1095

Ribet ME, Copin MC, Gosselin BH (1995) Bronchogenic cysts of the mediastinum. J Thorac Cardiovasc Surg 109:1003–1010

Ribet ME, Copin MC, Gossclin BH (1996) Bronchogenic cysts of the lung. Ann Thorac Surg 61:1636–1640

Sadohara J, Fujimoto K, Muller NL, Kato S, Takamori S, Ohkuma K, Terasaki H, Hayabuchi N (2006) Thymic epithelial tumors: comparison of CT and MR imaging findings of low-risk thymomass, high-risk thymomas, and thymic carcinomas. Eur J Radiol 60:70–79

Sakai F, Sone S, Kiyono K, Kawai T, Maruyama A, Ueda H, Aoki J, Honda T, Morimoto M, Ishii K, Ikeda S (1991) MR imaging of thymoma: radiologic-pathologic correlation. Am J Roentgenol 158:751–756

Sakai F, Sone S, Kiyono K, Maruyama A, Ueda H, Aoki J, Kawai T, Ishii K, Morimoto M, Haniuda M, Koizumi T (1992) Intrathoracic neurogenic tumors: MR-pathologic correlation. Am J Roentgenol 159:279–283

Sakai S, Murayama H, Soeda H, Matsuo Y, Ono M, Masuda K (2002) Differential diagnosis between thymoma and non-thymoma by dynamic MR imaging. Acta Radiol 43:262–268

Salo JA, Ala-Kulju K (1987) Congenital esophageal cysts in adults. Ann Thorac Surg 44:135–138

Sasaka K, Kurihara Y, Nakajima Y, Seto Y, Endo I, Ishikawa T, Takagi M (1998) Spontaneous rupture; a complication of benign mature teratomas of the mediastinum. Am J Roentgenol 170:323–328

Schowengerdt CG, Suyemoto R, Main FB (1969) Granulomatous and fibrous mediastinitis – a review and analysis of 180 cases. J Thorac Cardiovasc Surg 57:365–379

Serra AD, Rafal RB, Markisz JA (1992) MRI characteristics of two cases of adrenal ganglioneuromas. Clin Imaging 16:37–39

Shaffer K, Smith D, Kirn D, Kaplan W, Canellos G, Mauch P, Shulman LN (1996) Primary mediastinal large-B-cell lymphoma:radiologic findings at presentation. Am J Roentgenol 167:425–430

Shahian DM, Rossai R (1988) Posterior mediastinal goiter. Chest 94:599–602

Sherrck AD, Brown LR, Harms GF, Myers JL (1994) Radiologic findings of fibrosing mediastinitis. Chest 106:484–489

Shimosato Y, Mukai K (1997a) Epithelial tumors. In: Rosai J (ed) Tumors of the mediastinum, 3rd edn. Armed Forces Institute of Pathology, Washington, DC, pp. 40–157

Shimosato Y, Mukai K (1997b) Germ cell tumors. In: Rosai J (ed) Tumors of the mediastinum, 3rd edn. Armed Forces Institute of Pathology, Washington, DC, pp. 183–206

Shimosato Y, Mukai K (1997c) Malignant lymphoma. In: Rosai J (ed) Tumors of the mediastinum, 3rd edn. Armed Forces Institute of Pathology, Washington, DC, pp. 207–226

Shirkhoda A, Chasen MH, Eftekhari F, Goldman AM, Decaro LF (1987) MR imaging of mediastinal thymolipoma. J Comput Assist Tomogr 11:364–365

Siegel MJ, Glazer HS, Wiener JI, Molina PL (1989) Normal and abnormal thymus in childhood: MR imaging. Radiology 172:367–371

Siegel MJ, Jamroz GA, Glazer HS, Abramson CL (1986) MR imaging of intraspinal extension of neuroblastoma. J Comput Assist Tomogr 10:593–595

Spizarny DL, Rebner M, Gross BH (1987) CT evaluation of enhancing mediastinal masses. J Comput Assist Tomogr 11:990–993

Spritzer CE, Geffer WB, Hamilton R, Greenberg BM, Axel L, Kressel H (1987) Abnormal parathyroid glands: high-resolution MR imaging. Radiology 162:487–491

St-Georges R, Deslauriers J, Duranceau A, Vaillancourt R, Deschamps C, Beauchamp G, Page A, Brisson J (1991) Clinical spectrum of bronghogenic cysts of the mediastinum and lung in the adult. Ann Thorac Surg 52:6–13

Strollo DC, Rosado-de-Christenson ML, Jett JR (1997) Primary mediastinal tumors: part II. Tumors of the middle and posterior mediastinum. Chest 112:1344–1357

Strollo DC, Rosado-de-Christenson ML, Jett JR (2002) Primary mediastinal malignant germ cell neoplasms: imaging features. Chest Surg Clin North Am 12:645–658

Suster S, Rosai J (1991) Multilocular thymic cyst: an acquired reactive process. Am J Surg Pathol 15:388–398

Takahashi K, Inaoka T, Kamishima T (1998) Mature teraoma of the mediastinum: relationship of inflammatory process around the tumor with clinical, radiologic, and pathologic findings. Jpn J Clin Radiol 43:163–170

Takahashi K, Inaoka T, Murakami N, Hirota H, Iwata K, Nagasawa K, Yamada T, Mineta M, Aburano T (2003) Characterization of the normal and hyperplastic thymus on chemical-shift MR imaging. Am J Roentgenol 180:1265–1269

Takahashi K, Al-Janabi NJ (2010) Computed tomography and magnetic resonance imaging of mediastinal tumors. J Magn Reson Imaging 32(6):1325–1339

Takeda S, Miyoshi S, Minami M, Ohta M, Masaoka A, Matsuda H (2003) Clinical spectrum of mediastinal cysts. Chest 124:125–132

Tan MH, Kirk G, Archibold P, Kennedy P, Regan MC (2002) Cardiac compromise due to a pancreatic mediastinal pseudocyst. Eur J Gastroenterol Hepatol 14:1279–1282

Tanaka A, Takeda R, Utsunomiya H, Kataoka M, Mukaihara S, Hayakawa K (2000) Severe complilcations of mediastinal pancreatic pseudocyst: report of esophagobronchial fistula and hemothorax. J Hepato-Biliary-Pancreat Surg 7:86–91

Tateishi U, Muller NL, Johkoh T, Onishi Y, Arai Y, Satake M, Matuno Y, Tobinai K (2004) Primary mediastinal lymphoma: characteristic features of the various histological subtypes on CT. J Comput Assist Tomogr 28:782–789

Tiffet O, Nicholson AG, Ladas G, Sheppard MN, Goldstraw P (2003) A clinicopathologic study of 12 neuroendocrine tumors arising in the thymus. Chest 124:141–146

Travis WD, Brambilla E, Muller-Hermelink HK, Harris CC (2004) WHO classification of tumors. Pathology and genetics of tumors of the lung, pleura, thymus and heart. IARC Press, Lyon

Yamazaki K, Yoshino I, Oba T, Yohena T, Kameyama T, Tagawa T, Kawano D, Koso H, Maehara Y (2006) Ectopic pleural thymoma presenting as a giant mass in the thoracic cavity. Ann Thorac Surg 83:315–317

Yernault JC, Kuhn G, Dumortier P, Rocmans P, Ketelbant P, De Buyst P (1986) "Solid" mediastinal bronchogenic cyst: mineralogic analysis. Am J Roentgenol 146:73–74

Yoshioka N, Minami M, Inoue Y, Kawauchi N, Nakajima J, Oka T, Yoshioka K, Ohtomo K (2000) Pedunculated Bronchogenic cyst mimicking pleural lesion. J Comput Assist Tomogr 24:581–583

Wang ZF, Reddy GP, Gotway MB, Yeh BM, Hetts SW, Higgins CB (2003) CT and MR imaging of pericardial disease. RadioGraphics 23:s167–s180

Wychulis AR, Payne WS, Clagett OT, Woolner LB (1971) Surgical treatment of mediastinal tumors: a 40-year experience. J Thorac Cardiovasc Surg 62:379–392

Pulmonary Infections: Pneumonia

Roger Eibel and Jan Mueller

Contents

Abstract

The different appearances of pneumonia such as ill-defined nodules, ground-glass opacities, and consolidations can be easily detected and differentiated with MRI. Since very small nodules and calcifications are extremely challenging due to rather thick slices and loss of signal, MRI is highly recommended as a follow-up tool, to avoid repetitive investigations using ionizing radiation. With the sensitivity of T2-weighted sequences and the potential of contrast-enhanced T1-weighted sequences, important differential diagnostic considerations can be provided. Additionally, developing complications, such as pericardial or pleural effusions, empyema or lung abscess, are easily recognized. Current and future studies are to demonstrate that MRI is well suited as a monitoring and follow-up tool during and after therapy and compares favorably with CT or other imaging methods regarding sensitivity and specificity.

R. Eibel, MD (✉)
Department of Radiology, Pediatric- and Neuroradiology, HELIOS Kliniken Schwerin, Teaching Hospital of the University of Rostock, Wismarsche Str. 393, 19049 Schwerin, Germany
e-mail: roger.eibel@helios-kliniken.de

J. Mueller, MD
Diagnostic and Interventional Radiology, University Hospital Heidelberg,
Im Neuenheimer Feld 110, 69120 Heidelberg, Germany
e-mail: jan.mueller@med.uni-heidelberg.de

Key Points

The different appearances of pneumonia such as ill-defined nodules, ground-glass opacities, and consolidations can be easily detected and differentiated with MRI. Since very small nodules and calcifications are extremely challenging due to rather thick slices and loss of signal, MRI is highly recommended as a follow-up tool, to

avoid repetitive investigations using ionizing radiation. With the sensitivity of T2-weighted sequences and the potential of contrast-enhanced T1-weighted sequences, important differential diagnostic considerations can be provided. Additionally, developing complications, such as pericardial or pleural effusions, empyema or lung abscess, are easily recognized. Current and future studies are to demonstrate that MRI is well suited as a monitoring and follow-up tool during and after therapy and compares favorably with CT or other imaging methods regarding sensitivity and specificity.

1 Definition

Pneumonia is an infection of the gas-exchanging units of the lung, caused most commonly by bacteria but occasionally by viruses, fungi, parasites, and other infectious agents.

Pneumonia is the sixth leading cause of death in the United States, and the leading cause of death from infectious disease (Niederman et al. 2001). In hospitalized patients, particularly those who are mechanically ventilated, pneumonia is the leading cause of death from nosocomial infection (Campbell et al. 1996).

2 Pathogenesis

Pneumonia can result whenever the pulmonary defense mechanisms are impaired or the resistance of the host in general is lowered. Factors that affect resistance in general include:

- Chronic diseases
- Immunologic deficiency
- Treatment with immunosuppressive agents
- Leukopenia
- Unusually virulent infections

The clearing mechanisms can be interfered with by many factors, such as the following:

- Loss or suppression of the cough reflex (coma, drugs)
- Injury to the mucociliary apparatus (cigarette smoke, gas inhalation, viral diseases)
- Interference with the phagocytic or bactericidal action of alveolar macrophages (alcohol, smoke)
- Pulmonary congestion and edema
- Accumulation of secretions (cystic fibrosis, bronchial obstruction)

Some other points need to be emphasized, before listing the different classification schemes. (1) One type of pneumonia sometimes predisposes to another, especially in debilitated patients. (2) Although the portal of entry for most pneumonias is the respiratory tract, hematogenous spread from other organs can occur. (3) Many patients with chronic disease acquire terminal pneumonias while hospitalized.

3 Classification

Pneumonias are classified by the specific etiologic agent which determines the treatment, or, if no pathogen can be isolated, by the clinical setting in which the infection occurs. In the following text, the different entities of the pneumonia syndromes are briefly discussed to clarify the terms, the characteristics, and the peculiarities.

3.1 Community-Acquired Acute Pneumonia (CAP)

CAP may be bacterial or viral. Often, the bacterial infection follows an upper respiratory tract viral infection. Bacterial invasion of the lung parenchyma causes the alveoli to be filled with an inflammatory exudate, thus causing consolidation of the pulmonary tissue (Husain and Kumar 2005). Predisposing conditions include extremes of:

- Age
- Chronic diseases (congestive heart failure, COPD, and diabetes)

- Congenital or acquired immune deficiencies
- Decreased or absent splenic function (post-splenectomy, sickle cell disease)

It is beyond the scope of this chapter to describe the different pneumonias caused by various organisms, but with regard to MRI it is necessary to mention the different morphologic features common to most pneumonias.

According to the anatomic distribution in the lung, the two major categories are lobar versus bronchopneumonia. *Lobar pneumonia* is a classic manifestation of pneumococcal pneumonia in which an entire lobe is affected by the inflammatory infiltrate, with extension to the pleura or a major fissure. In patients with this type, the stages of pneumonia progress from

- Edema to
- Red hepatization (alveolar fibrin, neutrophils, lymphocytes, and pneumocyte hyperplasia)
- Gray hepatization (predominantly neutrophilic infiltrates with lysis of erythrocytes and inflammatory cells)
- Resolution (organizing pneumonia, macrophages, proliferation of loose connective tissue in distal airspaces)

The basic *radiographic pattern* of this type of pneumonia is a homogeneous consolidation with or without air bronchogram. The consolidation is bounded by the fissure and in contrast to an atelectasis no shrinkage or volume loss can be observed in the acute phase.

Bronchopneumonia is also known as lobular or focal pneumonia. It is characterized by centrilobular inflammation that is concentrated around respiratory bronchioles, with spread to the surrounding alveolar ducts and alveolar spaces. When lobular pneumonia becomes confluent, it may be difficult to separate from lobar pneumonia. From a clinical standpoint, it is sometimes difficult to apply these classic categories, more important for imaging is the determination of the extent of disease and the delineation of complications (abscess formation, empyema, organization, and dissemination, e.g., Fig. 1).
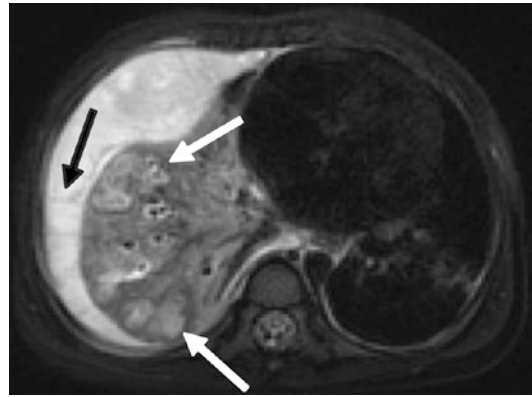
Fig. 1 A 3-year-old child with complicated pneumonia. T2-weighted MRI sequence clearly delineates intrapulmonary abscesses as focal areas of increased intensity with a hypointense rim in the right lower lobe (*white arrows*) and a large septated pleural effusion consistent with empyema (*black arrow*)

Common *radiographic findings* are nodular and patchy patterns due to involvement and sparing of acini. Sometimes volume loss can be found.

3.2 Community-Acquired Atypical Pneumonias

The term "atypical" refers to the following findings:

- Moderate amount of sputum
- No physical findings of consolidation
- Only moderate elevation of white cell count
- Lack of alveolar exudate

Most commonly this type of pneumonia is caused by *Mycoplasma pneumoniae*, viruses, and *Chlamydia pneumoniae*. These agents produce primarily an interstitial inflammation within the walls of the alveoli, resulting in thickening of the alveolar septa, later fluid accumulation, and cellular exudate into the alveolar spaces. Superimposed bacterial infection modifies the histologic and the subsequent radiologic picture (Husain and Kumar 2005).

Interpreting chest films and especially CT, *radiographic patterns* that can be found in this category are peribronchial, reticular, and

reticulonodular thickening; ground-glass opacification with filling of the acini; and sometimes a crazy-paving pattern. In some cases also a subsegmental collapse can be delineated.

3.3 Nosocomial Pneumonia

In 1995, the American Thoracic Society published a consensus statement defining nosocomial or hospital-acquired pneumonia (HAP) as a pneumonia that is

- Not incubating at the time of hospital admission
- Begins more than 48 h after admission (Campbell et al. 1996)

There are 300,000 cases of HAP annually in the United States, and it carries an associated mortality of 30–70% (McEachern and Campbell 1998). HAP is common in patients with severe underlying disease, prolonged antibiotics, intravascular devices, and mechanical ventilation. The latter is also termed ventilator-associated pneumonia (VAP). In a prospective study of 1014 mechanically ventilated patients, VAP developed in 177 patients. The mean time to onset was 9 days, with a median time to onset of 7 days after ICU admission. However, when the daily hazard rate of infection was calculated, it was estimated to be 3.3% at day 5, 2.3% at day 10, and 1.3% at day 15 (Cook et al. 1998). This documents a significant decline in pneumonia risk with time. Because the risk for pneumonia is so high early after intubation, pneumonias beginning within the first 5 days (*early-onset infection*) account for 50% of all episodes of VAP, and the natural history and pathogens of this infection differ from those associated with VAP of *late onset* (Prod'hom et al. 1994). Common isolates are gram-negative bacteria and *Staphylococcus aureus*. Typical radiologic patterns cannot be described. This is due to the different circumstances and risk factors, which contribute to the development of HAP. The other explanations are the different organisms responsible for the pneumonia. Within the first days the more common organisms are *Streptococcus pneumoniae*, *Moraxella catarrhalis*, *Staphylococcus aureus*, and

Hemophilus influenzae (Craven and Steger 1995). Later on, gram-negative rods predominate.

Microaspiration of contaminated oropharyngeal secretions seems to be the most frequent cause of HAP (McEachern and Campbell 1998). After macroaspiration, another subtype of pneumonia can occur, termed *aspiration pneumonia*. The resultant pneumonia is partly chemical, owing to the extremely irritating effects of the gastric acid appearing like pulmonary edema, and partly bacterial (from the oral flora). This type of pneumonia is often necrotizing, with abscess formation as a common complication (Husain and Kumar 2005). Typical radiographic pattern in this particular type of pneumonia are patchy consolidations in dependent portions of the lung with a multilobar and bilateral distribution.

Diagnosing HAP is difficult because there is no method for obtaining a diagnosis that is reliable in all cases. The diagnosis is initially made on clinical grounds by the finding of a new infiltrate on chest radiograph, fever, purulent sputum, or other signs of clinical deterioration. Unfortunately, this clinical method was shown to be specific for HAP in only 27 of 84 patients in a series reported by Fagon et al. (1993) because many other conditions such as congestive heart failure, pulmonary embolism, atelectasis, ARDS, pulmonary hemorrhage, or drug reactions may mimic pneumonia, particularly in critically ill patients. While there are many different testing modalities that may be employed, all have their limitations and none is sufficiently sensitive and specific to be considered a "gold standard" test (Rello et al. 2001).

3.4 Chronic Pneumonia

Chronic pneumonia results from granulomatous inflammation, due to bacteria (e.g., *Mycobacterium tuberculosis,* Fig. 2) or fungi (e.g., *Histoplasma capsulatum*, *Blastomyces dermatidis*, *Coccidioides immitis*). It is most often a localized lesion in the immunocompetent patient. Unlike tuberculosis, the abovementioned fungal species are geographic as they cause disease in particular areas in the United States and in Mexico.

In the lungs, these infections produce epithelioid cell granulomas, which usually undergo
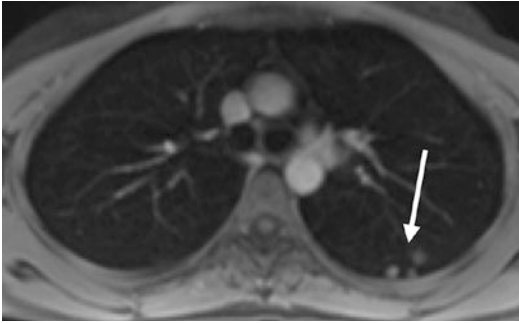
Fig. 2 A 31-year-old immunocompetent woman 12 months after exposure to tuberculosis. Positive QuantiFERONE test. Persistent sharply defined noduli in the posterior segment of the left upper lobe, consistent with tuberculomas (*arrow*). Tuberculomas can be found in primary and postprimary disease and may eventually calcify

coagulative necrosis and coalesce to produce larger areas of consolidation. Furthermore, they can liquefy to form cavities. Spontaneously or during therapy, these lesions can undergo fibrosis and concentric calcification. As a consequence, the typical *radiographic appearance* of this type of pneumonia is single or multiple lung nodules with or without calcification.

3.5 Pneumonia in the Immunocompromised Host

The appearance of pulmonary infiltrates and signs of infection (e.g., fever) are one of the most common and serious complications in patients whose immune and defense systems are limited by disease, immunosuppression for organ transplantation and tumors, or irradiation (Rosenow 1990).

The host defense system includes physical and chemical barriers to infection, the inflammatory response, and the immune response. Physical barriers, such as the skin and mucous membranes, prevent invasion by most organisms. Chemical barriers include lysozymes and hydrochloric acid. Lysozymes destroy bacteria by removing cell walls. Hydrochloric acid breaks down food and mucus that contains pathogens. The inflammatory response involves polymorphonuclear leukocytes, basophils, mast cells, platelets, and, to some extent, monocytes and macrophages. The immune response primarily involves the interaction of lymphocytes (T and B), macrophages, and macrophage-like cells and their products. These cells may be circulating or may be localized in the immune system's tissues and organs (Springhouse 2007). Primary immune deficiency diseases are disorders in which part of the body's immune system is missing or does not function properly. In contrast to secondary immune deficiency disease in which the immune system is compromised by factors outside the immune system, such as viruses or chemotherapy, the primary immune deficiency diseases are caused by intrinsic or genetic defects in the immune system.

Primary immunodeficiencies are complex diseases. Since each one can be traced to the failure of one or more parts of the immune system, one of the more convenient ways to group them is according to the part of the immune system that is insufficient:

- B cell (antibody) deficiencies
- Combined T cell and B cell (antibody) deficiencies
- T cell deficiencies
- Defective phagocytes
- Complement deficiencies
- Deficiencies/cause unknown

Antibody deficiencies can hinder or prevent the immune system from recognizing and marking for destruction bacteria, viruses, and other foreign invaders. X-linked agammaglobulinemia, an inherited deficiency that appears in the first 3 years of life, leaves infants and young children with recurrent infections of the ears, lungs, sinuses and bones, and increased susceptibility to such viruses as hepatitis and polio.

Combined immunodeficiencies occur in people who lack the T lymphocytes that develop into killer cells that destroy infected cells or become helper cells that communicate with other immune cells. X-linked severe combined immunodeficiency, most often diagnosed during the first year of life, allows organisms that do not affect people with healthy immune systems to cause frequent and life-threatening infections.

Complement deficiencies usually involve an absence of one or several of the proteins that contribute to the complement system's ability to

attach to antibody-coated foreign invaders. In childhood or early adulthood, a complement deficiency can result in severe infections such as meningitis, or it can contribute to an autoimmune disease such as lupus erythematosus.

Phagocytic cell deficiencies result in the inability of cells that engulf and kill antibody-coated invaders to act efficiently to remove pathogens or infected cells from the body. Chronic granulomatous disease, the most severe form of phagocytic deficiency, usually appears in early childhood. It causes frequent and severe infections of the skin, lungs, and bones, leaving swollen collections of inflamed tissue called granulomas.

In comparison to the secondary syndromes, primary immunodeficiencies are rare.

There are a number of common conditions associated with *secondary immunodeficiency* (Bonilla et al. 2014).

A wide variety of so-called opportunistic infectious agents, many of which rarely cause infection in normal hosts, can cause these pneumonias where often more than one agent is involved. The mortality from these opportunistic infections is high. On the other hand, the list of differential diagnoses of such infiltrates is long and includes drug reactions, cardiac failure, and involvement of the lung by tumor or other underlying conditions. Table 1 lists some of the opportunistic agents according to their prevalence and whether they cause local or diffuse pulmonary infiltrates. The large group of immunocompromised patients sometimes is divided into AIDS and non-AIDS causes of immunosuppression. The types of infection to which HIV-positive patients become susceptible vary as cell-mediated immunity becomes less effective at eradicating viruses, fungi, protozoa, and facultative intracellular bacteria, such as *Mycobacterium tuberculosis*. Knowledge of the CD4 lymphocyte count can thus be helpful for interpretation of radiologic images in AIDS patients (Marquardt and Jablonowski 2003). Table 2 gives a short overview of the CD4 counts and corresponding infections.

As mentioned previously, the radiographic patterns in most of the cases are not pathognomonic and the pattern approach is limited by underlying and concomitant diseases, by the

Table 1 Causes of pulmonary infiltrates in immunocompromised hosts

Diffuse infiltrates	Focal infiltrates
Common	*Common*
Cytomegalovirus	Gram-negative rods
Pneumocystis jiroveci	*Staphylococcus aureus*
Drug reaction	*Aspergillus*
	Candida
	Malignancy
Uncommon	*Uncommon*
Bacteria	Cryptococcus
Aspergillus	Mucor
Cryptococcus	*Pneumocystis jiroveci*
Malignancy	*Legionella pneumophila*

The table was published in Husain and Kumar (2005)

Table 2 Overview of the CD4 counts and corresponding infections

HIV: complications at CD4 >500/mm³	HIV: complications at CD4 200–500/mm³
Infectious	*Infectious*
Acute retroviral syndrome	Pneumococcal pneumonia
Candida vaginitis	Tuberculosis
	Herpes zoster
	Kaposis sarcoma
	Oral hairy leukoplakia (OHL)
	Oropharyngeal candidiasis (thrush)
Other	*Noninfectious*
Generalized lymphadenopathy	Cervical carcinoma
Guillain-Barre (very rare)	Lymphomas
Vague constitutional symptoms	Immune thrombocytopenic purpura (ITP)

severity and time factor of manifestation, and by the treatment. It is frequently impossible for the clinician to identify the causative organism of a pneumonic infiltrate. Narrowing of the etiologic differential diagnosis may be possible using *radiologic pattern* recognition and the integration with clinical and laboratory information. Although with pattern recognition, specific etiologic diagnoses can hardly ever be established, patterns help to classify groups of potentially underlying organisms.

As a general rule of thumb, localized segmental or lobar alveolar densities can be attributed to typical or atypical bacterial infections. Diffuse bilateral interstitial and/or interstitial alveolar infiltrates most commonly are caused by viruses, atypical bacteria, and protozoa.

Micronodular disease is most often caused by military tuberculosis (miliary pattern), candidiasis, and histoplasmosis (small nodules), or viruses such as herpes or varicella zoster virus (diffuse nodules with hazy borders). Large, nodular lesions may represent bacterial abscesses, and in immunocompromised patients, may be caused by invasive aspergillosis and nocardia.

In conclusion, the important tasks of imaging the lung with respect to pneumonia are:

- Detection of pulmonary abnormalities
- Support in narrowing the etiology or differential diagnosis
- Recognition of developing complications
- Demonstration of a therapeutic effect (cave: radiographic patterns may change, even deteriorate with improvement of the immunologic status of the patient)

Looking at MRI for detection of pneumonia, the next part of this chapter is divided into a historical overview mentioning older and recent MR imaging concepts and a comparison of MRI with CT in the detection of pulmonary abnormalities suspicious for pulmonary infection.

4 MRI: Historical Development of Imaging Concepts

Moore et al. (1986) investigated the differentiation of various causes of pulmonary consolidations with MRI. They analyzed patients with pulmonary edema, postobstructive pneumonitis, alveolar proteinosis, *Pneumocystis* pneumonia, lobar nonobstructive pneumonia, pulmonary hemorrhage, and acute radiation pneumonitis. The study was performed with a 0.35-T MR scanner, using spin-echo pulse sequences with repetition times of 500 and 2000 ms and echo times (TE) of 28 and 56 ms. The authors could

demonstrate that measuring T1 and T2 values for different entities showed considerable overlap. The two patients with pulmonary alveolar proteinosis showed much lower values of T1, which probably reflects the relative absence of water within the airspaces and the presence of lipoprotein. In general, T1 and T2 values increase in proportion to the water content of fluids or tissue, but they are also influenced by the presence of lipids and by interaction between water and both large and small molecules with which they come in contact (Moore et al. 1986).

High-resolution computed tomography (HRCT) had become the gold standard in the evaluation of chronic infiltrative lung diseases, and it was shown that it accurately reflects the pathologic abnormalities. The aim of a study from Müller et al. (1992) was to compare MRI with HRCT in the assessment of these entities. All MR studies were performed on a 1.5-T MR imager. Cardiac-gated proton density-weighted and relatively T2-weighted images were obtained at two or three RR intervals. The slice thickness was 10 mm, with a 1- or 2-mm interslice gap. In comparison to this, the CT scans were obtained by using 1.5-mm collimation scans and 10-mm intervals.

As a result, MRI was consistently inferior in the anatomic assessment of lung parenchyma and in showing interstitial abnormalities, particularly fibrosis. Furthermore, areas of mild interstitial abnormalities seen on CT were often not apparent on MRI. But, on the other hand, MRI was comparable to CT in the assessment of air-space abnormalities. In all patients, areas with ground-glass opacities or air-space consolidation on CT corresponded to areas of increased signal intensity on MRI (Müller et al. 1992).

Primack et al. noticed that the use of MRI in the assessment of infiltrative lung disease has been limited by the low proton density of lung parenchyma and by loss of signal due to motion and the difference in diamagnetic susceptibility of air and soft tissue. On the other hand, the presence of pulmonary infiltrates leads to a marked increase in signal intensity. This is due to both the increase in proton density and a decrease in magnetic susceptibility effects. This study demonstrated that the MRI findings correlate with the pathologic

findings and that parenchymal opacification on MRI usually indicates an inflammatory process, and therefore potentially treatable disease (Primack et al. 1994).

One of the earlier studies that focused on contrast-enhanced pulmonary MRI was published by Haraldseth et al. (1999). They reviewed different forms of contrast agent enhancement: MR perfusion imaging, contrast-enhanced MR angiography, and MR ventilation imaging. In the clinical context of pneumonia, they included 13 patients. The MR perfusion was obtained with a standard low flip-angle gradient-echo sequence with an inversion prepulse. The time-intensity curves after intravenous application of a gadolinium-based nonspecific contrast agent showed that in pneumonic tissue there was a steep increase without first passage peak; the dynamics of the contrast agent passage was different from normal lung tissue. The authors did not suggest replacement of chest X-rays for routine pneumonia diagnosis, but in cases where the differential diagnosis between pulmonary embolism and pneumonia were two main options, patients might benefit from an MR perfusion examination (Haraldseth et al. 1999).

A more detailed description of MRI of the pulmonary parenchyma was published by Kauczor and Kreitner (1999). As a brief summary of the technical considerations, the authors noticed the following three factors hampering the application of MRI to the lung and suggested the following strategies to resolve the problems:

1. *Low proton density*: This is valid for the normal lung parenchyma and especially for lung diseases with loss of tissue such as emphysema. In all other lung diseases, the amount of tissue, fluid, and/or cells is increased. The recommended investigation techniques are:
   (a) T1-weighted spin-echo sequences with short echo times (<7 ms)
   (b) T1-weighted gradient-echo sequences, such as fast low-angle shot (FLASH), with short echo times (3 ms)
   (c) Higher number of acquisitions
   (d) Administration of contrast agents
2. *Signal loss due to physiological motion*:
   (a) Breath-hold imaging with fast sequences like FLASH or half-Fourier acquisition single-shot turbo spin echo (HASTE)
   (b) Respiratory gating with navigating techniques, gating in expiration using a belt, and respiratory compensation using reordering of phase encoding
   (c) ECG triggering
3. *Susceptibility artifacts because of the multiple air-tissue interfaces*: As mentioned previously, these artifacts degrade imaging of normal lung tissue. After loss of air and concomitant increase of tissue, cells or fluid significantly reduces the number of air-tissue interfaces and the degree of susceptibility artifacts.
   (a) Use of short echo times for T1-weighted spin-echo or gradient-echo sequences
   (b) Use of T2-weighted turbo-spin-echo (TSE) sequences or T2-weighted ultrafast TSE-sequences with high turbo factors

With regard to infiltrations, the authors concluded that MRI can be used for the detection and characterization of inflammatory pulmonary round infiltrates in immunocompromised patients. Postcontrast T1-weighted FLASH showed a strongly enhancing, ill-defined round infiltration (Fig. 3), and with HASTE sequence moderate signal intensity was
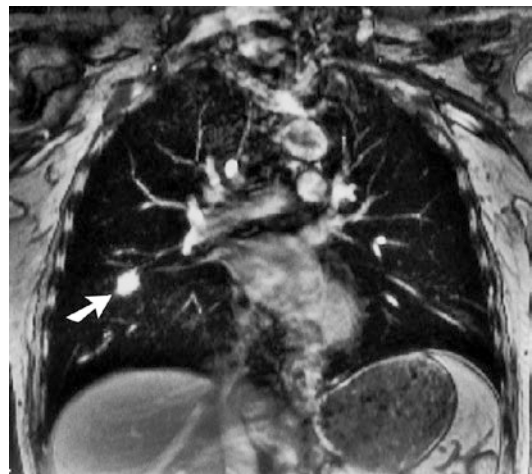
Fig. 3 A 45-year-old male patient with invasive aspergillosis. Postcontrast T1-weighted FLASH (TR >200 ms, TE = 4 ms, FA = 80°) shows a strongly enhancing, ill-defined round infiltration (*arrow*) (With permission of Springer: Kauczor and Kreitner 1999)
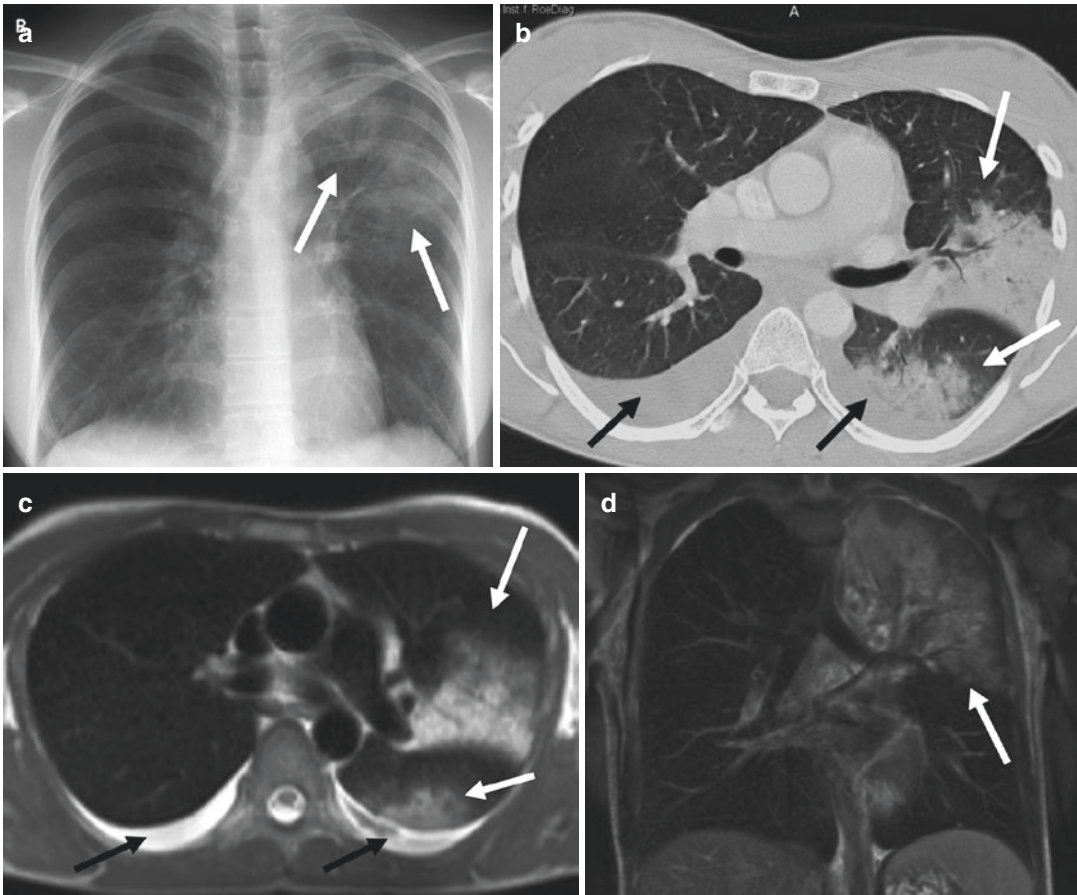
Fig. 4 A 29-year-old female with bilobar pneumonia of the left lung (*white arrows*) and bilateral pleural effusions (*black arrows*). A pathogen could not be identified. (**a**) X-ray of the chest, (**b**) helical CT (slice thickness 3 mm), and corresponding MRI (HASTE, TE 48 ms, slice thickness 6 mm) in (**c**) axial, and (**d**) coronal direction (With permission of Springer: Kauczor and Kreitner 1999)

found in a patient with bronchopneumonia (Fig. 4a–d) (Kauczor and Kreitner 1999).

Gaeta et al. (2000) revisited the value of gadolinium-enhanced MRI in the evaluation of chronic infiltrative lung disease. They found out that the presence of enhancing lesions on gadolinium-enhanced T1-weighted MRI studies may be a reliable indicator of inflammation and, consequently, indicates potentially treatable disease. Their study was performed on a 1.5-T scanner obtaining a spoiled gradient-echo T1-weighted sequence during full inspiration (TR 168 ms, TE 4.8 ms, FA 75°, slice thickness 5 mm) (Gaeta et al. 2000).

Another topic in literature is the differentiation between benign and malignant nodular lesions of the lung. Growth factors and calcification pattern are only two of the noninvasive diagnostic criteria to separate benign from suspicious lesions and avoid unnecessary invasive tests. To overcome the limitation of morphological features, Li et al. (2000) included 62 patients to be evaluated for suspicious lung nodules with CT and dynamic Gd-DTPA-enhanced MRI. Axial T1-weighted images (TR 500 ms, TE 10 ms) with a slice thickness of 5 mm at 0, 15, 45, 75, 110, and 140 s, and 3, 5, 8, and 10 min were obtained. Additional T2-weighted images (TR 3000 ms, TE 80 ms) were acquired before contrast application. After correlation with pathological findings, they found that nodular fibrosis, inflammatory granulomas, cryptococcoma, and inflammatory pseudotumor had a more or less low rate of contrast uptake.

On the other hand, focal organizing pneumonia and sclerosing hemangioma had a significant and early enhancement. Taking into account that malignant nodules are characterized by a fast increase in signal intensity during the first pass of the contrast agent (Gückel et al. 1996), malignancy of some nodular lesions could be excluded by dynamic MRI (Li et al. 2000).

Rupprecht et al. (2002) performed a study without contrast agent and investigated a steady-state free precession sequence (true FISP) as a potential alternative to the conventional X-ray in pediatric patients with suspected pneumonia. A true FISP sequence was chosen because of its high spatial resolution and signal-to-noise ratio (S/N) in fluid- and thus T2-dominated infectious pulmonary disease. To overcome breathing artifacts in this particular patient group and to increase the S/N ratio, they obtained slice thicknesses of 30–55 mm at a 0.2-T low-field MR system. The true FISP sequence had the following parameters: TR 6 ms, TE 3 ms, FA 90°. The acquisition time for a triple slice scan was 4.8 s, and the door-to-door time was between 10 and 15 min. All pathological findings in the conventional chest X-ray could be identified in the corresponding MR investigation, and the MRI was superior in demonstrating pleural and pericardial effusions. Two small retrocardial pneumonic infiltrates were noted in the MRI only. The authors concluded that this technique could represent an alternative to the conventional chest X-ray (Rupprecht et al. 2002). Such an alternative might be of special interest in children with Nijmegen-Breakage syndrome. This entity is an autosomal recessive chromosomal instability syndrome, characterized by microcephaly, growth retardation, skin abnormalities, immunodeficiency, radiation sensitivity, and a strong predisposition to lymphoid malignancy. Because of their sensitivity to ionizing radiation, X-ray and CT examination should be avoided (Alibek et al. 2007).

Whether it is possible not only to detect but also to quantify pulmonary lesions due to pneumococcal pneumonia was investigated in a murine model by Marzola et al. (2005). Infection was induced in a group of mice ($N = 5$) by intranasal administration of a sus-

pension containing *Streptococcus pneumoniae*, and a group of noninfected animals ($N = 5$) was used as a control group. Axial, ECG-gated, spoiled GRE images with 1.2-mm slice thickness were acquired with a 4.7-T scanner. After sacrifice and histological evaluation, a good concordance with regard to the anatomical localization and a good correlation between the volume of the pneumoniae by histology and MRI was found (Marzola et al. 2005).

Another interesting experimental study was published by Tournebize et al. (2006). The aim of this work was to prove if MRI is able to provide spatiotemporal visualization of edema and inflammation caused by *Klebsiella pneumoniae*–induced pneumonia in mice. The study was performed with a 7-T scanner. After inoculation with avirulent and virulent strains of *Klebsiella*, treatment by bactericidal doses of antibiotics was initiated. Images were acquired up to 8 days post infection. The virulent strain caused an intense inflammation within 2 days in the whole lungs, while an avirulent strain did not show significant changes. The increase in cell density accompanied with extravascular leakage results in an increase in high water content detectable by MRI. After treatment with antibiotics, the inflammation disappeared after a week. The lesions observed by MRI correlated with the damage seen by histological analysis. In summary, MRI allows observing the appearance and regression of inflammation (Tournebize et al. 2006).

The next important topic was the investigation of the sensitivity of MRI in detecting alveolar infiltrates. To provide reliable data, Biederer et al. (2002) performed an experimental study using porcine lung explants and a dedicated chest phantom to evaluate the signal intensity of artificial alveolar infiltrates with T1- and T2-weighted MRI sequences. Ten porcine lung explants were examined with MRI at 1.5 T before and after intratracheal instillation of either 100 or 200 ml gelatine-stabilized liquid to simulate alveolar infiltrates. Control studies were acquired with helical CT.

After administration of the gelatine-stabilized liquid, the CT images demonstrated patchy areas of ground-glass opacities in both lungs. The 2D and 3D T1-weighted sequences could not

sufficiently visualize the infiltrates. In contrast, the T2-weighted sequences showed clearly visible infiltrates with an increase in signal intensity of approximately 30% at 100 ml (p <0.01) and 60% at 200 ml (p <0.01). For practical reasons, T2-weighted sequences can be highly recommended for the delineation of infiltrates in the lung. T1-weighted sequences without intravenous application of contrast agents are not sufficient for this task. Because of the extremely different acquisition times between HASTE and the T2-TSE, the HASTE sequence has to be preferred.

Based on these technical developments, it is necessary to evaluate the potential of MRI in detecting pneumonia in the immunocompromised patient. Especially in this particular group of patients, pneumonia is an important cause of morbidity and mortality. The imaging of infiltrates is very challenging, because the immunosuppression decreases the response of the lung to infectious agents. On the other hand, the patterns of pneumonia are highly variable and depend on multiple factors, like underlying diseases, time course, and treatment. By now, a considerable proportion of pulmonary fungal infections are not diagnosed antemortem in cancer patients. In addition, especially patients after bone marrow transplantation are often younger, and repetitive CT examinations carry an additional radiation burden.

Leutner et al. (2000) tried to find out how MRI compares with CT regarding the depiction of typical features of pneumonia and the detectability of lesions. MRI studies were performed with a 1.5-T system, and the imaging protocol consisted of a transversal T2-weighted ultrashort turbo spin-echo sequence (TR 2000–4000 ms, TE 90 ms, slice thickness 6 mm, and six numbers of excitation). In comparison to helical CT (slice thickness 8 mm), they evaluated presence, number, and location of pulmonary infiltrates (nodular, reticular, cysts, cavitation, consolidation, and ground-glass infiltration). In summary, most of the CT and MR examinations (75%) were rated as showing identical results concerning not only the number but also the morphology of different lesions that were due to opportunistic pneumonia. In addition, MRI was able to differentiate between consolidation and ground-glass infiltration (Leutner et al. 2000).

5 MRI: Comparison with CT

The advent of multidetector CT and the implementation of parallel imaging in MRI pushed the limits towards new possibilities with regard to examination volume, time, and slice thickness. Multidetector CT offers the opportunity to investigate the entire lung with 1-mm slice thickness or less in a couple of seconds. Parallel imaging in MRI reduced the examination time dramatically and made MRI of the lungs in a few seconds a reality.

Multidetector CT with thin sections is the gold standard for the evaluation of the lung even for very subtle lesions like small ground-glass opacities around lung nodules. That means, to classify the value of MRI of the lung, studies are necessary that compare MRI with the best CT techniques that are available nowadays.

Eibel et al. (2006b) performed a study where they investigated pulmonary abnormalities in 30 immunocompromised patients with parallel MRI and thin-section helical CT. It was not the intention of this study to investigate the lung comprehensively. In order not to exceed 1-min examination time, only the HASTE sequence was selected. The resulting in-room-time was not more than 10 min. The motivation was that MRI can only serve as a real alternative to CT, when the examination time is short.

One of the inclusion criteria for this study was an X-ray of the chest that was either normal or did not show abnormalities suggestive of pulmonary infection. Ill-defined nodules, ground-glass opacity areas, and consolidations, their location and distribution, and their lesion characteristics (e.g., margin contour, cavitation, calcification) were systematically analyzed. Twenty-two patients had pulmonary abnormalities on CT. In 21 (95%) patients, pneumonia was correctly diagnosed with MRI. One false-negative finding occurred in a patient with ill-defined nodules smaller than 1 cm at CT. One false-positive finding with MR was the result of blurring and respiratory artifacts. That results in a sensitivity of MRI in comparison to 1-mm CT slices of 95%, specificity of 88%, positive predictive value of 95%, and a negative predictive value of 88% (Eibel et al. 2006a). In the detection of ground-glass opacity areas (Figs. 5 and 6), consolidations (Fig. 7),
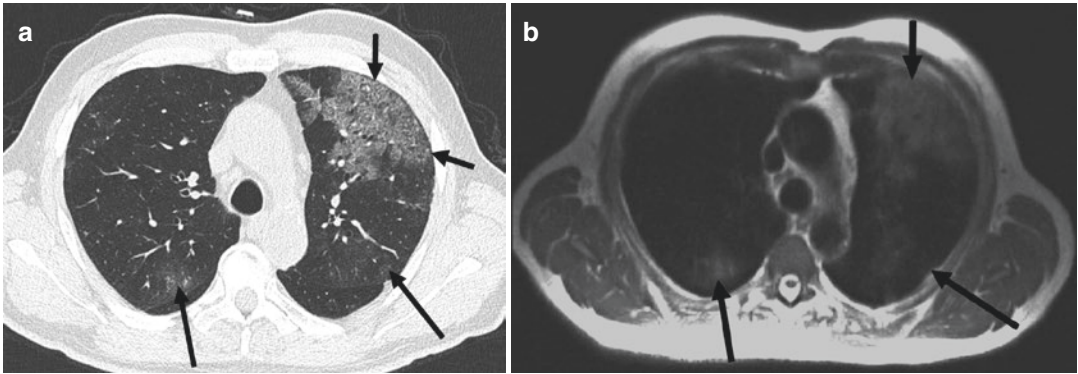
Fig. 5 A 76-year-old patient with myelodysplasia suffering from *Pneumocystis jiroveci* pneumonia (With the permission of Springer: Eibel et al. 2006a). (**a**) Thin-section CT above the level of the carina. Ground-glass opacity is the predominant finding in the ventral portion of the left upper lobe (*short arrows*). Please note also the more subtle lesions in the dorsal parts of the both upper lobes (*long arrows*). (**b**) Axial HASTE sequence at the same level (TE 27 ms). All lesions in the upper lobes are easily detectable
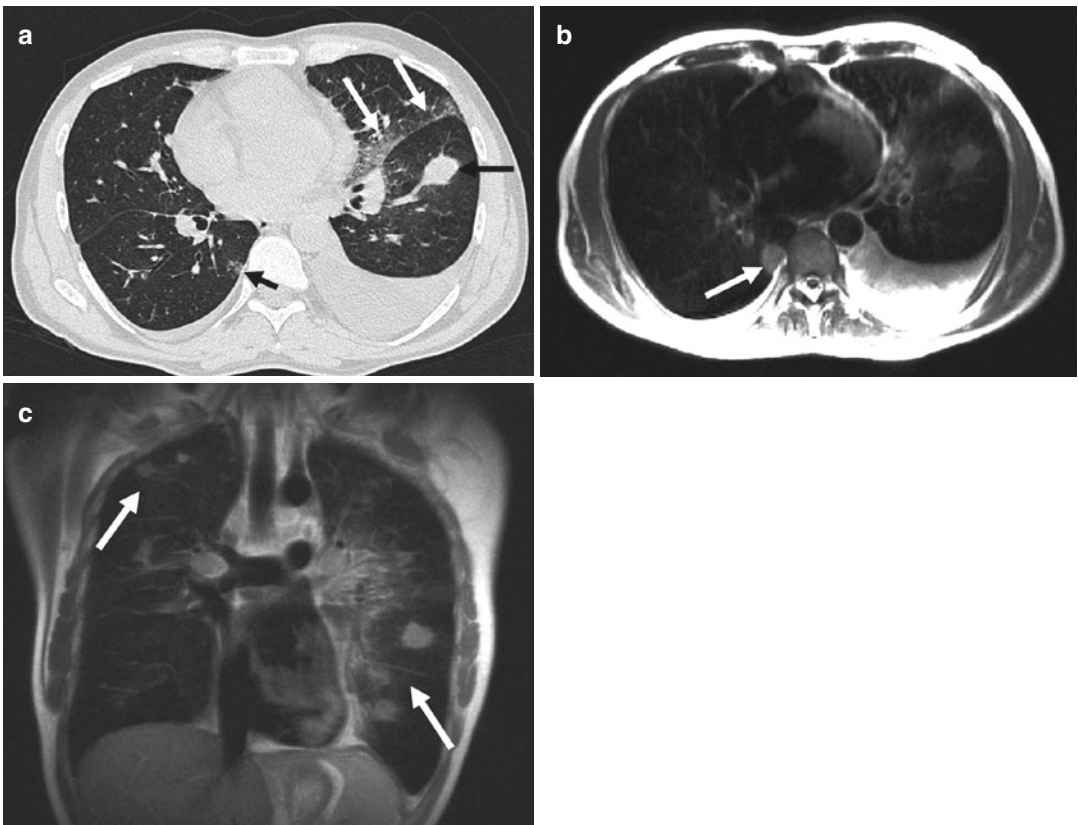
Fig. 6 A 45-year-old male with chronic lymphatic leukemia, now suffering from angioinvasive aspergillosis (With the permission of Springer: Eibel et al. 2006a). (**a**) Thin-section CT below the level of the carina shows a consolidation in the left lower lobe (*black arrow*), ground-glass opacity in the lingula adjacent to the fissure (*white arrows*), and both-sided pleural effusions. Please note also the subtle lesion in the right lower lobe adjacent to the spine (*short arrow*). (**b**) Axial HASTE. (**c**) Coronal HASTE. The pathologic findings are again comprehensively delineated by MRI (*arrow*), even the subtle lesion in the right lower lobe adjacent to the spine (axial HASTE)

Fig. 7 A 15-year-old girl with hyper IgE syndrome. Pneumectomy of the right lung due to recurrent complicated pneumonia (axial true FISP sequence). Preexisting thin-walled cavitary lesion in the left upper lobe with a new ovoid nodule in the dependent portion demonstrating the "air-crescent sign" in aspergilloma (*arrows*). The development of an "air-crescent sign" in a pulmonary nodule may also be interpreted as a sign of recovery when found in angioinvasive aspergillosis

and pleural effusion, MRI seems to be equal to thin-section CT. But the overall detection rate of nodules with MRI was only 72% (186/259). Detailed analyses found out that all nodules larger than 10 mm were reliably detected. The mean size of nodular lesions not found with MRI was 4 mm. This difference likely relates to the section thickness used with CT (1 mm) and MR imaging (6 mm). After this study, the authors came to the conclusion that pulmonary imaging for the detection and quantification of infiltrates is highly reliable with modern MR scanners (Eibel et al. 2006b).

Despite these encouraging results, it is important to keep in mind that CT has to be preferred in the detection of calcification, which can indicate some special disease entities and can be a sign of pulmonary scarring.

6 Morphology of Different Types of Pneumonia in MR Imaging

Before summarizing briefly the different MR features of pneumonia, already mentioned in the paragraphs before, the following statements are valid for MR imaging of pneumonia:

- Nodules larger than 1 cm in diameter, consolidations, and ground-glass opacifications are

Table 3 MRI findings and corresponding likely causative organisms

MRI findings	Likely causative organisms
Lobar consolidation = lobar pneumonia	*Streptococcus pneumoniae*, *Klebsiella pneumoniae*, *Legionella pneumophilia*, *Mycoplasma pneumoniae*
Patchy, sometimes bilateral interlobular consolidation = bronchopneumonia	Streptococci, gram-negative bacilli, *Legionella*, anaerobes, virus
Ground-glass opacification and reticular pattern = interstitial pneumonia	Virus, *Mycoplasma pneumoniae*, *Pneumocystis jiroveci* (Fig. 5)
Cavitation	*Staphylococcus aureus*, *Mycobacterium tuberculosis*, gram-negative bacilli, anaerobic bacteria
Round consolidation, halo, air-crescent sign, reverse target sign	*Aspergillus fumigatus* (Fig. 7)

detectable on MR images with a nearly identical sensitivity and accuracy with regard to lesion size and contour compared to CT. Obviously the definition of nodule, consolidation, and ground-glass according to the Fleischner Society seems to be valid even for MRI (Hansell et al. 2008).

- With MR images, it might be more challenging to delineate small nodules (<10 mm) and especially small areas of air or calcifications within lung nodules or consolidations in comparison to multidetector CT.

In Table 3, the most common and important features of pneumonia on MR images, derived from the findings on CT examinations, and the likely causative organisms are summarized. Of course, host conditions must been taken into account too.

Fungal pneumonia is an important topic, necessary to go a little bit more into detail, especially when dealing with MR imaging. Some organisms like *Histoplasma capsulatum* and *Coccidioides immitis* are primary pathogens, but are found only in specific geographic areas. On the other hand, organisms like *Aspergillus* and *Candida* species are opportunistic agents that affect

patients that already suffer from an underlying pulmonary disease or are immunocompromised. As invasive organisms, the latter can cause severe tissue destruction and can influence the clinical outcome dramatically.

The pathogenesis of *Aspergillus* infection is complex, but worthy to know is the fact that this fungus causes necrosis in lung parenchyma due to extensive vascular permeation and occlusion of small to medium arteries. This permeation and especially the separation of necrotic lung from viable parenchyma in the recovery phase of the patient can cause life-threatening intraalveolar hemorrhage.

Because of the different therapeutic approaches in patients with fungal pneumonia and because of the high morbidity and mortality in immunosuppressed patients with invasive aspergillosis, it is necessary to know the signs of this type of infection in imaging studies:

- Single or multiple nodular infiltrates
- Nodule with halo phenomenon
- Homogeneous consolidation in segmental or subsegmental spread
- Cavitation (air-crescent sign, Fig. 7)
- Reverse target sign

The ground-glass attenuation surrounding some of the nodules is termed as halo. Histopathologic studies delineated that the cause for this finding is hemorrhage around the nodule. With MR, the halo sign is clearly detectable and thus can help to differentiate the causative agents. Air crescent is a finding more commonly detectable in the recovery phase and relates to resorption of necrotic tissue in the periphery of the lesion or to retraction of the sequestrum from viable lung parenchyma (Kim et al. 2001). This crescent like air collection is associated with a higher risk of massive hemoptysis.

Blum et al. (1994) observed another characteristic feature of necrotizing pneumonia. On T2-weighted images, higher signal intensity in the center combined with comparatively lower signal intensity in the rim outlined a characteristic feature that they called "reverse target sign." While the halo phenomenon is strongly suggestive of invasive aspergillosis in its early course, the reverse target sign is detectable in later stages.

Probably because of the excellent soft-tissue contrast on MR imaging, Leutner et al. (2000) found that MRI is superior to contrast-enhanced CT in diagnosing necrotizing pneumonia.

Barreto et al. summarized the correlation between common CT and MRI findings of parenchymal lung disease in patients suffering from pneumonia (Barreto et al. 2013).

Up to now, no comprehensive study compared the sensitivity and specificity of different imaging modalities for the diagnosis of invasive aspergillosis. Blum et al. (1994) found out that MRI may be of diagnostic value in later stages of the disease and for the follow-up of nodular infiltrates on unknown etiology in immunocompromised patients. So, further studies are necessary to lower the high mortality of angioinvasive aspergillosis by making the diagnosis earlier and with a higher reliability.

7   Protocol

In this paragraph, a short protocol recommendation (Table 4) is listed, confirmed, and illustrated by an upper lobe pneumonia (Fig. 8).

The T2-weighted HASTE sequence is the workhorse, necessary for detection and characterization of infectious lesions of the lung. Performing only the topogram and the axial HASTE in patients that are severely ill and breathless, the investigation time is below 2 min. The T1-weighted FLASH sequence with and without intravenous application of gadolinium is helpful for further characterization of infiltrates. This extends the investigation time to 15 min. The STIR and true FISP sequences can give additional information selected cases, but they are not required in routine settings.

8   Further Developments

This chapter deals with some remarkable results of recent research and promising new applications and sequences of MRI in pulmonary infection imaging. Despite the benefits of CT in delineating abnormalities in the pulmonary parenchyma, the power in differentiating benign

Table 4 Suggested investigation protocol at a 1.5 T MR scanner

Sequence	Acronyms	Weighting	Slice orientation	TR (ms)	TE (ms)	Flip angle	FS	Slice thickness (mm)	Gd IV
Topogram									
Ultra-fast SE	UFSE, HASTE, SS-FSE	T2	Axial	1000	84	180		6	
		T2	Coronal	1000	84	180		6	
		T2	Sagittal	1000	84	180		6	
Spoiled GE	T1-FFE, FLASH, SPGR	T1	Axial	118	2	70		6	
		T1	Coronal	78	2	70	+	6	
STIR	STIR	T2	Axial	3980	100	150	+	6	
Balanced GE	Balanced FFE, true FISP, FIESTA	T2	Axial	3	1	60		6	
		T2	Coronal	3	1	60		6	
Spoiled GE	T1-FFE, FLASH, SPGR	T1	Axial	118	2	70	+	6	+
		T1	Coronal	78	2	70	+	6	+

Abbreviations: *FFE* fast field echo, *FIESTA* fast imaging employing steady-state acquisition, *FLASH* fast low-angle shot, *FS* fat saturation, *Gd IV* gadolinium intravenously, *GE* gradient echo, *HASTE* half-Fourier acquisition single-shot turbo spin echo, *IR* inversion recovery, *SE* spin echo, *SPGR* spoiled gradient recalled echo, *SS-FSE* single-shot fast spin echo, *STIR* short TI inversion recovery, *TE* time to echo, *TR* repetition time, *true FISP* true fast imaging with steady-state precession, *UFSE* ultra-fast spin echo
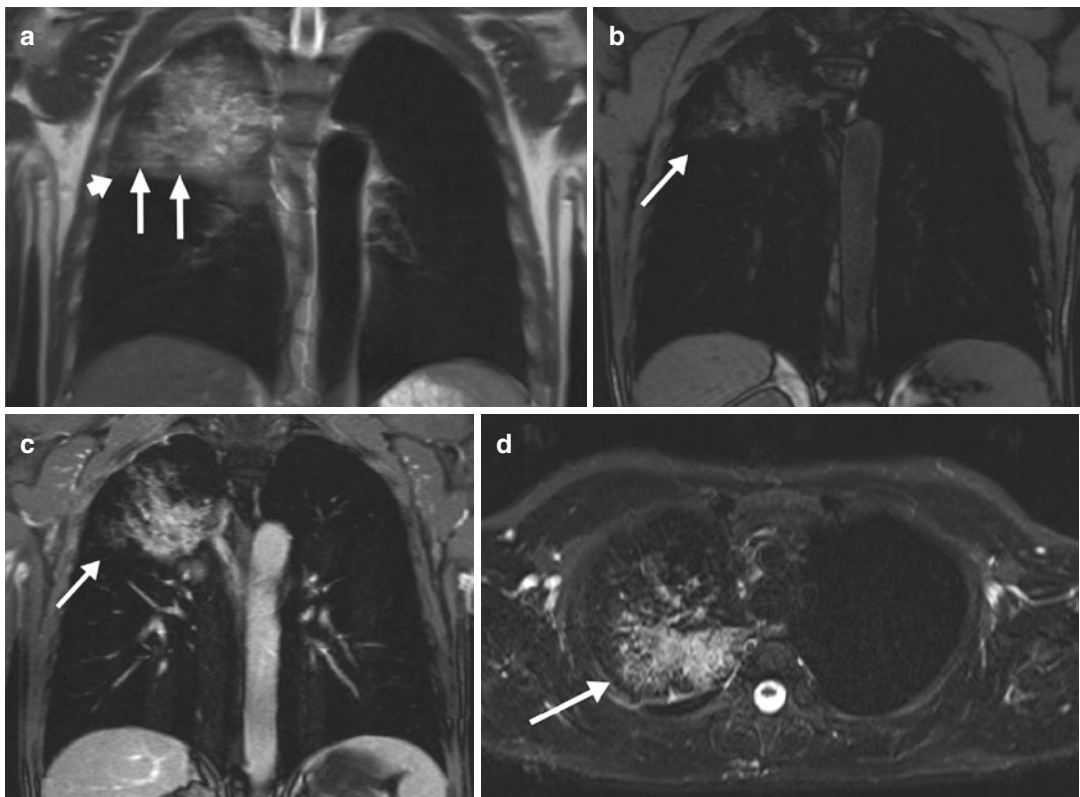
Fig. 8 A 51-year-old male with right upper lobe pneumonia (*Streptococcus*). (**a**) Coronal HASTE. The horizontal fissure (*short arrow*) is not exceeded by the pneumonia (*arrows*). (**b**) Coronal FLASH with spectral fat saturation, before intravenous contrast administration. (**c**) Coronal FLASH, after delivery of 14 ml gadolinium IV (0.1 mmol/kg). (**d**) Axial STIR. The edema is clearly detectable in the right upper lobe pneumonia (*arrow*), but the degree of artifacts and noise is higher in comparison to the HASTE sequence. (**e**) Coronal true FISP. The vessels are clearly detectable (*short arrows*). So this sequence can be an alternative to the contrast-enhanced FLASH to delineated adjacent vasculature. The pneumonia itself is not better appreciable in comparison to the HASTE and contrast-enhanced FLASH
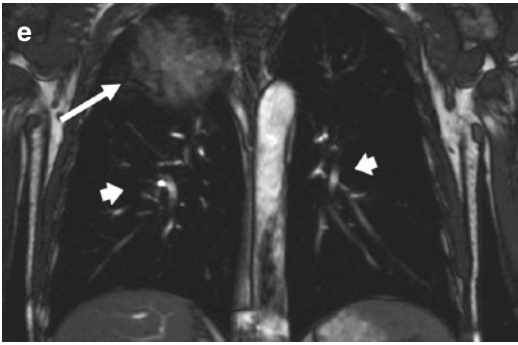
Fig. 8 (continued)

from malignant lesions is limited. This is especially true for the differentiation of pneumonia-like mucinous adenocarcinoma and infectious pneumonia. This type of carcinoma has a rising incidence and carries a poor prognosis. Because of the similarities to pneumonia at radiography and CT, the correct diagnosis is often performed with delay. Gaeta et al. found out that water-sensitive sequences (axial HASTE and coronal RARE) can add substantial information. In this study, the correct diagnoses of mucinous adenocarcinomas and pneumonia on CT images were possible in 74% and 73% for reader 1 and 65% and 80% reader 2, whereas both readers could make the correct diagnosis in 100% of cases with the aid of these two MR sequences. The most important finding was the so-called white lung sign, which is positive due to the high intratumoral content of mucin, but is negative in pneumonia (Gaeta et al. 2011).

An important topic is the use of MRI in young patients. It is known from a study of Pearce et al. (2012) that MDCT, which can deliver a cumulative radiation dose of approximately 50 mGy, may triple the risk of development of leukemia and that doses of approximately 60 mGy may triple the risk of brain cancer in children. So a major advantage of MRI is the lack of ionizing radiation. But therefore it is necessary to make confident diagnoses on MR images. Gorkem et al. could demonstrate that with contrast-enhanced MDCT findings as the reference standard, unenhanced MRI with fast-imaging-sequences accurately depicted 94%

lung abnormalities (consolidation, cystic hydatid disease, bronchiectasis, lung masses and nodules), 100% mediastinal masses, 100% pleural effusions, and 100% chest wall masses. The two undiagnosed findings with MRI were mild bronchiectasis and small pulmonary nodule (3 mm). Taking these results into account, the authors concluded that unenhanced MRI can be the first-line cross-sectional imaging in lieu of contrast-enhanced MDCT. This seems particularly true for pediatric patients who need multiple imaging studies for monitoring diseases (Gorkem et al. 2013).

In addition, Wielpütz et al. focused on a particular disease in the pediatric and adolescent group, the cystic fibrosis (CF). Demirkazik et al. (2001) found out that MDCT is more sensitive than chest radiograph in delineating the CF-associated pulmonary alterations. In recent development, MRI is increasingly replacing MDCT as the technique for diagnosing complications or monitoring the disease (Wielpütz et al. 2013). MRI shows the typical changes of bronchiectasis, wall thickening, mucus plugging, and infiltrates ("plus pathologies" on MRI) sensitively and with comparable clinical relevance compared to MDCT (Puderbach et al. 2007). Furthermore, MR perfusion imaging making use of hypoxic pulmonary vasoconstriction (Euler-Liljestrand reflex) shows potentially reversible perfusion and ventilation impairment. At present, MRI is being used for the first time in a German multicenter study in the framework of the neonatal cystic fibrosis screening program, providing a secondary surrogate endpoint for preventive treatment strategies (Wielpütz et al. 2014).

Despite further developments in MR imaging, CT outnumbers MRI in pulmonary imaging by far. Explanations are manifold like higher resolution, shorter scan times, availability, patient access during examination, and of course economic factors. Reducing artifacts, receiving more signal, and observing a higher degree of anatomical information will result in longer examination times which on the other hand is limited by the time the patient is able to stop breathing. Therefore, free breathing would be necessary which may lead to respiratory and blurring artifacts.

To overcome this problem, Völker et al. (2015) published a feasibility study using a versatile multishot radial TSE sequence under free breathing with modified golden-ratio-based reordering designed to prevent coherent streaking. They investigated healthy volunteers and patients with lung cancer and pneumonia, while the data were acquired during free respiration in a 90-s scan time. In conclusion, the authors found that this radial TSE sequence in combination with a modified golden-ratio-based reordering offers improved robustness towards motion. This allows for longer scan times over several respiratory cycles, thereby improving the SNR and facilitating high-quality morphological lung MRI which may help to improve the diagnosis of subtle disease. Restrictively, the performance with regard to making the diagnosis of pneumonia or lung cancer earlier, or with more confidence, was not evaluated in this study. Here further work is necessary.

References

Alibek S, Holter W, Staatz G (2007) The radiosensitive child: pulmonary MR tomography in EBV-induced lymphoproliferation in Nijmegen-breakage syndrome. FortschrRöntgenstr 179:1075–1077

Barreto MM, Rafful PP, Rodrigues RS, Zanetti G, Hochhegger B, Souza AS, Guimaraes MD, Marchiori E (2013) Correlation between computed tomographic and magnetic resonance imaging findings of parenchymal lung diseases. Eur J Radiol 82:492–501

Biederer J, Busse I, Grimm J, Reuter M, Muhle C, Freitag S, Heller M (2002) Sensitivity of MRI in detecting alveolar infiltrates: experimental studies. FortschrRöntgenstr 174:1033–1039

Blum U, Windfuhr M, Buitrago-Tellez C, Sigmund G, Herbst EW, Langer M (1994) Invasive pulmonary aspergillosis. MRI, CT, and plain radiographic findings and their contribution for early diagnosis. Chest 106:1156–1161

Bonilla FA, Stiehm ER, Feldweg AM (2014) Secondary immunodeficiency due to underlying disease states, environmental exposures, and miscellaneous causes. In: UpToDate Wolters Kluwer, Alphen aan den Rijn, NL

Campbell GD, Niederman MS, Broughton WA et al (1996) Hospital-acquired pneumonia in adults: diagnosis, assessment of severity, initial antimicrobial therapy, and preventative strategies: a consensus statement. Am J Respir Crit Care Med 153:1711–1725

Cook DJ, Walter SD, Cook RJ et al (1998) Incidence of and risk factors for ventilator-associated pneumonia in critically ill patients: results from a multicenter prospective study on 996 patients. Ann Intern Med 129:433–440

Craven DE, Steger KA (1995) Epidemiology of nosocomial pneumonia. New perspectives on an old disease. Chest 108:1S–16S

Demirkazik FB, Ariyürek OM, Ozçelik U, Göçmen A, Hassanabad HK, Kiper N (2001) High resolution CT in children with cystic fibrosis: correlation with pulmonary functions and radiographic scores. Eur J Radiol 37(1):54–59

Eibel R, Herzog P, Dietrich O, Rieger C, Ostermann H, Reiser M, Schoenberg S (2006a) Magnetic resonance imaging in the evaluation of pneumonia. Radiologe 46:267–270. , 272–274

Eibel R, Herzog P, Dietrich O, Rieger CT, Ostermann H, Reiser MF, Schoenberg SO (2006b) Pulmonary abnormalities in immunocompromised patients: comparative detection with parallel acquisition MR imaging and thin-section helical CT. Radiology 241:880–891

Fagon JY, Chastre J, Hance AJ, Domart Y, Trouillet JL, Gibert C (1993) Evaluation of clinical judgment in the identification and treatment of nosocomial pneumonia in ventilated patients. Chest 103:547–553

Gaeta M, Blandino A, Scribano E, Minutoli F, Barone M, Andò F, Pandolfo I (2000) Chronic infiltrative lung diseases: value of gadolinium-enhanced MRI in the evaluation of disease activity–early report. Chest 117:1173–1178

Gaeta M, Ascenti G, Mazziotti S, Contiguglia R, Barone M, Mileto A (2011) MRI differentiation of pneumonia-like mucinous adenocarcinoma and infectious pneumonia. Eur J Radiol 81(11):3587–3591

Gorkem SB, Coskun A, Yikilmaz A, Zurakowski D, Mulkern RV, Lee EY (2013) Evaluation of pediatric thoracic disorders: comparison of unenhanced fast-imaging-sequence 1.5-T MRI and contrast-enhanced MDCT. Am J Roentgenol 200(6):1352–1357

Gückel C, Schnabel K, Deimling M, Steinbrich W (1996) Solitary pulmonary nodules: MR evaluation of enhancement patterns with contrast-enhanced dynamic snapshot gradient- echo imaging. Radiology 200:681–686

Hansell DM, Bankier AA, MacMahon H, McLeod TC, Müller NL, Remy J (2008) Fleischner Society: glossary of terms for thoracic imaging. Radiology 246:697–722

Haraldseth O, Amundsen T, Rinck PA (1999) Contrast-enhanced pulmonary MR imaging. MAGMA 8:146–153

Husain AN, Kumar V (2005) The lung. In: Kumar V, Abbas AK, Fausto N (eds) Robbins and Cotran pathologic basis of disease, 7th edn. Elsevier Saunders, Philadelphia, USA. pp 711–772, table 15–9

Kauczor HU, Kreitner KF (1999) MRI of the pulmonary parenchyma. Eur Radiol 9:1755–1764

Kim MJ, Lee KS, Kim J, Jung KJ, Lee HG, Kim TS (2001) Crescent sign in invasive pulmonary

aspergillosis: frequency and related CT and clinical factors. J Comput Assist Tomogr 25:305–310

Leutner CC, Gieseke J, Lutterbey G, Kuhl CK, Glasmacher A, Wardelmann E, Theisen A, Schild HH (2000) MR imaging of pneumonia in immunocompromised patients: comparison with helical CT. AJR Am J Roentgenol 175:391–397

Li F, Sone S, Maruyama Y, Takashima S, Yang ZG, Hasegawa M, Honda T, Yamanda T, Kubo K (2000) Correlation between high-resolution computed tomographic, magnetic resonance and pathological findings in cases with non-cancerous but suspicious lung nodules. Eur Radiol 10:1782–1791

Marquardt T, Jablonowski H (2003) Opportunistic diseases. Risk can be estimated. MMW Fortschr Med 145:33–37

Marzola P, Lanzoni A, Nicolato E, Di Modugno V, Cristofori P, Osculati F, Sbarbati A (2005) (1)H MRI of pneumococcal pneumonia in a murine model. J Magn Reson Imaging 22:170–174

McEachern R, Campbell GD Jr (1998) Hospital-acquired pneumonia: epidemiology, etiology, and treatment. Infect Dis Clin North Am 12:761–779

Moore EH, Webb WR, Muller N, Sollitto R (1986) MRI of pulmonary airspace disease: experimental model and preliminary clinical results. AJR Am J Roentgenol 146:1123–1128

Müller NL, Mayo JR, Zwirewich CV (1992) Value of MR imaging in the evaluation of chronic infiltrative lung diseases: comparison with CT. AJR Am J Roentgenol 158:1205–1209

Niederman MS, Mandell LA, Anzueto A et al (2001) Guidelines for the management of adults with community-acquired lower respiratory tract infections: diagnosis, assessment of severity, antimicrobial therapy and prevention. Am J Respir Crit Care Med 163:1730–1754

Pearce MS, Salotti JA, Little MP, McHugh K, Lee C, Kim KP, Howe NL, Ronckers CM, Rajaraman P, Sir Craft AW, Parker L, Berrington de González A (2012) Radiation exposure from CT scans in childhood and subsequent risk of leukaemia and brain tumours: a retrospective cohort study. Lancet 380(9840):499–505

Primack SL, Mayo JR, Hartman TE, Miller RR, Müller NL (1994) MRI of infiltrative lung disease: comparison with pathologic findings. J Comput Assist Tomogr 18:233–238

Prod'hom G, Leuenberger P, Koefer J et al. (1994) Nosocomial pneumonia in mechanically ventilated patients receiving antacid, ranitidine, or sucralfate as prophylaxis for stress ulcer: a randomized controlled trial. Ann Intern Med 120:653–662

Puderbach M, Eichinger M, Haeselbarth J, Ley S, Kopp-Schneider A, Tuengerthal S, Schmaehl A, Fink C, Plathow C, Wiebel M, Demirakca S, Müller FM, Kauczor HU (2007) Assessment of morphological MRI for pulmonary changes in cystic fibrosis (CF) patients: comparison to thin-section CT and chest x-ray. Invest Radiol 42(10):715–725

Rello J, Paiva JA, Baraibar J et al (2001) International conference for the development of consensus on the diagnosis and treatment of ventilator-associated pneumonia. Chest 120:955–970

Rosenow EC III (1990) Diffuse pulmonary infiltrates in the immunocompromised host. Clin Chest Med 11:55–64

Rupprecht T, Böwing B, Kuth R, Deimling M, Rascher W, Wagner M (2002) Steady-state free precession projection MRI as a potential alternative to the conventional chest X-ray in pediatric patients with suspected pneumonia. Eur Radiol 12:2752–2756

Springhouse (2007) Professional guide to disease. An up-to-date encyclopedia of illnesses, disorders, and injuries and their treatments. Lippincott Williams and Wilkins, Philadelphia, USA

Tournebize R, Doan BT, Dillies MA, Maurin S, Beloeil JC, Sansonetti PJ (2006) Magnetic resonance imaging of Klebsiella pneumoniae-induced pneumonia in mice. Cell Microbiol 8:33–43

Völker M, Ehses P, Weick S, Breuer FA, Blaimer M, Hintze C, Biederer J, Jakob PM (2015) Free breathing 1H MRI of the human lung with an improved radial turbo spin-echo. MAGMA 28(3):227–238

Wielpütz MO, Eichinger M, Puderbach M (2013) Magnetic resonance imaging of cystic fibrosis lung disease. J Thorac Imaging 28(3):151–159

Wielpütz MO, Heußel CP, Herth FJ, Kauczor HU (2014) Radiologische Diagnostik von Lungenerkrankungen. Betrachtung der Therapieoption bei Wahl des Verfahrens. Dtsch Arztebl Int 111(11):181–187

Interstitial Lung Disease

Francesco Molinari

Contents

Key Points

Imaging is important in the differential diagnosis as well as in the assessment of functional constraints and therapy response in interstitial lung disease. Imaging has to address three main topics: (1) visualization and recognition of morphological changes and their patterns; (2) assessment of pulmonary function, i.e., restrictive ventilatory impairment, reduction of perfusion, and gas exchange; and (3) assessment of inflammatory activity. MRI is capable to provide image-based answers to all three topics. Typical patterns, such as reticular and reticulonodular changes, ground glass, consolidation, and honeycombing, are easily visualized. Functional imaging using contrast-enhanced perfusion MRI and ventilation MRI with hyperpolarized gases or oxygen is available for the assessment of restrictive constraints. Routine contrast-enhanced MRI allows estimating inflammatory activity in different types of interstitial lung disease which is a clear advantage over CT which has limitations in this regard.

F. Molinari
Centre Hospitalier de Tourcoing, Lille, France
e-mail: francescomolinari.dr@gmail.com

1   Introduction

The use of MRI in the assessment of interstitial lung diseases (ILD) has been limited by the low proton density of the lungs, resulting in low signal-to-noise ratios, and signal loss due to respiratory and cardiac motion artifacts as well as susceptibility artifacts due to air-tissue interfaces (Kauczor and Kreitner 1999). These restrictions lead to a much lower spatial resolution compared to thin-section CT which, with its supreme ability to reflect the macroscopic pathologic abnormalities in ILD, remains the mainstay for diagnosis and differential diagnosis of these disorders. However, evidence suggests that MRI may play a role in the assessment of disease activity in ILD, and recent technological refinements have led to a considerable improvement of MRI image quality, which may enable the use of MRI in selected patients with ILD. This chapter reviews reports on the application of MRI to different ILD and considers potential future applications for morphological and functional MRI imaging in patients with ILD.

2   Role of MRI for Morphologic Imaging in ILD

Since the beginning of the 1990s, a number of studies have addressed the use of MRI for depiction of morphologic changes in patients with ILD. Primack et al. (1994) investigated five patients with idiopathic pulmonary fibrosis, three patients with hypersensitivity pneumonitis, four patients with sarcoidosis, and ten patients with miscellaneous infiltrative lung diseases and recorded the predominant patterns of abnormality seen on proton-weighted and T1-weighted MRI (parenchymal opacification with or without reticulation, a reticular pattern, nodularity, and interlobular septal thickening). The authors found that the MRI patterns correlated well with pathologic features seen on lung biopsy: the majority of patients with parenchymal opacification showed active inflammation on biopsy, whereas in a minority of patients parenchymal opacification represented fibrosis. Thus, MRI can depict treatable disease with reasonably high sensitivity (Kauczor and Kreitner 1999; Primack et al. 1994). Architectural distortion in patients with fibrosis was also depicted on MRI. All patients with reticulation showed fibro-

sis on biopsy, and nodularity was found in patients with sarcoidosis. Interlobular septal thickening, however, was seen in patients with lymphangitic carcinomatosis and Churg-Strauss syndrome, respectively (Primack et al. 1994).

Another study compared the value of proton-weighted and T1-weighted MRI compared to that of thin-section CT in the assessment of chronic infiltrative lung diseases and found that in the majority of the patients gross assessment of morphologic changes and distribution of disease was feasible (Müller et al. 1992). In that study, nine patients with usual interstitial pneumonia, six patients with sarcoidosis, four patients with hypersensitivity pneumonitis, and six patients with miscellaneous diseases were included. The authors found that MRI was inferior to CT in demonstrating mild fibrosis, and also inferior in the anatomic assessment of the pulmonary parenchyma. However, MRI was comparable to CT in the assessment of air-space opacification, and proved to be a suitable tool for longitudinal studies: In six patients, follow-up scans were obtained with both MRI and CT and revealed equal degrees of air-space opacification over time (Müller et al. 1992).

A number of studies have also focused on the differentiation of the active (alveolitic) and inactive (fibrotic) stages of ILD. In an early study, McFadden et al. (1987) studied patients with interstitial lung disease and found that signal intensity on MRI correlated with disease severity and response to treatment, as a decrease in signal intensity could be observed on follow-up in some patients. Further evidence that MRI is a suitable tool for the assessment of disease activity comes from experimental studies. Kersjes et al. (1999) investigated rabbits with bleomycin-induced lung damage and correlated MRI findings with histopathology. They demonstrated that lesions in the alveolitic phase displayed high pre- and post-contrast signal intensity on T1-weighted and also on T2-weighted images, whereas with progressive fibrosis the signal intensity and contrast enhancement showed a marked decrease. In detail, the authors observed a marked increase in signal intensity on T1- and T2-weighted images after instillation of bleomycin, corresponding to interstitial and alveolar pulmonary edema (acute alveolitis). Fourteen days later, the progressive fibrotic transformation of the pulmonary parenchyma was paralleled by a decrease in signal intensity on both

T1- and T2-weighted images (Kersjes et al. 1999). Vinitski et al. (1986) who chose a similar experimental approach in rats demonstrated a close correlation between signal intensities at different stages of the disease and lung water content. Other studies, however, failed to show differentiation of acute and chronic changes in ILD by calculating T1 and T2 proton relaxation times (Shioya et al. 1990; Taylor et al. 1987). In another experimental study, macromolecular contrast agents could be shown to improve further differentiation between alveolitis and pulmonary fibrosis (Berthezene et al. 1992). In the early alveolitic phase after bronchial instillation of cadmium chloride, rats demonstrated a gradually increasing contrast enhancement over 45 min, indicating leakage of the contrast agent into the extravascular space. By contrast, in the fibrotic phase markedly lower enhancement was observed and attributed to a decrease in plasma volume in the fibrotic lung (Berthezene et al. 1992).

The time course demonstrated in bleomycin-induced lung damage is comparable to radiation pneumonitis (Kauczor and Kreitner 1999). Preliminary clinical studies have addressed the value of MRI in the assessment of radiation-induced fibrosis and differentiation of fibrosis from recurrent disease. Early on, Glazer et al. (1984) investigated 21 patients who had undergone radiotherapy and compared the findings with 15 patients with untreated tumors. T2-weighted images proved suitable for differentiation of fibrosis and tumor, as radiation fibrosis showed low signal intensity on both T1- and T2-weighted images, whereas the signal intensity of untreated tumor was much higher. In another study, the surrounding pulmonary parenchyma in patients receiving radiotherapy for lung cancer displayed a steady increase in signal intensity on T1- and T2-weighted images over several months, followed by a decrease in signal intensity (Yankelevitz et al. 1994).

The following paragraphs review the MRI appearance of the most important interstitial lung diseases.

3   Sarcoidosis

Sarcoidosis is a systemic disorder characterized by the presence of non-caseating granulomas, which may resolve spontaneously or progress to fibrosis (Colby and Carrington 1994). As many as 90% of patients show pulmonary manifestations (Webb 2001). Pathologically, granulomas are found in a perilymphatic or lymphatic distribution and display a center of histiocytes, surrounded by lymphocytes and mononuclear cells (Colby and Carrington 1994). The intervening lung parenchyma is normal.

Granulomatous disease is closely mirrored by high-resolution CT (HRCT), which is the method of choice for assessment of patients with sarcoidosis (Webb 2001). The most characteristic abnormality consists of small pulmonary nodules in a perilymphatic or peribronchovascular distribution. These nodules are usually well defined. Furthermore, nodules show a predilection for the fissures, the subpleural parenchyma, and the center of the secondary pulmonary lobule. Their size normally does not exceed a few millimeters; however, nodules may coalesce forming larger opacities 1–4 cm in diameter or confluent masses surrounded by confluent small nodules (Grenier et al. 1991). Upper lobe predominance is a frequent finding, but not invariably present. The characteristic location of the granulomas often causes smooth or nodular peribronchovascular interstitial thickening. Furthermore, nodules are seen along the interlobular septa, causing irregular or nodular interlobular septal thickening which is a common albeit minor feature in patients with sarcoidosis. Patchy areas of ground glass opacity result from interstitial disease rather than alveolitis (Leung et al. 1993). Airway involvement is common and commonly presents as bronchial wall thickening (often indistinguishable from peribronchovascular thickening) and bronchial luminal abnormalities (Webb 2001; Dawson and Müller 1990; Miller et al. 1995).

The MRI appearance of sarcoidosis was reported in previous studies. As early as in 1988, Craig et al. (1988) investigated nine patients with pulmonary sarcoidosis and compared the findings with chest radiographs. In that study, MRI detected hilar and mediastinal lymphadenopathy as well as coalescent parenchymal disease but failed to show widespread interstitial disease. A more meaningful comparison of MRI and HRCT features was performed in other studies in a total of ten patients. In the study by Primack et al. (1994), MRI findings in sarcoidosis included parenchymal opacification, peribronchovascular thickening and nodularity, as well as parenchymal opacification with mild architectural distortion (Fig. 1). They could show that
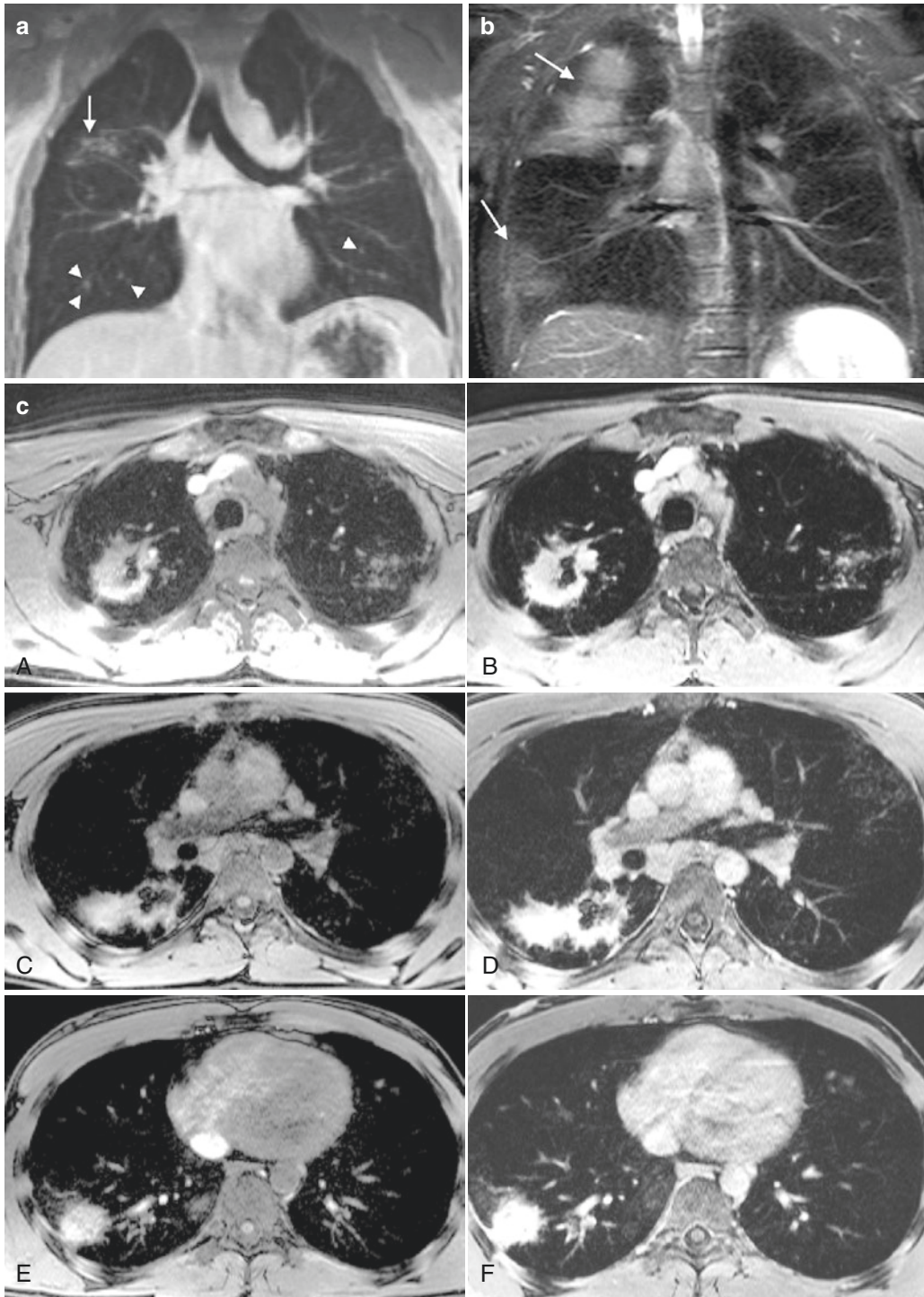
Fig. 1 (**a**–**d**) A 26-year-old male patient with sarcoidosis. (**a**) Post-contrast T1-weighted 3D FLASH coronal image displays peribronchovascular thickening (*arrow*) and nodularity (*arrowheads*). Note mediastinal lymphadenopathy. (**b**) IR-HASTE (inversion recovery half-Fourier acquisition single-shot turbo spin-echo) coronal image shows areas of consolidation (*arrows*). (**c**) Pre- (A–C) and post-contrast (D–F) T1-weighted VIBE (volumetric interpolated breath-hold examination) axial images show vivid contrast enhancement of the larger nodular lesions in the right upper lobe and the diffuse nodularity in the left upper lobe. (**d**) Post-contrast T1-weighted 3D FLASH coronal images (**a**: before initiation of steroid therapy, **b**: 8 weeks later) show regression of the parenchymal manifestations of sarcoidosis
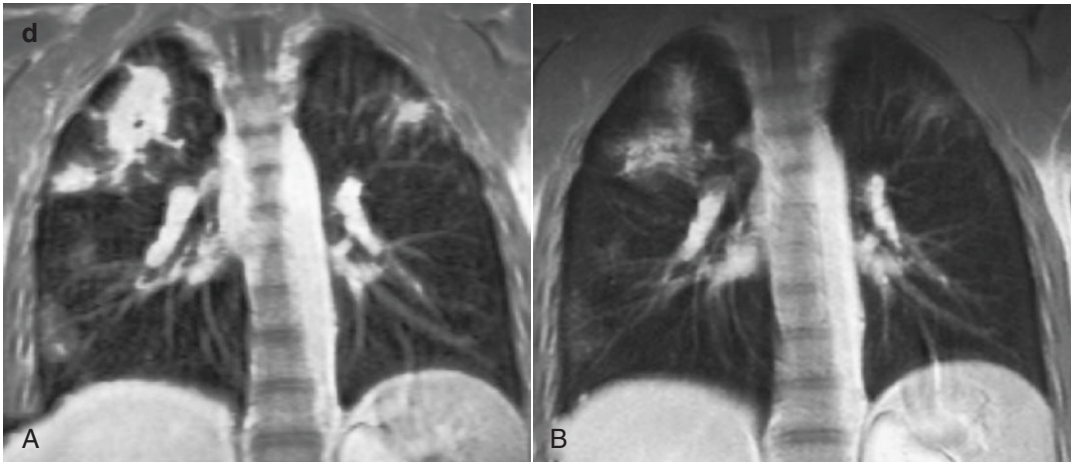
Fig. 1 (continued)

parenchymal opacification reflected the presence of non-caseating granulomas on open lung biopsy. Peribronchovascular nodularity was seen in four of five patients; MRI appearances in the remaining patient were normal. Müller et al. (1992) reported ground-glass opacities in a patient with sarcoidosis which improved on follow-up, whereas another patient with sarcoidosis showed no appreciable change. Gaeta et al. (2000) focused on the disease activity in chronic infiltrative lung disease and evaluated ten patients with sarcoidosis. They found that unenhancing lesions at contrast-enhanced MRI could be confidently considered as inactive disease. More recently, Chung et al. (2013) evaluated the agreement between the imaging appearance of pulmonary sarcoidosis on MRI and CT in 29 patients using a visual scoring method on a lobar basis. The authors found substantial correlation and agreement between total disease scoring on the two imaging modalities. The mediastinal and hilar lymph node appearance and involvement in sarcoidosis have also been investigated with MRI. A typical MRI appearance of a peripheral hyperintensity together with central low signal intensity (the so-called *dark lymph node sign*) was recently described by Chung et al. (2014) in approximately 50% of patients with sarcoidosis (25/51) on both contrast-enhanced T1-weighted (VIBE) and fat-suppressed T2-weigheted (BLADE) sequences. Gümüştaş et al. (2013) assessed 27 patients with mediastinal and hilar lymph nodes and reported that, based on the value of apparent diffusion coefficient, diffusion-weighted MRI may add to the differentiation of lymphoma from sarcoidosis.

Because MRI is the modality of choice for imaging of patients with suspected cardiac sarcoidosis, and cardiac and lung involvement in sarcoidosis may be concurrent, MRI has been recently proposed as a comprehensive imaging modality for cardiopulmonary assessment of sarcoidosis (Kouranos et al. 2015). Taken together, despite its lower spatial resolution compared to HRCT, MRI can depict cardinal features of pulmonary sarcoidosis such as nodularity, peribronchovascular thickening, as well as confluent masses. Furthermore, lesions in sarcoidosis usually show vivid contrast enhancement in MRI (Fig. 1), and it is therefore conceivable that MRI may play a role in staging disease activity in patients with sarcoidosis and in longitudinal studies of younger patients (Fig. 1), particularly when its lack of ionizing radiation is considered.

4 Idiopathic Interstitial Pneumonias

Idiopathic interstitial pneumonias (IP) form a heterogeneous group of interstitial lung diseases. In 2013, the American Thoracic Society and European Respiratory Society have regrouped idiopathic IP into five categories: (1) chronic fibrosing IP, which includes the morphologic pattern of usual IP (idiopathic pulmonary fibrosis) and nonspecific IP (idiopathic NSIP); (2) smoking-related IP, which includes the desquamative IP pattern (desquamative IP) and respiratory bronchiolitis (respiratory bronchiolitis ILD); (3) acute/subacute IP, which includes the organiz-

ing pneumonia pattern (cryptogenic organizing pneumonia) and diffuse alveolar damage (acute IP); (4) rare entities, which include lymphoid IP (idiopathic LIP) and pleuroparenchymal fibroelastosis (idiopathic pleuroparenchymal fibroelastosis); and (5) unclassifiable idiopathic IP (ATS/ERS 2000; ATS/ERS/JRS/ALAT 2011).

UIP is the most common type of idiopathic interstitial pneumonia (McAdams et al. 1996). Histopathologically, it shows a heterogeneous pattern of normal and inflammatory lung, fibroblastic foci, interstitial fibrosis, and honeycombing. This "temporal heterogeneity" is a characteristic feature (Katzenstein and Myers 1998; Kadota et al. 1995). Fibrosis and honeycombing in UIP display a striking basal and subpleural predominance. UIP is the most common histopathological pattern in patients with the clinical picture of idiopathic pulmonary fibrosis (IPF); however, it may also occur secondary to environmental or drug exposure, radiation, or in association with collagen-vascular diseases (Colby and Carrington 1994).

On HRCT, UIP/IPF is characterized by the presence of irregular reticular abnormalities reflecting fibrosis (Webb et al. 1988). The most important HRCT features are honeycombing and intralobular septal thickening (Webb et al. 1988). These findings indicate progressive disease and a poor prognosis (Wells et al. 1993; Terriff et al. 1992). Ground-glass opacities are less conspicuous findings and, if present, may indicate the presence of active inflammation or, alternatively, may reflect very fine fibrosis beyond the spatial resolution of HRCT (Leung et al. 1993). Honeycombing refers to thick-walled, wall-sharing cysts which are usually 2–20 mm in diameter, and which occur in layers in a subpleural location. Differentiation from traction bronchiolectasis is not always straightforward. Intralobular septal thickening results in a fine reticular pattern and is often associated with traction bronchiolectasis (Webb et al. 1988). Irregular interfaces between the pulmonary parenchyma and vasculature result from thickening of the intralobular interstitium. If fibrosis is severe, larger bronchi become dilated and distorted, a finding referred to as traction bronchiectasis.

The major HRCT features in patients with UIP/IPF are also depicted with MRI (Fig. 2).

Primack et al. (1994) investigated five patients with IPF using MRI and reported peripheral reticulation with or without areas of parenchymal opacification, dense reticulation, or architectural distortion. Peripheral reticulation was identified in all patients and reflected fibrosis on biopsy. If reticulation occurred in association with parenchymal opacification, biopsy demonstrated both fibrosis and active alveolitis (Primack et al. 1994). Müller et al. (1992) showed that at that time, MRI was slightly inferior to HRCT in the depiction of fibrosis and honeycombing: of 15 patients with reticulation on CT, 13 and 12 showed abnormalities on T1-weighted and proton density-weighted MRI, respectively. Furthermore, of ten patients with the HRCT finding of honeycombing, nine and six patients displayed honeycombing on T1-weighted and proton density-weighted MRI (Müller et al. 1992). The relative inferiority of conventional MRI techniques compared to HRCT in the assessment of morphologic changes of UIP was also confirmed by King et al. (1996).

More recently, Buzan et al. (2015) and Mirsadraee et al. (2016) have investigated relaxation features of lung abnormalities in patients with UIP/IPF. By using multi-echo turbo SE sequence for T2 mapping (Buzan et al. 2015) and a lock-locker inversion-recovery sequence for T1 mapping (Mirsadraee et al. 2016), these authors were able to image the relaxation times of the entire lung in patients with lung fibrosis. The interest of using relaxation MRI for characterization of ILD is that the relaxation maps may improve the differentiation of patterns of lung changes which might represent precursors to lung fibrosis, and provide a quantitative method for monitoring of progression of the disease and its response to treatment.

In conclusion, fibrotic changes of UIP/IPF can be easily depicted by modern MRI scanners especially after gadolinium contrast injection, whereas all conventional techniques are less reliable for the assessment of mild interstitial disease and in particular of ground-glass opacities. Validation of quantitate methods that assess T1 and T2 relaxation times of the lung is still required for clinical applicability.
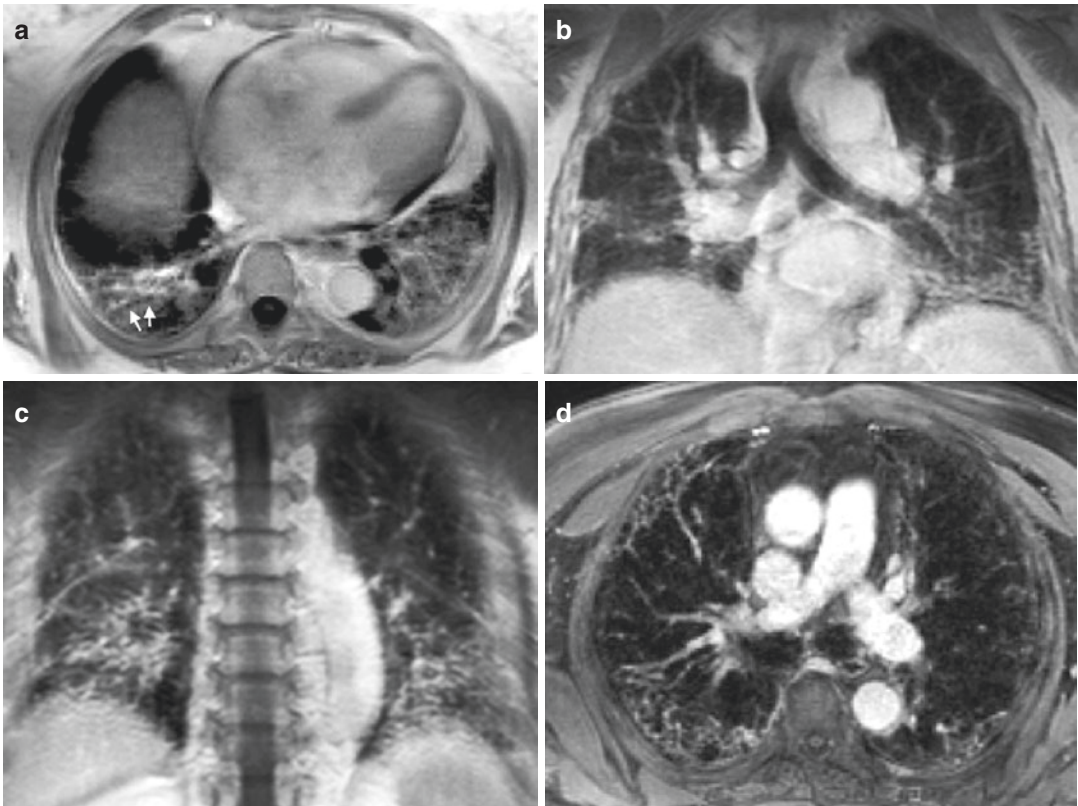
Fig. 2 (**a**–**d**) A 74-year-old female patient with usual interstitial pneumonia associated with rheumatoid arthritis. (a) Post-contrast T1-weighted 3D FLASH axial image displays a reticular pattern with extensive traction bronchiectasis/bronchiolectasis (*arrowheads*). (**b**) Post-contrast T1-weighted 3D FLASH coronal image depicts typical basal and subpleural predominance of the findings. (**c**) Post-contrast T1-weighted 3D FLASH coronal image shows extensive architectural distortion in the dorsal parts of the lungs. (**d**) Post-contrast T1-weighted 3D FLASH axial image indicating typical fibrotic changes in a patient with IPF. Note the extensive reticulation and architectural distortion predominant in the subpleural regions of the lung

5 Collagen-Vascular Diseases

Interstitial lung disease is a common feature in patients with underlying collagen-vascular disorders (CVD). As CVD are sharing common imaging features, the MRI appearances of interstitial lung disease associated with rheumatoid arthritis, scleroderma, and systemic lupus erythematosus are summarized at the end of this paragraph after a brief introduction of the different entities.

5.1 Rheumatoid Arthritis

Rheumatoid arthritis is a chronic inflammatory autoimmune disorder which is commonly associated with thoracic disease, e.g., interstitial fibrosis, necrobiotic nodules, pleural disease, bronchiectasis, and obliterative bronchiolitis (Remy-Jardin et al. 1994; Perez et al. 1998). The prevalence of radiologically evident interstitial lung disease is around 10%, with the most common histopathologic pattern being UIP. A small percentage of patients, however, have findings of NSIP on lung biopsy (Katzenstein and Fiorelli 1994). In a study by Remy-Jardin et al. (1994), HRCT findings of fibrosis (with or without honeycombing) were seen in 10% of patients. Ground-glass opacities were found in 14%. Bronchial abnormalities including bronchiectasis were present in 21% of patients, consolidation in 6%, lymphadenopathy in 9%, and pleural disease in 16%. Another frequent finding was predominantly subpleural nodularity (22%).

5.2 Progressive Systemic Sclerosis (Scleroderma)

Progressive systemic sclerosis is an autoimmune disorder characterized by excessive amounts of collagen fibers in different organs. The vast majority of patients with progressive systemic sclerosis (PSS) show some degree of interstitial fibrosis, although pulmonary function tests are frequently normal (Taorimina 1981; Arroliga et al. 1992). PSS is commonly associated with a pattern of NSIP, pulmonary vasculitis, and pulmonary hypertension. HRCT findings include honeycombing, reticulation, ground-glass opacities, and subpleural predominance (Webb et al. 1988). In a recent study, CT features of lung disease in PSS were compared with IPF and NSIP (Desai et al. 2004). In PSS, interstitial lung disease was shown to be less extensive, less coarse, and characterized by a greater proportion of ground-glass opacification than that in patients with IPF. CT features closely resembled those in patients with idiopathic NSIP (Desai et al. 2004). Other findings in patients with PSS include esophageal dilatation, diffuse pleural thickening, and mediastinal lymphadenopathy.

5.3 Systemic Lupus Erythematosus

Systemic lupus erythematosus (SLE) is a multisystemic autoimmune disorder associated with increased serum antinuclear antibodies. It is commonly associated with pleuropulmonary abnormalities. Up to 85% of autopsy cases show pleuritis or pleural fibrosis, and pleural effusion is a common feature on chest radiographs of patients with SLE (Wiedemann and Matthay 1992). Pulmonary complications in SLE are common and include pneumonia, lupus pneumonitis, and pulmonary hemorrhage (Kim et al. 2000). Organizing pneumonia and pulmonary fibrosis may occur in patients with SLE (Gammon et al. 1992).

HRCT shows findings of fibrosis, albeit less frequently than in patients with IPF, rheumatoid arthritis, or PSS. Other abnormalities include ground-glass opacities, pulmonary nodules, bronchiectasis or bronchial wall thickening, and pleural disease (Bankier et al. 1995). The incidence of pulmonary fibrosis is estimated to be 30–35% (Bankier et al. 1995; Fenlon et al. 1996; Sant et al. 1997). Frequent findings are interlobular or intralobular septal thickening (33%), and architectural distortion (88%) (Bankier et al. 1995). Honeycombing is uncommon. The findings of ground-glass opacification and consolidation may be caused by pneumonia, lupus pneumonitis, or pulmonary hemorrhage, and may also occur in organizing pneumonia (Primack et al. 1994). Airway abnormalities occur in 18–20% and pleuropericardial disease in 15–17% of patients (Fenlon et al. 1996; Sant et al. 1997).

There are currently no systematic data available on the use of MRI in patients with ILD associated with collagen-vascular diseases. From our experience, morphological features such as fibrosis with architectural distortion or honeycombing, as well as ground-glass opacities, can easily be depicted with MRI (Figs. 3, 4 and 5), whereas subtle fibrosis may go undiagnosed. Architectural distortion, consolidation, nodularity, and interlobular septal thickening are other abnormalities which can reliably be seen by MRI. In addition, findings pointing to the underlying disorder such as esophageal dilatation in PSS or pleuropulmonary disease in SLE are readily depicted. Interestingly, ground-glass opacities in collagen-vascular disorders may show intense contrast enhancement, and it is presumed albeit not proven that in this case an active inflammatory process, i.e., alveolitis, is the underlying pathology. In this context, it is conceivable that contrast-enhanced MRI may play a role in longitudinal studies investigating new therapeutic regimens, as differentiation between inflammation and fibrosis may be facilitated.
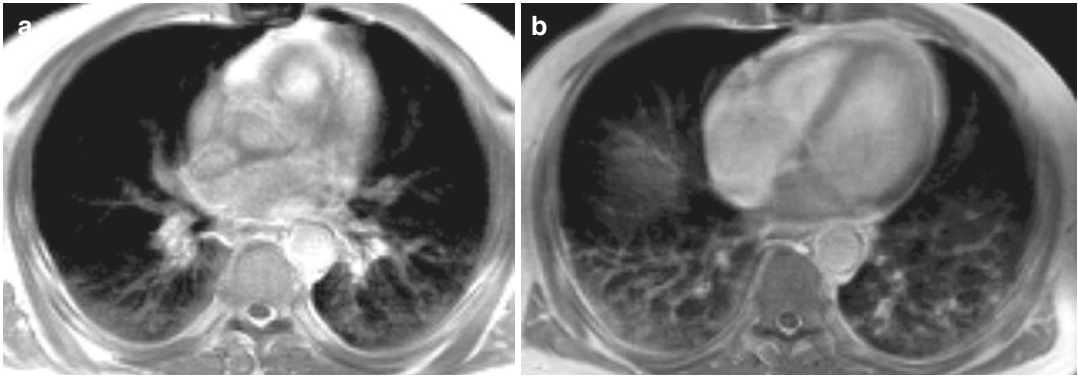
Fig. 3 A 61-year-old male patient with interstitial lung disease associated with rheumatoid arthritis, with MR findings suggestive of nonspecific interstitial pneumonia. Post-contrast T1-weighted 3D FLASH axial images depict subpleural ground-glass opacification with reticulation in the apical lower lobes (**a**) as well as extensive fibrosis with no evident honeycombing in the dorsobasal parts of the lungs (**b**)
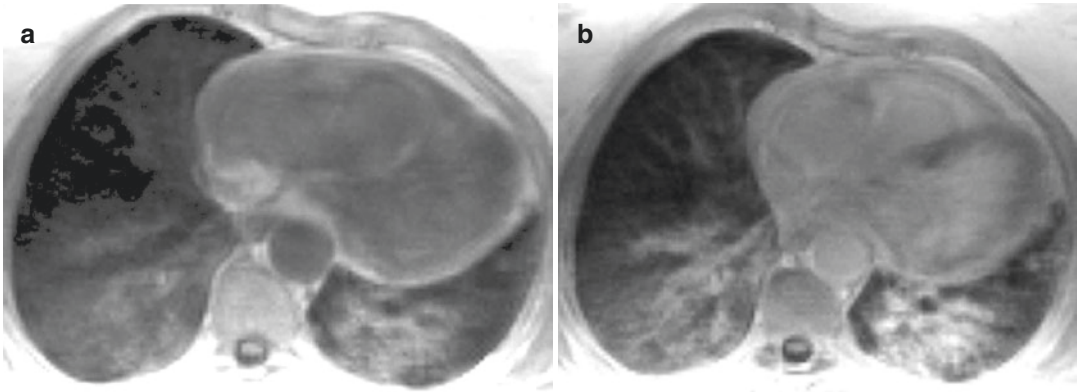
Fig. 4 A 70-year-old female patient with interstitial lung disease associated with systemic lupus erythematosus. Pre-contrast (**a**) and post-contrast (**b**) T1-weighted 3D FLASH axial images display bilateral subpleural and basal dense fibrosis with substantial contrast enhancement
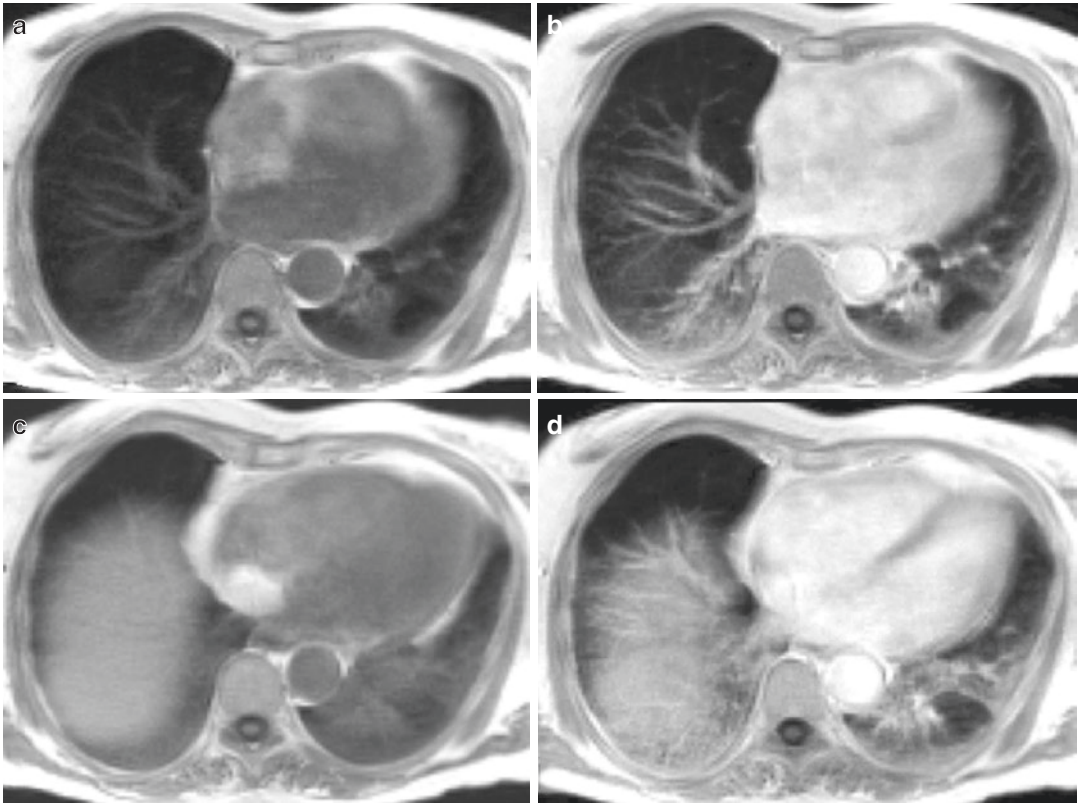
Fig. 5 A 68-year-old female patient with interstitial lung disease associated with progressive systemic sclerosis (scleroderma). Pre- (**a**, **b**) and post-contrast (**c**, **d**) T1-weighted 3D FLASH axial images show a subpleural and basal reticular pattern with architectural distortion suggestive of frank fibrosis with vivid contrast enhancement

6   Miscellaneous Interstitial Lung Diseases

Progressive massive fibrosis (PMF) in coal worker's pneumoconiosis was studied in 12 patients using MRI. The majority of lesions were isointense to skeletal muscle on T1-weighted images with post-contrast enhancement. On T2-weighted images, signal intensity was low, with central high signal intensity corresponding to necrosis (Matsumoto et al. 1998).

In *Wegener's granulomatosis*, pulmonary nodules are depicted with MRI and may show post-contrast enhancement (Kalaitzoglou et al. 1998). MRI in patients with *asbestosis* may show round atelectasis and interstitial fibrosis, along with pleural plaques which appear hyperintense on T1- and T2-weighted images and do not enhance (Bekkelund et al. 1998).

7   MR Strategies to Investigate Lung Function in ILD

The assessment of lung function is critically important for the diagnosis and management of ILD patients. ILDs include a wide spectrum of pathologic entities which often manifest with overlapping clinicoradiologic patterns (ATS/ERS 2002; Wells and Hogaboam 2007; ATS/ERS/JRS/ALAT 2011). At the presentation of the disease, the diagnosis is difficult and usually requires careful analysis of clinical and HRCT data, and the knowledge of the type of functional impairment of the lung. Invasive procedures, such as lung biopsy with video-assisted thoracic surgery (VATS), may also be needed, primarily to exclude the unfavorable occurrence of IPF/UIP pattern (Hunninghake et al. 2001). Biopsy specimens can also provide valuable information

on the disease activity. However the procedure is associated with known issues. Mortality and complication rates for lung biopsy in ILD patients have been reported, with complications being more frequent in patients dependent on oxygen and having pulmonary hypertension (Kreider et al. 2007). An experienced pathologist is required for the assessment of the biopsy specimens. Inconclusive results may also be possible when the distribution of the disease is highly heterogeneous (Wells and Hogaboam 2007). Therefore, the decision of performing lung biopsy for the diagnosis of ILD is largely dependent on the clinical condition of the patient. In particular, when the patient is old and has numerous comorbidities that may significantly outweigh the risk of complications against the benefit of obtaining histological samplings, the diagnosis and prognosis of the disease are determined clinically by serial monitoring of lung function and follow-up HRCT examinations.

Lung function is commonly evaluated with a broad range of techniques, known as pulmonary function tests (PFTs). PFTs of static lung volumes, gas diffusion, arterial blood gas analysis, and exercise capacity are typically assessed in ILD patients (Chetta et al. 2004). Some general limitations of these tests include a degree of variability of the results and the need of patient cooperation (Ulmer et al. 1993). The standardized technique and relatively inexpensive equipment required for testing ensure large clinical applicability for studying the ventilatory and gas exchange abnormalities of ILD.

The ventilatory defect in ILD is a consequence of several mechanisms, such as loss of lung volume, reduction in alveolar distensibility and/or size, and increased surface tension caused by surfactant alterations (Gibson and Pride 1977; Knudson and Kaltenborn 1981; Thompson and Colebatch 1989; McCormack et al. 1991). These pathophysiologic changes cause a global impairment of lung mechanics that is known as restrictive ventilatory pattern. At rest, ventilation is characterized by rapid breathing frequency to compensate the small tidal volumes and the reduced alveolar distensibility. Static lung volumes are not uniformly altered. Possibly as a consequence of premature closure of small air-

ways caused by peribronchial fibrosis or cystic modification of the lung, functional residual capacity (FRC) and residual volume (RV) are less decreased than vital capacity (VC). Total lung capacity (TLC) is therefore less reduced than VC. The RV/TLC ratio may be greater than normal. Because large airways are usually patent, dynamic lung volumes and particularly volume-corrected indices of airflow (forced expiratory volume in 1 s to VC, FEV1/VC) are normal or greater than normal.

The impairment of gas exchange depends on both ventilation/perfusion mismatch and alveolar-capillary damage. Gas diffusion through the alveolar-capillary barrier is estimated with high sensitivity from the diffusing capacity for carbon monoxide (DLCO) (Chetta et al. 2004; Gross and Hunninghake 2001). However, the DLCO decrease reflects partly the poor distribution of inspired gas and reduced lung volumes also. Using the carbon monoxide transfer coefficient (KCO is not dependent from the lung volume) the diffusing abnormality is assessed even more accurately (Hughes 2003). Oxygen desaturation is possible at resting, but it is more evident during exercise. Because of the ventilatory and gas exchange abnormalities, and concurrent cardiac dysfunction, the overall exercise tolerance is markedly reduced.

The PFTs alterations in ILD are typical but rather unspecific. They more likely express a general dysfunctional pattern of the lung that occurs in different pathological conditions evolving towards fibrosis. In serial functional monitoring of ILD patients, the PFTs show variable accuracy as prognostic factors. The capability to predict patient survival depends on the form of ILD. In sarcoidosis, for instance, the use of pulmonary function testing to predict the course of the disease is controversial (Chetta et al. 2004). In experimental treatment studies, the assessment of therapeutic effects on the sole basis of functional monitoring with PFTs is also difficult (Wells and Hogaboam 2007). Considering that conventional therapies for ILDs are associated with significant risks, the research of new diagnostic strategies to assess lung function is largely needed for both patient management and treatment control. Recently introduced treatment schemes based on antifibrotic agent (i.e.: pirfenidone) that appear to

slow the progression of IPF in patients with mild-to-moderate disease and have a possible mortality benefit might also require a more effective therapy control method than that based on PFTs.

Despite the technical issues that in the past have limited the clinical application of lung MRI, the potential of this imaging modality in assessing pulmonary function has been widely investigated. Along with the obvious advantage of providing information on regional morphology with a radiation-free diagnostic tool, the most attractive feature of lung imaging with MR consists in its flexibility to combine different data acquisition techniques with the use of new classes of contrast agents. Of particular interest in recent years has been the introduction of inhalatory paramagnetic contrast media, such as hyperpolarized gases and molecular oxygen to explore lung ventilation and diffusion. Concurrently, time-resolved three-dimensional visualization of the lung parenchyma during intravenous administration of gadolinium-based contrast agents has been established as a clinical tool to assess pulmonary perfusion. Since technical improvements in MR systems have largely reduced data acquisition times, imaging protocols that include morphologic and functional assessment of the lung are recently accessible for clinical application (Puderbach et al. 2007). To date, few studies have explored the potential of MRI to investigate lung function in ILD patients. In the following paragraphs the MR techniques that have been investigated for the assessment of lung function in ILD patients will be addressed.

8 Imaging of Lung Function with Hyperpolarized Gases

The use of exogenous inhalatory contrast agents in lung MRI was first demonstrated in the mid-1990s with the introduction of hyperpolarized or laser-polarized noble gasses, such as xenon-129 (Xe) and helium-3 (He) (Albert et al. 1994; Middleton et al. 1995; MacFall et al. 1996; Black et al. 1996; Kauczor et al. 1996). The polarization process, achieved by optical pumping, causes a nonequilibrium state in the nuclei of the gas which represents the source of the MR signal (Guenther et al. 2000). The gas inhalation allows for the direct assessment of the venti-

lated airways and pulmonary airspaces. In this setting the proton density of lung tissues (i.e., blood and interstitium) is neglected. A dedicated RF coil and an MR system adapted to the frequency of resonance of the gas are required. The sequence design is based on gradient echo techniques. For a detailed description of the principles, design and practical implementation of the laser polarization techniques, and the setup for MR imaging of the lung with hyperpolarized gasses, the reader is referred to the reviews in the literature (Goodson 2002; Moller et al. 2002) and to other chapters of this book.

Although He-3 is less abundant in nature than Xe-129, its use has been preferred because of its larger gyromagnetic ratio and polarization levels (Kauczor et al. 2002). The images obtained from hyperpolarized He-3 MRI of the lung are generally characterized by excellent SNR and good spatial and temporal resolution. Additionally, He-3 is not absorbed by the lung and can be inhaled in relatively large quantities without substantial risks. Different strategies to explore lung function with hyperpolarized He-3 have been established (Kauczor et al. 2002). By simple visualization of lung areas that exhibit signal enhancement, ventilated lung tissue is demonstrated (spin or gas density imaging). Other techniques have also been developed including the calculation of ventilated lung volume, assessment of the diffusion of gas molecules in the pulmonary airspaces (diffusion-weighted imaging), dynamic ventilation imaging, and measurement of the alveolar pO2 (Kauczor et al. 2002).

Because lung function imaging with hyperpolarized noble gases primarily allows for the depiction of airways and ventilated airspaces, it is not surprising that most of the studies focused on the application of this diagnostic modality for COPD, asthma, and chronic bronchitis. Although reports on the use of hyperpolarized gases MRI are continuously emerging in the literature, those studies are mostly conducted in animal models and in experimental settings (Stephen et al. 2010; Cleveland et al. 2014). ILD patients have not been investigated systematically by hyperpolarized gas MRI (Kauczor et al. 2001). All current literature available on the clinical application of this imaging tool to the study of lung fibrosis derives from few reports and results from patients that have been treated with single-lung

transplantation (Markstaller et al. 2002; Gast et al. 2003, 2007; Zaporozhan et al. 2004, 2005; Bink et al. 2007). In these studies, the most typical alteration reported was an inhomogeneous distribution of the signal generated by the gas in ventilated regions of the lung and of the ADC values calculated from diffusion imaging. These alterations have been interpreted as focal ventilatory defects caused by fibrotic obstruction of peripheral bronchi. These areas of heterogeneous signal contain information about ventilatory state as well as other parameters (i.e., time constants, compliance, and alveolar oxygen concentration). Functional and clinical significance of these findings is still to be investigated.

9 Imaging of Lung Function with Oxygen

Indirect assessment of lung function using molecular oxygen as an inhaled contrast agent was first proposed by Edelman et al. (1996). Since then, the technical feasibility and clinical relevance of oxygen-enhanced MRI of the lung have been investigated in animals, healthy volunteers, and patients with various diseases. Because oxygen causes signal changes in the lung after diffusing through the alveolar-capillary barrier (Ohno et al. 2002; Jakob et al. 2004), this technique is potentially suitable for the functional assessment of pulmonary diseases that lead to an altered gas diffusion. The physical characteristics of molecular O2 and the physiological basis that explain its paramagnetic effect in the lung are described in other chapters of this book. The following paragraphs offer a survey on the research relevant for understanding the potential of oxygen-enhanced MRI in the functional evaluation of ILD.

To date, ILD patients have been investigated with oxygen ventilation imaging only in a limited number of studies. A correlation between the results of this technique and the DLCO was firstly assessed by Muller et al. (2002). In their study, either the SI slope calculated by imaging the lung during the wash-in phase of oxygen or the overall SI change from room air ventilation to the maximal oxygen enhancement correlated with DLCO. Similar results have been found also in another recent study conducted in patients with

IPF and sarcoidosis (Molinari et al. 2007). From the analysis of the extent of the areas that showed oxygen enhancement in the lung, a semiquantitative parameter was correlated with the tests that characterize the gas exchange impairment of ILD. A good correlation was found with the DLCO, KCO, arterial partial pressure, and saturation of oxygen. The higher correlation was found between the results of oxygen-enhanced MRI and KCO. This is particularly interesting considering that, as mentioned above, KCO is generally regarded as more sensitive to the alteration of the alveolar-capillary gas exchange. In a more recent study, Ohno et al. (2014) compared oxygen-enhanced MRI with thin-section CT for pulmonary functional loss and disease severity assessment in 45 patients with connective tissue disease. The authors found that mean relative enhancement ratio after oxygen ventilation was significantly different between patients with interstitial lung disease (36) and those without ILD (9). Moreover, mean relative enhancement ratio correlated with pulmonary function parameters and serum KL-6. These studies seem to confirm the possibility to obtain information from oxygen-enhanced MRI that can be used clinically to predict the loss of lung function in ILD.

A quantitative model to assess the pulmonary gas exchange was also developed by Jakob and colleagues using multiple oxygen concentrations and a T1 mapping procedure (Jakob et al. 2001, 2004; Arnold et al. 2007). Based on the linear proportionality between the longitudinal relaxivity of the lung (i.e., R1) and the local oxygen concentration, the model allows for the calculation of an "oxygen transfer function" (OTF) which represents the slope of the plot of R1 versus O_2 concentration. The OTF has been proposed as an indicator of the gas transfer ability of the lung. Although the study was conducted in a small group of patients with cystic fibrosis, the approach relies on general principles of lung physiology and it might be also considered for the evaluation of ILD. Research has to be conducted to confirm the clinical applicability of this quantitative method for oxygen-enhanced MRI of the lung. Additionally, other more general aspects of oxygen ventilation imaging that might require further investigation have also been indicated (Jakob

et al. 2004). In particular, the amount of O2 physically dissolved in pulmonary blood is a function of the diffusing capacity of the lung, but also of the local ventilation-perfusion ratio (Jakob et al. 2004). Hence, oxygen ventilation imaging should not be regarded as a direct surrogate test for the assessment of lung diffusion. The assessment of lung function with this technique in combination with perfusion MRI has been suggested.

10 MR Protocol for Clinical Imaging of the Lung in ILD

The technical requirements and basic MR sequences for imaging the lung at 1.5 T have been reviewed (Puderbach et al. 2007). A routine MRI protocol based on short echo times (TE) to counteract the rapid signal decay of the lung and acquisitions within single or multiple consecutive breath-holds has been proposed. The basic protocol comprises a localizer, a coronal T2-weighted single-shot half-Fourier turbo spin-echo sequence, a transversal T1-weighted three-dimensional (3D) gradient echo, a coronal steady-state free precession, and a transversal T2-weighted short-τ inversion-recovery (STIR). An extension of this protocol includes a post-contrast transversal T1-weighted 3D gradient-echo sequence. With this approach the assessment of a variety of lung diseases including ILD is feasible in a reasonable time (approximately 20 min).

The infiltrative processes and fibrotic changes which represent the common manifestations of many ILDs are well depicted by the T2-weighted images, such as those obtained with partial-Fourier (HASTE) technique. The reticular pattern caused by thickening of interstitial septa, potentially associated to ground-glass opacities, traction bronchiectases/bronchiolectases, cystic changes with honeycombing, and overall architectural distortion of the lung, can be visualized easily by transversal or coronal images. In the coronal plane, the dorsal and basal location of the peripheral reticulations is demonstrated in full extent by few images, giving immediate perception of the distribution of the disease (Fig. 2). T1 contrast-enhanced images, used primarily to characterize focal masses among the interstitial changes, are similar to CT in depicting the subpleural reticulations (Fig. 2). The use of fat saturation increases the visualization of contrast-enhanced fibrotic changes and vascular distortion against the low-signal chest wall. The nodular pattern (for instance, in sarcoidosis) can be demonstrated using non-enhanced 3D T1-weighted gradient echo sequences (T1-GRE). On most scanners equipped with parallel imaging technique 3D–T1-GRE are capable of isotropic voxels of 2 mm^3 or even lower in-plane spatial resolution (Puderbach et al. 2007). Large focal consolidations or fibrotic masses are usually well depicted in both T2-HASTE and non-enhanced T1-GRE images. As mentioned, contrast administration at the end of the protocol may be considered when the nature of the consolidation is unclear. The coronal steady-state free precession sequence visualizes with high sensitivity the restricted motion of the lung, which is typically associated with fibrosis. The transversal T2-weighted STIR images are generally used to visualize enlarged mediastinal and hilar lymph nodes.

Most of the current systems are equipped with time-resolved echo-shared fast gradient-echo techniques, which can be used to image lung perfusion with a minimal extension to the total examination time of the basic contrast-enhanced protocol. Immediate qualitative assessment of these images in ILD may indicate lung perfusion defects in areas of advanced architectural distortion. In some cases large or multiple perfusion changes are visualized even with mild parenchymal alterations as a consequence of perivascular fibrosis. This may help understanding the functional impairment of the patient. As described in other chapters of this book, quantitative parameters of lung perfusion can be obtained in a post-processing phase.

An improvement to the imaging protocol illustrated in the previous paragraphs has been recently considered. Conventional MR sequences have relatively long TEs compared to the short T2* of lung tissue. Consequently, these techniques can only measure a limited amount of lung signal. An alternative approach to counteract the rapid dispersion of lung signal is to combine half-radiofrequency excitations and subsequent radial mapping from the center of the k-space (Robson and Bydder 2006; Bergin et al. 1992; Gewalt et al. 1993; Kuethe et al. 2007; Takahashi et al. 2010; Togao et al.

2010; Zurek et al. 2010). This alternative approach minimizes the delay between the end point of the excitation pulse and the data sampling, which allows for a reduction of the TE below the limit of clinical detectability provided by conventional gradient-echo techniques (approximately 0.1 ms vs. 1–2 ms of fast spin-echo and gradient-echo techniques) (Robson and Bydder 2006). Ultrashort TE MRI (UTE-MRI) of the lung has been demonstrated in experimental settings and in living lungs (Bergin et al. 1991; Gewalt et al. 1993; Kuethe et al. 2007; Takahashi et al. 2010; Togao et al. 2010; Zurek et al. 2010; Molinari et al. 2014). Quantitative analysis of lung water content using UTE-MRI has also been reported (Molinari et al. 2014). Clinical application of UTE-MRI has been recently shown in a cohort of 85 patients with vari-ous pulmonary diseases including ILD (Ohno et al. 2016). Substantial intermethod agreement between UTE-MRI and standard-dose and low-dose CT was found in pulmonary findings including ground-glass opacities, reticular opacities, traction bronchiectasis, and honeycombing (Ohno et al. 2016). Indeed, UTE-MRI could significantly improve the visualization of areas of ground-glass infiltrates in mild forms of interstitial disease and of cystic changes in advanced lung fibrosis. Normally, the air content in the cystic spaces reduces proton density and increases susceptibility artifacts which limit the overall image quality for visualizing of these cystic alterations. Because UTE-MRI is relatively insensitive to local rapid decay of lung signal, visualization of interstitial distortion and cystic changes can be improved (Figs. 6 and 7).
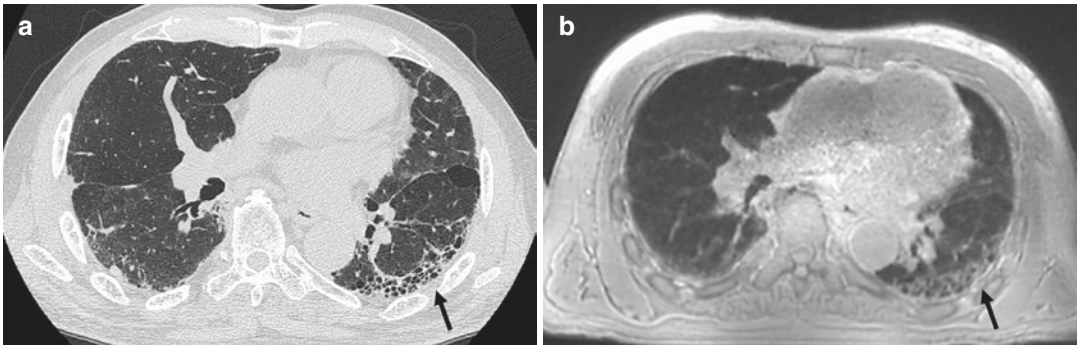
Fig. 6 A 82-year-old female patient with UIP. Thin-section CT (**a**) and thin-section MR imaging with ultrashort TE (**b**) demonstrate honeycomb lesions (*arrows*). *Courtesy of Dr. Y. Ohno, Kobe, Japan*
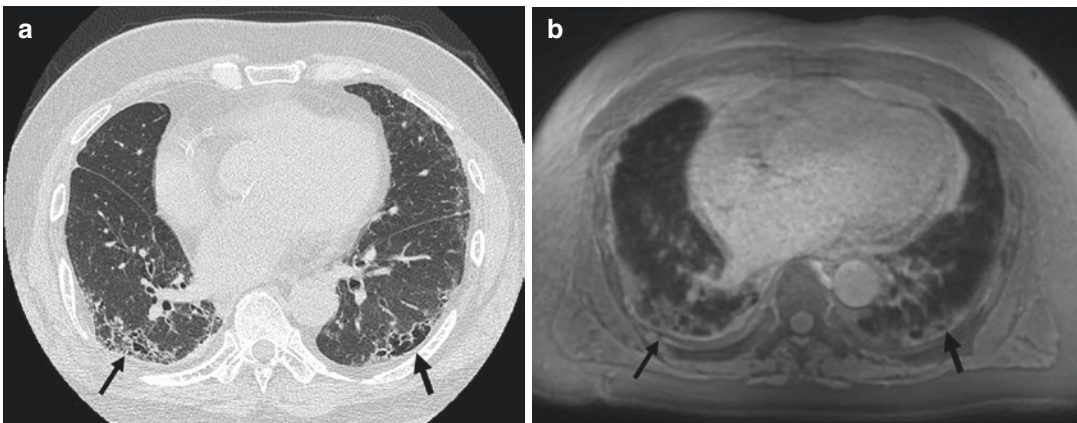
Fig. 7 A 74-year-old female patient diagnosed with mixed connective tissue disease (MCTD). Thin-section CT (**a**) and pulmonary thin-section MR imaging with ultrashort TE (**b**) demonstrate reticulation (*small arrows*) and destruction of secondary lobules (*large arrows*). *Courtesy of Dr. Y. Ohno, Kobe, Japan*

References

Albert MS, Cates GD, Driehuys B et al (1994) Biological magnetic resonance imaging using laser-polarized 129Xe. Nature 370:199–201

Arnold JF, Kotas M, Fidler F et al (2007) Quantitative regional oxygen transfer imaging of the human lung. J Magn Reson Imaging 26:637–645

Arroliga AC, Podell DN, Matthay RA (1992) Pulmonary manifestations of scleroderma. J Thorac Imag 7:30–45

ATS/ERS (2000) American Thoracic Society. Idiopathic pulmonary fibrosis: diagnosis and treatment. International consensus statement. American Thoracic Society (ATS), and the European Respiratory Society (ERS). Am J Respir Crit Care Med 646–664

ATS/ERS (2002) American Thoracic Society/European Respiratory Society International multidisciplinary consensus classification of the idiopathic interstitial pneumonias. Am J Respir Crit Care Med 165:277–304

ATS/ERS/JRS/ALAT (2011) Statement: idiopathic pulmonary fibrosis: evidence-based guidelines for diagnosis and management. AJRCCM 183:788–824

Bankier AA, Kiener HP, Wiesmayr MN et al (1995) Discrete lung involvement in systemic lupus erythematosus: CT assessment. Radiology 196:835–840

Bekkelund SI, Aasebo U, Pierre-Jerome C et al (1998) Magnetic resonance imaging of the thorax in the evaluation of asbestosis. Eur Respir J 11:194–197

Bergin CJ, Glover GH, Pauly JM (1991) Lung parenchyma: magnetic susceptibility in MR imaging. Radiology 180:845–848

Bergin CJ, Noll DC, Pauly JM et al (1992) MR imaging of lung parenchyma: a solution to susceptibility. Radiology 183:673–676

Berthezene Y, Vexler V, Kuwatsuru R et al (1992) Differentiation of alveolitis and pulmonary fibrosis with a macromolecular MR imaging contrast agent. Radiology 185:97–103

Bink A, Hanisch G, Karg A et al (2007) Clinical aspects of the apparent diffusion coefficient in 3He MRI: results in healthy volunteers and patients after lung transplantation. J Magn Reson Imaging 25:1152–1158

Black RD, Middleton HL, Cates GD et al (1996) In vivo He-3 MR images of guinea pig lungs. Radiology 199:867–870

Buzan MT, Eichinger M, Kreuter M et al (2015) T2 mapping of CT remodelling patterns in interstitial lung disease. Eur Radiol 25:3167–3174

Chetta A, Marangio E, Olivieri D (2004) Pulmonary function testing in interstitial lung diseases. Respiration 71:209–213

Chung JH, Cox CW, Forssen AV et al (2014) The dark lymph node sign on magnetic resonance imaging: a novel finding in patients with sarcoidosis. J Thorac Imaging 29:125–129

Chung JH, Little BP, Forssen AV et al (2013) Proton MRI in the evaluation of pulmonary sarcoidosis: comparison to chest CT. Eur J Radiol 82:2378–2385

Cleveland ZI, Virgincar RS, Qi Y et al (2014) 3D MRI of impaired hyperpolarized 129Xe uptake in a rat model of pulmonary fibrosis. NMR Biomed 27:1502–1514

Colby TV, Carrington CB (1994) Infiltrative lung disease. In: Thurlbeck WM (ed) Pathology of the lung. Thieme Medical Publishers, New York, pp 589–737

Craig DA, Colletti PM, Ratto D et al (1988) MRI findings in pulmonary sarcoidosis. Magn Reson Imaging 6:567–573

Dawson WB, Müller NL (1990) High-resolution computed tomography in pulmonary sarcoidosis. Semin Ultra CT MR 11:423–429

Desai SR, Verraraghavan S, Hansell DM et al (2004) CT features of lung disease in patients with systemic sclerosis: comparison with idiopathic pulmonary fibrosis and non-specific interstitial pneumonia. Radiology 232:560–567

Edelman RR, Hatabu H, Tadamura E et al (1996) Noninvasive assessment of regional ventilation in the human lung using oxygen-enhanced magnetic resonance imaging. Nat Med 2:1236–1239

Fenlon HM, Doran M, Sant SM et al (1996) High-resolution chest CT in systemic lupus erythematosus. AJR Am J Roentgenol 166:301–307

Gaeta M, Blandino A, Scribano E et al (2000) Chronic infiltrative lung diseases: value of gadolinium-enhanced MRI in the evaluation of disease activity-early report. Chest 117:1173–1178

Gammon RB, Bridges TA, al-Nezir H et al (1992) Bronchiolitis obliterans organizing pneumonia associated with systemic lupus erythematosus. Chest 102:1171–1174

Gast KK, Biedermann A, Herweling A et al (2007) Oxygensensitive (3)He-MRI in bronchiolitis obliterans after lung transplantation. Eur Radiol 18:530–537

Gast KK, Puderbach MU, Rodriguez I et al (2003) Distribution of ventilation in lung transplant recipients: evaluation by dynamic 3He-MRI with lung motion correction. Investig Radiol 38:341–348

Gewalt SL, Glover GH, Hedlund LW et al (1993) MR microscopy of the rat lung using projection reconstruction. Magn Reson Med 29:99–106

Gibson GJ, Pride NB (1977) Pulmonary mechanics in fibrosing alveolitis: the effects of lung shrinkage. Am Rev Respir Dis 116:637–647

Glazer H, Levitt RG, Lee JK et al (1984) Differentiation of radiation fibrosis from recurrent pulmonary neoplasm by magnetic resonance imaging. AJR Am J Roentgenol 143:729–730

Goodson BM (2002) Nuclear magnetic resonance of laser-polarized noble gases in molecules, materials, and organisms. J Magn Reson 155:157–216

Grenier P, Valeyre D, Cluzel P et al (1991) Chronic diffuse interstitial lung disease: diagnostic value of chest radiography and high-resolution CT. Radiology 179:123–132

Gross TJ, Hunninghake GW (2001) Idiopathic pulmonary fibrosis. N Engl J Med 345:517–525

Guenther D, Hanisch G, Kauczor HU (2000) Functional MR imaging of pulmonary ventilation using hyperpolarized noble gases. Acta Radiol 41:519–528

Gümüştaş S, Inan N, Akansel G et al (2013) Differentiation of lymphoma versus sarcoidosis in the setting of mediastinal-hilar lymphadenopathy: assessment with diffusion-weighted MR imaging. Sarcoidosis Vasc Diffuse Lung Dis 30:52–59

Hughes JM (2003) The single breath transfer factor (Tl, co) and the transfer coefficient (Kco): a window onto the pulmonary microcirculation. Clin Physiol Funct Imaging 23:63–71

Hunninghake GW, Zimmerman MB, Schwartz DA et al (2001) Utility of a lung biopsy for the diagnosis of idiopathic pulmonary fibrosis. Am J Respir Crit Care Med 164:193–196

Jakob PM, Hillenbrand CM, Wang T et al (2001) Rapid quantitative lung (1)H T(1) mapping. J Magn Reson Imaging 14:795–799

Jakob PM, Wang T, Schultz G et al (2004) Assessment of human pulmonary function using oxygen-enhanced T(1) imaging in patients with cystic fibrosis. Magn Reson Med 51:1009–1016

Kadota J, Kusano S, Kawakami K et al (1995) Usual interstitial pneumonia associated with primary Sjögren's syndrome. Chest 108:1756–1758

Kalaitzoglou I, Drevelengas A, Palladas P et al (1998) MRI appearance of pulmonary Wegener's granulomatosis with concomitant splenic infarction. Eur Radiol 8:367–370

Katzenstein AL, Fiorelli RF (1994) Nonspecific interstitial pneumonia/fibrosis: histologic features and clinical significance. Am J Surg Pathol 18:136–147

Katzenstein AL, Myers JL (1998) Idiopathic pulmonary fibrosis: clinical relevance of pathologic classification. Am J Respir Crit Care Med 157:1301–1315

Kauczor HU, Chen XJ, van Beek EJ et al (2001) Pulmonary ventilation imaged by magnetic resonance: at the doorstep of clinical application. Eur Respir J 17:1008–1023

Kauczor HU, Hanke A, Van Beek EJ (2002) Assessment of lung ventilation by MR imaging: current status and future perspectives. Eur Radiol 12:1962–1970

Kauczor HU, Hofmann D, Kreitner KF et al (1996) Normal and abnormal pulmonary ventilation: visualization at hyperpolarized He-3 MR imaging. Radiology 201:564–568

Kauczor U, Kreitner KF (1999) MRI of the pulmonary parenchyma. Eur Radiol 9:1755–1764

Kersjes W, Hildebrandt G, Cagil H et al (1999) Differentiation of alveolitis and pulmonary fibrosis in rabbits with magnetic resonance imaging after intrabronchial administration of bleomycin. Investig Radiol 34:13–21

Kim JS, Lee KS, Koh EM et al (2000) Thoracic involvement of systemic lupus erythematosus: clinical, pathologic, and radiologic findings. J Comput Assist Tomogr 24:9–18

King MA, Bergin CJ, Ghadishah E et al (1996) Detecting pulmonary abnormalities on magnetic resonance images in patients with usual interstitial pneumonitis: effect of varying window settings and gadopentetate dimeglumine. Acad Radiol 3:300–307

Knudson RJ, Kaltenborn WT (1981) Evaluation of lung elastic recoil by exponential curve analysis. Respir Physiol 46:29–42

Kouranos V, Hansell DM, Sharma R et al (2015) Advances in imaging of cardiopulmonary involvement in sarcoidosis. Curr Opin Pulm Med 21:538–545

Kreider ME, Hansen-Flaschen J, Ahmad NN et al (2007) Complications of video-assisted thoracoscopic lung biopsy in patients with interstitial lung disease. Ann Thorac Surg 83:1140–1144

Kuethe DO, Adolphi NL, Fukushima E (2007) Short data-acquisition times improve projection images of lung tissue. Magn Reson Med 57:1058–1064

Leung AN, Staples CA, Müller NL (1993) Parenchymal opacification in chronic infiltrative lung diseases: CT-pathologic correlation. Radiology 188:209–214

MacFall JR, Charles HC, Black RD et al (1996) Human lung air spaces: potential for MR imaging with hyperpolarized He-3. Radiology 200:553–558

Markstaller K, Kauczor HU, Puderbach M et al (2002) 3He- MRI-based vs. conventional determination of lung volumes in patients after unilateral lung transplantation: a new approach to regional spirometry. Acta Anaesthesiol Scand 46:845–852

Matsumoto S, Mori H, Miyake H et al (1998) MRI signal characteristics of progressive massive fibrosis in silicosis. Clin Radiol 53:510–514

McAdams HP, Rosado-de-Christenson ML, Wehunt WD et al (1996) The alphabet soup revisited: the chronic interstitial pneumonias in the 1990s. Radiographics 16:1009–1034

McCormack FX, King TE Jr, Voelker DR et al (1991) Idiopathic pulmonary fibrosis. Abnormalities in the bronchoalveolar lavage content of surfactant protein A. Am Rev Respir Dis 144:160–166

McFadden R, Carr TJ, Wood TE (1987) Proton magnetic resonance imaging to stage activity of interstitial lung disease. Chest 92:31–39

Middleton H, Black RD, Saam B et al (1995) MR imaging with hyperpolarized 3He gas. Magn Reson Med 33:271–275

Miller BH, Rosado-de-Christenson ML, McAdams HP et al (1995) From the archives of the AFIP. Thoracic sarcoidosis: radiologic-pathologic correlation. Radiographics 15:421–437

Mirsadraee S, Tse M, Kershaw L et al (2016) T1 characteristics of interstitial pulmonary fibrosis on 3T MRI-a predictor of early interstitial change? Quant Imaging Med Surg 6:42–49

Molinari F, Eichinger M, Risse F et al (2007) Navigatortriggered oxygen-enhanced MRI with simultaneous cardiac and respiratory synchronization for the assessment of interstitial lung disease. J Magn Reson Imaging 26:1523–1529

Molinari F, Madhuranthakam AJ, Lenkinski R et al (2014) Ultrashort echo time MRI of pulmonary water content: assessment in a sponge phantom at 1.5 and 3.0 Tesla. Diagn Interv Radiol 20:34–41

Moller HE, Chen XJ, Saam B et al (2002) MRI of the lungs using hyperpolarized noble gases. Magn Reson Med 47:1029–1051

Müller N, Mayo JR, Zwirewich CV (1992) Value of MR imaging in the evaluation of chronic infiltrative lung disease: comparison with CT. AJR Am J Roentgenol 158:1205–1209

Muller CJ, Schwaiblmair M, Scheidler J et al (2002) Pulmonary diffusing capacity: assessment with oxy-

gen-enhanced lung MR imaging preliminary findings. Radiology 222:499–506

Ohno Y, Hatabu H, Takenaka D et al (2002) Dynamic oxygen enhanced MRI reflects diffusing capacity of the lung. Magn Reson Med 47:1139–1144

Ohno Y, Koyama H, Yoshikawa T et al (2016) Pulmonary high-resolution ultrashort TE MR imaging: comparison with thin-section standard- and low-dose computed tomography for the assessment of pulmonary parenchyma diseases. J Magn Reson Imaging 43:512–532

Ohno Y, Nishio M, Koyama H et al (2014) Oxygen-enhanced MRI for patients with connective tissue diseases: comparison with thin-section CT of capability for pulmonary functional and disease severity assessment. Eur J Radiol 83:391–397

Perez T, Remy-Jardin M, Cortet B (1998) Airways involvement in rheumatoid arthritis: clinical, functional, and HRCT findings. Am J Respir Crit Care Med 157:1658–1665

Primack S, Mayo JR, Hartman TE et al (1994) MRI of infiltrative lung disease: comparison with pathologic findings. J Comput Assist Tomogr 18:233–238

Puderbach M, Hintze C, Ley S et al (2007) MR imaging of the chest: a practical approach at 1.5T. Eur J Radiol 64:345–355

Remy-Jardin M, Remy J, Cortet B et al (1994) Lung changes in rheumatoid arthritis: CT findings. Radiology 193:375–382

Robson MD, Bydder GM (2006) Clinical ultrashort echo time imaging of bone and other connective tissues. NMR Biomed 19:765–780

Sant SM, Doran M, Fenelon HM et al (1997) Pleuropulmonary abnormalities in patients who have systemic lupus erythematosus: assessment with high resolution computed tomography, chest radiography and pulmonary function tests. Clin Exp Rheumatol 15:507–513

Shioya S, Haida M, Fukuzaki M et al (1990) A 1-year time course study of the relaxation times and histology for irradiated rat lungs. Magn Reson Med 14:358–368

Stephen MJ, Emami K, Woodburn JM et al (2010) Quantitative assessment of lung ventilation and microstructure in an animal model of idiopathic pulmonary fibrosis using hyperpolarized gas MRI. Acad Radiol 17:1433–1443

Takahashi M, Togao O, Obara M et al (2010) Ultra-short echo time (UTE) MR imaging of the lung: comparison between normal and emphysematous lungs in mutant mice. J Magn Reson Imaging 32:326–333

Taorimina VJ (1981) Progressive systemic sclerosis subgroups: variable pulmonary features. AJR Am J Roentgenol 137:277–285

Taylor CR, Sostman HD, Gore JC et al (1987) Proton relaxation times in bleomycin-induced lung injury. Investig Radiol 22:621–626

Terriff BA, Kwan SY, Chan-Yeung MM et al (1992) Fibrosing alveolitis: chest radiography and CT as predictors of clinical and functional impairment at follow-up in 26 patients. Radiology 184:445–449

Thompson MJ, Colebatch HJ (1989) Decreased pulmonary distensibility in fibrosing alveolitis and its relation to decreased lung volume. Thorax 44:725–731

Togao O, Tsuji R, Ohno Y, Dimitrov I et al (2010) Ultrashort echo time (UTE) MRI of the lung: assessment of tissue density in the lung parenchyma. Magn Reson Med 64:1491–1498

Ulmer WT, Gillissen A, Reichel G et al (1993) Lung function and normal values [in German]. Pneumologie 47:403–408

Vinitski S, Pearson MG, Karlik SJ et al (1986) Differentiation of parenchymal lung disorders with in vitro proton nuclear magnetic resonance. Magn Reson Med 3:120–125

Webb WR (2001) Sarcoidosis. In: Webb WR, Müller NL, Naidich DP (eds) High-resolution CT of the lungs. Lippincott William and Wilkins, Philadelphia, pp 286–303

Webb WR, Stein MG, Finkbeiner WE et al (1988) Normal and diseased isolated lungs: high-resolution CT. Radiology 166:81–87

Wells AU, Hogaboam CM (2007) Update in diffuse parenchymal lung disease 2006. Am J Respir Crit Care Med 175:655–660

Wells AU, Rubens MB, du Bois RM et al (1993) Serial CT in fibrosing alveolitis: prognostic significance of the initial pattern. AJR Am J Roentgenol 161:1159–1165

Wiedemann HP, Matthay RA (1992) Pulmonary manifestations of systemic lupus erythematosus. J Thorac Imaging 7:1–18

Yankelevitz D, Henschke CI, Batata M et al (1994) Lung cancer: evaluation with MR imaging during and after irradiation. J Thorac Imaging 9:41–46

Zaporozhan J, Ley S, Gast KK et al (2004) Functional analysis in single-lung transplant recipients: a comparative study of high-resolution CT, 3He-MRI, and pulmonary function tests. Chest 125:173–181

Zaporozhan J, Ley S, Gast KK et al (2005) Visual assessment of functional lungs parenchyma on HRCT and (3)He-MRI in patients after single lung transplantation: comparison with quantitative volumetric results. Fortschr Röntgenstr 177:516–523

Zurek M, Bessaad A, Cieslar K et al (2010) Validation of simple and robust protocols for high-resolution lung proton MRI in mice. Magn Reson Med 64:401–407

Diseases of the Pleura and the Chest Wall

Claus Peter Heussel, Mark Oliver Wielpütz, and Hans-Ulrich Kauczor

Contents

C.P. Heussel • Mark Oliver Wielpütz
Hans-Ulrich Kauczor (✉)
Department of Interventional and Diagnostic
Radiology with Nuclear Medicine, Clinic for
Thoracic Diseases, University Heidelberg,
Heidelberg 69126, Germany

Department of Diagnostic and Interventional
Radiology, University Hospital Heidelberg,
Heidelberg 69120, Germany

Translational Lung Research Center, Member of the
German Center of Lung Research, University of
Heidelberg, Heidelberg 69120, Germany
e-mail: heussel@uni-heidelberg.de; Hans-Ulrich.
Kauczor@med.uni-heidelberg.de

Key Points

Primary tumours of the chest wall and pleura are rare in comparison to tumours of the lung such as bronchial carcinomas. Chest wall tumours are a heterogeneous group that pose an interesting diagnostic challenge for radiologists. They make up less than 5% of thoracic malignancies and vary widely in pathology as they arise from all anatomic structures of the chest wall. Since chemotherapy is rarely effective and local control is the most important prognostic factor, wide local excision might be the solely curative treatment. Therefore, the margins need to be identified by imaging prior to surgery and adjuvant radiation, which might be applied in cases with positive margins. Malignant pleural mesothelioma is an aggressively growing tumour and a rising incidence is expected in the next decades. CT is still the general diagnostic tool for staging and therapy planning of malignant pleural mesothelioma. However, within the last years novel MRI techniques have been developed and introduced into clinical routine to improve tumour delineation and characterization in order to optimize individual therapy planning. Typical findings of those tumours using modern MRI techniques are discussed. Techniques are compared with CT and modern PET techniques, especially concerning characterization, precision of tumour delineation, therapy planning, and monitoring.

1 Asbestosis

In general, asbestos fibres cause an inflammation of the parietal pleura, leading to pleural plaques, diffuse pleural fibrosis, rounded atelectasis, pleural effusion, bronchogenic carcinoma, and malignant pleural mesothelioma (MPM) (Schwartz 1991; Mossmann and Gee 1989). Bilateral scattered eventually calcified pleural plaques are pathognomonic signs for asbestos exposure (Peacock et al. 2000). Pleural plaques are the most commonly observed signs after asbestos exposure, observed in 60–70% of exposed workers (Falaschi et al. 1995). The average latency period is about 15 years for non-calcified and at least 20 years for calcified plaques (Müller 1993) (Fig. 1a). Their detection is important because

asbestos-exposed patients have an approximately three fold higher risk of developing lung cancer and MPM if plaques are evident (Kishimoto et al. 2003). Therefore, pleural plaques may be regarded as risk indicators of possibly asbestos-related tumours in an asbestos-exposed population. The average latency period from the first asbestos exposure to detection of a malignant tumour ranges from 20 to 43 years (Kishimoto et al. 2003; Soeberg et al. 2016). Since the pleural lesions associated with asbestos exposure might be subtle, the detection is a challenging task for the radiologist. Even in cardiac or abdominal imaging or even chest imaging with indications different than diagnosis of interstitial lung disease plaques are an incidental finding of grave importance. Basing upon these specific findings, the radiologist has to
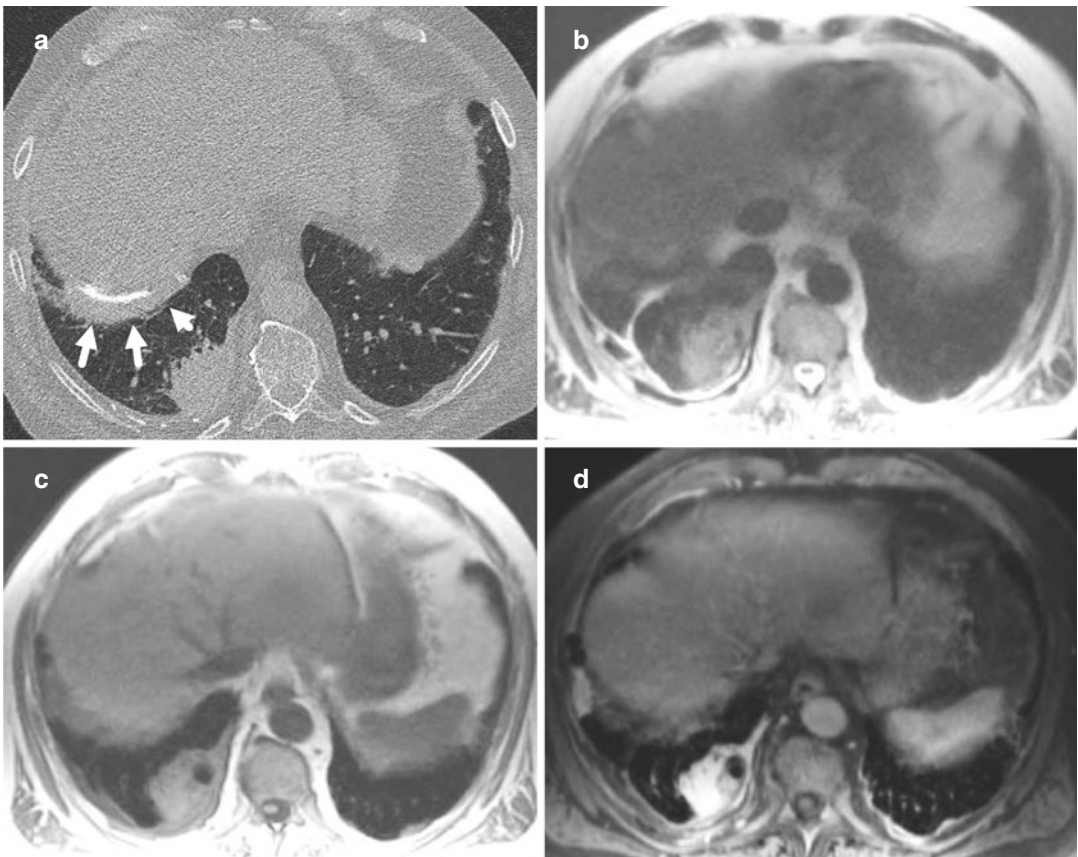
Fig. 1 Intraindividual comparison of pleural plaque and round atelectasis in a 76-year-old male. (**a**) CT demonstrates a mass with soft tissue density, (**b**) T2 SE shows subpleural fat, (**c**) T1 SE reveals no effusion but pleural plaque, and (**d**) T1 GE fat-sat depicts contrast enhance-

ment of the pleura and the pleural plaque and high and homogeneous enhancement of the mass indicating round atelectasis. *Published with kind permission of © Claus-Peter Heussel 2017. All Rights Reserved*

raise the suspicion of an occupational disease, which may result in screening programmes for malignancy and financial compensation of the patient. Conventional chest radiography has a sensitivity as low as 13–53% caused by superimposition. This is combined with a low specificity due to lack of calibrated density measurement to separate fat from soft tissue (Fig. 1a), which is easy in CT. In general, magnetic resonance imaging (MRI) is rarely used for the diagnosis of pleural plaques, also because of lack of confidence of depicting fine calcifications. Currently, computed tomography (CT) is the gold standard tool for the detection of benign asbestos-induced changes of the pleura (Lynch et al. 1989) (Fig. 1a). However, in cases of pleural plaques combined with either pleural effusion or with round atelectasis (Fig. 1a–d), the high soft tissue contrast of MRI can be helpful to distinguish effusion from soft tissue, i.e. malignant tumour, and atelectasis from carcinoma (Fig. 1a–d).

1.1 Mesothelioma

Malignant pleural mesothelioma (MPM) is the most common cancer in persons that have been exposed to asbestos. It is 1000 times more common in a population exposed to asbestos with no correlation to smoking history. Since regulatory restrictions have been introduced in the 1990s, the incidence is expected to peak in 2020 in industrialized countries (Bibby et al. 2016). Imaging plays a major role in the assessment of patients with suspected MPM, and can contribute both diagnostic and staging information. Typical radiological signs are pleural effusion, loss of hemithoracic volume, nodular or focal pleural and fissural thickening, and eventually including infiltration of the diaphragm and chest wall (Bibby et al. 2016) (Fig. 2). The major differential diagnosis is metastatic adenocarcinoma in terms of pleural carcinomatosis (Fig. 3). The presence of pleural plaques may alert to prior asbestos exposure, even in the absence of known exposure. However, radiological interpretation can be difficult if pleural thickening is minimal or absent, and even cross-sectional imaging is challenged by the heterogeneous growth pattern. Since MPM biomarkers have been found of limited clinical use and cytological yield is low, biopsies are required for diagnosis and identification of the histological sub-type (Bibby et al. 2016). There is no curative treatment for
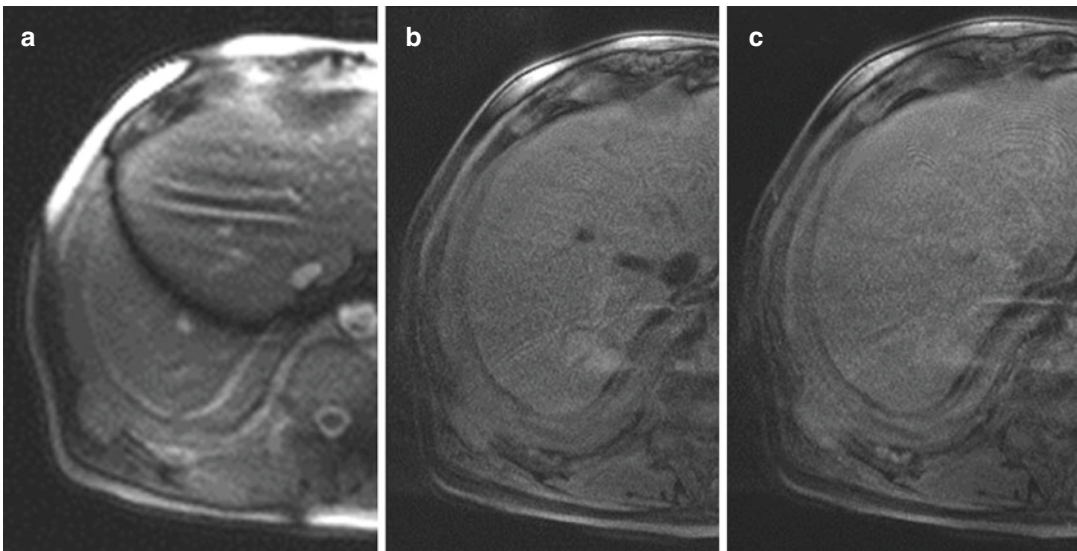
Fig. 2 Chest wall invasion by mesothelioma in a 73-year-old male: T2w image demonstrates soft tissue signal in the pleural space indicating pleural tumour and dorsolateral infiltration of the intercostal muscle (**a**). T1w GE fat-saturated without (**b**) and with (**c**) contrast demonstrate enhancement of the tumour. *Published with kind permission of © Claus-Peter Heussel 2017. All Rights Reserved*
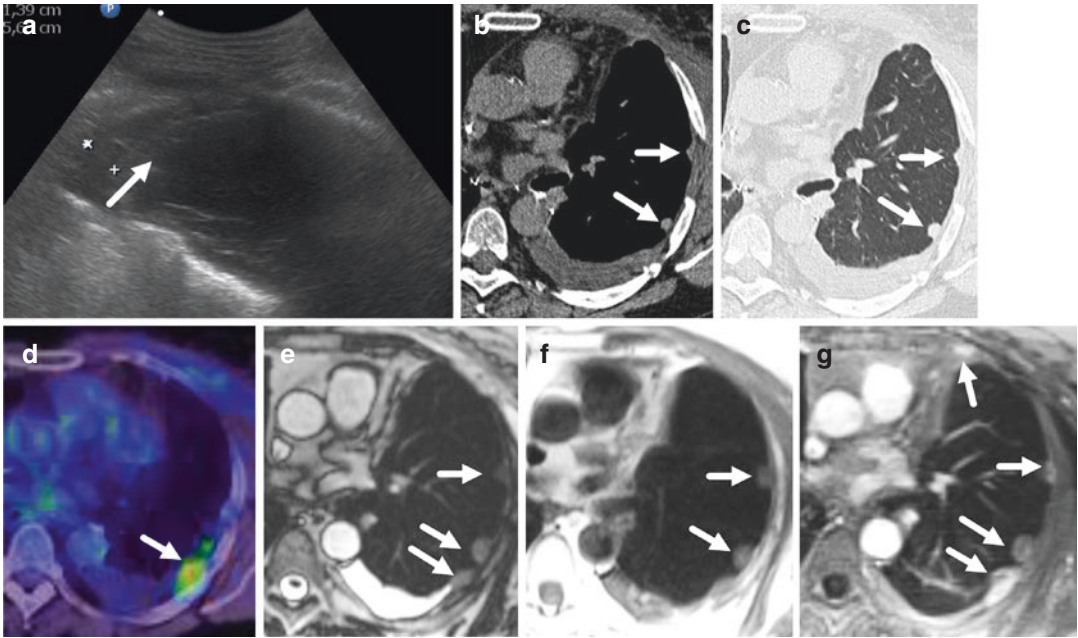
Fig. 3 Ultrasound (**a**), non-enhanced CT (**b**, **c**), FDG-PET/CT, (**d**) and MRT (**e**, **f**, **g**) were performed in a 53-year-old female suffering from non-small cell lung cancer with pleural carcinomatosis. Note the difference in signal intensity in the true-FISP sequence between the pleural nodules and the effusion (**e**) and the significant contrast enhancement (**g**). *Published with kind permission of © Claus-Peter Heussel 2017. All Rights Reserved*

MPM. Systemic treatment options include chemotherapy, targeted therapy, and radiotherapy and should be discussed at a specialist mesothelioma multidisciplinary team. Surgery is controversial and limited to patients with early-stage disease and good functional status (Bibby et al. 2016).

2 Tumour Imaging

Imaging plays an important role in the detection, diagnosis, staging, response assessment, and surveillance of MPM. The aetiology, biology, and growth pattern of mesothelioma present unique challenges for each modality used to capture various aspects of this disease. Those goals are early detection of disease, optimizing sensitivity and specificity for anatomic involvement of unresectable planes to identify patients who are suitable for surgical resection, improving prognosis, and assessing response to treatment

as a surrogate for therapeutic benefit. Clinical implementation of techniques and information derived from ultrasound, CT, PET/CT, and MRI evolve based on active research in this field worldwide (Armato et al. 2016). Thoracic ultrasound is commonly performed by respiratory physicians to assess pleural fluid volume, distribution, and echogenicity, and to determine a safe site for aspiration (Havelock et al. 2010). Thoracic ultrasound allows also for visualization of pleural thickening and nodularity with a specificity of >95% with regard to malignancy while sensitivity is low at 40% (Bibby et al. 2016). The advantages of MRI include high soft tissue contrast, *early* contrast enhancement features of the pleura that might be characteristic of early-stage mesothelioma as well as diffusion-weighted imaging (DWI), which is being used to compute tumour volume (Armato et al. 2016). On the basis of the present literature and own experience a basic MRI protocol to image MPM is recommended (Table 1).

Table 1 Recommended protocol for MRI of malignant pleural mesothelioma (see http://mriquestions.com)

Sequence	Intention
HASTE, SS-FSE (single-shot fast spin echo) coronal and axial	Investigation of the whole lung, parenchyma, and short overview of the thorax
VIBE (volume interpolated breath-hold examination) or 3D spoiled gradient-echo post-contrast coronal and sagittal	Demonstration of well-perfused tumour areas
T1-TSE (Turbo spin echo) non-breath-hold coronal	High-resolution images of the thorax and the MPM
T2-TSE respiratory gated coronal	Ultra high-resolution images of the thorax and the MPM. Detection of a potential infiltration of vessels, chest wall, brachial plexus, etc.
DWI (diffusion-weighted imaging) axial	Measurement of apparent diffusion coefficient (ADC) as sign of increased cellularity and therefore possible malignancy
Optional: dynamic TrueFISP (true Fast Imaging with Steady-state Precession) or steady-state GRE sequences (e.g. GRASS/FISP) coronal	Investigation of mobility of lung, diaphragm, and chest wall

Table 2 Staging system by Butchart et al. (1976)

Stage	Description
I	Tumour confined within the "capsule" of the parietal pleura, i.e. involving only ipsilateral pleura, lung, pericardium, and diaphragm
II	Tumour invading chest wall or involving mediastinal structures, e.g. oesophagus, heart, opposite pleura. Lymph node involvement within the chest
III	Tumour penetrating diaphragm to involve peritoneum; involvement of opposite pleura. Lymph node involvement outside the chest
IV	Distant blood-borne metastases

which has gained universal acceptance (Tables 3 and 4) (Rusch 1996; Pass et al. 2016).

A T1 descriptor indicates that there is usually a free pleural space, and these patients often present with a large pleural effusion. However, the presence of pleural fluid has no effect on staging. By non-invasive staging it is rather difficult to make a distinction between T1a, T1b, and T2 disease. Correct estimation of the extent of disease is therefore only possible during thoracotomy. In case of T1b disease, pleurectomy and decortication are usually feasible. In case of a T2 tumour there is more extensive involvement of the visceral pleura and lung, often necessitating a pleuropneumonectomy. T3 implies locally advanced but potentially respectable MPM, whereas T4 characterizes a non-resectable tumour. The identification of an intercostal infiltration by the tumour is crucial for the surgical planning as inoculation metastasis develop, e.g. after transthoracic drainage. Furthermore, the extension of the tumour into the recess is an underestimated problem since this is crucial for radiation planning. Since MPM mass is often difficult to distinguish at CT from chest wall, diaphragm, pleural effusions, or atelectasis, the high soft tissue contrast of MRI is very helpful here (Plathow et al. 2008). The prognosis of a T4 tumour is similar to M1 disease, and for this reason it is included in stage IV. In the IMIG system, lymph node staging is similar but not identical to the staging of non-small cell lung cancer. N1 disease relates to the involvement of the ipsilateral bronchopulmonary and/or hilar

2.1 Staging

Objective radiologic response rate is the key efficacy endpoint in the development of new therapies. The morphology and growth characteristics of mesothelioma, however, differ from many other solid tumours in that the disease often forms a rind around the pleural cavity, with a sheet-like rather than spherical growth pattern (Armato et al. 2016). There are at least five different staging systems for MPM: Butchart introduced a classification system into four stages, which became widely used (Table 2) (Butchart et al. 1976). However, in an attempt to distinguish patients who would benefit from surgical resection with curative intent from those needing palliative treatment, the International Mesothelioma Interest Group (IMIG) has introduced a staging system for MPM

Table 3 Staging system for diffuse malignant pleural mesothelioma introduced by the International Mesothelioma Interest Group (IMIG) (Rusch 1996)

Primary Tumour (T)

Tx	Primary tumour cannot be assessed
T0	No evidence of primary tumour
T1	Tumour involves ipsilateral parietal pleura, with or without focal involvement of visceral pleura
	T1a tumour involves ipsilateral parietal (mediastinal, diaphragmatic) pleura. No involvement of the visceral pleura (i.e. fissures are free)
	T1b tumour involves ipsilateral parietal (mediastinal, diaphragmatic) pleura, with focal involvement of the visceral pleura
T2	Tumour involves any of the ipsilateral pleural surfaces with at least one of the following
	Confluent visceral pleural tumour (including fissure)
	Invasion of diaphragmatic muscle or lung parenchyma
T3	Tumour involves any of the ipsilateral pleural surfaces, with at least one of the following:
	Invasion of the endothoracic fascia or into mediastinal fat
	Solitary focus of tumour invading the soft tissue of the chest wall
	Non-transmural involvement of the pericardium
T4	Tumour involves any of the ipsilateral pleural surfaces, with at least one of the following:
	Diffuse or multifocal invasion of soft tissues of the chest wall or rib
	Invasion through the diaphragm to the peritoneum, into the spine, myocardium, or brachial plexus
	Direct extension to the contralateral pleura
	Extension to the internal surface of the pericardium
	Pericardial effusion with positive cytology

Regional Lymph Nodes (N)

NX	Regional lymph nodes cannot be assessed
N0	No regional lymph node metastases
N1	Metastases in the ipsilateral bronchopulmonary or hilar lymph node
N2	Metastases in the subcarinal ipsilateral internal mammary or mediastinal lymph node
N3	Metastases in the contralateral mediastinal, internal mammary, or hilar lymph node, any supraclavicular or scalene lymph node

(continued)

Table 3 (continued)

Distant Metastases (M)

MX	Distant metastases cannot be assessed
M0	No distant metastasis
M1	Distant metastases

Table 4 Stage grouping of malignant pleural mesothelioma (Rusch 1996)

Stage I	T1	N0	M0
Stage IA	T1a	N0	M0
Stage IB	T1b	N0	M0
Stage II	T2	N0	M0
Stage III	T1, T2	N1	M0
	T1, T2	N2	M0
	T3	N0, N1, N2	M0
Stage IV	T4	Any N	M0
	Any T	N3	M0
	Any T	Any N	M1

lymph node(s). N2 disease includes invasion of the ipsilateral mediastinal, subcarinal, or the ipsilateral internal mammary nodes, while N3 disease includes the contralateral hilar, mediastinal, internal mammary nodes and/or the ipsilateral or contralateral supraclavicular or scalene lymph nodes. Precise evaluation of the peritracheal mediastinal lymph nodes often requires mediastinoscopy. Not only for mediastinal nodal involvement but also in the case of early mesothelioma, there is a discrepancy between noninvasive (clinical, imaging based) and subsequent surgical staging. The IMIG classification presumes that early tumours are evaluated surgically to determine local extension and subsequent treatment. It should also be stated that within a specific T and N subset differences in tumour biology are possible, resulting in a variable prognosis within the same group.

2.2 Response Evaluation Using Modified RECIST

Objective tumour size response evaluation remains nowadays the most often used primary endpoint in many clinical trials, allowing determining the efficacy of a treatment regimen. The widespread

RECIST (Response Evaluation Criteria in Solid Tumors) guidelines version 1.0 (Therasse et al. 2000) as well as its update to version 1.1 use unidimensional tumour measurements. RECIST, however, requires a measurement of a tumour's longest diameter, and the underlying assumption is of a spherical growth pattern. The poor suitability of RECIST for measurement of mesothelioma leads to the modified RECIST criteria for mesothelioma (Byrne and Nowak 2004) to address this drawback (Armato et al. 2016). The modified RECIST criteria are as follows. Tumour thickness perpendicular to the chest wall or mediastinum measured in two

positions at three separate levels on transverse sections of a CT scan, preferably above the level of division of the main bronchi (Tsao et al. 2011). The sum of the six measurements defined a pleural unidimensional measure. Transverse sections at least 1 cm apart and related to anatomical landmarks in the thorax are assumed to allow reproducible assessment at later time points. If measureable tumour is present, transverse cuts in the upper thorax, above the level of division of the main bronchi, were preferred. At reassessment, pleural thickness was measured at the same position at the same level and by the same observer.
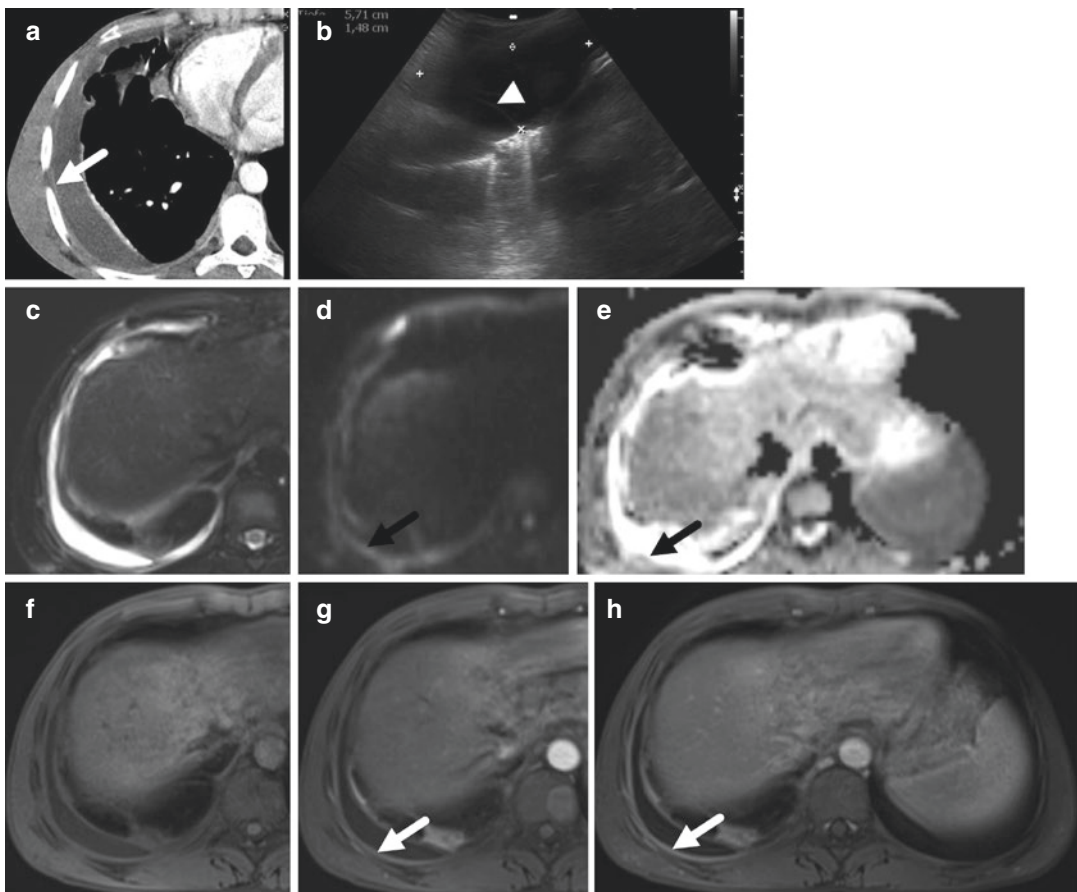
Fig. 4 Pleural effusion was detected in CT of a 28-year-old male with an enhancing thickened pleura (**a**, *white arrow*). Ultrasound (**b**) and T2w MR (**c**) verified the liquid while ultrasound revealed septation (*arrow-head*). Diffusion-weighted MR demonstrated high cellularity (**d**, b = 1000 ms, *black arrow*) and short ADC values (**e**, *black arrow*). In T1w MRI, the signal of the liquid is low, thus neither hematoma nor chylothorax was suspected. Significant contrast enhance-

ment was observed after contrast application (early: **g**, late: **h**, *white arrow*). While pleural thickening, diffusion, and contrast enhancement would be compatible with malignancy, the lack of nodules and the evidence of septations indicated infection. However, clinical symptoms of infection were missing. After thoracocentesis, *M. tuberculosis* was identified as the underlying agent of an empyema. *Published with kind permission of © Claus-Peter Heussel 2017. All Rights Reserved*

This was not necessarily the greatest tumour thickness at that level. Nodal, subcutaneous, and other bidimensionally measurable lesions are measured unidimensionally as per the RECIST criteria. Unidimensional measurements are added to obtain the total tumour measurement (Byrne and Nowak 2004). In the RECIST system adopted for MPM staging, CR was defined as the disappearance of all target lesions with no evidence of tumour elsewhere, and PR was defined as at least a 30% reduction in the total tumour measurement. Progressive disease (PD) was defined as an increase of at least 20% in the total tumour measurement over the nadir measurement, or the appearance of one or more new lesions. Patients with stable disease (SD) were those who fulfilled the criteria for neither PR nor PD (Byrne and Nowak 2004).

3 MRI of Other Pleural Diseases

Pleural fluid collections can be determined by MRI as being either transudates or exudates to some extent. Exudative pleural effusions show a higher degree of enhancement after IV gadolinium-based contrast administration than transudative pleural effusions (Fiola et al. 1997) (Fig. 4). Diffusion-weighted imaging with an echoplanar imaging sequence may differentiate exudates from transudates based on the apparent diffusion coefficient (ADC) value (Baysal et al. 2003). High signal intensity on T1-weighted images identifies a chylothorax (McLoud and Flower 1991). Subacute and chronic hematoma can be recognized in the pleural space based on its signal characteristics related to the blood breakdown products (Mitchell 2003). The use of MRI herein is mainly supplemental to ultrasound.

3.1 Solitary Fibrous Tumour of the Pleura

Solitary fibrous tumour (SFT), also known as hemangiopericytoma, is a fibroblastic mesenchymal tumour accounting for <2% of all soft tissue sarcomas and in the vast majority shows benign behaviour. Tumour size varies at time of resection with an average of around 9 cm. Since the symptoms are variable and non-specific, its diagnosis is often incidental. SFTs appear usually well-defined, cystic or solid mass with low T1, inhomogeneous high T2 signal while contrast enhancement is heterogeneous (Mitchell 2003; Wei Ge et al. 2016). Complete surgical resection remains the therapy of choice for both the benign and malignant variants. The morphology and relationship of large lesions to adjacent mediastinal and major vascular structures may be better delineated using MRI compared with CT. MRI is helpful in differentiating tumour from other structures and in confirming the intrathoracic localization (Figs. 5 and 6). In general, on T2-weighted images benign lesions have
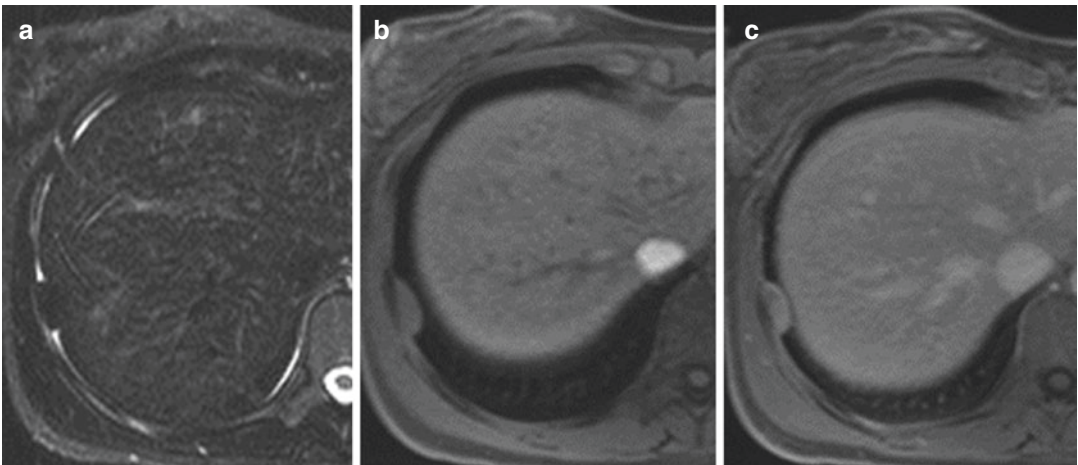
Fig. 5 Pleural lesion with low T2 signal (**a**), intermediate T1 signal (**b**), and significant contrast uptake (**c**) in a 20-year-old female. Neither pleural effusion nor chest wall invasion was detected. Surgical resection revealed solitary fibrous tumour (SFT). *Published with kind permission of © Claus-Peter Heussel 2017. All Rights Reserved*
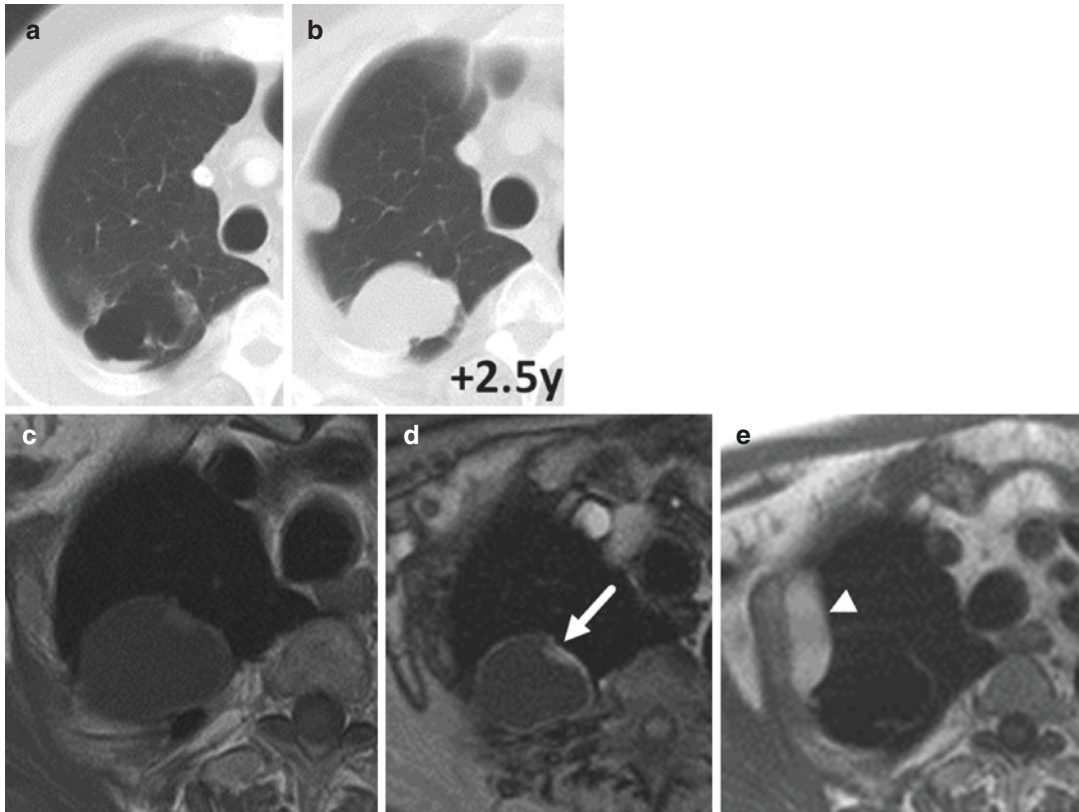
Fig. 6 A new filling was observed within an apical cyst at CT after 2.5 years in a 65-year-old male (**a**, **b**). MRI was performed for further characterization and revealed a contrast enhancing lesion at the rim (**c**, **d**, *arrow*). This was verified as adenocarcinoma after surgery. MRI also revealed a similar lesion (**e**) suspicious for pleural carcinomatosis; however, a xanthomatoid fibrous inflammation was confirmed by histology reflecting the different signal characteristics (*arrowhead*). *Published with kind permission of © Claus-Peter Heussel 2017. All Rights Reserved*

low signal intensity, whereas malignant SFT invariably appears with high signal intensity because of increased vascularity, edema, and cellularity. Benign and malignant lesions have low signal intensity on T1-weighted images. Unfortunately, benign solitary fibrous tumours of the pleura often can also have areas of high signal intensity on T2-weighted images because of intratumoural necrosis or myxoid degeneration and thus may not be differentiable from malignant formations. They also might show significant enhancement after contrast administration on T1-weighted images.

4 Chest Wall Diseases

Tumours of the chest wall can vary from benign to malignant and histologically originate from any soft tissue or bony structure. Besides breast, malignant and benign chest wall tumours, tumours like elastofibroma (Müller et al. 1999), SAPHO (Laiho et al. 2001), and sarcomas (Koenigkam-Santos et al. 2014) are to be imaged and treated according to musculoskeletal procedures. However, more than 50% of chest wall tumours are malignant, typically involving direct invasion or metastases from adjacent thoracic tumours (David and Marshall 2011). In general, MRI and CT have complementary roles in the evaluation of sternal and rib tumours: While CT is useful for imaging the cortical bone and calcified tumour matrix, multiplanar MRI with its inheritably superior tissue-resolving features is the technique of choice for evaluating the extent of medullary and extraosseous tumour extent as well as its relationship to adjacent structures with regard to operability (Aslam et al. 2002). Due to the rarity of chest wall tumours, the use of PET has not been formally

established as a diagnostic tool in the evaluation. However, in the case of malignant disease and other radiographic abnormalities, PET may be useful for staging (David and Marshall 2011).

4.1 Imaging of the Chest Wall

Frequently, a palpation finding or pain is reported by the patient as the main symptom initiating diagnostic work-up. This clinical information should be taken seriously since the identification of the affected localization can help of find the tumour fast and reliable. Sequences, e.g. for lesion characterization, can be limited to the tumour site improving image quality with shorter acquisition time, e.g. by using thinner slice thickness, higher signal, or smaller field-of-view. MR-visible markers should be placed at the suspected site to ensure imaging of the correct place. MR-sequences for tissue characterization include estimation of fat content, measurement of apparent diffusion coefficient, and quantification of contrast enhancement. For the proof of contrast uptake, pre- and post-contrast sequences should be planned completely identical, which includes TR, TE, fat-sat, and localization. This enables the assessment of contrast enhancement and even image subtraction to show even minimal enhancement (Table 1). Breath-hold imaging is usually necessary in supine position; however, prone position might be helpful to reduce breathing artefacts if the tumour is located anteriorly, if the patient tolerates this position (Fig. 7). Rib lesions need special attention in MR planning and may require individualized double angulated data acquisition. Image acquisition in at least two planes is essential, while one plane is usually transversal and the second perpendicular to the affected chest wall. In case of sternal or sternoclavicular lesions, coronal thin sections angulated to the course of the sternum are of additional use. In each of these entities, MRI helps in delineation of normal anatomical structures and is helpful in guiding surgery or biopsy (Figs. 7, 8, and 9). Therefore, the anatomical relationship of the lesion to the surrounding structures needs to be demonstrated and available in the operating theatre.
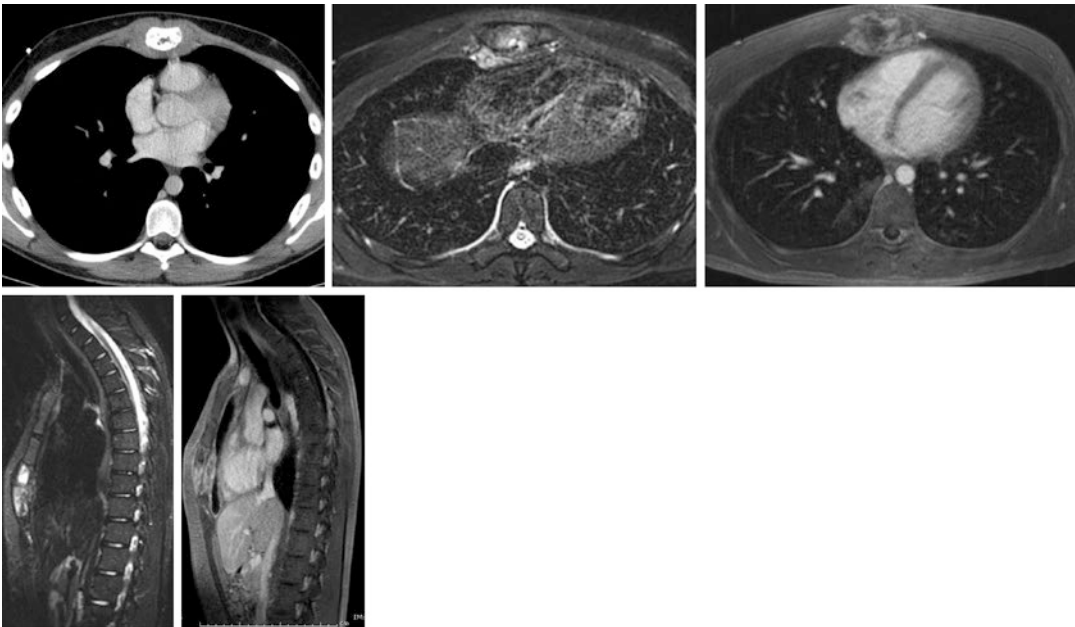
Fig. 7 A soft tissue mass surrounding and infiltrating the corpus sterni was detected at CT of a 21-year-old male and verified at T2 and T1 after contrast enhancement. Transversal and sagittal plane were acquired in prone position to avoid breathing artefacts and for best visualization of tumour extent prior to surgical resection of the Ewing sarcoma. *Published with kind permission of © Claus-Peter Heussel 2017. All Rights Reserved*
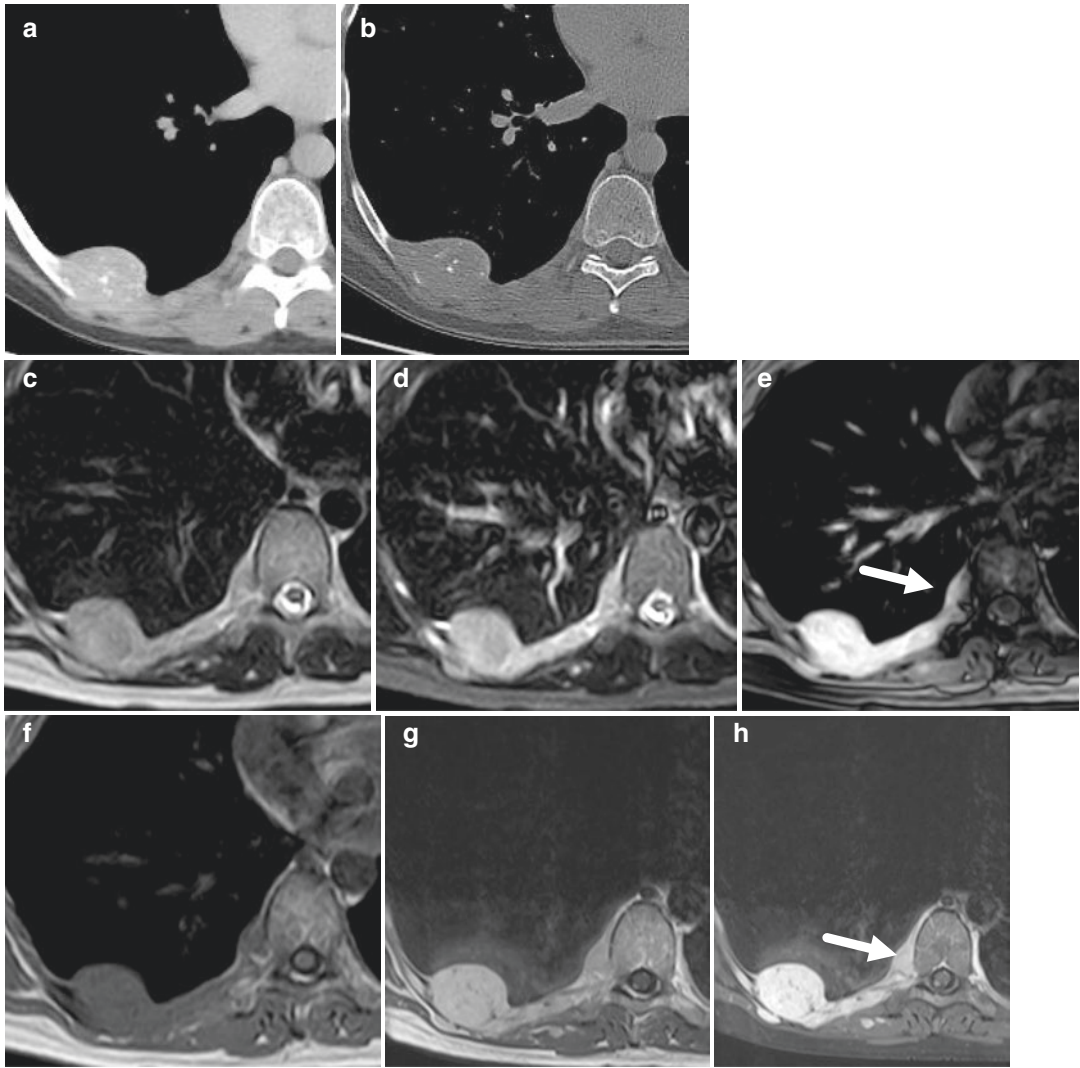
Fig. 8 Nodular mass of 3 cm was detected at CT of a 33-year-old female with destruction of and along the rib and calcification dots (**a**, **b**). T2 signal was homogeneously high (**c–e**), especially after fat supression (**e**). T1 signal was homogeneously intermediate (**f**) with significant uptake of contrast agent (**g**, **h**), especially after fat suppression (**h**). Extent of the tumour along the rib towards the vertebral body is depictable best after fat suppression (**e**, **h**, *arrow*). Chondrosarcoma was identified after complete surgery. *Published with kind permission of © Claus-Peter Heussel 2017. All Rights Reserved*
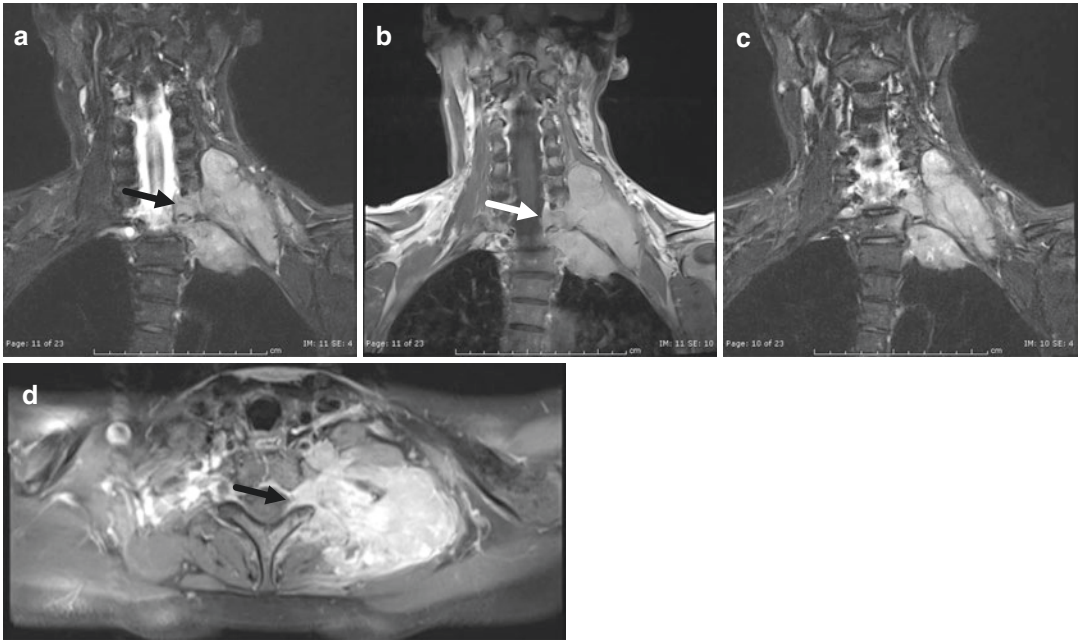
Fig. 9 A mass of 7 cm was detected in the lung apex of a 44-year-old female encasing the left plexus brachiocervicalis, infiltrating several cervical vertebra and the neuroforamen towards the dural sac (**a**, **b**, **d**, *arrow*). Extent of the tumour is depictable best after fat suppression (**a**, **c**, **d**) for surgical planning. *Published with kind permission of © Claus-Peter Heussel 2017. All Rights Reserved*

References

Armato SG 3rd, Blyth KG, Keating JJ, Katz S, Tsim S, Coolen J, Gudmundsson E, Opitz I, Nowak AK (2016) Imaging in pleural mesothelioma: a review of the 13th international conference of the international mesothelioma interest group. Lung Cancer 101:48–58

Aslam M, Rajesh A, Entwisle J et al (2002) Pictorial review: MRI of the sternum and sternoclavicular joints. Br J Radiol 75:627–634

Baysal T, Bulut T, Gokimak M et al (2003) Diffusion-weighted MR imaging of pleural fluid: differentiation of transudative vs. exudative pleural effusions. Eur Radiol 14:890–896

Bibby AC, Tsim S, Kanellakis N, Ball H, Talbot DC, Blyth KG, Maskell NA, Psallidas I (2016) Malignant pleural mesothelioma: an update on investigation, diagnosis and treatment. Eur Respir Rev 25(142):472–486

Butchart EG, Ashcroft T, Barnsley WC et al (1976) Pleuropneumonectomy in the management of diffuse malignant mesothelioma of the pleura. Experience with 29 patients. Thorax 31:15–24

Byrne MJ, Nowak AK (2004) Modified RECIST criteria for assessment of response in malignant pleural mesothelioma. Ann Oncol 15:257–260

David EA, Marshall MB (2011) Review of chest wall tumors: a diagnostic, therapeutic, and reconstructive challenge. Semin Plast Surg 25(1):16–24

Falaschi F, Boraschi P, Neri S et al (1995) High-resolution computed tomography (HRCT) in the detection of "early asbestosis". Eur Radiol 5:291–296

Fiola C, Cantoni S, Turtulici I et al (1997) Transudative vs exudative pleural effusions: differentiation using Gd-DTPA-enhanced MRI. Eur Radiol 7:860–867

Ge W, Yu D-C, Chen G, Ding Y-T (2016) Clinical analysis of 47 cases of solitary fibrous tumor. Oncol Lett 12:2475–2480

Havelock T, Teoh R, Laws D, Gleeson F (2010) Pleural procedures and thoracic ultrasound: British Thoracic Society pleural disease guideline 2010. Thorax 65:i61–i76

Kishimoto T, Ohnishi K, Saito Y (2003) Clinical study of asbestos-related lung cancer. Ind Health 41:94–100

Koenigkam-Santos M, Sommer G, Puderbach M, Safi S, Schnabel PA, Kauczor HU, Heussel CP (2014) Primary intrathoracic malignant mesenchymal tumours: computed tomography features of a rare group of chest neoplasms. Insights Imaging 5:237–244

Laiho K, Soini I, Martio J (2001) Magnetic resonance imaging findings of manubriosternal joint involvement in SAPHO syndrome. Clin Rheumatol 20:232–233

Lynch DA, Gamsu G, Aberle DR (1989) Conventional and high resolution computed tomography in the diagnosis of asbestos-related diseases. Radiographics 9:523–551

McLoud TC, Flower CD (1991) Imaging of the pleura: sonography, CT, and MR imaging. Am J Roentgenol 156:1145–1152

Mitchell JD (2003) Solitary fibrous tumor of the pleura. Semin Thorac Cardiovasc Surg 15:305–309

Mossman BT, Gee JB (1989) Asbestos-related diseases. N Engl J Med. 320:1721–1730

Müller NL (1993) Imaging of the pleura. Radiology 186:297–309

Müller LP, Wolf HK, Heussel CP et al (1999) Bilateral elastofibroma dorsi. Chirurg 70:1357–1360

Pass H, Giroux D, Kennedy C, Ruffini E, Cangir AK, Rice D, Asamura H, Waller D, Edwards J, Weder W, Hoffmann H, van Meerbeeck JP, Nowak A, Rusch VW IASLC Staging and Prognostic Factors Committee, Advisory Boards and Participating Institutions. The IASLC mesothelioma staging project: improving staging of a rare disease through international participation. J Thorac Oncol 2016;11(12):2082–2088

Peacock C, Copley SJ, Hansell DM (2000) Asbestos-related benign pleural disease. Clin Radiol 55:422–432

Plathow C, Klopp M, Zuna I, Schmähl M, Kauczor HU (2008) Therapy response in malignant pleural mesothelioma – role of MRI using RECIST, Modified RECIST and volumetric approaches in comparison with CT. Eur Radiol 18:1635–1643

Rusch V (1996) A proposed new International TNM Staging System for malignant pleural mesothelioma from the International Mesothelioma Interest Group. Lung Cancer 14:1–12

Schwartz DA (1991) New developments in asbestos-induced pleural disease. Chest 99:191–198

Soeberg MJ, Leigh J, van Zandwijk N (2016) Malignant mesothelioma in Australia 2015: current incidence and asbestos exposure trends. J Toxicol Environ Health B Crit Rev 19(5–6):173–189

Therasse P, Arbuck SG, Eisenhauer EA, Wanders J, Kaplan RS, Rubinstein L, Verweij J, Van Glabbeke M, van Oosterom AT, Christian MC, Gwyther SG (2000) New guidelines to evaluate the response to treatment in solid tumors. J Natl Cancer Inst 92:205–216

Tsao AS, Garland L, Redman M, Kernstine K, Gandara D, Marom EM (2011) A Practical Guide of the Southwest Oncology Group to Measure Malignant Pleural Mesothelioma Tumors by RECIST and Modified RECIST Criteria. J Thorac Oncol 6:598–601

Magnetic Resonance Imaging in Animal Models of Respiratory Diseases

Nicolau Beckmann and Yannick Crémillieux

Contents

Abstract

With the incidence of respiratory diseases increasing throughout the world, new therapies are needed. This chapter provides a short overview of different MRI techniques of interest for drug discovery and development within the pulmonary disease area. The focus is on studies performed both in animals and humans, which are of importance to understand pathophysiological aspects and to evaluate new drugs. Rather than emphasizing particular lung diseases, the noninvasive diagnosis and quantification of a number of characteristics related to several pathological conditions of the lung are addressed: inflammation, mucus secretion and clearance, emphysema, ventilation, perfusion, fibrosis, airway remodeling, and pulmonary arterial hypertension. Techniques are discussed based on their present use or potential future utilization in the context of drug studies.

N. Beckmann (✉)
Novartis Institutes for BioMedical Research,
Musculoskeletal Diseases Department,
CH-4056 Basel, Switzerland
e-mail: nicolau.beckmann@novartis.com

Y. Crémillieux
Institut des Sciences Moléculaires, Université de
Bordeaux, CNRS, F-33076 Bordeaux, France

1   Introduction

Diseases of the airways such as asthma and chronic obstructive pulmonary disease (COPD) involve a complex interplay of many inflammatory and structural cell types, all of which can release inflammatory mediators including cytokines, chemokines, growth factors, and adhesion molecules. Activated eosinophils are considered particularly

important in asthma, contributing to epithelial cell damage, bronchial hyperresponsiveness, plasma exudation, and edema of the airway mucosa, as well as smooth muscle hypertrophy and mucus plugging, through the release of enzymes and proteins (Barnes 2008a, b). In COPD, inflammation of the small airways and lung parenchyma with the involvement of neutrophils, macrophages, and T-lymphocytes results in chronic obstructive bronchitis, destruction of the lung parenchyma by proteolytic enzymes (emphysema), and mucus hypersecretion, leading to severe airflow limitation (Barnes 2008a, b). Pulmonary fibrosis is a progressive and lethal lung disease involving an overexuberant repair process, characterized by accumulation of inflammatory cells, excessive fibroblast proliferation, increase in collagen content, and deposition of extracellular matrix in the lungs (Strieter and Mehrad 2009; King et al. 2011).

Laboratory animals provide models for airways diseases in humans to help developing novel therapies. Terminal procedures such as bronchoalveolar lavage (BAL) fluid analysis, histology, and weighing of lungs are commonly used to analyze such models. Pulmonary function is assessed either noninvasively in conscious, unrestrained animals (plethysmography), or invasively requiring intubation or tracheotomy and artificial ventilation (Hoymann 2007). The main concern with whole body plethysmography is that it provides global respiratory measures that are so tenuously linked to respiratory mechanics that it is debatable if they can be considered as meaningful indicators of lung function (Hoymann 2007). Having access to noninvasive, spatially resolved readouts is therefore highly desirable for both ethical and scientific reasons.

A potentially improved diagnosis capability is the motivation for the introduction of magnetic resonance imaging (MRI) in the context of development of new therapies for respiratory diseases. The present contribution addresses the use of MRI in animal models. The main focus is on applications aiming to derive information on several aspects of pulmonary diseases, ranging from inflammation to fibrosis, with the ultimate objective to support and facilitate the drug discovery and development process in this medical area.

2 Lung Imaging of Small Rodents: Basic Considerations

For ethical reasons, animals are kept anesthetized during imaging investigations. One needs to consider what influence anesthesia may have on functional readouts and whether it may interfere with the development of the disease model, especially under repeated inductions. Therefore, generally speaking, it is recommended to keep the anesthesia time to ≤30 min in each imaging session.

A challenge in lung imaging is that cardiac and respiratory motion can cause marked image artifacts. In humans, image acquisition may be performed during breath-holding, or by gating it by an electrocardiogram. Problems are more evident in small rodents, because of their higher cardiac and respiratory rates, even under anesthesia. To address this issue, measurements are often performed in artificially ventilated animals to maintain a constant breathing rate and/or image acquisition is triggered by the electrocardiogram. However, for compound testing in vivo in animal models of airways diseases, it is important to keep acquisition conditions as simple as possible, so that repeated measurements interfering minimally with the physiology and the well-being of the animals can be performed longitudinally. For instance, one needs to carefully consider possible interferences between the pathophysiology of the disease models and lung injury complications that might potentially be caused by mechanical ventilation (Walder et al. 2005), especially if this is applied repeatedly. Indeed, it has been reported that mechanical ventilation of healthy rats can cause an increase of neutrophils in bronchoalveolar lavage (BAL) fluid, pulmonary edema, and even hypoxemia that may lead to progressive circulatory failure and death. Consequently, mechanical ventilation should be avoided whenever possible for the longitudinal investigation of lung disease models with expected inflammatory responses. Signal averaging allows the acquisition of lung images from spontaneously breathing rats and mice, without any gating (Beckmann et al. 2001a; Blé et al. 2008; Zurek et al. 2010).

The advantages of imaging the lungs of freely breathing animals are threefold: absence of invasive and potentially traumatic intubation, simplification and time savings of protocols leading to increased throughput, and use of a constant repetition time in imaging sequence. The last point is especially important when a fixed image contrast weighting is needed for quantitative measurements.

Besides cardiac and respiratory motion, lung MRI faces two main issues, namely (i) the rapid dephasing of transverse magnetization (transverse relaxation times measured in lung tissue are typically ranging between 0.5 and 2 ms, depending on the strength of the static magnetic field (Kveder et al. 1988; Hatabu et al. 1999; Beckmann et al. 2001b; Olsson et al. 2007) and (ii) the lower spin density (<30 %) related to the presence of alveolar space as compared to other organs of interest such as the heart or brain. Dedicated proton or nonproton nuclei MR techniques are available and can help overcome these difficulties.

Proton MRI sequences referred to as UTE (ultrashort-echo time) techniques are associated with echo times below 1 ms that allow the acquisition of the MRI signal from lung parenchyma before decay of the magnetization. When performed with a radial scanning of k-space, UTE sequences are less sensitive to respiratory and cardiac motion as compared to Cartesian acquisition (Bergin et al. 1992; Zurek et al. 2010). With UTE, 2D or 3D imaging of the lungs of spontaneously breathing small rodents is feasible within a few minutes (Zurek et al. 2010: Zurek and Crémillieux 2011; van Echteldand Beckmann 2011; Egger et al. 2013, 2014). Typical echo times achieved are of about 300 µs for 2D acquisitions and <20 µs for 3D images.

Alternatively, MRI of nuclei located on gaseous molecules or of atoms can be performed to image ventilated lung. MRI of fluorinated gases associated with a large number of ^{19}F nuclei (SF$_6$, C$_2$F$_6$, CF4 or C$_3$F$_8$) have been demonstrated in animal and human studies (Mosbah et al. 2008). Hyperpolarization techniques based on optical pumping approaches can be used to further improve the detection sensitivity of a gas [see (Goodson 2002; Möller et al. 2002) for reviews on HP techniques]. Following hyperpolarization, ^{3}He and ^{129}Xe MR signals can be increased by five orders of magnitude. MRI of hyperpolarized (HP) gases has been applied in animal models of airways diseases and in emphysema, cystic fibrosis (CF), or asthma patients. Most small rodent studies have been performed in artificially ventilated animals to better control gas delivery; however, measurements can be performed in spontaneously breathing animals as well (Stupar et al. 2007; Mosbah et al. 2010; Imai et al. 2011).

3 MRI in Small Animal Models of Respiratory Diseases

The use of imaging to noninvasively characterize several aspects of lung diseases will be discussed next. Whenever possible, references are made of pharmacological studies involving imaging. For many applications, however, studies involving compounds have not been reported. Nonetheless, the applications are addressed because of their potential in becoming useful tools for drug discovery in the near future.

3.1 Airway Inflammation

A characteristic feature of lung inflammation is edema in the airways due to an increase in the permeability of the microvasculature. Proton MRI has been used to quantify edema in the lungs of spontaneously breathing mice (Blé et al. 2008; Conti et al. 2010) or rats (Beckmann et al. 2001a; Tigani et al. 2002; Quintana et al. 2006a) actively sensitized to and challenged with ovalbumin (OVA). The MRI signals following OVA challenge correlated significantly with a variety of inflammatory parameters determined in the BAL fluid recovered from the same animals. Importantly, the fluid signals detected by MRI correlated significantly with the perivascular edema assessed by histology (Tigani et al. 2003a; Blé et al. 2008).

When assessing the effects of anti-inflammatory drugs administered prior to disease induction in these models, a dose-related reduction of

the MRI signals has been shown for compounds such as the glucocorticosteroids, budesonide (Beckmann et al. 2001a; Tigani et al. 2003a; Blé et al. 2009a) and mometasone (Tigani et al. 2003b), and a mitogen-activated protein kinase inhibitor (Tigani et al. 2003b). Moreover, the pharmacology of sphingosine-1 receptors has been studied in vivo using MRI (Blé et al. 2009a). Imaging data correlated with changes in the parameters of inflammation assessed in the BAL fluid. MRI was also applied to address the effects of compounds on established allergic inflammation. Treatment with budesonide, mometasone, or with a phosphodiesterase-4 inhibitor at 24 h after OVA challenge reduced MRI signals already at 3 h after drug administration. The decline in MRI signals correlated significantly with a reduction in perivascular edema quantified by histology (Beckmann et al. 2001a; Tigani et al. 2003a, b). No changes in BAL parameters were observed at this early time point. These observations indicate that proton MRI is more suitable to detect early effects of compounds on established inflammation than the traditional BAL fluid analysis. Effects of corticosteroid treatment on airway inflammation and mechanics in an allergic mouse model have also been reported using hyperpolarized ^{3}He MRI (Thomas et al. 2012).

Compared to single dosing, repeated OVA challenge in actively sensitized rats induced an attenuation of the inflammatory response as evidenced by proton MRI and BAL fluid analysis (Tigani et al. 2007). Moreover, vascular remodeling has been detected by MRI in the model: the decrease in vascular permeability assessed by dynamic contrast-enhanced (DCE)-MRI was consistent with the thickening of the vascular wall for vessels of diameter up to 300 μm as revealed histologically (Tigani et al. 2007).

While MRI can be efficiently used to image the exudative component of acute inflammation in the lungs, very few imaging techniques are available to estimate the leukocyte activity in acute or chronic lung inflammation. It has been reported that detection of lung inflammation in COPD was feasible using ^{18}fluoro-deoxyglucose (^{18}FDG) and positron emission tomography (PET). Since inflammatory cells utilize glucose as a source of energy during their activation, it was suggested that ^{18}FDG uptake by inflammatory cells in the lung has been suggested as an in vivo measurement of regional lung inflammation (Labiris et al. 2003; Chen and Schuster 2004; Chen et al. 2009). Ebner et al. (2010) investigated the lipopolysaccharide (LPS)-induced inflammation process by means of emulsified perfluorocarbons (PFC). Intravenous application of PFC particles in mice resulted in their accumulation in inflammatory regions of the lungs as detected with ^{19}F MRI. The authors showed that PFC particles were transported to the site of inflammation via circulating monocytes/macrophages. The regions where PFC infiltration was detected showed the presence of edema on proton MR images at the later time points, indicating that this approach was able to selectively localize the cellular components of inflammation in the lungs. Additionally, the authors demonstrated the ability of the technique to monitor the effect of anti-inflammatory therapies in this animal model of lung inflammation.

3.2 Airway Remodeling

Asthma is a chronic disease characterized by bronchial hyperresponsiveness (BHR), bronchial inflammation, and remodeling. Bianchi et al. (2013) applied UTE proton MRI to study a chronic model of asthma in mice in which the animals were sensitized with OVA over a period of 75 days. Parameters assessed were inflammatory volumes and bronchial remodeling (peribronchial signal intensity index, PBSI). Plethysmography was performed to assess BHR to methacholine. The average inflammatory volume measured by MRI in OVA-sensitized mice was significantly increased relative to control mice on days 38 and 78. PBSI was significantly higher in the OVA group on day 78, but not on day 38. After sensitization, asthmatic mice presented BHR to methacholine on days 39 and 79. Penh ratios correlated significantly with the inflammatory volume on day 39 and with the PBSI on day 79 (Bianchi et al. 2013). This study showed that UTE MRI allows the noninvasive quantification of

peribronchial eosinophilic inflammation with airways occlusion by mucus and of bronchial remodeling in a murine asthma model that correlates with functional parameters.

Proton MRI detected, in spontaneously breathing rats, the effects of bronchomodulating agents or of inflammation-induced airway remodeling and hyporesponsiveness in OVA-challenged or LPS-challenged animals, respectively (Beckmann et al. 2004, 2006). The approach consists in detecting modulations of lung parenchymal proton signals induced by changes in oxygenation levels (Edelman et al. 1996).

3.3 Mucus Secretion and Clearance

Chronic mucus hypersecretion and dysfunction in mucociliary clearance are associated with the accelerated loss of lung function in several respiratory diseases. Exposure of Brown Norway rats to LPS induces mucus release (Tesfaigzi et al. 2000). MRI can detect secreted mucus in the lungs of spontaneously respiring rats up to 16 days following a single LPS challenge (Beckmann et al. 2002; Tigani et al. 2002). Bi-labeled amino dextran-based probes binding specifically to mucus have been synthetized to extract information on mucus dynamics in this model (Blé et al. 2009b).

An upregulation of sensory-efferent neural pathways is implicated in asthma and COPD. The acute effects of sensory nerve stimulation by capsaicin in the rat lung have been studied by MRI (Karmouty-Quintana et al. 2007a). Capsaicin-induced MRI signals reflected the release of mucus following activation of sensory nerves. The transient receptor potential vanilloid-1 antagonist, capsazepine, the dual neurokinin-1,2 receptor antagonist, DNK333, and the mast cell stabilizer, disodium cromoglycate, blocked the effects of capsaicin in the airways.

The epithelial sodium channel (ENaC) regulates airway mucosal hydration and mucus clearance. The lack of such regulation in CF patients leads to desiccation of the airway lumen, resulting in mucostasis that establishes the environment for infections (Boucher 2007). Osmotic agents and negative ENaC regulators can be used to restore mucosal hydration. Proton MRI has been shown to provide a target-related readout to study modulators of lung fluid hydration in spontaneously breathing rats (Blé et al. 2010).

3.4 Emphysema

Emphysema is characterized by lung parenchyma destruction, enlarged alveolar space, impaired ventilation, and reduced gas exchange. The lung tissue density, as assessed with CT, is considered as a reliable quantitative imaging biomarker. For instance, the percentage of the relative area of the lungs with attenuation values below −950 Hounsfield units (HU) is used by radiologists and clinicians for evaluating the extent of the disease and for following up its progression at millimeter spatial resolution (Parr et al. 2004).

Efforts have been made to develop MRI techniques as an alternative without ionizing radiation. Diffusion-weighted MRI of polarized noble gas (He-3 and Xe-129) have been proposed and applied as an original approach for assessing lung structure at a subpixel level. The principle of the technique relies on the MRI signal attenuation due to the Brownian motion of gas atoms in the presence of a sensitizing magnetic field gradient. The signal attenuation can be assigned to a mean diffusion length (or to an apparent diffusion coefficient) of gas atoms. The size and the boundaries of the bronchoalveolar structures are imposing an upper limit on the mean diffusion length of gas. From the restricted diffusion of the polarized gas measured using MRI, one can then derive the alveolar dimensions. In the case of emphysema disease and of enlargement of airspaces, an increase in the restricted apparent diffusion coefficient (ADC) is then expected. This approach has been applied and validated against histomorphometry in elastase-induced emphysema in rats and mice (Chen et al. 2000; Dugas et al. 2004; Peces-Barba et al. 2003).

Submillisecond echo time proton MRI sequences aiming at detecting parenchymal signals have also been applied successfully to small
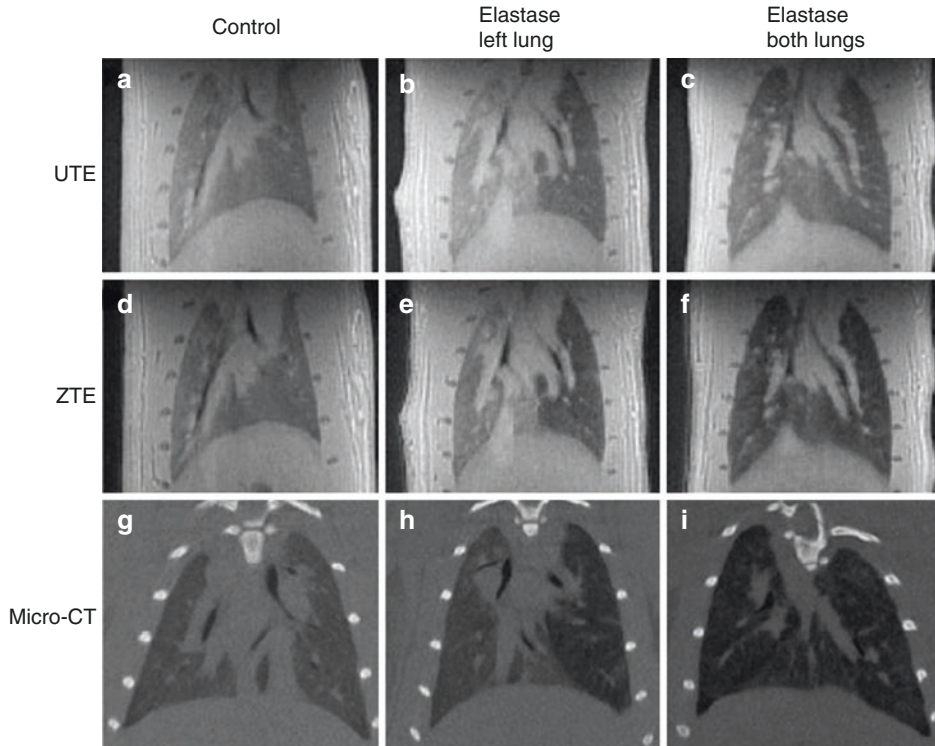
Fig. 1 Comparison of ultrashort echo time (UTE), zero echo time (ZTE), and μ-CT images from male Wistar rats. Images were acquired from a control animal or 4 weeks after administration of elastase at a dose of 75 U/100 g body weight. The elastase-treated lungs appear darker due to the reduction of proton density caused by the emphysematous changes (Reproduced with permission from Bianchi et al. (2015a). Copyright © 2015 John Wiley & Sons, Ltd.)

rodent emphysema models. Gradient-echo proton MRI has been used to detect elastase-induced changes in the lungs of spontaneously breathing rats (Quintana et al. 2006b). Reductions in MRI signal intensity of the lung parenchyma detected from 2 to 8 weeks following the insult correlated significantly with the loss of alveolar structure assessed by histology, suggesting that the MRI signal reflected elastase-induced alveolar destruction (Beckmann et al. 2007). Treatment with retinoic acid did not elicit a reversal of lung damage as measured by MRI and histology. Using a single-point imaging technique, Olsson et al. (2007) determined the relaxation time T_2^* to detect emphysematous changes in the lungs of tight-skin mice, which spontaneously develop emphysema-like alveolar enlargement. Tight-skin mice displayed significantly shorter T_2^* values than control, age-matched mice, because their larger alveoli resulted in an increased air/tissue ratio

and hence an increase in the internal susceptibility gradients. UTE MRI has been used to compare normal and emphysematous lungs in mutant mice (Takahashi et al. 2010) as well as in elastase-instilled mice (Zurek et al. 2012) and rats (Bianchi et al. 2015a, b). The results showed an excellent agreement between MR findings and histological morphometry and indicated that proton MRI allows structural changes at alveolar level to be monitored longitudinally. Moreover, UTE MRI has been shown to be as sensitive as the gold standard micro-CT to detect lung density changes associated to parenchymal destruction by elastase (Bianchi et al. 2015a) (Fig. 1).

These recent results obtained in animal models of emphysema illustrate the potential of MRI for assessing tissue density losses. Although the spatial resolution and the sensitivity of MRI remain currently inferior to the ones obtained using the gold standard micro-CT, tissue density

measurements using MRI can be advantageously supplemented with perfusion or ventilation MRI acquisitions in order to have a more comprehensive view of the lung function.

3.5 Lung Ventilation and Perfusion

Ventilation and perfusion distribution in the lungs form the foundation of pulmonary physiology and remain cornerstones in pathology. Efficient gas exchange in the lungs can only occur through intimate matching of regional ventilation and perfusion. The nonuniform distribution of regional lung blood flow and ventilation were first demonstrated utilizing radioactive tracers and external scintillation detectors that registered the distribution of radioactivity within the lung. After intravenous injection, particles larger than red blood cells (RBCs) are trapped in the first capillary bed that they encounter.

3.5.1 Ventilation

Ventilation imaging has been shown to be sensitive to a variety of lung disease models, including asthma in mice (Haczku et al. 2005), emphysema in rats (Spector et al. 2005), and pulmonary embolism in sheep (Wellman et al. 2010). Ventilation can be quantified from the dynamic change in image signal following application of an inhaled contrast agent. For instance, ventilation imaging has been demonstrated in animals with ^{3}He MRI (Haczku et al. 2005).

Hyperpolarized ^{3}He MRI has been used to measure the fractional ventilation in artificially ventilated small rodents (Deninger et al. 2002; Emami et al. 2008). The approach detected early changes of lung function and structure in a rat model of elastase-induced emphysema at mild and moderate severities (Emami et al. 2008). The fractional ventilation declined primarily in the first 5 weeks, while enlargement of alveolar diameters appeared primarily between the 5th and 10th week post elastase. Further, HP ^{3}He MRI studies focused on airway constriction induced chemically. High-resolution ^{3}He MRI was used to depict regional ventilation changes

and airway narrowing in artificially ventilated mice (Mistry et al. 2010) or rats (Chen and Johnson 2004) challenged with methacholine. Mosbah et al. (2010) demonstrated in a spatially resolved manner the effects of serotonin-induced bronchoconstriction on lung ventilation in spontaneously breathing rats (Fig. 2). Dynamic ventilation ^{3}He MR images spanning a respiratory cycle with 100 ms temporal resolution were obtained using a retrospective Cine-type image reconstruction procedure (Stupar et al. 2007).

Noncontrast-enhanced functional lung imaging can be used to extract information about ventilation from the difference in parenchymal signal between full inspiration and full expiration data sets (Bauman et al. 2009). This has been proven as a valid instrument to diagnose ventilation-related changes in humans (Zapke et al. 2006; Bauman et al. 2009), showing a good agreement with other methods for functional lung assessment, such as ^{3}He MRI (Bauman et al. 2013). Recently, Bianchi et al. (2015b) have applied this approach to derive ventilation-related maps in rats challenged with elastase. The MRI protocol comprised a 2D UTE sequence (acquisition time of 30 min), from which inspiration and expiration images were reconstructed after the extraction of a self-gating signal. Inspiration images were registered to images at expiration, and expansion maps were created by calculating the specific difference in signal intensity. The lungs were segmented, and the mean specific expansion calculated as an established surrogate for fractional ventilation. The calculated ventilation-related maps showed a reduction of function in elastase-treated lungs, both compared to the nontreated lungs and to the baseline values. Moreover, a good agreement between MRI-measured mean specific expansion, micro-CT, and histology data quantitatively supported the presence of ventilation deficit in emphysematous lungs.

3.5.2 Perfusion

The combined challenges of high temporal and spatial resolution have rendered routine quantitative perfusion imaging difficult in small rodents. MRI perfusion assessments in animals have been primarily accomplished using con-

trast-enhanced techniques comprising the dynamic acquisition of images in combination with the intravenous administration of a paramagnetic contrast agent (Neeb et al. 2009). Such an approach has been used to analyze a rabbit model of pulmonary embolism (Keilholz et al. 2009) and a newborn piglet model of pulmonary hypertension (Ryhammer et al. 2007). Mistry et al. (2008) developed a Cine technique based on the acquisition of radial images during repeated contrast agent injection matched to the

physiology of the animal using a micro-injector, enabling perfusion imaging at high spatial and temporal resolution in artificially ventilated small rodents. The feasibility of lung perfusion with arterial spin labeling precluding the administration of contrast material has been demonstrated in rabbit models of pulmonary embolism (Altes et al. 2005), and during repeated balloon occlusion of a segmental pulmonary artery as well as during pharmacological stimulation in pigs (Roberts et al. 2001).
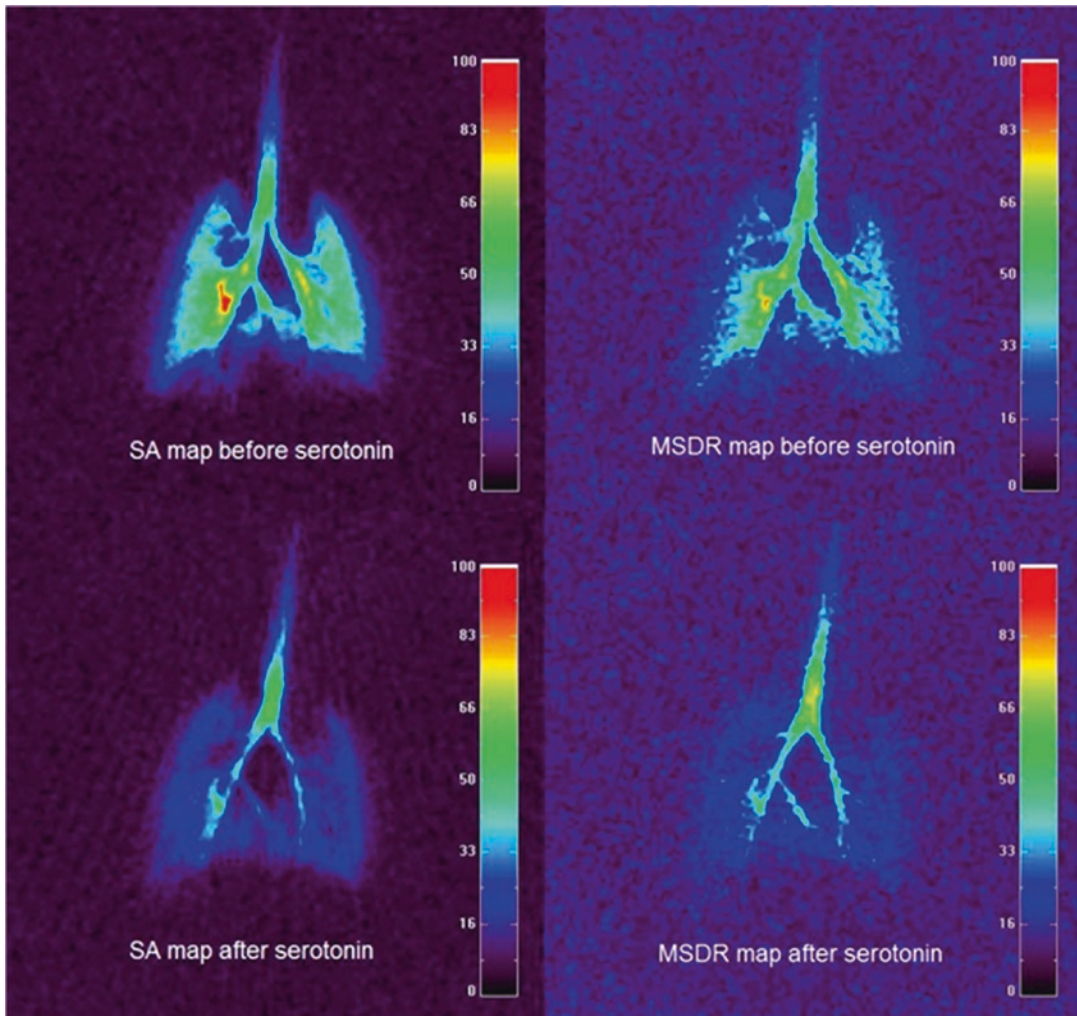
Fig. 2 Parametric ^{3}He ventilation maps obtained in a spontaneously breathing Sprague–Dawley rat. The SA (signal amplitude) parameter is related to the amount of helium gas entering the lung and the MSDR (maximum signal decay rate) parameter to the maximum helium gas expiratory airflow. Parametric maps were obtained from an animal before and after intravenous injection (50 μg/kg) of serotonin. A global decrease of the SA and MSDR parameters can clearly be seen and are related to a decrease of the tidal volume and of the expiratory airflow subsequently to the injection of serotonin (Reproduced with permission from Mosbah et al. (2010). Copyright © 2010 Wiley-Liss, Inc.)

Driehuys et al. (2009) showed in artificially ventilated rats that regional evaluation of pulmonary perfusion and gas exchange can be obtained by intravenous injection of saline saturated with HP ^{129}Xe and subsequent MRI of the gas phase in the alveolar airspaces. After a single injection, the emerging ^{129}Xe gas could be detected separately from ^{129}Xe remaining in the blood because of chemical shift differences. The features observed in dissolved-phase ^{129}Xe MR images are consistent with gravity-dependent lung deformation, which produces increased ventilation, reduced alveolar size (i.e., higher surface-to-volume ratios), higher tissue densities, and increased perfusion in the dependent portions of the lungs. These results suggest that dissolved HP ^{129}Xe imaging reports on pulmonary function at a fundamental level.

3.6 Lung Fibrosis

Currently, no efficacious treatment leading to disease remission exists for lung fibrosis. Animal models are important to investigate pathological mechanisms and for preclinical evaluation of novel therapies. The best characterized and most commonly adopted model in small rodents is of bleomycin-elicited injury. Bleomycin, a derivative of *Streptomyces verticillus*, is an antineoplastic antibiotic that has been used clinically for over 30 years (Lazo et al. 1996). It has the well-known side effect of producing inflammation and fibrosis specific to the lung (O'Sullivan et al. 2003). Local instillation of bleomycin in rodents is often used to model lung fibrosis (Chua et al. 2005; Moore and Hogaboam 2008).

The ability of proton MRI to noninvasively quantify the course of lung injury induced by bleomycin administration to mice (Babin et al. 2012; Egger et al. 2013) and rats (Babin et al. 2011; Egger et al. 2013, 2014; Jacob et al. 2010; Karmouty-Quintana et al. 2007b) has been reported. Increased MRI signals, detected up to 70 days post bleomycin, reflected tissue remodeling involved in fibrosis development, as evidenced by histology revealing prominent collagen deposition in the same areas where MRI signals had been detected in vivo. Initially, gradient-echo sequences were used to detect the long-lasting bleomycin-induced injury in the lungs of spontaneously breathing animals (Babin et al. 2011, 2012; Karmouty-Quintana et al. 2007b). The sensitivity for detecting lesions elicited by bleomycin increased dramatically by using UTE (Egger et al. 2013) (Fig. 3). Importantly, proton MRI has been
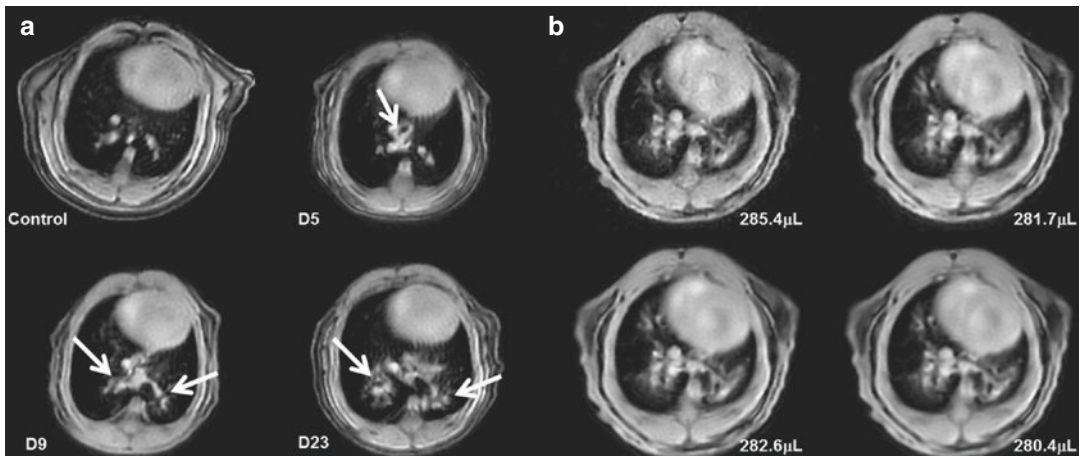
Fig. 3 Detection of bleomycin-induced lung injury by UTE-MRI in BALB/c mice. (**a**) Measurements (4-min acquisition time) on comparable slices before and at different time points (5, 9, and 23 days) after oropharyngeal aspiration of 6 × 1.0 mg/kg bleomycin. *White arrows* point to bleomycin-induced lung injury. (**b**) Comparison of UTE acquisitions with different numbers of averages in a bleomycin-treated animal. The volumes of signals in the lungs evaluated from these images were comparable for all acquisition conditions: 1-min acquisition time (285.4 μL), 2-min acquisition time (281.7 μL), 4-min acquisition time (282.6 μL), 16-min acquisition time (280.4 μL)(Reproduced from Egger et al. (2013). Copyright © 2013 Egger et al.)
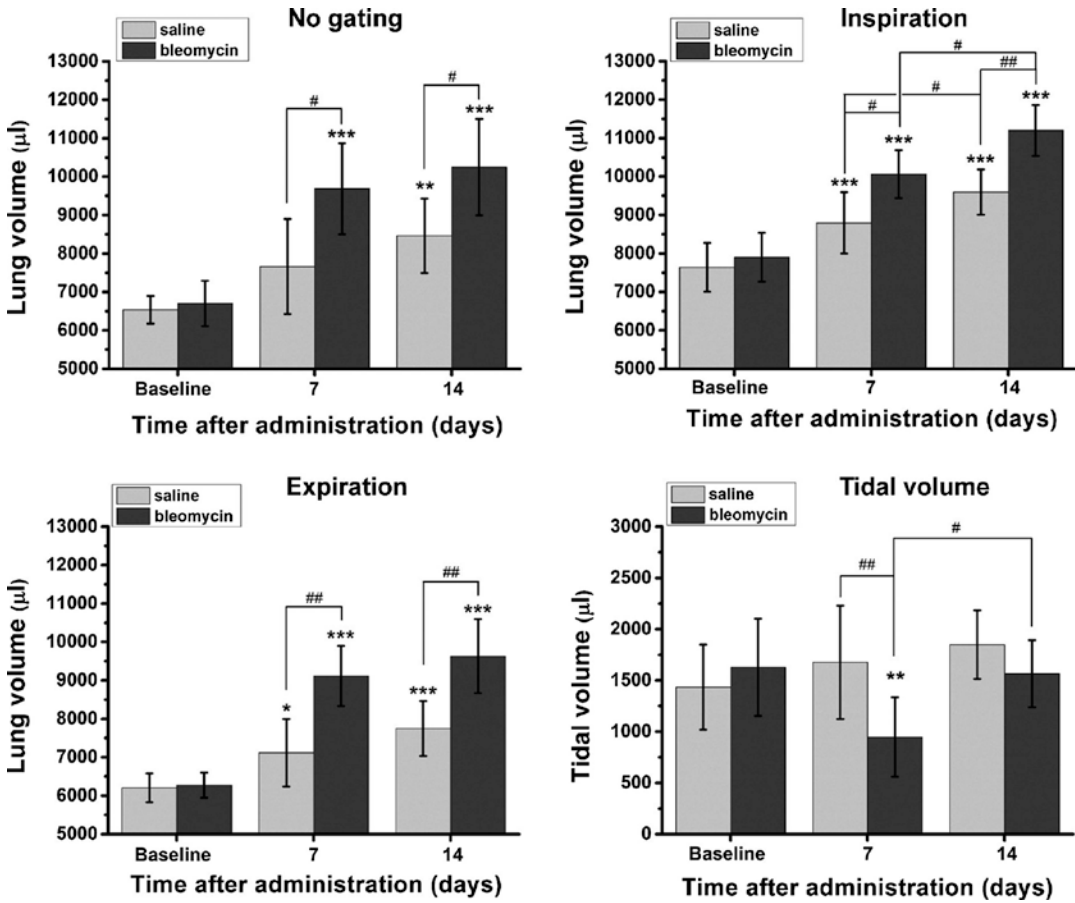
Fig. 4 Lung volumes assessed in Sprague–Dawley rats from nontriggered acquisitions as well as from gated acquisitions at the inspiratory and expiratory phases. Tidal volumes were derived by subtracting volumes at inspiration and expiration. Values are expressed as means ± SD (n = 6 rats per group). The levels of significance

$*0.01 < P < 0.05$, $**0.001 < P < 0.01$, and $***P < 0.001$ refer to ANOVA comparisons to baseline values in the same group. $\#0.01 < P < 0.05$, and $\#\#0.001 < P < 0.01$ correspond to ANOVA comparisons as indicated (Reproduced with permission from Egger et al. (2014). Copyright © 2014 the American Physiological Society)

shown to be as sensitive as micro-CT in detecting bleomycin-induced lesions in the lungs (Vande Velde et al. 2014).

Changes in lung structure accompanying fibrotic processes lead to a severe impairment of lung function related to a decreased elasticity. Indeed, increased lung elastance as well as decreased compliance (the reciprocal of elastance) have been reported in small rodent pulmonary fibrosis models (Ask et al. 2008; Manali et al. 2011). Egger et al. (2014) reported an increase of MRI-derived total lung volume in bleomycin-challenged small rodents, consistent with increased *postmortem* dry and wet lung weights, hydroxyproline content, as well as collagen amount

assessed by histology. In bleomycin-treated rats, MRI acquisitions gated by the respiration showed an increased volume of the lung in the inspiratory and expiratory phases of the respiratory cycle, and a temporary decrease of tidal volume. Using a flexyVent® system for the assessment of lung function in tracheotomized and mechanically ventilated animals (terminal procedure), decreased dynamic lung compliance was found in bleomycin-challenged rats (Egger et al. 2014). Overall speaking, bleomycin-induced increase of MRI-detected lung volume was consistent with tissue deposition during fibrotic processes resulting in decreased lung elasticity, while influences by edema or emphysema could be excluded (Fig. 4). In

OVA-challenged rats, total lung volume quantified by MRI remained unchanged (Egger et al. 2014).

Thus, proton MRI provided potential to facilitate in vivo pharmacological studies in the bleomycin model. Repetitive measurements opened new avenues in testing compounds, as the responses at several time points during the course of treatment could be easily compared. Specifically, studies at the chronic phase, when fibrosis was already established, became amenable. MRI supported the evaluation of several compounds in the bleomycin model, for example, steroids, hyaluronidase, and the somatostatin analog, SOM230 (Babin et al. 2011; Egger et al. 2014, 2015). Of note, SOM230 was shown to have therapeutic effects on established bleomycin-induced fibrosis in rats by reducing both lesion volume and total lung volume, the latter indicating an effect on lung elasticity and thus improvement of lung function (Egger et al. 2014) (Fig. 5). Moreover, knockout mouse lines were investigated in the bleomycin model using proton MRI with the aim of providing potential therapeutic targets (Babin et al. 2012).

Effective pulmonary gas exchange relies on the free diffusion of gases across the thin tissue barrier separating airspace from the capillary RBCs. An increased blood–gas barrier thickness is present in pathologies such as inflammation, fibrosis, and edema. Driehuys et al. (2006) demonstrated in a rat model of unilateral bleomycin lung injury the feasibility of detecting such impairment using ^{129}Xe MRI and by exploiting the fact that ^{129}Xe resonates at three distinct frequencies in the airspace, tissue barrier, and RBC compartments. Based on a simple diffusion model, the authors estimated that this MRI method for measuring ^{129}Xe alveolar–capillary transfer is sensitive to changes in blood–gas barrier thickness of ≈ 5 μm.

Gd-based contrast agents were used as well for detecting and characterizing lung fibrosis in animal models. Hence, Caravan et al. (2013) performed intravenous injection of collagen-targeted Gd-based probe and nonbinding Gd-based control probes to bleomycin-instilled mice. Following injection of contrast agent and using UTE MRI sequences, they were able to measure a twofold higher signal-to-noise ratio increase in the lungs of fibrotic mice after collagen-targeted probes administration as compared to animal injected with control probes. The authors point out that this contrast-enhanced MRI technique offers the potential of directly imaging collagen and staging pulmonary fibrosis.

Similarly, Tassali et al. (2016) investigated the application of UTE MRI sequence combined with the intratracheal administration of Gd-based nanoparticles in bleomycin-induced fibrotic mice. The authors reported a MRI signal enhancement of 120 % in fibrotic lesions as compared to 50 % in healthy tissues and a twofold increase of contrast-to-noise ratio between fibrotic and healthy tissue. They also assessed the clearance of Gd-based contrast agents and observed that elimination time constant was 54 % higher in fibrotic lesions. As mentioned by the authors, passive targeting of fibrotic lesions might help monitor the efficacy of antifibrotic drugs and therapeutic molecules targeting this disease.

3.7   Infections

Research on the pathogenesis and therapy of influenza and other emerging respiratory viral infections would be aided by methods that directly visualize pathophysiological processes. MRI has the potential to advance in vivo studies of respiratory viral infections in animals.

MRI can be used to track the development of pulmonary lesions and characterize inflammatory responses in murine models of bacterial infection. Marzola et al. (2005) reported inflammatory lesions localized mainly in the apical part of the lungs, in medial and peribronchial regions, 48 h after intranasal administration of about 10^6 colony-forming units of *Streptococcus pneumoniae*. The anatomical localization of the lesions was confirmed by histology. Tournebize et al. (2006) followed the development and regression of inflammatory lesions caused by infection by *Klebsiella pneumoniae* in mouse lungs. A virulent strain caused an intense inflammation within 2 days in the whole lungs, while an avirulent strain did not show significant changes. Mice infected with the virulent strain and subsequently treated with antibiotics presented a severe
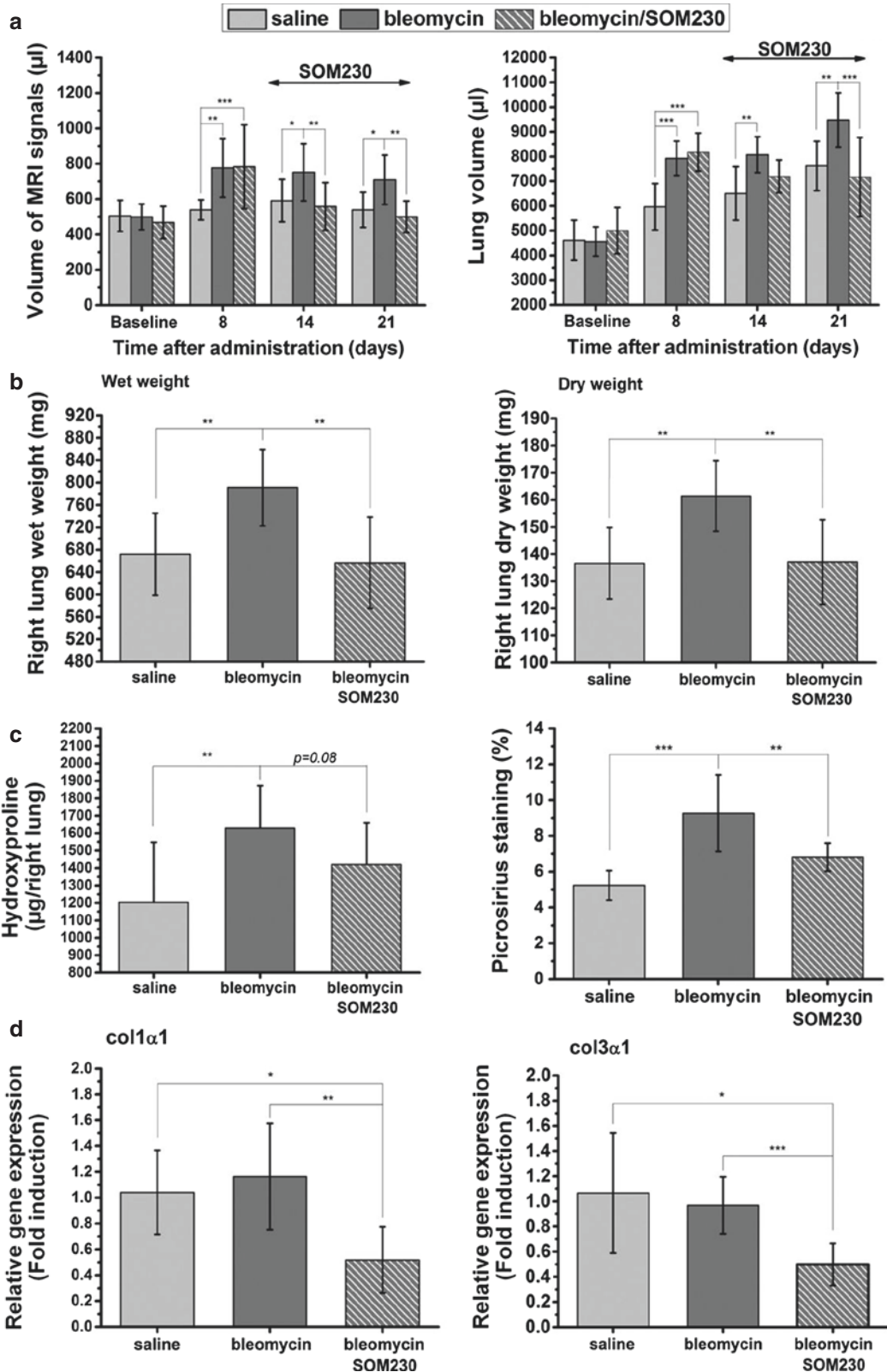
inflammation localized mainly in the left lung that disappeared after a week. The lesions observed by MRI correlated with the damage seen by histological analysis, and a 3D representation of the tissue allowed better visualization of the development and healing of inflammatory lesions.

Using UTE sequences, T_2^* effects of superparamagnetic iron oxide (SPIO) nanoparticles can be neglected, while T_1 shortening effects can be used for signal detection. Strobel et al. (2012) applied a 3D UTE sequence to a mouse model of lung inflammation, which was induced by systemic bacterial infection with *Staphylococcus aureus*. The bacteria cause a systemic infection, resulting in inflammation of the lung (Yi et al. 2009). Following the systemic application of SPIO, a significant signal increase in the lung of infected animals was detected already at 24 h post infection, compared to control mice (17 %, $P < 0.001$). Iron accumulation in the lung parenchyma as a consequence of the host immune response was histologically confirmed. The fact that by conventional T_2^*-weighted and T_2-weighted imaging, neither structural changes nor formation of substantial edema were observed indicates the potential of UTE in combination with the administration of SPIO to increase the sensitivity to detect inflammatory processes.

This publication suggests that the use of UTE-like sequences in combination with MRI-compatible cell labeling may provide the unique opportunity to study pulmonary influenza or other respiratory viral infections as well as potential therapies. For example, inflammatory cells loaded ex vivo with antiviral drugs or nanoparticles have been demonstrated to localize to sites of infection. The effectiveness of antiretroviral therapies (ART) depends on its ultimate ability to clear reservoirs of continuous human immunodeficiency (HIV) virus infection. Dou et al. (2006, 2007) demonstrated that, being a principal vehicle for viral dissemination, the mononuclear phagocytes could also serve as an ART transporter and as such improve therapeutic indices. A nanoparticle-indinavir (NP-IDV) formulation was made and taken up into and released from vacuoles of human monocyte-derived macrophages. Following a single NP-IDV dose, drug levels within and outside monocyte-derived macrophages remained constant for 6 days without cytotoxicity. Administration of NP-IDV when compared to equal drug levels of free-soluble indinavir significantly blocked induction of multinucleated giant cells, production of reverse transcriptase activity in culture fluids, and cell-associated HIV-1p24 antigens after HIV-1 infection. After a single administration, single-photon emission computed tomography (SPECT), histology, and reverse-phase high-performance liquid chromatography demonstrated robust bone marrow-derived macrophages and drug distribution in the lung, liver, and spleen of mice. These data provide proof of concept for the use of macrophage-based nanoparticle delivery systems for human HIV-1 infections. Labeling the bone marrow macrophages with, for example, SPIO instead of with [111]indium oxyquinoline for SPECT would provide the opportunity to perform measurements at higher spatial resolution using UTE-MRI.

3.8 Lung Cancer

Lung cancer is the most common cancer in the world today, accounting for 12.6 % of all new cancers and 17.8 % of all cancer deaths (World Health Organization 2004). The prognosis of the most common form of lung cancer, nonsmall-cell lung cancer (NSCLC) or adenocarcinoma, is dis-

Fig. 5 Effects of SOM230 on established lung injury elicited by bleomycin in Sprague–Dawley rats. (**a**) MRI signals and lung volume quantified from the 3D UTE-MRI data sets. (**b**) Wet and dry weights of right lungs at day 21 after saline or bleomycin challenge. (**c**) Hydroxyproline and Picrosirius staining levels at day 21 after saline or bleomycin administration. (**d**) Relative gene expression of collagen in lung tissue. All values provided as means ± SD for $n = 6$, saline-challenged, $n = 9$, bleomycin-challenged, and $n = 9$, bleomycin-challenged, SOM230-LAR-treated rats. The levels of significance *$0.01 < P < 0.05$, **$0.001 < P < 0.01$, and ***$P < 0.001$ refer to ANOVA comparisons as indicated (Reproduced with permission from Egger et al. (2014). Copyright © 2014 the American Physiological Society)

mal, with a 5-year survival rate which remained unchanged in the last two decades and which is constantly under 15 %. One of the main reasons is related to the late diagnosis of this pathology (Molina et al. 2008) that, in its first stages, often appears with rather generic symptoms (e.g. coughing, weight loss, and shortness of breath) common to other lung diseases. Imaging-based techniques play a fundamental role as they allow clinical detection, noninvasive assessment of several features of lung carcinogenic formations, and follow-up of treatments efficacy.

In contrast to human studies, MRI investigations of lung cancer in animal models are very few. As a matter of fact, until now DCE-MRI or DWI studies of orthotopic animal models of lung cancer have not been reported. This sparsity of preclinical investigations can probably be attributed to the challenges of lung MRI in small animals. Despite these difficulties, Garbow et al. (2004, 2008) were able to show that respiratory-gated proton MRI can be used to detect small-lung neoplastic lesions in vivo in mice using Cartesian spin-echo acquisitions and follow up their longitudinal progression in time. More recently, Bianchi et al. (2014a) evaluated the potential of UTE lung MRI techniques for NSCLC MRI in vivo detection and follow-up in a mouse model of lung adenocarcinoma that expresses the luciferase gene. In this study, the UTE MRI free-breathing acquisitions were compared to standard gradient-echo lung MRI using respiratory-gated protocols. The MRI findings were validated against bioluminescence imaging (BLI) and gold-standard conventional histopathological analysis. The authors reported that adenocarcinoma-like pathological tissue was successfully identified in all mice with gated-FLASH and nongated UTE MRI, and good tumor colocalization was found between MRI, BLI, and histological analyses. An excellent or good correlation was found between the measured bioluminescent signal and the total tumor volumes quantified with UTE MRI or gated-FLASH MRI, respectively. These findings illustrate the potential of UTE MRI for detecting, quantifying, and longitudinally monitoring the development of submillimeter NSCLCs in freely breathing mice.

To evaluate the effects of radiotherapy and chemotherapy on lung tumors, CT or X-rays are routinely applied, and the tumor size is a widely used imaging biomarker for evaluating the efficacy of these therapies. However, these techniques are limited for differentiating between necrotic and viable tumor tissue. Contrast-enhanced MRI with injection of Gd-based contrast agents have been shown to be better suited for evaluating the efficacy of treatment (Ohno et al. 2000) and to distinguish between necrosis and viable tumor. The passive targeting of contrast agent to tumor tissue is attributed to the enhanced permeability and retention (EPR) effect, combining the enhanced permeability of tumor vasculature, with prolonged retention due to poor or absent lymphatic pathways for drainage of contrast agent from the tumor interstitium. In a similar way, theranostic molecules can be delivered passively to lung tumor tissue. Bianchi et al. (2014b) reported the passive targeting of lung tumors in an orthotopic mouse model of lung cancer. The authors evaluated two administration routes for theranostic Gd-based nanoparticles, namely intravenous injection and intratracheal administration and found that the intratracheal route was more effective for targeting and detecting the lung tumor (Fig. 6). Following intrapulmonary administration of these radiosensitizing nano-assemblies, the animals were exposed to radiotherapy, and a 45 % increase of the mean survival time was reported (Dufort et al. 2015).

Regarding characterization of types or grades of lung tumor, Togao et al. (2013) applied amide proton transfer (APT), one of the chemical exchange saturation transfer (CEST) methods, for imaging the exchange between protons of free tissue water and the amide groups (−NH) of endogenous mobile proteins and peptides. In this study, they reported the feasibility of in vivo APT imaging of lung tumor and were able to differentiate the tumoral types on orthotopic tumor xenografts from two malignant lung cancer cell lines in mice. The measured APT effect was higher in the tumor, which exhibited more active proliferation than the other (Fig. 7). As underlined by the authors, this approach might reduce the need of invasive needle biopsy or resection for lung cancer.
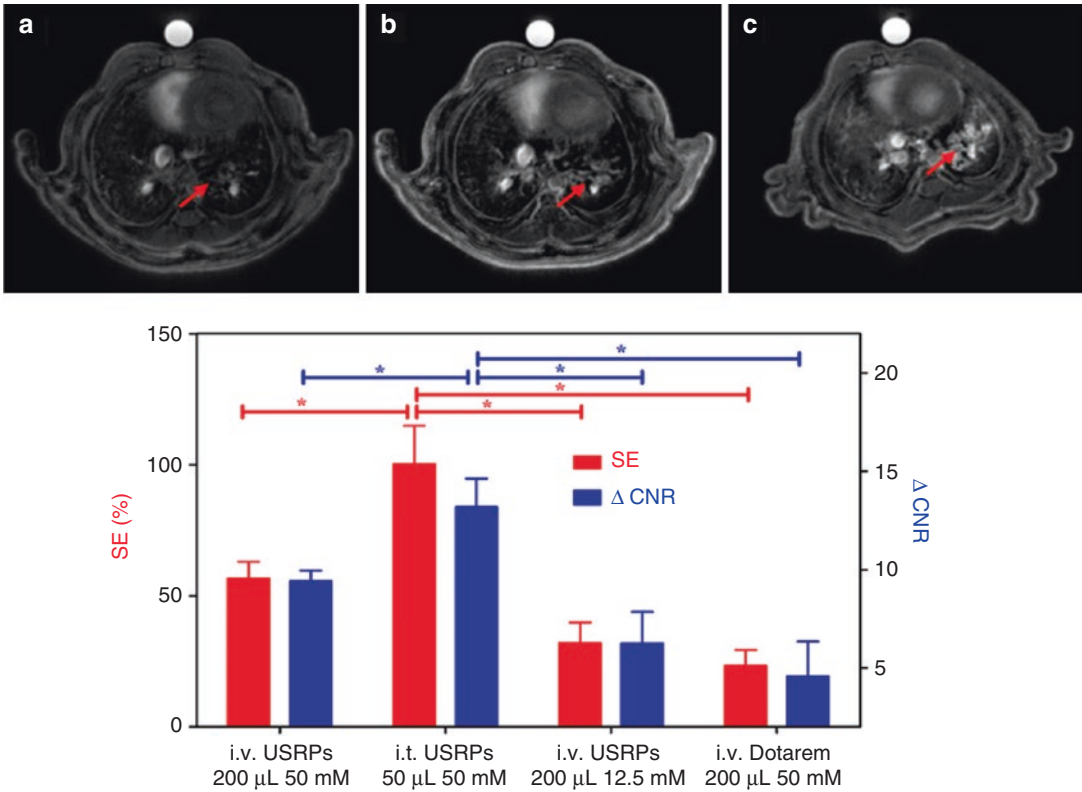
Fig. 6 UTE MRI axial slices of a tumor-bearing mouse (**a**) before and (**b**) after the intravenous administration of 200 μL of 50 mM [Gd3+] Gd-based nanoparticles (USRP) or (**c**) the orotracheal administration of 50 μL of 50 mM [Gd3+] USRP. The *arrows* indicate the tumor in the left lung. *Bar plots*, below the images, compare the signal enhancement (*red, left scale*) and the ΔCNR (*blue, right scale*) for intratracheal (i.t.) and intravenous (i.v.) administration of USRPs and commercial contrast agent (Dotarem, Guerbet, France). *Asterisks* indicate significant differences ($P < 0.05$). Data are presented as mean value ± SEM (Reproduced with permission from Bianchi et al. (2014b). Copyright @ 2014 National Academy of Sciences, USA)

4   Final Remarks

In the past few years, lung MRI methods have been considerably refined, allowing examinations in humans and small rodents at the anatomical, functional, and even molecular or target levels at high spatial and temporal resolution. The main challenge in using such techniques within the framework of drug discovery and development is twofold: (i) like any biomarker, imaging signatures need to be properly validated and qualified. In animal models, this involves a proper characterization of the readouts against invasive markers like cell influx into BAL fluid and histology. Then, the ability of modulating a given imaging signature by reference pharmacological agents of known activity needs to be demonstrated, to verify the sensitivity of the potential biomarker; (ii) it needs to be shown that the increased technical capabilities of imaging translate into improved disease diagnosis as compared to standard approaches. The hope is that with imaging, earlier phases of the disease can be diagnosed, thus enhancing the chance of pharmacological interventions. Moreover, imaging could facilitate patient stratification in preclinical investigations with animals and in clinical trials. In general terms, preclinical and clinical activities should be mutually supportive (translational research). For instance, small animal imaging may help to improve the characterization of clinical readouts and, conversely, imaging in humans may support the improvement of animal models.
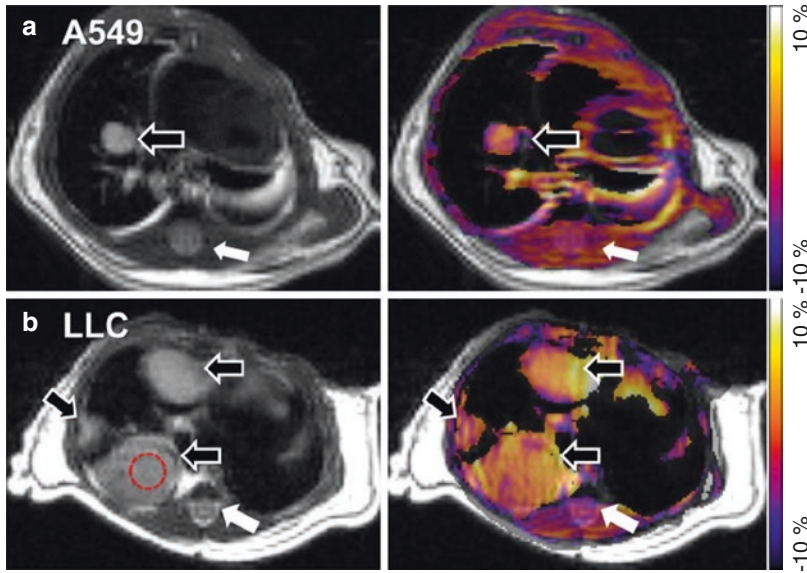
Fig. 7 In vivo amide proton transfer (APT) imaging of lung tumors in the orthotopic mouse model. Representative T2-weighted images (*left*) and APT-weighted images (*right*, MTRasym map at 3.5 ppm) of A549 (**a**) and LLC (**b**) where the tumors (*open arrows*) are delineated brighter than the surrounding tissues including spinal cord (*closed arrows*) and skeletal muscles. A typical region of interest to measure signal intensity on a tumor is demonstrated (**b**) (Reproduced with permission from Togao et al. (2013). © 2013 Togao et al.)

By adopting MRI in the area of small rodent models of airways diseases, a win–win situation between animal welfare and the relevance of data obtained from animal studies can be achieved. Noninvasive imaging results in a significant reduction in the number of animals used for experimentation. Depending on the application, a reduction between 80 and 90 % is estimated. Since repeated measurements are feasible, each animal can serve as its own control, thereby reducing the variability of the data. Moreover, as exemplified by the study of anti-inflammatory compounds on established inflammation, imaging provides potential to obtain information not accessible to conventional, *postmortem* assessments. Such an experimental refinement is often the consequence of the fact that imaging provides information of the organ in situ in the intact organism. Thus, data that are more relevant to address therapeutic effects can be obtained using imaging.

Besides therapy testing, in vivo toxicology, encompassing the identification of adverse effects of air pollutants, compounds or nanoparticles for medical use, will largely profit from imaging (Hockings and Powell 2013; Reid 2006; Wang and Yan 2008). Indeed, noninvasive small rodent imaging is in line with the concept and strategy of toxicity testing in the twenty-first century developed by the US National Academy of Sciences, the US National Academy of Engineering, the Institute of Medicine, and the US National Research Council (http://dels.nas.edu/dels/rpt_briefs/Toxicity_Testing_final.pdf). Some targeted testing in animals will be needed to sufficiently understand how chemicals are broken down in the body. Combined with imaging techniques, such assays will ensure an adequate toxicological evaluation of chemicals. As an example, it has been shown that the presence and biological effects of carbon nanotubes can be detected in vivo by noninvasive MRI techniques (Al Faraj et al. 2009, 2010, 2011).

In summary, efforts in developing imaging biomarkers for respiratory diseases are going to benefit both drug development and diagnosis. Patients will certainly profit from advancements in this field of research.

References

Al Faraj A, Cieslar K, Lacroix G et al (2009) In vivo imaging of carbon nanotube biodistribution using magnetic resonance imaging. Nano Lett 9:1023–1027

Al Faraj A, Bessaad A, Cieslar K et al (2010) Long-term follow-up of lung biodistribution and effect of instilled SWCNTs using multiscale imaging techniques. Nanotechnology 21(17):175103

Al Faraj A, Fauvelle F, Luciani N et al (2011) In vivo biodistribution and biological impact of injected carbon nanotubes using magnetic resonance techniques. Int J Nanomedicine 6:351–361

Altes TA, Mai VM, Munger TM et al (2005) Pulmonary embolism: comprehensive evaluation with MR ventilation and perfusion scanning with hyperpolarized helium-3, arterial spin tagging, and contrast-enhanced MRA. J Vasc Interv Radiol 16:999–1005

Ask K, Labiris R, Farkas L et al (2008) Comparison between conventional and "clinical" assessment of experimental lung fibrosis. J Transl Med 6:16

Babin AL, Cannet C, Gérard C et al (2011) Noninvasive assessment of bleomycin-induced lung injury and the effects of short-term glucocorticosteroid treatment in rats using MRI. J Magn Reson Imaging 33:603–614

Babin AL, Cannet C, Gérard C et al (2012) Bleomycin-induced lung injury in mice investigated by MRI: model assessment for target analysis. Magn Reson Med 67:499–509

Barnes PJ (2008a) Immunology of asthma and chronic obstructive pulmonary disease. Nat Rev Immunol 8:183–192

Barnes PJ (2008b) The cytokine network in asthma and chronic obstructive pulmonary disease. J Clin Invest 118:3546–3556

Bauman G, Puderbach M, Deimling M et al (2009) Non-contrast-enhanced perfusion and ventilation assessment of the human lung by means of fourier decomposition in proton MRI. Magn Reson Med 62:656–664

Bauman G, Scholz A, Rivoire J et al (2013) Lung ventilation- and perfusion-weighted Fourier decomposition magnetic resonance imaging: in vivo validation with hyperpolarized 3He and dynamic contrast-enhanced MRI. Magn Reson Med 69:229–237

Beckmann N, Tigani B, Ekatodramis D et al (2001a) Pulmonary edema induced by allergen challenge in the rat: noninvasive assessment by magnetic resonance imaging. Magn Reson Med 45:88–95

Beckmann N, Tigani B, Mazzoni L et al (2001b) MRI of lung parenchyma in rats and mice using a gradient-echo sequence. NMR Biomed 14:297–306

Beckmann N, Tigani B, Sugar R et al (2002) Noninvasive detection of endotoxin-induced mucus hypersecretion in rat lung by MRI. Am J Physiol Lung Cell Mol Physiol 283:L22–L30

Beckmann N, Cannet C, Zurbruegg S et al (2004) Proton MRI of lung parenchyma reflects allergen-induced airway remodeling and endotoxin-aroused hyporesponsiveness: a step toward ventilation studies in spontaneously breathing rats. Magn Reson Med 52:258–268

Beckmann N, Crémillieux Y, Tigani B et al (2006) Lung MRI in small rodents as a tool for the evaluation of drugs in models of airways diseases. In: Beckmann N (ed) In vivo MR techniques in drug discovery and development. Taylor & Francis, New York, pp 351–372

Beckmann N, Cannet C, Karmouty-Quintana H et al (2007) Lung MRI for experimental drug research. Eur J Radiol 64:381–396

Bianchi A, Ozier A, Ousova O et al (2013) Ultrashort-TE MRI longitudinal study and characterization of a chronic model of asthma in mice: inflammation and bronchial remodeling assessment. NMR Biomed 26:1451–1459

Bianchi A, Dufort S, Fortin PY et al (2014a) In vivo MRI for effective non-invasive detection and follow-up of an orthotopic mouse model of lung cancer. NMR Biomed 27:971–979

Bianchi A, Dufort S, Lux F et al (2014b) Targeting and in vivo imaging of non-small-cell lung cancer using nebulized multimodal contrast agents. Proc Natl Acad Sci U S A 111:9247–9252

Bianchi A, Tibiletti M, Kjørstad Å et al (2015a) Three-dimensional accurate detection of lung emphysema in rats using ultra-short and zero echo time MRI. NMR Biomed 28:1471–1479

Bianchi A, Tibiletti M, Kjørstad Å et al (2015b) Functional proton MRI in emphysematous rats. Invest Radiol 50:812–820

Blé FX, Cannet C, Zurbruegg S et al (2008) Allergen-induced lung inflammation in actively sensitized mice assessed with MR imaging. Radiology 248:834–843

Blé FX, Cannet C, Zurbruegg S et al (2009a) Activation of the lung S1P(1) receptor reduces allergen-induced plasma leakage in mice. Br J Pharmacol 158:1295–1301

Blé FX, Schmidt P, Cannet C et al (2009b) In vivo assessment of mucus dynamics in the rat lung using a Gd-Cy5.5-bilabeled contrast agent for magnetic resonance and optical imaging. Magn Reson Med 62:1164–1174

Blé FX, Cannet C, Collingwood S et al (2010) ENaC-mediated effects assessed by MRI in a rat model of hypertonic saline-induced lung hydration. Br J Pharmacol 160:1008–1015

Bergin CJ, Noll DC, Pauly JM et al (1992) MR imaging of lung parenchyma: a solution to susceptibility. Radiology 183:673–676

Boucher RC (2007) Airway surface dehydration in cystic fibrosis: pathogenesis and therapy. Annu Rev Med 58:157–170

Caravan P, Yang Y, Zachariah R et al (2013) Molecular magnetic resonance imaging of pulmonary fibrosis in mice. Am J Respir Cell Mol Biol 49:1120–1126

Chen XJ, Hedlund LW, Moller HE et al (2000) Detection of emphysema in rat lungs by using magnetic reso-

nance measurements of 3He diffusion. Proc Natl Acad Sci U S A 97:11478–11481

Chen BT, Johnson GA (2004) Dynamic lung morphology of methacholine-induced heterogeneous bronchoconstriction. Magn Reson Med 52:1080–1086

Chen DL, Schuster DP (2004) Positron emission tomography with [18F]fluorodeoxyglucose to evaluate neutrophil kinetics during acute lung injury. Am J Physiol Lung Cell Mol Physiol 286:L834–L840

Chen DL, Bedient TJ, Kozlowski J (2009) [18F]fluorodeoxyglucose positron emission tomography for lung antiinflammatory response evaluation. Am J Respir Crit Care Med 180:533–539

Chua F, Gauldie J, Laurent GJ (2005) Pulmonary fibrosis: searching for model answers. Am J Respir Cell Mol Biol 33:9–13

Conti G, Tambalo S, Villetti G et al (2010) Evaluation of lung inflammation induced by intratracheal administration of LPS in mice: comparison between MRI and histology. MAGMA 23:93–101

Deninger AJ, Mansson S, Petersson JS et al (2002) Quantitative measurement of regional lung ventilation using 3He MRI. Magn Reson Med 48:223–232

Dou H, Destache CJ, Morehead JR et al (2006) Development of a macrophage-based nanoparticle platform for antiretroviral drug delivery. Blood 108:2827–2835

Dou H, Morehead J, Destache CJ et al (2007) Laboratory investigations for the morphologic, pharmacokinetic, and anti-retroviral properties of indinavir nanoparticles in human monocyte-derived macrophages. Virology 358:148–158

Driehuys B, Cofer GP, Pollaro J et al (2006) Imaging alveolar-capillary gas transfer using hyperpolarized 129Xe MRI. Proc Natl Acad Sci U S A 103:18278–18283

Driehuys B, Möller HE, Cleveland ZI et al (2009) Pulmonary perfusion and xenon gas exchange in rats: MR imaging with intravenous injection of hyperpolarized 129Xe. Radiology 252:386–393

Dufort S, Bianchi A, Henry M et al (2015) Nebulized gadolinium-based nanoparticles: a theranostic approach for lung tumor imaging and radiosensitization. Small 11:215–221

Dugas JP, Garbow JR, Kobayashi DK et al (2004) Hyperpolarized (3)He MRI of mouse lung. Magn Reson Med 52:1310–1317

Ebner B, Behm P, Jacoby C et al (2010) Early assessment of pulmonary inflammation by 19F MRI in vivo. Circ Cardiovasc Imaging 3:202–210

Edelman RR, Hatabu H, Tadamura E et al (1996) Noninvasive assessment of regional ventilation in the human lung using oxygen-enhanced magnetic resonance imaging. Nat Med 2:1236–1239

Egger C, Cannet C, Gérard C et al (2013) Administration of bleomycin via the oropharyngeal aspiration route leads to sustained lung fibrosis in mice and rats as quantified by UTE-MRI and histology. PLoS One 8(5):e63432

Egger C, Gérard C, Vidotto N et al (2014) Lung volume quantified noninvasively by MRI reflects extracellular-matrix deposition and al-tered pulmonary function in small rodent bleomycin models of fibrosis. Am J Physiol Lung Cell Mol Physiol 306:L1064–L1077

Egger C, Cannet C, Gérard C et al (2015) Hyaluronidase modulates bleomycin-induced lung injury detected non-invasively in small rodents by radial proton MRI. J Magn Reson Imaging 41:755–764

Emami K, Cadman RV, Woodburn JM et al (2008) Early changes of lung function and structure in an elastase model of emphysema –a hyperpolarized 3He MRI study. J Appl Physiol (1985) 104:773–786

Garbow JR, Zhang Z, You M (2004) Detection of primary lung tumors in rodents by magnetic resonance imaging. Cancer Res 64:2740–2742

Garbow JR, Wang M, Wang Y et al (2008) Quantitative monitoring of adenocarcinoma development in rodents by magnetic resonance imaging. Clin Cancer Res 14:1363–1367

Goodson BM (2002) Nuclear magnetic resonance of laser-polarized noble gases in molecules, materials, and organisms. J Magn Reson 155:157–216

Haczku A, Emami K, Fischer MC et al (2005) Hyperpolarized 3He MRI in asthma measurements of regional ventilation following allergic sensitization and challenge in mice–preliminary results. Acad Radiol 12:1362–1370

Hatabu H, Alsop DC, Listerud J et al (1999) T2* and proton density measurement of normal human lung parenchyma using submillisecond echo time gradient echo magnetic resonance imaging. Eur J Radiol 29:245–252

Hockings PD, Powell H (2013) In vivo MRI/S for the safety evaluation of pharmaceuticals. In: Garrido L, Beckmann N (ed) New applications of NMR in drug discovery and develop-ment. Royal Society of Chemistry Publishing, Cambridge, UK, pp 361–375

Hoymann HG (2007) Invasive and noninvasive lung function measurements in rodents. J Pharmacol Toxicol Methods 55:16–26

Imai H, Kimura A, Hori Y et al (2011) Hyperpolarized 129Xe lung MRI in spontaneously breathing mice with respiratory gated fast imaging and its application to pulmonary functional imaging. NMR Biomed 24:1343–1352

Jacob RE, Amidan BG, Soelberg J et al (2010) In vivo MRI of altered proton signal intensity and T2 relaxation in a bleomycin model of pulmonary inflammation and fibrosis. J Magn Reson Imaging 31:1091–1099

Karmouty-Quintana H, Cannet C, Sugar R et al (2007a) Capsaicin-induced mucus secretion in rat airways assessed in vivo and non-invasively by magnetic resonance imaging. Br J Pharmacol 150:1022–1030

Karmouty-Quintana H, Cannet C, Zurbruegg S et al (2007b) Bleomycin-induced lung injury assessed non-invasively and in spontaneously breathing rats by proton MRI. J Magn Reson Imaging 26:941–949

Keilholz SD, Bozlar U, Fujiwara N et al (2009) MR diagnosis of a pulmonary embolism: comparison of P792 and Gd-DOTA for first-pass perfusion MRI and con-

trast-enhanced 3D MRA in a rabbit model. Korean J Radiol 10:447–454

King TE Jr, Pardo A, Selman M (2011) Idiopathic pulmonary fibrosis. Lancet 378:1949–1961

Kveder M, Zupančič I, Lahajnar G et al (1988) Water proton relaxation mechanisms in lung tissue. Magn Reson Med 7:432–441

Labiris NR, Nahmias C, Freitag AP et al (2003) Uptake of 18fluorodeoxyglucose in the cystic fibrosis lung: a measure of lung inflammation? Eur Respir J 21:848–854

Lazo JS, Sebti SM, Schellens JH (1996) Bleomycin. Cancer Chemother Biol Response Modif 16:39–47

Manali ED, Moschos C, Triantafillidou C et al (2011) Static and dynamic mechanics of the murine lung after intratracheal bleomycin. BMC Pulm Med 11:33

Marzola P, Lanzoni A, Nicolato E et al (2005) (1)H MRI of pneumococcal pneumonia in a murine model. J Magn Reson Imaging 22:170–174

Mistry NN, Pollaro J, Song JY et al (2008) Pulmonary perfusion imaging in the rodent lung using dynamic contrast-enhanced MRI. Magn Reson Med 59: 289–297

Mistry NN, Thomas A, Kaushik SS et al (2010) Quantitative analysis of hyperpolarized 3He ventilation changes in mice challenged with methacholine. Magn Reson Med 63:658–666

Molina JR, Yang P, Cassivi SD et al (2008) Non-small cell lung cancer: epidemiology, risk factors, treatment, and survivorship. Mayo Clin Proc 83:584–594

Möller HE, Chen XJ, Saam B et al (2002) MRI of the lungs using hyperpolarized noble gases. Magn Reson Med 47:1029–1051

Moore BB, Hogaboam CM (2008) Murine models of pulmonary fibrosis. Am J Physiol Lung Cell Mol Physiol 294:L152–L160

Mosbah K, Ruiz-Cabello J, Berthezène Y et al (2008) Aerosols and gaseous contrast agents for magnetic resonance imaging of the lung. Contrast Media Mol Imaging 3:173–190

Mosbah K, Stupar V, Berthezène Y et al (2010) Spatially resolved assessment of serotonin-induced bronchoconstrictive responses in the rat lung using 3He ventilation MRI under spontaneous breathing conditions. Magn Reson Med 63:1669–1674

Neeb D, Kunz RP, Ley S et al (2009) Quantification of pulmonary blood flow (PBF): validation of perfusion MRI and nonlinear contrast agent (CA) dose correction with H(2)15O positron emission tomography (PET). Magn Reson Med 62:476–487

Ohno Y, Adachi S, Kono M et al (2000) Predicting the prognosis of non-small cell lung cancer patient treated with conservative therapy using contrast-enhanced MR imaging. Eur Radiol 10:1770–1781

Olsson LE, Lindahl M, Onnervik PO et al (2007) Measurement of MR signal and T2* in lung to characterize a tight skin mouse model of emphysema using single-point imaging. J Magn Reson Imaging 25: 488–494

O'Sullivan JM, Huddart RA, Norman AR et al (2003) Predicting the risk of bleomycin lung toxicity in patients with germ-cell tumours. Ann Oncol 14: 91–96

Parr DG, Stoel BC, Stolk J et al (2004) Influence of calibration on densitometric studies of emphysema progression using computed tomography. Am J Respir Crit Care Med 170:883–890

Peces-Barba G, Ruiz-Cabello J, Crémillieux Y et al (2003) Helium-3 MRI diffusion coefficient: correlation to morphometry in a model of mild emphysema. Eur Respir J 22:14–19

Quintana HK, Cannet C, Schaeublin E et al (2006a) Identification with MRI of the pleura as a major site of the acute inflammatory effects induced by ovalbumin and endotoxin challenge in the airways of the rat. Am J Physiol Lung Cell Mol Physiol 291: L651–L657

Quintana HK, Cannet C, Zurbruegg S et al (2006b) Proton MRI as a noninvasive tool to assess elastase-induced lung damage in spontaneously breathing rats. Magn Reson Med 56:1242–1250

Reid D (2006) MRI in pharmaceutical safety assessment. In: Beckmann N (ed) In vivo MR techniques in drug discovery and development. Taylor & Francis, New York, pp 537–554

Roberts DA, Rizi RR, Lipson DA et al (2001) Dynamic observation of pulmonary perfusion using continuous arterial spin-labeling in a pig model. J Magn Reson Imaging 14:175–180

Ryhammer P, Pedersen M, Ringgaard S et al (2007) Regional pulmonary perfusion using model-free analysis of contrast-enhanced MRI in meconium-aspirated piglets. J Magn Reson Imaging 26:296–303

Spector ZZ, Emami K, Fischer MC et al (2005) Quantitative assessment of emphysema using hyperpolarized 3He magnetic resonance imaging. Magn Reson Med 53:1341–1346

Strieter RM, Mehrad B (2009) New mechanisms of pulmonary fibrosis. Chest 136:1364–1370

Strobel K, Hoerr V, Schmid F et al (2012) Early detection of lung inflammation: exploiting T1-effects of iron oxide particles using UTE MRI. Magn Reson Med 68:1924–1931

Stupar V, Canet-Soulas E, Gaillard S et al (2007) Retrospective cine 3He ventilation imaging under spontaneous breathing conditions: a non-invasive protocol for small-animal lung function imaging. NMR Biomed 20:104–112

Takahashi M, Togao O, Obara M et al (2010) Ultra-short echo time (UTE) MR imaging of the lung: comparison between normal and emphysematous lungs in mutant mice. J Magn Reson Imaging 32:326–333

Tassali N, Bianchi A, Lux F et al (2016) MR imaging, targeting and characterization of pulmonary fibrosis using intra-tracheal administration of gadolinium-based nanoparticles. Contrast Media Mol Imaging 11:396–404. doi:10.1002/cmmi.1703

Tesfaigzi Y, Fischer MJ, Martin AJ et al (2000) Bcl-2 in LPS- and allergen-induced hyperplastic mucous cells in airway epithelia of Brown Norway rats. Am J Physiol Lung Cell Mol Physiol 279:L1210–L1217

Thomas AC, Kaushik SS, Nouls J et al (2012) Effects of corticosteroid treatment on airway inflammation, mechanics, and hyperpolarized ³He magnetic resonance imaging in an allergic mouse model. J Appl Physiol (1985) 112:1437–1444

Tigani B, Schaeublin E, Sugar R et al (2002) Pulmonary inflammation monitored noninvasively by MRI in freely breathing rats. Biochem Biophys Res Commun 292:216–221

Tigani B, Cannet C, Zurbrugg S et al (2003a) Resolution of the oedema associated with allergic pulmonary inflammation in rats assessed noninvasively by magnetic resonance imaging. Br J Pharmacol 140:239–246

Tigani B, Di Padova F, Zurbrügg S et al (2003b) Effects of a mitogen-activated protein kinase inhibitor on allergic airways inflammation in the rat studied by magnetic resonance imaging. Eur J Pharmacol 482:319–324

Tigani B, Cannet C, Karmouty-Quintana H et al (2007) Lung inflammation and vascular remodeling after repeated allergen challenge detected noninvasively by MRI. Am J Physiol Lung Cell Mol Physiol 292:L644–L653

Togao O, Kessinger CW, Huang G et al (2013) Characterization of lung cancer by amide proton transfer (APT) imaging: an in-vivo study in an orthotopic mouse model. PLoS One 15:e77019

Tournebize R, Doan BT, Dillies MA et al (2006) Magnetic resonance imaging of *Klebsiellapneumoniae*-induced pneumonia in mice. Cell Microbiol 8:33–43

van Echteld CJ, Beckmann N (2011) A view on imaging in drug research and development for respiratory diseases. J Pharmacol Exp Ther 337:335–349

Vande Velde G, De Langhe E, Poelmans J et al (2014) Magnetic resonance imaging for noninvasive assessment of lung fibrosis onset and progression: cross-validation and comparison of different magnetic resonance imaging protocols with micro-computed tomography and histology in the bleomycin-induced mouse model. Invest Radiol 49:691–698

Walder B, Fontao E, Totsch M et al (2005) Time and tidal volume-dependent ventilator-induced lung injury in healthy rats. Eur J Anaesthesiol 22:785–794

Wang YX, Yan SX (2008) Biomedical imaging in the safety evaluation of new drugs. Lab Anim 42:433–441

Wellman TJ, Winkler T, Costa EL et al (2010) Measurement of regional specific lung volume change using respiratory-gated PET of inhaled 13 N-nitrogen. J Nucl Med 51:646–653

World Health Organization (2004) Classification of tumours. In: Travis WD, Brambilla E, Müller-Hermelink HK, Harris CC (eds) Pathology and genetics of tumours of the lung, pleura, thymus and heart. IARC Press, Lyon. https://www.iarc.fr/en/publications/pdfs-online/pat-gen/bb10/BB10.pdf

Yi C, Cao Y, Mao SH et al (2009) Recombinant human growth hormone improves survival and protects against acute lung injury in murine *Staphylococcus aureus* sepsis. Inflamm Res 58:855–862

Zapke M, Topf H, Zenker M et al (2006) Magnetic resonance lung function–a breakthrough for lung imaging and functional assessment? A phantom study and clinical trial. Respir Res 7:106

Zurek M, Bessaad A, Cieslar K et al (2010) Validation of simple and robust protocols for high-resolution lung proton MRI in mice. Magn Reson Med 64:401–407

Zurek M, Crémillieux Y (2011) MRI of the lung: noninvasive protocols and applications to small animal models of lung disease. Methods Mol Biol 771:459–474

Zurek M, Boyer L, Caramelle P et al (2012) Longitudinal and noninvasive assessment of emphysema evolution in a murine model using proton MRI. Magn Reson Med 68:898–904

Pulmonary MRI in Clinical Trials

Dante P.I. Capaldi, Rachel L. Eddy,
and Grace Parraga

Contents

Abstract

Until very recently, pulmonary MRI has played
a limited clinical role for patients with chronic
lung diseases such as COPD and asthma. The
reasons for this are numerous and complex; yet,
because of a concerted effort of a number of key
research sites, pulmonary MRI endpoints are
increasingly being used as research tools and bio-
markers in clinical trials. A number of previous
landmark studies focused on the development
and validation of biomarkers to provide a better
understanding of structural and functional infor-
mation. These biomarkers are now being applied
in emerging cohort studies to forge a better
understanding of lung disease in cross-sectional
and longitudinal evaluations and in the evalu-
ation of localized treatment and regional treat-
ment responses. Pulmonary MRI biomarker use
has certainly been increasing, but gaps remain
between the research bench and clinical work-
flows to patient care. Advancing pulmonary MRI
toward clinical implementation will require the
concerted, globally collaborative development
and validation of clinically relevant biomarkers
in multinational cohort studies and clinical trials.

D.P.I. Capaldi, BSc • R.L. Eddy, BEng
G. Parraga, PhD (✉)
Robarts Research Institute and Department
of Medical Biophysics, Western University,
1151 Richmond St N, London, Canada, N6A 5B7
e-mail: gparraga@robarts.ca

1 Introduction and Rationale

Randomized controlled clinical trials provide the
gold standard evidence for health care providers,
regulatory bodies, and other agencies to provide

marketing approval and prescribe new therapeutic drugs and devices. Moreover, the publication of the results of these trials provides the evidence needed to rationalize therapy decisions in complex patients like those with lung disease. Observational and cohort studies while not typically classified as "clinical trials" also provide a wealth of evidence to generate new understandings about disease mechanisms and further expand our knowledge related to diagnosis, treatment, and prevention. All of this research evidence is weighed and debated by consensus panels as well as national and international guideline committees that together generate the policies regarding therapy and patient management approaches that dominate the medical care of patients with lung disease. Together, multinational clinical research trials and consensus guidelines reinforce the overwhelming opinion that chronic lung diseases such as chronic obstructive pulmonary disease (COPD) and asthma can be managed but not cured for patients with all grades of disease severity (Vestbo et al. 2013a). Albeit a very hopeful and yet practical position, existing management strategies for patients with chronic lung disease have not improved long-term outcomes for many patients. Unfortunately, lung disease costs, hospitalization, and mortality rates continue to rise, and health economists warn that this upward trend will continue and very soon will overwhelm global health care systems (Khakban et al. 2015). In light of this dire situation, new management strategies are urgently required to combat this growing personal and public health crisis.

In part, because of these concerns for all patients with chronic diseases, novel precision medicine methods are being developed. Importantly, precision medicine depends on a deeper understanding of the underlying genetic and molecular mechanisms in individual patients, and it is thought that this has the potential to deliver the "right" treatment to the right patient at the right time. A better understanding of underlying disease will also allow for better patient management, and perhaps more importantly, will also open doors for the discovery of new drugs and interventions. This may also enable or drive the development of larger cohort studies and trials to evaluate specific underlying pathologies that accompany chronic disease, including respiratory diseases. Another important issue is the need for an in-depth understanding of how distinct underlying biological mechanisms manifest in the individual patient – the disease "phenotype." Such phenotype measurements currently include clinical and functional biomarkers, and more recently, pulmonary imaging structure–function imaging phenotypes, including those provided by pulmonary MRI.

The technical development, clinical and commercial translation of MRI methods and technologies and the more recent development of quantitative imaging methods, have led to their increased use in the diagnosis and management of many chronic diseases. Until very recently however, for patients with chronic lung diseases such as COPD and asthma, medical imaging has not played a major role. The reasons for this are numerous and complex. While the reasons underlying the clinical situation are not the main focus of this chapter, as summarized in Fig. 1, it is important to note that the slow progress of lung MRI development relative to other body system imaging is reflected by a limited number of clinical trials that utilize lung MRI biomarkers. Moreover, although lung MRI has been under clinical development for over two decades, there have been no pivotal trials of new lung disease treatments that have utilized MRI biomarkers. Given the paucity of lung MRI clinical trials experience, here we highlight the potential of pulmonary imaging with MRI for clinical trials, some limitations and challenges, as well as recent experience and future goals. We also discuss how pulmonary MRI can be used to generate novel, regional, and noninvasive biomarkers of lung disease growth, development, and aging, as well as disease progression. Finally, we challenge the research and clinical communities to enable five key requirements in the next 5 years (coined Five for Five) that we think will be important to change the dismal outcomes currently in place for patients with lung disease as well as for the physicians and health care systems that care for them.
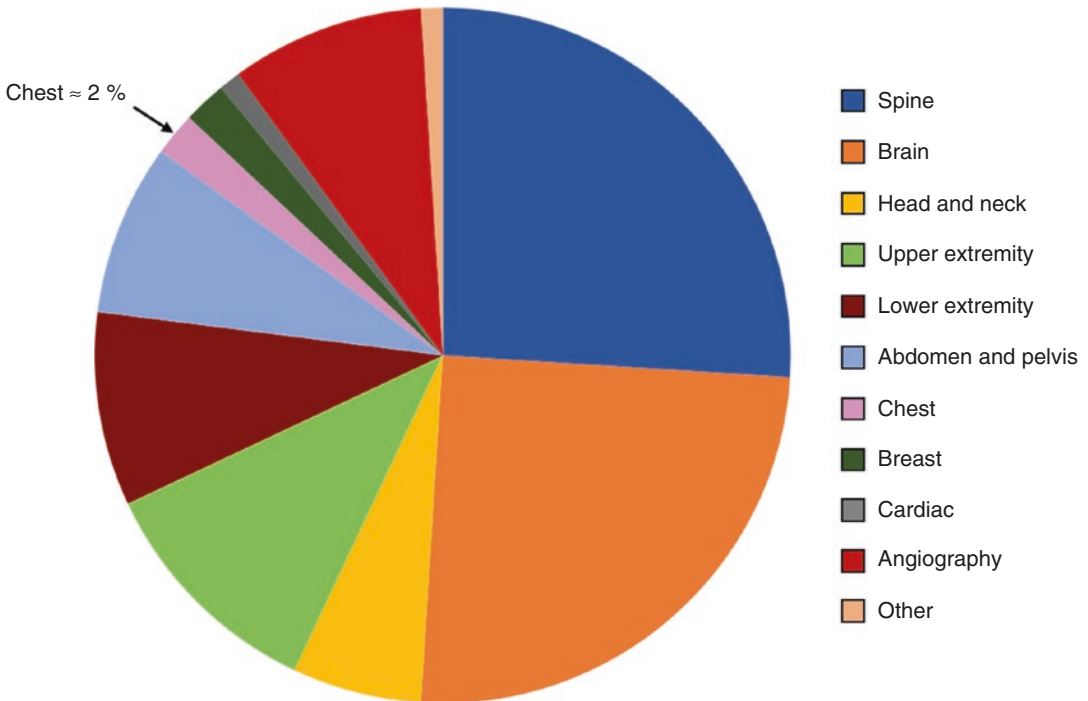
Fig. 1 MRI examinations by body region. MRI of the chest/lungs accounts for approximately 2 %, while half of all MR exams are dominated by imaging of the spine and brain. *Source*: Magnetic resonance: a peer-reviewed, critical introduction. 9th edn. Chapter 21–01 What is the Organ Distribution of MRI Studies? 2016. http://www.magnetic-resonance.org/ch/21-01.html

2 Current Role of Pulmonary MRI in Clinical Trials

For patients with chronic lung disease, pulmonary function tests provide the clinical standard for diagnosis, evaluation of response to treatment, and longitudinal monitoring. Pulmonary function tests have well-understood reproducibility (Pauwels et al. 2001); these are relatively straightforward to implement and inexpensive, and because of this, these tests are universally accepted for clinical use. Such lung volumes and capacities provide global lung measurements which are important, because very recently we have come to understand that at least for COPD, disease may initiate in a spatially heterogeneous manner and mainly within the smaller airways. This fundamental information is reflected by the limitation of spirometry measurements with respect to relative insensitivity to early disease stages (Vestbo et al. 2013b) and weak relationships with important clinical outcomes and health status (Jones 2009; Agusti et al. 2010), such as symptoms, exercise capacity, quality-of-life, exacerbations, and hospitalizations.

To overcome these limitations, X-ray computed tomography (CT) has been used for at least a decade in large cohort studies, including CanCOLD (Bourbeau et al. 2014), ECLIPSE (Vestbo et al. 2008), SPIROMICS (Couper et al. 2014), COPDGene (Regan et al. 2010), MESA Lung Study (Bild et al. 2002), SARP (Jarjour et al. 2012), and a study out of the Difficult Asthma Clinic in the UK (Gupta et al. 2009), to evaluate and identify regional pulmonary abnormalities in patients with COPD and asthma. Overall, the main rationale for including CT in COPD and asthma cohort studies is to provide objective measurements of regional and heterogeneous lung pathologies in the airways and parenchyma to better understand clinical phenotypes. There are a number of technical hurdles

related to the application of lung MRI in larger clinical studies, including low proton density (Bergin et al. 1991) and susceptibility artifacts caused by multiple air–tissue interfaces (Bergin et al. 1993). Some of these technical challenges have been overcome based on novel applications including inhaled inert or hyperpolarized noble gas contrast agents (Albert et al. 1994) and zero or ultrashort echo time (ZTE/UTE) imaging applications (Bergin et al. 1991) described in more detail in earlier chapters in this volume. It is important to stress however that MRI has significant advantages compared to CT – the current clinical standard, due in part to the increased availability of clinical MRI systems (OECD 2007) and the fact that MRI does not rely on ionizing radiation for contrast. This is extremely important for serial studies of treatment response and longitudinal studies, particularly in children and younger adults with chronic lung disease. Before the applications of pulmonary MRI in clinical trials are summarized, it is important to understand its strengths and limitations.

3 Strengths and Limitations

Among the many obvious strengths of clinical MRI, a hallmark feature is excellent soft tissue contrast that may be provided with relatively high spatial and temporal resolution, making MRI the modality of choice for brain, musculoskeletal, and nervous system examinations. In fact, as shown in Fig. 1, imaging of these body systems alone comprises over 75 % of all clinical MRI investigations, whereas MRI of the chest accounts for approximately 2 % of annual examinations. Pulmonary MRI comprises a small minority of clinical examinations, and some of the reasons for this may be gleaned from the key limitations of pulmonary MRI, summarized in Table 1. These are important to discuss, because some of these pulmonary MRI shortcomings have certainly slowed clinical translation and made clinical use challenging. It is also important to point out that while chest X-ray and CT have been long considered the gold standard for lung imaging for both research and clinical uses, MRI

Table 1 Strengths and limitations of MR imaging of the lungs in clinical trials

Strengths	Limitations
+ Safe + Well-tolerated (even in very compromised patients) + Fast + Well suited for pediatric populations + Provides both functional and anatomical images that are intrinsically coregistered + Numerous contrasts (Gd, ^{3}He, ^{129}Xe, ^{19}F) + High temporal and spatial resolution	- Quality control (calibration) of MR equipment for multicenter trials - Specialized readers for MR thoracic imaging - Software pipeline for image analysis - Validated imaging biomarkers - Coil inhomogeneities - Harmonizing across sites/vendors - Regulatory approval (in North America) - Cost/accessibility of MR specialized equipment for thoracic imaging

has the added advantage of providing pulmonary images without the burden of ionizing radiation. This is especially important for pediatric lung disease in that MRI makes possible both serial and longitudinal imaging in this vulnerable patient group. Furthermore, pulmonary MRI is well understood to be safe and well tolerated in healthy volunteers and even the most compromised patients with respiratory disease (Lutey et al. 2008; Driehuys et al. 2012; Shukla et al. 2012). The speed with which pulmonary MRI can be acquired is similar to CT in the simultaneous morphological and functional images of the chest volume in a single breath-hold, as described in this edition. There are also numerous contrast agents that have been applied to generate more information about the lung using MRI, such as intravenous gadolinium for pulmonary perfusion imaging (Hatabu et al. 1996) and inhaled gas for ventilation imaging, including ^{3}He (Ebert et al. 1996), ^{129}Xe (Mugler et al. 1997), and ^{19}F (Soher et al. 2010). Despite the undeniable opportunities for clinically relevant pulmonary biomarkers that these approaches provide, a number of key limitations have hampered the use of pulmonary MRI in clinical trials including the following: (1) techniques are still in development and restricted to a few specialized research centers, (2) inhaled gases incur relatively higher costs and require

access to multinuclear MR hardware and analysis software, (3) different vendor platforms and intellectual property issues have made harmonization complex and slow, and (4) requirement for standardized and validated image analysis software and quality control phantoms for hardware calibration.

Unlike the MRI pulse sequences and contrast agents approved for clinical use in brain, cardiac, body, and musculoskeletal applications, most pulmonary MRI methods are still in the developmental phase and restricted to research use only. For example, while inhaled hyperpolarized gas MRI is now approved for clinical use in the UK, it is not yet approved for clinical use in Asia, North America, or the rest of the EU, despite numerous demonstrations of safety and efficacy in chronic lung disease patients (Lutey et al. 2008; Driehuys et al. 2012). In addition, for inhaled gas MRI, relatively higher costs and the need for access to multinuclear MR hardware and analysis software have limited its use to a few research sites in the EU and North America. There are, however, opportunities for conventional proton lung imaging, including ultrashort echo time (UTE) (Bergin et al. 1991), Fourier decomposition (FD) (Bauman et al. 2009), and O_2-enhanced MRI (Edelman et al. 1996), as well as MR angiography (Meaney et al. 1997) and pulmonary MR perfusion (Hatabu et al. 1996). It is also important to consider and recognize that the different MRI vendor platforms and intellectual property issues have made harmonization across different platforms and sites complex and slow. Finally, standardization of software used to analyze images and quality control phantoms to calibrate the MR equipment are both needed. Because of this and other reasons, the validation of pulmonary imaging biomarkers across multiple centers has been an ongoing challenge and limited large-scale clinical trials using pulmonary MRI.

Despite these challenges, as shown in Sects. 5.2 and 5.3, there are a number of active clinical studies now ongoing that investigate the utility of pulmonary MRI in observational and interventional studies. There is still, however, a large opportunity for collaboration and standardization

between pulmonary and radiology research sites, as well with vendors and clinical trial sponsors to address many of these roadblocks. This ongoing collaboration is critically required to accelerate pulmonary MRI translation from the research workbench and workstation to clinical workflows and patient care.

4 Methodology

We performed a systematic review of clinical studies that included pulmonary MRI endpoints using PubMed and the NIH reporting website ClinicalTrials.gov by employing subject and text word search terms for "MRI" and "lung" with no restrictions on the study date or target population. We excluded studies and trials that were for the purpose of technical and pulse sequence design and development. Clinical studies and trials in four broad categories based on study design included in this chapter included: (1) validation studies and those designed to develop and validate MRI biomarkers of lung disease, (2) observational studies, including both cross-sectional and longitudinal designs, (3) interventional studies, including those evaluating treatment response and using MRI to guide pulmonary therapies, and (4) studies that developed or used MRI biomarkers in lung disease diagnoses and as diagnostic criteria. In the following sections, the goals of these clinical studies and their key findings are highlighted and summarized.

5 MRI Applications in Clinical Trials

5.1 Discovering, Developing, and Validating Disease Biomarkers

To date, pulmonary MRI has been used in a number of key clinical trials, and, as summarized in Table 2, these pioneering development and validation studies provided an essential first step in understanding the structural and functional information that can be derived from pulmonary

Table 2 Included clinical trials and studies that developed or validated biomarkers

Author	Biomarker	Type	Mechanism
Woodhouse et al.	PVV	Development	–
Kirby et al.	VDP	Development	–
Parraga et al.	^{3}He VDP, healthy	Reproducibility	Same Day, 7 Day
Mathew et al.	^{3}He VDP and ADC, COPD	Reproducibility	Same Day, 7 Day
de Lange et al.	^{3}He VDP, asthma	Reproducibility	7 Day
Kirby et al.	^{3}He VDP, CF	Reproducibility	7 Day
Kirby et al.	^{129}Xe VDP	Validation	^{3}He VDP
Couch et al.	^{19}F VDP	Validation	^{3}He VDP
Mugler III et al.	^{3}He ADC	Development	–
Woods et al.	^{3}He ADC	Validation	Histology
Diaz et al.	^{3}He ADC	Reproducibility	7 Day
Kirby et al.	^{129}Xe ADC	Validation	^{3}He ADC
Deninger et al.	^{3}He P_{AO2}	Development and validation	Blood Gases
Ishii et al.	^{3}He P_{AO2}	Reproducibility	Same Day
Bauman et al.	FD perfusion	Validation	DCE MRI
	FD ventilation	Validation	^{3}HeVDP
Lederlin et al.	FD perfusion, ventilation	Reproducibility	1 Day
Ma et al.	UTE signal intensity	Reproducibility	3 Week
Jobst et al.	^{1}H perfusion	Reproducibility	24 h
Edelman et al.	O_2-enhanced ventilation	Development	–
Hatabu et al.	Gadolinium perfusion	Development	–

MRI. From these initial studies, other clinical studies emerged that focused on the identification of MRI biomarkers, as shown in Fig. 2, of chronic lung disease and their relationship to clinically relevant measurements of lung disease.

Lung functional biomarkers include those that reflect regional ventilation such as hyperpolarized noble gas MRI percent ventilation volume (PVV) (Woodhouse et al. 2005) and ventilation abnormalities using ventilation-defect percent (VDP) (Kirby et al. 2010b). Until these biomarkers were shown to be measurable both objectively and quantitatively, qualitative subjective scoring systems were in place (Donnelly et al. 1999; de Lange et al. 2006; McMahon et al. 2006). The advantage of quantitative, continuous variables for clinical trial protocol development and the fact that these variables can be validated and automatically measured across research sites cannot be overestimated. The pulmonary ventilation MRI measurements of PVV and VDP reflect well-ventilated and poorly ventilated regions of the parenchyma, respectively. These may be rapidly and

automatically generated by combining the functional information from hyperpolarized noble gas MRI with the structural information from conventional proton MRI. These have been studied and validated as imaging biomarkers related to pulmonary function tests, lung volumes, and DL_{CO} (de Lange et al. 2006; Mathew et al. 2011; Kirby et al. 2012). In addition, the reproducibility of VDP has been shown and validated in healthy subjects (Parraga et al. 2008), as well as in COPD (Mathew et al. 2008), asthma (de Lange et al. 2007), and cystic fibrosis (Kirby et al. 2011b). While these studies focused on ^{3}He MRI, they provided a validation framework for ^{129}Xe (Kirby et al. 2012) and ^{19}F studies (Couch et al. 2014). Using diffusion-weighted MRI, apparent diffusion coefficients (ADC) can be derived and are a common measure of tissue integrity, especially in the brain. However, ADC has also been applied to pulmonary MRI using inhaled gas contrast as a biomarker of the extent of emphysema in the lungs, as generated using hyperpolarized noble gas imaging (Mugler III 1998). ^{3}He ADC in the
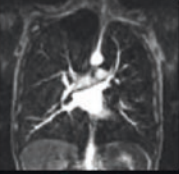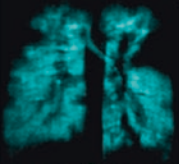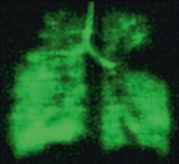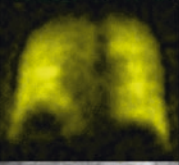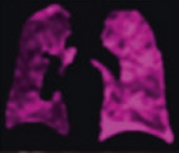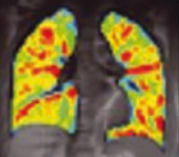
Technique	Biomarkers	Strengths	Challenges
MRA	• Pulmonary blood distribution • Perfusion • Exclusion of PE	• Radiation free (compared to CTA) • Morphologic and functional information	• Inferior spatial resolution • Longer scan/breath-hold times • Contraindications for critically ill patients
MR Perfusion	• Pulmonary blood flow • Perfusion • 3D perfusion changes	• Radiation free (compared to scintigraphy) • Morphologic and functional information • Rapid acquisition	• Requires high temporal resolution • Difficult quantification • Cardiac artefacts
³He	• Ventilation • VV • VDP • PVV	• Functional information • High SNR	• Expensive • Requires specialized equipment
¹²⁹Xe	• Ventilation • VV • VDP • PVV	• Functional information • Less expensive than ³He • Gas exchange parameters can be measured	• Requires specialized equipment • Lower SNR than ³He
¹⁹F	• Ventilation • VV • VDP • PVV	• Functional information • Does not require polarization	• Requires specialized coil • Low SNR
Proton UTE	• Tissue density	• Morphologic information • Inexpensive • Non-contrast enhanced	• No functional information • Low spatial resolution • Signal intensity is not normalized
Proton FD	• Ventilation • VV • VDP • PVV • Perfusion	• Functional information • Inexpensive • Non-contrast enhanced • Dynamic	• Indirect interpretation • Extensive post-processing
O₂-enhanced	• Ventilation • VV • VDP • PVV	• Functional information • Inexpensive • Non-contrast enhanced • Generally available tools, ie O₂ supply	• Indirect interpretation • Low signal enhancement • Complex contrast mechanism

Fig. 2 Pulmonary MRI techniques and their associated biomarkers, advantages, and disadvantages. MRA, MR Perfusion and O$_2$-enhanced from 1st Ed (^{19}F image courtesy of Mitch Albert)

lungs have been validated using histology (Woods et al. 2006) and were shown to be highly reproducible (Morbach et al. 2005; Parraga et al. 2007; Diaz et al. 2009). Moreover, ^{3}He ADC values have been used to validate ^{129}Xe ADC measurements (Kirby et al. 2014a). As shown in Fig. 3,

Fig. 3 Static ventilation and diffusion-weighted images in healthy volunteers using inhaled gas contrast agents. (**a**) Hyperpolarized ³He, (**b**) hyperpolarized ¹²⁹Xe, and (**c**) ¹⁹F (courtesy of MS Albert) inhaled gas contrast-enhanced techniques

³He   ¹²⁹Xe   ¹⁹F

Ventilation

Diffusion

0.00 cm²/s 0.88 cm²/s   0.00 cm²/s 0.14 cm²/s   0.00 cm²/s 0.06 cm²/s
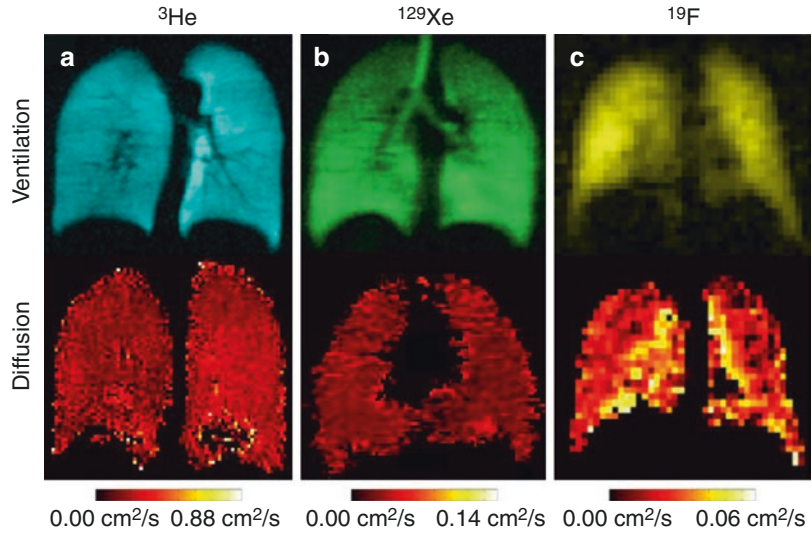
inhaled gas ventilation images and ADC maps for ³He, ¹²⁹Xe, and ¹⁹F in healthy volunteers show the relative image quality differences for the contrast agents inhaled. Another important biomarker that is generated by exploiting the tissue solubility of hyperpolarized ¹²⁹Xe has made it possible to image the xenon exchange between the airspaces (gas phase) and parenchyma/blood (dissolved phase) (Mugler et al. 1997). This provides a way to visualize simultaneous regional ventilation and perfusion function (Driehuys et al. 2006; Mugler et al. 2010). Measurements of regional alveolar partial pressure of oxygen (P_{AO2}) can also be derived from hyperpolarized gas pulmonary MRI, and was first demonstrated and validated using ³He in 1999 (Deninger et al. 1999), and reproducibility was more recently demonstrated (Ishii et al. 2015).

While the majority of pulmonary MRI biomarkers published in clinical studies derive from inhaled gas contrast MRI, other methods based on ¹H MRI are also under development. Fourier decomposition of free-breathing proton MRI (FDMRI) (Bauman et al. 2009) provides a way to evaluate pulmonary perfusion and ventilation, without exogenous contrast. Both ventilation and perfusion maps derived from FDMRI were validated using dynamic contrast-enhanced and hyperpolarized ³He MRI (Bauman et al. 2013b). Moreover, this approach was shown to be

reproducible in healthy volunteers (Lederlin et al. 2013), while the signal intensity of proton UTE MRI was also shown to be reproducible in COPD and bronchiectasis (Ma et al. 2015). Proton perfusion MRI was shown to be reproducible within 24 h when assessing COPD patients (Jobst et al. 2015). Oxygen-enhanced ¹H MRI measurements (Edelman et al. 1996) and gadolinium (Hatabu et al. 1996) have also been used to visualize biomarkers related to ventilation and perfusion.

5.2 Observational Studies

Table 3 summarizes observational studies that utilize both cross-sectional and longitudinal approaches to study lung aging, natural disease progression, and relationships with the clinical gold standard measurements.

5.2.1 Single Time Point and Other Cross-Sectional Studies

Some of the first-in-human studies that utilized pulmonary MRI involved single time point and cross-sectional evaluations of healthy volunteers and patients with chronic lung disease. The bulk of experience was first obtained using hyperpolarized inhaled gas MRI using ³He gas which is completely biologically inert, and provides very good

Table 3 Title, disease specification, and NCT number of included clinical trials and studies classified as observational

Title	Disease	NCT
Cross-sectional		
Normal and abnormal pulmonary ventilation: visualization in hyperpolarized He-3 MR imaging	Healthy young	–
Hyperpolarized ^{3}He magnetic resonance imaging of ventilation defects in healthy elderly volunteers: initial findings at 3.0 Tesla	Healthy elderly	–
Detection of age-dependent changes in healthy adult lungs with diffusion-weighted ^{3}He MRI	Healthy	–
Combined helium-3/proton magnetic resonance imaging measurement of ventilated lung volumes in smokers compared to never-smokers	COPD	NCT02279329
Hyperpolarized ^{3}He and ^{129}Xe MR imaging in healthy volunteers and patients with chronic obstructive pulmonary disease	COPD	NCT02279329
COPD: Do imaging measurements of emphysema and airway disease explain symptoms and exercise capacity?	COPD	NCT02279329
Pulmonary ventilation visualized using hyperpolarized helium-3 and xenon-129 magnetic resonance imaging: differences in COPD and relationship to emphysema	COPD	NCT02279329
Hyperpolarized ^{3}He ventilation defects used to predict pulmonary exacerbations in mild-to-moderate chronic obstructive pulmonary disease	COPD	NCT02279329
Pulmonary imaging biomarkers of gas trapping and emphysema in COPD: ^{3}He MR imaging and CT parametric response maps	COPD	NCT02279329
Hyperpolarized 3He MRI versus HRCT in COPD and normal volunteers: PHIL trial	COPD	–
Alterations of regional alveolar oxygen tension in asymptomatic current smokers: assessment with hyperpolarized ^{3}He MR imaging	Smokers	NCT01731015
The variability of regional airflow obstruction within the lungs of patients with asthma: assessment with hyperpolarized helium-3 magnetic resonance imaging	Asthma	–
Evaluation of asthma with hyperpolarized helium-3 MRI: correlation with clinical severity and spirometry	Asthma	–
Evaluation of structure–function relationships in asthma using multidetector CT and hyperpolarized He-3 MRI	Asthma	–
Hyperpolarized ^{3}He MR lung ventilation imaging in asthmatics: preliminary findings	Asthma	–
The difference in ventilation heterogeneity between asthmatic and healthy subjects quantified using hyperpolarized He-3 MRI	Asthma	–
What are ventilation defects in asthma?	Asthma	–
Is ventilation heterogeneity related to asthma control?	Asthma	–
Detection of longitudinal lung structural and functional changes after diagnosis of radiation-induced lung injury using hyperpolarized ^{3}He magnetic resonance imaging	RILI	–
Detection of radiation-induced lung injury in nonsmall-cell lung cancer patients using hyperpolarized helium-3 magnetic resonance imaging	RILI	–
Magnetic resonance imaging biomarkers of chronic obstructive pulmonary disease prior to radiation therapy for nonsmall-cell lung cancer	NSCLC	NCT02002052
Hyperpolarized ^{3}He magnetic resonance imaging: comparison with four-dimensional X-ray computed tomography imaging in lung cancer	Lung cancer	–
Hyperpolarized ^{3}He pulmonary functional magnetic resonance imaging prior to radiation therapy	Lung cancer	–
Free-breathing pulmonary ^{1}H and hyperpolarized ^{3}He MRI: comparison in COPD and bronchiectasis	COPD, bronchiectasis	NCT02282189 NCT02282202

(continued)

Table 3 (continued)

Title	Disease	NCT
Performance of perfusion-weighted Fourier decomposition MRI for detection of chronic pulmonary emboli	PE	–
Noncontrast-enhanced preoperative assessment of lung perfusion in patients with nonsmall-cell lung cancer using Fourier decomposition magnetic resonance imaging	NSCLC	–
Ultrashort echo-time pulmonary MRI: evaluation and reproducibility in COPD subjects with and without bronchiectasis	COPD, bronchiectasis	NCT02282189 NCT02282202
Lung morphology assessment of cystic fibrosis using MRI with ultrashort echo-time at submillimeter spatial resolution	CF	–
Detection of small pulmonary nodules with ultrashort echo-time sequences in oncology patients by using a PET/MR system	Nodules	–
Magnetic resonance imaging detects changes in structure and perfusion, and response to therapy in early cystic fibrosis lung disease	CF	NCT00760071
Longitudinal		
Thoracic imaging network of Canada (TINCan)	COPD	NCT02279329
Severe asthma research program (SARP)	Asthma	NCT01716494 NCT01760915
Differences in hyperpolarized ^{3}He ventilation imaging after 4 years in adults with cystic fibrosis	CF	–
Longitudinal observational study on the course of cystic fibrosis lung disease in patients following newborn screening (TRACK-CF)	CF	NCT02270476
Longitudinal ^{3}He MRI of healthy lung	Healthy	NCT02483403
Structure and function of asthma	Asthma	NCT02351141

image quality with relatively low doses. In healthy volunteers, ventilation was shown to be homogeneously distributed in young adults (Kauczor et al. 1996), while other work also identified peripheral ^{3}He ventilation defects related to aging in healthy elderly never-smokers (Parraga et al. 2008). Furthermore, another study showed that ^{3}He ADC in healthy volunteers was shown to increase with age (Fain et al. 2005). In patients with asthma (Teague et al. 2014), COPD (Parraga et al. 2007), lung cancer (Sheikh et al. 2015), radiation-induced lung injury (Mathew et al. 2010), and cystic fibrosis (CF) (Bannier et al. 2010), ventilation shown using hyperpolarized gas imaging is characteristically heterogeneous and has been quantified using VDP. PVV should be decreased in COPD patients compared to never-smokers (Woodhouse et al. 2005), while VDP was shown to be related to spirometry (Kirby et al. 2012), symptoms and exercise capacity (Kirby et al. 2015), CT-derived emphysema measurements (Kirby et al. 2013), and exacerbations (Kirby et al. 2014b) using ^{3}He and ^{129}Xe. In COPD

patients with mild disease, VDP was also shown to be related to parametric response map (PRM) measurements of gas-trapping, while in more severe COPD, VDP reflected PRM measurement of gas-trapping and emphysema (Capaldi et al. 2016). In addition, the Polarized Helium to Image the Lungs (PHIL) trial also demonstrated that ^{3}He MRI accurately distinguished COPD patients and healthy volunteers (van Beek et al. 2009). The utility of hyperpolarized ^{3}He MRI P_{AO2} maps was also shown for differentiating nonsmokers, asymptomatic smokers, and symptomatic smokers (Hamedani et al. 2015). This work revealed that the P_{AO2} measurement variance was correlated with PFT measurements including FEV_1/FVC and DL_{CO}, and this was significantly greater in asymptomatic smokers and diminished in symptomatic smokers as compared to never-smokers.

In patients with asthma, ventilation defects have been shown to be temporally persistent (de Lange et al. 2007, 2009; Wheatley et al. 2008) and to significantly correlate with spirometry (de Lange et al. 2006; Tgavalekos et al. 2007; Fain

et al. 2008), disease severity (de Lange et al. 2006), and CT measurements of gas trapping (Fain et al. 2008). Importantly, numerous studies showed that in asthma patients, ventilation is characteristically heterogeneous (Altes et al. 2001; de Lange et al. 2006; Tzeng et al. 2009; Teague et al. 2014) and worse than that in healthy volunteers. In asthmatics as well, ventilation defects are larger and more numerous in older patients, with greater inflammation and worse airway remodeling (Svenningsen et al. 2014a), and MRI ventilation defects were also shown to be related to asthma control and quality of life (Svenningsen et al. 2016a).

In lung cancer patients, hyperpolarized noble gas MRI has been used to evaluate radiation-induced lung injury (Mathew et al. 2010; Ireland et al. 2010) and to phenotype subjects prior to radiation therapy (Sheikh et al. 2015), and has been compared to four-dimensional X-ray CT, another method of generating functional information using MRI (Mathew et al. 2012c). It has been shown that the functional improvements evaluated using MRI were observed in the contralateral lung of lung cancer patients that underwent radiation therapy, while the ipsilateral lung remained stable (Mathew et al. 2010). Furthermore, patients with ^{3}He MRI measurements of COPD had a lower than expected 1-year survival rate based on previous published survival rates (Mathew et al. 2012b).

The clinical relevance of the biomarkers derived from inhaled gas MRI as well as the associated cost and the perceived complexity is driving the development of pulmonary ^{1}H MRI methods. Importantly, in COPD patients, ventilation defects derived using FDMRI are strongly correlated and spatially related to ventilation defects derived using inhaled gas MRI (Capaldi et al. 2015). Perfusion defects measured using FDMRI have also been shown to regionally correlate with dynamic contrast-enhanced MRI in patients with chronic pulmonary emboli (Schonfeld et al. 2014), non-small cell lung cancer (Sommer et al. 2013), and cystic fibrosis (Bauman et al. 2013a). UTE signal intensity measurements are also quantitatively related to CT measurements of tissue density in patients with COPD and bronchiectasis

(Ma et al. 2015). As shown in Fig. 4, ^{3}He ventilation, ^{1}H UTE, and FDMRI in the same participants reveal regional similarities for ^{3}He MRI ventilation defects, diminished UTE MRI signal intensity, and FDMRI ventilation defects. Other work that compared UTE with CT measurements in CF patients showed that there was good agreement when considering abnormal findings (Dournes et al. 2016). In patients with extrathoracic malignancies, UTE outperformed a dual-echo GRE sequence when detecting small pulmonary nodules (4–8 mm) and exhibited a high detection rate of pulmonary nodules greater than or equal to 4 mm in diameter when using CT as the reference standard (Burris et al. 2016). Relations between UTE and FDMRI measurements have yet to be shown. Perfusion MRI abnormalities were detected early in CF patients (NCT00760071) (Wielputz et al. 2014), and described in more detail in Chap. 13 "Pulmonary MRI in Clinical Trials" in this volume.

5.2.2 Longitudinal Studies

Longitudinal pulmonary MRI is particularly valuable for monitoring of respiratory disease progression because of the excellent safety profile of MRI. As shown in Fig. 5, a wealth of knowledge has been generated about regional phenotypes and biomarkers in both healthy and diseased lungs, and how these change over time. An important comparison in this case is that of typical clinical measurements, such as FEV_1, FVC, and lung volumes, with pulmonary MRI biomarkers, such as VDP, and how the change in one over time compares to the other. In fact, in a small group of COPD ex-smokers, ^{3}HeVDP was shown to worsen over 2 years, while FEV_1 remained stable (Kirby et al. 2010a). This result is currently being further investigated in a relatively large COPD cohort study (Kirby et al. 2014c) (NCT02279329), which was designed to be complementary to the large-scale CT studies such as COPDGene (Regan et al. 2010) and CanCOLD (Bourbeau et al. 2014). Overall, the aim of TINCan was to validate pulmonary MRI biomarkers that can be considered as intermediate endpoints for future studies of COPD therapy. A similar study is currently underway as part of
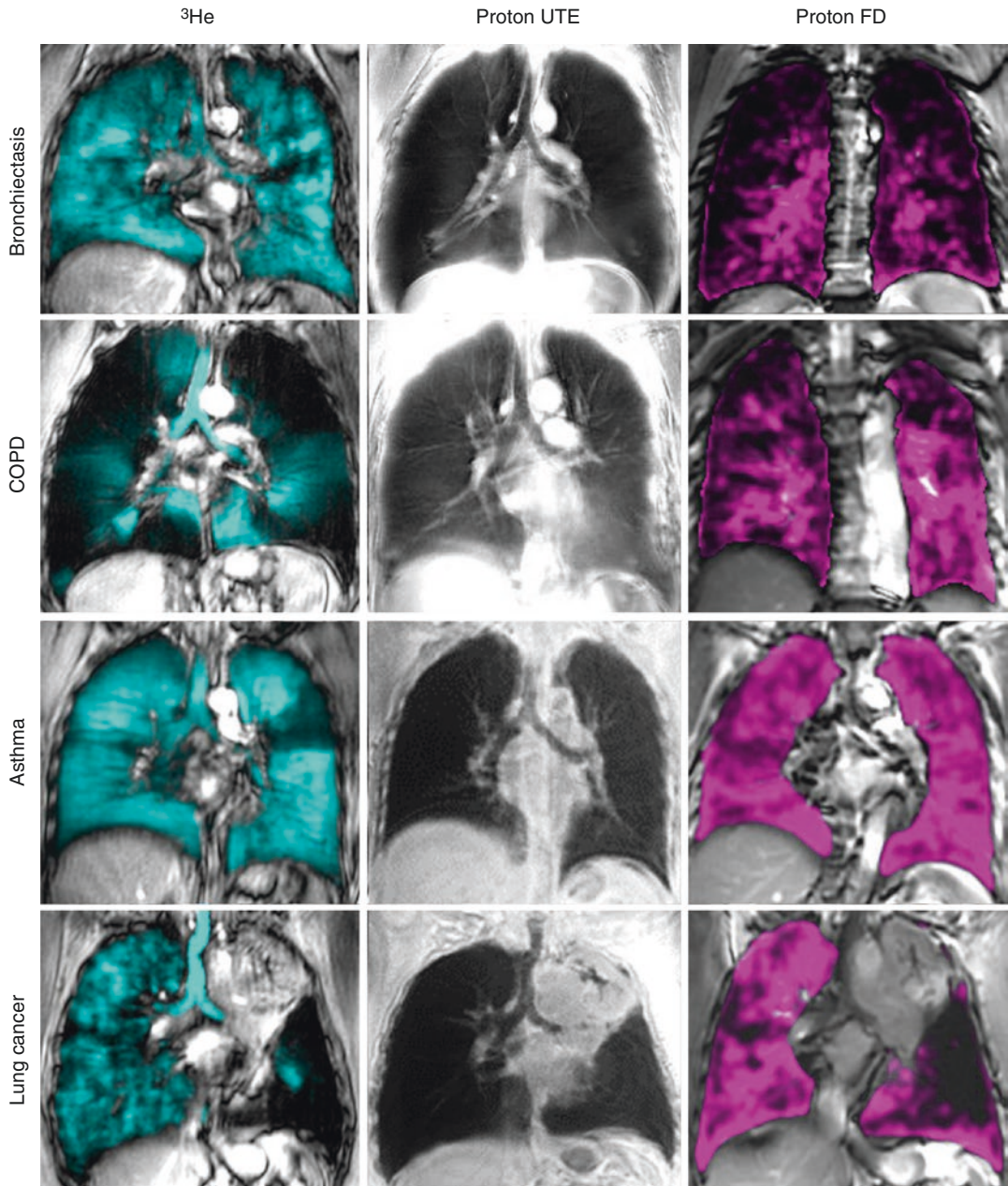
Fig. 4 Hyperpolarized ³He, proton ultrashort echo-time (UTE) and proton Fourier decomposition (FD) MRI in lung disease. Cross-sectional monitoring of bronchiectasis (62 y/o male), COPD (50 y/o male), asthma (44 y/o female), and lung cancer (72 y/o female) using hyperpolarized ³He contrast-enhanced, proton UTE and proton FD MRI. In this case, hyperpolarized ³He provides ground truth for validation of proton UTE and FD techniques

the NHLBI's Severe Asthma Research Program (SARP), and is evaluating airway remodeling and exacerbations in asthma and how each contributes to disease progression using hyperpolarized gas MRI at baseline versus 3 years (NCT01716494) (Fain et al. 2009). While MRI is performed only at a subset of study locations (NCT0760915, NCT01716494), this study will

Fig. 5 Longitudinal monitoring of ventilation using inhaled ³He MRI. ³He static ventilation at baseline and longitudinal follow-up of a healthy subject (62 y/o female over 2 years), ex-smoker without disease (72 y/o female over 2 years), and patients with COPD (68 y/o female over 2 years), asthma (26 y/o male over 3 years), and cystic fibrosis (29 y/o female over 4 years)
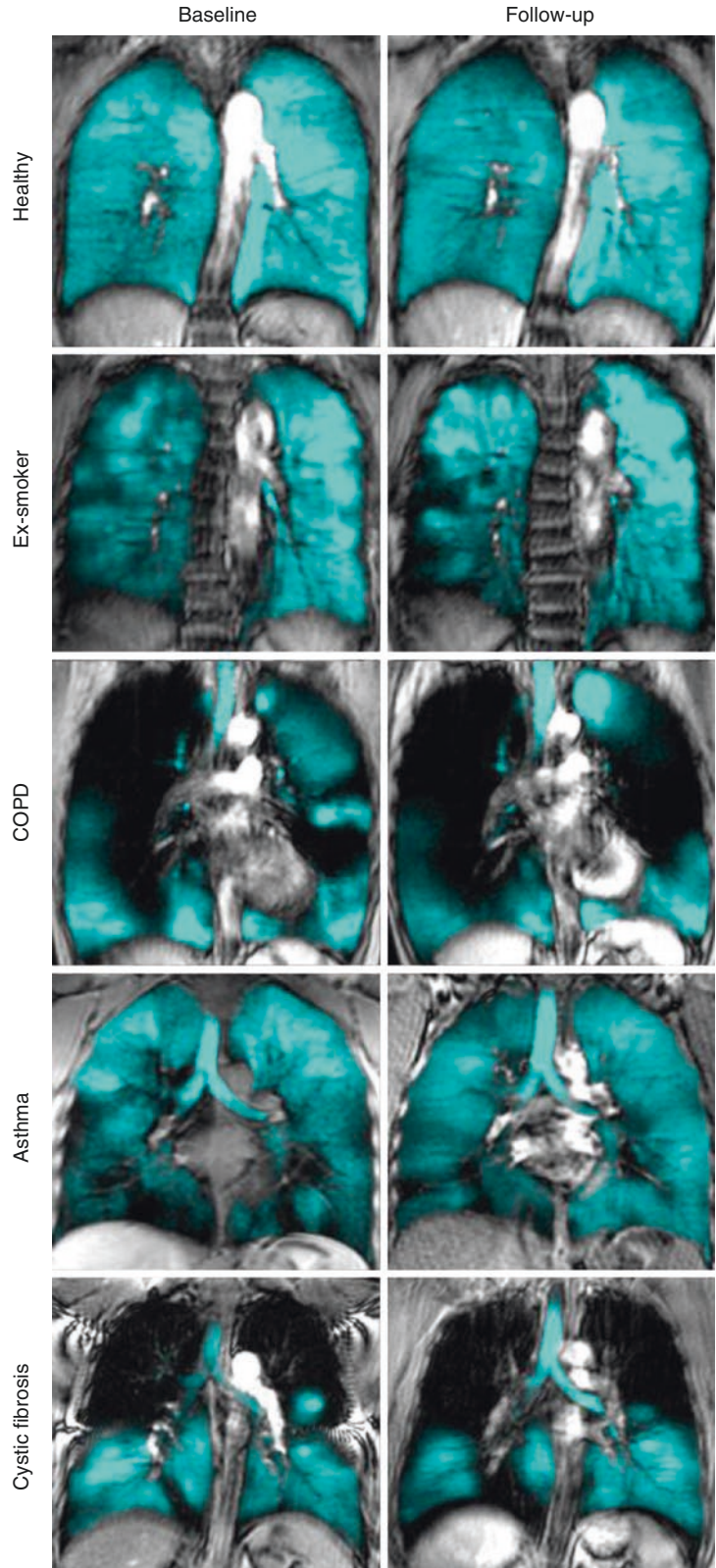
also be the first MRI-CT comparison study in severe asthma. SARP aims to combine asthma endotypes with CT and MRI phenotypes to improve the understanding of severe asthma and develop better treatments. While large studies following patients with CF over time are very limited in number, a proof-of-concept study in CF showed that ^{3}He VDP was strongly related to longitudinal changes in FEV_1 in a group of five CF patients (Paulin et al. 2015). Another study in CF patients (TRACK-CF) from age 1 to 10 investigates morphological and perfusion changes derived from chest MRI, although longitudinal results are not yet published (NCT02270476). There are also ongoing 3-year longitudinal studies monitoring healthy lung (NCT02483403) and asthma (NCT02351141) to track changes in lung function with hyperpolarized gas MRI, but results are not yet published. While most of these studies employed hyperpolarized gas MRI, to our knowledge, there have been no other longitudinal lung disease studies using other novel proton MRI techniques.

5.3   Interventional Studies

Table 4 summarizes interventional studies that interrogate therapy response and the potential impact of integrating MRI guidance for lung disease therapy.

5.3.1   Evaluation of Treatment Response

Perhaps, the largest impact of MRI of the lung in traditional clinical trials thus far has been the ability to provide regional information about response to various treatments – information that was previously unattainable using the clinical standard, spirometry measurements. As one example, and because FEV_1 is relatively insensitive to the effects of airway clearance techniques (ACT), as shown in Fig. 6, the efficacy of an oscillatory positive expiratory pressure (oPEP) device has been evaluated in patients with COPD (Svenningsen et al. 2016b) (NCT02282189) and bronchiectasis (Svenningsen et al. 2014b) (NCT02282202) using ^{3}He MRI. Other studies

have also demonstrated that ventilation defects in COPD were reduced following administration of bronchodilator (Kirby et al. 2011a) and following bronchoscopic airway bypass (Mathew et al. 2012a). Pioneering MRI studies of asthma first demonstrated that hyperpolarized gas MRI measurements of ventilation following methacholine and exercise challenges revealed worsening (Samee et al. 2003), while ADC was also worse following methacholine challenge (Costella et al. 2012). Both studies along with another (Svenningsen et al. 2013) have also demonstrated that ^{3}He and ^{129}Xe ventilation defects are reduced or resolved following bronchodilation. Studies such as these have promoted the use of MRI endpoints in large-scale clinical trials evaluating investigational new drugs. As one example, in a prospective, double-blind, placebo-controlled, multinational study, regional treatment response to oral montelukast in mild asthma was evaluated using ^{3}He MRI (Kruger et al. 2014). As shown in Fig. 7 in two representative patients, oral montelukast resulted in improved FEV_1 and MRI ventilation after exercise-induced bronchoconstriction when compared to placebo. A more recent treatment for severe asthma, bronchial thermoplasty, has also been evaluated using pulmonary MRI. As an example of these study results, Fig. 8 shows segmental ^{3}He ventilation improvements following whole-lung therapy (Thomen et al. 2015), suggesting that ventilation abnormalities may serve as an intermediate endpoint for asthma clinical trials. In patients with cystic fibrosis, bronchodilator and ACT treatments have also been shown to improve ^{3}He MRI ventilation defects (Mentore et al. 2005), and antibiotic therapy in pulmonary exacerbation has been shown to reduce perfusion abnormalities in patients aged 0–6 years (Wielputz et al. 2014).

As summarized in Table 5, numerous recent and ongoing studies have evaluated inhaled ^{129}Xe gas MRI (NCT01280994, NCT02606487, NCT01833390, NCT02723500, NCT02740868, NCT02723513). However, as of May 2016, there have been no treatment studies published using other (noninhaled gas) pulmonary MRI methods. Nevertheless, ongoing studies aim to improve our understanding of lung disease response to ther-

Table 4 Title, disease specification, and NCT number of included clinical trials and studies classified as interventional

Title	Disease	NCT
Evaluation of treatment response		
Longitudinal study of oscillatory positive expiratory pressure (oPEP)	COPD Bronchiectasis	NCT02282189 NCT02282202
Chronic obstructive pulmonary disease: quantification of bronchodilator effects by using hyperpolarized ^{3}He MR imaging	COPD	–
Hyperpolarized ^{3}He functional magnetic resonance imaging of bronchoscopic airway bypass in chronic obstructive pulmonary disease	COPD	–
Imaging the lungs in asthmatic patients by using hyperpolarized helium-3 magnetic resonance: assessment of response to methacholine and exercise challenge	Asthma	–
Regional pulmonary response to a methacholine challenge using hyperpolarized ^{3}He magnetic resonance imaging	Asthma	–
Hyperpolarized ^{3}He and ^{129}Xe MRI: differences in asthma before bronchodilation	Asthma	–
Hyperpolarized helium-3 MRI of exercise-induced bronchoconstriction during challenge and therapy	Asthma	–
Regional ventilation changes in severe asthma after bronchial thermoplasty with ^{3}He MR imaging and CT	Asthma	–
Hyperpolarized HHe-3 MRI of the lung in cystic fibrosis: Assessment at baseline and after bronchodilator and airway clearance treatment	CF	–
Magnetic resonance imaging detects changes in structure and perfusion, and response to therapy in early cystic fibrosis lung disease	CF	NCT00760071
MRI-guided therapy		
Hyperpolarized MRI in asthma pre- and post-bronchial thermoplasty	Asthma	NCT02263794
Bronchial thermoplasty for severe asthmatics guided by HXe MRI (HXe-BT)	Asthma	NCT01832363
Functional lung avoidance for individualized radiotherapy (FLAIR): a randomized, double-blind clinical trial	NSCLC	NCT02002052
Lung HeXeRT: Advanced proton, hyperpolarized 3-helium and 129-xenon MRI for lung cancer radiation planning and evaluation	NSCLC	NCT01859650

apy with the goal of providing a framework or foundation for the use of MRI to guide focal lung treatments.

5.3.2 Image-Guided MRI Intervention and Therapy Trials

While image-guided therapy for chronic vascular disease is common, image-guided treatment for respiratory disease is not yet the clinical standard of care. However, we now know that in chronic lung disease, pulmonary structural and functional abnormalities are spatially heterogeneous. Thus, there is enormous potential for MRI-guided procedures in respiratory disease that, until now, has not been exploited. In patients with asthma, and as

shown in Fig. 9, two studies have been designed to evaluate the utility of hyperpolarized noble gas MRI-derived ventilation defects to guide treatments to specific segmental ventilation defects (NCT02263794, NCT01832363). In these studies, and as shown in Fig. 10, a graphical user interface can be generated to identify target airways based on segmental VDP derived from hyperpolarized gas MRI. In addition, pulmonary MRI can also be used to identify regions of the lung where therapy should be avoided. In this regard, two studies have been designed that use hyperpolarized gas MRI to determine regions where radiation therapy should be avoided, including well-ventilated regions in patients with nonsmall-cell lung cancer (Hoover

Fig. 6 Treatment response to oscillatory positive expiratory pressure (oPEP) device in bronchiectasis and COPD using hyperpolarized ³He. Improvements in ventilation as shown by hyperpolarized ³He contrast-enhanced MRI can be seen in representative bronchiectatic (80 y/o female) and COPD (56 y/o female) patients
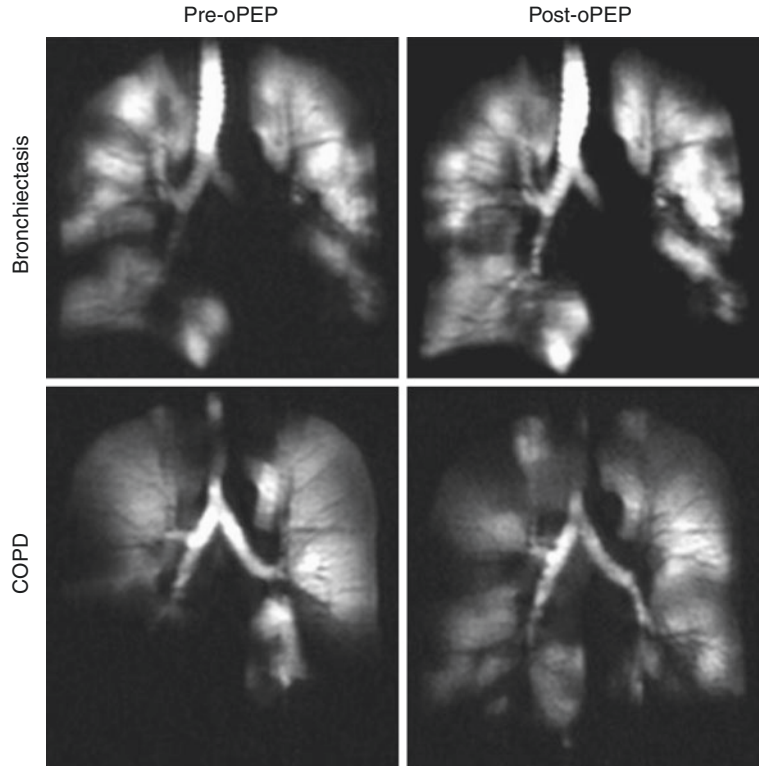
Fig. 7 Treatment response to montelukast during exercise-induced bronchoconstriction in two asthma subjects. Improvements in ventilation as shown by hyperpolarized ³He contrast-enhanced MRI can be seen in two representative asthma subjects (Subject 1:21 y/o female; Subject 2:28 y/o male)
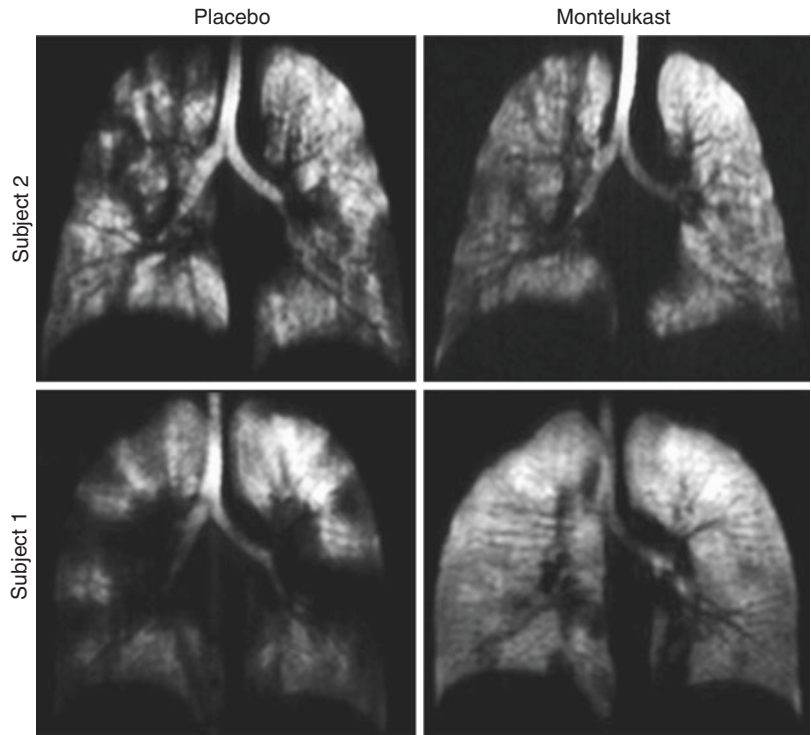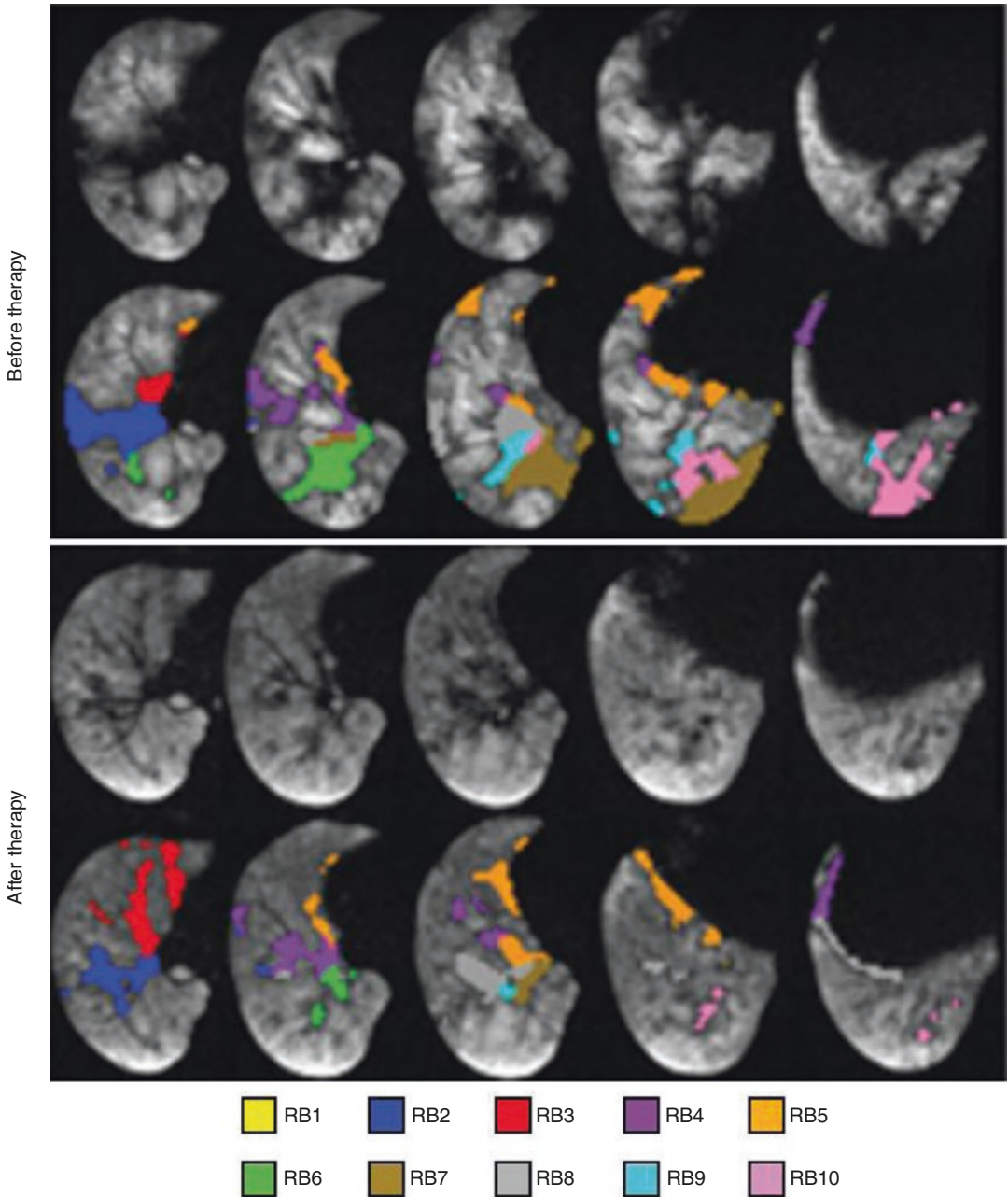
Fig. 8 Treatment response to bronchial thermoplasty in an asthmatic subject. Segmental ³He ventilation is improved in a representative asthmatic (42 y/o male), 91 days following bronchial thermoplasty. Colors identify different bronchial segments (Adapted from Thomen et al. *Radiology*. 2015:274(1);250–259)

et al. 2014) and comorbid COPD (NCT02002052, NCT01859650). These studies open up the door for MRI to be used as a tool to guide other regional therapies, including bronchoscopic lung volume reduction and bronchoscopic valve or stent placement. Clinical trials using MRI-guided therapy to target regions to treat and/or avoid will likely follow a general outline shown in Fig. 11.

Table 5 Studies employing ^{129}Xe MRI to evaluate treatment response in lung disease

Title	Disease	NCT
Hyperpolarized ^{129}Xe MRI for imaging pulmonary function	All Diseases	NCT01280994
Hyperpolarized xenon MRI in cystic fibrosis pulmonary exacerbations	CF	NCT02606487
MagniXene MRI use in patients with asthma and COPD to assess regional lung function by delineating ventilation defects (HXe-VENT)	Asthma, COPD	NCT01833390
^{129}Xenon MRI in chronic lung disease	All Diseases	NCT02723500
Xenon-129 lung MRI: study of healthy volunteers and participants with pulmonary disease	Asthma, CF	NCT02740868
Bronchopulmonary dysplasia: from neonatal chronic lung disease to early onset adult COPD	BPD	NCT02723513
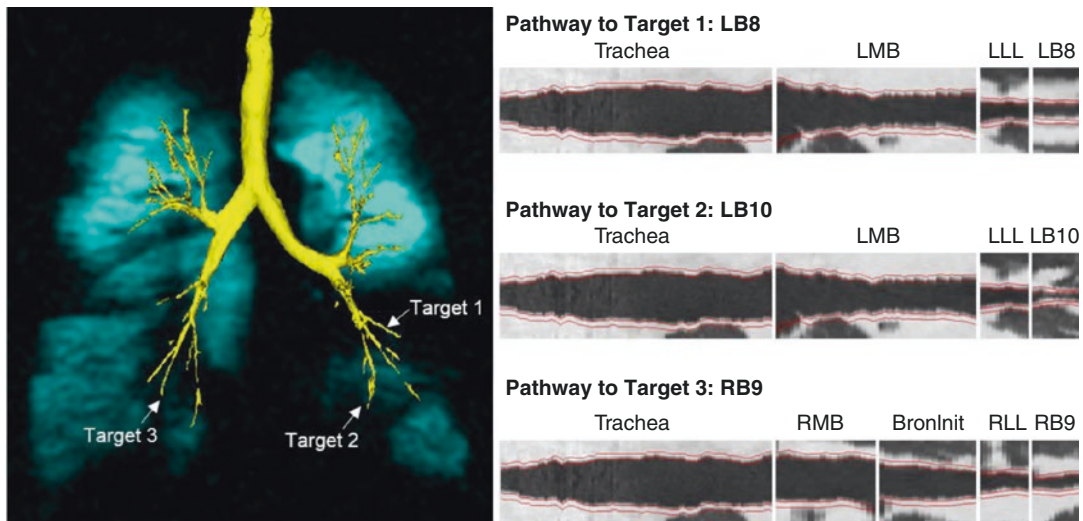
Fig. 9 ^{3}He ventilation defects and corresponding airways as targets for MRI-guided bronchial thermoplasty. ^{3}He static ventilation (*blue*) coregistered to the 3D–rendering of the airway tree (*yellow*) generated using CT. Three abnormal airways (LB8, LB10, and RB9) corresponding to localized ventilation defects can be identified as MRI-guided treatment targets using ^{3}He MRI and outlined and measured using CT

5.4 Using MRI Biomarkers to Change Diagnostic Criteria and Improve Diagnosis

As summarized in Table 6, diagnostic studies are by far the least explored avenue for clinical trials that incorporate the use of pulmonary MRI. Therefore, the question remains, *can currently identified pulmonary MRI biomarkers be used to diagnose lung disease and discriminate among lung disease biomarkers/phenotypes?* In other words, how sensitive are MRI biomarkers to the important features of lung disease, and how can this information be used to help patients and improve outcomes? The cur-

rent standard for the diagnosis of lung disease relies on spirometry measurements. Such measurements are well understood to be limited in part because disease often originates deep in the smaller airways and acinar ducts (Hogg et al. 1968, 2004), and spirometry is not engineered to capture or measure these abnormalities. In addition, because the lungs are relatively over-engineered for day-to-day tasks, patients often do not experience the symptoms until the disease is very advanced. This leaves a very small window of opportunity to diagnose such diseases or perhaps to generate screening trials. Given this context, pulmonary MRI may prove its greatest value in early detection or perhaps in the deeper
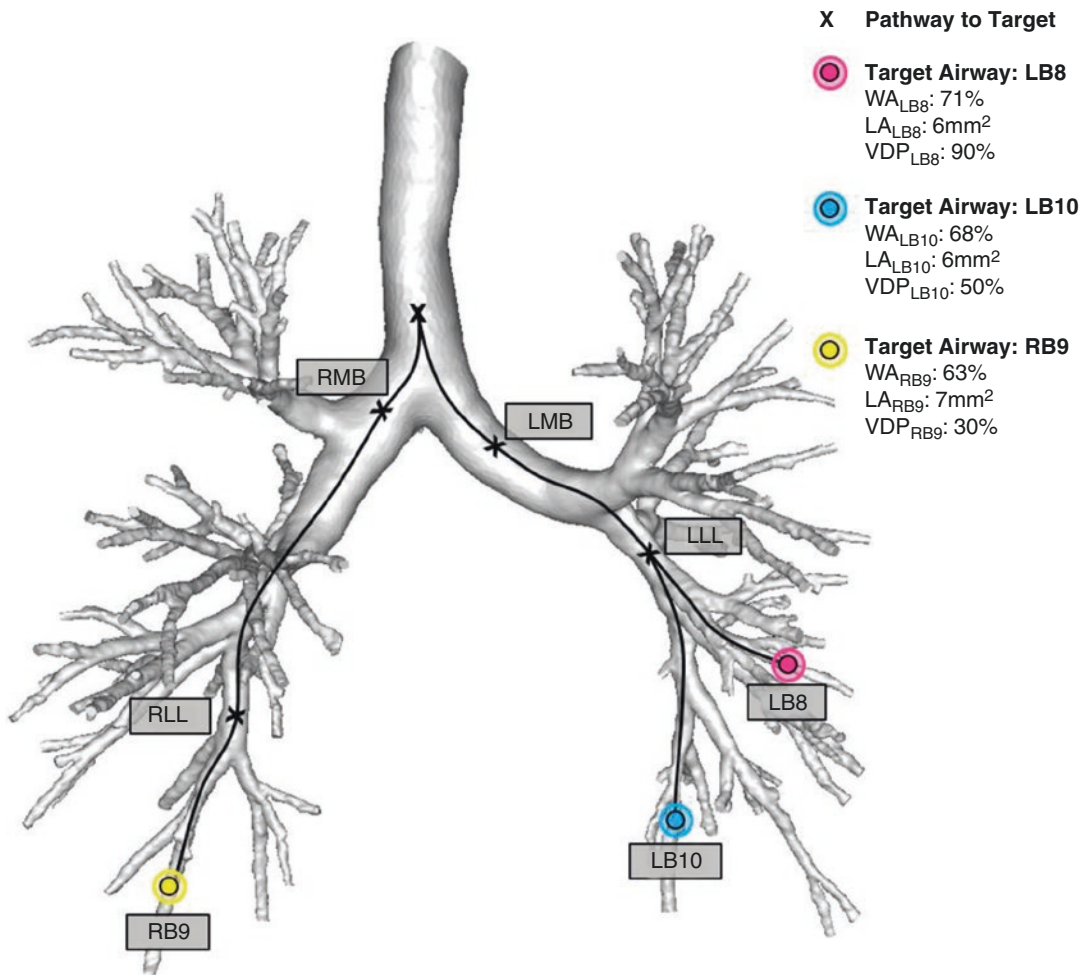
Fig. 10 Graphical user interface for MRI-guided bronchial thermoplasty. As shown in Fig. 9, LB8, LB10, and RB9 are potential targets for image-guided bronchial thermoplasty. A graphical user interface (GUI) shows the pathway to each targeted airway and measurements for airway morphometry. *WA* wall area percent, *LA* lumen area, *VDP* segmental ventilation defect percent

phenotyping of patients once diagnosed to allow for stratification to therapy. In childhood lung disease, such as bronchopulmonary dysplasia, cystic fibrosis, and asthma, the potential to help change outcomes is quite significant. As one example, a small bore high-field MRI that was engineered to be embedded within a neonatal intensive care unit (Tkach et al. 2012) aims to evaluate the underdeveloped lungs of neonates at high risk for chronic respiratory disease, and in whom longitudinal CT is not an option. Recent work with this unique small footprint MRI has investigated the utility of pulmonary MRI in evaluating bronchopulmonary dysplasia (Walkup et al. 2015). Preliminary results of another study demonstrated that ^{1}H chest MRI is comparable to CT for visualizing morphological changes in CF, including bronchiectasis, bronchial wall thickening, mucus plugging, air fluid level, consolidation, and segmental/lobar destruction (Puderbach et al. 2007), which have led to studies evaluating morphological and functional MRI for early diagnosis of CF patients (NCT00760071). Importantly, this work was also used to generate a CF disease scoring system that is reproducible and applicable for a
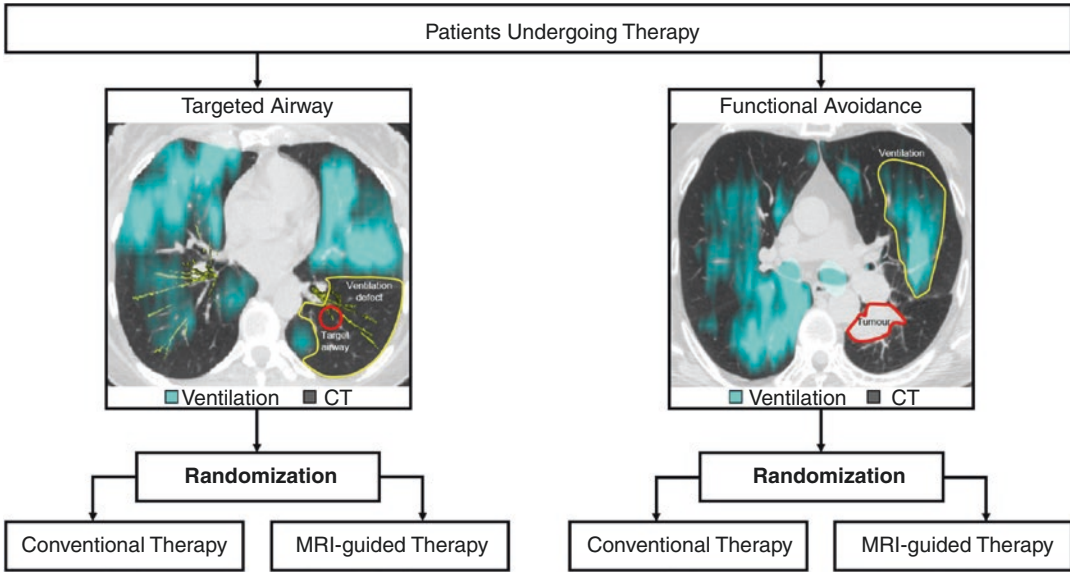
Fig. 11 General clinical trial outline for using MRI to guided localized therapy. Patients undergoing therapy as a part of their normal clinical care will be randomized to receive conventional or image-guided treatment, based on the type of treatment for a particular disease. For example, ventilation abnormalities can be used for targeted bronchial thermoplasty treatment, or regions of normal ventilation can be used as regions to avoid during radiotherapy of lung cancer

Table 6 Title, disease specification, and NCT number of included clinical trials and studies classified as diagnostic

Title	Disease	NCT
An MRI system for imaging neonates in the NICU	All diseases	NCT01801865
Quantitative MRI of bronchopulmonary dysplasia in the neonatal intensive care unit environment	BPD	–
Morphological and functional scoring of cystic fibrosis lung disease using MRI	CF	–
Magnetic resonance imaging (MRI) for early diagnosis of cystic fibrosis (CF)	CF	NCT00760071
Image-based structural and functional phenotyping of the COSYCONET cohort using MRI and CT	COPD	NCT02629432

large range of CF severity (Eichinger et al. 2012). Another study in older adults (Karch et al. 2016) aimed to compare the sensitivity and specificity of MRI for the diagnosis of emphysema-predominant versus airway-predominant COPD phenotypes in a subset of the large COSYCONET COPD cohort (NCT02629432).

6 Future Directions and Opportunities

In most clinical and academic centers, numerous small-scale collaborations form the basis of MRI research, and the gap between the research bench and clinical workflow remains significant. One key to narrowing this gap lies in multicenter, large-scale clinical trials, because single-center trials do not have the ability to generate the large sets of data required to fully exploit and understand MRI biomarkers. This is important because the advancement of pulmonary MRI toward clinical implementation will require the development and validation of clinically relevant biomarkers. There are obvious requirements to successfully launch and complete multicenter trials, including the availability of specialized personnel and equipment as well as standardized phantoms and image analysis software. It is not clear yet if all of these key ingredients are in

place to proceed. Nonetheless, in Europe and, in particular, in Germany, multiple research centers have taken the steps toward a standardized pulmonary MRI protocol to be implemented at each site in preparation for a multicenter trial (NCT02629432) (Karch et al. 2016). This crucial first step could set the foundation for other centers in the EU, Asia, and North America to follow, and include as many novel MRI pulmonary methods as possible. What is clear is that together and globally, we are on the threshold of taking the necessary and likely sufficient steps toward the validation of clinically meaningful lung MRI biomarkers and phenotypes, with the overarching goal of clinical translation and improved patient outcomes.

References

Agusti A, Calverley PM, Celli B, Coxson HO, Edwards LD, Lomas DA, MacNee W, Miller BE, Rennard S, Silverman EK, Tal-Singer R, Wouters E, Yates JC, Vestbo J, Evaluation of CLtIPSEi (2010) Characterisation of COPD heterogeneity in the ECLIPSE cohort. Respir Res 11:122. doi:10.1186/1465-9921-11-122

Albert MS, Cates GD, Driehuys B, Happer W, Saam B, Springer CS, Wishnia A (1994) Biological magnetic-resonance-imaging using laser polarized Xe-129. Nature 370(6486):199–201. doi:10.1038/370199a0

Altes TA, Powers PL, Knight-Scott J, Rakes G, Platts-Mills TA, de Lange EE, Alford BA, Mugler JP 3rd, Brookeman JR (2001) Hyperpolarized 3He MR lung ventilation imaging in asthmatics: preliminary findings. J Magn Reson Imaging 13(3):378–384

Bannier E, Cieslar K, Mosbah K, Aubert F, Duboeuf F, Salhi Z, Gaillard S, Berthezene Y, Cremillieux Y, Reix P (2010) Hyperpolarized 3He MR for sensitive imaging of ventilation function and treatment efficiency in young cystic fibrosis patients with normal lung function. Radiology 255(1):225–232. doi:10.1148/radiol.09090039

Bauman G, Puderbach M, Deimling M, Jellus V, Chefd'hotel C, Dinkel J, Hintze C, Kauczor HU, Schad LR (2009) Non-contrast-enhanced perfusion and ventilation assessment of the human lung by means of fourier decomposition in proton MRI. Magn Reson Med 62(3):656–664

Bauman G, Puderbach M, Heimann T, Kopp-Schneider A, Fritzsching E, Mall MA, Eichinger M (2013a) Validation of Fourier decomposition MRI with dynamic contrast-enhanced MRI using visual and automated scoring of pulmonary perfusion in young cystic fibrosis patients. Eur J Radiol 82(12):2371–2377. doi:10.1016/j.ejrad.2013.08.018

Bauman G, Scholz A, Rivoire J, Terekhov M, Friedrich J, de Oliveira A, Semmler W, Schreiber LM, Puderbach M (2013b) Lung ventilation-and perfusion-weighted Fourier decomposition magnetic resonance imaging: in vivo validation with hyperpolarized 3He and dynamic contrast-enhanced MRI. Magn Reson Med 69(1):229–237

Bergin CJ, Pauly JM, Macovski A (1991) Lung parenchyma: projection reconstruction MR imaging. Radiology 179(3):777–781. doi:10.1148/radiology.179.3.2027991

Bergin CJ, Glover GM, Pauly J (1993) Magnetic resonance imaging of lung parenchyma. J Thorac Imaging 8(1):12–17

Bild DE, Bluemke DA, Burke GL, Detrano R, Diez Roux AV, Folsom AR, Greenland P, Jacob DR Jr, Kronmal R, Liu K, Nelson JC, O'Leary D, Saad MF, Shea S, Szklo M, Tracy RP (2002) Multi-Ethnic Study of Atherosclerosis: objectives and design. Am J Epidemiol 156(9):871–881

Bourbeau J, Tan WC, Benedetti A, Aaron SD, Chapman KR, Coxson HO, Cowie R, Fitzgerald M, Goldstein R, Hernandez P, Leipsic J, Maltais F, Marciniuk D, O'Donnell D, Sin DD, Cancold Study G (2014) Canadian Cohort Obstructive Lung Disease (CanCOLD): fulfilling the need for longitudinal observational studies in COPD. COPD 11(2):125–132. doi:10.3109/15412555.2012.665520

Burris NS, Johnson KM, Larson PE, Hope MD, Nagle SK, Behr SC, Hope TA (2016) Detection of Small Pulmonary Nodules with Ultrashort Echo Time Sequences in Oncology Patients by Using a PET/MR System. Radiology 278(1):239–246. doi:10.1148/radiol.2015150489

Capaldi DP, Sheikh K, Guo F, Svenningsen S, Etemad-Rezai R, Coxson HO, Leipsic JA, McCormack DG, Parraga G (2015) Free-breathing pulmonary 1H and Hyperpolarized 3He MRI: comparison in COPD and bronchiectasis. Acad Radiol 22(3):320–329. doi:10.1016/j.acra.2014.10.003

Capaldi DP, Zha N, Guo F, Pike D, McCormack DG, Kirby M, Parraga G (2016) Pulmonary Imaging Biomarkers of Gas Trapping and Emphysema in COPD: (3)He MR Imaging and CT Parametric Response Maps. Radiology 279(2):597–608. doi:10.1148/radiol.2015151484

Costella S, Kirby M, Maksym GN, McCormack DG, Paterson NA, Parraga G (2012) Regional pulmonary response to a methacholine challenge using hyperpolarized (3)He magnetic resonance imaging. Respirology (Carlton, Vic) 17(8):1237–1246. doi:10.1111/j.1440-1843.2012.02250.x

Couch MJ, Ball IK, Li T, Fox MS, Ouriadov AV, Biman B, Albert MS (2014) Inert fluorinated gas MRI: a new pulmonary imaging modality. NMR Biomed 27(12):1525–1534. doi:10.1002/nbm.3165

Couper D, LaVange LM, Han M, Barr RG, Bleecker E, Hoffman EA, Kanner R, Kleerup E, Martinez FJ, Woodruff PG, Rennard S, Group SR (2014) Design of the Subpopulations and Intermediate Outcomes in COPD Study (SPIROMICS). Thorax 69(5):491–494. doi:10.1136/thoraxjnl-2013-203897

de Lange EE, Altes TA, Patrie JT, Gaare JD, Knake JJ, Mugler JP 3rd, Platts-Mills TA (2006) Evaluation of asthma with hyperpolarized helium-3 MRI: correlation with clinical severity and spirometry. Chest 130(4):1055–1062. doi:10.1378/chest.130.4.1055

de Lange EE, Altes TA, Patrie JT, Parmar J, Brookeman JR, Mugler JP, Platts-Mills TAE (2007) The variability of regional airflow obstruction within the lungs of patients with asthma: assessment with hyperpolarized helium-3 magnetic resonance imaging. J Allergy Clin Immunol 119(5):1072–1078. doi:10.1016/j.jaci.2006.12.659

de Lange EE, Altes TA, Patrie JT, Battiston JJ, Juersivich AP, Mugler JP 3rd, Platts-Mills TA (2009) Changes in regional airflow obstruction over time in the lungs of patients with asthma: evaluation with 3He MR imaging. Radiology 250(2):567–575. doi:10.1148/radiol.2502080188

Deninger AJ, Eberle B, Ebert M, Grossmann T, Heil W, Kauczor H, Lauer L, Markstaller K, Otten E, Schmiedeskamp J, Schreiber W, Surkau R, Thelen M, Weiler N (1999) Quantification of regional intrapulmonary oxygen partial pressure evolution during apnea by (3)He MRI. J Magn Reson 141(2):207–216. doi:10.1006/jmre.1999.1902

Diaz S, Casselbrant I, Piitulainen E, Magnusson P, Peterson B, Wollmer P, Leander P, Ekberg O, Akeson P (2009) Validity of apparent diffusion coefficient hyperpolarized 3He-MRI using MSCT and pulmonary function tests as references. Eur J Radiol 71(2):257–263. doi:10.1016/j.ejrad.2008.04.013

Donnelly LF, MacFall JR, McAdams HP, Majure JM, Smith J, Frush DP, Bogonad P, Charles HC, Ravin CE (1999) Cystic fibrosis: combined hyperpolarized 3He-enhanced and conventional proton MR imaging in the lung–preliminary observations. Radiology 212(3):885–889. doi:10.1148/radiology.212.3.r99se20885

Dournes G, Menut F, Macey J, Fayon M, Chateil JF, Salel M, Corneloup O, Montaudon M, Berger P, Laurent F (2016) Lung morphology assessment of cystic fibrosis using MRI with ultra-short echo time at submillimeter spatial resolution. Eur Radiol. doi:10.1007/s00330-016-4218-5

Driehuys B, Cofer GP, Pollaro J, Mackel JB, Hedlund LW, Johnson GA (2006) Imaging alveolar-capillary gas transfer using hyperpolarized 129Xe MRI. Proc Natl Acad Sci U S A 103(48):18278–18283. doi:10.1073/pnas.0608458103

Driehuys B, Martinez-Jimenez S, Cleveland ZI, Metz GM, Beaver DM, Nouls JC, Kaushik SS, Firszt R, Willis C, Kelly KT, Wolber J, Kraft M, McAdams HP (2012) Chronic obstructive pulmonary disease: safety and tolerability of hyperpolarized 129Xe MR imaging in healthy volunteers and patients. Radiology 262(1):279–289. doi:10.1148/radiol.11102172

Ebert M, Grossmann T, Heil W, Otten WE, Surkau R, Leduc M, Bachert P, Knopp MV, Schad LR, Thelen M (1996) Nuclear magnetic resonance imaging with hyperpolarised helium-3. Lancet 347(9011):1297–1299

Edelman RR, Hatabu H, Tadamura E, Li W, Prasad PV (1996) Noninvasive assessment of regional ventilation in the human lung using oxygen-enhanced magnetic resonance imaging. Nat Med 2(11):1236–1239

Eichinger M, Optazaite DE, Kopp-Schneider A, Hintze C, Biederer J, Niemann A, Mall MA, Wielputz MO, Kauczor HU, Puderbach M (2012) Morphologic and functional scoring of cystic fibrosis lung disease using MRI. Eur J Radiol 81(6):1321–1329. doi:10.1016/j.ejrad.2011.02.045

Fain SB, Altes TA, Panth SR, Evans MD, Waters B, Mugler JP 3rd, Korosec FR, Grist TM, Silverman M, Salerno M, Owers-Bradley J (2005) Detection of age-dependent changes in healthy adult lungs with diffusion-weighted 3He MRI. Acad Radiol 12(11):1385–1393. doi:10.1016/j.acra.2005.08.005

Fain SB, Gonzalez-Fernandez G, Peterson ET, Evans MD, Sorkness RL, Jarjour NN, Busse WW, Kuhlman JE (2008) Evaluation of structure-function relationships in asthma using multidetector CT and hyperpolarized He-3 MRI. Acad Radiol 15(6):753–762. doi:10.1016/j.acra.2007.10.019

Fain SB, Peterson ET, Sorkness RL, Wenzel S, Castro M, Busse WW (2009) Severe asthma research program – phenotyping and quantification of severe asthma. Imaging Decis MRI 13(1):24–27. doi:10.1111/j.1617-0830.2009.01124.x

Gupta S, Siddiqui S, Haldar P, Raj JV, Entwisle JJ, Wardlaw AJ, Bradding P, Pavord ID, Green RH, Brightling CE (2009) Qualitative analysis of high-resolution CT scans in severe asthma. Chest 136(6):1521–1528. doi:10.1378/chest.09-0174

Hamedani H, Kadlecek SJ, Ishii M, Xin Y, Emami K, Han B, Shaghaghi H, Gopstein D, Cereda M, Gefter WB, Rossman MD, Rizi RR (2015) Alterations of regional alveolar oxygen tension in asymptomatic current smokers: assessment with hyperpolarized (3)He MR imaging. Radiology 274(2):585–596. doi:10.1148/radiol.14132809

Hatabu H, Gaa J, Kim D, Li W, Prasad PV, Edelman RR (1996) Pulmonary perfusion: qualitative assessment with dynamic contrast-enhanced MRI using ultra-short TE and inversion recovery turbo FLASH. Magn Reson MedOffJ Soc Magn Reson MedSocMagn ResonMed 36(4):503–508

Hogg JC, Macklem PT, Thurlbeck WM (1968) Site and nature of airway obstruction in chronic obstructive lung disease. N Engl J Med 278(25):1355–1360. doi:10.1056/NEJM196806202782501

Hogg JC, Chu F, Utokaparch S, Woods R, Elliott WM, Buzatu L, Cherniack RM, Rogers RM, Sciurba FC, Coxson HO, Pare PD (2004) The nature of small-airway obstruction in chronic obstructive pulmonary disease. N Engl J Med 350(26):2645–2653. doi:10.1056/NEJMoa032158

Hoover DA, Capaldi DP, Sheikh K, Palma DA, Rodrigues GB, Dar AR, Yu E, Dingle B, Landis M, Kocha W, Sanatani M, Vincent M, Younus J, Kuruvilla S, Gaede S, Parraga G, Yaremko BP (2014) Functional lung avoidance for individualized radiotherapy (FLAIR): study

protocol for a randomized, double-blind clinical trial. BMC Cancer 14:934. doi:10.1186/1471-2407-14-934

Ireland RH, Din OS, Swinscoe JA, Woodhouse N, van Beek EJ, Wild JM, Hatton MQ (2010) Detection of radiation-induced lung injury in non-small cell lung cancer patients using hyperpolarized helium-3 magnetic resonance imaging. Radiother OncolJ Eur Soc Ther RadiolOncol 97(2):244–248. doi:10.1016/j.radonc.2010.07.013

Ishii M, Hamedani H, Clapp JT, Kadlecek SJ, Xin Y, Gefter WB, Rossman MD, Rizi RR (2015) Oxygen-weighted Hyperpolarized (3)He MR imaging: ashort-term reproducibility study in human subjects. Radiology 277(1):247–258. doi:10.1148/radiol.2015142038

Jarjour NN, Erzurum SC, Bleecker ER, Calhoun WJ, Castro M, Comhair SA, Chung KF, Curran-Everett D, Dweik RA, Fain SB, Fitzpatrick AM, Gaston BM, Israel E, Hastie A, Hoffman EA, Holguin F, Levy BD, Meyers DA, Moore WC, Peters SP, Sorkness RL, Teague WG, Wenzel SE, Busse WW, Program NSAR (2012) Severe asthma: lessons learned from the National Heart, Lung, and Blood Institute Severe Asthma Research Program. Am J Respir Crit Care Med 185(4):356–362. doi:10.1164/rccm.201107-1317PP

Jobst BJ, Wielputz MO, Triphan SM, Anjorin A, Ley-Zaporozhan J, Kauczor HU, Biederer J, Ley S, Sedlaczek O (2015) Morpho-functional 1H-MRI of the lung in COPD: short-term test-retest reliability. PLoS One 10(9):e0137282. doi:10.1371/journal.pone.0137282

Jones PW (2009) Health status and the spiral of decline. COPD 6(1):59–63. doi:10.1080/15412550802587943

Karch A, Vogelmeier C, Welte T, Bals R, Kauczor HU, Biederer J, Heinrich J, Schulz H, Glaser S, Holle R, Watz H, Korn S, Adaskina N, Biertz F, Vogel C, Vestbo J, Wouters EF, Rabe KF, Sohler S, Koch A, Jorres RA, Group CS (2016) The German COPD cohort COSYCONET: aims, methods and descriptive analysis of the study population at baseline. Respir Med 114:27–37. doi:10.1016/j.rmed.2016.03.008

Kauczor HU, Hofmann D, Kreitner KF, Nilgens H, Surkau R, Heil W, Potthast A, Knopp MV, Otten EW, Thelen M (1996) Normal and abnormal pulmonary ventilation: visualization at hyperpolarized He-3 MR imaging. Radiology 201(2):564–568

Khakban A, Sin DD, FitzGerald JM, Ng R, Zafari Z, McManus B, Hollander Z, Marra CA, Sadatsafavi M (2015) Ten-year trends in direct costs of COPD: apopulation-based study. Chest 148(3):640–646. doi:10.1378/chest.15-0721

Kirby M, Mathew L, Wheatley A, Santyr GE, McCormack DG, Parraga G (2010a) Chronic obstructive pulmonary disease: longitudinal hyperpolarized (3)He MR imaging. Radiology 256(1):280–289. doi:10.1148/radiol.10091937

KirbyM, WheatleyA, McCormackDG, ParragaG (2010b) Development and application of methods to quantify spatial and temporal hyperpolarized 3He MRI ventilation dynamics: preliminary results in chronic obstructive pulmonary disease. In: SPIE Medical Imaging. International Society for Optics and Photonics, pp 762605–762605-762609

Kirby M, Mathew L, Heydarian M, Etemad-Rezai R, McCormack DG, Parraga G (2011a) Chronic obstructive pulmonary disease: quantification of bronchodilator effects by using hyperpolarized (3)He MR imaging. Radiology 261(1):283–292. doi:10.1148/radiol.11110403

Kirby M, Svenningsen S, Ahmed H, Wheatley A, Etemad-Rezai R, Paterson NA, Parraga G (2011b) Quantitative evaluation of hyperpolarized helium-3 magnetic resonance imaging of lung function variability in cystic fibrosis. Acad Radiol 18(8):1006–1013. doi:10.1016/j.acra.2011.03.005

Kirby M, Svenningsen S, Owrangi A, Wheatley A, Farag A, Ouriadov A, Santyr GE, Etemad-Rezai R, Coxson HO, McCormack DG, Parraga G (2012) Hyperpolarized 3He and 129Xe MR imaging in healthy volunteers and patients with chronic obstructive pulmonary disease. Radiology 265(2):600–610. doi:10.1148/radiol.12120485

Kirby M, Svenningsen S, Kanhere N, Owrangi A, Wheatley A, Coxson HO, Santyr GE, Paterson NA, McCormack DG, Parraga G (2013) Pulmonary ventilation visualized using hyperpolarized helium-3 and xenon-129 magnetic resonance imaging: differences in COPD and relationship to emphysema. J Appl Physiol (Bethesda, Md : 1985) 114(6):707–715. doi:10.1152/japplphysiol.01206.2012

Kirby M, Ouriadov A, Svenningsen S, Owrangi A, Wheatley A, Etemad-Rezai R, Santyr GE, McCormack DG, Parraga G (2014a) Hyperpolarized 3He and 129Xe magnetic resonance imaging apparent diffusion coefficients: physiological relevance in older never- and ex-smokers. Physiol Rep 2(7). doi:10.14814/phy2.12068

Kirby M, Pike D, Coxson HO, McCormack DG, Parraga G (2014b) Hyperpolarized (3)He ventilation defects used to predict pulmonary exacerbations in mild to moderate chronic obstructive pulmonary disease. Radiology 273(3):887–896. doi:10.1148/radiol.14140161

Kirby M, Pike D, McCormack DG, Lam S, Sin DD, Coxson HO, Parraga G (2014c) Longitudinal computed tomography and magnetic resonance imaging of COPD: Thoracic Imaging Network of Canada (TINCan) study objectives. Chron Obstruct Pulmon Dis J COPD Found 1(2):200–211

Kirby M, Pike D, Sin DD, Coxson HO, McCormack DG, Parraga G (2015) COPD: do imaging measurements of emphysema and airway disease explain symptoms and exercise capacity? Radiology 277(3):872–880. doi:10.1148/radiol.2015150037

Kruger SJ, Niles DJ, Dardzinski B, Harman A, Jarjour NN, Ruddy M, Nagle SK, Francois CJ, Sorkness RL, Burton RM, Munoz del Rio A, Fain SB (2014) Hyperpolarized Helium-3 MRI of exercise-induced bronchoconstriction during challenge and therapy. J MagnReson Imaging 39(5):1230–1237. doi:10.1002/jmri.24272

Lederlin M, Bauman G, Eichinger M, Dinkel J, Brault M, Biederer J, Puderbach M (2013) Functional MRI using

Fourier decomposition of lung signal: reproducibility of ventilation-and perfusion-weighted imaging in healthy volunteers. Eur J Radiol 82(6):1015–1022

Lutey BA, Lefrak SS, Woods JC, Tanoli T, Quirk JD, Bashir A, Yablonskiy DA, Conradi MS, Bartel ST, Pilgram TK, Cooper JD, Gierada DS (2008) Hyperpolarized 3He MR imaging: physiologic monitoring observations and safety considerations in 100 consecutive subjects. Radiology 248(2):655–661. doi:10.1148/radiol.2482071838

Ma W, Sheikh K, Svenningsen S, Pike D, Guo F, Etemad-Rezai R, Leipsic J, Coxson HO, McCormack DG, Parraga G (2015) Ultra-short echo-time pulmonary MRI: evaluation and reproducibility in COPD subjects with and without bronchiectasis. JMagn Reson Imaging 41(5):1465–1474. doi:10.1002/jmri.24680

Mathew L, Evans A, Ouriadov A, Etemad-Rezai R, Fogel R, Santyr G, McCormack DG, Parraga G (2008) Hyperpolarized 3He magnetic resonance imaging of chronic obstructive pulmonary disease: reproducibility at 3.0 tesla. Acad Radiol 15(10):1298–1311. doi:10.1016/j.acra.2008.04.019

Mathew L, Gaede S, Wheatley A, Etemad-Rezai R, Rodrigues GB, Parraga G (2010) Detection of longitudinal lung structural and functional changes after diagnosis of radiation-induced lung injury using hyperpolarized 3He magnetic resonance imaging. Med Phys 37(1):22–31. doi:10.1118/1.3263616

Mathew L, Kirby M, Etemad-Rezai R, Wheatley A, McCormack DG, Parraga G (2011) Hyperpolarized (3)He magnetic resonance imaging: preliminary evaluation of phenotyping potential in chronic obstructive pulmonary disease. Eur J Radiol 79(1):140–146. doi:10.1016/j.ejrad.2009.10.028

Mathew L, Kirby M, Farquhar D, Licskai C, Santyr G, Etemad-Rezai R, Parraga G, McCormack DG (2012a) Hyperpolarized 3He functional magnetic resonance imaging of bronchoscopic airway bypass in chronic obstructive pulmonary disease. Can RespirJ J Can Thorac Soc 19(1):41–43

Mathew L, Vandyk J, Etemad-Rezai R, Rodrigues G, Parraga G (2012b) Hyperpolarized (3)He pulmonary functional magnetic resonance imaging prior to radiation therapy. Med Phys 39(7):4284–4290. doi:10.1118/1.4729713

Mathew L, Wheatley A, Castillo R, Castillo E, Rodrigues G, Guerrero T, Parraga G (2012c) Hyperpolarized (3) He magnetic resonance imaging: comparison with four-dimensional x-ray computed tomography imaging in lung cancer. Acad Radiol 19(12):1546–1553. doi:10.1016/j.acra.2012.08.007

McMahon CJ, Dodd JD, Hill C, Woodhouse N, Wild JM, Fichele S, Gallagher CG, Skehan SJ, van Beek EJ, Masterson JB (2006) Hyperpolarized 3helium magnetic resonance ventilation imaging of the lung in cystic fibrosis: comparison with high resolution CT and spirometry. Eur Radiol 16(11):2483–2490. doi:10.1007/s00330-006-0311-5

Meaney JF, Weg JG, Chenevert TL, Stafford-Johnson D, Hamilton BH, Prince MR (1997) Diagnosis of pulmonary embolism with magnetic resonance angiography. N Engl J Med 336(20):1422–1427. doi:10.1056/NEJM199705153362004

Mentore K, Froh DK, de Lange EE, Brookeman JR, Paget-Brown AO, Altes TA (2005) Hyperpolarized HHe 3 MRI of the lung in cystic fibrosis: assessment at baseline and after bronchodilator and airway clearance treatment1. Acad Radiol 12(11):1423–1429

Morbach AE, Gast KK, Schmiedeskamp J, Dahmen A, Herweling A, Heussel CP, Kauczor HU, Schreiber WG (2005) Diffusion-weighted MRI of the lung with hyperpolarized helium-3: a study of reproducibility. J Magn Reson Imaging 21(6):765–774. doi:10.1002/jmri.20300

Mugler III J(1998) Optimization of gradient-echo sequences for hyperpolarized noble gas MRI. In: Proceedings of the 6th annual meeting of ISMRM, Sydney, p 1904

Mugler JP 3rd, Driehuys B, Brookeman JR, Cates GD, Berr SS, Bryant RG, Daniel TM, de Lange EE, Downs JH 3rd, Erickson CJ, Happer W, Hinton DP, Kassel NF, Maier T, Phillips CD, Saam BT, Sauer KL, Wagshul ME (1997) MR imaging and spectroscopy using hyperpolarized 129Xe gas: preliminary human results. Magn Reson Med 37(6):809–815

Mugler JP 3rd, Altes TA, Ruset IC, Dregely IM, Mata JF, Miller GW, Ketel S, Ketel J, Hersman FW, Ruppert K (2010) Simultaneous magnetic resonance imaging of ventilation distribution and gas uptake in the human lung using hyperpolarized xenon-129. Proc Natl Acad Sci U S A 107(50):21707–21712. doi:10.1073/pnas.1011912107

OECD OfEC-oaD (2007) Computed Tomography (CT) and Magnetic Resonance Imaging (MRI) Census. Benchmark Report: IMV, Limited, Medical Information Division

Parraga G, Ouriadov A, Evans A, McKay S, Lam WW, Fenster A, Etemad-Rezai R, McCormack D, Santyr G (2007) Hyperpolarized 3He ventilation defects and apparent diffusion coefficients in chronic obstructive pulmonary disease: preliminary results at 3.0 Tesla. Invest Radiol 42(6):384–391. doi:10.1097/01.rli.0000262571.81771.66

Parraga G, Mathew L, Etemad-Rezai R, McCormack DG, Santyr GE (2008) Hyperpolarized 3He magnetic resonance imaging of ventilation defects in healthy elderly volunteers: initial findings at 3.0 Tesla. Acad Radiol 15(6):776–785. doi:10.1016/j.acra.2008.03.003

Paulin GA, Svenningsen S, Jobse BN, Mohan S, Kirby M, Lewis JF, Parraga G (2015) Differences in hyperpolarized (3) He ventilation imaging after 4 years in adults with cystic fibrosis. J Magn Reson Imaging 41(6):1701–1707. doi:10.1002/jmri.24744

Pauwels RA, Buist AS, Calverley PM, Jenkins CR, Hurd SS, Committee GS (2001) Global strategy for the diagnosis, management, and prevention of chronic obstructive pulmonary disease. NHLBI/WHO Global Initiative for Chronic Obstructive Lung Disease (GOLD) Workshop summary. Am J Respir Crit Care Med 163(5):1256–1276. doi:10.1164/ajrccm.163.5.2101039

Puderbach M, Eichinger M, Gahr J, Ley S, Tuengerthal S, Schmahl A, Fink C, Plathow C, Wiebel M, Muller FM, Kauczor HU (2007) Proton MRI appearance of cystic fibrosis: comparison to CT. Eur Radiol 17(3):716–724. doi:10.1007/s00330-006-0373-4

Regan EA, Hokanson JE, Murphy JR, Make B, Lynch DA, Beaty TH, Curran-Everett D, Silverman EK, Crapo JD (2010) Genetic epidemiology of COPD (COPDGene) study design. COPD 7(1):32–43. doi:10.3109/15412550903499522

Samee S, Altes T, Powers P, de Lange EE, Knight-Scott J, Rakes G, Mugler JP 3rd, Ciambotti JM, Alford BA, Brookeman JR, Platts-Mills TA (2003) Imaging the lungs in asthmatic patients by using hyperpolarized helium-3 magnetic resonance: assessment of response to methacholine and exercise challenge. J Allergy Clin Immunol 111(6):1205–1211

Schonfeld C, Cebotari S, Voskrebenzev A, Gutberlet M, Hinrichs J, Renne J, Hoeper MM, Olsson KM, Welte T, Wacker F, Vogel-Claussen J (2014) Performance of perfusion-weighted Fourier decomposition MRI for detection of chronic pulmonary emboli. J Magn Reson Imaging. doi:10.1002/jmri.24764

Sheikh K, Capaldi DP, Hoover DA, Palma DA, Yaremko BP, Parraga G (2015) Magnetic resonance imaging biomarkers of chronic obstructive pulmonary disease prior to radiation therapy for non-small cell lung cancer. Eur J Radiol Open 2:81–89. doi:10.1016/j.ejro.2015.05.003

Shukla Y, Wheatley A, Kirby M, Svenningsen S, Farag A, Santyr GE, Paterson NA, McCormack DG, Parraga G (2012) Hyperpolarized 129Xe magnetic resonance imaging: tolerability in healthy volunteers and subjects with pulmonary disease. Acad Radiol 19(8):941–951. doi:10.1016/j.acra.2012.03.018

SoherBJ, AinslieM, MacFallJ, HashoianR, CharlesHC (2010) Lung imaging in humans at 3 T using perfluorinated gases as MR contrast agents [abstr]. In: Proceedings of the Eighteenth Meeting of the International Society for Magnetic Resonance in Medicine Berkeley, Calif: International Society for Magnetic Resonance in Medicine:3389

Sommer G, Bauman G, Koenigkam-Santos M, Draenkow C, Heussel CP, Kauczor HU, Schlemmer HP, Puderbach M (2013) Non-contrast-enhanced preoperative assessment of lung perfusion in patients with non-small-cell lung cancer using Fourier decomposition magnetic resonance imaging. Eur J Radiol 82(12):E879–E887. doi:10.1016/j.ejrad.2013.06.030

Svenningsen S, Kirby M, Starr D, Leary D, Wheatley A, Maksym GN, McCormack DG, Parraga G (2013) Hyperpolarized (3) He and (129) Xe MRI: differences in asthma before bronchodilation. J Magn Reson Imaging 38(6):1521–1530. doi:10.1002/jmri.24111

Svenningsen S, Kirby M, Starr D, Coxson HO, Paterson NA, McCormack DG, Parraga G (2014a) What are ventilation defects in asthma? Thorax 69(1):63–71. doi:10.1136/thoraxjnl-2013-203711

Svenningsen S, Paulin G, Wheatley A, Pike D, Suggett J, McCormack D, Parraga G (2014b) Oscillating positive expiratory pressure (oPEP) therapy in chronic obstructive pulmonary disease and bronchiectasis. Eur Respir J 44(Suppl 58):P3679

Svenningsen S, Nair P, Guo F, McCormack DG, Parraga G (2016a) Is ventilation heterogeneity related to asthma control? Eur Respir J. doi:10.1183/13993003.00393-2016

Svenningsen S, Paulin GA, Sheikh K, Guo F, Hasany A, Kirby M, Etemad Rezai R, McCormack DG, Parraga G (2016b) Oscillatory positive expiratory pressure in chronic obstructive pulmonary disease. COPD 13(1):66–74. doi:10.3109/15412555.2015.1043523

Teague WG, Tustison NJ, Altes TA (2014) Ventilation heterogeneity in asthma. J Asthma 51(7):677–684. doi:10.3109/02770903.2014.914535

Tgavalekos NT, Musch G, Harris RS, Melo MFV, Winkler T, Schroeder T, Callahan R, Lutchen KR, Venegas JG (2007) Relationship between airway narrowing, patchy ventilation and lung mechanics in asthmatics. Eur Respir J 29(6):1174–1181. doi:10.1183/09031936.00113606

Thomen RP, Sheshadri A, Quirk JD, Kozlowski J, Ellison HD, Szczesniak RD, Castro M, Woods JC (2015) Regional ventilation changes in severe asthma after bronchial thermoplasty with (3)He MR imaging and CT. Radiology 274(1):250–259. doi:10.1148/radiol.14140080

Tkach JA, Hillman NH, Jobe AH, Loew W, Pratt RG, Daniels BR, Kallapur SG, Kline-Fath BM, Merhar SL, Giaquinto RO, Winter PM, Li Y, Ikegami M, Whitsett JA, Dumoulin CL (2012) An MRI system for imaging neonates in the NICU: initial feasibility study. Pediatr Radiol 42(11):1347–1356. doi:10.1007/s00247-012-2444-9

Tzeng YS, Lutchen K, Albert M (2009) The difference in ventilation heterogeneity between asthmatic and healthy subjects quantified using hyperpolarized He-3 MRI. J Appl Physiol 106(3):813–822. doi:10.1152/japplphysiol.01133.2007

van Beek EJ, Dahmen AM, Stavngaard T, Gast KK, Heussel CP, Krummenauer F, Schmiedeskamp J, Wild JM, Sogaard LV, Morbach AE, Schreiber LM, Kauczor HU (2009) Hyperpolarised 3He MRI versus HRCT in COPD and normal volunteers: PHIL trial. Eur Respir J 34(6):1311–1321. doi:10.1183/09031936.00138508

Vestbo J, Anderson W, Coxson HO, Crim C, Dawber F, Edwards L, Hagan G, Knobil K, Lomas DA, MacNee W, Silverman EK, Tal-Singer R, investigators E (2008) Evaluation of COPD Longitudinally to Identify Predictive Surrogate End-points (ECLIPSE). Eur Respir J 31(4):869–873. doi:10.1183/09031936.00111707

Vestbo J, Hurd SS, Agusti AG, Jones PW, Vogelmeier C, Anzueto A, Barnes PJ, Fabbri LM, Martinez FJ, Nishimura M, Stockley RA, Sin DD, Rodriguez-Roisin R (2013a) Global strategy for the diagnosis, management, and prevention of chronic obstructive pulmonary disease GOLD executive summary. Am J Respir Crit Care Med 187(4):347–365. doi:10.1164/rccm.201204-0596PP

Walkup LL, Tkach JA, Higano NS, Thomen RP, Fain SB, Merhar SL, Fleck RJ, Amin RS, Woods JC (2015) Quantitative magnetic resonance imaging of bronchopulmonary dysplasia in the neonatal intensive care unit environment. Am J Respir Crit Care Med 192(10):1215–1222. doi:10.1164/rccm.201503-0552OC

Wheatley A, Mckay S, Mathew L, Santyr G, McCormack DG, Parraga G (2008) Hyperpolarized helium-3 magnetic resonance imaging of asthma: Short-term reproducibility – art. no. 69161X. P Soc Photo-Opt Ins 6916:X9161–X9161. doi:10.1117/12.771138

Wielputz MO, Puderbach M, Kopp-Schneider A, Stahl M, Fritzsching E, Sommerburg O, Ley S, Sumkauskaite M, Biederer J, Kauczor HU, Eichinger M, Mall MA (2014) Magnetic resonance imaging detects changes in structure and perfusion, and response to therapy in early cystic fibrosis lung disease. Am J Respir Crit Care Med 189(8):956–965. doi:10.1164/rccm.201309-1659OC

Woodhouse N, Wild JM, Paley MN, Fichele S, Said Z, Swift AJ, van Beek EJ (2005) Combined helium-3/proton magnetic resonance imaging measurement of ventilated lung volumes in smokers compared to never-smokers. J Magn Reson Imaging 21(4):365–369. doi:10.1002/jmri.20290

Woods JC, Choong CK, Yablonskiy DA, Bentley J, Wong J, Pierce JA, Cooper JD, Macklem PT, Conradi MS, Hogg JC (2006) Hyperpolarized 3He diffusion MRI and histology in pulmonary emphysema. Magn Reson Med 56(6):1293–1300. doi:10.1002/mrm.21076

Challenges of Using 3 T MR Systems and Whole-Body MRI for Lung Imaging

Yoshiharu Ohno, Masaya Takahashi,
Hisanobu Koyama, and Takeshi Yoshikawa

Contents

Y. Ohno (✉) • T. Yoshikawa
Division of Functional and Diagnostic Imaging
Research, Department of Radiology, Kobe University
Graduate School of Medicine, Kobe, Japan

Advanced Biomedical Imaging Research Center, Kobe
University Graduate School of Medicine, Kobe, Japan
e-mail: yosirad@kobe-u.ac.jp, yosirad@med.kobe-u.ac.jp

M. Takahashi
Advanced Imaging Research Center, Department of
Radiology, University of Texas, Southwestern
Medical Center at Dallas, Dallas, TX, USA

H. Koyama
Division of Radiology, Department of Radiology,
Kobe University Graduate School of Medicine,
Dallas, TX, USA

Abstract

Ever since the clinical application of magnetic resonance (MR) imaging became an essential diagnostic tool, the lung has been a challenging area. Although many physicists and radiologists tried to assess different lung diseases as well as mediastinal and cardiac diseases by means of MR imaging during the 1980s and early 1990s, they could neither produce convincing image quality within a reasonable examination time nor demonstrate that MR imaging could serve as a substitute for computed tomography (CT), pulmonary angiography, and/or nuclear medicine studies. However, improvement of the 1.5-tesla (T) MR system and sequences, clinical application of new techniques such as parallel imaging, and utilization of more effective contrast media have continued since the late 1990s. These developments have made it possible to apply lung MR imaging to not only oncologic but also other pulmonary diseases, as well as to not only morphological but also functional assessment of various pulmonary and cardiopulmonary diseases. Moreover, these improvements have been continuing, resulting in the gradual shifting to the use of a higher magnetic strength field (≥ 3 T) for lung MR imaging during the 2000s.

1   Introduction

Ever since the clinical application of magnetic resonance (MR) imaging became an essential diagnostic tool, the lung has been a challenging area. Although many physicists and radiologists tried to assess different lung diseases as well as mediastinal and cardiac diseases by means of MR imaging during the 1980s and early 1990s, they could neither produce convincing image quality within a reasonable examination time nor demonstrate that MR imaging could serve as a substitute for computed tomography (CT), pulmonary angiography, and/or nuclear medicine studies. However, improvement of the 1.5-tesla (T) MR system and sequences, clinical application of new techniques such as parallel imaging, and utilization of more effective contrast media have continued since the late 1990s. These developments have made it possible to apply lung MR imaging to not only oncologic but also other pulmonary diseases, as well as to not only morphological but also functional assessment of various pulmonary and cardiopulmonary diseases. Moreover, these improvements have been continuing, resulting in the gradual shifting to the use of a higher magnetic strength field ($\geq$3 T) for lung MR imaging during the 2000s.

It is anticipated that the use of higher magnetic strength fields in MRI will result in improvement in signal-to-noise ratio (SNR) due to higher signal intensity (SI), the most significant of which is a reduction in the length of time required to obtain images (Takahashi et al. 2003). This may make a higher spatial resolution achievable. Since the late 1990s and early 2000s, several studies have reported and discussed the advantages of a higher magnetic strength field for imaging of not only the brain but also other organs, while many theoretical and experimental studies have attempted to demonstrate the existence and significance of magnetic field dependencies. In addition to SNR, magnetic field dependence has been well documented for tissue relaxation times (Duewell et al. 1995, 1996; Jezzard et al. 1996), as well as for the efficacy of MR contrast agents (e.g., R1, R2, or R2* relaxivities) (Lauffer 1990; Vander Elst et al. 1998).

The question is whether switching from 1.5 to 3 T for the chest field will lead to improvement or whether it will have practical advantages.

In this chapter, we describe (1) the basics of 3 T MR imaging and (2) new challenges for clinical lung MR imaging for morphological, functional, and metabolic assessments by using the 3 T MR system.

2   Basics of 3 T MR Imaging

2.1   Signal Intensity (SI) and Signal-To-Noise Ratio (SNR)

The question of optimum field strength has been a subject of intense controversy for over a decade. The interest in higher magnetic strength fields stems from the fact that SNR increases with an increase in field strength (ω), where SI and noise have different magnetic field dependencies.

$$SI \infty \left(\text{number of spins}\right) \times \left(\text{voltage induced by each spin}\right) \tag{1}$$

As shown in Eq. 1, the signal intensity from an MR experiment is in theory proportional to the square of the static magnetic field (ω^2) since both "number of spins" that can be observed and "voltage induced by each spin" increase linearly as the magnetic field (ω) increases. Noise is proportional to the static magnetic field (ω) when all noise comes from a sample, thus resulting in an SNR that is proportional to v in the case. On the other hand, noise is proportional to one-quarter of ω ($\omega^{1/4}$) when all noise comes from the RF coil, resulting in an SNR that is proportional to $\omega^{7/4}$. Therefore, SNR can be theoretically expected to increase by at least a factor of two when 3 T rather than 1.5 T is used. Unlike relaxation time and MR contrast agent effects, the benefit for SI at a higher magnetic strength field should be compared under nearly identical experimental conditions. Therefore, it is imperative to quantify the practical differences in terms of SNR and contrast-to-noise ratios (CNR) between 3 T and 1.5 T magnetic fields for various MR

sequences and examinations (Frydrychowicz et al. 2010; Londy et al. 2012; Nayak et al. 2004, Rakow-Penner et al. 2006; Yarnykh et al. 2006). However, only a few studies have been conducted using direct comparisons between SNRs and CNRs in terms of the combined effect of several magnetic field-dependent parameters at different fields in comparison with the theoretical values. Hence, it is still unclear how much benefit can be gained for SNR or what can or should be done when switching from 1.5 to 3 T MR systems.

2.2 Relaxation Time

SNR in biological tissue was found to be approximately proportional to field strength. However, the practically achievable SNR gain may be somewhat less since the underlying theory assumes that all parameters except the magnetic field are constant. One reason for the discrepancy is the increase in T1 relaxation time in conjunction with an increase in field strength (Stanisz et al. 2005). Based on the findings of a direct comparison of relaxation times for 1.5 T and 3 T MR systems (Stanisz et al. 2005), a few studies have suggested that SI is a function of relaxation time and thus magnetic field dependent (Noeske 2000; Stanisz et al. 2005). Table 1, modified from the previous manuscript (Stanisz et al. 2005), shows a summary of differences in relaxation time between two magnetic field strengths. These

differences suggest that T1 relaxation times are prolonged with a higher magnetic strength field, while T2 relaxation times are somewhat shortened in any tissue. Therefore, the CNR of lung lesions observed on conventional black-blood T1- and T2-weighted turbo SE sequences is generally reduced on a 3 T MR system in comparison with that on a 1.5 T MR system (Fig. 1). On the other hand, the increase in T1 relaxation time for a 3 T MR system is considered to be one of the advantages of non-contrast-enhanced (non-CE) MR angiography.

Although T2 values were substituted for T2* in the phantom study because T2 and T2* values should be theoretically identical in phantoms in either magnetic field (Fernandez-Seara et al. 2000), it is thought that conditions differ in some tissues where the T2* value is much shorter than the T2 value. The magnitude of susceptibility (g) is thus proportional to the magnetic field as shown in the following equation (Ludeke et al. 1985):

$$\gamma = \Delta x \Big/ 2 \times B_0 \Big/ RB_z \tag{2}$$

where Δx is the difference in magnetic susceptibility of adjoining substances, B_0 ($=\omega$) is the static magnetic field, R is the cross-sectional radius, and G_z is the readout gradient. However, this effect on T2* depends on T2 for the tissue since 1/T2* is a function of T2 and T2′ (R2*=R2+/R2′) (Takahashi et al. 2000). The shorter T2 and

Table 1 T2 and T1 relaxation times at 3 and 1.5 T measured at 37 °C

| | 3 T system | | 1.5 T system | |
| | Relaxation time | | Relaxation time | |
Tissue	T2 (ms)	T1 (ms)	T2 (ms)	T1 (ms)
Liver	42±3	812±64	46±6	576±30
Skeletal muscle	50±4	1412±13	44±6	1008±20
Heart	47±11	1471±31	40±6	1030±34
Kidney	56±4	1194±31	55±3	690±30
White matter	69±3	1084±45	72±4	884±50
Gray matter	99±7	1820±114	95±8	1124±50
Optic nerve	78±5	1083±39	77±9	815±30
Spinal cord	78±2	993±47	74±6	745±37
Blood	275±50	1932±85	290±30	1441±120

Modification of Table 1 in Stanisz et al. (2005)
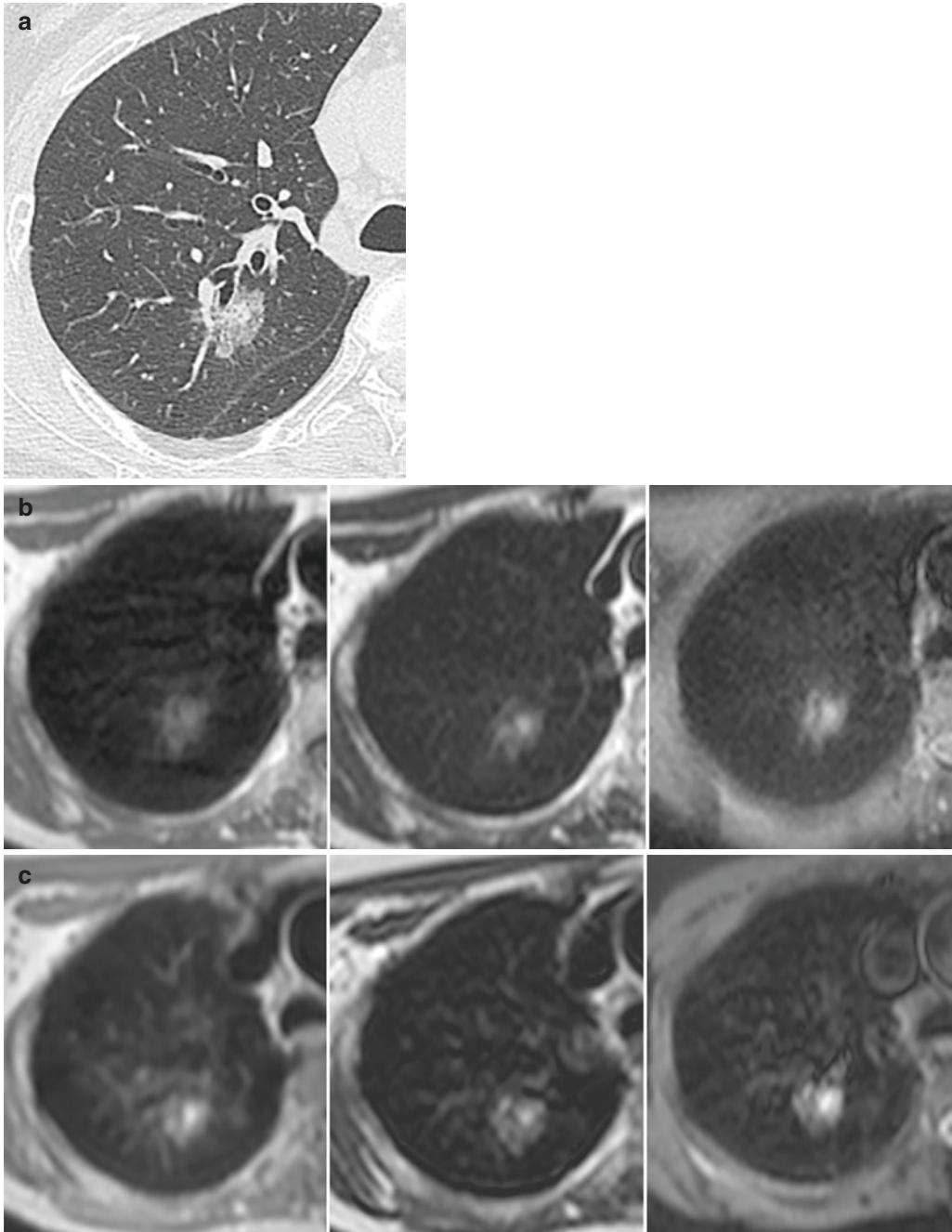
Fig. 1 A 67-year-old female with minimally invasive ade-nocarcinoma. (**a**) Thin-section CT shows a part-solid nod-ule 21 mm in diameter in the right upper lobe. Solid component 5 mm in diameter is observed within the nod-ule. (**b**) (L to R: T1-weighted, T2-weighted, and STIR TSE images at 1.5 T) The nodule is shown as a homogeneous low signal intensity area on T1-weighted TSE images and as a relatively high signal intensity area with a higher signal intensity component on T2-weighted and STIR TSE images. The higher signal intensity component within the nodule on T2-weighted and STIR TSE images showed a good match with pathologically proven stromal invasion. (**c**) (L to R: T1-weighted, T2-weighted, and STIR TSE images at 3 T) The nodule is shown as a low signal intensity area with a high signal intensity component on T1-weighted TSE images and as relatively high signal intensity area with a higher signal intensity component on T2-weighted and STIR TSE images. The higher signal intensity component within the nodule on all images on 3 T system showed a good match with pathologically proven stromal invasion

T2* values at a higher magnetic strength field may cause a larger reduction in the SNR and CNR than might be expected in some tissues such as the lung. Previously, it was found that the CNR increased in the central arteries of the lung, but not in the pulmonary peripheral arteries at 4 T as the dose of the contrast agent increased, ranging from 0.05 to 0.2 mmol/kg body weight (Uematsu et al. 2001). Therefore, the optimal imaging parameters for the clinical application should be carefully considered, particularly when an undesirable T2* effect may be involved.

2.3 Relaxivity of Gadolinium Contrast Media

The R1 relaxivity of gadolinium (Gd) contrast agent depends on various parameters, such as the type of contrast agent (Takahashi et al. 1996; De León-Rodríguez et al. 2015), temperature, and tissue environment as well as magnetic field strength (Lauffer et al. 1990; Vander Elst et al. 1998). While R1 relaxivity of a paramagnetic contrast agent is higher at a lower field strength (Lauffer et al. 1990), R2 and R2* values should be theoretically identical in phantoms in any magnetic field (Fernandez-Seara et al. 2000). Takahashi et al. used a phantom study to compare the effects of various contrast agents (Takahashi et al. 2003). For an accurate determination of the efficacy of Gd complex (R1, R2, and R2*), only some of the relaxation times (T1, T2) with an excellent fit to the curve ($r > 0.995$) were reciprocally plotted against the concentrations of Gd at both 4 and 1.5 T. In addition, R1 at 4 T was lower ($\approx 25\%$) than R1 at 1.5 T, while R2 at 4 T was almost the same as that at 1.5 T. Hence, R1 relaxivity decreases as the magnetic field strength increases, while R2 relaxivity does not change much (Fernandez-Seara et al. 2000, Takahashi et al. 2003; De León-Rodríguez et al. 2015). On the other hand, R2 and R2* may change considerably depending upon the type of contrast agent (e.g., superparamagnetic iron oxide [SPIO] and ultrasmall superparamagnetic iron oxide [USPIO]) and its applications. This suggests that the use of the MR contrast agent should also be taken into

consideration, although it is not clear whether this change is substantially effective in current clinical usage with a higher magnetic strength field.

2.4 Safety Considerations

Theoretical calculations of the interaction of high magnetic strength fields with human subjects have been reviewed. To date, few harmful physical or physiological phenomena have been observed when 3 T MR systems when appropriately used in routine clinical practice. The features examined included orientation of macromolecules and membranes, effects on nerve conduction, electrocardiograms and electroencephalograms, and blood flow.

If higher magnetic strength fields are to be used to obtain higher spatial resolution, the strength of the gradient must be increased. For the combination of a statistically higher magnetic strength field and gradients, the strength may be an issue in some applications due to limitations in the current FDA guidelines for the specific absorption rate (SAR). SAR is defined as follows:

$$SAR = \frac{\sigma \times |E|^2}{2\rho} \times \left(\frac{\tau}{TR}\right) \times N_P \times N_S \quad (3)$$

where σ is conductivity, E is the electric field, ρ is tissue density, τ is pulse duration, and N_P and N_S are the number of pulses and image slices, respectively. Since E is proportional to the static magnetic field, SAR increases significantly for higher magnetic strength fields, which may limit the application of the system in terms of number of slices, selection of flip angle, etc. Additionally, since RF energy is absorbed more effectively at higher frequencies, RF absorption, as expressed by SAR, must be carefully monitored. This could be a major concern for any application using high magnetic strength field (Bottomley et al. 1978; Takahashi et al. 2003). Currently, all clinical applications using a 3 T MR system need to take into consideration or check the SAR level, while appropriate modification of the sequence itself, the sequence parameters, as well as utilization of parallel imaging is warranted. For this reason,

every vendor is continuously taking safety issues into consideration for their new clinical applications on 3 T MR systems.

3 Challenges for 3 T Lung MR Imaging

With the aforementioned basics for the 3 T MR system as a major consideration, lung MR imaging is currently performed with 3 T systems as well as 1.5 T systems. Basically, the protocols for thoracic oncology and cardiopulmonary diseases are very similar, although individual vendors modify some sequence parameters and apply special new techniques for improving B0 and B1 inhomogeneities as well as employing new coils. Therefore, examination protocols dealt with in other chapters can also be used for 3 T lung MR examination in routine clinical practice, although SNR and CNR are slightly modified by changing relaxation time, relaxivities of the Gd complex, and other details. This chapter will therefore deal only with new challenges that have emerged since the mid-2000s for morphological, functional, and metabolic imaging when using 3 T MR systems.

3.1 Non-Contrast MR Angiography and Perfusion MR Imaging

Contrast-enhanced (CE-) MR angiography with Gd contrast media has been widely accepted since 1994 for body MR angiography with the use of a moving table and parallel imaging techniques for not only the abdomen but also the thorax (Prince 1994). On the other hand, since the early days of clinical MRI and long before the development of CE-MR angiography techniques, traditional non-contrast-enhanced (non-CE) MR angiography techniques, such as time of flight (TOF) and phase contrast (PC), have been developed and widely applied for various purposes. Three-dimensional (3D) TOF is currently used in intracranial MR angiography, two-dimensional (2D) MR angiography is used in carotid and

distal peripheral MR angiography (Laub 1995, Masaryk et al. 1990), and 2D (≈3D) or 3D (≈4D) PC-MR angiography is used mostly for quantitative flow measurements in various applications (Dumoulin et al. 1989, 1990). Although long acquisition time and almost unavoidable motion artifacts are drawbacks of these techniques, the renaissance of interest in non-CE-MR angiography for other parts of the body is attributable to various factors including improved MR hardware and sequence and parallel imaging (Sodickson et al. 1997; Pruessmann et al. 1999). In addition, a serious concern about nephrogenic systemic fibrosis (NSF) observed in patients with renal insufficiency (Buhaescu et al. 2008) has stimulated further development of alternative techniques that do not require exogenous contrast material. The original non-CE-MR angiography research was initiated in Japan due to the relatively high cost and dose limitations of gadolinium-based contrast material (Urata et al. 2001) in addition to a basic desire of healthcare professionals and patients to perform and receive completely noninvasive and contrast-free examinations (Miyazaki et al. 2012).

The balanced steady-state free precession (bSSFP) sequences, initially described as early as 1958 (Carr 1958), became commercially available in the early 2000s and have been used with 1.5 T and 3 T MR systems in a wide range of applications for many organs including the chest (Scheffler et al. 2003). The high signal-to-noise ratio (SNR) and intrinsic T2/T1 contrast, which are relevant for non-contrast MR angiography (NC-MRA) with minimal flow dependency (Scheffler et al. 2003), provide high blood signal efficiency, which makes the bSSFP sequence an appropriate choice for angiography applications. The sequence consists of an $\alpha/2$ preparation pulse, dummy pulses for spin conditioning, and an alternating RF excitation pulse train, which offers fully balanced spins in all three directions for high SNR and high contrast for blood signal. While the advantages of this application are obvious, the sensitivity of bSSFP to B0 field inhomogeneity makes this technique, unlike turbo or fast spin-echo (TSE or FSE)-based sequences, susceptible to off-resonance banding artifacts.

However, recent advances in software and hardware to shorten the TR of the excitation pulse train have helped to improve the robustness of bSSFP in the presence of inhomogeneous B0 fields. Nevertheless, because of the differences in B0 inhomogeneity between 3 T and 1.5 T systems, the bSSFP sequence theoretically reduces image quality at 3 T. In addition, and compared with CE-MR angiography with the 3 T system, the bSSFP sequence reduces the depiction of peripheral pulmonary vasculature rather than central pulmonary vessels (Fig. 2). Therefore, this technique should be used with a combination of following two methods.

The 3D FSE-based sequences using electrocardiographic (ECG) gating were developed in the early 2000s to provide 3D non-CE-MR angiography with bright blood vessels by triggering encoding of every slice at the same cardiac phase (Miyazaki et al. 2000, 2003; Ohno et al. 2014a). This technique was later extended by using different cardiac trigger delay times to separate arteries from veins as fresh blood imaging (FBI) (Fig. 3). In addition, the prolonged T1 relaxation time of blood at 3 T is considered one of the advantages of this technique as compared with the 1.5 T MR system.

FBI using an ECG-gated 3D half-Fourier FSE sequence relies on the signal difference between systolic- and diastolic-triggered acquisitions (Miyazaki et al. 2000, 2003; Ohno et al. 2014a). This technique also relies on the black arterial signal, or flow void, due to the spin-dephasing effects of the fast arterial flow during systole. During diastole, arteries are characterized by a slow flow and are thus depicted with a high signal. Venous blood, on the other hand, is bright throughout the cardiac cycle, due to its moderately constant slow flow. Because this technique thus relies on the blood flow velocity, ECG gating or peripheral pulse gating (PPG) is required for selectively acquiring data during the desired cardiac phase. To obtain each slice at the same cardiac phase, slice encoding is triggered with the same cardiac delay time for the 3D half-Fourier FSE sequence. The contrast of the image in half-Fourier FSE is determined by the effective echo time (TE_{eff}); moderately or heavily T2-weighted images are

thus obtained by selecting short or long TE_{eff}s. To effectively attain bright blood imaging by means of the ECG-gated half-Fourier FSE technique, a combination of the following techniques is used: short echo train spacing, reduction of the acquisition window by means of parallel imaging, and rectilinear k-space ordering. Lastly, and depending on the application, additional prepulses, such as short tau inversion recovery (STIR), can be used in conjunction with 3D half-Fourier FSE to achieve fat suppression. Furthermore, FSE-based sequences allow for election of the TE_{eff} to control the contrast in T2-weighted images. Moreover, for pulmonary FBI, appropriate ECG delays for diastolic and/or systolic triggering need to be selected for the various applications because this is a fundamental requirement for correctly performing non-CE-MR angiography at pulmonary arterial, parenchymal, and pulmonary venous phases. Therefore, a preparatory, or "ECG-prep," sequence that produces 2D single-shot images at incrementally increasing triggering times of arbitrary steps can be used to find the specific trigger delay (TD) for systole, when arterial blood is black (flow voids), and for diastole when arteries are bright (Miyazaki et al. 2000). Each single-shot 2D is acquired for 2 or 3 RR intervals at incremental delays to produce separate images for each phase. Depending on preference, the 2D PC technique can be used to determine the systolic and diastolic delays as an alternative to the ECG-prep scan.

To depict particular vessels, the arterial spin labeling (ASL) method was originally developed using spin-echo (SE) - and gradient-echo (GRE) - type sequences for carotid angiography (Nishimura et al. 1987; Edelman et al. 1994). In the late 1980s, Nishimura et al. introduced a method which uses one image, acquired with a selective inversion recovery (IR) pulse to tag the vessel of interest, combined with another image, acquired with a nonselective IR pulse, to generate image contrast after subtraction (Nishimura et al. 1987). Later this method was expanded to an ASL technique called signal targeting with alternating radio frequency (STAR) (Edelman et al. 1994; Wielopolski et al. 1995). Both the half-Fourier FSE and bSSFP sequences allow
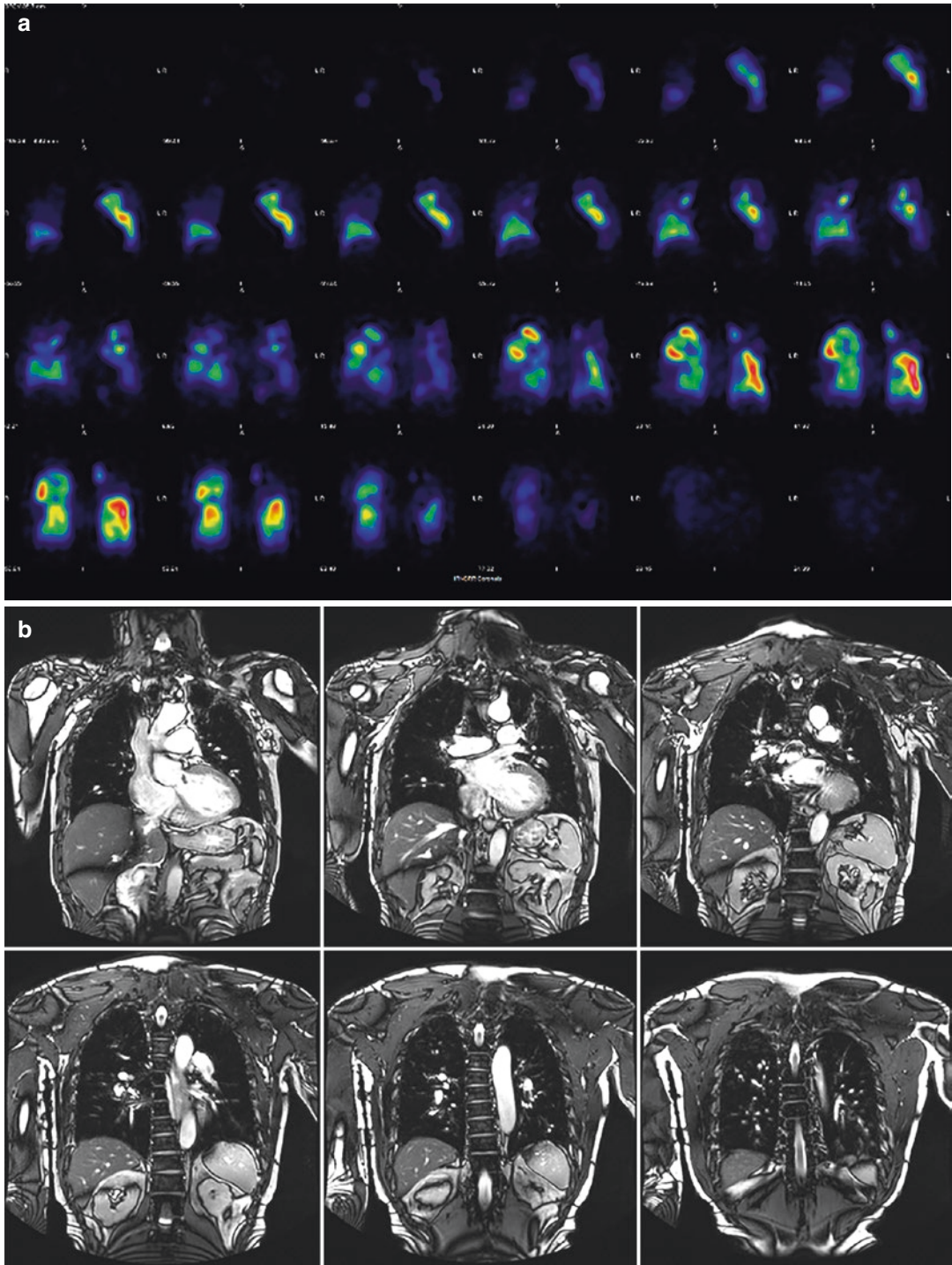
Fig. 2 A 48-year-old male patient with chronic thromboembolic pulmonary hypertension. (**a**) Coronal reformatted perfusion SPECT images with ⁹⁹ᵐTc-MAA show heterogeneous parenchymal perfusion due to chronic pulmonary thromboembolism. (**b**) (Upper line images from ventral to central slices and lower line images from central to dorsal slices) Balanced FFE (bFFE) images obtained from the main trunk, lobar, and segmental levels at 3 T clearly show large vessels such as aorta, superior vena cava, and pulmonary arteries and veins. However, pulmonary parenchymal perfusion abnormalities are not visualized
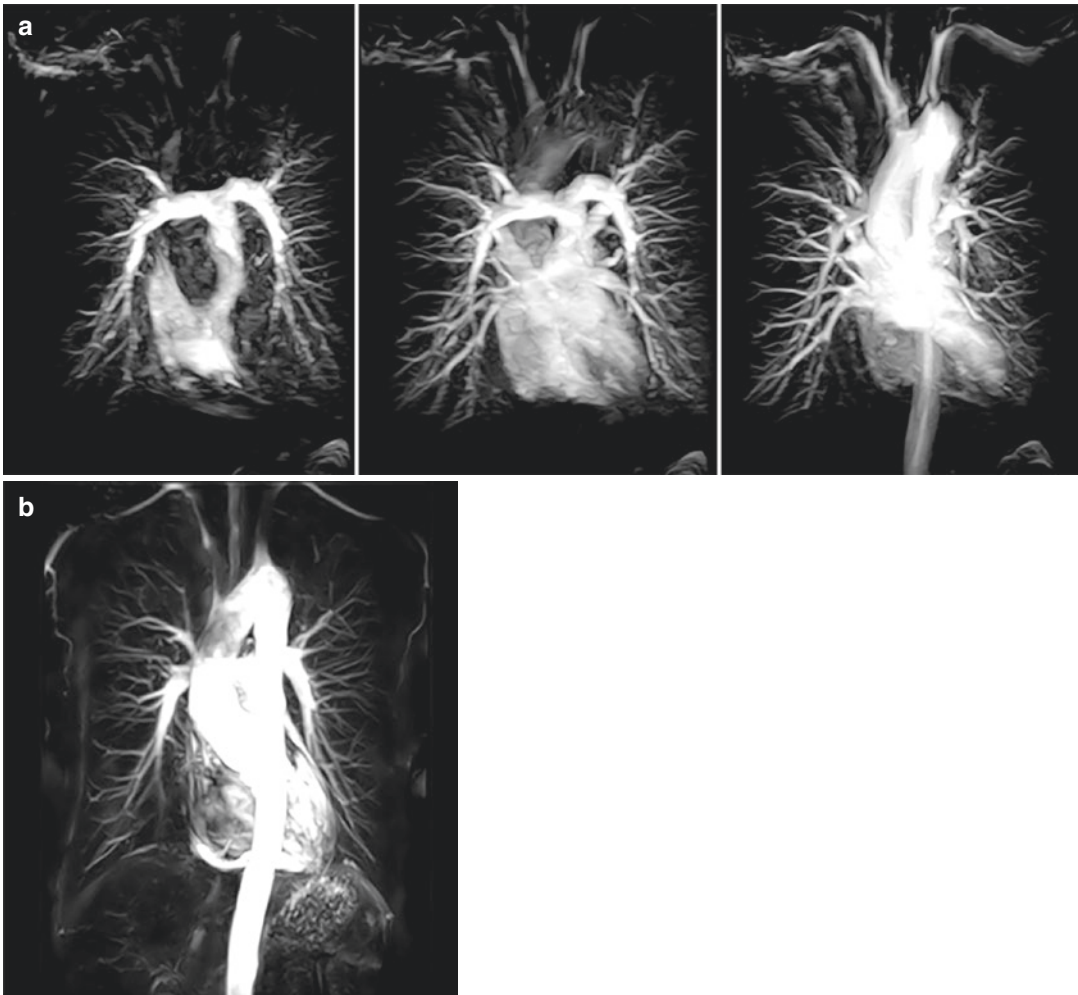
Fig. 3 A 67-year-old male healthy volunteer. (**a**) (L to R: pulmonary arterial and parenchymal and systemic circulation phases) Time-resolved CE-MR angiography at 3 T clearly depicts pulmonary vasculatures at pulmonary arterial and parenchymal and systemic circulation phases. (**b**) Non-CE-MR angiography performed with the ECG-gated fresh blood imaging (FBI) method at the same 3 T demonstrates pulmonary vasculatures as well as ascending and descending aorta with high spatial resolution similar to that on time-resolved CE-MR angiography

for single-shot imaging by acquiring multiple echoes (Stuber et al. 2002; Miyazaki et al. 2012). This feature makes short scan times possible as well as the addition of various prepulses, such as a fat suppression pulse, an inversion pulse, and/or a spin labeling pulse. Both half-Fourier FSE and bSSFP sequences offer bright blood imaging, but unless they are combined with a spin labeling technique, the background signal still interferes with depiction of blood vessels.

With regard to non-CE-MR angiography and venography with spin labeling, there are several characteristic differences between half-Fourier FSE and bSSFP. As mentioned above, bSSFP requires good B0 field homogeneity (Scheffler et al. 2003), which is not a problem for half-Fourier FSE. However, since flow dependency and dependency of the PE direction on the orientation of the vessels are limitations of half-Fourier FSE, the use of half-Fourier FSE is suitable only for imaging relatively slower flow vessels like pulmonary vessels. In contrast, bSSFP allows for acquisition in arbitrary cardiac phases. In addition, the characteristic flow independency of bSSFP allows for imaging of fast flow vessels,

such as for cardiac, aortic arch, aorta, and renal non-CE-MR angiography. However, application of these techniques requires other considerations, such as arterial and venous flow patterns, T1 and T2 of blood compared with the background tissues, and relative susceptibility of the different parts of the body (i.e., air/tissue interface in lungs). Therefore, it has been suggested that the time-spatial labeling inversion pulse (time-SLIP) method is the only suitable method for ASL-based pulmonary non-CE-MR angiography with the 3 T MR system (Ohno et al. 2014a).

Currently, the three types of spin labeling techniques available for time-SLIP are the flow-in, flow-out, and alternate tag-on/tag-off subtraction techniques (Miyazaki et al. 2012). All time-SLIP techniques can be combined with half-Fourier FSE or bSSFP sequences and with 2D or 3D acquisition, as well as with ECG (or PPG) gating and with respiratory gating, or both. The characteristic difference of these techniques is that the flow-in and flow-out techniques require careful selection of TI to null the background signal, whereas the alternate tag-on/tag-off technique generates images without any background signals (removed by means of subtraction) regardless of the selection of TI. This independency from TI selection allows for the study of perfusion in a time-resolved manner by repeated acquisitions with many different TIs. However, the main drawback of the alternate tag-on/tag-off technique is that the scan time is doubled. When the tag position and appropriate TI selection are taken into consideration, different anatomical or targeted pulmonary vasculatures can be visualized with non-CE-MR angiography (Fig. 4).

Application of non-CE-MR angiography with the abovementioned techniques for the 3 T MR system has been initiated for several organs during the last several years (Ohno et al. 2014a, 2015a; Albert et al. 2015; Kurata et al. 2016). However, only one study has been conducted to test all non-CE-MR angiography techniques for pulmonary vasculature assessment in comparison with CE-CT angiography as well as CE-MR angiography. The findings of this study revealed that there were no significant differences in pulmonary vasculature depiction and pulmonary vascular anomaly assessment among these techniques when used in routine clinical practice
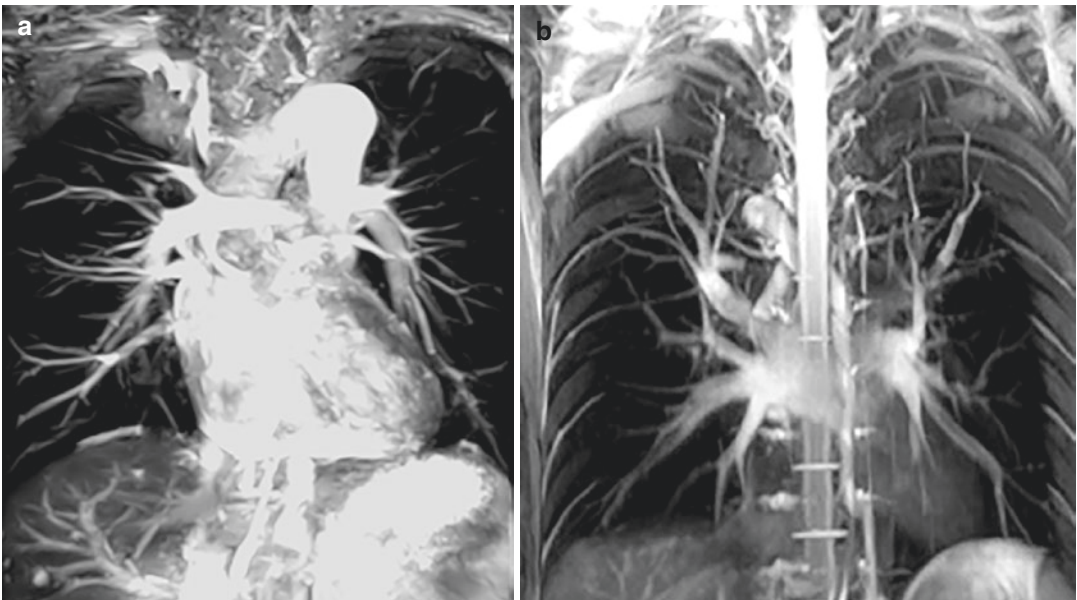
Fig. 4 A 42-year old healthy male volunteer. By changing tag-pulse position as well as inflow time, pulmonary arterial (**a**) and venous (**b**) phase images are clearly distinguished by non-CE-MR angiography with the time-spatial labeling inversion pulse (time-SLIP) method at 3 T

(Ohno et al. 2014a). Therefore, further development of these techniques for the 3 T systems will challenge CE-CT angiography as well as CE-MR angiography in the near future.

Since 1999, the applicability of non-CE perfusion MR imaging has been studied and tested mainly academically by using arterial spin tagging (Roberts et al. 1999), STAR half-Fourier acquisition single-shot TSE (HASTE) (Hatabu et al. 2000), flow-sensitive alternating inversion recovery with and without an extra-radio frequency pulse (FAIRER and FAIR), 2D ECG-gated subtraction, and Fourier decomposition (FD) (Bauman et al. 2013; Bauman Puderbach et al. 2013; Sommer et al. 2013; Kjørstad et al.

2014; Schönfeld et al. 2015) at 1.5 T. However, all these techniques were 2D, time consuming, and/or of low spatial resolution and could therefore not yet function as substitutes for dynamic CE-perfusion MR imaging, whether for academic or clinical purposes.

We recently developed a 3D ECG- and respiratory-gated non-CE-perfusion MR imaging method based on the 3D FBI method combined with subtraction between the diastolic and the systolic phase for the 3 T MR system (Ohno et al. 2015b) (Fig. 5). This technique showed good inter-method agreements for regional perfusion evaluation using dynamic CE-perfusion MR imaging and perfusion scanning (Ohno et al.
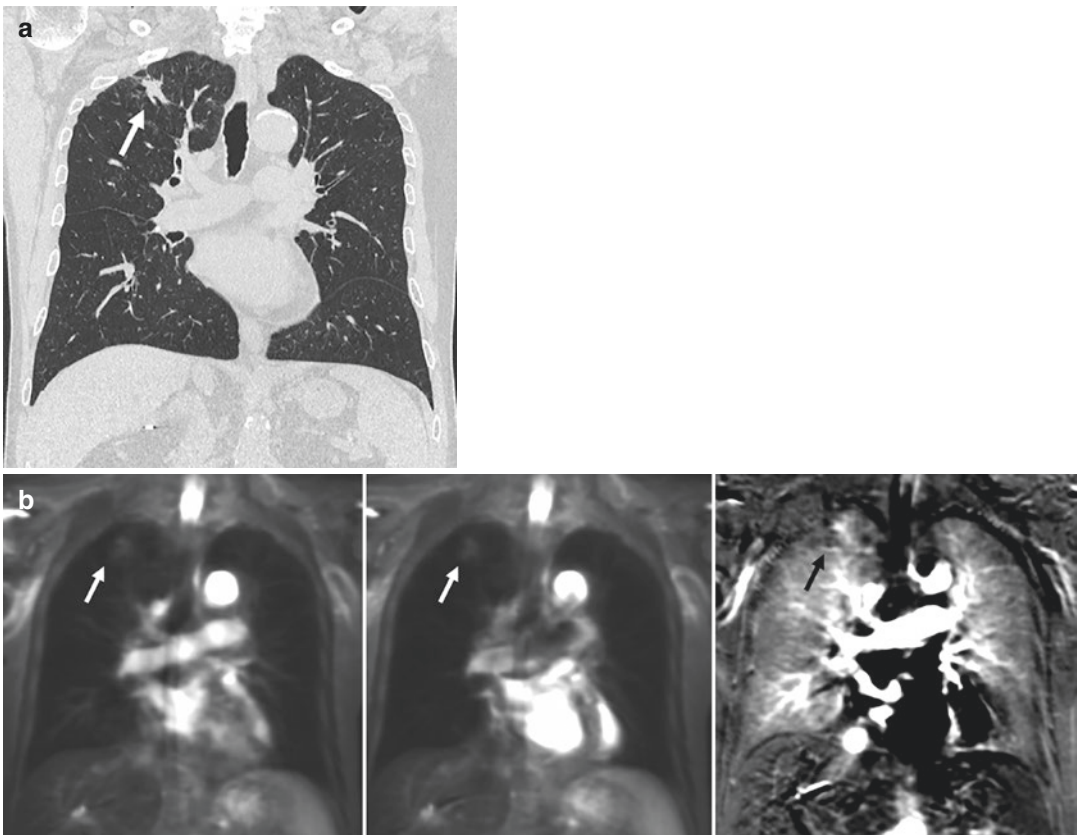
Fig. 5 A 76-year-old female patient with invasive adenocarcinoma. (**a**) Thin-section multi-planar reformatted (MPR) image at the coronal plane shows a nodule (*white arrow*) in the right upper lobe. The nodule features notches, spiculae, and pleural indentations and was pathologically diagnosed as invasive adenocarcinoma. (**b**) (L to R: systolic and diastolic images and non-CE-perfusion image) Systolic and diastolic original images obtained with the 3D ECG-gated fresh blood imaging (FBI) method show a lung adenocarcinoma (*white arrows*) in the right upper lobe. Non-CE-perfusion MR image obtained as a subtraction image obtained by subtracting systolic from diastolic images clearly shows lung parenchymal perfusion without lung adenocarcinoma (*black arrow*)

2015b). In addition, the prediction capability of postoperative lung function based on non-CE-perfusion MR imaging with this technique was almost similar to that based on quantitatively assessed thin-section CT and dynamic CE-perfusion MR imaging and higher than that based on qualitatively assessed thin-section CT and perfusion scan (Ohno et al. 2015b). Although further investigation is warranted, this new technique may become an option for perfusion assessment in various pulmonary diseases.

3.2 Whole-Body MR Imaging and PET/MRI for Lung Cancer Management

Since 2007, whole-body MR imaging has become clinically feasible after the introduction of fast imaging and moving table equipment and is considered to be the single, most cost-effective imaging test using 1.5 T and 3 T systems for patients with lung cancer (Ohno et al. 2007, 2008, 2013a, 2015c; Yi et al. 2008, 2013; Takenaka et al. 2009; Sommer et al. 2012). It has also been suggested that it might play a complementary role in the management of lung cancer staging, recurrence assessment, and/or metastases surveillance (Ohno et al. 2007, 2008, 2013a, 2015c; Yi et al. 2008, 2013; Takenaka et al. 2009; Sommer et al. 2012). In addition, PET/MRI has been tested for the same clinical purposes, and the benefits of this hybrid imaging method have been demonstrated in several studies during recent years (Ohno et al. 2015c; Schaarschmidt et al. 2015, 2016).

A few studies have compared the diagnostic performance of whole-body MRI for the T-factor using PET/CT as well as PET/ MRI (Yi et al. 2008; Sommer et al. 2012; Heusch et al. 2014; Ohno et al. 2015c). These studies found that the diagnostic accuracy of whole-body MR imaging with the 3 T system ranged from 89% to 94.3% and that of PET/CT from 86% to 91.4% (Yi et al. 2008; Sommer et al. 2012). In addition, one study has assessed both morphological and metabolic information obtained with the two modalities (Ohno et al. 2015c). This study found that the

diagnostic accuracy was 94.3% for whole-body MRI; 94.3% and 91.4%, respectively, for PET/ MRI with and without signal intensity (SI) assessment; and 91.4% for PET/CT, showing that there were no significant differences in diagnostic accuracy among these methods.

For whole-body MR imaging with and without diffusion-weighted imaging (DWI), N-factor assessment has been performed for NSCLC patients on 1.5 T and 3 T MR systems since 2008 (Yi et al. 2008, 2013; Sommer et al. 2012; Ohno et al. 2015c). Yi et al. directly compared the diagnostic performance of N-factor assessment for lung cancer patients by whole-body MR imaging with the 3 T system and by PET/CT and found that the respective diagnostic accuracies were 68% and 70%, respectively, and concluded that there was no significant difference in diagnostic performance (Yi et al. 2008). A more recent study, which made a direct comparison of diagnostic performance for N-factor assessment for NSCLC patients among whole-body MR imaging, PET/MRI, and PET/CT, found that the diagnostic accuracy of the three modalities was 98.6% for MR imaging; 98.6% and 92.1% for PET/MRI with and without SI assessment, respectively; and 92.1% for PET/CT (Ohno et al. 2015c). The accuracy of whole-body MR imaging and PET/ MRI with SI assessment was thus significantly higher than that of whole-body PET/MRI without SI assessment and of PET/CT. In addition, the sensitivity of whole-body MR imaging (100%) and PET/MRI with SI assessment (100%) was significantly higher than that of whole-body PET/MRI without SI assessment (93.8%) and of PET/CT (93.8%).

A comparative study of the diagnostic performance of whole-body MR imaging for M-factor assessment with that of FDG PET/CT found that the diagnostic accuracy of the two modalities was only 86% and significantly different from their diagnostic performance for N-factor assessment in lung cancer patients (Yi et al. 2008). Another study found that the sensitivity and accuracy of whole-body MR imaging (sensitivity, 100%; accuracy, 98.6%) and PET/MRI with SI assessment (sensitivity, 100%; accuracy, 98.6%) were higher than those of PET/MRI

without SI assessment (sensitivity, 92.7%; accuracy, 91.4%) and PET/CT (sensitivity, 92.7%; accuracy, 90.7%) (Ohno et al. 2015c).

In addition, this study compared the assessment of operability and found that the sensitivity and accuracy of whole-body MR imaging (sensitivity, 100%; accuracy, 97.1%) and PET/MRI with SI assessment (sensitivity, 100%; accuracy, 97.1%) were higher than those of PET/MRI without SI assessment (sensitivity, 86.3%; accuracy, 85.0%) and PET/CT (sensitivity, 86.3%; accuracy, 85.0%) (Ohno et al. 2015c).

Although the number of studies using the 3 T MR system is limited, we suggest that the addition of SI assessment for either whole-body MR imaging or PET/MRI can improve the diagnostic performance for lung cancer staging as well as operability assessment as compared with the mere morphological and metabolic information obtained from PET/MRI and PET/CT (Ohno et al. 2015c).

Whole-body MR imaging at 3 T was also tested for the assessment of postoperative lung cancer recurrence in NSCLC patients and directly compared with PET/CT (Ohno et al. 2013a). In this study, contrast-enhanced (CE) whole-body MR imaging was compared with in-phase T1-weighted GRE, the newly developed segmented 3D T1-weighted spoiled GRE sequence (Quick 3D), and a double fat suppression (DFS) RF pulse technique for enhancing fat-free capability (Ohno et al. 2013a). Moreover, specificity (100%) and accuracy (95.5%) of whole-body MR imaging with CE-Quick 3D and DFS sequence were significantly higher than those of FDG PET/CT (specificity, 93.6%; accuracy, 89.6%) and conventional radiological examinations (specificity, 92.7%; accuracy, 91.0%). In addition, specificity of whole-body MR imaging with the CE-in-phase T1-GRE sequence (100%) was significantly higher than that of FDG PET/CT and conventional radiological examinations (Ohno et al. 2013a). This study therefore concluded that whole-body MR imaging as a "one-stop-shopping" examination can be considered at least as valuable as PET/CT and more useful than conventional radiological examinations of lung cancer patients (Fig. 6).

As for the abovementioned whole-body MR imaging and/or PET/MRI for the 3 T system, no study has been conducted that deals with the complementary application of whole-body DWI. Further investigations are thus warranted to determine the actual clinical relevance as well as cost-effectiveness for lung cancer or other thoracic malignancies.

3.3 New Diffusion-Weighted MR Imaging at 3 T

During the past decade, it has been suggested that DWI is useful for thoracic oncology as well as the detection of pulmonary nodules at 1.5 T although few papers have dealt with the application of DWI on a 3 T system (Ohno et al. 2015d; Yuan et al. 2016). One study used a conventional DWI technique for intravoxel incoherent motion (IVIM) for a direct comparison with dynamic CE-MR imaging (Yuan et al. 2016). Several DWI-based indices were assessed, including the diffusion parameter representing pure molecular diffusion (D, i.e., the slow component of diffusion), the pseudo-diffusion parameter representing incoherent microcirculation within the voxel (D*, i.e., the fast component of the diffusion-weighted signal decay), fraction of perfusion (*f*), and apparent diffusion coefficient (ADC), as well as dynamic CE-MR-based indices such as extravascular extracellular volume fraction (Ve), blood plasma volume fraction (Vp), transfer constant (K^{trans}), and efflux rate constant (K_{ep}). It was found that sensitivity and accuracy of D (72.2% and 91.3%, respectively) for discriminating lung cancer from benignity were significantly higher than those of the other indices (accuracy, 55.5–68.0%; sensitivity, 41.3–78.3%; all $p < 0.01$) except for the accuracy of K_{ep} (70.8%; $p > 0.05$). In addition, K^{trans} showed significantly higher specificity (84.6%) than the other indices (38.5–73.1%; $p < 0.01$) and that these results can be improved even further by combining D and K^{trans}, resulting in sensitivity, specificity, and accuracy of 94.2%, 92%, and 93.5%, respectively. Although IVIM assessments in the thorax involve several problematic factors such as B0, B1, and
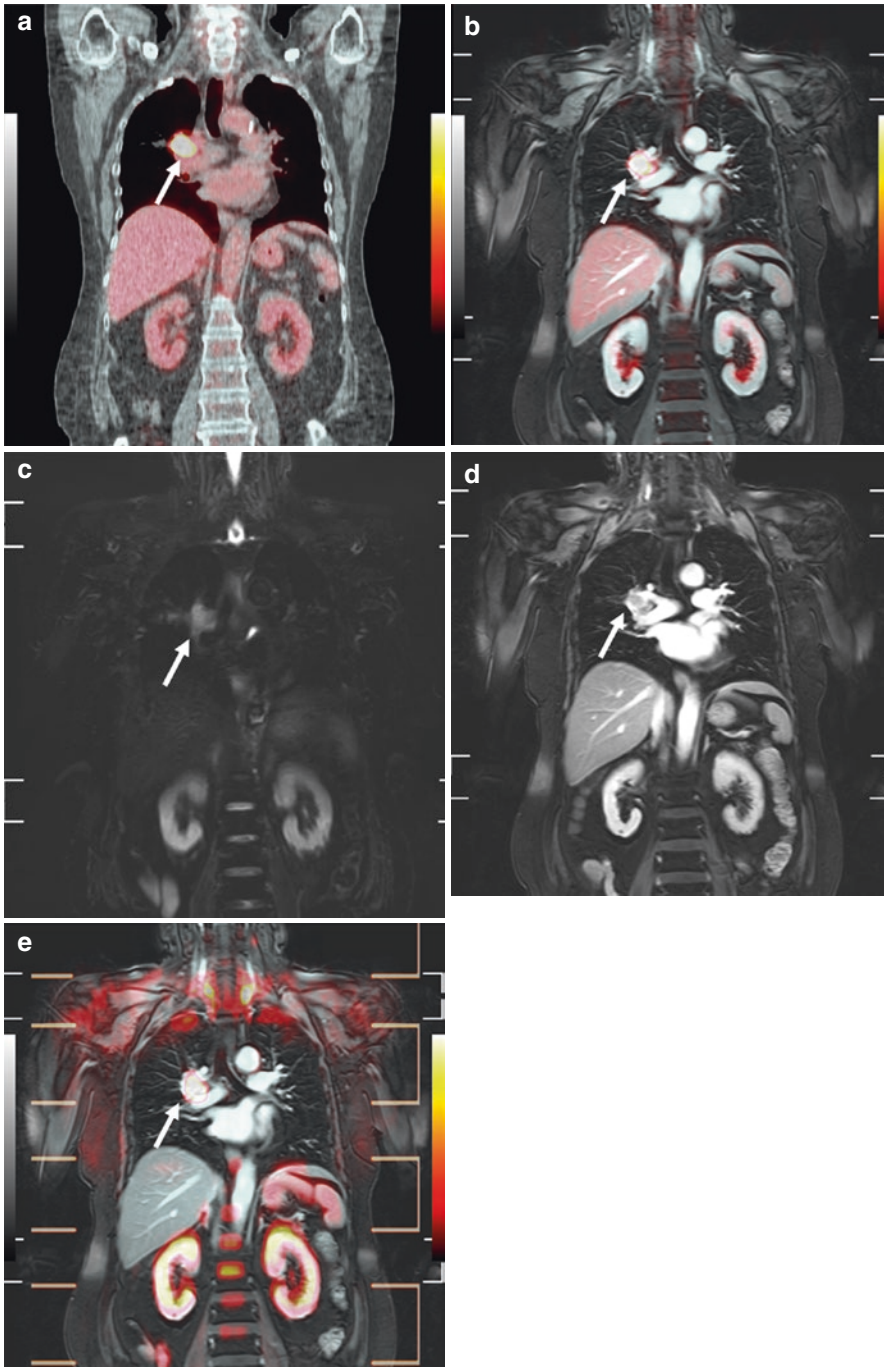
Fig. 6 A 65-year-old female patient with right hilar lymph node metastasis due to squamous cell carcinoma. (**a**) PET/CT shows enlarged right hilar lymph node metastasis (*arrow*) with high FDG uptake. (**b**) PET/MRI, a combination of PET and contrast-enhanced (CE) fast and segmented 3D T1-weighted spoiled GRE (i.e. Quick 3D) sequence data, shows enlarged right hilar lymph node metastasis (*arrow*) with high FDG uptake. (**c**) Whole-body STIR FASE image shows enlarged right hilar lymph node metastasis (*arrow*) as high signal intensity. (**d**) Whole-body contrast-enhanced (CE)-GRE (i.e. Quick 3D) image shows enlarged right hilar lymph node metastasis (*arrow*). (**e**) Whole-body MR image, a combination of diffusion-weighted image (DWI) and CE-Quick 3D data, shows enlarged right hilar lymph node metastasis (*arrow*) with high signal intensity on DWI. With any of these five modalities, this patient was correctly assessed as N1 disease

diffusion gradient inhomogeneities, cardiac and respiratory motion, susceptibility and/or blurring artifacts depending on the sequences used, SAR level, and prolonged examination time, IVIM assessment is considered to be a valid new option for DWI assessment at 3 T for patients with thoracic cancer, and its clinical relevance is anticipated to be validated in the near future.

When considering DWI at 3 T, several of the problematic factors mentioned above are aggravated, depending on acquisition methods, SAR level, and image distortion, when the echo-planar
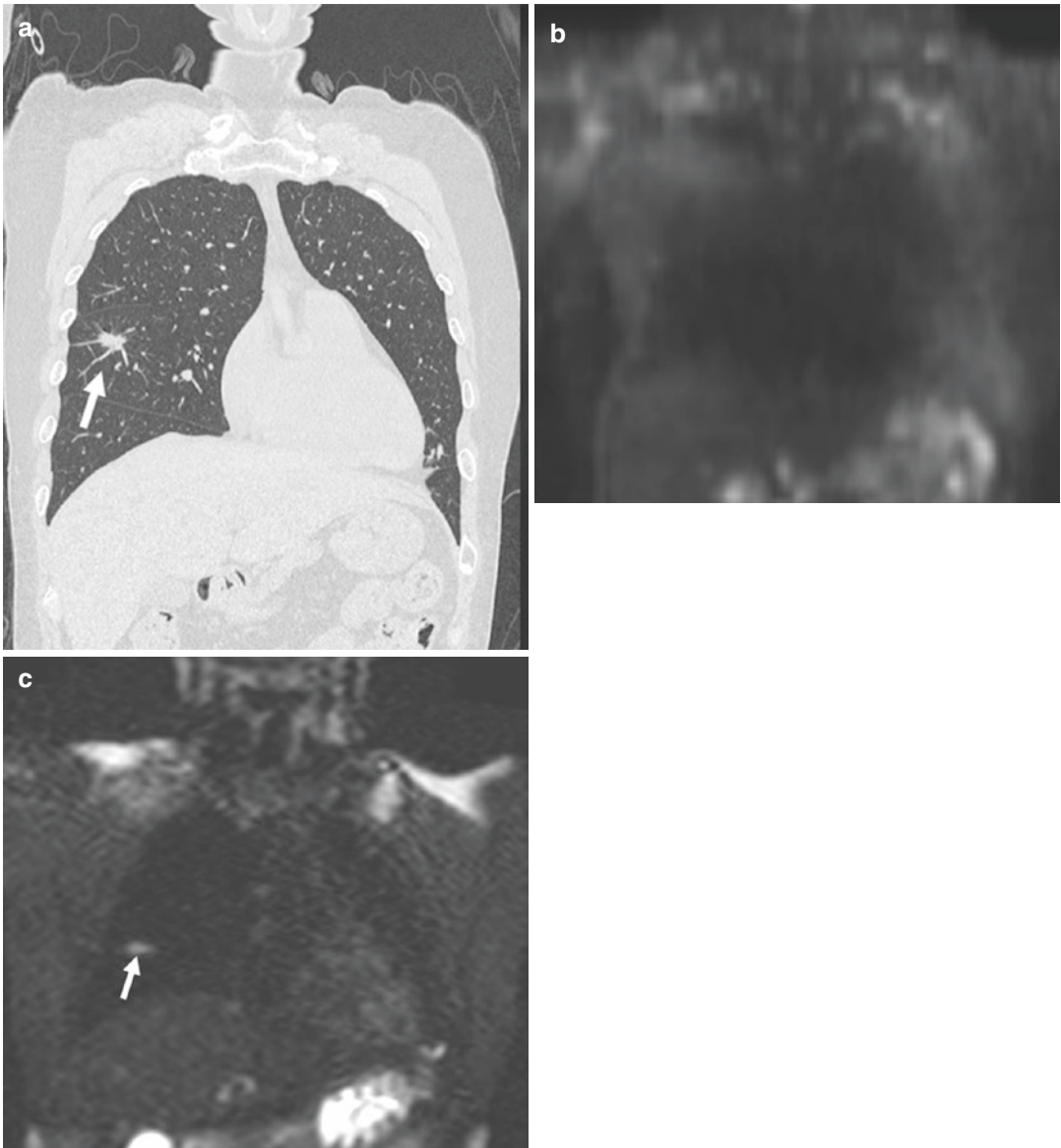
Fig. 7 A 62-year-old female patient with invasive adenocarcinoma. (**a**) Thin-section MPR image at the coronal plane shows a nodule (*arrow*) with spiculae and pleural indentations in the right middle lobe. This nodule was pathologically diagnosed as invasive adenocarcinoma. (**b**) Diffusion-weighted image (DWI) obtained with the echo-planar imaging (EPI) sequence does not show the nodule in the right lung due to severe image distortion and susceptibility artifacts. (**c**) DWI obtained with the fast advanced spin echo (FASE) sequence clearly shows the nodule (*arrow*) as high signal intensity and produced a diagnosis of malignant nodule

imaging (EPI) sequence is used. It has recently been suggested that computed DWI and the multi-shot EPI sequence at 3 T are useful for improving the clinical potential of DWI for other organs (Ueno et al. 2013, 2015; Filli et al. 2016; Rosenkrantz et al. 2016). However, no clear evidence has been presented as yet that these techniques may be useful for lung MR imaging.

DWI acquired by means of the fast advanced spin echo (FASE) sequence was recently suggested as being useful as one of the new DWI techniques that could lead to a new type of DWI at 3 T (Ohno et al. 2015d) (Fig. 7). In this study, the capability for N-stage assessment of STIR, DWI obtained by EPI, and FASE sequences at 3 T systems and FDG PET/CT was directly compared. It was shown that the accuracy of N-stage assessment using STIR (84.2%) and FASE (83.2%) was significantly higher than that with DWI using EPI (76.8%) and PET/CT (73.7%). Therefore, qualitative N-stage assessments of lung cancer patients obtained with DWI using FASE as well as STIR are more sensitive and/or accurate than those obtained with DWI using EPI and FDG PET/CT. DWI using FASE has several advantages and only a few disadvantages in comparison with DWI using EPI and is now beginning to be used in the clinical setting with the 3 T system for thoracic oncologic patients. Therefore, testing new sequences for DWI is now viewed as a challenging field in lung MR imaging using the 3 T system.

3.4 MR Imaging with Ultrashort Echo Time (UTE) and/or TEs

3.4.1 Pulmonary Thin-Section MR Imaging with UTE

Since MR imaging was first put into practice, its usefulness for evaluation of different lung diseases as well as mediastinal and pleural diseases was tested until in the early 1990s, but adequate image quality within reasonable examination time could not be attained. Due to the extremely short T2* of lung parenchyma, which originates from multiple tissue/air interfaces, very low signal intensity (SI) is obtained in the lung when

conventional pulse sequences are utilized (Bergin et al. 1991a, b; Mayo et al. 1992; Müller et al. 1992; Alsop et al. 1995; Hatabu et al. 1999). To overcome this fundamental problem, continuous sequence development as well as MR system improvement, especially with the 1.5 T system, has been tried for chest radiology by means of TSE and/or FSE with short echo time (TE) (Mayo et al. 1992; Müller et al. 1992; Alsop et al. 1995), single-shot half-Fourier TSE and/or FSE (Hatabu et al. 1999), two-dimensional (2D) SSFP with ultrashort repetition time (TR) and echo time (TE) (Failo et al. 2009), and radio-frequency-spoiled 3D fat-suppressed GRE sequences such as volumetric interpolated breath-hold examination (VIBE) (Fink et al. 2007; Ley-Zaporozhan et al. 2010). These studies clearly revealed that the capability for evaluation of lung parenchymal tissues increases as TE becomes shorter (Takahashi et al. 2010) although visualization of lung structures and assessment of radiological findings could not be attained to the same extent as with CT.

Under these circumstances, pulmonary MR imaging with ultrashort echo time (UTE) was introduced, and its capability for qualitative assessment of changes in lung parenchyma has been tested, using not only 1.5 T but also 3 T systems, for patients with lung diseases (Johnson et al. 2013; Ohno et al. 2016a). Projection acquisition of the FID in conjunction with radial readout technically makes it possible to reduce the TE to less than 200 ms, so that signal decay caused by short T2* can be minimized, and produces a higher signal-to-noise ratio (SNR) than that produced by a conventional image sequence with a short TE (c.a., 1–2 ms) (Togao et al. 2010). In addition, the sequence is (relatively) insensitive to the motion that is one of the most difficulties in pulmonary imaging by means of MRI (Takahashi et al. 2010; Ohno et al. 2013b; Ohno et al. 2014b). A few investigators have reported that pulmonary MR imaging with UTE has potential for visualization of lung parenchyma as well as assess radiological findings as is also possible with CT (Johnson et al. 2013; Dournes et al. 2015; Ohno et al. 2016a).

One of these studies directly compared the capability for visualization of lung parenchyma of

pulmonary thin-section MR imaging using ultra-short TE with that of standard- and low-dose thin-section CTs for patients with various pulmonary diseases (Ohno et al. 2016a) (Fig. 8). In this study, interobserver agreement for pulmonary nodules or masses, ground-glass opacities, micronodules, patchy shadows or consolidations, emphysema or bullae, bronchiectasis, reticular opacities, honey-combing, traction bronchiectasis, aneurysms, pericardial or pleural effusion, pleural thickening or tumor, and lymphadenopathy were significant and determined as either "substantial" or "excellent" (standard-dose CT, $0.74 \leq \kappa \leq 0.98$; low-dose CT, $0.73 \leq \kappa \leq 0.98$; pulmonary MR imaging with UTE, $0.66 \leq \kappa \leq 0.94$). On the other hand, inter-method agreements for pulmonary MR imaging with UTE using standard-dose CT and low-dose CT were also significant and determined as "sub-stantial" or "excellent" (versus standard-dose CT, $0.67 \leq \kappa \leq 0.94$; versus low-dose CT, $0.69 \leq \kappa \leq 0.95$), so that these agreements between standard- and low-dose CTs were assessed as significant and excellent ($0.85 \leq \kappa \leq 0.98$). Therefore, pulmonary thin-section MR imaging with ultrashort TE was found to be as reproducible as either type of thin-section CT, and its radiological finding assess-ment capability was considered sufficient to be used in routine clinical practice. Moreover, this study showed there were no significant differ-ences in diagnostic performance among these three methods for patients with lung nodule and/or mass, pulmonary emphysema and/or bullae, interstitial lung disease and/or pulmonary fibrosis, and infectious diseases. The 3 T system theoreti-cally produces more susceptibility artifacts and increases SI from lesions, but has a higher SNR and better image quality in comparison with the 1.5 T system. With regard to the future of lung MR imaging, ultrashort TE sequence will become the basis at 1.5 T and 3 T systems.

3.4.2 Pulmonary MR Imaging with UTEs

In vivo studies, conducted during the last several years and based on the findings from animal and human studies, have indicated that pulmonary MR imaging using UTEs is theoretically capable of assessing signal intensity or changes in T2* values within lung parenchyma due to pulmonary emphysema as well as smoking-related COPD and connective tissue disease (CTD) (Togao et al. 2010, 2011; Takahashi et al. 2010; Ohno et al. 2011, 2013b, 2014b).

Of the few animal studies performed, one showed that the signal intensity and T2* were reduced as the positive end-expiratory pressure increased. Furthermore, these parameters were found to strongly correlate with changes in lung volume (percentage of lung expansion). These findings indicated that the MR signal acquired
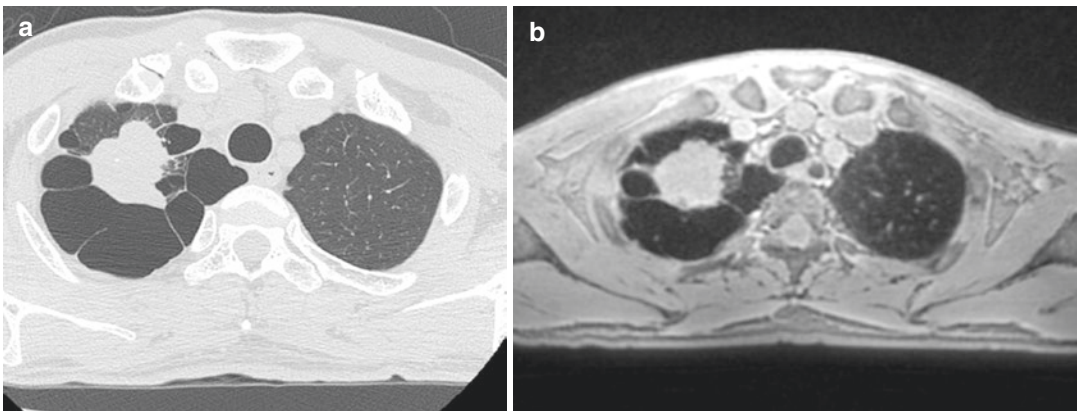
Fig. 8 A 58-year-old male patient with invasive adeno-carcinoma. (**a**) Thin-section CT shows invasive adenocar-cinoma with notches and surrounding bullae. (**b**) Thin-section MR imaging with ultrashort TE less than 200 μsec also shows invasive adenocarcinoma with notches and surrounding bullae. In the left lung, periph-eral pulmonary vasculatures are clearly shown, similar to the result for thin-section CT

with UTE in the lung parenchyma represents interstitial tissue density including blood (Togao et al. 2010). Another study measured the SI and T2* of the lung parenchyma at various echo times (TEs) ranging from 100 μs to 2 ms (Takahashi et al. 2010). The authors demonstrated that the SI of the lung parenchyma was adequate at UTE of 100 μs, thus making measurement of the short T2* in the parenchyma (< 1 ms) feasible with a 3 T system. Moreover, emphysematous lungs could be differentiated from controls due to reduced SIs and T2* in particular at the end-expiratory phase. The results of this study suggest that both SI and T2* in lung parenchyma measured with this method using a UTE of 100 μs represent the fractional volume of lung tissue.

These animal study results prompted us to use this technique for patients with smoking-related COPD and/or interstitial lung disease (ILD) based on connective tissue disease (CTD) for determination of its potential utility for quantitative morphological assessment of the lung parenchyma and the effect of ultrashort echo space in this setting (Ohno et al. 2011, 2013b, 2014b). When ultrashort echo spacing was changed from 0.5 to 1.0 ms and to 1.5 ms, it had a significant effect onto T2* measurements with UTEs, ($p < 0.05$) (Ohno et al. 2014b). In addition, the increase in ultrashort echo spacing showed significant but less correlation between the mean T2* value and CT-based functional lung volume (FLV). The findings of this study also suggested that a shorter ultrashort echo space equal to or less than 1.0 ms had better assessment capability for pulmonary functional loss as well as clinical stage differentiation than the one at 1.5 ms ($p < 0.05$). This study further suggested that inter-ultrashort echo space should be set as short as possible in this setting, which is consistent with the finding of a previous animal study (Takahashi et al. 2010). In addition, two studies showed that quantitative T2* values correlate with pulmonary functional loss and can identify significant differences among clinical stages of smoking-related COPD patients as well as CT-based FLV and that these results are reproducible (Ohno et al. 2011, 2014b).

Another study found that quantitatively assessed T2* values obtained by means of pulmonary MR imaging with UTEs show potential for assessment of pulmonary functional loss and disease severity of CTD patients with ILD (Ohno et al. 2013b). Comparisons of T2* values for normal subjects and these patients showed that the mean T2* values as well as radiological parameters on qualitatively assessed thin-section CT and other clinical parameters, including pulmonary function and blood test results, were significantly different for the two groups (Ohno et al. 2013b). This indicates that this technique may be able to play a complementary role in the management of CTD patients.

The success of MR imaging with UTE at 3 T will have positive implications for the direct assessment of the parenchymal architecture and to assist in the detection of early and localized pathological destruction of lung tissue architecture observed in various pulmonary disorders and to serve as a complement for thin-section CT in the near future.

3.5 Chemical Exchange Saturation Transfer Imaging

Contrast agents are widely used in MR imaging for signal enhancement. They allow for better differentiation between normal or healthy tissue and diseased tissue, as well as better visualization of different structures. Most of the agents in clinical use today are Gd contrast media that shorten the relaxation time of the free water protons. Since these agents are not selective, they distribute uniformly throughout the extracellular space after intravenous injection (Caravan et al. 1999).

In addition to the use of relaxation-based contrast agents, MR imaging offers a variety of contrast techniques based on the intrinsic properties of tissue, such as coupling to neighboring nuclei, chemical exchange saturation transfer, or flow (Vinogradov et al. 2013). Magnetization transfer (MT) contrast applies an off-resonance RF pulse to saturate a broad water signal that lies beneath a sharper bulk water signal in many tissues (Henkelman et al. 2001). This method employs a

technique utilizing saturation transfer (ST) mainly via dipolar exchange and has been widely used to produce modified tissue contrast for MR imaging in clinical settings. In the early 1990s, chemical exchange saturation transfer (CEST) was introduced as a new type of method, which has drawn considerable attention as a novel mechanism to produce modified tissue contrast for MR imaging based upon exchangeable protons (−NH, −OH, −SH, others) on endogenous or exogenous molecules. Since this method is also a technique utilizing ST but via chemical exchange, it uses an RF pulse at a specific frequency so that the target molecule is selectively saturated and the saturation is transferred to the bulk water (Ward et al. 2000a). This method provides more detailed physiological and functional information such as pH (Aime et al. 2002a, b; Zhou et al. 2003a) and metabolite levels (Aime et al. 2002c; Zhang et al. 2003a, b; Van Zijl et al. 2007) than conventional MR imaging and has gained attention in the field of molecular imaging (Sagiyama et al. 2014). This method is a current topic of interest for research using in vivo and in vitro studies into a variety of disorders (Mcmahon et al. 2008; Mcmahon et al. 2008; Jones et al. 2006; Sun et al. 2007a; Ling et al. 2008; Sheth et al. 2012; Togao et al. 2013, 2014; Ohno et al. 2016b).

3.5.1 CEST Mechanism

Exchangeable solute protons (s) that resonate at a frequency different from the bulk water protons (w) are selectively saturated using an RF pulse. This saturation is subsequently transferred to bulk water when exchange of solute protons with water protons occurs (exchange rate) and the water signal becomes slightly attenuated. In view of the low concentration of solute protons (μM to mM range), a single saturation transfer would be insufficient to show any discernable effect on water protons with their concentration of about 110 M. However, because the water pool is much larger than the saturated solute proton pool, each exchanged saturated solute proton is replaced by a non-saturated water proton. If the solute protons have a relatively fast exchange rate (residence time in the millisecond range) and the

saturation time is sufficiently long (in the second range), prolonged irradiation leads to substantial enhancement of the saturation effect, which eventually becomes visible on the water signal, thus allowing for indirect imaging of the presence of low-concentration solutes. These frequency-dependent saturation effects are visualized by plotting the water saturation (S_{sat}) normalized by the signal without saturation (S_0) as a function of saturation frequency. This yields what has been dubbed as Z-spectrum (Bryant et al. 1996) or CEST spectrum. Such a spectrum is assumed to be symmetrical and is characterized by the magnetization transfer ratio (MTR) at each frequency surrounding the water frequency, with 0 ppm assigned to the water frequency. The effect of CEST is addressed by employing the symmetry of the water saturation through an MT ratio asymmetry analysis (Guivel-Scharen et al. 1998) with respect to the water frequency. Such an analysis inherently assumes independent contributions of solute and water protons, which need not be the case, but it is satisfactory as a first approximation. Using the literature definition of MTR ($= 1 - S_{sat}/S_0$), this process is characterized by subtracting MTRs at the negative ($-\Delta\omega$) and positive ($\Delta\omega$) side of frequencies (Guivel-Scharen et al. 1998):

$$MTR_{asym}\left(\Delta\omega\right) = MTR\left(\Delta\omega\right) - MTR\left(-\Delta\omega\right) = S_{sat}\left(-\Delta\omega\right)/S_0 - S_{sat}\left(\Delta\omega\right)/S_0 \quad (4)$$

in which $\Delta\omega$ is the difference in frequency with that of water. It should be noted that this asymmetry analysis is based on an inherent assumption of symmetry of non-CEST contributions around the water signal, which often is incorrect, especially in vivo and also in vitro. Therefore, the magnitude of CEST effect is often determined from the difference of MTR_{asym} at the target tissue (e.g., lesion) and the reference tissue (e.g., normal) in many studies (Togao et al. 2013). Further, similar to MT imaging, it has to be realized that this type of quantification is often difficult to reproduce results in different laboratories because, unless saturation efficiency is 100%, the effect depends on the strength of the applied RF field (B1). This difficulty can be somewhat

ameliorated by taking left/right ratios of the signal attenuation, but doing this complicates quantification in terms of exchange rates and concentrations.

3.5.2 CEST Classification

CEST constitutes a powerful sensitivity enhancement mechanism in which low-concentration solutes can be visualized on the water signal. The enhancement, which depends on the agent proton concentration and the rate of exchange, enables the specific design of agents, constructs, and MRI pulse sequences to optimize the contrast based on the two parameters. CEST is therefore inherently suitable as a molecular and cellular imaging approach and can employ both paramagnetic species (exogenous agents) (Aime et al. 2002a, b; Zhang et al. 2001, 2003a, b) and diamagnetic species (endogenous agents) (Ward et al. 2000a, b; Goffeney et al. 2001; Snoussi et al. 2003; Zhou et al. 2003a, b), which has led to the nomenclature of paraCEST (Zhang et al. 2003b) and diaCEST (Zhou et al. 2006), respectively. This useful classification relates mostly to the size of the chemical shift difference with that of water, which can be greatly enlarged when using paramagnetic shift agents, thereby allowing for much higher exchange rates to be used while maintaining the slow-intermediate MR exchange regime. For diaCEST compounds, the range is generally 0–7 ppm from water (hydroxy [−OH], amine [−NH$_2$], amide [−NH], and imino [−SH] groups, but this can be extended to 18–19 ppm or even much higher (>50 ppm) through hydrogen bonding or exchange of water molecules. With respect to nomenclature, early classifications were made on the basis of molecular size, endogenous occur-

rence, and type of molecular construct (Terreno et al. 2010a, b). In addition, many approaches have been named specifically for the target molecule or mechanism involved by adding CEST to the name, e.g., glycoCEST for glycogen (Van Zijl et al. 2007), gagCEST for glycosaminoglycans (Ling et al. 2008), and lipoCEST for liposomes (Aime et al. 2005). As many of the proposed methods target the same exchange groups, it probably would have been more appropriate to use a different nomenclature based on the type of exchange group, i.e., glycoCEST (i.e., −OH group), gagCEST (i.e., −OH and/or –NH groups), gluCEST (−NH$_2$ group), and APT (−CONH$_2$ group). These methods are summarized in Table 2. However, there is overlap between the types since there are both macromolecular and liposome applications for paraCEST and diaCEST agents and many of the same approaches can be applied to either group. An additional issue is that saturation transfer is only one of many possible magnetic label-transfer approaches and that the "CEST" nomenclature for the agents is technically incorrect. Although a classification based on the exchange mechanism, namely, atomic (protonic) exchange, molecular exchange, and compartmental exchange, is suggested, only atomic (protonic) exchange has been tested not only for the brain but also other organs including the thorax (Togao et al. 2014; Yuan et al. 2014; Donahue et al. 2016; Ohno et al. 2016b).

3.5.3 Amide Proton Transfer (APT)

Amide proton transfer (APT) imaging is one subset of CEST imaging that applies specifically to the chemical exchange between protons of free tissue water (bulk water) and amide

Table 2 Examples of endogenous diaCEST contrast, exchange groups, off-resonance values, and exchange rates. The exchange rates are approximate and may strongly depend on physiological conditions such as pH and temperature

Type	Target	Exchange group	Exchange rate	Off resonance (ppm)
glycoCEST	Glycogen	−OH	>10^3/s	0.5–1.5
gagCEST	Glycosaminoglycan	−OH	>10^3/s	0.9–1.9
		−NH	10–30/s	3.2
gluCEST	Glutamate	−NH$_2$	5500/s	3
APT	Intracellular proteins, pH	−CONH$_2$	10–200/s	3.5

Modification of Table 1 in Vinogradov et al. (2013)

(−NH) groups. It is assumed that amide protons of endogenous mobile proteins and peptides in the cytoplasm are the major source of the APT signal (Zhou et al. 2003b) in tissues. This assumption was supported by the finding of a nuclear magnetic resonance (NMR) study reporting that the amide protons of mobile protein/peptide side chains (Gln, Asn) and backbone amides resonate at 6.8 ppm and 8.2–8.4 ppm (2.1 ppm and 3.5–3.7 ppm downfield of water resonance), respectively (Van Zijl et al. 2003). The APT effect strongly correlates with pH because proton exchange in –NH groups slows dramatically with a decrease in pH (Vinogradov et al. 2013). The relation between the pH and the CEST effect (MTR_{asym}) can be expressed in the equation, which was derived using phosphorus spectroscopy to determine intracellular pH values:

$$pH = 9.4 + \log\left[MTR_{asym}\Big/5.73\right] \qquad (5)$$

Many studies have used APT imaging to study ischemia in animal as well as human stroke studies (Zhou et al. 2003a, 2011; Sun et al. 2007a, b).

It has also been reported that such exchangeable protons are more abundant in tumor tissues than in healthy tissues (Zhou et al. 2003a, b). When applied to rats implanted with 9 L gliosarcoma tumors in brain, APT imaging could distinguish between pathology-confirmed regions of tumor and tissue edema, whereas standard T1W, T2W, and FLAIR imaging or DWI could not. Other previous studies have demonstrated that the APT signal increased by 3–4% in tumor compared to peritumoral brain tissue in an experimental rat glial tumor at 4.7 T (Van Zijl et al. 2003) and human brain tumor at 3 T (Gillies et al. 2000). Another study in patients with diffuse glioma showed that the APT signal increased with the WHO grade (II to IV) and clearly distinguished low-grade (II) from high-grade (III and IV) tumors (Togao et al. 2014).

Although the method is sensitive to motion and B0 inhomogeneity, a few studies have applied APT imaging to the thorax. Togao et al. conducted an animal study and reported that APT imaging can be used to quantify lung tumors in the moving lung. They reported that the measured APT effect was higher in tumors which exhibited more active proliferation than others and suggested that APT imaging has the potential to serve as a characterization test to differentiate types or grade of lung cancer noninvasively, which may eventually reduce the need for invasive needle biopsy or resection for lung cancer (Togao et al. 2013). In addition, we demonstrated the potential of APT imaging for the differentiation of malignant from benign thoracic lesions as well as distinguishing squamous cell carcinoma from adenocarcinoma when using the threshold values of MTR_{asym} at 3.5 ppm (Ohno et al. 2016a, b). This indicates that CEST imaging may serve as a new MR-based molecular imaging technique, although further investigations are warranted to confirm its potential (Fig. 9).

Conclusion

Although the 3 T MR system entails some theoretical differences, difficulties, and drawbacks for lung MR imaging as compared with the 1.5 T MR system, technical advancements as well as applications of new MR techniques make lung MR imaging at 3 T more attractive for clinical and academic purposes. In addition, continuous efforts by basic and clinical researchers as well as various manufacturers will open new fields for lung MRI, provide answers to basic and clinical needs through new and less invasive methods, and demonstrate the clinical significance of MRI of the lung at 3 T for patients with a wide range of thoracic diseases.
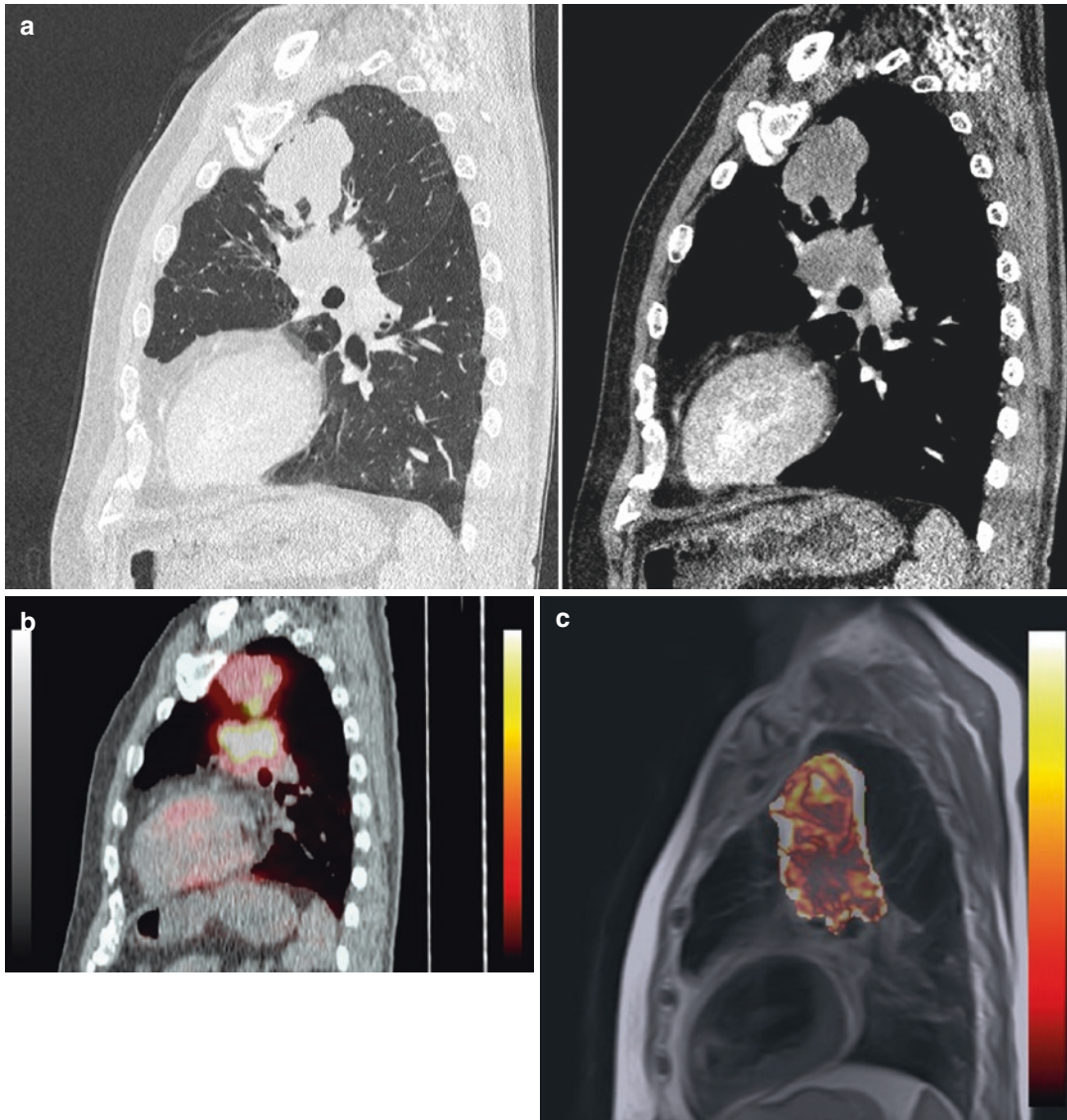
Fig. 9 A 72-year-old male patient with squamous cell carcinoma and left hilar lymph node metastasis. (**a**) Thin-section MPR images (L to R: lung window to mediastinal window setting) at the sagittal plane show primary lesion with left hilar lymph node metastasis. (**b**) PET/CT at the sagittal plane shows primary lesion and lymph node metastasis as high FDG uptakes. (**c**) CEST image at the sagittal plane shows primary lesion and lymph node metastasis as heterogeneous and high MTR_{asym}

References

Aime S, Barge A, Delli Castelli D, Fedeli F, Mortillaro A, Nielsen FU, Terreno E (2002a) Paramagnetic lanthanide(III) complexes as pH-sensitive chemical exchange saturation transfer (CEST) contrast agents for MRI applications. Magn Reson Med 47:639–648

Aime S, Delli Castelli D, Terreno E (2002b) Novel pH-reporter MRI contrast agents. Angew Chem Int Ed Eng 41:4334–4336

Aime S, Delli Castelli D, Fedeli F, Terreno E (2002c) A paramagnetic MRI-CEST agent responsive to lactate concentration. J Am Chem Soc 124:9364–9365

Aime S, Delli Castelli D, Terreno E (2005) Highly sensitive MRI chemical exchange saturation transfer agents using liposomes. Angew Chem Int Ed Eng 44:5513–5515

Albert TS, Akahane M, Parienty I, Yellin N, Catalá V, Alomar X, Prot A, Tomizawa N, Xue H, Katabathina VS, Lopera JE, Jin Z (2015) An international multi-center comparison of time-SLIP unenhanced MR angiography and contrast-enhanced CT angiography for assessing renal artery stenosis: the renal artery contrast-free trial. AJR Am J Roentgenol 204:182–188

Alsop DC, Hatabu H, Bonnet M, Listerud J, Gefter W (1995) Multi-slice, breathhold imaging of the lung with submillisecond echo times. Magn Reson Med 33:678–682

Bauman G, Scholz A, Rivoire J, Terekhov M, Friedrich J, de Oliveira A, Semmler W, Schreiber LM, Puderbach M (2013a) Lung ventilation- and perfusion-weighted Fourier decomposition magnetic resonance imaging: in vivo validation with hyperpolarized 3He and dynamic contrast-enhanced MRI. Magn Reson Med 69:229–237

Bauman G, Puderbach M, Heimann T, Kopp-Schneider A, Fritzsching E, Mall MA, Eichinger M (2013b) Validation of Fourier decomposition MRI with dynamic contrast-enhanced MRI using visual and automated scoring of pulmonary perfusion in young cystic fibrosis patients. Eur J Radiol 82:2371–2377

Bergin CJ, Pauly JM, Macovski A (1991a) Lung parenchyma: projection reconstruction MR imaging. Radiology 179:777–781

Bergin CJ, Glover GH, Pauly JM (1991b) Lung parenchyma: magnetic susceptibility in MR imaging. Radiology 180:845–848

Bottomley PA, Andrew ER (1978) RF magnetic field penetration, phase shift and power dissipation in biological tissue: implications for NMR imaging. Phys Med Biol 23:630–643

Bryant RG (1996) The dynamics of water-protein interactions. Annu Rev Biophys Biomol Struct 25:29–53

Buhaescu I, Izzedine H (2008) Gadolinium-induced nephrotoxicity. Int J Clin Pract 62:1113–1118

Caravan P, Ellison JJ, McMurry TJ, Lauffer RB (1999) Gadolinium(III) chelates as MRI contrast agents: structure, dynamics, and applications. Chem Rev 99:22932–22352

Carr HY (1958) Steady-state free precession in nuclear magnetic resonance. Phys Rev 112:1693–1701

De León-Rodríguez LM, Martins AF, Pinho MC, Rofsky NM, Sherry AD (2015) Basic MR relaxation mechanisms and contrast agent design. J Magn Reson Imaging 42:545–565

Donahue MJ, Donahue PC, Rane S, Thompson CR, Strother MK, Scott AO, Smith SA (2016) Assessment of lymphatic impairment and interstitial protein accumulation in patients with breast cancer treatment-related lymphedema using CEST MRI. Magn Reson Med 75:345–355

Dournes G, Grodzki D, Macey J, Girodet PO, Fayon M, Chateil JF, Montaudon M, Berger P, Laurent F (2015) Quiet Submillimeter MR Imaging of the Lung Is Feasible with a PETRA Sequence at 1.5 T. Radiology 276:258–265

Duewell SH, Ceckler TL, Ong K, Wen H, Jaffer FA, Chesnick SA, Balaban RS (1995) Musculoskeletal MR imaging at 4 T and at 1.5 T: comparison of relaxation times and image contrast. Radiology 196:551–555

Duewell S, Wolff SD, Wen H, Balaban RS, Jezzard P (1996) MR imaging contrast in human brain tissue: assessment and optimization at 4 T. Radiology 199:780–786

Dumoulin CL, Souza SP, Walker MF, Wagle W (1989) Three-dimensional phase contrast angiography. Magn Reson Med 9:139–149

Dumoulin CL, Yucel EK, Vock P, Souza SP, Terrier F, Steinberg FL, Wegmuller H (1990) Two- and three-dimensional phase contrast MR angiography of the abdomen. J Comput Assist Tomogr 14:779–784

Edelman RR, Siewert B, Adamis M, Gaa J, Laub G, Wielopolski P (1994) Signal targeting with alternating radiofrequency (STAR) sequences: application to MR angiography. Magn Reson Med 31:233–238

Failo R, Wielopolski PA, Tiddens HA, Hop WC, Mucelli RP, Lequin MH (2009) Lung morphology assessment using MRI: a robust ultra-short TR/TE 2D steady state free precession sequence used in cystic fibrosis patients. Magn Reson Med 61:299–306

Fernandez-Seara MA, Wehrli FW (2000) Postprocessing technique to correct for background gradients in image-based $R^*(2)$ measurements. Magn Reson Med 44:358–366

Filli L, Ghafoor S, Kenkel D, Liu W, Weiland E, Andreisek G, Frauenfelder T, Runge VM, Boss A (2016) Simultaneous multi-slice readout-segmented echo planar imaging for accelerated diffusion-weighted imaging of the breast. Eur J Radiol 85:274–278

Fink C, Puderbach M, Biederer J, Fabel M, Dietrich O, Kauczor HU, Reiser MF, Schönberg SO (2007) Lung MRI at 1.5 and 3 Tesla: observer preference study and lesion contrast using five different pulse sequences. Investig Radiol 42:377–383

Frydrychowicz A, Russe MF, Bock J, Stalder AF, Bley TA, Harloff A, Markl M (2010) Comparison of gadofosveset trisodium and gadobenate dimeglumine during time-resolved thoracic MR angiography at 3 T. Acad Radiol 17:1394–1400

Gillies RJ, Bhujwalla ZM, Evelhoch J, Garwood M, Neeman M, Robinson SP, Sotak CH, Van Der Sanden B (2000) Applications of magnetic resonance in model systems: tumor biology and physiology. Neoplasia 2:139–151

Goffeney N, Bulte JW, Duyn J, Bryant LH Jr, van Zijl PC (2001) Sensitive NMR detection of cationic-polymer-based gene delivery systems using saturation transfer via proton exchange. J Am Chem Soc 123:8628–8629

Guivel-Scharen V, Sinnwell T, Wolff SD, Balaban RS (1998) Detection of proton chemical exchange between metabolites and water in biological tissues. J Magn Reson 133:36–45

Hatabu H, Gaa J, Tadamura E, Edinburgh KJ, Stock KW, Garpestad E, Edelman RR (1999) MR imaging of pul-

monary parenchyma with a half-Fourier single-shot turbo spin-echo (HASTE) sequence. Eur J Radiol 29:152–159

Hatabu H, Tadamura E, Prasad PV, Chen Q, Buxton R, Edelman RR (2000) Noninvasive pulmonary perfusion imaging by STAR-HASTE sequence. Magn Reson Med 44:808–812

Henkelman RM, Stanisz GJ, Graham SJ (2001) Magnetization transfer in MRI: a review. NMR Biomed 14:57–64

Heusch P, Buchbender C, Köhler J, Nensa F, Gauler T, Gomez B, Reis H, Stamatis G, Kühl H, Hartung V, Heusner TA (2014) Thoracic staging in lung cancer: prospective comparison of 18F-FDG PET/MR imaging and 18F-FDG PET/CT. J Nucl Med 55:373–378

Jezzard P, Duewell S, Balaban RS (1996) MR relaxation times in human brain: measurement at 4 T. Radiology 199:773–779

Johnson KM, Fain SB, Schiebler ML, Nagle S (2013) Optimized 3D ultrashort echo time pulmonary MRI. Magn Reson Med 70:1241–1250

Jones CK, Schlosser MJ, van Zijl PC, Pomper MG, Golay X, Zhou J (2006) Amide proton transfer imaging of human brain tumors at 3 T. Magn Reson Med 56:585–592

Kjørstad Å, Corteville DM, Fischer A, Henzler T, Schmid-Bindert G, Zöllner FG, Schad LR (2014) Quantitative lung perfusion evaluation using Fourier decomposition perfusion MRI. Magn Reson Med 72:558–562

Kurata Y, Kido A, Fujimoto K, Kiguchi K, Takakura K, Moribata Y, Shitano F, Himoto Y, Fushimi Y, Okada T, Togashi K (2016) Optimization of non-contrast-enhanced MR angiography of the renal artery with three-dimensional balanced steady-state free-precession and time-spatial labeling inversion pulse (time-SLIP) at 3 T MRI, in relation to age and blood velocity. Abdom Radiol (NY) 41:119–126

Laub GA (1995) Time-of-flight method of MR angiography. Magn Reson Imaging Clin N Am 3:391–398

Lauffer RB (1990) Magnetic resonance contrast media: principles and progress. Magn Reson Q 6:65–84

Ley-Zaporozhan J, Ley S, Eberhardt R, Kauczor HU, Heussel CP (2010) Visualization of morphological parenchymal changes in emphysema: comparison of different MRI sequences to 3D-HRCT. Eur J Radiol 73:43–49

Ling W, Regatte RR, Navon G, Jerschow A (2008) Assessment of glycosaminoglycan concentration in vivo by chemical exchange-dependent saturation transfer (gagCEST). Proc Natl Acad Sci U S A 105:2266–2270

Londy FJ, Lowe S, Stein PD, Weg JG, Eisner RL, Leeper KV, Woodard PK, Sostman HD, Jablonski KA, Fowler SE, Hales CA, Hull RD, Gottschalk A, Naidich DP, Chenevert TL (2012) Comparison of 1.5 and 3.0 T for contrast-enhanced pulmonary magnetic resonance angiography. Clin Appl Thromb Hemost 18:134–139

Ludeke KM, Roschmann P, Tischler R (1985) Susceptibility artefacts in NMR imaging. Magn Reson Imaging 3:329–343

Masaryk TJ, Laub GA, Modic MT, Ross JS, Haacke EM (1990) Carotid-CNS MR flow imaging. Magn Reson Med 14:308–314

Mayo JR, MacKay A, Müller NL (1992) MR imaging of the lungs: value of short TE spin-echo pulse sequences. AJR Am J Roentgenol 159:951–956

McMahon MT, Gilad AA, DeLiso MA, Berman SM, Bulte JW, van Zijl PC (2008) New "multicolor" polypeptide diamagnetic chemical exchange saturation transfer (DIACEST) contrast agents for MRI. Magn Reson Med 60:803–812

Miyazaki M, Sugiura S, Tateishi F, Wada H, Kassai Y, Abe H (2000) Non-contrast-enhanced MRA using 3D ECG-synchronized half-Fourier fast spin echo. J Magn Reson Imaging 12:776–783

Miyazaki M, Takai H, Sugiura S, Wada H, Kuwahara R, Urata J (2003) Peripheral MR angiography: separation of arteries from veins with flow-spoiled gradient pulses in electrocardiography-triggered three-dimensional half-Fourier fast spin-echo imaging. Radiology 227:890–896

Miyazaki M, Akahane M (2012) Non-contrast enhanced MR angiography: established techniques. J Magn Reson Imaging 35:1–19

Müller NL, Mayo JR, Zwirewich CV (1992) Value of MR imaging in the evaluation of chronic infiltrative lung diseases: comparison with CT. AJR Am J Roentgenol 158:1205–1209

Nayak KS, Cunningham CH, Santos JM, Pauly JM (2004) Real-time cardiac MRI at 3 tesla. Magn Reson Med 51:655–660

Nishimura DG, Macovski A, Pauly JM, Conolly SM (1987) MR angiography by selective inversion recovery. Magn Reson Med 4:193–202

Noeske R, Seifert F, Rhein KH, Rinneberg H (2000) Human cardiac imaging at 3 T using phased array coils. Magn Reson Med 4:978–982

Ohno Y, Koyama H, Nogami M, Takenaka D, Yoshikawa T, Yoshimura M, Kotani Y, Nishimura Y, Higashino T, Sugimura K (2007) Whole-body MR imaging vs FDG-PET: comparison of accuracy of M-stage diagnosis for lung cancer patients. J Magn Reson Imaging 26:498–509

Ohno Y, Koyama H, Onishi Y, Takenaka D, Nogami M, Yoshikawa T, Matsumoto S, Kotani Y, Sugimura K (2008) Non-small cell lung cancer: whole-body MR examination for M-stage assessment--utility for whole-body diffusion-weighted imaging compared with integrated FDG PET/CT. Radiology 248:643–654

Ohno Y, Koyama H, Yoshikawa T, Matsumoto K, Takahashi M, Van Cauteren M, Sugimura K (2011) T2* measurements of 3-T MRI with ultrashort TEs: capabilities of pulmonary function assessment and clinical stage classification in smokers. AJR Am J Roentgenol 197:W279–W285

Ohno Y, Nishio M, Koyama H, Yoshikawa T, Matsumoto S, Takenaka D, Seki S, Tsubakimoto M, Sugimura K (2013a) Comparison of the utility of whole-body MRI with and without contrast-enhanced Quick 3D and

double RF fat suppression techniques, conventional whole-body MRI, PET/CT and conventional examination for assessment of recurrence in NSCLC patients. Eur J Radiol 82:2018–2027

Ohno Y, Nishio M, Koyama H, Takenaka D, Takahashi M, Yoshikawa T, Matsumoto S, Obara M, van Cauteren M, Sugimura K (2013b) Pulmonary MR imaging with ultra-short TEs: utility for disease severity assessment of connective tissue disease patients. Eur J Radiol 82:1359–1365

Ohno Y, Nishio M, Koyama H, Yoshikawa T, Matsumoto S, Seki S, Sugimura K (2014a) Journal Club: Comparison of assessment of preoperative pulmonary vasculature in patients with non-small cell lung cancer by non-contrast- and 4D contrast-enhanced 3-T MR angiography and contrast-enhanced 64-MDCT. AJR Am J Roentgenol 202:493–506

Ohno Y, Nishio M, Koyama H, Yoshikawa T, Matsumoto S, Seki S, Obara M, van Cauteren M, Takahashi M, Sugimura K (2014b) Pulmonary 3 T MRI with ultra-short TEs: influence of ultrashort echo time interval on pulmonary functional and clinical stage assessments of smokers. J Magn Reson Imaging 39:988–997

Ohno T, Isoda H, Furuta A, Togashi K (2015a) Non-contrast-enhanced MR portography and hepatic venography with time-spatial labeling inversion pulses: comparison at 1.5 Tesla and 3 Tesla. Acta Radiol Open 4: 2058460115584110

Ohno Y, Seki S, Koyama H, Yoshikawa T, Matsumoto S, Takenaka D, Kassai Y, Yui M, Sugimura K (2015b) 3D ECG- and respiratory-gated non-contrast-enhanced (CE) perfusion MRI for postoperative lung function prediction in non-small-cell lung cancer patients: a comparison with thin-section quantitative computed tomography, dynamic CE-perfusion MRI, and perfusion scan. J Magn Reson Imaging 42:340–353

Ohno Y, Koyama H, Yoshikawa T, Takenaka D, Seki S, Yui M, Yamagata H, Aoyagi K, Matsumoto S, Sugimura K (2015c) Three-way Comparison of Whole-Body MR, Coregistered Whole-Body FDG PET/MR, and Integrated Whole-Body FDG PET/CT Imaging: TNM and Stage Assessment Capability for Non-Small Cell Lung Cancer Patients. Radiology 275:849–861

Ohno Y, Koyama H, Yoshikawa T, Takenaka D, Kassai Y, Yui M, Matsumoto S, Sugimura K (2015d) Diffusion-weighted MR imaging using FASE sequence for 3 T MR system: preliminary comparison of capability for N-stage assessment by means of diffusion-weighted MR imaging using EPI sequence, STIR FASE imaging and FDG PET/CT for non-small cell lung cancer patients. Eur J Radiol 84:2321–2331

Ohno Y, Koyama H, Yoshikawa T, Seki S, Takenaka D, Yui M, Lu A, Miyazaki M, Sugimura K (2016a) Pulmonary high-resolution ultrashort TE MR imaging: comparison with thin-section standard- and low-dose computed tomography for the assessment of pulmonary parenchyma diseases. J Magn Reson Imaging 43:512–532

Ohno Y, Yui M, Koyama H, Yoshikawa T, Seki S, Ueno Y, Miyazaki M, Ouyang C, Sugimura K (2016b) Chemical exchange saturation transfer MR imaging: preliminary results for differentiation of malignant and benign thoracic lesions. Radiology 279:578–589

Prince MR (1994) Gadolinium-enhanced MR aortography. Radiology 191:155–164

Pruessmann KP, Weiger M, Scheidegger MB, Boesiger P (1999) SENSE: sensitivity encoding for fast MRI. Magn Reson Med 42:952–962

Rakow-Penner R, Daniel B, Yu H, Sawyer-Glover A, Glover GH (2006) Relaxation times of breast tissue at 1.5 T and 3 T measured using IDEAL. J Magn Reson Imaging 23:87–91

Roberts DA, Gefter WB, Hirsch JA, Rizi RR, Dougherty L, Lenkinski RE, Leigh JS Jr, Schnall MD (1999) Pulmonary perfusion: respiratory-triggered three-dimensional MR imaging with arterial spin tagging-preliminary results in healthy volunteers. Radiology 212:890–895

Rosenkrantz AB, Parikh N, Kierans AS, Kong MX, Babb JS, Taneja SS, Ream JM (2016) Prostate cancer detection using computed very high b-value diffusion-weighted imaging: How High Should We Go? Acad Radiol 23:704–711

Sagiyama K, Mashimo T, Togao O, Vemireddy V, Hatanpaa KJ, Maher EA, Mickey BE, Pan E, Sherry AD, Bachoo RM, Takahashi M (2014) In vivo chemical exchange saturation transfer imaging allows early detection of a therapeutic response in glioblastoma. Proc Natl Acad Sci U S A 111:4542–4547

Schaarschmidt BM, Buchbender C, Nensa F, Grueneisen J, Gomez B, Köhler J, Reis H, Ruhlmann V, Umutlu L, Heusch P (2015) Correlation of the apparent diffusion coefficient (ADC) with the standardized uptake value (SUV) in lymph node metastases of non-small cell lung cancer (NSCLC) patients using hybrid 18F-FDG PET/MRI. PLoS One 10:e0116277

Schaarschmidt BM, Grueneisen J, Metzenmacher M, Gomez B, Gauler T, Roesel C, Heusch P, Ruhlmann V, Umutlu L, Antoch G, Buchbender C (2016) Thoracic staging with F-FDG PET/MR in non-small cell lung cancer – does it change therapeutic decisions in comparison to F-FDG PET/CT? Eur Radiol. [Epub ahead of print]

Scheffler K, Lehnhardt S (2003) Principles and applications of balanced SSFP techniques. Eur Radiol 13:2409–2418

Schönfeld C, Cebotari S, Voskrebenzev A, Gutberlet M, Hinrichs J, Renne J, Hoeper MM, Olsson KM, Welte T, Wacker F, Vogel-Claussen J (2015) Performance of perfusion-weighted Fourier decomposition MRI for detection of chronic pulmonary emboli. J Magn Reson Imaging 42:72–79

Sheth VR, Li Y, Chen LQ, Howison CM, Flask CA, Pagel MD (2012) Measuring in vivo tumor pHe with CEST-FISP MRI. Magn Reson Med 67:760–768

Sodickson DK, Manning WJ (1997) Simultaneous acquisition of spatial harmonics (SMASH): fast imaging

with radiofrequency coil arrays. Magn Reson Med 38:591–603

Sommer G, Wiese M, Winter L, Lenz C, Klarhöfer M, Forrer F, Lardinois D, Bremerich J (2012) Preoperative staging of non-small-cell lung cancer: comparison of whole-body diffusion-weighted magnetic resonance imaging and 18F–fluorodeoxyglucose-positron emission tomography/computed tomography. Eur Radiol 22:2859–2867

Sommer G, Bauman G, Koenigkam-Santos M, Draenkow C, Heussel CP, Kauczor HU, Schlemmer HP, Puderbach M (2013) Non-contrast-enhanced preoperative assessment of lung perfusion in patients with non-small-cell lung cancer using Fourier decomposition magnetic resonance imaging. Eur J Radiol 82:e879 e8–87

Snoussi K, Bulte JW, Guéron M, van Zijl PC (2003) Sensitive CEST agents based on nucleic acid imino proton exchange: detection of poly(rU) and of a dendrimer-poly(rU) model for nucleic acid delivery and pharmacology. Magn Reson Med 49:998–1005

Stanisz GJ, Odrobina EE, Pun J, Escaravage M, Graham SJ, Bronskill MJ, Henkelman RM (2005) T1, T2 relaxation and magnetization transfer in tissue at 3 T. Magn Reson Med 54:507–512

Stuber M, Börnert P, Spuentrup E, Botnar RM, Manning WJ (2002) Selective three-dimensional visualization of the coronary arterial lumen using arterial spin tagging. Magn Reson Med 47:322–329

Sun PZ, Zhou J, Sun W, Huang J, van Zijl PC (2007a) Detection of the ischemic penumbra using pH-weighted MRI. J Cereb Blood Flow Metab 27:1129–1136

Sun PZ, Zhou J, Huang J, van Zijl P (2007b) Simplified quantitative description of amide proton transfer (APT) imaging during acute ischemia. Magn Reson Med 57:405–410

Takahashi M, Tsutsui H, Murayama C, Miyazawa T, Fritz-Zieroth B (1996) Neurotoxicity of gadolinium contrast agents for magnetic resonance imaging in rats with osmotically disrupted blood-brain barrier. Magn Reson Imaging 14:619–623

Takahashi M, Wehrli FW, Hwang SN, Wehrli SL (2000) Relationship between cancellous bone induced magnetic field and ultrastructure in a rat ovariectomy model. Magn Reson Imaging 18:33–39

Takahashi M, Uematsu H, Hatabu H (2003) MR imaging at high magnetic fields. Eur J Radiol 46:45–52

Takahashi M, Togao O, Obara M, van Cauteren M, Ohno Y, Doi S, Kuro-o M, Malloy C, Hsia CC, Dimitrov I (2010) Ultra-short echo time (UTE) MR imaging of the lung: comparison between normal and emphysematous lungs in mutant mice. J Magn Reson Imaging 32:326–333

Takenaka D, Ohno Y, Matsumoto K, Aoyama N, Onishi Y, Koyama H, Nogami M, Yoshikawa T, Matsumoto S, Sugimura K (2009) Detection of bone metastases in non-small cell lung cancer patients: comparison of whole-body diffusion-weighted imaging (DWI), whole-body MR imaging without and with DWI,

whole-body FDG-PET/CT, and bone scintigraphy. J Magn Reson Imaging 30:298–308

Terreno E, Castelli DD, Aime S (2010a) Encoding the frequency dependence in MRI contrast media: the emerging class of CEST agents. Contrast Media Mol Imaging 5:78–98

Terreno E, Castelli DD, Viale A, Aime S (2010b) Challenges for molecular magnetic resonance imaging. Chem Rev 110:3019–3042

Togao O, Tsuji R, Ohno Y, Dimitrov I, Takahashi M (2010) Ultrashort echo time (UTE) MRI of the lung: assessment of tissue density in the lung parenchyma. Magn Reson Med 64:1491–1498

Togao O, Ohno Y, Dimitrov I, Hsia CC, Takahashi M (2011) Ventilation/perfusion imaging of the lung using ultra-short echo time (UTE) MRI in an animal model of pulmonary embolism. J Magn Reson Imaging 34:539–546

Togao O, Kessinger CW, Huang G, Soesbe TC, Sagiyama K, Dimitrov I, Sherry AD, Gao J, Takahashi M (2013) Characterization of lung cancer by amide proton transfer (APT) imaging: an in-vivo study in an orthotopic mouse model. PLoS One 8:e77019

Togao O, Yoshiura T, Keupp J, Hiwatashi A, Yamashita K, Kikuchi K, Suzuki Y, Suzuki SO, Iwaki T, Hata N, Mizoguchi M, Yoshimoto K, Sagiyama K, Takahashi M, Honda H (2014) Amide proton transfer imaging of adult diffuse gliomas: correlation with histopathological grades. Neuro-Oncology 16:441–448

Uematsu H, Dougherty L, Takahashi M, Ohno Y, Nakatsu M, Song HK, Ferrari VA, Gefter WB, Schnall MD, Hatabu H (2001) Pulmonary MR angiography with contrast agent at 4 Tesla: a preliminary result. Magn Reson Med 46:1028–1030

Ueno Y, Takahashi S, Kitajima K, Kimura T, Aoki I, Kawakami F, Miyake H, Ohno Y, Sugimura K (2013) Computed diffusion-weighted imaging using 3-T magnetic resonance imaging for prostate cancer diagnosis. Eur Radiol 23:3509–3516

Ueno Y, Takahashi S, Ohno Y, Kitajima K, Yui M, Kassai Y, Kawakami F, Miyake H, Sugimura K (2015) Computed diffusion-weighted MRI for prostate cancer detection: the influence of the combinations of b-values. Br J Radiol 88:20140738

Urata J, Miyazaki M, Wada H, Nakaura T, Yamashita Y, Takahashi M (2001) Clinical evaluation of aortic diseases using nonenhanced MRA with ECG-triggered 3D half-Fourier FSE. J Magn Reson Imaging 14:113–119

van Zijl PC, Zhou J, Mori N, Payen JF, Wilson D, Mori S (2003) Mechanism of magnetization transfer during on-resonance water saturation. A new approach to detect mobile proteins, peptides, and lipids. Magn Reson Med 49:440–449

van Zijl PC, Jones CK, Ren J, Malloy CR, Sherry AD (2007) MRI detection of glycogen in vivo by using chemical exchange saturation transfer imaging (glycoCEST). Proc Natl Acad Sci U S A 104:4359–4364

Van der Elst L, Laurent S, Muller RN (1998) Multinuclear magnetic resonance characterization of paramagnetic

contrast agents. The manifold effects of concentration and counterions. Invest Radiol 33:828–834

Vinogradov E, Sherry AD, Lenkinski RE (2013) CEST: from basic principles to applications, challenges and opportunities. J Magn Reson 229:155–172

Ward KM, Aletras AH, Balaban RS (2000a) A new class of contrast agents for MRI based on proton chemical exchange dependent saturation transfer (CEST). J Magn Reson 143:79–87

Ward KM, Balaban RS (2000b) Determination of pH using water protons and chemical exchange dependent saturation transfer (CEST). Magn Reson Med 44:799–802

Wielopolski PA, Adamis M, Prasad P, Gaa J, Edelman R (1995) Breath-hold 3D STAR MR angiography of the renal arteries using segmented echo planar imaging. Magn Reson Med 33:432–438

Yarnykh VL, Terashima M, Hayes CE, Shimakawa A, Takaya N, Nguyen PK, Brittain JH, McConnell MV, Yuan C (2006) Multicontrast black-blood MRI of carotid arteries: comparison between 1.5 and 3 tesla magnetic field strengths. J Magn Reson Imaging 23:691–698

Yi CA, Shin KM, Lee KS, Kim BT, Kim H, Kwon OJ, Choi JY, Chung MJ (2008) Non-small cell lung cancer staging: efficacy comparison of integrated PET/CT versus 3.0-T whole-body MR imaging. Radiology 248:632–642

Yi CA, Lee KS, Lee HY, Kim S, Kwon OJ, Kim H, Choi JY, Kim BT, Hwang HS, Shim YM (2013) Coregistered whole body magnetic resonance imaging-positron emission tomography (MRI-PET) versus PET-computed tomography plus brain MRI in staging resectable lung cancer: comparisons of clinical effectiveness in a randomized trial. Cancer 119:1784–1791

Yuan J, Chen S, King AD, Zhou J, Bhatia KS, Zhang Q, Yeung DK, Wei J, Mok GS, Wang YX (2014) Amide proton transfer-weighted imaging of the head and neck at 3 T: a feasibility study on healthy human subjects and patients with head and neck cancer. NMR Biomed 27:1239–1247

Yuan M, Zhang YD, Zhu C, Yu TF, Shi HB, Shi ZF, Li H, Wu JF (2016) Comparison of intravoxel incoherent motion diffusion-weighted MR imaging with dynamic contrast-enhanced MRI for differentiating lung cancer from benign solitary pulmonary lesions. J Magn Reson Imaging 43:669–679

Zhang S, Winter P, Wu K, Sherry AD (2001) A novel europium(III)-based MRI contrast agent. J Am Chem Soc 123:1517–1518

Zhang S, Trokowski R, Sherry AD (2003a) A paramagnetic CEST agent for imaging glucose by MRI. J Am Chem Soc 125:15288–15289

Zhang S, Merritt M, Woessner DE, Lenkinski RE, Sherry AD (2003b) PARACEST agents: modulating MRI contrast via water proton exchange. Acc Chem Res 36:783–790

Zhao X, Wen Z, Huang F, Lu S, Wang X, Hu S, Zu D, Zhou J (2011) Saturation power dependence of amide proton transfer image contrasts in human brain tumors and strokes at 3 T. Magn Reson Med 66:1033–1041

Zhou J, Payen JF, Wilson DA, Traystman RJ, van Zijl PC (2003a) Using the amide proton signals of intracellular proteins and peptides to detect pH effects in MRI. Nat Med 9:1085–1090

Zhou J, Lal B, Wilson DA, Laterra J, van Zijl PC (2003b) Amide proton transfer (APT) contrast for imaging of brain tumors. Magn Reson Med 50:1120–1126

Zhou J, van Zijl P (2006) Chemical exchange saturation transfer imaging and spectroscopy. Prog Nucl Magn Reson Spectrosc 48:109–136

Index